Transactions of the ASME®

Transactions of the ASME, Journal of Heat Transfer (ISSN 0022-1481) is published quarterly (Feb., May, Aug., Nov.) for $220.00 per year by The American Society of Mechanical Engineers, 345 East 47th Street, New York, NY 10017. Periodicals postage paid at New York, NY and additional mailing offices. POSTMASTER: Send address changes to Transactions of the ASME, Journal of Heat Transfer, c/o THE AMERICAN SOCIETY OF MECHANICAL ENGINEERS, 22 Law Drive, Box 2300, Fairfield, NJ 07007-2300.
CHANGES OF ADDRESS must be received at Society *headquarters seven weeks before they are* to be effective. Please send old label and new address. **PRICES:** To members, $40.00, annually: to nonmembers, $220.00. Add $40.00 for postage to countries outside the United States and Canada.

Journal of Heat Transfer

Published Quarterly by The American Society of Mechanical Engineers

VOLUME 120 • NUMBER 1 • FEBRUARY 1998

(Contents continued on Outside Back Cover)

This journal is printed on acid-free paper, which exceeds the ANSI Z39.48-1992 *specification for permanence of paper and library materials.* ♾™

♻ 85% recycled content, including 10% post-consumer fibers.

(Contents continued)

(Contents continued on Inside Back Cover)

(Contents continued)

TECHNICAL NOTES

DISCUSSION

ANNOUNCEMENTS

1996 Max Jakob Memorial Award Lecture

Transient Thermal Effects of Radiant Energy in Translucent Materials

R. Siegel
Research and Technology Directorate,
NASA Lewis Research Center,
Mail Stop 5-9,
21000 Brookpark Road,
Cleveland, OH 44135
robert.siegel@lerc.nasa.gov

When a solid or stationary fluid is translucent, energy can be transferred internally by radiation in addition to heat conduction. Since radiant propagation is very rapid, it can provide energy within a material more quickly than diffusion by heat conduction. Radiation emitted in a hot material can also be distributed rapidly in the interior. The result is that transient temperature responses including radiation can be significantly different from those by conduction alone. This is important for evaluating the thermal performance of translucent materials that are at elevated temperatures, are in high temperature surroundings, or are subjected to large incident radiation. Detailed transient solutions are necessary to examine heat transfer for forming and tempering of glass windows, evaluating ceramic components and thermal protection coatings, studying highly backscattering heat shields for atmospheric reentry, porous ceramic insulation systems, ignition and flame spread for translucent plastics, removal of ice layers, and other scientific and engineering applications involving heating and forming of optical materials. Radiation effects have been studied less for transients than for steady state because of the additional mathematical and computational complexities, but an appreciable literature has gradually developed. This paper will review the applications, types of conditions, and geometries that have been studied. Results from the literature are used to illustrate typical radiation effects on transient temperatures, and comparisons are made of transient measurements with numerical solutions.

Introduction

Within a translucent material, energy can be transferred by radiation in addition to heat conduction. The discussion here is primarily for solids, with some information for fluids without convection. Of interest is their transient thermal behavior when internal radiative effects are important. The behavior of translucent materials is influenced by their surroundings in which they can be heated internally by incident radiation, or they can be losing energy internally by radiation to a cooler environment. Convective heating or cooling can also be applied at the boundaries. Radiant effects are accentuated as temperatures rise; it can be the temperature of the material, the temperature of the surroundings, or both. Examples are heating a window by radiation emitted at high temperature from the sun, heating translucent plastic with infrared lamps to soften it for a manufacturing process, cooling a white hot ceramic by radiative loss to lower temperature surroundings, or heating an insulating shield during atmospheric reentry.

Since the interaction of a translucent material with radiation is a volume process, incident energy can be absorbed directly within the material similar to heating food in a microwave oven. During a transient, internal heating by radiation can be much more rapid than by having only conduction transfer energy into the interior. When a hot translucent body cools by radiation to lower temperature surroundings, energy loss can arise from within the body, and the interior can cool more rapidly than for conduction alone. Hence, for a translucent material, the nature of the radiative surroundings can act to provide a positive or negative internal heat source.

If the material is hot, there is also significant internal emission. Each part of the volume emits radiation, and this is transmitted to other locations within the material where it is partially absorbed. The ability to transfer to other locations depends on the transparency of the material. If it is not very transparent, radiation will pass only to nearby locations before being absorbed. It can then continue along its journey by being emitted again. Scattering can also occur along a radiation path; this redirects energy as a result of interactions of electromagnetic energy with local inhomogeneities such as grain boundaries. From the combination of these processes, radiation transports energy within the material and this acts along with heat conduction. For most materials, transparency depends on the radiation wavelength or frequency, so it is usually important to include spectral property variations. For example, glass obviously transmits visible radiation very well, but it is highly absorbing and hence poorly transmitting for radiation at longer infrared wavelengths.

Radiation effects on heat transfer transients have been studied less than for steady state, since time dependency adds another dimension of complexity. However, a significant literature has gradually developed over the last 40 years, and illustrative results are discussed here. Detailed time-accurate transient solutions are needed to examine heat transfer and thermal stresses for applications as in Table 1. One of the most evident is for the glass forming industry, and this is where the early transient studies were concentrated. To obtain strong windows for modern automobiles requires a detailed knowledge of the heat transfer behavior during cooling of glass plates. Glass or quartz envelopes for high intensity lamps, and production of optical fibers and components, are other applications. Some ceramic components for high temperature use, such as in advanced turbine engines, are somewhat translucent. This is also true of some thin ceramic thermal barrier coatings. Transient radiative

Contributed by the Heat Transfer Division for publication in the JOURNAL OF HEAT TRANSFER. Manuscript received by the Heat Transfer Division August 22, 1997; revision received November 3, 1997; Keywords: Heat Transfer; Participating Media; Radiation; Transient. Technical Editor: J. R. Howell.

Table 1 Applications involving transient response with internal radiative transfer

1. Processing and forming of tempered glass for automobile and plate glass windows.
2. Ceramic parts in aircraft and automotive engines.
3. Processing translucent plastics and ceramics at elevated temperatures or by infrared heating.
4. Highly backscattering protective insulation systems for reentry into the atmosphere.
5. Understanding flash experiments for obtaining properties of translucent materials.
6. Seals and envelopes for high-intensity lamps.
7. Ceramic thermal protection coatings for turbine engines.
8. Ignition and flame spread for translucent plastics and solid fuels.
9. Cooling performance of liquid-drop radiators in outer space.
10. Heating of lenses in solar concentrators and solar furnaces.
11. Heating of observation windows in laboratory metallurgical furnaces.
12. Interpretation of transient laser diagnostic methods for translucent materials.
13. Transient performance of fibrous insulation.
14. Manufacture of optical fibers and other optical components.
15. Cooling of high-temperature air in shock waves and after strong explosions.
16. Melting and removal of ice layers by solar or infrared heating.
17. Processing of multilayer semiconductors.

effects are important in heat shields for spacecraft during atmospheric reentry. Another application is for interpreting flash experiments for obtaining properties of translucent materials. Unknown transient temperature distributions must be determined that are spatially and time accurate. Since internal emission is large for many of the applications, small errors in temperature can be significant in the accuracy during transient calculations because of the strong temperature dependence of internal emission in the transient energy balance.

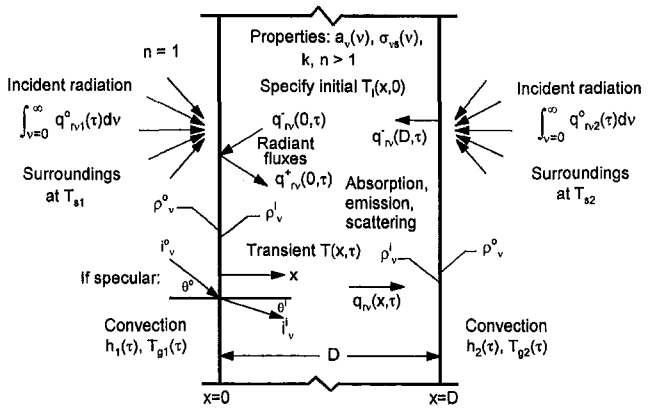

Fig. 1 Plane layer of translucent material with convection and incident radiation at its boundaries

Energy Relations and Boundary Conditions

With regard to theory and methods of analysis, the intent of this review is only to briefly provide some analytical relations to indicate some of the physical, mathematical, and numerical considerations. More detailed mathematical treatments are in textbooks such as Siegel and Howell (1992). Since the general radiative transfer relations become rather complex, the forms used here to illustrate the mathematical considerations are limited to one dimension as in Fig. 1. The relations are written in terms of frequency, which is a convenient spectral variable since it does not change when radiation travels across an interface into a material with a different refractive index. This avoids confusion when specifying spectral limits in materials with various refractive indices.

Nomenclature

a_ν, a_λ = spectral absorption coefficient, m^{-1}
B = height of a rectangle, m
c = specific heat of translucent material, J/kg·K
c_m = radiant propagation speed in a medium, m/s
D = thickness of plane layer; total thickness of a composite; width of a rectangle, m
D_1, D_2 = thicknesses of two layers in a composite, m
$e_{\nu b}$ = blackbody spectral energy for material with $n = 1$, W·s/m^2
E_1, E_2 = exponential integral functions
G = the flux quantity $2(q_r^+ + q_r^-)$, W/m^2
h_1, h_2 = convective heat transfer coefficients at $x = 0$ and D, W/m^2·K
i_ν = spectral radiant intensity, W·s/m^2·sr
I_ν = spectral radiative source function including scattering, W·s/m^2·sr
k = thermal conductivity, W/m·K
K_ν = spectral extinction coefficient, $a_\nu + \sigma_{s\nu}$, m^{-1}
N = conduction-radiation parameter
n = refractive index
q_r^+, q_r^- = diffuse radiative fluxes in the + and − x-directions, W/m^2
$q_{r\nu}$ = spectral radiative flux, W·s/m^2
q_{r1}^o, q_{r2}^o = external radiation fluxes incident at $x = 0$ and D, W/m^2
Q_{gen} = internal heat generation (chemical, electrical, nuclear), W/m^3
r_i, r_o = inner and outer radii of an annular region, m
S_r = internal radiant energy source, W/m^3
T = absolute temperature, K
T_{g1}, T_{g2} = gas temperatures for convection at $x = 0$ and D, K
T_i = initial temperature distribution, K
T_s = temperature of blackbody surroundings, K
x = coordinate in direction across plane layer, m; $X = x/D$
x, y, z = rectangular coordinate system, m

Greek Symbols

α_ν = spectral absorptivity
ϵ_ν = spectral emissivity
$\epsilon_{\nu t}$ = emittance of a translucent layer at uniform temperature
θ = angle measured from the x-direction, rad
λ = wavelength of radiation; λ_c cutoff wavelength, μm
ν = frequency of radiation, s^{-1}
ρ = density of translucent material, kg/m^3
ρ^o, ρ^i = external and internal reflectivities at a boundary
σ = Stefan-Boltzmann constant, W/m^2·K^4
$\sigma_{s\nu}$ = spectral scattering coefficient, m^{-1}
τ = time, s
Ω_ν = spectral scattering albedo, $\sigma_{s\nu}/(a_\nu + \sigma_{s\nu})$

Subscripts

m = in a medium; mean value
S, L = short and long wavelength regions
1, 2 = first and second layers; external environments at $x = 0$ and D

Superscripts

i, o = inside, outside
+, − = in the + and − coordinate directions

Energy Equation. The transient energy equation for a semitransparent solid has the same heat capacity and conductivity terms as in usual heat conduction analyses, but there is the addition of a radiative volumetric internal energy source term given by the last term on the right in Eq. (1),

$$\rho c \frac{\partial T(x,\tau)}{\partial \tau} = \frac{\partial}{\partial x}\left[k(T)\frac{\partial T(x,\tau)}{\partial x}\right] + Q_{\text{gen}}(x,\tau) + \int_{\nu=0}^{\infty} S_{r\nu}(x,\tau)d\nu. \quad (1)$$

The spectral radiative energy source, $S_{r\nu}(x, \tau)$, arises from absorption, emission, and scattering processes. The source must be evaluated as a function of frequency and integrated over all frequencies to obtain the total radiative energy needed for the energy balance. The energy equation also contains an internal heat generation term, $Q_{\text{gen}}(x, \tau)$, from chemical, electrical, or nuclear energy.

Radiative Internal Energy Source Relations. To solve the energy equation, the radiative internal energy source must be related to the instantaneous temperature distribution. Scattering is very important for some applications such as crystalline ceramics and backscattering heat shields. For the special case of isotropic scattering in a material with refractive index n, the spectral radiative energy source is

$$S_{r\nu}(x,\tau)d\nu = -4\frac{a_\nu}{\Omega_\nu}[n^2 e_{\nu b}(x,\tau)d\nu - \pi I_\nu(x,\tau)d\nu], \quad (2a)$$

where $e_{\nu b}(x, \tau)d\nu$ is the spectral emission from a blackbody in vacuum, and is a function of the local instantaneous temperature in the material. The source function $I_\nu(x, \tau)$ on the right side of Eq. (2a) includes effects of local emission, absorption, and scattering. It is governed by an integral equation, and for simplicity is given here for diffuse boundaries,

$$I_\nu(x,\tau)d\nu = \frac{a_\nu}{K_\nu}\frac{n^2 e_{\nu b}(x,\tau)d\nu}{\pi} + \frac{\sigma_{s\nu}}{2K_\nu}\left[\frac{q^+_{r\nu}(0,\tau)d\nu}{\pi}E_2(K_\nu x) + \frac{q^-_{r\nu}(D,\tau)d\nu}{\pi}E_2[K_\nu(D-x)] + K_\nu\int_{x^*=0}^{D} I_\nu(x^*,\tau)d\nu E_1(K_\nu|x^*-x|)dx^*\right]. \quad (2b)$$

The K_ν is the extinction coefficient that includes both absorption and scattering. During a transient, Eq. (2b) must be solved by numerical iteration at each time step as a function of frequency. For simplicity, the spectral absorption and scattering coefficients, a_ν and $\sigma_{s\nu}$, are independent of x; an optical coordinate can be used to include property variations as described in Siegel and Howell (1992). The terms on the right side of $I_\nu(x, \tau)$ result from local internal emission, energy leaving the boundaries at $x = 0(q^+_{r\nu}(0, \tau)d\nu)$ and $x = D(q^-_{r\nu}(D, \tau)d\nu)$ that reaches and interacts with the material at x, and the effect that the source function $I_\nu(x^*, \tau)$ at all x^* has on the source function $I_\nu(x, \tau)$ at x. The exponential integral functions E_1 and E_2, specify attenuation within the layer. The diffuse spectral fluxes at the boundaries, $q^+_{r\nu}(0, \tau)d\nu$ and $q^-_{r\nu}(D, \tau)d\nu$, are obtained from the radiative boundary conditions as will be discussed.

Without scattering, the radiative source in a plane layer, for the special case of diffuse boundaries, is

$$S_{r\nu}(x,\tau)d\nu = -4a_\nu n^2 e_{\nu b}(x,\tau)d\nu + 2a_\nu\left[q^+_{r\nu}(0,\tau)d\nu E_2(a_\nu x) + q^-_{r\nu}(D,\tau)d\nu E_2[a_\nu(D-x)] + a_\nu\int_{x^*=0}^{D} n^2 e_{\nu b}(x^*,\tau)d\nu E_1(a_\nu|x^*-x|)dx^*\right]. \quad (3)$$

If Eq. (3) is substituted into Eq. (1), the result is an integrodifferential equation for $T(x, \tau)$, where $T(x, \tau)$ is also in the blackbody function $e_{\nu b}(x, \tau)$.

In the derivations of Eqs. (2) and (3), the radiant intensity i_ν is considered along paths in the material; the i_ν is the spectral energy along a path passing through an area per unit solid angle and per unit projected area normal to the path. As pointed out in Siegel and Howell (1992), in the equation for the propagation of i_ν along a path, there is a transient term $(1/c_m)(\partial i_\nu/\partial\tau)$ in the transfer equation, where c_m is the radiant propagation speed in the medium. This term has not been included in the derivations of Eqs. (2) and (3). The c_m is so large that the local storage of radiative energy is usually much smaller than the energy storage in the semitransparent material that depends on its heat capacity; hence, the $(1/c_m)(\partial i_\nu/\partial\tau)$ can usually be neglected. As discussed in Kumar and Mitra (1995), this term may be significant when interpreting diagnostics using the propagation of extremely short laser pulses within absorbing and scattering materials. It has been included by Longtin and Tien (1997) for investigating laser heating of liquids.

Two-Flux Relations for the Radiative Source. As a simplification to using the exact radiative transfer relations, as in Eqs. (2) and (3), to obtain the radiative internal energy source $S_{r\nu}(x, \tau)d\nu$, approximate techniques have been used. The methods are the same as for steady-state calculations, and they include multi-flux formulations, radiative diffusion, and spherical harmonic expansions. For example, the two-flux method was found to provide accurate results for transient calculations in plane layers with diffuse boundaries, Siegel (1995a, 1996a). The two-flux relations have the advantage that they include scattering without needing an additional scattering equation such as Eq. (2b) that is time consuming to evaluate. Isotropic scattering is in the basic two-flux equations, and modified forms include nonisotropic scattering as in Cornelison and Howe (1992). By assuming the flux distribution is isotropic in each of the $+x$ and $-x$ directions, the two-flux relation for the heat source term is (the Milne-Eddington approximation),

$$S_{r\nu}(x,\tau) = -a_\nu[4n^2 e_{\nu b}(x,\tau) - G_\nu(x,\tau)]. \quad (4)$$

The $G_\nu(x, \tau)$ is a radiative flux function that is found at each time as a function of location, from the following second order differential equation,

$$\frac{\partial^2 G_\nu(x,\tau)}{\partial^2 x} - 3(a_\nu+\sigma_{s\nu})a_\nu G_\nu(x,\tau) = -4(a_\nu+\sigma_{s\nu})a_\nu n^2 e_{\nu b}(x,\tau). \quad (5)$$

Since the local blackbody function $e_{\nu b}(x, \tau)$ depends on the local instantaneous temperature, Eqs. (4) and (5) are coupled with the energy equation, Eq. (1).

Two Sets of Boundary Conditions. As is usual for transient solutions, an initial temperature distribution must be specified. With radiation included, two sets of boundary conditions are necessary. One set has the requirements for conventional heat conduction solutions of the transient energy equation that the interaction of external convection is related to internal conduction at the boundaries, and that both temperature and conduction heat flux are continuous at internal interfaces of a composite. The second set of boundary conditions is for radiative

fluxes that are reflected and transmitted at each boundary: this provides the $q^+_{r\nu}(0, \tau)$ and $q^-_{r\nu}(D, \tau)$ needed for Eqs. (2*b*) and (3), that are radiative fluxes inside the material leaving the boundaries, Fig. 1. For composites, these boundary conditions also include radiative relations across internal interfaces.

As radiation passes through a semitransparent boundary, energy is not absorbed exactly at the boundary plane because the boundary itself has no volume for absorption. Hence, if there are no spectral regions in which the material is assumed opaque, the boundary condition for Eq. (1) connecting external convection with internal conduction is the same as without radiation. For example, at $x = 0$ in Fig. 1,

$$-\left[k(T)\frac{\partial T(x,\tau)}{\partial x}\right]_{x=0} = h_1(\tau)[T_{g1}(\tau) - T(x=0,\tau)]. \quad (6)$$

When there are highly absorbing spectral regions in which the semitransparent material can be considered opaque, there is radiative exchange at the surface in the opaque regions that combines with the convection and conduction. If there is an externally incident spectral radiative flux distribution, $q^o_{r\nu 1}(\tau)d\nu$, and the surface is in surroundings with refractive index $n = 1$, this gives the boundary condition for the energy equation, Eq. (1), as

$$-\left[k(T)\frac{\partial T(x,\tau)}{\partial x}\right]_{x=0} = h_1(\tau)[T_{g1}(\tau) - T(0,\tau)] + \int_{\text{opaque }\nu\text{ regions}} [\alpha_\nu q^o_{r\nu 1}(\tau) - \epsilon_\nu e_{\nu b}(0,\tau)]d\nu, \quad (7)$$

where radiative absorption and emission at the surface has been included for the opaque regions.

The radiative boundary conditions for the partially transparent spectral regions (the spectral regions that are not included in Eq. (7)) are used in the calculation of the radiative internal heat source distributions $S_{r\nu}(x, \tau)$ in Eq. (1). These conditions depend on the surface reflection and transmission behavior. They can be complicated by a change in refractive index across an interface that produces reflections, changes the direction of transmitted rays, and can provide total internal reflection for part of the energy at an interface. For specular behavior at an optically smooth interface such as the surface of a glass window, the magnitudes of the reflected and transmitted radiative intensities are provided by the Fresnel optical equations, and they depend on the refractive indices on the two sides of the interface (Siegel and Howell, 1992). A rough interface may partly diffuse the transmitted energy in a manner that is difficult to define quantitatively, and the diffuse assumption is often made. For an interface that is diffuse for both reflected and transmitted energy, the diffuse flux inside the material leaving the boundary is the sum of reflected and transmitted fluxes. This gives at $x = 0$ in Fig. 1,

$$q^+_{r\nu}(0,\tau) = (1 - \rho^o_\nu)q^o_{r\nu 1}(\tau) + \rho^i_\nu q^-_{r\nu}(0,\tau). \quad (8)$$

When specifying the surface reflectivities for Eq. (8), it is important to include the behavior for radiation crossing an interface from a medium of higher to one of lower refractive index; the behavior is that some of the radiation arrives at the interface at angles larger than the critical angle for total reflection. Hence, an appreciable energy fraction approaching a boundary may be totally internally reflected. This compensates for the spectral emission within a solid having a maximum of $n^2 e_{\nu b}d\nu$, while spectral radiation exiting into a vacuum cannot exceed blackbody radiation, $e_{\nu b}d\nu$. At elevated temperatures, total internal reflection can be quite significant in ceramics where refractive indices are usually in the range 1.5–2.5. Total internal reflections must be included in the relations for radiation crossing an interface into a material with a smaller refractive index.

Specification of Properties Needed for Calculations

As for transient heat conduction calculations, the specific heat, density, and thermal conductivity must be specified, and they may need to be a function of temperature depending on the material and temperature range. For a translucent material, the thermal conductivity must have been determined to not include any contribution from radiant transmission. For the radiative source, the absorption and scattering coefficients must be specified as a function of frequency, and they may depend on temperature. For many translucent materials other than perhaps glass and some optical window materials, these properties are not known very well, and values may not be available at elevated temperatures. If the material is nonhomogeneous, granular, or porous, the angular behavior of its internal scattering may be difficult to determine with good accuracy. The reflection properties at surfaces must be specified, which include the fraction reflected, and how reflection varies with the angle of incidence. The angular nature of the transmitted energy may be important in some instances. The reflection and transmission behavior depends on the refractive indices of the materials on either side of the interface and on the texture of the interface that is often difficult to quantify. As a result, it may be difficult to specify the reflection and transmission properties with confidence. The refractive index is known for many optical materials, but may not be known accurately for some translucent ceramics. The refractive index is also important for internal emission in hot materials, as its square is in the emission term. Many assumptions are often necessary before a calculation can be performed.

Numerical Methods for Transient Solutions

The preceding relations briefly illustrate the equations used to model transient heat transfer including radiation. Having described the nature of the equations, boundary conditions, and properties required, the solution methods are discussed. The transient energy equation including a radiative internal energy source must be solved using the boundary conditions relating external convection and internal conduction.

When solving the energy equation, the radiative source must be calculated at all locations for each time, and it becomes more difficult and/or time consuming to evaluate if the geometry is two or three-dimensional. Including scattering and spectrally dependent properties provide additional complexity. The radiative source must be evaluated from relations such as Eqs. (2) or (3) in each spectral region where there is significant radiant energy. The radiative boundary relations such as Eq. (8) are included in the source evaluation to provide the radiative fluxes at the boundaries. Some of the methods used for source evaluation are direct numerical integration (Siegel, 1996b), integration of the two-flux equations (Matthews et al., 1985; Cornelison and Howe, 1992; Siegel, 1995a, 1996a), various expansion methods (Lii and Özişik, 1972; Frankel, 1995), the differential approximation (Wu and Ou, 1994), discrete ordinates (Su, 1995; Gorthala et al., 1994), radiative diffusion (Petrov, 1997), and Monte Carlo (Derevyanko and Koltun, 1991). These are the same as for steady-state calculations, and are described in textbooks such as Siegel and Howell (1992), and in the references cited here.

For solving the time-dependent energy equation, many transient analyses have used some type of time-marching finite-difference procedure. To start the calculations, a common procedure is to use the specified initial temperature distribution to evaluate the radiative source. Then the energy equation is solved with that source to move ahead one time increment. The new temperature distribution is used to reevaluate the source, and the energy equation then solved for the next time increment. Hence, the temperatures are being extrapolated forward by using a source evaluated with the current temperatures. With this procedure, the temperature distribution is known to evaluate the

Table 2 Types of solutions that have been obtained (with a few typical references)

I. *Single plane layers.*
   1. Glass plates with and without surface coatings (Heping and Lallemand (1989)).
   2. Layers with specified boundary temperatures (Schwander et al. (1990)).
   3. Layers with convection and incident radiation at boundaries (Field and Viskanta (1993), Fowle et al. (1969)).
   4. Surface subjected to a radiation pulse—flash method (Andre and Degiovanni (1995), Heping et al. (1991)).
   5. High-temperature insulating layer with scattering (Cornelison and Howe (1992), Matthews et al. (1985), Petrov (1997)).
   6. Heating of translucent plastics (Manohar et al. (1995)).
   7. Convective heating with internal radiation to cool surroundings (Siegel (1995a)).
   8. Liquid-drop radiators for energy dissipation in space (Siegel (1987a)).

II. Composites of multiple plane layers with interface reflections (Timoshenko and Trener (1986), Siegel (1996c, d), Song and Viskanta (1990)).

III. Semi-infinite regions with a plane boundary (Heinisch and Viskanta (1968), Kubo and Hayashiguchi (1981)).

IV. One-dimensional cylinders and concentric cylindrical regions (Siegel (1989a), Fernandes and Francis (1982), Gordaninejad and Francis (1984)).

V. Spheres and concentric spherical regions (Tsai and Özişik (1987), Chu and Weng (1992)).

VI. Highly backscattering spherical heat shields for atmospheric reentry (Cornelison and Howe (1992)).

VII. Two-dimensional square and rectangular regions (Siegel and Molls (1992), Wu and Ou (1994)).

VIII. Regions undergoing phase change (Habib (1971), Seki et al. (1978)).

source. This is especially convenient when dealing with spectral regions to account for spectral property variations since the blackbody energy in the spectral region can be evaluated from the known temperature distribution.

The numerical solution of the energy equation in its simplest form can be explicit, but this presents the difficulty that small time increments are necessary for stability. The spatial increments may need to be especially small in certain regions with large temperature gradients, and this requires using even smaller time increments; the calculations then become long and possibly inaccurate. It is usually better to use an implicit method to march the energy equation ahead. For one-dimensional geometries, this requires the solution of a tridiagonal matrix to simultaneously solve for the temperatures at the next time. Although implicit methods are often thought to be stable for arbitrary time increments, this only applies for simple situations. When using the nonlinear radiative transfer equations with the energy equation, it is usually necessary for stability to limit the time increment size. An approach to improve stability is to make the solution fully implicit without any time lag for evaluating the radiative source term. This has been done in a few instances, and adds considerable complexity (Siegel, 1996b). Even then, the solutions have not been found stable if large time increments are used in an effort to reduce the number of radiative source evaluations during the transient. In addition to stability, it is necessary to provide enough spatial and temporal increments so the solutions will be numerically accurate.

Summary of Geometries and Applications That Have Been Analyzed

The review that follows provides an overview of investigations and typical results for transient effects of radiation in translucent materials. Transient results have been obtained for various applications, geometries, and boundary conditions, as summarized in Table 2. The largest number of results are for single plane layers that includes glass plates, plastics, and ceramics. Boundary temperatures can be specified, or, more generally, the translucent material is subjected to convection and/or external radiation so that the boundary temperatures are obtained during the solution. There are some results available for composites of multiple plane layers. A limited number of transient solutions have been obtained for long cylinders and concentric cylindrical layers, and for spheres and concentric spherical layers. A few transient studies are available for two-dimensional rectangles. Both gray and spectral results have been obtained, especially for plane layers. Spectral properties are included for materials like glass where the transparency varies considerably with frequency. Both diffuse and specular boundaries have been examined for some geometries.

Transient Predictions and Measurements for Plane Layers

In view of the assumptions in analytical modeling and the uncertainties in specifying properties, experimental verification is very important if possible. Additional measurements are needed for both transient and steady conditions. A small number of the transient analyses have been made in conjunction with radiation experiments, and comparisons are shown here of the transient measurements with calculated values.

Heating and Cooling of Glass Plates.

Analytical Investigations. Radiation plays an important role in the glass forming industry, as in the fabrication of curved and tempered glass automobile windows. The heat transfer behavior must be understood to perfect annealing and quenching procedures. Some of the earliest conduction-radiation analyses for transient conditions were for understanding the heat treatment of glass plates (Gardon, 1958). An analysis for transient temperatures in spacecraft windows during atmospheric reentry conditions was performed by Fowle et al. (1969) using similar methods. Computational techniques have continued to be developed for important design applications in the glass industry. Results are in the literature for a variety of thermal conditions that include both external radiation and convection, with and without surface coatings.

Transient calculations for glass plates were made by Heping and Lallemand (1989) to investigate internal radiation effects for various boundary conditions. Several spectral bands were included to account for the glass absorption properties, and a nodal analysis was used based on the zonal radiative calculation method. A variety of conditions were considered to better understand heat transfer processes that can be used by the glass industry. The results in Figs. 2(a) and 2(b) demonstrate the effect on cooling a glass plate of putting coatings on its boundaries so they are opaque and do not allow radiant transmission. This was part of a study to determine how coatings can be used to regulate heat transfer processes in manufacturing with translucent materials. The initial temperature distribution was uniform in the hot glass so the dimensionless temperatures start at 1. Equal convective cooling was then provided at both surfaces. The solid lines are predicted temperatures when both internal radiation and conduction are included. These results are compared with the dot-dashed lines for internal heat conduction only. The conduction-radiation parameter, $N = k/4Dn^2\sigma T_i^3$, is an attempt to characterize the relative importance of conduction and radiation. In Fig. 2(a), the $N = 0.05$ is small enough that there is a significant effect of internal radiation that makes the temperatures more uniform during transient cooling. The layer also cools more rapidly with combined radiation and conduc-

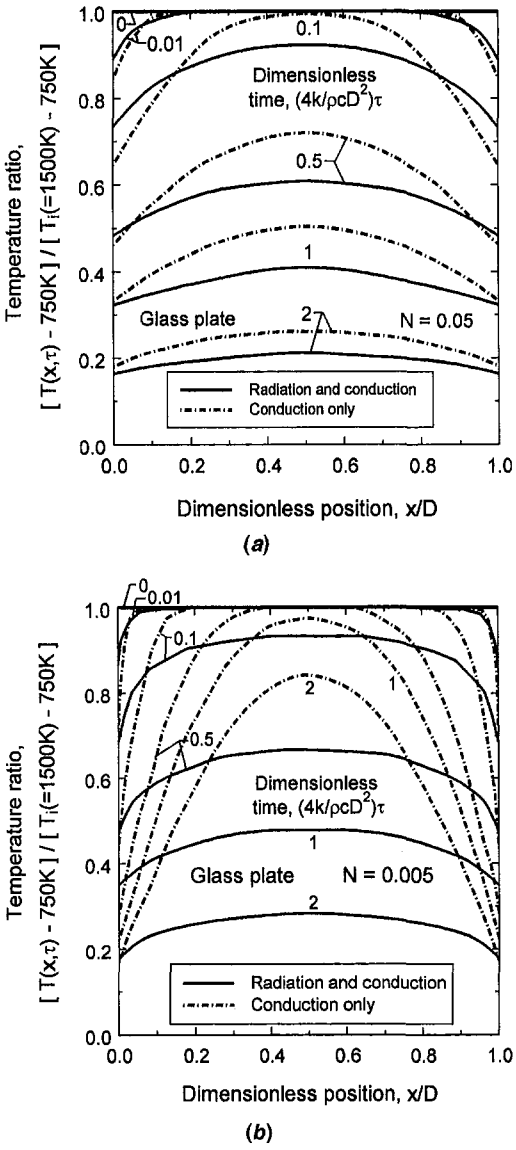

Fig. 2 Transient temperature distributions for cooling a glass plate, showing comparison of combined radiation-conduction analysis with that for conduction only, $T_{s1} = T_{s2} = 1500$ K, $h_1D/k = h_2D/k = 0.1$ (replotted from Heping and Lallemand, 1989): (*a*) conduction-radiation parameter, $N = k/4Dn^2\sigma T_i^3 = 0.05$ and (*b*) conduction-radiation parameter, $N = k/4Dn^2\sigma T_i^3 = 0.005$

tion. In Fig. 2(*b*), the conduction-radiation parameter is decreased to $N = 0.005$, therefore there is less effect of conduction, and the glass cools somewhat more slowly. Internal radiation makes the temperatures much more uniform than for conduction alone. These results illustrate both the importance of internal radiation and the detailed and accurate transient temperatures that are needed to quantify combined radiation and conduction effects for manufacturing processes.

The effects of the thermal conditions at the boundaries of a translucent layer were also investigated by Schwander et al. (1990) for a gray layer and for molten glass with four spectral bands. The gray layer was between two parallel opaque walls at temperatures T_1 and T_2, and three conditions were considered: (1) direct contact with the walls with heat conduction across both layer boundaries, (2) direct contact at only one side, and (3) no contact with either of the opaque walls. Diffuse and specular surface reflections were both considered, and the layer temperature was initially uniform at T_2. A parameter of importance is the optical thickness of the layer that characterizes its ability to attenuate radiation along a path by absorption and scattering. The radiation undergoes an exponential attenuation according to the optical thickness of the path length. When the translucent layer analyzed here was in direct contact with both walls, the directional nature of the surface reflections had little effect on the transient temperature distributions. When there was no contact of a layer boundary with one or both opaque walls, the type of surface reflections affected the temperature distributions when the optical thickness of the glass plate was small, such as 0.2. As the optical thickness of the layer increased, the boundary characteristics had less influence in the interior. For an optical thickness of 1, only a small effect of the type of surface reflections was found on temperature distributions, and the effect became very small when the optical thickness increased to 5. The same conclusions were found for a molten glass layer. This helps to define the conditions where it is necessary to be concerned with the details of the directional reflection and transmission at the boundaries of a semitransparent layer. The directional behavior is difficult to define for moderately rough surfaces.

In the analysis by Su and Sutton (1995) for transient heating of a window, one boundary was heated for 5 seconds by convection in high-speed flow. For convective heating by a nonradiating gas, the highest transient temperatures were at the heated boundary, not within the glass interior. The increase in surface temperature is of interest to predict when the glass will start to soften, and, hence, when its optical characteristics may begin to be distorted.

The transient analysis for glass by Su (1995) is for the early part of a transient following the sudden application of a large external radiative flux. The discrete ordinate method was used to compute the radiative source distribution, but the formulation is only briefly described.

Comparisons With Measurements for Cooling a Glass Window. Experimental results for cooling a window are in Fig. 3 from Field and Viskanta (1993). A glass plate was heated to a temperature near its softening point, a little over 500°C. It was then exposed on the front side to the ambient room to cool by convection and radiation, and on the back side to convection and a radiant heater. Three thermocouples were used on each test plate, and they were carefully installed to minimize, as much as possible, disturbing the radiative transfer, especially for transient conditions. To avoid the use of bonding materials such as ceramic cements, the thermocouples were fused into the glass by placing them in 0.25 mm grooves and heating to 650°C in a helium atmosphere. One thermocouple was fused into each surface, and the third molded into the window at its center plane by fusing it between two layers of glass.

The measurements showed that internal radiation effects are very significant during transient cooling, as predicted by calculations using five translucent spectral bands in the wavelength range 0–5 μm and the glass opaque at larger wavelengths. This is demonstrated in Fig. 3(*a*) where temperatures measured at the front surface of a 11.68 mm thick window are compared with predictions when radiation has either been included or omitted in the analysis. With radiation omitted (dot-dashed curve) the calculations are very far from the data. In contrast, the solid curve shows very good agreement when radiation is included in the analysis.

From the same study, Fig. 3(*b*) shows the difference in transient temperatures between the center plane and the front surface of the window for three different window thicknesses. This temperature difference is relatively small throughout the cooling process and, as expected, increases with window thickness. The predicted temperature difference is greater than measured, and the deviation increases with thickness. The differences between analysis and measurements are attributed by the authors to uncertainty in the thermophysical properties of glass, most likely the thermal conductivity, since the temperature difference pre-

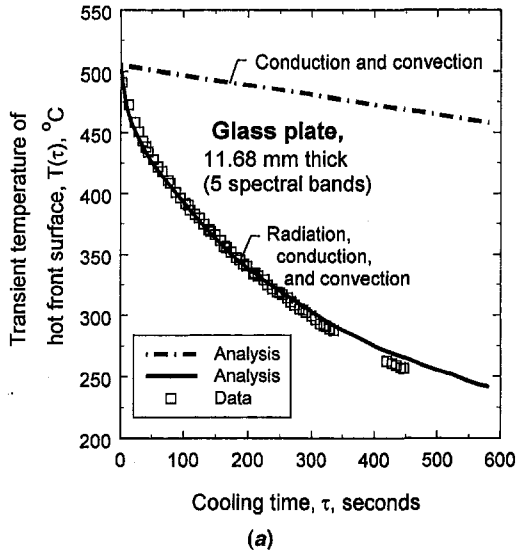

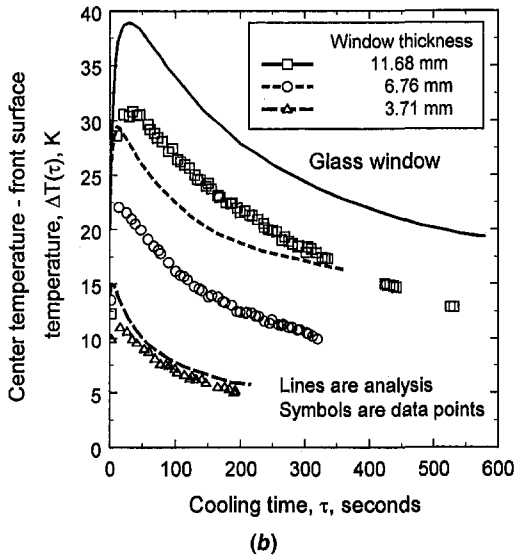

Fig. 3 Comparisons of measurements and calculations for cooling a glass window from near its melting temperature (replotted from Field and Viskanta, 1993): (*a*) temperatures at front surface of window 11.68 mm thick and (*b*) temperature difference between center plane and front surface for three window thicknesses

dictions are sensitive to this property. Further discussion on this is in Mann et al. (1992). The radiative analysis and computation techniques appear capable of providing good predictions if the properties are known accurately.

Comparisons With Measurements for Transient Heating of Glass. Measurements and calculations were made by Rubtsov et al. (1978) for a glass plate subjected to heating by external radiation suddenly applied at one side. The data were taken with 0.05 mm diameter platinum-platinum rhodium thermocouples that were sealed into the glass at different depths. The small thermocouple size was used to disturb local radiation and conduction as little as possible. The results for window glass are in Fig. 4 for a window 12.37 mm thick that was mounted on a cooled support and irradiated by an external source at 1017 K. The data are compared with calculations (solid lines) that used detailed spectral properties for window glass. Comparisons with measured transient surface temperatures for quartz and alumosilicate glass are also included from Fowle et al. (1969) (dashed and dot-dashed lines), where measurements were taken with narrow thin-film gold resistance ther-

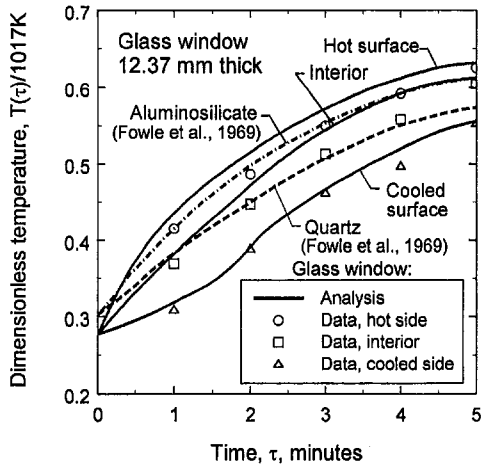

Fig. 4 Comparisons of measurements for sudden radiative heating at one side of a plane layer of glass 12.37 mm thick (from Rubtsov et al., 1978)

mometers coated on the glass surfaces. The gold strip width was small in order to minimize obstruction of radiation by the strip. The data from Rubtsov et al. (1978) agree reasonably well with the calculations; the curves are for temperatures at both surfaces and for one internal location. Only qualitative comparisons can be made with the data from Fowle et al. (1969) taken for similar conditions at the hot surface of two windows, but the general heating response is comparable.

Heating a Quartz Window.

Analysis for Heating a Spacecraft Window. Another example of transient thermal behavior for a window is in Fig. 5, that shows a simulated heating of a spacecraft fused silica windshield during reentry in the terrestrial atmosphere (Heping and Lallemand, 1989). Heating is on the boundary $x = D$, and is by convection and radiation by gas assumed to be a blackbody at 1200 K. The windshield, initially at 311 K, is 3 cm thick and its radiation properties were modeled with six spectral absorption bands. The variation was included of the quartz refractive index as a function of frequency; this affects both internal emission that depends on n^2 and surface reflectivities. The dot-

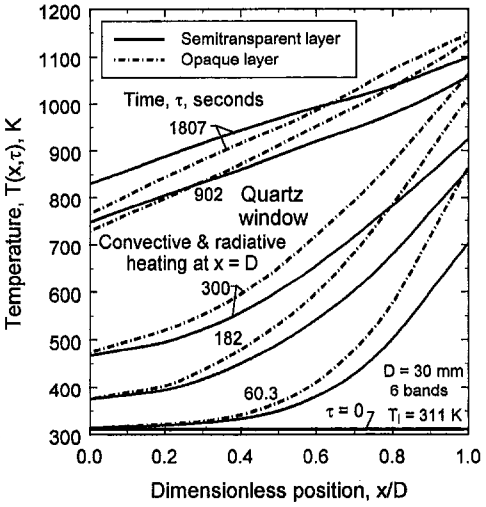

Fig. 5 Transient temperature distributions for heating a quartz window (at $x/D = 1$) during atmospheric reentry, showing comparison of analyses for semitransparent and opaque layers. Temperature of the flow = $T_{g2} = T_{s2} = 1200$ K, $h_1 = 10$ W/m^2·K, $h_2 = 100$ W/m^2·K (replotted from Heping and Lallemand, 1989)

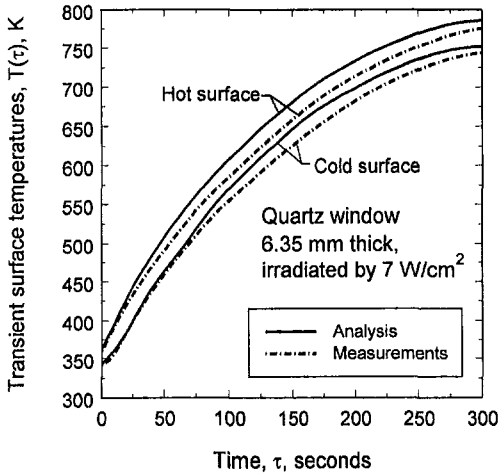

Fig. 6 Comparisons of measurements and calculations for transient surface temperatures of a quartz window after exposure to a radiation source at 1308 K on one side (replotted from Fowle et al., 1969)

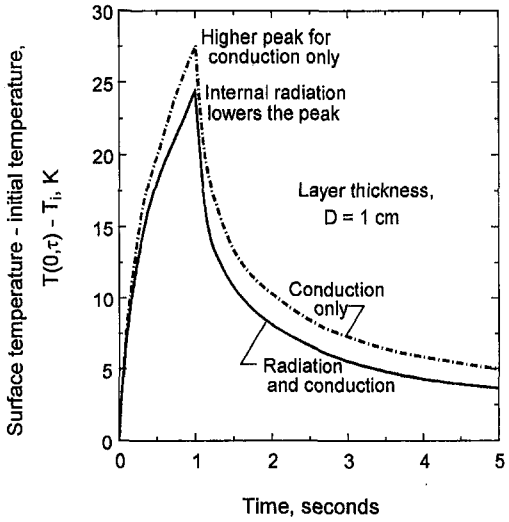

Fig. 7 Effect of internal radiative transport on the transient surface temperature of a glass plate exposed to a radiation pulse of 50 kW/m² at normal incidence for 1 s; the glass boundaries are opacified (replotted from Heping et al., 1991)

dashed lines are for an opaque layer where internally there is only conduction, but there is radiation exchange at its boundaries. For the solid lines, the layer is semitransparent; this causes the temperature of the heated boundary to increase less rapidly. Internal radiation acts somewhat like enhanced heat conduction so the temperature gradients are reduced. Internal reflections also tend to equalize the transient temperatures by providing multiple passes of radiation within the material that produce a more uniform distribution of absorbed internal energy. Hence, internal radiation produces somewhat more uniform temperatures during the transient heating process.

Comparisons With Measurements for Heating a Quartz Window. The results in Fig. 6 from Fowle et al. (1969) are for a quartz window with conditions that simulate heating a spacecraft window during atmospheric reentry. The window was exposed to radiation on one side from a high temperature source, and transient temperatures of the window surfaces were measured. For the results shown, a quartz window 6.35 mm thick in vacuum was suddenly placed in front of a blackbody source and kept there for 300 seconds. The source temperature was 1308 K, which specifies the incident spectral distribution, and the window received a radiative flux of about 7 W/cm^2. Very narrow gold thin-film resistance grids were used to measure the window surface temperatures. Results were compared with a numerical simulation for one-dimensional heat flow with diffuse incident radiation. Data on refractive index, density, and thermal conductivity and specific heat as a function of temperature were taken from technical publications of the manufacturer of the quartz sample. The spectral absorption coefficient was deduced from transmission data of the manufacturer. Reasonably good agreement was obtained for all of the tests, with the accuracy of the predicted results being within 5 percent or less, relative to the absolute temperatures. With few exceptions, the measured temperatures for the entire series of tests were lower than the predicted values. It was thought that this might be the result of deviations from one-dimensional heat flow caused by the finite size of the blackbody source.

Transient Response of a Translucent Solid to a Pulse or Step in External Radiation.

Analyses for Transient Response. The effect of a pulse or a step in radiation incident on a translucent layer has been analyzed by Andre and Degiovanni (1995), Heping et al. (1991), Darby (1983), and Saito et al. (1976). An application of the response to an energy pulse is for the flash heating method to measure the thermal diffusivity of materials. In this method, the front side of a sample is irradiated by a short laser pulse, and the temperature response is measured at the back side. Since the thermal diffusivity is deduced from the back-side response, it is desirable to have high energy absorption at the front to provide a significant response; hence, the front side is often coated with a strongly absorbing material. For a semitransparent layer, radiative transfer from the front to the back surface is avoided as much as possible by first coating the boundaries with a highly reflecting material such as gold, and then applying the absorbing coating. Although direct radiation between the surfaces can be made small, there still may be radiative transport within the material if it is at an elevated temperature. This makes the interpretation of flash heating data much more difficult than for an opaque material, especially when the translucent material scatters radiation (Hahn et al., 1997). For the results in Fig. 7 (Heping et al., 1991), three spectral bands were used with properties similar to glass. The transient response of the surface temperature is shown for heating by a square-wave radiative pulse for 1 second at normal incidence. For these results, both boundaries of the translucent layer have an opaque coating as used for the flash heating method, but semitransparent boundaries were also considered. The solid line is for radiation and conduction in the material, and the dot-dashed curve is for conduction only. There is a higher surface temperature peak for conduction only, than there is for a translucent material where energy transfer is augmented by radiative transfer.

The flash experiments of Andre and Degiovanni (1995) were interpreted by using a transient analysis including radiation and conduction, where a Crank-Nicholson method was used for extrapolation forward in time. For the experiments, a frosted (diffuse surfaces) glass sample was either coated with gold (highly reflecting), or was sprayed with black paint (highly absorbing). It was found that by using highly reflecting boundaries and a layer with a small optical thickness, internal radiative effects were small, and the flash technique provided a direct measurement of the thermal diffusivity of glass in the same way as for an opaque material. This was for a temperature range of about 400 K to 800 K.

The penetration of radiation is also of interest for the ignition of solid fuels. The analysis of Park and Tien (1990) includes radiation in the pyrolyzed absorbing gas that is formed, and the in-depth absorption of incident radiation by the solid fuel. Natural convection at the fuel boundary was shown to retard ignition. The importance of in-depth radiative absorption on the ignition

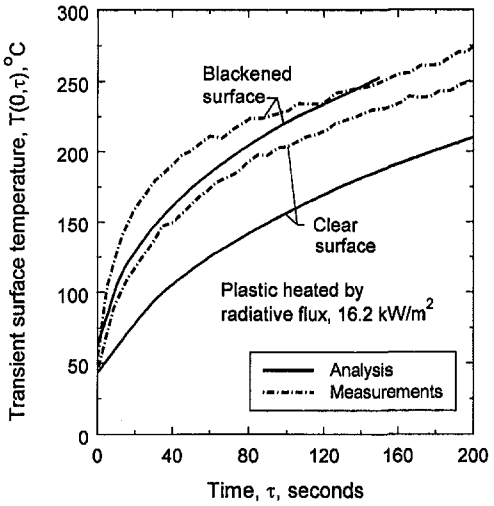

Fig. 8 Comparisons of measurements and calculations for temperature response of translucent plastic following a suddenly applied incident radiation flux of 16.2 kW/m² on one surface (replotted from Manohar et al., 1995)

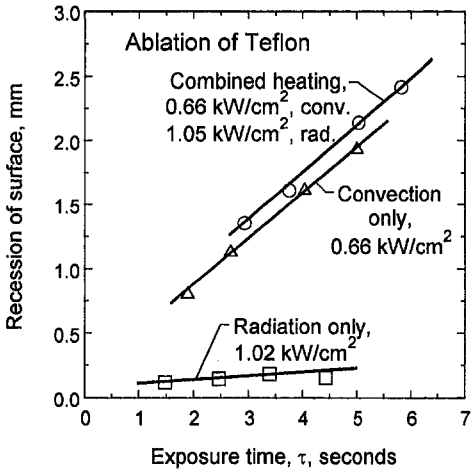

Fig. 9 Effect of radiative backscattering on reducing the ablation of Teflon (from Howe et al., 1973)

of solid fuel has also been shown by the ignition model of Kashwagi (1974) and by Kindelan and Williams (1977).

Comparison With Measurements for Penetration of External Radiative Heating. The study in Manohar et al. (1995) was to investigate the spreading of a flame with regard to the ignition of translucent plastic where radiation plays a significant role. An important feature is the transient penetration of radiation from an external source into the translucent plastic. During flame spread along a surface, radiation emitted by the high-temperature combustion products contributes to the process by which the flame advances. Radiative penetration into the plastic polymethylmethacrylate (PMMA) was computed numerically using properties specified by fourteen bands, and it was compared with measurements. Two cases were considered for differing surface conditions: the surface is clear for radiant transmission, or the surface is covered with soot from adjacent combustion. When the surface is soot covered, most of the incident external radiation is absorbed by the soot that radiates some of the energy into the semitransparent plastic. This produced a much smaller internal radiation effect than for a clear surface where radiation could enter directly. In the experiments, transient surface temperatures were measured for a PMMA layer subjected to a large radiation flux of 16.2 kW/m^2. Thermocouples 100 μm in diameter were used embedded in surface grooves and covered with a thin PMMA layer. A temperature measurement error estimate was made considering the size of the thermocouple, uncertainty in its location in a region with a significant temperature gradient, and the difference in emissivities of the thermocouple and the PMMA surface. The estimated error was ± 5 to 25 K. Comparisons of computed and measured transient surface temperatures for clear and blackened surfaces of the plastic are in Fig. 8. The surface temperature increases more rapidly when the surface is blackened, thereby providing surface absorption. The analytical predictions have the same trends as the measurements, but the computations indicate a somewhat slower response. After about 120 seconds the analysis for the blackened surface is in good agreement with experiment; for a clear surface, the prediction is not as good. An earlier experimental study by Mutoh et al. (1978) explored radiation induced ignition of PMMA as a result of irradiation by a beam from a CO_2 laser. The temperature and fuel concentration distributions were examined in the gas plume formed adjacent to the surface. A critical heat flux was found; above this value ignition occurred in the plume somewhat away from the surface, while for lower fluxes it occurred very close to the surface. A related investigation is in Qian et al. (1994), but their transient model does not include internal radiation effects.

Analysis for Radiant Heating of a Polytetrafluoroethylene (Teflon) Layer. Teflon has been considered as a heat shield against incident radiation. At temperatures below 600 K, Teflon consists of 80 percent crystallites that provide radiative backscattering. Experimental results from Howe et al. (1973) that illustrate the effectiveness of backscattering in reflecting away incident radiation are in Fig. 9. Teflon was subjected to radiation from an argon arc and convective heating. The incident radiation was larger than the convection, but, as shown the ablation of the Teflon surface by radiation, was considerably smaller than by convection. The combined effect of radiation and convection was almost the same as by convection alone; similar results are in Arai (1979). Hence, Teflon was very effective in scattering away incident radiation. When its temperature reaches 600 K, the Teflon structure changes from polycrystalline to amorphous and its volume reflecting ability is lost. To account for this, Arai (1979) used a two-layer analysis where scattering became very small in the amorphous region: $\sigma_s = 18$ and $\leq 10^{-6}$ cm^{-1} for the polycrystalline and amorphous states, respectively.

The analysis by Yuen et al. (1990) was to examine when any location in a Teflon layer reached the transition temperature 600 K during transient heating. Results are shown in Fig. 10 of the sudden application of a strong collimated radiant heating flux of 42 W/cm^2 at the front side ($x = 0$) of a Teflon layer. There was no convection at the front side, and the back side was insulated and black for the results shown here. The properties of Teflon were gray with an extinction coefficient of $a + \sigma_s = 18.06$ cm^{-1} and a high albedo, $\Omega = 0.99$, with isotropic scattering. During the transient, energy was absorbed near the front surface, and there was partial radiant energy penetration through the layer with absorption at the back side. For thin layers, such as $D = 2$ and 5 mm in Fig. 10, heating to 600 K occurred first at the insulated black boundary at the back side. For a layer 9.5 mm thick, $T = 600$ K was reached simultaneously at both boundaries. For larger thicknesses, the maximum temperature is at the front surface. The switch with increasing thickness of the maximum temperature from the back to the front boundary was observed experimentally for layers with high scattering by Seki et al. (1979). For the conditions in Fig. 10, the minimum temperatures for the transient profiles were always within the layer interior, and not at a boundary.

Analysis for Zirconia Heated by Intense Radiation. Zirconia is a somewhat translucent ceramic that has been used for thermal barrier coatings to protect metals in high temperature

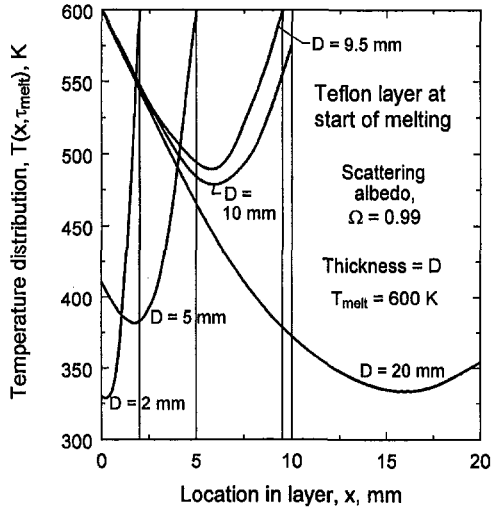

Fig. 10 Transient temperature distribution at the time when the melting point of 600 K is reached locally in Teflon layers of various thicknesses, D, following sudden application of collimated radiant heating at the surface $x = 0$ (replotted from Yuen et al., 1990)

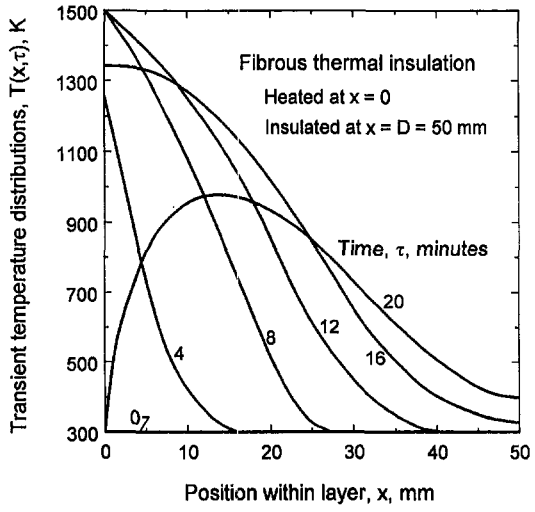

Fig. 12 Transient response of high temperature fibrous thermal insulation for heating at $x = 0$ by conditions of space shuttle reentry into the earth's atmosphere (replotted from Petrov, 1997)

applications such as in gas turbine or diesel engines. Transient thermal behavior for cyclic conditions was analyzed by Thomas (1992) for a ceramic cylinder liner in a diesel engine. Although radiation is significant, conduction is more dominating in zirconia with low porosity as used for thin thermal barrier coatings. Radiation is more important when the insulation is porous.

The analysis of Matthews et al. (1985) was to study the transient insulating behavior of zirconia with a high porosity in the range of 80 to 90 percent. The results in Fig. 11 show transient temperatures in a plane layer 12.7 mm thick following the sudden application of intense concentrated solar radiation on one side at $x = 0$ with a flux of 400 kW/m^2. Zirconia is highly scattering, especially in a porous form, and a scattering albedo of $\Omega = 0.99$ was used for these calculations. Zirconia is translucent for wavelengths up to about 5 μm, which includes essentially all of the energy in the solar spectrum; at larger wavelengths it can be assumed opaque. With both surfaces of the layer cooled by convection and some backscattering included in the radiation formulation, the internal heating by radiative penetration through the front surface produces a maximum temperature inside the layer near the front surface. This can produce thermal stresses in that region. Radiation effects were dominating near the front surface, while both conduction and radiation were important at the back of the layer away from the incident radiation. The optical thickness $(a + \sigma_s)D$ of the layer was about 100 including absorption and scattering, but with an albedo of 0.99 the absorption optical thickness was only about 1. However, with a large optical thickness, scattering can often act like absorption because it increases the radiation path lengths in the material; this is shown in some results that follow. For this study, the transient energy equation was solved with a finite-difference method, with the radiative source term obtained from a modified two-flux method that includes backscattering.

For additional information on anisotropic scattering, some effects on transients in plane layers were investigated by Tsai and Lin (1990). Effects of a linearly anisotropic scattering phase function and Rayleigh scattering were both examined. The initial temperature was uniform, and the boundaries were then each changed to a different constant temperature. It was found that a medium with strong backscattering required a longer time to reach steady state than a medium with forward scattering. The difference between having specular and diffuse boundary reflections was found negligible; scattering evidently diffused the radiation sufficiently that the directional characteristics of the boundaries were not important. This agrees with the findings of Schwander et al. (1990), and is of practical significance as it is often difficult to quantify with good accuracy the directional nature of interface reflections and transmission.

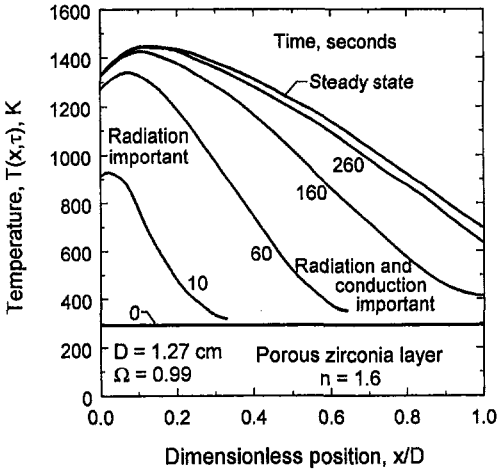

Fig. 11 Transient temperature distributions in porous zirconia 1.27 cm thick suddenly heated at $x = 0$ by intense solar radiation with a flux of 400 kW/m^2 (replotted from Matthews et al., 1985)

Analysis for Fibrous Protective Insulation Heated to Simulate Atmospheric Reentry. In a related analysis, Petrov (1997) investigated possible methods to calculate the transient thermal response of fiber thermal insulation. Considering the optical properties of the insulation, which has considerable scattering, it was found that a type of radiative diffusion analysis worked best. Using this method, the results in Fig. 12 were obtained for transient temperatures in a layer of space shuttle thermal insulation 50 mm thick composed of silica fibers having a density of 144 kg/m^3 and a porosity of 93.4 percent. The boundary at $x = 0$ has a thin opaque black coating, and the boundary at $x = 50$ mm is perfectly reflecting with its exterior insulated. On the boundary at $x = 0$, the heating conditions simulate a space shuttle entering the earth's atmosphere. The insulation layer starts at $T_i = 300$ K, and the boundary temperature at $x = 0$ increases to 1500 K over a 5 min interval. It stays at this temperature for 10 min, after which there is cooling for 5 min. The results in Fig. 12 show that the material being protected, which is at $x = 50$ mm, increases to only about 400

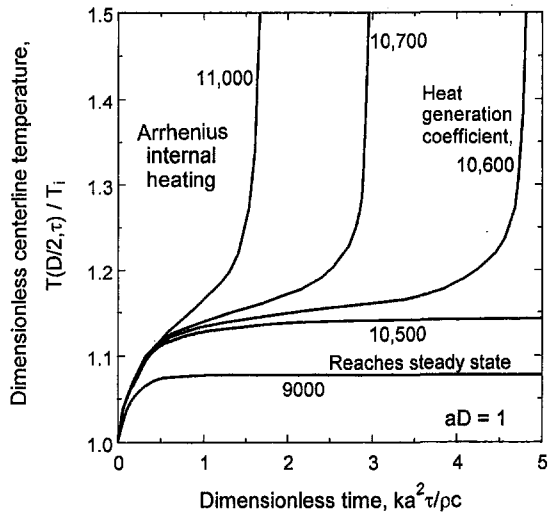

Fig. 13 Transient behavior of the centerline temperature in a semitransparent layer with an Arrhenius internal heat generation rate below and above the value to reach steady-state thermal equilibrium. (replotted from Crosbie and Pattabongse, 1987)

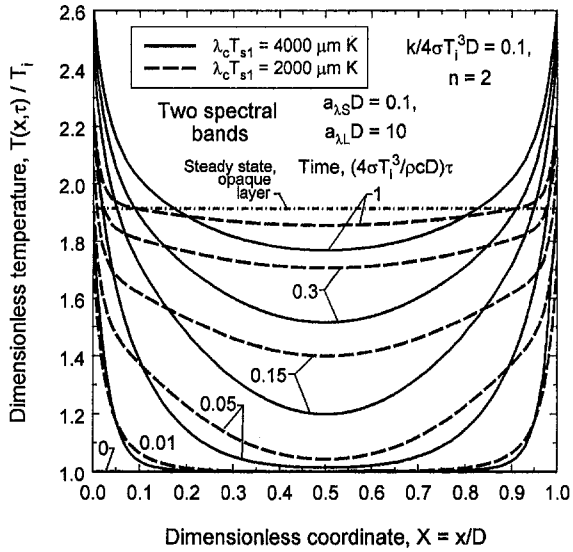

Fig. 14 Transient temperatures in a semitransparent layer, initially at uniform temperature, after exposure to convection by hot gas on both sides and to cold surroundings, $T_{g1}/T_i = T_{g2}/T_i = 4$, $T_{s1}/T_i = T_{s2}/T_i = 1$, $h_1/\sigma T_i^3 = h_2/\sigma T_i^3 = 5$ (from Siegel, 1995a)

K during the simulated reentry heating process. The behavior during the 15 minutes of heating somewhat resembles that in Fig. 11, but, without any convective cooling at $x = 0$, the temperature maximum is at the surface. The surface temperature decreases substantially after 15 min when cooling begins.

Analysis for Plane Layer With Internal Heat Generation. As indicated by the energy equation, Eq. (1), there can be internal heating such as by chemical reaction or electrical currents in addition to internal radiation effects. The investigation by Crosbie and Pattabongse (1987) considers the interaction of heat generation within a semitransparent material, with the heat source by radiative absorption. Transient conduction and radiation effects are analyzed in a gray absorbing and emitting material between black walls with the layer initially at uniform temperature. The transient is produced by the material starting to release internal energy in a temperature dependent manner according to the Arrhenius relation, $A_h \exp(-E/RT)$, where A_h is the heat generation coefficient, E is the activation energy, R is the universal gas constant, and T is the absolute temperature. As temperatures in the layer increase, the heat losses increase by conduction and radiation to the layer boundaries, and the internal generation also increases. If the losses increase to the level of the instantaneous internal generation, a steady state is reached. If, however, the internal generation rate exceeds a critical level, a steady condition cannot be reached; the material continues to increase in temperature and ignition occurs. This is illustrated by the results in Fig. 13 that show the layer centerline temperature as time increases. The heat generation coefficient is a measure of the magnitude of the internal Arrhenius heating. For these results, when this coefficient is about 10,500 or less, a steady condition is reached where energy losses can equal internal generation. Above this heating level, the temperatures continue to rise as the internal generation continues to increase with temperature.

Analysis for Convective Heating With Radiative Cooling. The results in Fig. 14 demonstrate the interesting effect of radiative cooling from within a translucent material that is being heated by convection at its boundaries. An absorbing-emitting layer, initially at uniform temperature, was subjected to large convective heating by a transparent gas with the same elevated temperature on both sides (Siegel, 1995a). Throughout the transient, the surroundings were retained at the initial temperature that is much lower than the gas temperature. This occurs in some high temperature tests of ceramics by heating them in a transparent gas flame with the surroundings at room temperature. As the layer temperatures increase, cooling to the surroundings occurs by radiation leaving from within the layer. Throughout the transient this produces a temperature minimum within the layer as a result of the negative heat source provided by radiative loss from within the layer interior. At steady state there is a balance of convective heating at the surface, that is transferred into the layer by conduction, and radiation out to the surroundings. This produces a much different temperature distribution than the uniform temperature shown by the dot-dash line in Fig. 14 for an opaque layer where radiation is lost only from the layer boundaries. These results are for a two-spectral-band calculation with optical thicknesses of $a_\lambda D = 0.1$ and 10 at short and long wavelengths, and temperature distributions are given for two cutoff wavelengths separating the two bands. For a smaller cutoff wavelength (dashed lines), the layer is less transmitting, and the results show how internal radiative cooling is reduced so the temperatures at large time are closer to the steady-state uniform value for an opaque layer. The two-flux method was used to calculate the radiative source in the layer. The differential equation, Eq. (5), for the radiative flux function in this method was solved by deriving a Green's function that satisfied boundary conditions derived from Eq. (8). An implicit finite-difference numerical procedure was used to solve the transient energy equation with the radiative source evaluation one time increment behind the temperature calculation.

Transient Cooling of Nongray Gas Layer.

Analysis for Cooling a Gas Layer. Transient cooling of a stationary nongray gas between parallel boundaries was analyzed by Tiwari et al. (1989). The layer was initially at a uniform high temperature, and the temperature of one boundary was suddenly decreased to initiate the transient. For the example in Fig. 15, the initial temperature was $T_i = 1000$ K, and the boundary was decreased to 500 K; the gas pressure was 1 atm. The gas cooled until steady state was reached with a steady energy transfer by combined radiation and conduction through the gas produced by the boundaries at differing temperatures. The transient decrease in dimensionless centerline temperature is shown for four gases. To investigate the importance of heat conduction relative to radiation, two sets of curves are provided;

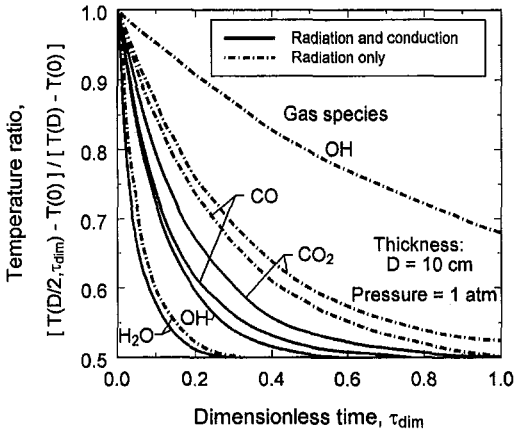

Fig. 15 Comparison of cooling of various nongray gases; the centerline temperature variation with time is shown for a plane layer 10 cm thick. Cooling with radiation and conduction after sudden reduction in one boundary temperature is compared with that for radiation alone; $T(D, \tau > 0) = T_i = 1000$ K, $T(0, \tau > 0) = 500$ K, $D = 10$ cm, pressure = 1 atm (replotted from Tiwari et al., 1989)

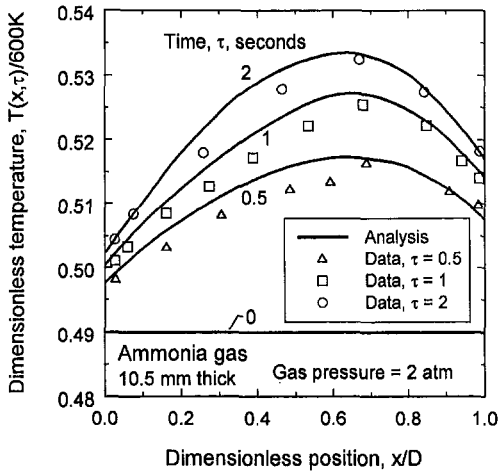

Fig. 16 Comparisons of measurements for sudden radiative heating of a layer of gaseous ammonia 10.5 mm thick through one transparent boundary with radiative cooling through the other boundary (from Rubtsov et al., 1978)

the dot-dashed curves are for radiation only, while the solid curves show the additional effect of conduction. Water vapor was found to have the most rapid transient cooling response. It has high radiative transfer relative to conduction so the addition of conduction increased transient cooling by only a small amount. The large radiative transfer arises from water vapor having five strong vibration-rotation bands. However, CO with one fundamental band was found to be a better radiating gas in this situation than CO_2, although CO_2 has three vibration-rotation bands. This is because for this example the CO_2 had a relatively large optical density, and was less effective in transferring radiation because of self absorption along the radiation paths.

Comparisons With Measurements for Transient Heating of Gaseous Ammonia. The measurements and calculations in Fig. 16 were made by Rubtsov et al. (1978) for a layer of gaseous ammonia suddenly subjected to heating by external radiation suddenly applied at one side. The layer was horizontal, and the radiative heating was through a transparent upper boundary at $x = D$; the ammonia was cooled by radiating energy through a transparent lower boundary at $x = 0$. The gas layer remained stable and did not flow during the heating process. Temperature distributions across the layer thickness are shown during a 2 second heating period; the data were taken with 0.05 mm diameter platinum–platinum rhodium thermocouples. Calculations were made using detailed spectral properties of gaseous ammonia. The ammonia gas had a pressure of 2 atm and was 10.5 mm thick. As shown in Fig. 16, the agreement of predictions with measurements is quite good.

Analysis of Plane Layer Without Heat Conduction.

Liquid-Drop Radiator Geometry. For a heat transfer analysis at elevated temperatures in a material like glass, it is very important to include both radiation and conduction, as demonstrated in Figs. 2 and 5. A novel application dominated only by radiation is the transient cooling of a layer of hot liquid drops. The "liquid-drop" heat radiator has been proposed as a compact, light-weight device for dissipating waste heat from equipment operating in the cold vacuum of outer space or on the moon. As shown in Fig. 17(a), the radiator uses a droplet generator that contains a perforated plate driven by pressure pulsations; this forms the hot working fluid of a space power system into a moving layer of very small drops. The droplet layer travels through outer space until it cools sufficiently by radiation. The cooled layer is then collected by another part of the structure, and the drops are combined into a continuous liquid for recirculation through the power system.

Radiative Cooling of a Droplet Layer. For the thermal analysis of a radiating droplet sheet, scattering was included to evaluate its effect within the droplet cloud. Heat conduction does not occur between drops, which simplifies the transient energy equation somewhat. The radiative source was evaluated numerically at each time step using the full equations of radiative transfer such as Eq. (2) with the addition of isotropic scattering, and the energy equation was integrated forward to the next time step with a finite-difference method.

Typical results for radiative cooling are in Fig. 17(b) (Siegel, 1987a) for a gray droplet layer with an optical thickness of $(a + \sigma_s)D = 2$. The layer is initially at a uniform temperature, and it is then exposed to the cold environment of outer space. An optical thickness of 2 was found to be about the optimum value for heat dissipation; a thinner layer does not radiate well, and a thicker layer has too much self absorption that reduces radiative dissipation relative to its mass. For this optical thickness there is a very significant effect of increasing the scattering albedo, and for a large albedo, $\Omega = 0.9$, the cooling rate is substantially decreased. Note that for these results the optical thickness is constant, so an increase in the scattering coefficient corresponds to a decrease in the absorption coefficient, thereby reducing the emitting ability of the layer that depends on the absorption coefficient. A large albedo also makes the transient temperature distributions more uniform. The effect of increasing Ω is quite different for larger optical thickness, as shown in Fig. 17(c) for $(a + \sigma_s)D = 10$. In this case, a large albedo decreases the cooling rate only a small amount, and provides somewhat more uniform temperature profiles only during the early part of the transient. Later in the transient, scattering has little effect on the temperature distribution. This is because, in a somewhat optically thick layer, scattering tends to enhance absorption by increasing the path length traveled by radiation within the medium. As a result, scattering acts partially like absorption, and there is not a large effect of albedo in Fig. 17(c), as compared with Fig. 17(b).

Emittance of the Droplet Layer. Further analysis of the numerical results in Siegel (1987a) revealed an interesting transient behavior for this type of radiative cooling. The layer emittance, defined as the instantaneous radiative heat loss divided by the blackbody flux corresponding to the instantaneous mean temperature, became constant with time. This was true even though the instantaneous heat loss and the layer mean tempera-

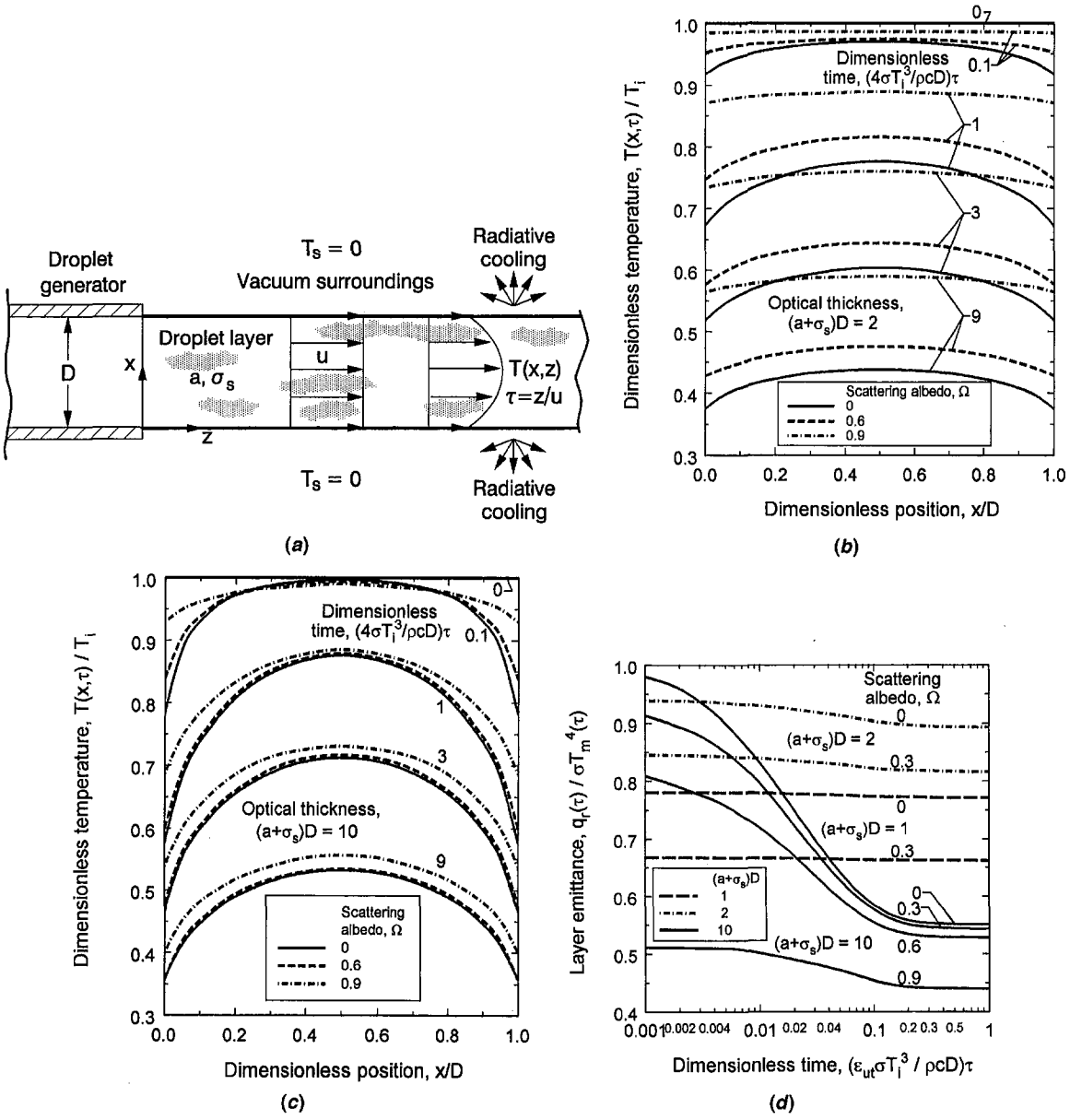

Fig. 17 Radiative cooling of a liquid-drop layer in a radiator for heat dissipation in outer space (Siegel, 1987a): (*a*) liquid-drop layer moving through space with a uniform velocity *u* for radiative heat dissipation ($\tau = z/u$); (*b*) transient temperature distributions for radiative cooling of a liquid-drop layer in a cold vacuum environment, layer optical thickness = 2; (*c*) transient temperature distributions for radiative cooling of a liquid-drop layer in a cold vacuum environment, layer optical thickness = 10; (*d*) transient emittance based on instantaneous heat loss and mean temperature

ture were both changing with time. Transient emittance values from the numerical solution are in Fig. 17(*d*) for various optical thicknesses and scattering albedos. The highest emittance is at the start of the transient when the layer is at uniform temperature. For a small optical thickness, the emittance does not change much with time since the transient temperature profiles tend to remain somewhat uniform, especially as scattering is increased. A mathematical proof that the layer emittance becomes independent of time as the transient proceeds was obtained in Siegel (1987b). A similarity solution was shown to develop with time for conditions where the transient heat loss is only by radiation, there is no heat conduction, and the surroundings are at low temperature. More generally, this similarity behavior was shown to exist (Siegel, 1995b) for a layer that has a refractive index larger than $n = 1$ so there are internal reflections at the boundaries.

One can make the liquid-drop radiator most efficient for energy dissipation by retaining a high layer emittance and having the drops remain at as high a temperature as possible while radiating energy to space. For this it was proposed to have the drops solidify and, thus, release energy at uniform temperature while changing phase. Transient radiative cooling was analyzed in Siegel (1987c, d) using three transient zones starting with drops at the freezing temperature. The layer starts to cool by losing latent heat until the outermost drops become solid, since they cool the most rapidly. Cooling then continues by loss of both latent and sensible heat depending on the droplet position across the layer. After all drops have solidified they continue to cool by loss of sensible heat. The emittance of the layer begins to decrease as soon as the outer regions of the layer become solid since their temperature then decreases by loss of sensible heat.

Multi-Layer Composites

Analyses for Plane-Layer Composites. The investigations in the previous section were for single plane layers. Several

studies have been made of transients in translucent multi-layer composites. In Tsai and Nixon (1986), the radiative transfer equations without scattering were solved numerically in combination with the energy equation for a composite of layers with diffuse boundaries. An example was given for transient heating of a four-layer aircraft windshield where the layers are gray. The layers all have the same refractive index so there are no reflections at the interfaces between the layers. A multilayered composite where some of the layers may not be in contact was analyzed by Timoshenko and Trener (1986). The boundaries were diffuse, scattering was not included, and the layers could have spectral properties. A brief example was given for radiative heating of a five-layer composite. The solution was obtained by a finite-difference method using a variable grid size. A two-layer composite was analyzed by Ho and Özişik (1987), where the composite was subjected to external radiation at one of its boundaries. Each of the external boundaries was covered by a thin opaque layer, isotropic scattering was included, and the layers were gray. A Galerkin method was used to evaluate the radiative source, and the transient energy equation was solved with a finite-difference method.

The two-flux relations, as in Eqs. (4) and (5), were used by Siegel (1996c, d) to obtain transient temperatures in two-layer composites with gray and spectral layers. The two-flux differential equation was solved by deriving a Green's function for the composite with boundary conditions including external radiation. The Green's function solution for the radiative source was combined with an implicit finite-difference solution of the transient energy equation. The refractive index was larger than one in each layer, and diffuse surface reflections were included. The internal interface produces reflections within the composite that were included. The transient results in Fig. 18 illustrate how a scattering layer can be used for some conditions to reflect away incident radiation and reduce temperatures in an adjacent translucent layer. For the two parts of Fig. 18, scattering added to the first layer of thickness, D_1 shields the second layer of thickness D_2 from radiation incident on the boundary at $x = 0$. The absorption optical thickness is kept at $a_1 D_1 = 0.1$ in the first layer, while scattering is added so its optical thickness $(a_1 + \sigma_{s1})D_1$ increases from 0.1 to 10. The properties of the second layer remain unchanged. The transient starts by suddenly applying diffuse radiative heating at $x = 0$, while both boundaries of the composite ($x = 0$ and $x = D_1 + D_2$) are strongly cooled by convection. During most of the transient in Fig. 18(a), which is without scattering, the maximum temperature is in the second layer near the internal interface. This is produced by radiation that penetrates through the first layer that has a small optical thickness, and is absorbed in the second layer with a larger optical thickness. The temperature distributions change considerably in Fig. 18(b), where large scattering has been added in the first layer. Radiation penetration to the second layer is reduced, and the maximum temperature is now always in the first layer.

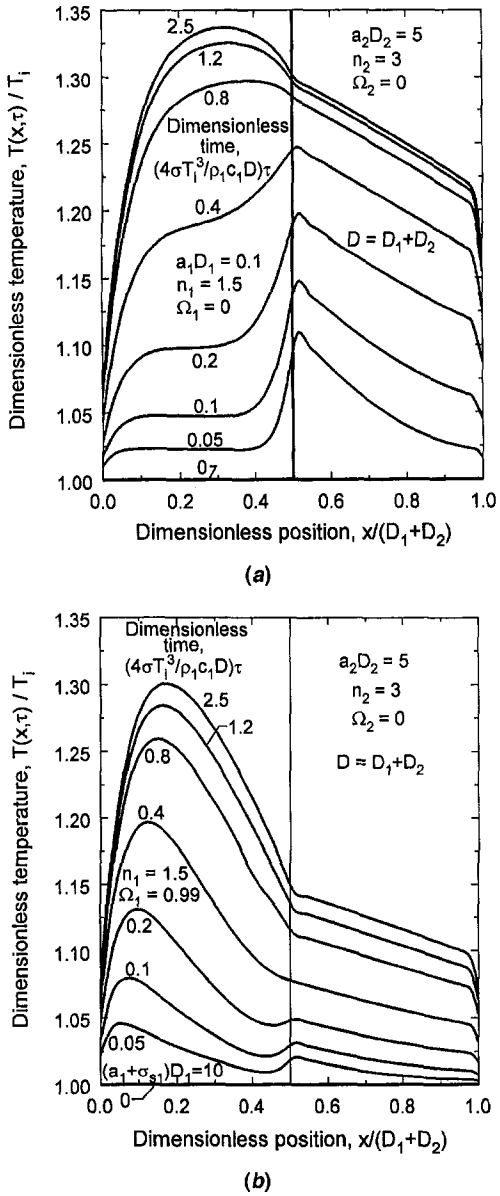

Fig. 18 Transient temperatures in a two-layer semitransparent composite following the sudden application of radiation at the boundary $x = 0$; $q_1^o/\sigma T_i^4 = 1.5$, $h_1/\sigma T_i^3 = h_2/\sigma T_i^3 = 5$, $k_1/4\sigma T_i^3 D = k_2/4\sigma T_i^3 D = 0.025$ (from Siegel, 1996c); (a) no scattering in the first layer; and (b) effect of scattering in the first layer on shielding the second layer from incident radiation

In Chan and Cho (1978), two semitransparent absorbing-emitting media, each at a different uniform temperature, are suddenly placed in contact. The media are gray, and they are gases or particulate suspensions so heat conduction in them is neglected and there are no reflections at their contact interface. Each medium is thick, relative to its radiation penetration length, so there is radiative transfer across the contact interface, but no penetration of radiative energy to the interface region from other boundaries.

Transient Measurements for a Composite–Heating of Ice on a Lucite Wall. For a composite of two translucent materials, comparisons of experimental measurements with analytical predictions are in Fig. 19. This study by Song and Viskanta (1990) was for examining radiative heating as a means for removing an ice layer frozen onto a wall. Incident external radiation can be used to penetrate through an ice layer and heat its interface with a wall. When the interface reaches the freezing temperature, or somewhat above, the ice detaches. An experiment was performed starting with an ice layer frozen onto a transparent plastic (Lucite) plate. Since the temperatures are low, internal emission in the layers was neglected in the analysis. Twenty-one spectral bands were used in the calculations. Surface reflectivities were calculated from the Fresnel equations for radiation incident in the normal direction. Comparisons of measurements and predictions are in Fig. 19 for ice layers starting with three different thicknesses frozen onto a Lucite plate, and for two radiant fluxes that are normally incident. The incident radiation was from lamps that simulated the spectrum of solar radiation. The predictions are reasonably good for the transient temperature rise of the ice-solid interface. In the analysis, the transient calculations were terminated when the interface reached 0°C. The measurements were continued to somewhat longer times required for the ice to detach. It was postulated

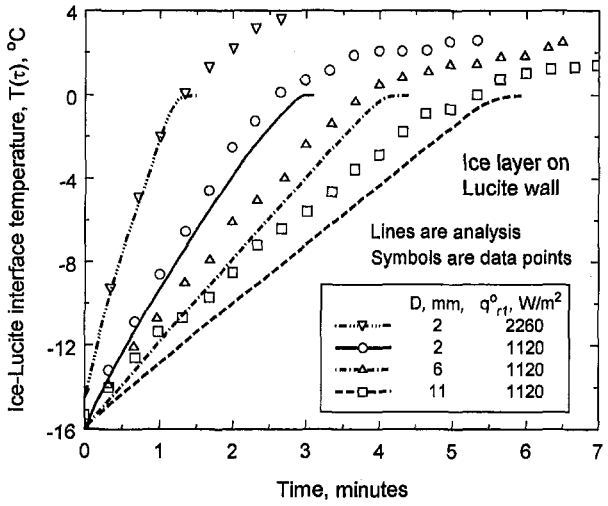

Fig. 19 Comparisons of predicted and measured temperatures of the ice-substrate interface during irradiation in the normal direction of an ice layer frozen onto a Lucite plate in surroundings at 23°C (replotted from Song and Viskanta, 1990)

that extra time and a somewhat higher interface temperature were required to overcome surface tension that was keeping the ice attached.

Radiative heating plays an important role in the breaking up of ice in lakes and rivers, as discussed by Gilpin et al. (1977). Solar energy absorbed within the ice causes internal melting at grain boundaries, and the ice structure is thereby weakened and breaks apart. This is a different process than producing melting at an ice-substrate interface for removal of an ice layer from a structure. The spatial distribution where energy is absorbed within the ice depends on the spectral absorption and scattering properties of the ice, and on the spectral distribution of the incident energy. Experimental results are in Gilpin et al. (1977) for the properties of clear and cloudy ice when exposed to heating by a tungsten lamp and by a simulated solar energy source.

Analyses for Semi-Infinite Regions With a Plane Boundary

The investigations in the previous sections were for single and multiple plane layers. Several studies are now considered for transients in translucent semi-infinite media with a plane boundary. In Lick (1965), the medium was gray, and scattering was not included. Initially, the medium was at zero temperature, the plane boundary was raised to a finite temperature, and an incident external radiation source was imposed. When radiation was dominant over conduction, the maximum temperature propagated in a wave-like fashion within the semi-infinite medium. Heinisch and Viskanta (1968) used an approximate analysis to study transient radiation and conduction in a semi-infinite gray medium with variable properties. The medium was optically thick and the diffusion approximation was used for the radiative flux. Initially, the medium was at uniform temperature, and its surface temperature was then changed to a new value. By using a similarity relation, the energy equation was transformed into a second-order ordinary differential equation that was solved by Runge-Kutta integration.

The effect of isotropic scattering on transient radiative transfer in a gray medium was analyzed by Kubo and Hayashiguchi (1981) for a translucent semi-infinite volume, such as an absorbing and radiating gas or particulate suspension bounded by a semitransparent plate. The transient begins by suddenly changing the temperature of the bounding plate and providing a radiative energy beam through the plate into the medium. There is no heat conduction, so the conclusions regarding scattering effects apply for radiation dominated conditions. For scattering albedos less than 0.8, the albedo had little effect on the transient temperatures; only the extinction coefficient was significant, so scattering acted much the same as absorption. In another study by Kubo (1984), results were obtained for large albedos, such as $\Omega = 0.99$, and a separate effect of albedo was found. The effect of scattering albedo agrees with the behavior in Fig. 17(c) for transient radiative cooling of a layer without heat conduction.

Analyses for Cylindrical and Spherical Regions

The previous sections have been for one-dimensional media with plane boundaries; this section considers one-dimensional shapes that are nonplanar.

Transients in Cylinders and Cylindrical Layers. Radiative cooling was discussed earlier for a plane layer of many small liquid drops for radiative heat dissipation in outer space. A radiator of this type was analyzed in Siegel (1989a) consisting of a cylindrical cloud of gray absorbing, emitting, and isotropically scattering drops. As the cloud cools by radiation from an initially uniform temperature, partial solidification occurs, and a two-phase region is formed without temperatures decreasing below the solidification temperature. Retaining this high uniform temperature maintains a high emissive ability for the cylindrical cloud.

Several analyses have been made for transients in a medium in the annular space between two cylinders. Chang and Smith (1970) considered a heat conducting, emitting, and absorbing gray medium between two long coaxial cylinders. The boundaries were diffuse with specified emissivities, and the medium refractive index was one. Initially, the medium was at uniform temperature, and each boundary was then suddenly changed to a different temperature. A two-flux approximation was used, where the radiative source distribution was obtained by solving a differential equation such as Eq. (4). By using Green's functions the solutions for both the source differential equation and the transient energy equation were expressed as integral relations and solved by successive approximations.

Isotropic scattering was included by Fernandes and Francis (1982) in an analysis of transient radiation and conduction in a gray annular medium. The boundaries were gray, diffuse, and at uniform temperature. The temperature in the annulus was initially uniform, and the transient followed sudden changes in the boundary temperatures. A finite-element method was used to compute temperature and radiant intensity distributions, and the transient term in the energy equation was integrated forward in time with a Crank-Nicolson procedure.

To illustrate transient results in an annular region, typical temperatures in a cylindrical annulus with black boundaries are in Fig. 20 (Gordaninejad and Francis, 1984). Initially, the region was at a low uniform temperature. Then, the inner boundary was raised to $T(r_i)$, and the outer boundary to one-tenth of that value, $T(r_o)/T(r_i) = 0.1$. The medium was gray, without scattering, and its refractive index was one. The optical thicknesses of the inner and outer radii were $ar_i = 1$ and $ar_o = 3$, so the region has considerable curvature. At steady state, the temperature distribution has an "S" shape that is also typical of a plane layer between boundaries at differing temperatures. The comparison with the logarithmic curve for steady-state heat conduction (dot-dash line) shows there is an appreciable radiation effect.

Transients in Spheres and Spherical Layers. Radiation within a gray translucent medium with isotropic scattering that is within a sphere was considered by Tsai and Özişik (1987); the sphere had a black internal boundary. The medium was initially at uniform temperature; then, the boundary temperature was suddenly changed to a different uniform value. A colloca-

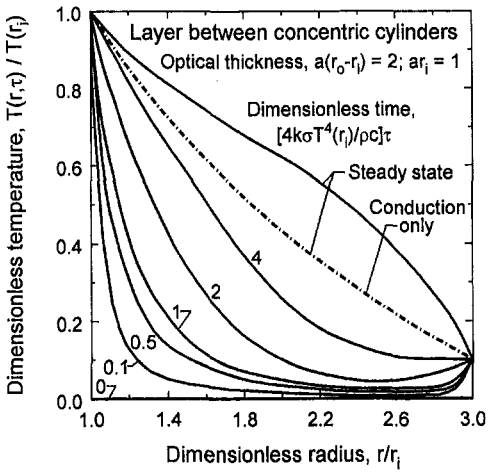

Fig. 20 Transient temperature distributions in a cylindrical annular region after the boundary temperatures are suddenly changed; the initial temperature distribution is uniform; $T(r_o)/T(r_i) = 0.1$ for $\tau > 0$, $ka/4\sigma T^3(r_i) = 0.01$ (replotted from Fernandes and Francis, 1982)

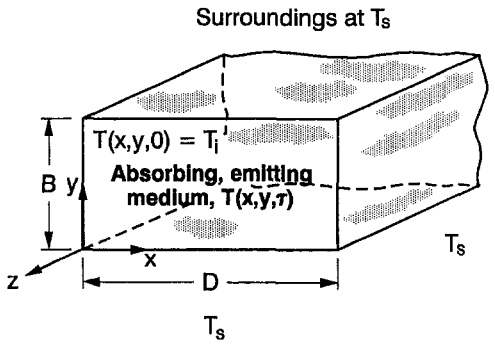

Fig. 21 Geometry of a two-dimensional rectangular region in surroundings at T_s

tion method was used to obtain the radiative source, and an implicit finite-difference method to solve the energy equation that included heat conduction. Effects were shown of optical thickness, scattering albedo, and the conduction-radiation parameter. An earlier transient analysis for radiative cooling of a sphere of high temperature gas is by Viskanta and Lall (1965). The gas was gray, without scattering, and heat conduction was not included. The results showed how the gas cooling rate decreased with increasing optical radius and how the cooling depended on the initial temperature distribution. References are given for earlier Russian literature on the cooling of high-temperature air.

Bayazitoglu and Suryanarayana (1989) considered transient heat transfer in an opaque sphere surrounded by a translucent concentric spherical layer. The surrounding layer partially insulated the internal sphere from radiative heat loss from its surface. The translucent concentric spherical layer was gray with absorption, emission, and isotropic scattering, but without heat conduction. Since the internal sphere was opaque, heat transfer within it was only by conduction, and temperatures were obtained numerically with an explicit finite-difference method.

A gray annular region between two concentric spheres was analyzed by Chu and Weng (1992) including conduction, absorption, emission, and anisotropic scattering. The region was initially at uniform temperature; then, the inner and outer boundary temperatures were each changed to a different uniform value. Emphasis was given to the effect of anisotropic scattering. It was found that increased time was required to reach steady state for a strongly backscattering medium compared with one that is strongly forward scattering; this agrees with the results of Tsai and Lin (1990). This behavior was attributed to the radiant energy emitted by the medium being transferred to the boundaries more easily if the medium is forward scattering.

A highly backscattering material was also considered by Cornelison and Howe (1992) for radiative transfer in a concentric spherical heat shield for reentry through a planetary atmosphere. The shield was highly backscattering to reflect away incident radiation. Internal emission was neglected compared with the large externally incident radiant flux, and spectral properties were included. The composition of the heat shield was determined by selecting a translucent material that had spectral properties such that it transmitted almost all, and hence absorbed very little, of the incident radiation. The material can be pulverized into a fine powder with optimum particle sizes for backscattering as determined by scattering theory. The powder can then be reformed into a solid material with densely packed scattering sites. Zinc selenide was used for the calculations; it has a low absorption coefficient of 0.005 cm^{-1} over a broad wavelength range and a scattering coefficient as high as 800 cm^{-1}. For some calculations, the shield had a uniform initial temperature of 300 K, and was 10 cm thick with an inner radius of curvature of 100 cm. It was exposed to a radiative heat flux of 300 W/cm^2 and a convective flux of 100 W/cm^2. The maximum temperatures were found to be at the external surface. With large internal backscattering, there was considerable scattering away of the incident radiation and it required 40 seconds for the external surface to reach the shield melting temperature. Without internal scattering and with an opaque and black external surface, the heating time to melting is only 7 seconds. Earlier research on the transient behavior of backscattering heat shields is in Howe et al. (1973).

Analyses for Two-Dimensional Rectangular Geometries

As might be expected because of the additional computational effort, especially for computing the radiative energy source distribution from relations such as Eqs. (2) or (3), investigations of transients in multidimensional geometries including radiation effects are much less than for plane layers. The geometry in Fig. 21 is a two-dimensional rectangular region investigated by Siegel and Molls (1992). The volume is a gray emitting and absorbing medium that is heat conducting, and the transient temperatures are functions of x and y, but not the z-direction. The medium refractive index was 1, so there were no internal reflections at the boundaries. A finite-difference method was used for integrating the energy equation, with solutions obtained with an alternating-direction-implicit method. Variable time increments and grid sizes were used so that small time increments could be used in the early part of the transient, with longer increments in the later stages of the transient where temperature changes were more gradual; this conserved computer time. The spatial grid points were concentrated in regions where large temperature gradients were expected. Two-dimensional Gaussian integration was used to evaluate the local radiative source from the instantaneous temperature distribution.

Illustrative transient temperature distributions along the boundary of a square are in Fig. 22. The region is initially at uniform temperature, and is then placed in a cold vacuum environment such as for experiments utilizing cooling in outer space. Radiative cooling is the only means for energy loss from the volume, since there is no surrounding medium to conduct energy away. Heat conduction, however, is an additional means to equalize internal temperatures depending on the relative magnitude of conduction and radiation. The optical side length in Fig. 22 is $aD = 10$, and because of symmetry, values are shown only along one-half of a side. When the transient begins and the hot region is suddenly subjected to a cold black environment, the outer parts of the square cross section begin to cool

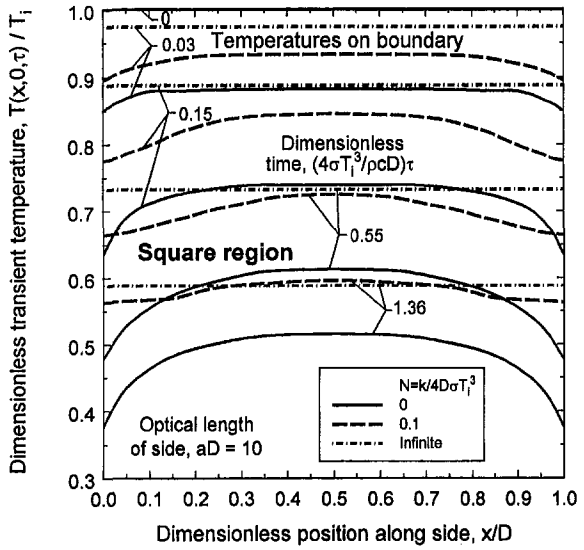

Fig. 22 Transient temperatures along the boundary of a square region following placement into cold vacuum surroundings; initial temperature distribution is uniform (from Siegel and Molls, 1992)

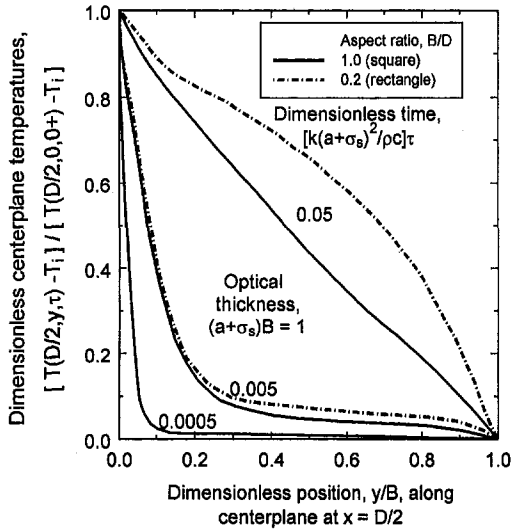

Fig. 23 Transient temperatures along the center plane of a square or rectangular region (across the short dimension), following an equal temperature increase on three sides, $N = k(a + \sigma_s)/n^2\sigma T_i^3 = 0.04$, $\Omega = 0.5$ (replotted from Wu and Ou, 1994)

most rapidly. Temperature distributions are shown at four times during the transient, corresponding to when 3, 10, 25, and 40 percent of the initial internal energy has been radiated away. The figure includes the limits for radiation without conduction, $N = 0$, and for radiation with infinite conduction, $N \to \infty$. For finite internal heat conduction, $N > 0$, the external conditions without convection or conduction impose a zero internal temperature gradient normal to the boundaries as from Eq. (6). Although it is not shown by these results that are along the boundary, the internal temperature distribution can be quite curved near the boundary as N approaches zero, which is the limit for radiation only. For $N = 0.1$, heat conduction is large enough to provide significant equalization of the temperature distribution across the region and also along the boundary. There is less temperature equalization early in the transient when temperature distributions are influenced more by the rapid action of radiative transfer than by the slower action of internal diffusion by heat conduction.

A two-dimensional rectangular region was analyzed by Wu and Ou (1994) including isotropic scattering. The medium is gray and has a refractive index larger than one, but the boundaries are black so there are no internal reflections. A modified differential approximation was used for the radiative source evaluation, and the energy equation was solved with a finite-difference method. Dimensionless temperature distributions are in Fig. 23 for a square cross section, and for a rectangular region with an aspect ratio $B/D = 0.2$. The transient is produced by starting with the region at uniform temperature and then raising the temperatures of three sides by the same amount; the temperature of the lower side (at $y = 0$ in Fig. 21) remains at its original value. Temperatures are shown that extend across the short dimension and are centrally located along a plane half way between the short sides. The temperatures are nondimensionalized such that the distributions extend from 1 to 0 as y in Fig. 21 increases from 0 to B. For short times, there is an insignificant difference in temperatures between the square and rectangular geometries. At long times, the temperature profile across the short dimension of the rectangle becomes somewhat like that for a translucent layer at steady state between infinite parallel boundaries with unequal specified temperatures. This limit is approached as B/D becomes very small, but the behavior is already evident for $B/D = 0.2$.

The study by Derevyanko and Koltun (1991) is for a rectangular region that is assumed to be two-dimensional. Two opposite boundaries transmit radiation, while the other two are bounded by opaque walls that are assumed black. The semi-transparent medium is gray, without scattering, and heat conduction is included. The radiative energy source is evaluated with a Monte Carlo type of method, and it lags one time increment behind the finite-difference solution procedure used for integrating the energy equation.

Analyses for Regions Undergoing Phase Change

Some phase change materials, such as ice, are translucent so that during solidification or melting, radiative transport may be combined with conduction in the energy transfer to or from a solidification interface. Depending on the temperatures involved, internal emission may not be important, but the material may be subjected to external radiation sources such as an ice layer exposed to the sun. Phase change was analyzed by Habib (1971, 1973), Seki et al. (1978), and Shih et al. (1986) for solidification in plane and cylindrical geometries. The liquid was initially at the freezing temperature, and remained at that temperature throughout solidification. A boundary of the semi-transparent medium was decreased in temperature to initiate the solidification process. In Habib (1971), the boundary and the solidification interface were each given an emissivity value, while in Seki et al. (1978) both of these interfaces were assumed black. The solidified material was gray and without scattering.

A finite-difference analysis was used by Abrams and Viskanta (1974) to investigate this type of problem in more detail for optical materials such as fluorite. A spectral-band model was used for a calculation with solidification, and gray properties were used when analyzing melting. Radiative transfer was found to have a significant effect for the thermal conditions associated with solidification and melting for many of these materials. During solidification, radiative transport can produce a temperature profile within the liquid phase that leads to unstable interfacial growth.

Another effect of internal radiation on phase change within translucent materials was investigated analytically by Chan et al. (1983). A proposed feature was that for radiative penetration producing internal melting, a two-phase zone may exist in which partial phase change occurs; this zone is contained between the liquid and solid phases. A gray translucent semi-infinite medium was analyzed, bounded by a black surface, and the medium was assumed to have a distinct melting point. The medium was

initially liquid at the melting point, and the temperature of the black boundary was then decreased. Since the refractive index was assumed to remain unchanged during phase change, scattering was neglected from liquid-solid interfaces within the two-phase mixture. The radiative portion of the analysis was limited to using an optically thin approximation.

Concluding Remarks

Transient effects of thermal radiation in translucent materials are important for many applications such as glass manufacturing, ceramics at high temperature, and radiative heat shields, as summarized in Table 1. In the presence of radiation, internal temperature responses for translucent materials can be considerably different than for heat conduction alone. Transient temperature distributions can have unusual shapes, and must be investigated to be assured that temperature limits are not exceeded and to permit evaluation of transient thermal stresses. During the past 40 years an appreciable literature has developed, but because of the additional mathematical and computational complexities that transients impose, it is substantially less than for steady conditions. Much of the literature is for one-dimensional shapes, mostly plane layers, with some results for cylinders and spheres. There are less results for multilayer composites and multidimensional shapes, especially when spectral calculations are considered. There is a modest amount of transient experimental data obtained for plane layers and compared with analyses using the experimental conditions. More transient measurements are needed to verify analytical modeling and computations. Agreement of calculations with experiments is often good if the internal and surface properties of the semitransparent material are known in detail for use in the theory.

A transient solution involves two parts: (1) the evaluation of the spatial distribution of the internal radiative energy source at each time, and (2) the solution of the transient energy equation. In a finite-difference time-marching solution, the radiative source evaluation is usually at one time increment earlier than the energy equation forward integration, so the temperature distribution is known for the source computation. This is especially convenient when including spectral property variations since the amounts of energy in the spectral bands depend on temperature. Because of the time lag in the evaluation of the radiative source, the complete solution method for the temperatures is not fully implicit even if an implicit solution is used for the energy equation with a known radiative heat source. Hence, for computational stability, it is usually necessary to have small time increments during the forward time marching of the solution; this can result in long computer times.

The transient radiative source in the material has been evaluated by the same procedures used for steady-state solutions. This includes direct numerical integration, discrete ordinates, Monte Carlo methods, and approximate methods such as expansions in spherical harmonics, radiative diffusion, and two-flux methods for plane layers. Approximate methods can save considerable computer time, but additional verification of accuracy is needed for their application to transient situations.

As expected, radiative penetration can provide rapid temperature responses within a material, and the maximum temperature is often not at a boundary. For simultaneous radiative heating and convective cooling, there can be large temperature gradients near surfaces that can cause difficulties with thermal stresses. When there is large convective heating at the boundaries in the presence of cool surroundings, there can be radiative cooling from within the translucent material. This can yield temperature distributions considerably different than those physically possible when there is only internal heat conduction. For some conditions, internal radiation can make the transient temperature distributions more uniform than for convective heating or cooling.

In the limit of small heat conduction relative to radiation, such as for radiative cooling of a layer filled with drops or particles, a similarity solution can develop during the transient for some conditions. The instantaneous heat loss becomes proportional to the fourth power of the instantaneous mean temperature so the layer emittance becomes constant with time.

Internal reflections can be important when the translucent material has a refractive index larger than one. Reflections can tend to equalize absorption of radiation within the material, producing more uniform temperature distributions as the refractive index is increased. The spectral nature of the material is important since regions of moderate transparency permit multiple reflections before the radiation is absorbed. These regions also allow the penetration of external radiation into the material, and still provide a large enough absorption coefficient to absorb energy and produce a local transient heat source within the interior.

There is a very significant need for additional experimental measurements and comparisons with results computed using the experimental conditions. This is especially true for transients in multidimensional shapes. The comparisons shown here indicate that reasonable predictions can often be made if the material properties can be specified in detail. Unfortunately, spectral properties are not known very well for materials like translucent ceramics, especially at elevated temperatures. Surface reflection and transmission characteristics are difficult to define for somewhat rough surfaces.

The development of faster computers will enable transient calculations to be carried out in a reasonable time since the radiative source distribution must be evaluated in detail at each time. As the literature continues to develop, it is expected that more information will become available on transients in multidimensional shapes including spectral property variations and scattering. Only a few multidimensional shapes have been investigated at present, and there is a lack of experimental data.

References

Arai, N., 1979, "Transient Ablation of Teflon in Intense Radiative and Convective Environments," *AIAA Journal,* Vol. 17, No. 6, pp. 634–640.

Abrams, M., and Viskanta, R., 1974, "The Effects of Radiative Heat Transfer Upon the Melting and Solidification of Semitransparent Crystals," ASME JOURNAL OF HEAT TRANSFER, Vol. 96, pp. 184–190.

Andre, S., and Degiovanni, A., 1995, "A Theoretical Study of the Transient Coupled Conduction and Radiation Heat Transfer in Glass: Phonic Diffusivity Measurements by the Flash Technique," *International Journal of Heat and Mass Transfer,* Vol. 38, No. 18, pp. 3401–3412.

Bayazitoglu, Y., and Suryanarayana, P. V. R., 1989, "Transient Radiative Heat Transfer From a Sphere Surrounded by a Participating Medium," ASME JOURNAL OF HEAT TRANSFER, Vol. 111, pp. 713–718.

Chan, S. H., and Cho, D. H., 1978, "Transient Radiative Heat Transfer Between Two Emitting-Absorbing Media," *Heat Transfer 1978, Proceedings of the 6th International Heat Transfer Conference,* Paper R-10, Vol. 3, Hemisphere Publishing Corp., Washington, DC, pp. 367–372.

Chan, S. H., Cho, D. H., and Kocamustafaogullari, G., 1983, "Melting and Solidification with Internal Radiative Transfer—A Generalized Phase Change Model," *International Journal of Heat and Mass Transfer,* Vol. 26, pp. 621–633.

Chang, Y. P., and Smith, R. S., Jr., 1970, "Steady and Transient Heat Transfer by Radiation and Conduction in a Medium Bounded by Two Coaxial Cylindrical Surfaces," *International Journal of Heat and Mass Transfer,* Vol. 13, pp. 69–80.

Chu, H.-S., and Weng, L.-C., 1992, "Transient Combined Conduction and Radiation in Anisotropically Scattering Spherical Media," *Journal of Thermophysics and Heat Transfer,* Vol. 6, pp. 553–556.

Cornelison, C. J., and Howe, J. T., 1992, "Analytic Solution of the Transient Behavior of Radiation-Backscattering Heat Shields," *Journal of Thermophysics and Heat Transfer,* Vol. 6, pp. 612–617.

Crosbie, A. L., and Pattabongse, M., 1987, "Transient Conductive and Radiative Transfer in a Planar Layer with Arrhenius Heat Generation," *Journal of Quantitative Spectroscopy and Radiative Transfer,* Vol. 37, pp. 319–329.

Darby, M. I., 1983, "Analysis of Thermal Conductivity Experiments on Glass at High Temperatures," *High Temperatures—High Pressures,* Vol. 15, pp. 629–644.

Derevyanko, G. V., and Koltun, P. S., 1991, "Radiative-Conductive Heat Transfer of Semitransparent Bodies," *Journal of Engineering Physics,* Vol. 61, pp. 680–684.

Fernandes, R., and Francis, J., 1982, "Combined Conductive and Radiative Heat Transfer in an Absorbing, Emitting, and Scattering Cylindrical Medium," ASME JOURNAL OF HEAT TRANSFER, Vol. 104, pp. 594–601.

Field, R. E., and Viskanta, R., 1993, "Measurement and Prediction of Dynamic Temperatures in Unsymmetrically Cooled Glass Windows," *Journal of Thermophysics and Heat Transfer,* Vol. 7, pp. 616–623.

Fowle, A. A., Strong, P. F., Comstock, D. F., and Sox, C., 1969, "Computer Program to Predict Heat Transfer Through Glass," *AIAA Journal,* Vol. 7, pp. 478–483.

Frankel, J. I., 1995, "Cumulative Variable Formulation for Transient Conductive and Radiative Transport in Participating Media," *Journal of Thermophysics and Heat Transfer,* Vol. 9, pp. 210–218.

Gardon, R., 1958, "Calculation of Temperature Distributions in Glass Plates Undergoing Heat Treatment," *Journal of the American Ceramic Society,* Vol. 41, pp. 200–209.

Gilpin, R. R., Robertson, R. B., and Singh, B., 1977, "Radiative Heating in Ice," ASME JOURNAL OF HEAT TRANSFER, Vol. 99, pp. 227–232.

Gordaninejad, F., and Francis, J., 1984, "A Finite Difference Solution to Transient Combined Conductive and Radiative Heat Transfer in an Annular Medium," ASME JOURNAL OF HEAT TRANSFER, Vol. 106, pp. 888–891.

Gorthala, R., Harris, K. T., Roux, J. A., and McCarty, T. A., 1994, "Transient Conductive, Radiative Heat Transfer Coupled with Moisture Transport in Attic Insulations," *Journal of Thermophysics and Heat Transfer,* Vol. 8, No. 1, pp. 125–132.

Habib, I. S., 1971, "Solidification of Semi-Transparent Materials by Conduction and Radiation," *International Journal of Heat and Mass Transfer,* Vol. 14, pp. 2161–2164.

Habib, I. S., 1973, "Solidification of a Semitransparent Cylindrical Medium by Conduction and Radiation," ASME JOURNAL OF HEAT TRANSFER, Vol. 95, pp. 37–41.

Hahn, O., Raether, F., Arduini-Schuster, M. C., and Fricke, J., 1997, "Transient Coupled Conductive/Radiative Heat Transfer in Absorbing, Emitting and Scattering Media: Application to Laser-Flash Measurements on Ceramic Materials," *International Journal of Heat and Mass Transfer,* Vol. 40, pp. 689–698.

Heinisch, R. P., and Viskanta, R., 1968, "Transient Combined Conduction-Radiation in an Optically Thick Semi-Infinite Medium," *AIAA Journal,* Vol. 6, pp. 1409–1411.

Heping, T., and Lallemand, M., 1989, "Transient Radiative-Conductive Heat Transfer in Flat Glasses Submitted to Temperature, Flux and Mixed Boundary Conditions," *International Journal of Heat and Mass Transfer,* Vol. 32, pp. 795–810.

Heping, T., Maestre, B., and Lallemand, M., 1991, "Transient and Steady-State Combined Heat Transfer in Semi-Transparent Materials Subjected of a Pulse or a Step Irradiation," ASME JOURNAL OF HEAT TRANSFER, Vol. 133, pp. 166–173.

Ho, C.-H., and Özişik, M. N., 1987, "Combined Conduction and Radiation in a Two-Layer Planar Medium with Flux Boundary Condition," *Numerical Heat Transfer,* Vol. 11, pp. 321–340.

Howe, J. T., Green, M. J., and Weston, K. C., 1973, "Thermal Shielding by Subliming Volume Reflectors in Convective and Intense Radiative Environments," *AIAA Journal,* Vol. 11, No. 7, pp. 989–994.

Kashiwagi, T., 1974, "A Radiative Ignition Model of a Solid Fuel," *Combustion Science and Technology,* Vol. 8, pp. 225–236.

Kindelan, M., and Williams, F. A., 1977, "Gas-Phase Ignition of a Solid with In-depth Absorption of Radiation," *Combustion Science and Technology,* Vol. 16, pp. 47–58.

Kubo, S., 1984, "Unsteady Radiative Heat Transfer in a Scattering-Dominant Medium," *AIAA Journal,* Vol. 22, pp. 1804–1809.

Kubo, S., and Hayashiguchi, E., 1981, "Effect of Scattering on Unsteady Radiative Heat Transfer," *Journal of the Physical Society of Japan,* Vol. 50, pp. 850–854.

Kumar, S., and Mitra, K., 1995, "Transient Radiative Transfer," *Radiative Transfer-I, Proceedings of the First International Symposium on Radiative Transfer,* Begell House, Inc., New York, pp. 488–504.

Lick, W., 1965, "Transient Energy Transfer by Radiation and Conduction," *International Journal of Heat and Mass Transfer,* Begell House, Inc., New York, Vol. 8, pp. 119–127.

Lii, C. C., and Özişik, M. N., 1972, "Transient Radiation and Conduction in an Absorbing, Emitting, Scattering Slab with Reflective Boundaries," *International Journal of Heat and Mass Transfer,* Vol. 15, pp. 1175–1179.

Longtin, J. P., and Tien, C.-L., 1997, "Efficient Laser Heating of Transparent Liquids Using Multiphoton Absorption," *International Journal of Heat and Mass Transfer,* Vol. 40, pp. 951–959.

Mann, D., Field, R. E., and Viskanta, R., 1992, "Determination of Specific Heat and True Conductivity of Glass from Dynamic Temperature Data," *Wärme- und Stoffübertragung,* Vol. 27, pp. 225–231.

Manohar, S. S., Kulkarni, A. K., and Thynell, S. T., 1995, "In-Depth Absorption of Externally Incident Radiation in Nongray Media," ASME JOURNAL OF HEAT TRANSFER, Vol. 117, pp. 146–151.

Matthews, L. K., Viskanta, R., and Incropera, F. P., 1985, "Combined Conduction and Radiation Heat Transfer in Porous Materials Heated by Intense Solar Radiation," *ASME Journal of Solar Energy Engineering,* Vol. 107, pp. 29–34.

Mutoh, N., Hirano, T., and Akita, K., 1978, "Experimental Study on Radiative Ignition of Polymethylmethacrylate," *Seventeenth Symposium (International) on Combustion,* The Combustion Inst., Pittsburgh, PA, pp. 1183–1190.

Park, S. H., and Tien, C. L., 1990, "Radiation Induced Ignition of Solid Fuels," *International Journal of Heat and Mass Transfer,* Vol. 33, pp. 1511–1520.

Petrov, V. A., 1997, "Combined Radiation and Conduction Heat Transfer in High Temperature Fiber Thermal Insulation," *International Journal of Heat and Mass Transfer,* Vol. 40, pp. 2241–2247.

Qian, C., Ishida, H., and Saito, K., 1994, "Upward Flame Spread Along PMMA Vertical Corner Walls, Part II: Mechanism of "M" Shape Pyrolysis Front Formation," *Combustion and Flame,* Vol. 99, pp. 331–338.

Rubtsov, N. A., Burka, A. L., and Stepanenko, P. I., 1978, "Transient Radiation-Conductive Heat Transfer in Selectively-Absorbing Media," *Heat Transfer 1978, Proceedings of the 6th International Heat Transfer Conference,* Vol. 3, Paper R-9, Hemisphere Publishing Corp., Washington, DC, pp. 361–365.

Saito, A., Mani, N., and Venart, J. E. S., 1976, "Combined Transient Conduction/Radiation Effects with the Line Source Technique of Measuring Thermal Conductivity," presented at the 16th National Heat Transfer Conference, St. Louis, August 8–11, Paper No. 76-CSME/CSChE-6.

Schwander, D., Flamant, G., and Olalde, G., 1990, "Effects of Boundary Properties on Transient Temperature Distributions in Condensed Semitransparent Media," *International Journal of Heat and Mass Transfer,* Vol. 33, pp. 1685–1695.

Seki, N., Sugawara, M., and Fukusako, S., 1978, "Radiative Melting of Horizontal Clear Ice Layer," *Wärme-und Stoffübertragung,* Vol. 11, pp. 207–216.

Seki, N., Sugawara, M., and Fukusaka, S., 1979, "Back-Melting of a Horizontal Cloudy Ice Layer with Radiative Heating," ASME JOURNAL OF HEAT TRANSFER, Vol. 101, pp. 90–95.

Shih, T. M., Hsu, I. C., and Cunnington, G. R., 1986, "Combined Conduction and Radiation with Phase Change in Teflon Slabs," *Radiation in Energy Systems,* T. W. Tong and M. F. Modest, eds., ASME, NY, pp. 25–31.

Siegel, R., 1987a, "Transient Radiative Cooling of a Droplet-Filled Layer," ASME JOURNAL OF HEAT TRANSFER, Vol. 109, pp. 159–164.

Siegel, R., 1987b, "Separation of Variables Solution for Non-Linear Radiative Cooling," *International Journal of Heat and Mass Transfer,* Vol. 30, pp. 959–965.

Siegel, R., 1987c, "Transient Radiative Cooling of a Layer Filled with Solidifying Drops," ASME JOURNAL OF HEAT TRANSFER, Vol. 109, pp. 977–982.

Siegel, R., 1987d, "Radiative Cooling of a Solidifying Droplet Layer Including Absorption and Scattering," *International Journal of Heat and Mass Transfer,* Vol. 30, pp. 1762–1765.

Siegel, R., 1989a, "Solidification by Radiative Cooling of a Cylindrical Region Filled with Drops," *Journal of Thermophysics and Heat Transfer,* Vol. 3, pp. 340–344.

Siegel, R., 1995a, "Two-Flux and Green's Function Method for Transient Radiative Transfer in a Semitransparent Layer," *Radiative Transfer-I, Proceedings of the First International Symposium on Radiative Heat Transfer,* Begell House, Inc., New York, pp. 473–487.

Siegel, R., 1995b, "Transient Emittance Limit for Cooling a Semitransparent Radiating Layer," *Journal of Thermophysics and Heat Transfer,* Vol. 9, pp. 373–375.

Siegel, R., 1996a, "Two-Flux Method for Transient Radiative Transfer in a Semitransparent Layer," *International Journal of Heat and Mass Transfer,* Vol. 39, pp. 1111–1115.

Siegel, R., 1996b, "Transient Heat Transfer in a Semitransparent Radiating Layer with Boundary Convection and Surface Reflections," *International Journal of Heat and Mass Transfer,* Vol. 39, pp. 69–79.

Siegel, R., 1996c, "Green's Function and Two-Flux Transient Analysis for a Composite," *Proceedings of the National Heat Transfer Conference,* ASME HTD-Vol. 325, ASME, NY, pp. 35–43.

Siegel, R., 1996d, "Two Flux Green's Function Analysis for Transient Spectral Radiation in a Composite," *Journal of Thermophysics and Heat Transfer,* Vol. 10, pp. 681–688.

Siegel, R., and Howell, J. R., 1992, *Thermal Radiation Heat Transfer,* 3rd ed, Hemisphere/Taylor and Francis, Washington, D.C.

Siegel, R., and Molls, F. B., 1992, "Finite Difference Solution for Transient Radiative Cooling of a Conducting Semitransparent Square Region," *International Journal of Heat and Mass Transfer,* Vol. 35, pp. 2579–2592.

Song, D., and Viskanta, R., 1990, "Deicing of Solids Using Radiant Heating," *Journal of Thermophysics and Heat Transfer,* Vol. 4, pp. 311–317.

Su, M.-H., 1995, "High Heat Flux in Glass," *International Communications in Heat and Mass Transfer,* Vol. 22, pp. 907–917.

Su, M.-H., and Sutton, W. H., 1995, "Transient Conductive and Radiative Heat Transfer in a Silica Window," *Journal of Thermophysics and Heat Transfer,* Vol. 9, pp. 370–373.

Thomas, J. R., Jr., 1992, "Coupled Radiation/Conduction Heat Transfer in Ceramic Liners for Diesel Engines," *Numerical Heat Transfer,* Part A, Vol. 21, pp. 109–120.

Timoshenko, V. P., and Trener, M. G., 1986, "A Method for Evaluating Heat Transfer in Multilayer Semitransparent Materials," *Heat Transfer-Soviet Research,* Vol. 18, pp. 44–57.

Tiwari, S. N., Singh, D. J., and Kumar, A., 1989, "Transient Energy Transfer by Conduction and Radiation in Nongray Gases," *Journal of Thermophysics and Heat Transfer,* Vol. 3, pp. 167–174.

Tsai, J.-H., and Lin, J.-D., 1990, "Transient Combined Conduction and Radiation with Anisotropic Scattering," *Journal of Thermophysics and Heat Transfer,* Vol. 4, pp. 92–97.

Tsai, C.-F., and Nixon, G., 1986, "Transient Temperature Distribution of a Multilayer Composite Wall with Effects of Internal Thermal Radiation and Conduction," *Numerical Heat Transfer,* Vol. 10, pp. 95–101.

Tsai, J. R., and Özişik, M. N., 1987, "Transient Combined Conduction and Radiation in an Absorbing, Emitting, and Isotropically Scattering Solid Sphere," *Journal of Quantitative Spectroscopy and Radiative Transfer,* Vol. 38, pp. 243–251.

Viskanta, R., and Lall, P. S., 1965, "Transient Cooling of a Spherical Mass of High Temperature Gas by Thermal Radiation," *Journal of Applied Mechanics,* Vol. 32, pp. 740–746.

Wu, C.-Y., and Ou, N.-R., 1994 "Transient Two-Dimensional Radiative and Conductive Heat Transfer in a Scattering Medium," *International Journal of Heat and Mass Transfer,* Vol. 37, pp. 2675–2686.

Yuen, W. W., Khatami, M., and Cunnington, G. R. Jr., 1990, "Transient Radiative Heating of an Absorbing, Emitting, and Scattering Material," *Journal of Thermophysics and Heat Transfer,* Vol. 4, pp. 193–198.

Additional References on Transient Radiation Effects in Translucent Materials

Barker, C., and Sutton, W. H., 1985, "The Transient Radiation and Conduction Heat Transfer in a Gray Participating Medium with Semitransparent Boundaries," *Radiation Heat Transfer,* B. F. Armaly and A. F. Emery, eds., ASME HTD-Vol. 49, ASME, NY, pp. 25–36.

Bathla, P. S., and Viskanta, R., 1968, "Effect of Surroundings on the Transient Energy Transfer in a Layer of Radiating Gas," *Applied Scientific Research,* Vol. 19, pp. 182–197.

Bathla, P. S., and Viskanta, R., 1969, "Transient Energy Transfer in Hot and Cold Layers of Radiating Gas During Expansion," *Acta Mechanica,* Vol. 7, pp. 119–136.

Burka, A. L., Rubtsov, N. A., Stepanenko, P. I., and Khripunov, A. D., 1976, "Investigation of Transient Radiation-Conduction Heat Transfer," *Proceedings of the 5th All-Union Heat Transfer Conference,* Minsk, Vol. 8, pp. 103–112.

Doornink, D. G., and Hering, R. G., 1972a, "Transient Combined Conductive and Radiative Heat Transfer," ASME JOURNAL OF HEAT TRANSFER, Vol. 94, pp. 473–478.

Doornink, D. G., and Hering, R. G., 1972b, "Transient Radiative Heat Transfer in a Nongray Medium," *Journal of Quantitative Spectroscopy and Radiative Transfer,* Vol. 12, pp. 1161–1174.

Glass, D. E., Özişik, M. N., and McRae, D. S., 1987, "Combined Conduction and Radiation with Flux Boundary Condition for a Semi-Transparent Medium Covered by Thin Radiating Layers," *Journal of Quantitative Spectroscopy and Radiative Transfer,* Vol. 38, pp. 201–208.

Hazzah, A. S., and Beck, J. V., 1970, "Unsteady Combined Conduction-Radiation Energy Transfer Using a Rigorous Differential Method," *International Journal of Heat and Mass Transfer,* Vol. 13, pp. 517–522.

Lall, P. S., and Viskanta, R., 1967, "Transient Energy Transfer in a Gray Radiating Gas During Expansion," *Physics of Fluids,* Vol. 10, pp. 98–107.

Melnikov, V. I., and Sukhovich, E. P., 1978, "Transient Heat Exchange Between a Radiating Plate and a High-Temperature Gas Flow," *Heat Transfer-Soviet Research,* Vol. 10, pp. 11–20.

Nemchinov, I. V., 1960, "Some Nonstationary Problems of Radiative Heat Transfer," *Zhurnal Prikladnoi Mekhaniki i Tekhnicheskoi Fiziki,* Vol. 1, pp. 36–57.

Prasad, K. K., and Hering, R. G., 1969, "Transient Radiative Heat Transfer in a Plane Layer," *International Journal of Heat and Mass Transfer,* Vol. 12, pp. 1331–1337.

Siegel, R., 1988, "Transient Radiative Cooling of an Absorbing and Scattering Cylinder—A Separable Solution," *Journal of Thermophysics and Heat Transfer,* Vol. 2, pp. 110–117.

Siegel, R., 1989b, "Some Aspects of Transient Cooling of a Radiating Rectangular Medium," *International Journal of Heat and Mass Transfer,* Vol. 32, pp. 1955–1966.

Siegel, R., 1990, "Emittance Bounds for Transient Radiative Cooling of a Scattering Rectangular Region," *Journal of Thermophysics and Heat Transfer,* Vol. 4, pp. 106–114.

Siegel, R., 1991, "Transient Cooling of a Square Region of Radiating Medium," *Journal of Thermophysics and Heat Transfer,* Vol. 5, pp. 495–501.

Siegel, R., 1992, "Finite Difference Solution for Transient Cooling of a Radiating-Conducting Semitransparent Layer," *Journal of Thermophysics and Heat Transfer,* Vol. 6, pp. 77–83.

Siegel, R., 1995c, "Refractive Index Effects on Transient Cooling of a Semitransparent Radiating Layer," *Journal of Thermophysics and Heat Transfer,* Vol. 9, pp. 55–62.

Sutton, W. H., 1986, "A Short Time Solution for Coupled Conduction and Radiation in a Participating Slab Geometry," ASME JOURNAL OF HEAT TRANSFER, Vol. 108, pp. 465–466.

Tong, T. W., McElroy, D. L., and Yarbrough, D. W., 1985, "Transient Conduction and Radiation Heat Transfer in Porous Thermal Insulations," *Journal of Thermal Insulation,* Vol. 9, pp. 13–19.

Tong, T. W., McElroy, D. L., and Yarbrough, D. W., 1986, "Analysis of Transient Heat Transfer Measurements Through Porous Thermal Insulations," *Journal of Thermal Insulation,* Vol. 10, pp. 31–46.

Tong, T. W., Yarbrough, D. W., McElroy, D. L., and Hou, Y. M., 1987, "Transient Conductive and Radiative Heat Transfer Through a Porous Layer with One Boundary Subject to a Time-Varying Temperature Condition," *Thermal Conductivity,* Vol. 19, pp. 467–479.

Tsukada, T., Kakinoli, K., and Hozawa, M., 1995, "Effect of Internal Radiation Within Crystal and Melt on Czochralski Crystal Growth of Oxide," *International Journal of Heat and Mass Transfer,* Vol. 38, No. 5, pp. 2707–2714.

Viskanta, R., and Anderson, E. E., 1975, "Heat Transfer in Semitransparent Solids," *Advances in Heat Transfer,* Vol. 11, pp. 317–441.

Viskanta, R., and Bathla, P. S., 1967, "Unsteady Energy Transfer in a Layer of Gray Gas by Thermal Radiation," *Z. Angew. Math. Phys.,* Vol. 18, pp. 353–367.

Weston, K. C., and Hauth, J. L., 1973, "Unsteady, Combined Radiation and Conduction in an Absorbing, Scattering, and Emitting Medium," ASME JOURNAL OF HEAT TRANSFER, Vol. 95, pp. 357–364.

Far-Infrared Radiation Modulators Using High-T_c Superconductors

Z. M. Zhang
Department of Mechanical Engineering,
University of Florida,
P.O. Box 116300,
Gainesville, FL 32611-6300
zzhang@cimar.me.ufl.edu

The potential of using high-T_c superconductors as intensity modulators for far-infrared radiation is investigated in this work. Reflectance and transmittance for several design structures are computed using the published optical constants of the superconductor $YBa_2Cu_3O_7$ and substrate materials. Notable differences in the reflectance and transmittance between the superconducting state and the normal state are illustrated. The best results are obtained based on the reflectance of thin films (10 nm–50 nm thick) on thin substrates (less than 100 μm thick) and for radiation incident on the substrate. This study demonstrates that high-T_c superconductive thin films can be used to build far-infrared radiation modulators. Future experimental study is recommended in order to materialize this promising thermo-optical device.

Introduction

A superconductor is in the superconducting state only at temperatures below the critical temperature (T_c), under either no bias current or a bias current less than the critical current, and subject to either no magnetic field or a magnetic field not to exceed the critical field. The transport and other properties of superconductors change abruptly between the superconducting and normal states, which could be used to make electronic and optical devices. For example, superconducting bolometers use the change of the electrical resistance of a superconductor in the transition region to measure the radiant power (Zhang and Frenkel, 1994, and references therein). High-T_c superconductors have been used to fabricate microwave switches and modulators based on the sudden change of microwave surface resistance (or transmission) between the superconducting and normal states (Karparkov et al., 1993; Poulin et al., 1995). These switching devices can be made very fast by optical or current pulses (Karasik et al., 1995). The high reflectivity of superconducting films in the far-infrared region has been explored for use in radiation shields and Fabry-Perot resonators (Malone et al., 1993a, 1993b, and references therein). However, the potential of using high-T_c films as radiation modulators in the far-infrared (30 μm–1000 μm wavelength) has not been investigated.

Radiation modulators or switches are important devices for spectroscopic and laser applications (Alius and Dodel, 1994; Grossman, 1989; Pankove, 1975). Far-infrared modulators are important devices for spectroscopic studies in the terahertz frequency range (Datla et al., 1995). Their applications include remote sensing of the earth's atmosphere, space temperature measurement, automotive and military radars, and molecular spectroscopy for materials characterization and process control. In the near and mid-infrared regions, oxides of vanadium, such as VO_2 and V_2O_3, have been used to build optical switches based on the phase transition from the semiconductor state to the metallic state (Lewis et al., 1995; De Natale, 1995). The far-infrared reflectance of an optically thick (opaque) superconducting film changes only a few percent from the normal state to the superconducting state (Renk et al., 1991; Van der Marel et al., 1991). The reflectance and transmittance of thin films, however, exhibited more striking changes (Flik et al., 1992; Gao et al., 1991; Hadni et al., 1995; Moser et al., 1993). This work investigates the feasibility of far-infrared radiation modulators based on high-T_c superconducting films, by evaluating the reflectance and transmittance for various designs in both the superconducting and normal states. The superconductor $YBa_2Cu_3O_7$ ($T_c \approx 90$ K) is used because it has been studied the most among all high-T_c superconductive materials.

The frequency- and temperature-dependent complex dielectric function recommended by Zhang et al. (1994a) is used to obtain the optical constants of $YBa_2Cu_3O_7$ in the superconducting state. This model accounts for the absorption by residual normal-state electrons, a finite electron scattering rate, and a mid-infrared absorption band due to interband electronic transitions. The Drude free-electron model is used for the normal state and for the residual normal electrons at temperatures lower than T_c. Different device arrangements and substrates are considered and compared. This study presents a promising thermo-optical device based on high-T_c superconducting thin films, and it suggests future theoretical and experimental research for realization of this kind of device.

Optical Constants

Optical Constants of the Superconductor $YBa_2Cu_3O_7$. Zhang et al. (1994a) used a dielectric function model with adjustable parameters for the *ab* plane of $YBa_2Cu_3O_7$, and obtained good agreement with the reflectance and absorptance data reported by many groups on *c*-axis oriented epitaxial films and single crystals. The frequency-dependent dielectric function can be expressed by a linear superposition (Tanner and Timusk, 1992):

$$\epsilon(\omega) = \epsilon_\infty + \epsilon_{\text{mir}}(\omega) + f_n\epsilon_n(\omega) + (1 - f_n)\epsilon_s(\omega), \quad (1)$$

where ϵ_n and ϵ_s are the contributions of the normal and superconducting electrons, respectively, and f_n is the fraction of normal electrons. The high-frequency dielectric constant $\epsilon_\infty \approx 4$. The mid-infrared band ϵ_{mir} is assumed to be a Lorentzian phonon oscillator with a center frequency of 1800 cm^{-1} (5.56 μm wavelength), a damping coefficient of 5000 cm^{-1}, and a plasma frequency of 18,000 cm^{-1} (Zhang et al., 1994a).

In the normal state, $f_n = 1$ and the last term in Eq. (1) is zero. The contribution of normal-state carriers is modeled using the Drude free-electron model. Two parameters, the dc conductivity σ_0 and the carrier scattering rate γ, are needed to calculate ϵ_n. A frequency-independent scattering rate is used in this study.

Contributed by the Heat Transfer Division for publication in the JOURNAL OF HEAT TRANSFER and presented at IMECE 1996, Atlanta. Manuscript received by the Heat Transfer Division September 17, 1996; revision received October 31, 1997; Keywords: Cryogenics; Heat Transfer; Radiation; Thermophysical. Associate Technical Editor: T. Tong.

The dc conductivity and the scattering rate change almost linearly with temperature in the normal state (Flik et al., 1992). The parameters are chosen to be $\sigma_0 \approx 1.6 \times 10^6\ (\Omega\ \text{m})^{-1}$ and $\gamma \approx 155\ \text{cm}^{-1}$ (2.91×10^{13} rad/s) at 100 K, and $\sigma_0 \approx 5.0 \times 10^5\ (\Omega\ \text{m})^{-1}$ and $\gamma \approx 500\ \text{cm}^{-1}$ at 300 K (Tanner and Timusk, 1992).

At temperatures below the critical temperature T_c, the contribution of the superconducting electrons ϵ_s is calculated from the algorithm developed by Zimmermann et al. (1991). The input parameters besides wavelength and temperature are the critical temperature T_c, the energy gap at 0 K, the dc conductivity σ_0, and the scattering rate γ. The parameters are taken from Zhang et al. (1994a): the critical temperature is $T_c = 91$ K and the frequency corresponding to the energy gap at 0 K is 500 cm^{-1} (20 μm wavelength). The dc conductivity and the scattering rate below T_c are obtained based on a fitting procedure described in the work of Flik et al. (1992). Near 0 K, the dc conductivity is taken to be $2.5 \times 10^6\ (\Omega\ \text{m})^{-1}$, and the scattering rate is 100 cm^{-1}. Due to defects, impurities, and possibly the free carriers in the CuO chains, the high-T_c superconductors exhibit residual absorption, even at temperatures much lower than T_c (Renk et al., 1991; Flik et al., 1992). This is accounted for by using a fraction of noncondensing (i.e., residual normal) electrons f_n. Below T_c, f_n is the ratio of the residual normal electron density to the total electron density, and it does not depend on temperature. Flik et al. (1992) obtained $f_n = 0.5$ for a set of thin films (10 nm–200 nm thick) at 10 K and 78 K. Zhang et al. (1994a) determined f_n to be between 0.15 and 0.3 for five high-quality opaque samples at temperatures from 10 K to 45 K.

The complex refractive index N is the square root of the dielectric function, i.e.,

$$N(\omega) = n(\omega) + i\kappa(\omega) = \sqrt{\epsilon(\omega)}, \qquad (2)$$

where n is the refractive index, and κ is the extinction coefficient. The calculated optical constants (n and κ) are plotted as functions of λ (the wavelength in vacuum) in Fig. 1 for different temperatures and f_n. The optical constants are almost independent of temperature at wavelengths less than the gap wavelength ($\approx$20 μm). At $\lambda > 30$ μm, n becomes much smaller, whereas κ becomes greater in the superconducting state than in the normal state. For an ideal superconductor, the dielectric function is a real negative, and the complex refractive index is purely imaginary ($n = 0$). It is the zero refractive index that makes an ideal superconductor lossless (nonabsorbing). Due to the mid-infrared band and residual normal electrons, the refractive index is not zero at low temperatures. The differences in optical constants between 10 K and 60 K are relatively small for $f_n = 0.2$. For $f_n = 0$, the refractive index at 10 K decreases towards long wavelengths. The key issue of using high-T_c superconductors as far-infrared modulators is whether changes in the optical constants could cause sufficient differences in the reflectance and transmittance between the superconducting and normal states. The change from the superconducting state to the normal state may be driven by a pulsed electrical current, magnetic field, or optical irradiation. Optical properties of high-T_c superconductors under strong current, field, or laser pulses need to be further investigated.

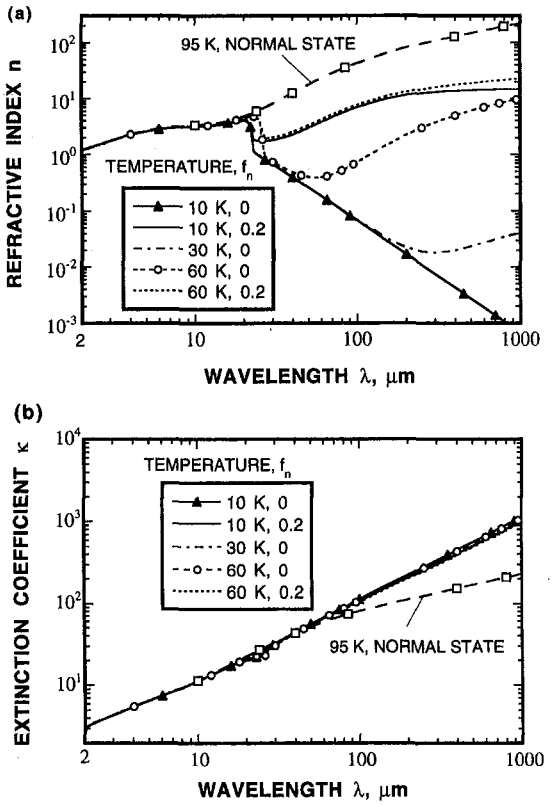

Fig. 1 Optical constants of the superconductor $YBa_2Cu_3O_7$: (*a*) refractive index n; (*b*) extinction coefficient κ.

Although the model discussed above is advantageous over the Mattis-Bardeen theory and the conventional two-fluid model (Phelan et al., 1992; Zhang et al., 1992; 1994a), there are several unresolved issues related to the optical properties of high-T_c superconductors. Examples are the existence of the energy gap, the mid-infrared and residual absorption mechanisms, the vortex dynamics, the controversy of s-wave versus d-wave, strong coupling versus weak coupling, and the dependence of the scattering rate upon temperature and frequency (Bonn et al., 1992; Hadni et al., 1995; Karrai et al., 1992; Tanner and Timusk, 1992). Other theories have been used in the literature (Akis et al., 1991; Gao et al., 1991). For films as thin as 35 nm and in the normal state, the refractive index of bulk materials can be used to calculate the radiative properties of thin films (Phelan et al., 1992). Thin films (<25 nm thick), however, often possess inferior properties, e.g., a slightly lower T_c, a lower electrical conductivity, and a larger scattering rate (Flik et al., 1992; Zhang et al., 1992). These effects are not consid-

Nomenclature

d = thickness, m
f_n = fraction of normal electrons
$i = (-1)^{1/2}$
N = complex refractive index
n = refractive index, i.e., real part of N
R = reflectance
T = transmittance
T_c = critical temperature, K
γ = electron scattering rate, rad/s
ϵ = dielectric function
ϵ_0 = electrical permittivity of free space, 8.854×10^{-12} C/(V m)
ϵ_{mir} = mid-infrared absorption band due to interband electronic transitions
ϵ_n = contributions of the normal electrons to the dielectric function
ϵ_s = contributions of the superconducting electrons to the dielectric function
ϵ_∞ = high-frequency dielectric constant
κ = extinction coefficient, i.e., imaginary part of N
λ = wavelength in vacuum, m
ρ_F = reflectivity at the air-film interface
σ_0 = dc conductivity, $(\Omega\ \text{m})^{-1}$
ω = angular frequency, rad/s

Subscripts

F = film
S = substrate

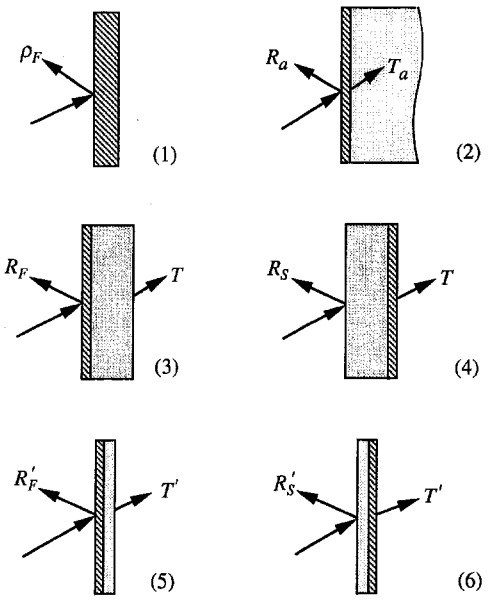

Fig. 2 Illustration of the reflectance and transmittance for six different designs: (1) an optically thick film; (2) a thin film on a semi-infinite substrate; (3) a thin film on a thick substrate, incident on the film; (4) a thin film on a thick substrate, incident on the substrate; (5) a thin film on a thin substrate, incident on the film; (6) a thin film on a thin substrate, incident on the substrate.

ered in the present paper. However, the predicted results are compared with published data whenever possible.

Optical Constants of Substrates. The best films made so far are on $SrTiO_3$ and $LaAlO_3$ substrates. $SrTiO_3$ is not a suitable substrate for thin-film applications due to its large dielectric constant (highly reflecting in the far-infrared). In the present study, the optical constants of $LaAlO_3$ are calculated from the Lorentzian phonon model obtained by Zhang et al. (1994b). Perhaps Si and MgO are the most suitable substrates since they are transparent in the far-infrared region, and they can be used to grow films of relatively high quality. The far-infrared complex refractive index of MgO has been determined by Cunsolo et al. (1992) from transmittance and reflectance measurements. MgO is opaque in the mid-infrared due to phonon absorption, and becomes transparent in the far infrared. The onset wavelength is $\lambda \approx 100$ μm at room temperature and $\lambda \approx 30$ μm at 20 K. At temperatures below 100 K, the absorption is very small and the refractive index changes less than 5 percent between 20 K and 100 K for 100 μm $< \lambda <$ 300 μm (Cunsolo et al., 1992). Silicon has a wide transparent window in the mid and far infrared, can be used to grow high-quality films, and can be made very thin by micromachining techniques (Fenner et al., 1992). A buffer layer, such as yttria-stabilized zirconia (YSZ) or CeO_2, is needed due to the lattice mismatch between $YBa_2Cu_3O_7$ and Si. Since this layer is of the order of 50 nm thick, the absorption and dispersion by the buffer layer are insignificant in the far infrared because of the small κ values of the dielectric materials in the far infrared. The absorption of undoped Si is negligibly small, and the change of the refractive index is less than 1 percent from room temperature down to 1.5 K for 30 μm $< \lambda <$ 300 μm (Loewenstein et al., 1973). Therefore, the refractive index of Si is $\approx$3.4 and its extinction coefficient is $\approx$0.

Reflectance and Transmittance

Six possible design structures for radiation modulation are shown in Fig. 2. Design 1 is based on an optically thick film. The penetration depth ($\lambda/4\pi\kappa$) of the superconductor $YBa_2Cu_3O_7$ is $\approx$100 nm at 100 K and at $\lambda = 100$ μm, and reduces as temperature decreases. A film of thickness greater than 400 nm would be essentially opaque, though the penetration depth increases with wavelength in the normal state. Design 2 consists of a thin film on a semi-infinite substrate. The substrate may be optically thick or wedged so that multiple reflections in the substrate are eliminated. The equations for computing ρ_F, R_a, and T_a are from Heavens (1965). Designs 3 and 4 are composed of thin films on thick transparent substrates. The interference effects in the substrate are eliminated either by using a lower instrumental resolution or by using a numerical averaging method. Therefore, radiation in the substrate is incoherent. This approach is applicable to $d_S \geq 0.5$ mm and $\lambda \leq 300$ μm. The reflectance for incidence on the film (R_F in design 3) is different from that for incidence on the substrate (R_S in design 4), but the transmittance (T) is the same for either incidence. The values R_F, R_S, and T are calculated using the expressions presented by Choi et al. (1992) and Zhang et al. (1995). Designs 5 and 6 are for thin substrates ($d_S <$ 100 μm) and for long wavelengths ($\lambda >$ 100 μm). In this case, the interference effects of the substrate are significant and must be taken into account. Radiation may be incident either on the film or on the substrate (see Fig. 2). The expressions for R'_F, R'_S, and T' can be derived from thin-film optics (Heavens, 1965).

Partial coherence theory may be used to calculate optical properties of layered structures with intermediate degrees of coherence (Chen and Tien, 1992; Zhang, 1994). For demonstration purposes, radiation in the substrate is treated as either completely coherent or completely incoherent. Transmittance and reflectance of multilayer structures may be calculated using the matrix formulation described by Zhang and Flik (1993). Since the buffer layer has little effect on the far-infrared properties, only two layers (film and substrate) are considered. The reflectance and transmittance depend on the angle of incidence, and the superconductor $YBa_2Cu_3O_7$ is anisotropic. The optical properties of metallic materials for random polarization change little with the angle of incidence unless it is close to 90 deg. Malone et al. (1993b) calculated the radiation exchange between two parallel surfaces (at least one is made of a high-T_c superconducting film), and found that the influence of the c-axis optical constants was small ($\leq$5 percent). Therefore, the direction of incidence is assumed to be normal to the film.

Results and Discussions

The calculated reflectivity for design 1 with opaque films is shown in Fig. 3, together with measured data at 10 K and 95 K from Renk et al. (1991). The predicted reflectivity agrees well with those measured within the experimental uncertainty of 0.005. The reflectivity is quite high in the far-infrared, even in the normal state. This is because of the metallic behavior of $YBa_2Cu_3O_7$ in the normal state, i.e., large n and κ (as shown in Fig. 1). Notice that with $f_n = 0.2$, the calculated reflectivity

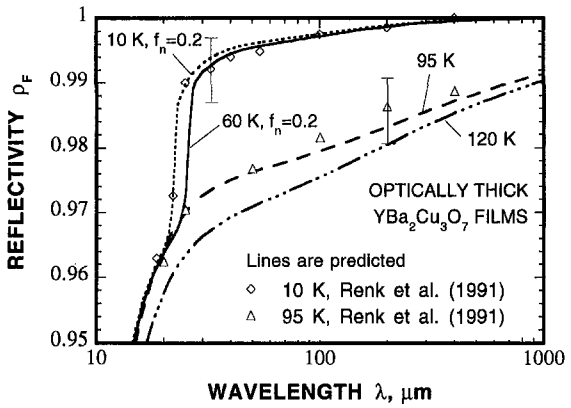

Fig. 3 Reflectance for optically thick films (design 1 in Fig. 2)

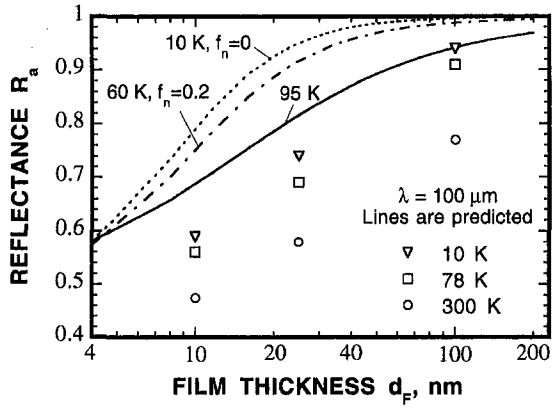

Fig. 4 Reflectance for films on semi-infinite $LaAlO_3$ substrates (design 2) at $\lambda = 100$ μm, the data are from Flik et al. (1992)

at 10 K is similar to that at 60 K. The reflectivity at 10 K is less than 1 at wavelengths longer than the gap wavelength due to absorption by the mid-infrared band and residual normal electrons. The difference between the superconducting and normal states is less than 0.03, which is too small for modulation applications.

The reflectance of thin films on semi-infinite substrates (design 2) exhibits a distinct difference between the superconducting and normal states, as shown in Fig. 4. The complex refractive index of a $LaAlO_3$ is taken to be $5.5 + i2.6 \times 10^{-2}$ at temperatures from 10 K to 95 K (Zhang et al., 1994b). The predicted maximum difference in reflectance between 60 K and 95 K is 0.10 for a $LaAlO_3$ substrate. Flik et al. (1992) measured the reflectance for several thin films on $LaAlO_3$ substrates at wavelengths up to 100 μm, which is shown in Fig. 4. Although the measured R_a is consistently lower than the calculated, the temperature dependence of R_a is consistent between the measured and the predicted reflectance. Using different values of σ_0, f_n, and γ, Flik et al. (1992) fitted the data to an agreement of 2–3 percent at wavelengths between 10 μm and 100 μm. Since the objective of the present study is to evaluate different designs, all the parameters are fixed for the calculation of the optical constants. The optical constants of thin films in the far-infrared region (beyond 100 μm) merit further investigation. Calculations of the wavelength-dependent reflectance for a 20 nm film showed that the reflectance at 95 K increases slightly, whereas the reflectance in the superconducting state increases rapidly as wavelength increases. Therefore, the difference in reflectance increases with wavelength.

The predicted transmittance as a function of film thickness at $\lambda = 200$ μm is shown in Fig. 5 for thick MgO substrates

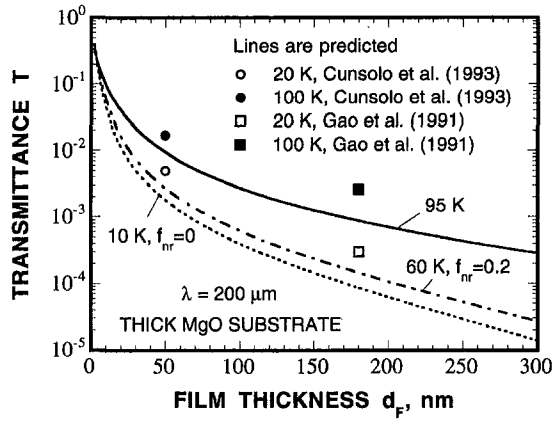

Fig. 5 Transmittance versus film thickness at $\lambda = 200$ μm for thick MgO substrates (design 3)

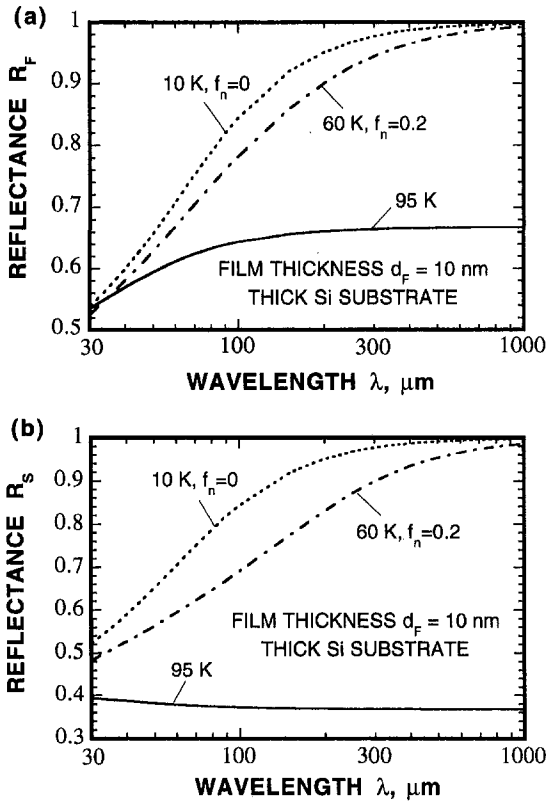

Fig. 6 Reflectance of thin-film/thick-substrate structures: (*a*) radiation incident on the film (design 3); (*b*) radiation incident on the substrate (design 4).

(design 3) together with data from Cunsolo et al. (1993) and Gao et al. (1991). The transmittance decreases as d_F increases. Cunsolo et al. (1993) measured the transmittance for a 50 nm film on a 0.5 mm MgO substrate. The values at $\lambda = 200$ μm are ≈0.005 at 20 K and ≈0.017 at 100 K. Gao et al. (1991) measured the far-infrared transmittance for a 180 nm thick film on a wedged 1 mm thick MgO substrate using a synchrotron source. At $\lambda = 200$ μm, they obtained a transmittance of 0.0003 at 20 K and 0.0026 at 100 K. As shown in Fig. 5, the predicted values are lower than the measured data because of the large σ_0 and small f_n used in calculating the optical constants. Although the change in transmittance is significant for $d_F > 20$ nm, the absolute value of transmittance is too low for practical applications. The penetration depth in the normal state increases as the wavelength increases (since $\kappa \propto \lambda^{1/2}$ for large λ as predicted by the Drude model), whereas the penetration depth in the superconducting state does not change significantly (Zhang et al., 1994a). Hence, the transmittance change is more distinct in the microwave region (Hangyo et al., 1993; Moser et al., 1993).

In Figs. 6 to 8, the substrate is taken to be Si, with a refractive index of 3.4 and an extinction coefficient of 0 (Loewenstein, 1973). The calculated results using MgO substrates are similar because the refractive indices of MgO and Si for $\lambda > 100$ μm are not very different at temperatures below 100 K. The reflectance of a film on a thick substrate is shown in Fig. 6 for radiation incident either on the film (design 3) or on the substrate (design 4). Notice that R_F is always higher than R_S. The differences in reflectance between the superconducting and normal states are significant, especially for R_S. The difference increases with wavelength quickly from 30 μm to 100 μm and slowly from 100 μm to 1000 μm. Calculation showed that there exists an optimized film thickness which yields the largest difference in R_F or R_S. The optimized d_F is somewhere between 10 nm and 20 nm. Cunsolo et al. (1993) observed a difference

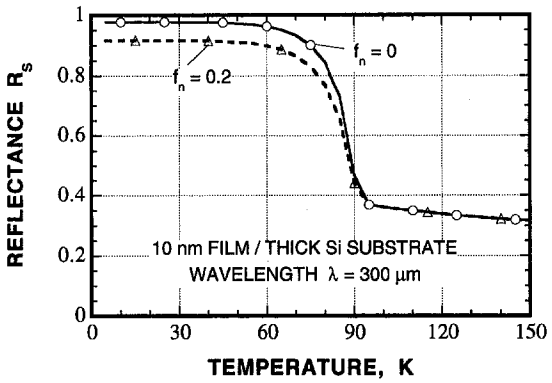

Fig. 7 Temperature-dependent reflectance at λ = 300 μm for f_n = 0 and 0.2 (design 4)

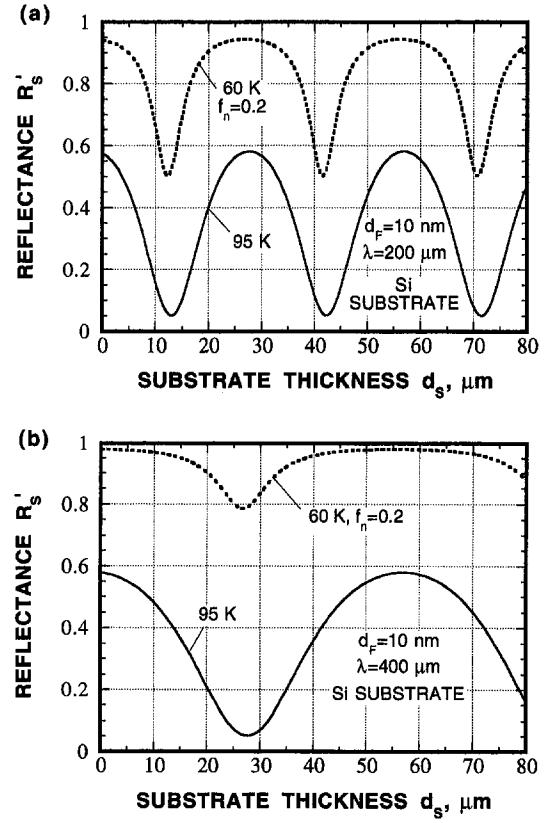

Fig. 8 Reflectance versus substrate thickness for d_F = 10 nm (design 6): (*a*) λ = 200 μm; (*b*) λ = 400 μm.

in R_F of about 0.08 between 20 K and 100 K at 50 μm ≤ λ ≤ 100 μm with a 50 nm thick $YBa_2Cu_3O_7$ film on a 0.5 mm thick MgO substrate. The calculated difference in R_F for a 50 nm thick film on a thick MgO substrate is ≈0.1 between 10 K and 100 K at λ = 100 μm, which is consistent with the measured difference. The absolute values of the predicted reflectance, however, are always higher than the experimental data for the reason discussed above.

The temperature dependence of R_S is evident in Fig. 7 (d_F = 10 nm at λ = 300 μm), i.e., it decreases more than 0.5 from 60 K to 95 K. The large difference has not been observed by experiments because all data reported so far are for incidence on the film. It has been noticed that incidence from the substrate side could increase the absorptance of film/substrate composites (Zhang and Frenkel, 1994). The change in the reflectance is sufficient for intensity modulation of far-infrared radiation.

The free spectral range (FSR), i.e., the spacing between two interference extrema, for a 0.5 mm thick Si substrate is $(2n_Sd_S)^{-1} \approx 3\ \text{cm}^{-1}$. It increases as d_S decreases. In the far-infrared measurements, the instrumental resolution is often comparable to the FSR, resulting in notable interference fringes (Hadni et al., 1995). Far-infrared lasers are often used because of their high intensity. In this case, the radiation is confined in a narrow spectral width and is coherent in both the film and the substrate. Therefore, interference effects in the substrate must be included. The reflectance of thin-film/thin-substrate composites (design 6) is shown in Fig. 8. The reflectance R_S' changes periodically with d_S. The period is $\Delta d_S = \lambda/2n_S$ (Bonn and Wolf, 1980), which is ≈30 μm for λ = 200 μm and ≈59 μm for λ = 400 μm. The contrast in reflectance between 60 K and 95 K is distinct, in particular, at the reflectance minimum. At λ = 200 μm, the reflectance changes from ≈0.05 (at 95 K) to ≈0.5 (at 60 K) for $d_S \approx$ 13 μm, 43 μm, 72 μm, and so on. At λ = 400 μm, the reflectance changes from ≈0.05 (at 95 K) to ≈0.79 (at 60 K) for $d_S \approx$ 27.5 μm, 86 μm, and so on. The change in R_F' is not as prominent because R_F' is much greater than R_S' in the normal state. For a given d_S, the reflectance and transmittance depend on wavelength. Hence, far-infrared modulators based on thin-film/thin-substrate structures are sensitive to wavelength. The notable differences in reflectance illustrate that high-T_c superconductors can be used to build far-infrared intensity modulators. The reflectance for incidence on the substrate must be experimentally investigated to verify the predicted results.

The calculated transmittance for design 5 at λ = 400 μm and d_F = 10 nm changes from ≈0.0064 (at 95 K) to ≈0.058 (at 60 K) for a Si substrate with d_S = 56 μm (where the transmittance is minimum). The transmittance for the thin-film/thin-substrate structure is also too small to be used for far-infrared modulators. Hadni et al. (1995) measured the transmittance spectra for a 20 nm thick film on a 0.53 mm thick MgO substrate, and observed spectral oscillations in the far-infrared region from 250 μm to 1000 μm wavelength. At λ ≈ 470 μm, where the transmittance is minimum, the transmittance changes from ≈0.07 at 53 K to ≈0.2 at 105 K (Hadni et al., 1995). Since the radiation in the substrate is partially coherent in this case, it is possible that the measured transmittance minima are greater than the predicted ones using the expression for completely coherent situation. The optical constants of thin films may differ from those for bulk materials as discussed above.

Conclusions

This work demonstrates a promising application of high-T_c superconductive thin films as far-infrared intensity modulators by calculating the reflectance and transmittance in both the superconducting and normal states for several possible device arrangements. The differences in reflectance at temperatures from 60 K to 95 K are substantial, especially for radiation incident on the substrate. The difference could be further enhanced by optimizing the thicknesses of both the film and the substrate for any given wavelength. For example, at λ = 400 μm, the reflectance could be reduced by nearly 16 times (from 0.79 to 0.05) when the temperature is increased from 60 K to 95 K. Measurements of the reflectance of thin-film/thin-substrate structures for incidence on the substrate are required to realize this type of device. The optical constants for thin films could be different from those obtained for opaque samples. Further studies are needed to accurately determine the optical constants of thin films (10 nm–50 nm thick) in the far-infrared region.

Acknowledgments

The author would like to thank Professor D. B. Tanner for valuable discussions and B. C. Johnson for carefully reviewing the manuscript. The official reviewers' comments are much

appreciated. This work has been supported by the University of Florida through an Interdisciplinary Research Initiative award.

References

Akis, R., Carbotte, J. P., Timusk, T., 1991, "Superconducting Optical Conductivity for Arbitrary Temperature and Mean Free Path," *Phys. Rev. B,* Vol. 43, pp. 12804–12808.

Alius, H., and Dodel, G., 1994, "Far-Infrared Modulation Techniques Based on Optical Excitation of Semiconductors," *Infrared Phys. Technol.,* Vol. 35, pp. 73–78.

Bonn, D. A., Dosanjh, P., Liang, R., and Hardy, W. N., 1992, "Evidence of Rapid Suppression of Quasiparticle Scattering below T_c in $YBa_2Cu_3O_{7-\delta}$," *Phys. Rev. Lett.,* Vol. 68, pp. 2390–2393.

Born, M., and Wolf, E., 1980, *Principles of Optics,* 6th ed., Pergamon Press, Oxford, UK, pp. 1–66.

Chen, G., and Tien, C. L., 1992, "Partial Coherence Theory of Thin Film Radiative Properties," ASME JOURNAL OF HEAT TRANSFER, Vol. 114, pp. 636–643.

Choi, B. I., Zhang, Z. M., Flik, M. I., and Siegrist, T., 1992, "Radiative Properties of Y-Ba-Cu-O Films with Variable Oxygen Content," ASME JOURNAL OF HEAT TRANSFER, Vol. 114, pp. 958–964.

Cunsolo, S., Dore, P., Lupi, S., Maselli, P., and Varsamis, C. P., 1992, "Complex Refractive Index of MgO in the Far Infrared from Transmittance and Reflectance Measurements," *Infrared Phys.,* Vol. 33, pp. 539–548.

Cunsolo, S., Dore, P., Lupi, S., Trippetti, R., Varsamis, C. P., and Sherman, A., 1993, "Infrared Conductivity of YBCO from Transmittance and Reflectance Spectra of Thin Films," *Physica C,* Vol. 211, pp. 22–28.

Datla, R., Grossman, E., and Hobish, M. K., 1995, "Metrology Issues in Terahertz Physics and Technology," *J. Res. Natl. Inst. Stand. Technol.,* Vol. 100, pp. 717–723.

De Natale, J. F., 1995, "Thin Film Optical Switching Materials," *MRS Symp. Proc.,* Vol. 374, pp. 87–97.

Fenner, D. B., Li, Q., Hamblen, W. D., Johansson, M. E., Hamblen, D. G., Lynds, L., Budnick, J. I., 1992, "Optical and Thermal Performance Advantages for Silicon Substrates in YBCO Bolometer Devices," *IEEE Trans. Appl. Supercond.,* Vol. 3, pp. 2104–2106.

Flik, M. I., Zhang, Z. M., Goodson, K. E., Siegal, M. P., and Phillips, J. M., 1992, "Electron Scattering Rate in Epitaxial $YBa_2Cu_3O_7$ Superconducting Films," *Phys. Rev. B,* Vol. 46, pp. 5606–5614.

Gao, F., Carr, G. L., Porter, C. D., Tanner, D. B., Etemad, S., Venkatesan, T., Inam, A., Dutta, B., Wu, X. D., Williams, G. P., and Hirschmugl, C. J., 1991, "Far-Infrared Transmittance and Reflectance Studies of Oriented $YBa_2Cu_3O_{7-\delta}$ Thin Films," *Phys. Rev. B,* Vol. 43, pp. 10383–10389.

Grossman, E. N., 1989, "Optically Illuminated Dielectric Interfaces as High-Speed Far-Infrared Modulator," *Intl. J. Infrared and Millimeter Waves,* Vol. 10, pp. 803–820.

Hadni, A., Gerbaux, X., Cudraz, H. M., Tazawa, M., Mage, J. C., Marcilhac, B., Mercandalli, L., and Mansart, D., 1995, "Residual Losses of Superconducting Thin Films of $YBa_2Cu_3O_{7-\delta}$ in the Far Infrared and Microwaves: Applications," *Physica C,* Vol. 245, pp. 219–230.

Hangyo, M., Nagashima, T., Nagasaki, N., Nakashima, S., Enami, H., and Murakami, Y., 1993, "Transmittance of $YBa_2Cu_3O_7$ Thin Films in the Millimeter Wave Region," *IEEE Trans. Appl. Supercond.,* Vol. 3, pp. 1737–1740.

Heavens, O. S., 1965, *Optical Properties of Thin Solid Films,* Dover Publications, Inc., N.Y., pp. 46–95.

Karasik, B. S., Milostnaya, I. I., Zorin, M. A., Elantev, A. I., Gol'tsman, G. N., and Gershenzon, E. M., 1995, "High Speed Current Switching of Homogeneous YBaCuO Film Between Superconducting and Resistive States," *IEEE Trans. Appl. Supercond.,* Vol. 5, pp. 3042–3045.

Karparkov, D. I., Kuznetsov, V. V., Löfgren, M., and Vendik, I. B., 1993, "Nonreflective High-T_c Superconductor Modulator," *Electronics Lett.,* Vol. 29, pp. 1006–1007.

Karrai, K., Choi, E., Dunmore, F., Liu, S., Ying, X., Li, Q., Venkatesan, T., Drew, H. D., Li, Q., and Fenner, D. B., 1992, "Far-Infrared Magneto-Optical Activity in Type-II Superconductors," *Phys. Rev. Lett.,* Vol. 69, pp. 355–358.

Lewis, K. L., Pitt, A. M., Wyatt-Davies, T., and Milward, J. R., 1995, "Thin Film Thermochromic Materials for Non-Linear Optical Devices," *MRS Symp. Proc.,* Vol. 374, pp. 105–116.

Loewenstein, E. V., Smith, D. R., and Morgan, R. L., 1973, "Optical Constants of Far Infrared Materials 2: Crystalline Solids," *Appl. Opt.,* Vol. 12, pp. 398–406.

Malone, C. G., Zhang, Z. M., Flik, M. I., and Cravalho, E. G., 1993a, "Optimized Design of Far-Infrared Fabry-Perot Resonators Fabricated From $YBa_2Cu_3O_7$," *IEEE Trans. Appl. Supercond.,* Vol. 3, pp. 2852–2855.

Malone, C. G., Whale, M. D., Flik, M. I., and Cravalho, E. G., 1993b, "Performance of Widely Spaced High-T_c Superconductor Radiation Shields," ASME Paper No. 93-WA/HT-64, pp. 1–9.

Moser, E. K., Tomasch, W. J., Furdyna, J. K., Coffey, M. W., and Clem, J. R., 1993, "Transmittance and Reflectance of Superconducting $YBa_2Cu_3O_{7-x}$ Films at 35 GHz," *IEEE Trans. Appl. Supercond.,* Vol. 3, pp. 1119–1122.

Pankove, J. I., 1975, *Optical Processes in Semiconductors,* Dover Publications, Inc., NY, pp. 391–407.

Phelan, P. E., Flik, M. I., and Tien, C. L., 1991, "Radiative Properties of Superconducting Y-Ba-Cu-O Thin Films," ASME JOURNAL OF HEAT TRANSFER, Vol. 113, pp. 487–493.

Phelan, P. E., Chen, G., and Tien, C. L., 1992, "Thickness-Dependent Radiative Properties of Y-Ba-Cu-O Thin Films," ASME JOURNAL OF HEAT TRANSFER, Vol. 114, pp. 227–233.

Poulin, G. D., Hegmann, F. A., Lachapelle, J., Moffat, S. H., Preston, J. S., 1995, "A Superconducting Microwave Switch," *IEEE Trans. Appl. Supercond.,* Vol. 5, pp. 3046–3048.

Renk, K. F., Gorshunov, B., Schützmann, J., Prückl, A., Brunner, B., Betz, J., Orbach, S., Klein, N., Müller, G., and Piel, H., 1991, "Far-Infrared and Microwave Intragap Absorption in a $YBa_2Cu_3O_{7-\delta}$ Thin Film at Low Temperature," *Europhys. Lett.,* Vol. 15, pp. 661–666.

Tanner, D. B., and Timusk, T., 1992, "Optical Properties of High-Temperature Superconductors," in *Physical Properties of High-Temperature Superconductors,* Vol. 3, D. M. Ginsberg, ed., World Scientific Publishing Co., Singapore, pp. 363–469.

Van der Marel, D., Habermeier, H.-U., Heitmann, D., König, W., and Wittlin, A., 1991, "Infrared Study of the Superconducting Phase Transition in $YBa_2Cu_3O_{7-x}$," *Physica C,* Vol. 176, pp. 1–18.

Zhang, Z. M., Choi, B. I., Le, T. A., Flik, M. I., Siegal, M. P., and Phillips, J. M., 1992, "Infrared Refractive Index of Thin $YBa_2Cu_3O_7$ Superconducting Films," ASME JOURNAL OF HEAT TRANSFER, Vol. 114, pp. 644–652.

Zhang, Z. M., and Flik, M. I., 1993, "Predicted Absorptance of $YBa_2Cu_3O_7$/YSZ/Si Multilayer Structures for Infrared Detectors," *IEEE Trans. Appl. Supercond.,* Vol. 3, pp. 1604–1607.

Zhang, Z. M., 1994, "Optical Properties of Layered Structures for Partially Coherent Radiation," in *Heat Transfer 1994—Proceedings of the Tenth International Heat Transfer Conference,* Vol. 2, G. F. Hewitt, ed., Taylor & Francis, PA, pp. 177–182.

Zhang, Z. M., and Frenkel, A., 1994, "Thermal and Nonequilibrium Responses of Superconductors for Radiation Detectors," *Journal of Superconductivity,* Vol. 7, pp. 871–884.

Zhang, Z. M., Le, T. A., Flik, M. I., and Cravalho, E. G., 1994a, "Infrared Optical Constants of the High-T_c Superconductor $YBa_2Cu_3O_7$," ASME JOURNAL OF HEAT TRANSFER, Vol. 116, pp. 253–257.

Zhang, Z. M., Choi, B. I., Flik, M. I., and Anderson, A. C., 1994b, "Infrared Refractive Indices of $LaAlO_3$, $LaGaO_3$, and $NdGaO_3$," *J. Opt. Soc. Amer. B,* Vol. 11, pp. 2252–2257.

Zhang, Z. M., Datla, R. U., and Hanssen, L. M., 1995, "Development of Neutral-Density Infrared Filters Using Metallic Thin Films," *MRS Symp. Proc.,* Vol. 374, pp. 117–122.

Zimmermann, W., Brandt, E. H., Bauer, M., Seider, E., and Genzel, L., 1991, "Optical Conductivity of BCS Superconductors with Arbitrary Purity," *Physica C,* Vol. 183, pp. 99–104.

M. Asheghi

M. N. Touzelbaev

K. E. Goodson

goodson@vk.stanford.edu
Mechanical Engineering Department,
Stanford University,
Stanford, CA 94305-3030

Y. K. Leung

S. S. Wong

Electrical Engineering Department,
Stanford University,
Stanford, CA 94305-3030

Temperature-Dependent Thermal Conductivity of Single-Crystal Silicon Layers in SOI Substrates

Self heating diminishes the reliability of silicon-on-insulator (SOI) transistors, particularly those that must withstand electrostatic discharge (ESD) pulses. This problem is alleviated by lateral thermal conduction in the silicon device layer, whose thermal conductivity is not known. The present work develops a technique for measuring this property and provides data for layers in wafers fabricated using bond-and-etch-back (BESOI) technology. The room-temperature thermal conductivity data decrease with decreasing layer thickness, d_s, to a value nearly 40 percent less than that of bulk silicon for $d_s = 0.42$ μm. The agreement of the data with the predictions of phonon transport analysis between 20 and 300 K strongly indicates that phonon scattering on layer boundaries is responsible for a large part of the reduction. The reduction is also due in part to concentrations of imperfections larger than those in bulk samples. The data show that the buried oxide in BESOI wafers has a thermal conductivity that is nearly equal to that of bulk fused quartz. The present work will lead to more accurate thermal simulations of SOI transistors and cantilever MEMS structures.

1 Introduction

Silicon-on-insulator (SOI) circuits promise advantages in speed and processing expense compared to circuits made from bulk silicon (e.g., Peters, 1993). The buried silicon-dioxide layer in SOI circuits has a very low thermal conductivity, which results in a large thermal resistance between the device and the chip packaging. This is a major problem for transistors that experience brief pulses of heating, such as ESD protection devices (e.g., Amerasekera et al., 1992), for which the temperature rise is dominated by conduction within micrometers of active regions. Lateral conduction parallel to the plane of the wafer in the silicon device layer can strongly reduce the temperature rise in active regions, such as the transistor channel (Goodson et al., 1995). However, this effect cannot be accurately predicted at present because the thermal conductivity of the device layer is not known. The lateral thermal conductivity of the silicon layer in SOI substrates is also important for the design of many MicroElectroMechanical Systems (MEMS) which use single-crystal silicon cantilevers that are etched from SOI substrates. One example is the cantilever of Chui et al. (1996), which uses heat pulses to make sub-micrometer pits in PMMA for high-density data storage.

Heat conduction in silicon is dominated by phonon transport, even in the presence of large concentrations of free charge carriers. The device-layer thermal conductivity is reduced compared to that of bulk silicon due to scattering mechanisms in the layer that are not present in the bulk material, such as those depicted in Fig. 1. Phonon-boundary scattering is particularly important at low temperatures, where the mean free path would otherwise become arbitrarily large. While phonon-boundary interactions govern the thermal conductivity of any silicon sample at low enough temperatures, the reduction is more severe and extends to higher temperatures for thin layers than for bulk samples. Also important is phonon scattering on imperfections, which exist in larger concentrations in SOI substrates than in bulk material. The higher concentrations result from steps in the wafer fabrication process, such as SIMOX implantation (e.g., Cellar and White, 1992) and the epitaxial growth process of BESOI wafers (Maszara, 1991). While the impact of these imperfections on electrical transport has been studied, there has been little progress on modeling or measuring their impact on heat transport. Finally, the impurities and additional free carriers in doped semiconducting regions impede heat transport compared to that in bulk intrinsic silicon (Goodson and Cooper, 1995). There are data available for the thermal conductivity of bulk doped samples (Touloukian et al., 1970a) which show a strong reduction for impurity concentrations greater than about 5×10^{19} cm^{-3}, but it is not clear if the bulk data are appropriate for layers doped using thin-film implantation and diffusion techniques.

Previous work (Paul et al., 1993, 1994; Von Arx and Baltes, 1992; Von Arx et al., 1995; Mastrangelo and Müller, 1988; Tai et al., 1988) measured the lateral thermal conductivity of doped polysilicon layers. These authors reported a reduction of up to 80 percent compared to the conductivity of bulk intrinsic silicon. While it is not clear which of the mechanisms shown in Fig. 1 is responsible for the reduction in the polysilicon layers for which data are available, it is likely that the grain boundaries are responsible for a fraction of the reduction. It would therefore be inappropriate to assume that the thermal conductivity of the crystalline layers in SOI substrates can be determined using the existing data for polycrystalline samples.

Very few data are available for the thermal conductivity of single-crystal silicon samples with submillimeter dimensions. Savvides and Goldsmid (1973) measured the thermal conductivity of pure and neutron-irradiated crystalline silicon with dimensions comparable to 20, 40, 60, and 100 μm at temperatures of 200 and 300 K. They did not observe a size effect on the thermal conductivity even for the thinnest pure silicon specimen at 200 K. Yu et al. (1996) measured the thermal diffusivity of a 4 μm thick, free-standing silicon film at room temperature and observed no significant reduction in the thermal diffusivity compared to that of bulk samples. However, a recent study reported a two orders of magnitude reduction in the thermal conductivity of a 0.15 μm thick silicon layer made using SIMOX technology at temperatures between 330 and 380 K

Contributed by the Heat Transfer Division for publication in the JOURNAL OF HEAT TRANSFER and presented at the 1996 ASME IMECE. Manuscript received by the Heat Transfer Division August 21, 1996; revision received September 23, 1997; Keywords: Conduction; Measurement Techniques; Thermophysical Properties. Associate Technical Editor: A. S. Lavine.

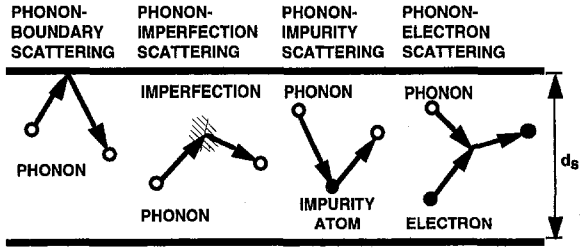

Fig. 1 Phonon scattering mechanisms which reduce the thermal conductivity of SOI device layers compared to that of bulk intrinsic silicon. The thermal conductivity of silicon is dominated by phonon transport.

(Zheng et al., 1996). These data motivate the present study, which provides a systematic measurement of the thermal conductivities of single-crystal silicon layers of thickness comparable to and less than one micrometer. The resulting data are of practical relevance for SOI devices and are of fundamental interest because of the information they provide about phonon free paths in the bulk material.

This work develops a technique for measuring the lateral thermal conductivity of SOI device layers. The technique has the advantage that it uses doping and photolithography techniques that are compatible with CMOS technology, such that it can be directly integrated onto an SOI wafer for parallel device and thermal-property characterization. The measurements yield the vertical thermal resistance of the buried silicon dioxide as well as the lateral thermal conductivity of the silicon device layer using two separate structures. This manuscript reports data for BESOI silicon layers of thickness between 0.4 and 1.6 μm at temperatures between 20 and 300 K. The range of thicknesses and temperatures aids with the determination of the relative importance of the phonon-boundary scattering mechanism. The data provided here assist with the study of self heating in thin-film SOI transistors. They are also important for the design of the large variety of microscopic thermal sensors and actuators that are made from SOI substrates. From a more fundamental viewpoint, study of the thermal conductivity in thin crystalline silicon films provides an opportunity to more directly determine the spectrum of phonon mean free paths in this material, by means of the conductivity reduction due to phonon boundary scattering. The potential for such fundamental study is particularly large in SOI wafers, whose device layers resemble the bulk material in purity and microstructural quality.

2 Experimental Structures and Procedure

Figure 2 shows a cross-sectional schematic and an electron micrograph of the experimental structure used to measure the lateral thermal conductivity of the SOI device layer. The wafers in the present study are fabricated using BESOI technology, in which a p^+ epitaxial layer doped with about 10^{20} boron atoms cm^{-3} serves as the etch stop. The device layer is grown on the etch-stop layer and is doped with less than 10^{15} boron atoms cm^{-3} due to the residual boron in the chamber. After the bonding, the silicon substrate is etched with a KOH/isopropyl alcohol solution which stops at the p^+ layer. The p^+ layer is then removed using a 1:3:8 solution of 49 percent HF, 70 percent HNO_3, and 98 percent CH_3COOH. This solution selectively etches the p^+ region and stops at the undoped layer. The moderately doped bridge, which is used here as a heater for the thermal conductivity measurements, is fabricated using a 50 keV implantation of BF_2^+ with dosage 5×10^{15} cm^{-2} and a subsequent 30 minute anneal at 1220 K. Two sets of structures are used in the present study, distinguished by the die from which they are fabricated. Data reported here over the temperature range of 20 to 300 K are obtained from die no. 1 with silicon device layer thicknesses d_s = 0.42, 0.83, and 1.6 μm and buried oxide thickness d_o = 3 μm. Data are obtained from die no. 2 at room temperature, with silicon device layer thicknesses d_s = 0.42, 0.72, and 1.42 μm. The dies are attached within a 68-pin leadless chip carrier device package, wire bonded, and mounted on the chip-carrier assembly of an open-circuit MTD-160 cryogenic test system. The cryogenic system thermometer has an accuracy of $\pm$0.5 K from 10 K to 100 K and 1 percent from 100 to 350 K.

During the measurement heat is generated by electrical current sustained in a doped region within the silicon device layer, yielding a temperature rise in the layer that decays rapidly with increasing x. The temperatures at two locations above the device layer are detected using electrical-resistance thermometry in the patterned aluminum bridges A and B, shown in Fig. 2(a). The lengths of the bridges in the direction normal to Fig. 2(a) are 1100 μm. The electrical current in the aluminum bridges is kept

Nomenclature

C_V = phonon-specific heat per unit volume, J m^{-3} K^{-1}
d_o = thickness of buried silicon-dioxide layer, m
d_s = thickness of silicon device layer, m
F = mean free path reduction ratio due to boundary scattering, Eq. (5)
h_P = Planck's constant divided by 2π = 1.055×10^{-34} J s
k = thermal conductivity, W m^{-1} K^{-1}
k_B = Boltzmann constant = 1.38×10^{-23} J K^{-1}
k_o = normal thermal conductivity of buried silicon-dioxide layer, W m^{-1} K^{-1}
k_s = lateral thermal conductivity of silicon device layer, W m^{-1} K^{-1}
L_H = healing length along SOI device layer, $(d_s d_o k_s / k_o)^{1/2}$, m
M = atomic mass of the host atom, kg
n = concentration of point defects, m^{-3}
p = specular reflection coefficient, Eq. (6)
P' = heater power per unit length, W m^{-1}
T = temperature, K
T_A = temperature at $x = x_A$, K
T_B = temperature at $x = x_B$, K
T_0 = temperature at the silicon substrate/silicon dioxide interface
V = volume of host atom, m^3
v_s = phonon velocity, m s^{-1}
x = separation from center of the bridge, m
x_A = location of the aluminum bridge A, m
x_B = location of the aluminum bridge B, m
x_0 = fitting parameter for approximation to analytical solution, Eq. (1), m
x_ω = dimensionless phonon frequency
δ = dimensionless parameter = d_s / Λ_{NB}
ΔM = mass difference between the impurity and the host atom, kg
η = mean surface roughness, m
λ = phonon wavelength, m
Λ_{NB} = phonon mean free path in the absence of boundary scattering, m
θ = angle of incidence, rad
Θ = Debye temperature, K
τ = phonon relaxation time, s
τ_D = phonon relaxation time due to defects, s
$\tau_{D,\mathrm{BULK}}$ = phonon relaxation time due to intrinsic defects, s
$\tau_{D,\mathrm{SOI}}$ = phonon relaxation time due to defects introduced during fabrication process, s
τ_{NB} = phonon relaxation time in the absence of boundary scattering, s
τ_U = phonon relaxation time due to Umklapp processes, s
ω = phonon angular frequency, rad s^{-1}

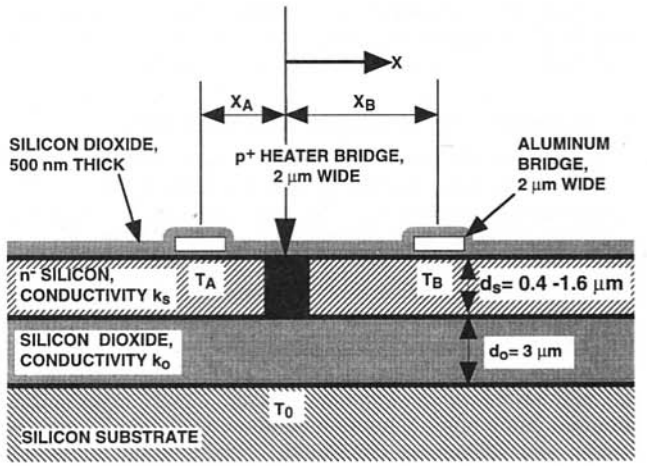

(a)

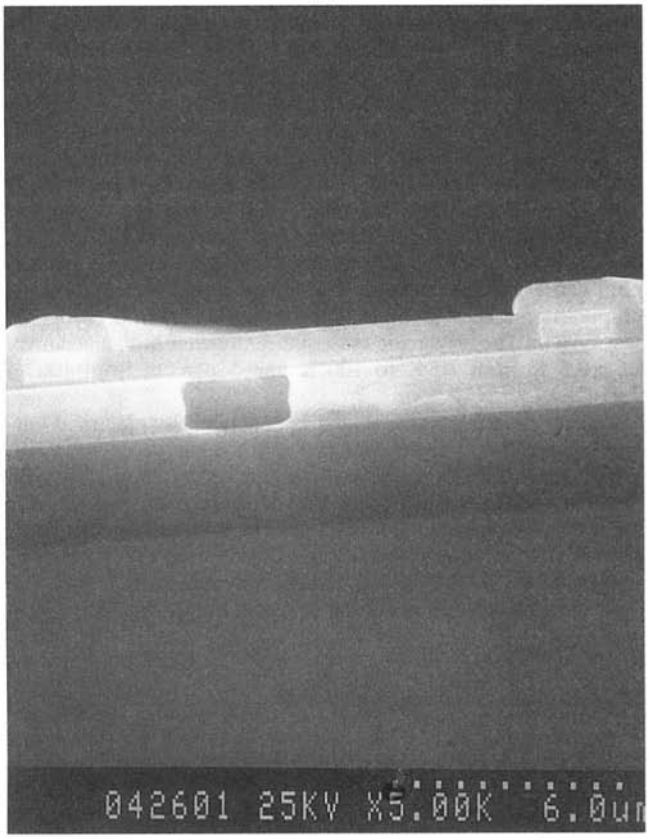

(b)

Fig. 2 Cross sectional diagram (*a*) and electron micrograph (*b*) of the experimental structure used to measure the lateral thermal conductivity of the SOI silicon device layer. To achieve a small uncertainty, the separations x_A and x_B need to be somewhat less than the thermal healing length in the device, $L_H = (d_s d_o k_s/k_o)^{1/2}$. The present study uses x_A = 5 and x_B = 10 μm.

very small to ensure negligible Joule heating. Convective and radiative heat loss from the surfaces of the aluminum bridges is negligible (Goodson et al., 1995), which causes the bridge temperatures to be nearly equal to those of the silicon overlayer at $x = x_A$ and $x = x_B$.

Thermal conduction in the experimental structure is modeled most rigorously in the present work using an analytical solution to the steady-state two-dimensional heat conduction equation in the silicon device layer, the underlying silicon dioxide layer, and the silicon substrate. The two-dimensional analysis can be very well approximated using a closed-form solution to the one-dimensional heat conduction equation in the x-direction along the device layer if three conditions are met. The first condition is that the temperature variation in the silicon substrate just beneath the buried oxide is small compared to that within the silicon device layer, which allows the use of an isothermal boundary condition at the bottom interface of the buried silicon dioxide. The more rigorous two-dimensional analysis is used to show that this condition is satisfied in the present work. The temperature variation at this interface, within a 100 μm width centered below the heater, is less than 0.1 percent of that between the silicon heater and the substrate for measurements performed within the temperature range of 20 K to 300 K. The second condition is that the temperature variation in the silicon device layer normal to the substrate at any position x is negligible compared to that in the buried silicon dioxide layer. This condition is satisfied when the thermal resistance for conduction normal to the silicon is much less than that for conduction normal to the underlying oxide, which requires $(d_s/k_s)/(d_o/k_o) \ll 1$. The length d_o is the oxide thickness, and k_o and k_s are the thermal conductivities of the silicon dioxide and the silicon layers, respectively. This condition is satisfied in the present work, for which this ratio is always smaller than 0.002. The third condition is that the lateral conduction in the silicon dioxide is negligible compared to that within the silicon device layer, which is satisfied given a small ratio of the lateral conductances $(d_o k_o/d_s k_s) \ll 1$. The value of this ratio in the present work is always less than 0.08. Since each of these conditions is satisfied, a one-dimensional solution to the thermal-conduction equation in the x direction along the device layer is appropriate. The thermal healing length in the device layer, $L_H = (d_s d_o k_s/k_o)^{1/2}$, is defined here as the characteristic lateral lengthscale of the temperature decay to the substrate temperature within the device layer. For 2 μm $< x <$ L_H, the temperature rise predicted using the more rigorous two-dimensional heat conduction analysis is approximated within 1.5 percent by

$$T(x) - T_0 = \frac{P'}{2}\sqrt{\frac{d_o}{k_o d_s k_s}}\exp\left(-\frac{x - x_0}{L_H}\right), \qquad (1)$$

where P' is the heater power per unit length and T_0 is the substrate temperature beneath the experimental structure. The length x_0 is a parameter between 0.4 and 0.6 μm which is used to match the temperature distribution from Eq. (1) to the exact solution of the one-dimensional heat conduction equation that includes the 2 μm wide heated region. The 1.5 percent difference between Eq. (1) and the more rigorous solution to the two-dimensional heat equation is neglected here because it is much smaller than the experimental uncertainty resulting from other factors. When the width of the aluminum bridge is much smaller than the healing length, which is satisfied in the present study, the temperature rises in the two aluminum bridges are approximately equal to those in the silicon overlayer at locations $x = x_A$ and $x = x_B$. The thermal resistance of the buried silicon dioxide is obtained independently, as described in the following paragraph. Knowledge of this resistance leaves only T_0 and k_s as unknowns in Eq. (1). The two equations which are needed to extract the unknowns k_s and T_0 are derived using Eq. (1) with $T(x_A) = T_A$ and $T(x_B) = T_B$, where T_A and T_B are the temperatures measured by the two metal bridges. The lateral thermal conductivity of the silicon device layer is calculated by solving these two equations simultaneously.

The buried oxide thermal conductivity, k_o, is measured on the same die using the structure shown in Fig. 3. Steady-state Joule heating and thermometry are performed using a 40 μm wide doped silicon bridge. Thermometry is also performed in two lightly doped silicon thermometers, each of 2 μm width, which experience negligible Joule heating. The substrate temperature beneath the heater is calculated from the temperature

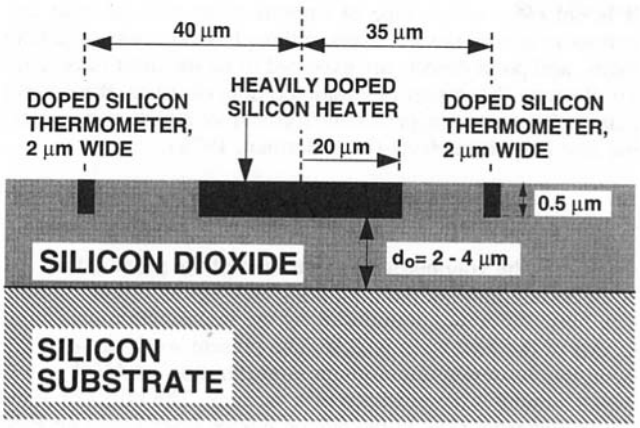

Fig. 3 Experimental structure for measuring the vertical thermal conductivity of the buried silicon dioxide.

measured in the two narrow thermometers. The silicon-dioxide thermal conductivity is calculated from the heater power per unit area normal to the substrate and the temperature drop between the heater and the substrate. The major improvement of this technique compared to that of Goodson et al. (1993), who used aluminum bridges for the heating and thermometry, is the fabrication of doped heaters and thermometers directly within the silicon device layer. This causes the geometry and materials of the conduction problem to more closely resemble those in a SOI transistor than in the previous work. But there are two problems associated with the use of the lightly doped silicon thermometers. At temperatures below 50 K the strongly diminished concentration of thermally excited carriers causes the bridge electrical resistance to exceed 6 MΩ, which is too large to be handled using common voltage sources. Another problem is that lightly doped silicon has a relatively small temperature derivative of the electrical resistance between 190 K and 250 K, where the sign of the derivative actually changes, yielding a very low sensitivity. This introduces relatively large uncertainties in the measurement of the buried-silicon dioxide thermal resistance in this temperature range. This shortcoming of the doped thermistors for $T < 50$ K and 190 K $< T <$ 250 K was not a major problem because all of the data in the other ranges of temperature agree quite closely with that of bulk fused quartz. For this reason the thermal conductivity of fused quartz is used to extract the silicon thermal conductivity in the ranges of temperature where the oxide structure is ineffective.

The relative uncertainties of the measured values of k_s are near 21 percent at room temperature. At very low temperatures the uncertainty of the measured values of k_s is as large as 25 percent due to the uncertainty in the thermal conductivity of the 3 μm thick buried oxide. The important contributors to the uncertainty are the lack of precise knowledge of the width of the doped heater, the thickness of the silicon layer, and the distance between the doped and metal bridges.

3 Model for the Thermal Conductivity of Thin Silicon Films

The thermal conductivity of the silicon layers is predicted using an approximate solution to the phonon Boltzmann transport equation in the relaxation time approximation together with the Debye model for phonon specific heat. This approach was developed by Callaway (1959) and refined for silicon by Holland (1963), who used a more detailed description of the phonon dispersion relations in this material to better capture the temperature dependence of thermal conductivity. The present work modifies the model of Holland (1963) to account for the increase in the scattering rate due to the small separation between the layer boundaries. The conductivity reduction due to phonon-boundary scattering is calculated independently for each differential step in the phonon frequency spectrum using the solution to the Boltzmann equation. The model of Holland (1963) is a refinement of the general expression for the phonon thermal conductivity (e.g., Berman, 1976), as follows:

$$k = \tfrac{1}{3} v_s^2 \int_0^{\Theta/T} C_V \tau \, dx_\omega, \tag{2}$$

where $x_\omega = h_p \omega / k_B T$ is the nondimensional phonon frequency, $k_B = 1.38 \times 10^{-23}$ J K^{-1} is the Boltzmann constant, $h_P = 1.602 \times 10^{-34}$ J s is Planck's constant divided by 2π, C_V is the phonon-specific heat per unit volume and nondimensional frequency, v_s is the phonon group velocity, Θ is the Debye temperature of the solid, and τ is the phonon relaxation time. Holland (1963) separated the conductivity into three integrals of the form of Eq. (2) that account for longitudinal, low-frequency transverse, and high-frequency transverse phonons. The three contributions to the conductivity modeled by Holland (1963) differ in the value of the sound velocity and the dependence of the relaxation time on nondimensional frequency and temperature. The present work uses the model of Holland (1963), including all of the parameters that govern the relaxation time, with an important modification that accounts for the reduction of the relaxation time due to phonon-boundary scattering. The relaxation time is reduced using

$$\tau(\omega, T, d_s, p) = \tau_{NB}(\omega, T) F\left(\frac{d_s}{\Lambda_{NB}(\omega, T)}, p \right), \tag{3}$$

where d_s is the film thickness and $\tau_{NB}(\omega, T)$ is the relaxation time in the absence of phonon-boundary scattering. The boundary scattering reduction factor F depends on the ratio of the layer thickness, d_s, and the phonon mean free path, $\Lambda_{NB}(\omega, T) = v_s \tau_{NB}(\omega, T)$, as well as the specular reflection coefficient p. If the remaining scattering mechanisms are independent, which is a valid assumption as long as the responsible scattering centers are distributed homogeneously in the layer, then the scattering rate in the absence of boundary scattering is

$$\tau_{NB}^{-1} = \tau_D^{-1} + \tau_U^{-1}. \tag{4}$$

The scattering rates τ_D^{-1} and τ_U^{-1} are due to phonon scattering on defects and other phonons, respectively, and are taken from the manuscript of Holland (1963). Equation (3) uses the exact solution to the Boltzmann equation for the mean-free path reduction along a thin free standing layer (Sondheimer, 1952):

$$F(\delta, p) = 1 - \frac{3(1-p)}{2\delta} \int_1^\infty \left(\frac{1}{t^3} - \frac{1}{t^5} \right) \frac{1 - \exp(-\delta t)}{1 - p \exp(-\delta t)} \, dt, \tag{5}$$

where the reduced thickness is $\delta = d_s / \Lambda_{NB}$. The heat transport along a thin layer is influenced by that of adjacent layers if the interface is not totally diffuse. The importance of this effect for the SiO_2-Si-SiO_2 multilayer system studied here is estimated using the model of Chen (1997) for this phenomenon. The results for diffuse and specular interfaces differ by less than 5 percent at temperatures below 30 K, where the probability of specular reflection from the interface becomes appreciable. The error is estimated to be less than 1 percent at temperatures above 30 K. Equation (5) is used for comparison with the data obtained here because it is considerably easier to implement and the error in the predictions is well below the uncertainty of the measurements.

Diffuse reflection is caused by the interference of phonon wavepackets reflected by an interface that has a characteristic roughness comparable to or larger than the phonon wavelength. The fraction of phonons reflected diffusely therefore depends

strongly on the surface roughness and on the wavelength of the phonons under consideration. The specular reflection coefficient can be very approximately estimated from the characteristic dimension of surface roughness, η, and the wavelength, λ, using (Berman et al., 1955)

$$p(\lambda, \eta) = \exp\left(-\frac{16\pi^3\eta^2}{\lambda^2}\right). \quad (6)$$

This expression is strictly valid only for phonons whose path before striking the surface is normal to the surface. To estimate the error due to the use of Eq. (6) for all angles of incidence, it is helpful to refer to research on the interaction of electromagnetic waves with surfaces. The light scattered by a rough surface contains information on the surface roughness. Statistical information about the deviation perpendicular to the surface is contained in the amplitude density function, and the behavior of the surface in the lateral direction is presented by the autocorrelation function (Marx and Vorburger, 1989). The autocorrelation function can be represented by an exponential function which approximates the degree of phase incoherence at some distance above the surface. The argument of the exponential function in Eq. (6) is the square of the phase change of the phonons incident at the peak and the bottom of an asperity. The height distribution is usually assumed to be Gaussian about the mean value, with width specified using the root-mean-squared height deviation, η. The fraction of phonons that are specularly reflected decreases rapidly with increasing η, and is far less than unity when this lengthscale is equal to the phonon wavelength λ. Equation (6) treats both incident and scattered waves as if they are normal to the surface and it has been successfully used (e.g., Ziman 1960, Chen and Tien, 1993) to correlate P, η, and λ. But a rigorous model that accounts for other angles of incidence and reflection seems to be more appropriate (Ziman, 1960). Beckmann and Spizzichino (1963) derived

$$p(\lambda, \eta, \theta) = \exp\left(-\frac{16\pi^3\eta^2}{\lambda^2}(\cos\theta)^2\right), \quad (7)$$

where θ is the angle of incidence with respect to the normal. Equation (7) is in a good agreement with the experimental results for stainless steel specimens with $\eta = 0.064 - 0.4$ μm and $\theta \approx \pi/3$ (Marx and Vorburger, 1989). Equation (7) can be incorporated into the solution of the Boltzmann equation for the mean-free path reduction along a thin layer and integrated over all angles of incidence. The specular reflection coefficient for the large angle of incidence predicted by Eq. (7) is greater, by far, than those predicted by Eq. (6) for the same η and λ. This causes the predicted thermal conductivity of silicon layers to increase more rapidly with decreasing temperature than predictions using Eq. (6). But this difference is due primarily to the differences between the Eqs. (6) and (7) for large angles of incidence, where the assumptions used to derive Eq. (7) (Beckmann and Spizzichino, 1963) are not satisfied. For this reason the present work uses Eq. (6) and cautions the reader that the impact of specular reflection can only be approximately considered due to the lack of a theory that is appropriate for all angles of incidence. The integral in Eq. (2) is over the nondimensional phonon frequency such that each differential step accounts for phonons with different wavelengths, $\lambda = 2\pi v_s h_P/(x_\omega k_B T)$.

To estimate the effect of additional scattering sites in the silicon device layer not present in the bulk material, the scattering rate in Eq. (4) can be augmented using

$$\tau_D^{-1} = \tau_{D,\mathrm{BULK}}^{-1} + \tau_{D,\mathrm{SOI}}^{-1} \quad (8)$$

The relaxation time $\tau_{D,\mathrm{BULK}}$ is that for bulk crystals provided by Holland (1963). The relaxation time $\tau_{D,\mathrm{SOI}}$ is the relaxation time on additional imperfections present in SOI device layers. It is not clear which type of imperfections will be most important in silicon device layers, although dislocations, stacking faults, and point defects are expected to be the most important. To illustrate the impact of additional imperfections, the present manuscript uses the approximate formula for the phonon scattering rate on point defects (e.g., Berman, 1976),

$$\tau_{D,\mathrm{SOI}}^{-1} = \frac{nV^2\Delta M^2}{4\pi v_s^3 M^2}\omega^4, \quad (9)$$

where n is the volumetric concentration of the point defects, M is the atomic mass of the host atom, and V is its lattice volume. The mass difference introduced by the imperfection compared to that of the host atom is ΔM. The present work assumes the strongest scattering for a given concentration ($\Delta M/M = 1$), which simulates the presence of a vacancy. The effect of additional scattering sites in the silicon device layer based on Eqs. (8) and (9) is used only in the final figure presented in this manuscript.

4 Results and Discussion

Figure 4 compares thermal-conductivity data for the buried silicon dioxide measured in the present study with the recommended values for bulk silicon dioxide (Touloukian et al., 1970b). The lack of data in the temperature ranges $T < 70$ K and $180 < T < 250$ K is associated with practical limitations of the lightly doped silicon thermistors in the structure in Fig. 3 and is discussed in section 2. The data agree quite well with the recommended bulk values at all of the temperatures for which the experimental structure is effective. At low temperatures it is expected that phonon scattering on the boundaries of the silicon dioxide may increase the total resistance compared to that calculated using the recommended bulk conductivity. This results in part from phonon scattering due to the mismatch of acoustic properties at the two boundaries of the layer. Also important is the reduction of phonon free paths due to the presence of two boundaries in close proximity, which renders the use of the bulk thermal conductivity inappropriate within the layer. The problem of thermal conduction normal to thin amorphous layers at low temperatures was studied by Goodson et al. (1994). These authors found that for 3 μm thick silicon dioxide layers, the relative impact of these phenomena on the thermal resistance normal to the layer could be as large as 20

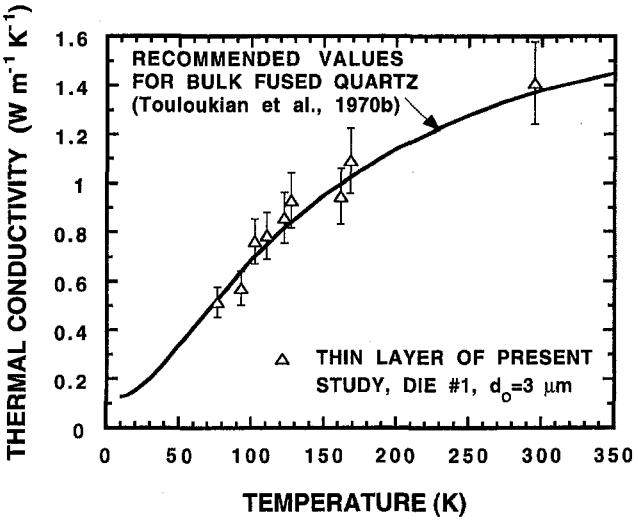

Fig. 4 Thermal conductivity data for the 3 μm thick buried silicon dioxide layers in the BESOI wafers of the present study. The data are compared with those recommended for bulk silicon dioxide. The lack of data in the temperature ranges $T < 50$ K and $180 < T < 250$ K is discussed in section 2.

and even 50 percent at temperatures 45 K and 20 K, respectively. These reductions in the effective oxide conductivity are treated as sources of uncertainty in the present work, and therefore augment the uncertainty in the extracted thermal conductivity of the silicon device layer. While the relative effect on the oxide resistance is quite large at 20 K, the contribution to relative uncertainty in the silicon conductivity at that temperature is considerably smaller, less than 24 percent. But the large uncertainty in the oxide resistance at the lowest temperatures contributes significantly to the uncertainty in the temperature of the structure during the measurement, and therefore influences the width of temperature error bars in subsequent plots.

Figure 5 shows thermal-conductivity data for the silicon device layers as a function of temperature. The maximum in the conductivity occurs near 70 K and separates the low-temperature region, where scattering is dominated by imperfections and surfaces, from the high temperature region, where phonon-phonon scattering is dominant. A portion of the recommended thermal conductivity curve for bulk silicon is provided for reference (Touloukian et al., 1970a). The recommended bulk conductivity reaches a much higher maximum, 5500 W m^{-1} K^{-1} at the temperature of 30 K. The thermal conductivities of the silicon device layers are significantly lower than the values recommended for bulk samples due to the much stronger reduction of phonon mean free path by boundary scattering. The data clearly show that this effect is more prominent for thinner layers. The figure also shows the predictions calculated using the theory developed in Section 3. It must be emphasized that the predictions are not the result of fitting to the data, but rather are a prediction based only on the theory of Holland (1963) and the modification to account for boundary scattering. The only adjustable parameter is the roughness of the boundaries η, which was estimated to be between 2 to 10 Å for BESOI wafers (Maszara, 1991). The predicted thermal conductivity curves are plotted for η = 5 and 10 Å. Increasing η beyond 10 Å has a negligible effect on the predicted thermal conductivity at temperatures down to 20 K, indicating that the use of η = 10 Å effectively models completely diffuse scattering. The fraction of the phonons that are specularly reflected increases as the surface roughness dimension decreases, thus diminishing the impact of boundary scattering on the thermal conductivity. The effect of surface roughness is more significant at lower temperatures where the population of the long wavelength phonons increases. In this figure no additional scattering due to fabrication-related imperfections is introduced. Figure 5 shows that

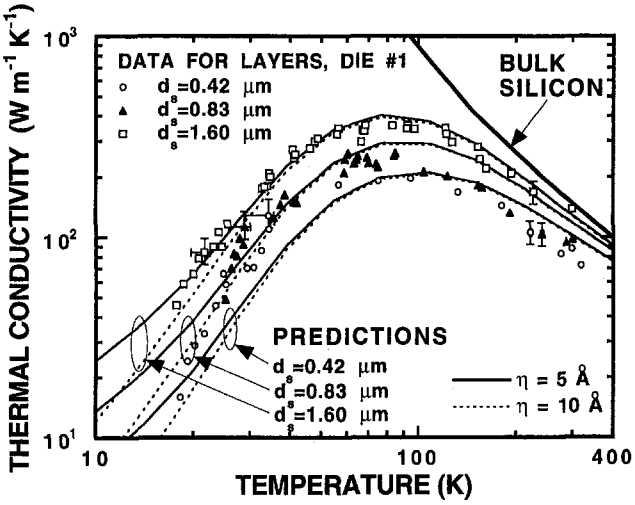

Fig. 5 Thermal conductivities of the silicon device layers with thicknesses 0.42, 0.83, and 1.6 μm. The data are compared with the predictions of the phonon-boundary scattering analysis.

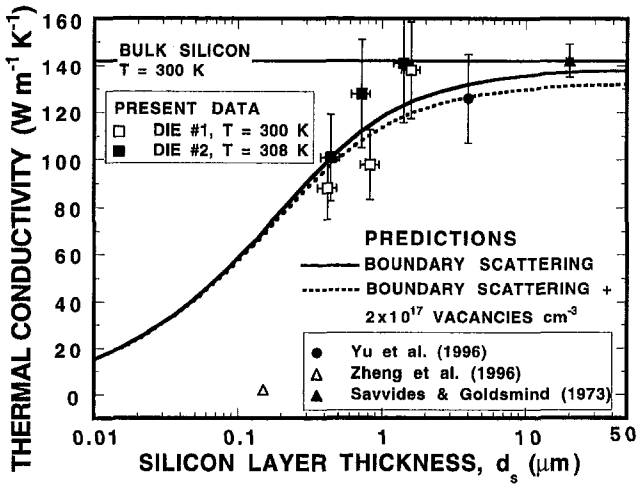

Fig. 6 Room-temperature thermal conductivity data for silicon layers as a function of their thickness. Also plotted are conductivity predictions that account for phonon-boundary scattering and phonon scattering on vacancies.

the data agree well with predictions for the 1.6 μm thick silicon overlayer over the entire temperature range. The poorer agreement for the 0.42 μm and 0.83 μm thick silicon layers may be due to the higher concentrations of imperfections associated with epitaxial silicon growth in these layers. BESOI device layers contain a large concentration of dislocations and stacking faults collected near the former interface with the heavily doped etch stop layer (Maszara, 1991). These imperfections may more strongly reduce the conductivity of thinner layers. The importance of scattering on these imperfections is nearly impossible to assess without more detailed information about the types of defects and the variation of their concentrations within layers.

Figure 6 shows the measured lateral thermal conductivities of silicon layers as a function of thickness near room temperature. The impact of phonon-boundary scattering is predicted using the theory described in section 3 and plotted as a solid line in the same graph. Previous experimental data for a 20 μm thick silicon specimen (Savvides and Goldsmid, 1973) and a 4 μm thick free-standing silicon film (Yu et al., 1996) are consistent with the predictions. However, the lateral thermal conductivity measured in a 0.15 μm thick SIMOX device layer at temperatures between 330 and 380 K (Zheng et al., 1996) shows nearly two orders of magnitude reduction compared to the bulk value and is far below the predictions of the phonon-boundary scattering model. This disparity could be explained by a high concentration of lattice imperfections in the sample of Zheng et al. (1996) or by uncertainty in the measurements of the layer thickness or the thermal conductivity.

The lateral thermal conductivities measured in the BESOI device layers of the present study are consistent with the phonon-boundary scattering predictions. For the thickest layers the reduction is small and not experimentally significant, suggesting a microstructure and purity that closely resemble those in bulk crystals. This shows that thermal simulations of SOI transistors with device layers thicker than about 1.5 μm should use the thermal conductivity of bulk silicon. However, the bulk conductivity overpredicts the data for the thinnest silicon overlayer by nearly 40 percent, indicating a potential for a large error in device simulations. The reduction is significant even considering the experimental uncertainty and may be due to any of the mechanisms shown in Fig. 1. A strong reduction due to impurities is unlikely because the boron concentration in the device layer is below that at which the thermal conductivity of bulk crystals is reduced by scattering on impurities (Goodson and Cooper, 1995). While boundary scattering analysis yields predictions consistent with the data in Figs. 5 and 6, a more con-

vincing confirmation of this model near room temperature will require data for thinner layers. The predominant additional imperfection in BESOI silicon device layers may be dislocations. Dislocations due to the epitaxial growth process are assumed to account for the observed warping of the device layer across a wafer (Ma et al., 1991) and provide a potential explanation for the difference in the thermal conductivity values obtained for samples on dies nos. 1 and 2. A study involving BESOI layers of thickness 0.1 μm and below would be particularly helpful since the predicted relative conductivity reduction will exceed 60 percent. Data for such layers would not resolve the situation, however, because it would be difficult to ensure that the concentration of fabrication-related imperfections is the same in the layers of different thicknesses. Figure 6 includes a very approximate prediction of the effect of evenly distributed fabrication-related imperfections, which is based on Eqs. (8) and (9). A concentration of 2×10^{17} cm^{-3} vacancies can reduce the thermal conductivity by more than 10 percent.

5 Conclusions

The data provided in this manuscript are of practical importance for SOI technology and for MEMS that are made using SOI wafers. The data are needed most urgently for thermal simulation of SOI transistors that must withstand the temperature rise during ESD pulses. The impact of this study is greatest for silicon device layers thinner than about 0.5 μm, for which the relative reduction in the conductivity due to phonon-boundary scattering exceeds 40 percent. The reduction for SOI technologies with very thin device layers is more dramatic, as shown in Fig. 6. It must be noted that the temperature rise in active regions cooled by lateral conduction in the silicon actually scales with the inverse of the square root of the silicon thermal conductivity (Goodson and Cooper, 1995), such that the relative change in the temperature rise will be less than the relative reduction in the thermal conductivity.

The data and analysis documented here are also of considerable fundamental importance because they can be used to extract the phonon mean free path in silicon for shorter phonon wavelengths than has been possible previously. The Boltzmann equation solution used here relates the impact of boundary scattering on heat transport by phonons of a given wavelength to the ratio of the free path to the layer thickness. Since SOI wafers provide silicon layers that approach bulk silicon in purity and microstructural perfection, the data provide the opportunity to determine the wavelengths of phonons that have free paths comparable to the layer thickness. The agreement of the predictions with the data provides an important confirmation of the free paths obtained by means of the conductivity integrals of Holland (1963).

Acknowledgments

The authors are warmly appreciative of the research group of J. D. Plummer for the use of the cryogenic stage. M. Asheghi appreciates the help of H. Khalkhali of University of Dayton with finite-element simulations of the temperature distribution in the experimental structure. This work was sponsored by the Semiconductor Research Corporation under contracts 97-SJ-461 and 96-PJ-357. K.E.G. appreciates support from the Office of Naval Research Young Investigator Program and the National Science Foundation through the CAREER Program and grant CTS-9622178.

References

Amerasekera, A., Van Abeelen, W., Van Roozendaal, L., Hannemann, M., and Schofield, P., 1992, "ESD Failure Modes: Characteristics Mechanisms, and Process Influences," *IEEE Trans. Electron Devices,* Vol. 39, pp. 430–436.

Beckmann, P., and Spizzichino, A., 1963, *The Scattering of Electromagnetic Waves from Rough Surfaces,* Pergamon Press Inc., New York, pp. 29, 81.

Berman, R., 1976, *Thermal Conduction in Solids,* Oxford University Press, Oxford, United Kingdom, pp. 23, 73–75.

Berman, R., Foster, E. L., and Ziman, J. M., 1955, "Thermal Conduction in Artificial Sapphire Crystals at Low Temperatures," *Proc. Roy. Soc. A,* Vol. 231, pp. 130–144.

Callaway, J., 1959, "Model for Lattice Thermal Conductivity at Low Temperatures," *Phys. Rev.,* Vol. 113, pp. 1046–1051.

Cellar, G. K., and White, A. E., 1992, "Buried Oxide and Silicide Formation by High-Dose Implantation in Silicon," MRS Bulletin, Vol. 17, No. 6, pp. 40–46.

Chen, G., 1997, "The Size and Interface Effects on the Thermal Conductivity of Superlattices and Periodic Thin-Film Structures," ASME JOURNAL OF HEAT TRANSFER, Vol. 119, pp. 220–229.

Chen, G., and Tien, C. L., 1993, "Thermal Conductivities of Quantum Well Structures," *Journal of Thermophysics and Heat Transfer,* Vol. 7, No. 2, pp. 311–318.

Chui, B. W., Stowe, T. D., Kenny, T. W., Mamin, H. J., Terris, B. D., and Rugar, D., 1996, "Low-Stiffness Silicon Cantilevers for Thermal Writing and Piezoresistive Readback with the Atomic Force Microscope," *Applied Physics Letters,* Vol. 69, pp. 2767–2769.

Goodson, K. E., and Cooper, P. T., 1995, "The Effect of High-Energy Electrons on Lattice Conduction in Semiconductor Devices," *Proceedings of the Symposium on Thermal Science and Engineering in Honor of Chancellor Chang-Lin Tien,* R. Buckius, ed., Office of Printing Services, University of Illinois at Urbana-Champaign, pp. 153–159.

Goodson, K. E., Flik, M. I., Su, L. T., and Antoniadis, D. A., 1993, "Annealing Temperature Dependence of Thermal Conductivity of CVD Silicon-Dioxide Layers," *IEEE Electron Device Letters,* Vol. 14, pp. 490–492.

Goodson, K. E., Flik, M. I., Su, L. T., and Antoniadis, D. A., 1994, "Prediction and Measurement of the Thermal Conductivity of Amorphous Dielectric Layers," ASME JOURNAL OF HEAT TRANSFER, Vol. 116, pp. 317–324.

Goodson, K. E., Flik, M. I., Su, L. T., and Antoniadis, D. A., 1995, "Prediction and Measurement of Temperature Fields in Silicon-on-Insulator Electronic Circuits," ASME JOURNAL OF HEAT TRANSFER, Vol. 117, pp. 574–581.

Holland, M. G., 1963, "Analysis of Lattice Thermal Conductivity," *Phys. Rev.,* Vol. 132, No. 6, pp. 2461–2471.

Ma, D. I., Campisi, J. G., Qadri, S. B., and Peckerar, M. C., 1991, "Characterization of Silicon on Insulator Substrates Using Reflection Mode Double-Crystal X-ray Topography," *Thin Solid Films,* Vol. 206, pp. 27–33.

Marx, E., and Vorburger, T. V., 1989, "Direct and Inverse Problems for Light Scattered by Rough Surfaces," *Applied Optics,* Vol. 29, No. 25, pp. 3613–3626.

Mastrangelo, C. H., and Müller, R. S., 1988, "Thermal Diffusivity of Heavily Doped Low Pressure Chemical Vapor Deposited Polycrystalline Silicon Films," *Sensors and Materials,* Vol. 3, pp. 133–141.

Maszara, W. P., 1991, "Silicon-On-Insulator by Wafer Bonding: A Review," *J. Electrochem. Soc.,* Vol. 138, No. 1, pp. 341–347.

Paul, O. M., Korvink, J., and Baltes, H., 1993, "Thermal Conductivity of CMOS Materials for the Optimization of Microsensors," *Journal of Micromechanics and Microengineering,* Vol. 3, No. 3, pp. 110–12.

Paul, O. M., Korvink, J., and Baltes, H., 1994, "Determination of the Thermal Conductivity of CMOS IC Polysilicon," *Sensors and Actuators A (Physical),* Vol. A41, No. 1–3, pp. 161–164.

Peters, L., 1993, "SOI Takes Over Where Silicon Leaves Off," *Semiconductor International,* Vol. 16, pp. 48–51.

Savvides, N., and Goldsmid, H. J., 1973, "The Effect of Boundary Scattering on the High-Temperature Thermal Conductivity of Silicon," *J. Phys. C: Solid State Phys.,* Vol. 6, pp. 1701–1708.

Sondheimer, E. H., 1952, "The Mean Free Path of Electrons in Metals," *Adv. Phys.,* Vol. 1, pp. 1–42.

Tai, Y. C., Mastrangelo, C. H., and Müller, R. S., 1988, "Thermal Diffusivity of Heavily Doped Low-Pressure Chemical Vapor Deposited Polycrystalline Silicon Films," *J. Appl. Phys.,* Vol. 63, pp. 1442–1447.

Touloukian, Y. S., Powell, R. W., Ho, C. Y., and Klemens, P. G., 1970a, "Thermal Conductivity of Metallic Elements and Alloys," *Thermophysical Properties of Matter,* Vol. 1, New York: IFI/Plenum, p. 333, 339.

Touloukian, Y. S., Powell, R. W., Ho, C. Y., and Klemens, P. G., 1970b, "Thermal Conductivity of Nonmetallic Solids," from Thermophysical Properties of Matter, Vol. 2, IFI/Plenum, New York, p. 193.

Von Arx, M., and Baltes, H., 1992, "A Microstructure for Measurement of Thermal Conductivity of Polysilicon Thin Films," *Journal of Microelectromechanical Systems,* Vol. 1, No. 4, pp. 193–6.

Von Arx, M., Paul, O. M., and Baltes, H., 1995, "Determination of the Heat Capacity of CMOS Layers for Optimal CMOS Sensor Design," *Sensors and Actuators A (Physical),* Vol. A47, No. 1–3, pp. 428–31.

Yu, X. Y., Zhang, L., and Chen, G., 1996, "Thermal-Wave Measurement of Thin-Film Thermal Diffusivity with Different Laser Beam Configurations," *Rev. Sci. Instrum.,* Vol. 67, No. 6, pp. 2312–2316.

Zheng, X. Y., Li, S., Chen, M., and Wang, K. L., 1996, "Giant Reduction in Lateral Thermal Conductivity of Thin Nitride/Silicon/Oxide Membrane Measured with a Micro Thermal Bridge," *Proc. Int. Mech. Eng. Congress and Exp.,* C. T. Avedisian et al., eds., ASME, New York, pp. 93–98.

Ziman, J. M., 1960, *Electrons and Phonons,* Oxford University Press, Oxford, United Kingdom, pp. 456–460.

Application of Diffuse Mismatch Theory to the Prediction of Thermal Boundary Resistance in Thin-Film High-T_c Superconductors

P. E. Phelan
phelan@asu.edu

Department of Mechanical and Aerospace Engineering,
Arizona State University,
PO Box 876106,
Tempe, AZ 85287-6106

Thermal boundary resistance (R_b) plays an important role in the design and performance of thin-film high-temperature superconducting devices, such as infrared detectors and optical switches, which rely upon the temperature rise of the film as the basis for their operation. Although there is general agreement on the magnitude of R_b from experimental data, there is at present no generally accepted theory capable of predicting R_b for these films, particularly at the intermediate cryogenic temperatures where they are likely to be used. Here, the Diffuse Mismatch Model (DMM), which considers that all phonons reaching the interface between the film and substrate scatter diffusely, is applied to the calculation of R_b. The results indicate that when employing the Debye model for the phonon density of states, the DMM yields results slightly more in agreement with data than the Acoustic Mismatch Model (AMM). Considering the measured phonon density of states, however, greatly increases R_b over that calculated assuming the Debye model, thus bringing the DMM results in relatively good agreement with the experimental data.

Introduction

The thermal boundary resistance (R_b) between high-temperature superconductor (HTS) thin films and their substrates is an important parameter for the design and operation of HTS electronic and optoelectronic devices, particularly bolometers and optical switches. Although a few studies have established the magnitude of R_b (Nahum et al., 1991; Phelan et al., 1994; Zeuner et al., 1995), there exists no generally accepted theoretical explanation of the results. That is, no model exists that can be used to accurately predict R_b for a given HTS film/substrate combination.

A theory which has been applied successfully to the prediction of R_b for other materials at extremely low temperatures is the acoustic mismatch model (AMM), also called the acoustic mismatch theory (Little, 1959). The AMM is applied to describe phonon heat transport across an interface and uses the approach from continuum acoustic theory to calculate the transmission probability for phonons striking the interface. A key assumption of the AMM is that all the phonons interact specularly with the interface, i.e., no scattering occurs at the interface. This is a reasonable assumption at very low temperatures, where the phonon wavelengths are much longer than the length scales associated with interfacial roughness and defects near the boundary, but becomes invalid as the temperature, and hence the phonon wavelength, decreases. At the temperatures where HTS devices are operated—typically around 70 to 80 K—the specularity assumption is suspect. Another theory which was introduced to overcome this problem is the diffuse mismatch model (DMM) (Swartz and Pohl, 1989), which considers that all the phonon interactions with the boundary are diffuse rather than specular.

The present study provides a review of the derivation of the DMM, including the key concepts and assumptions involved. Some of the assumptions are removed, particularly the temperature restrictions and the assumption of a Debye density of states, in order to determine their effects on the model's predictions. A direct comparison between the AMM and the DMM results and HTS experimental data is presented, which shows that although removing the temperature restrictions on the DMM yields only slightly improved agreement with experimental data, considering the measured density of states rather than the Debye density of states substantially increases the predicted R_b, thus bringing the DMM's predictions much closer to the experimental data.

Review of the Diffuse Mismatch Model (DMM)

A schematic diagram of the physical system to which the model is being applied is shown in Fig. 1. Material 1 is a $YBa_2Cu_3O_{7-\delta}$ (YBCO) HTS film, and material 2 is considered to be MgO, one of the typical substrates on which HTS films are deposited. In a typical application, the temperature of the film, T_1, increases relative to the substrate temperature, T_2, causing a heat flux, q, from the film to the substrate. The thermal boundary resistance, R_b, of concern is that at the interface between the film and substrate.

The applicability of the AMM and the DMM is determined, in general, by the ratio λ_d/σ, where λ_d is the dominant phonon wavelength at a given temperature, and σ is the mean interfacial roughness, or deviation from a perfect planar interface. The regions of applicability of the two models can be described succinctly as

$$\frac{\lambda_d}{\sigma} \gg 1 : \text{AMM applies}$$

$$\frac{\lambda_d}{\sigma} \leq 1 : \text{DMM applies.}$$

Contributed by the Heat Transfer Division for publication in the JOURNAL OF HEAT TRANSFER and presented at the 1996 International Mechanical Engineering Congress and Exposition (IMECE96). Manuscript received by the Heat Transfer Division February 28, 1997; revision received September 22, 1997; Keywords: Conduction; Cryogenics; Direct-Contact Heat Transfer. Associate Technical Editor: T. L. Bergman.

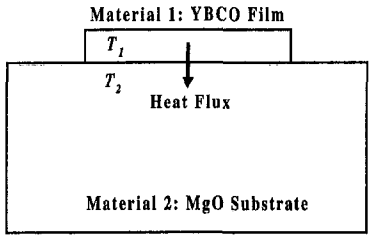

Fig. 1 Schematic diagram of the physical model

Thus, the AMM requires the interface to appear "smooth" to an oncoming phonon, whereas the DMM requires the interface to appear "rough". To give an approximate idea of the actual dimensions involved in such a categorization, λ_d can be estimated from (Rosenberg, 1988)

$$\lambda_d \approx \left(\frac{\theta_d}{T}\right) a, \tag{1}$$

where θ_d is the Debye temperature, T the temperature of interest, and a the lattice spacing. For YBCO, θ_d is approximately 410 K (von Molnár, 1988), while a is taken to be the average lattice constant in the a and b directions, and is equal to 3.9 Å. Equation (1) yields $\lambda_d \approx 40$ nm at 4 K, $\lambda_d \approx 3$ nm at 50 K, and $\lambda_d \approx 2$ nm at 77 K. Thus, at the typical operating temperatures of HTS devices, interfacial roughness would have to be held to length scales much less than $2 \sim 3$ nm for the AMM to be applicable. Since this is probably not the case, we shall assume that the DMM applies.

Phonon Transport Across an Interface. The derivation of the basic equation of phonon transport across an interface is the same for the AMM and the DMM. The energy transported per unit time from material 1 to material 2, $\dot{Q}_{1\to 2}$, is (Little, 1959; Swartz and Pohl, 1989; Burkhard et al., 1995)

$$\dot{Q}_{1\to 2}(T_1) = \tfrac{1}{2}\sum_j \int_A \int_{\theta=0}^{\pi/2} \int_{\omega=0}^{\omega_d} N_1(\omega, T_1, j)\hbar\omega c_{1,j}\alpha_{1\to 2}(\omega) \times \cos(\theta)\sin(\theta) d\omega d\theta dA, \tag{2}$$

where j is the phonon mode (either longitudinal or transverse), N_1 is the phonon number density in material 1, ω is the phonon frequency, θ is the angle between the incident phonon and the normal to the interface, A is the total area of the interface, $\hbar$ is Planck's constant divided by 2π, ω_d is the maximum phonon frequency, $c_{1,j}$ is the speed of a phonon of mode j in material 1, and $\alpha_{1\to 2}(\omega)$ is the transmission coefficient, which varies between 0 and 1. For now, $\alpha_{1\to 2}(\omega)$ is taken to be a function of ω and its detailed derivation will be presented later. Equation (2) is equivalent for both the AMM and the DMM; only $\alpha_{1\to 2}(\omega)$ changes.

The net heat flux across the interface, q, is given simply as the difference between the heat flux from material 1 to material 2, and that from material 2 to material 1:

$$q = \frac{\dot{Q}_{1\to 2}(T_1)}{A} - \frac{\dot{Q}_{2\to 1}(T_2)}{A}. \tag{3}$$

For $N_1(\omega, T_1, j)$ and $N_2(\omega, T_2, j)$, the Debye density-of-states function is multiplied by the Bose-Einstein occupation factor to yield

$$N_1(\omega, T_1, j) = \frac{\omega^2}{2\pi^2 c_{1,j}^3\left[\exp\left(\frac{\hbar\omega}{k_b T_1}\right) - 1\right]} \tag{4a}$$

$$N_2(\omega, T_2, j) = \frac{\omega^2}{2\pi^2 c_{2,j}^3\left[\exp\left(\frac{\hbar\omega}{k_b T_2}\right) - 1\right]}, \tag{4b}$$

where k_b is the Boltzmann constant. Substituting Eqs. (4a) and (4b) into Eq. (3) and simplifying gives

$$q = \frac{\hbar}{8\pi^2}\left\{\sum_j c_{1,j}^{-2}\int_{\omega=0}^{\omega_d} \frac{\omega^3\alpha_{1\to 2}(\omega)d\omega}{\exp\left(\frac{\hbar\omega}{k_b T_1}\right) - 1} - \sum_j c_{2,j}^{-2}\int_{\omega=0}^{\omega_d} \frac{\omega^3\alpha_{2\to 1}(\omega)d\omega}{\exp\left(\frac{\hbar\omega}{k_b T_2}\right) - 1}\right\}. \tag{5}$$

Note that since we are employing the Debye phonon density of states, ω_d is therefore the Debye frequency, which is related to the Debye temperature through $\hbar\omega_d = k_b\theta_d$. Moreover, according to the confines of the theory, phonons having $\omega > \omega_{d1}$, where ω_{d1} is the Debye frequency of material 1, cannot be transmitted into material 1; similarly, phonons having $\omega > \omega_{d2}$ cannot be transmitted into material 2. Therefore, ω_d is defined as the lower of the Debye frequencies of the two materials.

Nomenclature

a = lattice spacing [Å]
A = area [m^2]
c = phonon, or sound, speed [$m\ s^{-1}$]
c_v = specific heat at constant volume [$J\ kg^{-1}\ K^{-1}$]
g = measured phonon density of states [$s\ rad^{-1}\ m^{-3}$]
$\hbar$ = Planck's constant divided by 2π = 1.054496×10^{-34} J s
k_b = Boltzmann constant = 1.3805×10^{-23} J K^{-1}
n = conversion factor in Eq. (29) [m^{-3}]
N = phonon number density [$rad^2\ s\ m^{-3}$]
q = net heat flux [$W\ m^{-2}$]
$\dot{Q}$ = heat flow [W]
R_b = thermal boundary resistance [$m^2\ K\ W^{-1}$]
T = temperature [K]
U = lattice energy [$J\ m^{-3}$]
α = transmission coefficient
ρ = density [$kg\ m^{-3}$]
ΔT = temperature difference, $= T_1 - T_2$ [K]
$\Gamma_{1,\text{tot}}$ = integrated transmission coefficient for AMM
λ_d = dominant phonon wavelength [nm]
ω = phonon angular frequency [$rad\ s^{-1}$]
ω_d = phonon Debye frequency [$rad\ s^{-1}$]
σ = mean interfacial roughness [nm]
θ = incident angle [rad]
θ_d = Debye temperature [K]

Subscripts

1 = referring to the film, or material 1
2 = referring to the substrate, or material 2
$1 \to 2$ = from material 1 to material 2
$2 \to 1$ = from material 2 to material 1
j = phonon mode
l = longitudinal mode
t = transverse mode

The integrals in Eq. (5) are nondimensionalized with the variable $z = \hbar\omega/k_bT$, where T is either T_1 or T_2, to yield

$$q = \frac{k_b^4}{8\pi^2\hbar^3}\left\{T_1^4\sum_j c_{1,j}^{-2}\int_{z=0}^{\hbar\omega_d/k_bT_1}\frac{z^3\alpha_{1\to2}(z)dz}{\exp(z)-1} - T_2^4\sum_j c_{2,j}^{-2}\int_{z=0}^{\hbar\omega_d/k_bT_2}\frac{z^3\alpha_{2\to1}(z)dz}{\exp(z)-1}\right\}. \quad (6)$$

Equation (6) will simplify greatly under the most generous assumptions, but much less so when those assumptions are removed. In any case, R_b is determined by substituting Eq. (6) into the definition of R_b:

$$R_b = \frac{T_1 - T_2}{q} = \frac{\Delta T}{q}. \quad (7)$$

Various simplifications of Eq. (6) will be presented later with the detailed results. Now, let us turn our attention to the derivation of $\alpha_{1\to2}(\omega)$ and $\alpha_{2\to1}(\omega)$.

Derivation of Transmission Coefficients. What follows is taken almost entirely from Swartz and Pohl (1989). As discussed briefly in the Introduction, the key feature which distinguishes the DMM from the AMM is that all the phonons are scattered diffusely, rather than specularly, at the interface. This results in the phonons "forgetting" where they came from, except for their frequency (i.e., energy). In other words, at the moment a phonon reaches the interface from either material, it immediately has no memory of where it came from. Consequently, we can think figuratively of a phonon "resting" on the interface, and attempting to decide in which direction—material 1 or material 2—to continue its travels. From this picture we can write down a very useful relation between $\alpha_{1\to2}(\omega)$ and $\alpha_{2\to1}(\omega)$:

$$\alpha_{1\to2}(\omega) + \alpha_{2\to1}(\omega) = 1 \quad (8)$$

which we shall require to determine an expression for $\alpha_{1\to2}(\omega)$, and hence $\alpha_{2\to1}(\omega)$.

The number of phonons of frequency ω leaving material 1, per unit area and per unit time, is

$$\frac{1}{4\pi}\sum_j\int_{\varphi=0}^{2\pi}\int_{\theta=0}^{\pi/2}N_1(\omega, T_1, j)c_{1,j}\alpha_{1\to2}(\omega)\cos(\theta)\sin(\theta)d\theta d\varphi, \quad (9)$$

where φ is the azimuthal angle. Since the scattering at the interface is entirely diffuse, $\alpha_{1\to2}(\omega)$ is not a function of either θ or φ, and the integration can be carried out, yielding

$$\tfrac{1}{4}[\sum_j N_1(\omega, T_1, j)c_{1,j}]\alpha_{1\to2}(\omega). \quad (10)$$

For an interface in thermal equilibrium, such that $T_1 = T_2 = T$, the number of phonons of frequency ω leaving material 1 must be equal to the number of phonons of frequency ω leaving material 2, or

$$\tfrac{1}{4}[\sum_j N_1(\omega, T, j)c_{1,j}]\,\alpha_{1\to2}(\omega) = \tfrac{1}{4}[\sum_j N_2(\omega, T, j)c_{2,j}]\alpha_{2\to1}(\omega). \quad (11)$$

Equivalently, Eq. (11) can be derived using Eq. (2) and taking $\dot{Q}_{1\to2}(T) = \dot{Q}_{2\to1}(T)$. Upon substituting the relation in Eq. (8) into Eq. (11), we can solve for $\alpha_{1\to2}(\omega)$:

$$\alpha_{1\to2}(\omega) = \frac{\sum_j N_2(\omega, T, j)c_{2,j}}{\sum_j N_1(\omega, T, j)c_{1,j} + \sum_j N_2(\omega, T, j)c_{2,j}}. \quad (12)$$

Now employ the expressions in Eqs. (4*a*) and (4*b*) for $N_1(\omega, T_1, j)$ and $N_2(\omega, T_2, j)$ to obtain the final relation for $\alpha_{1\to2}(\omega)$:

$$\alpha_{1\to2}(\omega) = \alpha_{1\to2} = \frac{\sum_j c_{2,j}^{-2}}{\sum_j c_{1,j}^{-2} + \sum_j c_{2,j}^{-2}}. \quad (13)$$

Equation (13) is theoretically valid for all temperatures, within the confines of the Debye theory. However, it must be noted that Eq. (13) is derived for the case where $T_1 = T_2$, which is obviously not true when there is a finite heat flow from the film to the substrate. Equation (13) probably represents $\alpha_{1\to2}(\omega)$ adequately where $\Delta T = T_1 - T_2$ is small, and as can be seen, $\alpha_{1\to2}(\omega)$ loses its frequency dependence to become a constant value, $\alpha_{1\to2}$. For larger values of ΔT, Eq. (13) becomes less valid and $\alpha_{1\to2}$ probably regains its frequency dependence. Nevertheless, Eq. (13) is used to calculate all the results in the present study. Determining a more appropriate relation for $\alpha_{1\to2}(\omega)$ at large values of ΔT (without employing the Debye density of states) is left for a future publication.

Results

AMM and DMM Results for $T \ll \theta_d$, $\Delta T \to 0$. The most restrictive and commonly used assumptions for both the AMM and DMM are that the temperatures are much less than the lower Debye temperature of the two materials, $T \ll \theta_d$, and that the temperature difference is very small, $\Delta T \to 0$. Under these assumptions, $\alpha_{1\to2}$ and $\alpha_{2\to1}$ are both constant values, per Eq. (13), and the integrals in Eq. (6) can be evaluated to yield

$$q = \frac{k_b^4\pi^2}{120\hbar^3}\{T_1^4\sum_j c_{1,j}^{-2}\alpha_{1\to2} - T_2^4\sum_j c_{2,j}^{-2}\alpha_{2\to1}\}. \quad (14)$$

Furthermore, if $T_1 = T_2$, $q = 0$ and

$$\sum_j c_{1,j}^{-2}\alpha_{1\to2} = \sum_j c_{2,j}^{-2}\alpha_{2\to1}, \quad (15)$$

thus simplifying Eq. (14) further to

$$q = \frac{k_b^4\pi^2}{120\hbar^3}[\sum_j c_{1,j}^{-2}]\alpha_{1\to2}(T_1^4 - T_2^4). \quad (16)$$

Equation (16) is now substituted into the expression for R_b, Eq. (7), and after utilizing $\Delta T \to 0$ we are left with the final expression for R_b:

$$R_b = \left\{\frac{k_b^4\pi^2}{30\hbar^3}[\sum_j c_{1,j}^{-2}]\alpha_{1\to2}\right\}^{-1}T_2^{-3}, \quad (17)$$

which is strictly valid for $T_2 \ll \theta_d$ and $\Delta T \to 0$. Equation (17) is equivalent to that given in Swartz and Pohl (1989), where T_2, the substrate temperature, is arbitrarily used as the reference temperature.

In a similar manner, and for the same assumptions, a comparable result can be derived for the AMM (Little, 1959; Swartz and Pohl, 1989):

$$R_{b,\mathrm{AMM}} = \left\{\frac{k_b^4\pi^2}{15\hbar^3}\left[\frac{\Gamma_{1,\mathrm{tot}}}{c_{1,l}^2}\right]\right\}^{-1}T_2^{-3} \quad (18)$$

where $R_{b,\mathrm{AMM}}$ is the AMM result, $c_{1,l}$ the longitudinal speed of sound in material 1, and $\Gamma_{1,\mathrm{tot}}$ is the integrated transmission coefficient for the AMM.

The necessary properties for calculating the transmission coefficients for material 1, YBCO, are (Cankurtaran et al., 1989; von Molnár et al., 1988)

$$c_{1l} = 4780\ \mathrm{m\ s^{-1}}$$

$$c_{1t} = 3010\ \mathrm{m\ s^{-1}}$$

$$\rho_1 = 6338 \text{ kg m}^{-3}$$

$$\theta_{d1} = 410 \text{ K}$$

and those for material 2, MgO, are (Landolt-Börnstein, 1975; Landolt-Börnstein, 1982; American Institute of Physics Handbook, 1982)

$$c_{2l} = 9710 \text{ m s}^{-1}$$

$$c_{2t} = 6050 \text{ m s}^{-1}$$

$$\rho_2 = 3576 \text{ kg m}^{-3}$$

$$\theta_{d2} = 946 \text{ K}.$$

Note that a total of three phonon modes is assumed: two transverse and one longitudinal. However, the two transverse phonon speeds are taken to be equivalent, so that, for example, for material 1 we have

$$\sum_j c_{1,j}^{-2} = \frac{1}{c_{1,l}^2} + \frac{1}{c_{1,t}^2} + \frac{1}{c_{1,t}^2} = \frac{1}{c_{1,l}^2} + \frac{2}{c_{1,t}^2}. \quad (19)$$

The integrated transmission coefficient for the AMM, $\Gamma_{1,\text{tot}}$, is determined from the above properties and the tables in Cheeke et al. (1976) and is found to be 0.698. The transmission coefficient for the DMM, $\alpha_{1\to2}$, is calculated from Eq. (13) and is determined to be 0.198.

The results from both models are compared with some existing HTS experimental data in Fig. 2. The experimental data are for an Er-Ba-Cu-O thin film on an MgO substrate (Phelan et al., 1994), but the results are characteristic of other existing R_b data for HTS thin films. That is, R_b is roughly constant at around 10^{-7} m^2 K W^{-1}. As indicated in Fig. 2, the data lie as much as two orders of magnitude above both theoretical predictions. Although the DMM results are slightly closer to the data than those of the AMM, clearly they fail to accurately represent the data. Apparently, either some of the assumptions and limitations of the DMM must be removed in order to improve the agreement between theory and experiment, or other mechanisms in addition to diffuse scattering must be taken into account. The rest of this report will be concerned with removing some of the assumptions of the DMM and observing the resulting effects on the predictions of R_b.

DMM Results for Any T, $\Delta T \to 0$. One assumption that can be easily removed from the DMM is that which limits the temperature to $T \ll \theta_d$. As indicated in the upper scale of Fig. 2 and subsequent figures, the temperature range of interest for HTS devices is approximately $T/\theta_d = 0.2$, which arguably is outside the temperature range where the $T \ll \theta_d$ approximation

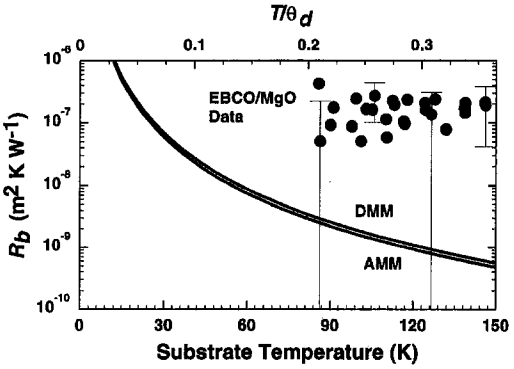

Fig. 2 Comparison of the Acoustic Mismatch Model (AMM), the Diffuse Mismatch Model (DMM), and HTS experimental data. The theoretical curves are based on the Debye model and are limited to the conditions that $T \ll \theta_d$ and $\Delta T \to 0$.

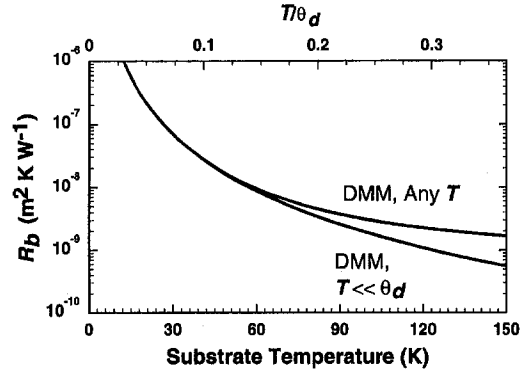

Fig. 3 Comparison of the Diffuse Mismatch Model (DMM) results, based on the Debye model, between the limiting case where $T \ll \theta_d$, $\Delta T \to 0$, and those for any T, $\Delta T \to 0$

is valid. Starting with the expression for q in Eq. (6), and utilizing the still valid relation in Eq. (15), results in

$$q = \frac{k_b^4}{8\pi^2\hbar^3}\left[\sum_j c_{1,j}^{-2}\right]\alpha_{1\to2}\left\{T_1^4\int_{z=0}^{\hbar\omega_d/k_bT_1}\frac{z^3dz}{\exp(z)-1} - T_2^4\int_{z=0}^{\hbar\omega_d/k_bT_2}\frac{z^3dz}{\exp(z)-1}\right\}. \quad (20)$$

Now, the integrals have to be evaluated numerically. However, since $\Delta T \to 0$, $T_1 \cong T_2$, so that the upper limits of integration for both integrals become equivalent, leaving

$$q = \frac{k_b^4}{8\pi^2\hbar^3}\left[\sum_j c_{1,j}^{-2}\right]\alpha_{1\to2}\left\{\int_{z=0}^{\hbar\omega_d/k_bT_2}\frac{z^3dz}{\exp(z)-1}\right\}(T_1^4 - T_2^4). \quad (21)$$

Then, utilizing $\Delta T \to 0$ as before yields the final expression for R_b:

$$R_b = \left\{\frac{k_b^4}{2\pi^2\hbar^3}\left[\sum_j c_{1,j}^{-2}\right]\alpha_{1\to2}\int_{z=0}^{\hbar\omega_d/k_bT_2}\frac{z^3dz}{\exp(z)-1}\right\}^{-1}T_2^{-3} \quad (22)$$

where again T_2, the substrate temperature, is used for convenience. Equation (22) is valid for $\Delta T \to 0$ and any T.

Figure 3 provides a graphical comparison between the DMM expression for $T \ll \theta_d$, and that for any T, but both of which are subject to the constraint that $\Delta T \to 0$. As expected, at low temperatures the two curves are equal, but above ~60 K, or $T/\theta_d \sim 0.15$, the curves diverge. The DMM expression for any T, Eq. (22), predicts values of R_b higher than those calculated using Eq. (17), since the integral is evaluated over a shorter range of limits. In physical terms, this is the effect that as the temperature increases above absolute zero, a smaller and smaller range of phonon frequencies is available for heat transport, leading to an increasing R_b. Yet, recalling that the experimental data in Fig. 3 are clustered around 10^{-7} m^2 K W^{-1}, there is still plenty of room for improving the theory. The next section will discuss removing another temperature restriction from the theoretical derivation.

DMM Results for any T, any ΔT. Now that the restriction that $\Delta T \to 0$ is lifted, we must employ Eq. (20) to calculate q, and then substitute the result into Eq. (7) to calculate R_b. First, however, it must be emphasized that $\alpha_{1\to2}$ is calculated from Eq. (13), which as discussed previously is strictly valid only for $\Delta T \to 0$. In every other way, though, the assumption that $\Delta T \to 0$ is removed, so that we capture the complete behavior

in R_b resulting from both the T^4 terms, as well as any effects due to keeping T_1 and T_2 in the upper limits to their respective integrals in Eq. (20). The results of this calculation are shown in Fig. 4, which also includes R_b calculated in the previous section (Eq. (22)) for any T, $\Delta T \to 0$.

Two interesting features are readily apparent, one at low temperatures and the other at high temperatures. Both features are due to the competing effects of (i) keeping the T^4 terms, rather than simplifying with $\Delta T \to 0$, and (ii) keeping both $\hbar\omega_d/k_bT_1$ and $\hbar\omega_d/k_bT_2$ as the upper limits to the integrals in Eq. (20). At low temperatures, R_b is relatively insensitive to changing the upper limits of integration, since the integrand, $z^3/[\exp(z) - 1]$, is effectively zero for $z > 12$, while at low temperatures the upper limits of integration are much larger than that. Thus, the changes in R_b at low temperatures, which decreases with increasing ΔT, are due entirely to the presence of the T^4 terms, or effect (i). At high temperatures, simplifying the T^4 terms using the $\Delta T \to 0$ approximation becomes more valid, since $\Delta T/T_2$ becomes much less than one. Therefore, the curves for finite ΔT tend to merge together at high temperatures. However, an interesting and unanticipated (at least by this author) feature results from effect (ii). Keeping T_1 and T_2 in the upper limits of integration in the two integrals in the calculation of q has a substantial effect at these higher temperatures, since at these temperatures the integrand changes rapidly with z. The interplay between the T^4 terms and the integrals produces a q that increases approximately linearly with increasing ΔT, a result in agreement with conventional behavior at higher temperatures. The difference between the set of curves for finite ΔT and that for $\Delta T \to 0$ at high temperatures is a consequence of approximating $\hbar\omega_d/k_bT_1$ by $\hbar\omega_d/k_bT_2$ in the first integral in Eq. (20).

Despite removing all the temperature restrictions, there is still considerable disagreement between the theoretical curves and the data shown in Fig. 2. The next step, therefore, is to remove the assumption of Debye densities of states for the two materials in contact, as discussed in the following section.

DMM Results for Measured Phonon Density of States. To employ a measured phonon density of states (DOS), we start with the general expression for $\dot{Q}_{1\to2}(T)$ in Eq. (2). Upon integrating over θ and A, we are left with

$$\frac{\dot{Q}_{1\to2}(T_1)}{A} = \frac{1}{4}\sum_j \int_{\omega=0}^{\infty} N_1(\omega, T_1)\hbar\omega c_{1,j}\alpha_{1\to2}\, d\omega \qquad (23)$$

where the limits of integration are from $\omega = 0$ to $\omega = \infty$, since there is no longer any restriction on ω. Also, N_1 loses its dependence on the phonon mode j. Now, in order to simplify the following derivation, the principle of detailed balance (Swartz and Pohl, 1989) is used to generate the expression for the net heat flux q:

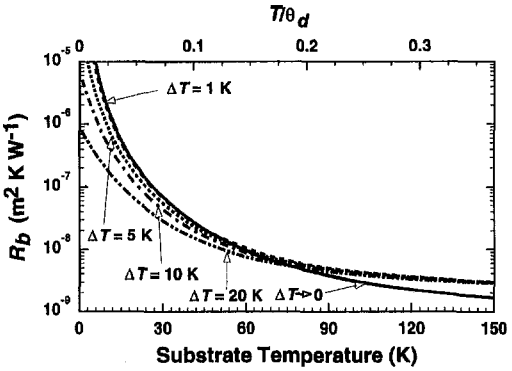

Fig. 4 Comparison of the Diffuse Mismatch Model (DMM) results, based on the Debye model, between the limiting case for any T, $\Delta T \to 0$, and those for any T, any ΔT

$$q = \frac{\dot{Q}_{1\to2}(T_1)}{A} - \frac{\dot{Q}_{1\to2}(T_2)}{A}. \qquad (24)$$

Equation (24) yields results equivalent to those from Eq. (3) and permits the calculation of q by considering only one side of the interface. The principle of detailed balance which enables this simplification can be understood by considering two scenarios: an interface at thermal equilibrium at T_1 and an interface at thermal equilibrium at T_2. Under these two conditions we have

$$\frac{\dot{Q}_{1\to2}(T_1)}{A} = \frac{\dot{Q}_{2\to1}(T_1)}{A} \quad \text{and} \quad \frac{\dot{Q}_{1\to2}(T_2)}{A} = \frac{\dot{Q}_{2\to1}(T_2)}{A}. \qquad (25)$$

Since from Eq. (13) $\alpha_{1\to2}$, and conversely, $\alpha_{2\to1}$, do not depend on the temperature on the other side of the interface, we can substitute $\dot{Q}_{1\to2}(T_2)$ for $\dot{Q}_{2\to1}(T_2)$ in Eq. (3), giving us Eq. (24). Note that a more rigorous derivation of $\alpha_{1\to2}$ for an interface where $T_1 \neq T_2$ would yield $\alpha_{1\to2} = \alpha_{1\to2}(T_1, T_2, \omega)$, so that Eq. (3) would not simplify to Eq. (24).

Combining Eqs. (23) and (24) yields

$$q = \tfrac{1}{4}\sum_j \int_{\omega=0}^{\infty} [N_1(\omega, T_1) - N_1(\omega, T_2)]\hbar\omega c_{1,j}\alpha_{1\to2}\, d\omega. \qquad (26)$$

For $N_1(\omega, T)$, use

$$N_1(\omega, T) = g(\omega)\cdot f(\omega, T) = \frac{g(\omega)}{\exp\left(\dfrac{\hbar\omega}{k_bT}\right) - 1}, \qquad (27)$$

where $g(\omega)$ is the measured phonon DOS, in [s m^{-3} rad^{-1}], and $f(\omega, T)$ is the Bose-Einstein occupation factor. Substituting Eq. (27) into Eq. (26) yields the final expression for q:

$$q = \frac{\hbar\alpha_{1\to2}}{4}\sum_j c_{1,j}\int_{\omega=0}^{\infty} g(\omega)\omega \times \left[\frac{1}{\exp\left(\dfrac{\hbar\omega}{kT_1}\right)} - \frac{1}{\exp\left(\dfrac{\hbar\omega}{kT_2}\right)}\right] d\omega, \qquad (28)$$

which is numerically integrated to yield a value for q, after which q is substituted into Eq. (7) to calculate R_b.

Measured values of $g(\omega)$ (Gompf et al., 1988) are reported in units of meV^{-1}. To establish $g(\omega)$ on a per unit volume basis, as required by Eq. (27), these measured values are multiplied by a factor n, defined by (Ashcroft and Mermin, 1976)

$$n = \frac{\text{number of primitive cells}}{\text{unit volume}}, \qquad (29)$$

as well as converted to s rad^{-1} from meV^{-1}. For YBCO, since only one formula unit is contained within the unit cell (Poole et al., 1995), the unit cell is taken to be the primitive cell and has the following dimensions (Poole et al., 1995):

$$a = 3.83 \text{ Å},$$

$$b = 3.88 \text{ Å},$$

and

$$c = 11.68 \text{ Å}, \qquad (30)$$

where a, b, and c are the lattice constants. Thus, upon conversion to SI units, this leads to $n = 5.7614 \times 10^{27}$ m^{-3}.

A comparison between the Debye DOS, and the measured $g(\omega)$, converted to appropriate units as discussed above, is

presented in Fig. 5. It is immediately apparent from Fig. 5 that, although the Debye DOS is limited to frequencies $\omega < \omega_d$, the Debye DOS is much greater than the measured $g(\omega)$, which peaks between 0.2 and 0.4 $\times$ 10^{14} rad s^{-1}, and drops to zero near 1.4 $\times$ 10^{14} rad s^{-1}. From Eq. (28), one can see that as $g(\omega)$ decreases, q decreases, which results in higher values for R_b. This is precisely what is observed in Fig. 6 (which shows a comparison between the same set of experimental data displayed in Fig. 2): a curve for any T and ΔT = 1 K based on the Debye DOS and curves resulting from Eq. (28) and using the measured $g(\omega)$. Considering the measured $g(\omega)$ drastically improves the agreement with the experimental data, signifying the failure of the Debye model at the temperatures appropriate for HTS's.

Some caution is warranted, however, in the interpretation of the results in Fig. 6. The specific heat at constant volume, c_v, as calculated from the measured $g(\omega)$ through

$$c_v = \frac{1}{\rho}\frac{\partial U}{\partial T} = \frac{3\hbar^2}{\rho k_b T^2}\int_{\omega=0}^{\infty} \frac{g(\omega)\omega^2 \exp\left(\frac{\hbar\omega}{k_b T}\right) d\omega}{\left[\exp\left(\frac{\hbar\omega}{k_b T}\right) - 1\right]^2}, \quad (31)$$

where U is the lattice energy, is much lower than measured specific heat data for YBCO, assuming that $c_v = c_p$, the specific heat at constant pressure. This creates some doubt about the validity of our measured $g(\omega)$, although it should be pointed out that while Eq. (31) considers only the harmonic contribution to c_v; the anharmonic contribution has been shown to be significant at low temperatures for aluminum and lead (Stedman et al., 1967). Thus, although there may be some uncertainty in the measured $g(\omega)$, this uncertainty does not erase the fact that considering a realistic phonon density of states greatly improves the agreement between the DMM and experimental data.

Although Fig. 6 shows that the DMM, when the measured $g(\omega)$ is taken into account, is relatively successful in its agreement with experimental data, some differences are still apparent between the theoretical results and the data. First of all, it must be noted that $\alpha_{1\to 2}$ in Eq. (28) is still calculated from Eq. (13), which is itself derived by assuming an interface at thermal equilibrium and Debye DOS's on both sides of the interface. The error caused by these assumptions will be evaluated in a future work, but this error will not undo the result that considering the measured $g(\omega)$ greatly increases R_b compared to assuming the Debye DOS. Secondly, the fact that the theoretical curves do not fall in the middle of the set of data, but rather somewhat below it, suggests that another mechanism is at play which effectively increases R_b. This mechanism is likely the increased scattering due to the imperfect crystal structure near the interface, such as that caused by defects or interdiffusion. This is also suggested by the relative independence of measured

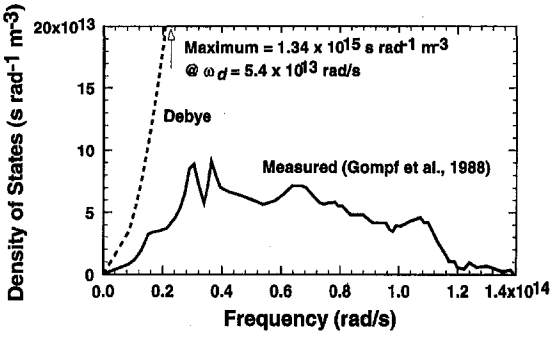

Fig. 5 Comparison of the YBCO phonon DOS calculated assuming the Debye model and the measured phonon DOS (Gompf et al., 1988)

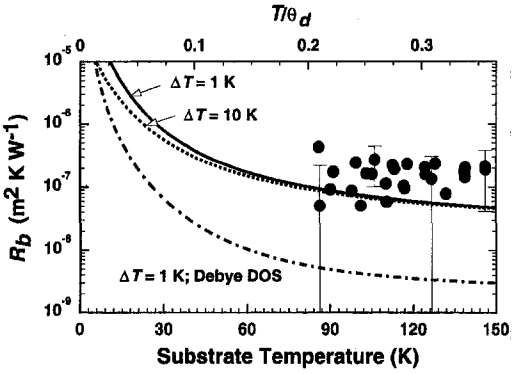

Fig. 6 Comparison of the Diffuse Mismatch Model (DMM) results considering either the Debye or measured phonon DOS and experimental data. The theoretical curves are valid for any T and the specified ΔT.

R_b on temperature, since phonon scattering by defects is essentially constant at high temperatures (Rosenberg, 1988).

An alternative approach to employing either the Debye or the measured DOS is to consider the phonon dispersion, such as that calculated using a simple oscillator model like the Born-von Kármán model (Ziman, 1960). However, the DOS derived from the Born-von Kármán model is actually greater than that from the Debye model over the same range of ω. With reference to Fig. 5, the greater DOS leads to a larger q at the same ΔT, or in other words, to a smaller R_b. Since the DMM results based on the Debye model already underpredict the measured R_b by as much as two orders of magnitude, considering the phonon dispersion in this way is apparently not a fruitful approach. Note that in general, by itself the Born-von Kármán model also fails to improve the prediction of the lattice specific heat (Ziman, 1960), although an oscillator model, combined with some consideration of the optical as well as the acoustic phonons, has recently been shown to yield relatively good agreement with specific heat data for GaAs (Chen, 1997). For R_b, it may be concluded that phonon dispersion must be portrayed more accurately than through a simple oscillator model if results better than those obtained from the Debye model are to be expected.

Conclusions

The Diffuse Mismatch Model (DMM) is applied to the prediction of the thermal boundary resistance (R_b) in thin-film high temperature superconductors. The results are compared with those of the Acoustic Mismatch Model (AMM), as well as with some existing experimental data. These comparisons indicate that when employing the Debye model for the phonon densities of state, the DMM predicts values of R_b that are slightly higher than those predicted by the AMM, but that both predictions are as much as two orders of magnitude less than the experimental data. Removing some of the assumptions inherent in the derivation of the DMM, particularly those limiting its application to temperatures much less than the Debye temperature and to small temperature differences, tends to slightly increase the predicted value of R_b, depending on the temperature range. Considering the measured phonon density of states, however, is shown to greatly increase R_b compared to that calculated assuming the Debye model, thus bringing the theoretical results in relatively good agreement with the experimental data.

Acknowledgments

The author gratefully acknowledges the support of the National Science Foundation through a Research Initiation Award (Grant No. CTS-9696002) and a CAREER Award (Grant No.

CTS-96960003). The author appreciates the assistance of Mr. Ravi Prasher in preparing Fig. 1.

References

American Institute of Physics Handbook, 3rd ed., 1982, D. E. Gray, coordinating ed., McGraw-Hill, NY, p. 4–115.

Angenheister, G., ed., 1982, *Landolt-Börnstein,* Vol. 1, Subvol. a, Springer-Verlag, Berlin, p. 33.

Ashcroft, N. W., and Mermin, N. D., 1976, *Solid State Physics,* Saunders College Publishing, Fort Worth, pp. 462–465.

Burkhard, G., Sawaoka, A. B., and Phelan, P. E., 1995, "The Effect of Umklapp-Processes on the Heat Transport of Solids: Evaluation of the Thermal Boundary Resistance of Two Joined Solids," *Proceedings of the Symposium on Thermal Science and Engineering in Honor of Chancellor Chang-Lin Tien,* pp. 145–152.

Cankurtaran, M., Saunders, G. A., Willis, J. R., Al-Kheffaji, A., and Almond, D. P., 1989, "Bulk Modulus and Its Pressure Derivative of $YBa_2Cu_3O_{7-x}$," *Physical Review B,* Vol. 39, No. 4, pp. 2872–2875.

Cheeke, J. D. N., Ettinger, H., and Hebral, B., 1976, "Analysis of Heat Transfer Between Solids at Low Temperatures," *Canadian Journal of Physics,* Vol. 54, pp. 1749–1771.

Chen, G., 1997, "Size and Interface Effects on Thermal Conductivity of Superlattices and Periodic Thin-Film Structures," ASME JOURNAL OF HEAT TRANSFER, Vol. 119, No. 2, pp. 220–229.

Gompf, F., Renker, B., and Gering, E., 1988, "Comparison of the Phonon Density of States of High-T_c $YBa_2Cu_3O_7$ With That of the Nonsuperconducting Reference System $YBa_2(Cu_{.9}Zn_{.1})_3O_7$," *Physica C,* Vol. 153–155, pp. 274–275.

Hellwege, K.-H., and Hellwege, A. M., eds., 1975, *Landolt-Börnstein,* Vol. 7, Part B, Springer-Verlag, Berlin, p. 26.

Little, W. A., 1959, "The Transport of Heat Between Dissimilar Solids at Low Temperatures," *Canadian Journal of Physics,* Vol. 37, pp. 334–349.

Nahum, M., Verghese, S., Richards, P. L., and Char, K., 1991, "Thermal Boundary Resistance for $YBa_2Cu_3O_{7-\delta}$ Films," *Applied Physics Letters,* Vol. 59, No. 16, pp. 2034–2036.

Phelan, P. E., Song, Y., Nakabeppu, O., Ito, K., Hijikata, K., Ohmori, T., and Torikoshi, K., 1994, "Film/Substrate Thermal Boundary Resistance for an Er-Ba-Cu-O High-T_c Thin Film," ASME JOURNAL OF HEAT TRANSFER, Vol. 116, No. 4, pp. 1038–1041.

Poole, C. P., Jr., Farach, H. A., and Creswick, R. J., 1995, *Superconductivity,* Academic Press, San Diego, CA pp. 180–183.

Rosenberg, H. M., 1988, *The Solid State,* 3rd ed., Oxford University Press, NY, pp. 97, 101.

Stedman, R., Almqvist, L., and Nilsson, G., 1967, "Phonon-Frequency Distributions and Heat Capacities of Aluminum and Lead," *Physical Review,* Vol. 162, No. 3, pp. 549–557.

Swartz, E. T., and Pohl, R. O., 1989, "Thermal Boundary Resistance," *Reviews of Modern Physics,* Vol. 61, No. 3., pp. 605–668.

von Molnár, S., Torressen, A., Kaiser, D., Holtzberg, F., and Penney, T., 1988, "Low-Temperature Specific Heat of Single-Crystal $YBa_2Cu_3O_{7-\delta}$," *Physical Review B,* Vol. 37, No. 7, pp. 3762–3765.

Zeuner, S., Lengfellner, H., and Prettl, W., 1995, "Thermal Boundary Resistance and Diffusivity for $YBa_2Cu_3O_{7-\delta}$ Films," *Physical Review B,* Vol. 51, No. 17, pp. 11903–11908.

Ziman, J. M., 1960, *Electrons and Phonons,* Oxford University Press, London, pp. 59–61.

Stokes' First and Second Problems for Rivlin-Ericksen Fluids With Nonclassical Heat Conduction

P. Puri
Professor.
ppma@uno.edu

P. K. Kythe
Professor.

Department of Mathematics,
University of New Orleans,
New Orleans, LA 70148

The nonclassical heat conduction equation based on the Maxwell-Cattaneo-Fox (MCF) model is used to study the Stokes' first and second problems for the Rivlin-Ericksen fluids. The discontinuities in velocity gradients in fluid flows induced by impulsive or sudden heating of a plate and the influence of the thermal relaxation time and elastic parameter of the fluid on the velocity field are investigated. The structure of the waves in the temperature and velocity fields is presented. An anomalous behavior of the medium is characterized by infinite or negative values of the group velocity for the wave packets as the frequency attains or exceeds a critical value. The displacement thickness and the rate of heat transfer at the plate are determined.

1 Introduction

Fourier's law of heat conduction, which has been used to derive the heat conduction equation in classical unsteady heat transfer problems, results in a parabolic equation for the temperature field and an infinite speed of heat propagation, thus violating the principle of causality. Maxwell (1867) derived the first generalization of Fourier's heat law for the dynamical theory of gases. Maxwell's heat flux equation contains a term proportional to the time derivative of the heat flux vector with the constant of proportionality known as the thermal relaxation time τ. Since τ had a very small magnitude in Maxwell's work, he took it to be zero. In justification he remarked, "The first term of this equation may be neglected, as the rate of conduction will rapidly establish itself." It appears that Maxwell did not investigate the implications of a nonzero relaxation time. Further progress was not made until 1917 when Nerest (1917) suggested for the first time the existence of thermal "inertia" in good thermal conductors at very low temperatures. In 1931, Onsager (1931) was the first to note that Fourier's heat law is only an approximation of the actual process of heat conduction. He was also the first to state that Fourier's heat law implies zero propagation time for thermal energy. Onsager conjectured that the time of propagation of a thermal disturbance is very small, but he did not suggest how Fourier's heat law could be modified. Between 1938 and 1944 researchers attempted to detect the "second sound" effect in liquid helium and superfluid helium II. This effect was first observed in 1944 by Peshkov (1944) in liquid helium. Cattaneo (1948) was the first to develop a precise mathematical modification of Fourier's theory of heat conduction by using a second-order approximation and aspects from the kinetic theory of gases to derive the equation. Cattaneo's theory allows for the existence of thermal waves which propagate at finite speeds and are the means by which heat flow occurs in gases.

Chester (1963), Kaliski (1965), Lord and Shulman (1967), Green and Lindsay (1972), and others have developed equations of thermoelasticity which permit finite speed of thermoelastic wave propagation. Ackerman et al. (1966) established the second sound in solid helium, which gave a finite speed of propagation of thermal waves. Although Lindsay and Straughan (1978) have investigated acceleration waves and second sound in a perfect fluid, no significant progress has been made in developing solutions for corresponding problems in fluid mechanics. A detailed history of the development of nonclassical generalizations of Fourier's law is given in Joseph and Preziosi (1989, 1990). They state that the Cattaneo equation is the most obvious and simple generalization of Fourier's law that gives rise to finite speeds of propagation. McTaggart and Lindsay (1985) used a non-Fourier heat flux law and analyzed the effect of modified heat conduction equations in the Bénard problem. They have shown that there is a major difference in the results of the Bénard problem when nonclassical effects are taken into account. This is due to the "major role played by the time constant of the Maxwell-Cattaneo theory." Puri and Kythe (1995) have studied an unsteady flow problem which deals with nonclassical heat conduction effects and the structure of waves in the Stokes' second problem. To the best of our knowledge the only study into the existence and propagation of discontinuities in viscous flows induced by nonclassical thermal effects has been done by Puri and Kythe (1997).

In this article we have studied the influence of generalized law of heat conduction, using the Maxwell-Cattaneo-Fox (MCF) model, on Stokes' first and second problems for the Rivlin-Ericksen fluids. The corresponding thermoelastic problems have been studied by several authors, some of the principal ones being Lord and Shulman (1967), and Norwood and Warren (1969). In the MCF model as developed in McTaggart and Lindsay (1985), the nonclassical constitutive equation for the heat-flux vector q is given by the Maxwell-Cattaneo equation

$$\tau(\dot{q}_i - \omega_{ij}q_j) = -q_i - \kappa\theta_{,i}. \tag{1}$$

The thermal relaxation time τ is "the time delay between the heat flux vector and the temperature gradient in the fast-transient process" (Tzou, 1997). If $\omega_{ij} = 0$, Eq. (1) reduces to that of the Cattaneo model, and for $\tau = 0$ it becomes Fourier's law (see Joseph and Preziosi (1989, 1990)). While there are other good models to choose from, the Cattaneo law, as stated in Joseph and Preziosi (1989, 1990), has many desirable properties. For example, the steady heat flow is induced by temperature gradients and gives rise to finite speeds of propagation. The dimensionless thermal relaxation time, defined as $\lambda = CP$, ex-

Contributed by the Heat Transfer Division for publication in the JOURNAL OF HEAT TRANSFER. Manuscript received by the Heat Transfer Division April 28, 1997; revision received September 23, 1997; Keywords: Flow; Heat Transfer; Non-Newtonian; Thermal; Unsteady. Associate Technical Editor: M. Kaviaany.

hibits a definite influence in the existence and speed of propagation of discontinuities in velocity gradients and temperature in fluid flows induced by impulsive heating (thermal impulse $\delta(t)$) or by sudden heating (thermal input $H(t)$) of the plate. The number λ also appears in generalized thermoelasticity (see Puri (1973, 1975) where it is defined as m) and is shown to be of order 10^{-2}. Again, as noted in McTaggart and Lindsay (1985), the Cattaneo number C may not be small in astrophysical applications. For example, C is of order 10^{-2} in a low temperature hydrogen gas. However, the thermal relaxation time λ does not appreciably change the magnitude of the temperature and velocity fields.

In Stokes' first problem a weak solution for velocity is found in the case of an impulsive heating of the plate, but a strong solution exists for sudden heating of the plate. The oscillatory nature of the flow in Stokes' second problem generates dispersive wave packets in both temperature and velocity fields. An interesting situation arises when the group velocity first becomes infinite at a critical frequency and negative thereafter, thus indicating an anomalous behavior, which is explained in the sequel. There is a growing interest in cooling and low temperature phenomena, especially in medical and space research.

2 Mathematical Analysis

We will consider the Stokes' first and second problems (see, e.g., Schlichting (1960)) for a viscoelastic incompressible fluid (Rivlin-Ericksen model (1955)). Let the fluid rest adjacent to a vertical flat plate in the yz-plane and occupy the space $x > 0$, with the z-axis in the vertical direction. The flow is induced by impulsive or sudden heating of the plate, or by time-dependent motion of the plate, or both. The plate which is initially at rest and at constant temperature θ_∞ is moved with a velocity $U_0 g(t)$ vertically in its own plane in the direction of the z-axis, and its temperature is subjected to heating of the form $(\theta_w - \theta_\infty)f(t)$.

The basic equations of continuity, momentum, and energy, governing such a flow, subject to the Boussinesq approximation, are

$$v_{i,i} = 0, \tag{2}$$

$$\rho \dot{v}_i = -p_{,i} + \mu \nabla^2 v_i - \rho[1 - \alpha(\theta - \theta_\infty)]g\delta_{i3} + t_{ki,k}, \tag{3}$$

$$\rho \dot{\epsilon} = -q_{i,i} + t_{ik} d_{ik}. \tag{4}$$

Although $t_{ik} = 0$ for viscous fluids as in Puri and Kythe (1997), in the case of Rivlin-Ericksen model considered here, $t_{ik} = \mathbf{T}$, which for the second-order approximation of the general constitutive equation for the Rivlin-Ericksen fluid is defined by

$$\mathbf{T} = -p\mathbf{I} + \mu\mathbf{A}_1 + \beta_1\mathbf{A}_1^2 + \beta_2\mathbf{A}_2, \tag{5}$$

where

$$\mathbf{A}_1 = \frac{\partial v_i}{\partial x_j} + \frac{\partial v_j}{\partial x_i},$$

$$\mathbf{A}_2 = \frac{\partial}{\partial x_j}\left(\frac{Dv_i}{Dt}\right) + \frac{\partial}{\partial x_i}\left(\frac{Dv_j}{Dt}\right) + 2\frac{\partial v_m}{\partial x_i}\frac{\partial v_m}{\partial x_j},$$

$$(i, j, m = 1, 2, 3).$$

Taking into account the geometry of the problem which results in the disappearance of the dissipative terms and dropping nonlinear terms, Eqs. (2)–(3) reduce to the following equation of motion:

$$u_t = \nu u_{xx} + k^* u_{xxt} + g\alpha(\theta - \theta_\infty), \tag{6}$$

where $k^* = \beta_2/\rho$ is the viscoelastic constant which measures the elasticity of the fluid. Equation (1), after substitution into (4), gives

$$\rho c_p \dot{\theta} = -q_{i,i}, \tag{7}$$

since $\epsilon = c_p\theta$ for the MCF model. If we drop the nonlinear terms $\tau\omega_{ij}q_j$ in (1), because τ and ω_{ij} are small quantities we get

$$\tau \dot{q}_{i,i} = -q_{i,i} - \kappa\theta_{,ii}. \tag{8}$$

Eliminating $q_{i,i}$ between (6) and (7) we find that

$$-\rho c_p \tau \ddot{\theta} = \rho c_p \dot{\theta} - \kappa\theta_{,ii}. \tag{9}$$

Since $\dot{\theta} = (\partial\theta/\partial t) + u_x(\partial\theta/\partial x) + u_y(\partial\theta/\partial y) + u_z(\partial\theta/\partial z) = \partial\theta/\partial t$ because $u_x = 0 = u_y$ and $\partial\theta/\partial z = 0$, Eq. (9) leads to

$$\tau\theta_{tt} + \theta_t = \frac{\kappa}{\rho c_p}\theta_{xx}. \tag{10}$$

Using the nondimensional quantities

$$x = \frac{\nu}{U_0}x', \quad u = U_0 u', \quad t = \frac{\nu}{U_0^2}t', \quad \frac{\theta - \theta_\infty}{\theta_w - \theta_\infty} = \theta',$$

$$k = \frac{k^* U_0^2}{\nu^2}, \quad G = \frac{\nu g\alpha(\theta_w - \theta_\infty)}{U_0^3}, \quad P = \frac{\nu\rho c_p}{\kappa},$$

$$C = \frac{\tau\kappa U_0^2}{\nu^2\rho c_p}, \quad \lambda = \frac{\tau U_0^2}{\nu} = CP,$$

Nomenclature

A_1, A_2 = first two Rivlin-Ericksen tensors
c_p = specific heat at constant pressure
C = Cattaneo number
d_{ik} = strain tensor
D/Dt = material time derivative (also denoted by dot)
$f(t)$ = arbitrary function of time
$g(t)$ = arbitrary function of time
G = Grashof number
$H(t)$ = Heaviside step function
I_1 = modified Bessel function of first kind
$\mathbf{I}$ = unit tensor
k = elastic parameter of the fluid
k^* = viscoelastic constant ($=\beta_2/\rho$)
p = pressure
P = Prandtl number
q = heat-flux vector
s = Laplace transform variable
S = magnitude of discontinuity (saltus)
t = time
t_{ij} = non-Newtonian stress tensor
u = z-component of velocity
U_0 = constant with dimensions of velocity
v_i = velocity components
$\mathbf{v}$ = velocity vector
x, y, z = cartesian coordinates
α = coefficient of thermal expansion
β_1, β_2 = material constants
$\delta(t)$ = Dirac delta function
δ_{ij} = Kronecker delta
δ^* = displacement thickness
ϵ = specific internal energy
θ = temperature
θ_∞ = free stream temperature
θ_w = constant temperature ($\neq\theta_\infty$)
κ = thermal conductivity
λ = dimensionless relaxation time ($=CP$)
μ = dynamic viscosity
ν = kinematic viscosity ($=\mu/\rho$)
ρ = density
τ = thermal relaxation time
ω = radian frequency
ω_c = critical frequency
ω_{ij} = components of vorticity tensor
$\mathcal{L}^{-1}$ = Laplace inverse
∇^2 = Laplacian

the governing equations (6) and (10) for the flow and heat conduction, after suppressing the primes, become

$$u_t = u_{xx} + kU_{xxt} + G\theta, \tag{11}$$

$$\lambda P\theta_{tt} + P\theta_t = \theta_{xx}, \tag{12}$$

where k measures of the strength of elastic forces relative to viscous forces.

Stokes' First Problem. The boundary conditions are

$$\theta(0, t) = f(t), \quad u(0, t) = g(t),$$

$$\theta(\infty, t) = 0 = u(\infty, t), \tag{13}$$

and the initial conditions are

$$u(x, 0) = 0 = \theta(x, 0) = \theta_t(x, 0). \tag{14}$$

By applying the Laplace transform to Eqs. (11) and (12), the solution in the transform domain is given by

$$\bar{\theta}(x, s) = \bar{f}(s)e^{-mx}, \tag{15}$$

$$\bar{u}(x, s) = \left[\bar{g}(s) + \frac{G\bar{f}(s)}{(1 + ks)m^2 - s}\right]e^{-x\sqrt{s/(1+ks)}}$$

$$- \frac{G\bar{f}(s)}{(1 + ks)m^2 - s}e^{-mx}$$

$$\equiv \bar{u}_1 - \bar{u}_2, \tag{16}$$

where a bar over a quantity denotes its Laplace transform with s as the transform variable and

$$m = \sqrt{\lambda Ps^2 + Ps}. \tag{17}$$

For $\bar{f}(s) = 1 = \bar{g}(s)$, the solution for θ has been obtained in Puri and Kythe (1997) and is given by

$$\theta(x, t) = H(t - b)abB(x, t) + \delta(t - b)e^{-at} \tag{18}$$

where

$$B(x, z) = e^{-az}\frac{I_1(a\sqrt{z^2 - b^2})}{\sqrt{z^2 - b^2}}, \quad a = 1/2\lambda, \quad b = x\sqrt{\lambda P}. \tag{19}$$

This solution represents the fundamental solution for this problem. All solutions for arbitrary $f(t)$ and $g(t)$ can be derived from it by applying Duhamel's theorem.

In order to obtain the inverse of $\bar{u}$, we first express $\bar{u}_1$ and $\bar{u}_2$ from (16) as follows:
for $P \neq 1$,

$$\bar{u}_1 = \left[1 + \frac{G}{\lambda kP}\left\{\frac{1}{\alpha\beta s} + \frac{1}{\alpha(\alpha - \beta)}\frac{1}{s + \alpha}\right.\right.$$

$$\left.\left. - \frac{1}{\beta(\alpha - \beta)}\frac{1}{s + \beta}\right\}\right]e^{-x\sqrt{s/(1+ks)}}, \tag{20}$$

$$\bar{u}_2 = \frac{G}{\lambda kP}\left\{\frac{1}{\alpha\beta s} + \frac{1}{\alpha(\alpha - \beta)}\frac{1}{s + \alpha}\right.$$

$$\left. - \frac{1}{\beta(\alpha - \beta)}\frac{1}{s + \beta}\right\}e^{-x\sqrt{Ps(1+\lambda s)}}, \tag{21}$$

and for $P = 1$,

$$\bar{u}_1 = \left[1 + \frac{G\lambda k}{(\lambda + k)^2}\left\{-\frac{1}{s} + \frac{\lambda + k}{\lambda k}\frac{1}{s^2}\right.\right.$$

$$\left.\left. + \frac{1}{s + 1/(\alpha + \beta)}\right\}\right]e^{-x\sqrt{s/(1+ks)}}, \tag{22}$$

$$\bar{u}_2 = \frac{G\lambda k}{(\lambda + k)^2}\left\{-\frac{1}{s} + \frac{\lambda + k}{\lambda k}\frac{1}{s^2}\right.$$

$$\left. + \frac{1}{s + 1/(\alpha + \beta)}\right\}e^{-x\sqrt{Ps(1+\lambda s)}}, \tag{23}$$

where

$$\alpha + \beta = \frac{\lambda + k}{\lambda k}, \quad \text{and} \quad \alpha\beta = \frac{P - 1}{\lambda kP}. \tag{24}$$

Using the Laplace inverses obtained in Puri (1984) and Puri and Kythe (1997), i.e.,

$$\mathcal{L}^{-1}e^{-x\sqrt{as/(s+a)}} = \frac{1}{\pi}\int_0^a e^{-\alpha t}\sin\left(x\sqrt{\frac{az}{a + z}}\right)dz, \tag{25}$$

and

$$\mathcal{L}^{-1}e^{-x\sqrt{Ps(1+\lambda s)}} = \frac{b}{2\lambda}B(x, t)H(t - b) + \delta(t - b)e^{-b/2\lambda}, \tag{26}$$

we get for $P \neq 1$

$$u_1 = \frac{1}{\pi}\int_0^{1/k}\left[e^{-zt} + \frac{G}{\lambda kP}\left\{\frac{\alpha(e^{-\alpha t} - e^{-zt})}{z(\alpha - z)}\right.\right.$$

$$\left.\left. - \frac{\beta(e^{-\beta t} - e^{-zt})}{z(\beta - z)}\right\}\right]\sin\left(x\sqrt{\frac{z}{1 - kz}}\right)dz$$

$$+ \frac{G}{\lambda kP}\left(\frac{1}{\alpha\beta} + \frac{e^{-\alpha t}}{\alpha(\alpha - \beta)} - \frac{e^{-\beta t}}{\beta(\alpha - \beta)}\right), \tag{27}$$

$$u_2 = \frac{H(t - b)G}{\lambda kP}\left[\frac{b}{2\lambda}\int_b^t\left\{\frac{1}{\alpha\beta} + \frac{e^{-\alpha(t-z)}}{\alpha(\alpha - \beta)} - \frac{e^{-\beta(t-z)}}{\beta(\alpha - \beta)}\right\}\right.$$

$$\left. \times B(x, z)dz + e^{-b/2\lambda}\left(\frac{1}{\alpha\beta} + \frac{e^{-\alpha(t-b)}}{\alpha(\alpha - \beta)} - \frac{e^{-\beta(t-b)}}{\beta(\alpha - \beta)}\right)\right], \tag{28}$$

and for $P = 1$

$$u_1 = \frac{1}{\pi}\int_0^{1/k}\left[e^{-zt} - \frac{G}{\lambda k(\alpha + \beta)}\right.$$

$$\left. \times\left\{\frac{1 - e^{-zt}}{z^2} - \frac{e^{-(\alpha+\beta)t} - e^{-zt}}{z(\alpha + \beta - z)}\right\}\right]\sin\left(x\sqrt{\frac{z}{1 - kz}}\right)dz$$

$$+ \frac{G}{\lambda k(\alpha + \beta)^2}[(\alpha + \beta)t - 1 + e^{-(\alpha+\beta)t}], \tag{29}$$

$$u_2 = \frac{H(t - b)G}{\lambda k(\alpha + \beta)^2}\left[\frac{b}{2\lambda}\int_b^t\{e^{-(\alpha+\beta)(t-z)} + (\alpha + \beta)(t - z) - 1\}\right.$$

$$\times B(x, z)dz - e^{-b/2\lambda}(1 - (\alpha + \beta)(t - b)$$

$$\left. - e^{-(\alpha+\beta)(t-b)})\right]. \tag{30}$$

For $\bar{f}(s) = 1/s = \bar{g}(s)$, the solutions for θ and $u = u_1 - u_2$ for $P \neq 1$, are given by

$$\theta = H(t-b)\left[e^{-ab} + ab\int_b^t B(b,\zeta)d\zeta\right], \quad (31)$$

$$u_1 = 1 + \frac{G}{\lambda kP}\left(\frac{t}{\alpha\beta} - \frac{\alpha+\beta}{\alpha^2\beta^2} - \frac{e^{-\alpha t}}{\alpha^2(\alpha-\beta)} + \frac{e^{-\beta t}}{\beta^2(\alpha-\beta)}\right) - \frac{1}{\pi}\int_0^{1/k}\left[\frac{e^{-zt}}{z} + \frac{G}{\lambda kP}\left\{\frac{1-e^{-zt}}{\alpha\beta z^2} + \frac{e^{-\alpha t} - e^{-zt}}{\alpha z(\alpha-\beta)(\alpha-z)} - \frac{e^{-\beta t} - e^{-zt}}{\beta z(\alpha-\beta)(\beta-z)}\right\}\right]\sin\left(x\sqrt{\frac{z}{1-kz}}\right)dz, \quad (32)$$

$$u_2 = \frac{H(t-b)G}{\lambda kP}\left[e^{-b/2\lambda}\left\{\frac{t-b}{\alpha\beta} - \frac{\alpha+\beta}{\alpha^2\beta^2} - \frac{e^{-\alpha(t-b)}}{\alpha^2(\alpha-\beta)} + \frac{e^{-\beta(t-b)}}{\beta^2(\alpha-\beta)}\right\} + \frac{b}{2\lambda}\int_b^t\left\{\frac{t-z}{\alpha\beta} - \frac{\alpha+\beta}{\alpha^2\beta^2} - \frac{e^{-\alpha(t-z)}}{\alpha^2(\alpha-\beta)} + \frac{e^{-\beta(t-z)}}{\beta^2(\alpha-\beta)}\right\}B(x,z)dz\right], \quad (33)$$

and for $P = 1$ by

$$u_1 = 1 + \frac{G}{\lambda k(\alpha+\beta)^3}\left(1 - (\alpha+\beta)t + \frac{(\alpha+\beta)^2}{2}t^2 - e^{-(\alpha+\beta)t}\right) - \frac{1}{\pi}\int_0^{1/k}\left[\frac{e^{-zt}}{z} + \frac{G}{\lambda k(\alpha+\beta)^2}\left\{\frac{1-e^{-zt}}{z^2} + \frac{(\alpha+\beta)}{z^2}\left(t - \frac{1}{z} + \frac{e^{-zt}}{z}\right) + \frac{e^{-(\alpha+\beta)t} - e^{-zt}}{z(\alpha+\beta-z)}\right\}\right] \times \sin\left(x\sqrt{\frac{z}{1-kz}}\right)dz, \quad (34)$$

$$u_2 = \frac{H(t-b)G}{\lambda k(\alpha+\beta)^3}\left[e^{-b/2\lambda}\left\{1 - (\alpha+\beta)(t-b) + \frac{(\alpha+\beta)^2}{2}(t-b)^2 - e^{-(\alpha+\beta)(t-b)}\right\} + \frac{b}{2\lambda}\int_b^t\left\{1 - (\alpha+\beta)(t-z) + \frac{(\alpha+\beta)^2}{2}(t-z)^2 - e^{-(\alpha+\beta)(t-z)}\right\}B(x,z)dz\right]. \quad (35)$$

Stokes' Second Problem. The flow is induced by oscillation of the plate, or by periodic heating, or both, while the plate initially at rest and at constant temperature θ_∞ is moved with a velocity $U_0 e^{i\omega t}$ in its own plane along the z-axis and its temperature is subject to a periodic heating of the form $(\theta_w - \theta_\infty)e^{i\omega t}$. We shall, therefore, solve Eqs. (11) – (12) subject to the boundary conditions (in nondimensional form) which are

$$u(x,t) = e^{i\omega t} = \theta(x,t), \quad u(\infty,t) = 0 = \theta(\infty,t). \quad (36)$$

Taking $u(x,t) = U(x)e^{i\omega t}$, and $\theta(x,t) = \Theta(x)e^{i\omega t}$, Eqs. (11) – (12) and the boundary conditions (36) reduce to

$$\Theta'' + (\lambda P\omega^2 - i\omega P)\Theta = 0, \quad (37)$$

$$(1 + ik\omega)U'' - i\omega U = -G\Theta, \quad (38)$$

$$U(0) = \Theta(0) = 1, \quad U(\infty) = \Theta(\infty) = 0. \quad (39)$$

The solution for $\theta(x,t)$ is the same as in Puri and Kythe (1995), i.e.,

$$\Theta(x) = e^{-(r_1+r_2)x}, \quad (40)$$

where

$$r_{1,2} = \sqrt{\frac{\omega P(\sqrt{1+\lambda^2\omega^2} \mp \lambda\omega)}{2}}. \quad (41)$$

The solution for $u(x,t)$ subject to the boundary conditions in (39) is given by

$$U(x) = e^{-(p_1+ip_2)x} - (G_1 + iG_2)[e^{-(p_1+ip_2)x} + e^{-(r_1+ir_2)x}], \quad (42)$$

where

$$p_{1,2} = \sqrt{\frac{\omega\sqrt{1+k^2\omega^2} \pm k\omega^2}{2(1+k^2\omega^2)}}, \quad (43)$$

and

$$G_1 + iG_2 = \frac{G[(\lambda+k)P\omega + i\{(1-\lambda k\omega^2)P - 1\}]}{(\lambda+k)^2P^2\omega^3 + \{(1-\lambda k\omega^2)P - 1\}^2\omega}. \quad (44)$$

Hence,

$$u(x,t) = [1 - (G_1 + iG_2)]e^{i\omega t - (p_1+ip_2)x} + (G_1 + iG_2)e^{i\omega t - (r_1+ir_2)x}, \quad (45)$$

with

$$\Re u(x,t) = [(1-G_1)\cos(\omega t - p_2 x) + G_2\sin(\omega t - p_2 x)]e^{-p_1 x} + [G_1\cos(\omega t - r_2 x) - G_2\sin(\omega t - r_2 x)]e^{-r_1 x}. \quad (46)$$

Note that the classical solution for $\lambda = k = 0$ and $P = 1$ cannot be derived from the above expression because the denominator of $G_1 + iG_2$ in (44) becomes zero (for a direct evaluation see Puri and Kythe (1995)).

3 Discussion

Stokes' First Problem. Using the Boley's criterion (see Boley (1962) and Boley and Tolins (1962)) and following the method of Puri and Kythe (1997), we investigate the discontinuities in the temperature and velocity gradients for $k \neq 0$ (which assures the non-Newtonian nature of the fluid). Table 1, where we have used the notation $E = (G/k\lambda P)\, e^{-x\sqrt{P/4\lambda}}$, summarizes the results for the magnitudes of discontinuities at the wave front $x = t/\sqrt{\lambda P}$ in the velocity gradients:

Table 1

$f(t)$	$S[\partial^2 u/\partial t^2]$	$S[\partial^2 u/\partial t\partial x]$	$S[\partial^2 u/\partial x^2]$	
$\delta(t)$	$-E$	$E\sqrt{\lambda P}$	$-E\lambda P$	
$f(t)$	$S[\partial^3 u/\partial t^3]$	$S[\partial^3 u/\partial t^2\partial x]$	$S[\partial^3 u/\partial t\partial x^2]$	$S[\partial^3 u/\partial x^3]$
$H(t)$	$-E$	$E\sqrt{\lambda P}$	$-E\lambda P$	$E(\lambda P)^{3/2}$

where $S[g(x,t)] = g(x^+,t) - g(x^-,t)$ denotes the magnitude of the discontinuity (saltus) in $g(x,t)$ at x, which implies that $(D/Dt)\, S[g(x,t)] = 0$ for continuous $g(x,t)$. Note that the first-order derivatives for $f(t) = \delta(t)$ and the second-order derivatives for $f(t) = H(t)$ are continuous. The Hadamard condition of compatibility for a continuous function $g(x,t)$ is given by

$$\frac{D}{Dt} S[g(x, t)] = S\left[\frac{\partial g}{\partial t}\right] + \frac{dx}{dt} S\left[\frac{\partial g}{\partial x}\right]. \quad (47)$$

(See Truesdell and Toupin (1960).) Since $S[g(x, t)]$ is zero, this condition reduces to

$$S\left[\frac{\partial g}{\partial t}\right] = -\frac{dx}{dt} S\left[\frac{\partial g}{\partial x}\right], \quad (48)$$

where dx/dt is the wave velocity which in this case is $1/\sqrt{\lambda P}$. It is obvious that the Hadamard condition is satisfied by the discontinuities given in Table 1.

For Stokes' first problem, the first-order derivatives are continuous and the discontinuities occur in the second-order derivatives for $f(t) = \delta(t)$ and in third-order derivatives for $f(t) = H(t)$.

Stokes' Second Problem. The oscillatory nature of the flow generates dispersive harmonic waves in both temperature and velocity fields. Although these waves decay rapidly, it is of some interest to analyze their structure. The wave structure of the thermal waves is the same as discussed in Puri and Kythe (1995). From (41), one can solve for ω in terms of r_2 and get

$$\omega = \frac{\sqrt{2}\, r_2^2}{\sqrt{P(P + 4\lambda r_2^2)}},$$

which implies that ω is proportional to r_2^2 for small r_2, but proportional to r_2 for large r_2. The dispersion for thermal waves is, therefore, anomalous at small and nondispersive at large wave numbers. In the velocity field, the solution (42) exhibits two types of dispersive wave trains: one has the wave front at $x = \omega t/p_2$, with velocity ω/p_2. This corresponds to the classical Stokes wave, with the difference that a layer at a distance x from the plate in the present case oscillates with a phase lag of $p_2 x - \psi$, where

$$\tan \psi = \frac{G[1 - P(1 - \lambda k\omega^2)]}{(\lambda + k)^2 P^2 \omega^3 + [1 - (1 - \lambda k\omega^2)P]^2 \omega - G(\lambda + k)P\omega}.$$

For $k = 0$ it reduces to the classical case. Note that there is no phase lag for $k = 0$ and $P = 1$. The group velocity of this wave is given by

$$v_g = \frac{2\sqrt{2}\,(1 + \omega^2 k^2)^{3/2} \sqrt{\omega\sqrt{1 + \omega^2 k^2} - \omega^2 k}}{\sqrt{1 + \omega^2 k^2} - 2\omega k}, \quad (49)$$

which for $k = 0$ reduces to the classical value $2\sqrt{2\omega}$. The other wave train is similar to the thermal wave, which is analyzed in Puri and Kythe (1995).

The group velocity v_g is greater than the phase velocity ω/p_2 for $\omega \leq 1/k\sqrt{3}$, after which the group velocity becomes negative. The frequency $\omega = 1/k\sqrt{3}$ can be regarded as the critical frequency (denoted by ω_c) because v_g has an infinite discontinuity at this value. It approaches $+\infty$ from the left and $-\infty$ from the right. In view of these observations, the wave structure exhibits an anomalous dispersion for frequencies less than ω_c. This means that the waves appear to emanate at the front of the wave packet and disappear at the rear. Since $v_g < 0$ for frequencies greater than ω_c, the phase and group velocities are directed in opposite directions. This is in agreement with the bulge in the Brillouin diagram (Fig. 1). It appears that the viscoelastic fluid becomes an absorbing medium for $\omega > \omega_c$ (see Brillouin (1960) and Smith (1970)). The phase and group velocities are independent of the Grashof number G.

The velocity field in Stokes' second problem consists of two components: one, corresponding to e^{-mx}, defines the Stokes-Rayleigh layer which is of order $O(1/p_1)$, and the other, corresponding to $e^{-(r_1+ir_2)x}$, represents the thermal layer which is of order $O(1/r_1)$. The effect of λ for $k = 0$ is exactly the same as in Puri and Kythe (1995). The effect of k can be seen from Figs. 2–3, which present graphs of $\Re u$ for $k = 0$ and $k = 0.01$ at different values of the other parameters. The velocities for $k = 0$ and $k \neq 0$ exhibit oscillatory behavior with decaying amplitudes. These graphs intersect before decaying. This implies that the influence of k is to alter the phase difference between the oscillations in velocity and in the plate. It tends to decrease this phase difference. Thus, the viscoelastic fluid oscillates in a phase different from that of the viscous fluid.

The difference $\phi = x(\sqrt{\omega/2} - p_2)$ between the phases at $k = 0$ and $k \neq 0$ can be seen in Fig. 4 at different values of x.

It should be noted that in these figures the values of $\Re u$ for $k = 0$ match with those in Puri and Kythe (1995).

The effect of G on the velocity field is presented in Fig. 5 for $k = 0.01$ and $\omega = 10$. For different values of ω this effect varies because of the phase difference, and for large frequencies

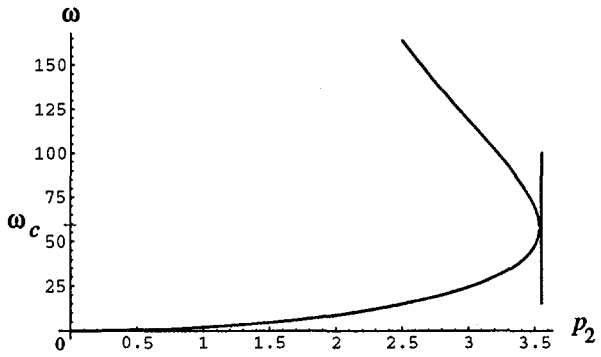

Fig. 1 Brillouin diagram for $k = 0.01$

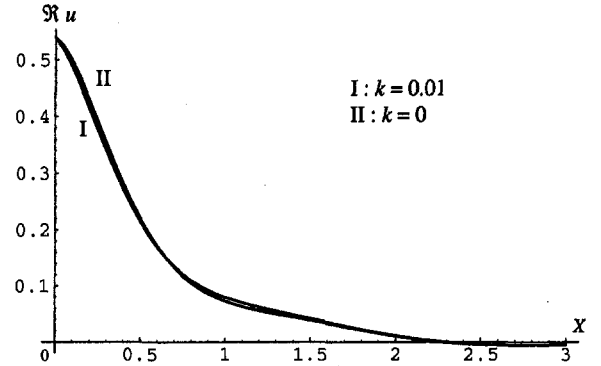

Fig. 2 Graphs of $\Re u$ for $G = -5$, $P = 0.7$, $\lambda = 0.01$, and $\omega = 10$ at $t = 0.1$

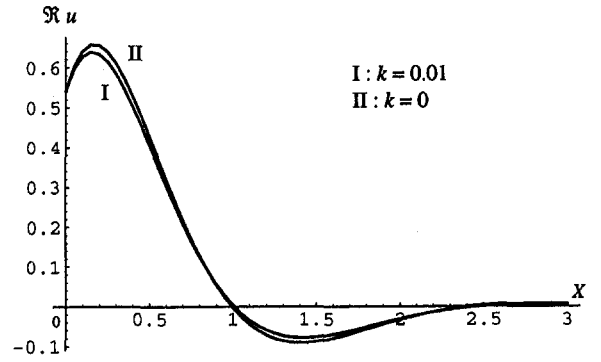

Fig. 3 Graphs of $\Re u$ for $G = 5$, $P = 0.7$, $\lambda = 0.01$, and $\omega = 10$ at $t = 0.1$

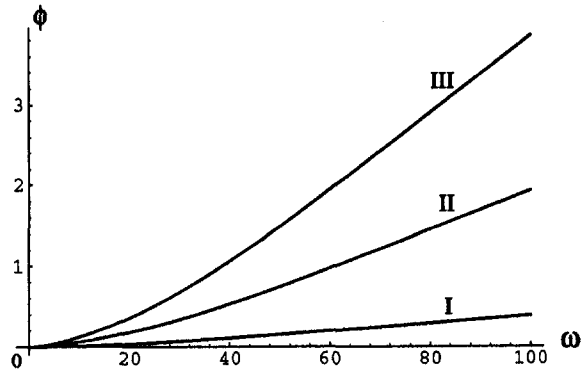

Fig. 4 Graphs of the phase difference ϕ: (I) at $x = 0.1$; (II) at $x = 0.5$, and (III) at $x = 1$.

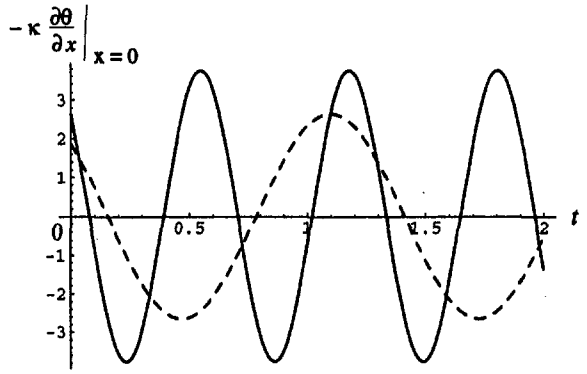

Fig. 6 Rate of heat transfer on the plate: dashed for $\omega = 5$; solid for $\omega = 10$; both at $\lambda = 0.01$, $P = 0.7$

the variation in the thermal effects almost disappears, as can be seen from (44) and (45).

The quantity p_2, defined in (43), increases with frequency up to ω_c and decreases thereafter. For large frequencies the phase difference between viscous and viscoelastic velocities approaches $\sqrt{\omega/2}$. For very large frequencies the viscoelastic layer oscillates in phase with the plate, since the phase lag $p_2 x - \psi$ approaches zero for large ω. Using the standard definition of the displacement thickness $\delta^* = \int_0^\infty (1 - (u/U_f))dx$, where U_f is the free-stream velocity, in our problem we have $\delta^* = \int_0^\infty u dx$, since the plate is moving while the free stream is stationary. Hence, the absolute value of the displacement thickness is given by

$$|\delta^*| = \left| \frac{1}{p_1 + ip_2} - \frac{G_1 + iG_2}{p_1 + ip_2} + \frac{G_1 + iG_2}{r_1 + ir_2} \right|. \quad (50)$$

This thickness in the classical case cannot be determined from (50) and must be obtained directly from the differential equation (38) by taking $P = 1$, $\lambda = k = 0$ (see Puri and Kythe (1995)).

The skin friction on the plate is proportional to

$$\Re \left. \frac{\partial u}{\partial x} \right|_{x=0} = [G_1(p_1 - r_1) - G_2(r_2 - p_2) - p_1] \cos \omega t$$

$$- [G_1(p_2 - r_2) + G_2(p_1 - r_1) - p_2] \sin \omega t. \quad (51)$$

The rate of the heat transfer on the plate is the same as in Puri and Kythe (1995), which is given by

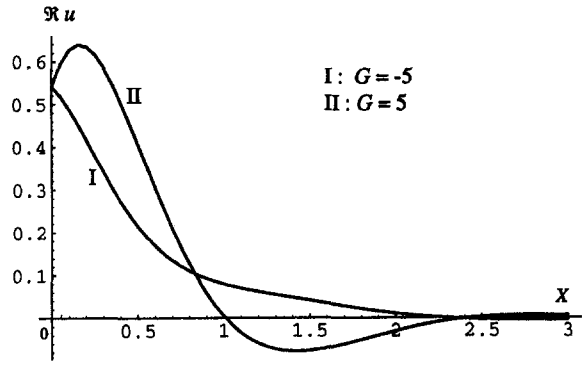

Fig. 5 Graphs of $\Re u$ for $P = 0.7$, $\lambda = 0.01$, $k = 0.01$, and $\omega = 10$ at $t = 0.1$

$$-\kappa \left. \frac{\partial \theta}{\partial x} \right|_{x=0} = \kappa(r_1 \cos \omega t - r_2 \sin \omega t) \quad (52)$$

and represented in Fig. 6. For $\lambda = 0$ it reduces to $\kappa\sqrt{\omega P} \times \cos(\omega t + \pi/4)$.

4 Conclusions

1 The temperature field is similar to that discussed in Puri and Kythe (1997) for Stokes' first problem and in Puri and Kythe (1995) for Stokes' second problem.
2 For flows induced by impulsive heating of the plate, the second-order gradients are discontinuous for $f(t) = \delta(t)$, and Eq. (11) has a weak solution. The discontinuities appear in the third-order gradients for $f(t) = H(t)$, and Eq. (11) has a strong solution in this case. An initial jump in temperature boundary condition propagates in the temperature and is transmitted to the velocity gradients of certain order as specified in Table 1. The jump in velocity boundary condition does not propagate.
3 For periodic heating or oscillations of the plate one can envision two layers, one of which is a thermal layer and the other corresponds to the viscoelastic flow.
4 The thermal layer disappears for large frequencies.
5 The viscoelastic layer oscillates with a phase difference of $p_2 x - \psi$ at a distance x from the plate. Note that $\psi = 0$ for $k = 0$ and $P = 1$, whereas $\psi \to \pi/2$ as $\omega \to 0$, and $\psi \to 0$ as $\omega \to \infty$. The viscoelastic property reduces the phase difference between the fluid layer and the plate. The phase lag for the viscous case ($k = 0$) at a distance x from the plate is $x\sqrt{\omega/2}$, while for the viscoelastic case ($k \neq 0$) it is given by $p_2 x$. Also $p_2 \leq \sqrt{\omega/2}$ for all k. This behavior remains the same even in the absence of heating.
6 The group velocity v_g for viscoelastic waves is greater than the phase velocity ω/p_2 for $\omega < \omega_c$. Also $v_g \to \infty$ as $\omega \to \omega_c^-$, and $v_g \to -\infty$ as $\omega \to \omega_c^+$. This implies an anomalous behavior in that the waves emanate in the front of the wave packet and disappear in its rear for $\omega < \omega_c$. For $\omega > \omega_c$ the group velocity is negative and the energy and the waves travel in opposite directions. The viscoelastic fluid is an absorbing medium for $\omega > \omega_c$. This is probably because the Rivlin-Ericksen model considered here is a slow flow approximation.

5 Acknowledgments

The authors are grateful to the referees for their helpful suggestions and to Professor R. S. Rivlin for a clarification.

References

Ackerman, C. C., Bertman, B., Fairbank, H. A., and Guyer, R. A., 1966, "Second Sound in Solid Helium," *Phys. Rev. Lett.,* Vol. 16, pp. 789–791.

Boley, B. A., 1962, "Discontinuities in Integral-Transform Solutions," *Quart. Appl. Math.,* Vol. 19, pp. 273–284.

Boley, B. A., and Tolins, I. S., 1962, "Transient Coupled Thermoelastic Boundary Value Problems in the Half-Space," ASME *J. Appl. Mech.,* Vol. 29, pp. 637–646.

Brillouin, L., 1960, *Wave Propagation and Group Velocity,* Academic Press, New York.

Cattaneo, C., 1948, "Sullacondizione del calore," *Atti del Semin. Matem. e Fis. della Univ. Modena,* Vol. 3, pp. 83–101.

Chester, M., 1963, "Second Sound in Solids," *Phys. Rev.,* Vol. 131, pp. 2013–2015.

Green, A. E., and Lindsay, K. A., 1972, "Thermoelasticity," *J. Elast.,* Vol. 2, pp. 1–7.

Joseph, D. D., and Preziosi, L., 1989, "Heat Waves," *Rev. Modern Phys.,* Vol. 61, pp. 41–73.

Joseph, D. D., and Preziosi, L., 1990, addendum to the paper "Heat Waves," *Rev. Modern Phys.,* Vol. 62, pp. 375–391.

Kaliski, S., 1965, "Wave Equations in Thermoelasticity," *Bull. Acad. Polon. Sci.,* Ser. Sci. Tech., Vol. 13, pp. 253–260.

Lindsay, K. A., and Straughan, B., 1978, "Acceleration Waves and Second Sound in a Perfect Fluid," *Arch. Rational Mech. Anal.,* Vol. 68, pp. 53–87.

Lord, H. W., and Shulman, Y., 1967, "A Generalized Dynamical Theory of Thermoelasticity," *J. Mech. Phys. Solids,* Vol. 15, pp. 299–309.

Maxwell, J. C., 1867, "On the Dynamical Theory of Gases," *Phil. Trans. Royal Soc.,* Vol. 157, pp. 49–88.

McTaggart, C. L., and Lindsay, K. A., 1985, "Nonclassical Effects in the Bénard Problem," *SIAM J. Appl. Math.,* Vol. 45, pp. 70–92.

Nerest, W., 1917, *Die theoretischen Grundlagen des n Wärmestatzes,* Knapp, Halle.

Norwood, F. R., and Warren, W. E., 1969, "Wave Propagation in the Generalized Dynamical Theory of Thermoelasticity," *Quart. J. Mech. and Applied Math.,* Vol. 22, pp. 283–290.

Onsanger, L., 1931, "Reciprocal Relations in Irreversible Processes," *Phys. Rev.,* Vol. 37, pp. 405–426.

Peshkov, V., 1944, "Second Sound in Helium II," *J. Phys. (Moscow),* Vol. 8, pp. 381.

Puri, P., 1973, "Plane Waves in Generalized Thermoelasticity," *Int. J. Engng. Sci.,* Vol. 11, pp. 735–744.

Puri, P., 1975, errata to "Plane Waves in Generalized Thermoelasticity," *Int. J. Engng. Sci.,* Vol. 13, pp. 339–340.

Puri, P., 1984, "Impulsive Motion of a Flat Plate in a Rivlin-Ericksen Fluid," *Rheol. Acta,* Vol. 23, pp. 451–453.

Puri, P., and Kythe, P. K., 1995, "Nonclassical Thermal Effects in Stokes' Second Problem," *Acta Mechanica,* Vol. 112, pp. 1–9.

Puri, P., and Kythe, P. K., 1997, "Discontinuities in Velocity Gradients and Temperature in the Stokes' First Problem With Nonclassical Heat Conduction," *Quart. Appl. Math.,* Vol. 55, pp. 167–176.

Rivlin, R. S., and Ericksen, J. L., 1955, *J Rational Mechanics and Analysis,* Vol. 4, p. 323.

Schlichting, H., 1960, *Boundary Layer Theory,* 4th Ed., McGraw-Hill Book Company, Inc., p. 72.

Smith, R. L., 1970, "The Velocities of Light," *Am. J. Phys.,* Vol. 38, pp. 978–984.

Truesdell, C., and Toupin, R. A., 1960, *The Classical Field Theories in Encyclopedia of Physics,* III/1, Springer-Verlag, Berlin.

Tzou, D. Y., 1997, *Macro- to Microscale Heat Transfer,* Taylor & Francis, 1997, p. 20.

Prediction of Thermal Contact Conductance in Vacuum by Statistical Mechanics

M. Leung

C. K. Hsieh

D. Y. Goswami

Department of Mechanical Engineering,
University of Florida
P.O. Box 116300
Gainesville, FL 32611-6300

Despite substantial theoretical studies of thermal contact conductance in the past, the application of statistical mechanics in this field has never been attempted. This paper addresses contact conductance from macroscopic and microscopic viewpoints in order to demonstrate the promise of the statistical mechanics approach. In the first part of the derivation, the Boltzmann statistical model is applied to determine the most probable distribution of asperity heights for a homogeneously, isotropically rough surface. The result found is equivalent to Gaussian distribution, which has only been assumed but not rigorously substantiated in the past. Subsequently, the Boltzmann statistical model is applied to predict the distribution of true contact spots when two such surfaces are pressed together, resulting in a relationship between the total thermal contact conductance and the relative interfacial pressure. The numerical results are compared to published empirical data, and a good order-of-magnitude agreement is found.

Introduction

When two solid bodies at different temperatures are brought into mechanical contact, a thermal resistance impedes the heat flow across the interface and results in a temperature drop as shown in Fig. 1. This resistance, commonly known as thermal contact resistance, is well-explained by the fact that the actual contact area is exceedingly small as compared to the apparent contact area due to the presence of roughness and waviness of the engaging surfaces. As the interstitial material, such as air, is a poor heat conductor and the radiative heat transfer is often insignificant (Fenech and Rohsenow, 1959), a large portion of the heat flow converges to the discrete solid-solid contact spots as illustrated in Fig. 2. Hence, the increase in the heat-flow path length causes the thermal contact resistance. Its reciprocal is called thermal contact conductance, defined as

$$h = \frac{q}{A\Delta T}, \tag{1}$$

where q is the heat flow rate, A is the apparent contact area, and ΔT is the temperature drop at the interface.

Thermal contact conductance plays an important role in all thermal systems where a mechanical contact is involved. Recently, such conductance has received special interest and attention in small-scale heat removal systems such as microelectronics (Lee et al., 1993; Fisher and Yovanovich, 1989; Eid and Antonetti, 1986) and in heat transfer between superconductor films and substrates (Phelan et al., 1994; Ochterback et al., 1992). Other active research areas include thermal rectification (Stevenson et al., 1991), metallic coating conductance enhancement (Lambert et al., 1995; Kang et al., 1990; Antonetti et al., 1985), and interstitial material effects (Das and Sadhal, 1992). Comprehensive overviews of the literature in these areas can be found in the papers presented by Snaith et al. (1986) and Madhusudana and Fletcher (1986). A more recent review presented by Fletcher (1988) surveys the works published since 1980.

In theoretical studies, substantial efforts have been made in the development of predictive models for thermal contact conductance between nominally flat surfaces. Some successful examples are the ones by Hsieh (1968), Yovanovich (1967, 1982), and McWaid and Marschall (1992). However, none of the existing models have attempted the use of statistical mechanics even though it is a potentially promising approach. The physical foundation of this statistical approach is based on the analogy that surface asperities are comparable to particles in the traditional sense of microscopic viewpoint. The focus of this investigation is thus directed toward the application of statistical mechanics to the prediction of contact conductance.

Leung (1995) has developed a predictive model of thermal contact conductance between nominally flat surfaces by statistical mechanics. The assumptions made for this modeling encompass the following:

- contacting surfaces are of similar physical properties
- conical asperities of constant slope and variable heights represent a flat rough surface
- touching asperities undergo pure plastic deformation
- contact spots are evenly distributed over the apparent contact area
- no interference is considered between neighboring contact spots
- load cycling and surface film effects are negligible

In this paper, the Boltzmann statistical model is first applied to derive the most probable distribution of the asperity heights for a flat, homogeneously, and isotropically rough surface. The Boltzmann model is used again to predict the distribution of true contact spots for two such surfaces pressed together. Then, by using the constriction resistance for a single contact, the relationship between the total thermal contact conductance and the relative interfacial pressure can be derived. The numerical results show that the predicted conductance agrees well with the published empirical data. Statistical mechanics is thus shown to be a feasible approach in predicting the thermal contact conductance.

Theoretical Basis for the Use of Statistical Mechanics

In theoretical physics, if a macroscopic (observable) property of a many-particle system in equilibrium can be characterized

Contributed by the Heat Transfer Division for publication in the JOURNAL OF HEAT TRANSFER. Manuscript received by the Heat Transfer Division March 20, 1996; revision received October 28, 1997; Keywords: Conduction; Direct-Contact Heat Transfer; Modeling and Scaling. Associate Technical Editor: A. S. Lavine.

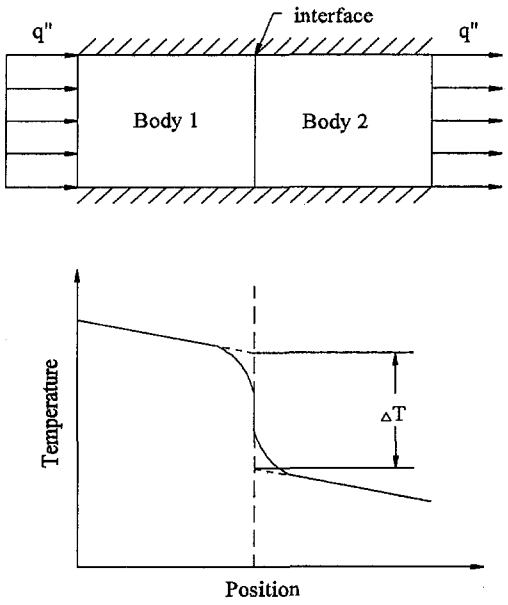

Fig. 1 Illustration of thermal contact conductance

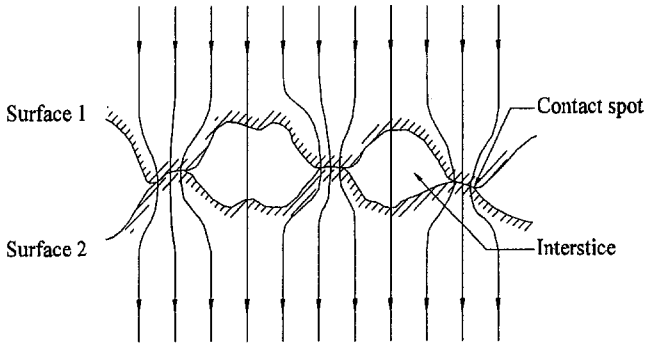

Fig. 2 Convergence of heat flow through contact spots

by other macroscopic properties, statistical mechanics can be applied to analyze the system. In this effort, the system is analyzed microscopically in terms of the most probable distribution of particles. In application of this concept to the field of mechanics, the asperities of the surfaces in contact can be taken as particles. The applied load at the interface is distributed over the microscopic contact spots formed by the touching asperities in a state of force "equilibrium." As a result of the distribution of the contact spots, the thermal contact conductance arises as a macroscopic property of this thermal system.

Substantial experimental studies have shown that for surfaces of given material properties, topographic characteristics, and loading conditions, the reduction in contact resistance behaves orderly and consistently as the loading interfacial pressure increases. This leads one to believe that the distribution of the contact spots is highly repeatable when the surfaces are brought into contact under a specific condition. In other words, the contact conductance can be considered a result of "the most probable distribution" of contacts. From this perspective, statistical mechanics is certainly an appropriate method to predict the thermal contact conductance.

In mechanical engineering, statistical mechanics is frequently applied to the prediction of equilibrium thermodynamic quantities. For this reason, an illustrative example in statistical thermodynamics will be introduced first in order to establish the links between the thermal contact conductance and statistical mechanics. The details of the statistical thermodynamics can be found in Sonntag and Van Wylen (1966).

Consider an isolated system comprised of N particles that are independently distributed among various energy levels. At energy level j there is a corresponding statistical weight g_j, which is the number of quantum states having energy u_j. Under an equilibrium state in thermodynamics, the two constraints which govern the activity of the particles in this system are that (1) the total number of particles must be conserved,

$$\sum_j N_j = N, \tag{2}$$

and (2) the internal energy must be conserved,

$$\sum_j N_j u_j = U, \tag{3}$$

where N_j represents the number of particles having energy u_j. The most probable distribution of the particles can then be determined by use of Boltzmann statistics as

$$N_j = \frac{N g_j e^{-\beta u_j}}{\sum_j g_j e^{-\beta u_j}}, \tag{4}$$

where β is a Lagrange multiplier.

Attention is now turned to the comparison of the features associated with contact conductance and its counterpart in statistical thermodynamics given above to demonstrate their similarities. They are listed side by side in Table 1. These comparisons provide further rationale of the modeling of contact conductance by statistical mechanics.

Most Probable Distribution of Summit Heights

Before studying the interaction between two contacting surfaces, the statistical features of each surface must be identified. Statistical mechanics can play a vital role in theoretical derivation of the distribution of asperity summit heights. In this inves-

Nomenclature

A = area
a = circular contact spot radius
b = cylindrical heat flow channel radius
F = loading force on a contact spot
$f(z)$ = probability density function of property z
g = statistical weight
H = Vickers microhardness
h = thermal contact conductance
k = thermal conductivity
m = asperity slope
N_j = number density of particles or asperities having property j
N = total number density of particles or asperities
P = applied pressure
q = heat rate
q'' = heat flux
S = shift of distribution curve
T = temperature
U = total internal energy of an isolated system
u_j = energy corresponding to energy level j
x = summit height

Greek Letters

α, β, γ = Lagrange multipliers
δ = asperity summit penetration depth
ξ = base plane separation
σ = standard deviation
μ = mean
ψ = constriction alleviation factor

Table 1 Analogies of statistical thermodynamics and thermal contact conductance

	Statistical Thermodynamics	Thermal Contact Conductance
1	Gas particles are independent of each other.	Asperities are independent of each other.
2	Number of particles is conserved in a isolated system, $\sum_j N_j = N.$	Number of asperities present on each surface is conserved, $\sum_j N_j = N.$
3	Total energy is conserved, $\sum_j N_j u_j = U.$	Sum of loads carried by asperities equals the applied pressure, $\sum_j N_j F_j = P.$
4	Most probable distribution of particles is found by the Boltzmann statistical model; other system characteristics can be determined accordingly.	Most probable distribution of true contact areas is found by the Boltzmann statistical model; thermal contact conductance can be determined accordingly.

tigation, the Boltzmann statistical model is used in conjunction with the surface roughness measurements as statistical constraints to characterize a rough surface.

The topography of a surface is commonly measured by the use of a profilometer. As the stylus of a profilometer travels along a straight path on a surface, the electromechanical transducer produces electrical signals proportional to the variation of surface heights resulting in a two-dimensional surface profile of the single trace. For a complete description of the surface roughness in three dimensions, a surface mapping scanning technique can supplement the measurement of the surface topography over an area. Based on this concept, Williamson (1968 and 1969) built an auxiliary stylus-lifter to record many closely spaced, parallel surface profiles with a unique reference height for a bead-blasted aluminum surface sample. Alternatively, Wyant et al. (1986) used a noncontact optical profiler to obtain the surface heights over an area of a computer tape surface. From the constructed surface contour maps, they were able to obtain the roughness summit locations and heights. The measurement results show that both surface height and summit height distribution curves are similarly bell shaped, as illustrated in Fig. 3. The mean summit height is greater than the mean

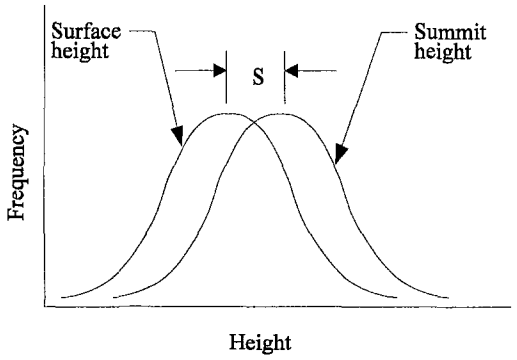

Fig. 3 Distributions of surface heights and summit heights of a bead-blasted surface

surface height and their standard deviations can be correlated as presented by McCool (1986). These results indicate that the rough surfaces possess the following characteristics:

- *Density of asperities.*

$$\sum_j N_j = N \tag{5}$$

- *Mean summit height.*

$$\sum_j N_j x_j = N\mu \tag{6}$$

- *Standard deviation of summit heights.*

$$\sum_j N_j (x_j - \mu)^2 = N\sigma^2 \tag{7}$$

N is the density of asperities (number per unit area) and N_j is the density of asperities having summit height x_j. These relationships can serve as the constraints imposed on the surface topography for the Boltzmann statistical analysis.

Following the standard mathematical procedures of statistical mechanics, Leung (1995) has derived the Boltzmann distribution of summit heights as

$$N_j = \frac{Ne^{-\beta x_j} e^{-\gamma x_j^2}}{\sum_j e^{-\beta x_j} e^{-\gamma x_j^2}}, \tag{8}$$

where β and γ are the Lagrange multipliers corresponding to Eqs. (6) and (7), respectively. Since the discrete values of x_j are so closely spaced as to form a continuum, the summation can be changed to an integration by the transformation means of Euler-Maclaurin summation formula. Then, the distribution given by Eq. (8) can be expressed in a probability density form by

$$\frac{dN_x}{Ndx} = \frac{e^{-\beta x} e^{-\gamma x^2}}{\int_0^\infty e^{-\beta x} e^{-\gamma x^2} dx}. \tag{9}$$

Substituting N_j from Eq. (8) into Eqs. (6) and (7) and then applying Euler-Maclaurin summation formula again, one can write, respectively,

$$\frac{\int_0^\infty e^{-\beta x} e^{-\gamma x^2} x dx}{\int_0^\infty e^{-\beta x} e^{-\gamma x^2} dx} = \mu, \tag{10}$$

and

$$\frac{\int_0^\infty e^{-\beta x} e^{-\gamma x^2} (x - \mu)^2 dx}{\int_0^\infty e^{-\beta x} e^{-\gamma x^2} dx} = \sigma^2. \tag{11}$$

By solving Eqs. (10) and (11) simultaneously, the unknowns β and γ are obtained as

$$\beta = -\frac{\mu}{\sigma^2},$$

and

$$\gamma = \frac{1}{2\sigma^2}.$$

Finally, the most probable distribution of summit heights, given by Eq. (9), can be expressed in terms of μ and σ by

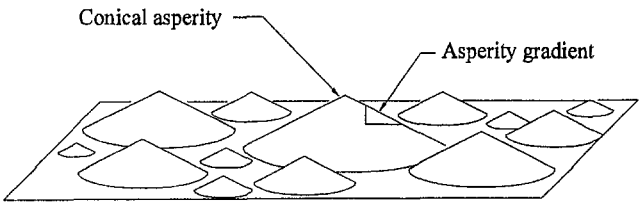

Fig. 4 Surface roughness modeled by conical asperities

$$\frac{dN_x}{Ndx} = f(x) = \frac{1}{\sqrt{2\pi}\sigma} \exp\left[-\frac{1}{2}\left(\frac{x-\mu}{\sigma}\right)^2 \right]. \quad (12)$$

It is found that the probability density function derived above for the Boltzmann distribution is identical to the one for a Gaussian distribution. As a result, the Boltzmann statistical model has provided a solid foundation for the use of Gaussian distribution of summit heights, which has hitherto been in widespread use but subjected to no rigorous validation.

Prediction of Thermal Contact Conductance

Surface Representation. In this investigation, the irregularities of a rough surface are modeled by conical asperities of an identical gradient m and various heights resting on a common flat plane, as illustrated in Fig. 4. This model has been proven to be a suitable representation for the surfaces processed by grinding, lapping, honing, bead blasting, anodizing, and accurate casting (Hsieh, 1974; D'yachenko et al., 1964). The summit height distribution given by Eq. (12) leads to some useful surface characteristics provided by Hsieh (1968) as follows:

- *Density of surface asperities (number per unit area).*

$$N = \left(\frac{m}{7.308\sigma}\right)^2 \quad (13)$$

- *Maximum summit height (peak-to-valley roughness).*

$$x_{max} = 8\sigma \quad (14)$$

- *Mean summit height.*

$$\mu = 4\sigma \quad (15)$$

It is noted that the asperities having heights beyond x_{max} are within 0.02 percent (negligibly small) of the total population described by Eq. (12).

Contact Interface Modeling. The formation of true contact areas are modeled as demonstrated in Fig. 5. Figure 5(a) shows that the contact spots often occur near the summits as found in Williamson (1968). The first step in modeling is to represent each rough surface by the conical asperities, as illustrated in Fig. 5(b). As expected, perfect alignment between a pair of touching asperities rarely occurs. Nevertheless, the degree of misalignments is expected to be statistically constant since the macroscopic properties, such as contact conductance, surface friction, etc., are consistently reproducible. It is thus justified to simplify the analysis by assuming that all touching asperities are perfectly aligned, as illustrated in Fig. 5(c). The theoretical prediction of contact conductance can be corrected, if necessary, by a multiplying factor, which is close to unity (Hsieh, 1968).

Mechanical and Thermal Analyses for a Single Contact. The fundamental unit for the study of conductance at an interface is a single contact formed by a pair of touching asperities as shown in Fig. 6. In the mechanical analysis, touching asperities

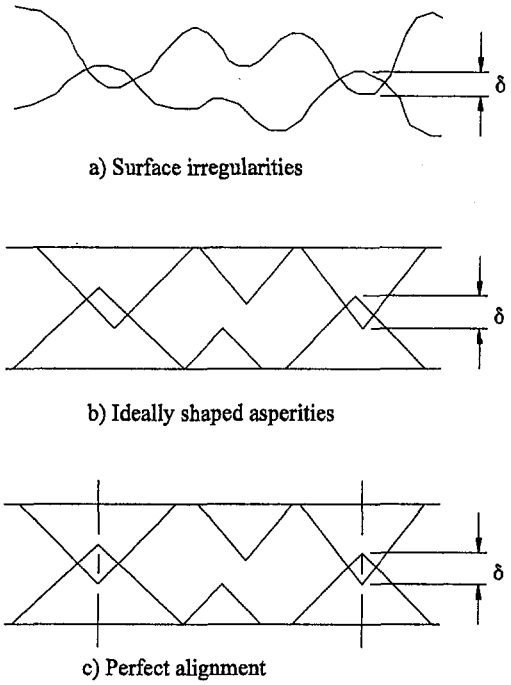

Fig. 5 Modeling technique used in contact area formation

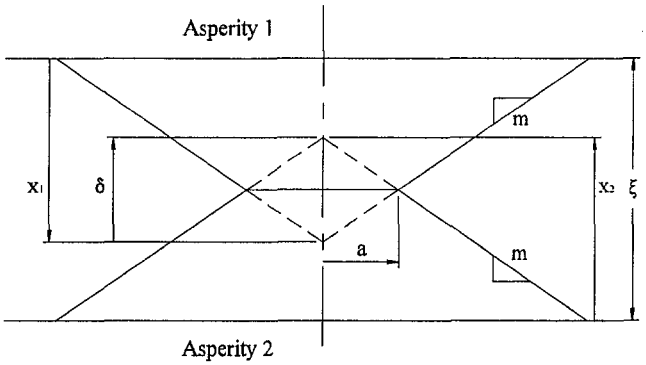

Fig. 6 Plastic deformation at asperity summits

resemble blunt indenters whose summit undergoes a plastic deformation. Based on simple geometry, this mechanism results in the contact spot radius

$$a = \begin{cases} 0 & \text{if } \delta \le 0 \\ \dfrac{\delta}{2m} & \text{if } \delta > 0 \end{cases} \quad (16)$$

and the contact force

$$F = \begin{cases} 0 & \text{if } \delta \le 0 \\ H\pi a^2 = \dfrac{\pi H \delta^2}{4\, m^2} & \text{if } \delta > 0, \end{cases} \quad (17)$$

where H is the (Vickers) microhardness of the material of the contacting surfaces and δ is the summit penetration depth depicted in Fig. 6. The value of δ less than zero implies that the two asperities are not in contact.

The thermal analysis calls for solving a Laplace equation with mixed boundary conditions. Gibson (1976) obtained the analytical thermal conductance for a single contact spot as

$$h = \begin{cases} 0 & \text{if} \quad \delta \le 0 \\ \dfrac{2ak}{\psi} = \dfrac{k\delta}{m\psi} & \text{if} \quad \delta > 0. \end{cases} \tag{18}$$

Here the constriction alleviation factor, ψ, is expressed by

$$\psi = 1 - 1.4091839(a/b) + 0.338010(a/b)^3 + 0.067902(a/b)^5, \tag{19}$$

where a/b is the ratio of the contact spot radius to the flow channel radius.

Application of the Boltzmann Statistical Model. The first step is to identify the constraints that govern the activities at the interface. For two contacting surfaces having the same surface texture, the number of potential contact spots formed are constrained by

$$\sum_j N_j = N, \tag{20}$$

where N is the density of all summit penetrations (Eq. 13) and N_j is the density of summit penetration δ_j. It is noted that a contact spot is physically formed only for δ_j greater than zero. The force balance condition is another constraint imposed on the interface,

$$\sum_j N_j F_j = \sum_j \left. \frac{N_j \pi H \delta_j^2}{4m^2} \right|_{\delta_j > 0} = P, \tag{21}$$

where P is the applied pressure.

These two constraints yield the following Boltzmann distribution of summit penetration,

$$N_j = \begin{cases} \dfrac{g_j N}{\sum_j g_j|_{\delta_j \le 0} + \sum_j g_j e^{-\beta\delta_j^2}|_{\delta_j > 0}} & \text{if} \quad \delta_j \le 0 \\ \dfrac{g_j N e^{-\beta\delta_j^2}}{\sum_j g_j|_{\delta_j \le 0} + \sum_j g_j e^{-\beta\delta_j^2}|_{\delta_j > 0}} & \text{if} \quad \delta_j > 0, \end{cases} \tag{22}$$

where β is the Lagrange multiplier and g_j is the statistical weight function for δ_j. Substituting Eq. (22) into Eq. (21) results in the relationship between P and β,

$$\frac{\pi HN}{4m^2} \left(\frac{\sum_j g_j e^{-\beta\delta_j^2} \delta_j^2|_{\delta_j > 0}}{\sum_j g_j|_{\delta_j \le 0} + \sum_j g_j e^{-\beta\delta_j^2}|_{\delta_j > 0}} \right) = P. \tag{23}$$

The corresponding total contact conductance is the sum of all individual constriction conductances,

$$h = \sum_j \left. \frac{N_j k \delta_j}{m\psi} \right|_{\delta_j > 0} = \frac{kN}{m\psi} \left(\frac{\sum_j g_j e^{-\beta\delta_j^2} \delta_j|_{\delta_j > 0}}{\sum_j g_j|_{\delta_j \le 0} + \sum_j g_j e^{-\beta\delta_j^2}|_{\delta_j > 0}} \right). \tag{24}$$

It is assumed that all contact spots are evenly spaced so that a/b is the same for each spot (Cooper et al., 1969),

$$\frac{a}{b} = \sqrt{\frac{P}{H}}. \tag{25}$$

In Eq. (24), ψ has been factored out from the summation sign and a/b in Eq. (19) can be replaced by $(P/H)^{1/2}$.

The asperity heights can be as much as $x_{\max}$ which is equal to 8σ (Eq. 14). Thus, asperity contacts will be initiated only if the surfaces are brought together with a base plane separation ξ (see Fig. 6) of less than 16σ. It is also expected that the lowest possible value of ξ is zero, meaning that the touching asperities completely penetrate into each other. Under these circumstances, the value of δ ranges from -16σ to 16σ. Equations (23) and (24) can be written in an integral form by

$$P = \frac{\pi HN}{4m^2} \left(\frac{\int_0^{16\sigma} g_\delta e^{-\beta\delta^2} \delta^2 d\delta}{\int_{-16\sigma}^{0} g_\delta d\delta + \int_0^{16\sigma} g_\delta e^{-\beta\delta^2} d\delta} \right) \tag{26}$$

and

$$h = \frac{kN}{m\psi} \left(\frac{\int_0^{16\sigma} g_\delta e^{-\beta\delta^2} \delta d\delta}{\int_{-16\sigma}^{0} g_\delta d\delta + \int_0^{16\sigma} g_\delta e^{-\beta\delta^2} d\delta} \right). \tag{27}$$

The multiplier β in Eqs. (26) and (27) serves as a parameter so that P and h can be related.

The final step is to define the statistical weight function g_δ. The product of g_δ and $d\delta$ should reflect the proportion of the probability of the event having a summit penetration depth between δ and $\delta + d\delta$. Following the steps for finding the probability of events, the statistical weight function can be derived as (Leung, 1995)

$$g_\delta = \begin{cases} \left(\int_{\delta/2}^{8\sigma} f(x) x^2 dx \right)^2 & \text{if} \quad \delta > 0 \\ \int_0^{8\sigma} f(x_1) x_1^2 \int_0^{16\sigma+\delta-x_1} f(x_2) x_2^2 dx_2 dx_1 & \text{if} \quad -8\sigma < \delta \le 0 \\ \int_0^{16\sigma+\delta} f(x_1) x_1^2 \int_0^{16\sigma+\delta-x_1} f(x_2) x_2^2 dx_2 dx_1 & \text{if} \quad -16\sigma < \delta \le -8\sigma, \end{cases} \tag{28}$$

where $f(x)$ is the probability density function given by Eq. (12).

Numerical Results and Discussion

Finding exact solutions to the equations derived above (Eqs. (26), (27), and (28)) is not successful because of the difficulty in evaluating the multiple integrations involved. For this reason, Simpson's rule is used to accomplish the numerical results. An initial and arbitrary number of equally spaced increments of the dummy variable of integration are selected to perform numerical integration. The computation is then repeated by using twice the number of increments until the termination criterion is reached. This criterion is that the errors between consecutive computations do not exceed 1 percent. It is found that a sufficient number of increments varies from 100 to 400. The truncation errors of Simpson's rule for the computed P in Eq. (26)

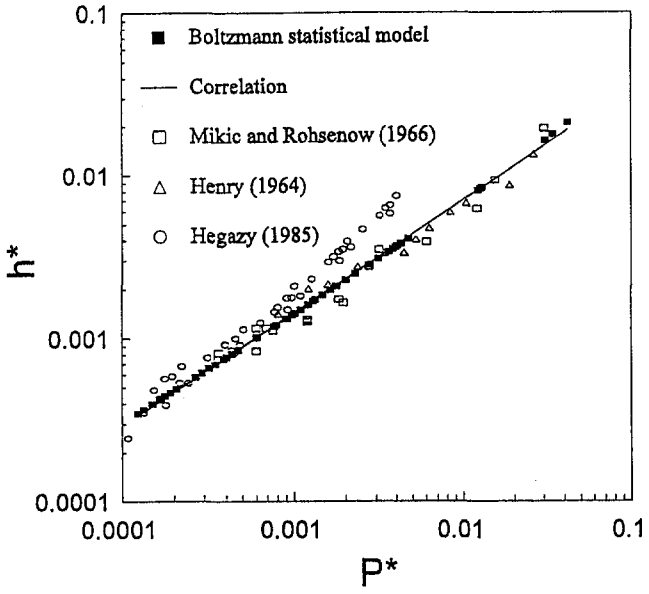

Fig. 7 Predicted and experimental thermal contact conductance

and h in Eq. (27) are estimated within 1 percent and 0.1 percent, respectively.

The numerical results are presented in Fig. 7 as the dimensionless contact conductance,

$$h^* = \frac{h\sigma}{mk}, \tag{29}$$

versus the dimensionless pressure,

$$P^* = \frac{P}{H}. \tag{30}$$

These dimensionless parameters are derived in previous correlation studies (Cooper et al., 1969; Tien, 1968). The correlation between the predicted h^* and P^* is expressed by

$$h^* = 0.170P^{*0.693}, \tag{31}$$

which is plotted as the solid line in Fig. 7. The load exponent of 0.693 is found for the dimensionless loading range between 0.0001 and 0.05.

Experimental data for tests of conductance in vacuum have been selected from the open literature and used for comparison. Since the surface slope is not commonly reported in the literature, only eleven sets of qualifying data are found useful for direct comparison, and they cover a wide range of surface roughness and material properties. The specimens include Stainless Steels 303, 304, and 416, Nickel 200, Zirconium-2.5 wt percent Nb, and Zircaloy-4 and the surface roughness varies from 0.338 μm (smooth) to 9.86 μm (rough). The surface characteristics and the sources of reference for all the selected data are given in Table 2. The experimental results are presented in Fig. 7, while individual comparisons can be found in Leung (1995).

Figure 7 shows that the Boltzmann statistical model yields accurate predictions as compared to the measurements by Mikic and Rohsenow (1966) and Henry (1964) for a wide range of pressures ($1 \times 10^{-4} < P^* < 3 \times 10^{-2}$). For Hegazy's (1985) data, good agreement is found when P^* is less than 6×10^{-4}. When P^* is greater than 6×10^{-4}, the model tends to underpredict the contact conductance and the deviation increases with P^*. The worst case found is at P^* approximately equal to 4×10^{-3}, where the experimental h^* is twice as high as the predicted h^*. While such a deviation is not uncommon in the field of contact conductance, it is safe to say that on the basis of this analysis, predictions of the contact conductance by the conical model at low loads ($P^* < 6 \times 10^{-4}$) are reliable. At high loads, since only one group of data deviates from the prediction, it is difficult to assess the accuracy of the predicting models. Nonetheless, the predictions are within the uncertainty in the experimental data.

As shown in Eq. (31), the load exponent of 0.693 is a dominant parameter in the prediction of the contact conductance. This value is relatively low as compared with the value (0.95) theoretically derived by Yovanovich (1982). However, comparisons with the results of corresponding empirical correlations as summarized in Table 3 show that the Boltzmann statistical model predicts a load exponent which is within the range that is listed in the table. It is noted that the present modeling of the contact conductance by Boltzmann statistics can be modified by the application of an elastic-plastic deformation mechanism (So and Liu, 1990; Ishigaki and Kawaguchi, 1979), which is essentially an alternative method to that of modeling the contact of rough surfaces. It is expected that the load exponent will change with the inclusion of the elastic component in the analysis.

The present work is somewhat handicapped by the lack of qualifying data for comparison —this is not without reasons. As seen in the literature, in the early stage of research in the field, the study of contact of individual asperities was given full attention and the characterization of the surface roughness was treated in detail in the papers. However, later works tended to deviate gradually from this course and recent efforts have been directed to the studies of surface coatings, surface rectification, and interstitial materials, among others. It is clear that for a thorough validation of the Boltzmann model developed in this

Table 2 Experiments for thermal contact conductance of nominally flat surfaces in a vacuum environment

Test	Specimen	σ (μm)	m	H (GPa)	k (W/mK)	References
1	SS 303	2.64	0.1500	2.28	17.3	Mikic and Rohsenow, 1966
2	SS 303	5.92	0.0998	2.28	17.3	Mikic and Rohsenow, 1966
3	SS 416	3.04	0.102	2.62	25.3	Henry, 1964
4	Ni 200	0.638	0.0778	3.67	75.1	Hegazy, 1985
5	Ni 200	9.86	0.165	2.17	75.1	Hegazy, 1985
6	SS 304	0.338	0.0509	4.11	19.3	Hegazy, 1985
7	SS 304	7.74	0.134	2.51	18.9	Hegazy, 1985
8	Zirconium	0.652	0.0587	3.14	19.8	Hegazy, 1985
9	Zirconium	6.23	0.141	2.17	20.0	Hegazy, 1985
10	Zircaloy-4	0.431	0.0346	2.32	16.6	Hegazy, 1985
11	Zircaloy-4	5.60	0.146	1.97	17.2	Hegazy, 1985

Table 3 Summary of load exponent reported in empirical correlations of thermal contact conductance for nominally flat surfaces in vacuum

Reference	Specimens	Load Exponent
Hegazy, 1985	Stainless steel, nickel, Zirconium, and Zircaloy-4	0.95
Edmonds et al., 1980	Stainless steel and copper	0.60
Popov, 1976	Steel, aluminum, and other materials	0.956
O'Callaghan and Probert, 1974	Stainless steel and aluminum	0.66
Thomas and Probert, 1972	Stainless steel	0.743
	Aluminum	0.72
Fletcher and Gyorog, 1971	Stainless steel and aluminum	0.56
Mal'kov, 1970	Metal contacts	0.66
Tien, 1968	Stainless steel and aluminum	0.85

paper, the surface characterization must be included in detail in future studies. Not only will this validate the Boltzmann model developed in this paper, but it will also benefit the study of other areas, such as surface grinding and micro heat transfer, among others.

Conclusions

This investigation has shown that the prediction of thermal contact conductance by statistical mechanics is viable. Considering surface asperities comparable to molecules in the traditional sense of microscopic viewpoint, the Boltzmann statistical model successfully determines the "most probable distribution" of the contact spots. Thus, a relationship between the contact conductance and the relative pressure can be derived. The disagreement between the predicted contact conductance and the published data is less than 30 percent when the dimensionless pressure (P/H) is less than 6×10^{-4}. The worst group of data is found at high test range where the empirical data is twice as much as the prediction.

The Boltzmann statistical model has been explored in this investigation and reasonably accurate predictions are obtained. The Bose-Einstein and Fermi-Dirac statistical models, assuming that the particles are indistinguishable, have been successfully applied in statistical thermodynamics. Thus, these two models may also play an important role in the field of contact conductance. Investigations of these two statistical models are recommended.

References

Antonetti, V. W., and Yovanovich, M. M., 1985, "Enhancement of Thermal Contact Conductance by Metallic Coatings: Theory and Experiment," ASME JOURNAL OF HEAT TRANSFER, Vol. 107, pp. 513–519.

Cooper, M. G., Mikic, B. B., Yovanovich, M. M., 1969, "Thermal Contact Conductance," *International Journal of Heat and Mass Transfer,* Vol. 12, pp. 279–300.

Das, A. K., and Sadhal, S. S., 1992, "Effect of Interfacial Fluid on Thermal Constriction Resistance," ASME JOURNAL OF HEAT TRANSFER, Vol. 114, pp. 1045–1048.

D'yachenko, P. E., Tolkacheva, N. N., Andreev, G. A., and Karpova, T. M., 1964, *The Actual Contact Area between Touching Surfaces,* Consultants Bureau, New York.

Edmonds, J. J., Jones, A. M., and Probert, S. D., 1980, "Thermal Contact Resistance for Hard Machined Surfaces Pressed Against Relatively Soft Optical-Flats," *Applied Energy,* Vol. 6, pp. 405–427.

Eid, J. C., and Antonetti, V. W., 1986, "Small Scale Thermal Contact Resistance of Aluminum Against Silicon," *Proceedings of the 8th International Heat Transfer Conference,* Hemisphere Publishing, PA, pp. 659–664.

Fenech, H., and Rohsenow, W. M., May 1959, *Thermal Conduction of Metallic Surfaces in Contact,* Report No. NYO-2136, for the United States Atomic Energy Commission by Heat Transfer Laboratory, M.I.T., Cambridge, MA.

Fisher, N. J., and Yovanovich, M. M., 1989, "Thermal Constriction Resistance of Sphere/Layered Flat Contacts: Theory and Experiment," ASME JOURNAL OF HEAT TRANSFER, Vol. 111, pp. 249–256.

Fletcher, L. S., 1988, "Recent Developments in Contact Conductance Heat Transfer," ASME JOURNAL OF HEAT TRANSFER, Vol. 110, pp. 1059–1070.

Fletcher, L. S., and Gyorog, D. A., 1971, "Prediction of Thermal Contact Conductance Between Similar Metal Surfaces," *AIAA Progress in Astronautics and Aeronautics,* Vol. 24, Heat Transfer and Spacecraft Thermal Control, pp. 273–288.

Gibson, R. D., 1976, "The Contact Resistance for a Semi-infinite Cylinder in a Vacuum," *Applied Energy,* Vol. 2, pp. 57–65.

Hegazy, A. A., 1985, Thermal Joint Conductances of Conforming Rough Surfaces: Effects of Surface Microhardness Variation, Ph.D. thesis, Department of Mechanical Engineering, University of Waterloo, Ontario.

Henry, J. J., 1964, *Thermal Contact Resistance,* A.E.C. Rep. No. 2079-2, M.I.T., Cambridge, MA.

Hsieh, C. K., 1968, Correlation and Prediction of Thermal Contact Conductance for Nominally Flat Surfaces, Ph.D. thesis, Purdue University, West Lafayette, IN.

Hsieh, C. K., 1974, "A Critical Evaluation of Surface Geometrical Parameters For a Nominally Flat Surface Model," *ASME Journal of Lubrication Technology,* Vol. 96, pp. 638–639.

Ishigaki, H., and Kawaguchi, I., 1979, "A Simple Estimation of the Elastic-Plastic Deformation of Contacting Asperities," *Wear,* Vol. 54, pp. 157–164.

Kang, T. K., Peterson, G. P., and Fletcher, L. S., 1990, "Enhancing the Thermal Contact Conductance Through the Use of Thin Metallic Coatings," ASME JOURNAL OF HEAT TRANSFER, Vol. 112, pp. 864–871.

Lambert, M. A., Marotta, E. E, and Fletcher, L. S., 1995, "The Thermal Contact Conductance of Hard and Soft Coat Anodized Aluminum," ASME JOURNAL OF HEAT TRANSFER, Vol. 117, pp. 270–275.

Lee, S., Song, S., Moran, K. P., and Yovanovich, M. M., 1993, "Analytical Modeling of Thermal Resistance in Bolted Joints," *ASME Enhanced Cooling Techniques for Electronics Applications,* HTD-Vol. 263, ASME, NY, pp. 115–122.

Leung, M., 1995, Prediction of Thermal Contact Conductance by Statistical Mechanics, Ph.D. dissertation, University of Florida, Gainesville, FL.

Madhusudana, C. V., and Fletcher, L. S., 1986, "Contact Heat Transfer—The Last Decade," *AIAA Journal,* Vol. 24, No. 3, pp. 510–523.

Mal'kov, V. A., 1970, "Thermal Contact Resistance of Machined Metal Surfaces in a Vacuum Environment," *Heat Transfer-Soviet Research,* Vol. 2, pp. 24–33.

McCool, J. I., 1986, "Comparison of Models for the Contact of Rough Surfaces," *Wear,* Vol. 107, pp. 37–60.

McWaid, T., and Marschall, E., 1992, "Thermal Contact Resistance Across Pressed Metal Contacts in a Vacuum Environment," *International Journal of Heat Mass Transfer,* Vol. 35, No. 11, pp. 2911–2920.

Mikic, B. B., and Rohsenow, W. M., 1966, *Thermal Contact Resistance,* Rep. No. 4542-41, M.I.T., Cambridge, MA.

O'Callaghan, P. W., and Probert, S. D., 1974, "Thermal Resistance and Directional Index of Pressed Contacts Between Smooth Non-Wavy Surfaces," *Journal of Mechanical Engineering Science,* Vol. 16, pp. 41–55.

Ochterbeck, J. M., Peterson, G. P., and Fletcher, L. S., 1992, "Thermal Contact Conductance of Metallic Coated BiCaSrCuO Superconductor/Copper Interfaces at Cryogenic Temperatures," ASME JOURNAL OF HEAT TRANSFER, Vol. 114, pp. 21–29.

Phelan, P. E., Song, Y., Nakabeppu, O., Ito, K., Hijikata, K., Ohmori, T., and Torikoshi, K., 1994, "Film/Substrate Thermal Boundary Resistance for an Er-Ba-Cu-O High-T_c Thin Film," ASME JOURNAL OF HEAT TRANSFER, Vol. 116, pp. 1038–1041.

Popov, V. M., 1976, "Concerning the Problem of Investigating TCR," *Power Engineering,* Vol. 14, No. 3, pp. 158–163.

Snaith, B., Probert, S. D., and O'Callaghan, P. W., 1986, "Thermal Resistances of Pressed Contacts," *Applied Energy,* Vol. 22, pp. 31–84.

So, H., and Liu, D. C., 1990, "Evaluation of Statistical Models for Elastic-Plastic Contact of Rough Surface with Hardening Effect," *Journal of the Chinese Society of Mechanical Engineers,* Vol. 11, No. 6, pp. 481–487.

Sonntag, R. E., and Van Wylen, G. J., 1966, *Fundamentals of Statistical Thermodynamics,* John Wiley & Sons, Inc., New York.

Stevenson, P. F., Peterson, G. P., and Fletcher, L. S., 1991, "Thermal Rectification in Similar and Dissimilar Metal Contacts," ASME JOURNAL OF HEAT TRANSFER, Vol. 113, pp. 30–36.

Thomas, T. R., and Probert, S. D., 1972, "Correlations for Thermal Contact Conductance in Vacuo, ASME JOURNAL OF HEAT TRANSFER, Vol. 94, pp. 276–281.

Tien, C. L., 1968, "A Correlation for Thermal Contact Conductance of Nominally-Flat Surface in a Vacuum," *Proceedings of the 7th Thermal Conductivity Conference,* U.S. Bureau of Standards, pp. 755–759.

Williamson, J. B. P., 1968, "Microphotography of Surfaces," *Proceedings of the Institution of Mechanical Engineers,* Pt. 3K, Vol. 182, pp. 21–30.

Williamson, J. B. P., 1969, "The Shape of Solid Surfaces," Proceedings of the ASME Annual Winter Meeting, ASME, NY, pp. 24–35.

Wyant, J. C., Koliopoulos, C. L., Bhushan, B., and Basila, D., 1986, "Development of a Three-Dimensional Noncontact Digital Optical Profiler," *ASME Journal of Tribology,* Vol. 108, pp. 1–8.

Yovanovich, M. M., 1967, Influence of Surface Roughness and Waviness upon Thermal Contact Resistance, Sc.D. thesis, Massachusetts Institute of Technology, Cambridge, MA, EPL Rep. No. 76361-48.

Yovanovich, M. M., 1982, "Thermal Contact Correlations," Spacecraft Radiative Transfer and Temperature Control, *AIAA Progress in Astronautics and Aeronautics,* Vol. 83, T. E. Horton, ed., New York, pp. 83–95.

Numerical Study of Shear-Induced Heating in High-Speed Nozzle Flow of Liquid Monopropellant

X. Shi[1]

O. M. Knio
Assistant Professor.
knio@jhu.edu
Assoc. Mem. ASME

J. Katz
Professor.
Mem. ASME

Department of Mechanical Engineering,
The Johns Hopkins University,
Baltimore, MD 21218-2686

A numerical study is performed which focuses on peak temperatures experienced by a liquid monopropellant during high-speed injection in a small-diameter nozzle. Attention is focused on short-duration injection during which the nozzle wall boundary layer is predominantly laminar. An unsteady 1D analysis of the temperature distribution associated with sudden fluid acceleration over a flat insulated boundary is first conducted. Expressions are provided which relate the normalized peak wall temperature to the prevailing Eckert and Prandtl numbers. Results reveal a quadratic dependence of the normalized wall temperature on impulse velocity, and a nonlinear variation with Prandtl number. Next, simulation of high-speed flow in an axisymmetric nozzle is performed. The numerical schemes are based on finite-difference discretization of a vorticity-based formulation of the mass, momentum, and energy conservation equations. Implementation of the numerical schemes to flow of LP 1846 in a 4 mm diameter nozzle indicates that preignition is likely to occur for velocities higher than 200 m/s. The effects of wall heat transfer and temperature-dependent properties are also discussed.

1 Introduction

One of the concerns in the design or operation of devices involving high-speed flow of a combustible liquid is the prevention or minimization of hazards associated with premature ignition of the mixture. Among the various phenomena that could lead to such an undesirable event, attention is focused here on shear-induced (or viscous) heating effects. The latter arise, for example, when the liquid is driven at high velocity within small gaps or is squeezed between two colliding boundaries. Thus, high shearing rates are established which may result in the generation of regions of sufficiently high temperature for ignition to occur.

A number of mechanisms leading to the formation of so called "hot spots" have been described in the literature. Most have been identified based on investigations of viscous heating due to the squeezing of liquid drops between two colliding parallel plates (Cherry, 1945; Eirich and Tabor, 1948; Field, 1992; Field et al., 1992; Yuan and Prosperetti, 1996; Field et al., 1982; Heavens and Field, 1974; Krishna Moan and Field, 1984). These studies have shown that the peak temperature experienced by the liquid occurs in thin layers adjacent to the solid surfaces where the velocity and shear are high and the viscosity is low.

The present study is motivated by safety concerns associated with viscous heating of liquid monopropellants in small-diameter nozzles (Knapton et al., 1992; Lisanov and Dubovic, 1986). As schematically illustrated in Fig. 1, we focus on the high-speed flow of LP 1846, a hydroxylammonium nitrate based monopropellant, in a 4 mm diameter, 2 cm long axisymmetric nozzle located downstream of pipe contraction with large area ratio. In addition, we restrict our attention on a transient operation regime of approximately 10 ms in duration, during which the monopropellant is rapidly accelerated through the nozzle to mean mixture velocity in the range 100–400 m/s. For such a scenario, simple scaling arguments show that the boundary layer thickness remains much smaller than the nozzle radius, and that transition to turbulence is not expected during the injection period (Shi, 1996). Consequently, viscous effects are confined to a small region close to solid boundaries, and the primary concern is the maximum temperature attained at or near the nozzle boundaries. Thus, the objective of the present effort is the development of a simplified computational model that can be used to conservatively predict the peak mixture temperature, and to investigate its dependence on the details of the injection event.

2 Formulation

In order to obtain conservative estimates of peak temperatures, and to render the analysis tractable, a number of simplifying assumptions are used. Specifically, the study is focused on limiting inlet conditions corresponding to an essentially flat velocity profile with vanishingly small boundary layer thickness. In addition, the initial flow acceleration transient is ignored, and the mixture is assumed to be impulsively accelerated through the nozzle. By doing so, detailed experimentation in a potentially large parameter space is avoided.

The flow field within the nozzle is thus analyzed using a simplified model which also assumes that (*i*) the mixture is incompressible and Newtonian, (*ii*) the nozzle has constant diameter, and (*iii*) the flow remains axisymmetric. Under the stated assumptions, fluid motion is governed by the mass, momentum, and energy conservation equations. In a vorticity based formulation, these are expressed as (Batchelor, 1967; Schlichting, 1979; Panton, 1984):

[1] Currently: Software Engineer, Newbridge Networks Inc., Herndon, VA 20170.

Contributed by the Heat Transfer Division for publication in the JOURNAL OF HEAT TRANSFER. Manuscript received by the Heat Transfer Division February 3, 1997; revision received August 8, 1997; Keywords: Conduction; Numerical Methods; Transient and Unsteady Heat Transfer. Associate Technical Editor: R. W. Douglass.

$$\frac{\partial \omega}{\partial t} + \frac{\partial v_r \omega}{\partial r} + \frac{\partial v_z \omega}{\partial z} = \frac{\nu^*}{\mathrm{Re}}\left[\frac{\partial^2 \omega}{\partial r^2} + \frac{\partial}{\partial r}\left(\frac{\omega}{r}\right) + \frac{\partial^2 \omega}{\partial z^2}\right] + \frac{1}{\mathrm{Re}}\left[\frac{\partial \nu^*}{\partial z}\frac{\partial \omega}{\partial z} + \frac{\partial \nu^*}{\partial r}\left(2\frac{\partial \omega}{\partial r} + \frac{\omega}{r}\right)\right] + \frac{1}{\mathrm{Re}}\left[\frac{\partial^2 \nu^*}{\partial z \partial r}\left(\frac{\partial v_r}{\partial r} - \frac{\partial v_z}{\partial z}\right) + \left(\frac{\partial v_z}{\partial r} + \frac{\partial v_r}{\partial z}\right)\left(\frac{\partial^2 \nu^*}{\partial z^2} - \frac{\partial^2 \nu^*}{\partial r^2}\right)\right] \quad (1)$$

$$\frac{\partial}{\partial r}\left(\frac{1}{r}\frac{\partial \psi}{\partial r}\right) + \frac{1}{r}\frac{\partial^2 \psi}{\partial z^2} = -\omega \quad (2)$$

$$\frac{\partial T}{\partial t} + v_r \frac{\partial T}{\partial r} + v_z \frac{\partial T}{\partial z} = \frac{1}{\mathrm{Re\,Pr}}\left[\frac{1}{r}\frac{\partial}{\partial r}\left(k^* r \frac{\partial T}{\partial r}\right) + \frac{\partial}{\partial z}\left(k^* \frac{\partial T}{\partial z}\right)\right] + \frac{\mathrm{Ec}}{\mathrm{Re}}\nu^* \Phi \quad (3)$$

where ω is the vorticity, ψ the streamfunction, T the temperature, $v_r = r^{-1}\partial\psi/\partial z$, and $v_z = r^{-1}\partial\psi/\partial r$ are the radial and streamwise velocity components, respectively, $\nu^* \equiv \tilde{\nu}(\tilde{T})/\tilde{\nu}(\tilde{T}_0)$ is a normalized viscosity, $k^* \equiv \tilde{k}(\tilde{T})/\tilde{k}(\tilde{T}_0)$ is a normalized thermal conductivity, and

$$\Phi \equiv 2\left[\left(\frac{\partial v_r}{\partial r}\right)^2 + \left(\frac{v_r}{r}\right)^2 + \left(\frac{\partial v_z}{\partial z}\right)^2\right] + \left(\frac{\partial v_r}{\partial z} + \frac{\partial v_z}{\partial r}\right)^2 \quad (4)$$

is the viscous dissipation function. $\mathrm{Re} \equiv \tilde{\rho}\tilde{U}\tilde{R}/\tilde{\mu}_0$, $\mathrm{Pr} \equiv \tilde{\nu}_0/\tilde{\alpha}_0$, and $\mathrm{Ec} \equiv \tilde{U}^2/\tilde{c}_p\tilde{T}_0$ denote the Reynolds, Prandtl, and Eckert numbers, respectively. Dimensional quantities are indicated using tildes and the subscript 0 is used to denote inlet conditions. Variables are normalized with respect to the appropriate combination of the mixture density, $\tilde{\rho}$, the nozzle radius, $\tilde{R}$, the maximum velocity at the nozzle inlet, $\tilde{U}$, and the mixture inlet temperature, $\tilde{T}_0$.

3 Numerical Schemes

Flowfield simulation is performed by numerically integrating the parabolized equations of motion on a radially stretched computational grid. To this end, the transformation from physical to computational plane,

$$r = 1 - \frac{\exp[a(1-\xi)] - 1}{\exp(a) - 1} \quad (5)$$

$0 \le \xi \le 1$ is used. The transformation, which concentrates grid points in the neighborhood of nozzle walls, is characterized by the grid stretching parameter a. In the computational plane, the governing equations are expressed as

$$\frac{\partial \omega}{\partial t} + \xi_r \frac{\partial}{\partial \xi}(v_\xi \omega) + \xi_z \frac{\partial}{\partial z}(v_z \omega) = \frac{\nu^*}{\mathrm{Re}}\left[\xi_r^2 \frac{\partial^2 \omega}{\partial \xi^2} + \xi_{rr}\frac{\partial \omega}{\partial \xi} + \frac{\xi_r}{r}\frac{\partial \omega}{\partial \xi} - \frac{\omega}{r^2}\right] + \frac{1}{\mathrm{Re}}\left[\xi_r \frac{\partial \nu^*}{\partial \xi}\left(2\xi_r \frac{\partial \omega}{\partial \xi} + \frac{\omega}{r}\right) + \omega\left(\xi_r^2 \frac{\partial^2 \nu^*}{\partial \xi^2} + \xi_{rr}\frac{\partial \nu^*}{\partial xi}\right)\right] \quad (6)$$

$$\xi_r^2 \frac{\partial^2 \psi}{\partial \xi^2} + \xi_{rr}\frac{\partial \psi}{\partial \xi} - \frac{\xi_r}{r}\frac{\partial \psi}{\partial \xi} = -\omega r \quad (7)$$

$$\frac{\partial T}{\partial t} + v_\xi \xi_r \frac{\partial T}{\partial \xi} + v_z \frac{\partial T}{\partial z} = \frac{1}{\mathrm{Re\,Pr}}\left[\frac{\xi_r}{r}\frac{\partial}{\partial \xi}\left(k^* r \xi_r \frac{\partial T}{\partial \xi}\right)\right] + \frac{\mathrm{Ec}}{\mathrm{Re}}\nu^* \Phi \quad (8)$$

where $v_\xi = -r^{-1}\partial\psi/\partial z$, $v_z = \xi_r r^{-}\partial\psi/\partial\xi$, $\Phi \simeq \xi_r^2(\partial v_z/\partial\xi)^2$, while $\xi_r \equiv \partial\xi/\partial r$ and $\xi_{rr} \equiv \partial^2\xi/\partial r^2$.

Numerical simulation of the above system of equations relies on a finite-difference methodology. The computational plane is spatially discretized using a rectangular grid with (N_r, N_z) points in the (ξ, z) directions. All internal spatial derivatives are discretized using second-order centered differences (Fletcher, 1988; Hirsch, 1990). A semi-implicit temporal discretization of the governing equations is adopted which is based on treating nonlinear convection terms using a third-order Adams-Bashforth scheme, and applying the second-order Crank-Nicolson scheme to remaining terms. Numerical simulation of the steady parabolized equations is also performed. A spatial discretization similar to that of unsteady simulations is used, and the equations are integrated by marching the solution in the streamwise direction, from the nozzle inlet towards the exit. Details of numerical implementations and results of a validation study are discussed by Shi (1996).

Equations (6–8) are solved subject to the following boundary conditions; at the nozzle wall, $r = 1$, no slip velocity boundary conditions are used, and the following thermal boundary condition is imposed: $k^*\partial T/\partial r = -\mathrm{Nu}[T(r=1) - 1]$, where $\mathrm{Nu} \equiv \tilde{h}\tilde{R}/\tilde{k}_0$ is the Nusselt number. Adiabatic wall conditions are simulated simply by setting $\mathrm{Nu} = 0$. At the inlet of the channel a uniform temperature profile is imposed, $T(r) = 1$. Meanwhile, stream function and vorticity boundary conditions are derived from a smooth velocity profile that is essentially flat, except for a thin boundary layer at the nozzle wall. In the computations, the thickness of this artificial layer at the nozzle inlet is decreased, and the grid resolution accordingly refined, until the computed solution becomes essentially independent of both the thickness of the artificial layer and of the grid size. The validity of the present approach has been examined in detail (Shi, 1996). Briefly, we find that "convergence" is reached whenever the thickness of the inlet profile drops to roughly 1 μm. The validity of the parabolized flow approximation is also established in Shi (1996), based on a detailed comparison of the predictions of the steady and unsteady parabolized codes with direct numerical simulations at moderate Reynolds number.

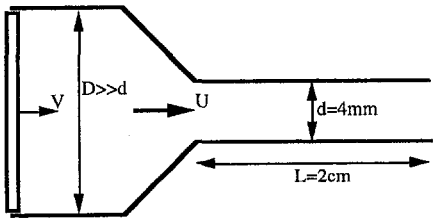

Fig. 1 Schematic illustration of the nozzle geometry

4 Quasi-One-Dimensional Approximation

In order to gain an appreciation for the role of governing parameters, we first examine the simplified problem of impul-

sively started motion over a flat insulated plate. This exercise is also motivated by the fact that the corresponding physical setting closely approximates the early stages of boundary layer formation at the nozzle walls. Assuming constant properties, the quasi-one-dimensional flow is expressed in terms of the well-known similarity solution (Carslaw and Jaeger, 1959),

$$\frac{u}{U_\infty} = \text{erf}\ (\eta) \tag{9}$$

where $\eta \equiv \tilde{y}/\sqrt{4\tilde{\nu}\tilde{t}}$. Meanwhile, the temperature distribution is obtained by inverting the corresponding energy equation,

$$\frac{\partial \tilde{T}}{\partial \tilde{t}} = \tilde{\alpha}\frac{\partial^2 \tilde{T}}{\partial \tilde{y}^2} + \frac{\tilde{U}^2}{\partial \tilde{c}_p \tilde{t}}\exp\left(-\frac{\tilde{y}^2}{2\tilde{\nu}\tilde{t}}\right) \tag{10}$$

using a Green's function approach. A closed-form expression for the wall temperature is thus obtained, and is expressed in normalized form as (Shi, 1996):

$$\frac{T_w}{T_0} = \begin{cases} 1 + \dfrac{\text{Ec}}{\pi}\sqrt{\dfrac{\text{Pr}}{2-\text{Pr}}}\left(\sin^{-1}(1-\text{Pr}) + \dfrac{\pi}{2}\right) & \text{Pr} < 2 \\ 1 + \dfrac{2\text{Ec}}{\pi} & \text{Pr} = 2 \\ 1 + \dfrac{\text{Ec}}{\pi}\sqrt{\dfrac{\text{Pr}}{\text{Pr}-2}}\ln\left(\sqrt{\text{Pr}(\text{Pr}-2)} + \text{Pr} - 1\right) & \text{Pr} > 2. \end{cases} \tag{11}$$

Thus, the wall temperature is time independent and, due to the absence of a characteristic flow lengthscale, the above expressions do not explicitly depend on the Reynolds number.

Equation (11) allows simple interpretation of the impact of Eckert and Prandtl numbers on shear heating during the early stages of boundary layer formation. In particular, linear variation of the normalized wall temperature with Eckert number reflects a quadratic dependence on impulse velocity. Meanwhile, the logarithmic divergence of the wall temperature as $\text{Pr} \to \infty$ underscores a concern for mixtures having high Prandtl number. This is particularly the case for some HAN-based liquid monopropellants such as LP 1846, which are characterized by Prandtl numbers exceeding 100.

5 Axisymmetric Flow

5.1 Effect of Injection Speed. The simulation schemes are applied to characterize shear induced heating during high-speed injection of LP 1846. Most computations are performed using the steady parabolized schemes on a stretched grid with a stretching parameter $a = 6.5$, $N_r = 401$ points in the radial direction, and $N_z = 8001$ points in the streamwise direction. The effect of injection velocity is first analyzed by considering four different injection speeds $\tilde{U} = 100$, 200, 300, and 400 m/s. In all of these cases an inlet temperature $\tilde{T}_0 = 298$ K is assumed and adiabatic wall conditions are imposed.

The computations are performed using two different models. In the first, the physical properties of LP 1846 are assumed constant; we use $\tilde{\rho} = 1{,}430\ \text{kg/m}^3$, $\tilde{c}_p = 2{,}300\ \text{J/kg}\cdot\text{K}$, $\tilde{k} = 0.15\ \text{W/m}\cdot\text{K}$, and $\tilde{\nu} = 4.988 \times 10^{-6}\text{m}^2/\text{s}$ (McQuaid, 1994; Freedman, 1986). In this model, the Prandtl number of the mixture is also constant, Pr = 109.4.

In the second model, the dependence of the physical properties of LP 1846 on temperature are accounted for. For LP 1846, the dynamic viscosity varies with temperature as (McQuaid, 1994; Freedman, 1986)

$$\tilde{\mu} = C\exp\left(\frac{D}{\tilde{T} - \tilde{T}_{\text{ref}}}\right) \tag{12}$$

where $\tilde{T}$ is the temperature in Kelvin, $\tilde{T}_{\text{ref}} = 164$ K is a reference temperature, while $C = 0.16773$cp and $D = 502.52$ K are constants. Unfortunately, the dependence of the thermal conductivity on temperature is not known and only a single value $\tilde{k}$ (298 K) is reported (McQuaid, 1994; Freedman, 1986). However, since for most liquids the dynamic viscosity decreases rapidly with increasing temperature with only small variation in the thermal conductivity, this uncertainty is realistically overcome by treating the thermal conductivity as temperature independent, and using the reported value at $\tilde{T} = 298$ K. Since both the density and heat capacity of LP 1846 vary slightly with temperature, the thermal diffusivity is consequently constant. Thus, the Prandtl number drops appreciably with increasing temperature and it is desired to analyze the impact of this variation.

Results of steady computations are summarized in Figs. 2(*a*) and 2(*b*), which show the wall temperature distribution computed using the constant and variable-viscosity models, respectively. The results reflect trends established for quasi-one-dimensional flow. In particular, temperature predictions exhibit a quadratic dependence on the injection velocity. Significant heating of the mixture, with temperature increases greater than 100 K, are predicted when the injection velocity exceeds 200 m/s. Thus, for these injection scenarios, prema-

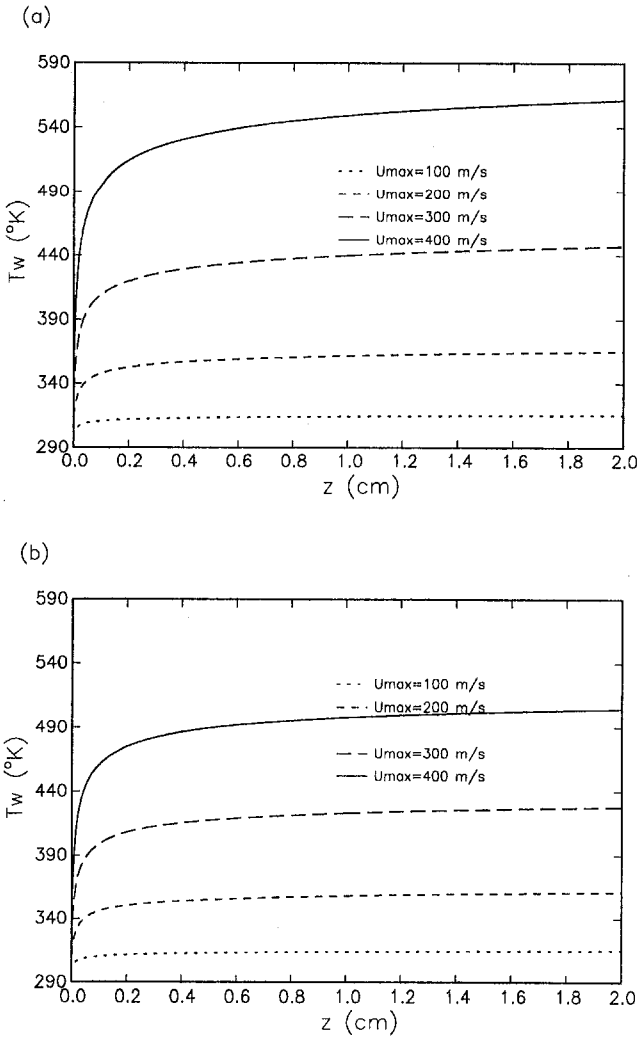

Fig. 2 Effect of inlet speed on the steady state wall temperature distribution for high-speed injection of LP 1846 at $\tilde{T}_0 = 298$°K: (*a*) constant viscosity; (*b*) temperature-dependent viscosity. In both cases adiabatic wall conditions are assumed.

ture ignition of the mixture due to severe shear heating is likely to occur.

The effect of temperature-dependent viscosity is analyzed by comparing Figs. 2(*a*) and 2(*b*). The comparison shows that for moderate injection speeds, $\tilde{U} \leq 200$ m/s, the predictions of both models are very close to each other. At higher injection speeds, large temperature variations induced by intense shear heating of the mixture cause a significant deviation between the predictions. The variable-viscosity model predicts lower steady-state peak temperatures than the corresponding constant-property simulation (Yuan and Prosperetti, 1996). The nature of this deviation is not surprising since the viscosity decreases with increasing temperature, resulting in a drop in the Prandtl number. Thus, by neglecting the temperature dependence of the viscosity, the constant property model yields more conservative estimates of shear heating.

Results of the steady-state computations were compared to predictions of unsteady simulations in order to check their validity (Shi, 1996). A sample of this exercise is shown in Fig. 3, which shows the evolution of the wall temperature distribution for injection at $\tilde{U} = 300$ m/s. The figure shows that the wall temperature exhibits a monotonic increase towards a steady state which is reached well before the end of the injection period. Specifically, for large times following injection, $t \geq 2$ ms, the wall temperature distribution in the unsteady computation ceases to increase, and coincides with the corresponding steady-state prediction (Fig. 2(*a*)). Thus, both steady and unsteady codes yield the same peak temperature prediction. It is also interesting to note that the steady and unsteady computations are performed with different grid refinement levels. Thus, the agreement between the two calculations also provides an indication that the predictions are essentially independent of discretization parameters.

5.2 Effect of Wall Heat Transfer. The impact of wall heat transfer on peak temperature predictions is also investigated. We use a simplified model in which wall heat transfer is taken into account through a prescribed heat transfer coefficient. Thus, the simplified model ignores the thermal resistance of finite thickness nozzle walls, and also ignores the associated heat storage capacity which may play an important role during the flow transient. The temperature of the nozzle surroundings is assumed to coincide with the mixture's inlet temperature. High speed LP 1846 injection experiments are repeated for

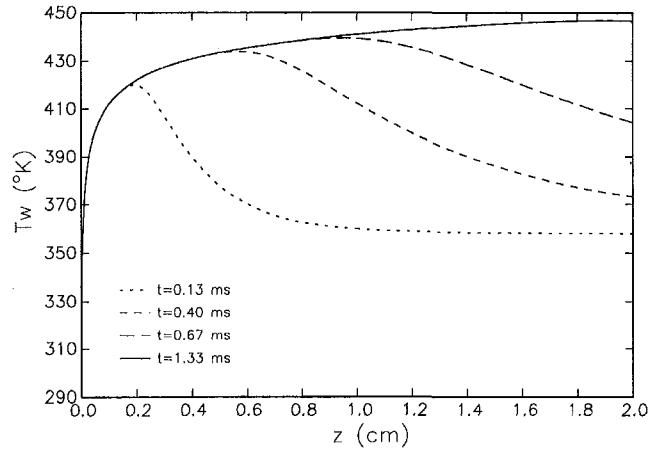

Fig. 3 Instantaneous wall temperature distribution for high-speed injection of LP 1846 with $\tilde{T}_0 = 298$ K and $\tilde{U} = 300$ m/s. The computations are performed on a stretched grid with $a = 6$, $N_r = 201$ points in the radial direction, and $N_z = 801$ points in the streamwise direction. Adiabatic wall conditions are assumed.

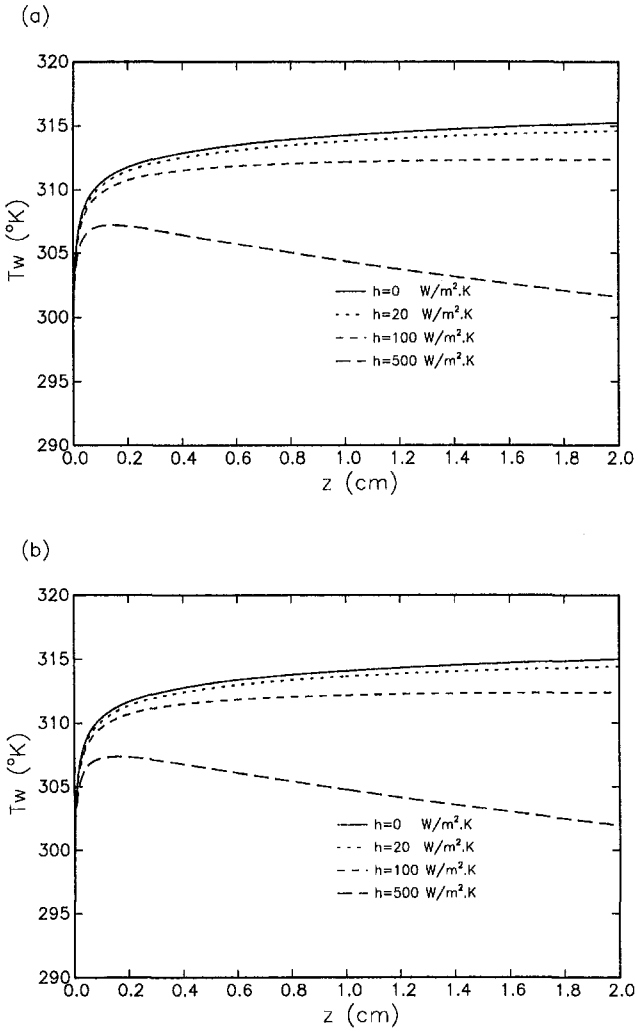

Fig. 4 Effect of wall heat transfer on the steady state peak temperature distributions for LP 1846 injection at $\tilde{T}_0 = 298$°K and $\tilde{U} = 100$ m/s: (*a*) constant viscosity; (*b*) temperature-dependent viscosity

different values of the heat transfer coefficient, $\tilde{h} = 20$, 100, and 500 W/m^2·K. These values are representative of free convection in air, forced air cooling at low speed, and forced liquid cooling at moderate speed (Burmeister, 1993; Incropera and DeWitt, 1990).

Results are shown in Figs. (4)–(6), which, respectively, show peak temperature distributions for LP 1846 injection at $\tilde{U} = 100$, 200, and 300 m/s. As in the previous section, the results of both constant property and temperature-dependent-viscosity models are shown. Examination of these results reveals that:

1 For very high injection speed ($\tilde{U} = 300$ m/s), wall heat transfer does not significantly reduce peak temperature predictions even for high heat transfer coefficient. Thus, conventional nozzle wall cooling means may not constitute an effective means of minimizing the likelihood of mixture preignition.

2 For low heat transfer coefficient, $\tilde{h} = 20$ W/m^2·K, the computed peak temperatures are very close to those obtained assuming adiabatic wall conditions. Accordingly, natural heat losses are not expected to significantly affect peak temperature predictions.

3 Large values of the heat transfer coefficient may appreciably reduce peak temperatures whenever the injection velocity is not extremely high. In these situations, forced cooling techniques may be especially tailored in order to effectively minimize the risk of mixture ignition.

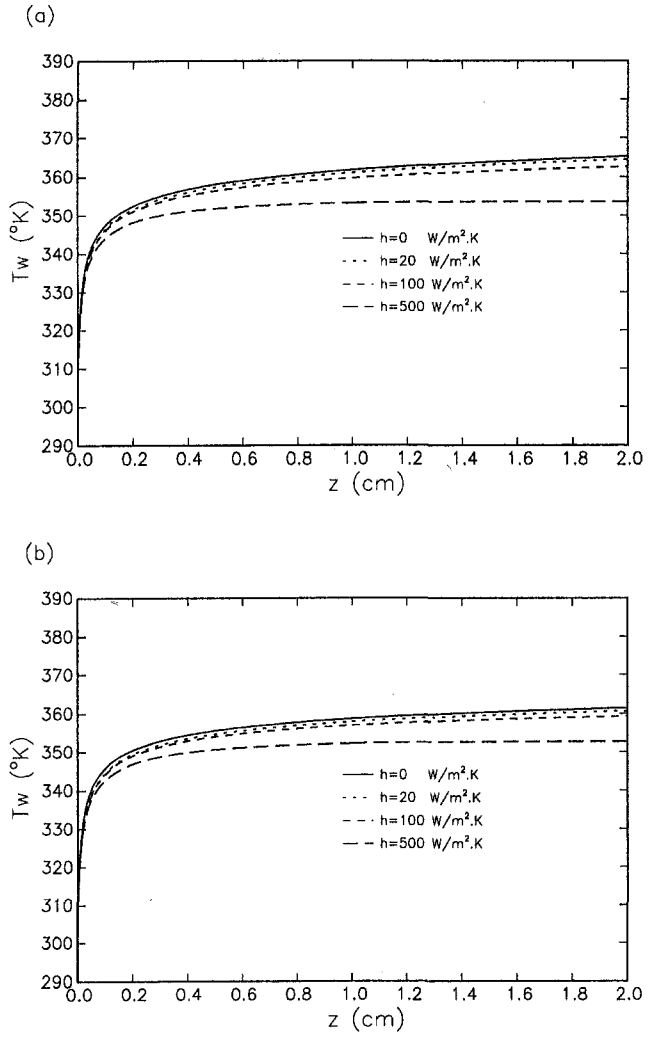

Fig. 5 Effect of wall heat transfer on the steady state peak temperature distributions for LP 1846 injection at $\tilde{T}_0$ = 298°K and $\tilde{U}$ = 200 m/s: (*a*) constant viscosity; (*b*) temperature-dependent viscosity

4 Comparison of constant viscosity and variable-viscosity results shows that when the injection speed is low, the predictions of both models are very close. For higher injection speeds, temperature increases are more substantial and the variable-viscosity model yields smaller peak temperature predictions than those obtained using constant-property simulations.

We finally note that when wall heat transfer is accounted for, the peak temperature achieved at a given streamwise location may not always coincide with the wall temperature. Generally, as heat losses increase, the maximum temperature location moves away from the wall into the thermal boundary layer. Thus, unlike insulated wall conditions, the peak temperature distributions plotted in Figs. (4)–(6) do not always correspond to wall temperature distributions.

5.3 Effect of Inlet Temperature. Finally, the effect of inlet temperature is investigated. We consider three injection speeds, $\tilde{U}$ = 100, 200, and 300 m/s, and assume adiabatic nozzle wall conditions. Results of steady parabolized approximations are shown in Figs. 7(*a*)–7(*c*), which show wall temperature distributions for three inlet temperatures; $\tilde{T}_0$ = 278, 298, and 318 K.

For low injection speed, $\tilde{U}$ = 100 m/s, the effects of shear-induced heating are essentially similar for all inlet temperatures. For these injection characteristics, moderate heating in the thermal boundary layer occurs, and the wall temperature distributions for different cases appear to be shifted vertically as the inlet temperature is varied. This result is in agreement with previous observations, since the temperature distribution and consequently the viscosity do not exhibit large variations.

At higher injection speed, $\tilde{U}$ = 200 m/s, variable viscosity effects start becoming more pronounced. Figure 7(*b*) indicates that shear heating of the mixture is more substantial as the inlet temperature is decreased. Note that, for lower inlet temperatures, the inlet viscosity of the mixture is higher. Therefore, shear stresses and viscous dissipation are also higher, leading to larger wall temperature increases. This trend can also be interpreted in terms of our earlier expectation that shear heating effects are more pronounced for mixtures with higher Prandtl number. The present results are consistent with this trend since the inlet Prandtl number increases with decreasing temperature.

Another interesting observation is that, at high injection velocities, all similarity between wall temperature distributions is lost as the inlet temperature is altered. This can be clearly observed in Fig. 7(*c*) which shows that the peak temperature developed at low injection temperature may exceed that corresponding to higher inlet temperature. This suggests that, for such extreme scenarios, preheating the

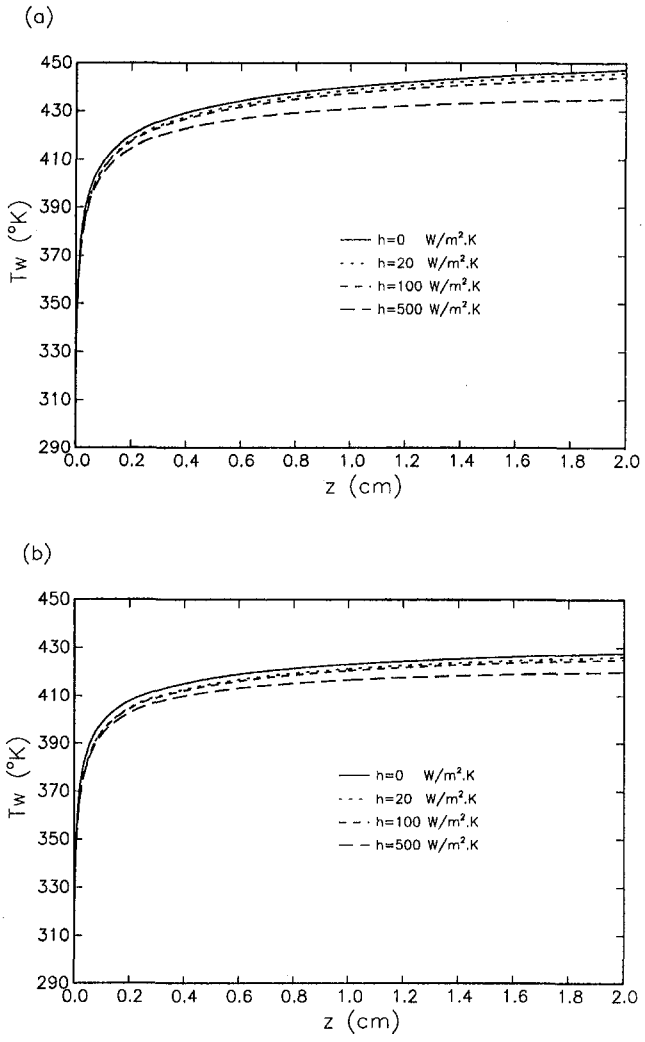

Fig. 6 Effect of wall heat transfer on the steady state peak temperature distributions for LP 1846 injection at $\tilde{T}_0$ = 298°K and $\tilde{U}$ = 300 m/s: (*a*) constant viscosity; (*b*) temperature-dependent viscosity

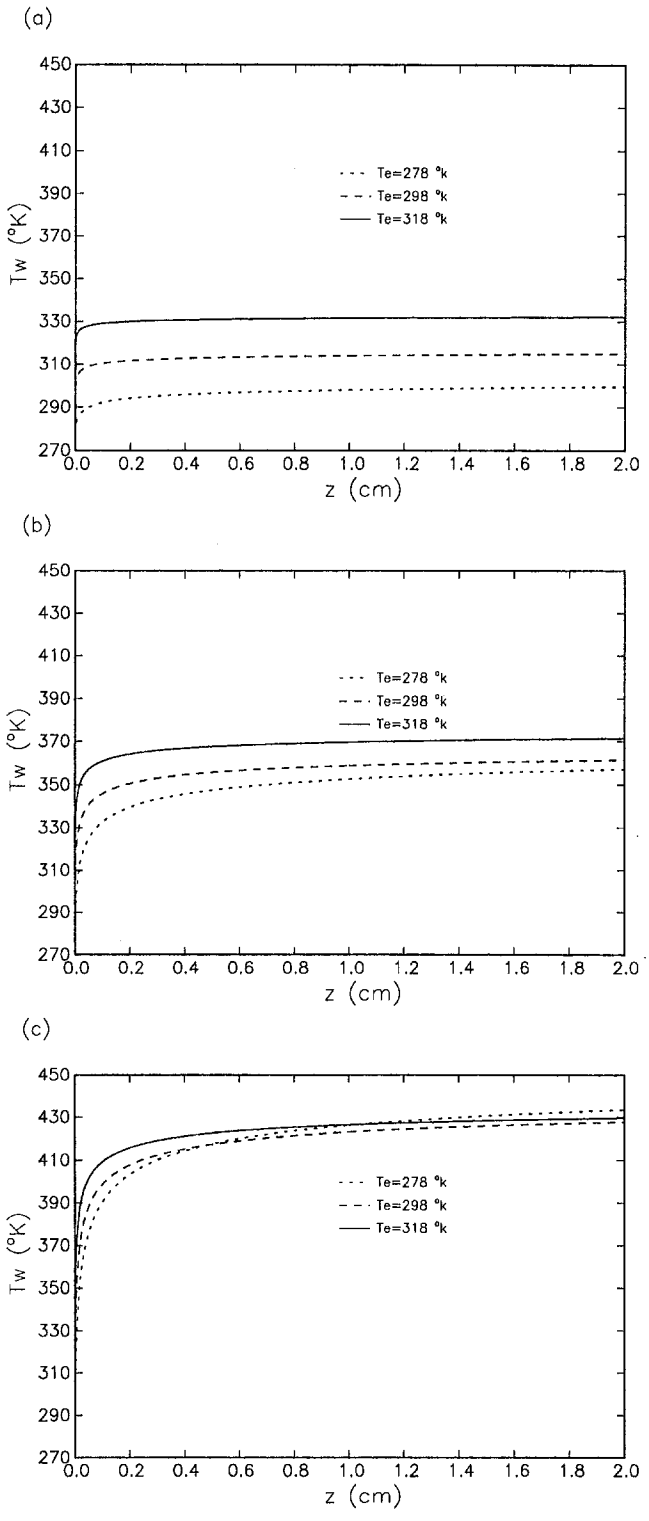

Fig. 7 Effect of inlet temperature on the steady state peak temperature distributions for LP 1846 injection: (*a*) $\bar{U}$ = 100 m/s; (*b*) $\bar{U}$ = 200 m/s; and (c) $\bar{U}$ = 300 m/s. A temperature-dependent viscosity is used, and adiabatic wall conditions are assumed

propellant prior to injection may help reduce the peak mixture temperature. Further examination of the origin of this phenomenon (not shown) indicates that it is due to different development of both the thermal and viscous boundary layers. Specifically, when intense shear heating of the mixture occurs, both the structure and spatial evolution of the boundary layer exhibit significant differences as the inlet temperature is varied.

Summary

Shear-induced heating of LP 1846 during high-speed injection in an axisymmetric nozzle is analyzed numerically. The numerical schemes are based on a finite-difference discretization of the vorticity transport and energy equations. Steady and unsteady codes are applied to predict peak temperatures of LP 1846 during high speed short-duration injection in a nozzle having 4 mm diameter and 2 cm length. When adiabatic wall conditions are assumed, computed results reveal a quadratic dependence of the peak temperature on injection velocity. Significant temperature increase, of the order of 100 K or more, is predicted for injection velocities higher than 200 m/s.

Wall heat transfer, modeled in terms of a wall heat transfer coefficient, is also analyzed. When the injection speed is very high, wall heat transfer does not significantly reduce peak temperature predictions even for high heat transfer coefficient. In addition, for low heat transfer coefficient, peak temperatures are close to those obtained assuming adiabatic wall conditions. On the other hand, large values of the heat transfer coefficient may appreciably reduce peak temperatures whenever the injection velocity is not extremely high.

The impact of a temperature-dependent viscosity is examined. Computed results show that for moderate injection speeds the predictions of both constant and variable-viscosity models are very close. However, for high injection speeds peak temperatures obtained using a variable-viscosity model are smaller than those obtained using constant-property simulation. This effect is related to the decrease of viscosity and Prandtl number with increasing temperature. Variation of the mixture inlet temperature also affects temperature predictions. In particular, it is found that shear heating effects are more pronounced for smaller inlet temperature, i.e., when the inlet Prandtl number is larger.

Acknowledgment

This work has been supported by the U.S. Army Research Office under Grant DAAH-93-G-0413. A perliminary version of this work was presented at the 31st JANNAF Combustion Subcommittee Meeting.

References

Batchelor, G., 1967, *Introduction to Fluid Dynamics,* Cambridge University Press, London.

Burmeister, L. C., 1993, *Convective Heat Transfer,* John Wiley & Sons, Inc., New York.

Carslaw, H. S., and Jaeger, J. C., 1959, *Conduction of Heat in Solids,* Oxford University Press, New York.

Cherry, T. M., 1945, "Flow and Generation of Heat in Compressed Films of Viscous Liquid," *Rep. Coun. Scient. Ind. Res. Austral.,* Vol. A 116, Rep. No. 8.

Eirich, F. R., and Tabor, D., 1948, "Collisions Through Liquid Films," *Proc. Camb. Phil. Soc.,* Vol. 44, pp. 566–580.

Fletcher, C. A. J., 1988, *Computational Techniques for Fluid Dynamics,* Springer-Verlag, New York.

Field, J. E., 1992, "Hot Spot Ignition Mechanisms for Explosives," *Accnts. Chem. Res.,* Vol. 25, pp. 489–496.

Field, J. E., Swallowe G. M., and Heavens, S. N., 1982, "Ignition Mechanisms of Explosives During Mechanical Deformation," *Proc. R. Soc. London,* Vol. A 382, pp. 231–244.

Field, J. E., Bourne, N. K., Palmer, S. J. P., and Walley, S. M., 1992, "Hot Spot Ignition Mechanisms for Explosives and Propellants," *Phil. Trans. R. Soc. London,* Vol. A 339, pp. 269–283.

Freedman, E., 1986, "A Skeleton Outline of the Physical Chemistry of HAN-Based Liquid Propellants," U.S. Army Research Laboratory Report.

Heavens, S. N., and Field, J. E., 1974, "The Ignition of a Thin Layer of Explosive by Impact," *Proc. R. Soc. London,* Vol. A 338, pp. 77–93.

Hirsch, C., 1990, *Numerical Computation of Internal and External Flows,* John Wiley & Sons, Inc., New York.

Incropera, F. C., and DeWitt, D. P., 1990, *Fundamentals of Heat and Mass Transfer,* John Wiley & Sons, Inc., New York.

Knapton, J. D., Messina, N. A., and Tarczynski, M., 1992, "Some Unresolved Problems on Ignition Mechanisms in Hydroxylammonium Nitrate Based Liquid

Monopropellants," *Proceedings of the 29th JANNAF Combustion Subcommittee Meeting,* Chemical Propulsion Information Agency, Columbia, MD.

Krishna Moan, V., and Field, J. E., 1984, "Impact Initiation of Hexanitrostilbene," *Comb. Flame,* Vol. 56, pp. 269–277.

Lisanov, M. V., and Dubovik, A. V., 1986, "Inflammation of Liquids Forced Through an Opening. II. Experimental Investigation," *Combustion, Explosion and Shock Waves,* Vol. 22, pp. 649–655.

McQuaid, M., 1994, private communication.

Panton, R., 1984, *Incompressible Flow,* John Wiley & Sons, Inc., New York.

Schlichting, H., 1979, *Boundary Layer Theory,* McGraw-Hill Companies, New York.

Shi, X., 1996, "Numerical Study of Shear-Induced Heating in High-Speed Nozzle Flow," Ph.D. thesis, Department of Mechanical Engineering, The Johns Hopkins University, Baltimore, MD.

Yuan, H., and Prosperetti, A., 1996, "Transient Viscous Heating of Liquid Layers Under Intense Shear," *Proc. R. Soc. London,* Vol. A 452, pp. 1–17.

Numerical Simulations of Heat Transfer in Taylor-Couette Flow

R. Kedia

M. L. Hunt
hunt@cco.caltech.edu

T. Colonius

Department of Engineering
and Applied Science,
California Institute of Technology,
Pasadena, CA 91125

Numerical simulations have been performed to study the effects of the gravitational and the centrifugal potentials on the stability of heated, incompressible Taylor-Couette flow. The flow is confined between two differentially heated, concentric cylinders, and the inner cylinder is allowed to rotate. The Navier-Stokes equations and the coupled energy equation are solved using a spectral method. To validate the code, comparisons are made with existing linear stability analysis and with experiments. The code is used to calculate the local and average heat transfer coefficients for a fixed Reynolds number (Re = 100) and a range of Grashof numbers. The investigation is primarily restricted to radius ratios 0.5 and 0.7 for fluids with Prandtl number of about 0.7. The variation of the local coefficients of heat transfer on the cylinder surface is investigated, and maps showing different stable states of the flow are presented. Results are also presented in terms of the equivalent conductivity, and show that heat transfer decreases with Grashof number in axisymmetric Taylor vortex flow regime, and increases with Grashof number after the flow becomes nonaxisymmetric.

Introduction

Since the publication of the classic experimental and analytical paper by Taylor (1923), numerous studies on the transitions in circular Couette flow have been made. The flow undergoes a series of transitions (Coles, 1965; Brandstater and Swinney, 1987) before it becomes fully turbulent at very high rotational rates of the inner cylinder. The flow becomes even more complex if either radial heating or superimposed axial flow (Shih and Hunt, 1992) are present or if the cylinders are eccentrically oriented. The effects of a radial temperature gradient on the stability of Taylor-Couette flows has been the subject of considerable investigation (Ali and Weidman, 1990; Chen and Kuo, 1990). The primary application of this research is in the cooling of electrical motor shafts and turbine rotors (Lee and Minkowycz, 1989). Other applications include modeling of atmospheric flows (Greenspan, 1968) and techniques of chemical vapor deposition (CVD) used in semiconductor device fabrication (Singer, 1984).

In Boiling Water Reactor (BWR) power plants, high speed pumps are used to transport water at high pressure and temperature. Over the past decade, maintenance inspections have revealed cracks up to 6 mm deep on both the shafts and the shaft covers of such pumps; these cracks arise after approximately 20,000 to 30,000 hours of operation (Kato et al., 1992; Gopalakrishnan et al., 1992). In extreme instances, these cracks actually cause pumps to fail. The manufacturers and operators of the pumps have surmised that the cracking is due to thermal loading caused by an unsteady flow. Some preliminary work in this area has shown that these cracks could be initiated by low-frequency, high-amplitude temperature fluctuations. To predict thermal fatigue in these pumps, a thermal stress analysis would require information about the frequencies and amplitudes of the thermal environment. A focus of this work is to obtain such frequency and amplitude information for the model.

Previous investigations of heated Taylor-Couette flows include theory, experiment, and numerical analysis. There are a number of parameters in this problem; among them are the Reynolds number ($\mathrm{Re} = \omega r_i b/\nu$) and the Grashof number ($\mathrm{Gr} = g\beta(T_1 - T_2)b^3/\nu^2$). Typically in an experiment, the Reynolds number is increased by increasing the angular velocity of the inner cylinder, and the Grashof number is increased by increasing the temperature difference between the inner and the outer cylinders. As these two parameters are varied, the flow changes from one state to another, and there is a subsequent change in momentum and heat transfer characteristics. There is a need to understand these transitions and document the transport properties.

Theoretical investigations include stability analyses for these flows. For high Reynolds number, previous work in this area neglected gravity and showed that the Taylor cells are stabilized when $T_1 > T_2$ and destabilized when $T_2 > T_1$. Roesner (1978) included the effect of gravity through the Boussinesq approximation (Gray and Giorgini, 1976) but only considered axisymmetric disturbances. This work showed that isothermal Taylor cells are stabilized by both negative and positive radial heating, and the stability boundaries revealed perfect symmetry with respect to the direction of radial heating. Ali and Weidman (1990) tested stability with respect to both toroidal and helical disturbances of uniform wavenumber. They found that the number of critical modes increased dramatically for large radius ratio. Chen and Kuo (1990) took into account the effects of both centrifugal and gravitational potential on the axisymmetric stability problem. They concluded that the stability boundary depended on the ratio of the centrifugal and the gravitational potentials, the Prandtl number, and the Grashof number.

An experimental study was performed by Kataoka et al. (1977) with the aid of an electrochemical technique under the assumption of analogy between heat and mass transfer. They reported that the regular sinusoidal variation of Sherwood number (Sh) is distorted by an added axial flow and both the mean and the amplitude are greatly reduced. Ball and co-workers (1989) performed a parametric study of the mean heat transfer rates across the annular gap for three different radius ratios. Their results show that the heat transfer can be described by a power-law relationship and correlated as functions of the Reynolds number and radius ratio.

Numerical simulations for axisymmetric, isothermal Taylor-Couette flow have been performed by Meyer (1967), using a finite difference technique. Moser et al. (1983) used a spectral method for solving the incompressible Navier-Stokes equations between concentric cylinders. In the present study, their method is extended to solve both the heat equation and the equations

Contributed by the Heat Transfer Division for publication in the JOURNAL OF HEAT TRANSFER and presented at '97 NHTC, Baltimore. Manuscript received by the Heat Transfer Division April 11, 1997; revision received October 23, 1997; Keywords: Flow Instability; Numerical Methods; Rotating Flows. Associate Technical Editor: R. W. Douglass.

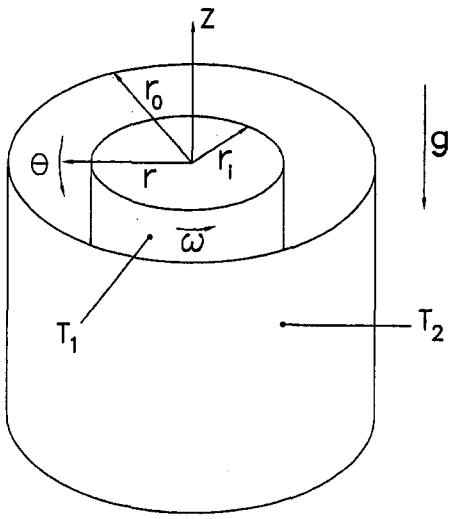

Fig. 1 Flow geometry and boundary conditions

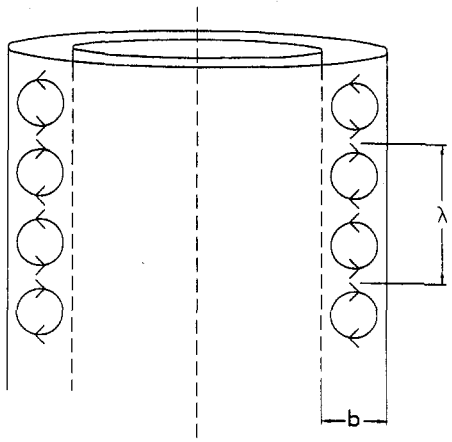

Fig. 2 Schematic of isothermal Taylor cells

of motion, which are coupled through the centrifugal and gravitational potentials. The effects of buoyancy on bifurcation in small-to-moderate aspect ratio Taylor-Couette systems have been studied numerically by Ball and Farouk (1987, 1988).

When the centrifugal acceleration is of the same order as the acceleration due to gravity, the density variation of the fluid becomes important for instabilities that are primarily centrifugal. The effect of this density variation is also accounted for in the centrifugal term. Therefore, the present study examines the interaction of gravity and centrifugal potentials with the radial temperature gradient. The simulations reported here are motivated by the need to characterize the thermal environment that is encountered during chaotic and fully turbulent flows.

Numerical Method

A sketch of the flow configuration in (r, θ, z) cylindrical coordinates is shown in Fig. 1. The radii of the inner and the outer cylinders are r_i and r_o, respectively, and the radius ratio is η. The inner cylinder rotates with a constant angular velocity ω about the vertical z-axis, while the outer cylinder is stationary. The two cylinders are at different uniform temperatures. The temperature of the inner cylinder is T_1 and that of the outer one is T_2. Gravity acts in the negative z-direction. The centrifugal force is parallel to the mean temperature gradient. The temperature difference can be assumed to be sufficiently small such that the density is treated as a constant everywhere in the Navier-Stokes equations with the exception of the gravitational (z-momentum equation) and the centrifugal (r-momentum equation) terms, i.e., the Boussinesq approximation is applied. All other fluid properties are assumed to be independent of temperature. The flow is axially periodic (i.e., infinite aspect ratio) and no slip boundary conditions are used at the inner and the outer cylinders. Figure 2 shows schematically the familiar axisymmetric counter-rotating isothermal Taylor cells. Without heating, the Taylor cells are of uniform size. The axial distance between a pair of Taylor cells is defined as axial wavelength (λ) and b is the gap width. The axial wavelength is normalized by the gap width to define L_z.

Nomenclature

A = acceleration ratio, $\omega^2 r_i/g$
b = gap width, $(r_o - r_i)$ [m]
C = Courant number
C_b = bulk concentration [mol/m^3]
C_w = concentration at the outer cylinder surface [mol/m^3]
c = nondimensional wave speed
D = mass diffusivity of the fluid [m^2/s]
f = frequency of heat transfer coefficient fluctuation [1/s]
f_c = inner cylinder frequency [1/s]
G = torque [N − m]
Gr = Grashof number, $g\beta(T_1 - T_2)b^3/\nu^2$
g = acceleration due to gravity [m/s^2]
h = local heat transfer coefficient, $q/(T_b - T_2)$ [W/m^{2}K]
$h_{\bar{\theta},\bar{z},\bar{t}}$ = spatially and temporally averaged heat transfer coefficient [W/m^{2}K]
K_{eq} = mean equivalent conductivity, $r_i \ln(1/\eta) h_{\bar{\theta},\bar{z},\bar{t}}/k$
k = thermal conductivity of the fluid [W/mK]
L_z = normalized axial wavelength, λ/b
m = local mass transfer coefficient, $N/(C_b - C_w)$ [m/s]
N = mass flux on the outer cylinder [mol/m^{2}s]
Nu = Nusselt number, $2hb/k$
n = number of starts, $2\pi r_o \tan \Psi/L_z$
P = nondimensional dynamic pressure
Pr = Prandtl number, ν/α
q = heat flux on the outer cylinder
Re = Reynolds number, $\omega r_i b/\nu$
$\mathrm{Re}_{\mathrm{crit}}$ = critical Reynolds number for the onset of Taylor vortex flow
r, θ, z = cylindrical coordinates
r_i = inner cylinder radius [m]
r_o = outer cylinder radius [m]
Sc = Schmidt number, ν/D
Sh = Sherwood number, $2mb/D$
T = nondimensional temperature
T_1 = inner cylinder temperature [K]
T_2 = outer cylinder temperature [K]
$\underline{T_b}$ = bulk temperature [K]
T_o = dimensionless reference temperature
u_r, u_θ, u_z = nondimensional velocity component in cylindrical coordinate system
ω = inner cylinder angular velocity [1/s]
ρ = density of the fluid [kg/m^3]
ν = kinematic viscosity of the fluid [m^2/s]
α = thermal diffusivity of the fluid [m^2/s]
β = thermal expansion coefficient of the fluid [1/K]
$\beta^* = \beta(T_1 - T_2)$
λ = wavelength of a pair of vortices [m]
η = radius ratio, r_i/r_o
Ψ = the angle of inclination of the cell from the horizontal
Δt = nondimensional time step of integration
$\Delta r, \Delta\theta, \Delta z$ = grid spacing in the radial, circumferential, and axial directions

The equations are made dimensionless by scaling lengths with b, time with $b/\omega r_i$, velocity with ωr_i, and temperature with $(T_1 - T_2)$, after subtracting the outer cylinder temperature and dynamic pressure with $\omega^2 r_i^2$. The nondimensional equations governing the flow for the nondimensional velocity components (u_r, u_θ, u_z), nondimensional dynamic pressure P and nondimensional temperature T (in rotational form) follow.

Continuity.

$$\frac{\partial u_r}{\partial r} + \frac{u_r}{r} + \frac{1}{r}\frac{\partial u_\theta}{\partial \theta} + \frac{\partial u_z}{\partial z} = 0 \tag{1}$$

Momentum.

$$\frac{\partial u_r}{\partial t} + \frac{u_\theta}{r}\frac{\partial u_r}{\partial \theta} + u_z\frac{\partial u_r}{\partial z} - u_z\frac{\partial u_z}{\partial r} - u_\theta\frac{\partial u_\theta}{\partial r} - (1 - \beta^*(T - \overline{T}_o))\frac{u_\theta^2}{r} = -\frac{\partial P}{\partial r} + \frac{1}{\mathrm{Re}}\left(\frac{1}{r^2}\frac{\partial^2 u_r}{\partial \theta^2} - \frac{1}{r^2}\frac{\partial u_\theta}{\partial \theta} - \frac{1}{r}\frac{\partial^2 u_\theta}{\partial \theta \partial r} + \frac{\partial^2 u_r}{\partial z^2} - \frac{\partial^2 u_z}{\partial r \partial z}\right) \tag{2}$$

$$\frac{\partial u_\theta}{\partial t} + \frac{u_r u_\theta}{r} + u_r\frac{\partial u_\theta}{\partial r} - \frac{u_r}{r}\frac{\partial u_r}{\partial \theta} - \frac{u_z}{r}\frac{\partial u_z}{\partial \theta} + u_z\frac{\partial u_\theta}{\partial z} = -\frac{1}{r}\frac{\partial P}{\partial \theta} + \frac{1}{\mathrm{Re}}\left(\frac{1}{r}\frac{\partial u_\theta}{\partial r} - \frac{u_\theta}{r^2} + \frac{\partial^2 u_\theta}{\partial r^2} + \frac{1}{r^2}\frac{\partial u_r}{\partial \theta} - \frac{1}{r}\frac{\partial^2 u_r}{\partial r \partial \theta} - \frac{1}{r}\frac{\partial^2 u_z}{\partial z \partial \theta} + \frac{\partial^2 u_\theta}{\partial z^2}\right) \tag{3}$$

$$\frac{\partial u_z}{\partial t} - u_r\frac{\partial u_r}{\partial z} + u_r\frac{\partial u_z}{\partial r} + \frac{u_\theta}{r}\frac{\partial u_z}{\partial \theta} - u_\theta\frac{\partial u_\theta}{\partial z} = -\frac{\partial P}{\partial z} + \frac{1}{\mathrm{Re}}\left(\frac{1}{r}\frac{\partial u_z}{\partial r} - \frac{1}{r}\frac{\partial u_r}{\partial z} - \frac{\partial^2 u_r}{\partial r \partial z} + \frac{\partial^2 u_z}{\partial r^2} + \frac{1}{r^2}\frac{\partial^2 u_z}{\partial \theta^2} - \frac{1}{r}\frac{\partial^2 u_\theta}{\partial z \partial \theta}\right) + \frac{\mathrm{Gr}}{\mathrm{Re}^2}(T - \overline{T}_o) \tag{4}$$

with $(u_r, u_\theta, u_z) = (0, 1, 0)$

at the nondimensional inner radius, $\eta/(1 - \eta)$

and $(u_r, u_\theta, u_z) = (0, 0, 0)$

at the nondimensional outer radius, $1/(1 - \eta)$

Energy.

$$\frac{\partial T}{\partial t} + u_r\frac{\partial T}{\partial r} + \frac{u_\theta}{r}\frac{\partial T}{\partial \theta} + u_z\frac{\partial T}{\partial z} = \frac{1}{\mathrm{Pr}\,\mathrm{Re}}\left(\frac{1}{r}\frac{\partial T}{\partial r} + \frac{\partial^2 T}{\partial r^2} + \frac{1}{r^2}\frac{\partial^2 T}{\partial \theta^2} + \frac{\partial^2 T}{\partial z^2}\right) \tag{5}$$

with $T = 1$ at the nondimensional inner radius, $\eta/(1 - \eta)$

and $T = 0$ at the nondimensional outer radius, $1/(1 - \eta)$

Geometric parameters include η and L_z. Another useful parameter is the acceleration ratio, $A = \omega^2 r_i/g$, which is the ratio of the centrifugal to gravitational accelerations. It can be derived from the independent parameters ($A = \mathrm{Re}^2\beta^*[1/\eta - 1]/\mathrm{Gr}$).

The three-dimensional incompressible equations of motion, together with the energy equation, are discretized using a Chebyshev/Fourier spectral method. Writing the solution V_s and T_s as a truncated series expansion, using trial functions as basis functions,

$$V_s(r, \theta, z, t) = \sum_{K_\theta}\sum_{K_z}\sum_{l=0}^{L} \alpha_{jml}(t)u_l(r; K_\theta, K_z)e^{iK_\theta\theta}e^{iK_z z} \tag{6}$$

$$T_s(r, \theta, z, t) = \sum_{K_\theta}\sum_{K_z}\sum_{l=0}^{L} \gamma_{jml}(t)\tau_l(r; K_\theta, K_z)e^{iK_\theta\theta}e^{iK_z z}, \tag{7}$$

where K_z and K_θ are the wave numbers, and L is the number of modes in the r-direction. The expansion coefficients are given by $\alpha_{jml}(t)$ and $\gamma_{jml}(t)$; $u_l(r; K_\theta, K_z)$ and $\tau_l(r; K_\theta, K_z)$ are the r-trial functions for the velocity and the temperature fields. This method uses spectral expansions that inherently satisfy the boundary conditions and Eq. (1) (Moser et al., 1983). Fourier series expansions are used in the z-direction and θ-direction, and modified Chebyshev polynomials are used in the r-direction. The equations of motion and the energy equation are coupled, but the method yields banded matrices, which can be efficiently solved at each time step. The viscous term is treated implicitly (Crank-Nicholson), whereas an explicit (Adams-Bashforth) scheme is used for the convective terms. The nonlinear terms act as a forcing term to the implicit part of the calculation and are computed using the pseudospectral (collocation) technique on a grid dense enough to eliminate aliasing by the 3/2 rule (Canuto et al., 1988). The calculations were performed using 32 Fourier modes each in z and θ-directions and Chebyshev polynomials through thirty-first degree in the r-direction. A nondimensional time step (Δt) of 0.05 was used in all the computations, which yielded a maximum Courant number of 0.75, where the Courant number C is defined as

$$C = \pi\Delta t\left(\left|\frac{u_r}{\Delta r}\right| + \left|\frac{u_\theta}{r\Delta\theta}\right| + \left|\frac{u_z}{\Delta z}\right|\right). \tag{8}$$

To establish convergence, a series of higher resolution simulations (64^3) with a smaller time step were performed. The three components of velocity and the temperature were monitored at the same physical location as for the coarser resolution. The two gave an identical time trace which proved the adequacy of the coarser (32^3) simulation. Full details of the numerical scheme are given in Kedia (1997).

Results and Discussion

Comparison With Linear Stability Theory. The accuracy of the code was checked by comparing it with a linear stability analysis (Chen et al., 1990) for $\eta = 0.9$, $L_z = 2.007$, and $\mathrm{Pr} = 0.71$. Chen and Kuo (1990) investigated the interaction of a radial temperature gradient with both gravity and centrifugal potentials. Their linear stability analysis showed that the critical Reynolds number depended on the ratio of the centrifugal and gravitational potentials, the Prandtl number, and the Grashof number. The results are summarized in Table I. Case (1) and (2) refer to constant density simulations ($\beta^* = 0$) and case (3) and (4) refer to simulations where density is allowed to depend on temperature. To check for the critical Reynolds number, perturbations are introduced in the simulation. If the perturbations decay in time (with the flow returning to the steady base flow), then the flow is stable. Otherwise, the flow is unstable. The error margin for critical Reynolds number (case 1) indicates that the disturbances died down for $\mathrm{Re} = 132.2$ and grew into Taylor cells for $\mathrm{Re} = 132.6$. The error margin for wave speed is based on the time step. The critical Reynolds number ($\mathrm{Re}_{\mathrm{crit}}$) for the onset of Taylor cells, and the computed wave speed (c) agree very well with the linear stability theory.

Comparison With Experiments. The code is also compared with experimental results. One of the results from Kataoka et al. (1977) is replotted in Fig. 3 (symbols). In their experi-

Table 1 Comparison with linear stability theory

Case# η=0.9 L_z=2.007 Pr=0.71	Stability Analysis of Chen and Kuo (1990)	Simulation
(1) Gr=200 β^*=0 Re_{crit}	132.39	132.4±0.2
c	0.00142	0.00142±0.00001
(2) Gr=-200 β^*=0 Re_{crit}	132.39	132.4±0.2
c	−0.00142	−0.00142±0.00001
(3) Gr=200 β^*=0.133 Re_{crit}	134.91	134.8±0.2
c	0.00130	0.00131±0.00001
(4) Gr=-200 β^*=-0.138 Re_{crit}	129.96	130.0±0.2
c	−0.00153	−0.00152±0.00001

ment, they measured the local coefficient of mass transfer on the outer cylinder. The Schmidt and Grashof numbers are not given in the paper, but are estimated to be of order 10^5 and 100, respectively (an approximate estimation was made from the range of values of ν, $CuSO_4$ molarity and wt% of Glycerin). The figure also shows (solid lines) the numerical results for the local Nusselt numbers obtained for the numerical simulation for the same η and L_z, but for Pr = 0.71. The axial wavelengths imposed in the simulation results shown in Fig. 3 are taken from the experiments of Kataoka et al. For Gr ≈ 100, the effect of natural convection is small, and the flow state remains axisymmetric; hence, in the heat transfer calculations, the Grashof number is taken to be zero. The local heat transfer coefficient is based on the temperature difference between the bulk of the fluid and the outer cylinder. The comparison between the mass transfer experiments and the heat transfer calculations show reasonable agreement. Some of the differences may be due to the assumption of Sc and Gr numbers. The simulations show that the adjacent Taylor cells are of equal size for Gr = 0. However, the relative size of Taylor cells varies with the increase in the differential heating of the two concentric cylinders. The slight difference in the relative size of Taylor cells is also seen in Fig. 3 from the experimental values of Kataoka et al. (1977). This difference is probably due to small Grashof number (based on mass transfer) effects. Note that the exponent has a value of 0.375, which was chosen to bring the results closer together. If the exponent is 0.333 (as used in the experiments), the values from the simulations were found to be smaller than the experimental values. The simulation can not be run for a very high Pr because the energy equation becomes stiff.

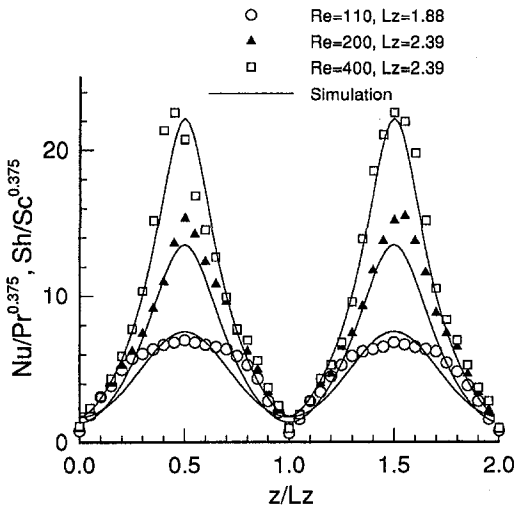

Fig. 3 Variation of heat (present simulation) and mass transfer (Kataoka et al., 1977) on the outer cylinder for η = 0.617

The second set of experiments used to validate the code is from the heat transfer experiments of Ball et al. (1989). In this experiment, the walls were maintained at uniform temperatures. The inner cylinder was heated by a cartridge heater and the outer cylinder was cooled by passing an ethylene glycol-water mixture through a flexible plastic hose coiled around it. The mean equivalent conductivity, K_{eq}, is defined as the ratio of the average convective heat transfer coefficient ($h_{\bar{r},\bar{r}\bar{l}}$) to the heat transfer coefficient for pure conduction. The average convective heat transfer coefficient is based on the temperature difference between the inner and the outer cylinders. In Fig. 4, K_{eq} is plotted versus Re^2 for η = 0.565, L_z = 1.991, Gr = 1900, and

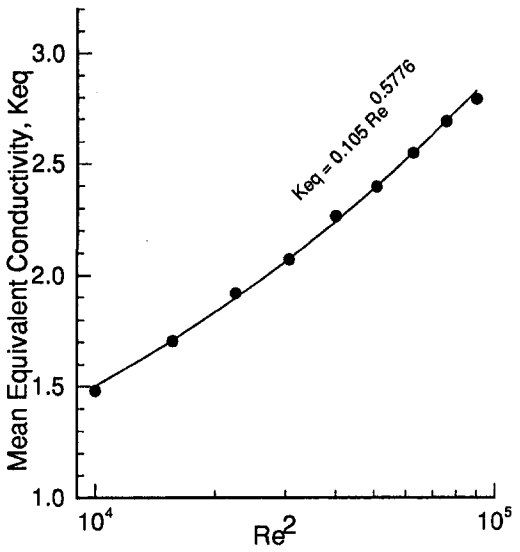

Fig. 4 Variation of heat transfer rate with Re^2 for η = 0.565, L_z = 1.991, Gr = 1900, and β^* = 0.053

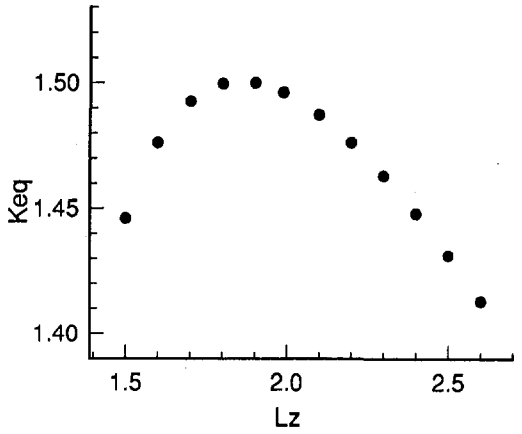

Fig. 5 Variation of mean equivalent conductivity with L_z for $\eta = 0.5$, Re = 100, Gr = 1700, and $\beta^* = 0.0128$

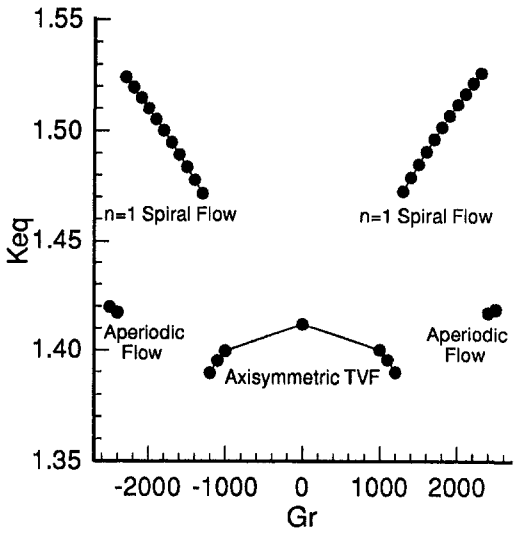

Fig. 6 Map showing different stable states present in the flow for $\eta = 0.5$, $L_z = 1.988$, Re = 100, Pr = 0.7, and $A = 0.1285$

$\beta^* = 0.053$. The normalized wavelength of approximately 1.991 is the critical wavelength corresponding to the critical Reynolds number for a radius ratio of 0.565, as given by the linear stability analysis. It is assumed that the axial wavelength remains fairly constant in the range of Reynolds number studied here, and this critical wavelength is chosen as the axial period of the flow. The result shows a power law behavior, which has a lower coefficient and a higher exponent than the result presented by Ball et al. This discrepancy arises because of the variation of axial wavelength with axial distance resulting from the thermal conditions at the ends of the experimental apparatus. The simplifying assumption of no axial temperature gradient could be another source of discrepancy between the experiment and the numerics. The simulations also show that for Gr = 1900, as the Reynolds number is varied, the relative size of the adjacent counter-rotating Taylor cells change. This agrees qualitatively with the flow visualization studies of Ball et al. (1989).

Figure 5 shows that the heat transfer results are very sensitive to the imposed axial wavelength. Plotted is the variation of the calculated K_{eq} with L_z. The same average heat transfer coefficient can be achieved by two different wavelengths, one below the isothermal critical value ($L_z = 1.988$), and the other above it. A similar result was shown by Meyer (1967) in numerical calculations of torque. The author concluded that the experimentally observed torque is somewhat lower than the numerical torque; it is speculated that the same is true for the heat transfer as well.

Flow States for Varying Gr. Apart from calculating the local and the average heat transfer coefficients, it is important to know how the flow evolves from one state to another as Gr is varied. Figure 6 presents a map of different stable states in the flow for a fixed Reynolds number and different Gr. The circular Couette flow was the base flow, and the steady-state conduction field was the base temperature field. A random disturbance of magnitude one percent of the velocity of the inner cylinder was introduced to the laminar state (circular Couette flow) and allowed to grow into Taylor vortices. Reynolds number was slowly increased (in steps of 5) to achieve the desired Reynolds number. The result with the lower Reynolds number was used as initial condition for the next higher Reynolds number. Once the desired Reynolds number was reached, another random disturbance of magnitude one percent of the temperature difference between the two cylinders was imposed on the temperature initial condition in order to trigger transitions. For low $|\mathrm{Gr}|$, axisymmetric Taylor Vortex Flow (TVF) is the stable state. Outside this range, $n = 1$ stripes are formed. Figure 7 shows a schematic of spiral flows for $n = 1$ and $n = 2$. These spirals move an axial distance of nL_z for one rotation around the inner cylinder. The flow becomes aperiodic for higher Gr.

Similar stripes were also seen in the flow visualization experiments of Snyder and Karlsson (1964) and Ball et al. (1989). Stripes of larger inclination angle, up to $n = 6$, were observed by Snyder and co-workers for higher heating in a small annulus ($\eta = 0.957$). Higher spiral modes are formed for narrower gaps (Ali et al., 1990).

Increasing Gr decreases the heat transfer coefficient (K_{eq}) within the axisymmetric TVF regime. The increase in the axial velocity as a result of increasing Gr not only delays the onset of Taylor vortices but also causes a damping effect on the heat transfer. A similar effect of decreasing of the average Sherwood number by an added axial flow was also observed by Kataoka et al. The mean equivalent conductivity, K_{eq}, increases significantly with the formation of $n = 1$ spiral flow, and it continues to increase with Gr until the flow becomes aperiodic with a subsequent decrease in K_{eq} near $\mathrm{Gr} = \pm 2400$. The map is nearly symmetric about the Gr = 0 axis.

A similar map is shown for $\eta = 0.7$ in Fig. 8. Again, axisymmetric Taylor vortex flow is seen for low $|\mathrm{Gr}|$, but the $n = 1$ spiral flow is formed for a broader negative range of Gr and for a narrower positive Gr. The $n = 2$ spiral flow is formed for higher negative Gr, and is not formed for positive Gr. The flow becomes aperiodic outside this range. The heat transfer has similar effects as for $\eta = 0.5$ (Fig. 6) in the TVF regime. However, instead of K_{eq} increasing monotonically in the $n = 1$ spiral flow regime, it attains a maximum for both positive and

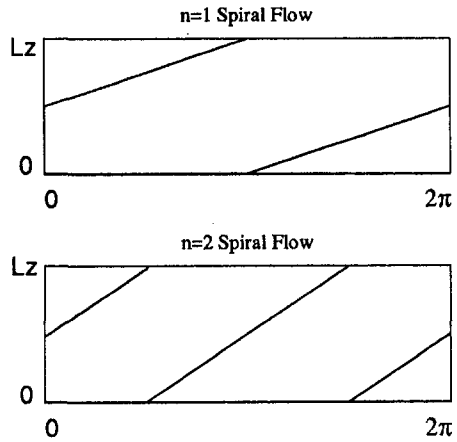

Fig. 7 Schematic of spiral flows

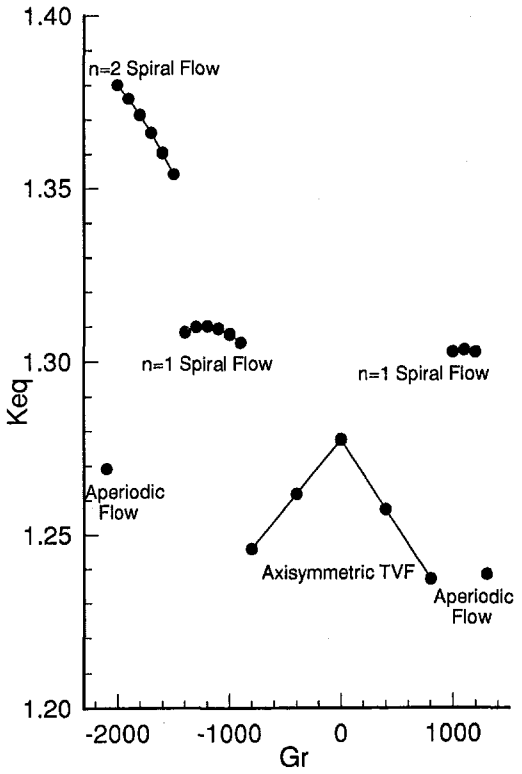

Fig. 8 Map showing different stable states present in the flow for η = 0.7, L_z = 2.001, Re = 100, Pr = 0.7, and A = 0.67

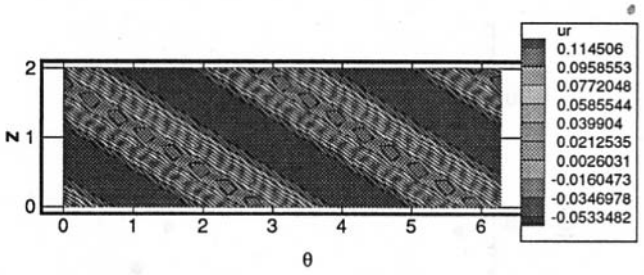

Fig. 10 Radial velocity contours at the mid radial section of the two cylinders for η = 0.7, L_z = 2.001, Re = 100, Pr = 0.7, and Gr = −1700

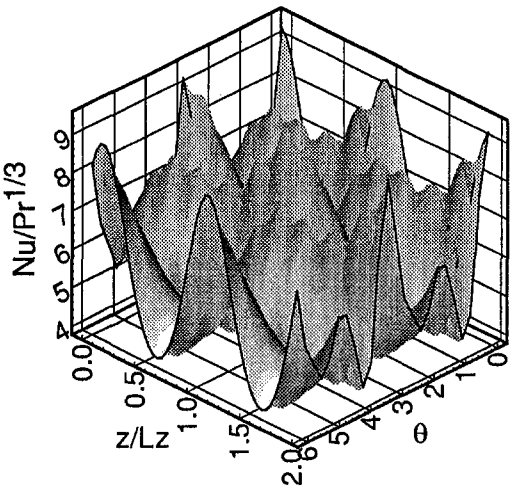

Fig. 11 Variation of heat transfer on the outer cylinder for η = 0.7, L_z = 2.001, Re = 100, Pr = 0.7, and Gr = −2100

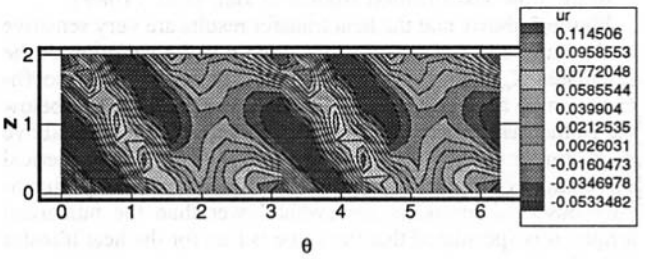

Fig. 12 Radial velocity contours at the mid-radial section of the two cylinders for η = 0.7, L_z = 2.001, Re = 100, Pr = 0.7, and Gr = −2100

negative Grashof numbers. A significant increase in K_{eq} is observed with the formation of $n = 2$ spiral flow, and K_{eq} increases with further increase in Gr in this regime of flow. This map is not symmetrical about the Gr = 0 axis. The asymmetry grows with the increase in the value of A. The onset of spirals correlate with both $|\mathrm{Gr}/\mathrm{Re}^2|$ and A. For higher A, the spirals start at lower $|\mathrm{Gr}/\mathrm{Re}^2|$.

The choice of L_z to determine the flow states (Figs. 6 and 8) was based on previously published linear stability analyses (DiPrima and Swinney, 1981). At the outset, it was unclear whether the flow states (n = 1 spiral, n = 2 spiral, or aperiodic) would be sensitive to the imposed axial wavelength, L_z. However, numerical experiments showed that the flow states were invariant as L_z was varied by as much as 50 percent, despite

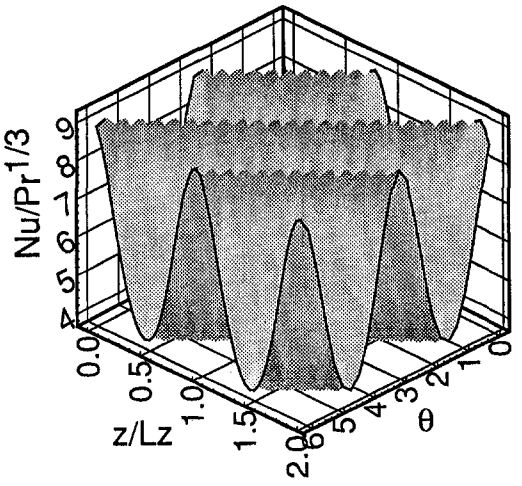

Fig. 9 Variation of heat transfer on the outer cylinder for η = 0.7, L_z = 2.001, Re = 100, Pr = 0.7, and Gr = −1700

the fact that K_{eq} varied by as much as 6 percent (see Fig. 5). The results presented here are all based on the critical wavelength for L_z.

The variation of heat transfer as a function of z and θ is shown in Fig. 9 (Gr = −1700, n = 2 spiral flow) and Fig. 11 (Gr = −2100, aperiodic flow). For Gr = −1700 the variation is sinusoidal in both z and θ. For Gr = −2100, the Nusselt number varies with z and θ in a more complicated way. The radial velocity contours corresponding to Figs. 9 and 11 are plotted in Figs. 10 and 12, respectively. For Gr = −1700 the two stripes are clearly evident, while for Gr = −2100 the flow is wavy and there is no single dominant frequency.

Finally, the frequencies and the amplitudes of local fluctuations of heat transfer coefficient (h) present in the flow are shown in Fig. 13. The frequency is normalized by the rotation frequency of the inner cylinder and the amplitude is normalized by the spatially and temporally averaged heat transfer coefficient. The figure shows that $f/f_c \simeq 0.35$ for n = 1 and the amplitude of local fluctuations of heat transfer is about 95 per-

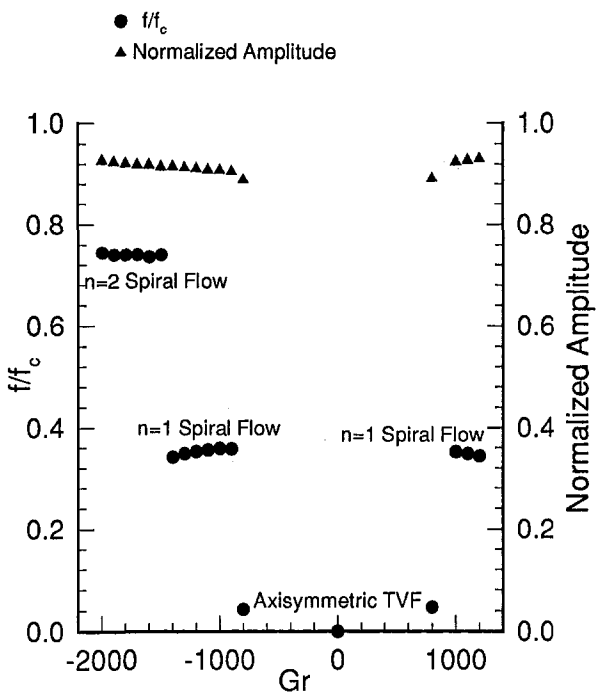

Fig. 13 Variation of frequency and amplitude with Grashof number for $\eta = 0.7$, $L_z = 2.001$, Re = 100, Pr = 0.7, and $A = 0.67$

cent of $h_{\bar{\theta},z\bar{T}}$. The above information of the frequency and the amplitude of local fluctuations of heat transfer is required as boundary conditions for thermal stress analysis of the shaft and cover of BWR pumps. With the assumption that the frequency fluctuation is about 10 to 100 percent of rotating speeds, the predictive models (Gopalakrishnan et al., 1992) revealed crack depths which were comparable to field observations for the shaft and cover.

Conclusion

Heat transfer in an incompressible, three-dimensional Taylor-Couette flow with a rotating inner cylinder has been numerically investigated to study the interaction of gravity and centrifugal potentials with the radial temperature gradient. Calculation of critical Reynolds number and wave speed obtained from these simulations agree well with linear stability theory. For a certain range of Gr, the spatial variation of heat transfer on the inner and the outer cylinder is sinusoidal, and the magnitude of the Nusselt number increases with Reynolds number. The space and time averaged heat transfer from the inner to the outer cylinder is reported and is found to be sensitive to the imposed axial wavelength. The average heat transfer decreases with increased heating in the axisymmetric TVF regime. The equivalent conductivity increases significantly with the formation of higher order spirals. When the centrifugal acceleration becomes of the same order of magnitude as the acceleration due to gravity ($A \simeq 1$), higher mode spirals are formed when the outer cylinder is heated. Hence, the thermal environment present in the flow may be the cause for thermal stress fatigue in primary-loop recirculation pumps in BWR power plants. The results also show that when the flow is within the spiral flow regime (with either $n = 1$ or $n = 2$), the heat flux to the surface of the shaft is periodic with a period that is at frequencies of approximately 35 percent ($n = 1$) and 74 percent ($n = 2$) of the rotational frequency of the shaft. The local variation of the heat flux to the surface may be as much as 95 percent of the average.

Acknowledgments

This research was performed in part using the CSCC parallel computer system operated by Caltech on behalf of the Concurrent Supercomputing Consortium. Access to this facility was provided by Caltech. The authors would also like to thank Dr. A. Leonard at Caltech and Dr. R. D. Moser at University of Illinois at Urbana-Champagne for valuable discussions.

References

Ali, M., and Weidman, P. D., 1990, "On the Stability of Circular Couette Flow With Radial Heating," *J. Fluid Mech.*, Vol. 220, pp. 53–84.

Ball, K. S., and Farouk, B., 1987, "On the Development of Taylor Vortices in a Vertical Annulus With a Heated Rotating Inner Cylinder," *Int. J. Num. Meth. Fluids*, Vol. 7, pp. 857–867.

Ball, K. S., and Farouk, B., 1988, "Bifurcation Phenomena in Taylor-Couette Flow With Buoyancy Effects," *J. Fluid Mech.*, Vol. 197, pp. 479–501.

Ball, K. S., Farouk, B., and Dixit, V. C., 1989, "An Experimental Study of Heat Transfer in a Vertical Annulus With a Rotating Inner Cylinder," *Int. J. Heat Mass Transfer*, Vol. 32, No. 8, pp. 1517–1527.

Brandstater, A., and Swinney, H. L., 1987, "Strange Attractors in Weakly Turbulent Couette-Taylor Flow," *Phys. Rev. A*, Vol. 35, No. 5, pp. 2207–2220.

Canuto, C., Hussaini, M. Y., Quarteroni, A., and Zang, T. A., 1988, *Spectral Methods in Fluid Dynamics*, 3rd ed., Springer-Verlag, Berlin.

Chen, J., and Kuo, J., 1990, "The Linear Stability of Steady Circular Couette Flow With a Small Radial Temperature Gradient," *Phys. Fluids A*, Vol. 2, No. 9, pp. 1585–1591.

Coles, D., 1965, "Transition in Circular Couette Flow," *J. Fluid Mech.*, Vol. 21, pp. 385–425.

DiPrima, R. C., and Swinney, H. L., 1981, "Instabilities and Transition in Flow Between Concentric Rotating Cylinders," *Hydrodynamic Instabilities and the Transition to Turbulence*, H. L. Swinney and J. P. Gollub, eds., Springer-Verlag, Berlin, pp. 139–180.

Gopalakrishnan, S., Vaghasia, G. K., and Reimers, C. R., 1992, "Crack Propagation in Main Coolant Pumps," presented at Fifth Int. Workshop on Main Coolant Pumps, April 21–24, Orlando, FL.

Gray, D. D., and Giorgini, A., 1976, "The Validity of the Boussinesq Approximation for Liquids and Gases," *Int. J. Heat Mass Transfer*, Vol. 19, pp. 545–551.

Greenspan, H. P., 1968, *The Theory of Rotating Fluids*, Cambridge University Press, New York.

Kataoka, K., Doi, H., and Komai, T., 1977, "Heat/Mass Transfer in Taylor Vortex Flow With Constant Axial Flow Rates," *Int. J. Heat Mass Transfer*, Vol. 20, pp. 57–63.

Kato, H., Kanno, H., Hosokawa, M., Watanabe, A., Shitara, C., Ashizawa, K., Miyano, H., Narabayashi, T., Iikura, T., Hayashi, M., Endoh, A., and Takehara, H., 1992, "The Development of Advanced Nuclear Primary Loop Recirculating Pump (PLR Pump) for BWR Plant Considering Thermal Fatigue Problem," *Industrial and Environmental Applications of Fluid Mechanics*, Proc. of the ASME Winter Annual Meeting, FED-Vol 145, Sherif et al., eds., pp. 157–162.

Kedia, R., 1997, "An Investigation of Velocity and Temperature Fields in Taylor-Couette Flows," Ph.D. thesis, California Institute of Technology, Pasadena, CA.

Kreith, F., 1968, "Convection Heat Transfer in Rotating Systems," *Advances in Heat Transfer 5*, Academic Press, New York, pp. 129–251.

Lee, Y. N., and Minkowycz, W. J., 1989, "Heat Transfer Characteristics of the Annulus of Two-Coaxial Cylinders With One Cylinder Rotating," *Int. J. Heat Mass Transfer*, Vol. 32, pp. 711–722.

Meyer, K. A., 1967, "Time-Dependent Numerical Study of Taylor Vortex Flow," *Phys. Fluids*, Vol. 10, No. 9, pp. 1874–1879.

Moser, R. D., Moin, P., and Leonard, A., 1983, "A Spectral Numerical Method for the Navier-Stokes Equations With Applications to Taylor-Couette Flow," *J. Comput. Phys.*, Vol. 52, pp. 524–544.

Roesner, K. G., 1978, "Hydrodynamic Stability of Cylindrical Couette-Flow," *Arch. of Mech.*, Vol. 30, pp. 619–627.

Shih, A. C., and Hunt, M. L., 1992, "High-Taylor-Number Couette Flows With a Superposed Isothermal or Heated Axial Flow," *Proc. of the ASME National Heat Transfer Conf., General Papers in Heat Transfer*, HTD-Vol. 204, M. Jensen et al., eds. San Diego, CA.

Singer, H. P., 1984, "Techniques of Low Pressure Chemical Vapor Deposition," Semiconductor International, Denver, CO, May 1984, pp. 72–77.

Taylor, G. I., 1923, "Stability of a Viscous Liquid Contained Between Two Rotating Cylinders," *Phils. Trans. R. Soc. London*, Ser. A, Vol. 223, pp. 289–343.

Heat Transfer From a Circular Cylinder at Low Reynolds Numbers

V. N. Kurdyumov
Universidad Politecnica de Madrid,
E.T.S.I. Aeronáuticos,
Plaza Cardenal Cisneros 3,
28040 Madrid, Spain

E. Fernández
Instituto Nacional de Técnica Aeroespacial,
División de Propulsión,
Torrejón de Ardoz, Spain

A correlation formula, $Nu = W_0(Re)Pr^{1/3} + W_1(Re)$, that is valid in a wide range of Reynolds and Prandtl numbers has been developed based on the asymptotic expansion for $Pr \to \infty$ for the forced heat convection from a circular cylinder. For large Prandtl numbers, the boundary layer theory for the energy equation is applied and compared with the numerical solutions of the full Navier Stokes equations for the flow field and energy equation. It is shown that the two-terms asymptotic approximation can be used to calculate the Nusselt number even for Prandtl numbers of order unity to a high degree of accuracy. The formulas for coefficients W_0 and W_1 are provided.

1 Introduction

Pure forced convection about a single circular cylinder of uniform temperature suspended in an infinite fluid medium has been studied both experimentally and analytically for several decades and, more recently, numerical techniques have been applied. Applying Oseen's approximation to the energy equation, Cole and Roshko (1954) were the first who computed the heat transfer from a circular cylinder. The solution for the temperature field was obtained in terms of an infinite series of modified Bessel and trigonometric functions. Based on this solution, they calculated the total heat transfer. For the case of small Peclet numbers (the product of Reynolds and Prandtl numbers) they obtained

$$\mathrm{Nu} = \ln^{-1}(4/\gamma\ \mathrm{Re\ Pr}). \tag{1}$$

The same technique was employed by Illingworth (1963) who obtained the next term in this expansion.

Also employing Oseen's approximation, Wood (1968) applied it to the momentum equations and obtained the next order terms in the velocity field. Taking into account these higher-order terms in the velocity field, he obtained a two-terms expansion for the Nusselt number using modified Bessel functions.

Hieber and Gebhart (1968) treated the circular cylinder via the method of matched asymptotic expansion and considered two limiting cases. In the first one, when Pr is fixed and $\mathrm{Re} \to 0$, they obtained the expression

$$\mathrm{Nu} = [1 - a_3(\mathrm{Pr}) \ln^{-2}(4/\gamma\ \mathrm{Re\ Pr})] \ln^{-1}(4/\gamma\ \mathrm{Re\ Pr}). \tag{2}$$

In the second case they considered the limit $\mathrm{Pr} = \mathrm{Re}^{-\alpha}$, $(0 < \alpha < 1)$, $\mathrm{Re} \to 0$. For different Reynolds numbers and for a large fixed Prandtl number, the parameter α can be determined as $\alpha = \ln(\mathrm{Pr})/\ln(1/\mathrm{Re})$. The two-terms expression for the Nusselt number was

$$\mathrm{Nu} = \{1 - b_3(\alpha) \ln^{-2}[4/\gamma(1-\alpha)\ \mathrm{Re\ Pr}]\} \times \ln^{-1}[4/\gamma(1-\alpha)\ \mathrm{Re\ Pr}], \tag{3}$$

where $b_3(\alpha) = (1 - 2\alpha)\ln 2 + (1/2 - \ln\gamma)(1-\alpha) + \ln(1-\alpha) + (1 + \ln(\gamma/2))$.

Employing the method of joining the circumferential average temperature in the concentric layer around the cylinder governed mainly by conduction to that in the wake governed mainly by convection, Nakai and Okazaki (1975) obtained the following formula:

$$\mathrm{Nu} = (1 - \ln(\mathrm{Re\ Pr}))^{-1}, \tag{4}$$

which, taking into account that $\ln 4/\gamma = 0.809$, is very close to Eq. (1). Additional references and correlation formulae can be found in Morgan (1975).

For different values of Prandtl number, Dennis et al. (1968) performed calculations of full Navier-Stokes and energy equations, obtaining accurate results in good agreement with experiments conducted by Collis and Williams (1959), ascertaining that discrepancies with the previous theoretical works was due to the improper flow field assumptions.

In the present work, we treat the circular cylinder at Reynolds numbers ranging from much smaller than one to values close to the critical Reynolds number, when the flow is attached to the cylinder and the recirculation region does not appear yet. First of all, the case of large Prandtl numbers is under consideration, and the boundary layer approximation for the energy equation is adopted. Then, the asymptotic formula so obtained is applied to the case when the Prandtl numbers are of order unity and compared with the results of the numerical calculation of the complete equations. It is found that the two-terms asymptotic formula is applicable, even for Prandtl numbers as low as order unity, in a wide range of Reynolds numbers (before the appearance of the recirculation region) with high accuracy.

2 Problem Statement

We consider the case of a steady flow in the x-axis direction around a horizontal circular wire of radius a and temperature T_w. The undisturbed flow is taken to have uniform velocity U_∞ and temperature T_∞ and the fluid is considered to be incompressible, viscous dissipation is neglected, and transport properties are taken as constant.

Taking the scales for coordinates and velocity components as ν/U_∞ and U_∞, respectively, and defining $\theta = (T - T_\infty)/(T_w - T_\infty)$ as the nondimensional temperature rise, the governing equations take, in cylindrical coordinates (r, φ), the nondimensional form

$$v_r \frac{\partial\omega}{\partial r} + \frac{v_\varphi}{r}\frac{\partial\omega}{\partial\varphi} = \Delta\omega, \quad \omega = -\Delta\psi \tag{5}$$

$$v_r \frac{\partial\theta}{\partial r} + \frac{v_\varphi}{r}\frac{\partial\theta}{\partial\varphi} = \frac{1}{\mathrm{Pr}}\Delta\theta, \tag{6}$$

Contributed by the Heat Transfer Division for publication in the JOURNAL OF HEAT TRANSFER. Manuscript received by the Heat Transfer Division March 10, 1997; revision received November 3, 1997; Keywords: Conjugate Heat Transfer; Flow Separation; Forced Convection. Associate Technical Editor: P. S. Ayyaswamy.

where $v_r = r^{-1}\psi_\varphi$ and $v_\varphi = -\varphi_r$. The nondimensional radius of the wire aU_∞/ν, is equal to the Reynolds number, Re, of the flow. For the boundary conditions, we shall impose that $v_r = -\cos\varphi$, $v_\varphi = \sin\varphi$, $\theta = 0$ at $r \to \infty$ and $v_r = v_\varphi = 0$, $\theta = 1$ at $r = \mathrm{Re}$.

The Nusselt number, defined as $\mathrm{Nu} = q/2\pi\kappa(T_w - T_\infty)$, can be written in terms of the dimensionless variables defined above as

$$\mathrm{Nu} = -\frac{1}{\pi}\int_0^\pi \left(r\frac{\partial\theta}{\partial r}\right)\bigg|_{r=\mathrm{Re}} d\varphi. \tag{7}$$

3 The Case of Small Reynolds Number, Re $\ll$ 1

The small Reynolds number flow in the vicinity of the cylinder can be described by the asymptotic Stokes solution (see Van-Dyke 1975), which for the stream function takes the form

$$\varphi = -r\left\{1 - \frac{\ln r}{\ln \mathrm{Re}} + \frac{1}{2\ln \mathrm{Re}}\left(1 - \left(\frac{\mathrm{Re}}{r}\right)^2\right)\right\}\sin\varphi. \tag{8}$$

This solution is valid for $\mathrm{Re} \le r \le O(1)$, $\mathrm{Re} \ll 1$.

Employing a transformation $r = \mathrm{Re}\,\hat{r}$ with $\hat{r} = O(1)$ for the inner region, it is obtained that

$$\hat{v}_r\frac{\partial\theta}{\partial\hat{r}} + \hat{v}_\varphi\hat{r}'\frac{\partial\theta}{\partial\varphi} = \frac{1}{\sigma}\left(\frac{\partial^2\theta}{\partial\hat{r}^2} + \frac{1}{\hat{r}}\frac{\partial\theta}{\partial\hat{r}} + \frac{1}{\hat{r}^2}\frac{\partial^2\theta}{\partial\varphi^2}\right), \tag{9}$$

where $\sigma = \mathrm{Pr\,Re}/\ln(1/\mathrm{Re})$ is the effective Peclet number, and

$$\hat{v}_r = \{-\ln\hat{r} + (1 - \hat{r}^{-2})/2\}\cos\varphi,$$
$$\hat{v}_\varphi = \{1 + \ln\hat{r} - (1 + \hat{r}^{-2})/2\}\sin\varphi. \tag{10}$$

3.1 The Boundary Layer Approximation, $\sigma \gg 1$. For large values of σ, the boundary layer approximation for (9)–(10) was adopted. Introducing the variable $z = \sigma^{1/3}(\hat{r} - 1)$, the temperature distribution has been found as an expansion in the form $\theta = \theta_0 + \sigma^{-1/3}\theta_1 +$, where for $0 < \varphi < \pi$ and $0 < z < \infty$, θ_0 and θ_1 satisfy, the equations

$$2z\sin\varphi\frac{\partial\theta_0}{\partial\varphi} = \frac{\partial^2\theta_0}{\partial z^2} + z^2\cos\varphi\frac{\partial\theta_0}{\partial z} \tag{11}$$

$$2z\sin\varphi\frac{\partial\theta_1}{\partial\varphi} = \frac{\partial^2\theta_1}{\partial z^2} + z^2\cos\varphi\frac{\partial\theta_1}{\partial z} + \left(4z^2\sin\varphi\frac{\partial\theta_0}{\partial\varphi} - \frac{5}{3}z^3\cos\varphi\frac{\partial\theta_0}{\partial z} + \frac{\partial\theta_0}{\partial z}\right). \tag{12}$$

The Nusselt number is given by

$$\mathrm{Nu} = w_0\sigma^{1/3} + w_1 + \ldots, \tag{13}$$

where $w_0 = -\pi^{-1}\int_0^\pi (\partial\theta_0/\partial z)|_{z=0}d\varphi$ and $w_1 = -\pi^{-1}\int_0^\pi (\partial\theta_1/\partial z)|_{z=0}d\varphi$.

The parabolic Eqs. (11)–(12) were solved numerically, for $\delta_1 \le \varphi \le \pi - \delta_2$ with $\delta_1 \ll 1$, $\delta_2 \ll 1$ and $0 \le z \le z_{\max}$, using a finite difference method with uniform grid in both φ and z, marching in φ with initial conditions obtained by solving (11)–(12) for $\varphi = 0$. The values of δ_1 and δ_2 were varied between 10^{-2} and 10^{-4} to insure solution independence on these parameters. The value of $z_{\max}$ was varied between 5 and 10 and no variation in the solution was observed. To test the grid independence, calculations were carried out using 1000 × 1000, 5000 × 5000, and 10,000 × 10,000 grids, and negligible differences were found. Using the finest grid, the values of w_0 and w_1 were found to be 0.579 ± 0.001 and 0.0917 ± 0.0001, respectively. The formula (13) for the Nusselt number is shown in Fig. 1 by a solid line. For the case of water, Pr = 6.82; Eq. (13) is plotted in Fig. 4 by a solid line 2. One can see that it has a more satisfactory overall behavior when the Reynolds number is less than $10^{-1.5}$, lying closer to the solid line 3, which represents the results of the calculation of the full equations (5)–(6). For Re $\ll$ 1, the asymptotic limit of all results converge in a unique curve, except for (13), but for $10^{-5} < \mathrm{Re} < 10^{-1.5}$ the agreement is good. It fails to give an accurate solution for Re = $O(1)$ when the Stokes approximation (8) for the flow field is not valid.

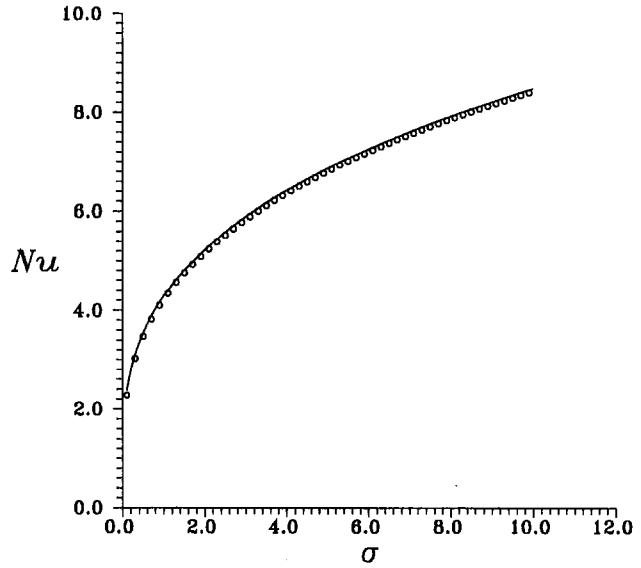

Fig. 1 Nusselt number as a function of σ, Stokes flow field (8); *circles*—calculation of full heat transport equation (6); *solid line*—boundary layer theory (13)

3.2 The Case $\sigma = O(1)$. When Re Pr $\ge$ 1 or $\sigma \ge O(1)$, the problem in (9)–(10) was solved numerically using a second-order finite-difference method. To obtain the temperature distribution, the unsteady form of (9) was used, after writing the equation in terms of $\eta = \ln\hat{r}$, in the domain $0 \le \varphi \le \pi$ and $1 \le \hat{r} \le \hat{r}_{\max}$. We considered that the stationary distribution had been reached when $\max_{i,j}|\theta_{i,j} - \hat{\theta}_{i,j}| < 10^{-9}$, where θ and $\hat{\theta}$ are the values of the temperature at the current and previous time levels with $\Delta t = 0.01$. The typical grid size was 101 × 101, $\hat{r}_{\max} = 10^2$. To test the grid independence, calculations were carried out using 131 × 131 and 151 × 151 grid. The domain size, $\hat{r}_{\max}$, was also varied from 10^2 to 10^3 to insure that its influence on the solution is negligible.

Nomenclature

a = radius of the cylinder
Nu = Nusselt number based on a
Pr = Prandtl number
q = total heat transfer per unit length
r = radial coordinate
Re = Reynolds number based on a
T = temperature
U = dimensional velocity
v = velocity component
z = boundary layer variable
γ = Euler's constant, $\ln\gamma = 0.577\ldots$
κ = thermal conductivity
ν = kinematic viscosity
θ = nondimensional temperature
ψ = stream function
φ = azimuthal coordinate
σ = Re Pr/ln (1/Re)
ω = vorticity
$\zeta = \log_{10}(\mathrm{Re})$

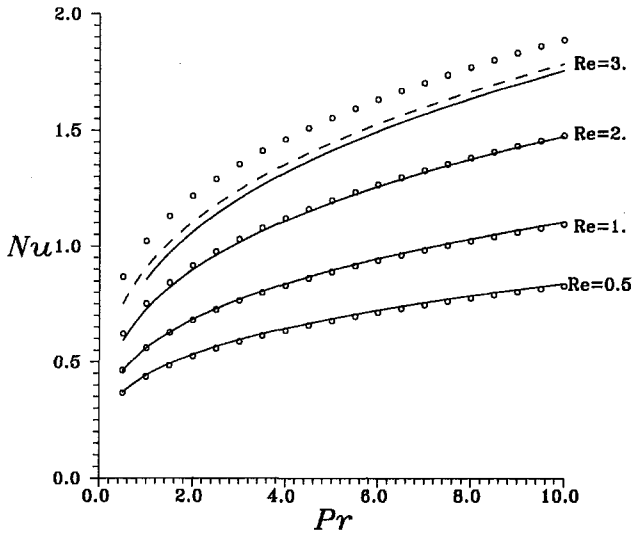

Fig. 2 Nusselt number for Reynolds number of order unity: *solid line*—full Navier-Stokes and energy equations; *circles*—boundary layer theory for the energy equation; *dashed line*—correlation formula (16), (18), and (19) for Re = 3

The calculated Nusselt numbers as a function of σ are shown in Fig. 1 by circles. The result, which could hardly be expected beforehand, is that the two terms asymptotic formula (13), plotted as a solid line, achieves 1 percent accuracy, even for σ as low as 0.5.

4 The Case of Moderately Small Reynolds Numbers

In this section, we shall consider the case when the Reynolds number is of order unity and the Stokes approximation (8) fails to describe the flow field around the cylinder. It is therefore necessary to solve the full Navier-Stokes equations (5)–(6). To obtain the stationary distributions of all the variables the pseudounsteady form of the governing equations and a second order finite difference method were used. Firstly, the fluid dynamic part was solved and then the calculated flow field was used to obtain the temperature distributions around the cylinder. The domain and the grid were chosen like in the previous section, where only the energy equation was solved, and the same tests were conducted. In addition, comparison with Dennis et al. (1968) revealed a negligible difference for air. The critical Reynolds number for the appearance of the recirculating region was found to be close to 3.14 ± 0.01. The calculated Nusselt numbers, as functions of Pr, are plotted in Fig. 2 with solid lines.

Alternatively, the boundary layer theory was applied to the energy equation (6) when $\mathrm{Pr} \gg 1$. Introducing the boundary variable $z = \mathrm{Pr}^{1/3}(r - \mathrm{Re})$, the temperature in the boundary layer can be found as $\theta = \theta_0 + \mathrm{Pr}^{-1/3}\theta_1$, where θ_0 and θ_1 depend on the distribution of the vorticity at the surface of the cylinder. Here, the designations $\omega_0(\varphi) = \omega|_{r=\mathrm{Re}}$, $\omega_1(\varphi) = (\partial\omega/\partial r)|_{r=\mathrm{Re}}$ are used.

Using the Taylor expansion for v_r and v_φ at $\mathrm{Pr}^{-1} \ll 1$, the equations for θ_0 and θ_1 are

$$\omega_0(\varphi)\frac{z}{\mathrm{Re}}\frac{\partial\theta_0}{\partial\varphi} = \frac{\partial^2\theta_0}{\partial z^2} + \frac{1}{2}\omega_0'(\varphi)\frac{z^2}{\mathrm{Re}}\frac{\partial\theta_0}{\partial z} \tag{14}$$

$$\omega_0(\varphi)\frac{z}{\mathrm{Re}}\frac{\partial\theta_1}{\partial\varphi} = \frac{\partial^2\theta_1}{\partial z^2} + \frac{1}{2}\omega_0'(\varphi)\frac{z^2}{\mathrm{Re}}\frac{\partial\theta_1}{\partial z} + \frac{1}{\mathrm{Re}}\left(1 - \frac{2}{3}\omega_0'(\varphi)\frac{z^3}{\mathrm{Re}} + \frac{1}{6}\omega_1'(\varphi)z^3\right)\frac{\partial\theta_0}{\partial z} + \frac{z^2}{\mathrm{Re}}\left(\frac{3}{2}\frac{\omega_0(\varphi)}{\mathrm{Re}} - \frac{1}{2}\omega_1(\varphi)\right)\frac{\partial\theta_0}{\partial\varphi} \tag{15}$$

Table 1 The values of W_0 and W_1 for different Reynolds numbers

Re	W_0	W_1	Re	W_0	W_1
2.5	0.6929	0.1297	0.5	0.3417	$0.9752 \cdot 10^{-1}$
2.0	0.6302	0.1266	0.3	0.2738	$0.9473 \cdot 10^{-1}$
1.5	0.5556	0.1169	0.1	0.1723	$0.9246 \cdot 10^{-1}$
1.0	0.4640	0.1063	0.01	$0.6878 \cdot 10^{-1}$	$0.9184 \cdot 10^{-1}$

and the corresponding two terms formula for the Nusselt number takes the form

$$\mathrm{Nu} = W_0(\mathrm{Re})\mathrm{Pr}^{1/3} + W_1(\mathrm{Re}). \tag{16}$$

Here, $W_0(\mathrm{Re}) = -\pi^{-1}\int_0^\pi (\partial\theta_0/\partial z)|_{z=0}d\varphi$ and $W_1(\mathrm{Re}) = -\pi^{-1}\int_0^\pi (\partial\theta_1/\partial z)|_{z=0}d\varphi$ are functions of the Reynolds number only. The equations (14)–(15) have been solved numerically for $0 < \varphi < \pi$, and the values of W_0 and W_1 for the different Reynolds numbers are shown in Table 1.

The functions $W_0(\mathrm{Re})$ and $W_1(\mathrm{Re})$ are plotted in Fig. 3 with solid lines. A comparison of (16) and (13) gives

$$W_0(\mathrm{Re}) \to \left(\frac{\mathrm{Re}}{\ln(1/\mathrm{Re})}\right)^{1/3} w_0,$$

$$W_1(\mathrm{Re}) \to w_1 \quad \mathrm{Re} \to 0, \tag{17}$$

shown in Fig. 3 with dashed lines.

To get a description applicable for small and order unity Reynolds numbers, one can combine the asymptotic formulas with an ad hoc correlation by merging at $\mathrm{Re} = 10^{-2}$:

$$W_0(\mathrm{Re}) = \begin{cases} 0.46271\exp(1.01633\zeta + 0.05121\zeta^2) \\ \qquad 10^{-2} \le \mathrm{Re} \le 3.14, \\ 0.597(\mathrm{Re}/\ln(1/\mathrm{Re}))^{1/3} \quad \mathrm{Re} < 10^{-2} \end{cases} \tag{18}$$

$$W_1(\mathrm{Re}) = \begin{cases} 0.10666\exp(0.41285\zeta + 0.43847\zeta^2 \\ \quad + 0.19150\zeta^3 + 0.01802\zeta^4 - 0.005225\zeta^5) \\ \qquad 10^{-2} \le \mathrm{Re} \le 3.14, \\ 0.0917 \quad \mathrm{Re} < 10^{-2} \end{cases} \tag{19}$$

this is shown in Fig. 3 by circles and squares. Even though

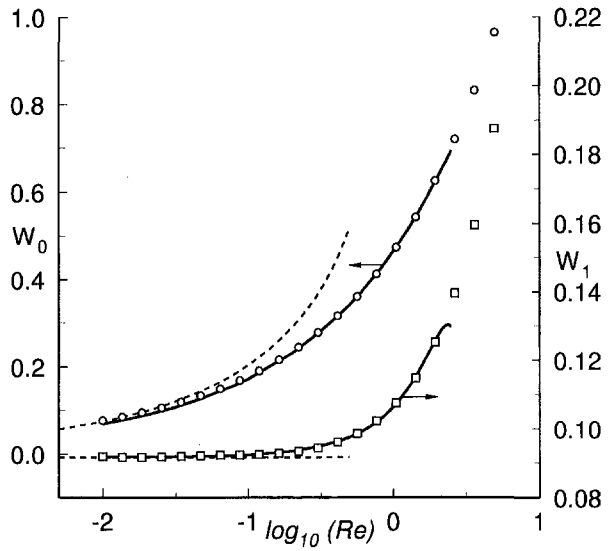

Fig. 3 Functions W_0(Re) and W_1(Re): *solid line*—calculated values; *circles and squares*—correlation (18) and (19); *dashed line*—asymptotic expressions (17)

there is no simple analytical representation for W_0 and W_1, this functional form was chosen in this way for simplicity but, of course, there may exist a functional representation that fits the curves better.

The function W_1 has a very acute maximum near the critical Reynolds number, when recirculation appears. This maximum is not reproduced by the correlation in (19). The correlations cope successfully with the problem of calculating the Nusselt number in the range of $10^{-2} \leq \mathrm{Re} \leq 2.5$, as can be seen in Fig. 2, where the circles correspond to the two terms expression (16) of the Nusselt numbers and the solid lines correspond to the results obtained from the calculation of the full equations (5)–(6). For Reynolds numbers below 2.5, the difference between the asymptotic formula (16) and the full equations simulation is negligible. When the Reynolds number approaches the critical value for detachment of the stream and the boundary layer equation is not valid anymore, there is a significant difference between both calculations, as can be seen for the case Re = 3.0. The correlations in (18) and (19) give very good results in the range of validity of the Boundary Layer theory, and reasonable results, which are better than those for the pure Boundary Layer theory, for the values of the Reynolds numbers close to the critical one—as can be seen for the case Re = 3.0, in which the correlation is plotted by a dashed line. This better behavior of the correlation is explained by the fact that the correlation for W_1 does not follow the sharp maximum near the critical Reynolds number. Analogously to the case $\sigma = O(1)$, the correlations can be used for Prandtl numbers of order unity, even though the boundary layer theory is only appropriate, in principle, for $\mathrm{Pr} \gg 1$.

The validity of (16), (18), and (19) can be seen in Fig. 4, where it has been plotted by circles for Pr = 6.82 (water) and Pr = 0.72 (air). The solid line 3 corresponds to the full Navier-Stokes and energy equations solution. The agreement is reasonably close even for Reynolds near the critical value and Prandtl of order unity. The numerical results for air of Dennis et al. (1968), shown by squares, are almost coincident with the curve obtained in this work. In the same figure it can be seen that the correlations for air obtained by Collis and Williams (1959), shown by black triangles, also compare favorably with our results, taking their parameter $T_m/T_\infty = 1$, as was done by Dennis et al. (1968).

5 Conclusions

An analysis has been done to calculate the heat transfer from a wire to a fluid stream. The boundary layer approximation has been used for the case of $\sigma \gg 1$ using a small Reynolds number (Stokes) flow field. It was shown that the formula (13) gives good results, even for $\sigma = O(1)$. Even though the global behavior of the solution so obtained is more satisfactory, it is found to differ somewhat from the real solution for the case Re = $O(1)$. Then, the case of the moderately small Reynolds number has been studied, trying to cover a wider range. Even though there is no simple analytical description for this regime, it is still possible to obtain an asymptotic description in terms of the functions $W_0(\mathrm{Re})$ and $W_1(\mathrm{Re})$ for large Prandtl numbers and moderately small Reynolds numbers, in principle. It has been demonstrated that the Nusselt number can be calculated accurately not only for the large Prandtl numbers, but also for the values of order unity and, using an approximate correlation for W_0 and W_1, for Reynolds numbers close to the critical value, just by extrapolating the correlation curves (18) and (19).

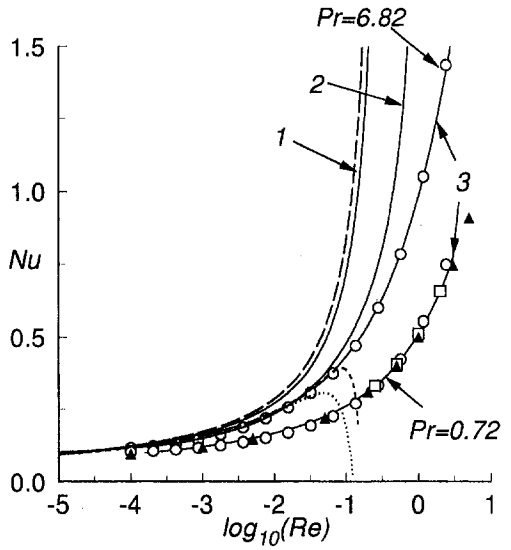

Fig. 4 Comparison of results obtained with different procedures for Pr = 6.82: *long dashed line*—Cole and Roshko (1954) (1); *dotted line*—Wood (1968); *short dashed line*—Hieber and Gebhart (1968) (3); *solid line* 1—Nakai and Okazaki (1975) (4); *solid line 2*—boundary layer solution (13). Calculation of full equations (5)–(6) (solid lines 3) for Pr = 6.82 and Pr = 0.72; *circles*—formulae (16), (18), and (19); *squares*—Dennis et al. (1968) (for air); *black triangles*—Collis and Williams (1959) (for air).

Acknowledgments

V. Kurdyumov wishes to express his gratitude to the DGICYT of the Ministry of Education and Science (Spain) for a postdoctoral fellowship at UPM. Useful discussions with Prof. A. Liñán were very important for the definition of the problem. The authors also wish to thank INTA (Spain) for the use of its computing facilities.

References

Cole, J., and Roshko, A., 1954, "Heat Transfer From Wires at Reynolds Numbers in the Oseen Range," *Proceeding of Heat Transfer and Fluid Mechanics Institute,* University of California, Berkeley, CA, pp. 13–23.

Collis, D. S., and Willams, M. J., 1959, "Two-Dimensional Convection From Heated Wires at Low Reynolds Numbers," *J. Fluid Mech.,* Vol. 6, pp. 357–384.

Dennis, S. C. R., Hudson, J. D., and Smith, N., 1968, "Steady Laminar Forced Convection From a Circular Cylinder at Low Reynolds Numbers," *Physics of Fluids,* Vol. 11, pp. 933–940.

Hieber, C. N., and Gebhart, B., 1968, "Low Reynolds Number Heat Transfer From a Circular Cylinder," *J. Fluid. Mech.,* Vol. 32, pp. 21–28.

Illingworth, C. R., 1963, "Flow at Small Reynolds Number," in *Laminar Boundary Layers* L. Rosenhead, ed., Claredon Press, Oxford.

Morgan, V. T., 1975, "The Overall Convection Heat Transfer from Smooth Circular Cylinder," *Advances in Heat Transfer,* Vol. 11, Academic Press, NY, pp. 199–264.

Nakai, S., and Okazaki, T., 1975, "Heat Transfer From a Horizontal Circular Wire at Small Reynolds and Grashof Numbers," *Int. J. Heat and Mass Transfer,* Vol. 18, pp. 387–396.

Van Dyke, M., 1975, *Perturbation Methods in Fluid Mechanics,* The Parabolic Press, Stanford, CA, p. 152.

Wood, W. W., 1968, "Calculation for Anemometry With Fine Hot Wires," *J. Fluid Mech.,* Vol. 32, pp. 9–22.

Second Law Analysis of Laminar Viscous Flow Through a Duct Subjected to Constant Wall Temperature

A. Z. Şahin
Department of Mechanical Engineering,
King Fahd University of Petroleum
and Minerals,
P.O. Box 1461,
Dhahran 31261, Saudi Arabia
azsahin@dpc.kfupm.edu.sa

Entropy generation for a fully developed laminar viscous flow in a duct subjected to constant wall temperature is investigated analytically. The temperature dependence on the viscosity is taken into consideration in the analysis. The ratio of the pumping power to the total heat flux decreases considerably and the entropy generation increases along the duct length for viscous fluids. The variation of total exergy loss due to both the entropy generation and the pumping process is studied along the duct length as well as varying the fluid inlet temperature for fixed duct length. For low heat transfer conditions the entropy generation due to viscous friction becomes dominant and the dependence of viscosity with the temperature becomes essentially important to be considered in order to determine the entropy generation accurately.

Introduction

Efficient utilization of exergy is one of the primary objectives in designing any thermodynamic system. Minimization of entropy generation in a thermodynamic system provides efficient use of exergy that is available. The irreversibilities associated with fluid flow through a duct are usually related to heat transfer and viscous friction. The contributions of various mechanisms and design features on the different irreversibility terms often compete with one another (Bejan, 1988). Therefore, there may exist an optimal thermodynamic design which minimizes the amount of entropy generation. For a given thermodynamic system, a set of thermodynamic parameters which optimize operating conditions could be obtained.

Second-law analysis in heat transfer and thermal design was outlined in detail by Bejan (1980, 1982). He presented the basic steps for the procedure of entropy generation minimization at the system-component level. Nag and Mukherjee (1987) studied the thermodynamic optimization of convective heat transfer through a duct with constant wall temperature. In their study, they plotted the variation of entropy generation with the difference of bulk flow inlet and the surface temperatures using a duty parameter. In the case they considered, the duty parameter was also a function of this temperature difference through the heat transfer. They studied the effect of the inlet and the wall temperature difference for small values of this temperature difference.

Heat transfer enhancement techniques that are used to increase the rate of heat transfer are known to increase friction factor. Minimization of the total entropy generation for two typical heat transfer enhancement problems related to the variation of heat transfer area and the variation of temperature difference was studied by Perez-Blanco (1984).

The irreversibility associated with the viscous friction is directly proportional to the viscosity of the fluid in laminar flow. On the other hand, the viscosity of fluids may vary significantly with temperature and, to the best of this author's knowledge, this variation has not yet been considered in exergy analysis in the literature. Thus, as an extention to the Bejan's work (Bejan, 1980; Bejan, 1982) it is required to investigate the effect of change of viscosity during a heating process for a more accurate determination of entropy generation and pumping power required.

Total Entropy Generation

Consider the constant cross-sectional area duct shown in Fig. 1. The surface temperature of the duct is kept constant at T_w. An incompressible viscous fluid with mass flow rate, $\dot{m}$, and inlet temperature, T_o, enters the duct of length l. Heat transfer to the bulk of the fluid occurs through the average heat transfer coefficient, $\bar{h}$, which is not constant but is a function of the viscosity variation. On the other hand, density ρ, thermal conductivity k, and specific heat C_p of the fluid are assumed to be constant within the range of temperatures considered in this study (Table 1). We would like to analyze the entropy generation for different duct lengths and fluid inlet temperatures considering the variation of viscosity with temperature.

The heat transfer rate to the fluid inside the control volume shown in Fig. 1 is

$$\delta\dot{Q} = \dot{m}C_p dT = \bar{h}\pi D(T_w - T)dx, \tag{1}$$

where $\dot{m}$ is the mass flow rate given by

$$\dot{m} = \rho\bar{U}\frac{\pi D^2}{4}.$$

It should be noted that in writing Eq. (1) the duct is assumed to have a circular cross section; however, the analysis is not affected, assuming cross-sectional areas other than circular.

Integrating Eq. (1), the bulk temperature variation of the fluid along the duct can be obtained as

$$T = T_w - (T_w - T_o)\exp\left(-\frac{4\bar{h}}{\rho\bar{U}DC_p}x\right). \tag{2}$$

Equation (2) can be rewritten as

$$\theta = \exp\left(-4\frac{\mathrm{St}}{D}x\right), \tag{3}$$

where θ is the dimensionless temperature defined as

Contributed by the Heat Transfer Division for publication in the JOURNAL OF HEAT TRANSFER. Manuscript received by the Heat Transfer Division March 19, 1996; revision received October 31, 1997; Keywords: Forced Convection; Heat Exchangers; Thermodynamics and Second Law. Associate Technical Editor: R. D. Boyd.

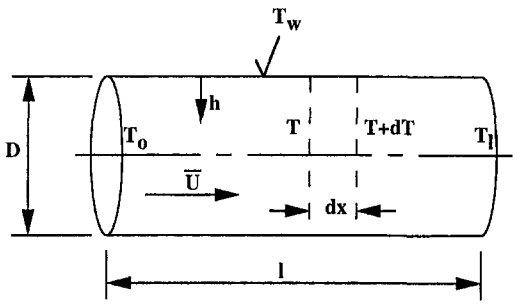

Fig. 1 Schematic view of duct

$$\theta = \frac{T - T_w}{T_o - T_w},$$

and St is the Stanton number defined as

$$\mathrm{St} = \frac{\overline{h}}{\rho \overline{U} C_p}.$$

The temperature variation along the duct approaches the duct wall temperature exponentially.

The average heat transfer coefficient, $\overline{h}$, being a function of viscosity variation along the duct length, can be evaluated for each set of duct length (l) and fluid inlet temperature (T_o) values. The effect of viscosity on the average heat transfer coefficient is given by Kays and Perkins (1973) as

$$\frac{\overline{h}}{\overline{h}_{c.p.}} = \frac{\overline{Nu}}{Nu_{c.p.}} = \left(\frac{\mu_b}{\mu_w}\right)^{0.14}, \tag{4}$$

where $\overline{h}_{c.p.} = k\overline{\mathrm{Nu}}_{c.p.}/D$ and $\overline{\mathrm{Nu}}_{c.p.} = 3.66$ for fully developed laminar flow. μ_b in Eq. (4) is a function of mean bulk fluid temperature, which is also initially unknown and depends on $\overline{h}$. Therefore, a trial and error procedure is followed to determine $\overline{h}$ making use of Eqs. (1) and (4).

The entropy generation within the control volume in Fig. 1 can be written as

$$d\dot{S}_{\mathrm{gen}} = \dot{m} ds - \frac{\delta \dot{Q}}{T_w}, \tag{5}$$

where for an incompressible fluid

$$ds = \frac{C_p dT}{T} - \frac{dP}{\rho T}.$$

Substituting Eq. (1) in Eq. (5), the total entropy generation becomes

Table 1 Thermophysical properties and parameters used

	Water	*Glycerol*
a (N s/m^2)	9.93×10^{-4}	1.48
b (N s/m^2 K)	8.9438×10^{-6}	0.0182
B	4700	23100
C_p (J/kg K)	4182	2428
D (m)	0.0254	0.0254
$\overline{h}_{c.p.}$ (W/m^{2}K)	86	38
k (W/m K)	0.6	0.264
n	8.9	52.4
T_{ref} (K)	293	293
T_w (K)	373	373
$\overline{U}$ (m/s)	0.025	0.5
$\mu(T_{ref})$ (N s/m^2)	9.93×10^{-4}	1.48
Π_1	0.0 – 0.5	0.0 – 0.5
ρ (kg/m^3)	998.2	1260
τ	0.0 – 0.2	0.0 – 0.2

$$d\dot{S}_{\mathrm{gen}} = \dot{m} C_p \left(\frac{T_w - T}{T T_w} dT - \frac{1}{\rho C_p T} dP\right). \tag{6}$$

The pressure drop in Eq. (6) is given by Kreith and Bohn (1993):

$$dP = -\frac{f \rho \overline{U}^2}{2D} dx, \tag{7}$$

where f is the friction factor.

Integrating Eq. (6) along the duct length, l, using Eqs. (2) and (7) and assuming that the viscosity remains constant along the duct, the total entropy generation is obtained as

$$\dot{S}_{\mathrm{gen}} = \dot{m} C_p \left\{ \ln\left(\frac{1 - \tau e^{-4\mathrm{St}\lambda}}{1 - \tau}\right) - \tau(1 - e^{-4\mathrm{St}\lambda}) + \frac{1}{8}\frac{f \tau \mathrm{Ec}}{\mathrm{St}} \ln\left(\frac{e^{4\mathrm{St}\lambda} - \tau}{1 - \tau}\right)\right\}, \tag{8}$$

where τ is the dimensionless temperature difference

Nomenclature

C_p = specific heat capacity (J/kg K)
D = diameter (m)
Ec = Eckert number $[\overline{U}^2/[C_p(T_w - T_o)]]$
f = friction factor
$\overline{h}$ = average heat transfer coefficient (W/m^2 K)
$\overline{h}_{c.p.}$ = constant property average heat transfer coefficient (W/m^2 K)
k = thermal conductivity (W/m K)
l = length of the duct (m)
$\dot{m}$ = mass flow rate (kg/s)
P = pressure (N/m^2)
$\mathcal{P}_r$ = pumping power to heat transfer rate ratio
$\dot{Q}$ = total heat transfer rate (W)
Re = Reynolds number $[\rho \overline{U} D/\mu]$
s = entropy (J/kg K)
$\dot{S}_{\mathrm{gen}}$ = entropy generation (W/K)
St = Stanton number $[\overline{h}/(\rho \overline{U}(C_p)]$
T = temperature (K)
T_o = inlet fluid temperature (K)
T_{ref} = reference temperature (= 293 K)
T_w = wall temperature of the duct (K)
$\overline{U}$ = fluid bulk velocity (m/s)
x = axial distance (m)
ΔT = increase of fluid temperature (K)
μ = viscosity (N/s m^2)
μ_b = viscosity of fluid at bulk temperature (N/s m^2)
μ_w = viscosity of fluid at wall temperature (N/s m^2)
λ = dimensionless axial distance $[l/D]$
Π_1 = modified Stanton number [St λ]
Π_2 = dimensionless group [Ec/(St Re)]
Ψ = dimensionless entropy generation $[\dot{S}_{\mathrm{gen}}/[\dot{Q}/(T_w - T_o)]]$
Ψ' = modified dimensionless entropy generation $[\dot{S}_{\mathrm{gen}}/(\dot{Q}/\Delta T)]$
ρ = density (kg/m^3)
τ = dimensionless inlet wall-to-fluid temperature difference $[(T_w - T_o)/T_w]$
θ = dimensionless temperature $[(T - T_w)/(T_o - T_w)]$

$$\tau = \frac{T_w - T_o}{T_w},$$

λ is the dimensionless length of duct,

$$\lambda = \frac{l}{D},$$

and Ec is the Eckert number defined as

$$\mathrm{Ec} = \frac{\bar{U}^2}{C_p(T_w - T_o)}.$$

The total heat transfer rate to the fluid is obtained by integrating Eq. (1) along the duct length and can be written as

$$\dot{Q} = \dot{m}C_p(T_w - T_o)(1 - e^{-4\mathrm{St}\lambda}). \tag{9}$$

Now, defining a dimensionless entropy generation as

$$\Psi = \frac{\dot{S}_{\mathrm{gen}}}{\dot{Q}/(T_w - T_o)},$$

Eq. (8) can be written as

$$\Psi = (1 - e^{-4\mathrm{St}\lambda})\left\{\ln\left(\frac{1 - \tau e^{-4\mathrm{St}\lambda}}{1 - \tau}\right) - \tau(1 - e^{-4\mathrm{St}\lambda}) + \frac{1}{8}\frac{f\tau\mathrm{Ec}}{\mathrm{St}}\ln\left(\frac{e^{4\mathrm{St}\lambda} - \tau}{1 - \tau}\right)\right\}. \tag{10}$$

For fully developed laminar flow in a duct, assuming μ = constant for the time being, the friction factor is related to the Reynolds number (Kreith and Bohn, 1993) as

$$f = \frac{64}{\mathrm{Re}}, \tag{11}$$

where Reynolds number is defined as

$$\mathrm{Re} = \frac{\rho\bar{U}D}{\mu}.$$

Therefore, two dimensionless groups naturally arise in Eq. (10) in fully developed laminar flow as

$$\Pi_1 = \mathrm{St}\lambda \tag{12}$$

and

$$\Pi_2 = \frac{\mathrm{Ec}}{\mathrm{St}\ \mathrm{Re}}. \tag{13}$$

Thus, Eq. (10) can be written in a compact form for the constant viscosity assumption as

$$\Psi = (1 - e^{-4\Pi_1})\left\{\ln\left(\frac{1 - \tau e^{-4\Pi_1}}{1 - \tau}\right) - \tau(1 - e^{-4\Pi_1}) + 8\tau\Pi_2\ln\left(\frac{e^{4\Pi_1} - \tau}{1 - \tau}\right)\right\}, \tag{14}$$

which is a function of three nondimensional parameters, namely, τ, Π_1, and Π_2. Among these parameters, τ represents the fluid inlet temperature, (T_o, Π_1) represents the duct length l, and the product ($\tau\Pi_2$) is independent of T_o. Once the type of the fluid and the mass flow rate are fixed, ($\tau\Pi_2$) is constant and τ and Π_1 are the only two design parameters that can be varied for determining the effects of duct length and/or inlet fluid temperature.

Viscosity Dependence on Temperature

Experimentally, it is evident that the viscosity of liquids vary considerably with temperature. Around room temperature (293 K), for instance, a 1 percent change in temperature produces a 7 percent change in viscosity of water and approximately a 26 percent change in viscosity of glycerol (Sherman, 1990).

If the variation of viscosity with temperature is to be linear,

$$\mu(T) = a - b(T - T_{\mathrm{ref}}), \tag{15}$$

where a and b are positive fluid dependent dimensional constants and T_{ref} is a reference temperature (= 293 K).

The pressure drop in Eq. (7) for fully developed laminar flow, using Eq. (11), becomes

$$dP = -\frac{32\bar{U}}{D^2}[a - b(T - T_{\mathrm{ref}})]dx. \tag{16}$$

Integrating Eq. (6) along the duct length using Eqs. (2) and (16), the total entropy generation in this case is obtained as

$$\Psi = (1 - e^{-4\Pi_1})\left\{\ln\left(\frac{1 - \tau e^{-4\Pi_1}}{1 - \tau}\right) - \tau(1 - e^{-4\Pi_1}) + 8\tau\Pi_2\left[\ln\left(\frac{e^{4\Pi_1} - \tau}{1 - \tau}\right) + \left(\frac{bT_{\mathrm{ref}}}{a}\right)\ln\left(\frac{e^{4\Pi_1} - \tau}{1 - \tau}\right) - 4\left(\frac{bT_w}{a}\right)\Pi_1\right]\right\}, \tag{17}$$

where Re number in Π_2 is defined based on the constant a in Eq. (15); that is, $a = \mu(T_{\mathrm{ref}})$.

A reasonably accurate empirical correlation of liquid viscosity with the temperature is given by Sherman (1990) as

$$\mu(T) = \mu(T_{\mathrm{ref}})\left(\frac{T}{T_{\mathrm{ref}}}\right)^n \exp\left[B\left(\frac{1}{T} - \frac{1}{T_{\mathrm{ref}}}\right)\right], \tag{18}$$

where n and B are fluid dependent constant parameters.

Substituting Eq. (18) and Eq. (11) into Eq. (7), the pressure drop for fully developed laminar flow becomes

$$dP = -\frac{32\bar{U}}{D^2}\mu(T_{\mathrm{ref}})\left(\frac{T}{T_{\mathrm{ref}}}\right)^n \exp\left[B\left(\frac{1}{T} - \frac{1}{T_{\mathrm{ref}}}\right)\right]dx. \tag{19}$$

Integrating Eq. (6) along the duct length using Eq. (19), the total entropy generation is obtained as

$$\Psi = (1 - e^{-4\Pi_1})\left\{\ln\left(\frac{1 - \tau e^{-4\Pi_1}}{1 - \tau}\right) - \tau(1 - e^{-4\Pi_1}) + 32\Pi_2\int_0^l \frac{\Pi_1}{l}\frac{T_w - T_o}{T_{\mathrm{ref}}^n}T^{n-1} \times \exp\left[B\left(\frac{1}{T} - \frac{1}{T_{\mathrm{ref}}}\right)\right]dx\right\}, \tag{20}$$

where T is given in Eq. (2) and Re number in Π_2 is defined based on $\mu(T_{\mathrm{ref}})$. The integration in Eq. (20) must be done numerically.

It should be noted that, the dimensionless entropy generation, Ψ, in the above analysis is a function of the total heat transfer rate, $\dot{Q}$, which in turn depends on the length of the duct and inlet fluid temperature. However, a modified dimensionless entropy generation can be defined on the basis of unit mass flow rate of fluid in the duct as

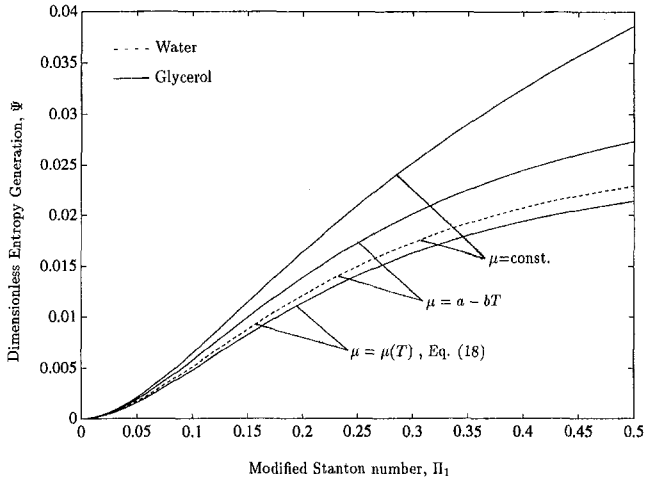

Fig. 2 Dimensionless entropy generation, Ψ, versus modified Stanton number, Π_1, for water and glycerol with three cases of viscosity dependence. (Effect of viscosity variation with temperature for water is negligible.)

$$\Psi' = \frac{\dot{S}_{\text{gen}}}{(\dot{Q}/\Delta T)}, \tag{21}$$

where ΔT is the increase of the bulk temperature of the fluid in the duct, $T(l) - T_o$. Noting that

$$\frac{\dot{Q}}{\Delta T} = \dot{m}C_p$$

is constant for fixed mass flow rate and

$$\Psi' = \frac{\Psi}{1 - e^{-4\Pi_1}}, \tag{22}$$

Ψ' indicates the total entropy generation along the duct that is expected to increase with the increase in duct length.

Pumping Power to Heat Transfer Rate Ratio

The ratio of pumping power to heat transfer rate is

$$\mathcal{P}_r = \frac{(\pi D^2/4)\Delta P \bar{U}}{\dot{Q}}. \tag{23}$$

Using Eqs. (7), (9), and (11), the pumping power to heat transfer rate ratio, $\mathcal{P}_r$, for fully developed laminar flow and constant viscosity is obtained as

$$\mathcal{P}_r = 32\Pi_2 \frac{\Pi_1}{1 - e^{-4\Pi_1}}. \tag{24}$$

When the variation of viscosity with temperature is assumed to be linear, as given by Eq. (15), the $\mathcal{P}_r$ ratio becomes

$$\mathcal{P}_r = 32\Pi_2 \frac{\Pi_1}{1 - e^{-4\Pi_1}} \left\{ 1 - \frac{b}{a}(T_w - T_o)\left[1 - \frac{1 - e^{-4\Pi_1}}{4\Pi_1} \right] - \frac{b}{a}(T_o - T_{\text{ref}}) \right\}. \tag{25}$$

For the relationship of viscosity with temperature given by Eq. (18), this ratio becomes

$$\mathcal{P}_r = 32\Pi_2 \frac{\Pi_1}{1 - e^{-4\Pi_1}} \left\{ \int_0^l \frac{1}{l} \left(\frac{T}{T_{\text{ref}}} \right)^n \times \exp\left[B\left(\frac{1}{T} - \frac{1}{T_{\text{ref}}} \right) \right] dx \right\}, \tag{26}$$

where T is given in Eq. (2) and the integration must be done numerically.

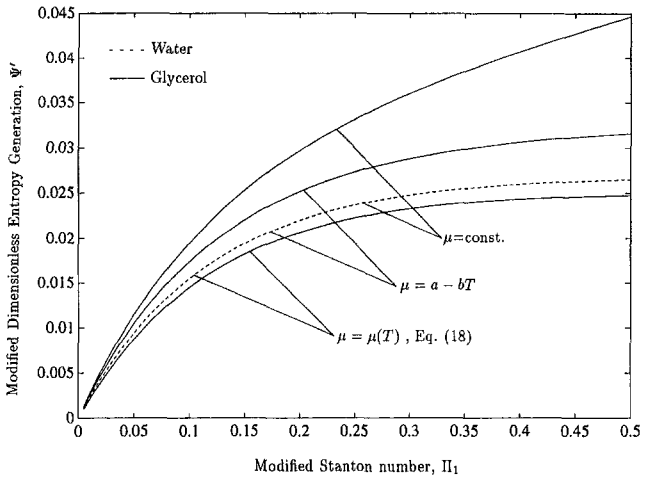

Fig. 3 Modified dimensionless entropy generation, Ψ', versus modified Stanton number, Π_1, for water and glycerol with three cases of viscosity dependence. (Effect of viscosity variation with temperature for water is negligible.)

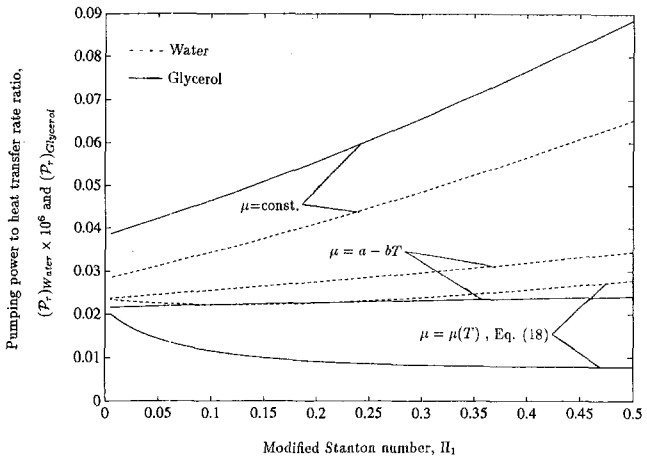

Fig. 4 Pumping power to heat transfer rate ratio, $\mathcal{P}_r$, versus modified Stanton number, Π_1, for water and glycerol with three cases of viscosity dependence

Discussions

In order to demonstrate the effect of viscosity on the entropy generation, two incompressible fluids, namely, water and glycerol, were selected. The parameters and the thermophysical properties used in the numerical example are given in Table 1. The surface temperature, the velocity of the incompressible fluid, and the cross-sectional area of the duct were fixed. The length of the duct and the inlet fluid temperature are left as variables to be studied.

The convergence criterion used during the evaluation of viscosity-dependent heat transfer coefficient $\bar{h}$ through Eqs. (1) and (4) is $|(T_k - T_{k-1})| < \epsilon$, where $\epsilon = 0.1$ K and k are the iteration counter. The integrals in Eqs. (20) and (26) were evaluated using the trapezoidal rule with 100 subintervals.

Figure 2 shows the variation of dimensionless entropy generation, Ψ, versus modified Stanton number, Π_1, for water and glycerol with three cases of viscosity dependence. Since the viscosity of water is low, the three curves corresponding to constant, linear, and variable viscosity dependence on tempera-

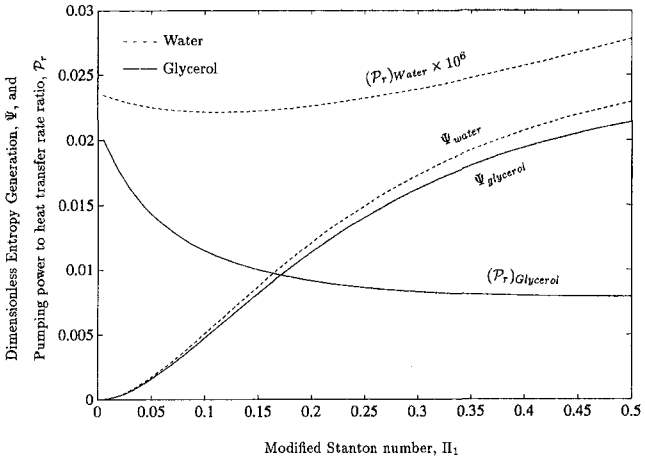

Fig. 5 Dimensionless entropy generation, Ψ and pumping power to heat transfer rate ratio, $\mathcal{P}_r$, versus modified Stanton number, Π_1, for water and glycerol using temperature dependent viscosity in Eq. (18)

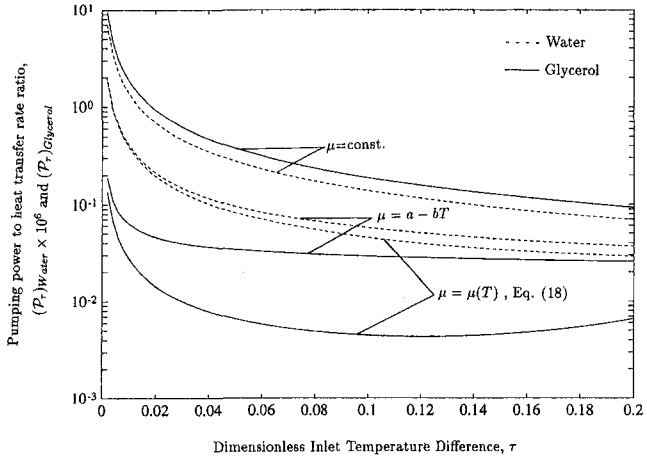

Fig. 7 Pumping power to heat transfer rate ratio, $\mathcal{P}_r$, versus Dimensionless inlet wall-to-fluid temperature difference, τ, for water and glycerol with three cases of viscosity dependence

ture are essentially the same. That means the last term in Eq. (14) is negligible for water. The effect of the assumed variation of viscosity on Ψ, however, is apparent in Fig. 2 for glycerol. The dimensionless entropy generation, Ψ, calculated based on the constant viscosity assumption, yields higher values than those calculated for temperature dependent viscosity. Since Π_1 represents the length of the duct, the dimensionless entropy generation defined on the basis of total heat transfer rate to the duct, Ψ, increases along the duct length. The rate of increase in entropy generation decreases and approaches a constant value as the total heat transfer rate to the fluid approaches its maximum value of

$$\dot{Q}_{\max} = \dot{m}C_p(T_w - T_o).$$

For long ducts where $e^{4\Pi_1} \gg \tau$, it can be shown from Eq. (14) that the entropy generation increases linearly with the slope

$$\frac{d\Psi}{d\Pi_1} = 32\tau\Pi_2.$$

The modified dimensionless entropy generation defined based on heat transfer rate per degree temperature difference along the duct, Ψ', is given in Fig. 3 as a function of modified Stanton number, Π_1, for water and glycerol for the three cases of viscosity dependence. The effect of viscosity is negligible in the case of water. However, apparent in the case of glycerol, as shown in Fig. 3, Ψ' adds up along the duct length and shows a general increase. As in the case of Ψ, the assumption of a constant viscosity yields considerably higher values of Ψ' compared with those for temperature dependent viscosity. Ψ' and Ψ differ only for small values of Π_1. For large values of Π_1, $\Psi' = \Psi$, as can be seen from Eq. (22).

The pumping power to heat transfer rate ratio, $\mathcal{P}_r$, is shown in Fig. 4 for water and glycerol. In both cases, the constant viscosity assumption yields unreasonably high pumping power ratios as expected. Due to an increase in the bulk temperature and a decrease in viscosity, the pumping power to heat transfer rate ratio may decrease for small values of Π_1, but then increase as the total heat transfer rate to the fluid decreases as the bulk temperature approaches the wall temperature. For large values of Π_1, it can be shown from Eq. (24) that the pumping ratio, $\mathcal{P}_r$, increases linearly with the slope

$$\frac{d\mathcal{P}_r}{d\Pi_1} = 32\Pi_2.$$

The dimensionless entropy generation, Ψ, and pumping power to heat transfer rate ratio, $\mathcal{P}_r$, are shown in Fig. 5 for

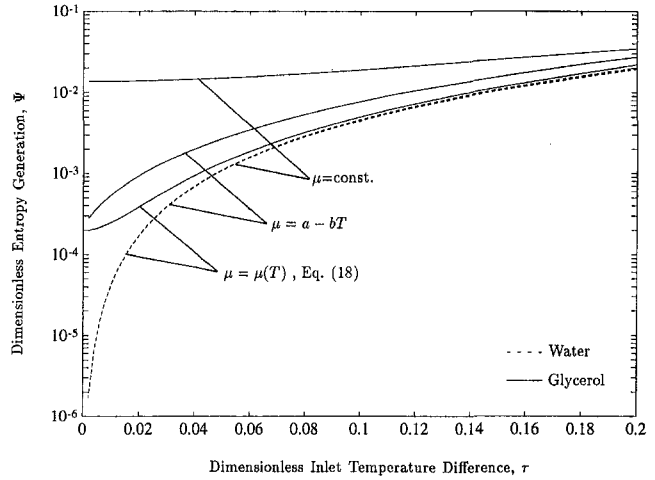

Fig. 6 Dimensionless entropy generation, Ψ, versus dimensionless inlet wall-to-fluid temperature difference, τ, for water and glycerol with three cases of viscosity dependence. (Effect of viscosity variation with temperature for water is negligible.)

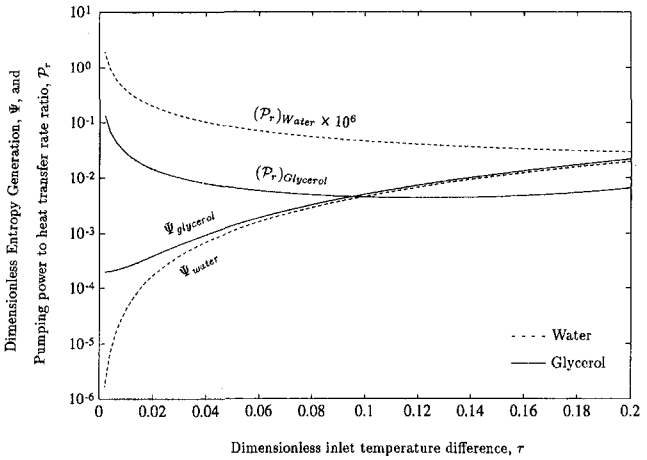

Fig. 8 Dimensionless entropy generation, Ψ, and pumping power to heat transfer rate ratio, $\mathcal{P}_r$, versus dimensionless inlet wall-to-fluid temperature difference, τ, for water and glycerol using temperature dependent viscosity in Eq. (18)

Table 2 Variation of total loss of exergy and pumping power consumed per unit amount of heat transfer rate for the case of water for (*a*) fixed inlet temperature and (*b*) fixed duct length

(a)

Inlet temperature, T_o = 293 K					
Π_1	l (m)	Ψ	Ψ'	$\mathcal{P}_r \times 10^6$	$\Psi + \mathcal{P}_r$
0.025	0.6634	0.0005	0.0052	0.02293	0.0005
0.05	1.3416	0.0017	0.0094	0.02252	0.0017
0.075	2.0321	0.0033	0.0128	0.02227	0.0033
0.1	2.7331	0.0051	0.0155	0.02216	0.0051
0.125	3.4429	0.0069	0.0177	0.02216	0.0069
0.15	4.1603	0.0088	0.0194	0.02224	0.0088
0.175	4.8842	0.0105	0.0208	0.02240	0.0105
0.2	5.6137	0.0121	0.0220	0.02261	0.0121
0.225	6.3481	0.0136	0.0229	0.02287	0.0136
0.25	7.0869	0.0149	0.0236	0.02318	0.0149
0.275	7.8294	0.0162	0.0243	0.02352	0.0162
0.3	8.5753	0.0173	0.0247	0.02390	0.0173
0.325	9.3241	0.0183	0.0252	0.02431	0.0183
0.35	10.0756	0.0192	0.0255	0.02475	0.0192
0.375	10.8295	0.0200	0.0257	0.02521	0.0200
0.4	11.5856	0.0207	0.0260	0.02569	0.0207
0.425	12.3436	0.0214	0.0261	0.02620	0.0214
0.45	13.1033	0.0219	0.0263	0.02672	0.0219
0.475	13.8646	0.0225	0.0264	0.02726	0.0225
0.5	14.6273	0.0229	0.0265	0.02782	0.0229

(b)

Duct length, l=15 m					
τ	T_o(°C)	Ψ	Ψ'	$\mathcal{P}_r \times 10^6$	$\Psi + \mathcal{P}_r$
0.01	369.27	0	0	0.38555	0.0000
0.02	365.54	0.0002	0.0002	0.19589	0.0002
0.03	361.81	0.0004	0.0005	0.13277	0.0004
0.04	358.08	0.0007	0.0008	0.10128	0.0007
0.05	354.35	0.0011	0.0013	0.08245	0.0011
0.06	350.62	0.0016	0.0018	0.06995	0.0016
0.07	346.89	0.0022	0.0025	0.06108	0.0022
0.08	343.16	0.0029	0.0033	0.05448	0.0029
0.09	339.43	0.0037	0.0042	0.04939	0.0037
0.10	335.70	0.0046	0.0053	0.04536	0.0046
0.11	331.97	0.0056	0.0064	0.04211	0.0056
0.12	328.24	0.0067	0.0077	0.03945	0.0067
0.13	324.51	0.0079	0.0091	0.03725	0.0079
0.14	320.78	0.0093	0.0107	0.03540	0.0093
0.15	317.05	0.0107	0.0123	0.03385	0.0107
0.16	313.32	0.0123	0.0141	0.03254	0.0123
0.17	309.59	0.0140	0.0161	0.03143	0.0140
0.18	305.86	0.0159	0.0182	0.03050	0.0159
0.19	302.13	0.0179	0.0204	0.02972	0.0179
0.20	298.40	0.0200	0.0228	0.02908	0.0200

water and glycerol for comparison. Both Ψ and $\mathcal{P}_r$ are required to be minimized in actual applications. Therefore, there may exist a certain operating duct length which will minimize the total cost due to both the entropy generation and the pumping power, especially for the fluids having large viscosities. This observation is only possible using a temperature dependent viscosity. However, the constant viscosity assumption that yields increasing $\mathcal{P}_r$ with respect to Π_1 would not yield an operating duct length for which exergy losses were minimum.

Figure 6 shows the variation of the dimensionless entropy generation, Ψ, with dimensionless inlet wall-to-fluid temperature difference, τ, for water and glycerol with the three cases of viscosity dependence. Since the viscosity of water is low, the three curves corresponding to constant, linear, and variable viscosity dependence on temperature are essentially the same as mentioned above. The effect of the assumed variation of viscosity on Ψ is apparent in the case of glycerol. The dimensionless entropy generation, Ψ, calculated based on the constant viscosity assumption yields considerably higher values than those calculated for temperature dependent viscosity—especially for small values of τ. Since τ represents the difference between the temperature of the duct surface and that of the inlet fluid, the dimensionless entropy generation defined on the basis of total heat transfer rate to the duct, Ψ, increases as τ increases due to the increase in the total heat transfer rate to the fluid. For small values of τ, the total entropy change is due to the viscous friction; in the limit when $\tau = 0$, and noting that the product $\tau\Pi_2$ ($= \mu\bar{U}^2/\bar{h}DT_w$) is independent of the inlet fluid temperature, the total dimensionless entropy change using Eq. (14) becomes

$$\Psi = 32(\tau\Pi_2)\Pi_1(1 - e^{-4\Pi_1}).$$

For large values of τ, the contribution of the heat transfer to the total entropy generation becomes dominant and the gap between the curves in Fig. 6 that is due to the different viscosity dependence get smaller.

The modified dimensionless entropy generation defined based on heat transfer rate per degree temperature difference along the duct, Ψ', shows a similar behaviour as that of Ψ. This was expected since Ψ' and Ψ are related through a constant factor of $(1 - e^{-4\Pi_1})$, as given in Eq. (22).

Variation of the pumping power to heat transfer rate ratio, $\mathcal{P}_r$, with respect to the dimensionless inlet wall-to-fluid temperature difference, τ, is shown in Fig. 7 for water and glycerol. As noted above, the constant viscosity assumption yields unreasonably high pumping power ratios in both cases. Recalling that the product $\tau\Pi_2$ is invariable with varying inlet fluid tempera-

Table 3 Variation of total loss of exergy and pumping power consumed per unit amount of heat transfer rate for the case of glycerol for (*a*) fixed inlet temperature and (*b*) fixed duct length

(a)

Inlet temperature, T_o = 293 K					
Π_1	l (m)	Ψ	Ψ'	$\mathcal{P}_r$	$\Psi + \mathcal{P}_r$
0.025	14.7397	0.0005	0.0048	0.0169	0.0174
0.05	30.6999	0.0016	0.0087	0.0143	0.0159
0.075	47.7085	0.0031	0.0119	0.0126	0.0157
0.1	65.6209	0.0048	0.0145	0.0115	0.0163
0.125	84.3152	0.0065	0.0166	0.0106	0.0171
0.15	103.6884	0.0082	0.0182	0.0100	0.0182
0.175	123.6536	0.0098	0.0196	0.0095	0.0193
0.2	144.1368	0.0114	0.0206	0.0092	0.0206
0.225	165.0752	0.0128	0.0215	0.0089	0.0217
0.25	186.4148	0.0140	0.0222	0.0086	0.0226
0.275	208.1097	0.0152	0.0228	0.0085	0.0237
0.3	230.1198	0.0162	0.0232	0.0083	0.0245
0.325	252.4110	0.0172	0.0236	0.0082	0.0254
0.35	274.9533	0.0180	0.0239	0.0081	0.0261
0.375	297.7207	0.0187	0.0241	0.0081	0.0268
0.4	320.6905	0.0194	0.0243	0.0080	0.0274
0.425	343.8429	0.0200	0.0245	0.0080	0.0280
0.45	367.1604	0.0205	0.0246	0.0080	0.0285
0.475	390.6274	0.0210	0.0247	0.0080	0.0290
0.5	414.2303	0.0214	0.0247	0.0080	0.0294

(b)

Duct length, l=500 m					
τ	T_o(°C)	Ψ	Ψ'	$\mathcal{P}_r$	$\Psi + \mathcal{P}_r$
0.01	369.27	0.0002	0.0003	0.0276	0.0278
0.02	365.54	0.0004	0.0004	0.0144	0.0148
0.03	361.81	0.0006	0.0007	0.0100	0.0106
0.04	358.08	0.0009	0.0011	0.0079	0.0088
0.05	354.35	0.0014	0.0016	0.0066	0.0080
0.06	350.62	0.0019	0.0022	0.0058	0.0077
0.07	346.89	0.0025	0.0029	0.0053	0.0078
0.08	343.16	0.0032	0.0037	0.0049	0.0081
0.09	339.43	0.0041	0.0046	0.0046	0.0087
0.10	335.70	0.0050	0.0057	0.0045	0.0095
0.11	331.97	0.0061	0.0069	0.0044	0.0105
0.12	328.24	0.0073	0.0082	0.0043	0.0116
0.13	324.51	0.0086	0.0097	0.0044	0.0130
0.14	320.78	0.0100	0.0113	0.0044	0.0144
0.15	317.05	0.0116	0.0131	0.0046	0.0162
0.16	313.32	0.0134	0.0150	0.0048	0.0182
0.17	309.59	0.0152	0.0170	0.0051	0.0203
0.18	305.86	0.0173	0.0193	0.0054	0.0227
0.19	302.13	0.0195	0.0217	0.0060	0.0255
0.20	298.40	0.0220	0.0243	0.0066	0.0286

tures, it can be concluded from Eq. (24) that the pumping power ratio is inversely proportional to τ. However, in the case of large values of τ, $\mathcal{P}_r$ may start increasing due to increases in the viscosity for the incoming low temperature fluid. This is apparent in Fig. 7 for the case of glycerol.

The dimensionless entropy generation, Ψ, and the pumping power to heat transfer rate ratio, $\mathcal{P}_r$, for water and glycerol are shown in Fig. 8 for the case of the temperature-dependent viscosity given in Eq. (18). Since both Ψ and $\mathcal{P}_r$ are required to be minimized, there may exist a certain dimensionless inlet wall-to-fluid temperature difference, τ, which will minimize the total cost due to both the entropy generation and the pumping power—especially for fluids having large viscosities. This was observed even with the constant viscosity case; increases in Ψ but decreases in $\mathcal{P}_r$ resulted when τ increased.

Exergy, also referred to as availability, can be viewed as the useful work potential of an amount of energy at a specified state (Saad, 1997; Cengel and Boles, 1994). This potential is not generally conserved but is destroyed by irreversibilities (Moran and Shapiro, 1995). In order to show the total loss of exergy due to entropy generation and the pumping process for determining the actual cost and assuming unit cost for both, consider the following addition:

$$\Psi + \mathcal{P}_r = \frac{\dot{S}_{\text{gen}}(T_w - T_o)}{\dot{Q}} + \frac{(\pi D^2/4)\Delta P \bar{U}}{\dot{Q}},$$

which is tabulated in Tables 2 and 3 for water and glycerol, respectively. Two cases were considered in each table: fixed fluid inlet temperature for varying duct length and fixed duct length for varying fluid inlet temperature. During the computations, Re numbers were calculated to make sure that fully developed laminar flow is maintained within the range of parameters used. For water, $\Psi + \mathcal{P}_r$ shows a continuous increase with both duct length and inlet fluid temperature, however, a minimum value of $\Psi + \mathcal{P}_r$ can be determined for glycerol for the two cases as shown in Table 3.

Finally, the significance of using viscosity-dependent average heat transfer coefficient $\bar{h}$ was studied. Comparisons of some of the results for constant property average heat transfer coefficient $\bar{h}_{c.p.}$ and viscosity dependent average heat transfer coefficient $\bar{h} = \bar{h}(\mu)$ were made. The difference in results for water was only noticable in the pumping power to heat transfer rate ratio, $\mathcal{P}_r$ values. This is expected because the viscosity change of water within the temperature ranges used is not significant, therefore, the effect of viscosity on the dimensionless entropy generation (Ψ and Ψ') is negligible (less than 2.5 percent). Within the range of parameters used (see Table 1), the maximum difference between $\bar{h} = \bar{h}(\mu)$ and $\bar{h}_{c.p.}$ was found to be 10.2 percent. The resulting difference in $\mathcal{P}_r$ was obtained to be less than 18 percent. For the case of glycerol, the effect of using constant property average heat transfer coefficient $\bar{h}_{c.p.}$ on the dimensionless entropy generation values (Ψ and Ψ') was still small (less than 5 percent). However, a significant difference

(up to 73 percent) was observed in the values of pumping power to heat transfer rate ratio, $\mathcal{P}_r$. The maximum difference between $\overline{h} = \overline{h}(\mu)$ and $\overline{h}_{c,p}$, in the case of glycerol was found to be 31.4 percent.

Conclusions

Entropy generation for a viscous flow in a duct subjected to constant surface temperature was investigated. The entropy generation was found to be a function of three dimensionless numbers, namely, Π_1, Π_2 and τ.

For constant viscosity flow in the duct, both the entropy generation, Ψ', and the pumping power ratio, $\mathcal{P}_r$, increased along the length of the duct. For viscous fluids, however, the pumping power ratio, $\mathcal{P}_r$, decreased along the duct length. Therefore, for a certain duct length, exergy losses due to both the entropy generation and the pumping process becomes minimum.

It was found that entropy generation, Ψ, increased with increasing the dimensionless temperature difference between the inlet fluid and surface temperature, τ. However, the pumping power ratio decreased with increasing τ. Therefore, in each of the constant and temperature dependent viscosity models, a certain fluid inlet temperature exists for which the exergy losses are minimum.

In the case of low heat transfer rate for which $\tau \ll 1$, the entropy generation due to viscous friction becomes dominant. In this case, the dependence of viscosity with the temperature becomes the more important issue to be considered in order to determine the entropy generation accurately.

Acknowledgment

The author acknowledges the support of King Fahd University of Petroleum and Minerals, Dhahran, Saudi Arabia for this work.

References

Bejan, A., 1980, "Second-Law Analysis in Heat Transfer," *Energy,* Vol. 5, pp. 721–732.

Bejan, A., 1982, "Second-Law Analysis in Heat Transfer and Thermal Design," *Adv. Heat Transfer,* Vol. 15, pp. 1–58.

Bejan, A., 1988, *Advanced Engineering Thermodynamics,* John Wiley & Sons, Inc., New York, pp. 594–602.

Cengel, Y. A., and Boles, M. A., 1994, *Thermodynamics, An Engineering Approach,* McGraw-Hill Co., New York, p. 388.

Kays, W. M., and Perkins, H. C., 1973, "Forced Convection, Internal Flow in Ducts," in *Handbook of Heat Transfer,* W. M. Rohsenow, and J. P. Hartnett, eds., McGraw-Hill Co., New York, pp. 7-156–7-157.

Kreith, F., and Bohn, M. S., 1993, *Principles of Heat Transfer,* 5th ed., *West Publ. Co.,* New York, p. 386.

Moran, M. J., and Shapiro, H. N., 1995, *Fundamentals of Engineering Thermodynamics,* John Wiley & Sons, Inc., New York, p. 277.

Nag, P. K., and Mukherjee, P., 1987, "Thermodynamic Optimization of Convective Heat Transfer Through a Duct With Constant Wall Temperature," *Int. J. Heat Mass Transfer,* Vol. 30, No. 2, pp. 401–405.

Perez-Blanco, H., 1984, "Irreversibility in Heat Transfer Enhancement," in *Second Law Aspects of Thermal Design,* HTD Vol. 33, ASME, NY, pp. 19–26; also presented at The 22nd National Heat Transfer Conference and Exhibition, Niagara Falls, New York, August 5–8, 1984.

Saad, M. A., 1997, *Thermodynamics, Principles and Practice,* Prentice Hall, New Jersey, p. 309.

Sherman, F. S., 1990, *Viscous Flow,* McGraw Hill Co., New York, pp. 71–72.

D. L. Thomson

Y. Bayazitoglu

A. J. Meade, Jr.

Department of Mechanical Engineering
and Material Science,
Rice University,
P.O. Box 1892, MS 321,
Houston, TX 77251-1892

Low Dean Number Convective Heat Transfer in Helical Ducts of Rectangular Cross Section

Flow in a torroidal duct is characterized by increased convective heat transfer and friction compared to a straight duct of the same cross section. In this paper the importance of the nonplanarity (torsion) of a helical duct with rectangular cross section is investigated. A previously determined low Dean number velocity solution is used in the decoupled energy equation for the hydrodynamically fully developed, thermally developing case. Torsion, known to increase the friction factor, is found to cause a decrease in the fully developed Nusselt number compared to pure torroidal flow. Therefore, it is recommended that torsion be minimized to enhance heat transfer.

Introduction

During experimental studies on the production of fine metal powders by electromagnetic vaporization proposed by Bayazitoglu and Cerny (1992, 1994), it was found that the cooling of a levitating coil used to produce an alternating magnetic field posed a significant mechanical problem. A coil of rectangular cross section was recommended by Stickel and Bayazitoglu (1995) to minimize the stacking space for a given duct perimeter while maximizing the levitating effect. The electric current used to levitate an object within the helix causes extreme heating, so fluid was pumped through the coil to remove this heat. The resulting flow rate through such a coil was less than would be expected for a straight duct of the same length.

According to a recent survey (Shah and Joshi, 1987), curved tubes, whether torroidal or helical (i.e., with or without torsional effects) have higher heat transfer rates and friction factors than equivalent straight ducts. These phenomena are the result of increased mixing caused by secondary Dean-type flow due to centrifugal effects. A large number of investigations into ducts with negligible torsion have been completed. The first analytical investigation on flow in a curved duct with a circular cross section was performed by Dean (1927). While many of the later analytical and numerical studies involved more complicated geometries and extensions to heat transfer characteristics, torsion was either neglected or artificially introduced in an effective radius parameter until recently.

One of the first analytical studies to legitimately include the torsion effect was performed by Wang (1981). His analysis used a nonorthogonal coordinate system that complicated the solution process. Germano (1982) introduced an orthogonal coordinate system that has become the standard for later analyses (Germano, 1989; Tuttle, 1990; Thomson, 1996). Previous numerical extensions to heat transfer (Eason et al., 1994) have been limited by the time required to calculate the velocity solution in the duct. Using the velocity solution given by Thomson (1996) allows the velocity field to be calculated in a negligible amount of time.

In this paper a numerical solution of the developing temperature profile in a helical duct with rectangular cross section is obtained for hydrodynamically fully developed flow. The temperature is based on axially constant wall heat flux and a peripherally uniform wall temperature (the H1 boundary condition). This temperature profile is used to determine the local Nusselt number. Comparisons are made with previously obtained results.

Contributed by the Heat Transfer Division for publication in the JOURNAL OF HEAT TRANSFER. Manuscript received by the Heat Transfer Division June 17, 1996; revision received November 13, 1997; Keywords: Augmentation and Enhancement; Forced Convection; Heat Exchangers. Associate Technical Editor: S. Ramadhyani.

Approach

The governing equations are solved to determine the velocity and temperature profile. A coordinate system previously developed by Germano (1982) is used here. The fluid properties for forced convection are approximately constant, so the energy equation may be decoupled from the continuity and momentum equations. The velocity profile previously determined for small curvature and low Dean numbers is used in this analysis. Further observations and assumptions are made which reduce the complexity and generality of the energy equation.

Helical Coordinate System

The duct being considered is a right handed helix as shown in Fig. 1. The centerline of the helix (the axis of the duct) is written in parametric form using the angle of the helix in radians (Φ) as $\vec{R} = R_H \cos \Phi \hat{e}_X + R_H \sin \Phi \hat{e}_Y + P_H \Phi \hat{e}_Z$, where the radius and pitch of the helix are R_H and P_H. The arclength is defined in the usual manner as $d\tilde{s} \equiv \sqrt{d\vec{R} \cdot d\vec{R}}$, thus $\tilde{s} = \Phi\sqrt{R_H^2 + P_H^2}$.

The Frenet formulas for a general space curve define the tangent ($\hat{T} \equiv d\vec{R}/d\tilde{s}$), normal ($\hat{N} \equiv \tilde{\kappa}^{-1} d\hat{T}/d\tilde{s}$), and binormal ($\hat{B} \equiv \hat{T} \times \hat{N}$) directions with respect to the centerline of that curve where the curvature, $\tilde{\kappa}$, is defined to enforce normality. The magnitude of the change in the binormal direction with respect to the centerline is defined as the torsion, $\tilde{\tau}$ ($d\hat{B}/d\tilde{s} \equiv -\tilde{\tau}\hat{N}$). For a regular helix these are determined as $\tilde{\kappa} = R_H/(R_H^2 + P_H^2)$ and $\tilde{\tau} = P_H/(R_H^2 + P_H^2)$. The Frenet triad can then be rewritten using the helix centerline as $\hat{T} = [\tilde{\kappa}(-\sin \Phi \hat{e}_X + \cos \Phi \hat{e}_Y) + \tilde{\tau}\hat{e}_Z]\sqrt{R_H^2 + P_H^2}$, $\hat{N} = -\cos \Phi \hat{e}_X - \sin \Phi \hat{e}_Y$, and $\hat{B} = [\tilde{\tau}(\sin \Phi \hat{e}_X - \cos \Phi \hat{e}_Y) + \tilde{\kappa}\hat{e}_Z]\sqrt{R_H^2 + P_H^2}$.

To avoid the difficulties inherent in a nonorthogonal system, the helical coordinate system introduced by Germano (1982) for a circular cross section and used later by Germano (1989) and Tuttle (1990) for an elliptical cross section and Thomson (1996) for a rectangular cross section is used here. To uncouple the torsion effects, the $\tilde{q} - \tilde{r}$ axes are rotated through a prescribed angle about the tangent direction, $\phi = -\tilde{\tau}\tilde{s} = -\Phi P_H/\sqrt{R_H^2 + P_H^2}$, as Φ increases. Relating any point in the plane normal to $\hat{T}$ to the global coordinate system gives $\vec{Q} = \vec{R}(\tilde{s}) + [\tilde{q} \cos \phi(\tilde{s}) - \tilde{r} \sin \phi(\tilde{s})]\hat{N}(\tilde{s}) + [\tilde{r} \cos \phi(\tilde{s}) + \tilde{q} \sin \phi(\tilde{s})]\hat{B}(\tilde{s})$, which results in the orthogonal metric $d\vec{Q} \cdot d\vec{Q} = d\tilde{q}^2 + d\tilde{r}^2 + d\tilde{s}^2[1 - \tilde{\kappa}\tilde{q} \cos \phi(\tilde{s}) + \tilde{\kappa}\tilde{r} \sin \phi(\tilde{s})]^2$.

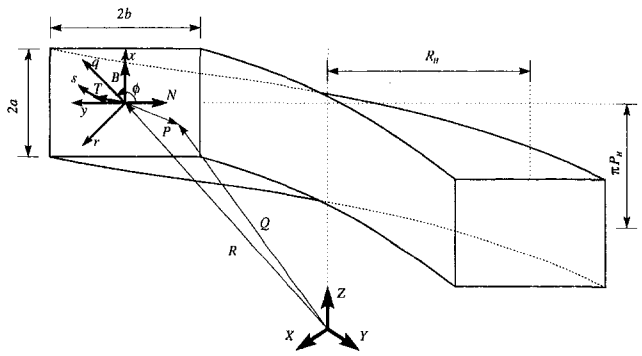

Fig. 1 Helical coordinate system

Formulation

Consider a laminar, incompressible flow through a helical duct of constant cross section neglecting buoyancy. These assumptions uncouple the energy equation from the momentum and continuity equations. Assume also that the flow is time independent. The driving force for the flow is a pressure gradient that is assumed constant in the axial direction of the duct ($\tilde{s}$ in Fig. 1). Such a system corresponds to Poiseuille flow through a helical duct. The velocity component in the $\tilde{s}$, $\tilde{q}$, $\tilde{r}$, $\tilde{x}$, and $\tilde{y}$ directions are denoted as $\tilde{u}$, $\tilde{v}_q$, $\tilde{v}_r$, and $\tilde{v}_x$, and $\tilde{v}_y$, respectively. The temperature at any location in the duct is T. The characteristic velocity, U, is the average velocity in a straight duct with the same cross section and pressure gradient as the helical duct being considered. The characteristic length is the hydraulic diameter, D_H. The dimensionless temperature, θ, is defined in the same way as the thermal entry region of a straight duct.

The dimensionless incompressible continuity equation for any orthogonal coordinate system is

$$\nabla \cdot \vec{V} = 0,$$

the dimensionless momentum equations are

$$(\vec{V} \cdot \nabla)\vec{V} = -\nabla p - \frac{1}{\mathrm{Re}} \nabla \times \nabla \times \vec{V},$$

and the energy equation is

$$\frac{DT}{Dt} = \alpha \nabla^2 T + \frac{\mu}{\rho c} \Omega.$$

From the metric of the helical coordinate system, the following terms apply:

n	1	2	3
ξ_n	s	q	r
h_n	$1 - \kappa q \cos\phi + \kappa r \sin\phi$	1	1
v_n	u	v_q	v_r

Since the q-r axes are rotating with respect to the cross section, the velocities are difficult to interpret, and the boundary conditions are difficult to apply. The equations are converted to a notation which corresponds more directly to the boundaries

Nomenclature

B = binormal unit vector, $\hat{B} = [\tilde{\tau}(\sin\Phi\hat{e}_X - \cos\Phi\hat{e}_Y) + \tilde{\kappa}\hat{e}_Z]\sqrt{R_H^2 + P_H^2}$

C = even eigenfunction, $C_m(t) \equiv (\cosh \lambda_m t/\cosh \frac{1}{2}\lambda_m) - (\cos \lambda_m t/\cos \frac{1}{2}\lambda_m)$

D = substantial derivative, $D/Dt \equiv (\partial/\partial t) + \vec{V}\cdot\nabla$

D = coefficient in axial velocity solution

De = Dean number, $\mathrm{De} \equiv \kappa^{1/2}\,\mathrm{Re}$

D_H = hydraulic diameter (characteristic length), $D_H \equiv (4 \times \text{area})/\text{perimeter} = 4ab/(a+b)$

Nu = Nusselt number, $\mathrm{Nu} \equiv hD_H/k$

N = normal unit vector, $\hat{N} = -\cos\Phi\hat{e}_X - \sin\Phi\hat{e}_Y$

P = vector from cross section origin to arbitrary point in cross section

Pe = Péclet number, $\mathrm{Pe} = \mathrm{Re}\,\mathrm{Pr}$

P_H = pitch of the helix

Pr = Prandtl number, $\mathrm{Pr} \equiv \mu/\rho\alpha$

Q = vector from global origin to arbitrary point in cross section

R = vector from global origin to cross-section origin

R_H = radius of the helix

Re = Reynolds number, $\mathrm{Re} \equiv UD_H\rho/\mu$

S = odd eigenfunction, $S_m(t) \equiv (\sinh \mu_m t/\sinh \frac{1}{2}\mu_m) - (\sin \mu_m t/\sin \frac{1}{2}\mu_m)$

T = temperature

T = tangent unit vector, $\hat{T} = [\tilde{\kappa}(-\sin\Phi\hat{e}_X + \cos\Phi\hat{e}_Y) + \tilde{\tau}\hat{e}_Z]\sqrt{R_H^2 + P_H^2}$

U = average velocity in a straight duct (characteristic velocity)

V = velocity

X, Y, Z = global coordinate system

a = half height of cross section

b = half width of cross section

c = arbitrary vector or scalar

c_p = specific heat

d = differential

d = coefficient in stream function solution

e = unit vector

h = heat transfer coefficient

h = scale factors of orthogonal curvilinear coordinates

k = thermal conductivity

m, n = dummy indices

p = pressure, $p \equiv \tilde{p}/(\rho U^2)$

$\dot{q}''$ = heat flux

q, r = coordinates in helical system, $q \equiv \tilde{q}/D_H$ and $r \equiv \tilde{r}/D_H$

s = arclength, $\tilde{s} = \Phi\sqrt{R_H^2 + P_H^2}$, $s \equiv \tilde{s}/D_H$, $s^* \equiv s/\mathrm{Pe}$

t = time

u = axial velocity component, $u \equiv \tilde{u}/U$

v = cross-sectional (secondary) velocity component, $v \equiv \tilde{v}/U$

x, y = rectangular coordinates, $x \equiv \tilde{x}/D_H$ and $y \equiv \tilde{y}/D_H$

Greek Letters

Λ = aspect ratio of rectangular cross section (height/width), $\Lambda \equiv a/b$

Φ = angle of the helix (in radians)

Ω = viscous dissipation function

α = thermal diffusivity

γ = relative torsion, $\gamma \equiv (\tau/\kappa)\,\mathrm{Re}^{-1}$

θ = dimensionless temperature, $\theta \equiv (T - T_{\text{entry}})k/\overline{\dot{q}''_w}D_H$

κ = curvature, $\tilde{\kappa} = R_H/(R_H^2 + P_H^2)$, $\kappa \equiv \tilde{\kappa}D_H$

λ = eigenvalue of even eigenfunction, $\tanh \frac{1}{2}\lambda + \tan \frac{1}{2}\lambda = 0$

μ = eigenvalue of odd eigenfunction, $\coth \frac{1}{2}\mu - \cot \frac{1}{2}\mu = 0$

μ = viscosity

ξ = orthogonal curvilinear coordinate

ρ = density

τ = torsion, $\tilde{\tau} = P_H/(R_H^2 + P_H^2)$, $\tau \equiv \tilde{\tau}D_H$

ϕ = angle of rotation of the cross-section coordinate system, $\phi(\tilde{s}) \equiv -\int_0^{\tilde{s}} \tilde{\tau}(\tilde{s}')d\tilde{s}'$

ψ = cross-sectional pseudo stream function

ω = reciprocal of scale factor from s direction, $\omega \equiv 1/h_1 = 1/(1 + \kappa y)$

of the duct (x, y, s). Writing q, r, and the secondary velocities in terms of this x-y notation results in

$$q = x \sin \phi - y \cos \phi, \quad r = x \cos \phi + y \sin \phi,$$

$$v_q = v_x \sin \phi - v_y \cos \phi, \quad \text{and} \quad v_r = v_x \cos \phi + v_y \sin \phi.$$

The related partial derivative terms are then determined as

$$\frac{\partial}{\partial q} \Rightarrow \sin \phi \frac{\partial}{\partial x} - \cos \phi \frac{\partial}{\partial y},$$

$$\frac{\partial}{\partial r} \Rightarrow \cos \phi \frac{\partial}{\partial x} + \sin \phi \frac{\partial}{\partial y},$$

$$\text{and} \quad \frac{\partial}{\partial s} \Rightarrow \frac{\partial}{\partial s} - \tau\left(x \frac{\partial}{\partial y} - y \frac{\partial}{\partial x}\right).$$

All partial derivatives with respect to s in the new coordinate system contain an additional term based on the dimensionless torsion.

The fluid properties are considered to be temperature independent so that the energy and velocity equations are uncoupled. The problem is simplified further by assuming that the velocity field is fully developed when the heat is first applied (velocity terms are axially invariant). Even for thermally and hydrodynamically developing flow, this is a good assumption for fluids with large Prandtl numbers (Kays and Crawford, 1993). A pseudo stream function can be defined to satisfy continuity in the cross section as $\partial\psi/\partial y \equiv \mathrm{Re} v_x/\omega + \gamma\ \mathrm{De}^2\ yu$ and $-\partial\psi/\partial x \equiv \mathrm{Re} v_y/\omega - \gamma\ \mathrm{De}^2\ xu$. Substituting the stream function definition into the momentum equations and then rearranging results in (Thomson, 1996):

$$\frac{1}{\omega}\nabla^2 u = \mathrm{Re}\frac{\partial p}{\partial s} + \mathrm{De}^2\,\gamma\left(y\frac{\partial p}{\partial x} - x\frac{\partial p}{\partial y}\right) + \frac{\partial u}{\partial x}\frac{\partial \psi}{\partial y} - \frac{\partial u}{\partial y}\frac{\partial \psi}{\partial x} - \kappa\left(\omega u\frac{\partial \psi}{\partial x} + \frac{\partial u}{\partial y}\right) - \kappa^2\omega u + 2\kappa^2\omega^2\gamma\left(y\frac{\partial^2\psi}{\partial x\partial y} + x\frac{\partial^2\psi}{\partial y^2} - \frac{\partial\psi}{\partial y}\right) - \kappa\omega\gamma^2\,\mathrm{De}^2\left(y^2\frac{\partial^2 u}{\partial x^2} + x^2\frac{\partial^2 u}{\partial y^2} + 2u - 2xy\frac{\partial^2 u}{\partial x\partial y}\right) - 3\kappa^3\omega^3 x\gamma\frac{\partial\psi}{\partial y} + \kappa\omega\gamma(\nabla^2\psi + \mathrm{De}^2\,xu^2) - 3\kappa^3\omega^3\gamma^2\,\mathrm{De}^2\,x^2 u + \kappa^2\omega^2\gamma^2\,\mathrm{De}^2\left(3xy\frac{\partial u}{\partial x} - 2x^2\frac{\partial u}{\partial y}\right) \quad (1)$$

and

$$\frac{1}{\omega}\nabla^4\psi = \left[\frac{\partial\psi}{\partial y}\frac{\partial}{\partial x} + \left(2\kappa - \frac{\partial\psi}{\partial x}\right)\frac{\partial}{\partial y}\right] \times \left[\nabla^2\psi - \gamma\,\mathrm{De}^2\left(y\frac{\partial u}{\partial y} + x\frac{\partial u}{\partial x} + 3u\right)\right] + \frac{2}{\omega}\mathrm{De}^2 u\frac{\partial u}{\partial x} + \gamma\,\mathrm{De}^2\left[\frac{4}{\omega}\nabla^2 u + \frac{1}{\omega}\left(x\frac{\partial}{\partial x} + y\frac{\partial}{\partial y}\right)(\nabla^2 u)\right] + \left(y\frac{\partial u}{\partial y} - x\frac{\partial u}{\partial x}\right)\frac{\partial^2\psi}{\partial x\partial y} + x\frac{\partial u}{\partial y}\frac{\partial^2\psi}{\partial x^2} - y\frac{\partial u}{\partial x}\frac{\partial^2\psi}{\partial y^2} + 3\kappa y\nabla^2 u - 2\kappa\left(y\frac{\partial^2 u}{\partial y^2} + x\frac{\partial^2 u}{\partial x\partial y} + 2\frac{\partial u}{\partial y}\right)\Bigg] + O(\kappa^3), \quad (2)$$

subject to the rectangular, no slip boundary conditions

$$@x = \pm\frac{1+\Lambda}{4}, \quad \psi = 0, \quad \frac{\partial\psi}{\partial x} = 0, \quad u = 0$$

$$\text{and} \quad @y = \pm\frac{1+\Lambda}{4\Lambda}, \quad \psi = 0, \quad \frac{\partial\psi}{\partial y} = 0, \quad u = 0. \quad (3)$$

For negligible viscous dissipation, the steady flow energy equation may be written as

$$\frac{4}{(1+\Lambda)^2}\left(\frac{\partial^2\theta}{\partial x^2} + \Lambda^2\frac{\partial^2\theta}{\partial y^2}\right) + \omega^2\gamma^2\,\mathrm{De}^2\,\kappa\left(\Lambda^2 x^2\frac{\partial^2\theta}{\partial y^2} + \frac{y^2}{\Lambda^2}\frac{\partial^2\theta}{\partial x^2} - y\frac{\partial\theta}{\partial y} - x\frac{\partial\theta}{\partial x} - 2xy\frac{\partial^2\theta}{\partial x\partial y}\right) + \omega^3\gamma^2\,\mathrm{De}^2\,\kappa^2 x\frac{1+\Lambda}{2} \times \left(\frac{y}{\Lambda}\frac{\partial\theta}{\partial x} - x\Lambda\frac{\partial\theta}{\partial y}\right) + \kappa\omega\frac{2\Lambda}{1+\Lambda}\frac{\partial\theta}{\partial y}$$

Nomenclature (cont.)

Subscripts

- 1, 2 . . . = order of the component, direction
- H = helical component
- T = torroidal component
- m, n = dummy indices
- q, r, s, x, y = component in the designated direction
- w = at the wall

Symbols

- # = arbitrary character, below
- #″ = second derivative of #
- $\vec{\#}$ = vector, #
- $\bar{\#}$ = averaged quantity, #
- $\hat{\#}$ = unit vector, #
- $\tilde{\#}$ = dimensional quantity, #
- #* = dimensionless entry length, #
- ∂ = partial derivative of
- Δ = step size in a direction
- ∇ = gradient operator, $\nabla = (1/h_1)(\partial/\partial\xi_1)\hat{e}_1 + (1/h_2)(\partial/\partial\xi_2)\hat{e}_2 + (1/h_3)(\partial/\partial\xi_3)\hat{e}_3$
- $\nabla\cdot$ = divergence operator, $\nabla\cdot\vec{c} = (1/h_1h_2h_3)[(\partial/\partial\xi_1)(c_1h_2h_3) + (\partial/\partial\xi_2)(c_2h_3h_1) + (\partial/\partial\xi_3)(c_3h_1h_2)]$
- $\nabla\times$ = curl operator, $\nabla\times\vec{c} = (1/h_1h_2h_3) \times \begin{vmatrix} \hat{e}_1h_1 & \hat{e}_2h_2 & \hat{e}_3h_3 \\ \partial/\partial\xi_1 & \partial/\partial\xi_2 & \partial/\partial\xi_3 \\ h_1c_1 & h_2c_2 & h_3c_3 \end{vmatrix}$
- $\bar{\nabla}^2$ = Laplacian operator, $\bar{\nabla}^2 c = (1/h_1h_2h_3)[(\partial/\partial\xi_1)((h_2h_3/h_1)(\partial c/\partial\xi_1)) + (\partial/\partial\xi_2)((h_3h_1/h_2)(\partial c/\partial\xi_2)) + (\partial/\partial\xi_3)((h_1h_2/h_3)(\partial c/\partial\xi_3))]$
- ∇^2 = Laplacian operator in the x-y plane, $(\partial^2/\partial x^2) + (\partial^2/\partial y^2)$
- ∇^4 = Biharmonic operator in the x-y plane, $(\partial^4/\partial x^4) + 2(\partial^4/\partial x^2\partial y^2) + (\partial^4/\partial y^4)$

$$= u\omega \frac{\partial \theta}{\partial s} + \frac{4\Lambda\omega \,\mathrm{Pr}}{(1+\Lambda)^2}\left(\frac{\partial \psi}{\partial y}\frac{\partial \theta}{\partial x} - \frac{\partial \psi}{\partial x}\frac{\partial \theta}{\partial y}\right)$$

$$- \frac{1}{\mathrm{Pe}}\left[2\omega^2\gamma\kappa\,\mathrm{Re}\left(\frac{y}{\Lambda}\frac{\partial^2\theta}{\partial x \partial s} + x\Lambda\frac{\partial^2\theta}{\partial y \partial s}\right)\right.$$

$$\left. + \omega^3\gamma\kappa^2\,\mathrm{Re}x\frac{1+\Lambda}{2}\frac{\partial \theta}{\partial s}\right] - \frac{1}{\mathrm{Pe}^2}\omega^2\frac{\partial^2\theta}{\partial s^2}. \quad (4)$$

The H1 boundary condition, implying axially constant wall heat flux and peripherally uniform wall temperature, is imposed as

$$\Lambda^2\overline{\left(\frac{\partial \theta}{\partial y}\right)}\bigg|_{y=-(1/2)} - \Lambda^2\overline{\left(\frac{\partial \theta}{\partial y}\right)}\bigg|_{y=(1/2)}$$

$$+ \overline{\left(\frac{\partial \theta}{\partial x}\right)}\bigg|_{x=-(1/2)} - \overline{\left(\frac{\partial \theta}{\partial x}\right)}\bigg|_{x=(1/2)}$$

$$= (1+\Lambda)^2 \quad \text{at} \quad s^* > 0,$$

$$\theta_w = \theta_w(s^*) \quad \text{at} \quad s^* > 0,$$

and

$$\theta(x, y) = 0 \quad \text{at} \quad s^* = 0. \quad (5)$$

Solution Technique

The velocity field was previously determined for noncreeping ($\mathrm{Re}^2 \gg 1$), low Dean number flows through ducts with small curvature ($\kappa \ll 1$) and relative torsion, at most on the order of one ($\gamma \leq 1$) (Thomson, 1996). The method of successive approximations was used to convert the two nonlinear equations into a number of linearized equations. The axial velocity and pseudo stream function, Eqs. (1) and (2), were decomposed into harmonic and biharmonic equations, respectively. The individual equations were solved using known eigenfunction expansions. All equations were converted to the dimensionless square $-\frac{1}{2} \leq x \leq \frac{1}{2}$ and $-\frac{1}{2} \leq y \leq \frac{1}{2}$. The pseudo stream function and velocity are written as

$$\psi \approx \mathrm{De}^2(\psi_{1T} + \gamma\psi_{1H}) + \mathrm{De}^4(\psi_{2T} + \gamma\psi_{2HA} + \gamma^2\psi_{2HB}) \quad (6)$$

and

$$u \approx u_0 + \mathrm{De}^2(u_{1T} + \gamma u_{1H}) + \mathrm{De}^4(u_{2T} + \gamma u_{2HA} + \gamma^2 u_{2HB}). \quad (7)$$

The linear components of the equation are determined as

$$u_0 = \sum_{m=1}^{\infty}\sum_{n=1}^{\infty} D_{0,mn}\cos(2m-1)\pi x \cos(2n-1)\pi y,$$

$$u_{1T} = \sum_{m=1}^{\infty}\sum_{n=1}^{\infty} D_{1T,mn}\cos(2m-1)\pi x \sin 2n\pi y,$$

$$\psi_{1T} = \sum_{m=1}^{\infty}\sum_{n=1}^{\infty} d_{1T,mn}S_m(x)C_n(y),$$

$$u_{1H} = \sum_{m=1}^{\infty}\sum_{n=1}^{\infty} D_{1H,mn}\sin 2m\pi x \sin 2n\pi y,$$

$$\psi_{1H} = \sum_{m=1}^{\infty}\sum_{n=1}^{\infty} d_{1H,mn}C_m(x)C_n(y),$$

$$u_{2T} = \sum_{m=1}^{\infty}\sum_{n=1}^{\infty} D_{2T,mn}\cos(2m-1)\pi x \cos(2n-1)\pi y,$$

$$\psi_{2T} = \sum_{m=1}^{\infty}\sum_{n=1}^{\infty} d_{2T,mn}S_m(x)S_n(y),$$

$$u_{2HA} = \sum_{m=1}^{\infty}\sum_{n=1}^{\infty} D_{2HA,mn}\sin 2m\pi x \cos(2n-1)\pi y,$$

$$\psi_{2HA} = \sum_{m=1}^{\infty}\sum_{n=1}^{\infty} d_{2HA,mn}C_m(x)S_n(y),$$

$$u_{2HB} = \sum_{m=1}^{\infty}\sum_{n=1}^{\infty} D_{2HB,mn}\cos(2m-1)\pi x \cos(2n-1)\pi y,$$

$$\psi_{2HB} = \sum_{m=1}^{\infty}\sum_{n=1}^{\infty} d_{2HB,mn}S_m(x)S_n(y),$$

where all of the coefficients of the solution are determined by substituting into the partial differential equations, separating by like powers of the Dean number and torsion parameter, and taking the inner products as described by Thomson (1996).

For large Péclet numbers, the final two terms in Eq. (4) may be neglected. This is a very reasonable assumption for water (with $\mathrm{Pr} \sim 10$) in noncreeping flow (as required by the velocity solution). This assumption eliminates axial conduction from the equation so marching techniques may be used in the axial direction. Also, no axial boundary condition is required at the end of the duct. The axial direction of the energy, Eq. (4), is discretized using the DuFort-Frankel scheme, which is similar to that described by Hoffman and Chiang (1993). At each cross section of the duct, the equation is discretized by a standard second-order central difference scheme. The gradient boundary condition in the cross section is enforced by a second-order forward or backward difference formulation, depending on the boundary involved. Each step in the axial direction requires the previous two axial steps. The entry condition is used for the first two axial steps to preclude the need for a separate starter algorithm.

The axially local, peripherally averaged Nusselt number, Nu, can be determined as

$$\mathrm{Nu}(s^*) = 1/(\overline{\theta_w} - \theta_{\mathrm{mixed}}) \quad (8)$$

where the dimensionless mixed mean temperature is found as

$$\theta_{\mathrm{mixed}} = \int_{-1/2}^{1/2}\int_{-1/2}^{1/2} u\theta\,dx\,dy \Big/ \int_{-1/2}^{1/2}\int_{-1/2}^{1/2} u\,dx\,dy.$$

The solution should proceed for a given length of duct or until the Nusselt number approaches a steady value (thermally fully developed).

For all of the solutions shown, the cross section of the duct is discretized using a 41×41 grid, which was found to provide sufficient accuracy in a point successive over relaxation (PSOR) solution of the velocity (Thomson, 1996). The maximum allowable step size in the axial direction depends on the Dean number, relative torsion parameter, and cross sectional aspect ratio. The maximum axial step size used for any of the solutions shown is $\Delta s^* = 5 \times 10^{-5}$. For combinations of parameters that did not converge, the step size was decreased until convergence was achieved. To estimate the error in the results, comparisons were made between the Nusselt number calculated using the standard number of grid points and an increased number of grid points. For each case, the maximum error is shown at several locations along the entry length ($s^* \geq 10^{-4}$, 10^{-3}, 10^{-2}, and 10^{-1}). The maximum differences in Nu between a 41×41 grid and an 81×81 grid (both with $\Delta s^* = 1 \times 10^{-5}$) were 6.3 percent, 4.3 percent, 1.1 percent, and 0.50 percent. The maximum differences in Nu between $\Delta s^* = 1 \times 10^{-5}$ and $\Delta s^* = 1 \times 10^{-6}$ (both with a 41×41 cross sectional grid) were 1.8 percent, 0.17 percent, 1.1×10^{-2} percent, and 1.8×10^{-4} percent. The maximum differences in Nu when using a 41×41 grid, $\Delta s^* = 1 \times 10^{-5}$ and an 81×81 grid, $\Delta s^* = 1 \times 10^{-6}$ were 7.1 percent, 4.5 percent, 1.2 percent, and 0.50 percent.

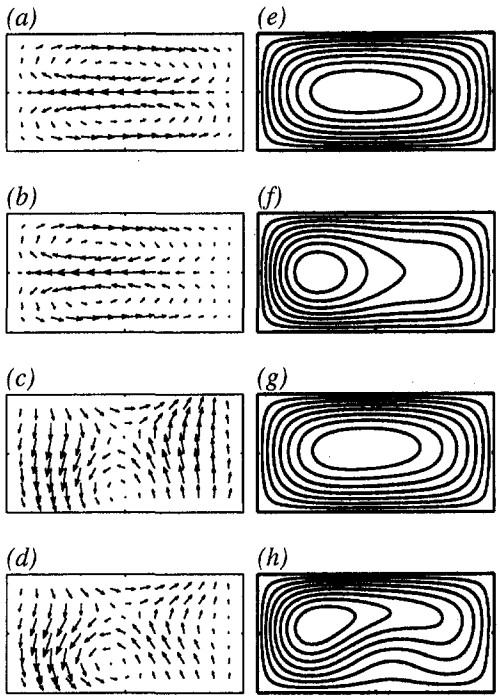

Fig. 2 Secondary flow (*a*, *b*, *c*, *d*) and axial velocity (*e*, *f*, *g*, *h*), Λ = 0.5. (*a*, *e*) De = 20, γ = 0; (*b*, *f*) De = 35, γ = 0; (*c*, *g*) De = 20, γ = 0.5; (*d*, *h*) De = 35, γ = 0.5.

Results and Discussion

A sample solution of the velocity profile is shown in Fig. 2. It is clear that torroidal effects cause a secondary, two-cell flow in the duct cross section, similar to that in a circular helical duct (Thomson, 1996). The fluid in the center of the cross section has a higher axial velocity than the fluid near the walls. Inertial effects invoked by the curvature of the duct cause this fluid to move toward the outside wall. Fluid moves back toward the inside wall along the upper and lower walls to preserve continuity within the cross section. Torsional effects distort this two cell pattern toward a one cell pattern, similar to that found in a straight twisted duct. While the torsional geometry still creates cross-sectional flow, less mixing between the center of the cross section and the walls occurs for higher torsion. These secondary flow profiles strongly influence the heat transfer in helical ducts.

The numerical heat transfer method was calibrated with straight duct flow (κ = 0 and γ = 0) results made available by Shah and Bhatti (1987). The solution for the flow through a straight duct was dependent on only one parameter, Λ, the aspect ratio of the cross section. For flow through a torroidal duct, the Dean number became an additional parameter. The flow through a helical duct introduced another parameter, the relative torsion γ. Ideally, only one additional parameter, the Prandtl number, would need to be introduced to the helical flow solution to characterize the heat transfer effects. (Only results pertaining to Pr = 10 are shown within.) However, the curvature, κ, still appears explicitly in the energy equation. Several tests were made to see if the curvature really needed to be varied in subsequent experiments. Figure 3 shows that for a torroidal duct in the range of Dean numbers available from the velocity solution, the Nusselt number varies little with curvature for $\kappa \leq 0.3$. The correspondence is better at lower Dean numbers. For a helical duct, curvature has a more noticeable effect on the Nusselt number (Fig. 4). However, the differences decrease dramatically in the range of torsion usually encountered (i.e., $\gamma < 0.1$). More importantly, the differences become negligible as the temperature becomes fully developed. Since the

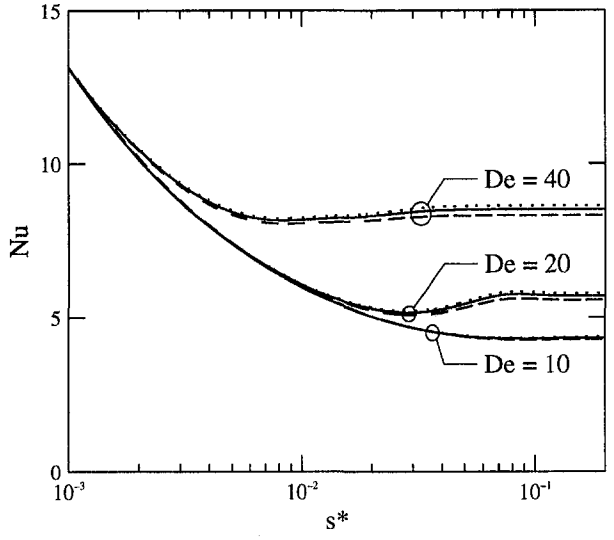

Fig. 3 Variation of the Nusselt number with curvature in a torroidal duct (Λ = 0.5, γ = 0). . . . κ = 0.001, —— κ = 0.1, - - κ = 0.3.

explicit effects of the curvature (as opposed to the effects of the curvature embedded in the Dean number) are nearly negligible, a constant curvature of κ = 0.1 was used for the remainder of the trials. Fully developed Nusselt numbers for a range of ducts configurations are shown in Table 1.

The variation of the Nusselt number with the Dean number in the thermally developing region is shown in Fig. 5 for the torroidal case. The oscillations in the developing Nusselt number that appear at higher Dean numbers have been observed for all cross sections and boundary conditions previously considered (Shah and Joshi, 1987). For a straight duct without the secondary flow, the peripherally averaged Nusselt number asymptotically decreases as the fluid near the wall warms up. Propagation of the heat from the wall into the interior is due to conduction alone for the constant property straight duct case. For the torroidal duct, however, the cross flow from the velocity solution brings cooler fluid (not yet appreciably affected by conduction) from the interior of the duct toward the outside wall. The cooler fluid impinging on the outside wall causes an increase in the Nusselt number until the warmer fluid originally near the inside wall reaches the outside wall. Smaller oscilla-

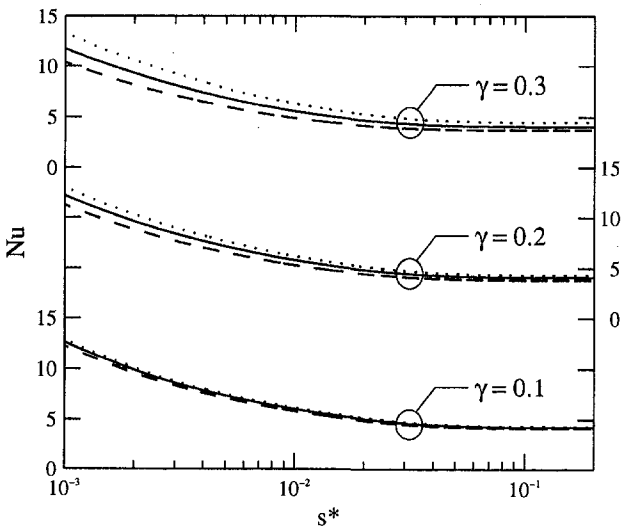

Fig. 4 Variation of the Nusselt number with curvature in a helical duct (Λ = 0.5, De = 20). . . . κ = 0.001, —— κ = 0.1, - - κ = 0.3.

Table 1 Fully developed Nusselt numbers for helical ducts, H1 boundary condition

	$Nu_{fully\ developed}$											
	De = 5				De = 20				De = 35			
Λ	γ = 0	γ = 0.05	γ = 0.1	γ = 0.2	γ = 0	γ = 0.05	γ = 0.1	γ = 0.2	γ = 0	γ = 0.05	γ = 0.1	γ = 0.2
1/10	6.79	6.78	6.76	6.69	6.80	6.72	6.58	6.35	7.14	6.72	6.40	6.12
1/5	5.75	5.75	5.74	5.71	5.95	5.86	5.74	5.53	7.13	6.03	5.71	5.61
1/3	4.81	4.81	4.81	4.80	5.60	5.12	4.90	4.70	7.62	5.26	4.94	
1/2	4.14	4.14	4.14	4.13	5.71	4.51	4.24	4.09	7.86	4.71		
2/3	3.82	3.82	3.81	3.80	5.79	4.18	3.88	3.73	8.08			
3/4	3.74	3.74	3.73	3.71	5.78	4.09	3.77	3.60	8.18			
9/10	3.67	3.66	3.65	3.63	5.72	4.01	3.66	3.46	8.23			
1	3.66	3.65	3.64	3.62	5.67	4.01	3.64	3.42	8.11			
10/9	3.67	3.67	3.66	3.63	5.61	4.04	3.65	3.44	7.86			
4/3	3.75	3.75	3.74	3.71	5.50	4.15	3.76	3.57	7.17			
3/2	3.83	3.83	3.82	3.80	5.44	4.26	3.87	3.70	6.72	3.89		
2	4.15	4.15	4.15	4.14	5.38	4.54	4.23	4.07	6.13	4.48	4.19	
3	4.81	4.81	4.81	4.80	5.40	5.02	4.86	4.68	6.37	5.07	4.84	4.96
5	5.75	5.75	5.74	5.71	5.89	5.80	5.70	5.51	6.40	5.82	5.62	5.54
10	6.78	6.78	6.76	6.70	6.82	6.72	6.57	6.34	7.02	6.63	6.34	6.09

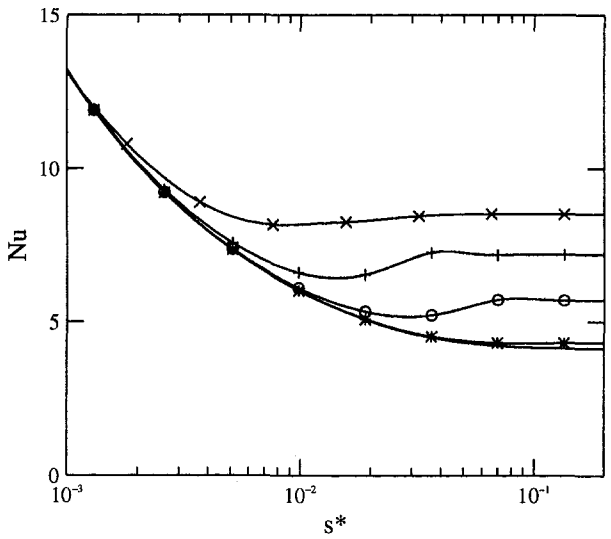

Fig. 5 Variation of the Nusselt number with the Dean number in a torroidal duct (Λ = 0.5, γ = 0). —— De = 5, -*- De = 10, -○- De = 20, -+- De = 30, -×- De = 40.

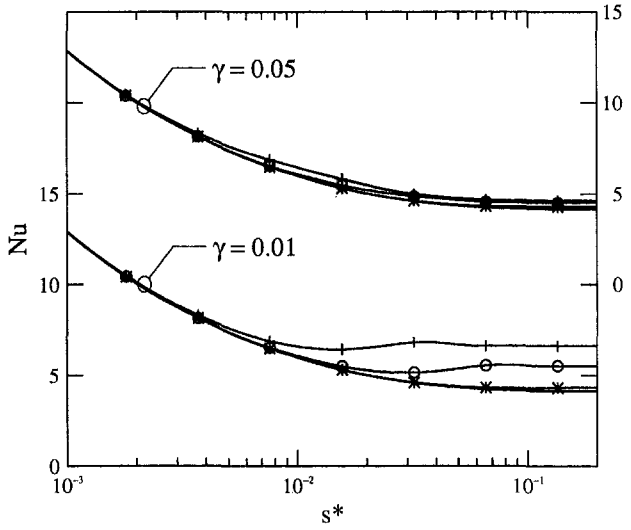

Fig. 6 Variation of the Nusselt number with the Dean number in a helical duct (Λ = 0.5). —— De = 5, -*- De = 10, -○- De = 20, -+- De = 30.

tions occur when other cool pockets impinge on the wall. A stronger secondary flow, present at moderate Dean numbers, results in larger oscillations. At higher Dean numbers, the oscillations decrease in magnitude because mixing results in weaker transient cool pockets. The oscillations eventually damp out to a Nusselt number higher than the straight duct value due to the continual mixing of the fluid in the cross section.

For rectangular cross sections of any aspect ratio, increasing the Dean number causes a significant increase in the Nusselt number for the torroidal configuration. However, previous results (Thomson, 1996) showed that the movement of the higher velocity fluid toward the outside wall increases the friction factor in these ducts as well. To determine whether a torroidal configuration is beneficial for heat transfer, a comparison between these effects must be made. For example, raising the Dean number from 5 to 40 for a cross section of Λ = 0.5 causes the fully developed Nusselt number to increase by 100 percent, while the friction factor is increased by only 10 percent. Thus, the secondary flows in these hypothetical torroidal ducts significantly enhance the heat transfer characteristics for a minimal increase in required pumping.

The necessity of a real duct configuration requires nonnegligible torsion to be included in the analysis. For very small torsion, the limit provided from the torroidal solution is approached. For larger torsion, however, the Nusselt number changes dramatically. As seen in Fig. 6 for the case of moderate torsion, even at higher Dean numbers the Nusselt number drops considerably compared to the torroidal duct. This should be expected from the velocity profile. While secondary flow still occurs for the helical duct, less flow is directed from the interior toward the walls. Moreover, the friction factor increases in a helical duct compared to a torroidal duct (Thomson, 1996). This means that extreme helicity should be avoided in applications where heat transfer needs to be enhanced while minimizing the pumping requirements. The duct should be shaped as close to the torroidal model as physically possible.

The variations of the Nusselt number for several cross-sectional aspect ratios are shown in Figs. 7 and 8. As expected from the straight duct results, cross sections with more extreme aspect ratios generally have greater Nusselt numbers at smaller Dean numbers because of the shorter distance of the center to the closest wall. For these smaller Dean number cases with less secondary flow, the orientation of the cross section with respect

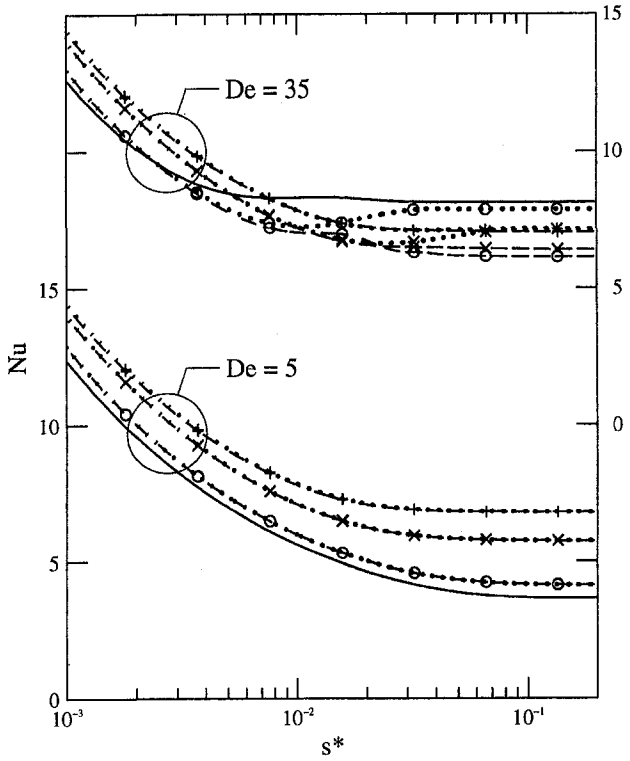

Fig. 7 Variation of the Nusselt number with the aspect ratio of the cross section in a torroidal duct (γ = 0). ··+·· Λ = 0.1, ··×·· Λ = 0.2, ··○·· Λ = 0.5, —— Λ = 1, -○- Λ = 2, -×- Λ = 5, -+- Λ = 10.

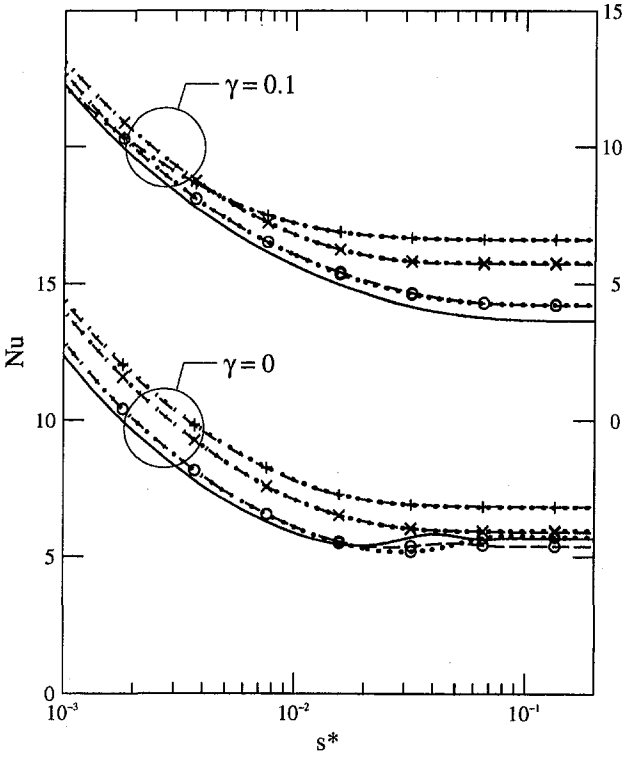

Fig. 8 Variation of the Nusselt number with the aspect ratio of the cross section in a helical duct (De = 20). ··+·· Λ = 0.1, ··×·· Λ = 0.2, ··○·· Λ = 0.5, —— Λ = 1, -○- Λ = 2, -×- Λ = 5, -+- Λ = 10.

to the axis of the helix is not important. For larger Dean numbers with purely torroidal flow or small torsion, the horizontal alignment (i.e., with the longer length of the cross section perpendicular to the axis of the helix) results in increased heat transfer compared to the vertical alignment. This is due to the greater centrifugal effect of this configuration, which increases the magnitude of the secondary velocity. The cross-sectional aspect ratio required for an optimal Nusselt number is Dean number dependent. At smaller Dean numbers, more extreme cross sections give greater Nusselt numbers than less extreme cross sections because the distance to the closest wall is small. As the Dean number increases, the Nusselt number of less extreme cross sections increases faster since the greater mixing decreases the importance of physical distance from the wall. The horizontal alignment also allows better stacking, resulting in lower torsion parameters than are physically possible for the vertically aligned ducts. As torsion increases, it begins to dominate the secondary velocity profile, and the cross section's angle of orientation loses significance when compared to the aspect ratio.

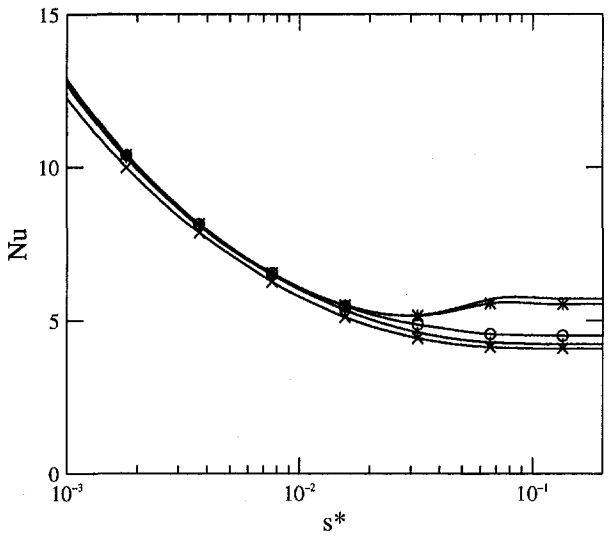

Fig. 9 Variation of the Nusselt number with the relative torsion parameter in a helical duct (Λ = 0.5, De = 20). —— γ = 0, -*- γ = 0.01, -○- γ = 0.05, -+- γ = 0.1, -×- γ = 0.2.

The effect of the relative torsion parameter on the Nusselt number is shown explicitly in Fig. 9. For the torroidal duct, increasing the Dean number increases the Nusselt number. As the torsion is increased, however, the heat transfer does not increase as much at higher Dean numbers. Increasing the torsion further may actually cause the heat transfer to be worse than in a straight duct. While this may seem counter intuitive, it can be explained as follows. For straight rectangular ducts, the center is only half the distance of the shortest side (say a) away from the walls. Heat must propagate through a before the center is affected. For the twisted profile that the torsion causes in extreme helical ducts, the fluid near the walls tends to remain near the walls (as in straight duct flow). Moreover, since the fluid continuously rotates about the center, the fluid, initially only a away from the center, will also be b and $(a^2 + b^2)^{1/2}$ (for example) away from the center at certain locations along the axial length. The fluid in the center can effectively be at an angularly averaged distance which is larger than a or b.

Conclusion

The continuity, momentum, and energy equations were written in the revised helical coordinate system. Boundary conditions were established corresponding to a helical duct of rectangular cross section. Simplifying assumptions included a fully developed velocity profile; time independent, laminar flow; temperature independent properties; and constant heat flux (H1) boundary condition. The assumptions uncoupled the energy equation from the momentum and continuity equations. A pre-

viously determined velocity profile, valid for fully developed low Dean number flows, was used in the analysis.

The energy equation was discretized using the DuFort-Frankel finite difference method. Preliminary tests indicated that the curvature of the duct did not alter the Nusselt number significantly (as an independent parameter) for the small curvatures allowed by the velocity solution. However, the curvature of the duct is important in its effect on the Dean number.

Various helical and torroidal ducts were investigated. The hypothetical torroidal duct was found to have a large increase in the Nusselt number with a mild increase in the friction factor compared to a straight duct of the same cross section. The oscillatory pattern in the developing Nusselt numbers observed by other investigators was observed in the present solution as well. Torsion in the duct decreases the heat transfer characteristics while increasing the friction factor compared to a torroidal duct. The nonplanarity of the helical coil should be minimized if the Nusselt number is to remain high. Also, a rectangular duct with its longer side oriented horizontally (perpendicular to the axis of the helix) was seen to have increased heat transfer compared to a duct with a vertically oriented cross section. Since this also allows the torsion of the duct to be reduced by decreasing the pitch of the helix, this arrangement is very beneficial.

Acknowledgments

This work was supported by the Texas Advanced Technology Program, Grant No. 003604-041 and 056.

References

Bayazitoglu, Y., and Cerny, R., 1992, "Vaporization of Molten-Copper Drops Due to Alternating Electromagnetic Field," *Journal of Materials Processing and Manufacturing Science,* Vol. 1, No. 2, pp. 227–244.

Bayazitoglu, Y., and Cerny, R., 1994, "Numerical Simulation of Electromagnetic Melting and Evaporation of Spherical Metal Particles," *Numerical Heat Transfer,* Part A, Vol. 25, No. 2, pp. 135–150.

Dean, W. R., 1927, "Note on the Motion of Fluid in a Curved Pipe," *Philosophical Magazine,* Series 7, Vol. 4, No. 20, pp. 208–223.

Eason, R. M., Bayazitoglu, Y., and Meade, A. J., Jr., 1994, "Enhancement of Heat Transfer in Square Helical Ducts," *International Journal of Heat and Mass Transfer,* Vol. 37, No. 14, pp. 2077–2087.

Germano, M., 1982, "On the Effect of Torsion on a Helical Pipe Flow," *Journal of Fluid Mechanics,* Vol. 125, pp. 1–8.

Germano, M., 1989, "The Dean Equations Extended to a Helical Pipe Flow," *Journal of Fluid Mechanics,* Vol. 203, pp. 289–305.

Hoffmann, K. A., and Chiang, S. T., 1993, *Computational Fluid Dynamics for Engineers,* Vol. 1, Engineering Education System, Wichita, KS.

Kays, W. M., and Crawford, M. E., 1993, *Convective Heat and Mass Transfer,* McGraw-Hill, New York.

Shah, R. K., and Bhatti, M. S., 1987, "Laminar Convective Heat Transfer in Ducts," Chap. 3 in *Handbook of Single-Phase Convective Heat Transfer,* S. Kakac, R. K. Shah, and W. Aung, eds., John Wiley & Sons, Inc., New York.

Shah, R. K., and Joshi, S. D., 1987, "Convective Heat Transfer in Curved Ducts," chap. 5 in *Handbook of Single-Phase Convective Heat Transfer,* S. Kakac, R. K. Shah, and W. Aung, eds., John Wiley & Sons, Inc., New York.

Stickel, V. G., Jr., and Bayazitoglu, Y., 1995, "Sublimation of an Electrically Conducting Droplet Through the Use of an External Alternating Magnetic Field," *Journal of Metallurgical and Materials Transactions B,* Vol. 26, pp. 1209–1216.

Thomson, D. L., 1996, "Low Dean Number Flows in Helical Ducts of Rectangular Cross Section," M.S. thesis, Rice University, Houston, TX.

Tuttle, E. R., 1990, "Laminar Flow in Twisted Pipes," *Journal of Fluid Mechanics,* Vol. 219, pp. 545–570.

Wang, C. Y., 1981, "On the Low-Reynolds-Number Flow in a Helical Pipe," *Journal of Fluid Mechanics,* Vol. 108, pp. 185–194.

Spray Cooling Enhancement by Addition of a Surfactant

Y. M. Qiao

S. Chandra
chandra@mie.utoronto.ca

Department of Mechanical and Industrial Engineering, University of Toronto, Toronto, Ontario, Canada, M5S 3G8

An experimental study was done on the effect of dissolving a surfactant in water sprays used to cool a hot surface. A copper surface was heated to an initial temperature of 240°C and then rapidly cooled using a spray of either pure water or an aqueous solution containing 100 ppm by weight of sodium dodecyl sulfate. The variation of surface temperature was measured during cooling, and spray impact was photographed. Addition of the surfactant was found to enhance nucleate boiling heat flux by up to 300 percent. The surface temperature required to initiate vapor bubble nucleation was reduced from 118°C to 103°C. These effects were attributed to the surfactant promoting bubble nucleation and foaming in spray droplets. Nucleate boiling heat transfer enhancement was observed at all liquid mass fluxes and droplet velocities in the range of our experiments. The surfactant slightly reduced transition boiling heat transfer, and also reduced the temperature at which spray droplets started to wet the surface. Changing the orientation of the surface with respect to gravity had no effect on heat transfer.

1 Introduction

Spraying droplets of water on a hot surface provides very high heat transfer rates at a relatively low surface temperature, making spray cooling a very useful technique in a number of industrial applications such as the quenching of metal slabs during continuous casting, emergency core cooling of nuclear reactors, electronic cooling, and fire extinguishment using sprinkler systems. The importance of these applications has motivated research into understanding the mechanism of heat removal by sprays and developing methods to enhance heat transfer. One method of improving spray cooling efficiencies, into which little research has been done, is by dissolving additives (such as surfactants) in the water.

Adding surfactants, commonly known as "wetting agents," to water sprays is known to improve their fire suppression abilities (Bryan, 1993). However, the mechanism by which this happens is not well understood. Most experimental studies into the use of additives to enhance boiling heat transfer have investigated pool or flow boiling rather than spray cooling. All these studies have shown that heat transfer is significantly enhanced by the addition of a surfactant. However, there is no agreement as to the mechanism responsible for this increase and several conflicting theories have been proposed. Much of the experimental data has been tabulated and discussed by Wu et al. (1995). The earliest hypothesis was that reduction in surface tension caused by the surfactant enhances nucleate pool boiling (Morgan et al. 1949). However, additives that did not change surface tension were also found to promote pool boiling (Lowery and Westwater, 1957; Jontz and Myers, 1960) suggesting that the increase in heat transfer was due to solute particles promoting nucleation in the liquid. Heat transfer to water films flowing on heated vertical plates was found to increase linearly with surfactant concentration (Shah and Darby, 1973), but the increase in heat transfer could not be correlated with changes in surface tension and was attributed to foaming in the liquid. Despite this, Shibayama et al. (1980) measured heat transfer from a hot surface to an impinging water jet and correlated increases in heat transfer coefficient due to adding surfactants with reductions in surface tension. Other proposed reasons for heat transfer enhancement include the following: local increases in viscosity because of the surfactant (Dunskus and Westwater, 1961); changes in "dynamic surface tension" because of variation in surfactant concentration at the surface of expanding vapor bubbles (Yang and Maa, 1983; Tzan and Yang, 1990; Yang, 1990); and increased convection at the heater surface (Frost and Kippenhan, 1967; Ammerman and You, 1996)

To determine which of these effects is relevant to spray cooling, we have examined in an earlier study (Qiao and Chandra 1997) the effect of adding a surfactant (sodium dodecyl sulfate (SDS)) to 2 mm diameter water droplets deposited individually on a hot stainless steel surface. Experiments were done using solutions containing 100 ppm and 1000 ppm by weight of surfactant, and the results compared with those for droplets of pure water. Addition of the surfactant significantly enhanced nucleate boiling heat transfer so that the lifetime of surfactant solution droplets placed on a heated surface was only about a third of those of pure water. Photographs of droplets showed that addition of a surfactant to water reduces surface tension and liquid-solid contact angle and promotes nucleation of vapour bubbles and foaming. Each of these effects was examined in turn to determine which was responsible for heat transfer enhancement. Earlier studies (Roy Chowdhury and Winterton, 1985; Wang and Dhir, 1993) have demonstrated that reduction of liquid-solid contact angle (from 90 deg for pure water to 55 deg for 100 ppm SDS solution and 20 deg for 1000 ppm SDS solution) diminishes rather than augments nucleate boiling since it makes it easier for the liquid to flood cavities in the heated solid surface, suppressing heterogeneous nucleation caused by vapour trapped in these cavities. Furthermore, increased heat transfer could not be correlated with surface tension changes. Adding 100 ppm of the surfactant produced very little change in surface tension (reducing it by 4 percent), while greatly increasing heat flux; adding 1000 ppm produced a large change in surface tension (reducing it by 30 percent), with little additional increase in heat transfer. It has previously been shown (Lowery and Westwater, 1957) that dissolving additives that do not affect surface tension in methanol can increase boiling heat transfer. Jontz and Myers (1960) found that organic additives, not necessarily surfactants, that have molecules large enough to act as critical-sized nuclei promote bubble nucleation. We concluded (based on inspection of droplet photographs) that the principal effect of the surfactant was to promote homogeneous nucleation of vapour bubbles throughout the bulk of the liquid drop. Sur-

Contributed by the Heat Transfer Division for publication in the JOURNAL OF HEAT TRANSFER. Manuscript received by the Heat Transfer Division November 25, 1996; revision received September 22, 1997; Keywords: Augmentation and Enhancement; Boiling; Sprays/Droplets. Associate Technical Editor: B. W. Webb.

factants also produce foaming in the liquid and enhance surface wetting, which further enhances heat transfer.

Our objective in the present study was to determine whether addition of a surfactant, which increased boiling heat transfer in single droplets, could also enhance spray cooling efficiency. We observed the quenching of a flat 25.4 mm diameter copper surface using a water spray. Experiments were done using both pure water and aqueous solutions containing 100 ppm by weight of sodium dodecyl sulfate (SDS). We did not attempt to use higher concentrations of surfactant since single droplet experiments (Qiao and Chandra, 1997) have shown that increasing surfactant concentration produces little additional heat transfer enhancement. The hot surface was cooled from an initial temperature of 240°C, when spray droplets were in a state of film boiling and did not wet the surface, to below 100°C, when nucleate boiling ceased. We varied the water mass flux (0.5 or 2.8 kg/m^{2}s), mean impact velocity of droplets in the spray (17, 20, or 23 m/s), and orientation of the test surface with respect to gravity (facing up, down, or vertical) in our experiments. We recorded the variation in test surface temperature, and from these measurements calculated the surface heat flux. Spray impact on the surface was photographed using both 35 mm and video cameras.

2 Experimental Method

Figure 1 is a schematic diagram of the apparatus used for spray cooling experiments. The spray nozzle and test surface were enclosed in an aluminum chamber (152 mm long × 152 mm wide × 254 mm high) which was mounted on a rotation stage so that the orientation of the test surface with respect to gravity could be varied. The front of the chamber was kept open, while a clear plastic window in the rear wall allowed the test surface to be illuminated by a video light.

Water was supplied by a turbine pump to the spray nozzle via stainless steel tubing after passing through a 60 micron filter. The water delivery pressure was measured by a pressure gauge (with an uncertainty of ±7 kPa) located near the spray nozzle, and it was adjusted by a pressure regulator. The water flow rate was measured by a flowmeter and could be controlled with a resolution of 1 ml/min by a micrometer valve. Any excess flow was recirculated through a release valve to the liquid supply tank.

The cooled surface was the flat face of a 25.4 mm diameter copper cylinder, electroplated with a 10 μm thick layer of nickel to prevent oxidation. It was placed at a distance of 50 mm from the nozzle tip, centered along the axis of the spray. Four 0.5 mm diameter chromel-alumel (type K) thermocouples were inserted into holes drilled 6.35 mm apart along the axis of the cylinder, with the top hole positioned 0.4 mm below the spray cooled surface. The holes were filled with a high thermal conductivity paste before inserting the thermocouples to minimize thermal contact resistance. The lower end of the cylinder was bolted to a copper heater block that housed two 500 W cartridge heaters. Power to the cartridge heaters was regulated by a temperature controller, holding the surface temperature constant to within ±1°C before water was sprayed on it. The heater block was insulated with mineral wool to reduce heat losses. The

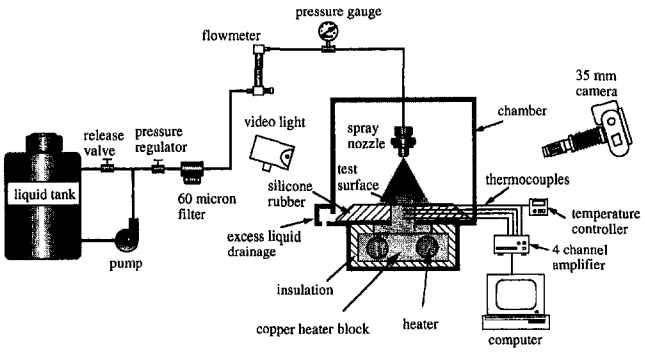

Fig. 1 Schematic diagram of the spray cooling apparatus

sides of the cylindrical test surface were insulated with mineral wool to reduce heat losses. The sides of the cylindrical test surface were insulated with a silicone rubber sheet machined to the required shape; it provided a seal sufficient to prevent any leakage of water into the heater block. Water running off the surface was removed from the chamber through a drainage tube.

Two commercially available full-cone spray nozzles (Unijet TG 0.6 and 0.7, Spray Systems Co., Wheaton, Illinois) were employed to achieve two different values of liquid mass flux (m_l) sprayed on the test surface: 0.5 and 2.8 kg/m^{2}s, respectively. The nozzles provided uniform coverage over the test surface. The mass flux of water was measured by replacing the test surface with a copper tube whose internal diameter was the same as the diameter of the surface. The spray was turned on and water flowing through the tube collected in a 100 ml measuring cylinder. The time required to fill the cylinder was recorded, and the spray mass flux calculated by dividing the mass of water in the cylinder by the filling time and the test surface area. The error in this measurement of m_l was estimated to be ±4 percent. When surfactant was added to the spray water the change in measured mass flux was found to be less than the uncertainty in measurement.

The mean velocity of droplets impacting on the test surface (U_m) was estimated by using a simple energy balance analysis developed by Ghodbane and Holman (1991), which we extended (Qiao, 1996) to include gravitational potential energy. The droplet impact velocity was calculated from the following equation:

$$U_m = \left(U_o^2 + \frac{2\Delta p}{\rho} - \frac{12\sigma}{\rho d_{05}} - 2gh \sin(\alpha) \right)^{1/2}. \quad (1)$$

Only the second term on the right hand side of Eq. (1) ($2\Delta p/\rho$) was significant in our experiments: neglecting the other three produced an error of less than 1 percent. We used three different nozzle pressures (138, 207, and 276 kPa) to obtain mean droplet velocities of 17, 20, and 23 m/s, respectively. In this pressure range the measured mass flux remained constant for a given nozzle, within the resolution of our measurement. Increasing

Nomenclature

d = droplet diameter (m)
d_{05} = mass median droplet diameter (m)
d_{32} = Sauter mean diameter (m)
g = acceleration due to gravity (m/s^2)
h = distance from nozzle to surface (m)
m_l = spray mass flux (kg/m^{2}s)
Δp = pressure drop across spray nozzle (kPa)
q'' = surface heat flux (W/m^2)
T_l = liquid temperature (°C)
T_w = surface temperature (°C)
U_0 = mean velocity of water entering nozzle (m/s)
U_m = mean droplet impact velocity (m/s)

Greek Symbols

α = angle of inclination of the surface with respect to gravity [°]
ρ = density [kg/m^3]
σ = surface tension [N/m]

pressure increased the spray cone angle rather than the mass flux along the axis of the spray.

Spray cooling experiments were done using both pure water and solutions containing 100 ppm by weight of surfactant. The surfactant used was sodium dodecyl sulfate, which is available as a powdered solid. Fresh surfactant solution was prepared before each experiment by weighing and dissolving 80 mg of surfactant in 800 g of water which had been distilled immediately before use to minimize the presence of dissolved gases.

A transient spray cooling experiment was started by cleaning the test surface with metal polish and washing it first with acetone and then with distilled water. The heaters in the heater block were powered until the surface temperature, as measured by the uppermost thermocouple, reached 240°C. The heaters were then switched off and the water pump activated, with a metal plate held in front of the nozzle to block the spray. Once the water pressure at the nozzle inlet reached a steady value, the metal shield was withdrawn and the spray was allowed to hit the surface. Water impinging on the test surface quenched it to a temperature below 100°C in a period of 10 s–100 s, depending on the spray parameters used. Signals from the thermocouples inserted into the surface were amplified and recorded using a data acquisition system during spray cooling.

Though most of the tests we did were on transient cooling, a limited number of steady-state surface cooling experiments were also carried out. In these, the water spray was started before heating the surface. The heaters were then switched on and the voltage applied to the heaters was slowly increased, using a transformer, until the temperature of the heater block reached steady state. The increase in power supplied to the heaters (measured directly using a wattmeter) equaled the heat transfer to the impinging spray. Also, the temperature profile below the heated surface was linear, and surface temperature and heat flux could easily be calculated. The steady-state heat flux at a given surface temperature was found to be very close to that calculated in the transient cooling experiments, the difference between the two being less than the uncertainty in measurement of heat flux.

Photographs of spray droplets impacting on the hot surface were taken using a 35 mm camera. The 35 mm camera was equipped with a motordrive that could advance the film at speeds of up to 6 frames per second. A 850 Watt Halogen video light was used to provide illumination. The rear window of the spray chamber was covered with white paper to diffuse the incoming light. Photographs were taken using Kodak TMAX 400 film and exposure times ranging from 1/250 to 1/1000 s, with the lens aperture set to f-22. The camera was triggered manually using an electronic circuit that simultaneously sent a signal to the data acquisition system recording surface temperatures. Therefore, the exact time and surface temperature at which each photograph was taken could be ascertained. Spray impingement on the hot surface was also recorded using a video camera.

To determine whether adding a surfactant had any significant effect on spray atomization, droplet size distributions in sprays were measured using a Malvern 2600 particle analyzer. This instrument uses a 9 mm diameter laser beam to probe the spray, which was aligned perpendicular to the axis of the spray nozzle 50 mm from its tip (the location of the test surface). Diameters of all droplets passing through this beam are recorded by the particle analyzer and averages calculated. The uncertainty in droplet diameter measurement was ± 5 μm.

3 Results and Discussion

Adding 100 ppm of surfactant produced negligible changes in properties such as density and viscosity, and reduced the surface tension by only 4 percent (Qiao and Chandra, 1997). In fact, experiments on deformation of surfactant solution droplets during impact on a solid surface (Pasandideh-Fard et al., 1996) suggest that the surface tension of a freshly exposed surface, to which surfactant has not had time to migrate, may approach that of pure water. We therefore did not expect the surfactant to have a significant influence on droplet size distributions in the spray. Measurements with a particle size analyzer confirmed that this was indeed the case. Figure 2 shows the droplet size distribution in a spray produced by the TG 0.6 nozzle at two different pressures—138 and 276 kPa. At both pressures addition of a surfactant produced a small increase in droplet size. Averaging of droplet diameters showed that the Sauter mean diameter (d_{32}, defined as the diameter of a drop whose volume-to-surface-area ratio is the same as that for the entire spray) increased by approximately 10 percent when surfactant was added to the spray water. This was true over a wide range of pressures, as seen in Fig. 3 which displays the variation of d_{32} with nozzle inlet pressure. Each symbol in Fig. 3 represents the average of three measurements; the variation between then was less than ± 2 μm.

A variation of 10 percent in droplet size has a negligible effect on spray cooling heat transfer. Extensive spray cooling experiments by Mudawar and Valentine (1989) and Klinzing et al. (1992), using nozzles and spray parameters similar to those used in our experiments and a wide range of droplet diameters (d_{32} varying from 0.4 to 2 mm), showed that nucleate boiling heat flux was independent of droplet size. The correlations they proposed to predict heat transfer do not include droplet diameter as a parameter. Hoogendorn and den Hond (1974) also found that varying Sauter mean diameters in the range 0.2 to 1 mm had little impact on spray cooling. Yao and Choi (1987), studying cooling using monodispersed sprays, came to a similar conclusion. We therefore assumed that any spray cooling enhancement caused by a surfactant is because of its influence on boiling, rather than changes to the droplet size distribution.

Figure 4 displays typical temperature measurements made during spray cooling of a surface using pure water with a mass flux $m_1 = 0.5$ kg/m^{2}s. The temperature variation recorded by each of the four thermocouples (T_1 to T_4) is shown. Prior to cooling, the surface was heated to 240°C until steady state was reached. At this time, temperature gradients in the test surface were very small: temperatures measured by the four thermocouples differed by less than 1°C. Time $t = 0$ marks the instant that the spray was turned on. The temperature measured by the thermocouple closest to the surface (T_1) dropped from 240°C to 110°C in approximately 100 s.

Figure 5 shows the surface heat flux (q'') and temperature (T_w) during spray cooling, calculated from the interior temperature measurements of Fig. 4 using the sequential function specification method (Beck et al., 1985) to solve the inverse heat

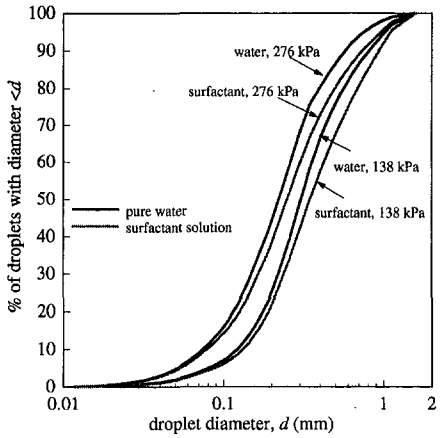

Fig. 2 Droplet size distribution in sprays of water and surfactant solution at nozzle pressures of 138 and 276 kPa

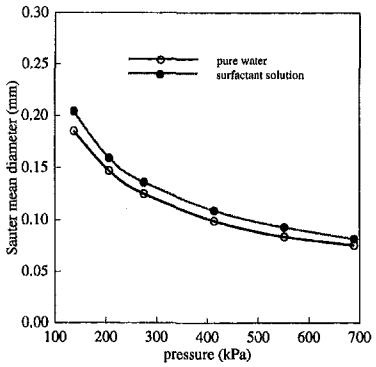

Fig. 3 Sauter mean droplet diameter (d_{32}) variation with pressure in sprays of water and surfactant solution

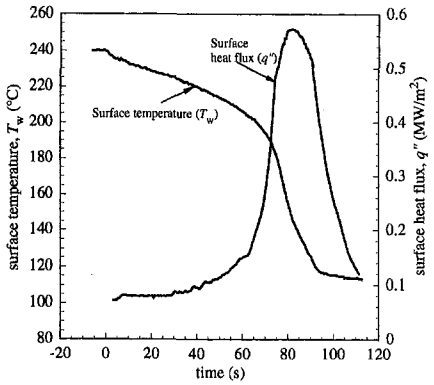

Fig. 5 Calculated surface heat flux and temperature during spray cooling with pure water (mass flux m_1 = 0.5 kg/m^{2}s)

conduction problem. Details of the calculation procedure have been given by Qiao (1996). The accuracy of our temperature measurements were estimated to be ±0.5°C, and the locations of the thermocouples could be established to within ±0.15 mm. An error analysis (Qiao, 1996) showed that these uncertainties could create an error in our calculation of heat flux of, at most, 10 percent, with the largest errors occurring at the start and end of cooling where the relative magnitude of heat flux was small. At an initial surface temperature of 240°C, spray droplets were in a state of film boiling, bouncing off the surface after impact, and the heat flux was low (q'' = 0.08 MW/m^2). Heat transfer to the spray was in the transition boiling regime for 140°C < T_w < 200°C, and surface heat flux increased rapidly until it reached its maximum value, called the critical heat flux (CHF), at T_w = 140°C. Heat transfer at lower surface temperatures was by nucleate boiling, and q'' decreased with further reductions in surface temperature.

Photographs taken of the test surface during spray cooling under the same conditions as those in Figs. 4 and 5 are shown in Fig. 6, in which each column shows successive stages during quenching of the surface using sprays of both pure water (column a) and surfactant solution (column b). When quenched with pure water, the temperature of the test surface, initially at 240°C, began to decrease relatively slowly after the spray started (see Fig. 5, 0 < t < 60 s). Spray droplets were in a state of film boiling and contacted the surface only momentarily before rebounding. The residence time of droplets on the surface was much less than the exposure time of the photographs we took of the impacting spray: therefore, no droplets are visible on the surface at 240°C in Fig. 6. Droplets were first seen on the surface at T_w = 185°C for pure water sprays, which is very close to the so-called "rewetting temperature" measured for falling films of water on a copper surface (Yu et al., 1977).

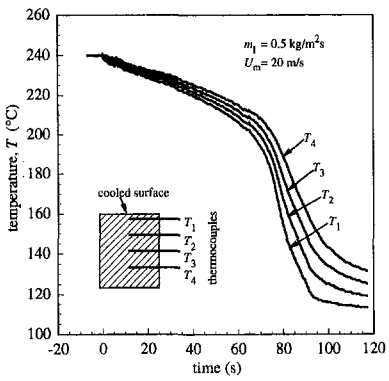

Fig. 4 Surface temperatures recorded by four thermocouples (T_1 to T_4) inserted in the test surface during spray cooling using pure water

Since the liquid-solid contact angle for pure water droplets is large (~90 deg, droplets after impact did not spread but recoiled, finally coming to rest as hemispherical liquid masses on the surface (see Fig. 6(a) at 184°C) instead of forming a continuous liquid film on the surface. The size of droplets on the surface increased as impinging droplets coalesced with them. The estimated average volume of droplets visible on the surface at 160°C in Fig. 4(a) was approximately three times that of a median sized droplet in the spray. The CHF point (T_w = 140°C) corresponded to the appearance of liquid patches on the periphery of the surface, formed by the agglomeration of droplets (Fig. 6(a) at 135°C). The thin liquid film, which was in a state of nucleate boiling, prevented direct contact between impinging droplets and the metal surface so that heat transfer was progressively reduced as larger portions of the surface became covered with liquid. Ultimately, as the surface temperature fell below 118°C, which was the minimum required to initiate boiling, nucleation was suppressed and the surface was covered by a continuous layer of water (Figure 6(a) at 105°C).

Adding a surfactant to the water in the spray made several visible changes to the quenching process. Photographs taken of a surface cooled with surfactant solution are displayed in Fig. 6(b). The temperature at which droplets were first seen on the surface was reduced to 175°C, from the value of 185°C measured for pure water. Experiments on the boiling of single drops on a hot surface (Qiao and Chandra, 1997) have shown that the presence of a surfactant promotes homogeneous nucleation of vapor bubbles in the bulk liquid, but at the same time heterogeneous nucleation at the liquid-solid interface is suppressed because the liquid-solid contact angle decreases. The net effect of adding the surfactant was to reduce the so called "Leidenfrost temperature" above which droplets were in stable film boiling. It is possible that the surfactant had a similar effect on spray droplets, reducing the temperature at which droplets rewet the surface. At lower surface temperatures the number of droplets observed on the surface was greater, and their size smaller, than in the case of pure water, indicating that the surfactant reduced coalescence of spray droplets after impact. In addition, the amount of light reflected from the surface being photographed appeared to be reduced by adding a surfactant to the spray water (see Fig. 4(a) and (b) at 160°C). Adding 100 ppm of surfactant to water decreases the liquid-solid contact angle from 90 deg to approximately 55 deg (Qiao and Chandra, 1997), increasing surface wetting. It is likely, therefore, that adding the surfactant reduced coalescence of droplets, which instead spread on the surface creating a thin liquid film that reduced the reflection of incident light. Finally, during nucleate boiling the surfactant produced vigorous foaming in the water film covering the surface (Fig. 6(b) at 115°C). Bubble nucleation could not be observed in the pure water spray below a surface temperature of 118°C; however, bubbles could be seen in the surfactant

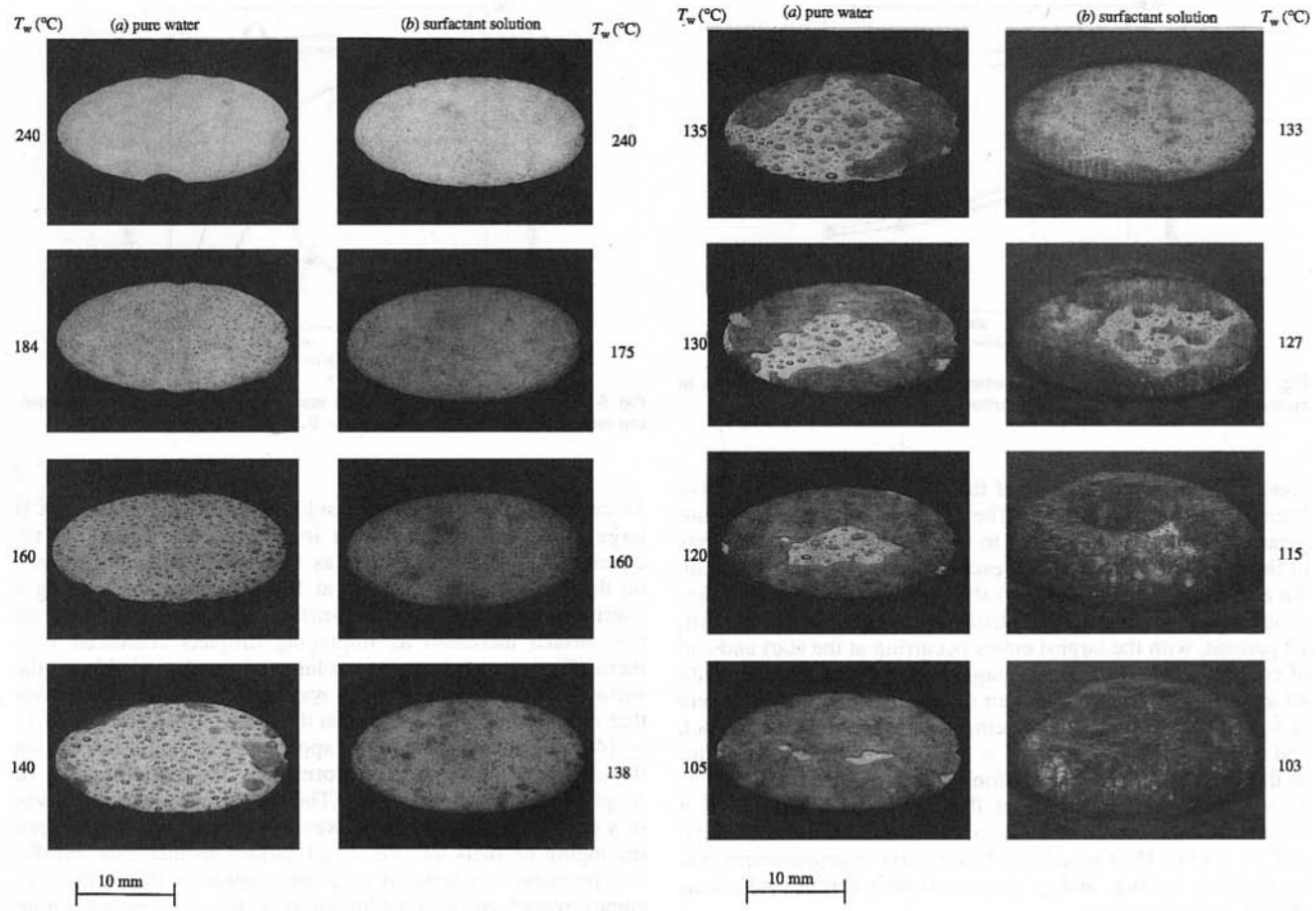

Fig. 6 Photographs taken of test surface during spray cooling using: (*a*) pure water and (*b*) surfactant solution

solution spray at surface temperatures as low as 103°C (Fig. 6(*b*) at 103°C).

The effect of adding a surfactant on spray cooling heat transfer is shown in Fig. 7, where the measured variation of surface heat flux with surface temperature is plotted for both pure water and surfactant solution at two different mass fluxes (m_1 = 2.8 kg/m^{2}s and 0.5 kg/m^{2}s). The most significant effect the surfactant had on boiling heat transfer was to substantially increase both the nucleate boiling heat flux and critical heat flux (CHF) during spray cooling: for surface temperatures between 100°C and 120°C, the surface heat transfer rate was increased by up to 300 percent. These results agreed with earlier experiments on the evaporation of single droplets of water in which SDS had been dissolved (Qiao and Chandra, 1997), where it was found that the surfactant promoted homogeneous nucleation in droplets and enhanced nucleate boiling. The observation that the superheat required to initiate nucleate boiling was reduced by adding SDS (from a surface temperature of 118°C to 103°C) is also consistent with an increase in bubble nucleation rate because of dissolved surfactant molecules. Because of the increased rate of vapor production the critical heat flux, above which the liquid is in a state of transition boiling, occurs at a lower surface temperature (see Fig. 7).

Heat transfer in the transition boiling region was found to be slightly reduced by the addition of surfactant (e.g., see Fig. 7 for m_1 = 2.8 kg/m^{2}s, 160°C < T_w < 200°C). This effect, though small, was consistently reproducible. At such high wall superheats spray droplets impact on the surface only momentarily before rebounding. Heat transfer from the surface to impinging droplets occurs largely because of heterogeneous bubble nucleation at the liquid-solid interface. The surfactant decreases the liquid-solid contact angle from 90 deg to 55 deg, thereby reducing the heterogeneous nucleation rate by several orders of magnitude (Yao and Henry, 1976). Photographs of single droplets impacting a hot surface (Qiao and Chandra, 1997) have confirmed that heterogeneous bubble nucleation is reduced by dissolving a surfactant.

The effect of adding a surfactant on surface temperature variation during quenching is shown in Fig. 8 for both m_1 = 0.5 and 2.8 kg/m^{2}s. Starting from an initial temperature of 240°C, the cooling rate was relatively slow initially because spray droplets were in transition boiling and rebounded off the surface after impact. The rewetting temperature for pure water (marked on Fig. 8) was approximately 185°C, and did not change with liquid mass flux. Addition of SDS reduced the rewetting temper-

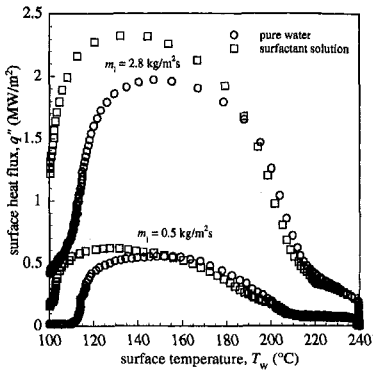

Fig. 7 Effect of a surfactant on spray cooling heat transfer at two different mass fluxes (mean impact velocity U_m = 20 m/s)

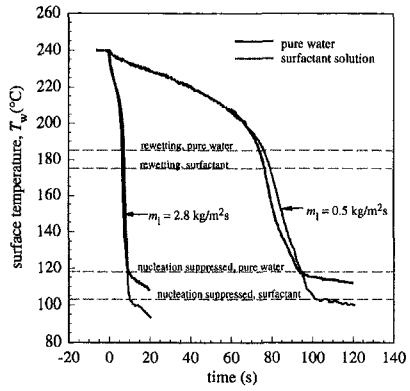

Fig. 8 Effect of adding a surfactant on the surface temperature variation during spray cooling. Both the rewetting temperature and the incipient nucleation temperature were reduced by the surfactant.

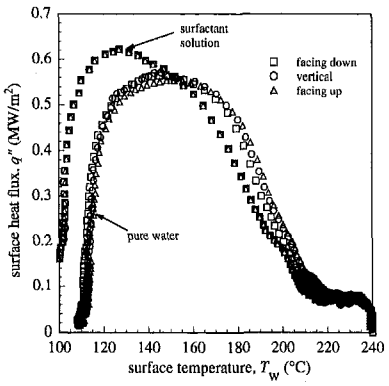

Fig. 10 Effect of surface orientation on spray cooling heat transfer using both pure water and surfactant solution. The liquid mass flux m_l = 0.5 kg/m²s and mean impact velocity U_m = 20 m/s.

ature to 175°C. Once rewetting occurred, heat transfer was by nucleate boiling and the surface cooling rate increased. Cooling was more rapid when surfactant solution was used instead of pure water, a result of the surfactant increasing nucleate boiling heat transfer. The surface cooling rate again decreased when its temperature fell below the minimum required to sustain nucleate boiling. This temperature was 118°C for pure water sprays and was independent of liquid mass flux. Nucleate boiling persisted to temperatures as low as 103°C when surfactant was added to the water. The termination of nucleate boiling coincided with the surface being flooded by liquid (see Fig. 6).

Spray cooling experiments were conducted to investigate the effect of droplet velocity on heat flux. Figure 9 shows our measurements of heat flux at three different values of mean droplet impact velocity (17, 20, and 23 m/s), holding m_l constant at 2.8 kg/m²s. Tests were done using both pure water and surfactant solution. Increasing impact velocity enhanced heat transfer for surface temperatures above 120°C when the surface was not flooded. At lower temperatures most of the surface was covered with a liquid film. Droplets impacted on top of this film and their velocity had relatively little effect on heat transfer from the surface. Our observations confirm the findings of Mudawar and Valentine (1989) and Klinzing et al. (1992) who reported that nucleate boiling heat transfer during spray cooling depends only on surface temperature. They correlated their heat flux measurements with the following equation:

$$q'' = 1.87 \times 10^{-5}(T_w - T_l)^{5.55}, \qquad (2)$$

where q'' is in W/m², and $(T_w - T_l)$ is in °C. Equation (2) accurately predicts our measured values of heat flux (see Fig. 7). However, our measurement of the critical heat flux was only about half that observed by Mudawar and Valentine (1989), even though the spray parameters in our experiments were similar to theirs. The difference may be due to due to differences in surface roughness and wettability, which are known to have a strong influence on CHF in spray cooling (Pais et al., 1992). Addition of the surfactant enhanced nucleate boiling at all velocities in the range of our experiments. Our measurements of nucleate boiling heat flux during spray cooling with a surfactant solution could be correlated by an expression similar in form to Eq. (2):

$$q'' = 0.56 \times 10^{-5}(T_w - T_l)^6. \qquad (3)$$

Changing surface orientation with respect to gravity had no measurable effect on heat transfer in spray cooling. Fig. 10 shows the heat flux measured during spray cooling of a surface held in three different orientations: horizontal facing up; vertical; and horizontal facing down. No significant difference in heat transfer was observed between the three cases. These results differ from those of Choi and Yao (1987) who found that that in film boiling the spray cooling efficiency on a horizontal upward facing surface was up to 50 percent greater than that on a vertical surface. They attributed the difference to rebounding droplets impacting several times on an upward facing surface (increasing heat transfer), whereas they fell off a vertical surface after the initial impact. This effect would be highly dependent on surface geometry and spray parameters. In our experiments the cooled surface was smaller and impact velocities were much higher than those used by Choi and Yao (1987): rebounding droplets probably did not strike the surface again after their initial impact, even when the surface was facing upwards. We also found that surface orientation had no effect on nucleate boiling, corroborating the findings of Choi and Yao (1987). Nucleate boiling in spray cooling is therefore unlike pool boiling, where heat transfer from a downward facing surface has been found to be much lower than that from a vertical or upward facing surface because of accumulation of vapor at the heater surface (Nishikawa et al., 1983). This difference reflects the fact that buoyancy forces do not play a significant role in movement of vapor during nucleate boiling of impacting spray droplets. Experiments on droplet impact on a hot surface in a low gravity environment (Qiao and Chandra, 1996) have shown that vapor bubbles nucleating on the heated surface are transported away, even in the absence of buoyancy, by inertial and surface tension forces.

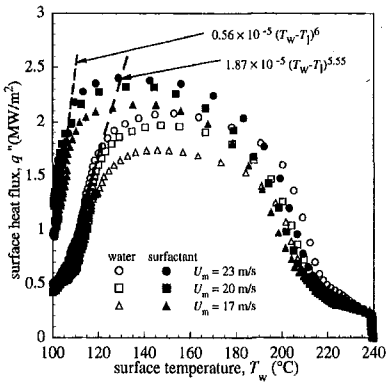

Fig. 9 Effect of surfactant addition on spray cooling heat transfer at three different values of mean droplet impact velocity (U_m). The liquid mass flux m_l = 2.8 kg/m²s.

4 Conclusions

We conducted experiments on the spray cooling of a hot surface by water sprays in which 100 ppm by weight of a

surfactant (sodium dodecyl sulfate) was dissolved. The results were compared with those obtained using pure water sprays. Adding a surfactant significantly enhanced nucleate boiling during spray cooling: for surface temperatures between 100°C and 120°C the surface heat transfer rate was increased by up to 300 percent. Heat transfer enhancement was attributed to the promotion of homogeneous vapor bubble nucleation and foaming by surfactants. The increase in nucleate boiling heat transfer was observed at all mass fluxes and impact velocities in our experiments. Heat transfer during transition boiling were reduced slightly because the surfactant reduced liquid-solid contact angle, suppressing heterogeneous bubble nucleation. Wetting of the surface by liquid droplets occurred at a temperature of 185°C for pure water and 175°C for the surfactant solution. Droplets on the surface coalesced to form a continuous film when the surface cooled below 118°C, corresponding to the onset of nucleation boiling. This temperature was lowered to 103°C by adding the surfactant. Changing surface orientation with respect to gravity had no measurable effect on spray cooling heat transfer.

Acknowledgments

Funding for his project was provided by a grant from the Natural Sciences and Engineering Research Council of Canada. We gratefully acknowledge the assistance of Dr. M. D'Souza and Mr. K. McAlpine of the National Research Council, Ottawa, for their assistance in making droplet size measurements.

References

Ammerman, C. N., and You, S. M., 1996, "Determination of the Boiling Enhancement Mechanism Caused by Surfactant Addition to Water," ASME JOURNAL OF HEAT TRANSFER, Vol. 118, pp. 429–435.

Beck, J. V., Blackwell, B., and St. Clair, Jr., C. R., 1985, *Inverse Heat Conduction,* Wiley-Interscience, NY.

Bryan, J. L., 1993, *Fire Suppression and Detection Systems,* Macmillan Publishing Co., NY, pp. 331–334.

Dunskus, T., and Westwater, J. W., 1961, "The Effect of Trace Additives on the Heat Transfer to Boiling Isopropanol," *Chemical Engineering Progress Symposium Series,* Vol. 57(32), pp. 173–181.

Choi, J., and Yao, S. C., 1987, "Mechanism of Film Boiling of Normally Impacting Spray," *International Journal of Heat and Mass Transfer,* Vol. 30, pp. 311–318.

Frost, W., and Kippenhan, C. J., 1967, "Bubble Growth and Heat Transfer Mechanisms in the Forced Convection Boiling of Water Containing a Surface Active Agent," *International Journal of Heat and Mass Transfer,* Vol. 10, pp. 931–949.

Ghodbane, M., and Holman, J. P., 1991, Experimental Study of Spray Cooling With Freon-113," *International Journal of Heat and Mass Transfer,* Vol. 34, pp. 1163–1174.

Hoogendorn, C. J., and den Hond, R., 1974, "Leidenfrost Temperature and Heat Transfer Coefficients for Water Sprays Impinging on a Hot Surface," *Proceedings of the 5th International Heat Transfer Conference,* Vol. 4, JSME, Tokyo, pp. 135–138.

Jontz, P. D., and Myers, J. E., 1960, "The Effect of Dynamic Surface Tension on Nucleate Boiling Coefficients," *A. I. Ch. E. Journal,* Vol. 6, pp. 34–38.

Klinzing, W. P., Rozzi, J. C., and Mudawar, I., 1992, "Film and Transition Boiling Correlations for Quenching of Hot Surfaces With Water Sprays," *Journal of Heat Treatment,* Vol. 9, pp. 91–103.

Lowery, A. J., and Westwater, J. W., 1957, "Heat Transfer to Boiling Methanol—Effect of Added Agents," *Industrial and Engineering Chemistry,* Vol. 49, pp. 1445–1448.

Morgan, A. I., Bromley, L. A., and Wilke, C. R., 1949, "Effect of Surface Tension on Heat Transfer in Boiling," *Industrial and Engineering Chemistry,* Vol. 41, pp. 2767–2769.

Mudawar, I., and Valentine, W. S., 1989, "Determination of the Local Quench Curve for Spray-Cooled Metallic Surfaces," *Journal of Heat Treatment,* Vol. 7, pp. 107–121.

Nishikawa, K., Fujita, Y., Uchida, S., and Ohta, H., 1983, "Effect of Heating Surface Orientation On Nucleate Boiling Heat Transfer," *ASME-JSME Thermal Engineering Joint Conference Proceedings,* Vol. 1, ASME, NY, pp. 245–250.

Pais, M. R., Chow, L. C., and Mahefkey, E. T., 1992, "Surface Roughness and its Effect on the Heat Transfer Mechanism in Spray Cooling," ASME JOURNAL OF HEAT TRANSFER, Vol. 114, pp. 211–219.

Pasandideh-Fard, M., Qiao, Y. M., Chandra, S., and Mostaghimi, J., 1996, "Capillary Effects During Droplet Impact on a Solid Surface," *Physics of Fluids,* Vol. 8, pp. 650–659.

Qiao, Y. M., 1996, "Effect of Gravity and Surfactant on Spray Cooling of Hot Surfaces, Ph.D. thesis, University of Toronto, Toronto, Ontario, Canada.

Qiao, Y. M., and Chandra, S., 1996, "Boiling of Droplets on a Hot Surface in Low Gravity," *International Journal of Heat and Mass Transfer,* Vol. 39, pp. 1379–1393.

Qiao, Y. M., and Chandra, S., 1997, "Experiments on Adding a Surfactant to Water Droplets Boiling on a Hot Surface," *Proceedings of the Royal Society of London,* Vol. 453, pp. 673–689.

Roy Chowdhury, S. K., and Winterton, R. H. S., 1985, "Surface Effects in Pool Boiling," *International Journal of Heat and Mass Transfer,* Vol. 28, pp. 1881–1889

Shah, B. S., and Darby, R., 1973, "The Effect of Surfactant on Evaporative Heat Transfer in Vertical Film Flow," *International Journal of Heat and Mass Transfer,* Vol. 16, pp. 1889–1903.

Shibayama, S., Katsuta, M., Suzuki, K., Kurose, T., and Hatano, Y., 1980, "A Study of Boiling Heat Transfer in a Thin Liquid Film: Part 1—In the Case of Pure Water and an Aqueous Solution of a Surface Active Agent as the Working Liquid," *Heat Transfer—Japanese Research,* Vol. 9, pp. 12–40.

Tzan, Y. L., and Yang, Y. M., 1990, "Experimental Study of Surfactant Effects on Pool Boiling Heat Transfer," ASME JOURNAL OF HEAT TRANSFER, Vol. 112, pp. 207–212.

Wang, C. H., and Dhir, V. K., 1993, "Effect of Surface Wettability on Active Nucleation Site Density During Pool Boiling of Water on a Vertical Surface," ASME JOURNAL OF HEAT TRANSFER, Vol. 115, pp. 659–669.

Wu, W. T., Yang, Y. M., and Maa, J. R., 1995, "Enhancement of Nucleate Boiling Heat Transfer and Depression of Surface Tension by Surfactant Additives," ASME JOURNAL OF HEAT TRANSFER, Vol. 117, pp. 526–529.

Yang, Y. M., and Maa, J. R., 1983, "Pool Boiling of Dilute Surfactant Solutions," ASME JOURNAL OF HEAT TRANSFER, Vol. 105, pp. 190–192.

Yang, Y. M., 1990, "Dynamic Surface Effect on Boiling of Aqueous Surfactant Solutions," *International Communications in Heat and Mass Transfer,* Vol. 17, pp. 711–727.

Yao, S. C., and Henry, R. E., 1976, "Hydrodynamic Instability Induced Liquid-Solid Contacts in Film Boiling," ASME Paper 76-WA/HT-25.

Yao, S. C., and Choi, K. J., 1987, "Heat Transfer Experiments of Mono-Dispersed Vertically Impacting Sprays," *International Journal of Multiphase Flow,* Vol. 13, pp. 639–648.

Yu, S. K., Farmer, P. R., and Coney, M. W. E., 1977, "Methods and Correlations for the Predicting of Quenching Rates on Hot Surfaces," *International Journal of Multiphase Flow,* Vol. 3, pp. 415–443.

Thermal Aspects of a Novel Viscous Pump

M. C. Sharatchandra
Postdoctoral Research Associate.

M. Sen
Professor.
Mem. ASME

M. Gad-el-Hak
Professor.
mohamed.gad-el-hak.1@nd.edu
Fellow ASME

Department of Aerospace and Mechanical Engineering,
University of Notre Dame,
Notre Dame, IN 46556

We have previously introduced a novel method for pumping fluids via a viscous mechanism. The device essentially consists of a cylindrical rotor eccentrically placed in a channel, and it is suited for hauling highly viscous polymers in macroducts, or more common fluids in microducts. Under certain operating conditions, viscous dissipation can be important, and a significant attendant temperature rise can have adverse effects on the pump operation. For this reason, we have conducted a numerical experiment to characterize the associated phenomena. The coupled system of the two-dimensional Navier-Stokes equations, with temperature-dependent viscosity, and the energy equation, with viscous dissipation terms retained, are solved using a finite-volume method. Different types of thermal boundary conditions at the rotor-fluid interface are explored in the numerical scheme. An approximate theoretical model is also developed to analyze flow in the region between the rotor and the nearest plate (for small gaps). The results indicate that although the bulk temperature rise is minimal for typical microscale situations, significantly steep temperature gradients are observed in the region between the rotor and the nearest channel wall where the most intense shear stress occurs. For certain combinations of Re, Ec, and Pr, temperature rises along the channel wall of the order of 30 K were calculated. Moreover, for very small values of this gap, large errors in the computed flowrates and pumping power estimates can arise for large Brinkman numbers, if the effects of viscous dissipation are ignored. Furthermore, the existence of an optimum value of rotor position, such that the bulk velocity is a maximum, is demonstrated. These findings are significant, as they are indicative of trends associated with the flow of highly viscous polymeric liquids, where much larger temperature rises and their attendant degradation in performance are likely to occur.

1 Introduction

In recent years, the technology for production of micromachines, machines which are microns or tens of microns in size, has progressed by leaps and bounds (Hogan, 1996). While there are many of these devices in actual use, other potential applications are still in the pipeline. One of the uses to which such a machine may be put is the pumping of liquids for biological or medical purposes. Special pumping mechanisms have to be sought since microfluid mechanics has some aspects that are different from usual macroscale phenomena. Reciprocating pumps are difficult to fabricate because of the size of the valves; turbomachines that depend on separation and other inertial effects do not work at low Reynolds numbers. These difficulties are avoided in a viscous-action pump consisting of a rotating cylinder eccentrically placed within a channel (Sen et al., 1996; Sharatchandra et al., 1997). Macroscopic experiments and numerical computations of the hydrodynamics of this device have been carried out by the authors. The device also works at larger scales with fluids of higher viscosity as long as the Reynolds number is not much larger than unity. In the present work, we study the thermal aspects of the pump to determine its feasibility for specific uses where temperature control is a necessity.

For viscous micropumps, the thermal aspect is much more important than for pumps that are of the reciprocating or turbomachine type. Firstly, viscous action is large since that is what drives the flow. Secondly, since the rotor and other pieces of the pump are small in size, it does not take much energy to raise their temperature. Finally, even small increases in temperature may be detrimental to the fluid being pumped if it is thermosensitive, as would be the case for some biological fluids; this aspect is also important for viscous pumps of larger size.

Viscous dissipation is the mechanism that generates heat, and unless this energy is advected away by the fluid or otherwise conducted out through the fully submerged rotor, it will raise the temperature of the fluid. A consequence of the temperature rise is its effect on fluid viscosity. For liquids, generally, the viscosity decreases when the temperature rises; thus, there is an attendant loss of performance of the viscous pump. Though the nondimensional parameters determining viscous dissipation will be discussed later, at this stage it is sufficient to remember that it is produced by work done by the viscous stresses. Thus, it depends both on the fluid viscosity and on the strain rate. Highly viscous fluids, such as polymers or glycerin, in macropumps at low rotational speeds would be susceptible to significant temperature increases. Larger increases would be registered for higher pump speeds. Low viscosity fluids in micropumps can similarly suffer if rotor speeds are high. Micromotor operating speeds of 50,000 rpm have been achieved so far (Ho and Tai, 1994), and such speeds can be expected to increase in the future.

Fluid mechanical studies of microgeometries have been made by, among others, Beskok and Karniadakis (1994) using CFD and by Piekos and Breuer (1995) using a Monte Carlo noncontinuum technique; viscous dissipation was not taken into account. There have been many numerical and experimental studies of macroflows in which the thermal effect due to viscosity is significant. Balachandar et al. (1995) were interested in geophysical applications, Lee and Jaluria (1996) in the process of optical fiber drawing, and de Araujo et al. (1990) in flow between two eccentric cylinders. Recently, Cho et al. (1993) made a theoretical and experimental study of viscous energy dissipation in a laterally oscillating planar microstructure.

In the present work, we will numerically study the thermal aspects of the viscous pumping mechanism. To simulate actual

Contributed by the Heat Transfer Division for publication in the JOURNAL OF HEAT TRANSFER. Manuscript received by the Heat Transfer Division August 16, 1996; revision received October 17, 1997; Keywords: Compressors and Pumps; Enclosure Flows; Numerical Methods. Associate Technical Editor: S. Ramadhyani.

conditions, we will include both viscous dissipation and temperature-dependent viscosity effects in our finite-volume computations. The parameters which determine temperature rises and conditions under which they will be significant will be determined.

2 Mathematical Formulation

Figure 1 shows the geometrical configuration of the problem under investigation. Clockwise rotation of the cylinder A, which is in virtual contact with the bottom wall B, induces a flow from left to right in the channel, the height of which is varied by vertical translation of the plate C. The Navier-Stokes and thermal energy equations describing the laminar, incompressible, steady flow of a fluid with a temperature-dependent viscosity, may be expressed in coordinate-invariant dimensionless form as

$$\nabla \cdot \mathbf{V} = 0 \tag{1}$$

$$\nabla \cdot \left[\mathbf{VV} - \frac{F_\nu(\theta)}{\mathrm{Re}} [(\nabla \mathbf{V}) + (\nabla \mathbf{V})^T] \right] + \nabla p = 0 \tag{2}$$

and

$$\nabla \cdot \left(\mathbf{V}\theta - \frac{1}{\mathrm{Re\ Pr}} \nabla \theta \right) - \frac{\mathrm{Ec} F_\nu(\theta)}{\mathrm{Re}} \nabla \mathbf{V} : [(\nabla \mathbf{V}) + (\nabla \mathbf{V})^T] = 0, \tag{3}$$

where the viscosity variation with temperature is characterized by

$$F_\nu(\theta) = \frac{\nu(T)}{\nu_o(T_o)} = e^{-C_\nu(1-(1/\theta))}. \tag{4}$$

The viscosity ν_o is evaluated at some reference temperature T_o, usually of the order of 290 K. The constant C_ν is taken to be equal to 28 in this study based on that of glycerin. This value may also be regarded as typical of other viscous oils and of even more viscous polymeric liquids.

In the above equations, $\mathbf{V}$ and ∇ are the dimensionless velocity vector and spatial gradient operator, respectively. Here, the velocity and length scales are, respectively, the rotor surface speed $U = \omega a$ and diameter $d = 2a$. Pressure is normalized with respect to ρU^2, and the dimensionless temperature is defined as

$$\theta = \frac{T}{T_o}. \tag{5}$$

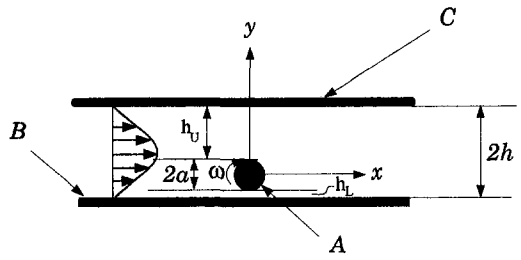

Fig. 1 Schematic of flow configuration

The Reynolds, Prandtl, and Eckert numbers are defined as

$$\mathrm{Re} = \frac{2\omega a^2}{\nu_o}; \quad \mathrm{Pr} = \frac{\nu_o}{\alpha}; \quad \text{and} \quad \mathrm{Ec} = \frac{(\omega a)^2}{cT_o}, \tag{6}$$

where c and α are, respectively, the (constant) specific heat and thermal diffusivity of the fluid. In addition, the following geometric and dynamic parameters may be defined, with regard to Fig. 1, as

$$s = \frac{2h}{d} \tag{7}$$

$$\epsilon = \frac{h_U + a - h}{2a} \tag{8}$$

$$\delta_L = \frac{h_L}{2a} \tag{9}$$

$$\Delta p^* = 4 \frac{(P_2 - P_1)a^2}{\rho \nu_o^2}, \tag{10}$$

where the subscripts 1 and 2 denote the inlet and exit stations of the channel. The fluid bulk velocity is normalized with respect to ωa and designated $\bar{u}$.

2.1 Boundary Conditions. No-penetration and no-slip boundary conditions are assumed to hold for the normal and tangential velocity components at the solid surfaces corresponding to the rotor A and the plates B and C. At the inflow and outflow boundaries, zero streamwise gradients were imposed for the streamwise velocity component. These conditions essentially yield parabolic velocity profiles at distances $|x| \geq 4$ from the rotor (Sen et al., 1996). A fixed temperature, taken equal to the reference temperature T_o, was prescribed at the inlet, and

Nomenclature

a = rotor radius (m)
Br = Brinkman number
c = specific heat (J/kg·K)
C_M = rotor moment coefficient
d = diameter (m)
Ec = Eckert number
$F_\nu(\theta)$ = dimensionless function that characterizes viscosity variation with temperature
h = channel half height (m)
h_L, h_U = lower and upper gap heights (m)
K = thermal conductivity (W/m·K)
l = rotor length (m)
Nu* = modified Nusselt number
p = pressure (N/m²)
Pr = Prandtl number
$\dot{q}$ = cooling flux at rotor ends (W/m²)
r, ϕ, z = cylindrical coordinates
Re = Reynolds number
R_t = wall temperature ratio, T_1/T_o
s = ratio of channel height to rotor diameter
T = temperature (K)
U = rotor surface tangential velocity (m/s)
$\mathbf{V}$ = dimensionless velocity vector
x, y, z = Cartesian coordinates

Greek Symbols

α = thermal diffusivity (m²/s)
δ_L, δ_U = lower and upper (dimensionless) gap heights
ϵ = dimensionless rotor eccentricity
θ = dimensionless temperature
ν = kinematic viscosity (m²/s)
ξ, η = dimensionless nonorthogonal curvilinear coordinates
τ = dimensionless shear stress
ω = angular velocity (s⁻¹)

Subscripts

c = rotor surface condition
f = fluid
o = channel inlet condition

a vanishing streamwise temperature gradient was assumed at the exit. The upper and lower surfaces are assumed to be adiabatic.[1]

At the rotor surface, the net heat flux imparted to the rotor by the fluid is equated to the cooling flux applied to the rotor ends. In other words, a steady-state heat transfer condition is assumed. With respect to Fig. 2, setting $\dot{Q} = 2\dot{q}$ yields the following condition for the rotor surface temperature:

$$K_f l a \int_0^{2\pi} \left.\frac{\partial T}{\partial r}\right|_a d\phi = 2\pi a^2 h (T_c - T_o), \qquad (11)$$

where T_c is the (constant) rotor surface temperature, K_f is the thermal conductivity of the fluid being pumped, and l is the rotor length. For simplicity, the "ambient" temperature corresponding to that of the cooling flux at the ends is taken equal to the pump inlet temperature T_o. In addition, the entire rotor surface is considered to be at the (as such unknown) temperature T_c.

Slip flow is not considered in this study since it has been recently shown (Pfahler et al., 1991; Wilding et al., 1994) that the Navier-Stokes equations are applicable without modification to compute liquid flows in channels greater than 20 μ in width.

2.2 Comments on Solution Methodology. The method of solution of Eqs. (1)–(3) in a generalized nonorthogonal curvilinear coordinate system that we have used, has been described before (Sharatchandra and Rhode, 1994; Sharatchandra, 1995; Sharatchandra et al., 1997) and will not be discussed here. The comments below are only for the thermal aspects of the problem which are new.

The integral in the LHS of Eq. (11) is discretized according to

$$a \int_0^{2\pi} \left.\frac{\partial T}{\partial r}\right|_a d\phi = \sum_{k=1}^{N_r} W^k (\theta_{a+\Delta_{kr}} - \theta_c), \qquad (12)$$

where $\theta_{a+\Delta_{kr}}$, $k = 1, N_r$, are the temperatures at the nodal centers of the N_r control volumes adjacent to the rotor surface. The factor W^k is a contravariant metric scale factor associated with the coordinate direction at the kth point at which Eq. (12) is evaluated. An expression for the dimensionless surface temperature θ_c can then be written as

$$\theta_c = \frac{\mathrm{Nu}^* + \sum_{i=1}^{N_r} W^k \theta_{a+\Delta_{kr}}}{\mathrm{Nu}^* + \sum_{i=1}^{N_r} W^k}, \qquad (13)$$

where $\mathrm{Nu}^* \equiv \pi(ha/K_f)(a/l)$ is a modified Nusselt number. Clearly, when $\mathrm{Nu}^* = 0$, the rotor surface is thermally insulated in a global sense, whereas when $\mathrm{Nu}^* \gg 1$, $\theta_c \to 1$ and an estimate of the cooling flux required to maintain the rotor surface at levels close to the pump inlet temperature can be obtained as

$$\frac{\dot{q}}{K_f a T_o} = \mathrm{Nu}^*(\theta_c - 1). \qquad (14)$$

2.3 Validation of the Numerical Methodology. To the best of the authors' knowledge, no known closed form solution exists even for the simplest flow configuration involving both variable viscosity and viscous dissipation. However, if either of these features is eliminated, exact solutions can be obtained for Couette and Poiseuille-type flows. Consider flow in a plane channel with isothermal walls maintained at unequal temperatures T_o and T_1. Butler and McKee (1973) have shown that an exact closed form solution of flow without viscous dissipation is possible when the viscosity and thermal conductivity variations with temperature are described by

$$F_\nu(\theta) = \theta^{-n} \qquad (15)$$

and

$$\frac{k}{k_o} = \frac{1}{\theta}. \qquad (16)$$

For plane Couette flow subject to the above constitutive relations, the dimensionless velocity and temperature distributions in the channel are given by

$$u = \frac{e^{n \ln R_t y} - 1}{e^{n \ln R_t} - 1} \qquad (17)$$

and

$$\theta = e^{\ln R_t y}, \qquad (18)$$

where u is normalized with respect to the velocity of the (upper) driven wall, and $R_t = T_1/T_o$ is the wall temperature ratio.

The computational domain was discretized by a highly skewed 21 × 21 grid generated elliptically.[2] The exact solution given by Eqs. (17) and (18) is imposed on the domain boundaries, and the full Navier-Stokes and energy equations are solved for the velocity and temperature distributions, based on the property variations described by Eqs. (15) and (16). In the absence of significant numerical errors due to grid skewness and curvature, the computed and exact distributions must be in good agreement. Figure 3 shows that this is indeed the case, as exemplified by the excellent agreement between the computed and exact distributions at the location $x = L/2$, L being the length of the domain. As a more rigorous check, the average errors in the velocity gradient at the upper wall are tabulated in Table 1, for various values of the exponent n. These errors correspond to those obtained from the grid-independent solu-

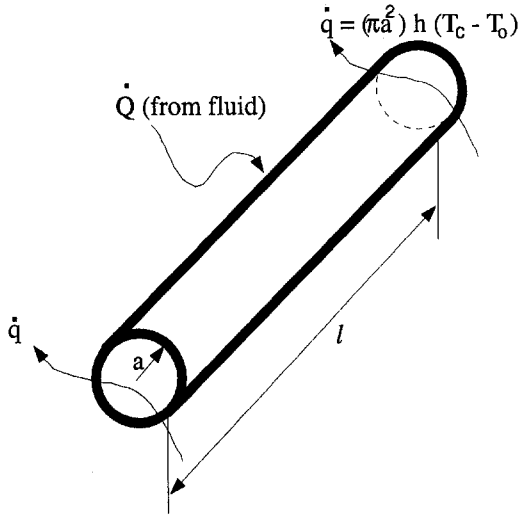

Fig. 2 Thermal energy balance about the rotor

[1] Though other thermal boundary conditions can be assumed, an adiabatic boundary condition in which the heat generated by the viscous action would not be conducted through the walls is the worst-case scenario. If, on the other hand, infinite cooling were available at the walls, viscous heating may not be a problem. Furthermore, accounting for heat loss from the walls would entail a host of attendant questions about the wall surface heat transfer coefficients or the conjugate conduction problem in the wall, which would detract from the main focus of the present study. Finally, at the length scales that we are interested in here, the Grashof number values would be minuscule, rendering surface cooling by natural convection negligible.

[2] Such a grid is not required in this particular rectilinear flow problem, but is used to provide an extreme test of the present code which has to employ a highly skewed grid in order to achieve sufficient resolution in the vicinity of the rotor particularly near the narrow gap.

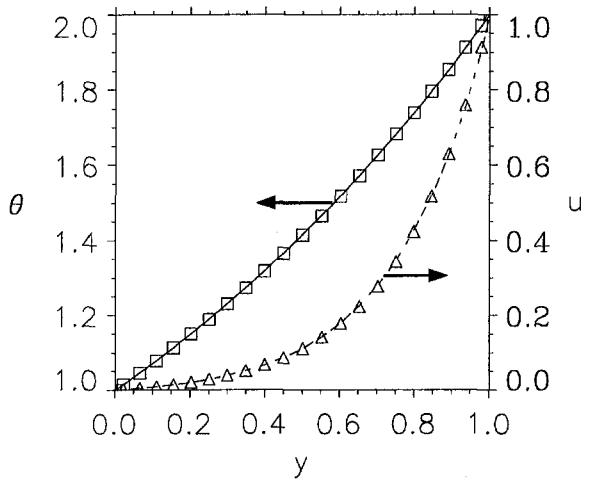

Fig. 3 Comparison of computed and exact u and θ distributions for variable viscosity Couette flow. Re = Pr = 10, n = 6, R_t = 2. Symbols: exact solution; lines: computations.

tions, obtained on a 41 × 41 grid isomorphically similar to the 21 × 21 grid. The results of Table 1 demonstrate the ability of the present methodology to accurately and reliably capture the effects of variable viscosity flows in complex geometrical configurations. In essence, the lack of significant errors due to grid skewness and curvature demonstrated above justifies the application of the present numerical method to complex geometrical configurations, where grid skewness and curvature arise naturally.

In addition, the present numerical code, without the energy equation, has already been thoroughly validated against the Wannier solution (Wannier, 1950) for flow past a rotating cylinder in the vicinity of a flat plate. This problem bears a close geometric resemblance to the present one. See Sharatchandra et al. (1997) for details.

3 Analysis of Flow in the Gap Region

The most intense shear stresses occur between the rotor and the lower plate. Consequently, the effects of viscous dissipation are most significant in this region and it is reasonable to anticipate that the highest temperature gradients (and hence the largest viscosity variations) will occur here as well. Therefore, it is of importance to analyze the flow and heat transfer in this region in detail to develop an enhanced understanding of the phenomena involved. To this end, an approximate analytical model is developed based on several simplifying assumptions. Specifically, it is assumed that the flow in the narrow-gap region is both thermally and hydrodynamically fully developed and that the curvature along the rotor segment adjacent to the gap region may be neglected. The former assumption is valid only when the walls are isothermal. Accordingly, the momentum and energy equations governing the flow in the gap region may be approximated by

$$\Delta p_g = \frac{d}{dy_g}\left[F_\nu(\theta_g)\frac{du_g}{dy_g}\right], \quad 0 \le y_g \le 1 \tag{19}$$

and

$$\frac{d^2\theta_g}{dy_g^2} + \mathrm{Br}F_\nu(\theta_g)\left(\frac{du_g}{dy_g}\right)^2 = 0, \tag{20}$$

where Br = Ec Pr is the Brinkman number, and the subscript g is used to denote the gap region. The viscosity variation with temperature is given by Eq. (4). Based on the aforementioned assumptions of fully developed flow, the boundary conditions appropriate to the problem are

$$u_g(0) = \frac{d\theta_g}{dy_g}(0) = 0$$

$$-u_g(1) = \theta_g(1) = 1, \tag{21}$$

which corresponds to the limit Nu* → ∞ in Eq. (13). Despite this, it will be apparent in a later section that the analysis is not necessarily constrained to very large values of Nu* because it turns out that $\theta_c \approx 1$, even for Nu* = 0.

The velocity field in the gap region is then obtained as

$$u_g = \Delta p_g \int_o^{y_g} F_\nu^{-1}\eta d\eta + A\int_o^{y_g} F_\nu^{-1} d\eta \tag{22}$$

where

$$A = \frac{1 + \Delta p_g \int_o^1 F_\nu^{-1} y_g dy_g}{\int_o^1 F_\nu^{-1} dy_g}. \tag{23}$$

The temperature field may be expressed in terms of a Fourier series as

$$\theta_g = 1 + \theta_w(1 - y) + \sum_{k=1}^{\infty} a_k \sin(k\pi y_g), \tag{24}$$

where the lower wall temperature θ_w is treated as a constant and determined from a Newton-Raphson iterative scheme such that the condition $(d\theta_g/dy_g)(0) = 0$ is satisfied. This approach facilitates the evaluation of the Fourier coefficients a_k by exploiting the orthogonality of $\sin(k\pi y_g)$, $k = 1, 2, \ldots$, on the interval [0, 1] as

$$a_k = \frac{2\,\mathrm{Br}}{(\pi k)^2}\int_0^1 F_\nu^{-1}(\Delta p_g y_g + A)\sin(k\pi y_g)dy_g,$$

$$k = 1, 2, \ldots, N. \tag{25}$$

The above method of evaluating a_k is preferable, when compared to solving a system of linear equations for a_k, since such a system is likely to be stiff for large truncation numbers N of the Fourier series. The nonlinearity of the coupled system of Eqs. (19)–(20) requires an iterative scheme to determine the coefficients using Eq. (25). Here, F_ν (and hence A) are evaluated using the values of the Fourier coefficients from the previous iteration, designated a_k^*. The convergence criterion was

$$\sum_{k=1}^{N}(a_k - a_k^*)^2 \le 10^{-15}. \tag{26}$$

With values of Δp_g estimated from the Navier-Stokes simulations for appropriate values of Br and C_ν, the integrals in Eqs. (22)–(25) are evaluated using Gauss-Legendre quadrature rules.

It should be mentioned that comparisons between the numerical and analytical predictions of velocity and temperature fields in the gap region are not expected to be in exact quantitative agreement. What we are seeking here is reasonable qualitative agreement that facilitates an understanding of the underlying physical phenomena involved. Such a comparison will be made in the following section.

Table 1 Average velocity gradient errors for Re = Pr = 10, and R_t = 2

n	Exact $\frac{\partial u}{\partial y}\|_{y=1}$	Avg. Comptd. $\frac{\partial u}{\partial y}\|_{y=1}$	Avg. % Error
2	1.846	1.848	0.11
4	2.953	2.962	0.28
6	4.199	4.213	0.59

4 Results and Discussion

In this section, the effects of the parameters Br, s, δ_L, and Nu* on the pump performance are explored. Although Pr was varied while Ec was fixed, the results are presented in terms of the Brinkman number (Br = Ec Pr), as is typically done for liquid flows involving viscous dissipation. In order to assign reasonable values of Re and Ec for the computations, we first consider the effects of various fluids, pump sizes, and rotational speeds as summarized in Table 2.

For air and water, the ratio Ec/Re is too small to result in appreciable thermal effects, even at large pump speeds and over a fairly wide range of pump characteristic dimensions. For glycerin on the other hand, the ratio is considerably higher. The values in the table are based on thermophysical properties of the fluids at 293 K. For the present computations, we hold the values of Re and Ec fixed at those corresponding to case 7 because of the intermediate size. The Brinkman number variation was accomplished by varying the Prandtl number. This variation may then be regarded as representative of various high Prandtl number fluids whose ν versus θ relationships correspond more or less to that of Eq. (4). However, since the Ec/Re ratio is more or less constant over a large range of characteristic dimensions, the results herein may be regarded as representative of both micro and macro-pumps.

All the computations were performed on a 72 × 54 grid, greatly refined in the vicinity of the rotor. Grid independence was established, in that a less than 0.1 percent change in the computed bulk velocity was observed when the mesh was doubled, i.e., when a 144 × 108 grid was employed. The channel half-length to rotor diameter ratio L/d is taken to be equal to 8, so as to justify the imposition of the zero gradient condition at streamwise boundaries. In addition, the rotor is maintained at very small distances from the lower wall such that the eccentricity $\epsilon \sim \epsilon_{max}$; the study of Sharatchandra et al. (1997) indicates that the most effective pumping is obtained for this configuration. The parameter δ_L was varied keeping $\epsilon \sim \epsilon_{max}$, as the physics of the problem suggests that the flow and thermal characteristics are likely to be very sensitive to small changes in the rotor position away from the lower wall. The pump load Δp^* is kept equal to zero, meaning that the pressure rise across the rotor is balanced by the pressure drop in the upstream and downstream portions of the duct.

4.1 Velocity Field and Temperature Distribution. For the initial computations, we consider Nu* = 0 so that the rotor is, in effect, thermally insulated from its surroundings. The rotor is maintained at a distance from the lower plate corresponding to $\delta_L = 0.005$. Figure 4(a) shows the computed streamlines for $s = 1.5$ and Br = 0.015. The symmetry of Stokes flow apparent in the low Re results of Sharatchandra et al. (1997) is not present here since Re = 12.6 is clearly beyond the regime of Stokes flow and because of the temperature dependence of the viscosity. The flow structure with the two co-rotating vortices is, however, consistent with the results of the aforementioned study. The rather moderate effects of higher viscous dissipation are seen in Fig. 4(b), corresponding to Br = 1.5. The decrease in the viscosity at the rotor surface results in reduced shear

Table 2 Values of Re and Ec for different fluids and pump parameters

Case	Fluid	Rotor Dia. (μ)	Rotor RPM	Re	Ec
1	Air	100	40000	1.05	1.5×10^{-7}
2	Air	1000	50000	131	2.3×10^{-5}
3	Water	100	40000	21	7.3×10^{-8}
4	Water	1000	50000	2618	1.1×10^{-5}
5	Glycerin	100	30000	0.03	3.7×10^{-8}
6	Glycerin	1000	30000	3.14	3.7×10^{-5}
7	Glycerin	2000	30000	12.6	1.5×10^{-5}
8	Glycerin	5000	35000	91.6	1.3×10^{-4}

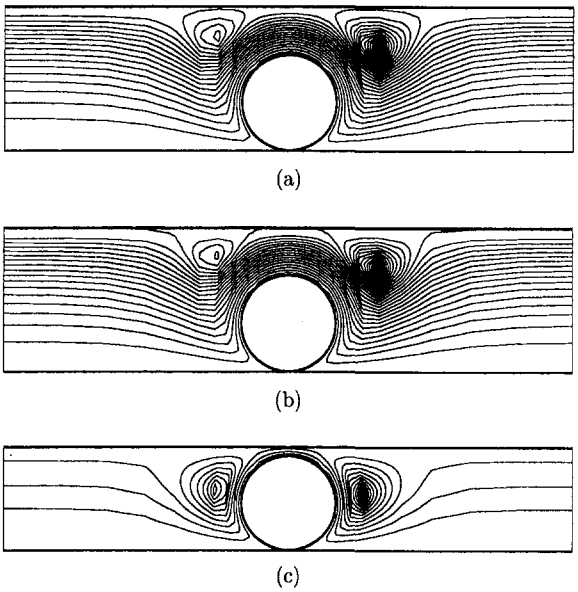

Fig. 4 Streamlines, for δ_L = 0.005 and Nu* = 0. (*a*) s = 1.5, Br = 0.015; (*b*) s = 1.5, Br = 1.5; (*c*) s = 1.1, Br = 0.75.

stresses there and, hence, in the thinning of the vortices above the rotor. In particular, the greater tendency of the upstream vortex to shrink is consistent with the increase in the effective Reynolds number as ν decreases, as evidenced in the earlier study of Sharatchandra et al. (1997). The near symmetry for $s = 1.1$ and Br = 0.75 in Fig. 4(c), as compared to $s = 1.5$, is due to the fact that the bulk velocity for $s = 1.1$ is about half the corresponding value for $s = 1.5$. This has the effect of reducing the effective Reynolds number by a factor of nearly two, which in turn causes the flow structure to be more or less symmetric.

Figure 5(a) shows the axial variation of the temperature along the lower plate for $\delta_L = 0.005$, $s = 1.5$, Br = 0.75, and Nu* = 0. Not surprisingly, the peak temperature occurs near $x = 0$, where the most intense shear stresses occur. If the reference temperature is taken to be 290 K, then Fig. 5(a) predicts an approximately 30 K temperature rise from pump inlet to rotor midpoint. For a pump L/d ratio of 8, as in the present case, this temperature rise occurs over a distance of about 15 mm. Furthermore, the very steep temperature gradients in the vicinity of $x = 0$ could be sources of thermal stress concentration, and under certain conditions they could cause the lower plate to warp and affect the pump performance. However, the axial bulk temperature variation was found to be almost negligible, hence, it is not plotted in the figure. The viscosity variation, also along the lower plate, is shown in Fig. 5(b). It is significant to note that at $x = 0$, the viscosity has dropped to about 10 percent of its inlet value. The effects of this steep viscosity drop will be explored in subsequent results (Sections 4.2 and 4.3).

4.2 Effect of Brinkman Number. In this section, we hold the following parameters fixed: $s = 1.5$, $\delta_L = 0.005$, and Nu* = 0. The Br variation shown in Fig. 6 and Table 3 indicates that there is a monotonic increase in the peak temperature along the lower plate. The range of Pr in Table 3 represents a fairly wide range of fluids from light oils to highly viscous polymers. Also shown in the figure by symbols are the peak lower wall temperatures—as predicted by the analytical model developed in Section 3 for the gap region. The rather remarkable agreement between the computations and the theoretical model is perhaps fortuitous since the gap region temperature profile for Br = 0.75, seen in Fig. 7, is in poor agreement except at the rotor surface and the wall. This indicates that the assumption of thermally fully developed flow is rather questionable due to the

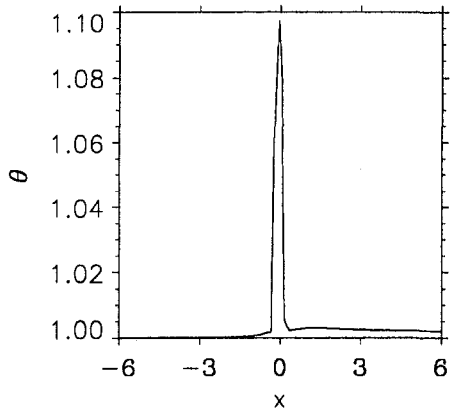

(a)

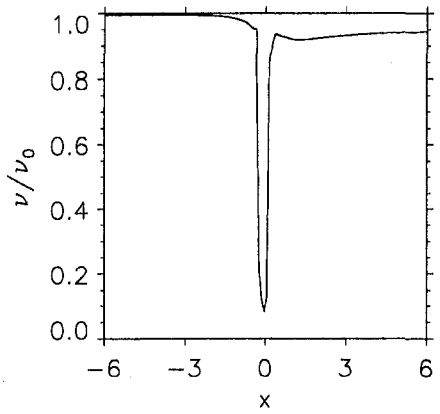

(b)

Fig. 5 Axial variation along the lower wall of (*a*) temperature; and (*b*) viscosity. For s = 1.5, Br = 0.75 and Nu* = 0.

rather steep temperature gradients in the gap region evidenced in Fig. 5(*a*).

The results of Fig. 7 are better explained in the context of Fig. 8, which shows the shear stress distribution around the rotor surface for Br = 0.225 and Br = 0.75. Here the angle ϕ is measured clockwise from the leftmost point of the rotor. The shear stresses in the gap region (between the rotor and the plate

Table 3 Effect of Br on pump performance for s = 1.5 and Nu* = 0

Pr	$Br = EcPr$	$\bar{u}$	θ_{max}	θ_c
1000	0.015	0.110	1.015	1.0032
5000	0.075	0.110	1.025	1.0033
15000	0.225	0.110	1.046	1.0033
25000	0.375	0.109	1.071	1.0033
50000	0.750	0.108	1.111	1.0033
75000	1.125	0.108	1.128	1.0033
100000	1.500	0.108	1.140	1.0035

in the neighborhood of 270°) are the lowest. This translates into low viscous dissipation and, hence, in relatively low temperatures in the vicinity of the rotor, as seen in Fig. 7, for all values of Br.

A more interesting feature is seen in Fig. 8. In the gap region, a sign change in the shear stress is observed for Br = 0.75. This implies that, in this region, the fluid velocities tangential to and in the neighborhood of the rotor are higher than the rotor surface speed itself. Referring to Fig. 9, we find that this is indeed the case. There are two mechanisms acting in tandem that are responsible for this phenomenon. Firstly, it should be noted that the Couette-Poiseuille flow in this region is aided by the pressure gradient between the delivery and suction sides of the pump that are immediately adjacent to the rotor. Secondly, as is easily inferred from Table 3 and Fig. 5(*b*), there is a large viscosity variation between the rotor and the lower wall. This reduced viscosity in the gap region tends to cause a channeling effect, as seen in the figure. Also seen in Fig. 9 is the velocity profile for Br = 0.75 predicted by the approximate theoretical model. The agreement here is somewhat better than in Fig. 7, particularly in the vicinity of the rotor surface, and suggests that the assumption of hydrodynamically fully developed flow is at least better than that of thermally fully developed flow. This reasoning is also justified on account of the Prandtl number ranges (10^3–10^5) under consideration.

No experimental heat transfer data exist to facilitate a comparison with the present numerical results. However, the flow-field computations of Sharatchandra et al. (1997) were in such excellent qualitative and quantitative agreement with the experimental results of Sen et al. (1996), that a very high degree of confidence may be placed on the validity of the present results. This rationale is augmented by the facts that (a) the energy equation is weakly nonlinear, and (b) variable viscosity effects have been considered in the mathematical model. Finally, a note of caution is in order—variable-viscosity Poiseuille flow has

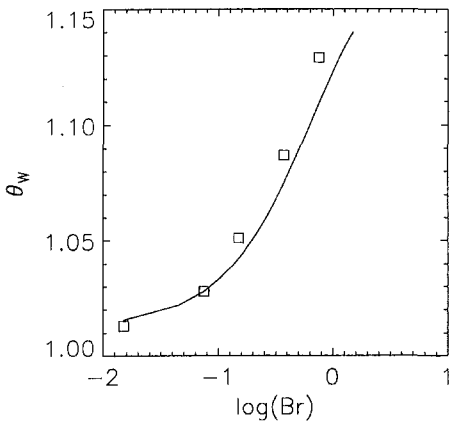

Fig. 6 Variation of peak lower wall temperature with Brinkman number for Nu* = 0, δ_L = 0.005 and s = 1.5. Line: computations; symbols: theoretical model.

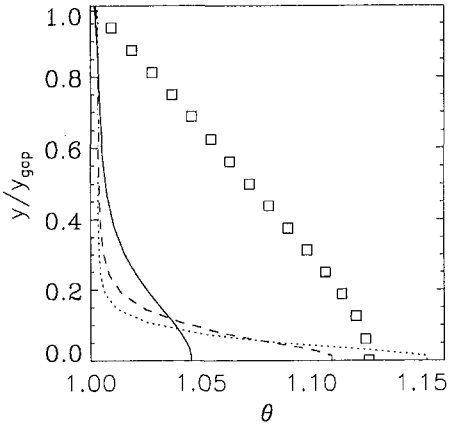

Fig. 7 Transverse variations of temperature in the gap region for s = 1.5 and Nu* = 0. Solid line: Br = 0.225; dashed line: Br = 0.75; dotted line: Br = 1.5; symbols: theoretical model, Br = 0.75.

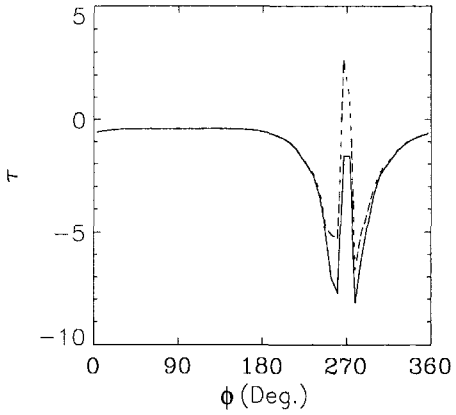

Fig. 8 Shear stress distribution around the rotor for s = 1.5 and Nu* = 0. Solid line: Br = 0.225; broken line: Br = 0.75.

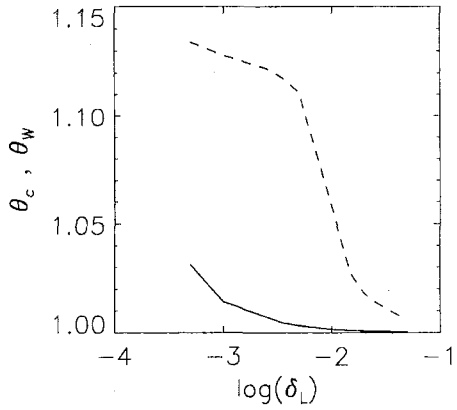

Fig. 10 Variations of rotor surface temperature (solid line) and peak lower wall temperature (dashed line) with rotor position for s = 1.5, Br = 0.75, and Nu* = 0.

been shown (Sen and Vasseur, 1989) to have multiple solutions depending on the values of C_v and the effective Brinkman number.

Interestingly, the bulk velocity is not significantly affected by Br, as shown in Table 3. The reason for this is that the rotor surface temperature remains virtually constant with an increase in Br, as also shown in the table. The latter effect is due to the fact that the rotor surface, unlike the wall, is moving and the heat gained in the gap region is dissipated to the bulk fluid above the rotor. Moreover, the effects of reduced shear at the rotor surface due to lower viscosity are offset by the far lesser resistance to flow offered by the lower wall due to the decrease in local viscosity there. It is worth noting that an almost negligible rise in the rotor temperature as Br increases from 0.015 to 1.5 translates into a nearly 3 percent drop in the bulk velocity. This is due to the exponential nature of the viscosity-temperature relationship.

4.3 Effect of Rotor Position. In this section, we hold the following parameters fixed: s = 1.5, Br = 0.75, and Nu* = 0. The strong effect of even a slight displacement of the rotor from the lower plate is seen in Fig. 10. This is cause for concern from a design standpoint because even if care is taken to position the rotor at the more benign position of say, δ_L = 0.1, a mild excursion from this position could result in rather steep temperature rises both at the rotor surface and lower plate. Clearly, the shear stresses in the gap region are very sensitive to rotor position, particularly in the neighborhood of δ_L = 0.01. What is interesting is the tendency of the peak lower-wall temperature to level off as $\delta_L \to 0$, while, on the other hand, the rotor surface temperature seems to rise almost exponentially in this limit. The following argument is used to explain this phenomenon. For very small gap heights, fairly accurate estimates of the lower wall and rotor surface velocity gradients may be obtained as

$$\tau_W = \frac{2\bar{u}_g}{y_g} \quad \text{and} \quad \tau_R = \frac{2(1 - \bar{u}_g)}{y_g}, \tag{27}$$

where y_g and $\bar{u}_g$ are the gap region height and bulk velocity, respectively. The gap region bulk velocity is defined as the flow rate in the gap region divided by the minimum gap cross-sectional area. As the gap region shrinks in size, the magnitude of the backflow there (characterized by $\bar{u}_g$ in the above expressions) tends to diminish. Consequently, the increase in the wall shear stress (due to decreased δ_L) is mitigated by the lower value of $\bar{u}_g$, whereas the shear stress at the rotor surface increases on both counts. The corresponding increases in viscous dissipation are responsible for the surface temperature rises seen in Fig. 10.

The variation of the global bulk velocity (defined as the volumetric flow rate divided by the channel cross-sectional area) with δ_L is shown in Fig. 11. The dashed line corresponds to Br = 0 (no viscous dissipation). The differences between the solid and dashed lines represent the error involved in a flow analysis that neglects the effects of viscous dissipation. Specifically, in this context it is seen that a 23 percent error is involved when δ_L = 0.001. The decrease in $\bar{u}$ with δ_L is due to the reduced viscosity accompanying the increase in rotor surface

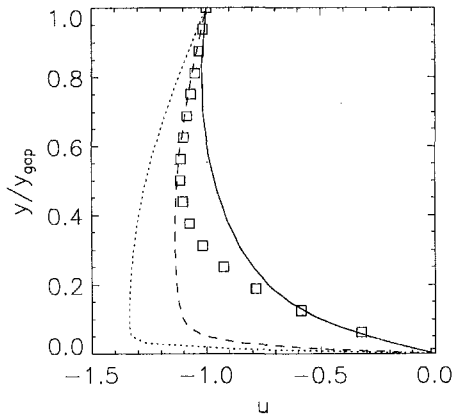

Fig. 9 Transverse variations of tangential velocity in the gap region for s = 1.5 and Nu* = 0. Solid line: Br = 0.225; dashed line: Br = 0.75; dotted line: Br = 1.5; symbols: theoretical model, Br = 0.75.

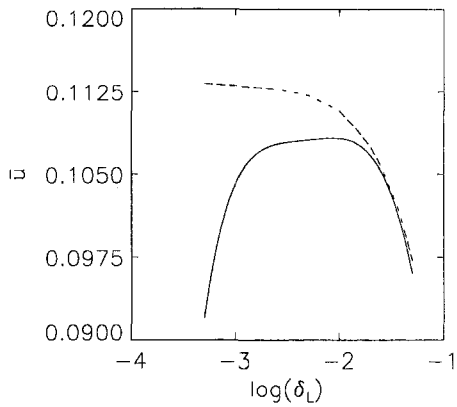

Fig. 11 Variation of bulk velocity with rotor position for s = 1.5 and Nu* = 0. Solid line: Br = 0.75; dashed line: Br = 0.

temperature seen in Fig. 10. A very interesting and significant aspect of the present analysis is the appearance of an optimum value of δ_L when the effects of viscous dissipation are significant. Given the extremely low pumping power requirements involved, it is meaningful to seek to maximize the bulk velocity itself, rather than the flow rate per unit pumping power input. While the entire parameter space of both Br and δ_L was not probed, it is clear that the optimum value tends to move away from the wall as Br increases.

The rotor moment coefficient defined as

$$C_M = \int_0^{2\pi} F_\nu(\theta_c)\tau d\phi \tag{28}$$

is a measure of the pumping power required. The integration is performed around the rotor periphery. This quantity is plotted in Fig. 12 with the dashed line again representing the case Br = 0. Once again, the error involved due to neglecting the effects of viscous dissipation is clearly seen in the figure. The errors involved translate into an approximately 60 percent overprediction in the pumping power estimate for $\delta_L = 0.001$.

4.4 Effect of Plate Spacing In this section, we hold the following parameters fixed: $\delta_L = 0.005$, Br = 0.225, and Nu* = 0. Here we consider the effect of varying the parameter s by keeping the spacing between the rotor and the lower plate fixed while displacing the upper plate. The physics of the problem suggests that the thermal aspects of the flow are not likely to be significantly affected by changes in s, if δ_L is held fixed. This is confirmed by the computations, and the results for this case are summarized in Table 4. The table shows the presence of an optimum value of s with respect to $\bar{u}$, similar to the constant viscosity case in Sharatchandra et al. (1997). It must be mentioned, however, that in the presence of a load acting on the pump (i.e., a nonzero Δp^*), the optimum tends to move towards a value of s lower than 1.5.

The temperature field, however, experiences virtually no change with s. This is because the spacing between the bottom of the rotor and the lower plate is unchanged as the upper plate position is varied. The marginal increases in the rotor surface temperature as s decreases is due to the increased shear stress on the upper surface of the rotor due to the proximity of the upper plate.

4.5 Effect of Cooling Flux. In this section, we hold the following parameters fixed: $s = 1.5$, $\delta_L = 0.005$, and Br = 0.225. Rather than maintaining the rotor surface insulated as assumed thus far, we explore the effects of a Robins-type boundary condition applied in terms of a convective cooling flux (whose magnitude is as such unknown) at the rotor ends, as depicted in Fig. 2 and explained earlier. Table 5 shows that

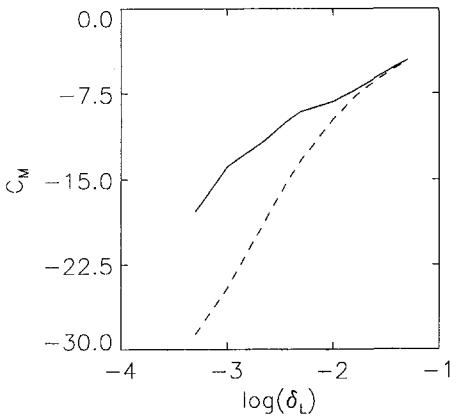

Fig. 12 Variation of rotor moment coefficient with rotor position for s = 1.5 and Nu* = 0. Solid line: Br = 0.75; dashed line: Br = 0.

Table 4 Effect on s on pump performance for Br = 0.225 and Nu* = 0

s	$\bar{u}$	θ_{max}	θ_c
2	0.101	1.111	1.0032
1.5	0.108	1.111	1.0033
1.25	0.091	1.111	1.0033
1.1	0.047	1.111	1.0037

the bulk velocity variation with increasing Nu* is similar to the corresponding variation of $\bar{u}$ with decreasing Br (Table 3). This may be explained as follows. The rotor surface conditions have the most significant influence on $\bar{u}$. A larger cooling flux results in lower rotor surface temperatures and, hence, in higher viscosity, which increases the bulk velocity. The same effect is observed in the context of lower Brinkman numbers. While the improvements in bulk velocity with Nu* are not particularly significant, it is conceivable that for lower values of δ_L outside the range of optimal values for Nu* = 0, a large enough cooling flux could lower the rotor surface temperature such that significant improvements in the pump flowrate are observed.

The very slight (and seemingly anamolous) increase in peak lower-wall temperature with Nu* may be explained by the increase in viscosity in the immediate vicinity of the rotor causing the fluid to take the path of lower resistance resulting in channeling near the wall. The enhanced wall shear stresses and attendant viscous dissipation cause an increase in the wall temperature. At any rate, this increase is too slight to be of significance.

Finally, Fig. 13 shows the variation of the rotor surface temperature as a function of Nu*. Two asymptotic trends are clear for extreme values of Nu*. The first corresponds to Nu* = 0, where the cooling flux decays to zero when the rotor surface is insulated. The second trend corresponds to the limit Nu* $\to \infty$, where $\theta_c \to 1$. Also plotted in the figure is the rotor surface heat flux. The trend towards asymptotic invariance as Nu* $\to \infty$ is seen again. It is worth noting here that the product Nu*(θ_c − 1) is constant in this limit and is the heat flux required to maintain the rotor at the pump inlet temperature. An estimate of the physical magnitude of the peak heat flux may be made in terms of the pump fluid thermal conductivity, rotor diameter, and inlet (reference) temperature. The heat flux per unit area, however, increases in inverse proportion to the square of the rotor diameter, and this could have drastic consequences, even for micropump diameters of the order of 100 μ.

5 Conclusions

A parametric study of the thermal aspects in a viscous pumping mechanism has been conducted. The coupled momentum and energy equations were solved using a finite-volume methodology. The analysis incorporated the effects of both variable viscosity and viscous dissipation. The computational method was validated and found suitable for the present application. An approximate theoretical model developed for the gap region between the rotor and the lower plate yielded satisfactory agreement with the computational results for the velocity profiles, but

Table 5 Effect on Nu* on pump performance for Br = 0.225 and s = 1.5

Nu^*	$\bar{u}$	θ_{max}
0	0.108	1.111
10	0.108	1.111
10^2	0.108	1.111
10^3	0.109	1.111
10^4	0.110	1.112
10^5	0.110	1.112
10^6	0.111	1.112

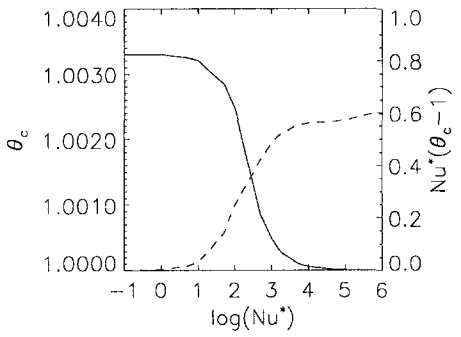

Fig. 13 Variation of rotor surface temperature (solid line) and cooling flux (broken line) with Nu*. Br = 0.225 and s = 1.5.

not for the temperature profiles. The model, however, provides a basis for an enhanced understanding of the important flow and heat transfer phenomena in the gap region. A very interesting observation is that the significance of the gap region increases in inverse proportion to its size. The most significant finding of this study is that neglecting the effects of viscous dissipation can lead to very large errors in the computed flow rates and pumping power estimates when the rotor is placed very close to the lower wall. Furthermore, an optimal value of δ_L is shown to exist for nonzero values of Br. While no significant rises in bulk temperature were observed even for rather large values of Br, very steep gradients were observed along the lower plate in the vicinity of the rotor. Temperature rises of the order of 30 K are predicted when the working fluid is highly viscous with a pump inlet temperature of 290 K. The plate spacing with fixed rotor position relative to the lower plate has virtually no effect on the thermal characteristics. Finally, the effects of a cooling flux do not appear to significantly improve the pump performance in terms of flowrate for a value of δ_L close to the optimum. Moreover, the cooling flux tends to slightly increase the lower wall temperature. In summary, it is concluded that viscous dissipation effects are indeed significant in the present context. Further study may be required, however, to fully explore the existence of optimal values of δ_L for a wide range of Br and Nu*.

Acknowledgments

This study was performed under a grant from the National Science Foundation, under the Small Grants for Exploratory Research initiative (SGER Grant No. CTS-95-21612). The technical monitors are Dr. Robert Powell and Dr. Roger E. A. Arndt. Different versions of this research have been presented at the ASME Computers in Engineering Conference, Irvine, California, 18–22 August 1996, and at the Annual Meeting of the Division of Fluid Dynamics, American Physical Society, Syracuse, New York, 24–26 November 1996.

References

Balachandar, S., Yuen, D. A., and Lauer, G. S., 1995, "Viscous Dissipation in Three-Dimensional Convection with Temperature-Dependent Viscosity," *Science,* Vol. 267, No. 5201, pp. 1150–1152.

Beskok, A., and Karniadakis, G. E., 1994, "Simulation of Heat and Momentum Transfer in Complex Micro-Geometries," *AIAA Journal of Thermophysics and Heat Transfer,* Vol. 8, No. 4, pp. 355–370.

Butler, H. W., and McKee, D. E., 1973, "An Exact Solution for the Flow of Temperature-Dependent Viscous Fluids in Heated Rectangular Ducts," ASME JOURNAL OF HEAT TRANSFER, Vol. 95, pp. 555–557.

Cho, Y.-H., Kwak, B. M., Pisano, A. P., and Howe, R. T., 1993, "Viscous Energy Dissipation in Laterally Oscillating Planar Microstructures: A Theoretical and Experimental Study," *Proceedings IEEE Micro Electro Mechanical Systems,* M. Esashi and J. Fluitman, eds., IEEE, NY, pp. 93–98.

de Araujo, J. H. C., Raus, V., and Vargas, A. S., 1990, "Finite Element Solution of Flow Between Eccentric Cylinders with Viscous Dissipation," *International Journal for Numerical Methods in Fluids,* Vol. 11, No. 6, pp. 849–866.

Ho, C.-M., and Tai, Y.-C., 1994, "MEMS—Science and Technology," in *Application of Microfabrication to Fluid Mechanics,* P. R. Bandyopadhyay et al., eds. ASME FED Vol. 197, ASME, NY, pp. 36–46.

Hogan, H., 1996, "Invasion of the Micromachines," *New Scientist,* Vol. 29 June, pp. 28–33.

Lee, S. H.-K., and Jaluria, Y., 1996, "Effects of Variable Properties and Viscous Dissipation During Optical Fiber Drawing," ASME JOURNAL OF HEAT TRANSFER, Vol. 118, No. 2, pp. 350–358.

Pfahler, J., Harley, J., Bau, H. H., and Zemel, J., 1991, "Gas and Liquid Flow in Small Channels," in *Symp. Micromechanical Sensors, Actuators, and Systems,* D. Cho et al., eds. ASME DSC Vol. 32, ASME, NY, pp. 49–60.

Piekos, E., and Breuer, K. S., 1995, "DSMC Modeling of Micromechanical Devices," AIAA Paper No. 95-2089, American Institute of Aeronautics and Astronautics, Reston, VA.

Sen, M., and Vasseur, P., 1989, "Analysis of Multiple Solutions in Plane Poiseuille Flow with Viscous Heating and Temperature Dependent Viscosity," *Heat Transfer in Convective Flows,* Proceedings of the 1989 National Heat Transfer Conference, R. K. Shah, ed. ASME, NY, pp. 267–272.

Sen, M., Wajerski, D., and Gad-el-Hak, M., 1996, "A Novel Pump for Low-Reynolds-Number Flows," *ASME Journal of Fluids Engineering,* Vol. 118, No. 3, pp. 624–627.

Sharatchandra, M. C., 1995, "A Strongly Conservative Finite-Volume Formulation for Fluid Flows in Irregular Geometries Using Contravariant Velocity Components," Ph.D. thesis, Texas A&M University, College Station, TX.

Sharatchandra, M. C., and Rhode, D. L., 1994, "A New Strongly Conservative Finite-Volume Formulation for Fluid Flows in Irregular Geometries using Contravariant Velocity Components. Part 1—Theory," *Numerical Heat Transfer,* Part B, Vol. 26, pp. 39–52.

Sharatchandra, M. C., Sen, M., and Gad-el-Hak, M. 1997, "Navier-Stokes Simulations of a Novel Viscous Pump," *ASME Journal of Fluids Engineering,* Vol. 119, No. 2, pp. 372–382.

Wannier, G. H., 1950, "A Contribution to the Hydrodynamics of Lubrication," *Quarterly of Applied Mathematics,* Vol. 8, pp. 1–18.

Wilding, P., Pfahler, J., Bau, H. H., Zemel, J. N., and Kricka, L. J., 1994, "Manipulation and Flow of Biological Fluids in Straight Channels Micromachined in Silicon," *Clinical Chemistry,* Vol. 40, No. 1, pp. 43–47.

Natural Convection of a Liquid Metal in Vertical Circular Cylinders Heated Locally From the Side

R. Selver

Y. Kamotani
yxk@po.cwru.edu

S. Ostrach

Department of Mechanical and Aerospace Engineering,
Case Western Reserve University,
10900 Euclid Avenue,
Cleveland, OH 44106-7222

An experimental study is made of natural convection in gallium melts enclosed by vertical circular cylinders with localized circumferential heating. Heating is done in an axial band at the mid-height, and both ends of the cylinder are cooled. In the present study, the cylinder aspect (Ar = height/diameter) ratio ranges from 2 to 10, and the Rayleigh number (Ra) ranges from 9.0×10^4 to 3.0×10^7. The Prandtl number is 0.021. Temperature measurements are made at six axial levels around the circumference of the cylinder to study thermal convection in the melt. A numerical analysis is also conducted to supplement the experimental information. When Ra is small, the melt is in steady toroidal motion. Above a certain Ra, the flow becomes nonaxisymmetric as a result of a thermal instability, in the case of Ar larger than 3. With increasing Ra, the motion becomes oscillatory, mainly in the upper half. When Ar is smaller than 3, the toroidal flow becomes nonaxisymmetric and oscillatory at the same time beyond a certain Ra. The conditions for the appearance of oscillations and the oscillation frequencies are investigated in detail.

1 Introduction

It is known that in crystal growth processes of solidification from a melt, natural convection can have a strong influence on the structure and quality of the resulting crystals (Hurle, 1972). Oscillatory or time-dependent convection is especially problematic because it can result in periodic inhomogeneities in crystals (Müller et al., 1984). In the past, several investigators have studied oscillatory natural convection of liquid metals in circular cylinders with differentially heated end walls because it is a basic configuration of several crystal growth systems (e.g., Müller et al., 1984; Crespo et al., 1989; Neumann, 1990; Kamotani et al., 1994). They found that the flow becomes oscillatory beyond a certain Rayleigh number (Ra) and that the critical Ra depends on the cylinder aspect (height/diameter) ratio (Ar). Kamotani et al. (1994) measured temperature around the circumference of the cylinder at several axial locations, from which the oscillatory flow structures were inferred. They showed various oscillation patterns depending on Ra, Ar, and the cylinder inclination angle.

The present study is an extension of our earlier work (Kamotani et al., 1994). In the present experimental work, gallium melts (Prandtl number = 0.021) are placed in vertical circular cylinders which are heated in an axial band at the mid-height. The experiment is designed to investigate convection in a simulated vertical zone melting configuration. In the zone melting technique of crystal growth, the aspect ratio of the melt zone is near unity (1 to 2), but the present experiment covers a much wider range of Ar than that in order to study oscillatory convection under more general conditions. Thermocouples are placed around the circumference to detect the onset of oscillations and to determine the oscillation flow structures and frequencies. In addition to the experiment, the flow in a two-dimensional configuration is analyzed numerically to help us obtain a better qualitative understanding of the basic steady flow field. Baumgartl et al. (1989) studied, both numerically and experimentally, steady and time-dependent convection in a configuration similar to the present one. However, their work was limited to the $Ar = 1$ condition and the flow and temperature fields were not studied experimentally in detail. The present paper is based on the work of Selver (1996).

2 Experimental Design

2.1 Important Dimensionless Parameters. The experimental configuration is sketched in Fig. 1. A fluid is placed in a vertical circular cylinder, and is heated at the mid-height and cooled uniformly at both ends of the cylinder. Except for the heated region, the cylinder wall is assumed to be thermally insulated. It can be shown that the important dimensionless parameters for the steady thermal convection inside the cylinder are: Rayleigh number (Ra), Prandtl number (Pr), cylinder aspect ratio (Ar), and relative heating zone size (Hr). The experiment is designed to study convection in a simulated vertical zone melting configuration of crystal growth. Therefore, we consider the situation where $\mathrm{Ra} \gg 1$, $Ar > 1$, and $Hr \ll Ar$ in the present work. Since oscillatory thermal convection tends to occur in crystal growth systems of low Prandtl fluids, we focus on such fluids.

2.2 Experimental Apparatus. The experimental setup is similar to the one used in our earlier work (Kamotani et al., 1994) with the exception of the heating configuration. The test section consists of two plexiglas cylinders, a ring heater, as well as cooled bottom and top walls. In order to cover wide ranges of Ra and Ar, test sections with four different inner diameters (1.27, 1.59, 1.91, and 2.54 cm) are used. Plexiglas tubes of 3.2 mm wall thickness are used for the test sections with foam insulation wrapped around them. Different length cylinders are used to vary Ar. The ring heater is made of copper with an internal channel for water circulation from a constant temperature bath, and its width is equal to half the cylinder inner diameter ($Hr = 0.5$). Two thermocouples are embedded in the heater at diametrically opposed positions to monitor the heater temper-

Contributed by the Heat Transfer Division for publication in the JOURNAL OF HEAT TRANSFER and presented at ASME IMECE, 1996. Manuscript received by the Heat Transfer Division April 11, 1997; revision received November 17, 1997; Keywords: Enclosure Flows; Flow Instability; Liquid Metals; Natural Convection. Associate Technical Editor: P. G. Simpkins.

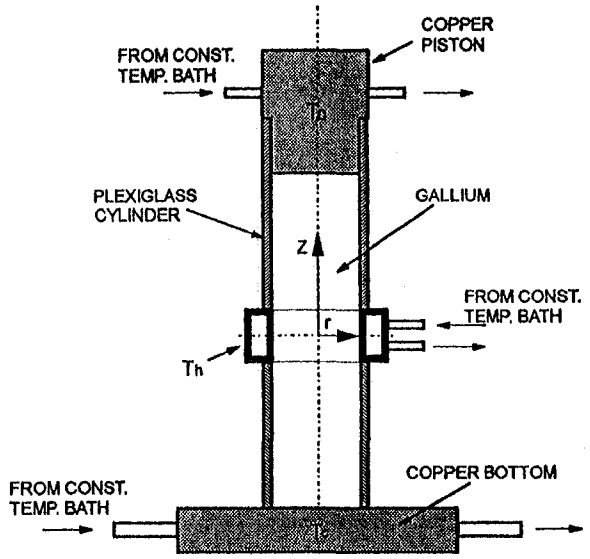

Fig. 1 Experimental configuration

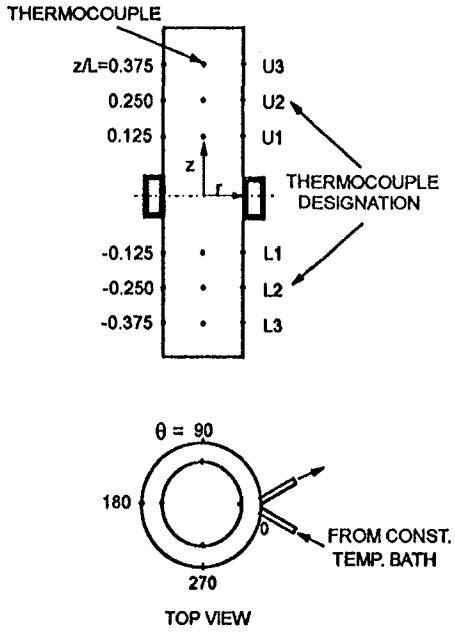

Fig. 2 Thermocouple locations

ature. The bottom plate is made of copper and has an internal channel for water circulation. A copper piston, whose temperature is maintained by running constant-temperature water through it, makes up the top wall. Both wall temperatures are monitored by embedded thermocouples. Gallium is used as the test fluid. Its Prandtl number is equal to 0.021. It is chosen because it is safe and its melting point (29.8°C) is near room temperature. Furthermore, its thermophysical properties are known (see, e.g., Platt et al., 1991).

Holes of diameter 0.72 mm are drilled around the circumference of each cylinder to allow thermocouples to access the liquid-wall interface. A total of 24 holes are drilled, 12 in each of the top and bottom cylinders. As shown in Fig. 2, the holes are located at six different heights with four symmetrically arranged holes at each height. The thermocouples are made from 0.08 mm diameter wire and protrude only slightly (about the size of the thermocouple bead, namely 0.15 mm) into the fluid in order to avoid affecting the oscillations. As shown by Kamotani et al. (1994), the effects of those thermocouples on the oscillation phenomenon are negligible within the experimental error. Before the installation in the test sections, the thermocouples are placed in water at various temperature levels from 0 to 70°C, and only the thermocouples whose readings are accurate to within ±0.05°C in that temperature range are used in the experiments.

2.3 Experimental Procedure. The experimental procedure is very similar to that in our past work (Kamotani et al., 1994). Solid clean gallium ingots are placed in the cylinder, melted, and then stirred to remove trapped air. The top piston is then inserted and pushed down so that the trapped air below the piston is expelled from small holes in the plexiglas wall. During a test, the bottom and top wall temperature is maintained at 35°C. A computer controls the temperature of the circulating water through the heater with a ramp setting lower than 1°C per hour. The existence or nonexistence of oscillations is usually obvious by examining the thermocouple outputs, and the flow is judged to be oscillatory if any one of the thermocouples shows oscillations. The tests are repeated at least three times to check repeatability of the data.

Parametric ranges covered by the present experiment are as follows: Pr = 0.021, Hr = 0.5, Ar = 2 − 10, and Ra = $9.0 \times 10^4 - 3.0 \times 10^7$. Experimental error in the temperature measurement is estimated to be ±0.05°C. The value of ΔT_{cr} (the critical temperature difference for the onset of oscillations) is reproducible within ±10 percent. Error in Ra is estimated to be ±4 percent. The error in the dimensionless frequency is estimated to be ±3 percent.

3 Numerical Analysis

The fluid motion in the present experiment is expected to be complex, but, since gallium is opaque, its motion cannot be easily visualized. An accurate three-dimensional numerical simulation of the present experiment is extremely time-consuming computationally, and beyond the scope of the present study. Instead, we consider only a two-dimensional version of the

Nomenclature

Ar = aspect ratio = L/D
Ar^* = aspect ratio based on half-height = $(L/2)/D$
D = cylinder diameter
f = oscillation frequency
f^* = dimensionless frequency = $f/(2g\beta\Delta T/L)^{1/2}$
g = gravitational acceleration
Hr = dimensionless heating zone length = L_H/D
L = cylinder height
L_H = heating zone length
Pr = Prandtl number = ν/α
Ra = Rayleigh number = $g\beta\Delta TL^3/\nu\alpha$
Ra* = Rayleigh number based on half-height = $g\beta\Delta T(L/2)^3/\nu\alpha$
Ra^*_{cr} = critical Ra* for onset of oscillations
(r, z) = coordinate system defined in Fig. 1
T = temperature
T_c = cold wall temperature
α = thermal diffusivity
β = coefficient of thermal expansion
ΔT = temperature difference between hot and cold walls
ΔT_{cr} = critical ΔT for onset of oscillations
ν = kinematic viscosity

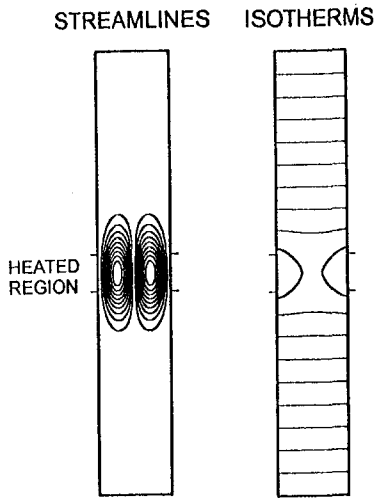

Fig. 3 Computed streamlines and isotherms at equal increments for two-dimensional configuration (Ra = 1.6×10^5, $Ar = 6$, and $Hr = 0.5$). The maximum stream function is equal to 4.32×10^{-3}.

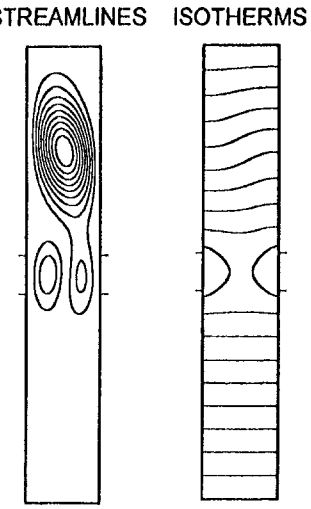

Fig. 4 Computed streamlines and isotherms at equal increments for two-dimensional configuration (Ra = 6.0×10^5, $Ar = 6$, and $Hr = 0.5$). The maximum stream function is equal to 3.34×10^{-2}.

present problem, namely, a fluid is placed in a rectangular container and heated by heaters at the mid-height. The two-dimensional simulation gives us only qualitative information about the present experiment, but it turns out to be quite useful, as will be discussed later.

Our numerical model is based on the SIMPLER scheme (Patanker, 1980). The continuity equation, the momentum equations with the Boussinesq approximation, and the energy equation are solved. In the analysis, the flow is assumed to be laminar and incompressible. Uniform meshes are employed in the horizontal direction, while a nonuniform grid system is used in the vertical direction with meshes graded toward the heated region. In the numerical analysis, the axial velocity, radial velocity, and stream function are nondimensionalized by $(g\beta\Delta TL)^{1/2}$, $(g\beta\Delta TL)^{1/2}/Ar$, and $(g\beta\Delta TL)^{1/2}D$, respectively. The time, axial location, and radial location are nondimensionalized by $(L/g\beta\Delta T)^{1/2}$, L, and D, respectively. The temperature is nondimensionalized as $(T - T_c)/\Delta T$. The dimensionless heat transfer rate, namely the Nusselt number, is defined as the ratio of the total heat transfer rate to the (computed) total heat transfer rate by conduction. Hr is set at 0.5 in the numerical analysis as in the experiment.

For the conditions of Ra = 2.1×10^5 and $Ar = 6$, the values of the maximum stream function computed with three different grids, 31×41 (horizontal by vertical), 51×71, and 81×111 with the smallest mesh sizes in the vertical direction of 0.0083, 0.0042, and 0.0028, respectively, are 4.96×10^{-3}, 4.83×10^{-3}, and 4.78×10^{-3}, respectively. With those grids, the computed Nusselt numbers are 1.01, 1.00, and 1.00, respectively. Therefore, the 51×71 grid system is used in the present analysis.

4 Results and Discussion

4.1 Computed Results. The numerical results are discussed first. In Fig. 3, the computed streamlines and isotherms are shown for the conditions of Ra = 1.6×10^5 and $Ar = 6$. As the isotherms show, the fluid temperature changes linearly with the vertical distance over most of the flow field, and noticeable horizontal temperature gradients exist only in the vicinity of the heated region. Consequently, the main fluid motion is confined to the region near the heater. Note that the nearly motionless fluid in the upper half is heated from below and cooled from above, which is thermally unstable. The condition in the lower half is thermally stable.

The flow structure remains basically the same with increasing Ra but beyond a certain Ra (about 4.4×10^5) the flow structure suddenly changes. The streamlines and isotherms presented in Fig. 4 are computed at Ra = 6.0×10^5, which shows that the whole upper-half region is in strong motion. The flow is a result of a thermal instability in that region. It is known that in the case of a fluid in a vertical cylinder which is heated at the bottom and cooled at the top, the fluid remains motionless up to a certain Rayleigh number and beyond that the fluid becomes unstable, and a unicellular flow appears (Kamotani et al., 1994). The situation in the present problem is similar to the heated-from-below case, except that the unicellular motion in the present problem interacts with the existing motion near the heater. After the instability, the isotherms in the upper half become distorted because of strong convection in that region (Fig. 4). Therefore, we detect the onset of the instability in the present experiment by measuring the side wall temperature distribution.

Since only the upper half becomes thermally unstable in the present configuration, we may be able to relate the upper half situation to the heated-from-below configuration that has been investigated in the past by several investigators. For that reason, we use the Rayleigh number and aspect ratio that are based on the half of the container height (Ra* and Ar^*) in conjunction with the thermal instability. Then, the computed Rayleigh number for the onset of the unicellular motion is $(5.5 \pm 0.1) \times 10^4$ for $Ar^* = 3$. The present numerical analysis deals also with the heated-from-below case with some modifications of the thermal boundary conditions (differentially heated bottom and top walls and insulated side walls). The computed Rayleigh number for the instability in that case is found to be $(4.6 \pm 0.1) \times 10^4$ (going from stability to instability) when the container height/width ratio is three. Therefore, by comparing the above two critical Rayleigh numbers one can conclude that the two situations are very similar.

It is not clear what determines the circulation direction of the cellular motion in the upper half in the numerical simulation. Experimentally, a slight nonuniformity in the thermal boundary conditions determines the circulation direction (Baumgartl et al., 1989). According to the present numerical analysis, the flow before the thermal instability and the value of Ra* for the onset of instability depend very strongly on the nonuniformity in the thermal conditions. For example, with only a 1 percent difference in the right and left heater temperatures (about the level of nonuniformity in the present experiment), the cellular flow near the slightly warmer heater has about a 42 percent larger stream function than the flow near the slightly colder heater at Ra = 1.6×10^5 ($Ar = 6$), and the critical Ra* is reduced by 10 percent. In contrast, the flow after the instability

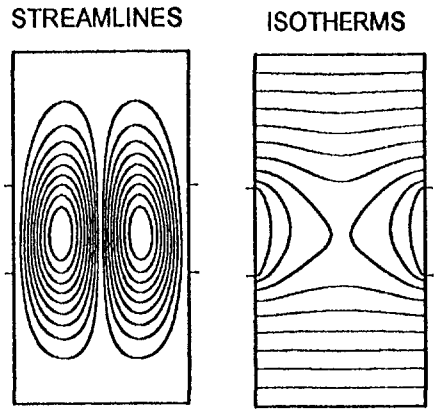

Fig. 5 Computed streamlines and isotherms at equal increments for two-dimensional configuration (Ra = 2.1 × 10^4, *Ar* = 2, and *Hr* = 0.5). The maximum stream function is equal to 3.66 × 10^{-2}.

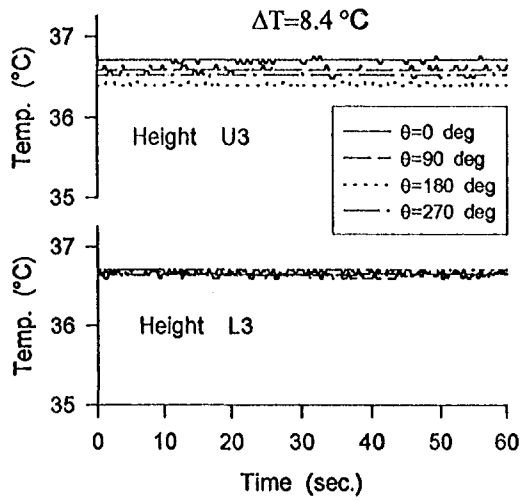

Fig. 7 Thermocouple outputs at Ra = 5.7 × 10^5 (Ra* = 7.1 × 10^4) for *Ar* = 4. Thermocouple locations are shown in Fig. 2.

is not so sensitive to the nonuniformity: with a 1 percent difference in the heater temperatures, the maximum stream function is only about a 2 percent larger than that in the uniform heating case at Ra = 1.0 × 10^6.

The situation is very different when *Ar* is near unity (*Ar* less than about 3). The computed streamlines and isotherms at Ra = 2.1 × 10^4 for *Ar* = 2 (the smallest *Ar* in the present experiment) are shown in Fig. 5. The fluid motion extends nearly all the way to the end walls so that there is no quiescent thermally unstable region as in the larger *Ar* case. The flow and isotherms are symmetric (left and right), and the isotherms are only slightly distorted by convection, especially in the upper half.

With increasing Ra, the velocity and temperature fields interact more strongly. Eventually, it becomes impossible to keep the two cells exactly balanced and the flow becomes nonsymmetric. The present analysis shows that the flow becomes unstable above about Ra = 4 × 10^4, and the flow oscillates after the instability. Figure 6 shows how the flow structure changes in one period of oscillation. The figure shows that the two cells undergo the same oscillation process, but with a 180 deg phase shift. What is happening is that the two cells compete against each other, each cell becoming alternately large and small. The oscillations are caused by an interaction of inertia and buoyancy forces in the following way. When one cell becomes stronger, it will bring more cold fluid to the lower half and, consequently, the region just below the heated region on the side of the stronger cell will become more thermally stratified. Eventually, the stable thermal stratification will slow down the cell and the other cell will then become stronger. Since the oscillations are associated with the heated-from-above condition in the lower half, there is no corresponding situation in the heated-from-below configuration.

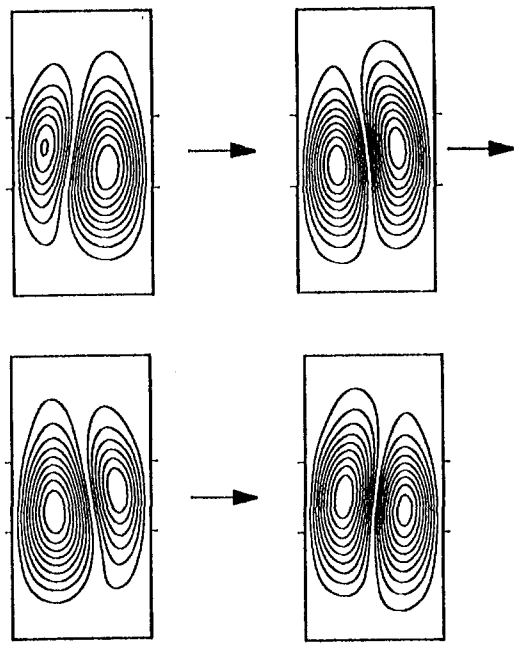

Fig. 6 Change of flow structure during oscillations in two-dimensional computation (Ra = 6 × 10^4, *Ar* = 2, and *Hr* = 0.5)

The computed dimensionless oscillation period for the conditions of Fig. 6 is 30.8 (the time here is nondimensionalized by $(L/2g\beta\Delta T)^{1/2}$), or the dimensionless oscillation frequency is 0.032. Based on the above discussion on the oscillation mechanism, the oscillation period should scale with the convection time scale. The time scale for convection is obtained by dividing the length scale between the hot and cold walls by the velocity scale, which gives $(L/2g\beta\Delta T)^{1/2}$. As for the effect of heating nonuniformity, with a 1 percent difference in the left and right heater temperatures, the computed critical Ra is reduced by about 10 percent for *Ar* = 2.

4.2 Experimental Results.

4.2.1 Temperature Traces. The present experimental information is based mainly on the outputs from the thermocouples located at various places along the cylinder side wall. Some temperature traces obtained in two typical tests (*D* = 1.59 cm, *Ar* = 4 and *D* = 1.91 cm, *Ar* = 2) are presented below, together with the information we derive from them.

The case of *Ar* = 4 is discussed first. When ΔT is small, it is found (Selver, 1996) that (i) the four thermocouple outputs at each height are all close, and the fluid temperature in the upper half is close to that at the corresponding location in the lower half, and (ii) the outputs at different heights show that the wall temperature changes nearly linearly in the axial direction. The information suggests that no or very weak flow exists in the cylinder.

Beyond about ΔT = 3.8°C (Ra = 2.6 × 10^5, Ra* = 3.2 × 10^4), the four outputs at some heights begin to differ in a systematic way. The temperature traces shown in Fig. 7 are obtained at ΔT = 8.4°C (Ra = 5.7 × 10^5, Ra* = 7.1 × 10^4). As seen from the outputs at the U3 location, the thermocouple located at 0 deg (see Fig. 2) shows the highest reading, and the thermocouple located at 180 deg shows the lowest at all times. The readings of the thermocouples located at 90 and 270 deg are between those two values. In comparison, the outputs

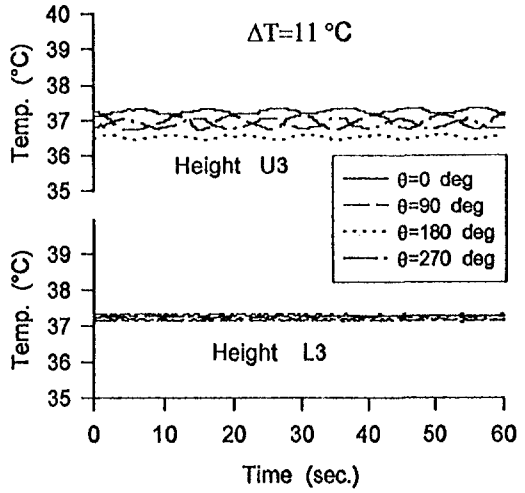

Fig. 8 Thermocouple outputs at Ra = 7.4 × 10^5 (Ra* = 9.3 × 10^4) for Ar = 4. Thermocouple locations are shown in Fig. 2.

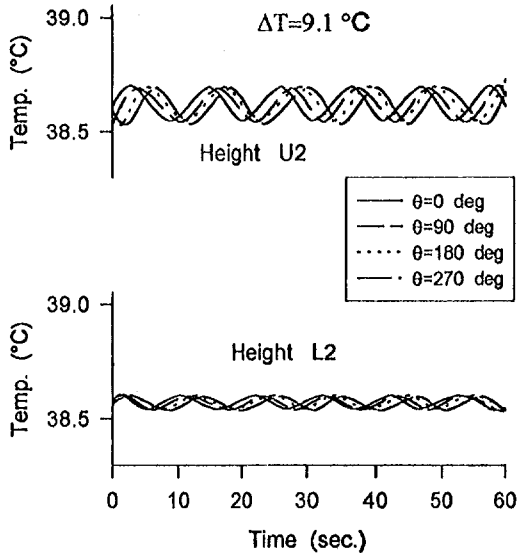

Fig. 9 Thermocouple outputs at Ra = 1.3 × 10^5 (Ra* = 1.6 × 10^4) for Ar = 2. Thermocouple locations are shown in Fig. 2.

from the four thermocouples at the L3 location (in the lower half) are very close. From the data, one can infer that a unicellular motion is generated in the upper half as a result of the aforementioned thermal instability in which the fluid moves up around a 0 deg angle and flows down around a 180 deg angle. No such motion exists in the lower half. The upflow region in the upper half coincides with the location where the circulating water enters the heater, and, thus, the temperature of the heater is highest. Although the heater temperature is measured to be less than 1 percent (of ΔT) higher at the water inlet than at the outlet, the circulation direction of the motion created by the instability is very sensitive to the nonuniformity in the thermal boundary conditions, as shown by the aforementioned numerical analysis. For $Ar^* = 3$ it is found that the instability occurs around $Ra^* = 10^5$ compared to the value of $Ra^* = 5.5 \times 10^4$ obtained from the two-dimensional numerical computation. The fact that the two-dimensional critical Rayleigh number is smaller is reasonable because the side wall effect is stronger in the cylindrical configuration.

With increasing ΔT, the differences in the thermocouple readings at the same height increase, suggesting that the unicellular motion becomes stronger. Then, beyond about $\Delta T = 10$°C ($Ra^* = 8.4 \times 10^4$), the outputs become oscillatory in time. Figure 8 shows the outputs of the thermocouples at the U3 and L3 locations for $\Delta T = 11$°C ($Ra^* = 9.3 \times 10^4$). The thermocouples at the L3 location suggest that no appreciable motion exists in the lower half, while the outputs from the U3 thermocouples show the following trends. The thermocouple outputs at 90 and 270 deg show the largest temperature oscillation amplitudes, and they are 180 deg out of phase from each other. The outputs at 0 and 180 deg show smaller oscillation amplitudes, and they are also 180 deg out of phase from each other. Note that the thermocouple at 0 deg is in the middle of the upflow region, and at 180 deg it is in the downflow region. Although not shown here, the outputs from other heights in the upper half show that they are all in-phase with what is happening at the U3 location. Therefore, the situation is very similar to that found in our earlier experiment in the heated-from-below configuration (Kamotani et al., 1994). Based on the work, one can say that the observed oscillation patterns are caused by the fact that the unicellular motion in the upper half is rotating back and forth around the cylinder axis so that the temperature oscillation amplitude is large in the regions where the azimuthal temperature gradient is large, namely, in the regions near the interfaces of the up and down flows.

In the case of $Ar = 2$, the basic flow structure is different from the above case, as shown by the two-dimensional numerical calculation. It is found in the present experiment that no change in the flow structure occurs before the onset of oscillations, that is, the flow remains in axisymmetric toroidal motion (Selver, 1996). But above around $Ra = 9 \times 10^4$, the flow becomes oscillatory. Typical oscillation patterns in the upper and lower half are presented in Fig. 9. Unlike the oscillations patterns in Fig. 8, all the outputs in the upper half in Fig. 9 have nearly the same amplitude of oscillations. Figure 9 shows that the oscillation patterns at different azimuthal locations are very similar, but they have phase lags. We have seen a similar oscillation pattern in our earlier work on oscillatory thermocapillary flow in the so-called half zone configuration (Kamotani et al., 1984). Such an oscillation pattern is associated with a rotating nonaxisymmetric toroidal flow pattern around the cylinder axis. The rotating pattern is very similar to the two-cell pattern shown in the present two-dimensional computation (Fig. 6). The fluid temperature along the wall goes up and down because the rotating pattern causes alternately strong and weak convection in a given meridian plane, as in the two-dimensional computation. That flow structure is also similar to the one predicted numerically by Baumgartl et al. (1989) for $Ar = 1$ in the cylindrical configuration. In the two-dimensional simulation, the oscillations appear around $Ra = 4 \times 10^4$ (3.6×10^4 with the heating nonuniformity), compared to $Ra = 9 \times 10^4$ for the cylindrical configuration which is considered to be due to larger wall effect in the latter configuration. As discussed earlier, the inertia and buoyancy forces compete to cause the oscillations.

4.2.2 Critical Rayleigh Numbers. The critical temperature difference for the appearance of oscillations is nondimensionalized as the critical Rayleigh number based on the half-height (Ra^*_{cr}) in order to compare with the heated-from-below configuration. Since the oscillation phenomenon is the main interest in the present work, the values of Ra^*_{cr} are measured under various conditions. The results are presented in Fig. 10 where Ra^*_{cr} is plotted against Ar^*. Although the present data are taken with four different size cylinders with overlapping aspect ratios, the dimensionless critical conditions are very consistent with each other. The present results are compared with the critical Rayleigh numbers measured by other investigators in the heated-from-below configuration. As seen in Fig. 10, the critical Rayleigh numbers for both configurations are rather close, which shows again that the oscillation phenomenon observed in the present configuration is similar to that found in the heated-

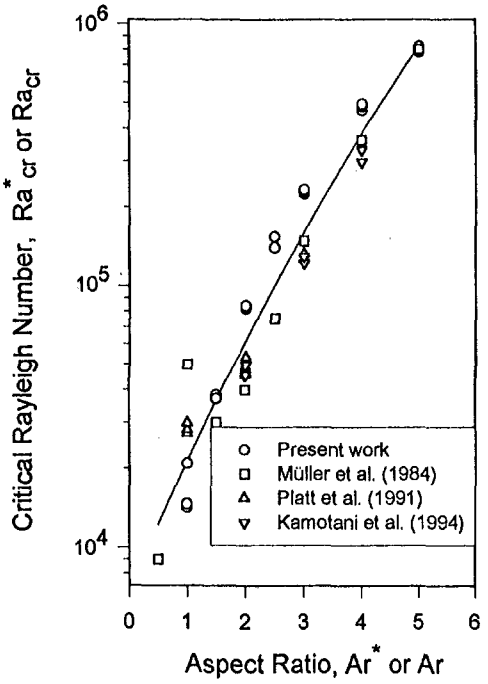

Fig. 10 Critical Rayleigh numbers for the onset of oscillatory convection. (Ra^*_{cr}, Ar^*) for the present data and (Ra_{cr}, Ar) for the other data.

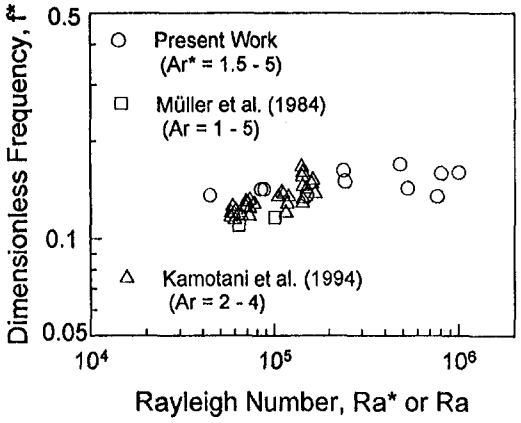

Fig. 11 Dimensionless oscillation frequencies. Ra* for the present data and Ra for the other data.

from-below tests. Ra^*_{cr} increases with increasing Ar^*, as the viscous retardation effect of the side wall increases.

As discussed earlier, the nonuniformity in the thermal boundary conditions influences the flow and its stability. In the large Ar case ($Ar > 3$), the flow structure before the thermal instability (the appearance of the unicellular motion) and the value of Ra for the onset of instability are very sensitive to the nonuniformity, but the flow after the instability is not so sensitive to it. Therefore, it is reasonable to expect that the onset of oscillatory flow, which is associated with the unicellular flow, is not very sensitive to the nonuniformity. In the small Ar case, the two-dimensional numerical computation shows that the critical Ra for the onset of oscillations is reduced by 10 percent with 1 percent difference in the heater temperatures. Therefore, the effect of the nonuniformity on the critical Ra in the present experiment is considered to be within its experimental reproducibility, which is ±10 percent.

As mentioned earlier, the critical Ra for the onset of oscillations in the two-dimensional computation for $Ar = 2$ ($Ar^* = 1$) is found to be about $Ra_{cr} = 9 \times 10^4$ ($Ra^*_{cr} = 1.1 \times 10^4$), which is close to the critical Ra* for $Ar^* = 1$ in Fig. 10 (about 1.5×10^4).

4.2.3 Oscillation Frequencies. The oscillation frequency is determined by applying a Fast Fourier Transform to the thermocouple outputs. The present data show that the frequency varies with the cylinder dimension and ΔT. It is attempted herein to correlate those data. As discussed earlier, the oscillation period is considered to scale with the convection time given by $(L/2g\beta\Delta T)^{1/2}$, and, thus, the oscillation frequency is nondimensionalized herein by $(2g\beta\Delta T/L)^{1/2}$. Figure 11 shows the dimensionless frequency versus Ra*. As noted by Kamotani et al. (1994) in their work, the oscillation frequency depends very much on the flow structure. Therefore, the present data in Fig. 11 are for $Ar \geq 3$ and only near the onset of oscillations, where the oscillatory flow is in back-and-forth motion. Although the data tend to scatter, they show that the dimensionless frequency is nearly constant, equal to about 0.15, in the parametric ranges of the present experiment, which means that the frequency scaling is proper. As Fig. 11 shows the dimensionless frequencies in the heated-from-below configuration are nearly equal to the present data within the data scatter.

5 Conclusions

An experimental study has been made of natural convection oscillations in gallium melts placed in circular cylinders heated locally from the side. Numerical analysis has also been performed in a two-dimensional configuration to obtain qualitative information about the flow in the present experiment. The present work has identified interesting buoyancy-driven flow phenomena in enclosures associated with low Pr fluids.

When Ar is larger than about 3, unicellular flow appears in the upper half of the cylinder beyond a certain Ra due to a thermal instability, and it interacts with the toroidal flow near the heater. The unicellular flow becomes oscillatory beyond Ra^*_{cr}. The oscillations are associated with back-and-forth rotation of the unicellular structure. Ra^*_{cr} increases with increasing Ar. The period of oscillations scales with the time of convection from the heater to the cold wall. The flow in the upper half is very similar to that found in the heated-from-below configuration, and Ra^*_{cr} and the dimensionless oscillation frequency in the present configuration are close to those for the latter configuration. In the case of Ar near unity, the axisymmetric toroidal flow occupies the whole cylinder. With increasing ΔT, the toroidal flow becomes nonaxisymmetric and rotates around the cylinder axis, which causes temperature oscillations at a fixed point. The oscillations are caused by an interaction of inertia and buoyancy forces.

Acknowledgments

We would like to gratefully acknowledge the financial support of NASA under grant NAG 3-886. We also thank Dr. J. P. Kizito for his assistance.

References

Baumgartl, J., Budweiser, W., Müller, G., and Neumann, G., 1989, "Studies of Buoyancy Driven Convection in a Vertical Cylinder with Parabolic Temperature Profile," *Journal of Crystal Growth,* Vol. 97, pp. 9–17.

Crespo del Arco, E., Bontoux, P., Sani, R. L., Hardin, G., Extremet, G. P., and Chikhaoui, A., 1989, "Finite Difference Solutions for Three-Dimensional Steady and Oscillatory Convection in Vertical Cylinders—Effect of Aspect Ratio," ASME HTD-Vol. 99, pp. 67–76.

Hurle, D. T. J., 1972, "Hydrodynamics, Convection, and Crystal Growth," *Journal of Crystal Growth,* Vol. 13/14, pp. 39–43.

Kamotani, Y., Ostrach, S., and Vargas, M., 1984, "Oscillatory Thermocapillary Convection in a Simulated Floating Zone Configuration," *Journal of Crystal Growth,* Vol. 66, pp. 83–90.

Kamotani, Y., Weng, F.-B., Ostrach, S., and Platt, J., 1994, "Oscillatory Natural Convection of a Liquid Metal in Circular Cylinders," ASME JOURNAL OF HEAT TRANSFER, Vol. 116, pp. 627–632.

Müller, G., Neumann, G., and Weber, W., 1984, "Natural Convection in Vertical Bridgman Configurations," *Journal of Crystal Growth,* Vol. 70, pp. 78–93.

Neumann, G., 1990, "Three-Dimensional Numerical Simulation of Buoyancy-Driven Convection in Vertical Cylinders Heated from Below," *Journal of Fluid Mechanics,* Vol. 214, pp. 559–578.

Patanker, S. V., 1980, *Numerical Heat Transfer and Fluid Flow,* Hemisphere, Washington, D.C.

Platt, J., Ostrach, S., and Kamotani, Y., 1991, "Oscillatory Natural Convection of a Liquid Metal Enclosed in a Right Circular Cylinder Heated From Below," Report EMAE/TR-91-203, Department of Mechanical and Aerospace Engineering, Case Western Reserve University, Cleveland, OH.

Selver, R., 1996, "Natural Convection of a Liquid Metal in Circular Cylinders Locally Heated from Side Wall," Ph.D. thesis, Department of Mechanical and Aerospace Engineering, Case Western Reserve University, Cleveland, OH.

O. J. Ilegbusi
Associate Professor.
ilegbusi@meceng.coe.neu.edu
Mem. ASME

M. D. Mat

Department of Mechanical, Industrial and Manufacturing Engineering,
360 Huntington Avenue, 334 SN,
Northeastern University,
Boston, MA 02115

A Two-Fluid Model of Mixing in a Two-Dimensional Enclosure

Mixing of fluids in a cavity under isothermal and nonisothermal conditions is studied with a two-fluid model. This model involves the solution of separate transport equations for zone-averaged variables of each fluid with allowance for interface transport of momentum and energy. The effects of thermal and potential energy driven convection as well as Prandtl number are investigated. The material interface is represented by the contour of the volume fraction separating the fluids. The effect of the buoyancy force due to the initial potential energy of the fluids is found to predominate over thermal buoyancy for comparable Grashof numbers.

Introduction

Research interest in buoyancy-driven convection in cavities has been motivated by its relevance in many applications including materials processing, oceanography and biotechnology. A variety of such convective flow phenomena can be produced by changing the orientation and magnitude of the temperature and concentration gradients. Most previous theoretical studies of these problems have often assumed perfectly mixed Boussinesq fluids at relatively small density gradients or Atwood numbers. However, such perfectly mixed conditions rarely exist in real systems. This paper examines an alternative model that allows for representation of buoyancy-driven flows for unlimited range of density gradients.

Buoyancy-driven flows resulting from thermosolutal convection have been thoroughly reviewed by Ostrach (1980). Bejan (1985) performed scale analysis to investigate the relative importance on the flowfield of dimensionless numbers including the Prandtl number (Pr), Lewis number (Le), aspect ratio (A_r), and buoyancy ratio (N). Hyun et al. (1990) numerically studied thermal and solutal buoyancy convection in a cavity aligned normal to the gravity vector. A layered flow structure was observed for particular values of N and Le with both opposing and cooperating buoyancy forces. The numerical results were consistent with the experimental data of Kamotoni et al. (1985) and Wu and Gau (1992).

The literature on fluid mixing is quite extensive. Mixing in the laminar regime has received considerable attention in recent years due to the relatively high power requirement for turbulent mixing and the shear sensitivity of some materials. Aref and Tryggvason (1984) studied the use of two alternating agitators for mixing. Chien et al. (1986) investigated chaotic mixing in moving boundary cavities. Ottino (1989) used an exponential increase of interface length to indicate chaotic mixing in a system. Duval (1992) demonstrated that three regimes could be identified depending on the Grashof number (Gr). These regimes are diffusive (at low Gr), convective (moderate Gr), and chaotic (high Gr).

Ilegbusi et al. (1997) studied a model isothermal problem comprising of two fluids meeting at a sharp density interface similar to that of Duval (1992). It was found that the Reynolds number (or equivalently, the Grashof number), plays a significant role on the flow characteristics and the interface evolution. Three flow regimes were observed as in Duval (1992) depending on the parametric range of the Reynolds number, namely, chaotic ($\mathrm{Re} > 500$, $\mathrm{Gr} > 10^5$), convective ($1 \leq \mathrm{Re} \leq 500$, $1 \leq \mathrm{Gr} \leq 10^5$), and diffusive ($\mathrm{Re} < 1$, $\mathrm{Gr} < 1$). It was also demonstrated that even without external agitators and moving boundaries, the initial orientation and configuration of the fluids in a cavity could produce chaotic mixing. Two vortices were observed at the center of the cavity that behaved like the agitators in Aref and Tryggvason's (1984) study. In another paper, Ilegbusi et al. (1996) demonstrated that the material interface and flow characteristics were strongly dependent on the Atwood number for a purely isothermal system.

In the present paper, the effects on the flowfield of Atwood number, Prandtl number, buoyancy ratio and aspect ratio are considered for a nonisothermal system. A model problem is considered similar to those of Ilegbusi et al. (1996, 1997) but with the fluids now subjected to a horizontal temperature gradient. The vertical side walls of the cavity are maintained at constant temperatures to produce an aiding effect on the buoyancy generated by the density gradient. A two-fluid model is employed to calculate the zone-averaged velocities, temperatures, and volume fractions of the fluids. The fluids are thus assumed to share occupancy of space but retain their identity throughout the mixing process. Transport equations are solved for the flow variables, and allowance is made for the interface transfer of momentum, mass, and energy. The calculated volume fraction (or existence probability) of each fluid coupled with the interface evolution provides a measure of the degree of mixing in the cavity.

This paper is divided into four sections of which this introduction is the first. Section 2 contains the mathematical formulation comprising the governing equations, boundary and initial conditions, and a summary of the numerical method. The computed results are presented and discussed in section 3. Section 4 contains the concluding remarks that summarize the major findings of the study.

Formulation

Consideration is given to two miscible fluids of different thermophysical properties inside a closed cavity initially separated by a valve, as shown in Fig. 1. The lighter fluid is on the right and the heavier fluid on the left. The two fluids initially are assumed to have the same temperature T_i. The temperatures at the two vertical walls are suddenly changed to T_{hot} and T_{cold}, and they are maintained at these levels thereafter. The top and bottom walls are well insulated and impermeable. It is further assumed that no initial perturbation of the interface occurs due to the removal of the valve. The flow subsequently evolves under the combined buoyancy forces due to density and temperature gradients.

This flow configuration has been chosen for several reasons. First, it is a Rayleigh-Taylor-type problem that is ideally suited for testing the two-fluid model, especially since a similar con-

Contributed by the Heat Transfer Division for publication in the JOURNAL OF HEAT TRANSFER and presented at the 1996 IMECE, Atlanta. Manuscript received by the Heat Transfer Division February 24, 1997; revision received September 30, 1997; Keywords: Natural Convection; Numberial Methods; Transient and Unsteady Heat Transfer. Associate Technical Editor: R. A. Nelson, Jr.

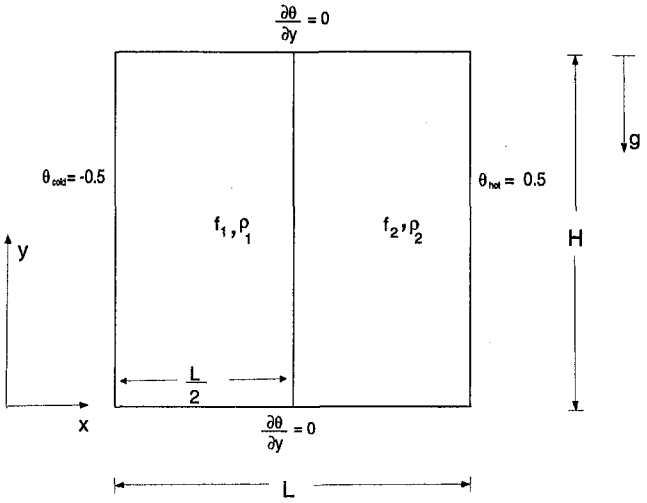

Fig. 1 The initial positions of the two fluids

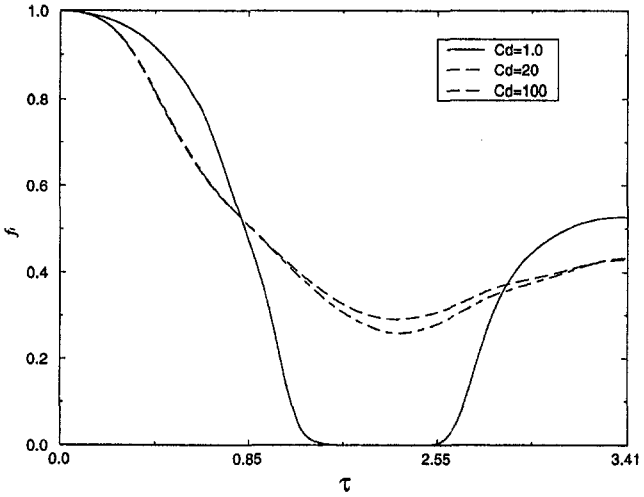

Fig. 2 Effect of interface friction coefficient c_d on volume fraction of the first fluid at ($L/2$, $H/2$, t). ($Gr_P = 3.7 \times 10^6$, $A_r = 1.0$)

figuration has been studied with a purely Boussinesq model (Duval, 1992). Second, it provides a mechanism for fundamentally studying the parametric range under which diffusive, convective, and chaotic mixing phenomena occur. In addition, this configuration has several features that are similar to the mushy/melt interface during phase transformation in alloy processing and crystal growth, as well as the slag/metal interface in ladle metallurgy.

To represent mixing in the system for a parametric range covering large density gradients, a two-fluid model (Ilegbusi et al., 1997) is employed. This model is based on the concept of two interpenetrating fluids mixing as a result of shear and "sifting" mechanisms. Sifting occurs due to imbalances between body forces and pressure gradients, and are believed to cause the Rayleigh-Taylor type of instabilities (Spalding, 1984). The two fluids are assumed to share space in proportion to their existence probabilities or volume fractions, f_1 and f_2, such that

$$f_1 + f_2 = 1. \tag{1}$$

In the above and subsequent equations, subscript 1 refers to fluid 1 and subscript 2 refers to fluid 2.

The fluids are regarded as two intermingled phases separated by sharp, flexible boundaries that interact with each other through the sharing of space and exchange of mass, momentum, and energy. Thus, at any location there is a pair of each flow variable, such as velocity components, temperatures, and volume fractions.

The pertinent transport equations can be nondimensionalized by defining the following scaling relations:

$$\tau = \frac{t}{H^2/\alpha_{\text{ref}}}, \quad \bar{x} = \frac{x}{L}, \quad \bar{y} = \frac{y}{H}$$

$$\overline{\rho_i} = \frac{\rho_i}{\rho_{i,\text{ref}}}, \quad \overline{u_i} = \frac{u_i}{\alpha_{\text{ref}}/L}, \quad \overline{v_i} = \frac{v_i}{\alpha_{\text{ref}}/H}$$

$$\bar{p} = \frac{p}{\alpha_{\text{ref}}^2 \rho_{i,\text{ref}}/H^2}, \quad \theta = \frac{T_i - T_{\text{ref}}}{T_{\text{hot}} - T_{\text{cold}}},$$

where L and H are the length and height of the cavity, respectively, $\rho_{i,\text{ref}}$ is the density of the fluid i at a reference temperature T_{ref}, p is the shared pressure, α_{ref} is thermal diffusivity at the reference temperature, and T_{hot} and T_{cold} are the temperatures of the hot and cold walls, respectively.

The governing transport equations expressing the conservation of mass, momentum, and energy can be expressed as (Ilegbusi et al., 1996, 1997)

Continuity.

$$\frac{\partial}{\partial \tau}(f_i\overline{\rho_i}) + A_r^2 \frac{\partial}{\partial \bar{x}}(f_i\overline{\rho_i u_i}) + \frac{\partial}{\partial \bar{y}}(f_i\overline{\rho_i v_i}) = 0 \tag{2}$$

U-Momentum.

$$\frac{\partial}{\partial \tau}(f_i\overline{\rho_i u_i}) + A_r^2 \frac{\partial}{\partial \bar{x}}(f_i\overline{\rho_i u_i}^2) + \frac{\partial}{\partial \bar{y}}(f_i\overline{\rho_i u_i v_i})$$

$$= -f_i \frac{\partial \bar{p}}{\partial \bar{x}} + \bar{F}(\overline{u_1} - \overline{u_2}) + \text{Pr}\left(A_r^2 \frac{\partial^2 \overline{u_i}}{\partial \bar{x}^2} + \frac{\partial^2 \overline{u_i}}{\partial \bar{y}^2}\right) \tag{3}$$

Nomenclature

A_r = aspect ratio
A_t = Atwood number
c_p = specific heat
f = volume fraction
F = interfluid friction coefficient
Gr_P = Grashof number based on the initial potential energy
Gr_T = thermal Grashof number
H = height of the cavity
k = thermal conductivity
l = length of the interface
L = length of the cavity
N = buoyancy ratio
p = static pressure
Pr = Prandtl number
Q = interface heat conduction coefficient
Re = Reynolds number
t = time
T = temperature
T_{ref} = reference temperature
u = x-direction velocity
v = y-direction velocity
V = generalized velocity
w = mixing width
x = horizontal coordinate
y = vertical coordinate

Greek Symbols

α = thermal diffusivity
α_{ref} = reference thermal diffusivity
μ = viscosity
ρ = fluid density
ρ = mixture density
ρ_{ref} = reference density
σ = Liapunov exponent
ν = kinematic viscosity
ψ = stream function

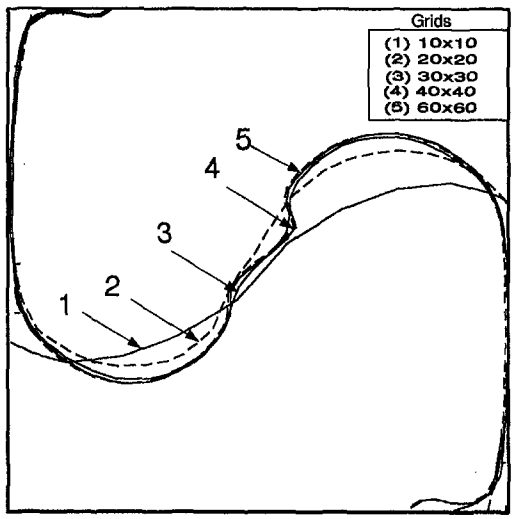

Fig. 3 Grid independence results

V-Momentum.

$$\frac{\partial}{\partial \tau}(f_i\overline{\rho_i v_i}) + A_r^2\frac{\partial}{\partial \bar{x}}(f_i\overline{\rho_i u_i v_i}) + \frac{\partial}{\partial \bar{y}}(f_i\overline{\rho_i v_i}^2)$$

$$= -f_i\frac{\partial \bar{p}}{\partial \bar{y}} + \bar{F}(\overline{v_1} - \overline{v_2}) + \mathrm{Gr}_T\,\mathrm{Pr}^2\,\theta_i + \mathrm{Pr}\left(A_r^2\frac{\partial^2\overline{v_i}}{\partial \bar{x}^2} + \frac{\partial^2\overline{v_i}}{\partial \bar{y}^2}\right) \quad (4)$$

Energy.

$$\frac{\partial}{\partial \tau}(f_i\overline{\rho_i}\theta_i) + A_r^2\frac{\partial}{\partial \bar{x}}(f_i\overline{\rho_i u_i}\theta_i) + \frac{\partial}{\partial \bar{y}}(f_i\overline{\rho_i v_i}\theta_i) = \frac{\alpha_{i,\mathrm{ref}}}{\alpha_{\mathrm{ref}}}\left(A_r^2\frac{\partial^2\theta_i}{\partial \bar{x}^2} + \frac{\partial^2\theta_i}{\partial \bar{y}^2}\right) + \bar{Q}(\theta_1 - \theta_2) \quad (5)$$

In Equations (2)–(5), subscript $i = 1, 2$ represents the first and the second fluid respectively, and u and v represent velocity components in the x and y-coordinate directions. The second terms on the right side of the momentum and energy equations are, respectively, the dimensionless interfluid exchange terms due to friction and heat conduction at the interface. The dimensionless interface friction coefficient F is here expressed as

$$\bar{F} = \frac{F_i}{\alpha_{\mathrm{ref}}\rho_{i,\mathrm{ref}}/H^2}, \quad (6)$$

where

$$F_1 = -F_2 = c_d\rho f_1 f_2, \quad (7)$$

in which ρ is a mixture (ensemble average) density defined as

$$\rho = f_1\rho_1 + f_2\rho_2. \quad (8)$$

The drag coefficient c_d in Eq. (7) was systematically established in a prior work to be approximately 20.0 by application of the two-fluid model to a range of Rayleigh-Taylor problems (Andrews, 1995). A typical result of a sensitivity test performed on this value for the present problem is presented in Fig. 2. It is seen that increasing c_d from 20 by an order of magnitude

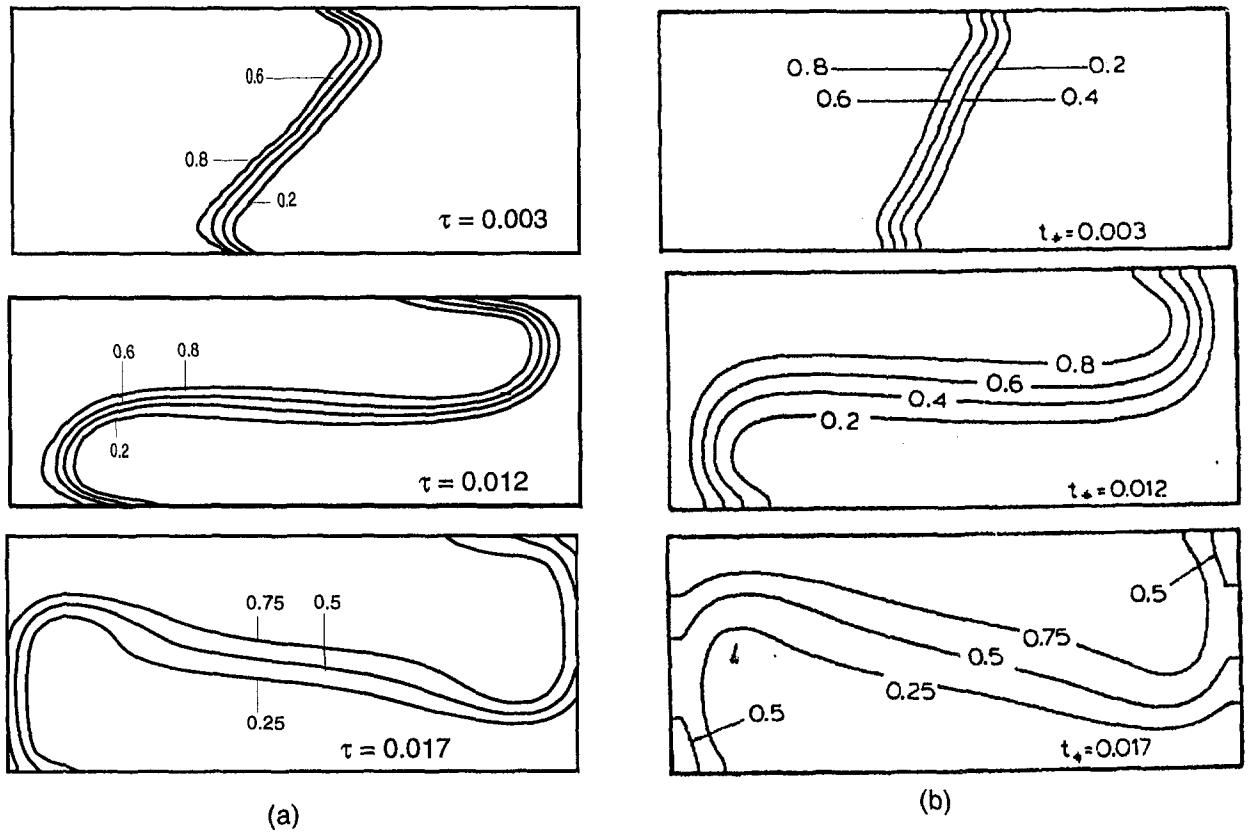

Fig. 4 Comparison of predicted isotherms with the numerical results of Litsek and Bejan (1988): (*a*) present study (*b*) Litsek and Bejan ($\mathrm{Ra} = 10^5$, $\mathrm{Pr} = 0.71$, $A_r = 0.5$)

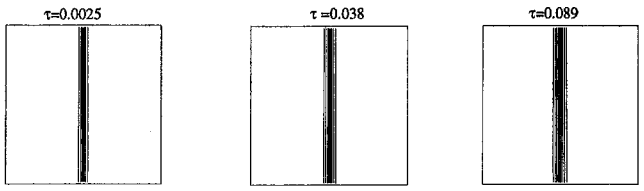

Fig. 5 Interface behavior in the diffusive regime (Gr_P = 0.37, A_r = 1.0)

does not significantly change the volume fraction at the monitored point. This result is typical of other locations in the system.

The dimensionless interface heat conduction coefficient takes the form of

$$\bar{Q} = \frac{Q_i}{\alpha_{\text{ref}}\rho_{i,\text{ref}}c_{p,i}/H^2}, \tag{9}$$

where

$$Q_1 = -Q_2 = c_p c_h F_1, \tag{10}$$

in which c_p is the mean specific heat, and c_h is an empirical constant relating interface heat conduction to the fluid variable. The coefficient c_h is necessary so that additional modification to the interface friction relation (Eq. 7) is not required. A value of c_h = 0.05 was systematically established in previous studies (Ilegbusi and Spalding, 1989; Ilegbusi, 1994; Ilegbusi, 1995) by comparison of predictions with a large set of experimental

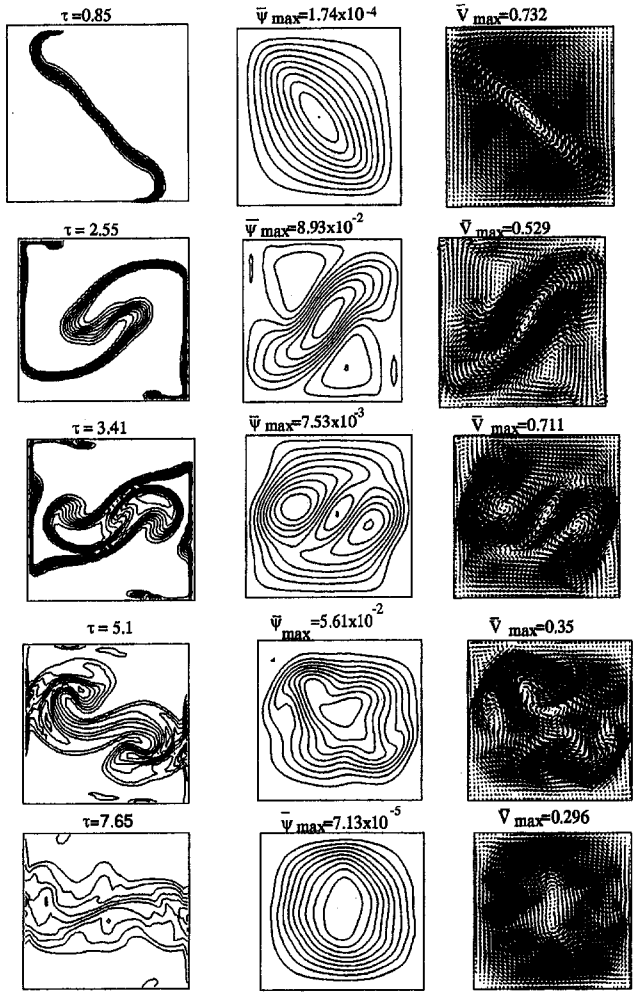

Fig. 6 Evolution of interface and flow pattern in the chaotic regime (Gr_P = 3.7 × 10^6, A_r = 1.0)

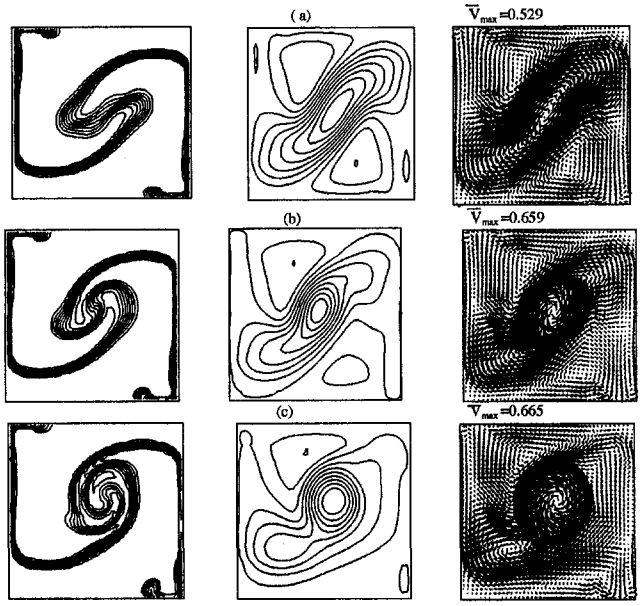

Fig. 7 Formation of tendril and whorl structure depending on Atwood number at τ = 2.55, Gr_P = 3.7 × 10^5: (*a*) A_t = 5.0 × 10^{-5}; (*b*) A_t = 0.13; and (*c*) A_t = 0.36

data on a range of problems. This value was adopted in this study after performing preliminary sensitivity tests, the results of which are not presented here for lack of space.

Thermal buoyancy is represented by allowing ρ_i to vary with temperature; thus,

$$\rho_i = \rho_{\text{ref},i}[1 - \beta(T_i - T_{\text{ref}})], \tag{11}$$

where β is the thermal expansion coefficient.

The generalized velocity used for the vector plots can be expressed as

$$\bar{V} = (\bar{u}^2 + \bar{v}^2)^{1/2}, \tag{12}$$

and the stream function is calculated from

$$\bar{\psi} = -\bar{v}d\bar{x} + \bar{u}d\bar{y}, \tag{13}$$

where u and v, appearing in Eqs. (12) and (13), are the mixture velocities calculated from the relation

$$\bar{u} = \bar{u}_1 f_1 + \bar{u}_2 f_2 \tag{14}$$

and

$$\bar{v} = \bar{v}_1 f_1 + \bar{v}_2 f_2 \tag{15}$$

The above equations indicate that the nonisothermal system can be characterized by the following dimensionless numbers:

$$\text{Aspect ratio:} \quad A_r \equiv H/L$$

$$\text{Grashof number (thermal):} \quad \text{Gr}_T \equiv \beta\Delta T g H^3/\nu^2$$

$$\text{Prandtl number:} \quad \text{Pr} \equiv \nu/\alpha$$

The additional dimensionless numbers may be determined by considering a purely isothermal system for which the buoyancy-driven flow results from the potential energy gradient of the system. This energy can be shown to be proportional to the gravity force and density difference between the two fluids; thus,

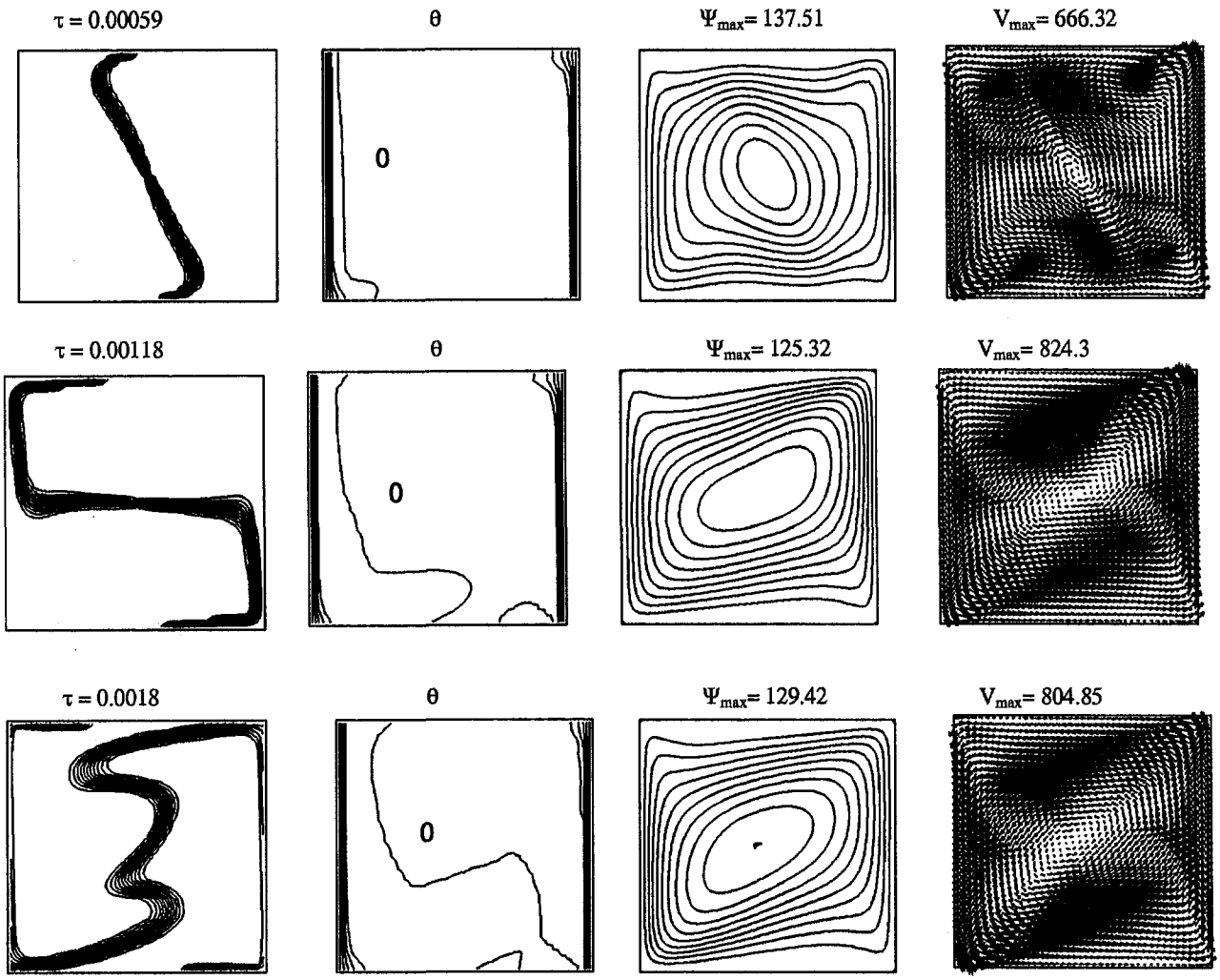

Fig. 8 Evolution of interface, temperature field, and flow pattern for pure thermal convection ($Gr_T = 3.7 \times 10^5$, $N = 0$, $A_t = 1.0$)

$$\Delta PE = \frac{gH^2L}{4}(\rho_1 - \rho_2). \tag{16}$$

Assuming no energy losses, the potential energy released is converted into kinetic energy, as follows:

$$KE = \frac{1}{2}\frac{HL}{2}(\rho_1 + \rho_2)V^2, \tag{17}$$

where V is a mean velocity in each fluid. Thus the maximum value (with no losses) for the velocity is readily obtained by equating (16) and (17) to give

$$V = \sqrt{gHA_t}. \tag{18}$$

This maximum velocity is then used for the velocity scale. This velocity also provides a useful kinematic time scale for the problem as

$$T_k = \frac{H}{V} = \sqrt{\frac{H}{gA_t}}. \tag{19}$$

The ratio $1/T_k$ is the Brunt-Väisälä frequency (Turner, 1973) that plays a key role in describing oceanographic fluid oscillations.

For this purely isothermal situation, it can be shown that the additional dimensionless groups that characterize the system are

Awood number (nominal): $A_t \equiv \Delta\rho/(\rho_1 + \rho_2)$

Grashof number (potential energy): $Gr_P \equiv A_t gH^3/\nu^2$

It should be noted that the Grashof number due to the potential energy depends on the Atwood number.

For the combined system, the relative significance of both thermal-buoyancy and potential energy convective sources can be expressed by a buoyancy ratio defined as

Buoyancy ratio: $N \equiv Gr_P/Gr_T \equiv A_t/\beta\Delta T$

The values of the dimensionless numbers used in the computation are summarized in Table 1.

Initial and Boundary Conditions. The two fluids are initially at rest at temperature θ_i. At $\tau = 0$, the left and right wall temperatures are suddenly changed to θ_{cold} and θ_{hot}, respectively. Thus, the initial conditions can be expressed mathematically as

$\tau = 0$: $0 < x < 1$, $0 < y < 1$

$$\bar{u}_1 = \bar{u}_2 = \bar{v}_1 = \bar{v}_2 = 0.0 \tag{20}$$

$$x < \tfrac{1}{2}: \quad f_1 = 1.0, \quad f_2 = 0.0 \tag{21}$$

$$x \geq \tfrac{1}{2}: \quad f_1 = 0.0, \quad f_2 = 1.0 \tag{22}$$

$$\theta_1 = \theta_2 = \theta_i = 0.5 \tag{23}$$

$\tau = 0$: $0 < y < 1$

$$x = 0: \quad \theta = \theta_{cold} \tag{24}$$

$$x = 1: \quad \theta = \theta_{hot} \tag{25}$$

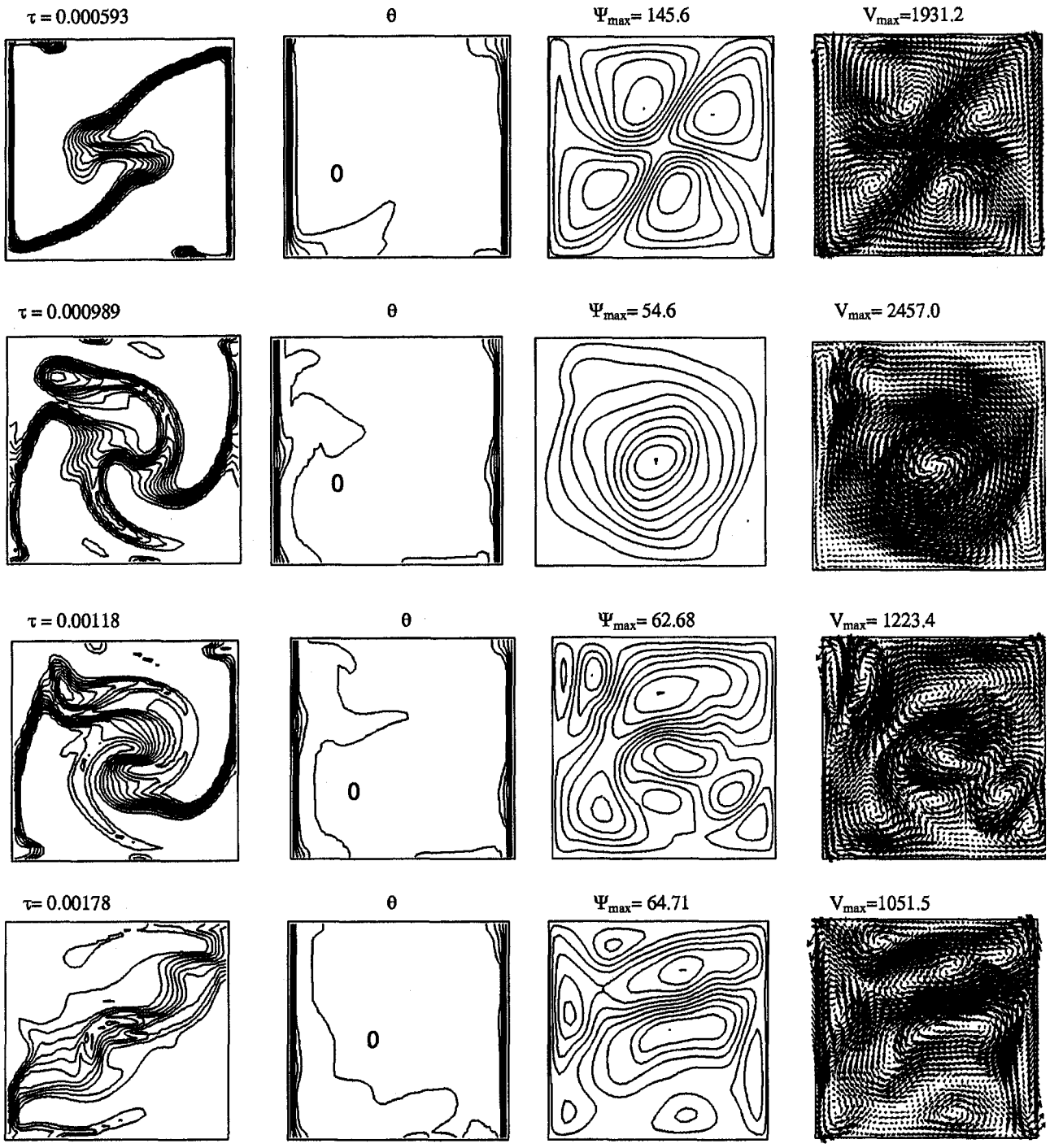

Fig. 9 Evolution of interface, temperature field, and flow pattern for $N = 0.5$ and $Pr = 10$ ($Gr_P = 3.7 \times 10^5$, $Gr_T = 1.85 \times 10^5$, $A_r = 1.0$)

The boundary walls are fixed and no-slip condition is imposed on all velocities. The left and right wall temperatures are fixed at θ_{cold} and θ_{hot}, respectively. The top and bottom walls are assumed to be adiabatic. These conditions can be expressed as

$$\bar{u}_1 = \bar{u}_2 = \bar{v}_1 = \bar{v}_2 = 0.0 \tag{26}$$

on all walls, and

$$x = 0: \quad \theta_1 = \theta_2 = \theta_{cold} = -0.5 \tag{27}$$

$$x = 1: \quad \theta_1 = \theta_2 = \theta_{hot} = 0.5 \tag{28}$$

$$y = 0, 1: \quad \partial\theta_1/\partial y = \partial\theta_2/\partial y = 0. \tag{29}$$

Mixing Characteristics. Following Ilegbusi et al. (1996, 1997), three parameters are used to quantify the state of mixing inside the cavity. These parameters are as follows: (i) dimensionless length l^*, defined as

$$l^* = \frac{(l - l_o)}{l_o} \tag{30}$$

in which l_o and l are, respectively, the material interface lengths at the initial and later time τ; (ii) dimensionless width, w^*, expressed as

$$w^* = \frac{(w - w_o)}{w_o}, \tag{31}$$

where w is the interface width defined as the average distance

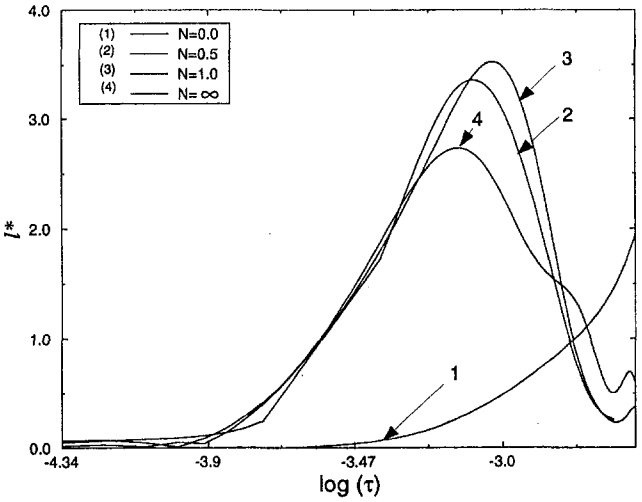

Fig. 10(*a*) Effect of buoyancy ratio on interface elongation

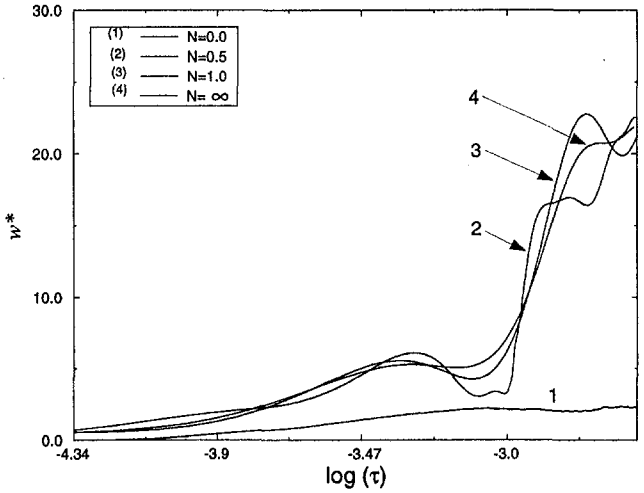

Fig. 10(*b*) Effect of buoyancy ratio on interface width

between the 0.05 and 0.95 contours of volume fraction of one of the fluids at time τ, and w_o is the initial width; and (iii) Lyapunov exponent σ, which is an indicator of chaos in the system. Ottino (1989) associated good mixing with rapid divergence of a material line from an initial position. The Lyapunov exponent expresses this divergence in the following form:

$$\sigma = \lim_{t\to\infty}\left(\frac{1}{t}\ln\frac{|ds|}{|dS|}\right), \tag{32}$$

in which $|dS|$ is the material length at the initial state and $|ds|$ is the length at a later time τ. A nonzero value of σ implies that the material line elongates exponentially.

Numerical Details

The choice of the appropriate numerical scheme is crucial due to the sharp density interface that exists in the system considered. A drawback of conventional high-order finite difference techniques for buoyancy-driven flows dominated by nonlinear advective terms (as in the present situation) is the numerical oscillation that may occur as the transported component can become negative during the course of the computation. This oscillation can lead to unphysical results, such that the volume fraction may be negative or exceed 1 over the domain. The van Leer method prevents such unphysical results, while maintaining high-order accuracy (Andrews, 1995); it is thus employed here in the computation of the convective terms. The governing equations are solved in two steps such that an intermediate value which is calculated from the convective terms is updated with Lagrangian source terms as described below.

The volume fractions of the fluids are calculated from the continuity equation (Eq. 2) in two stages of x-step followed by y-step as follows:

***x*-step.**

$$f^*_{1,P}m^*_P = f^n_{i,P}m^n_P + \delta V_{i,w} - \delta V_{i,e}. \tag{33}$$

***y*-step.**

$$f^{n+1}_{1,P}m^{n+1}_P = f^*_{i,P}m^*_P + \delta V^*_{i,w} - \delta V^*_{i,e}, \tag{34}$$

where m^n, m^*, m^{n+1} are old, intermediate, and new values of phase masses, respectively. The other terms represent the mass fluxes over the cell faces. For example, the mass flux over the east face for the first fluid is

$$\delta V_{1,e} = \Delta y\Delta t\rho_{\tilde{1},e}u_{\tilde{1},e}f_{\tilde{1},e}, \tag{35}$$

where the tilde denotes cell face values computed using a high-order van Leer scheme described in Andrews (1995) and Ilegbusi et al. (1997) instead of the upwind procedure often employed in many numerical schemes. By applying the van Leer method, the volume fraction of the first fluid on the east face can be expressed as

$$f_{1,e} = f_{1,\text{upwind}} + \text{sign}(\epsilon_{1,e})\left(\frac{1-|\epsilon_{1,e}|}{2}\right)\Delta xD_{1,e}, \tag{36}$$

where

$$D_{1,e} = S\min\left\{|D|, \frac{2|\Delta e|}{\Delta x}, \frac{2|\Delta w|}{\Delta x}\right\}$$

$$\Delta w = f^n_{1,p} - f^n_{1,w}, \quad \Delta e = f^n_{1,e} - f^n_{1,p} \tag{37}$$

$\epsilon_{1,e} = \delta V_{1,e}/V^n_{1,\text{upwind}}$

$\delta V_{1,e}$: volume flux on east cell face of fluid 1

$V^n_{1,\text{upwind}}$: volume of upwind cell occupied by fluid 1 at time n

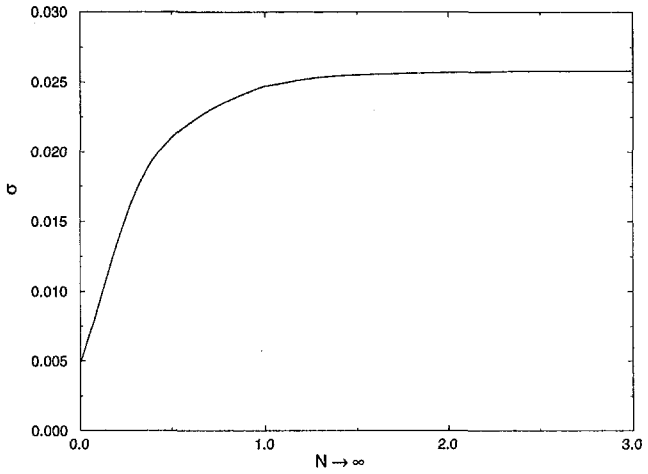

Fig. 11 Lyapunov exponent as a function of buoyancy ratio

and

$$S = \begin{cases} 1 & \text{if } \Delta e \text{ and } \Delta w > 0 \\ -1 & \text{if } \Delta e \text{ and } \Delta w < 0. \\ 0 & \text{otherwise} \end{cases} \quad (38)$$

The $|D|$ value in the van Leer limiter can be chosen as $D = 0.0$ for first-order accuracy, $D = (\Delta e + \Delta w)/2\Delta x$ for second-order accuracy, and

$$D = \begin{cases} \dfrac{1 + |\epsilon_{1,e}|\Delta w}{3} + \dfrac{2 - |\epsilon_{1,e}|\Delta e}{3} & \text{for} \quad \epsilon_{1,e} \geq 0 \\ \dfrac{1 + |\epsilon_{1,e}|\Delta e}{3} + \dfrac{2 - |\epsilon_{1,e}|\Delta w}{3} & \text{for} \quad \epsilon_{1,e} < 0 \end{cases} \quad (39)$$

for third order accuracy (Ilegbusi et al., 1997). The latter scheme has been employed in the computations presented here.

An intermediate cell mass is calculated by adding the x-step phase mass equations (Eq. 33) to give

$$m_p^* = m_p^n + \delta V_w - \delta V_e, \quad (40)$$

where δV_w and δV_e represent the net mass fluxed over the east and west faces, respectively. Similarly, the new value of the cell mass m^{n+1} can be calculated from the y-step phase mass equation (Eq. 34).

The calculation procedure for phase momentum and energy is similar to the phase mass explained above. The momentum and energy equations are then updated with the appropriate source terms. However, the velocities obtained after this source-term updates do not necessarily satisfy the continuity equation. Similar to the SIMPLE algorithm (Patankar and Spalding, 1972), a pressure correction equation is obtained by using phase velocity corrections such as

$$u_i^{n+1} = u_{i,e}^* + \Delta u_{i,e}, \quad v_{i,n}^{n+1} = v_{i,n}^* + \Delta v_{i,n}, \quad (41)$$

and a pressure correction

$$p_P^{n+1} = p_P^n + \Delta p_P. \quad (42)$$

These correction terms are then substituted into the momentum equations and substracted from the original momentum equations to yield the following velocity influence equations:

$$\Delta u_{i,e} = \frac{\Delta t}{\rho_i \Delta x}(\Delta p_P - \Delta p_E) \quad (43)$$

$$\Delta v_{i,n} = \frac{\Delta t}{\rho_i \Delta y}(\Delta p_P - \Delta p_N). \quad (44)$$

The following Poisson equation for pressure correction is obtained from substituting the above velocity influence equations in the continuity equation (Eq. 2); thus,

$$a_P \Delta p_P + a_E \Delta p_E + a_W \Delta p_W + a_N \Delta p_N + a_S \Delta p_S = -R, \quad (45)$$

with, for example,

$$a_E = -\frac{\Delta t \Delta y}{\Delta x}\left(\frac{f_{1,e}^{n+1}}{\rho_1} + \frac{f_{2,e}^{n+1}}{\rho_2}\right) \quad (46)$$

and, R is the mass residual evaluated from the starred velocities in the velocity correction equations. The Poisson equation is then solved with the Gauss-Seidel iteration method until the mass residuals over all the cells are less than a prescribed value (typically, 10^{-6}). Further details of the numerical method may be found in Andrews (1995) and Ilegbusi et al. (1997).

A numerically accurate result is obtained in each case with a 40×40 grid system. This grid system was selected from a systematic grid refinement test performed on 10×10, 20×20, 40×40, and 60×60 uniform grid systems. The results of this test at a typical time ($\tau = 2.5$) are presented in Fig. 3 showing plots of $f_1 = 0.5$ for the grids considered. It is seen that all the grids exhibit most of the qualitative features of the system. However, the detail features of the interface such as Kelvin-Helmoltz instability at the center and wall plumes at the top and bottom of the cavity are better represented with the larger grid numbers. The profiles do not appear to change significantly beyond the 40×40 grid system, indicating numerical accuracy of the results. This system corresponds to a 1.25 mm grid size.

Validation of the Two-Fluid Model

The validity of the two-fluid model was first demonstrated by repeating the calculation of Litsek and Bejan (1985) on transient natural convection between two zones in an insulated enclosure. Figure 4 presents a representative set of predictions of the isotherms based on the two-fluid model compared with the corresponding results of Litsek and Bejan (1985) which assumed Boussinesq fluid. It is seen that the two sets of results are qualitatively similar, although there are some qualitative differences in details. These differences are expected to become larger as the density gradient increases and the assumption of the Boussinesq fluid is no longer valid.

Results

The dynamics of the problem considered (Fig. 1) is governed by the five dimensionless parameters already identified: N, Gr_P, Gr_T, Pr, A_t, and A_r. While computation can be performed with any combination of these parameters, the objective here is to present sample results to illustrate their effects on the flow characteristics, as well as the thermal field and the interface evolution. Both isothermal and nonisothermal systems are considered. The results include velocity vectors, streamlines, and evolution of the interface and temperature field. The interface is demarcated by the 0.05 and 0.95 contour values of the volume fraction of the first fluid. A representative isotherm, here chosen as the mid-value between the hot and cold wall temperatures, is shown on each temperature contour plot. Note that the reference velocity in the vector plots is chosen as the maximum velocity.

Effect of Grashof Number Based on the Initial Potential Energy, Gr_p (Isothermal Case). The results for this flow situation are presented in Figs. 5–7 for the evolution of the interface, streamlines, and velocity vectors. A wide range of Gr_P values ranging from 0.37 to 3.7×10^5 are considered in the absence of thermal convection.

It is seen from Fig. 5 that for the lower limit of Grashof numbers ($\mathrm{Gr}_P < 1$), the initial potential energy of the system is too weak to generate flow. For this range of Grashof numbers, the nonlinear terms in the momentum equation are negligible, and fluid mixing occurs diffusively.

Figure 6 shows that interesting flow structures are formed at a larger Grashof number, $\mathrm{Gr}_p > 10^5$ (chaotic regime). The heavier fluid initially pushes the lighter one to form an internal wave. The internal wave subsequently breaks up producing a large mixing area. Figure 7 shows the significance of the Atwood number, A_t, on the interface morphology and the velocity field in the chaotic regime for $\mathrm{Gr}_p = 3.7 \times 10^5$. The material interface forms a tendril structure at low A_t similar to that observed using Boussinesq approximation by Duval (1992), and a whorl structure develops at large A_t. A vortex roll develops at the core region and stretches the interface. This vortex becomes relatively stronger as the Atwood number increases. It should be remarked that the similarity of the present results to those of Duval is another evidence of the validity of the two-fluid model.

Effect of Buoyancy Ratio, N. The results demonstrating the influence of the buoyancy ratio, N, on the flow characteristics are presented in Figs. 8–11. The flow and associated ther-

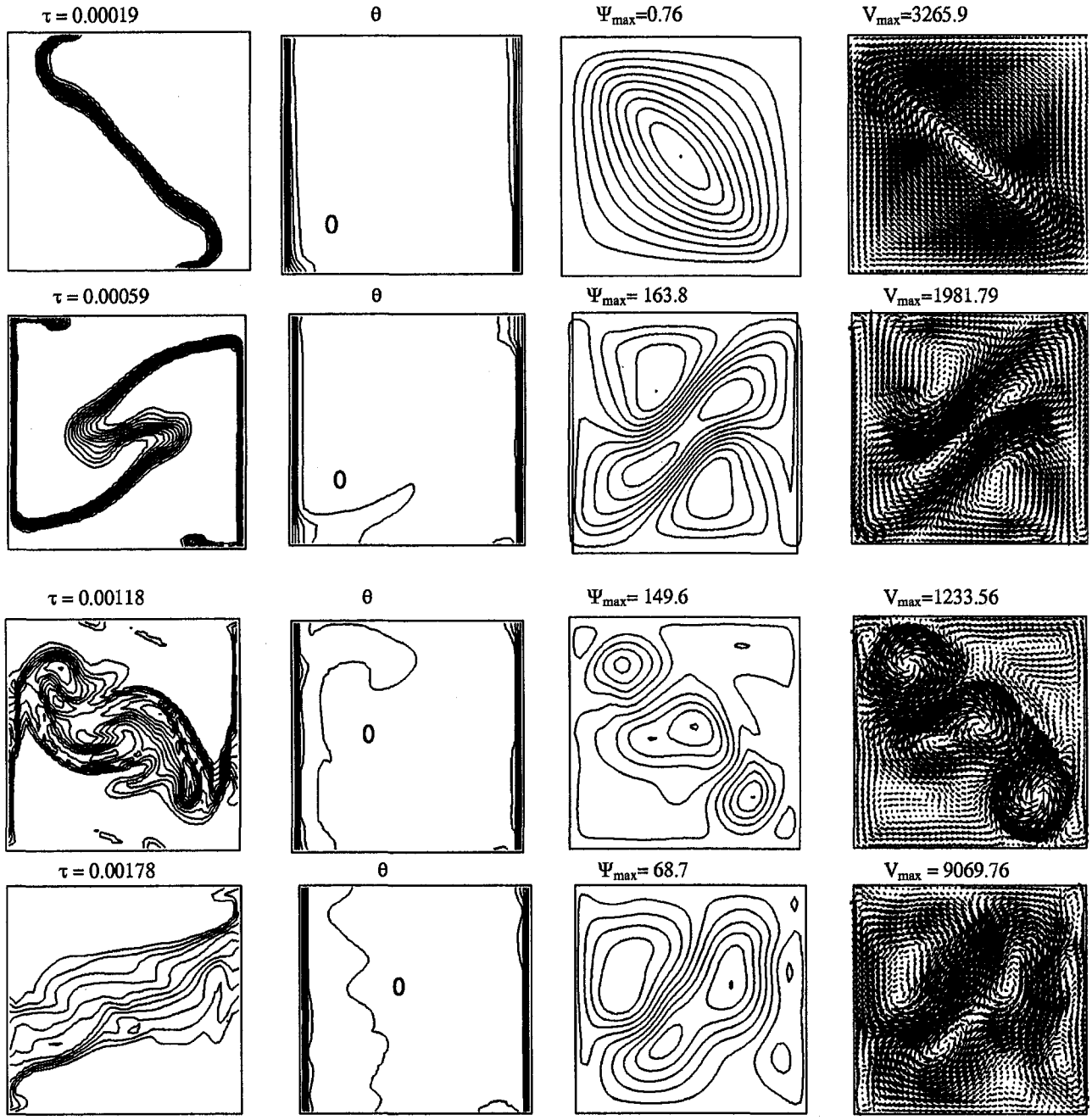

Fig. 12 Evolution of interface, temperature field, and flow pattern for $N = 1$ and Pr = 10 ($Gr_P = Gr_T = 3.7 \times 10^5$, $A_r = 1.0$)

mal field and interface evolution are shown for N ranging from 0 to 1000. The lower limit of the buoyancy ratio corresponds to pure thermal convection, while the upper limit corresponds to convection resulting purely from the initial potential energy of the system.

In the first set of calculations, the density difference between the two fluids is set to zero, while all other thermophysical properties remain constant. It is assumed that only density is affected by the thermal field. Figure 8 shows that in the pure thermal buoyancy situation a counter-clockwise circulation is formed in the system that pushes the fluid from the top and bottom of the cavity. The interface configuration takes a relatively longer time to develop in pure thermal convection compared to that due solely to the potential energy which was presented in the previous section. This result clearly indicates that for such systems Gr_P may indeed have a more dominant effect on the flow characteristics than Gr_T. Figure 8 also shows that the interface evolution with pure Gr_T is qualitatively similar to the behavior under pure Gr_P that was presented in Fig. 6.

The result for $N = 0.5$ is presented in Fig. 9. The effects of both buoyancy sources are generally complementary. It is seen that the clockwise-rotating circulation cell observed at $\tau = 0.00059$ in the pure thermal buoyancy situation (Fig. 8) is now replaced by four vortices around the corner region, with the diagonal vortices rotating in the same direction (at $\tau = 0.00059$). The interface breaks up at a later time (approximately $\tau = 0.00098$ in Fig. 9) as compared to pure potential-energy driven convection presented in Fig. 6. This result can be attributed to the strength of the inner vortices. Due to the additional effect of the thermal convection in the present situation, the heavier fluid pushes the interface downward at the left and upward at the right side for this low buoyancy ratio ($N = 0.5$). A comparison with Figs. 6 and 8 indicates that the counter-clockwise vortices combine as N increases, with a consequent

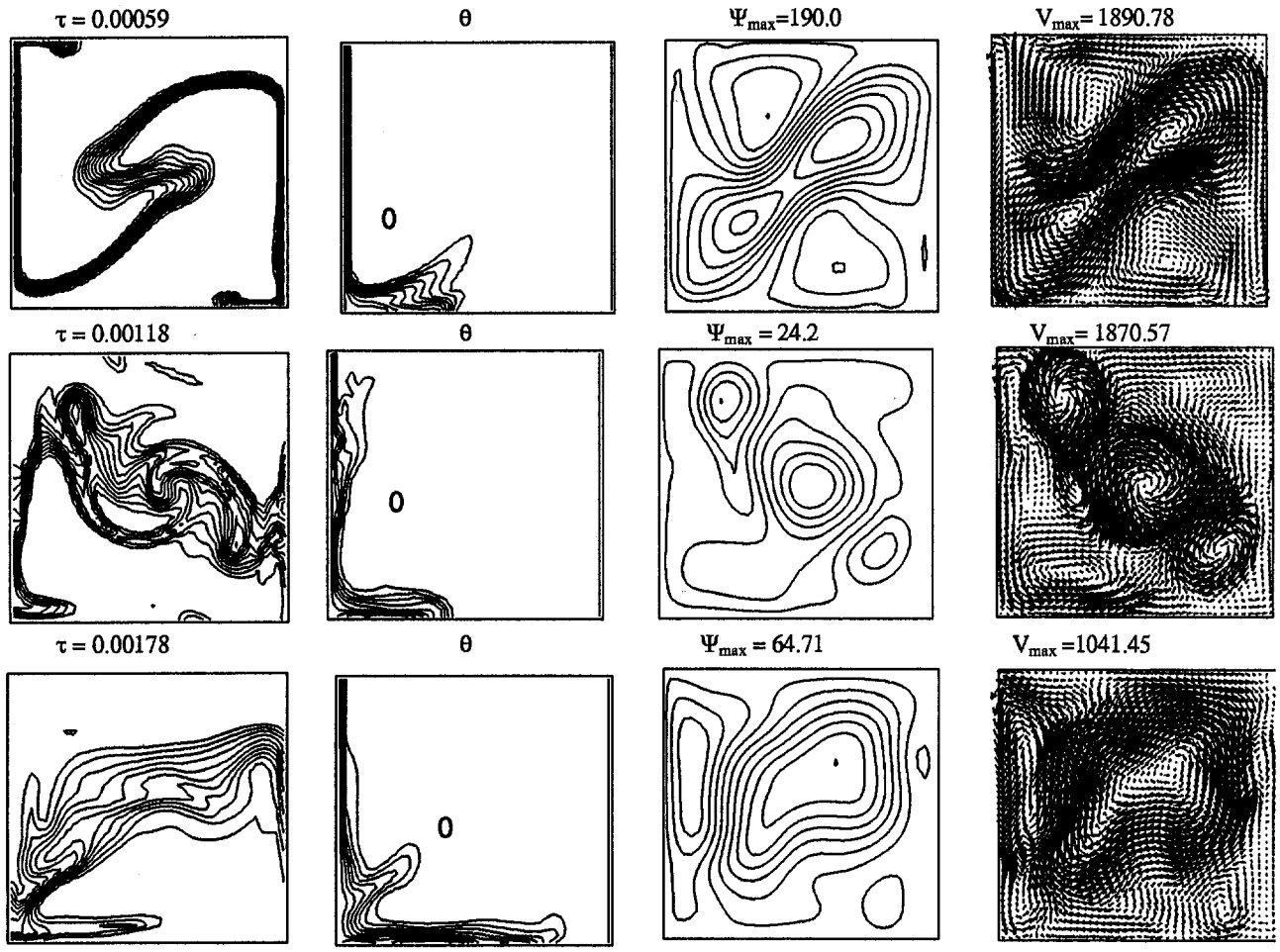

Fig. 13 Evolution of interface, temperature field, and flow pattern for $N = 1$ and Pr = 1000 ($Gr_P = Gr_T = 3.7 \times 10^5$, $A_r = 1.0$)

complementary effect on the interface evolution. It is seen from Fig. 9 that at a later time ($\tau = 0.00178$) two circulation patterns develop in the thermal boundary layers of the hot and cold walls and squeeze the potential-energy-induced circulation to the center of the cavity. Figure 8 also shows that a continuous oscillation of vortex cells occurs at this buoyancy ratio. The vortex cells merge and break up continuously in time. The system exhibits a more symmetrical behavior and reaches steady state faster with increasing buoyancy ratio, as seen by comparing Figs. 6, 8, and 9.

The interface elongation and mixing width are presented in Fig. 10. Figure 10(a) shows that the interface elongates exponentially when the buoyancy force due to the potential energy is effective ($N \to \infty$), but grows approximately linearly with time in pure thermal convection ($N \to 0$). The elongation reaches a maximum value at $N = 1$. This trend can be attributed to the combined effects of both buoyancy forces. Figure 10(a) also shows that the interface elongation at $N = \infty$ is greater than at $N = 0$. These results suggest that the convection induced by the initial potential energy has a larger effect on mixing than the thermal convection for the Prandtl number range considered. The abrupt change in interface elongation for curves 1, 2, and 3 indicates a breakup of the interface and rapid transition to a stratified configuration during chaotic mixing. Figure 10(b) shows that the interface width is approximately independent of N, except at $N = 0$ (i.e., pure thermal convection). The decrease of width observed in curves (2, 3, 4) represent the contraction of the interface due to stretching. Most of this contraction occurs before the breakup of the interface when the elongation reaches its maximum value. Subsequently, the mixing width increases rapidly due to the chaotic mixing.

Figure 11 shows the variation of the Lyapunov exponent σ with N. It is seen that while there is a step change in σ for low buoyancy ratios, it remains invariant at higher ratios. The step change indicates a transformation from relatively mild to strong mixing as N increases. It should be remarked that a positive value of the Lyapunov exponent indicates an exponential increase in the interface length as observed in Fig. 10(a), and is a signature of chaos in the system (Ottino, 1989).

Effect of Prandtl Number. The buoyancy ratio is kept constant at $N = 1$, and the Prandtl number is varied from 1 to 1000. The results for this case are presented in Figs. 12–14.

It is seen from Figs. 12 and 13 that the early-time behavior of the flow field (at $\tau = 0.00059$) is essentially independent of the Prandtl number. This result can be explained by the dominant role of potential-energy induced buoyancy at this stage. Figure 12 shows that the flow field is characterized by a counterclockwise vortex in the core region (at $\tau = 0.00019$). Subsequently, the large circulation cell is transformed into four vortices around the core region at $\tau = 0.00059$. It is apparent from the streamline plots at $\tau = 0.00059$ in Figs. 12 and 13 that, in contrast to the combined cell observed for $N \to \infty$ for potential-energy-induced convection, (Fig. 6), two separate vortex rolls are now formed at the diagonal between the top right corner and bottom left corner of the cavity, independent of the Prandtl number. Elliptic points (Ottino, 1989) are formed between these two cells. It is also interesting that a strong flow circulation now completely spans the two side walls rather than the weak structures localized at the top part of the left wall and the bottom part of the right wall that was observed in the pure potential energy-induced convection situation of Fig. 6.

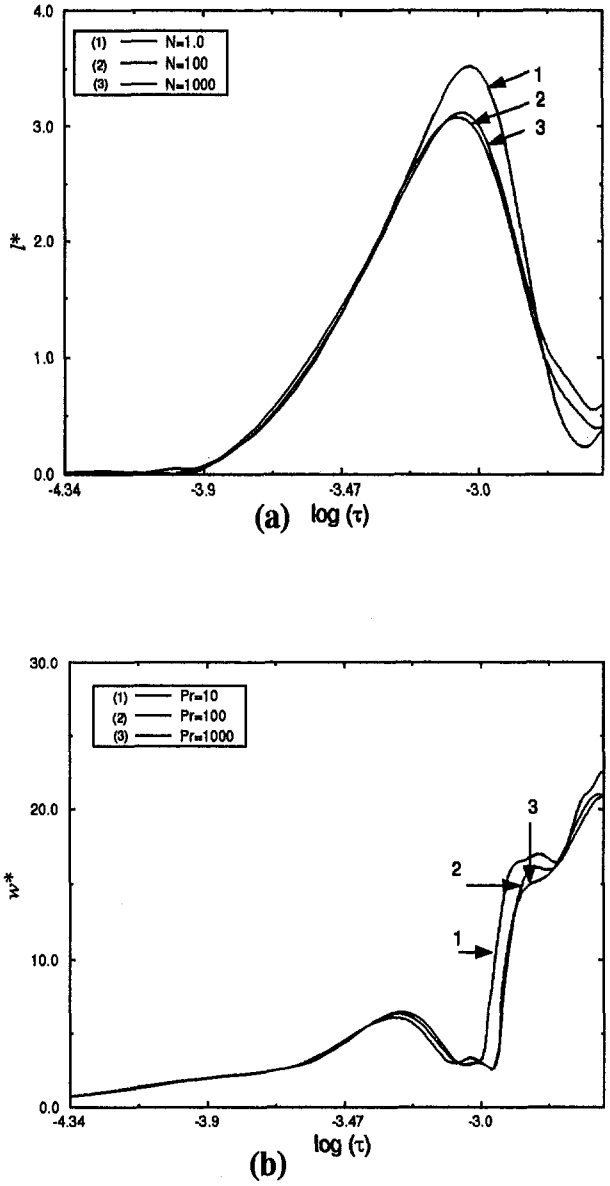

Fig. 14 Effect of Prandtl number on interface elongation (*a*) and width (*b*)

The effect of Prandtl number is very distinctive at $\tau = 0.0018$, as seen in Figs. 12 and 13. Three vortices are formed at the diagonal between the top left corner and bottom right corner, and the cell at the center is stronger at higher Prandtl numbers. However, the corner vortices are relatively stronger at low Prandtl numbers due to the stable temperature field. A close inspection of the interface pattern at $\tau = 0.00118$ in both figures shows that at the lower Prandtl number (Fig. 12) plumes extend towards the bottom of the left wall and the top of the right wall. The right plume disappears at the higher Prandtl number (Fig. 13) and a horizontal intrusion layer of the denser fluid is dragged from left to right by a secondary flow that develops at the bottom left corner. It is also seen that the fluid fragments from the remnants of the wall plumes at the top and bottom of the cavity move and partially diffuse in the flow field.

Figure 13 shows that the interface evolves faster than the temperature field at the higher Prandtl number. It is seen that a cold front develops at the bottom of the cavity that initially propagates into the core. This behavior is subsequently repeated at the top section when the velocity field changes direction. After about $\tau = 0.00178$ two thermal boundary layers develop near the side walls for the lower Prandtl number (Fig. 11), and the potential-energy-driven flow becomes dominant in the core region. At the higher Prandtl number (Fig. 13), only one boundary layer develops at the left wall. At a later stage, the denser cold fluid pushes the lighter hot one rightwards at the bottom section. An S-shaped temperature isotherm develops similar to the behavior typically observed in conventional thermosolutal convection phenomena (Hyun and Lee, 1990).

It is seen from Figs. 12 and 13 that the interface exhibits a more asymmetric behavior as Prandtl number increases. This trend may be attributed to the slower propagation of the thermal field than the velocity field at high Prandtl numbers. Since the system is initially at the temperature of the hot wall, the flow field that develops near the cold wall significantly influences the interface behavior.

The effect of Prandtl number on the interface elongation and the mixing width are presented in Fig. 14. The interface attains a maximum elongation at a relatively low Prandtl number. Beyond that, the effect of Prandtl number on the elongation is not quite distinctive. This result may be due to the oscillation of the interface prior to breakup at the high Pr range. Figure 14(*b*) shows that there is a slight increase in the mixing width at low Prandtl numbers perhaps due to enhanced diffusivity.

Conclusion

The mixing of fluids inside a cavity has been studied with a two-fluid model under isothermal and nonisothermal conditions. The effects of thermal and potential energy-induced buoyancy and Prandtl number have been considered.

For the isothermal system, mixing occurs diffusively at low values of potential energy-based Grashof number ($Gr_P < 1$), and the material interface remains essentially undistorted. At relatively large Grashof numbers ($Gr_P > 10^5$), the internal wave that forms at early stages subsequently breaks up to produce chaotic mixing. The chaotic regime is found to be most efficient for mixing.

For the nonisothermal system, the potential-energy induced buoyancy appears to play a dominant role in the mixing process for the system considered. The material interface requires a longer time to develop for pure thermal convection compared to potential-energy driven convection. The system exhibits asymmetric behavior at low buoyancy ratios and the interface elongation and the mixing width rapidly reach the pure potential-energy induced convection limit.

The results indicate that while Prandtl number does not significantly affect the mixing efficiency, it influences the flow pattern, the interface evolution, and the thermal field.

For low levels of Grashof numbers ($Gr_T < 1$ and $Gr_P < 1$), the flow field and the interface behavior are not affected by buoyancy forces. Such a situation would be ideal for crystal growth processes where flow control and minimal convection are desired.

While the configuration considered here is relatively simple, it serves several useful purposes. First, it provides a means of directly representing the two-fluid model. Second, it simplifies the study of the parametric range under which the basic mechanisms of mixing (diffusive, convective, chaotic) occur. This configuration is also of practical relevance in materials processing as it may represent, at a fundamental level, the mushy zone/melt interface in alloy solidification and crystal growth processes as well as the slag/metal interface in laddle metallurgy. The application of the two-fluid model to the latter situations will, of course, require modification to the interfacial sources and allowance for chemical reaction and species transport. Additional validation of the two-fluid model will also require a well-controlled experiment.

Acknowledgment

The authors would like to acknowledge the useful discussion with Dr. M. J. Andrews and the financial support provided by Nigde University, Turkey.

References

Andrews, M. J., 1995, "Accurate Computation of Convective Transport in Transient Two-Phase Flow," *International Journal for Numerical Methods in Fluids,* Vol. 21, No. 3, pp. 205–222.

Aref, H., and Tryggvason, G., 1984, "Vortex Dynamics of Passive and Active Interfaces," *Physica,* Vol. 12D, pp. 59–70.

Bejan, A., 1985, "Convection in a Vertical Cavity," *Int. J. Heat and Fluid Flow,* Vol. 6, pp. 149–159.

Chien, W. L., Rising, H., and Ottino, J. M., 1986, "Laminar Mixing and Chaotic Mixing in Several Cavity Flows," *J. Fluid Mech.,* Vol. 170, pp. 355–377.

Duval, W. M. B., 1992, "Numerical Study of Mixing of Two Fluids Under Low Gravity," NASA TM 105865.

Hyun, J. M., Lee, J. W., 1990, "Double-Diffusive Convection in a Rectangular Cavity with Cooperating Horizontal Gradient of Temperature and Concentration," *Int. J. Heat Mass Transfer,* Vol. 33, pp. 1605–1617.

Ilegbusi, O. J., and Spalding, D. B., 1989, "Prediction of Fluid Flow and Heat Transfer Characteristics of Turbulent Shear Flows with a Two-Fluid Model of Turbulence," *Int. J. Heat Mass Transf.,* Vol. 32/4, pp. 767–774.

Ilegbusi, O. J., 1994, "The Two-Fluid Model of Turbulence and its Application in Metals Processing," *J. Materials Processing and Manufacturing Science,* Vol. 3, pp. 143–157.

Ilegbusi, O. J., 1995, "Mathematical Modeling of Mixing and Unmixedness in Plasma Jets," *Materials Processing in the Computer Age—II,* V. R. Voller, S. P. Marsh, and N. El-Kaddah, eds., TMS Publications, Warrendale, PA, pp. 265–278.

Ilegbusi, O. J., Mat, M., and Andrews, M., 1996, "Effect of Atwood Number on the Kinematic Mixing of Two Fluids," *Int. J. of Materials Processing and Manufacturing Science,* Vol. 4, pp. 323–337.

Ilegbusi, O. J., Mat, M., and Andrews, M., 1997, "The Deformation and Kinematic Mixing of a Collapsing Interface," *Applied Mathematical Modelling,* Vol. 21, pp. 66–76.

Kamotani, Y., Wang, L. W., Ostrach, S., and Jiang, D., 1985, "Experimental Study of Natural Convection in a Shallow Enclosure with Horizontal Temperature and Concentration Gradient," *Int. J. Heat Mass Transfer,* Vol. 28, pp. 165–173.

Litsek, P. A., and Bejan, A., 1988, "Transient Natural Convection Between Two Zones in an Insulated Enclosure," ASME JOURNAL OF HEAT TRANSFER, Vol. 110, pp. 116–125.

Ostrach, S., 1980, "Natural Convection with Combined Driving Forces," *PCH PhysicoChemical Hydrodynamics,* Vol. 1, pp. 233–247.

Ottino, J. M., 1989, *The Kinematics of Mixing: Stretching, Chaos, and Transport,* Cambridge University Press, New York.

Patankar, S. V., and Spalding, D. B., 1972, "A Calculation Procedure for Heat, Mass, and Momentum Transfer in Three-Dimensional Parabolic Flows," *Int. J. Heat and Mass Transf.,* Vol. 15, pp. 1787–1806.

Spalding, D. B., 1984, "Two-Fluid Models of Turbulence," NASA, Langley Workshop of the Theoretical Approaches to Turbulence, Hampton, Virginia.

Turner, J. S., 1973, *Buoyancy Effects in Fluids,* Cambridge University Press, New York.

Wu, K. H., and Gau, C., 1992, "Thermosolutal Convection Flow and the Associated Heat and Mass Transfer Process in a Square Enclosure," Natural Convection in Enclosures, conference proceedings, ASME, HTD-Vol. 198, pp. 121–131.

Stability of Mixed Convection in a Differentially Heated Vertical Channel

Y.-C. Chen
Oriental Institute of Technology,
Panchiao, Taiwan, ROC

J. N. Chung
School of Mechanical and
Materials Engineering,
Washington State University,
P.O. Box 642920,
Pullman, WA 99164-2920
chung@mme.wsu.edu

In this study, the linear stability of mixed convection in a differentially heated vertical channel is investigated for various Prandtl numbers. The results indicate that this fully developed heated flow can become unstable under appropriate conditions. It is found that both the Prandtl number and Reynolds number hold very important effects on the critical Grashof number, wave number, wave speed, and instability mechanism for higher Prandtl numbers. For low Prandtl numbers, the effects from the Prandtl number and Reynolds number are relatively small. The most significant finding is that the local minimum wave numbers can be as high as eight for Pr = 1000, which is substantially higher than those found before for other heated flows. The existence of multiple local minimum wave numbers is responsible for the sudden jumps of the critical wave number and wave speed and the sudden shift of instability type for higher Prandtl numbers. The energy budget analysis shows that the thermal-shear and shear instabilities dominate at both low and high Reynolds numbers for Pr = 0.7 and 7. It is the thermal-buoyant instability for Re < 1365 and shear instability for Re ≥ 1365 for Pr = 100. The thermal-buoyant and mixed instabilities are the possible instability types for Pr = 1000. In general, for mixed convection channel flows, the instability characteristics of differentially heated flows are found to be substantially different from those of uniformly heated flows.

1 Introduction

Mixed convection flows in vertical channels and annuli are found in many engineering applications. The characteristics of thermal instability associated with these flows have been investigated extensively in recent years. Because of the distinctively different instability behaviors, two major categories have been examined: constant heat flux wall heating and differential heat flux wall heating (the two boundary walls are each kept at a constant but different temperature). For the former, the buoyancy-driven flow is either in the same direction as the pressure gradient-driven flow (buoyancy-assisted mixed convection) or in the opposite direction (buoyancy-opposed mixed convection). For the latter, the buoyancy-driven flow is in the same direction of the pressure gradient-driven flow in one-half of the channel and in the opposite direction in the other half, which simply means that the buoyancy-assisted and buoyancy-opposed flows exist simultaneously in the same channel. As a result, the laminar base velocity and temperature profiles are totally different between the two. Both profiles are symmetric with respect to the center line for the constant heat flux case while they are asymmetric for the constant temperature case.

For the constant heat flux case, the instability type is in general the thermal-buoyant instability for the buoyancy-assisted flow. They are the Rayleigh-Taylor instability and thermal-shear instability for the lower and higher Reynolds numbers, respectively, in the buoyancy-opposed flow. For the constant temperature case, thermal-shear instability is generally found for low to moderate Reynolds numbers and shear instability is for high Reynolds numbers. Furthermore, the instability character depends strongly on the Prandtl number for the buoyancy-assisted flow, and the Prandtl is a weak parameter for the buoyancy-opposed flow. Chen and Chung (1996) gave a detailed and updated review on the mixed convection instability, and therefore it is not repeated here.

One of the important characteristics of mixed convection instability is the existence of multiple local minimum wave numbers. This phenomenon is particularly significant for the constant temperature heating case and it directly affects the laminar-turbulent transition mechanisms. Double minimum wave numbers were found for natural convection in a vertical slot or plate by Nachtsheim (1963), Gill and Davey (1969), Bergholz (1978), and Ozisik (1985). They showed that the lower wave number minimum represents the thermal instability when the thermal disturbance (the effect of buoyancy) predominates, while the higher wave number minimum is associated with the hydrodynamic instability when the shear force predominates. Mohamad and Viskanta (1989) also reported double minimum wave numbers for the combined buoyancy and lid-driven shear flow in a shallow cavity where the top and bottom boundaries were maintained at constant but different temperatures. The two minimum wave numbers represent thermal and hydrodynamic instabilities, respectively. For the unstably stratified shear flow between two parallel plates, Fujimura and Kelly (1988) found double and triple local minimum wave numbers for relatively large Prandtl numbers and Reynolds numbers. As a result, the critical Rayleigh number curve contains a discontinuity when the instability mode switches from one to another. In this paper, we placed a strong emphasis on the identification and discussion of multiple local minimum wave numbers. We also examined the effects of the Prandtl on the instability, which has not been investigated in the past.

2 Formulation

The viscous flow investigated in this paper is the mixed convection, which is driven by an external pressure gradient and also by a buoyancy force, between two parallel long vertical plates separated by a distance, $2d$. The gravitational force is aligned in the negative x-direction. There is a fixed temperature difference ΔT, produced by maintaining the two vertical walls at different temperatures of T_1 and T_2, respectively. The sche-

Contributed by the Heat Transfer Division for publication in the JOURNAL OF HEAT TRANSFER. Manuscript received by the Heat Transfer Division January 21, 1997; revision received September 2, 1997; Keywords: Channel Flow; Heat Transfer; Mixed Convection. Associate Technical Editor: T. L. Bergman.

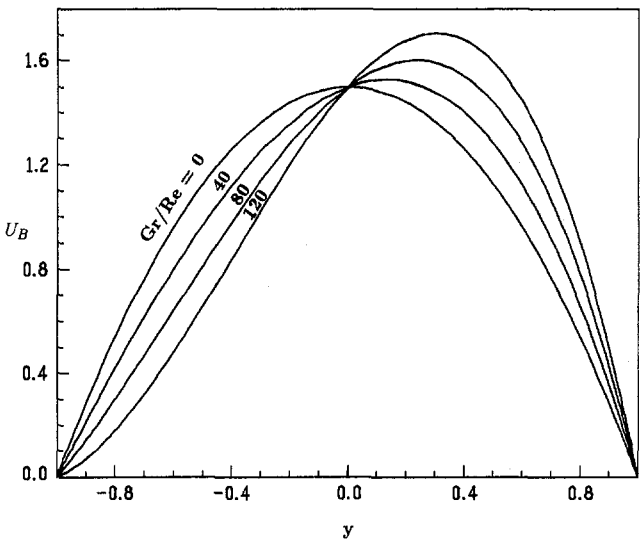

Fig. 1 Laminar base velocity profile

matic of this system, except for the boundary conditions, is given in Chen and Chung (1996). The dimensionless governing equations for continuity, momentum, and energy can be written as

$$\nabla \cdot \vec{V} = 0 \tag{1}$$

$$\frac{\partial \vec{V}}{\partial t} + \vec{V} \cdot \nabla \vec{V} = -\nabla P + \frac{1}{\mathrm{Re}} \nabla^2 \vec{V} + \frac{\mathrm{Gr}}{8\ \mathrm{Re}^2} \theta \vec{e}_x \tag{2}$$

$$\frac{\partial \theta}{\partial t} + \vec{V} \cdot \nabla \theta = \frac{1}{\mathrm{Re\ Pr}} \nabla^2 \theta, \tag{3}$$

where the coordinates are nondimensionalized by the half width of the channel d, the velocity ($\vec{V}$) by the average laminar base velocity $\bar{U}_B$, the pressure (P) by $\rho \bar{U}_B^2$, the time (t) by $d/\bar{U}_B$, and ρ is the fluid density. $\vec{e}_x$ is the unit vector in the x-direction. x, y, z are coordinates in the streamwise, cross streamwise (perpendicular to the walls), and spanwise directions, respectively. In the above, $\mathrm{Re} = \bar{U}_B d/\nu$ is the Reynolds number, where ν is the fluid kinematic viscosity. Also $\mathrm{Pr} = \nu/\alpha_T$ is the Prandtl number, and α_T is the thermal diffusivity. $\mathrm{Gr} = g\beta_T \Delta T (2d)^3/\nu^2$ is the Grashof number, where g is the gravitational acceleration and β_T is the thermal expansion coefficient. The Boussinesq approximation is used here, and viscous dissipation is neglected. $\theta = (T - T_m)/\Delta T$ is the dimensionless temperature. T_m is the mean temperature between the two vertical walls.

2.1 Laminar Base Flow. The base flow is the fully developed steady laminar flow, that is, it is a function of y only. Following the similar procedure as given in Chen and Chung (1996), the base flow velocity and temperature profiles are given as

$$U_B = 3(1 - y^2)/2 + \frac{1}{96} \frac{\mathrm{Gr}}{\mathrm{Re}} (y - y^3) \tag{4a}$$

$$\theta_B = y/2. \tag{4b}$$

The only parameter in Eq. (4) is Gr/Re. The laminar base flow velocity profiles for Gr/Re = 0, 40, 80, and 120 are plotted in Fig. 1. The velocity profile has an inflection point for Gr/Re $\geq$ 48.

2.2 Linear Stability Analysis. In the linear stability analysis, the infinitesimal disturbances are imposed on the fully developed laminar base flow, thus, the velocity, pressure, and temperature fields can be written as follows:

$$\vec{V} = U_B(y)\vec{e}_x + \vec{V}' \tag{5a}$$

$$P = P_B(x) + p' \tag{5b}$$

$$\theta = \theta_B(y) + \theta', \tag{5c}$$

where the prime denotes the infinitesimal disturbances. $\vec{V}' = (u', v', w')$ and (u', v', w') are the velocity disturbances in the x, y, and z-directions, respectively. By using the usual normal mode form, the disturbances can be represented by

$$\vec{V}' = \hat{\vec{V}}(y) e^{i(\alpha x + \beta z - \alpha c t)} \tag{6a}$$

$$p' = \hat{p}(y) e^{i(\alpha x + \beta z - \alpha c t)} \tag{6b}$$

$$\theta' = \hat{\theta}(y) e^{i(\alpha x + \beta z - \alpha c t)}, \tag{6c}$$

where $\hat{\vec{V}} = (\hat{u}, \hat{v}, \hat{w})$ and $(\hat{u}, \hat{v}, \hat{w})$ are the velocity components in the x, y, and z-directions, respectively. α (real) and β (real) are the wave numbers in the x and z-directions, respectively. $c = c_r + ic_i$ is the complex wave speed. Following the standard linear stability method as outlined in Chen and Chung (1996), the linearized stability equations become the following:

$$\frac{1}{\mathrm{Re}} \left[\frac{d^4\hat{v}}{dy^4} - 2(\alpha^2 + \beta^2) \frac{d^2\hat{v}}{dy^2} + (\alpha^2 + \beta^2)^2 \hat{v} \right]$$

$$+ i\alpha \left\{ U_B \left[-\frac{d^2\hat{v}}{dy^2} + (\alpha^2 + \beta^2)\hat{v} \right] + \frac{d^2 U_B}{dy^2} \hat{v} \right\}$$

$$- i\alpha \frac{\mathrm{Gr}}{8\ \mathrm{Re}^2} \frac{d\hat{\theta}}{dy} = -i\alpha c \left[\frac{d^2\hat{v}}{dy^2} - (\alpha^2 + \beta^2)\hat{v} \right] \tag{7}$$

$$- \frac{1}{\mathrm{Re\ Pr}} \left[\frac{d^2\hat{\theta}}{dy^2} - (\alpha^2 + \beta^2)\hat{\theta} \right] + \frac{d\theta_B}{dy} \hat{v} + i\alpha U_B \hat{\theta} = i\alpha c \hat{\theta}. \tag{8}$$

The associated boundary conditions are

$$\hat{v} = \frac{d\hat{v}}{dy} = \hat{\theta} = 0 \quad \text{at} \quad y = \pm 1. \tag{9}$$

Equations (7) and (8) and the corresponding boundary conditions constitute an eigenvalue problem.

2.3 Numerical Method. The Galerkin method is used to solve the above coupled equations, (7) and (8), and their associated boundary conditions. In this method, the test (weighted) functions are the same as the base (trial) functions. Thus, the $\hat{v}$ and $\hat{\theta}$ are expanded as follows:

$$\hat{v} = \sum_{n=0}^{N} a_n \xi_n(y) \tag{10a}$$

$$\hat{\theta} = \sum_{n=0}^{N} b_n \phi_n(y). \tag{10b}$$

We adopt the base function proposed by Singer et al. (1989) for $\hat{v}$. The base function for $\hat{\theta}$ have little different form. They are shown as follows:

$$\xi_n(y) = (1 - y^2)^2 P_n(y) \tag{11a}$$

$$\phi_n(y) = (1 - y^2) P_n(y). \tag{11b}$$

In the above, each base function ξ_n and ϕ_n satisfies the boundary conditions and $P_n(y)$ is the Legendre polynomial of order n. The other details can be found in Chen and Chung (1996). We verified our code first by comparing with the published results of an isothermal channel flow for the case of Gr/Re = 0. Our isothermal results of the critical Reynolds number Re_c = 3848.13 (Re_c = 5772.2 if based on the maximum velocity) and the critical wave number α_c = 1.0206 with N = 51 in Eq. (10)

agree exactly with those given by Orszag (1971). For verifying our code with heated flows, we first used the results of Korpela et al. (1973) and Lee and Korpela (1983). Both papers provide stability analyses for natural convection in a vertical slot. By setting Re → 0 in our code, we obtained 8038 and 1.4 (based on the half channel width) for the critical Grashof number and wave number, respectively. The results of our code show that the disturbances are stationary for Pr < 12.7 and oscillatory for Pr > 12.7. These results are all identical with those of Korpela et al. (1973) and Lee and Korpela (1983). For mixed convection flow, no data was available for a direct comparison. The results of Yao and Rogers (1989) for mixed convection in a vertical annulus with a very large aspect ratio of 100 were estimated from their figures and were used as approximations to our flat plate channel flows (aspect ratio is infinite). The comparison for Re = 1500 is as follows:

Table 1

	Current results	Yao and Rogers (1989)
$(Gr/Re)_c$	115.25	115
α_c	1.032	1.05
c_r	0.508	0.52

Based on the above three cases of comparison, we believe that our code is accurate for the study. Since in all the verification runs $N = 51$, we decided to keep that for the current study.

2.4 Energy Budget Analysis. In order to understand the role played by the heat transfer during the flow instability, it is necessary to keep track of the turbulent kinetic energy budget for the disturbances. The driving mechanisms of flow instability may be determined by the production and dissipation of disturbance kinetic energy (Hart 1971; Rogers and Yao 1993). The balance of disturbance kinetic energy for the infinitesimal disturbance is

$$\frac{\partial}{\partial t}\left\langle \frac{1}{2}(u'^2 + v'^2 + w'^2)\right\rangle = -\left\langle u'v'\frac{dU_B}{dy}\right\rangle + \frac{\mathrm{Gr}}{8\ \mathrm{Re}^2}\langle u'\theta'\rangle - \frac{1}{\mathrm{Re}}\langle(\nabla u')^2 + (\nabla v')^2 + (\nabla w')^2\rangle = E_s + E_b + E_d, \quad (12)$$

where the bracket $\langle\ \rangle$ implies integration over the volume of the disturbance wave. The first term on the right-hand-side of Eq. (12), E_s, represents the shear production of turbulent energy. The second term, E_b, represents the turbulent kinetic energy production due to the work done by the thermal buoyant potential of disturbance temperature field. The last term, E_d, represents the dissipation of energy through molecular viscosity. On the neutral stability curve ($c_i = 0$), the disturbances are neither growing nor decaying, thus the left-hand-side term (differentiation with time) is zero. More detailed discussion about the physical meanings of each term in Eq. (12) is provided in Chen and Chung (1996).

3 Results and Discussion

In addition to the Re and Gr, another dimensionless parameter in the system is the Pr. In this study, Pr of 0.7, 7, 100, and 1000 were chosen for sample calculations, which represent most gases and liquids. Because the stable and unstable domains are separated by the neutral stability curve ($c_i = 0$), we will basically present the neutral stability curves for various Pr numbers to demonstrate the characteristics of stability for the flow. Since the laminar velocity profile is only a function of Gr/Re, the c_i can be presented as $c_i = c_i(\mathrm{Re}, \mathrm{Gr/Re}, \alpha, \beta)$. We have included both integer and noninteger β values in this computation. The

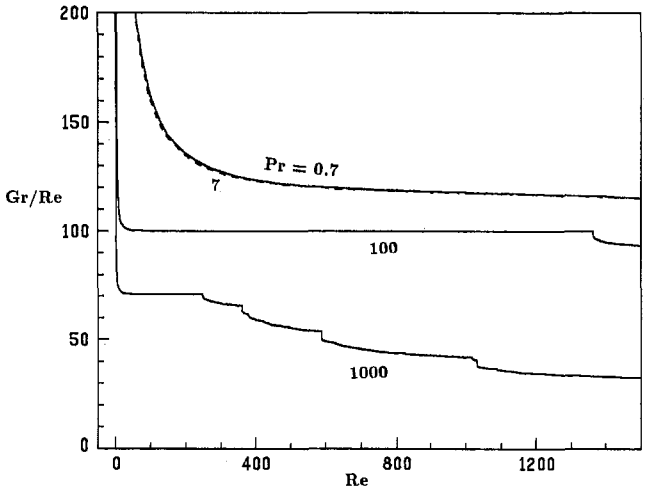

Fig. 2 The instability boundaries on the (Re, Gr/Re) plane

results show that $\beta = 0$ is the least stable mode, that is, the least stable disturbances are two-dimensional. Thus most of the neutral stability curves on both (Re, Gr/Re) and (Re, α) planes will be plotted for various Pr values.

The instability boundaries on the (Re, Gr/Re) plane are shown in Fig. 2. The results indicate that a heated channel flow would become unstable when the Gr is greater than a specific value (e.g., with Pr = 1000 fluids, Gr > 7083 for Re = 100 and Gr > 35240 for Re = 1500; with Pr = 0.7 fluids, Gr > 16225 for Re = 100 and Gr > 172890 for Re = 1500). In general, the higher the Prandtl number, the smaller the critical value of Gr/Re. The critical Grashof number Gr_c or $(Gr/Re)_c$ for Pr = 0.7 and 7 are very similar to each other, but the Gr_c's or $(Gr/Re)_c$'s for Pr = 7, 100, and 1000 are significantly different. This implies that the Prandtl number is a very important parameter for the stability characteristics of most liquids. It is noted that the $(Gr/Re)_c$ for Pr = 1000 is smaller than 48 for Re > 626; therefore, there is no inflection point in the laminar velocity profile for Re > 626. One important feature is that the Gr_c or $(Gr/Re)_c$ has one discontinuity on the (Re, Gr) plane at Re = 1365 for Pr = 100 and several more for Pr = 1000. It will be shown later in Fig. 3 and 4 that the critical wave number and wave speed also have sudden jumps corresponding to discontinuities on the (Re, Gr) plane. The physical

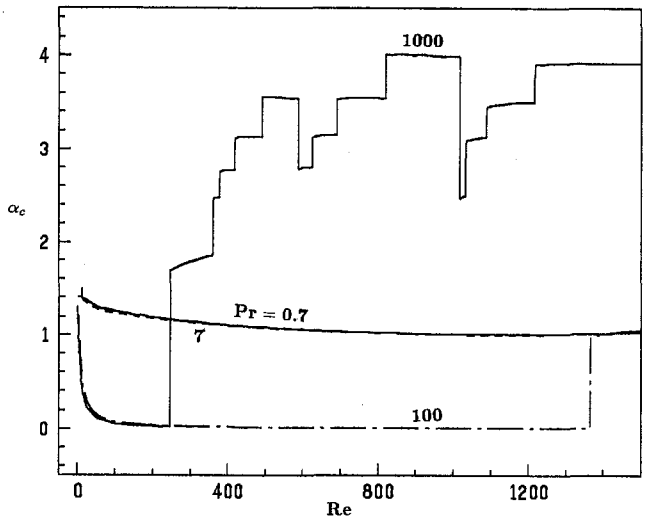

Fig. 3 The variation of wave number α_c with Re along the neutral stability curve (α_c = 1.0206 for isothermal flow)

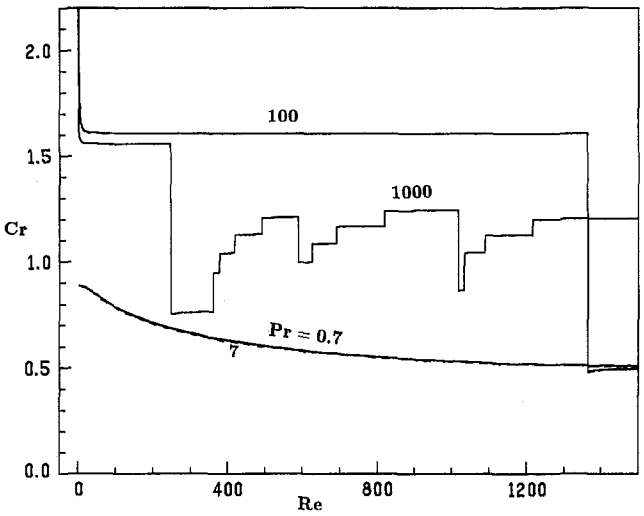

Fig. 4 The variation of wave speed c_r with Re along the neutral stability curve

meaning of the discontinuities is explained next. For instance, the instability types are distinctly different before and after the discontinuities at Re = 1365 for Pr = 100; it is a thermal-buoyant instability for Re < 1365, and it suddenly shifts to a shear instability for Re ≥ 1365 with Pr = 100 fluids. This behavior, that the Gr_c has discontinuities, is due to the multiple local minimum wave numbers as mentioned in the Introduction and will be shown and discussed later in Fig. 5. In general, the Gr_c increases with increasing Reynolds number except in some portions of Pr = 100 and 1000, where the Gr_c generally has discontinuities. Since the range of the Pr for water goes as high as 13, we have computed the stability characteristics for Pr = 13 in the Re range of 10 to 1500. We found that the critical Gr/Re's for Pr = 13 differ from those of Pr = 7 by less than 0.14 percent. This indicates that the stability characteristics for water are fairly constant.

The linear instability boundary on the (Re, α_c) plane, where α_c is the critical wave number, is plotted in Fig. 3. The curves on Fig. 3 demonstrate the variation of α_c with respect to the Re_c along the neutrally stable curve. It is seen that again the curves for Pr = 0.7 and 7 are very similar to each other and α_c decreases very slowly with increasing Reynolds number for Re > 25. The α_c reaches the minimum value of 1.004 at Re = 1150 for Pr = 0.7 and 1.003 at Re = 1150 for Pr = 7 and then increases very slightly with increasing Reynolds number. Thus, the α_c between Re = 600 and 1500 is close to the isothermal channel flow critical wave number of 1.0206. For Pr = 100, the α_c decreases very quickly with the increase of Reynolds number for Re < 100 and becomes vanishingly small (α_c = 0.008 for Re = 1000) between Re = 100 and 1364. After a big upward jump at Re = 1365, the α_c shifts to a value about 1, which is close to that of Pr = 0.7 or 7. The instability types for Pr = 0.7, 7, and 100 are also all the same (shear instability) for Re ≥ 1365 as shown in Table 2. The behavior of α_c for Pr = 1000 is very similar to that of Pr = 100 for Re < 248. After upward jumps at Re = 248 and 361, it can be seen that the α_c (α_c = 3.99 for Re = 1000) for Pr = 1000 is now much higher than that of Pr = 0.7, 7, or 100 for Re > 361, that is, the wavelength is the shortest for Re > 361. This implies that the instability for Pr = 1000 is caused by a local disruption of the velocity field which is induced by the temperature fluctuation. Roughly, the portion of the curve between Re = 361 and 1500 can be divided into three regions: one from Re = 361 to 587, one from Re = 588 to 1016, and one from Re = 1017 to 1500. Each region encounters about three small upward jumps. The behaviors of wave speed and instability mechanism in each region are also similar, as shown in Fig. 4 and Table 2.

The wave speed, c_r, along the instability boundary is plotted in Fig. 4. The wave speed curve for Pr = 0.7 and 7 gradually and smoothly decrease with the increase of the Reynolds number. For Pr = 100, the wave speed between Re = 25 and 1364 is nearly constant with a value of 1.6. It is noted that the c_r between Re = 248 and 1365 for Pr = 100 is the largest among all the critical wave speeds, while its wave number is the smallest as shown in Fig. 3. At Re = 1365, the c_r has a big drop and the wave speed is also close to that of Pr = 0.7 or 7 for Re ≥ 1365. The wave speed of Pr = 1000 is similar to that of Pr = 100 for Re < 248. After a substantial drop at Re = 248, the wave speed curve displays a very similar behavior as its wave number curve between Re = 361 and 1500. It is also seen that c_r's for Pr = 0.7, 7, and 100 are very similar for Re ≥ 1365. They are quite different from that of Pr = 1000.

As mentioned earlier, the analysis of the energy transfer budget for the neutral stability curve could provide some insights on the transport mechanisms during flow instability. A summary of the energy budget is given in Table 2. For Pr = 0.7 and 7, the instability type is the thermal-shear instability for lower Reynolds numbers, while it becomes the shear instability (similar to the isothermal flow) for higher Reynolds numbers. For Pr = 100, the thermal-buoyant instability dominates for Re < 1365, then it suddenly shifts to shear instability for Re ≥ 1365. It is noted that the instability types are the same for Pr = 0.7, 7, and 100 for Re ≥ 1365. This can be realized since α_c and c_r for Pr = 0.7, 7, and 100 are similar to one another for Re > 1365. The instability mechanism for Pr = 1000 reflects the characteristics of its wave number and speed. It is the thermal-buoyant instability, which is the same as that of Pr = 100 for Re < 248. After a big jump at Re = 248, the instability switches to the mixed instability between Re = 248 and 360. In this region, both E_s (shear production) and E_b (energy generation from buoyant source) play important roles in the flow instability, even E_s is larger than E_b. Between Re = 361 and 1500, the instability type can be divided into three regions: one from Re = 361 to 587, one from Re = 588 to 1016, and one from Re = 1017 to 1500. In each region, the instability begins with the mixed instability in which E_s is smaller than E_b, then it gradually switches to the thermal-buoyant instability. From the above discussion, we may conclude that the instability mechanisms among Pr = 7 (or 0.7), 100, and 1000 are significantly different, while they are similar for Pr = 0.7 and 7.

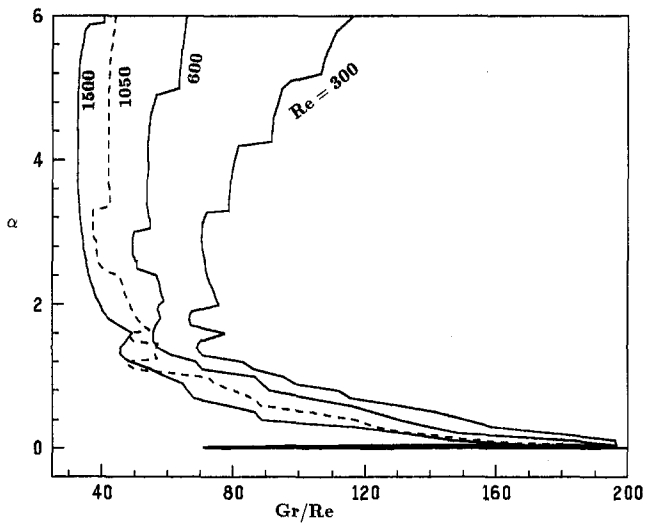

Fig. 5 The variation of wave number with Gr/Re at various Reynolds number for Pr = 1000

Table 2 Energy budget in the neutral stability curve. (TB—thermal buoyant instability, M—mixed instability, TS—thermal shear instability, S—shear instability)

Pr	Re	$(Gr/Re)_c$	α_c	E_s	E_b	E_d	Type
0.7	2	4023.27	1.403	0.94	0.06	−1.0	TS
0.7	10	816.55	1.40	0.94	0.06	−1.0	TS
0.7	100	162.25	1.26	0.96	0.04	−1.0	TS
0.7	1000	117.75	1.01	1.00	0.00	−1.0	S
0.7	1500	115.26	1.032	1.00	0.00	−1.0	S
7	10	800.11	1.378	0.81	0.19	−1.0	TS
7	100	160.42	1.244	0.94	0.06	−1.0	TS
7	1000	117.64	1.007	1.00	0.00	−1.0	S
7	1500	115.18	1.030	1.00	0.00	−1.0	S
100	10	111.26	0.67	0.01	0.99	−1.0	TB
100	100	100.11	0.075	0.01	0.99	−1.0	TB
100	500	100.00	0.015	0.01	0.99	−1.0	TB
100	1000	100.00	0.008	0.01	0.99	−1.0	TB
100	1300	100.00	0.006	0.01	0.99	−1.0	TB
100	1370	96.73	0.986	1.00	0.00	−1.0	S
100	1500	93.53	1.055	1.00	0.00	−1.0	S
1000	1	208.45	1.173	0.001	0.999	−1.0	TB
1000	240	70.82	0.023	0.003	0.997	−1.0	TB
1000	250	69.14	1.70	0.683	0.317	−1.0	M
1000	360	65.75	1.86	0.638	0.362	−1.0	M
1000	365	62.51	2.474	0.334	0.666	−1.0	M
1000	400	59.14	2.773	0.207	0.793	−1.0	TB
1000	445	57.05	3.132	0.129	0.871	−1.0	TB
1000	500	55.55	3.553	0.087	0.913	−1.0	TB
1000	550	54.39	3.548	0.068	0.932	−1.0	TB
1000	585	53.86	3.535	0.054	0.946	−1.0	TB
1000	588	50.12	2.78	0.360	0.640	−1.0	M
1000	600	49.13	2.80	0.355	0.645	−1.0	M
1000	650	46.91	3.15	0.289	0.711	−1.0	M
1000	800	43.85	3.543	0.239	0.761	−1.0	TB
1000	1000	42.16	3.99	0.214	0.786	−1.0	TB
1000	1025	40.95	2.49	0.300	0.700	−1.0	M
1000	1050	37.18	3.117	0.115	0.885	−1.0	TB
1000	1200	34.69	3.50	0.053	0.947	−1.0	TB
1000	1500	32.64	3.913	−0.004	1.004	−1.0	TB

The many discontinuities on the wave number curves and wave speed curves for Pr = 1000 prompt the investigation on the variation of wave number with Gr/Re for some typical Reynolds numbers, that is, the lowest value of Gr/Re to result in $c_i = 0$ for a given wave number. The results for Re = 300, 600, 1050, and 1500 are plotted in Fig. 5. As mentioned previously, double minimum wave numbers were found in the natural convection flow by Gill and Davey (1969), Bergholz (1978), and Ozisik (1985). Two or three local minimum wave numbers were found in the shear flow between horizontal plates heated from below by Mohamad and Viskanta (1989) and Fujimura and Kelly (1988). It is seen in Fig. 5 that multiple minimum wave numbers occur on every curve. Five local minimum wave numbers are found at α = 0.019, 1.4, 1.79, 2.9, and 3.33 for Re = 300, where α = 1.79 is the critical wave number to determine the critical Grashof number Gr_c, as shown in Fig. 2. It is noted that the number of local minimum wave numbers can be as high as eight for Re = 600 and 1050, which is substantially higher than those found before. They are located at α = 0.0053, 1.19, 1.32, 1.57, 2.81, 3.12, 3.98, and 4.6 for Re = 1050, where α = 3.12 is the critical wave number. Eight local minima are found at α = 0.009, 1.54, 1.94, 2.54, 2.8, 3.09, 3.53, and 4.07 for Re = 600. The behavior of multiple local minimum wave numbers for Pr = 1000 is responsible for the several discontinuities found on the critical Grashof number curve, several discontinuities on wave number and wave speed curves, as well as associated sudden switches of instability types as shown in Fig. 2, 3, 4, and Table 2. This is because the critical wave number can be one of those local minimum wave numbers for the different Reynolds and Grashof numbers. Furthermore, at Re = 1500, the number of local minima now goes down to four, which are found at α = 0.003, 1.34, 3.91, and 4.44 (where α = 3.91 is the critical wave number).

4 Conclusions

The linear instability analysis of mixed convection in a differentially heated vertical channel was investigated for the Prandtl number range of 0.7, 7, 100, and 1000. The results indicate that this fully developed heated flow can become unstable under appropriate conditions. It is found that both the Prandtl number and the Reynolds number are very important parameters in determining the critical Grashof number Gr_c, critical wave number α_c, wave speed c_r, and instability mechanism for higher Prandtl numbers. For lower Prandtl numbers, the effects of the Prandtl number and the Reynolds number are relatively small. For the overall trend, the Gr_c increases with increasing Reynolds number. In general, the higher the Prandtl number, the smaller the critical Grashof number Gr_c. For Pr = 1000, the $(Gr/Re)_c$ is smaller than 48 for Re > 625, therefore, there is no inflection point in the base laminar profile.

One important feature is the existence of multiple local minimum wave numbers. We found that the number of the local minimum wave numbers can be as high as eight for Pr = 1000, which are substantially larger than those (two or three local minimum wave numbers) found in natural convection or shear flow between horizontal plates heated from below. The fact that the Gr_c has several discontinuities, and α_c and c_r also have discontinuities, as well as sudden shift of instability types for Pr = 100 and 1000, are all attributed to the presence of multiple local minimum wave numbers. The α_c and c_r for Pr = 100 encounter a large jump at Re = 1365. Before that jump, the α_c is very small (α = 0.006 for Re = 1300) and the c_r is the largest among all curves, with a value of 1.6. In addition, the instability type is the thermal-buoyant instability between Re = 50 and 1365. After that jump, the α_c and c_r approach 1 and 0.5, respectively, and the instability also suddenly shifts

to shear instability. The α_c and c_r for Pr = 1000 go through substantially more discontinuities. Each discontinuity has a respective effect on the α_c, c_r, and instability type. The thermal-buoyant and mixed instabilities are the only instability types and they switch to each other at those discontinuities for different Reynolds numbers. It is emphasized that the α_c for Pr = 1000 is the highest (α_c = 3.99 for Re = 1000) or the wavelength is the shortest for medium and high Reynolds numbers. This implies that the instability is caused by the local disruption of the velocity field which is induced by the thermal fluctuation. The Gr_c, α_c, and c_r for Pr = 0.7 and 7 do not have discontinuities and the thermal-shear and shear instabilities dominate in low and high Reynolds number flows, respectively. It is noted that the α_c and c_r for Pr = 0.7, 7, and 100 are relatively close together and the instability types are the same for Re $\geq$ 1365, which is significantly different from those of Pr = 1000.

References

Bergholz, R. F., 1978, "Instability of Steady Natural Convection in a Vertical Fluid Layer," *J. Fluid Mech.*, Vol. 84, pp. 743–768.

Chen, Y. C., and Chung, J. N., 1996, "The Linear Stability of Mixed Convection in a Vertical Channel Flows," *J. Fluid Mech.*, Vol. 325, pp. 29–51.

Fujimura, K., and Kelly, R. E., 1988, "Stability of Unstably Stratified Shear Flow Between Parallel Plates," *Fluid Dyn. Res.*, Vol. 2, p. 281.

Gill, A. F., and Davey, A., 1969, "Instabilities of a Buoyancy-Driven System," *J. Fluid Mech.*, Vol. 75, pp. 775–793.

Hart, J. E., 1971, "Stability of the Flow in a Differentially Heated Inclined Box," *J. Fluid Mech.*, Vol. 47, pp. 547–576.

Korpela, S. A., Gozum, D., and Chandrakant, B. B., 1973, "On the Stability of the Conduction Regime of Natural Convection in a Vertical Slot," *Int. J. Heat Mass Transfer*, Vol. 16, pp. 1683–1689.

Lee, Y., and Korpela, S. A., 1983, "Multicellular Natural Convection in a Vertical Slot," *J. Fluid Mech.*, Vol. 126, pp. 91–121.

Mohamad, A. A., and Viskanta, R., 1989, "Stability of Lid-Driven Shallow Cavity Heated From Below," *Int. J. Heat Mass Transfer*, Vol. 32, pp. 2155–2166.

Nachtsheim, P. R., 1963, *Stability of Free-Convection Boundary-Layer Flows*, N.A.S.A. Tech. Note D-2089.

Orszag, S. A., 1971, "Accurate Solution of the Orr-Sommerfeld Stability Equation," *J. Fluid Mech.*, Vol. 50, pp. 689–703.

Ozisik, M. N., 1985, "Thermal Stability of a Vertical Fluid Layer With Volumetric Energy Sources," *Natural Convection Fundamentals and Applications* S. Kakac, W. Aung, and R. Viskanta, eds., Hemisphere, Washington, pp. 156–178.

Rogers, B. B., and Yao, L. S., 1993, "The Importance of Prandtl Number in Mixed-Convection Instability," ASME JOURNAL OF HEAT TRANSFER, Vol. 115, pp. 482–486.

Singer, B. A., Ferziger, J. H., and Reed, H. L., 1989, "Numerical Simulations of Transition in Oscillatory Plane Channel Flow," *J. Fluid Mech.*, Vol. 208, pp. 45–66.

Yao, L. S., and Rogers, B. B., 1989, "Mixed Convection in an Annulus of Large Aspect Ratio," ASME JOURNAL OF HEAT TRANSFER, Vol. 111, pp. 683–689.

Y. Bayazitoglu
Professor.
bayaz@rice.edu
Fellow ASME.

B. Y. Wang
Graduate Student.

Department of Mechanical Engineering and Materials Science,
Rice University,
6100 South Main Street,
Houston, TX 77005

Wavelets in the Solution of Nongray Radiative Heat Transfer Equation

The wavelet basis functions are introduced into the radiative transfer equation in the frequency domain. The intensity of radiation is expanded in terms of Daubechies' wrapped-around wavelet functions. It is shown that the wavelet basis approach to modeling nongrayness can be incorporated into any solution method for the equation of transfer. In this paper the resulting system of equations is solved for the one-dimensional radiative equilibrium problem using the P-N approximation.

Introduction

The exact solution of the equation of radiative transfer for a radiatively participating medium is impossible for most practical problems. Therefore, assumptions and approximations are made which lead to simpler solutions. The most common assumption is that of a gray medium, which eliminates the frequency dependencies. Since absorption in most gases and semitransparent solids is restricted to specific intervals of the spectrum, the gray gas assumption is limited in its use. Chan and Tien (1971), Tiwari (1977), and Crosbie and Viskanta (1970) used the band model approximation to solve nongray, nonisothermal media problems. Chan and Tien used the wide band Curtis-Godson technique, which is only useful when the temperature distribution is specified. Yuen and Rasky (1981) solved the radiative heat transfer problem in a nongray media using the P-1 approximation. Yucel and Bayazitoglu (1982) generalized the P-N approximation for nongray problems using the rectangular band model with P-1 and P-3 approximations. Kaminski and Moder (1989) gave an analysis of the P-N approximation for nongray problems by dividing the absorption coefficient spectrum into a finite number of bands. Earlier attempts were made by Hottel and Sarofim (1967) to apply the zonal method to a nongray medium with little success.

During the last decade the weighted-sum-of-gray-gases method was successfully applied to the solution of the equation of radiative transfer by Modest (1991). In addition, the effects of absorption-emission bands of molecular gases in some cases can be approximated by the box model, which is also called the picket fence model. A recent work of Modest and Sikka (1992) incorporates a general picket fence model into the P-1 approximation.

In order to accurately represent local variations, consider the emerging field of wavelet analysis (also known as "time scale atoms"). Concisely, wavelet analysis can be viewed as a multiresolution analysis that consists of a sequence of successive approximation spaces. Haar (1910) constructed an orthogonal system of localized functions defined between the interval from zero to one. Donoho (1993) showed that wavelets are unconditional bases for a very wide set of function classes. Particularly, when the functions exhibit localized variation, wavelets provide better approximations than conventional methods such as Fourier series approximations.

To construct a wavelet function ψ, Daubechies (1992) started from the dilation equation for the scaling function φ,

$$\varphi(x) = \sum_n h_n \varphi_{-1,n} = \sqrt{2} \sum_n h_n \varphi(2x - n) \quad n = 0, N-1 \quad (1)$$

and found that the wavelet function satisfies a similar dilation equation,

$$\psi(x) = \sqrt{2} \sum_n (-1)^{n-1} h_{N-n-1} \varphi(2x - n) \quad n = 0, N-1. \quad (2)$$

More importantly, a set of h_n coefficients, up to $N = 20$ (where N has to be even) are constructed. Since φ and ψ have finite support (i.e., they only have nonzero values in a finite interval), they are calculated numerically. Daubechies (1992) proved that wavelets, the family of functions $\psi(2^j x - k)$ (i.e., the dilated and translated version of $\psi(x)$, where $j, k \in Z$), construct a set of orthogonal bases for the L^2 function space, i.e., the square-integrable function space, and gave a detailed construction procedure for these wavelets.

Newland (1993) gave a wavelet series expansion of the L^2 function $f(t)$, as follows:

$$f(t) = b_0 + \sum_j \sum_k b_{2^j+k} W(2^j t - k),$$

$$0 \le t < 1, \quad j = 0, \infty \quad k = 0, 2^j - 1, \quad (3)$$

where $W(2^j t - k)$ are Daubechies' wavelets confined in the interval $0 \le t < 1$ and wrapped around the interval $0 \le t < 1$ as many times as necessary to ensure that their entire length is included in this unit interval; therefore, outside this interval these wrapped around wavelets vanish to zero. The inner product of any single wavelet or any two distinct wavelets from the same family are identically zero. These orthogonality properties are expressed as

$$\int_0^1 W(2^j t - k) W(2^{j'} t - k') dt = \delta_{jj'} \delta_{kk'} \quad (4a)$$

$$\int_0^1 W(2^j t - k) dt = 0, \quad (4b)$$

where δ is the Kronecker δ function. The general coefficients can be calculated by taking the inner product of the function and the wavelet basis as

$$b_0 = \int_0^1 f(t) dt \quad (5a)$$

$$b_{2^j+k} = \int_0^1 f(t) W(2^j t - k) dt. \quad (5b)$$

Mallat (1989) and Newland (1993) have developed a very efficient algorithm to compute the discrete wavelet transform Eq. (5) from the sampling points of the function. The wavelets

Contributed by the Heat Transfer Division for publication in the JOURNAL OF HEAT TRANSFER and presented at IMECE, Atlanta 1996. Manuscript received by the Heat Transfer Division October 23, 1996; revision received October 6, 1997; Keywords: Radiation; Radiation Interactions. Associate Technical Editor: B. W. Webb.

W_m are calculated numerically from the inverse discrete wavelet transform.

Figures 1 and 2 show the numerically calculated D20 (i.e., Daubechies, 20 h_n coefficients) wavelets at two different levels and locations. Figures 3 and 4 are examples of functions reconstructed by truncated wavelet series (Fig. 3 shows the function in part of the entire domain). The original functions are the absorption coefficient functions which will be used in the later analysis. The reconstruction is carried out by sampling the original functions at 16,384 points, doing the discrete wavelet transform, but only using 256 terms to approximately reconstruct the functions. (If all 16,384 terms are used, it will perfectly reproduce the sampling points.) It should be noted that the truncated wavelet series expansion of radiative intensity, not these reconstructed absorption coefficients, will be involved in the later analysis.

In thermal radiation analysis the absorption coefficients of most media are significant only in several discrete bands in the frequency domain. Since these absorption bands are typically very narrow, the radiative intensity is expected to vary locally. Wavelets have finite support which may be localized at any position in the frequency domain, so we can expect wavelets to provide a very good approximation for the radiative intensity in the frequency domain.

In this work the wavelet basis functions are introduced into the radiative transfer equation in the frequency domain. The resulting system of equations, which does not have frequency as a variable, could be solved by any method applicable for a gray medium. The P-N approximation method, which has previously been determined to be effective for gray media problems, is used here. The current method is applicable for any distribution of the absorption coefficient that is square integrable.

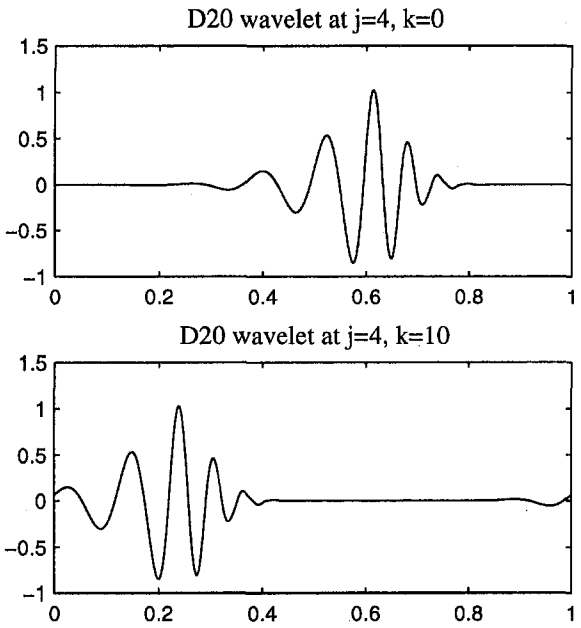

Fig. 1 Wrapped-around Daubechies' wavelets at level $j = 4$, $k = 0$ and 10

Mathematical Analysis and Formulation

In order to apply the discrete wavelet analysis presented by Newland (1993), we need a function which is square integrable ($L^2(R)$) and has a finite domain. The intensity of thermal radiation and the blackbody intensity are both square integrable functions. The intensity of thermal radiation is bounded in the wavelength domain between 0 − 1000 μm, while the blackbody intensity given by Planck's law is not in the bounded domain. The wavelength goes from zero to infinity. For mathematical simplification, we will assume that the blackbody intensity is equal to zero beyond a maximum wavelength, λ_M.

The transfer equation for a nongray, nonscattering medium is

$$\sum_{i=1}^{3} l_i \frac{\partial I_\lambda}{\partial x_i} = -\kappa_\lambda I_\lambda + \kappa_\lambda I_{b,\lambda}, \tag{6}$$

where I_λ is the radiative intensity, $I_{b,\lambda}$ is the blackbody intensity at the local temperature, κ_λ is the absorption coefficient, and $l_i (i = 1, 2, 3)$ are the direction cosines. Equation (6) is scaled in the region $[0, \lambda_M)$ as

$$\sum_{i=1}^{3} l_i \frac{\partial I_{\lambda_c}}{\partial x_i} = -\kappa_{\lambda_c} I_{\lambda_c} + \kappa_{\lambda_c} I_{b,\lambda_c}, \tag{7}$$

where $\lambda_c = \lambda/\lambda_M$ and $0 \le \lambda_c < 1$. Since $I_{\lambda_c} \in L^2(\lambda_c)$, it can be expanded in a wavelet basis series as

$$I_{\lambda_c} = b_0(\vec{x}, \omega) + \sum_j \sum_k b_{2^j+k}(\vec{x}, \omega) W(2^j \lambda_c - k). \tag{8}$$

Following the Galerkin finite element method, an approximate solution $\tilde{I}_{\lambda_c}$ is now assumed for I_{λ_c} by truncating the infinite wavelet series as

$$I_{\lambda_c} \approx \tilde{I}_{\lambda_c} = b_0(\vec{x}, \omega) + \sum_{j=0}^{J} \sum_{k=0}^{2^j-1} b_{2^j+k}(\vec{x}, \omega) W(2^j \lambda_c - k). \tag{9}$$

Nomenclature

$b_m(\vec{x}, \omega)$ = wavelet expansion coefficients of I_{λ_c}
$b_m^{(0)}$ = zeroth moment of b_m
$b_m^{(i)}$ = first moment of b_m
$b_m^{(ij)}$ = second moment of b_m
d = spectral line spacing
E = blackbody emissive power σT^4 evaluated at temperature $T(x^*)$
h_n = scaling function coefficients
I = total radiative intensity
I_λ = radiative intensity at wavelength λ
$I_{b,\lambda}$ = blackbody intensity at wavelength λ
$\tilde{I}_{\lambda_c}$ = approximate intensity
q_r = radiative heat flux
S = mean line intensity
$T_{w,1}$, $T_{w,2}$ = temperatures of black wall 1 and 2
$W_{m'}$, $W(2^j\lambda_c - k)$ = wrapped-around Daubechies' wavelets
$Y_l^{m'}(\omega)$ = spherical harmonics
$\phi_m^{(0)}$ = dimensionless zeroth moments
$\phi_m^{(1)}$ = dimensionless first moments
φ = scaling function
γ = line half-width
λ = spectral variable, wavelength
λ_c = dimensionless wavelength, $\lambda_c = \lambda/\lambda_M$
λ_M = a maximum wavelength
κ_λ = absorption coefficient
Θ = dimensionless temperature $T/T_{w,1}$
ω = solid angle
ψ = wavelet
η = wavenumber, $\eta = 1/\lambda$
ν = spectral variable, frequency
$\bar{\nu}$ = dimensionless frequency $h\nu/kT_{w,1}$
$\bar{\nu}_{co}$ = dimensionless cutoff frequency for box model A and B
τ_o = optical thickness, $\tau_o = \kappa_\lambda D$

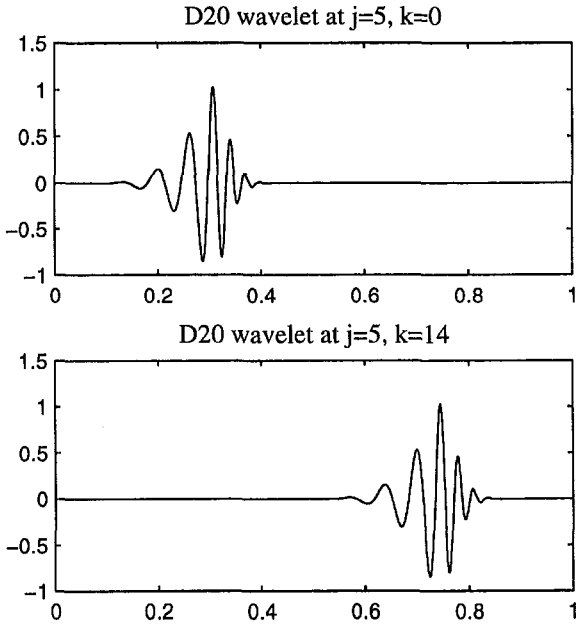

Fig. 2 Wrapped-around Daubechies' wavelets at level $j = 5$, $k = 0$ and 14

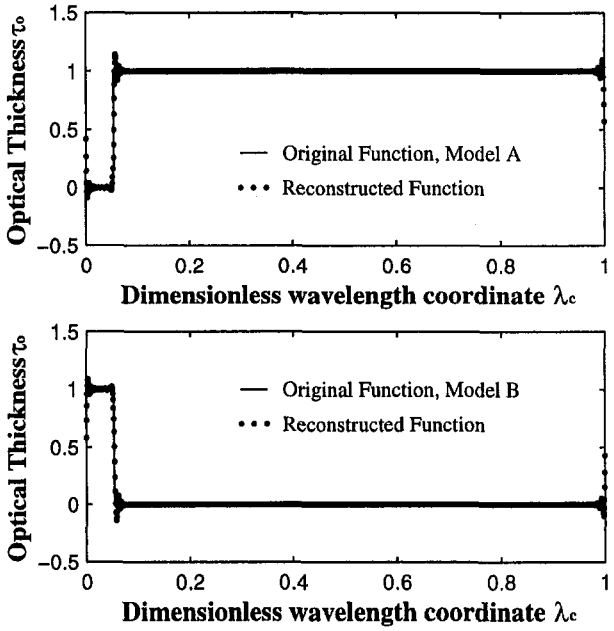

Fig. 4 Reconstruction of the box model absorption coefficient functions

In the double summation in Eq. (9), $2^j + k$ goes from 1 to $2^{J+1} - 1$. Defining $N \equiv 2^{J+1}$, Eq. (9) can be rewritten as

$$\tilde{I}_{\lambda_c} = b_0(\tilde{x}, \omega) + \sum_{m=1}^{N-1} b_m(\tilde{x}, \omega) W_m. \quad (10)$$

When this approximate solution is substituted into Eq. (7), there is a residual that depends on $\tilde{x}$, ω, and λ_c which is

$$\sum_{i=1}^{3} l_i \frac{\partial \tilde{I}_{\lambda_c}}{\partial x_i} + \kappa_{\lambda_c} \tilde{I}_{\lambda_c} - \kappa_{\lambda_c} I_{b,\lambda_c} = \text{Res}\ (\lambda_c, \tilde{x}, \omega). \quad (11)$$

Variational principles are applied to minimize the residual. A set of independent weighting functions are applied, and the residual is made orthogonal with respect to each of the weighting functions. According to the Galerkin finite element method, the weighting functions are chosen to be the same functions as the wavelet bases. This provides the following integrals, which are evaluated for each of the independent wavelet bases.

$$\int_0^1 \text{Res}\ (\lambda_c, \tilde{x}, \omega) d\lambda_c = 0 \quad m = 0 \quad (12a)$$

$$\int_0^1 \text{Res}\ (\lambda_c, \tilde{x}, \omega) W_m d\lambda_c = 0 \quad m = 1, N-1 \quad (12b)$$

Here unity can be treated as the zeroth wavelet basis. Equation (12) provides a system of equations for each of the wavelet basis functions as

$$\int_0^1 \left[\sum_{i=1}^{3} l_i \frac{\partial \tilde{I}_{\lambda_c}}{\partial x_i} + \kappa_{\lambda_c} \tilde{I}_{\lambda_c} - \kappa_{\lambda_c} I_{b,\lambda_c} \right] d\lambda_c = 0 \quad m = 0 \quad (13a)$$

$$\int_0^1 \left[\sum_{i=1}^{3} l_i \frac{\partial \tilde{I}_{\lambda_c}}{\partial x_i} + \kappa_{\lambda_c} \tilde{I}_{\lambda_c} - \kappa_{\lambda_c} I_{b,\lambda_c} \right] W_m d\lambda_c = 0$$

$$m = 1, N-1. \quad (13b)$$

Equation (13) provides N simultaneous equations for N coefficients of b_m,

$$\sum_{i=1}^{3} l_i \frac{\partial b_0}{\partial x_i} = I_0 - b_0 a_0 - \sum_{m'=1}^{N-1} b_{m'} a_{m'} \quad m = 0 \quad (14a)$$

$$\sum_{i=1}^{3} l_i \frac{\partial b_m}{\partial x_i} = I_m - b_0 a_m - \sum_{m'=1}^{N-1} b_{m'} c_{m,m'} \quad m = 1, N-1, \quad (14b)$$

where

$$I_0 = \int_0^1 \lambda_{\lambda_c} I_{b,\lambda_c} d\lambda_c \quad I_m = \int_0^1 \kappa_{\lambda_c} I_{b,\lambda_c} W_m d\lambda_c \quad (15a)$$

$$a_0 = \int_0^1 \kappa_{\lambda_c} d\lambda_c \quad a_m = \int_0^1 \kappa_{\lambda_c} W_m d\lambda_c \quad (15b)$$

$$c_{m,m'} = \int_0^1 \kappa_{\lambda_c} W_m W_{m'} d\lambda_c \quad \text{with} \quad m, m' = 1, N-1. \quad (15c)$$

For a nominal temperature, Eq. (15) can be calculated by the discrete wavelet transform or numerical quadrature. Equation

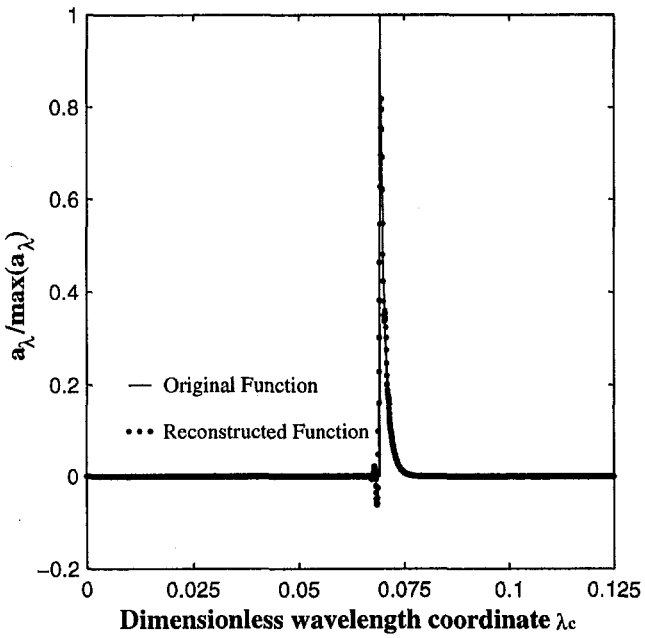

Fig. 3 Reconstruction of the normalized absorption coefficient function

(14) can be solved with the coupled energy equation and boundary conditions by using any solution method developed for gray media. In this work we choose to demonstrate the solution of the nongray radiative transfer equation using the one-dimensional P-N approximation.

Numerical Solution for a One-Dimensional Radiative Equilibrium Medium

The physical system under consideration consists of an absorbing, emitting, and nonscattering medium bounded by two infinite parallel black plates. The medium has a refractive index of unity ($n = 1$). The plate at $x = 0$ is maintained at temperature $T_{w,1}$, and the plate at $x = D$ is maintained at temperature $T_{w,2}$, where $T_{w,1}$ is larger than $T_{w,2}$.

In order to solve Eq. (14) the coefficients $b_m (m = 0, N - 1)$ are expanded in terms of normalized spherical harmonics, $Y_l^{m'}(\omega)$, as

$$b_m = \sum_{l=0}^{\infty} \sum_{m'=-l}^{l} A_{ml}^{m'}(S) Y_l^{m'}(\omega) \quad m = 0, N-1, \tag{16}$$

where the spherical harmonics themselves are expanded in terms of the associated Legendre polynomials of the first kind. For the P-1 approximation only the $l = 0$ and 1 terms are retained.

The moments of the wavelet basis coefficient b_m are

$$b_m^{(0)} = \int_{\omega=0}^{4\pi} b_m d\omega \tag{17a}$$

$$b_m^{(i)} = \int_{\omega=0}^{4\pi} l_i b_m d\omega \quad i = 1, 2, 3 \tag{17b}$$

$$b_m^{(ij)} = \int_{\omega=0}^{4\pi} l_i l_j b_m d\omega \quad i, j = 1, 2, 3 \quad m = 0, N-1, \tag{17c}$$

resulting in

$$b_m = \frac{1}{4\pi} (b_m^{(0)} + 3b_m^{(1)} \cos\theta + 3b_m^{(2)} \sin\theta \cos\phi + 3b_m^{(3)} \sin\theta \sin\phi). \tag{18}$$

The closure condition is

$$b_m^{(ij)} = \tfrac{1}{3}\delta_{ij} b_m^{(0)} \quad i, j = 1, 2, 3 \quad m = 0, N-1. \tag{19}$$

Equation (14) is multiplied by powers of the direction cosines individually and in combination, and the resulting equations are integrated over all solid angles to give

$$\sum_{i=1}^{3} \frac{\partial b_0^{(i)}}{\partial x_i} = 4\pi I_0 - b_0^{(0)} a_0 - \sum_{m'=1}^{N-1} b_{m'}^{(0)} a_{m'} \tag{20a}$$

$$\sum_{i=1}^{3} \frac{\partial b_0^{(ij)}}{\partial x_i} = -\left[b_0^{(j)} a_0 + \sum_{m'=1}^{N-1} b_{m'}^{(j)} a_{m'} \right] \quad j = 1, 2, 3 \tag{20b}$$

$$b_0^{(ij)} = \tfrac{1}{3}\delta_{ij} b_0^{(0)} \quad j = 1, 2, 3 \tag{20c}$$

$$\sum_{i=1}^{3} \frac{\partial b_m^{(i)}}{\partial x_i} = 4\pi I_m - b_0^{(0)} a_m - \sum_{m'=1}^{N-1} b_{m'}^{(0)} c_{m,m'} \tag{20d}$$

$$\sum_{i=1}^{3} \frac{\partial b_m^{(ij)}}{\partial x_i} = -\left[b_0^{(j)} a_m + \sum_{m'=1}^{N-1} b_{m'}^{(j)} c_{m,m'} \right] \quad j = 1, 2, 3 \tag{20e}$$

$$b_m^{(ij)} = \tfrac{1}{3}\delta_{ij} b_m^{(0)} \quad j = 1, 2, 3 \quad m = 1, N-1. \tag{20f}$$

For a one-dimensional medium between parallel plates whose temperatures are at $T_{w,1}$ and $T_{w,2}$, Eq. (20) becomes

$$\frac{db_0^{(1)}}{dx} = 4\pi I_0 - b_0^{(0)} a_0 - \sum_{m'=1}^{N-1} b_{m'}^{(0)} a_{m'} \tag{21a}$$

$$\frac{db_0^{(0)}}{dx} = -3\left[b_0^{(1)} a_0 + \sum_{m'=1}^{N-1} b_{m'}^{(1)} a_{m'} \right] \tag{21b}$$

$$\frac{db_m^{(1)}}{dx} = 4\pi I_m - b_0^{(0)} a_m - \sum_{m'=1}^{N-1} b_{m'}^{(0)} c_{m,m'} \tag{21c}$$

$$\frac{db_m^{(0)}}{dx} = -3\left[b_0^{(1)} a_m + \sum_{m'=1}^{N-1} b_{m'}^{(1)} c_{m,m'} \right] \quad m = 1, N-1. \tag{21d}$$

Equation (18) becomes

$$b_m = \frac{1}{4\pi} (b_m^{(0)} + 3b_m^{(1)} \cos\theta) \quad m = 0, N-1. \tag{22}$$

Marshak's (1947) boundary condition is applied for a one-dimensional black wall problem and yields

$$\int_0^{2\pi} \cos\theta \tilde{I}_{\lambda_c} d\omega = \int_0^{2\pi} \cos\theta I_{b,\lambda_c} d\omega. \tag{23}$$

The intensity of radiation for the P-1 approximation in terms of wavelets becomes

$$\tilde{I}_{\lambda_c} = \frac{1}{4\pi} [b_0^{(0)} + 3b_0^{(1)} \cos\theta] + \sum_{m=1}^{N-1} \left\{ \frac{1}{4\pi} [b_m^{(0)} + 3b_m^{(1)} \cos\theta] \right\} W_m. \tag{24}$$

Substituting Eq. (24) into Eq. (23), multiplying each of the independent wavelet bases, and integrating Eq. (23) in the wavelength domain provides the sufficient boundary condition for $b_m^{(0)}$ and $b_m^{(1)}$ given below.

$$\frac{b_0^{(0)}}{2} + b_0^{(1)} = 2\pi \int_0^1 I_{b,\lambda_c}(T_{w,1}) d\lambda_c \quad \text{at} \quad x = 0 \quad \text{for} \quad m = 0 \tag{25a}$$

$$\left(\frac{b_m^{(0)}}{2} + b_m^{(1)} \right) = 2\pi \int_0^1 W_m I_{b,\lambda_c}(T_{w,1}) d\lambda_c \quad \text{at} \quad x = 0 \quad \text{for} \quad m = 1, N-1 \tag{25b}$$

$$\frac{b_0^{(0)}}{2} - b_0^{(1)} = 2\pi \int_0^1 I_{b,\lambda_c}(T_{w,2}) d\lambda_c \quad \text{at} \quad x = D \quad \text{for} \quad m = 0 \tag{26a}$$

$$\left(\frac{b_m^{(0)}}{2} - b_m^{(1)} \right) = 2\pi \int_0^1 W_m I_{b,\lambda_c}(T_{w,2}) d\lambda_c \quad \text{at} \quad x = D \quad \text{for} \quad m = 1, N-1. \tag{26b}$$

The energy equation representing the radiative equilibrium is

$$\nabla \cdot q_r = 0. \tag{27}$$

For a one-dimensional system, introducing the radiative heat flux term

$$q_r = \hat{i} \int_{\omega=0}^{4\pi} I \cos\theta d\omega = \hat{i} \int_{\omega=0}^{4\pi} \int_0^1 \tilde{I}_{\lambda_c} \lambda_M d\lambda_c \cos\theta d\omega = \hat{i} \int_{\omega=0}^{4\pi} \frac{\lambda_M}{4\pi} [b_0^{(0)} + 3b_0^{(1)} \cos\theta] \cos\theta d\omega = \hat{i} b_0^{(1)} \lambda_M \tag{28}$$

gives

$$\lambda_M = \frac{db_0^{(1)}}{dx} = 0. \tag{29}$$

For convenience, the governing equations and the boundary conditions of this application are scaled with λ_M. The dimensionless moments and coordinate are defined as follows:

$$b_0^{(0)} = \left(\frac{E_1 - E_2}{\lambda_M}\right)\phi_0^{(0)} + \frac{4E_2}{\lambda_M} \quad \text{for} \quad m = 0 \tag{30a}$$

$$b_m^{(0)} = \left(\frac{E_1 - E_2}{\lambda_M}\right)\phi_m^{(0)} \quad \text{for} \quad m = 1, N-1 \tag{30b}$$

$$b_m^{(1)} = \left(\frac{E_1 - E_2}{\lambda_M}\right)\phi_m^{(1)} \quad \text{for} \quad m = 0, N-1 \tag{30c}$$

$$x^* = \frac{x}{D}, \tag{30d}$$

where $E_1 = \sigma T_{w,1}^4$ and $E_2 = \sigma T_{w,2}^4$. The scaled moment equations are as follows:

$$\frac{d\phi_0^{(1)}}{dx^*} = 4\pi F_0 - \phi_0^{(0)} A_0 - \sum_{m'=1}^{N-1} \phi_{m'}^{(0)} A_{m'} \tag{31a}$$

$$\frac{d\phi_0^{(0)}}{dx^*} = -3\left[\phi_0^{(1)} A_0 + \sum_{m'=1}^{N-1} \phi_{m'}^{(1)} A_{m'}\right] \tag{31b}$$

$$\frac{d\phi_m^{(1)}}{dx^*} = 4\pi F_m - \phi_0^{(0)} A_m - \sum_{m'=1}^{N-1} \phi_{m'}^{(0)} C_{m,m'} \tag{31c}$$

$$\frac{d\phi_m^{(0)}}{dx^*} = -3\left[\phi_0^{(1)} A_m + \sum_{m'=1}^{N-1} \phi_{m'}^{(1)} C_{m,m'}\right] \quad m = 1, N-1, \tag{31d}$$

where

$$A_0 = \int_0^1 D\kappa_{\lambda_c} d\lambda_c \tag{32a}$$

$$A_m = \int_0^1 D\kappa_{\lambda_c} W_m d\lambda_c \quad m = 1, N-1 \tag{32b}$$

$$F_0 = \int_0^1 \frac{(I_{b,\lambda_c}\lambda_M - E_2/\pi) D\kappa_{\lambda_c}}{E_1 - E_2} d\lambda_c \tag{32c}$$

$$F_m = \int_0^1 \frac{(I_{b,\lambda_c}\lambda_M - E_2/\pi) D\kappa_{\lambda_c} W_m}{E_1 - E_2} d\lambda_c \quad m = 1, N-1 \tag{32d}$$

$$C_{m,m'} = \int_0^1 D\kappa_{\lambda_c} W_m W_{m'} d\lambda_c \quad m, m' = 1, N-1 \tag{32e}$$

Table 1 Comparison of the dimensionless heat flux ($q/\sigma T_{w,2}^4$) for the two typical cases

	Case 1	Case 2
Chan and Tien (1971)	195.029	189.481
Yuen and Rasky (1981)	194.1	189.2
Wavelet method	194.1961	179.4396

Case 1: $T_{w,1}$=1500K,$T_{w,2}$=400K, P_{CO_2}=0.2atm,P_{N_2}=10atm, D=1 cm
Case 2: $T_{w,1}$=1500K,$T_{w,2}$=400K, P_{CO_2}=1.0atm,P_{N_2}=0, D=10 cm

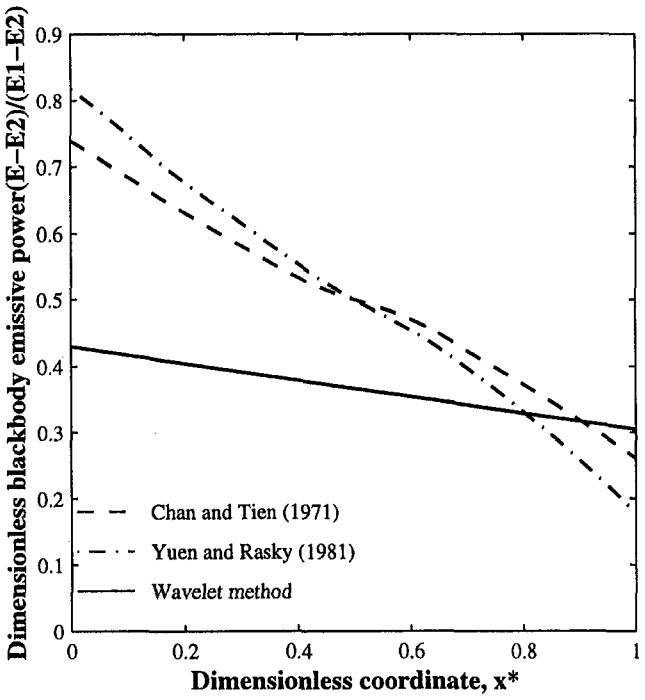

Fig. 5 Dimensionless blackbody emissive power distribution, $(E - E_2)/(E_1 - E_2)$ versus dimensionless coordinate x^*, Case 1

and the boundary conditions become

$$\frac{\phi_0^{(0)}}{2} + \phi_0^{(1)} = 2 \quad \text{at} \quad x^* = 0 \quad \text{for} \quad m = 0 \tag{33a}$$

$$\left(\frac{\phi_m^{(0)}}{2} + \phi_m^{(1)}\right) = 2\pi \int_0^1 \frac{I_{b,\lambda_c}(T_{w,1})\lambda_M W_m}{E_1 - E_2} d\lambda_c$$

$$\text{at} \quad x^* = 0 \quad \text{for} \quad m = 1, N-1 \tag{33b}$$

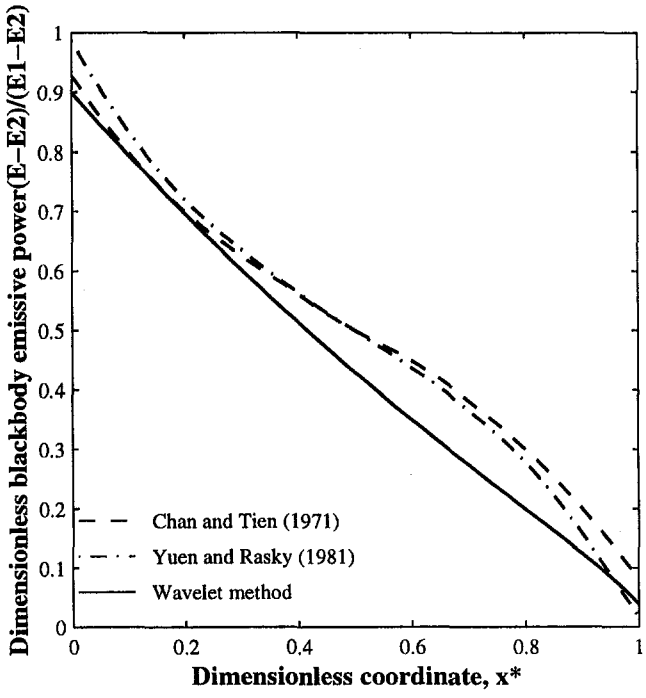

Fig. 6 Dimensionless blackbody emissive power distribution, $(E - E_2)/(E_1 - E_2)$ versus dimensionless coordinate x^*, Case 2

$$\frac{\phi_0^{(0)}}{2} - \phi_0^{(1)} = 0 \quad \text{at} \quad x^* = 1 \quad \text{for} \quad m = 0 \qquad (33c)$$

$$\left(\frac{\phi_m^{(0)}}{2} - \phi_m^{(1)}\right) = 2\pi \int_0^1 \frac{I_{b,\lambda_c}(T_{w,2})\lambda_M W_m}{E_1 - E_2}\, d\lambda_c$$

$$\text{at} \quad x^* = 1 \quad \text{for} \quad m = 1, N-1. \qquad (33d)$$

Finally, the energy equation is written as

$$\frac{d\phi_0^{(1)}}{dx^*} = 0. \qquad (34)$$

The modified quasi-linearization method, which is formulated by Miele and Iyer (1970) and used by Yucel and Bayazitoglu (1982) in solving radiation problems, is used to solve Eqs. (31)–(34).

Results and Conclusions

We assumed that for a nongray problem, the absorption coefficient is

$$\kappa_\eta = \left(\frac{\rho S}{d}\right) \frac{\sinh(2\pi\gamma/d)}{\cosh(2\pi\gamma/d) - 1}, \qquad (35)$$

which is given by Yuen and Rasky (1981), where ρ is the gas density, S/d is the mean-line-intensity-to-spacing ratio, and γ/d is the line-width-to-spacing ratio for the considered narrow band. Over a wide band, Edwards (1976) showed that S/d is a exponential function of wave number and γ/d is a function of temperature and pressure, and gave us several convenient tables for the parameters. This is the reason that this model has been selected. However, wavelet functions are the bases for the L^2 function space (square-integrable function space). Any absorption coefficient model, as long as it is square-integrable, can be used in this analysis. One drawback of Edwards' model in the current analysis is that the numerical integrals that involve exponential functions are relatively expensive to compute.

To demonstrate quantitatively the effectiveness and the accuracy of the wavelet method, solutions with CO_2 as the absorbing medium are now generated. Only one absorption band, the 4.3 μm band of CO_2, is used so that the results can be compared with references. Assuming that $T_{w,1} = 1500$K and $T_{w,2} = 400$K, λ_M is chosen according to the temperatures of the black walls. Computing the model on a sparcstation/20 machine took about 13,000 seconds of CPU time. Each case began with a linear initial temperature profile. The heat flux calculated from the present method for two specific cases and those obtained from other techniques by Chan and Tien (1971) and Yuen and Rasky (1981) are compared in Table 1. The blackbody emissive power distributions are illustrated in Figs. 5 and 6. In case 1 the heat flux matches the previous results, but the emissive power distributions have large differences. In case 2 the heat flux is lower than previous results, but the emissive power distributions are more closely matched. Yucel and Bayazitoglu (1982) pointed out that P-1 approximation has been shown to give satisfactory results for a one-dimensional optically thick medium. Therefore the results of case 2 are more convincing.

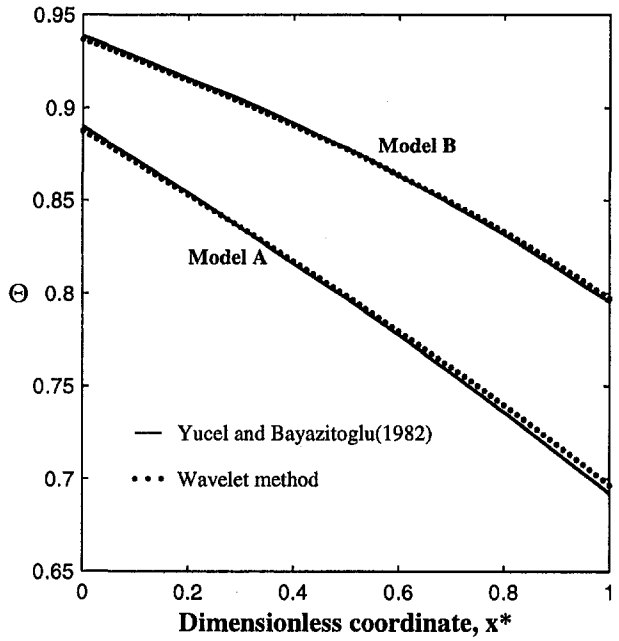

Fig. 7 Dimensionless temperature distributions for box model A and B

Table 2 Comparison of the dimensionless heat flux $Q_R = q/\sigma T_{w,1}^4$ for rectangular absorption coefficient model

	Model A	Model B
Yucel and Bayazitoglu (1982)	0.7921	0.6811
Wavelet Method	0.7894	0.6789

For Model A and B: $\bar{\nu}_{co} = 3$, $\tau_o = 1$, $\Theta_2 = 0.5$

We have to realize that in the first paper Chan and Tien (1971) used the isothermal band absorptance to evaluate the nonisothermal band absorptance by way of the wide-band Curtis-Godson method. The unknown dimensionless temperature profile is approximated by an nth degree polynomial. They also pointed out that an antisymmetric temperature distribution can be achieved by simplifying the total radiative heat flux formula with only one isothermal absorption band. Otherwise only the gray medium case has the same feature. However, this is not true when the temperature dependence of radiation properties is taken into consideration. In the second paper, Yuen and Rasky (1981) assumed that the zeroth moment of the radiative intensity is a third order polynomial in the spatial domain. This resulted in the simplification of the governing equations of the P-1 approximation, where the absorption coefficient was evaluated at the average temperature. The wavelet method allows the radiative problems to be calculated with fewer assumptions than required for the other methods shown. Therefore, the variation of the current results from previous, more approximate results, is not surprising.

The wavelet method is easily extensible to the multiband absorption coefficient model. The procedure is the same, although additional computer time is needed to calculate the integral of the individual bands in Eq. (32). Note that this could be quite involved using previous methods. For a line-by-line absorption coefficient model, wavelets can be used inside each narrow band. As for multidimensional problems, a partial differential equation solver for the first-order system is needed. The energy equation will be more complicated, but the modified quasi-linearization method is still applicable. Therefore, we conclude that the usage of wavelet basis functions in nongray, nonisothermal radiation problems is promising.

Numerical Error Analysis

Error analysis will be focused on the truncation of the wavelet series approximation. Three different levels of wavelet series are chosen: 64, 128, and 256. Numbers must be the power of 2. The results shown are computed using 256 wavelet terms. The heat flux differences are 0.43 percent and 0.091 percent (256 versus 64 and 128). The maximum temperature differences are 12.5 percent and 2.3 percent. It should be noticed that

when the absorption coefficient is a constant, Eqs. 21(a) and (b) with boundary conditions Eqs. 25(a) and 26(a) will recover the exact equations of the P-1 approximation for a gray problem. Therefore, we expect the same results by the current method as by the analytical P-1 method for the gray problem. The results from the trial calculations indeed show this identity. To further show the accuracy of current method, comparison with the box model absorption coefficients plus P-1 method by Yucel and Bayazitoglu (1982) is also carried out. Figure 4 shows the box model absorption coefficients. The cutoff frequency (the discontinuous points in the dimensionless wavelength domain) is $\bar{\nu}_{co} = 3$. The dimensionless temperature distribution and heat flux results shown in Fig. 7 and Table 2 match the analytical P-1 results very well in both model A and B.

Acknowledgments

This material is based in part, upon the work supported by the Texas Advanced Technology Program under Grants No. 003604-027, -041 and National Science Foundation Grant No. CTS 9312379.

References

Chan, S. H., and Tien, C. L., 1971, "Infrared Radiative Heat Transfer in Non-Gray Non-Isothermal Gases," *International Journal of Heat and Mass Transfer,* Vol. 14, pp. 19–26.

Crosbie, A. L., and Viskanta, R., 1970, "Nongray Radiative Transfer in a Planar Medium Exposed to a Collimated Flux," *Journal Quantitative Spectroscopy Radiation Transfer,* Vol. 10, pp. 465–485.

Daubechies, I., 1992, *Ten Lectures on Wavelets,* SIAM, Philadelphia, PA.

Donoho, D. L., 1993, "Unconditional Bases Are Optimal Bases for Data Compression and for Statistical Estimation," *Applied and Computational Harmonic Analysis,* Vol. 1 No. 1, pp. 100–115.

Dwight, H. B., 1961, *Tables of Integrals and Other Mathematical Data,* 4th ed., The Macmillan Company, New York.

Edwards, D. K., 1976, "Molecular Gas Band Radiation," *Advances in Heat Transfer,* Vol. 12, Academic Press, New York, pp. 116–195.

Haar, A., 1910, "Zur Theorie der orthogonalen Funktionen-Systeme," *Math. Ann.,* Vol. 69, pp. 331–371.

Hottel, H. C., and Sarofim, A. F., 1967, *Radiative Transfer,* McGraw-Hill, New York.

Kaminski, D. A., and Moder, J. P., 1989, "A Nongray P-N Approximation for Radiative Transfer," *National Heat Transfer Conference,* HTD-Vol. 106, pp. 27–34.

Mallat, S., 1989, "A Theory for Multiresolution Signal Recomposition: The Wavelet Representation," *IEEE Trans. Pattern Anal. and Machine Intell.,* Vol. 11, pp. 674–693.

Marshak, R. E., 1947, "Note on the Spherical Harmonics Methods as Applied to the Milne Problem for a Sphere," *Phys. Rev.,* Vol. 71, pp. 443–446.

Miele, A., and Iyer, R. R., 1970, "General Technique for Solving Non-linear, Two-Point Boundary-Value Problems via the Method of Particular Solutions," *Optimization Theory and Applications,* Vol. 5, pp. 382–399.

Modest, M. F., 1991, "The Weighted-Sum-Gray-Gases Model for Arbitrary Solution Methods in Radiative Transfer," ASME JOURNAL OF HEAT TRANSFER, Vol. 113, No. 3, pp. 650–656.

Modest, M. F., and Sikka, K. K., 1992, "The Stepwise-Gray P-1 Approximation for Multi-Dimensional Radiative Transfer in Molecular-Gas-Particulate Mixtures," *Journal of Quantitative Spectroscopy Radiation Transfer,* Vol. 48, No. 2, pp. 159–168.

Newland, D. E., 1993, *An Introduction to Random Vibrations, Spectral & Wavelet Analysis,* John Wiley & Sons, Inc., New York.

Tiwari, S. N., 1977, "Applications of Infrared Band Model Correlation to Non-Gray Radiation," *International Journal of Heat and Mass Transfer,* Vol. 20, pp. 741–751.

Yucel, A., and Bayazitoglu, Y., 1982, "P-N Approximation for Radiative Transfer in a Nongray Planar Medium," *AIAA Journal,* Vol. 21 No. 8, pp. 1196–1203.

Yuen, W. W., and Rasky, D. J., 1981, "Application of the P-1 Approximation to Radiative Heat Transfer in a Nongray Medium," ASME JOURNAL OF HEAT TRANSFER, Vol. 103, pp. 182–184.

Flow Boiling in Horizontal Tubes: Part 1—Development of a Diabatic Two-Phase Flow Pattern Map

N. Kattan

J. R. Thome
favrat@it.dgm.epfl.ch

D. Favrat

Laboratory for Industrial Energy Systems,
Department of Mechanical Engineering,
Swiss Federal Institute of Technology,
CH-1015 Lausanne, Switzerland

An improved two-phase flow pattern map is proposed for evaporation in horizontal tubes. The new map was developed based on flow pattern data for five different refrigerants covering a wide range of mass velocities and vapor qualities. The new map is valid for both adiabatic and diabatic (evaporating) flows and accurately identifies about 96 percent of the 702 data points. In addition, the new flow pattern map includes the prediction of the onset of dryout at the top of the tube during evaporation inside horizontal tubes as a function of heat flux and flow parameters.

1 Introduction

Numerous flow pattern maps have been developed for horizontal, adiabatic two-phase flows in tubes: Taitel and Dukler (1976), Hashizume (1983), and Steiner (1993), just to name a few. For flow boiling, a diabatic flow pattern map that includes the effects of heat flux, dryout, etc. on the flow pattern boundaries is desirable. Figure 1 from Collier and Thome (1994), depicts the typical flow patterns observed during evaporation inside a horizontal tube, including cross-sectional views of the flows. Depending on the operating conditions and fluid, only several of these flow patterns may be encountered from inlet to outlet of an evaporator tube. For a recent survey of flow pattern research, refer to Collier and Thome (1994).

The objective of the present study was to develop an accurate flow pattern map for refrigerants under evaporating conditions as the first step in the development of a new flow boiling model for horizontal tubes based on local flow pattern. Consequently, flow pattern data were obtained with observations directly at the exit of evaporator tube test sections with simultaneous measurement of heat transfer coefficients. A second objective was to investigate the flow stratification problem in horizontal flow boiling—in particular, the threshold for the formation of dry zones at the top of the tube periphery as the flow rate is decreased and also at high vapor qualities where dryout of the annular film occurs, both of which have a significant adverse effect on flow boiling heat transfer.

In order to develop a flow pattern database, a comprehensive test program was undertaken covering four new refrigerants (R134a, R-123, R-402A, and R-404A) and one old refrigerant (R-502). R-134a and R-123 are both single-component refrigerants, while R-402A and R-404A are each three-component, zeotropic refrigerant blends that are "near-azeotropes." R-502 is a binary azeotropic mixture of two refrigerants whose use has since been prohibited by the Montreal protocol and subsequent amendments.

Some of the flow pattern data presented here have previously been compared to flow pattern maps in Kattan et al. (1995b). The Taitel and Dukler and the Hashizume flow pattern maps yielded rather poor results. The Steiner (1993) flow pattern map, developed using R-12 and R-22 data, is a modified Taitel and Dukler map and compared quite favorably with the present flow pattern data but demonstrated several crucial weak points that will be discussed later. Based on these results, the Steiner map was selected for modification to improve accuracy and to incorporate diabatic effects of flow boiling on two-phase flow patterns.

2 Test Facility and Flow Pattern Observations

A detailed description of the test facility is presented in Part 2. For complete details of test procedures and data reduction methods refer to Kattan et al. (1995a) or Kattan (1996).

The sight glasses used in the study were 12.0 mm bore with a 100 mm length, mounted inline to the inlet and outlet of the two horizontal experimental evaporator tube test sections that were made of 3 m long and 12.0 mm diameter copper tubes. The transition between the copper tubes and sight glasses was also 12 mm in diameter with a short and smooth transition length. The present flow pattern data only refer to flows observed and videotaped at the exit of the two evaporator test sections. The sight glasses are not heated but the flow patterns observed are those leaving the evaporator test sections and thus can be considered to be diabatic flow pattern data, which are desired for development of a flow boiling heat transfer model based on flow pattern. Flow boiling heat transfer coefficients were measured simultaneously in the evaporation test sections to have a comprehensive heat transfer and flow pattern database for analysis (Part 2).

The flow patterns were recorded using a high quality video system. In addition, direct visual observations with written notes were taken in some cases. The videos could be viewed both on the videotape system and on the high-resolution monitor of a PC using a video card. The video system allowed slow-motion viewing of the flow patterns.

The flow patterns observed were classified as follows: stratified flow (S), stratified-wavy flow (SW), intermittent flow (I), annular flow (A), mist flow (MF), and transitions between these regimes. For instance, the transition between intermittent flow and annular flow was designated as "I/A." Flow rates were not low enough to detect stratified flows for the database, but several transition data points were obtained between stratified and stratified-wavy flow at low vapor quality (S/SW). In addition, bubbly flows and mist flows occur at mass velocities above the present evaporator test conditions. Intermittent flow is also referred to as slug flow (it is essentially a stratified-wavy flow pattern with large amplitude waves that wash the top of the tube). For a detailed definition of the flow patterns used here, refer to Collier and Thome (1994). The videos were also

Contributed by the Heat Transfer Division for publication in the JOURNAL OF HEAT TRANSFER. Manuscript received by the Heat Transfer Division October 1, 1996; revision received July 16, 1997; Keywords: Evaporation; Flow Visualization; Multiphase Flows. Associate Technical Editor: M. D. Kelleher.

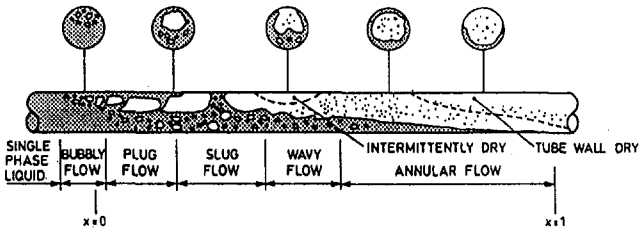

Fig. 1 Two-phase flow patterns in a horizontal evaporator tube from Collier and Thome (1994)

Table 1 Two-phase flow data compared to the new flow pattern map

Fluid	Tsat	Psat	G	x	q	Total	Points correct	% Correct
	°C	Bar	kg/s.m^2	%	kW/m^2	Points	(new map)	
R134a	10.3	4.19	100-500	4...90	3.20...36.54	106	100	94.3%
R134a	4.44	3.42	100-400	18...100	0.44...22.58	101	97	96.0%
R134a	2.0	3.14	300-500	5...57	7.83...25.58	60	60	100.0%
R134a	-1.3	2.79	100-300	12...82	4.62...18.91	32	29	90.6%
R402A	10.2	8.88	303	11...88	4.24...26.60	34	33	97.1%
R402A	2.4	7.05	100-318	9...91	3.36...22.18	94	88	93.6%
R402A	-1.3	6.30	317	13...63	5.7...20.84	24	24	100.0%
R404A	10.2	8.36	300	7...98	6.29...30.57	34	34	100.0%
R404A	2.4	6.61	100-318	7...92	3.42...30.55	95	90	94.7%
R404A	-1.3	5.89	320	12...63	7.78...21.78	24	24	100.0%
R502	2.5	6.19	100-300	8...97	3.29...27.72	60	60	100.0%
R123	30.7	1.12	100-300	7...98	3.7...24.65	38	36	94.7%
Total Points correct :						702	675	96.2%

viewed to determine whether or not the total circumference of the tube wall was all wet or not. For example, in Fig. 1 several cross-sectional views depict partially dry portions of the tube circumference. With respect to this, annular flow with partial dryout as depicted in Fig. 1 has been classified as stratified-wavy flow in order to conform to the Steiner flow pattern map definitions.

Particular care has been devoted to flow regimes occurring at high vapor quality, i.e., from 50 percent up to 100 percent (all vapor), to investigate dryout effects. The left side of Table 1 depicts the test conditions covered for each refrigerant.

3 New Flow Pattern Map

3.1 A New Graphical Representation of the Steiner Map. Figure 2 depicts the Steiner flow pattern map with some R134a test data. The data are identified as defined in section 2. F, T, and K in Fig. 2 are Taitel-Dukler (1976) parameters defined in numerous textbooks, such as Collier and Thome (1994).

To better identify flow patterns during the evaporation process at different mass velocities and to make the map a more

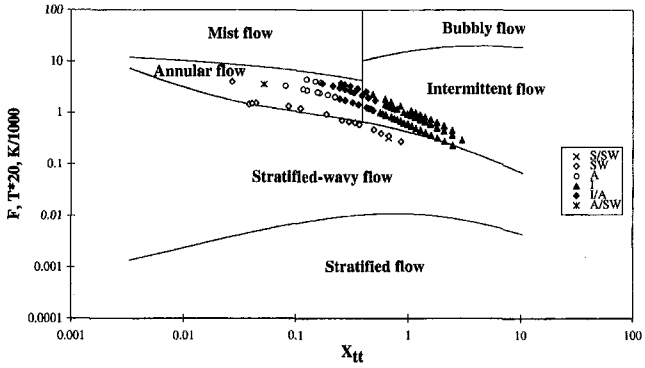

Fig. 2 R134a data compared to the Steiner map at 10.3°C and G = 100–500 kg/(s.m^2)

useful research and design tool, the axes of the Steiner flow pattern map have been converted to mass velocity G versus vapor quality x (similar to how local flow boiling coefficients are plotted, i.e., heat transfer coefficient versus vapor quality). For that purpose, the abscissa of the Steiner map, the Martinelli parameter, was converted into vapor quality using the thermodynamic and transport properties of the refrigerant at the saturation temperature. The three ordinate parameters of the Steiner map are a function of mass velocity, vapor quality, and thermodynamic and transport properties of the refrigerant at the saturation temperature. By equalizing the ordinate equations to the corresponding boundary curve equations, the mass velocity is extracted for each transition curve and plotted on the new form of graph versus the vapor quality.

Figures 3 and 4 show the transition curves of the transformed Steiner map for different refrigerants plotted at different saturation temperatures. With this new representation it is feasible to follow the change in flow pattern during the evaporation of a refrigerant at a fixed mass velocity. This is very useful for interpreting heat transfer data, typically plotted as heat transfer coefficient versus vapor quality, or for thermal design purposes, to avoid an undesired flow pattern such as stratified-wavy flow or mist flow.

3.2 Transition Curve Between Stratified-Wavy Flow and Annular Flow (Low Vapor Quality). Test results for R134a at saturation temperatures varying from −1.28°C to 10.33°C showed that the flow regime is always in stratified-wavy flow for a mass velocity fixed at G = 100 kg/(s.m^2). The Steiner flow pattern map in Fig. 3 has a transition from stratified-wavy to annular flow at about G = 100 kg/(s.m^2). Therefore, the transition curve between annular flow and stratified-wavy flow should be moved (with a translation move-

Nomenclature

A = cross-sectional area, m^2
b_{La} = Laplace constant $\{\sigma_L/[g(\rho_L - \rho_v)]\}^{0.5}$
D = tube internal diameter, m
g = acceleration of gravity, m/s^2
G = total mass velocity of liquid and vapor, kg/s m^2
h = liquid height, m
Δh_v = latent heat of vaporization, J/kg
P_{sat} = saturation pressure, Pa (or bar)
P_i = liquid-vapor interface, m
P_L = wetted perimeter, m
P_v = dry perimeter, m
q = heat flux, W/m^2
T_{sat} = saturation temperature, K (or °C)
x = vapor quality
X_{tt} = Martinelli parameter

Greek

μ = dynamic viscosity, N s/m^2
ξ = friction factor
ρ = density, kg/m^3
σ_L = surface tension, N/m
φ = inclination angle of the tube from horizontal, deg

Dimensionless Numbers

$F_1(q)$ = Nondimensional exponent
$F_2(q)$ = Nondimensional exponent
Fr_L = Froude number of liquid phase $[G^2/\rho_L^2 gD]$
Re_L = Reynolds number of liquid phase $[GD(1-x)/\mu_L]$
Re_v = Reynolds number of vapor phase $[GDx/\mu_v]$
We = Weber number $[G^2 D/\rho_L \sigma_L]$

Subscripts

crit = critical
d = dimensionless
L = liquid
sat = saturation
v = vapor

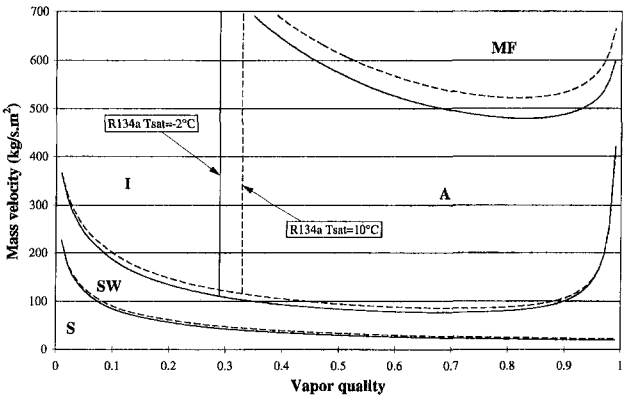

Fig. 3 The Steiner flow pattern map calculated for an inside tube diameter = 12 mm

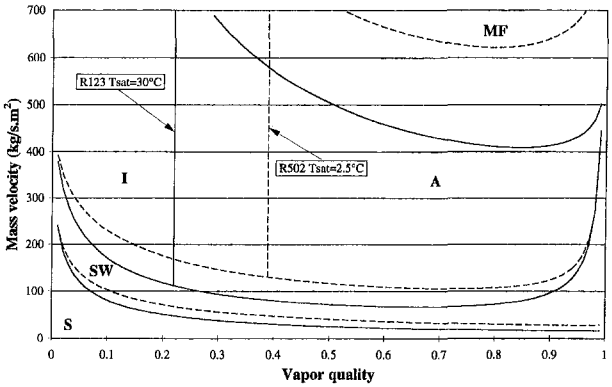

Fig. 4 The Steiner flow pattern map calculated for an inside tube diameter = 12 mm

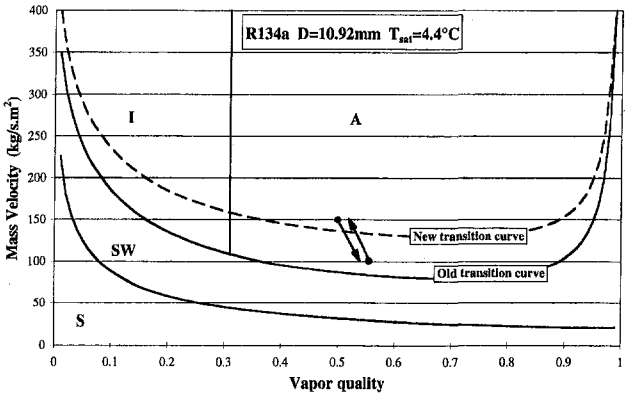

Fig. 5 The new transition curve between stratified-wavy flow and annular flow

ment) to a higher value to properly include these test data in the stratified-wavy region instead of the annular flow region. In addition, the test results showed that the transition from stratified-wavy to annular flow occurred at $G = 150$ kg/(s.m^2). To determine this transition threshold the mass velocity during some special tests was gradually varied from $G = 150$ kg/(s.m^2) to $G = 100$ kg/(s.m^2) at a vapor quality of about 50 percent. Flow patterns were observed at the outlet of the second test section to detect at which mass velocity the transition from annular flow to stratified-wavy flow occurred. Figure 5 shows the procedure used to find the new transition curve.

The tests were done in two directions, from annular to stratified-wavy flow and from stratified-wavy to annular flow, and

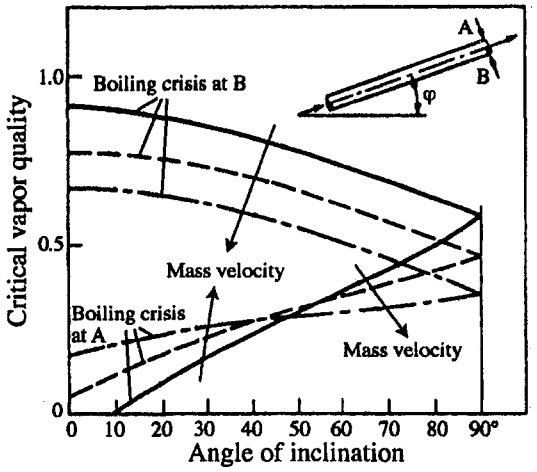

Fig. 6 Effect of the angle of inclination on the critical vapor quality (Auracher et al. (1993))

no hysteresis was detected. To fit these test data the new stratified-wavy boundary curve is moved up by adding a value of 50 kg/(s.m^2) to the previous curve obtained from the original Steiner map. The same test procedure should ideally be applied at other vapor qualities in order to confirm the offset value of 50 kg/(s.m^2) over the whole quality range.

3.3 Transition Curve Between Annular Flow and Annular Flow With Partial Dryout. Auracher et al. (1993) defined the critical vapor quality that corresponds to the boiling crisis in flow boiling as the point at which the liquid film disappears first at the top and then at the bottom of horizontal or inclined tubes. Figure 6, taken from their paper, shows that the boiling crisis in horizontal and inclined tubes is lower than in vertical tubes. In horizontal cases the crisis first occurs at the crest of the tube while the lower wall remains wetted, as can be seen in Fig. 1. The crisis differs from that in vertical tubes, in which the boiling crisis commences (at least ideally) all around the perimeter of the tube at one location. The higher the ratio of the force of gravity to the forces resulting from turbulent mixing, the greater the difference of behavior between flow in horizontal tubes compared to vertical tubes. Therefore, this ratio increases if the mass velocity is reduced or the tube diameter is increased.

To find the transition curve between annular flow and annular flow with partial dryout, test data results are plotted in Fig. 7 on the new representation of the Steiner map and compared with the Auracher et al. (1993) critical boiling method. Tests have been made with R134a at high vapor quality and a satura-

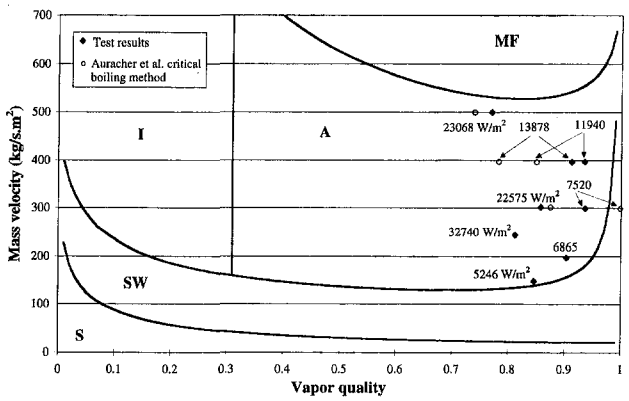

Fig. 7 Transition curve between annular flow and annular flow with partial dryout on the Steiner map (T_{sat} = 4.4°C, D = 10.92 mm)

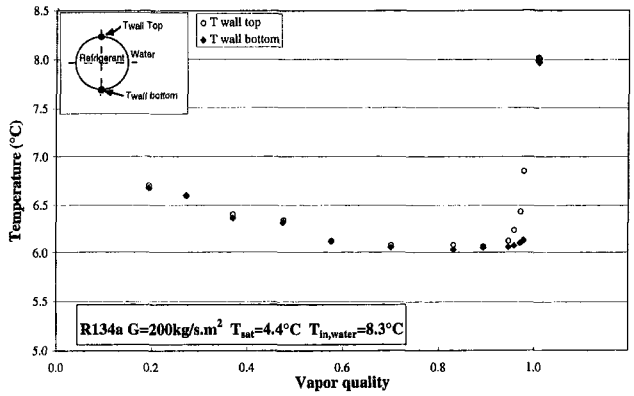

Fig. 8 Tube wall temperatures measured in annular flow with partial dryout

tion temperature of 4.4°C with thermocouples mounted in the test sections of zone 6 (see Part 2). The mass velocity was varied from 100 to 500 kg/(s.m^2), and the heat flux ranged between 5.2 and 33.0 kW/m^2. Test results are represented on this graph by solid diamond symbols. They indicate the vapor quality at which the thin liquid film in annular flow disappears at the crest of the tube but remains at the bottom of the tube until the end of the evaporation process (data are plotted for various heat fluxes and mass velocities). The circle symbols show results predicted by the Auracher et al. (1993) critical boiling method. This method seems unable to predict the critical vapor quality consistently because it was originally developed from water-steam data at much higher pressures, mass velocities, and heat fluxes than applicable for standard refrigeration applications.

The annular flow with partial dryout regime was observed by visualization through the sight glass tube and verified by measuring the tube wall temperatures with thermocouples (at the top and bottom at the end of the evaporator tube test section). Figure 8 shows the variation of the tube wall temperatures when varying the vapor quality. Annular flow with partial dryout is observed at about 90 percent vapor quality when the top and the bottom tube temperatures start to diverge. The two temperatures join again later when the refrigerant is completely vaporized and slightly superheated, i.e., $x > 1.0$.

Finally, the stratified-wavy flow boundary curve equation was modified to include the transition to partial dryout in annular flow into the Steiner flow pattern map, i.e., convert the adiabatic map into a diabatic map. The stratified-wavy flow boundary curve is represented by the following equation in kg/(s.m^2):

$$G_{\text{wavy}} = \left\{ \frac{16A_{vd}^3 g D \rho_L \rho_v}{x^2 \pi^2 (1 - (2h_{Ld} - 1)^2)^{0.5}} \times \left[\frac{\pi^2}{25 h_{Ld}^2} \left(\frac{\text{We}}{\text{Fr}} \right)_L + \frac{1}{\cos \varphi} \right] \right\}^{0.5} + 50 \quad (1)$$

The second part of the stratified-wavy flow boundary curve, located between stratified-wavy and annular flows, depends strongly on the ratio between the Froude number and the Weber number:

$$\left(\frac{\text{We}}{\text{Fr}} \right)_L = \frac{g D^2 \rho_L}{\sigma_L}, \quad (2)$$

where the Weber number is the ratio of the inertia to the surface tension forces and the Froude number is the ratio of inertia to gravity forces. Figure 9 shows the stratified-wavy boundary curve with several alternative modifications of the ratio (We/Fr).

The stratified-wavy flow boundary curve is shifted by using a multiplying factor for the original ratio of (We/Fr). This shift is undesirable because the objective is to keep the boundary curve unchanged until a vapor quality of about 60 percent is reached and then change the curvature depending on the heat flux at high vapor qualities. For this reason a relationship between the heat flux, the ratio (We/Fr), and the vapor quality is introduced into the equation of the stratified-wavy flow boundary curve.

Based on test data the ratio (We/Fr) in the stratified-wavy flow boundary equation can be replaced by the following expression:

$$(1 - x)^{F_1(q)} \left[\left(\frac{\text{We}}{\text{Fr}} \right)_L \right]^{F_2(q)}, \quad (3)$$

where

$$F_1(q) = 48.24 \left(\frac{q}{q_{\text{crit}}} \right) \quad (4a)$$

and

$$F_2(q) = 9.65 \left(\frac{q}{q_{\text{crit}}} \right) + 1.053. \quad (4b)$$

Note that in Eq. (1) the ratio (We/Fr) is part of the denominator. The factor $(1 - x)$ in Eq. (3) is to minimize the influence of the ratio (We/Fr) on the stratified-wavy flow boundary curve equation at low to medium vapor qualities while the curvature is augmented by the factor $F_2(q)$ at high vapor qualities. q_{crit} is the critical heat flux introduced here to make the exponents $F_1(q)$ and $F_2(q)$ nondimensional and is obtained from the Kutateladze (1948) correlation:

$$q_{\text{crit}} = 0.131 \rho_v^{1/2} \Delta h_v [g(\rho_L - \rho_v)\sigma_L]^{1/4}. \quad (5)$$

Note that the form of Eq. (3) has not been optimized but it still provides a good fit to our experimental data base. Figure 10 shows the new stratified-wavy flow boundary curve, for two different heat fluxes, plotted by using Eq. (1) and the modified ratio of (We/Fr) defined in Eq. (3).

Importantly, the exponents $F_1(q)$ and $F_2(q)$ defined in Eqs. (4a) and (4b) are based on the outlet vapor quality of the test zone (where the sight glass tube is located), quality at which the thin liquid film disappeared at the top of the horizontal tube. However, the experimental heat transfer coefficient is based on the mean vapor quality of the test zone. Consequently, the exponents $F_1(q)$ and $F_2(q)$ have to be modified to be able to predict the critical vapor quality at which the heat transfer coefficient begins to drop very rapidly, which was observed

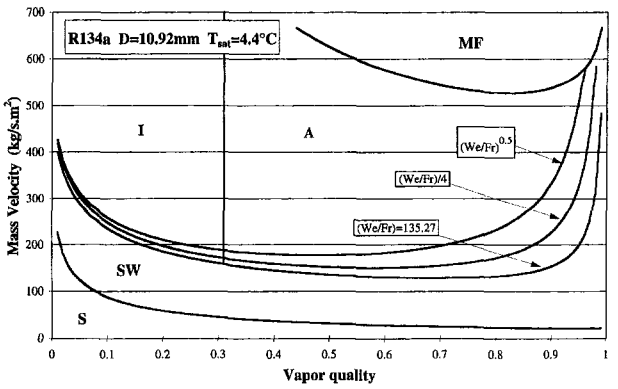

Fig. 9 The influence of the ratio (Fr/We) on the stratified-wavy flow boundary curve

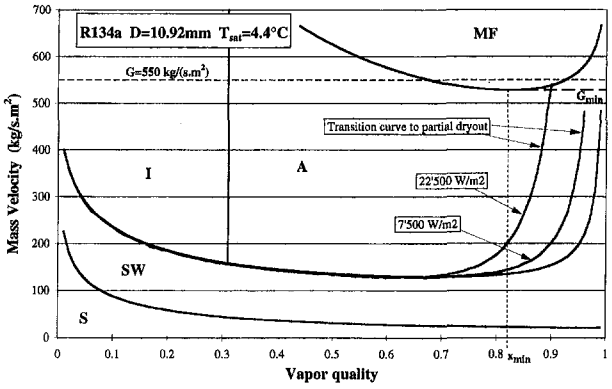

Fig. 10 The new stratified-wavy flow boundary curve plotted by using the modified ratio of (We/Fr) developed in Eq. (3)

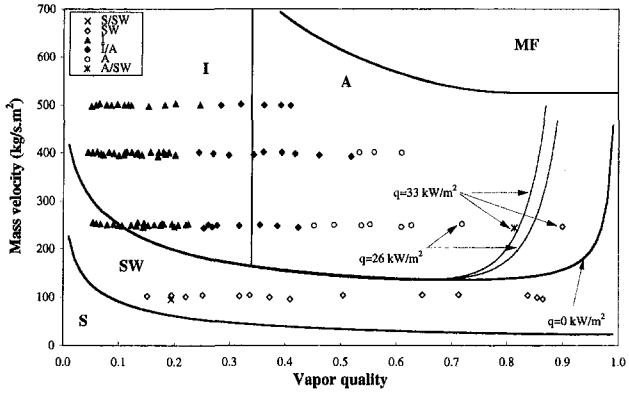

Fig. 11 R134a data compared to the new flow pattern map at 10.3°C (*D* = 12 mm)

experimentally (Part 2) to coincide with the onset of dryout. The solution is to use the mean vapor quality of the heat transfer test section instead of the outlet vapor quality; the exponents $F_1(q)$ and $F_2(q)$ become:

$$F_1(q) = 646.0\left(\frac{q}{q_{crit}}\right)^2 + 64.8\left(\frac{q}{q_{crit}}\right) \qquad (6a)$$

and

$$F_2(q) = 18.8\left(\frac{q}{q_{crit}}\right) + 1.023. \qquad (6b)$$

3.4 Modification of the Mist Flow Transition Curve. Observation of the flow patterns at $G = 550$ kg/(s.m^2) with a slow variation in test quality showed that the flow regime passed directly from annular flow to mist flow, at about 80 percent vapor quality, while the original flow pattern map predicted transition at about 65 percent (see Fig. 10). A second anomaly was observed for the mist flow transition curve shape. At $G = 550$ kg/(s.m^2) and $q = 0$ kW/m^2, according to the Steiner map, the flow pattern map changes from annular to mist flow and then back again to annular flow; keeping the same mass velocity and changing the heat flux to 22.5 kW/m^2, the flow pattern changes from annular to mist flow and then from mist flow to stratified-wavy flow. However, there is no physical reason to go back into the annular or stratified-wavy flow regime after the mist flow regime and no such transition was observed in the present experiments.

The heat transfer process in the mist flow regime and the transition curve between mist and annular flows were not specifically studied in the present study because they normally occur in a range of mass velocities beyond the operational limits of the test facility. However, based on the limited data available in the present tests and recalling the above mentioned contradiction of a mist flow reconverting to annular or stratified-wavy flow with increasing vapor quality, one solution for the second problem described above is proposed; that is, to keep the mass velocity constant from the minimum value of the mist flow transition curve (G_{min}) until the end of the evaporation process. The new mist flow limit is shown as a thick dashed line in Fig. 10. More data are required to study the location of the annular/mist flow transition curve and verify its position.

4 Comparison of the Flow Pattern Data With the New Flow Pattern Map

Test results for R134a and R502 are plotted on the new diabatic flow pattern map in Figs. 11 and 12, respectively. The stratified-wavy flow (SW) data, at high vapor quality, correctly fall now in the stratified-wavy region and the annular flow data lie in the annular region. The transition data, such as for intermittent to annular flow (I/A), are located at or near the transition line on the map. At low vapor quality the intermittent flow data are in the correct region, except for some R134a test results. At high vapor quality the stratified-wavy flow transition curve depends now on the heat flux of each test point. Only a few transition curves are plotted in Fig. 12 to keep the figure readable. The bubbly flow regime is located at higher mass velocities than shown in the graphs.

Table 1 shows the summary of the experimental test conditions for different refrigerants and the comparison to the new flow pattern map. The new flow pattern map correctly identifies 96.2 percent of the flow pattern data for the five refrigerants tested. Transition flow patterns, such as I/A, were considered to be correct if they were in the general vicinity of the transition curve, since transition is not a "step-change" but instead a gradual process occurring over a range of mass velocities and vapor qualities. At high vapor quality, all the flow pattern data are predicted correctly using the new stratified-wavy transition curve.

The test condition ranges covered by the new flow pattern map are: $1.12 \le P_{sat} \le 8.88$ bar, $100 \le G \le 500$ kg/(s.m^2), 4 percent $\le x \le 100$ percent, $0.4 \le q \le 36.54$ kW/m^2, $1.1 \le We_L \le 234.5$, and $0.037 \le Fr_L \le 1.36$. The equations for the new flow pattern map are summarized in the Appendix. (Only a 12 mm bore sight glass was tested, but since this map is a modified Taitel-Dukler-Steiner map that covered a range of diameters, this map can probably be applied to diameters over the range used in direct-expansion evaporators for the present fluids: 5—13.5 mm.)

Test data are plotted on the new flow pattern map in Figs. 13 to 17. The annular-stratified-wavy flow transition curve is

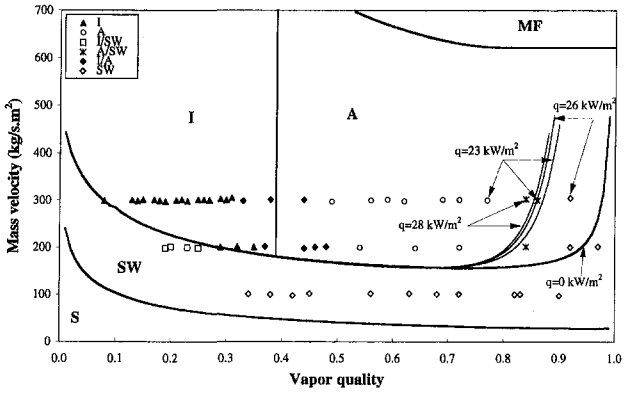

Fig. 12 R502 data compared to the new flow pattern map at 2.5°C (*D* = 12 mm)

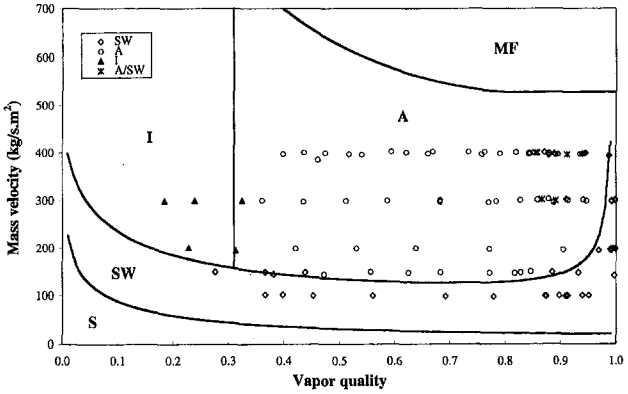

Fig. 13 R134a data at T_{sat} = 4.4°C and G = 100–400 kg/(s.m²)

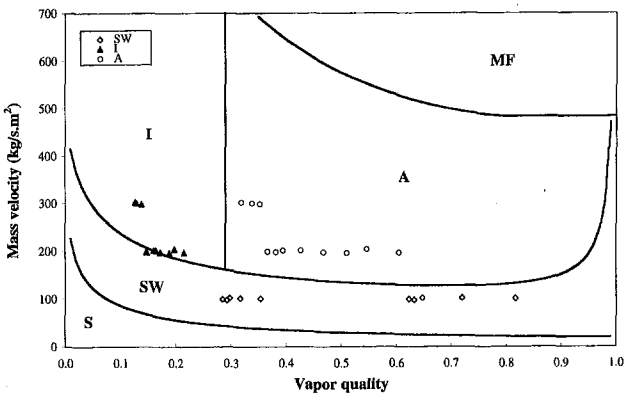

Fig. 14 R134a data at T_{sat} = −1.3°C and G = 100–300 kg/(s.m²)

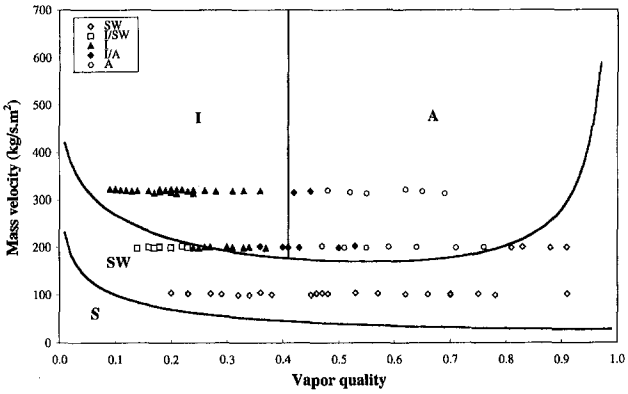

Fig. 15 R402A data at T_{sat} = 2.38°C and G = 100–318 kg/(s.m²)

showed only for the heat flux value of 0 kW/m² for simplicity, even though the data are for $q > 0$. Flow pattern data are presented here only to give an overall view of the flow configurations observed at different mass velocities, vapor qualities, and saturation temperatures. It is interesting to note that the stratified-wavy to annular flow transition curve that was translated upward by a value of 50 based only on R134a data also fits the other fluids well.

5 Existing Stratification Criteria Compared to the New Stratified-Wavy Flow Transition Curve

The stratification criteria cited by Shah (1982) (Fr_L = 0.04), Kandlikar (1990) (Fr_L = 0.04), Gungor and Winterton (1986, 1987) (Fr_L = 0.05), and Wattelet et al. (1992) (Fr_L = 0.25)

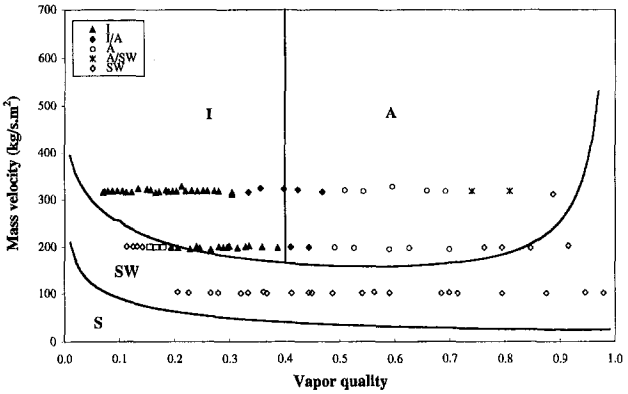

Fig. 16 R404A data at T_{sat} = 2.38°C and G = 100–318 kg/(s.m²)

in their flow boiling correlations use only the liquid Froude number as the threshold criterion to determine whether or not the wall of a horizontal evaporator tube is all wet or not. For the sake of comparison the liquid Froude number equation can be rearranged as follows:

$$Fr_L = \frac{G^2}{\rho_L^2 gD} \Rightarrow G = (\rho_L^2 gD\, Fr_L)^{1/2}. \quad (7)$$

The threshold criterion proposed by Klimenko-Fyodorov (1990) instead is a semiempirical expression to determine the transition from stratified to unstratified flow. Their threshold equation can be rearranged as follows:

$$G = \frac{[(\rho_L - \rho_v)gD]^{0.5}}{\left\{0.074\left(\frac{D}{b_{La}}\right)^{0.67}\frac{x^2}{\rho_v} + 8\left[1 - \left(\frac{\rho_v}{\rho_L}\right)^{0.1}\right]^2\frac{(1-x)^2}{\rho_L}\right\}^{0.5}}. \quad (8)$$

Figure 18 shows Eqs. (7) and (8) compared to the Steiner map and the new flow pattern map thresholds. The liquid Froude number criteria using Fr_L = 0.04 and 0.05 corresponds to the Steiner stratified-wavy transition curve from about 40 percent to 90 percent vapor quality and to the Klimenko-Fyodorov threshold from about 80 percent to 100 percent vapor quality. At low vapor quality these two criteria (Fr_L = 0.04 and 0.05) place the stratification threshold curve too low compared to the other curves. The liquid Froude number criterion using Fr_L = 0.25, instead, sets the stratification threshold curve too high, between 40 percent and 95 percent vapor quality, compared to the others. The new stratified-wavy flow transition curve proposed here is below the Klimenko-Fyodorov threshold for vapor qualities lower than 60 percent. In fact, above the new stratified-

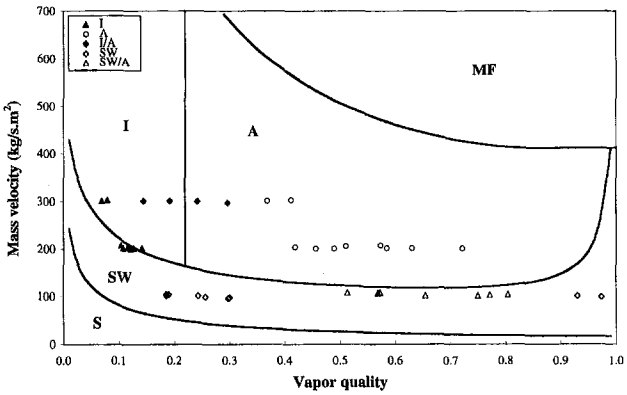

Fig. 17 R123 data at T_{sat} = 30.7°C and G = 100–300 kg/(s.m²)

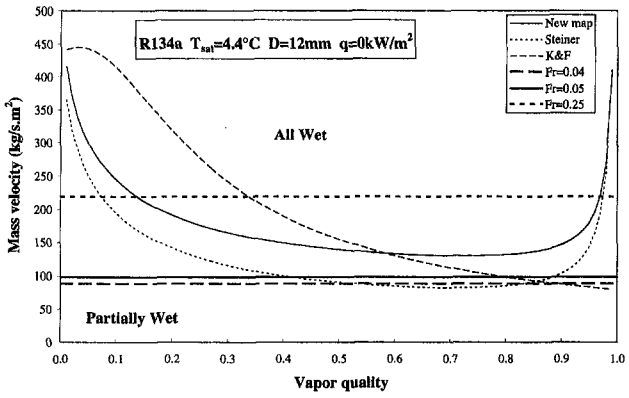

Fig. 18 Stratification criteria compared to the new stratified-wavy flow transition curve

wavy flow transition curve, an intermittent flow will exist up until 30 percent vapor quality. Depending on the amplitude of the periodic waves in intermittent flow, the top of the tube can be wetted or partially wetted. For this reason, in this zone, the frequency of the slugs is important in order to determine if the top of the horizontal tube is wetted all the time by the liquid (thin film or droplets) or not. To implement this new map refer to the Appendix for the equations and to Fig. 21 for the solution scheme.

6 Conclusions

The new flow pattern map includes four improvements to the Steiner map and extends its application to evaporating diabatic flows. It correctly identifies 96.2 percent of the flow pattern data for the five refrigerants tested over a wide range of pressures, vapor qualities, and mass velocities representative of direct-expansion evaporator design conditions. Compared to the original Steiner map, the transition boundary curve between the annular flow and the stratified-wavy flow region is raised by 50 kg/(s.m^2) and is modified to take into account the influence of the heat flux and onset of dryout at high vapor quality. Also, the mist flow to annular flow boundary has been modified to make a more realistic boundary. Importantly, the map was also transformed into a mass velocity versus vapor quality format, which is much more useful in identifying the flow patterns that will occur along an evaporator tube than the old format.

The Auracher et al. critical boiling method was shown not to be capable of predicting the critical vapor quality at which the liquid film at the top of the tube dries out in horizontal tube evaporation. One reason for this poor matching is that their method was developed for water-steam mixtures at high pressures, high mass velocities, and high heat fluxes, i.e., far from the conditions dealt with in the present study. The new method accurately predicts the location of the onset of dryout as evidenced by the coincidence with the peak in heat transfer coefficient versus vapor quality data that will be shown in Part 2.

Acknowledgments

The research was supported by the Swiss Federal Office of Energy (OFEN), Bern. The refrigerants were provided by DuPont de Nemours International S. A. of Geneva.

References

Auracher, H., Drescher, G., Hein, D., Katsaounis, A., Kefer, V., Köhler, W., and Ulrych, G., 1993, "Critical Boiling States in Flowing Liquids," *VDI-Wärmeatlas (VDI Heat Atlas)*, Verein Deutscher Ingenieure, VDI-Gesellschaft Verfahrenstechnik und Chemieingenieurwesen (GCV), Düsseldorf, Germany, (J. W. Fullarton, translator).

Collier, J. G., and Thome, J. R., 1994, *Convective Boiling and Condensation*, 3rd Edition, Oxford University Press, Oxford.

Gungor, K. E., and Winterton, R. H. S., 1986, "A General Correlation for Flow Boiling in Tubes and Annuli," *Int. J. Heat Mass Transfer*, Vol. 29, No. 3, pp. 351–358.

Gungor, K. E., and Winterton, R. H. S., 1987, "Simplified General Correlation for Saturated Flow Boiling and Comparison of Correlations to Data," *Chem. Eng. Res. Des*, Vol. 65, pp. 148–156.

Hashizume, K., 1983, "Flow Pattern and Void Fraction of Refrigerant Two-Phase Flow in a Horizontal Pipe," *Bulletin of JSME*, Vol. 26, No. 219, pp. 1597–1602.

Kandlikar, S. G., 1990, "A General Correlation of Saturated Two-Phase Flow Boiling Heat Transfer Inside Horizontal and Vertical Tubes," ASME JOURNAL OF HEAT TRANSFER, Vol. 112, pp. 219–228.

Kattan, N., 1996, "Contribution to the Heat Transfer Analysis of Substitute Refrigerants in Evaporator Tubes with Smooth or Enhanced Tube Surfaces," Thèse 1498 (1996), Ecole Polytechnique Fédérale de Lausanne, Switzerland (in English).

Kattan, N., Thome, J. R., and Favrat, D., 1995a, "R-502 and Two Near-Azeotropic Alternatives: Part I—Intube Flow Boiling Tests," *ASHRAE Trans.*, Vol. 101, Part 1, pp. 491–508.

Kattan, N., Thome, J. R., and Favrat, D., 1995b, "R-502 and Two Near-Azeotropic Alternatives: Part II—Two-Phase Flow Patterns," *ASHRAE Trans.*, Vol. 101, Part 1, pp. 509–519.

Klimenko, V. V., and Fyodorov, M., 1990, "Prediction of Heat Transfer for Two-Phase Forced Flow in Channels of Different Orientation," *Proceedings of the 9th International Heat Transfer Conference*, Jerusalem, Vol. 5, pp. 65–70.

Kutateladze, S. S., 1948, "On the Transition to Film Boiling Under Natural Convection," *Kotloturbostroenie*, No. 3, p. 10.

Shah, M. M., 1982, "Chart Correlation for Saturated Boiling Heat Transfer: Equations and Further Study," *ASHRAE Trans.*, Vol. 88, Part 1, pp. 185–196.

Steiner, D., 1993, "Heat Transfer to Boiling Saturated Liquids," *VDI-Wärmeatlas (VDI Heat Atlas)*, Verein Deutscher Ingenieure, ed., VDI-Gesellschaft Verfahrenstechnik und Chemieingenieurwesen (GCV), Düsseldorf, Germany, (J. W. Fullarton, translator).

Taitel, Y., and Dukler, A. E., 1976, "A Model for Predicting Flow Regime Transitions in Horizontal and Near Horizontal Gas-Liquid Flow," *AIChE Journal*, Vol. 22, No. 2, pp. 43–55.

Wattelet, J. P., Chato, J. C., Souza, A. L., and Christoffersen, B. R., 1992, "Evaporation Characteristics of R-12, R134a, and MP-39 at Low Fluxes," *ASHRAE Trans.*, Vol. 100, No. 1.

APPENDIX

New Flow Pattern Map

The equations of the new flow pattern map curves, shown in Fig. 19, are given as follows:

$$G_{\text{wavy}} = \left\{ \frac{16A_{vd}^3 gD\rho_L\rho_v}{x^2\pi^2(1-(2h_{Ld}-1)^2)^{0.5}} \left[\frac{\pi^2}{25h_{Ld}^2}(1-x)^{F_1(q)} \times \left(\frac{\text{We}}{\text{Fr}}\right)_L^{F_2(q)} + \frac{1}{\cos\varphi} \right] \right\}^{0.5} + 50 \quad (9)$$

$$G_{\text{mist}} = \left\{ \frac{7680A_{vd}^2 gD\rho_L\rho_v}{x^2\pi^2\xi_{Ph}} \left(\frac{\text{Fr}}{\text{We}}\right)_L \right\}^{0.5} \quad \text{at} \quad x < x_{\min} \quad (10a)$$

$$G_{\text{mist}} = G_{\min} \quad \text{at} \quad x > x_{\min} \quad (10b)$$

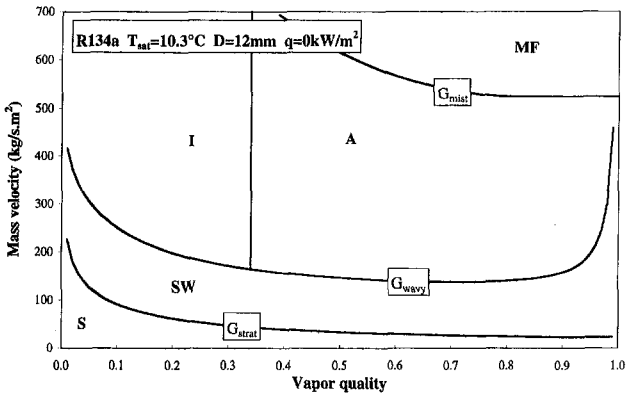

Fig. 19 New flow pattern map

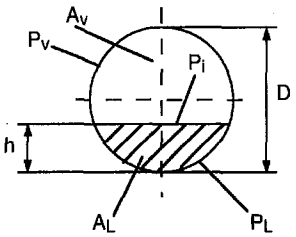

Fig. 20 Cross-sectional and peripheral fraction in a circular tube

$$G_{\text{strat}} = \left\{ \frac{(226.3)^2 A_{Ld} A_{vd}^2 \rho_v (\rho_L - \rho_v) \mu_L g \cos \varphi}{x^2 (1-x) \pi^3} \right\}^{1/3} \quad (11)$$

$$G_{\text{bubbly}} = \left\{ \frac{256 A_{vd} A_{Ld}^2 D^{1.25} \rho_L (\rho_L - \rho_v) g \cos \varphi}{0.3164 (1-x)^{1.75} \pi^2 P_{id} \mu_L^{0.25}} \right\}^{1/1.75}, \quad (12)$$

where

$$\left(\frac{\text{We}}{\text{Fr}} \right)_L = \frac{g D^2 \rho_L}{\sigma_L} \quad (13)$$

$$\xi_{Ph} \approx \left[1.138 + 2 \log \left(\frac{\pi}{1.5 A_{Ld}} \right) \right]^{-2} \quad (14)$$

and $F_1(q)$ and $F_2(q)$ are given by Eqs. (6*a*) and (6*b*). $x_{\min}$ is solved for using Eq. (10*a*) to find the minimum in G_{mist}, and hence the value of $x_{\min}$. For turbulent flow of both the vapor and the liquid phase, the boundary curve of the intermittent flow is defined by a fixed Martinelli parameter $X_{tt} = 0.34$ given by the following equation:

$$X_{tt} = \left(\frac{1-x}{x} \right)^{0.875} \left(\frac{\rho_v}{\rho_L} \right)^{0.5} \left(\frac{\mu_L}{\mu_v} \right)^{0.125}. \quad (15)$$

By extracting the vapor quality from Eq. (15), the boundary curve of the intermittent flow in the new flow map is calculated by

$$x = \left\{ \left[0.34^{1/0.875} \left(\frac{\rho_v}{\rho_L} \right)^{-1/1.75} \left(\frac{\mu_L}{\mu_v} \right)^{-1/7} \right] + 1 \right\}^{-1}. \quad (16)$$

As shown in Fig. 20, P_L is the wetted part of the perimeter while P_v is the complementary perimeter part in contact with vapor. Similarly, A_L and A_v are the corresponding cross-sectional areas, and P_i is the phase interface.

The following six dimensionless variables need to be defined:

$$h_{Ld} = \frac{h}{D}; \quad P_{Ld} = \frac{P_L}{D}; \quad P_{vd} = \frac{P_v}{D}; \quad P_{id} = \frac{P_i}{D};$$

$$A_{Ld} = \frac{A_L}{D^2}; \quad A_{vd} = \frac{A_v}{D^2}. \quad (17)$$

The dimensionless peripheral and cross-sectional area variables that are required for analysis can be derived from the geometry for a given height "h" of liquid or for a given reference liquid level h/D. For $h_{Ld} \le 0.5$,

$$P_{Ld} = (8(h_{Ld})^{0.5} - 2(h_{Ld}(1-h_{Ld}))^{0.5})/3, \quad P_{vd} = \pi - P_{Ld}$$

$$A_{Ld} = (12(h_{Ld}(1-h_{Ld}))^{0.5} + 8(h_{Ld})^{0.5}) h_{Ld}/15,$$

$$A_{vd} = \frac{\pi}{4} - A_{Ld}. \quad (18)$$

For $h_{Ld} > 0.5$,

$$P_{vd} = (8(1-h_{Ld})^{0.5} - 2(h_{Ld}(1-h_{Ld}))^{0.5})/3, \quad P_{Ld} = \pi - P_{vd}$$

$$A_{vd} = (12(h_{Ld}(1-h_{Ld}))^{0.5} + 8(1-h_{Ld})^{0.5})(1-h_{Ld})/15,$$

$$A_{Ld} = \frac{\pi}{4} - A_{vd}. \quad (19)$$

For $0 \le h_{Ld} \le 1$,

$$P_{id} = 2(h_{Ld}(1-h_{Ld}))^{0.5}. \quad (20)$$

An iterative method of resolution, on the basis of the following equation, is necessary to calculate the reference liquid level h_{Ld}:

$$X_{tt}^2 = \left[\left(\frac{P_{vd} + P_{id}}{\pi} \right)^{1/4} \left(\frac{\pi^2}{64 A_{vd}^2} \right) \left(\frac{P_{vd} + P_{id}}{A_{vd}} + \frac{P_{id}}{A_{Ld}} \right) - \frac{1}{T_v^2} \right] \times \left(\frac{\pi}{P_{Ld}} \right)^{1/4} \left(\frac{64 A_{Ld}^3}{\pi^2 P_{Ld}} \right), \quad (21)$$

where

$$T_v^2 = \left(\frac{\xi_v G^2 x^2}{2 D g \rho_v (\rho_L - \rho_v) \sin \varphi} \right)^{0.5}$$

$$\xi_v = \frac{0.3164}{\text{Re}_v^{0.25}} \text{ with } \text{Re}_v = \frac{GxD}{\mu_v}. \quad (22)$$

Once the reference liquid level h_{Ld} is known, the dimensionless variables are calculated from Eqs. (18) to (20); the equations of the boundary curves for the new flow pattern map are determined from Eqs. (9) to (12). The angle of inclination for horizontal tubes (as tested here) is 0 deg. For $\varphi = 0$ deg, $T_v^2 \to \infty$ and $1/T_v^2$ in Eq. (21) goes to zero. Figure 21 shows a solution scheme for the flow pattern map (we have implemented it as a computer program that steps along the map at small intervals to generate a tabular set of boundary points which are then displayed using a PC graphics program).

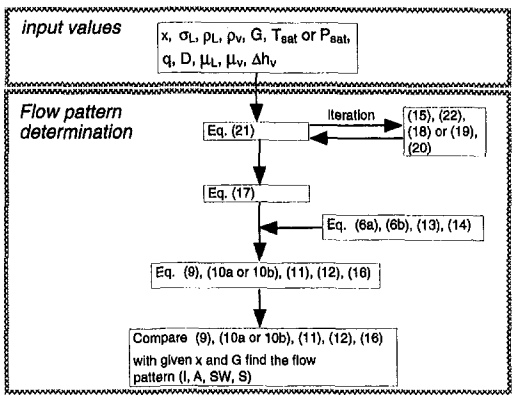

Fig. 21 Solution scheme for the flow pattern map

N. Kattan

J. R. Thome
favrat@it.dgm.epfl.ch

D. Favrat

Laboratory for Industrial Energy Systems,
Department of Mechanical Engineering,
Swiss Federal Institute of Technology,
CH-1015 Lausanne, Switzerland

Flow Boiling in Horizontal Tubes: Part 2—New Heat Transfer Data for Five Refrigerants

A summary of a comprehensive experimental study on flow boiling heat transfer is presented for five refrigerants (R134a, R123, R402A, R404A, and R502) evaporating inside plain, horizontal, copper tube test sections. The test data were obtained for both 12.00 mm and 10.92 mm diameters using hot water as the heating source. Besides confirming known trends in flow boiling heat transfer data as a function of test variables, it was also proven that the heat flux level at the dryout point at the top of the tube in annular flow has a very significant downstream effect on heat transfer coefficients in the annular flow regime with partial dryout.

1 Introduction

Numerous test data for flow boiling of new refrigerants are now becoming available in the literature. Some of the first measurements were obtained by Eckels and Pate (1991) for R134a, who measured average coefficients for large changes in vapor qualities in their test sections (quality change of about 70 percent). Using ten electrically heated test sections in series, Hambraeus (1991) measured local heat transfer coefficients for R134a. Her data covers the vapor quality range from 0.1 to 1.0, where the coefficient is plotted at the end of each identically heated tube adjusted for complete evaporation of the refrigerant at the exit of the last tube. Wattelet et al. (1992) measured heat transfer coefficients for R134a in both the stratified-wavy and the annular flow regimes, as observed at the exit of their test section. The annular flow heat transfer coefficients rise noticeably with increasing vapor quality while the stratified-wavy data are flat. Similar data for R12 showed the same trend. For a more detailed review of these tests and other recent papers, refer to Thome (1994, 1997).

Many, but not all, of the above test data for local flow boiling were obtained using electrical heated test sections. For test conditions with complete wetting of the internal perimeter of the evaporator tube, this is a reasonable approximation of a uniform heat flux boundary condition; however, for stratified and stratified-wavy flows, and for annular flow with partial tube dryout, the top part of the tube is dry and heat is conducted around the tube to the bottom, essentially turning the dry tube wall into a "fin". The boundary condition around the periphery of the tube with a partially wetted wall is therefore neither a uniform heat flux, nor a uniform temperature. In a real direct-expansion evaporator, the boundary condition will be close to a uniform wall temperature condition similar to test results obtained using counter-current flow of hot water to evaporate the refrigerant. (In the present tests it will also be demonstrated that there is a definite influence of the heat flux at the dryout point on downstream heat transfer coefficients, which shows that electrical heating is not at all appropriate for high vapor quality tests.)

The objectives of the present experimental study were to (*i*) develop an accurate flow boiling heat transfer database for several important new refrigerants, (*ii*) obtain test data at high vapor quality that are often scarce when compared to low vapor quality test conditions that are easier to measure, (*iii*) compare the thermal performances of R402A and R404A to R502 (which they replace) and (*iv*) investigate typical trends found in horizontal flow boiling data (such as the cause for the peak in heat transfer coefficient versus vapor quality, the near monotonic variation in heat transfer coefficient versus vapor quality found at other test conditions, etc.).

2 Description of Test Facility

Figure 1 depicts a simplified flow diagram of the test facility. It has four double-pipe test sections grouped in two pairs, with each pair having two double pipe test sections connected in series in a U-tube type of configuration (only two are shown). One pair is used with the test fluid (i.e., pure refrigerant or refrigerant mixture) flowing inside the inner tube (configuration for the present tests), and the other pair is used with the test fluid flowing in the annulus. Hot water can be directed to either pair of test sections. Two-phase experiments can be run for horizontal, vertical, or any inclined tube orientations by rotating the whole test section setup around a central pivot. Connections to the rest of the flow circuit are made by insulated, flexible, stainless-steel hoses.

The refrigerant passes through a 6 kW preheater before reaching the first test section. It then passes through one pair of the U-tube test sections before entering the condenser. Next, the refrigerant is drawn into a stainless steel pump with a magnetically driven rotor that operates without any lubricating oil on the fluid side, thus eliminating any possibility of oil entering the refrigerant. A speed controller on the pump is used to modify the refrigerant flow rate. The refrigerant passes through a calibrated Coriolis flow meter and back into the preheater. The latter device is used to precondition the refrigerant to the desired inlet conditions in the first test section.

The hot water heater circuit reheats the water after it passes through the two test sections. The water flow rate is measured by a calibrated Coriolis flow meter, and the water is circulated by a stainless steel pump. A by-pass system is used to modify the water flow rate. This system is carefully deaerated to eliminate any adverse effects on flow rate measurements and energy balances. The inlet water temperature to the second test section is controlled by two secondary water circuits (using two plate heat exchangers)—a hot water circuit from the heater and an industrial cold water circuit. A PID control system is used for the three-way valve, located in the secondary hot water circuit, to control the inlet water temperature to the second test section.

The refrigerated water-glycol solution, for the system's coiled tube-in-tube condenser, is maintained at a fixed inlet temperature by a refrigeration system (−15°C to +15°C) with a large

Contributed by the Heat Transfer Division for publication in the JOURNAL OF HEAT TRANSFER and presented in part (Section 7) at the ASHRAE & 10th International Heat Transfer Conference. Manuscript received by the Heat Transfer Division October 1, 1996; revision received July 16, 1997; Keywords: Evaporation; Flow Visualization; Multiphase Flows. Associate Technical Editor: M. D. Kelleher.

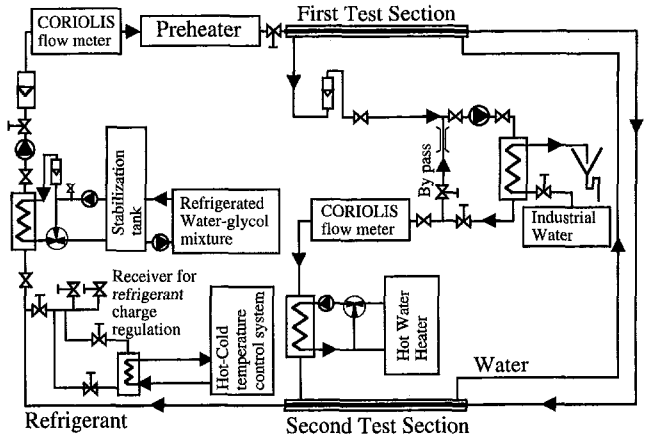

Fig. 1 Layout of the test facility flow circuits

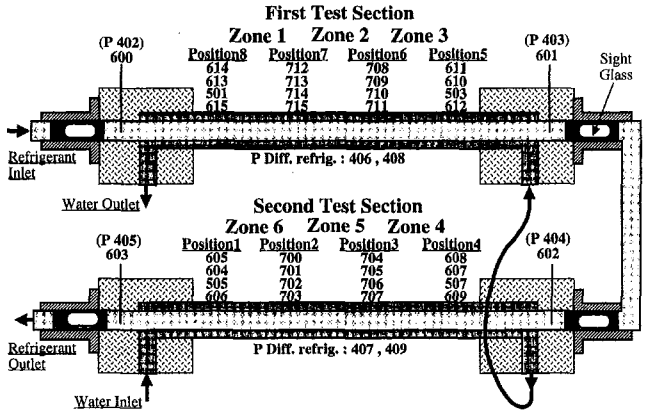

Fig. 2 Measurement locations in the test sections

water-glycol receiver (200 liters) in its flow circuit. This receiver eliminates cyclic temperature variations originating from the refrigeration system's on-off operating cycle from being passed on to the condenser, and hence to the test facility itself.

Figure 2 shows the test section measurement layout diagram for water flowing in the annulus with counter-current refrigerant flow inside the inner tube. At the refrigerant inlet, the temperature is measured by thermocouple #600 located in the refrigerant flow stream (the tube is well insulated from this point up to the location of the four water-side thermocouples, #614, #613, #501, and #615, with a tightly fitted Teflon sleeve. Similar arrangements exist for the refrigerant at the outlet of the first section, the inlet to the bottom test section, and the exit of the bottom test section—thermocouples #601, #602 and #603, respectively. At each of these locations the absolute pressures (gauges P402 to P405 on Fig. 2) of the refrigerant and the differential pressure drops (gauges 406 to 409 on Fig. 2) across the two test sections are measured.

3 Test Sections

The inner tubes of the double-pipe test sections are made of copper. The outside tubes are made of a very hard PVC that is precision machined into two halves. This gives a much greater dimensional uniformity and precision along the length of the test section than the standard piping used in other experimental test facilities. The PVC also acts to insulate the test section. An O-ring is compressed between the two halves to form the seal such that the faces of the two halves meet to form a circular annulus around the copper tube. O-ring sealed screws are inserted through the outer tube to center the copper tube inside. Figure 3 shows the detail of the screw in the PVC wall tube. Figure 4(*b*) shows the three centering screws in the tube section. The outside PVC tube is supported to maintain a perfectly straight test section.

Figure 4(*a*) shows the four thermocouples (0.5 mm diameter) installed at each measurement location in the annulus, located at 0°, 60°, 120°, and 180° from the top of the annulus. These are inserted through sealed screws installed in the thick PVC tube wall with the junctions positioned about 0.3 mm from the copper tube wall. There are four measurement locations on both the top and bottom test sections; thus, there are six test zones from which to obtain heat transfer coefficients. This allows measurements over narrow changes of vapor quality (essentially local values) during boiling tests (see Fig. 2, zones 1 to 6). This novel approach eliminates inlet, outlet, and "dead" zones formed at the connections to the mixing chambers used in conventional setups that change the local heat transfer coefficients over a significant percentage of the test section length in the annulus. Using this new set up minimizes the disruption of the water flow while accurate energy balances confirm the integrity of this approach. In addition, the mean temperature of the four temperatures for the heating water at the outlet of the second test section have been compared to the mean temperature for the heating water at the inlet to the first test section, i.e., after the water has passed through the insulated connecting pipe and becomes well mixed. These mean temperatures are very close to each other and are well within the experimental error of the temperature measurements.

Between test zone 5 and test zone 6, two thermocouples are located in the tube wall to check the wall temperature, and in particular the wall temperature difference between the top and the bottom of the tube. These 0.25 mm diameter thermocouples are tightly inserted in a short and narrow groove made in the tube wall and then glued. The thermocouple wire exits the annulus by passing through the joint between the two halves of the PVC tube, without creating any leaks on the water circuit (the O-ring joint assures the water seal). Tubular sight glass sections are installed inline with the tube to visualize the flow at four locations (inlet and outlet of each test section), allowing the visual determination of the flow patterns at these locations (see Fig. 2).

Figure 5 shows the thermocouple and the centering screw locations in the test sections corresponding to Fig. 2. The dis-

Nomenclature

c_p = specific heat, kJ/kg K
D = tube diameter, m
G = total mass velocity of liquid and vapor, kg/s m^2
h = heat transfer coefficient, W/m^2 K
H = enthalpy, kJ/kg
H_{Lv} = latent heat of vaporization, kJ/kg
P_{sat} = saturation pressure, Pa (or bar)
q = heat flux, W/m^2
T = temperature, K (or °C)
T_{bub} = bubble-point temperature, K (or °C)
T_{sat} = saturation temperature, K (or °C)
x = vapor quality

Subscripts

bub = bubble
L = liquid
Pos = position
ref = reference
sat = saturation
tp = two-phase
v = vapor
w = wall

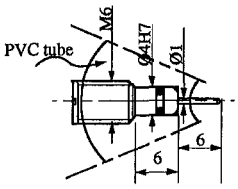

Fig. 3 Centering mechanism of the screw in the PVC wall tube (dimensions are in mm)

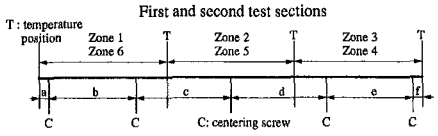

Fig. 5 Thermocouples and centering screws positions in the test sections

tance between the different locations and the tubes dimensions are given in Table 1. For further experimental details refer to Kattan (1996).

4 Measurements, Accuracies, and Operating Procedures

An HP 3852A data acquisition system together with a Macintosh II FX personal computer running the LabView III software are used to acquire, analyze, and store the data. All sensors are carefully calibrated. The thermocouples are calibrated using the double-precision method available in the acquisition system to obtain the highest accuracies possible, that is, 0.03°C. For adiabatic conditions after leaving the rig off all night, all temperatures are within a maximum deviation of ±0.10°C and most are within ±0.05°C of the average. For diabatic (i.e., heated) test conditions and for inside tube evaporation, the maximum variations between the four thermocouple readings, around the annulus at any one position, are normally within ±0.07°C and most are within ±0.05°C for $Re_D > 3000$. The uniformity of these temperature measurements also confirms the precision centering of the copper tube.

The thermocouples in the water annular channel (see Fig. 2) were then rewired and recalibrated while installed in place so that the four water-side thermocouples (for example 614, 613, 501, and 615) were circuited to read their mean temperature, thus reducing the acquisition time by a factor of four. A quartz thermometer, used as the reference absolute temperature, is located in the water circuit at the inlet of the second test section. Figure 6 depicts two temperature profiles measured for the test facility, illustrating the accuracy of the thermocouple measurements. As can be seen from the two diagrams for isothermal tests, the variation in temperature at the eight measurement positions is less than ±0.02°C from that measured by the quartz thermometer. Also, the deviation from one position to the next is very small; hence, the temperature measurement accuracy and energy balances used to get heat fluxes are very good for this large flow boiling test facility. Also, note that the mean water temperature leaving zone 4 matches that of the mean temperature entering zone 3, attesting to the validity of using thermocouples located directly in the annulus.

The refrigerant and hot water flow rates are both measured with an estimated accuracy of 0.2 percent, based on the specifications by the manufacturer of the Coriolis meters and our own calibrations. The energy balances between the water and refrigerant flows in the two test sections in liquid-liquid tests agree to within 2 percent maximum error (1 percent average error) when the water Reynolds number is maintained above 3000. Thus, heat losses (or gains) from the ambient air were negligible. Errors rose to 3–5% for $Re_D < 3000$ because of the thermal stratification effect due to natural convection in the hot water in the annulus, and hence this regime was avoided. The absolute pressures are measured to an accuracy of 0.5 percent according to our calibrations, while differential pressure drop measurements are accurate to 0.5 percent of full scale (meters of 0.1 and 0.5 bar were used). The mean relative uncertainty in the measured heat transfer coefficients determined from a propagation of error analysis is ±7.2 percent.

Traditional modified Wilson (1915) plot methods are based on the Dittus-Boelter type of turbulent flow heat transfer correlation (Dittus and Boelter, 1930). However, this can yield large scatter in the heating water data because this correlation cannot model the transition flow regime, i.e., a Reynolds number from 2300 to 10,000 is a common range for the hot water in refrigerant boiling tests. A new approach was thus developed based instead on the Gnielinski (1976) heat transfer correlation applicable for the range 2300 to 1,000,000. Thus, rather than using liquid-liquid data to find the empirical constant and exponent of the Dittus-Boelter correlation for the annulus, an empirical constant was obtained to correct the Gnielinski correlation for the annulus; both approaches were tested and the Gnielinski method gave better accuracy.

The computerized control system maintains the system at steady state during tests and is then used to bring the system to the next test condition. Data acquisitions of the test variables show that no significant fluctuations or cyclic changes in temperatures, pressures, or flow rates occur during tests. Repeatability of experimental data is very good for tests done on different days. The test conditions are summarized in Table 2.

A temperature controlled receiver is connected via a valve to the test fluid circuit to regulate the amount of refrigerant charge, and a high vacuum pump system (not shown) is also connected for evacuation and for leak detection tests during each change of refrigerants. Starting with a full vacuum in the refrigerant loop and using a very careful filling procedure to avoid air from entering into the loop, no venting to de-gas the refrigerant is normally required, which is confirmed by the close agreement between the measured saturation temperature and that predicted by the vapor pressure curve from the measured saturation pressure.

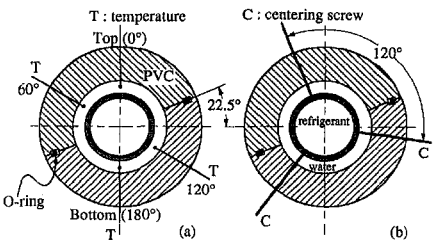

Fig. 4 (*a*) Thermocouple locations in the annulus, (*b*) centering screw locations

5 R134a Test Data

Local heat transfer coefficient data for horizontal flows of R134a are shown in Figs. 7 and 8. Note that with hot water heating, heat fluxes depend on the overall U_o and LMTD of each test zone and therefore cannot be preset by the experi-

Table 1 Main geometrical dimensions of the test sections

	Copper		PVC		Zone length			Section length	Centering screw location						Fluid
Tube	ID	OD	ID	OD	1 or 6	2 or 5	3 or 4	1or 2	a	b	c	d	e	f	
plain #1	12	14	19	46	997	1019	997	3013	70	683	753	753	680	74	R134a, R12, R123, R402A, R404A, R502
plain #2	10.92	12.7	16	46	1005	1004	1004	3013	70	690	750	750	680	73	R134a
Dimensions in mm			ID = inside diameter					OD = outside diameter							

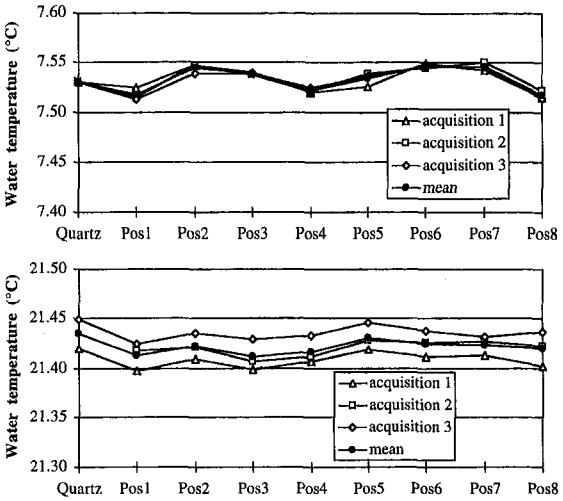

Fig. 6 Two temperature profiles measured after calibration and compared to a quartz thermometer

menter. Thus, data are presented for a range of heat flux to show the trends in the data (i.e., some of the "scatter" in data points is due to the range of heat fluxes plotted, not experimental error).

Figure 7 depicts the boiling data for R134a at mass velocities of 102.3, 201.2, and 301.6 kg/(s.m^2) for the heat flux range of 5 to 25 kW/m^2, a saturation temperature of 10.3°C, and a tube diameter of 12 mm. Figure 8 shows the boiling data for R134a at mass velocities of 100, 199, and 299 kg/(s.m^2) for the heat flux range of 4 to 14 kW/m^2, a saturation temperature of 4.4°C, and a tube diameter of 10.92 mm.

6 R123 Test Data

Figure 9 depicts the boiling data for R123 at mass velocities of 101.1, 201.4, and 300.5 kg/(s.m^2) for the heat flux range of 5 to 25 kW/m^2, a saturation temperature of 30.7°C, and a tube diameter of 12 mm.

7 R502, R402A, and R404A Test Data

Flow boiling of zeotropic refrigerant mixtures has become an increasingly important research topic for new heat pump designs as well as for the R22 or R502 substitutes. Note that work with other types of mixtures, principally binary and multicomponent hydrocarbon mixtures and aqueous mixtures, has already been under way for several decades. For a comprehensive review of forced convective boiling of pure fluids and mixtures, the reader is referred to Collier and Thome (1994) or specifically for mixture boiling fundamentals to Thome and Shock (1984) and to Thome (1990) for a survey of enhanced boiling of mixtures.

Table 2 Flow boiling test conditions (nominal values)

Fluid	T_{sat} (°C)	P_{sat} (bar)	Mass velocity (kg/s.m^2)	Heat flux (W/m^2)	Vapor quality (%)
R402A	-1.3	6.29	317	4503 - 20'836	1.7 - 54.7
	2.4	7.05	102 - 318	4387 - 22'897	1.7 - 90.0
	10.2	8.87	303	4588 - 28'597	2.8 - 83.6
R404A	-1.3	5.89	320	5323 - 21'777	1.9 - 54.7
	2.4	6.61	102 - 318	3418 - 30,551	1.7 - 92.1
	10.2	8.36	300	4372 - 30'573	1.6 - 89.3
R502	2.5	6.20	100 - 300	4257 - 27'720	1.8 - 98.6
R123	30.7	1.12	101 - 300	3700 - 24'650	7 - 98
R134a	-1.3	2.79	100 - 300	4620 - 18'910	12 - 82
R134a	2.0	3.14	300 - 500	7830 - 25'580	5 - 57
R134a	4.4	3.42	100 - 400	440 - 22'580	18 - 100
R134a	10.3	4.19	100 - 500	3200 - 36'540	4 - 90

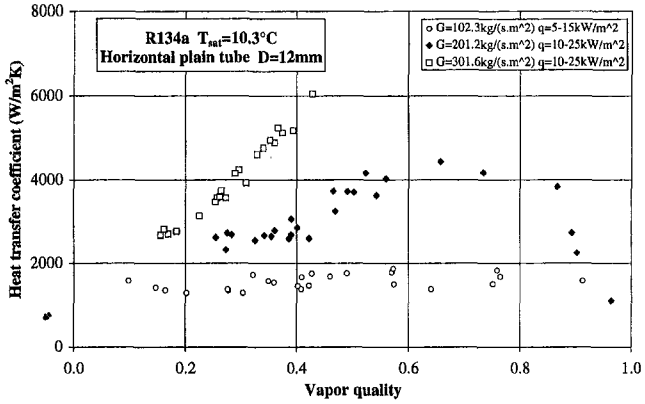

Fig. 7 R134a flow boiling data at T_{sat} = 10.2°C (D = 12 mm)

7.1 Test Fluids. R402A (60 percent R125, 2 percent R290, and 38 percent R22 by wt.) and R404A (44 percent R125, 52 percent R143a, and 4 percent R134a by wt.) are ternary "near-azeotropic" mixtures. Their boiling ranges or "glides" (dew-point temperature minus bubble-point temperature) are 1.01°C and 0.45°C, respectively. R502 (48.8 percent R22 and 51.2 percent R115) is a binary azeotropic mixture with, therefore, no boiling range. The tests were run at fixed saturation temperatures and mass velocities such that a direct comparison of the experimental heat transfer data for the three fluids could be made at similar heat fluxes over a wide range of local vapor qualities (see Table 2). The saturation temperatures for the near-azeotropic mixtures listed correspond to the bubble-point temperatures at the entrance of the first test section, while local bubble-point temperatures were used to reduce the test data to heat transfer coefficients.

The physical properties of the three fluids are compared in Table 3 at 2.4°C. The thermodynamic and transport properties of R502 are predicted from the ASHRAE Handbook (*Fundamentals,* 1993). The thermodynamic properties for R402A and R404A are obtained from tables provided by the manufacturer, and the transport properties are predicted using the computer program REFPROP (*REFPROP,* 1992). Since the program did not accurately predict the vapor pressure curves of R402A and R404A using its own internal binary interaction parameters, new binary interact parameters were found by trial and error until good agreement was obtained over the range of the present tests and data by DuPont, who furnished the fluids.

Handling of multicomponent mixtures must be done carefully in order to ensure that the composition of the sample does not change during its introduction into the test facility or during the experimental tests themselves. For example, as liquid is withdrawn from a closed vessel, part of the liquid remaining

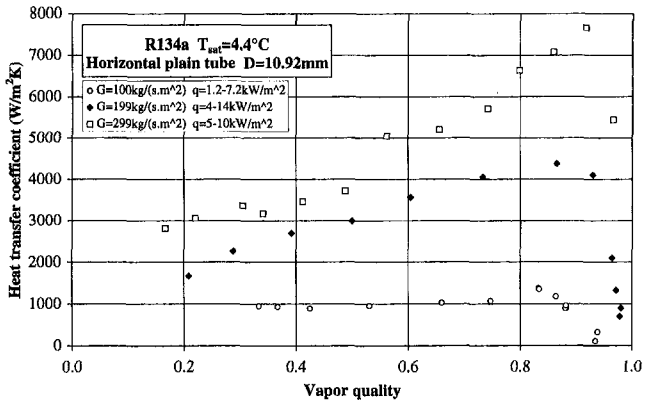

Fig. 8 R134a flow boiling data at T_{sat} = 3.9°C (D = 10.92 mm)

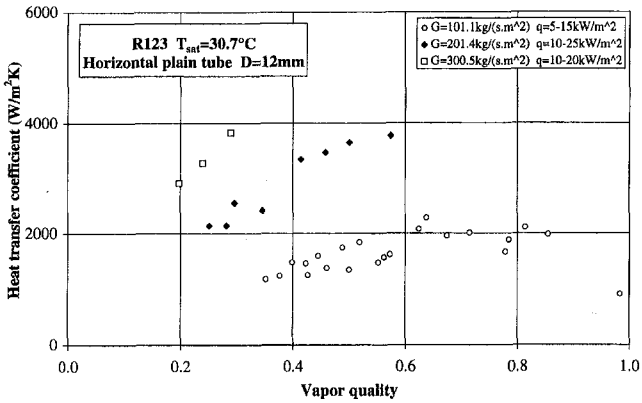

Fig. 9 R123 flow boiling data at T_{sat} = 29.6°C (D = 12 mm)

behind must evaporate in order to fill the volume originally occupied by this liquid. Since the vapor composition is not the same as that in the liquid phase for a nonazeotropic mixture, the liquid composition changes during this process. This effect is particularly acute for mixtures with large differences in vapor and liquid compositions, but is minor for near-azeotropics such as R402A and R404A. Vapor-phase system leaks are important to avoid.

In order to double check the present handling procedures, small liquid samples were obtained for the following fluids: (*i*) the original R402A as supplied by the manufacturer; (*ii*) the liquid within the test circuit midway through the R402A tests; and (*iii*) the liquid in the test circuit at the conclusion of the R402A tests. Two composition measurements of each of these three samples were then measured by the manufacturer. Table 4 shows the results. The average value of each sample tested was within the normal product range for R402A. Two minor unidentified components made up about 0.5 percent of the fluid. A small increment of 0.7 percent in the R125 composition was registered from the beginning to the end of the tests.

7.2 Definition of Mixture Boiling Heat Transfer Coefficient. The flow boiling heat transfer coefficient for a mixture is defined using the bubble-point temperature (instead of the saturation temperature for a pure fluid) corresponding to the local bulk liquid concentration at the local saturation pressure according to

$$h_{tp} = \frac{q}{(T_w - T_{\text{bub}})}, \tag{1}$$

where T_w is the tube wall temperature, T_{bub} is the bubble-point temperature, and q is the heat flux. During the evaporation of a zeotropic mixture, the vapor composition of the more volatile component (the fluid with the lower boiling point) is greater than its composition in the liquid phase. Consequently, the local bubble-point temperature increases as the composition of the less volatile component (the fluid with a higher boiling point) in the liquid phase rises during evaporation along a heated tube. The change in enthalpy, H, of the mixture during evaporation along the tube is thus composed of three terms, where

$$dH = H_{Lv}x + (1 - x)dT_{\text{bub}}c_{p,L} + xdT_{\text{bub}}c_{p,v}. \tag{2}$$

The terms are (*i*) the latent heat of vaporization of the amount vaporized, x; (*ii*) the sensible heating of the liquid phase, $(1 - x)$; and (*iii*) the sensible heating of the vapor phase, x. The values of the latent heat and specific heats are a function of the local liquid and vapor compositions. In calculating the local heat transfer coefficients along the tube, Eq. (1) must be used together with phase equilibria data to determine the local vapor quality, heat flux, and bubble-point temperature. Equation (2) reduces to only the latent heat for a pure fluid or an azeotrope, as expected. For boiling, the enthalpy or heat release curve given by Eq. (2) is known as the evaporation curve and a unique curve exists at each saturation pressure. For consistency, this curve is used to reduce test data to boiling heat transfer coefficients and should also be utilized for designing multicomponent evaporators to calculate local temperature and enthalpy changes. For R402A and R404A the heat release curves were determined using the computer program REFPROP (*REFPROP*, 1992) with user supplied binary interaction parameters determined from the vapor-liquid equilibria data provided by supplier of the fluids (see acknowledgment). These curves were then curvefit to produce expressions for local vapor quality and bubble-point temperature as a function of enthalpy as follows:

$$x = a_1(H + H_{\text{ref}})^2 + a_2(H + H_{\text{ref}}) + a_3 \tag{3}$$

$$T_{\text{bub}} = b_1(H + H_{\text{ref}})^3 + b_2(H + H_{\text{ref}})^2 + b_3(H + H_{\text{ref}}) + b_4. \tag{4}$$

The values of the constants for R402A and R404A at the three test conditions are given in Table 5. H_{ref} is the reference enthalpy at a vapor quality of 0 percent and H is the enthalpy relative to H_{ref}.

7.3 Test Procedures. The inlet condition at the first test zone for the refrigerant was 0.3°C of subcooling. Then, using the heat duty given by the hot water in the first test zone, the vapor quality and bubble-point temperature at the exit of the zone were calculated using Eq. (3) and Eq. (4). In this manner the local conditions at the end of the other zones were determined in successive steps. Using the inlet and outlet bubble-point temperatures and water temperatures for the zone, the boiling heat transfer coefficient is calculated for the zone by utilizing the water-side coefficient, the heat duty, and the log

Table 4 R402A sample compositions (by % weight)

Component	Sample			
	Normal	Initial	Intermediate	Final
R125	60.0%	61.0 / 61.0	61.4 / 61.5	61.7 / 62.7
Propane	2.0%	1.27 / 1.27	1.23 / 1.23	1.32 / 1.26
R22	38.0%	37.1 / 37.2	36.7 / 36.8	36.4 / 35.4
Unknown 1		0.24 / 0.25	0.26 / 0.26	0.25 / 0.24
Unknown 2		0.30 / 0.28	0.28 / 0.28	0.27 / 0.28

Table 3 Physical properties at 2.4°C

Property	Unit	Fluid		
		R402A	R404A	R502
Saturation pressure	bar	7.05	6.61	616.8
Liquid density	kg/m^3	1257	1164	1313
Vapor density	kg/m^3	37.2	32.9	34.9
Liquid viscosity	cp*	0.205	0.181	0.226
Vapor viscosity	cp	0.0122	0.0117	0.0121
Liquid specific heat	kJ / kg K	1.211	1.346	1.184
Vapor specific heat	kJ / kg K	0.817	0.939	0.708
Latent heat	kJ / kg	159.4	166.3	144.9
Surface tension	N / m	0.00875	0.00746	0.00992
Critical pressure	bar	41.35	37.32	40.75
Molecular weight	-	101.55	97.6	111.63
Dew point temperature	°C	3.4	2.8	2.4
Bubble point temperature	°C	2.4	2.4	2.4
* 1 cp=10^{-3} Pa.s				

Table 5 Constants for heat release curves of R402A and R404A

Fluid	P_{sat} (bar)	a_1 10^{-7}	a_2 10^{-3}	a_3	b_1 10^{-7}	b_2 10^{-5}	b_3	b_4	H_{ref} (kJ/kg)
R402A	6.30	-5.16	6.570	-1.313	0.000	-1.680	0.01650	-3.966	203.1
	7.05	-4.86	6.670	-1.363	0.000	-1.246	0.01410	-0.037	207.5
	8.88	0.00	6.515	-1.399	0.000	-1.690	0.01640	7.372	217.1
R404A	5.89	-2.52	6.029	-1.178	0.000	0.925	-0.00228	-1.199	197.1
	6.61	0.00	5.993	-1.209	-0.759	7.412	0.02047	4.117	202.0
	8.36	-2.79	6.410	-1.351	-1.362	12.580	-0.03530	13.37	212.7

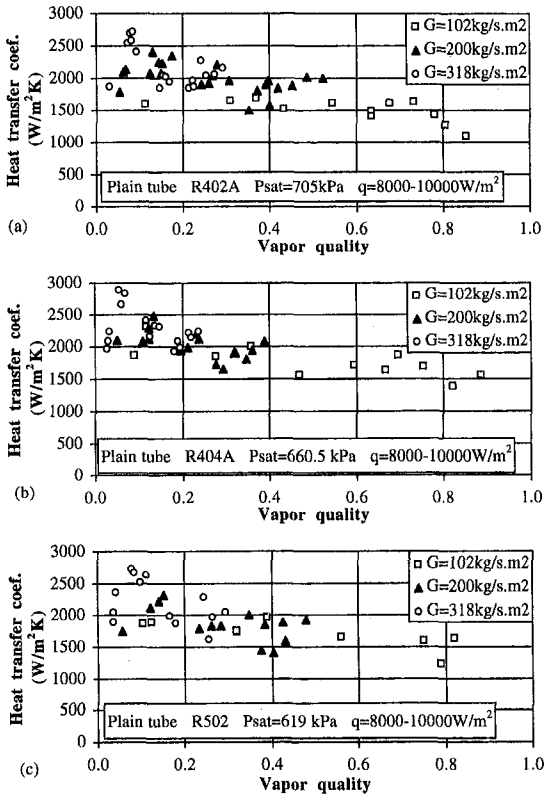

Fig. 10 R402A, R404A, and R502 results at three mass velocities

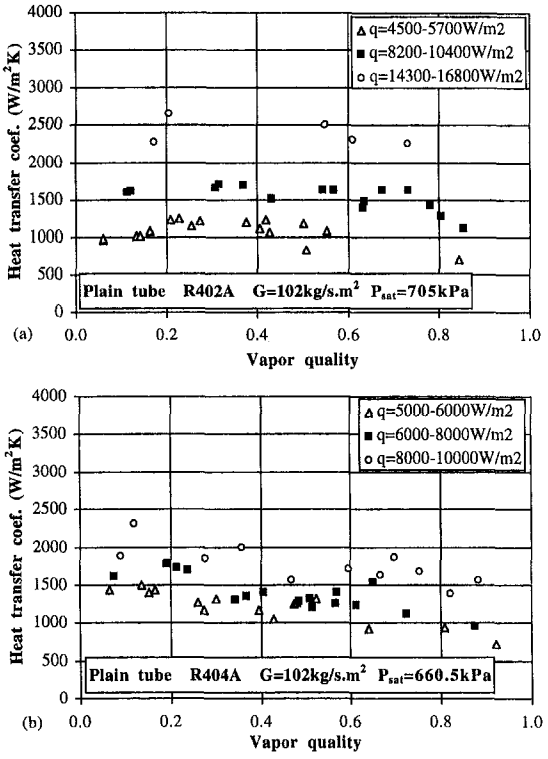

Fig. 11 R402A and R404A results at three heat fluxes

mean temperature difference (LMTD) for the zone, taking into account the wall resistance of the copper tube.

7.4 Experimental Results. Local boiling heat transfer coefficients are reported for R402A, R404A, and R502 evaporating inside a horizontal plain tube (the dimensions of the plain #1 tube are presented in Table 1). Figure 10(a) depicts the boiling data for R402A at mass velocities of 102, 200, and 318 kg/(s.m^2) for the heat flux range of 8 to 10 kW/m^2, a bubble-point temperature of 2.4°C, and a pressure of 7.05 bar. Figure 10(b) depicts the boiling data for R404A at mass velocities of 102, 200, and 318 kg/(s.m^2) for the heat flux range of 8 to 10 kW/m^2, a bubble-point temperature of 2.4°C, and a pressure of 6.61 bar. Figure 10(c) depicts the boiling data for R502 at mass velocities of 100, 200, and 300 kg/(s.m^2) for the heat flux range of 8 to 10 kW/m^2, a bubble-point temperature of 2.5°C, and a pressure of 6.20 bar.

The effect of heat flux is shown in Fig. 11(a) for the boiling data of R402A at a mass velocity of 102 kg/(s.m^2), a bubble-point temperature of 2.4°C, and a pressure of 7.05 bar. The three heat flux ranges are 4500 to 5700, 8200 to 10,400, and 14,300 to 16,800 W/m^2. A significant increase in the heat transfer coefficient with heat flux is observed, as expected. The heat transfer coefficients trail off to lower values at high vapor qualities. The heat flux effect on boiling of R404A at a mass velocity of 102 kg/(s.m^2), a bubble-point temperature of 2.4°C, and a pressure of 6.605 bar is depicted in Fig. 11(b). The three heat flux ranges are 5 to 6, 6 to 8, and 8 to 10 kW/m^2. An increase in the heat transfer coefficient with heat flux is again observed and the coefficients trail off to lower values at high vapor qualities.

The effect of saturation pressure on heat transfer is shown in Fig. 12(a) for R402A in a heat flux range of 14 to 17 kW/m^2. The pressures represented are 6.29, 7.05, and 8.87 bar. The corresponding dew-point temperatures are −1.3°C, 2.4°C, and 10.2°C. A small increase in the coefficients with rising pressure is found. Figure 12(b) illustrates a similar effect of saturation pressure on heat transfer for R404A for the heat flux range of 14 to 17 kW/m^2. The pressures represented are 5.89, 6.60, and 8.36 bar. The corresponding dew-point temperatures are −1.3°C, 2.4°C, and 10.2°C. A small increase in the coefficients with rising pressure is again evident.

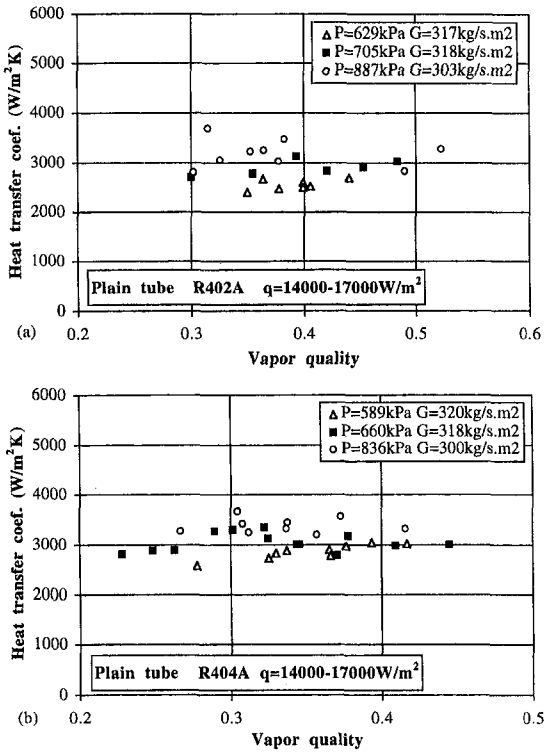

Fig. 12 R402A and R404A results at three pressures

Figure 13(a) depicts a direct comparison of the experimental boiling coefficients of R402A and R404A to those of R502 at a fixed inlet bubble-point temperature of 2.4°C to 2.6°C. The test conditions are for a mass velocity of 100 kg/(s.m^2) and a heat flux range of 8000 to 10,000 W/m^2. Figure 13(a) illustrates that the heat transfer coefficients are very similar over the vapor quality range from 10 percent to 88 percent. R402A tends to have a thermal performance slightly below that of R502, while that of R404A is slightly better. The average coefficients for the data in Fig. 13(a) are 1531, 1767, and 1703 W/m^{2}K for R402A, R404A, and R502, respectively; the values for R402A and R404A are −10 percent and +4 percent, relative to that of R502.

Figure 13(b) depicts the comparison for the heat flux range of 8000 to 10,000 W/m^2 at a mass velocity of 200 kg/(s.m^2). Figure 13(b) illustrates that the heat transfer coefficients are similar over the vapor quality range from 5 percent to 52 percent. Minor maxima in the heat transfer coefficient at a vapor quality of 12 percent to 15 percent are found for all three fluids. The average coefficients for the data in Fig. 13(b) are 1995, 2018, and 1856 W/m^{2}K for R402A, R404A, and R502, respectively (i.e., +8 percent and +9 percent relative to that of R502).

Figure 13(c) shows a comparison for the heat flux range of 8000 to 10,000 W/m^2 over a mass velocity of 300 to 318 kg/(s.m^2). Figure 13(c) again confirms that the heat transfer coefficients of the three refrigerants are very similar over vapor qualities from 3 percent to 29 percent. More prominent maxima in the heat transfer coefficients are found for all three fluids at this higher mass velocity but the location has shifted to lower vapor qualities of 5 percent to 7 percent. The average coefficients for the data in Fig. 13(c) are 2168, 2275, and 2200 W/m^{2}K for R402A, R404A, and R502, respectively (i.e., −1 percent and +3 percent relative to that of R502).

8 Discussion of the Results

In Figs. 10(a), 10(b), and 10(c), a distinct maximum in heat transfer coefficient at a vapor quality of about 8 percent is observed at the highest mass velocity, while a more moderate one occurs at about 15 percent at the medium mass velocity. The heat transfer coefficient is seen to decrease monotonically with increasing vapor quality at the lowest mass flow rate (G = 100 kg/(s.m^2)). The maxima at low vapor quality may be caused by a change in flow pattern or by a change in the contributions between nucleate boiling and convective boiling components. A moderate increase in the heat transfer coefficient is observed with mass velocity, as expected. At G = 200 and 300 kg/(s.m^2), data were not measured up to very high vapor qualities (a more powerful preheater was added after these tests allowing higher quality tests with R123 and R134a).

In Figs. 7, 8 and 9, the heat transfer coefficient is seen to increase with increasing vapor quality from about 20 percent. A distinct maximum in heat transfer coefficient is observed at a high vapor quality. The fall off in the heat transfer coefficient after the peak was observed to be caused by the transition from the annular flow regime to annular flow with partial dryout. This transition is predicted now by the new flow pattern map presented in Part 1.

In traditional test facilities, the refrigerant is heated by an electrical resistance wire wound around the tube or by direct electrical heating of the tube itself and the heat flux is fixed by the electrical power dissipated. Instead, in the present test facility, the refrigerant inside the tubes is heated by hot water flowing countercurrently in the annulus (which corresponds more closely to the real situation in a water chiller evaporator). In this case the heat flux is not an independent variable imposed by the experimenter, it comes from controlling the hot water inlet temperature and it also depends on the overall U_o and the logarithmic mean temperature difference (LMTD). Thus, the resulting heat flux is dependent on the unknown boiling heat transfer coefficient to be measured. Therefore, the influence of using electrical heating as opposed to a hot fluid stream, as in a real heat exchanger, is a controversial issue that needs to be addressed in tests using electrical heating.

Figure 14 shows the influence of the heat flux as observed in our experimental investigations during boiling of R134a at a saturation temperature of 4.4°C and mass velocity G = 400 kg/(s.m^2). Two different heat flux curves are generated by modifying the inlet water temperature of the test zone, which affects the LMTD of the zone. To facilitate the interpretation of the test data, each curve is divided into two parts at the maximum value of the heat transfer coefficient. Mean error ranges are also shown.

Before the maximum value of the heat transfer coefficient the tube wall is completely wet and the heat flux depends on the LMTD fixed by the inlet water temperature of the test zone. In this region the heat flux values are similar in magnitude. For the high heat flux curve, the heat flux varies from 19,846 to

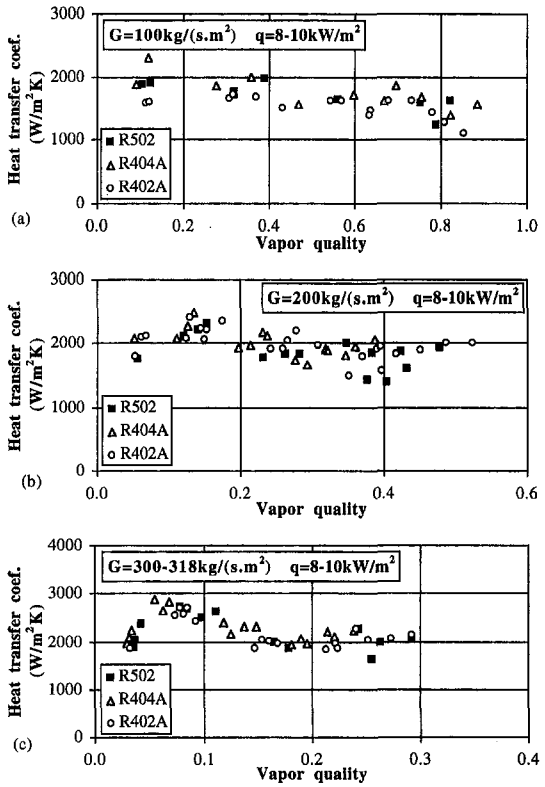

Fig. 13 R402A, R404A, and R502 results at the same mass velocity: (*a*) G = 100 kg/(s.m^2); (*b*) G = 200 kg/(s.m^2); and (*c*) G = 300–318 kg/(s.m^2)

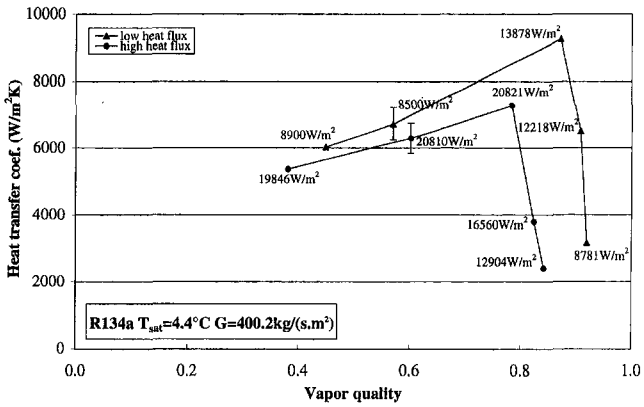

Fig. 14 The variation of the heat flux for R134a at G = 400 kg/(s.m^2) (tube diameter D = 10.92 mm)

20,821 W/m^2, while for the low heat flux curve the heat flux varies from 8500 to 13,878 W/m^2.

After the maximum value of the heat transfer coefficient, with the beginning of partial tube dryout, the measured heat flux values decrease even though the inlet water temperature is kept the same for each curve. In this region the heat flux depends on the flow pattern configuration inside the tube, i.e., how much of the tube wall is dry, which was observed to be a function of the value of the dryout heat flux upstream where dryout began.

Using an electrically heated tube the heat flux is kept artificially constant before and after the maximum value of the heat transfer coefficient so that the heat flux becomes an independent variable imposed by the experimenter. This means that in an annular flow with partial dryout the heat transfer coefficient at the top of the tube decreases while the electrical resistance tends to keep a constant heat flux, inducing a temperature increase of the tube wall.

The input variables for the general correlations found in the literature are the mass velocity, the saturation temperature, the heat flux, and the vapor quality. For the two curves in Fig. 14, the mass velocity and the saturation temperature are the same. Some values of the heat flux can be the same for data points after the maximum value of the heat transfer coefficient, in both the low and high heat flux curves (at similar vapor quality), depending on the heat flux where dryout began. For example, in the high heat flux curve the last data point has a heat flux value of 12,904 W/m^2, which corresponds to an intermediate value between 13,878 and 12,218 W/m^2 in the low heat flux curve. Since the vapor quality is very similar, the heat transfer coefficients predicted by existing correlations are essentially the same for the two data points located on the low and high heat flux curves; hence, these methods cannot distinguish between the two. Instead, there are several solutions or several heat transfer coefficients for the same mass velocity, saturation temperature, vapor quality, and heat flux since in this zone the local dry angle θ_{dry} (defined in Part 3) is dependent on the heat flux level upstream of the tube where dryout began. Electrically heated test sections cannot identify or measure these values.

9 Conclusions

Local boiling heat transfer coefficients as a function of test variables were presented for R134a, R123, R402A, R404A, and R502 evaporating inside a horizontal plain tube. Comparative results show that local flow boiling heat transfer coefficients for R404A are slightly larger than those for R502 under the same test conditions, while those for R402A are, on average, slightly smaller. At low vapor quality (from about 8 to 15 percent) a distinct maximum in heat transfer coefficient was observed and could be caused by a change in flow pattern or by a change in the contribution of the nucleate boiling and convective boiling components. At high vapor quality (>80 percent) the heat transfer coefficient decreases rapidly after the peak towards the pure vapor heat transfer coefficient. The fall off in the heat transfer coefficient after the peak is caused by the transition from annular flow to annular flow with partial dryout. The local heat transfer coefficients in annular flow with partial dryout were found to be a function of the upstream dryout heat flux.

Acknowledgments

The research was supported by the Swiss Federal Office of Energy (OFEN), Bern. The refrigerants were provided by DuPont de Nemours International S. A. of Geneva.

References

ASHRAE Handbook, 1993, ASHRAE, Atlanta, GA.

Collier, J. G., and Thome, J. R., 1994, *Convective Boiling and Condensation,* 3rd ed., Oxford University Press, Oxford.

Dittus, F. W., and Boelter, L. M. K., 1930, *University of California (Berkeley) Publications on Engineering,* Vol. 2, University of California, Berkeley, CA, p. 443.

Eckels, S. J., and Pate, M. B., 1991, "An Experimental Comparison of Evaporation and Condensation Heat Transfer Coefficients for HFC-134a and CFC-12," *Int. J. Refrigeration,* Vol. 14, pp. 70–77.

Gnielinski, V., 1976, "New Equations for Heat and Mass Transfer in Turbulent Pipe and Channel Flow," *Int. Chem. Eng.,* Vol. 16, pp. 359–368.

Hambraeus, K., 1991, "Heat Transfer Coefficient During Two-Phase Flow Boiling of HFC-134a," *Int. J. Refrigeration,* Vol. 14, pp. 357–362.

Kattan, N., 1996, *Contribution to the Heat Transfer Analysis of Substitute Refrigerants in Evaporator Tubes with Smooth or Enhanced Tube Surfaces,* Thèse 1498 (1996), Ecole Polytechnique Fédérale de Lausanne, Switzerland (in English).

REFPROP-Thermodynamic Properties of Refrigerants and Refrigerant Mixtures, version 3.04a, 1992, National Institute of Standards and Technology, Gaithersburg, MD.

Thome, J. R., and Shock, R. A. W., 1984, "Boiling of Multicomponent Mixtures," *Advances in Heat Transfer,* J. P. Hartnett and T. J. Irvine, eds., Academic Press, NY, Vol. 16, pp. 59–156.

Thome, J. R., 1990, *Enhanced Boiling Heat Transfer,* Hemisphere, NY.

Thome, J. R., 1994, "Two-Phase Heat Transfer to New Refrigerants," *10th Int. Heat Transfer Conf.,* Vol. 1, Brighton, pp. 19–41.

Thome, J. R., 1997, "Boiling of New Refrigerants: A State-of-the-Art Review," *Int. J. Refrigeration,* Vol. 19, No. 7, pp. 435–457.

Wattelet, J. P., Chato, J. C., Souza, A. L., and Christoffersen, B. R., 1992, "Evaporation Characteristics of R-12, R134a, and MP-39 at Low Fluxes," *ASHRAE Trans.,* Vol. 100, No. 1.

Wilson, E. E., 1915, "A Basis for Rational Design of Heat Transfer Apparatus," *Trans. ASME,* Vol. 37, pp. 47–70.

Flow Boiling in Horizontal Tubes: Part 3—Development of a New Heat Transfer Model Based on Flow Pattern

N. Kattan

J. R. Thome
favrat@it.dgm.epfl.ch

D. Favrat

Laboratory for Industrial Energy Systems,
Department of Mechanical Engineering,
Swiss Federal Institute of Technology,
CH-1015 Lausanne, Switzerland

A new heat transfer model for intube flow boiling in horizontal plain tubes is proposed that incorporates the effects of local two-phase flow patterns, flow stratification, and partial dryout in annular flow. Significantly, the local peak in the heat transfer coefficient versus vapor quality can now be determined from the prediction of the location of onset of partial dryout in annular flow. The new method accurately predicts a large, new database of flow boiling data, and is particularly better than existing methods at high vapor qualities ($x > 85$ percent) and for stratified types of flows.

1 Introduction

Most of the flow boiling correlations in the literature for horizontal flows are vertical tube methods with some correction to try to account for flow stratification at low flow rates. In vertical upflow, dryout in annular flow tends to occur at vapor qualities in the range from 50–75 percent and hence, few test data are taken above this threshold; consequently, these vertical tube methods are not particularly suitable for predicting local coefficients in horizontal tubes where complete evaporation of the fluid has to be modeled. In addition, most horizontal flow boiling data available in the literature were obtained with electrical heating of the test sections, which has an adverse influence on heat transfer coefficients measured with partially wetted tube walls in horizontal flows.

Recent reviews of in-tube flow boiling have been prepared by Steiner and Taborek (1992), Webb and Gupte (1992), and Thome (1994) while a summary of prediction methods can be found in Collier and Thome (1994). In Thome (1995), a critical review of flow boiling correlations for horizontal tubes was presented. The major deficiencies identified, in addition to those mentioned above, are as follows:

1 The predicted variations and peak in heat transfer coefficient versus vapor quality at a fixed mass velocity and heat flux often provide a poor match to those in the database.
2 The rapid falloff in heat transfer coefficient at high vapor quality is not predicted well.
3 The liquid convection coefficients h_L are determined with turbulent flow correlations based on tubular flow rather than film flow (i.e., as occurs in annular flow), and the two-phase convection multiplier should utilize the effective liquid velocity in the Reynolds number determined from the local void fraction to be consistent with the Dittus-Boelter correlation, rather than the Martinelli parameter which is not a function of liquid velocity.
4 Most correlations do not go to the natural limits of single-phase heat transfer at a vapor quality of 100 percent.
5 The effects of flow stratification on heat transfer have been developed primarily from statistical analysis of the underlying database using the liquid Froude number Fr_L, a criterion that alone has been proven to be ineffective for predicting the onset of flow stratification.
6 Existing correlations have no mist flow nor partial dryout threshold criteria, erroneously using wet-wall correlations for evaporation under these conditions.

In summary, while there are various positive aspects in the existing methods that can be retained in the new model, (e.g., the asymptotic approach used successfully by Steiner and Taborek (1992) for vertical upflow boiling, and the Cooper (1984) pool boiling correlation used in the correlations of Gungor and Winterton (1986, 1987)) many of the new flow boiling correlations (too numerous to mention here) are reformulations of the original methods presented by Chen (1963) for vertical tubes and by Shah (1982) for horizontal tubes.

The objective here is to develop a physically based model, albeit empirical, that incorporates three important features: (i) turbulent film flow heat transfer based on the liquid film velocity; (ii) flow pattern type; and (iii) partial wetting of the tube circumference by the evaporating liquid. For the present purposes, the complex intermittent flow pattern will be modeled as an annular flow since the trends in the heat transfer data are very similar. The stratified-wavy flow pattern and annular flow with partial dryout will be modeled as a stratified-wavy-arc flow where the wetted fraction of tube is predicted (i.e., essentially annular flow with flow boiling heat transfer around the wetted perimeter and vapor-phase heat transfer around the dry perimeter). The current heat transfer database does not include heat transfer coefficients for the stratified (S), bubbly (B), and mist flow (MF) regimes and hence, these are not yet included in the present model. In addition, local maxima in the heat transfer coefficient versus vapor quality were found in the data presented in Part 2 (see Fig. 13(c)) at very low vapor qualities. This maximum in heat transfer coefficient appears to be related to the transition from stratified-wavy flow to intermittent flow upon inspection of the new flow pattern map (comparing Fig. 13(c) in Part 2 to Figs. 15 an 16 in Part 1 at $G = 300$ kg/(s·m^2)); however, more study and test data are required to adequately confront the problem. Hence, the current flow boiling model has been limited to vapor qualities greater than 15 percent; this does not severely affect its application since the vapor quality entering direct-expansion evaporators after the expansion valve in refrigeration, air-conditioning, and heat pump systems is typically in the range from 15–30 percent.

2 Relationship Between Heat Transfer Coefficient and Flow Pattern

Figure 1 shows the local heat transfer coefficient plotted versus vapor quality at fixed mass velocity, heat flux, and saturation

Contributed by the Heat Transfer Division for publication in the JOURNAL OF HEAT TRANSFER. Manuscript received by the Heat Transfer Division October 1, 1996; revision received July 16, 1997; Keywords: Evaporation; Modeling and Scaling; Multiphase Flows. Associate Technical Editor: M. D. Kelleher.

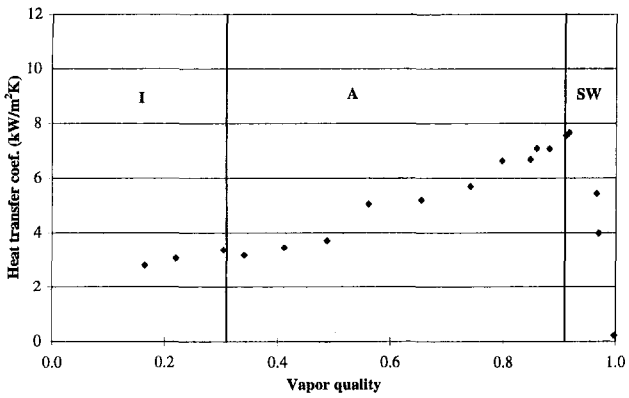

Fig. 1 R134a heat transfer coefficient at G = 300 kg/(s·m²) and T_{sat} = 4.4°C (D = 10.92 mm)

temperature with the flow pattern boundaries depicted as thick vertical lines (using the new flow pattern map in Part 1). In the annular (A) flow regime, the heat transfer coefficient rises rapidly as its evaporating liquid film thins. In the intermittent (I) flow regime, the trend in heat transfer coefficient versus vapor quality is an extension to that for annular flow. At the transition to stratified-wavy (SW) flow at the onset of partial dryout of the annular film, the heat transfer falls off very rapidly towards the data point for the vapor-phase heat transfer coefficient at x = 1.0. Therefore, it is very clear that the peak in heat transfer coefficient is determined by the point of onset of partial dryout at the top of the tube, confirmed by numerous other confrontations of heat transfer data to the new flow pattern map. The vapor quality at which the peak occurs is thus a function of fluid properties, local heat flux, and mass velocity. Accurate prediction of local heat transfer coefficients at vapor qualities after the peak is thus very dependent on being able to predict the location of the peak. In addition, in Part 2 it was shown that the local coefficient after the peak is a function of the local heat flux at the peak, since the heat flux controls the vapor quality at which partial tube dryout begins. Thus, this is another important aspect to include in the present model.

The new model proposed here is limited to the intermittent, annular, stratified-wavy and stratified flow patterns; no heat transfer data for the stratified flow regime were obtained experimentally in Part 2 and thus the method cannot be verified yet in that regime. The first step is to develop a physical model for each flow pattern type; the second step is to find a common formulation for all the flow patterns in order to build a comprehensive model with smooth transitions in the heat transfer coefficient as the flow changes from one pattern to another.

3 Heat Transfer Flow Models

Four models were developed to predict local heat transfer coefficients: an annular flow model, a stratified flow model, a stratified-wavy flow model and a separate stratified-wavy flow model for annular flow with partial dryout occurring at high vapor qualities.

Figure 2 illustrates the cross-sectional flow pattern configurations adopted for the model. Transition from annular (A) flow to stratified-wavy (SW) flow as the mass velocity is decreased or from annular flow to annular flow with partial dryout (classified as SW on the flow map) with increasing vapor quality, the liquid-vapor interface becomes unstable as a result of the Kelvin-Helmholz instability arising from the two fluid layers of different density flowing horizontally along the top of the tube at different velocities. Note that intermittent (I) flow is modeled as annular flow since the data trends in heat transfer coefficient versus vapor quality for these two regimes are very similar.

3.1 Stratified-Wavy Flow and Annular Flow With Partial Dryout Model. At a fixed vapor quality in Fig. 2, the transition from annular flow (A) to stratified flow (S) should generate the intermediate configurations in the stratified-wavy flow (SW) regime. Thus, in the stratified-wavy flow regime it

Nomenclature

A = cross-section area, m²
B_o = scaling factor (=1.0)
c_p = specific heat, J/kg K
C = convective boiling leading constant
D = tube diameter, m
F_c = mixture correction factor
g = acceleration of gravity, m/s²
G = mass velocity, kg/s m²
G_{high} = mass velocity at the transition annular flow curve, kg/s m²
G_{low} = mass velocity at the transition stratified-wavy flow curve, kg/s m²
h_{cb} = convective boiling heat transfer coefficient, W/m²K
h_{id} = ideal heat transfer coefficient, W/m²K
h_{nb} = nucleate boiling heat transfer coefficient, W/m²K
h_{tp} = two-phase heat transfer coefficient, W/m²K
h_v = vapor phase heat transfer coefficient, W/m²K
h_{wet} = liquid phase heat transfer coefficient, W/m²K
Δh_v = latent heat of vaporization, J/kg
k = thermal conductivity, W/mK
m = Reynolds number exponent
M = molecular weight, kg/kmol
P = pression, Pa
P_{crit} = critical pressure, Pa
P_r = reduced pressure [P/P_{crit}]
q = heat flux, W/m²
R = tube radius, m
T_{sat} = saturation temperature, K (or °C)
ΔT_{bp} = boiling range or temperature glide, K
u = velocity, m/s
x = vapor quality
$x_{all\ vapor}$ = 100 percent vapor quality
x_{max} = vapor quality at the intersection of annular flow and mist flow transition curves
x_{cr} = critical vapor quality

Greek

α = void fraction
β_L = liquid mass transfer coefficient (=0.0003 m/s), m/s
δ = liquid film thickness, m
ϵ = relative error
θ_{dry} = dry angle, radians
θ_{max} = dry angle for x_{max}, radians
θ_{strat} = stratified angle, radians
μ = dynamic viscosity, N s/m²
ρ = density, kg/m³
σ = standard deviation
σ_L = liquid surface tension, N/m

Dimensionless Numbers

Bo = boiling number ($q/\Delta h_v G$)
Fr_L = Froude number of liquid phase ($G^2/\rho_L^2 gD$)
Pr = Prandtl number ($c_p\mu/k$)
Re_L = Reynolds number of liquid phase ($4GD(1-x)\delta/(1-\alpha)\mu_L$)
Re_v = Reynolds number of vapor phase ($GD_x/\alpha\mu_v$)

Subscripts

cal = calculated
exp = experimental
id = ideal
L = liquid
sat = saturation
strat = stratified
tp = two phase
v = vapor

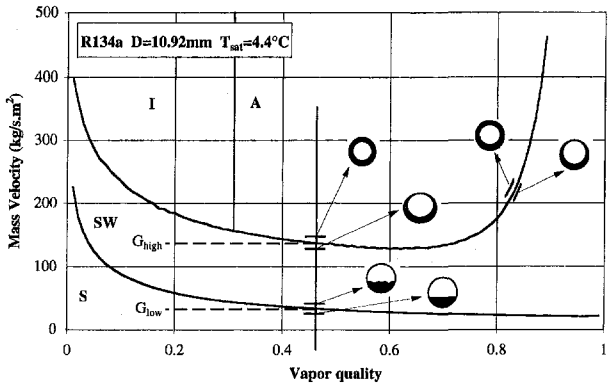

Fig. 2 The new flow pattern map plotted with the stratified-wavy transition curve at a heat flux of 22,500 W/m²

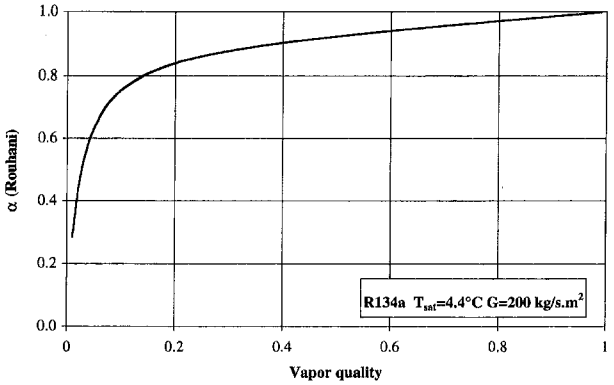

Fig. 4 Rouhani void fraction correlation for R134a at T_{sat} = 4.4°C and G = 200 kg/(s m²)

is assumed that the liquid will form a thin film of uniform thickness that partially wets the tube. This hypothesis, for the prediction of the stratified-wavy flow configuration (or annular flow with partial dryout configuration at high vapor quality), requires a new parameter linking the stratified flow configuration shown on the left in Fig. 3(a) to the annular flow configuration at the left in Fig. 3(b). One convenient parameter for this linking is the dry angle θ_{dry} represented in Fig. 3(b), which denotes the dry upper fraction of the tube.

According to Fig. 3(a) in the diagram at the left, the stratified angle is calculated by the following equation:

$$A_L = 0.5R^2[(2\pi - \theta_{strat}) - \sin(2\pi - \theta_{strat})], \qquad (1)$$

where $A_L = A(1 - \alpha)$ and is the liquid cross-sectional area calculated by using the Rouhani-Axelsson void fraction correlation (Rouhani and Axelsson, 1970) for α and θ_{strat} is in radians. Equation (1) is solved iteratively to find the value of the stratified angle θ_{strat}. This void fraction equation was selected among many others available based on its recommendation by Steiner (1993) and its use in various two-phase pressure drop correlations. It is given as

$$\alpha = \frac{x}{\rho_v}\left[\left(1 + 0.12(1 - x)\left(\frac{x}{\rho_v} + \frac{1 - x}{\rho_L}\right)\right) + \frac{1.18(1 - x)[g\sigma_L(\rho_L - \rho_v)]^{0.25}}{G\rho_L^{0.5}}\right]^{-1}. \qquad (2)$$

Figure 4 shows the void fraction variation for R134a, which for $x > 0.15$ varies only from 0.8 to 1.0.

The transition from annular flow to stratified flow, illustrated in Fig. 3(b), is based now on the concept of the dry angle θ_{dry} which is related to the stratified angle θ_{strat}. As can be discerned from Fig. 2 (at a fixed vapor quality), the dry angle θ_{dry} is a function of the mass velocity and varies from $\theta_{dry} = 0$ to $\theta_{dry} = \theta_{strat}$ corresponding to the mass velocities G_{high} and G_{low}, respectively, which in turn are functions of vapor quality. Different types of expressions, linking the dry angle to the mass velocity, were analyzed for the new heat transfer correlation without significant differences in the predictions. Therefore, a simple linear function is assumed between the values of G_{high} and G_{low}, defined as follows:

$$\theta_{dry} = \theta_{strat}\frac{(G_{high} - G)}{(G_{high} - G_{low})}. \qquad (3)$$

Figure 5 shows the basic model used to predict the heat transfer coefficient for stratified-wavy flow or annular flow with partial dryout configurations. The mean thin liquid film thickness is designated by δ, while θ_{dry} is the dry angle.

It is assumed that at a local cross section of the evaporator tube, the mean heat transfer around the periphery h_{tp} is a direct proration of the liquid and vapor heat transfer coefficients for the wet and dry perimeter segments; therefore, the basic equation is

$$h_{tp} = \frac{\theta_{dry}h_v + (2\pi - \theta_{dry})h_{wet}}{2\pi}. \qquad (4)$$

The heat transfer coefficient on the wetted portion of the tube

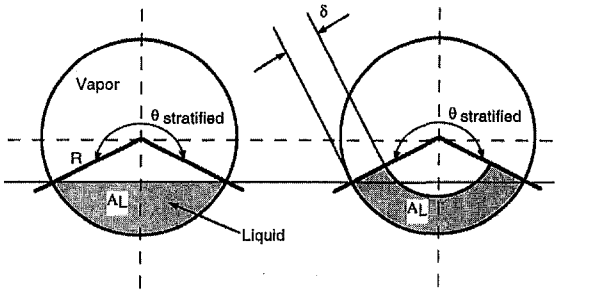

Fig. 3(a) Equivalent configuration of the stratified flow regime

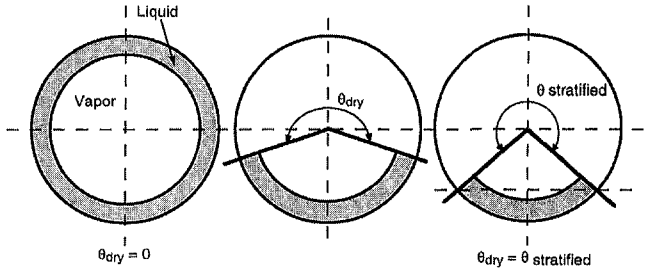

Fig. 3(b) Transition from annular flow to stratified flow

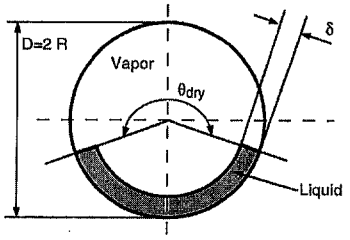

Fig. 5 Model for stratified-wavy flow and annular flow with partial dryout

is comprised of the nucleate boiling and the convective boiling contributions. The asymptotic model of Steiner and Taborek (1992) was selected to link these two heat transfer mechanisms according to the following equation:

$$h_{\text{wet}} = (h_{nb}^3 + h_{cb}^3)^{1/3}, \tag{5}$$

where h_{nb} is the nucleate pool boiling heat transfer coefficient defined by the Cooper (1984) dimensional correlation:

$$h_{nb} = 55 P_r^{0.12} (-\log_{10} P_r)^{-0.55} M^{-0.5} q^{0.67}, \tag{6}$$

where h_{nb} is in W/m^2K, P_r is the reduced pressure, M is the fluid molecular weight, and q is the heat flux in W/m^2. A surface roughness of 1 μm is assumed so the surface roughness correction is not required. This correlation was shown to accurately predict nucleate boiling coefficient of the new refrigerants in Thome (1994). No nucleate boiling suppression factor is used in Eq. (5) since the asymptotic model already, by itself, reduces the nucleate boiling contribution as the convective boiling contribution becomes dominant, i.e., using a boiling suppression factor would be redundant. The convective liquid flow boiling heat transfer coefficient h_{cb} is determined by the following equation:

$$h_{cb} = C \, \text{Re}_L^m \, \text{Pr}_L^{0.4} \frac{k_L}{\delta}, \tag{7}$$

while the vapor heat transfer coefficient h_v is determined with the Dittus-Boelter correlation (Dittus and Boelter, 1930) for tube flow, as follows:

$$h_v = 0.023 \, \text{Re}_v^{0.8} \, \text{Pr}_v^{0.4} \frac{k_v}{D}. \tag{8}$$

The leading constant C and the Reynolds number exponent m for the liquid heat transfer coefficient in Eq. (7) are determined later on the basis of the experimental data. The vapor Reynolds number is referred to the tube diameter as its characteristic dimension, while the liquid Reynolds number is referred to the thin liquid film thickness (similar to turbulent film condensation on a vertical plate such as defined in Incropera (1990)):

$$\text{Re}_L = \frac{4\rho_L u_L \delta}{\mu_L} \tag{9a}$$

$$\text{Re}_v = \frac{\rho_v u_v D}{\mu_v}. \tag{9b}$$

The liquid and the vapor velocity are calculated as follows:

$$u_L = \frac{AG(1-x)}{\rho_L A_L} = \frac{AG(1-x)}{\rho_L A(1-\alpha)} = \frac{G(1-x)}{\rho_L(1-\alpha)} \tag{10a}$$

$$u_v = \frac{AGx}{\rho_v A_v} = \frac{AGx}{\rho_v A\alpha} = \frac{Gx}{\rho_v \alpha}, \tag{10b}$$

such that the liquid and the vapor Reynolds numbers become

$$\text{Re}_L = \frac{4G(1-x)\delta}{(1-\alpha)\mu_L} \tag{11a}$$

$$\text{Re}_v = \frac{GxD}{\alpha\mu_v}. \tag{11b}$$

Finally, the liquid film flow convective boiling heat transfer coefficient h_{cb} and the vapor heat transfer coefficient h_v are reformulated as follows:

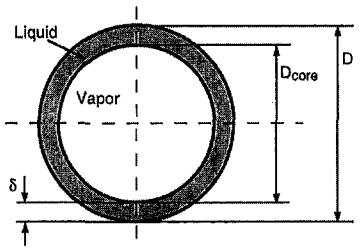

Fig. 6 Annular flow configuration

$$h_{cb} = C\left(\frac{4G(1-x)\delta}{(1-\alpha)\mu_L}\right)^m \left(\frac{c_{p_L}\mu_L}{k_L}\right)^{0.4} \frac{k_L}{\delta} \tag{12}$$

$$h_v = 0.023\left(\frac{GxD}{\alpha\mu_v}\right)^{0.8} \left(\frac{c_{p_v}\mu_v}{k_v}\right)^{0.4} \frac{k_v}{D}. \tag{13}$$

Using the Rouhani-Axelsson void fraction correlation, the thin liquid film thickness δ is calculated as follows:

$$\delta = \frac{A_L}{R(2\pi - \theta_{\text{dry}})} = \frac{A(1-\alpha)}{R(2\pi - \theta_{\text{dry}})} = \frac{\pi D(1-\alpha)}{2(2\pi - \theta_{\text{dry}})}. \tag{14}$$

Thus, the present model is based on turbulent liquid film flow rather than on tubular flow as in past correlations. In all previous correlations, h_{cb} was based on the inside tube diameter and multiplied by an empirical enhancement factor usually related to the Martinelli number, an approach that does not explicitly model the liquid velocity in two-phase flow and is thus inconsistent with the use of the Dittus-Boelter correlation. Instead in the present model, the void fraction is used to determine the thin liquid film thickness and the vapor and liquid velocities, without the need of any additional physically meaningless empirical enhancement factor. This new approach can be easily applied and the values of the film flow constants C and m determined via the heat transfer data.

3.2 Stratified Flow Model. For the stratified flow (S) model, the same procedure developed for stratified-wavy flow (SW) is applied for the entire stratified flow region, except for the calculation of the dry angle θ_{dry} predicted by Eq. (3) which is assumed to be equal to the stratified angle θ_{strat} calculated by using Eq. (1).

3.3 Annular and Intermittent Flow Model. For the annular flow model shown in Fig. 6, the dry angle θ_{dry} predicted by Eq. (3) is assumed to be equal to zero ($\theta_{\text{dry}} = 0$) in all the annular and intermittent flow regions. The same procedure developed for stratified-wavy flow is applied here, and the thin liquid film δ is assumed to be uniformly distributed. The liquid Reynolds number for film flow in Eq. (11(a)) reduces to the usual one for tubes only in the annular flow regime, but the characteristic dimension in Eq. (12) is the liquid film thickness δ, not the tube diameter D as in the following expression:

$$\text{Re}_L = G(1-x)D/\mu_L \tag{15}$$

used in other previous correlations.

3.4 Model of Annular Flow With Partial Dryout at High Vapor Quality. According to Eq. (3), the dry angle θ_{dry} in the stratified-wavy region is calculated proportional to the mass velocity using the dry angle equal to θ_{strat} at the stratified flow transition curve (S/SW) and the dry angle $\theta_{\text{dry}} = 0$ at the transition curve from annular to stratified-wavy flow (A/SW). This calculation is made "vertically" at a given vapor quality. Figure 7 shows the limit of the model at higher vapor quality

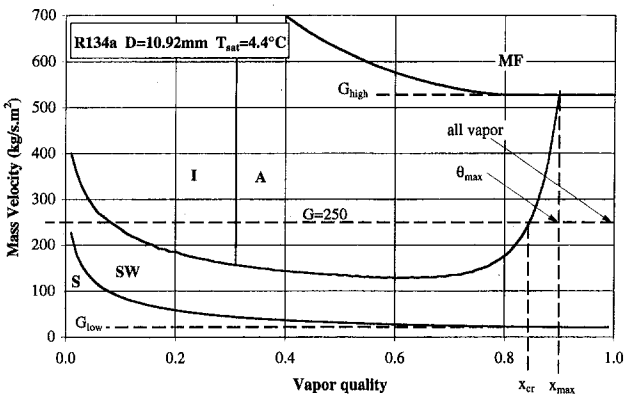

Fig. 7 Limit of the stratified-wavy flow model at high vapor quality (q = 22,500 W/m² for the new transition stratified-wavy curve)

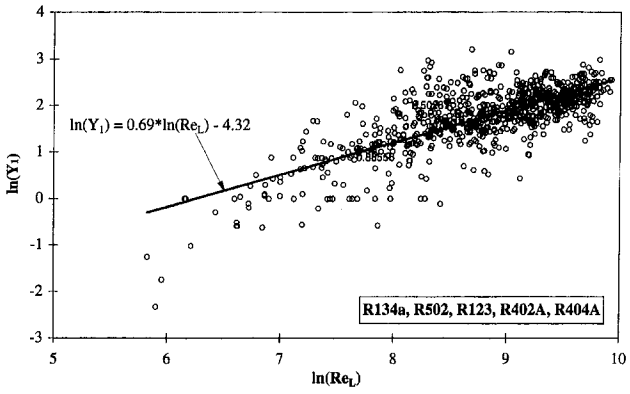

Fig. 8 Determination of the leading constant C and the Reynolds number exponent m

and high mass velocity when the transition curve (S/SW) intersects the mist flow transition curve. For vapor qualities higher than the vapor quality threshold x_{max}, the transition curve (S/SW) does not exist anymore and the mass velocity G_{high}, used in Eq. (3), is no longer defined. One solution is to calculate the dry angle θ_{dry} "horizontally" for these conditions, that means at a fixed mass velocity as a function of x (from x_{max} to the natural limit of 2π for completely dry wall at $x = 1.0$). For example, at $G = 250$ kg/(s·m²), the dry angle θ_{dry} is calculated by the "vertical" method, developed for the stratified-wavy region from x_{cr} to x_{max}, and by the "horizontal" method, explained below from x_{max} to $x_{all\ vapor} = 1.0$. At the vapor quality x_{max}, the connection between the two methods is respected by having the same dry angle in both directions. Thus, the dry angle θ_{max}, represented in Fig. 7 for $G = 250$ kg/(s·m²) and calculated by using Eq. (3), is kept the same for the calculation of θ_{dry} in the vapor quality zone from x_{max} to $x_{all\ vapor}$.

For qualities greater than x_{max} it will be assumed that the dry angle is a linear function of the vapor quality from θ_{max} to $\theta_{all\ vapor} = 2\pi$:

$$\theta_{dry} = (2\pi - \theta_{max}) \frac{(x - x_{max})}{(x_{all\ vapor} - x_{max})} + \theta_{max}. \quad (16)$$

x_{max} is the vapor quality calculated at the point of intersection of the stratified-wavy flow curve with the mist flow curve. However, as discussed in Part 1 the mist flow transition curve requires further experimental verification in this zone. In the present analysis, this problem is bypassed by fixing the maximum value of the mass velocity G_{high} at 500 kg/(s·m²), instead of using an untested mist flow curve. The calculation of the vapor quality x_{max} is hardly affected by this approximation because at the end of the stratified-wavy transition curve the slope tends to be nearly vertical. Note, however, that x_{max} is a function of q at x_{cr} in the calculation of h_{tp} after the peak in heat transfer coefficient versus vapor quality.

4 Heat Transfer Correlation Development

The leading constant C and the Reynolds number exponent m, defined in Eq. (7) for the heat transfer coefficient of the turbulent annular liquid film, are determined on the basis of the experimental data reported in Part 2 by the following method.

Equation (5) and Eq. (4) are rearranged as follows:

$$h_{wet} = \frac{2\pi h_{tp} - \theta_{dry} h_v}{(2\pi - \theta_{dry})} = (h_{nb}^3 + h_{cb}^3)^{1/3}. \quad (17)$$

Solving for h_{cb} in Eq. (17), h_{cb} is equated to Eq. (7), such that:

$$h_{cb} = \left[\left(\frac{2\pi h_{tp} - \theta h_v}{(2\pi - \theta)} \right)^3 - h_{nb}^3 \right]^{1/3} = C\, \mathrm{Re}_L^m\, \mathrm{Pr}_L^{0.4} \frac{k_L}{\delta}. \quad (18)$$

Equation (18) is then rearranged as follows:

$$\frac{\left[\left(\frac{2\pi h_{tp} - \theta h_v}{(2\pi - \theta)} \right)^3 - h_{nb}^3 \right]^{1/3}}{\mathrm{Pr}_L^{0.4} \frac{k_L}{\delta}} = Y_1 = C\, \mathrm{Re}_L^m. \quad (19)$$

In substituting Y_1 for the left-hand side of Eq. (19), and applying a logarithmic function to both sides of the equation, the following equation is obtained:

$$\ln(Y_1) = m \ln(\mathrm{Re}_L) + \ln(C). \quad (20)$$

The above equation has two unknowns (C and m) and has the form of a straight line of slope, m, and Y-intercept, ln (C). Y_1 and Re_L are calculated by using all the experimental data for the five refrigerants and the results are presented in Fig. 8. The Reynolds number exponent and the leading constant were found to be equal to $m = 0.69$ and $C = 0.0133$, respectively. Data with vapor quality lower than 15 percent were not treated in this analysis because the present model does not attempt to handle the processes involved in horizontal transition from stratified-wavy flow to intermittent flow at low vapor quality.

Only heat transfer test zones 2, 3, 5, and 6 (see Part 2) are considered in this evaluation to exclude possible entrance effects in zones 1 and 4. The heat transfer coefficient in test zone 4 is affected by the U-bend located between the test zone 3 and the test zone 4 and the heat transfer coefficient in test zone 1 may be affected by the inlet conditions induced by the electrical preheater and the connecting line.

The procedure for calculating the local heat transfer coefficient h_{tp} is summarized in Fig. 9. The input values are the mass

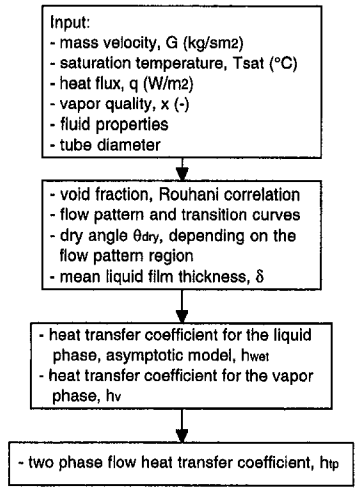

Fig. 9 Flow boiling heat transfer coefficient calculation

Table 1 Two-phase flow boiling data compared to new and existing methods

Correlations	Deviation	Refrigerants						Total
	%	R134a	R134a *	R502	R123	R402A	R404A	Mean error
Jung	Standard	41.3	88.2	45.1	30.2	27.4	23.2	42.6
	Mean	18.8	37.4	17.9	20.3	16.2	14.8	20.9
	Average	-0.6	25.3	1.7	6.8	-6.4	-5.4	3.6
Shah	Standard	21.6	47.7	23.2	28.4	18.2	15.0	25.7
	Mean	24.6	33.6	27.8	20.9	28.5	24.6	26.7
	Average	-18.7	-7.4	-22.5	-5.4	-25.4	-22.3	-16.9
VDI	Standard	27.4	47.0	32.1	27.9	28.4	20.1	30.5
	Mean	29.6	30.8	31.6	20.7	22.4	16.6	25.3
	Average	27.4	1.1	29.4	-4.2	-0.1	-1.7	8.6
GW86	Standard	33.4	58.9	33.6	23.4	29.7	26.4	34.2
	Mean	22.0	39.5	22.9	15.7	24.3	20.9	24.2
	Average	11.9	-1.7	10.9	0.0	18.7	13.4	8.9
GW87	Standard	24.2	48.6	23.8	26.1	17.5	15.3	25.9
	Mean	17.6	38.1	19.7	18.4	18.4	15.0	21.2
	Average	-7.1	-14.9	-13.1	-4.8	-14.2	-11.2	-10.9
Present	Standard	17.1	20.0	15.8	16.6	18.0	13.1	16.8
	Mean	12.8	13.6	12.8	14.9	14.9	11.0	13.3
	Average	2.4	4.3	1.4	-6.3	6.8	3.4	2.0
Data points		420	101	91	66	233	230	1141
T_{sat} (°C)		-1.3...10.3	4.44	2.50	30.7	-1.3...10.2	-1.3...10.2	
P_{sat} (bar)		2.8...4.2	3.42	6.19	1.12	6.3...8.9	5.9...8.4	
P_{crit} (bar)		41.35	41.35	40.75	36.07	41.35	37.32	
P_r (-)		0.068...0.102	0.083	0.152	0.031	0.152...0.215	0.158...0.225	
σ_L (mN/m)		11.87...10.2	11.04	9.3	14.5	9.2...7.67	7.95...6.41	
Pr_L (-)		3.94...3.76	3.84	3.65	5.47	3.99...3.65	3.18...3.14	
G (kg/(s.m^2))		100...500	100...400	100...300	100...300	100...318	100...318	
x (%)		4...90	18...100	8...97	7...98	9...91	7...98	
q (kW/m^2)		3.2...36.54	0.44...22.58	3.29...27.72	3.7...24.65	3.36...28.6	3.42...30.57	
M (kg/kmol)		102.03	102.03	111.63	152.93	101.55	97.60	
Re_L (-)		981...20399	199...10298	732...14222	961...7554	1705...16675	1601...18685	
Re_v (-)		21704...234583	38177...376804	35237...249786	25386...136766	40523...247297	41780...273245	
* tube diameter=10.92mm								

velocity, the saturation temperature, the heat flux, the vapor quality, and the fluid properties. The transition boundary curves on the flow pattern map are determined first, and then the flow pattern for the input conditions is determined. After that, the dry angle θ_{dry} is calculated with the corresponding model defined for each flow pattern region if necessary, using the void fraction correlation. Once the dry angle θ_{dry} is known, the heat transfer coefficients for the wet wall and the dry wall are determined using the void fraction and the asymptotic model. Finally, the two-phase flow heat transfer coefficient h_{tp} is calculated proportional to the liquid and the vapor heat transfer coefficients depending on the dry angle θ_{dry}.

5 Comparison of the New Correlation With the Experimental Flow Boiling Data

Comparisons with our data have been carried out with five existing correlations for horizontal flow boiling. The results are shown in Table 1. Note that since the mixture's mass transfer effect F_c of Thome (1986) (for flow boiling of zeotropic mixtures) is higher than 0.98, it was not included in evaluating the above correlations for R402A and R404A, but would have had little effect for these very small boiling range mixtures (<1.0°C). Note that Jung et al. (1989) and Steiner (1993) have their own mixture factors for refrigerant mixtures, also not included here for the same reason.

Three criteria were used to analyze the accuracy of each correlation: the standard deviation, the mean deviation, and the average deviation, defined, respectively, by the following equations:

$$\sigma = \frac{1}{n}\left(\sum_{i=1}^{n} \epsilon_i^2\right) - (\bar{\epsilon})^2, \tag{21a}$$

$$|\bar{\epsilon}| = \frac{1}{n}\sum_{i=1}^{n} |\epsilon_i|, \tag{21b}$$

and

$$\bar{\epsilon} = \frac{1}{n}\sum_{i=1}^{n} \epsilon_i, \tag{21c}$$

where the relative error for each data point is calculated as follows:

$$\epsilon_i = \frac{(h_{cal} - h_{exp})}{h_{exp}}, \tag{22}$$

where h_{cal} and h_{exp} are the calculated and the experimental values, respectively. The ratio of the calculated heat transfer coefficient to the measured heat transfer coefficient plotted versus the vapor quality is presented in Fig. 10.

The mean deviation in Table 1, for all the existing correlations tested for different fluids for all flow regimes, varies from 20.9 percent to 26.7 percent. The Jung et al. (1989) and the Gungor and Winterton (1987) correlations gave the smallest mean deviation values of about 21 percent. The mean deviation is 13.3 percent for the present correlation. The standard deviation for all the existing correlations varies from 25.7 percent to 42.6 percent, while for the present correlation the standard deviation is 16.8 percent. The average deviation is quite small

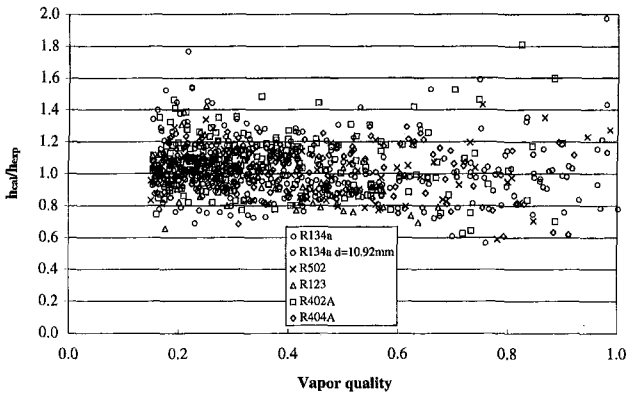

Fig. 10 The ratio of the calculated heat transfer coefficient to the measured heat transfer coefficient versus the vapor quality

for all correlations, i.e., the test data tend to be "centered" by the correlational predictions and not skewed. The larger standard deviations of the existing correlations therefore represent poor modelling of (i) the slope of the heat transfer coefficient as a function of the vapor quality, (ii) the peak in the heat transfer coefficient, (iii) the fall-off in the heat transfer coefficient with partial tube wetting after the peak, and (iv) the adverse effects of flow stratification.

The objective of the new correlation is to predict the heat transfer coefficient in the vapor quality range from 15 percent to 100 percent and to especially improve the heat transfer coefficient prediction at high vapor quality from 85 percent to 100 percent, where few data tend to be found in flow boiling databanks. Gungor and Winterton (1987) observed a larger error in the prediction of the heat transfer coefficient for data points having a vapor quality higher than 95 percent for all the existing correlations that they tested. This zone is very important in thermal design because the falloff in the heat transfer coefficient in the partial dryout region has a significant effect on the tube length of direct-expansion evaporators.

In Table 1, for the R134a results with the tube diameter of 10.92 mm, about 30 percent of those data (101 points) are for vapor qualities higher than 85 percent. The mean deviation of the present correlation is 13.6 percent for all the R134a data with the tube diameter of 10.92 mm and the standard deviation is 20 percent, while for all the other correlations the mean deviation varies from 30.8 percent to 39.5 percent and the standard deviation varies from 47.0 percent to 88.2 percent. Table 2 instead shows the statistical deviations estimated only for data points with the vapor quality lying between 85 percent to 100 percent. In this case, the mean deviation of the present correlation is 16.3 percent, while for the other correlations the mean deviation varies from 59.1 percent to 101.3 percent, and the standard deviation is even much more.

Table 3 shows the statistical deviations estimated only for data points in the intermittent and annular flow regime, which all of the methods predicted reasonably well. The present model, based on turbulent film flow of the annular liquid ring rather than tubular flow in the existing correlations, requires only the void fraction to be calculated to model the effect of liquid velocity on this process. In contrast, the existing correlations do not model this process mechanistically and utilize empirical factors such as E_1, E_2, E_3, and F_{tp}, but do not really predict the effect of two-phase flow on liquid velocity (as should be done in modifying the Dittus-Boelter type of correlation). Table 3 also again shows that the present test data are comparable to those in other independent studies used to develop these five existing correlations.

Table 4 shows the statistical deviations estimated only for data points in the stratified-wavy flow regime. The present model predicts the flow boiling data much better in this regime compared to the existing correlations. This means that the stratified flow correction factors in those correlations do not represent the data trends very well.

The new flow boiling model predicts the heat transfer coefficients well at high vapor quality, while all the other correlations tested have very large errors or are completely incapable of modeling this data since they do not recognize the onset of dryout. In this region, the heat transfer coefficient decreases rapidly with increasing vapor quality, and a small change in the vapor quality leads to a large variation in the heat transfer coefficient. Consequently, the predictive accuracy of the new model using only a linear function of the dry angle θ_{dry}, and not an empirically fit expression, can be considered to be good, considering the sensitivity of these data to small experimental errors in vapor quality. For data in the annular flow regime, the standard deviation of the new model is very similar to the Jung et al. (1989), Shah (1882), and Gungor and Winterton (1986, 1987) correlations. However, the mean deviation for all existing correlations tested varies from 12.5 percent to 25 percent while for the new model the mean deviation is only 11.9 percent.

6 Comparison of the New Correlation With Existing Correlations

The flow pattern map for R134a at a saturation temperature of 10°C and tube diameter of 12 mm is shown in Fig. 11. Figures 12 to 14 show the shapes of the curves of the new model evaluated at different mass velocities and compared to the five other correlations tested. Only the new correlation predicts the sharp peak and dropoff of the heat transfer coefficient at high vapor quality and high mass velocity, typical of those illustrated in Fig. 1 and also observed in many other published data sets. The slope of the Jung et al. correlation is similar to the new correlation from about 20 percent to 80 percent vapor quality and the heat transfer coefficient values are very close to those predicted by the new correlation for G = 300 kg/($s \cdot m^2$) and 200 kg/($s \cdot m^2$). The smallest difference between the heat transfer coefficient predicted by the correlations is located at about 50 percent vapor quality. Figure 15 shows a comparison of the new correlation to the Gungor and Winterton (1986), Jung et al., and Steiner correlations, evaluated with the R134a experimental data test conditions for each data point.

7 Influence of Heat Flux and Mass Velocity in the New Correlation

Figure 16 shows the influence of the heat flux on the R134a heat transfer coefficient predicted by the new plain tube correla-

Table 2 Statistical deviations for data points at vapor qualities higher than 85 percent

Correlations	Deviation	%
Jung	Standard	163.1
	Mean	101.3
	Average	86.6
Shah	Standard	85.8
	Mean	61.5
	Average	11.8
VDI	Standard	84.1
	Mean	59.1
	Average	15.7
GW86	Standard	102.2
	Mean	70.9
	Average	20.8
GW87	Standard	88.9
	Mean	66.4
	Average	6.7
Present	Standard	26.3
	Mean	16.3
	Average	8.2
Total Data points		27
R134a, D=10.92mm		

Table 3 Comparison of the new correlations with intermittent and annular flow boiling data

Correlations	Deviation	Refrigerants						Total
	%	R134a	R134a *	R502	R123	R402A	R404A	Mean error
Jung	Standard	13.7	9.3	13.6	14.5	12.9	10.8	12.5
	Mean	13.7	9.5	11.9	14.3	13.5	11.8	12.5
	Average	-9.2	-6.6	-7.4	-10.4	-10.3	-10.7	-9.1
Shah	Standard	12.6	11.2	12.1	13.2	10.9	9.7	11.6
	Mean	25.2	25.4	26.6	20.4	27.7	24.5	25.0
	Average	-24.3	-25.4	-26.5	-19.5	-27.6	-24.5	-24.6
VDI	Standard	20.5	18.1	23.2	16.7	21.6	16.9	19.5
	Mean	24.7	20.7	27.3	14.7	18.6	15.2	20.2
	Average	22.3	-15.9	24.9	-7.5	-2.5	-3.5	3.0
GW86	Standard	19.1	16.2	20.5	14.1	19.5	16.2	17.6
	Mean	14.8	26.7	18.1	12.2	17.1	13.6	17.1
	Average	2.9	-25.0	5.4	-3.8	10.2	6.0	-0.7
GW87	Standard	14.4	12.3	14.3	12.9	13.4	11.9	13.2
	Mean	16.1	33.0	17.8	15.6	17.5	13.9	19.0
	Average	-12.5	-33.0	-16.0	-14.1	-15.3	-12.8	-17.3
Present	Standard	16.4	11.0	13.6	16.2	14.6	10.8	13.8
	Mean	12.1	8.3	11.7	14.1	14.7	10.5	11.9
	Average	3.3	-1.1	4.9	-4.6	11.2	6.7	3.4
Data points		371	76	66	46	175	180	914
* tube diameter=10.92mm								

Table 4 Comparison of the new correlations with stratified-wavy flow boiling data

Correlations	Deviation	Refrigerants						Total
	%	R134a	R134a *	R502	R123	R402A	R404A	Mean error
Jung	Standard	81.9	131.9	74.0	32.1	43.9	37.1	66.8
	Mean	41.9	96.6	30.8	26.3	22.1	22.6	40.0
	Average	38.5	92.3	21.4	24.0	2.4	8.0	31.1
Shah	Standard	32.7	69.1	35.8	32.2	27.7	22.8	36.7
	Mean	21.8	51.8	30.3	21.5	30.2	24.9	30.1
	Average	6.6	29.9	-14.0	8.7	-20.7	-16.5	-1.0
VDI	Standard	39.9	66.4	44.2	35.5	39.0	26.2	41.9
	Mean	52.2	52.9	40.9	26.7	30.8	20.3	37.3
	Average	50.7	36.0	39.0	-1.0	5.4	3.0	22.2
GW86	Standard	50.0	82.2	49.5	29.5	38.2	36.0	47.6
	Mean	54.9	67.4	33.4	19.3	40.2	39.8	42.5
	Average	52.6	47.0	22.8	3.7	37.6	32.7	32.7
GW87	Standard	39.5	70.5	35.9	32.1	23.9	21.1	37.2
	Mean	24.2	49.5	23.6	21.3	20.4	17.9	26.1
	Average	17.4	22.7	-6.9	4.5	-11.8	-7.2	3.1
Present	Standard	19.5	28.1	17.4	16.8	20.7	14.7	19.5
	Mean	16.2	24.5	15.2	15.8	15.4	12.2	16.6
	Average	-1.9	15.9	-6.3	-8.1	-3.1	-5.0	-1.4
Data points		49	25	25	20	58	50	227
* tube diameter=10.92mm								

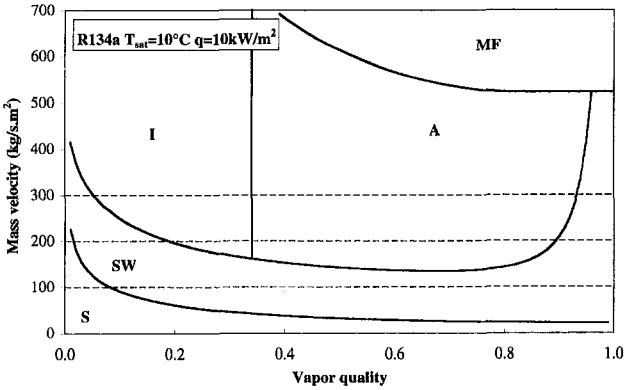

Fig. 11 The new flow pattern map for R134a

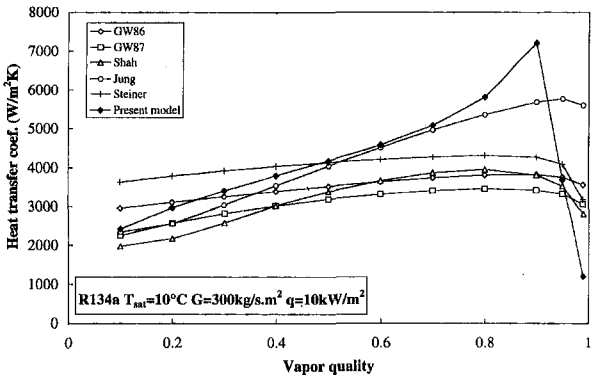

Fig. 12 Comparison of the new correlation for R134a at G = 300 kg/(s · m^2) with different existing correlations

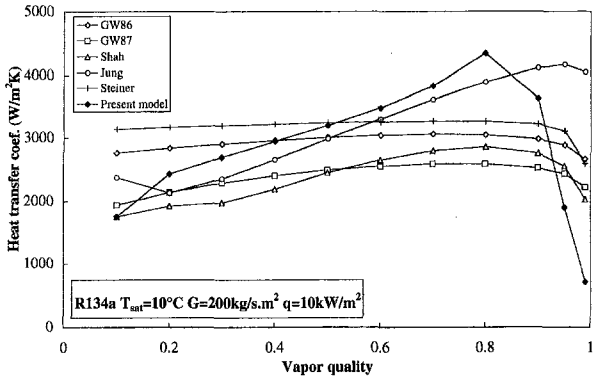

Fig. 13 Comparison of the new correlation for R134a at G = 200 kg/(s · m^2) with different existing correlations

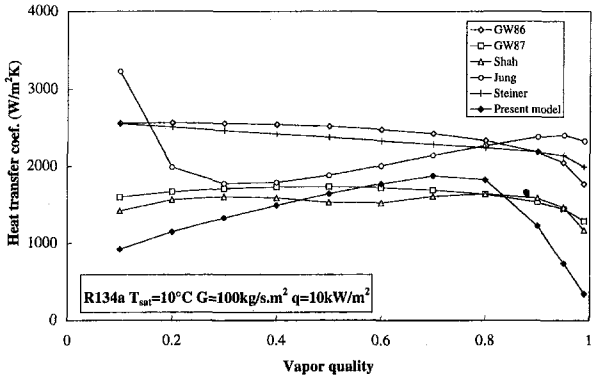

Fig. 14 Comparison of the new correlation for R134a at G = 100 kg/(s · m^2) with different existing correlations

tion for three different mass velocities and three different heat fluxes. As expected, the influence of the heat flux is more important at low vapor quality when the pool boiling contribution is dominant. At the same mass velocity this influence diminishes with increasing vapor quality where the convective boiling contribution becomes dominant. This tendency is less pronounced at high mass velocity, as shown in Fig. 16. Also, the shape of the curve of heat transfer coefficient versus vapor quality is shown to change appropriately as a function of mass velocity, heat flux, and flow pattern, similar to experimental data. In Fig. 16 the predicted effect of the heat flux and mass velocity on the location and magnitude of the peak in heat transfer coefficient versus vapor quality is also clearly shown. Note also that after the peak, the fall off in the heat transfer coefficient is sharper with a higher slope at higher mass velocity.

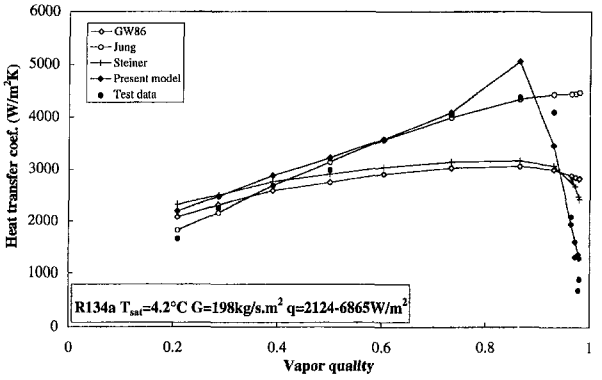

Fig. 15 Comparison of the new correlation with R134a experimental data at G = 198 kg/(s · m^2) and with three existing correlations

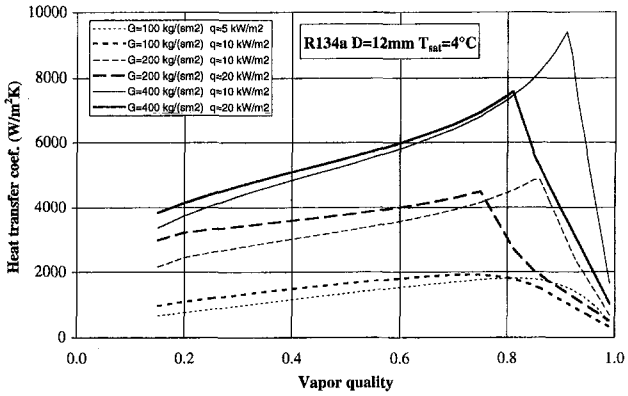

Fig. 16 Influence of the heat flux on the predicted heat transfer coefficient

8 Flow Boiling of Zeotropic Refrigerant Mixtures

To extend the present model to flow boiling of refrigerant blends and zeotropic mixtures in general, the Thome (1986, 1987) mixture boiling equation is recommended, which is an analytical expression given as

$$F_c = \left[1 + (h_{id}/q)\Delta T_{bp}\left[1 - \exp\left(\frac{-B_o q}{\rho_L \Delta h_v \beta_L} \right) \right] \right]^{-1} \quad (23)$$

that is valid for boiling ranges up to 30 K. The nucleate boiling heat transfer coefficient for zeotropic mixtures is thus obtained by including F_c in Eq. (6) to give

$$h_{nb} = F_c\, 55\, P_r^{0.12}(-\log_{10} P_r)^{-0.55} M^{-0.5} q^{0.67}, \quad (24)$$

where q is the flow boiling heat flux, ΔT_{bp} is the boiling range, (i.e., the dew point temperature minus the bubble point temperature of the mixture) the mass transfer coefficient β_L is set to a fixed value of 0.0003 m/s, and P_r and M are for the mixture. The ideal heat transfer coefficient h_{id} is determined with ΔT_{bp} set to 0.0, i.e., with F_c = 1 in Eq. (24).

9 Conclusions

A new flow boiling model and a correlation for predicting local heat transfer coefficients in horizontal tubes were developed, which include the effects of flow pattern, partial tube wall wetting, and partial tube dryout in annular flow. The method is much more accurate than existing methods for stratified types of flows and at high vapor qualities and, importantly, predicts most of the trends observed in experimental data sets. Compared to a new heat transfer database of 1141 points for five different refrigerants, the new method has a mean deviation of 13.3 percent, a standard deviation of 16.8 percent, and an average deviation of 2.0 percent.

Acknowledgments

The research was supported by the Swiss Federal Office of Energy (OFEN), Bern. The refrigerants were provided by DuPont de Nemours International S. A. of Geneva.

References

Chen, J. C., 1963, "A Correlation for Boiling Heat Transfer to Saturated Fluids in Convective Flow," paper presented at the 6th National Heat Transfer Conference, Boston, MA, August, 11–14.

Collier, J. G., and Thome, J. R., 1994, *Convective Boiling and Condensation*, 3rd ed., Oxford University Press, Oxford.

Cooper, M. G., 1984, "Saturation Nucleate Pool Boiling: A Simple Correlation," *1st U.K. National Conference on Heat Transfer*, Vol. 2, pp. 785–793.

Dittus, F. W., and Boelter, L. M. K., 1930, University of California (Berkeley) Publications on Engineering, Vol. 2, University of California, Berkeley, CA, p. 443.

Gungor, K. E., and Winterton, R. H. S., 1986, "A General Correlation for Flow Boiling in Tubes and Annuli," *Int. J. Heat Mass Transfer,* Vol. 29, No. 3, pp. 351–358.

Gungor, K. E., and Winterton, R. H. S., 1987, "Simplified General Correlation for Satureted Flow Boiling and Comparison of Correlations to Data," *Chem. Eng. Res. Des,* Vol. 65, pp. 148–156.

Incropera, F. P., and De Witt, D. P., 1990, *Fundamentals of Heat and Mass Transfer,* 3rd ed., John Wiley & Sons, Inc., NY.

Jung, D. S., McLinden, M., Radermacher, R., Didion, D., 1989, "A Study of Flow Boiling Heat Transfer With Refrigerant Mixtures," *Int. J. Heat Mass Transfer,* Vol. 32, No. 9, pp. 1751–1764.

Rouhani, Z., and Axelsson, E., 1970, "Calculation of Volume Void Fraction in the Subcooled and Quality Region," *International Journal of Heat and Mass Transfer,* Vol. 13, pp. 383–393.

Shah, M. M., 1982, "Chart Correlation for Saturated Boiling Heat Transfer: Equations and Further Study," *ASHRAE Transaction,* Part 1, Vol. 88, pp. 185–196.

Steiner, D., 1993, "Heat Transfer to Boiling Saturated Liquids," *VDI-Wärmeatlas (VDI Heat Atlas),* Verein Deutscher Ingenieure, ed., VDI-Gessellschaft Verfahrenstechnik und Chemieingenieurwesen (GCV), Düsseldorf, Germany, (J. W. Fullerton, translator).

Steiner, D., and Taborek, J., 1992, "Flow Boiling Heat Transfer in Vertical Tubes Correlated by an Asymptotic Model," *Heat Transfer Engineering,* Vol. 13, No. 2, pp. 43–69.

Thome, J. R., 1986, "Prediction of the Mixture Effect on Boiling in Vertical Thermosyphon Reboilers," Paper 127b, paper presented at the AIChE Winter National Meeting, Miami Beach, November, 2–7.

Thome, J. R., 1994, "Two-Phase Heat Transfer to New Refrigerants," *10th Int. Heat Transfer Conf.,* Vol. 1, Brighton, pp. 19–41.

Thome, J. R., 1995, "Flow Boiling in Horizontal Tubes: A Critical Assessment of Current Methodologies," *Int. Symposium of Two-Phase Flow Modelling and Experimentation,* Vol. 1, Rome, Edizioni ETS, Pisa, pp. 41–52.

Thome, J. R., and Shakir, S., 1987, "A New Correlation for the Boiling of Aqueous Mixtures," *AIChE Symp. Ser.,* Vol. 83, No. 257, pp. 46–51.

Webb, R. L., and Gupte, N. S., 1992, "A Critical Review of Correlations for Convective Vaporization in Tube and Tube Banks," *Heat Transfer Engineering,* Vol. 13, No. 3, pp. 58–81.

Experimental Study and Modeling of the Intermediate Section of the Nonisothermal Constrained Vapor Bubble

M. Karthikeyan

J. Huang

J. Plawsky

P. C. Wayner, Jr.
wayner@rpi.edu

The Isermann Department of Chemical Engineering, Rensselaer Polytechnic Institute, Troy, NY 12180

The generic nonisothermal constrained vapor bubble (CVB) is a miniature, closed heat transfer device capable of high thermal conductance that uses interfacial forces to recirculate the condensate on the solid surface constraining the vapor bubble. Herein, for the specific case of a large length-to-width ratio it is equivalent to a wickless heat pipe. Experiments were conducted at various heat loads on a pentane/quartz CVB to measure the fundamental governing parameter fields: temperature, pressure, and liquid film curvature. An "intermediate" section with a large effective axial thermal conductivity was identified wherein the temperature remains nearly constant. A one-dimensional steady-state model of this intermediate section was developed and solved numerically to yield pressure, velocity, and liquid film curvature profiles. The experimentally obtained curvature profiles agree very well with those predicted by the Young-Laplace model. The operating temperature of the CVB was found to be a function of the operating pressure and not a function of the heat load. Due to experimental design limitations, the fundamental operating limits of the CVB were not reached.

Introduction

A generic vapor bubble formed by underfilling an evacuated enclosure with a liquid has both isothermal and nonisothermal uses. For an enclosure with a small cross-sectional area, the walls constrain the bubble and thereby modify the interfacial force field. This "constrained vapor bubble" (CVB) is being used to characterize, experimentally, both the interfacial force field under equilibrium conditions (e.g., DasGupta et al., 1995) and steady-state transport processes under nonequilibrium conditions (Karthikeyan et al., 1996). For the specific case of a relatively large length-to-width ratio, the constrained vapor bubble forms the wickless heat pipe presented in Fig. 1.

The main objective of this research is to experimentally evaluate the details of the steady-state transport processes in thin liquid films controlled by interfacial forces and thereby evaluate the use of the Young-Laplace model. We note that under some conditions these thin film processes are like those in many other systems, e.g., the microlayer in boiling and the contact line region in rewetting. Therefore, although we focus herein on the wickless heat pipe form of the CVB, these studies are of more general use.

The concept of a wickless micro heat pipe was first proposed by Cotter (1984). He defined the micro heat pipe as one so small that the mean curvature of the vapor-liquid interface is necessarily comparable in magnitude to the reciprocal of the hydraulic radius of the total flow channel. Typically, the diameter of the noncircular channel is between 10 and 500 μm. The promise of high heat flux cooling combined with a relatively small temperature drop has generated considerable interest in the application of micro heat pipes both as efficient cooling devices and as heat spreaders. Although micro heat pipes need to be fabricated of a high thermal conductivity material such as a metal or ceramic to be a practical choice for cooling, this design would be unsuitable for our purposes which includes the microscopic optical observation of the critical meniscus region. A larger system fabricated of a transparent material is necessary. Herein, we report on our investigation of a larger version of Cotter's micro heat pipe in the form of a 3 × 3 × 40 mm (inside dimensions) fused quartz cell of square cross section. In our case the capillary driving force in a portion of the cell is of the same order of magnitude as the earth's gravity force, unlike a micro heat pipe for which the capillary force is much larger than the gravity force. From a fundamental point of view the CVB conveniently permits the study of interfacial transport concepts. We note that these studies are also a precursor to planned studies under microgravity conditions.

In particular we are concerned with the CVB presented in Fig. 1. For a completely wetting system, the liquid will adhere to the walls of the chamber. For a finite contact angle system, some of the walls will have only a small amount of adsorbed liquid that changes the surface properties at the solid-vapor interface. Liquid will fill a portion of the corners in both cases. If the temperature at end no. 2 is higher than at end no. 1 because of an external heat source, energy flows from end 2 to end 1 by means of conduction in the walls and by a combined evaporation, vapor flow, and condensation mechanism. Heat applied to end 2 of the CVB vaporizes the liquid in this region and the vapor is forced to move to end 1 where it condenses, releasing the latent heat of vaporization in the process. The curvature of the liquid-vapor interface changes continually along the axial length of the cell because of viscous losses, and the evaporation/condensation process. This capillary pressure difference between the evaporator (end 2) and the condenser (end 1) regions causes the working fluid to flow back to end 2 from end 1 along the right-angled corner regions. With a completely wetting fluid, additional flow occurs in thin films formed on the rest of the surfaces.

Our experiments with the CVB at different heat inputs indicate that there is an intermediate region of variable length located between the evaporator and condenser regions that has,

Contributed by the Heat Transfer Division for publication in the JOURNAL OF HEAT TRANSFER and presented at NHTC '96. Manuscript received by the Heat Transfer Division January 24, 1997; revision received October 7, 1997; Keywords: Heat Pipes and Thermosyphons; Phase-Change Phenomena; Thin Film Flow. Associate Technical Editor: R. A. Nelson, Jr.

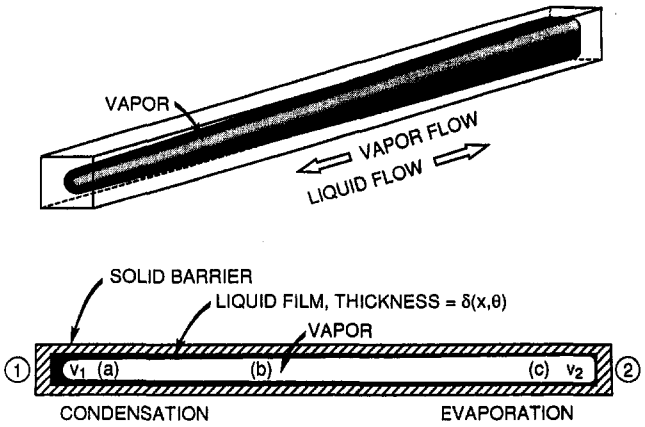

Fig. 1 Wickless heat pipe form of the nonisothermal constrained vapor bubble (CVB) concept for $g \to 0$

depending on the mode of operation, close to a constant temperature along its entire length. If the CVB is filled with the working fluid under vacuum (and there are no noncondensables in the system) and if thermoelectric coolers are used to remove the correct amount of heat from the condenser end of the CVB, this constant temperature has been found to be close to that of the environment. The energy flowing in from the evaporator end would leave the condenser end with an insignificant loss to the environment in the intermediate region. It should be noted that if there are noncondensables in the system, the temperature of the intermediate region, although still nearly constant, is universally higher than that of the environment. Pressure measurements indicate that we had less than 6 percent noncondensables. Therefore, in this case there is a small amount of heat loss to the environment and the intermediate region is not truly adiabatic.

Peterson (1992) and Faghri (1995) have written excellent reviews of micro heat pipe research and development that include both experimental investigations on micro heat pipes and modeling of micro heat pipe performance. Results have also been published on the experimental study of micro heat pipe arrays fabricated as an integral part of silicon wafers (Mallik et al., 1993; Peterson et al., 1991). On the other hand, many papers have also been published on the modeling of micro heat pipes. Cotter's original paper (Cotter, 1984) describes a model to predict the behavior of micro heat pipes. However, this model requires the knowledge of a parameter that behaves as a correction factor. Babin et al. (1990) present a steady-state model that assumes prior knowledge of the liquid film profile in order to compute the liquid and vapor pressure drops. Longtin et al. (1994) have also developed a one-dimensional model to predict the operating parameters of the micro heat pipe. Their analysis differs from ours mainly in the boundary conditions. Also, the factor they use to compare their model results to experiments is the macroscopic heat flux instead of a more fundamental parameter such as the film curvature profile, which we use. In essence, the enclosed study is more complete and informative than past studies. To the authors' knowledge this is the first time that the curvature gradient in a heat pipe under steady-state operation has been experimentally measured and used to obtain a heat balance.

Dunn and Reay (1994) and Faghri (1995) discuss the grouping of the properties of a working fluid to form a figure of merit that maximizes the heat transport capacity. Although pentane is relatively ineffective on this basis, we selected it for its convenient boiling point and its nonpolar nature. The boiling point of pentane is close to room temperature, hence its choice allowed valuable experiments to be performed using a relatively simple setup. Also, the nonpolar nature of pentane made the modeling of the interfacial force field easier.

In general, the performance of the CVB is based on the chemical potential profile which is a function of the temperature and pressure profiles. The pressure profile is connected to the film thickness profile by the augmented Young-Laplace equation, Eq. 11. In this paper we present the results of our ground-based nonisothermal studies which include the experimental measurement of the temperature and film thickness profiles of a CVB operating at various heat loads. We also present a model

Nomenclature

A = cross-sectional area
a = inner diameter of the CVB cell (3 mm)
d_h = hydraulic diameter
f = friction factor
g = acceleration due to gravity
h = heat transfer coefficient between the CVB cell and room
h_{st} = effective heat transfer coefficient between the stainless steel rod and room
K = curvature of liquid film
k = thermal conductivity or friction coefficient
L = perimeter
l_{int} = length of the intermediate section of CVB
l_e = length of the evaporator section of CVB
l_s = length of stainless steel rod for estimation of h_{st} (20 mm)
m = fin equation parameter
P = pressure
Q = heat input to the CVB
Q_{int} = heat input to the intermediate section of the CVB
Re = Reynolds number
r = radius of curvature
T = temperature
U = velocity
x = axial distance starting 1 mm from the heater end of the cell
y = distance in the direction normal to CVB axis

Greek Characters

α = angle at the corner of the CVB cell
β = angle of inclination of the CVB cell
δ = liquid film thickness
θ = temperature difference between the surface of the CVB cell and room
θ_c = contact angle between pentane liquid and the quartz surface
μ = viscosity
Π = disjoining pressure
ρ = density
σ_l = surface tension of liquid
τ = shear stress
ϕ = angle covered by the arc of the meniscus at the corner of the CVB cell

Subscripts

0 = beginning of the intermediate section
1 = arbitrary location 1 along the length of the CVB
2 = arbitrary location 2 along the length of the CVB
b = bottom of the CVB
e = evaporator
eff = effective
i = liquid-vapor interface
int = intermediate section
l = liquid
max = maximum
q = quartz (CVB cell)
sat = saturation condition
st = stainless steel rod
t = top of the CVB
v = vapor
w = wall
∞ = environment (room)

based on a simple mass and momentum balance coupled with the Young-Laplace equation to describe the intermediate region. The gravitational field effects and the slight deviation of the region from true "adiabatic" behavior are both taken into account. The results of this model agree very well with the experimental data for all values of heat loads studied, the film curvature profile being the comparison parameter between the experiments and the model.

Experimental Procedure and Data Analysis

CVB Experimental Setup. Figure 2 shows a schematic of a portion of the experimental setup. The whole assembly was mounted on an aluminum base plate that was in turn attached to the mechanical stage of an optical microscope. This arrangement enabled the movement of the assembly on the stage so that the inside top surface of the cell could be viewed under the microscope and the liquid film thickness profile at the top measured at various axial locations. The pentane working fluid was subjected to a vacuum distillation step to remove dissolved air before being charged into the CVB system. For additional information on the experimental setup, purification of pentane, cleaning of the cell, and charging, refer to Karthikeyan et al. (1996). After the setup was filled and a vapor bubble established, the 40 mm long CVB cell had about 90 percent vapor and the remaining liquid.

The CVB experimental setup consisted mainly of the quartz cell (square cross section; inside dimensions: 3 mm × 3 mm; outside dimensions: 5.5 mm × 5.5 mm; length: approximately 40 mm), a resistance heater, and four miniature (5 × 5 × 2.4 mm) thermoelectric coolers. The heater was a hollow cylinder of a Garolite (a glass fabric laminated with epoxy resin) approximately 60 mm long on which high-resistivity nichrome wire was tightly wound. A 4.76 mm diameter, stainless steel rod of 85 mm length was inserted into the heater in such a way that 25 mm of the rod projected out of one end. The contact resistance between the heater and the stainless steel rod was reduced by using a layer of thermally conductive paste between the surfaces. The projecting end of the stainless steel rod was then attached to the cell using high thermal conductivity silver epoxy. Finally, the heater and the projecting portion of the rod were insulated to minimize heat loss. This arrangement enables us to measure the heat input into the cell by measuring the temperature profile of the stainless steel rod and, subsequently, to fit it to the fin equation.

The temperature profiles of both the rod and the quartz cell were measured using closely spaced microscale (40 AWG) Chromel-Alumel thermocouple beads. These were attached to the cell and the rod using conductive silver epoxy, and the beads were then coated with regular epoxy to reduce the error in the measured temperature due to the effect of the environment. All the thermocouples were connected to a type K thermocouple indicator through a rotary switch. Altogether, 25 thermocouples were used—14 on the vertical side of the cell, five on the stainless steel rod, one at the cell-rod interface, four on the coolers, and one underneath the heater. Figure 2 shows the location of the thermocouples. The thermocouple manufacturer specifies the limits of error in the temperature readings measured by these thermocouples as 1.1°C. Since the thermocouple meter was calibrated and we only deal with temperature differences, θ, (not absolute temperatures), most of the bias error associated with the instruments would get canceled, leading to a much smaller overall uncertainty in θ. In single sample experiments such as ours, a statistical analysis is not possible, hence the random component of the uncertainty (precision error) can only be estimated. Based on our experience with both the temperature measurement system and the physical process being measured, the overall uncertainty in θ was estimated to be ±0.2°C.

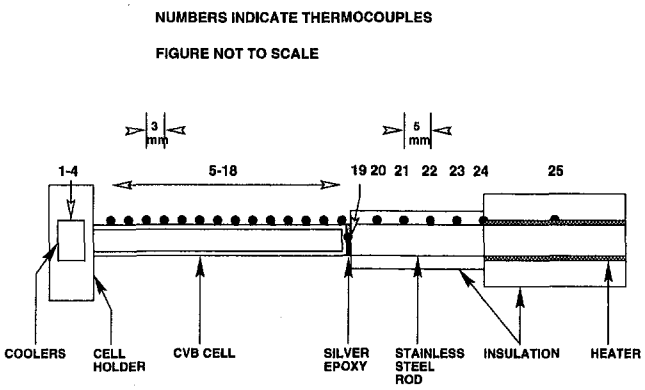

Fig. 2 Schematic of a portion of the experimental setup and the location of thermocouples

The coolers were first attached to the inside surface of two L-shaped aluminum blocks that also act as the cell holder. The coolers were then firmly pressed against the edges of cell and the blocks tightened. A thin coating of thermally conductive paste ensured good thermal contact between the cell and the coolers. It should be noted that the coolers were primarily used to help retain the bubble within the cell by maintaining a constant low temperature at the cooler end (Karthikeyan et al., 1996). The pressure inside the system was continuously monitored using a pressure transducer connected to a digital meter. These instruments were new and were precalibrated by the manufacturer with a specified uncertainty in the pressure data of ±1 torr. Under isothermal conditions, use of the known thermodynamic vapor pressure gives the fraction of noncondensables in the system. Temperature and thickness profiles were obtained at various heater and cooler power inputs. These data are presented and discussed in the next section.

A drawing of a corner of the CVB, where the film thickness profile was measured, is presented in Fig. 3. Details of this film thickness measurement, known as image analyzing interferometry (IAI), are elaborated elsewhere (DasGupta et al., 1995). Only a brief outline will be given here. This method works on the principle of interference of the reflected light waves from the solid-liquid and the liquid-vapor interfaces leading to patterns of dark and bright fringes. These interference images were captured from the microscope through a CCD camera, digitized, and stored. The stored images were later processed to yield plots of grey value versus distance. The grey value plots were further analyzed to get the film thickness profile. We could measure the liquid film thickness at the corner of the cell continuously from 0.1 μm to about 5 μm. The lower limit is set by the wavelength of light (546.1 nm in this case), while the higher limit is partially determined by the resolving power of the objective used.

Evaluation of Heat Input to the Intermediate region. As mentioned earlier, a stainless steel rod connecting the heater and the cell was employed to evaluate the heat input to the CVB and subsequently to the intermediate region. The measured stainless steel rod temperatures were fitted to the following classical fin equation with the temperatures at $x = -26$ mm and at $x = -6$ mm used as boundary conditions. Since the thermocouple at the interface, $x = -1$ mm was not actually on the stainless steel rod but buried in the silver paste, it was not used. The overall effective heat transfer coefficient between the steel rod and the environment, h_{st}, was evaluated from the least square fit of the experimental temperature data.

$$\frac{\theta}{\theta_b} = \frac{(\theta_{ls}/\theta_b)\sinh mx + \sinh m(l_s - x)}{\sinh ml_s}, \qquad (1)$$

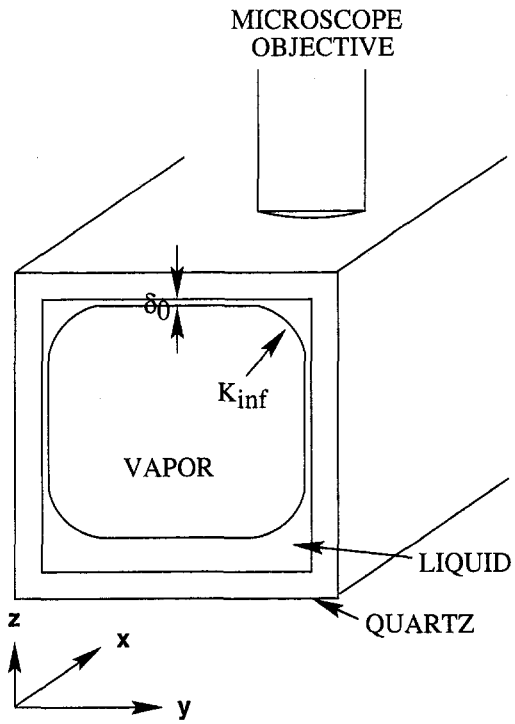

Fig. 3 Location of the microscope objective with respect to the CVB cell (all profile measurements were made through the top surface of the cell and the schematic of the liquid film profile is not to scale)

where m is defined by the equation

$$m^2 = \frac{h_{st} L_{st}}{k_{st} A_{st}}. \tag{2}$$

The heat going out from the end of the steel rod ($x = -1$ mm), Q_{out}, was calculated from the gradient of the temperature profile modeled by the fin equation. Note that the experimental temperature point at $x = -1$ mm was not used. There are two sources of heat loss that need to be accounted for. The first 1 mm of the cell is solid quartz and was not insulated. Secondly, the cell has a slightly larger cross-sectional area than that of the stainless steel rod, and there is a small amount of convection loss from the exposed portion of the end of the cell. The heat loss due to these factors was calculated and deducted from Q_{out} to get the actual heat flow rate Q into the quartz cell. Finally, the amount of energy entering the intermediate region, Q_{int}, can be determined by deducting the heat loss to the environment from the evaporator section of the CVB from Q. This is given as

$$Q_{int} = Q - \int_0^{l_e} L_q h \theta dx. \tag{3}$$

The heat transfer coefficient for the uninsulated quartz cell, h, was estimated by performing a dry run at the same heat input as that of the CVB and by fitting the dry run profile to the fin equation. The uncertainties in the heat inputs stem from the uncertainty in the values of thermal conductivity, heat transfer coefficient, and θ. The overall uncertainties in both Q and Q_{int}, calculated using the classical propagation equation of Kline and McClintock (1953), was about 18 percent.

Determination of Curvature. The interference images at different locations along the length of the CVB were analyzed to get the film thickness profile. The curvature of the film is defined as

$$K = \frac{\frac{d^2\delta}{dy^2}}{\left[1 + \left(\frac{d\delta}{dy}\right)^2\right]^{3/2}}. \tag{4}$$

However, in our case, the square of the slope of the film thickness is negligible compared to unity ($(d\delta/dy)^2 \ll 1$). For the results presented in this paper, the maximum value of $(\delta')^2$ is only 0.015. Hence, Eq. 4 can be simplified to yield

$$K = \frac{d^2\delta}{dy^2}. \tag{5}$$

For all the experiments we performed, the film thickness profiles appeared to be parabolic in a portion of the meniscus. This suggests that the curvature might be approximately a constant, at least, in the region where the pressure gradient in the y-direction was small. When the square root of film thickness, $\delta^{1/2}$, was plotted against the normal distance, y, we found that the profile appeared to be a straight line, at least in the thicker portion of the meniscus where $\delta > 1$ μm. This can be expressed as

$$\delta^{1/2} = a_1 y + a_2, \tag{6}$$

where a_1 and a_2 are constants. Squaring both sides of Eq. 6 leads to a less general parabolic expression for δ.

$$\delta = a_1^2 y^2 + 2a_1 a_2 y + a_2^2 \tag{7}$$

Upon differentiating the above equation twice, the curvature can be expressed as a function of the coefficient a_1, which is also the slope of $\delta^{1/2}$ versus y.

$$K = \frac{1}{r} = 2a_1^2 = 2\left(\frac{d\delta^{1/2}}{dy}\right)^2 \tag{8}$$

We, along with DasGupta et al., have found that this procedure yields consistent and reliable values for curvature. Figure 4 shows representative plots of film thickness (δ versus distance, y) and square root of film thickness ($\delta^{1/2}$, versus distance y) for one of the experiments conducted. The uncertainty in the value of δ for our measurement range was 2.5 percent. This stems from the uncertainties in the wavelength of light and in the refractive indices used in the calculation. However, the primary uncertainty in r is due to the error associated with locating the center of the reflectivity maxima and minima. This uncertainty,

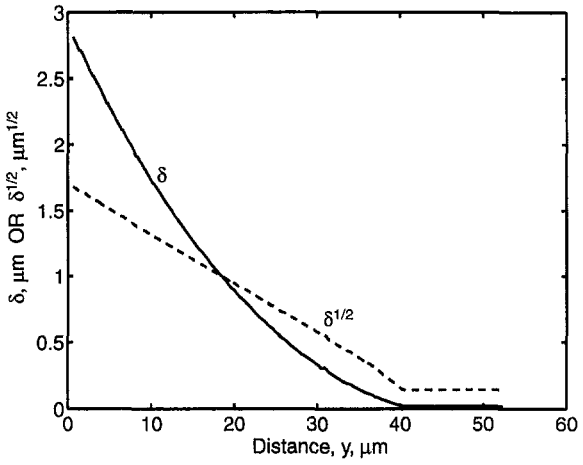

Fig. 4 Representative film thickness and square root of film thickness profiles for CVB, Q = 0.28 W, x = 25.5 mm (the uncertainty in δ is 2.5 percent)

an artifact of the image processing system, when combined with the the uncertainty in δ through the application of the propagation equation, yields an overall uncertainty in r of about 7.6 percent. Note that this value is applicable only for the range of radii of curvatures presented in this paper and that the uncertainty in measuring very small radii of curvature will be much higher.

Effective Thermal Conductivity Calculations. The local effective thermal conductivity of the CVB, which is a function of the position within the cell, was calculated for one of the CVB temperature profiles (Q = 0.28 W) in Fig. 5. First, the local axial heat flux was calculated as a function of x using the following equation:

$$q(x) = \frac{Q - \int_0^x L_q h \theta dx}{A}. \quad (9)$$

The heat transfer coefficient in the above equation was obtained from an equivalent dry cell experiment by fitting its temperature profile to the fin equation. The three regions of the CVB temperature profile (the evaporator, the intermediate region, and the condenser) were individually fitted as polynomials and the local slope of the temperature profile, $d\theta/dx$, obtained numerically. The local effective thermal conductivity was then obtained using the following equation:

$$k_{\text{eff}}(x) = -\frac{q(x)}{\frac{d\theta}{dx}}. \quad (10)$$

It was found that the intermediate region had a thermal conductivity that is many orders of magnitude greater than that of the evaporator and the condenser regions. The effective thermal conductivity throughout the intermediate region was found to be k_{eff} = 9200 W/mK, based on the inside cross-sectional area of the CVB, and k_{eff} = 2800 W/mK, based on the total cross-sectional area of the CVB. Since the temperature change in the intermediate region lies within the error of temperature measurements, only a best estimate for k_{eff} can be made.

Modeling of the Intermediate Region

A model was developed to predict the liquid and vapor pressure variations along the axial length of the intermediate region. In addition, the axial curvature variation of the liquid film adhering to the corners of the CVB was predicted by using the experimentally obtained curvature at the beginning of the intermediate region as a boundary condition. Figure 6 shows a schematic of the energy and mass flows into and out of every region of the CVB during its operation. The following assumptions were employed in the derivation of the governing equations for the intermediate region model:

- *Steady-state operation.*
- *Constant fluid properties*. All fluid properties were evaluated at the temperature of operation of the CVB.
- *Laminar, incompressible flow.* Since the Reynolds numbers of the liquid and vapor were found to be very small (<10) and the Mach number for the vapor $\ll 1$, this assumption is valid.
- *Single radius of curvature.* The interfacial radius of curvature parallel to the CVB axis can be neglected because it is much larger than that normal to the CVB axis.
- *Constant curvature.* The curvature is a function of x only ($K = K(x)$). However, the curvature at the top of the CVB is different from that at the bottom of the CVB due to gravity, which is accounted for in the present analysis.
- *Constant operating temperature.* Both liquid and vapor within the intermediate region are at equilibrium at a temperature equal to the measured surface temperature of the CVB.

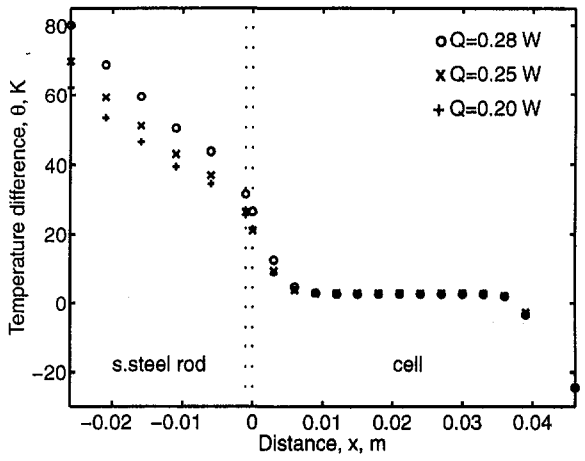

Fig. 5 Temperature profiles of CVB for various Q, pressure ≈ 540 torr

Young-Laplace Equation. The performance of the CVB depends on the liquid and vapor pressure profiles among other factors. The pressure profiles are a function of the film thickness profile and the augmented Young-Laplace equation:

$$P_v - P_l = \sigma_l \left[\frac{1}{r_2} - \frac{1}{r_1}\right] + \Pi_2 - \Pi_1. \quad (11)$$

However, in our case, the axial liquid flow in the thin adsorbed layer is expected to be negligible and most of the axial flow occurs in the thicker portion of the meniscus. Hence, we assume that the effect of the disjoining pressure on axial flow is negligible and the governing equation for the axial pressure gradient reduces to

$$\frac{dP_v}{dx} - \frac{dP_l}{dx} = -\frac{\sigma_l}{r^2}\frac{dr}{dx}. \quad (12)$$

We also note that the details of the variation of heat flux and of the disjoining pressure in the y-direction are not needed in this study. They will be addressed in a future paper.

Conservation of Mass. The mass flow rates of the liquid and vapor entering and leaving the intermediate region would be the same (except for a small effect due to axial pressure gradients), if the temperature of this region were identical to the environment temperature. However, in our experiments we noticed that the temperature in the intermediate region was slightly higher than that of the environment. We attribute this to the resistance to flow associated with a small air leak or some dissolved gas remaining in pentane. Our data indicate (see Table 1) that the maximum amount of noncondensables in the CVB was 6 percent. The temperature difference leads to a small heat loss from the intermediate region and hence a slight deviation from ideality. Based on the assumption that the liquid and vapor are at the saturation temperature, this heat loss can only be accounted for by some condensation of the vapor within the intermediate region. Hence, both the mass and energy balances are combined to yield one equation each for the liquid and vapor flows.

$$\rho_l U_l \frac{dA_l}{dx} + \rho_l A_l \frac{dU_l}{dx} - \frac{L_q h (T_{\text{int}} - T_\infty)}{h_{fg}} = 0 \quad (13)$$

$$\rho_v U_v \frac{dA_v}{dx} + \rho_v A_v \frac{dU_v}{dx} + \frac{L_q h (T_{\text{int}} - T_\infty)}{h_{fg}} = 0 \quad (14)$$

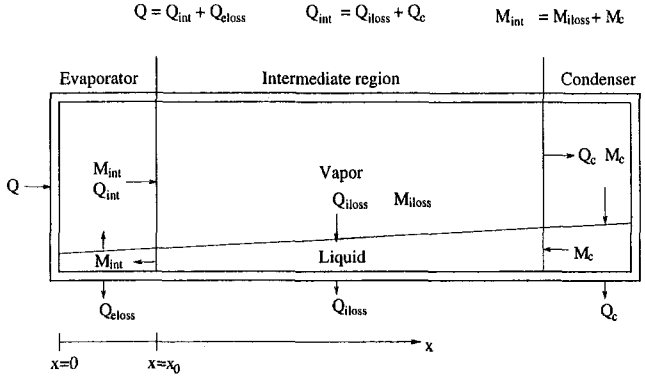

Fig. 6 Schematic of energy and mass flow in the CVB

In each of the above equations, the first two terms account for the difference between the inflow and outflow of mass into the control volume while the third term accounts for the condensation of vapor. The sign convention used is that the vapor velocity is positive with vapor flowing from the evaporator to the condenser, while the liquid velocity is negative with liquid flowing in the opposite direction.

Conservation of Momentum. The conservation of linear momentum for liquid and pure vapor flows over the control volume results in the following equations, respectively:

$$A_l \frac{dP_l}{dx} + \rho_l g A_l \sin\beta + \rho_l U_l^2 \frac{dA_l}{dx} + 2\rho_l A_l U_l \frac{dU_l}{dx} - L_i \tau_i - L_{l,w}\tau_{l,w} = 0 \quad (15)$$

$$A_v \frac{dP_v}{dx} + \rho_v U_v^2 \frac{dA_v}{dx} + 2\rho_v A_v U_v \frac{dU_v}{dx} + L_i \tau_i + L_{v,w}\tau_{v,w} = 0. \quad (16)$$

The first term of Eq. 15 is the pressure acting on the liquid cross-sectional area. The second term is a body force term that accounts for the gravity force where β is the angle of inclination of the axis of the CVB with respect to gravity. Since the CVB in our experiments is nearly horizontal, $\beta = 0$. The third and fourth terms of the first equation account for the change in the bulk momentum flow in the control volume. The last two terms are the tangential forces that arise due to the shear encountered at the liquid-vapor interface and the liquid-wall interface, respectively.

Equation 16 represents the momentum balance for the vapor flow and it differs from Eq. 15 in that the gravity force term is naturally absent. We expected the absolute values of the liquid and vapor velocities to be of the same order of magnitude over the entire length because of the large difference in the cross-sectional areas of the flow channels. Therefore, when calculating the tangential shear stress on the vapor at the liquid-vapor interface, τ_i, the relative velocity of the vapor with respect to the liquid was used. Figure 7 represents the geometry at one of the top corners of the CVB. Using the geometric factors shown in Fig. 7, the cross-sectional areas of the liquid and vapor flow channels were calculated. The calculation is simplified due to the fact that the liquid completely wets the solid surface, and hence the contact angle, θ_c, is 0. In addition, the liquid wall and the vapor-wall contact line lengths and the perimeter of the liquid-vapor interface were calculated. We note that the radius of curvature at the bottom of the CVB is higher than that at the top due to gravity, and the bottom radius was calculated by the application of Young-Laplace equation. This effect is included in the model simply by changing the geometric factors corresponding to the increase in the radius of curvature at the bottom while assuming the velocity of the liquid at the bottom to be the same as that at the top. The total liquid cross-sectional area increases while the vapor cross-sectional area decreases. The wetted perimeters of the liquid and the vapor flow channels also change resulting in a change in the hydraulic diameters used for shear stress calculations. We must point out that with our current experimental setup we could measure only the curvature at the top surface and not that at the bottom. The results of the model such as liquid and vapor pressure drops, and the liquid film curvature profiles are presented for the inside top surface of the CVB.

Since our model is one-dimensional, the radial velocity distribution within the liquid and vapor necessary to calculate the wall and interfacial shear stresses is unknown. Hence, we assume the liquid and vapor flows to be similar to fully developed duct flow. According to Longtin et al. (1994), this is justified because the convective terms are small and the liquid and vapor cross-sectional areas change slowly with x. The shear stress due to friction is given for both liquid and vapor flows as (Bejan, 1984)

$$\tau = \tfrac{1}{2}\rho U^2 f, \quad (17)$$

where the friction factor, f, is given as

$$f = \frac{k}{\mathrm{Re}}, \quad (18)$$

where, k, the constant, depends on the geometry of the flow channel. The liquid flow channel can be approximated to a 90–45–45 deg triangle, therefore, a value of $k = 13.1$ was used for the liquid. The vapor flow channel changes from almost a square to almost a circle as we go from the evaporator end to the condenser end. Hence, a value of $k = 15.1$ (average of the values for a square and a circular channel) was used for the vapor flow. These values were obtained from White (1986). Agreement between theory and experiment below support the use of these values. The Reynolds number, Re, is defined as

$$\mathrm{Re} = \frac{d_h U \rho}{\mu}, \quad (19)$$

where the hydraulic diameter, d_h, of both the liquid and vapor flow channels is computed based on the control volume geometry.

Boundary Conditions. Equations 12 through 16 constitute a set of five first order, nonlinear, coupled ordinary differential equations. In order to solve these equations simultaneously five boundary conditions are needed. These boundary conditions have all been taken at one point, i.e., the beginning of the intermediate section, the axial location of which is denoted as $x = x_0$. They are listed as follows:

- At the beginning of the intermediate region the radius of curvature at the top of the CVB, $r_{t,0}$, was obtained

Table 1 CVB experimental data

Experiment	Q (W)	Q_{int} (W)	T_{int} (°C)	T_∞ (°C)	P measured (torr)	P_{sat} at T_{int} (torr)
1	0.20 ± 0.018	0.17 ± 0.015	25.2	22.2	542 ± 1	515.3
2	0.25 ± 0.022	0.22 ± 0.020	25.0	22.0	538 ± 1	511.5
3	0.28 ± 0.025	0.25 ± 0.022	24.9	22.2	539 ± 1	509.6

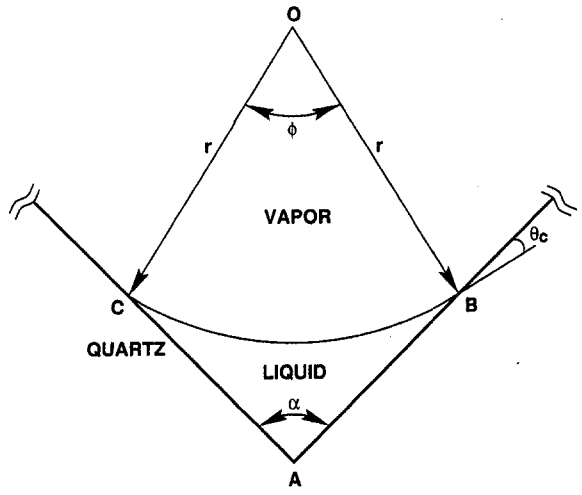

Fig. 7 Top corner geometry of the CVB

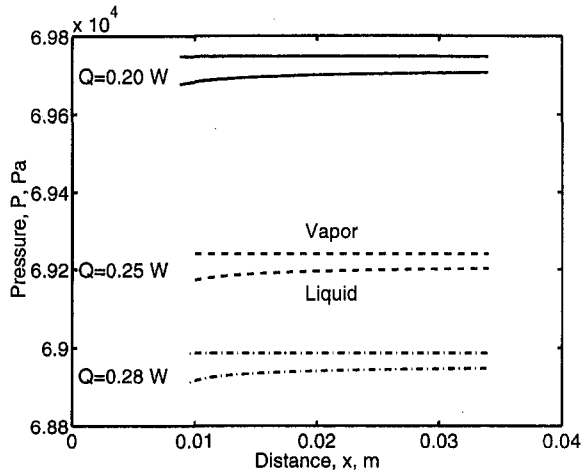

Fig. 8 Pressure drops within the intermediate section of the CVB for experiments 1, 2, and 3 of Table 1 (model prediction)

experimentally and the radius of curvature at the bottom, $r_{b,0}$, was calculated.

- The velocities of the vapor and the liquid at the beginning of the intermediate section, $x = x_0$, are calculated knowing the heat input to the intermediate section, Q_{int}.

$$U_{l,0} = \frac{-Q_{\text{int}}}{h_{fg}\rho_l A_{l,0}} \tag{20}$$

$$U_{v,0} = \frac{-Q_{\text{int}}}{h_{fg}\rho_v A_{v,0}}, \tag{21}$$

where $A_{l,0}$ and $A_{v,0}$ are the cross-sectional areas of the liquid and vapor flow channels at the beginning of the intermediate section, respectively.

- The vapor pressure at $x = x_0$ is assumed to be the saturation pressure of pentane at the temperature of operation of the CVB, and the liquid pressure at $x = x_0$ is obtained by application of the Young-Laplace equation.

$$P_{v,0} = P_{v,\text{sat}}\ (T = T_{\text{int}}) \tag{22}$$

$$P_{l,0} = P_{v,0} - \sigma_l / r_{l,0}. \tag{23}$$

Equations 12 through 16 and their boundary conditions were solved numerically for the five unknowns: r, U_l, U_v, P_l, and P_v.

Results and Discussion

Table 1 gives the values of overall heat input to the CVB and the heat input to the intermediate section of the CVB for each of three experiments. Also listed are the temperatures of the intermediate section and pressure readings as indicated by the pressure gauge. The fact that the measured pressure value for each of the three experiments was higher than the saturation pressure at the corresponding room temperature suggests the presence of a small leak in the system. Based on the pressure values the maximum amount of noncondensables in the CVB was estimated to be 6 percent. Due to the negligible amount of noncondensables we conclude that the effect of the leak on the observed trend in the experimental data was minimal and does not affect the conclusions listed below.

The measured temperature profiles for the experiments 1, 2, and 3, were already shown in Fig. 5. The flat portion in the profile corresponding to the intermediate section is very clear in all three plots. The length of this intermediate section for all three experiments, estimated from the temperature profiles, is about the same. Other experiments conducted at lower heat loads do show shorter intermediate sections, and for a certain minimum heat load this section is completely unnoticeable. On the other hand, the highest heat load we could operate at was restricted by our heating system and is close to that of experiment 3 in the table. Higher heat fluxes with a different heater are therefore possible. Since the resistance to vapor flow and evaporation are very small in the current design, the operating temperature can be set by the thermoelectric coolers. Therefore, the operating temperature is not a function of the heat load.

Figure 8 shows the pressure drops in the liquid and vapor phases along the length of the intermediate section of the CVB for the three experiments. The pressure drop in the vapor is very small and is hardly noticeable in these plots. A simple calculation shows that even at the condenser end of the intermediate region where the radii of curvature are the largest, the ratio of the cross-sectional area of the vapor to liquid flow channels, A_v/A_l, is at least 30. This means that although the curvature gradient along the axial direction is large, the cross-sectional area of the vapor flow channel itself changes very little with x. Also, as we shall see later, the vapor velocity gradient with respect to x is quite small. The fact that the vapor has a very low density and also a low velocity reduces the shear stress experienced by the vapor to be insignificant. Since the energy loss due to shear stress is very small, the pressure drop is also very small.

On the other hand, although the magnitude of the liquid pressure gradient is small ($\Delta P_l = 29.38$ Pa for experiment 2), it is

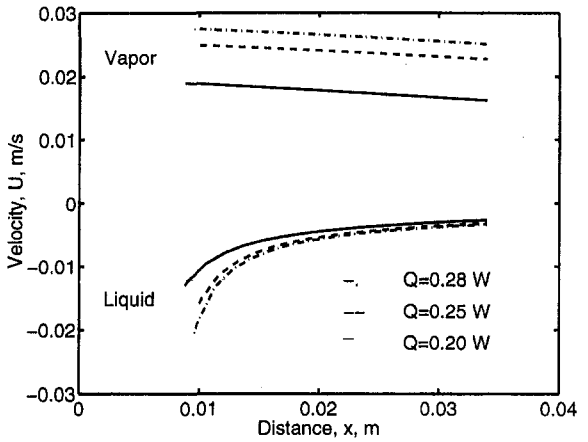

Fig. 9 Average velocity within the intermediate section of the CVB for experiments 1, 2, and 3 of Table 1 (model prediction)

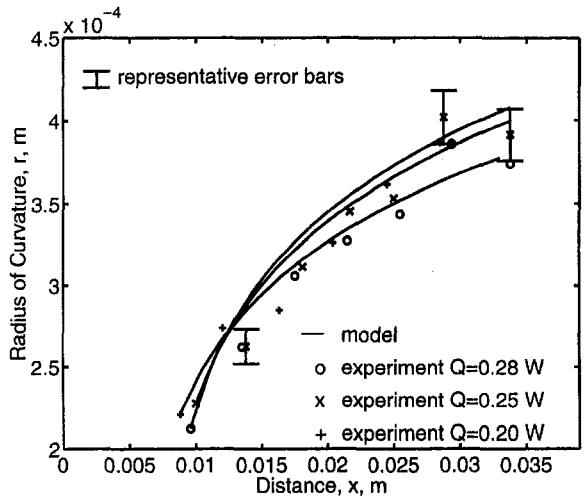

Fig. 10 Radii of curvature profiles within the intermediate section of the CVB for experiments 1, 2, and 3 of Table 1 (for comparison, the isothermal radius of curvature at the top of the cell, r_t, is 6.14 × 10^{-4} m, when the vertical distance between the top and bottom menisci is arbitrarily fixed at H = 2.4 × 10^{-3} m)

still many orders of magnitude greater than the pressure gradient in the vapor. (ΔP_v = 6.4 × 10^{-3} Pa for experiment 2). So, from the point of view of the liquid, the vapor has a constant pressure along the entire length of the intermediate section. Hence, the pressure drop in the liquid can be explained by the application of the Young-Laplace equation. At the evaporator end of the intermediate section where the radius of curvature is the smallest, the difference between the pressures in the vapor and liquid phases is the largest. Conversely, this difference, $P_v - P_l$, is the smallest at the condenser end of the intermediate section, where the radius of curvature is the largest.

Figure 9 shows the variation of the vapor and liquid velocities along the axial length, x, for the three experiments. Our sign convention forces the vapor velocities to be positive and the liquid velocities to be negative. As we can see the absolute values of the vapor and liquid velocities are the largest at the evaporator end of the intermediate section, while the absolute values of both velocities are the smallest at the condenser end of the intermediate section. The mass flow rate of the vapor decreases with increasing x because of condensation. Although the area of the vapor flow channel also decreases, the decrease in the mass flow rate is the dominant factor, and hence the velocity of the vapor decreases with increasing x. On the other hand, the mass flow rate of the liquid increases as we go from the condenser end to the evaporator end due to the condensation of vapor, while the area of the liquid flow channel decreases. These two factors act in the same direction to cause a rather large increase in the absolute value of the liquid velocity as we go from the condenser to the evaporator.

We can also see that the absolute values of the vapor and liquid velocities are of the same order of magnitude as expected. The maximum ratio of the absolute velocities of vapor to liquid, U_v/U_l, is less than 5, even at the condenser end. (This is because the liquid flow channel has a much smaller area than that of the vapor.) These two factors cancel each other to some extent to yield vapor and liquid velocity values that are not greatly disparate. This phenomenon is quite different from that predicted by Longtin et al. (1994) because they modeled much higher heat fluxes compared to our experimental values. Figure 10 shows both the experimental radii of curvature and those predicted by the model. There is good agreement between these experimental and predicted values for all three plots. This certainly indicates the soundness of the Young-Laplace and momentum models in describing the fluid-thermal behavior of the intermediate section of the CVB and the value of the friction coefficient, k. The measured radius of curvature at the top of the CVB in our experiments varies only from about 0.2 mm at the evaporator end to about 0.4 mm at the condenser end. The maximum possible radius of curvature is half the diameter of the CVB, 1.5 mm in our case, and if it is assumed that the evaporator and the condenser regions do not limit the performance of the CVB, there is room for substantial increase in the heat load that can be handled by the CVB. The above results demonstrate the ability of the presented techniques to evaluate the characteristics of the transport processes in a CVB.

Conclusions

1 Experimental techniques for direct measurement of the fundamental operating parameters of the nonisothermal constrained vapor bubble (CVB) were demonstrated.
2 Control of the operating temperature of the CVB is possible by varying the operating pressure using thermoelectric coolers to control the temperature level. The operating temperature is not a function of the heat load, at least within the range of our experimental heat loads.
3 Since the predicted radii of curvature values within the intermediate region agree very well with the experimental data for all values of the heat load, the presented Young-Laplace and momentum models describe the fluid-thermal behavior of the CVB.

Acknowledgment

This material is based on work supported by the National Aeronautics and Space Administration under grant # NAG3-1834. Any opinions, findings, and conclusions or recommendations expressed in this publication are those of the authors and do not necessarily reflect the view of NASA.

References

Babin, B. R., Peterson, G. P., and Wu, D., 1990, "Steady-State Modeling and Testing of a Micro Heat Pipe," ASME JOURNAL OF HEAT TRANSFER, Vol. 112, pp. 595–601.

Bejan, A., 1984, *Convection Heat Transfer,* John Wiley & sons, Inc., New York, pp. 77–78.

Cotter, T. P., 1984, "Principles and Prospects of Micro Heat Pipes," *Proc. 5th Int. Heat Pipe Conf.,* Tsukuba Science CZY, Japan, K. Oshima, Y. Kobayashi, M. Murakami, K. Negishi, eds., Japan Technology & Economics Center Inc., Tokyo, Japan, pp. 328–335.

DasGupta, S., Plawsky, J. L., and Wayner, P. C., Jr., 1995, "Interfacial Force Field Characterization in a Constrained Vapor Bubble Thermosyphon," *AIChE Journal,* Vol. 41, No. 9, pp. 2140–2149.

Dunn, P. D., and Reay, D. A., 1994, *Heat Pipes,* 4th ed., Pergamon, Oxford.

Faghri, A., 1995, *Heat Pipe Science and Technology,* 1st ed., Taylor and Francis, Washington, DC.

Karthikeyan, M., Huang, J., Plawsky, J. L., and Wayner, P. C., Jr., 1996, "Initial Non-isothermal Experimental Study of the Constarined Vapor Bubble Thermosyphon," ASME National Heat Transfer Conference, Vol. 5, HTD-Vol. 327, ASME, NY, pp. 121–129.

Kline, S. J., and McClintock, F. A., 1953, "Describing Uncertainties in Single-Sample Experiments," *Mechanical Engineering,* Vol. 75, Jan., pp. 3–8.

Longtin, J. P., Badran, B., and Gerner, F. M., 1994, "A One-Dimensional Model of a Micro Heat Pipe During Steady-State Operation," ASME JOURNAL OF HEAT TRANSFER, Vol. 116, pp. 709–715.

Mallik, A. K., Peterson, G. P., and Weichold, M. H., 1993, "Fabrication of Vapor Deposited Micro Heat Pipe Arrays as an Integral Part of Semiconductor Devices," *Journal of Microelectromechanical Systems,* Vol. 4, No. 3, pp. 119–131.

Peterson, G. P., Duncan, A. B., Ahmed, A. S., Mallik, A. K., and Weichold, M. H., 1991, "Experimental Investigation of Micro Heat Pipes in Silicon Wafers," presented at the ASME Winter Ann. Meet., Atlanta, GA, Dec. 1–6, ASME Vol. DSC-32.

Peterson, G. P., 1992, "Overview of Micro Heat Pipe Research and Development," *Appl. Mech. Rev.,* Vol. 45, No. 5, pp. 175–189.

White, F., 1986, *Fluid Mechanics,* 2nd ed., McGraw-Hill, New York.

H. S. Lee
Assistant Research Scientist.
The University of Michigan,
2250 G. G. Brown,
Ann Arbor, MI 48109-2125

H. Merte, Jr.
Professor.
The University of Michigan,
2148 G. G. Brown,
Ann Arbor, MI 48109-2125
merte@engin.umich.edu
ASME Life Fellow.

The Origin of the Dynamic Growth of Vapor Bubbles Related to Vapor Explosions

An explosive type of vapor bubble growth was observed during pool boiling experiments in microgravity using R-113. Photographs reveal that the liquid-vapor interface of the explosive bubbles are wrinkled and corrugated, leading to the conclusion that some type of instability mechanism is acting. The classical hydrodynamic instability theories of Landau and Rayleigh-Taylor do not consider the effect of heat transfer at the interface, which is believed to be responsible for the observed instability of the evaporating surface. This was confirmed by the mechanisms proposed by Prosperetti and Plesset, combined with a model of the early growth of spherical vapor bubbles.

1 Introduction

Rapid evaporation at superheats much lower than the homogeneous nucleation superheat limit was observed in transient boiling experiments conducted in short term microgravity. A limited number of vapor bubble growth experiments conducted at the superheat limit have been reported recently. The rapid evaporation rates observed have been described by various terms such as vapor explosion, explosive boiling, thermal explosion, rapid phase transitions (RPTs), and have been discussed by Reid (1983). In general, it has been presumed that potential high pressure water cooled nuclear reactor explosions, LNG spill explosions, and high pressure boiler accidents are related to vapor explosions. Answers are being sought to a number of questions: what are the mechanisms involved in vapor explosions, what are the conditions under which such can occur, and what can be done to prevent their occurrence? The present work is intended to assist in providing a better understanding of the mechanisms involved.

The vapor explosion type of behavior described here is considered to result from an increase in the liquid-vapor interface area arising from the instability of this interface. The process of vapor explosions can be enhanced further if the area of contact between the heat source and the liquid is increased by breakup of the heat source itself. This much more complex aspect of the phenomena will not be considered here.

An interface is unstable if it can be demonstrated that certain perturbations grow instead of decaying. One type of interface instability was first reported by Taylor (1950), deducing that when two superposed fluids of different densities are accelerated in a direction perpendicular to a *plane* interface, the interface is unstable for the acceleration directed from the lighter to the heavier fluid. This has been termed the *Rayleigh-Taylor instability*. Later, Plesset (1954), Birkhoff (1956), and Plesset and Prosperetti (1977) developed the corresponding Rayleigh-Taylor instability analysis for the spherical case, suggesting a closed form of instability criteria which included surface tension, viscosity, and acceleration. Shepherd and Sturtevant (1982) and Frost and Sturtevant (1986) discovered the vapor bubble explosion associated with a wrinkled surface and compared the instability criteria with measurements, using a classical bubble growth model. The results predicted the bubble growth to be stable for the case of *n*-butane at atmospheric pressure, while the experiments demonstrated obviously unstable behavior.

The hydrodynamic instability with rapid evaporation at a *plane* interface was approached from a different perspective by Miller (1973) and Palmer (1976). The former reported that a vaporizing planar interface can be unstable due to large density difference between phases, with the stability analysis showing the perturbation growth rate to be positive depending on the surface tension, density difference, and heat transfer at the interface. The latter introduced a *differential vapor recoil* mechanism to explain the plane instability, which is described as local surface depressions produced by the force exerted on the liquid surface by the vapor generation.

The roughening of a growing vapor *bubble* surface was first observed by Shepherd and Sturtevant (1982) with *n*-butane, with the measured average bubble growth rate of approximately 14.3 m/s being much greater than the classical bubble growth prediction. Rather than apply the Rayleigh-Taylor instability to their bubble growth problem, it was suggested that the instability theory of Landau (1944) be applied, which was originally developed for *plane* combustion flame propagation under the assumption of a thin flame. Istratov and Librovich (1969) developed the Landau theory for the *spherical* case, obtaining a closed form of instability criteria. Testing this criteria using the classical bubble growth model of Prosperetti and Plesset (1978) resulted in disagreement with the experiments of Shepherd and Sturtevant (1982). Photographs of the early bubble diameter of 0.15 mm at 10 μs clearly show a roughening of the liquid-vapor interface. The calculated evaporative mass flux, according to the measurements of Shepherd and Sturtevant (1982), is approximately 400 g/cm^2·s, which is extremely higher than the value calculated by the classical bubble growth model. McCann et al. (1989) repeated the experiments for the same conditions, but with a higher camera speed, and confirmed the results of Shepherd and Sturtevant (1982), with an average bubble growth rate of 23.8 m/s at 10 μs slowing down to 13.9 m/s at a later time.

A linearized instability analysis of the rapid evaporation to the superheat limit with a *plane* surface was carried out by Prosperetti and Plesset (1984) and Higuera (1987). The former asserted that the equivalence to the thin flame assumption of Landau (1944) was not appropriate for the problem of evaporation and consequently was not made. The analysis, however, depends on the undisturbed temperature distribution, which was unknown, and therefore could not be evaluated by comparison with experiments. Using several different temperature distributions, it was demonstrated that the surface of a rapidly evaporat-

Contributed by the Heat Transfer Division for publication in the JOURNAL OF HEAT TRANSFER and presented at IMECE, Atlanta '96. Manuscript received by the Heat Transfer Division December 16, 1996; revision received October 10, 1997; Keywords: Flow Instability; Microgravity Heat Transfer; Phase-Change Phenomena. Associate Technical Editor: M. S. Sohal.

ing liquid can become unstable for a range of wave numbers, and at a mass flux sufficiently large the growth resulting from the instability can be quite noteworthy, with characteristic growth times of a millisecond or less. Higuera (1987) included the effect of viscosity, which is stabilizing, and vapor motion, which reinforces the instability, and demonstrated that interfacial instabilities can occur, in agreement with Prosperetti and Plesset (1984).

Grolmes and Fauske (1974) observed violent free *plane* flashing at a liquid-vapor interface due to rapid depressurization of water to a low pressure of 0.004 atm. The flashing consisted of vapor and entrained liquid, and these observations contributed to an understanding of the phenomena of rapid evaporation. The effect of pressure on nucleation and vapor formation at the superheat limit was studied by Avedisian (1985), with the result that the violent bubble growth is suppressed by increasing the pressure. Frost and Sturtevant (1986) and Frost (1988) examined the relationship between the explosive bubble growth and the interface instability by means of the sensitive measurement of the far-field pressure. The onset of the instability during the smooth bubble growth was clearly demonstrated photographically by varying the ambient pressure, and supports the pressure effects observed by Avedisian (1985). Direct evidence was obtained by Frost (1988) that fine liquid particles are torn from the liquid-vapor interface during the violently unstable boiling, generating a vapor mass orders of magnitude greater than that characteristic of ordinary vapor bubble growth.

Although a considerable improvement in the understanding of rapid evaporation has been established in terms of interface instability, a definitive demonstration of the theory for the *spherical* case, with experimental confirmation, is not yet available. Experimental results have been obtained which reveal that rapid evaporation can occur at liquid superheats lower than the homogeneous nucleation superheat limit. These results are also described and presented in the works of Ervin (1991) and Ervin et al. (1992). As will be described in some detail below, both the Rayleigh-Taylor and the Landau instabilities criteria were tested, using a numerical model developed by Lee and Merte (1996a), with the result that stable conditions are predicted by both criteria, regardless of the spherical harmonic index, in disagreement with experimental observations. The mechanism for the rapid evaporation observed is interpreted here in terms of heat transfer combined with hydrodynamics. Any number of sources of perturbations or instability could be present, but once a perturbation occurs, it is believed that the heat transfer in the liquid at the interface can be a principal mechanism for the subsequent growth of this perturbation. To accommodate the above mentioned concern, the linearized planar instability theory of Prosperetti and Plesset (1984) was combined with a bubble growth model to provide the essential interfacial temperature distribution at the moment of the onset of the instability, to obtain the characteristic equation of the instability criteria. The results will discussed later. The important consequence here is that the explosive vapor bubble growth can occur at superheats much lower than the superheat limit in pool boiling, which seems to be not well recognized, and which perhaps implies that such events are more likely to take place in high temperature heat exchangers such as nuclear reactor cooling systems than in conventional boilers. According to the report of the Chernobyl disaster, the accident is obviously related to a vapor explosion, leading to the meltdown of the nuclear reactor core and eventually to the spreading of radioactivity.

2 Experiments and Results

Pool boiling experiments with R-113 were conducted in microgravity in the 132 m evacuated drop tower facility at the NASA Lewis Research Center, which provided 5.18 seconds of free fall with effective body forces on the order of 10^{-5} g, with the heating process being initiated following release. Photographs of the boiling process were obtained with a D. B. Milliken camera operating at 400 pictures per second. The drop vehicle, vessel, and associated electronics were designed to withstand the vacuum conditions and the 50 g impact at the bottom of the drop tower. The test vessel has internal dimensions of approximately 12.5 cm by 14 cm by 27.9 cm and consists of thick aluminum plates to assist in providing initially uniform internal temperatures. Two heater surfaces are installed in one wall of the test vessel; each consists of a 400 Å thick semitransparent gold film sputtered on a highly polished quartz substrate, and serves simultaneously as a heater, with an uncertainty of ±4 percent in the measurement of the heat flux, and a resistance thermometer, with an overall uncertainty of ±1.0°C. The heater is rectangular in shape, 1.91 cm by 3.81 cm. Degassed commercial grade R-113 (trichlorotrifluoroethane, CCl_2FCClF_2) was used because of its low normal boiling point (47.6°C), which minimized problems associated with heat loss to the surroundings, and because of its electrical nonconductivity, which made it compatible for direct contact with the thin gold film heater. A pressure transducer was employed to measure the system pressure, with an uncertainty of ±0.172 kPa. Calibrated chromel-constantan Teflon sheathed thermocouples

Nomenclature

c = specific heat
D = thermal diffusivity
g = gravity
G = unperturbed temperature gradient
h_{fg} = latent heat
J = mass flux
K = thermal conductivity
k = wavenumber ($=2\pi/\lambda$)
n = spherical harmonic index
P_∞ = system pressure
P_v = vapor pressure
q'' = heat flux
r = radial coordinate
$R(t)$ = bubble radius
R_c = critical radius
t = time
t^* = time at nucleation following onset of heating
t' = time for instability evolution
T = temperature
T_w^* = wall temperature at nucleation
T_v = vapor temperature
T_∞ = bulk liquid temperature
T_{bulk} = fluid temperature far from the liquid-vapor interface
T_{sat} = saturation temperature corresponding to system pressure
$\Delta T_{\text{sub}} = (T_{\text{sat}} - T_\infty)$, bulk liquid subcooling
$\Delta T_{\text{sup}} = (T_\infty - T_{\text{sat}})$, bulk liquid superheat
$\Delta T_{\text{wsup}} = (T_w - T_{\text{sat}})$, heater surface superheat
$\Delta T_{\text{wsup}}^* = (T_w^* - T_{\text{sat}})$, heater surface superheat at nucleation
$\Delta P = P_v - P_\infty$
V = velocity
z = coordinate

Subscripts

i = liquid-vapor interface
l = liquid
w = wall
v = vapor
∞ = infinite or far field
sub = subcooling
sup = superheat

Greek Letters

Ω = nondimensional growth rate
α = density ratio = ρ_v/ρ_l
Φ = velocity potential
ζ = surface tension
σ = perturbation growth rate
ν_l = liquid kinematic viscosity
λ = wavelength

with ice reference junctions were used to measure the liquid and vapor temperatures, with a total uncertainty of ±0.05°C. The desired subcooling was obtained by increasing the system pressure above the saturation pressure corresponding to the initial liquid temperature. In the absence of buoyancy, an initially motionless liquid remains stagnant upon heating until the onset of boiling, and the temperature distribution at the moment of incipient boiling can be determined from a conduction heat transfer analysis. Detailed descriptions of the experimental apparatus and procedure are given in Ervin et al. (1992) and in Merte and Lee (1997).

As is well known, conventional growing vapor bubbles have a smooth interface. However, under certain conditions with pool boiling in microgravity, the interface took on a rough appearance, accompanied by rapid growth rates. Figure 1 shows a typical roughened hemispherical vapor bubble 17.5 milliseconds after nucleation. This type of roughened surface has not been observed with boiling in earth gravity, most likely due to natural convection.

Two typical growth sequences, representative of these differences, are presented in Fig. 2(a) and (b) together with the operating conditions. The differences in the wall superheats at nucleation are particularly noteworthy, and are associated with the dramatic differences in the growth rates, especially obvious by comparing the bubble sizes at 7.5 milliseconds. It is of interest that the very first picture (A in Figure 2(a)) already exhibits a roughened surface, which implies that the onset of the interfacial instability is somewhere between 0 ~ 2.5 milliseconds. It is also to be noted that the bulk liquid is slightly subcooled in Fig. 2(a) and considerably subcooled in Fig. 2(b).

The growing bubble radii of Fig. 2(a) and (b) were measured approximately in the direction normal to the heater surface, and compared with several spherical vapor bubble growth models which assume a smooth interface, shown in Figs. 3 and 4, respectively. The initial uniform and nonuniform superheat models were developed by Lee and Merte (1996a, b) and consist of numerical solutions of the combined energy and momentum equations. For the initial uniform superheat model, the entire bulk liquid is assumed superheated at the level corresponding to the heater surface at nucleation; for the initial nonuniform superheat model, the radial superheat distribution surrounding the critical size vapor bubble is taken as that normal to the heater surface at nucleation. The former can be regarded as the upper limit of the bubble growth rate, while the latter can be regarded as the lower limit. For the analytical inertia dominated model of Rayleigh (1917), the pressure producing the bubble growth is assumed constant at the vapor pressure corresponding to the heater surface superheat at nucleation, an upper bound on the growth rate. The measured growth rate in Fig. 3 appears to be almost linear, with a mean velocity of approximately 2.14 m/s, and is much higher than that of both the uniform and nonuniform model predictions owing to the enhanced evaporation rate associated with the increased area of the roughened interface. Figure 4 corresponds to the experimental conditions of Fig. 2(b) and indicates that the actual bubble growth is close to the nonuniform superheat model for the early stages of the growth, since the bubble interface is smooth. This

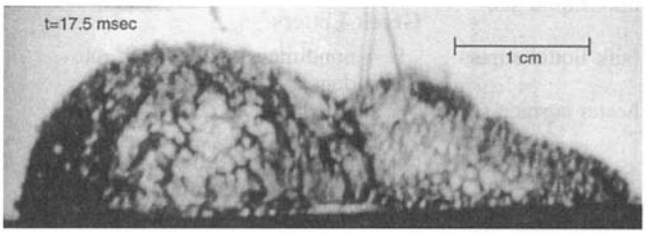

Fig. 1 Enlargement of a growing vapor bubble at 17.5 ms for experimental data code PBMT1102.800

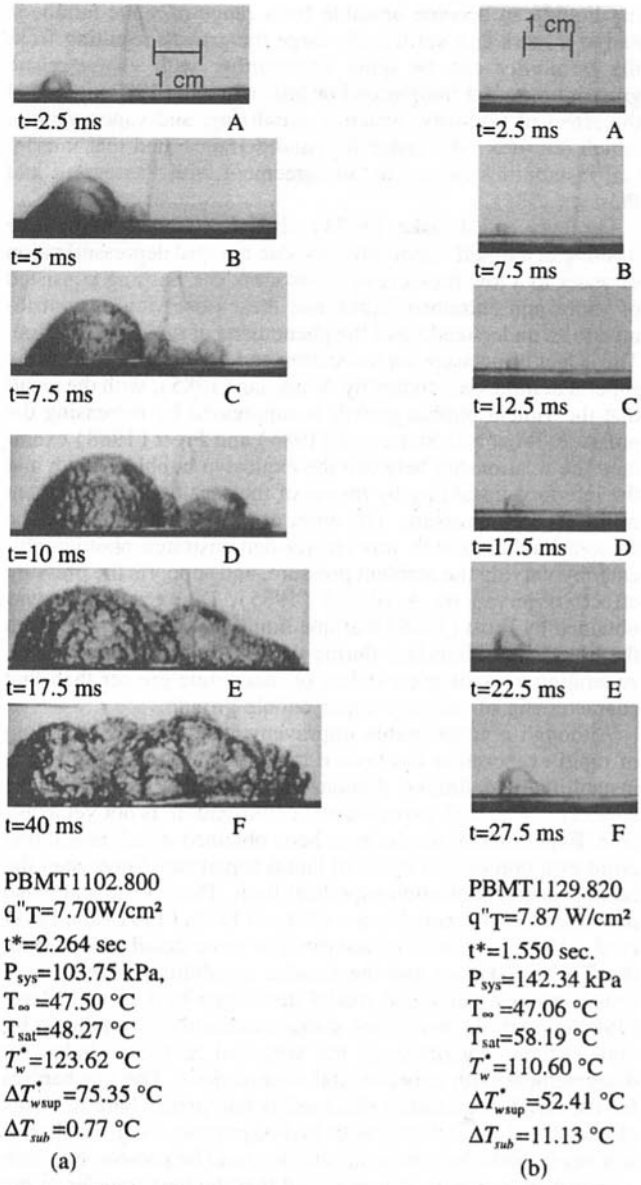

Fig. 2 Comparisons of early vapor bubble growth behavior under microgravity with different levels of heat flux and subcooling

supports the concept that the roughening of the bubble interface as a result of a surface instability leads to an increase in the evaporation rate.

Figure 5 shows the measured mean heater surface temperature and the measured pressure corresponding to the data in Fig. 2(a). Zero time indicates the onset of heating with a monotonically increasing heater surface temperature due to heat conduction and nucleation took place at 2.264 seconds. The dynamic vapor bubble growth due to the interfacial instability caused the bubble to lift slightly from the surface, as can be seen in Lee (1993), replacing the heated liquid by the cooler liquid, and resulting in the rapid surface temperature drop shown. A pressure jump at nucleation also results from the dynamic growth, with the pressure rise of 1.4 kPa in the figure. The actual pressure rise is believed to be much higher than this, since the sampling rate of the pressure measurement was not sufficiently high to capture the dynamic growth. According to more recent observations, the pressure rise should be greater than 15 kPa.

3 Bubble Dynamics

Several interesting aspects of the dynamics associated with vapor bubble growth were disclosed in the course of computing

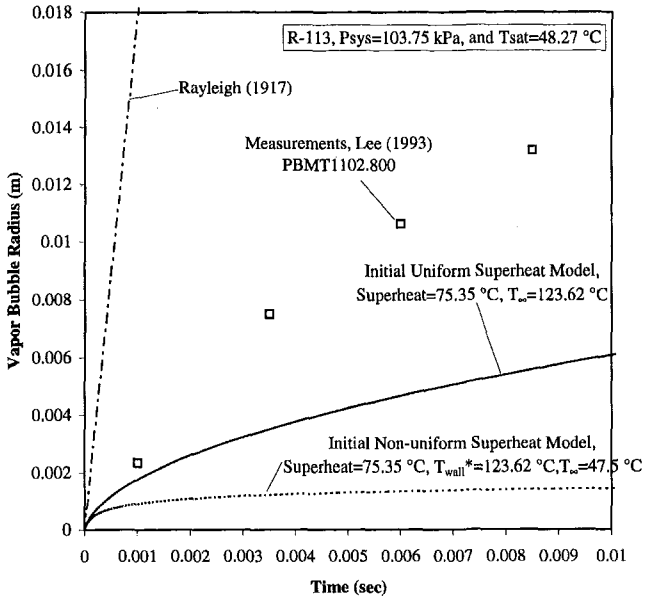

Fig. 3 Comparisons of experimental bubble growth data with several spherical vapor bubble growth models. Experimental conditions corresponds to Fig. 2(*a*).

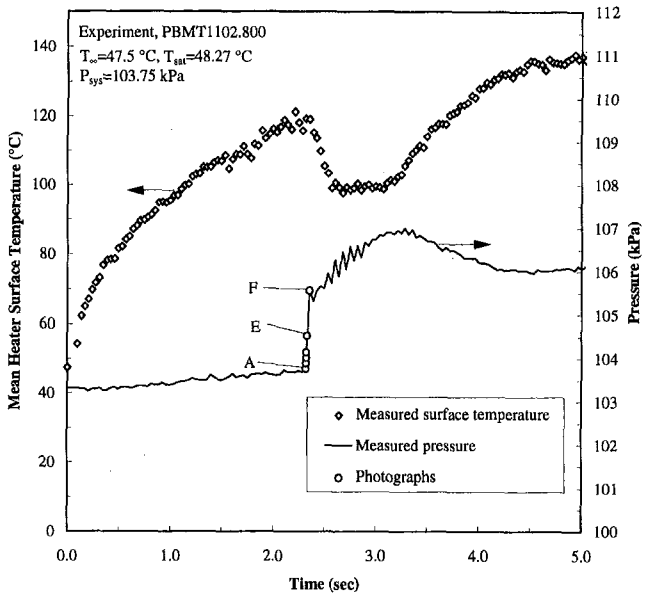

Fig. 5 Measured mean heater surface temperature and system pressure for Fig. 2(*a*) (A) – (F)

the vapor bubble growths for the two limits of initial uniform and nonuniform liquid superheats in Figs. 3 and 4. The elements of bubble radius and velocity, acceleration, and superheat at the liquid-vapor interface arising from the computations are plotted in Fig. 6 for the condition of Fig. 3. A logarithmic time scale is used in order to make more clear the events taking place in the early stages of growth.

It is seen in Fig. 6 that the initial critical size vapor bubble, in which the higher vapor pressure corresponding to the bulk temperature mechanically balances the surface tension, appears to sustain its critical size at a constant value for a certain period of time. In actuality it is growing, although very slowly with a velocity of 3×10^{-3} m/s, too small to be detected in this plot. The growth then suddenly increases to a velocity of approximately 12.5 m/s, due to the rapid reduction in the surface tension. The critical size bubble of 2.4×10^{-8} m radius in Fig. 6, which is beyond a measurable size, accelerates to a maximum value of 8×10^{8} m/s^2, imparting momentum to the liquid, which then leads to an overshoot, resulting in a rapid decrease in the liquid-vapor interface temperature.

In examining Fig. 6, it is noted that no significant difference exists between the initial uniform superheat model and the initial nonuniform superheat model with respect to both the interface accelerations and the interface temperatures. The radius

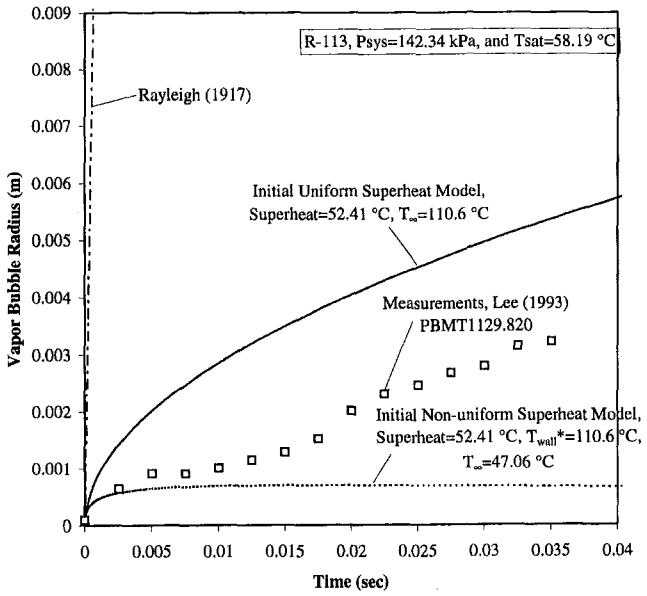

Fig. 4 Comparisons of experimental bubble growth data with several spherical vapor bubble growth models. Experimental conditions corresponds to Fig. 2(*b*).

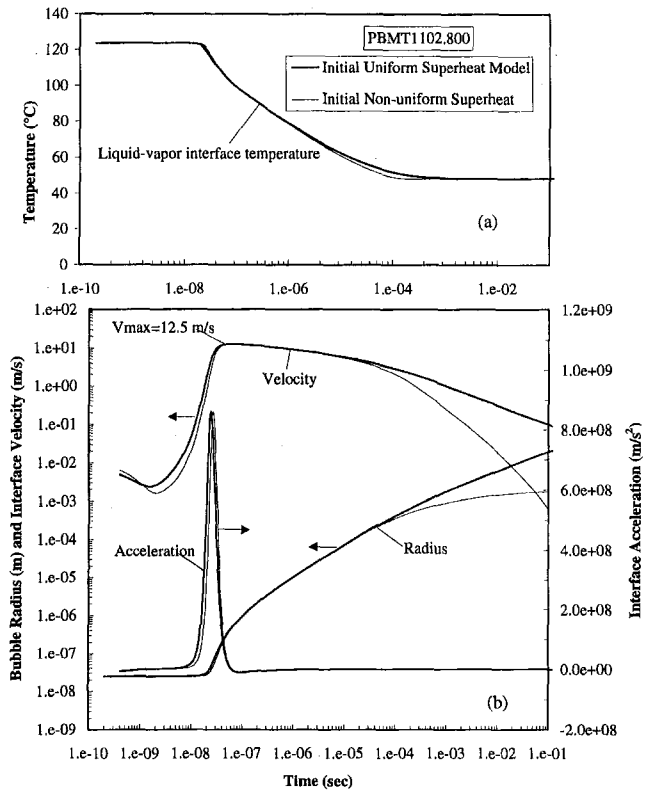

Fig. 6 Computed dynamics of vapor bubble growth model limits for R113, experimental data code PBMT1102.800

and velocity curves generated by both models coincide up to 3×10^{-5} seconds, which leads to the conclusion that the differences between the initially uniform and nonuniform liquid superheats have no effects on the early stages of bubble growth as long as the initial heater surface superheat is common to both. It is only in the latter stages of growth that significant differences arise.

4 Instability Considerations

Rapid evaporation is not prevalent in normal pool boiling processes, but has been observed when special steps are taken to maximize the degree of liquid superheat, which is termed the superheat limit. As described above, rapid evaporation of R-113 occurred at superheats much lower than the superheat limit, on the order of 70°C, whereas the computed superheat limits are in the range of 104–112°C for the pressures used, as given by Merte and Lee (1997). Analytical studies of a particular feature of the rapid evaporation at the superheat limit have been conducted, attempting to quantify the source of the instability which gives rise to the intense evaporation.

Shepherd and Sturtevant (1982) conducted experiments to achieve homogeneous nucleation by injecting a droplet of highly volatile *n*-butane into the bottom of a cylindrical vessel filled with hot immiscible ethylene glycol, so that the droplet temperature reaches the superheat limit as it rises due to buoyancy. Figure 7 shows the roughening of a *n*-butane vapor bubble at 12 μs following nucleation, which took place at a bulk temperature of 104.5°C and atmospheric pressure. Figure 7(*a*) depicts a *n*-butane liquid droplet 1 mm in diameter which contains a growing vapor bubble, and Fig. 7(*b*) is a photographic enlargement of the 150 μm diameter bubble. The resulting measured effective radius of a spherical bubble is plotted in Fig. 8, as a function of time, together with measurements of McCann et al. (1989), the momentum governed growth predicted by Rayleigh (1917), the approximate solution of Mikic et al. (1970), and the numerical solution of Lee and Merte (1996a). The measured growth rates appear to be linear, with a mean velocity of approximate 14.3 m/s, and with good agreement between the two sets of experiments. The growth rate is less than the momentum controlled growth of Rayleigh (1917), which is to be to be expected, but larger than the predictions of Mikic et al. (1970) and the numerical calculations of Lee and Merte (1996a). The numerical computations provide the velocity and acceleration in the early stages of growth for *n*-butane. The maximum interface acceleration is of the order of 2×10^{10} m/s^2, although for an exceedingly short time. The interface velocity reaches 32 m/s early and then decreases to 3 m/s at 1 ms. Using the information computed, both the Rayleigh-Taylor and Landau instability criteria can be examined on a time basis, determining the range of the index of spherical harmonics (n) necessary for instability. As indicated earlier, two closed-form descriptions of these instability criteria are available and will be summarized below.

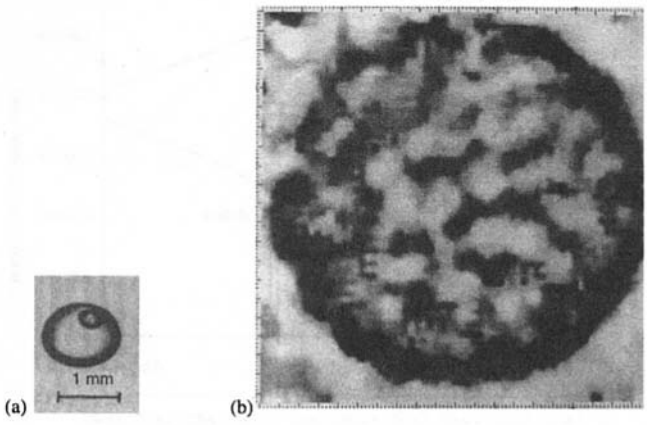

Fig. 7 Photographs of *n*-butane nucleating at the superheat limit (Shepherd and Sturtevant, 1982): (*a*) depicts a *n*-butane droplet containing a vapor bubble; (*b*) an image-enhanced photograph of a vapor bubble at $t = 12$ μs following nucleation

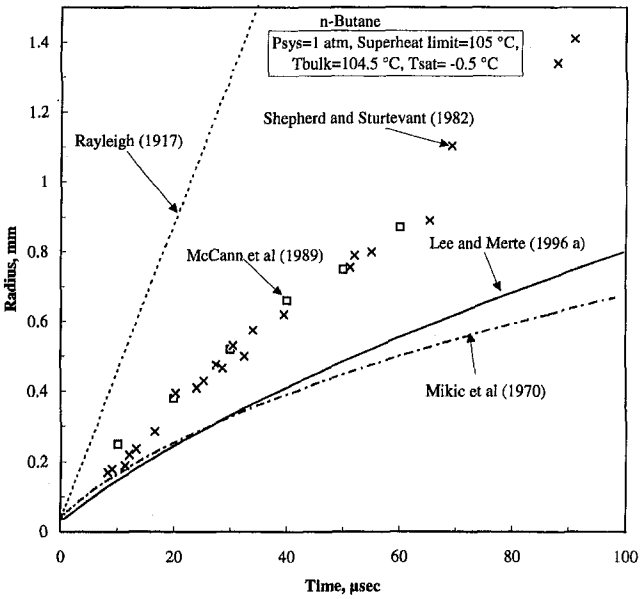

Fig. 8 Computations between extremely dynamic bubble growth experiments, a momentum controlled model, and approximate and numerical solutions of the energy and momentum equations for *n*-butane

4.1 Rayleigh-Taylor Instability. The Rayleigh-Taylor instability for a spherical interface has been established by considering whether a small amplitude disturbance on the interface grows or diminishes. It is understandable that as soon as spherical symmetry is excluded, the analysis of the various aspects of bubble dynamics becomes exceedingly complex, both from a theoretical and an experimental standpoint. An obvious possibility for circumventing this complexity is the use of an expansion in terms of spherical harmonics Y_n. The equation for the local interface of the bubble may be expressed as:

$$r_s = R(t) + a_n Y_n, \tag{1}$$

where $R(t)$ is the instantaneous average radius and a_n is the amplitude of the spherical harmonic of degree n. Equation (1) may be substituted into the governing equations and the basic equations subtracted so that only the disturbance equations remain. The detailed derivations may be obtained by reference to Plesset (1954), Birkhoff (1956), and Plesset and Prosperetti (1977). After some manipulations, the differential equation for a_n, from which the stability conditions can be deduced, is obtained as

$$\ddot{a}_n + \left[3\frac{\dot{R}}{R} + 2(n+2)(2n+1)\frac{\nu_l}{R^2}\right]\dot{a}_n - Aa_n = 0. \tag{2}$$

The original general stability criteria of Birkhoff (1956) indicate that oscillating bubbles are unstable when

$$A > 0, \quad \text{or} \tag{3}$$

$$A < 0 \quad \text{and} \quad \frac{d(R^6 A)}{dt} + 4(n+2)(2n+1)\nu_l R^4 A > 0, \tag{4}$$

where

$$A = (n-1)\left[\frac{\ddot{R}}{R} - (n+1)(n+2)\frac{\zeta}{\rho_l R^3} - 2(n+2)\frac{\nu_l \dot{R}}{R^3}\right]. \quad (5)$$

In the criterion of Eq. (4), in which the term including liquid viscosity is now included, the instability results in the surface perturbation oscillating with increasing amplitude. It is noted that the acceleration and surface tension are dominant parameters in Eq. (5).

Using the numerical calculations of Lee and Merte (1996a) for the operating conditions of n-butane in Fig. 8, the Rayleigh-Taylor instability criteria of Eqs. (3) and (4) predict that the vapor bubble should be stable throughout the growth period, contrary to the observation of interface instability shown in Fig. 7. This comparison was extended to the recent experiments with R-113 for the operating conditions in Fig. 2(a) and (b). Unconditional stable circumstances were also predicted regardless of the spherical harmonic index, again contrary to the unstable observations in Fig. 2(a). Shepherd and Sturtevant (1982) tested the criteria earlier in the same manner except that the classical bubble growth model of Prosperetti and Plesset (1978) was used, again with disagreement with the experimental observations. This implies that the Rayleigh-Taylor instability criteria for spherical bubbles should be reconsidered for the present case, in which the evaporation at the interface is given due cognizance.

4.2 Landau Instability. Frost and Sturtevant (1986) extended and applied the Landau stability theory as used by Istratov and Librovich (1969) for spherical flames to spherical vapor bubbles, expressing the perturbation amplitude as

$$\zeta \approx t^{\Omega}, \quad (6)$$

where Ω is the dimensionless algebraic growth rate.

The resulting dispersion relation is

$$\Omega^2 + b\Omega + c = 0 \quad (7)$$

where

$$b = 3 + \frac{n(1+2\alpha n)}{(n+1)\alpha + n} \quad (8)$$

$$c = 3 + \frac{\alpha(\alpha n+1)(n^2-1) - \alpha n^2(n-1)}{(n+1)\alpha + n} - \frac{n(n+1)\left[N_W - \frac{n(n+1)}{2}\right]}{[(n+1)\alpha + n]N_I} \quad (9)$$

$$\alpha = \frac{\rho_\nu}{\rho_l} \quad N_I = \frac{\rho_l R\dot{R}^2}{2\zeta} \quad N_W = \frac{(\rho_l - \rho_v)R^2\ddot{R}}{2\zeta}. \quad (10)$$

n is the spherical harmonic index. Positive values of Ω mean that the perturbation amplitude grows more rapidly than the radius, leading to instability. It is to be noted here that the density ratio (α) in Eq. (9) is a dominant parameter, as stated by Istratov and Librovich (1969).

The Landau instability criteria for spherical vapor bubble growth, expressed by Eq. (7), was tested for the same conditions as that for the Rayleigh-Taylor instability above, with the parameters of n-butane given in Fig. 8 and the numerical calculation procedure of Lee and Merte (1996a), with the prediction of a stable growth. Frost and Sturtevant (1986) applied the Landau criteria at the superheat limit earlier, with the result that the growing n-butane bubble also should be stable, in disagreement with their experiments. The Landau stability test was extended here to the experiments with R-113 shown in Fig. 2(a) and (b) as well, predicting stable growths, in all three cases regardless of the density ratio. It can be concluded from the above that the Landau instability criteria as applied to cases with evaporating interfaces should be reconsidered as well, for both the plane and the spherical cases.

4.3 Instability Model Including Heat Transfer. The lack of agreement with reality discussed in Sections 4.1 and 4.2 above suggest that some important mechanism is lacking in these models. Since the first observation of the roughened bubble in 1989, reported by Ervin et al. (1992), it was deduced that the local interfacial heat transfer would play an important role in the description of the interfacial instability. An analysis incorporating this mechanism was presented by Prosperetti and Plesset (1984), who directly solved the momentum and energy equations with appropriate interfacial boundary conditions. A number of common assumptions were made: the fluids are incompressible and inviscid, and Marangoni effects are neglected. Other essential assumptions include *linearization* and *normal mode*. Linearization restricts the analysis to amplitudes of perturbation which remain small, implying that if the later stages of perturbations are of interest, nonlinear terms must be considered. The assumption of linearization appears to be sufficiently justified for examining at least the onset of instability. The normal mode provides an exponential expression for the production of the perturbation growth rate (σ) and an evolution time duration (t) for the perturbation displacement. This assumption continues to be a subject of discussion in the literature, especially for basic transient systems. However, for present purposes the normal mode is associated with a quasi-steady assumption for the basic system. Higuera (1987) pointed out that the normal mode is applicable as an approximation.

The planar interfacial instability theory, including the heat transfer at the interface, proposed by Prosperetti and Plesset (1984), is combined with the present growing vapor bubble model here, with the assumption that the wavelength is sufficiently smaller than the bubble size. The perturbation displacement can be expressed as

$$\eta(x, y, t') = a_0 \exp(\sigma t') f(x, y). \quad (11)$$

It is necessary to determine the magnitude of $\mathrm{Re}(\sigma)$ since t' is always real and positive. The instability of the liquid-vapor interface depends totally on whether $\eta(x, y, t')$ is growing or decaying since it is presumed that sources of perturbations will always be present. $f(x, y)$ is a periodic function which satisfies $\nabla^2 f + k^2 f = 0$, and the function is eventually eliminated in the final characteristic equation. It is noted that the basic system prior to any perturbation is inherently one-dimensional, but becomes two or three-dimensional as the perturbation progresses. The small fluid motion is generally governed by the conservation of mass, the conservation of momentum, and the conservation of energy equations:

$$\nabla \cdot \mathbf{u} = 0 \quad (12)$$

$$\frac{\partial \mathbf{u}}{\partial t} + \mathbf{u} \cdot \nabla u = -\frac{1}{\rho}\nabla P + \mathbf{g} \quad (13)$$

$$\frac{\partial T}{\partial t} + \mathbf{u} \cdot \nabla T = \alpha \nabla^2 T. \quad (14)$$

The quantities for velocity, pressure, and temperature are decomposed by two components, which are vectors:

$$\mathbf{U} = \mathbf{U}_\mathbf{k} + \mathbf{U}', \quad (15)$$

where $\mathbf{U}_\mathbf{k}$ represents the quantity in the basic system, and $\mathbf{U}'$ the perturbed quantity, usually very small compared to $\mathbf{U}_\mathbf{k}$.

Equation (15) is applied to Eqs. (13) and (14) with the aid of Eq. (12). Using the linearization assumption, nonlinear terms and high-order terms are neglected, and subtracting the quantities in the basic system yields the *perturbation equations,* which are solved directly with interfacial boundary conditions. It is noted that the presence of surface tension was implied in the interfacial momentum boundary condition to account for the effect of curvature at the interface. The characteristic equation is obtained, following Prosperetti and Plesset (1984), as

$$S_1(\sigma) - S_2(\sigma) = 0, \tag{16}$$

where

$$S_1(\sigma) = [\rho_l(1 + I_l) + \rho_v(1 - I_l)]\sigma^2 + 2k[J + \rho_l(V_v - V_l)I_l]\sigma + (1 - I_l)[(\rho_l + \rho_v)\varpi_0^2 - k^2J(V_v - V_l)] - 2(\sigma + kV_v)J\left[\mu_l + \frac{1}{G_l}\left(\frac{\partial^2 T_l}{\partial z^2}\right)_0\right] \tag{17}$$

$$S_2(\sigma) = -\frac{K_l\mu_l + K_v\mu_v}{h_{fg}\partial J/\partial T_s}\{(\rho_l + \rho_v)(\sigma^2 + \omega_0^2) + kJ[2\sigma - k(V_v - V_l)]\} \tag{18}$$

$$\mu_l = \left[\left(\frac{V_l}{2D_l}\right)^2 + k^2 + \frac{\sigma}{D_l}\right]^{1/2} + \frac{V_l}{2D_l} \tag{19}$$

$$\mu_v = \left[\left(\frac{V_v}{2D_v}\right)^2 + k^2 + \frac{\sigma}{D_v}\right]^{1/2} - \frac{V_v}{2D_v}. \tag{20}$$

Surface tension appears in the expression for the natural frequency, ϖ_0.

$$\varpi_0^2 = [(\rho_l - \rho_v)/(\rho_l + \rho_v)]gk + [\zeta/(\rho_l + \rho_v)]k^3 \tag{21}$$

The function, I_l, which appears in several places in Eq. (17), has a significant physical meaning, and accounts for the effect of the distortion of the unperturbed temperature field caused by the liquid motion, given by

$$I_l = \frac{V_l}{D_l}\int_{-\infty}^{0} \exp[(k - \mu_l')z]\,\frac{\partial T/\partial z}{\partial T/\partial z|_0}\,dz, \tag{22}$$

where $\partial T/\partial z|_0$ is the liquid temperature gradient at the liquid-vapor interface in the basic system and

$$\mu_l' = \frac{V_l}{2D_l} - \left[\left(\frac{V_l}{2D_l}\right)^2 + k^2 + \frac{\sigma}{D_l}\right]^{1/2}. \tag{23}$$

It is interesting that the unperturbed temperature distribution appears in the perturbation equations. A difficulty arises in determining the unperturbed temperature field, $\partial T/\partial z$, at each moment in time. Since the unperturbed system is one-dimensional, it can be solved for $\partial T/\partial z$ using Laplace transforms, which are inserted into Eq. (22), giving

$$I_l(\tau, \beta) = \frac{2}{1 - \beta^2}[\text{erf}\,(\sqrt{\tau}) + \beta\{\text{erfc}\,(\beta\sqrt{\tau})\exp[(\beta^2 - 1)\tau] - 1\}], \tag{24}$$

where

$$\beta = \frac{2D_l}{V_l}\left[k + \left(\frac{V_l^2}{4D_l^2} + k^2 + \frac{\sigma}{D_l}\right)^{1/2}\right] \quad \text{and} \quad \tau = \frac{V_l^2}{4D_l}t.$$

It is noted that $I_l(\tau, \beta)$ is a function of the dimensionless β and τ, which have a significant meaning and relationship to the vapor velocity and liquid temperature distribution at the liquid-vapor interface, and hence arbitrary values of parameters having no physical basis may produce meaningless results. The original equation of Prosperetti and Plesset (1984) differs from Eq. (24), possibly due to an algebraic error.

It is also of interest to point out that the basic concepts of the Landau instability and those proposed by Prosperetti and Plesset (1984) may be viewed as identical, in the sense that when the space wise perturbed mass flux derived in the latter is taken as zero, the solution converges identically to the Landau dispersion equation for a plane interface, similar to Eq. (7) here. This corresponds to the case of uniform evaporation along the interface.

Using the instantaneous information given in Fig. 6, e.g., at 1×10^{-4} seconds, liquid-vapor interface velocity = 2.02 m/s, interface temperature = 48.87°C, and interface acceleration = -1.36×10^4 m/s^2, it is possible to compute the instability criteria, solving Eq. (16) for the perturbation growth rate, σ. The value of σ can be either real or complex. If σ is real and positive, the amplitude of any perturbation grows monotonically. If σ is complex the perturbation may decay or correspond to an oscillating surface wave of growing amplitude. Only positive values of $\text{Re}(\sigma)$ are considered here as describing unstable conditions. Both the real and imaginary components of σ are given in Fig. 9 at 0.1 ms for the conditions of Fig. 6, and positive values of $\text{Re}(\sigma)$ occur in a range of wave numbers (k) from 1.5×10^3 to 6×10^4 1/m, with the maximum wave number of 3×10^4 1/m corresponding to a perturbation growth rate of 4×10^3 1/s. The maximum growth rate with the corresponding wave number is considered to be the most unstable in practice, and is in agreement with measurements, as will be demonstrated below.

5 Stability Criteria

Microgravity experiments have the advantage of providing the instantaneous conditions at boiling nucleation, since the fluid is quiescent until the disturbance of boiling takes place, making it feasible to measure the heater surface temperature and compute the temperature distribution.

5.1 Most Unstable Regime. Using the information shown in Fig. 6, it is possible to compute the time-varing neutral stability curve, together with the wavenumbers which provide the maximum perturbation growth rate, given in Fig. 10. The growing bubble radius is included, together with the corresponding measurements, all of which have unstable interfaces, as shown in Figure 2(a). The apparent unstable regime exists over a wide interval of time. However, a constraint must be imposed

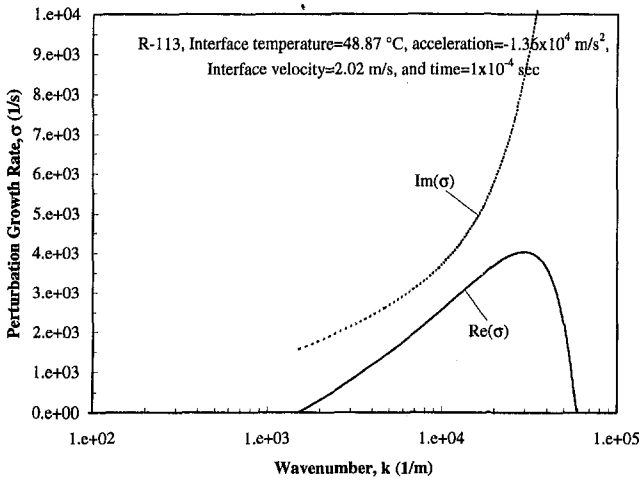

Fig. 9 Perturbation growth rate at 0.1 milliseconds for PBMT1102.800

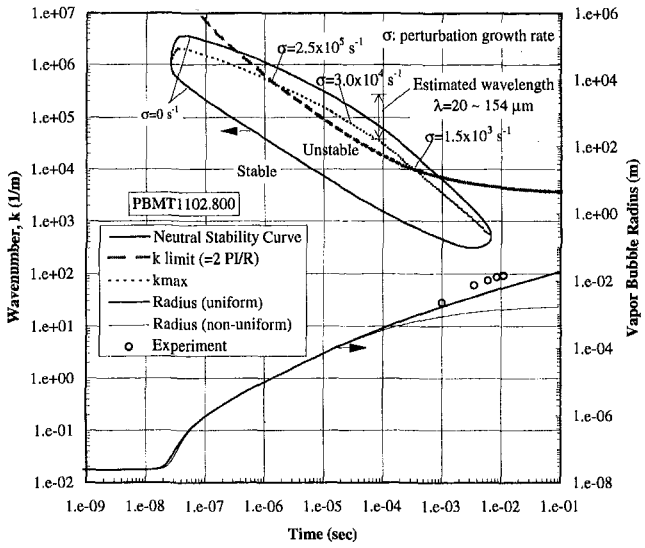

Fig. 10 Neutral stability diagram and growing bubble radius for R113, experimental data code PBMT1102.800, Fig. 2(*a*)

within this regime in that the wavelength cannot exceed the bubble diameter. This is called the "k limit", defined as $2\pi/R$, for practical reasons as discussed previously by Sturtevant and Shepherd (1982), and is included in Fig. 10. *The "most unstable regime"* is determined by the intersections between the "k limit curve" and the maximum wavenumber curve, giving a range of times between 1.2×10^{-6} and 3.0×10^{-4} seconds as the interval of instability. The radii measurements indicated are beyond this interval, demonstrating that the onset of the instability occurred earlier. The corresponding computations were carried out for the case of Fig. 2(b), which demonstrated a distinctive stable bubble growth, and the results are presented in Fig. 11. The conditions required for the "most unstable regime" are satisfied only marginally, which indicates that the probability for instability will be low, considering that the "k limit" curve is the lower bound. The result is in fair agreement with the measurements, in which the measured bubble radii are between the computational limits.

It is also possible now to consider the work of Shepherd and Sturtevant (1982) with n-butane. First of all, only the initially uniform model need be used to predict the bubble growth. As discussed above, the conventional instability theories fail to describe the behavior, which is obviously unstable. The present instability model, which includes the local heat transfer, was used to assess the stability criteria as a function of time. The results are given in Fig. 12, together with measurements of the bubble radius. The "*most unstable regime*" is in good agreement with the measurements, which are in the range of 1×10^{-5} to 1×10^{-4} seconds, as shown.

5.2 Wavelength Predictions. A question arises as to how well the wavelengths predicted by the instability theory compare with the measurements. According to the work of Shepherd and Sturtevant (1982), the wavelength (λ) of the growing vapor bubble shown in Fig. 7(b) ranges between 20 and 40 μm at the time of 12 μs following nucleation, for a bubble size of 150 μm in diameter. This corresponds to a range of wavenumbers of $3.14 \times 10^5 \sim 1.57 \times 10^5$ 1/m, which is indicated in Fig. 12, showing an agreement with the computed results, where the vertical range of wavenumber crosses the "kmax" curve within the "most unstable regime".

An attempt was made to apply the wavelength prediction to the present experiment of Fig. 10. However, since the measurements are temporally beyond the most unstable regime, a direct comparison cannot be made. If the number of wavelengths per bubble can be presumed to remain constant as the bubble grows, which is equivalent to the assumption of a linear circumferential stretch of the perturbations with bubble radius R, the wavelength at a certain earlier time can be calculated backward from the measurable size bubble. The bubble in Fig. 1, which has wavelengths in the range $\lambda = 0.5$ mm $\sim$ 4 mm for 17.5 ms, was selected, giving a range of estimated wavelengths of 20 $\sim$ 154 μm at 0.1 ms, corresponding to wavenumbers in the range of $4.0 \times 10^4 \sim 3.3 \times 10^5$ 1/m, which is in reasonable agreement with the theoretical predictions in Fig. 10. As a result, it would appear that the stability theory as presented here predicts not only the occurrence of the interfacial instability as a function of time, but also the corresponding wavelengths.

5.3 General Mechanisms of Instability. Presuming that a small perturbation in the form of a sinusoidal function arises at a liquid-vapor interface where evaporation is taking place,

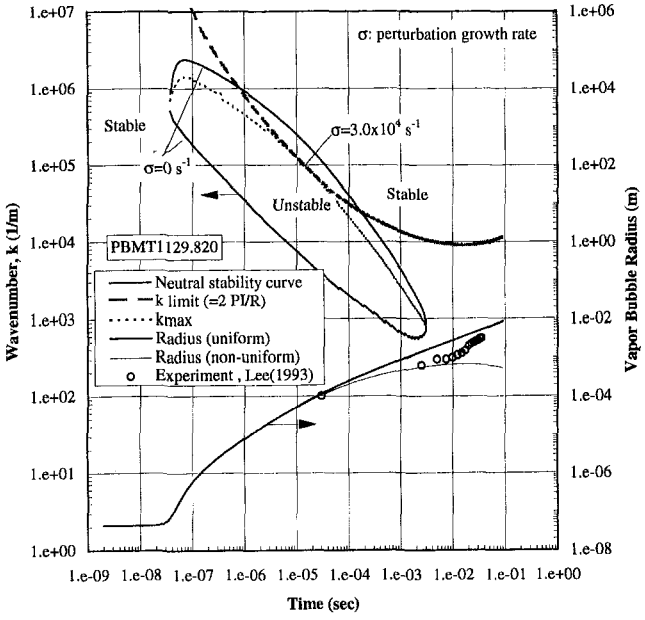

Fig. 11 Neutral stability diagram and growing bubble radius for R113, experimental data code PBMT1129.820, Fig. 2(*b*)

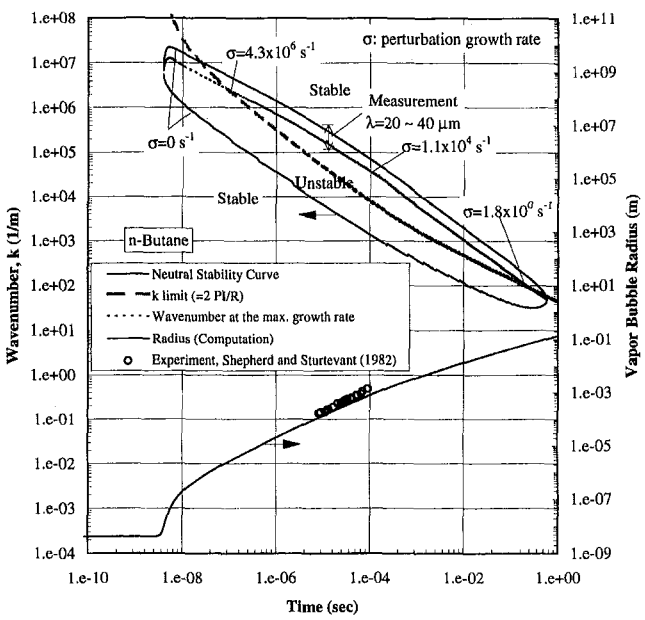

Fig. 12 Neutral stability diagram and growing bubble radius for *n*-butane

the instability theory described above incorporates the local heat transfer such that the evaporation at a crest differs from that at the trough, while the conventional hydrodynamic stability has a uniform mass flux along the interface. The temperature gradient in the liquid at a trough increases, promoting evaporation, while the evaporation at a crest decreases. The increased evaporation in the trough deepens the trough because of vapor recoil, leading to further increases in the temperature gradient. Although the linearized stability theory described here is mathematically restricted to small perturbations, it is sufficient to determine the onset of an instability over a short time interval. Once the theory predicts the interface to be unstable, it is speculated that the interfacial motion is enhanced, owing to the above mentioned phenomena, and the neck of a valley eventually becomes sufficiently narrowed so that a liquid droplet may be separated from the interface, becoming entrained with the departing vapor. The entrainment of such small liquid drops was directly observed by Frost (1988), and presumably explains why the mass flux of wrinkled bubbles is one or two orders greater than that predicted by the classical bubble growth theory.

In general, surface tension, gravity, viscosity, sphericity, and divergence of streamlines have stabilizing effects on vapor bubble growth, while Marangoni effects and moving boundaries are destabilizing factors, where the moving boundary refers to the liquid-vapor interface movement due to evaporation. The weak point of the present instability theory is that the plane theory is applied to the spherical bubble growth problem. This is compensated in part by the spherical constraint "k limit" discussed in Section 5.1 above. If an intrinsically spherical instability theory including heat transfer can be developed, it may be anticipated that it will have a tendency to be more stable.

6 Conclusions

The occurrence of extremely rapid evaporation at a vapor bubble interface has been demonstrated with superheats far below the superheat limit. This occurred with pool boiling in a microgravity environment, and is attributed to the growth of an interfacial instability. Such a process can produce an abrupt pressure rise and be quite destructive if a sufficiently large heater surface area is present.

Sources of perturbation growth other than an instability can arise at the liquid-vapor interface of a bubble. The present plane instability model including heat transfer reasonably predicts not only the occurrence of explosive bubble growth, but also the wavelength of the unstable interface. Local heat transfer at the interface is an essential mechanism to the instability, where the heat transfer increases at a trough while it decreases at the crest, which can produce differential vapor recoil. This can lead to the distortion of the crests such that liquid particles become entrained with the vapor, departing the interface, and which can then serve to further increase the evaporative flux.

References

Avedisian, C. T., 1985, "The Homogeneous Nucleation Limits of Liquids," *J. Phys. Chem. Ref. Data,* Vol. 14, No. 3, pp. 695–729.

Birkhoff, G., 1956, "Stability of Spherical Bubble," *Q. Appl. Math,* Vol. 13, pp. 451.

Ervin, J. S., 1991, "Incipient Boiling in Microgravity," Ph.D. thesis, University of Michigan, Ann Arbor, MI.

Ervin, J. S., Merte, H., Keller, R. B., and Kirk, K., 1992, "Transient Pool Boiling in Microgravity," *Int. J. Heat Mass Transfer,* Vol. 35, pp. 659–674.

Frost, D. L., 1988, "Dynamics of Explosive Boiling of a Droplet," *Phys. Fluids,* Vol. 31, pp. 2554–2561.

Frost, D., and Sturtevant, B., 1986, "Effects of Ambient Pressure on the Instability of a Liquid Boiling Explosively at the Superheat Limit," ASME JOURNAL OF HEAT TRANSFER, Vol. 108, pp. 418–424.

Grolmes, M. A., and Fauske, H. K., 1974, "Axial Propagation of Free Surface Boiling into Superheated Liquids in Vertical Tubes," *Proceeding of the Fifth International Heat Transfer Conference,* Vol. 4, JSME, Tokyo, pp. 30–34.

Higuera, F. J., 1987, "The Hydrodynamic Stability of an Evaporating Liquid," *Phys. Fluids,* Vol. 30, pp. 679–686.

Istratov, A. G., and Librovich, V. B., 1969, "On the Stability of Gasdynamic Discontinuities Associated with Chemical Reactions: The Case of a Spherical Flame," *Astronautica Acta,* Vol. 14, pp. 453–467.

Landau, L., 1944, "On the Theory of Slow Combustion," *Acta Physicochemica U.S.S.R.,* Vol. 19, pp. 76–85.

Landau, L., and Lifshitz, E. M., 1959, *Fluid Mechanics,* Pergamon, New York, pp. 479.

Lee, H. S., 1993, "Vapor Bubble Dynamics in Microgravity," Ph.D. thesis, The University of Michigan, Ann Arbor, MI.

Lee, H. S., and Merte, H., 1996a, "Spherical Bubble Growth in Liquids in Uniformly Superheated Liquids," *Int. J. Heat Mass Transfer,* Vol. 39, No. 12, pp. 2427–2447.

Lee, H. S., and Merte, H., 1996b, "Hemispherical Vapor Bubble Growth in Microgravity: Experiments and Model," *Int. J. Heat Mass Transfer,* Vol. 39, No. 12, pp. 2449–2461.

McCann, H., Clarke, L. J., and Masters, A. P., 1989, "An Experimental Study of Vapour Growth at the Superheat Limit Temperature," *Int. J. Heat Mass Transfer,* Vol. 32, pp. 1077–1093.

Merte, H., and Lee, H. S., 1997, "Quasi-Homogeneous Nucleation in Microgravity at Low Heat Flex: Experiments and Theory," ASME JOURNAL OF HEAT TRANSFER, Vol. 119, pp. 305–312.

Mikic, B. B., Rohsenow, W. M., and Griffith, P., 1970, "On Bubble Growth Rates," *Int. J. Heat Transfer,* Vol. 13, pp. 657.

Miller, C. A., 1973, "Stability of Moving Surface in Fluid Systems With Heat and Mass Transport," *AIChE Journal,* Vol. 19, No. 5, pp. 909–915.

Palmer, H. J., 1976, "The Hydrodynamic Stability of Rapidly Evaporating Liquids at Reduced Pressure," *J. Fluid Mech.,* Vol. 75, pp. 487–511.

Palmer, H. J., and Maheshri, J. C., 1981, "Enhanced Interfacial Heat Transfer by Differential Vapor Recoil Instabilities," *Int. J. Heat Transfer,* Vol. 4, pp. 117–123.

Plesset, M. S., 1954, "On the Stability of Fluid Flows With Spherical Symmetry," *J. Appl. Phys.,* Vol. 25, pp. 96–98.

Plesset, M. S., and Prosperetti, A., 1977, "Bubble Dynamics and Cavitation," *Ann. Rev. Fluid Mech.,* Vol. 9, pp. 145–185.

Plesset, M. S., and Zwick, S. A., 1954, "The Growth of Vapor Bubble in Superheated Liquid," *J. Appl. Phys.,* Vol. 25, pp. 493.

Prosperetti, A., and Plesset, M. S., 1978, "Vapor Bubble Growth in a Superheated Liquid," *J. Fluid Mech.,* Vol. 85, Part 2, pp. 349–368.

Prosperetti, A., and Plesset, M. S., 1984, "The Stability of an Evaporating Liquid Surface," *Phys. Fluids,* Vol. 27, pp. 1590–1602.

Rayleigh, 1917, *Phil. Mag.,* No. 34, p. 94.

Reid, R. C., 1983, "Rapid Phase Transitions from Liquid to Vapor," *Advances in Chemical Engineering,* Vol. 12, pp. 105–208.

Shepherd, J. E., and Sturtevant, B., 1982, "Rapid Evaporation at the Superheat Limit," *J. Fluid Mech.,* Vol. 121, pp. 379–402.

Sturtevant, B., and Shepherd, J. E., 1982, "Evaporative Instability at the Superheat Limit," *Appl. Sci. Res.,* Vol. 38, pp. 85–97.

Taylor, G. I., 1950, "The Stability of Liquid Surfaces When Accelerated in a Direction Perpendicular to Their Planes: I," *Proc. R. Soc. Lond.,* Vol. A201, pp. 192.

Numerical Simulation of Film Boiling Near Critical Pressures With a Level Set Method

G. Son

V. K. Dhir
vdhir@seas.ucla.edu

Department of Mechanical and Aerospace Engineering,
University of California, Los Angeles,
400 Westwood Plaza,
Box 95197,
Los Angeles, CA 90095-1597

Attempts have recently been made to numerically simulate film boiling on a horizontal surface. It has been observed from experiments and numerical simulations that during film boiling the bubbles are released alternatively at the nodes and antinodes of a Taylor wave. Near the critical state, however, hydrodynamic transition in bubble release pattern has been reported in the literature. The purpose of this work is to understand the mechanism of the transition in bubble release pattern through complete numerical simulation of the evolution of the vapor-liquid interface. The interface is captured by a level set method which is modified to include the liquid-vapor phase change effect. It is found from the numerical simulation that at low wall superheats the interface moves upwards, bubbles break off, and the interface drops down alternatively at the nodes and antinodes. However, with an increase in wall superheat, stable vapor jets are formed on both the nodes and antinodes and bubbles are released from the top of the vapor columns. The numerical results are compared with the experimental data, and visual observations reported in the literature are found to be in good agreement with the data.

Introduction

In recent years, significant efforts have been made to understand interfacial dynamics associated with phase change processes, such as film boiling, condensation on the underside of a horizontal surface, and melting or sublimation of a substrate placed beneath a pool of heavier liquid.

Berenson (1961) developed a semiempirical model of saturated film boiling on a horizontal surface. He assumed that vapor bubbles were placed on a square grid with a spacing equal to two-dimensional "most dangerous" Taylor wavelength, λ_{d2} $(=2\pi\sqrt{3\sigma/g(\rho_l - \rho_v)})$, and a thin vapor film of uniform thickness connected the neighboring bubbles. By further assuming that the mean bubble height and bubble diameter were proportional to the bubble spacing, and two bubbles were supported per λ_{d2}^2 area of the heater, he predicted the Nusselt number for film boiling as

$$\mathrm{Nu}_B = 0.425(\mathrm{Gr}\,\mathrm{Pr}/\beta)^{1/4}. \quad (1)$$

The predictions from Eq. (1) were found to compare well with Berenson's data. However, Berenson's model did not account for the time variation of either the film thickness and the bubble height or bubble diameter and the flow field in the liquid.

Dhir et al. (1977) studied pseudofilm boiling during sublimation of a slab of dry ice placed beneath a pool of warm liquid. The heat transfer rate was determined by noting a change in the enthalpy of the overlying liquid pool. Data were found to compare favorably with prediction from an equation similar to Eq. (1) when the lead constant was reduced to 0.36. It was argued that the reduction of about 15 percent in the lead constant resulted from the fact that during sublimation only one bubble was supported per λ_{d2}^2 area instead of $\lambda_{d2}^2/2$ as assumed by Berenson. This was based on their experimental observation that the bubbles were released from the same location rather than alternately from the nodes and antinodes as observed during film boiling on flat plates or during early period of sublimation.

Film boiling on a horizontal platinum wire in water near its critical state was investigated by Reimann and Grigull (1975). They observed that the vapor removal configurations were dependent upon the magnitude of heat flux from the wire. At low heat fluxes, discrete bubbles were released from the heater, which is similar to the observations during film boiling at one atmosphere pressure. However, with increase in heat flux, vapor left the heater in the form of jets. Similar transitions were subsequently observed by Dhir and Taghavi-Tafreshi (1981) during dripping of a liquid from underside of a horizontal tube.

Klimenko (1981) carried out a somewhat generalized analysis of film boiling on horizontal flat plates. Employing a basic formulation, similar to that of Berenson, Klimenko developed a correlation that included data near critical pressures. According to his correlation, Nusselt number data for film boiling on an upward facing horizontal surface was expressed within ±25 percent as

$$\mathrm{Nu}_K = 1.90 \times 10^{-1}\,\mathrm{Gr}^{1/3}\,\mathrm{Pr}^{1/3} f_1; \quad \text{for} \quad \mathrm{Gr} < 4.03 \times 10^5 \quad (2)$$

$$\mathrm{Nu}_K = 2.16 \times 10^{-2}\,\mathrm{Gr}^{1/2}\,\mathrm{Pr}^{1/3} f_2; \quad \text{for} \quad \mathrm{Gr} > 4.03 \times 10^5, \quad (3)$$

where

$$f_1 = 1 \quad \text{for} \quad \beta > 0.71$$
$$= 0.89\beta^{-1/3} \quad \text{for} \quad \beta < 0.71$$
$$f_2 = 1 \quad \text{for} \quad \beta > 0.50$$
$$= 0.71\beta^{-1/2} \quad \text{for} \quad \beta < 0.50.$$

Equations (2) and (3) suggest that for small values of $\beta(= c_{pv}\Delta T/h_{fg})$, the heat transfer coefficient should vary as $\Delta T^{-1/3}$ or $\Delta T^{-1/2}$ depending on the magnitude of Grashof number, Gr. For high values of β, the heat transfer coefficient is predicted to be independent of wall superheat.

The above described studies have provided us with data and semiempirical models for a description of film boiling on flat

Contributed by the Heat Transfer Division for publication in the JOURNAL OF HEAT TRANSFER and presented at '97 NHTC, Baltimore. Manuscript received by the Heat Transfer Division May 15, 1997; revision received August 28, 1997; Keywords: Boiling; Multiphase Flows; Phase-Change Phenomena. Associate Technical Editor: R. W. Douglass.

plates. However, many of the assumptions made in the models (e.g., constant film thickness between bubbles as assumed in Berenson's model for the heat transfer coefficient in film boiling) remain *not validated.* Very recently, Son and Dhir (1997) have carried out a complete numerical simulation of the evolution of the vapor-liquid interface during saturated film boiling on a horizontal surface. For an axisymmetric case they have used a coordinate transformation technique supplemented by a numerical grid generation method. In the method, the matching conditions at the interface can be imposed accurately as long as computational grids can be constructed numerically. From the numerical simulation, the film thickness and, in turn, the heat transfer coefficient are found to vary both spatially and temporally. Another numerical study of film boiling, independent of Son and Dhir's work, has been reported by Juric and Tryggvason (1996). They used a two-dimensional front-tracking method which could handle breaking of the interface. In their method, the interface was described as a transition region of finite thickness rather than as a surface separating two fluids. However, the heat transfer rates predicted from both numerical studies were lower than those predicted from Berenson's correlation. This underprediction could probably be caused by three-dimensional effects of the bubble release pattern. Generally, the front-tracking method, when the interface is described explicitly, is very hard to use for three-dimensional problems.

In this paper, a level set approach is adopted as a method that can not only handle break-off and merger of the interfaces, but can also be extended easily to three-dimensional problems. The numerical algorithm developed by Sussman et al. (1994) for incompressible two-phase flow is modified to include the effect of liquid-vapor phase change. Also, a stream function-based formulation for mass conservation is replaced by a pressure-based formulation which can be much more easily generalized to three-dimensional problems. Although the level set method is formulated for axisymmetric flows in this study, it can be easily generalized to three-dimensional flows. The objectives of this work are to apply the modified level set method to saturated film boiling near critical pressures and to understand the mechanism of transition in a bubble release pattern with an increase in heat flux or wall superheat.

Numerical Analysis

In this study, the computations are performed for two-dimensional incompressible flow, which is described in axisymmetric coordinates. The computation domain is chosen as the circular regions around the nodes and antinodes of the Taylor wave as shown in Fig. 1. Each circle has an area $\lambda_{d2}^2/2$ and its origin is located on the center of a node and an antinode where the bubbles are released. By using this configuration it is possible not only to describe vapor bubbles as spherical rather than cylindrical, but also the alternate release of bubbles from nodes and antinodes can be modeled. The axisymmetric approximation is not expected to be so restrictive for vapor bubbles during film boiling. As has been verified from the experimental observations, vapor bubbles during film boiling are nearly axisymmetric. However, the effect of lack of axisymmetry on the numerical results of heat transfer can be estimated quantitatively only when three-dimensional computations are performed, which

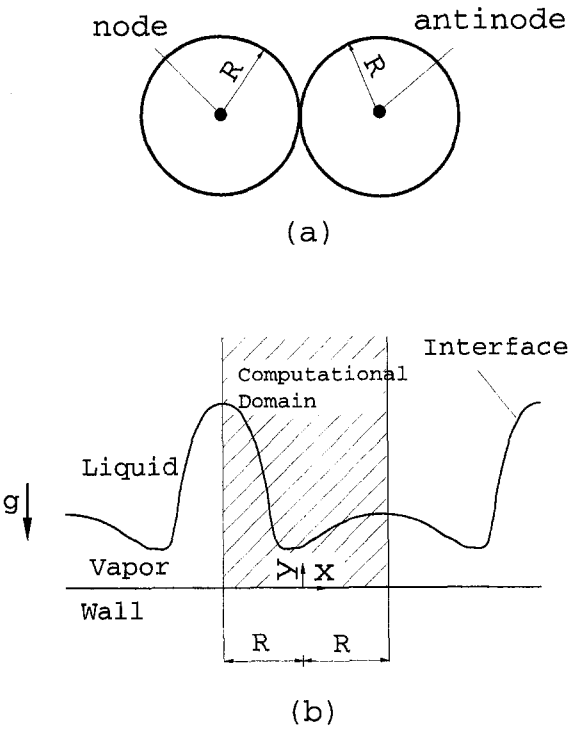

Fig. 1 Two-circular regions used in numerical simulations: (*a*) top view and (*b*) side view.

Nomenclature

$A = (V_v - V_l)/V_c$
a = radius of a vapor jet
c_p = specific heat at constant pressure
$\vec{g}$ = gravity vector
Gr = Grashof number, $(\rho_v^2 g l_o^3/\mu_v^2)(\rho_l/\rho_v - 1)$
H = step function
h = grid spacing
h_{fg} = latent heat of evaporation
k = thermal conductivity
l_o = characteristic length, $\sqrt{\sigma/g(\rho_l - \rho_v)}$
$\dot{m}$ = mass flux vector defined in Eq. (11)
Nu = Nusselt number, $l_o q_w/k_v \Delta T$
p = pressure
Pr = Prandlt number, $c_{pv}\mu_v/k_v$
q = heat flux
R = radius of each circular region
r = radial coordinate, $R - |x|$
Re = Reynolds number, $\rho_v u_o l_o/\mu_v$
$\tilde{S}_u$ = source term vector
T = temperature
ΔT = temperature difference, $T_w - T_{sat}$
u = x-directional velocity
$\vec{u}$ = velocity vector, (u, v)
$\vec{u}_i$ = interfacial velocity vector
u_o = characteristic velocity, $\sqrt{gl_o}$
V = base velocity
$\dot{V}$ = volume flow rate per jet
V_c = critical velocity
v = y-directional velocity
$v_{fg} = \rho_v^{-1} - \rho_l^{-1}$
x = horizontal coordinate
y = vertical coordinate
$\alpha = 2\pi a/\lambda$
β = the ratio of sensible heat to latent heat, $c_{pv}\Delta T/h_{fg}$
$\beta' = \beta/(1 + 0.5\beta)$
δ = vapor film thickness
κ = interfacial curvature
λ = wavelength
λ_{d2} = two-dimensional "most dangerous" wavelength
μ = viscosity
ρ = density
σ = surface tension
ϕ = level set function
ω = growth rate of interfacial disturbance

Subscripts

int = interface
l, v = liquid, vapor
sat, w = saturation, wall
t = partial differentiation with respect to t
x, y = partial differentiation with respect to x, y

will be done in the future. A horizontal coordinate, x, is defined in the interval of $-R \le x \le R$. Here the radius of each circle, R, is evaluated as

$$R = \lambda_{d2}/\sqrt{2\pi} = \sqrt{6\pi\sigma/g(\rho_l - \rho_v)}. \quad (4)$$

At the boundary of each circular region, $x = 0$, fluid velocity and temperature are assumed to be continuous. The equations describing the flow in both circular regions can be obtained if r and $\partial/\partial r$, included in the equations describing purely axisymmetrical flows, are replaced by $r = R - |x|$ and $\partial/\partial x$.

It is assumed that fluid properties, including density, viscosity and thermal conductivity, are constant in each phase. The interface separating the two phases is captured by a level set function, ϕ, which is defined as a signed distance from the interface: the negative sign is chosen for the vapor phase and the positive sign for the liquid phase.

The equations governing the momentum conservation including gravity and surface tension are written as

$$\rho(\vec{u}_t + \vec{u}\cdot\nabla\vec{u}) = -\nabla p + \rho\vec{g} - \sigma\kappa\nabla H + \nabla\cdot\mu\nabla\vec{u} + \vec{S}_u, \quad (5)$$

where $\vec{u} = (u, v)$ and $\vec{S}_u = (S_u, S_v)$. S_u and S_v are defined as

$$S_u = r^{-1}(r\mu u_x)_x + (\mu v_x)_y - \mu r^{-2}u$$

$$S_v = r^{-1}(r\mu u_y)_x + (\mu v_y)_y.$$

In Eq. (5), σ is the surface tension, H is a step function ($H = 0$ for $\phi < 0$ and $H = 1$ for $\phi > 0$) and κ is the interfacial curvature expressed as

$$\kappa = \nabla\cdot\frac{\nabla\phi}{|\nabla\phi|}. \quad (6)$$

The surface tension force, $-\sigma\kappa\nabla H$, is implemented in the volume form to avoid the need for explicit description of the interface (Brackbill et al., 1992). Also, density and viscosity are described as

$$\rho = \rho_v + (\rho_l - \rho_v)H \quad (7)$$

$$\mu^{-1} = \mu_v^{-1} + (\mu_l^{-1} - \mu_v^{-1})H. \quad (8)$$

Alexiades and Solomon (1993) have shown that the viscosity formulation given by Eq. (8) can be more effective in evaluating such transport properties as viscosity and conductivity than that is possible by the form given by Eq. (7). Also, this formulation for two-phase flow can be obtained by modifying the formulation for transport properties proposed by Patankar (1980). Patankar's formulation for transport properties at the interface was based on the continuity of fluxes. For example, the heat flux at point B in Fig. 2(a) is formulated numerically using a piecewise-linear temperature profile as

$$qh = \frac{T_A - T_D}{k^{-1}} = \frac{T_A - T_D}{k_v^{-1}(1 - f_B) + k_l^{-1}f_B},$$

where h is a grid spacing and $f_B = h_B/h$. From this equation, Patankar interpolated the conductivity at point B as

$$k^{-1} = k_v^{-1} + f_B(k_l^{-1} - k_v^{-1}).$$

However, for two-phase flow with a moving interface, the interface is more possibly located at point C between point A and point D, rather than at point B, as shown in Fig. 2(b). The heat flux at point B is formulated as

$$qh = \frac{T_A - T_D}{k^{-1}} = \frac{T_A - T_D}{k_v^{-1}(1 - f_C) + k_l^{-1}f_C},$$

where $f_C = h_C/h$, and it is changing with time. Thus, for two-phase flow the conductivity at point B is formulated as

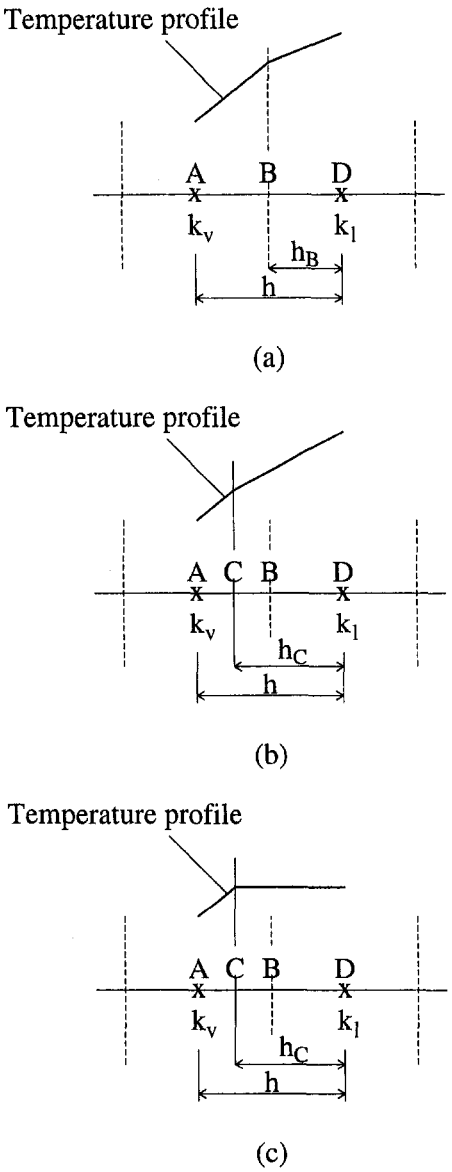

Fig. 2 Schematic diagram for the conductivity formulation: (*a*) proposed by Patankar (1980) (*b*) modified for two-phase flow and (*c*) modified for two-phase flow with $k_l^{-1} = 0$.

$$k^{-1} = k_v^{-1} + f_C(k_l^{-1} - k_v^{-1}).$$

When the interface thickness is h, f_C is equivalent to H.

The energy equation for film boiling is derived to satisfy the condition that the vapor-liquid interface is maintained at the saturation temperature:

$$\rho_v c_{pv}(T_t + \vec{u}\cdot\nabla T) = \nabla\cdot k\nabla T \quad \text{for} \quad H < 1$$

$$T = T_{\text{sat}} \quad \text{for} \quad H = 1, \quad (9)$$

where the effective thermal conductivity is evaluated by setting $k_l^{-1} = 0$ (no temperature gradient in the liquid) as

$$k^{-1} = k_v^{-1}(1 - H). \quad (10)$$

The condition $T = T_{\text{sat}}$ is imposed at the grids for $H = 1$. This simple implementation is good enough to get a correct heat flux while using the conductivity formulation given by Eq. (10), which is shown in Fig. 2(c). In this study, T_{sat} is defined as the saturation temperature at the system pressure. Considering interfacial curvature effects, the interface temperature at the

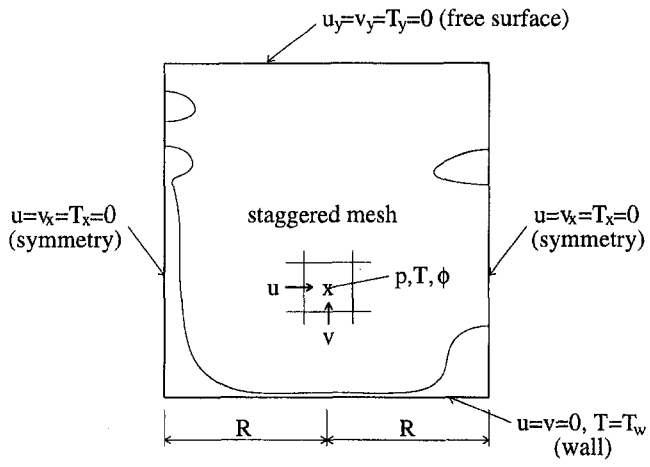

Fig. 3 Computational grid with boundary conditions

vapor side, $T_{\text{int},v}$, is obtained from the Clausius-Clapeyron relation as

$$T_{\text{int},v} = T_{\text{sat}}(p_v) = T_{\text{sat}}(p_l + \sigma\kappa) = T_{\text{sat}}(p_l) + \frac{T_{\text{sat}}\sigma\kappa v_{fg}}{h_{fg}}.$$

Even if κ is chosen as $100/\lambda_{d2}$, $(T_{\text{int},v} - T_{\text{sat}})/\Delta T$ for film boiling of water is less than 10^{-3} at 1 atm. pressure, and it is reduced up to 10^{-6} near the critical pressure. Also, the interface temperature at the liquid side, $T_{\text{int},l}$, is obtained from a kinetic theory as

$$T_{\text{int},l} = T_{\text{int},v} + q/h_{ev},$$

where h_{ev} is an evaporative coefficient. The magnitude of h_{ev} varies from 1.6×10^7 (W/m^{2}K) to 3.1×10^7 (W/m^{2}K) for film boiling of water at 1 atmosphere and critical pressure, respectively. Therefore, for film boiling the interface temperature at both the vapor side and the liquid side can be assumed to be $T_{\text{sat}}(p_l)$, within 0.1 percent error.

The equation governing the mass conservation should include the effect of volume expansion due to liquid-vapor phase change. It is derived from the conditions of the mass continuity and energy balance at the interface

$$\dot{m} = \rho_v(\vec{u}_i - \vec{u}_v) = \rho_l(\vec{u}_i - \vec{u}_l) \tag{11}$$

and

$$\dot{m} = -k\nabla T/h_{fg}. \tag{12}$$

Thereafter,

$$\vec{u}_l - \vec{u}_v = v_{fg}\dot{m}, \tag{13}$$

where $v_{fg} = \rho_v^{-1} - \rho_l^{-1}$. Using Eq. (13) in a manner similar to that used for implementation of the surface tension into the momentum equation, the equation governing mass conservation can be formulated as

$$\nabla \cdot \vec{u} = v_{fg}\dot{m} \cdot \nabla H. \tag{14}$$

The boundary conditions used in this study are as follows (refer to Fig. 3):

- *At the wall ($y = 0$):*

$$u = v = 0; \quad T = T_w \tag{15}$$

- *At the planes of axisymmetry ($x = \pm R$):*

$$u = v_x = T_x = 0 \tag{16}$$

- *At the top of computational domain (free surface):*

$$u_y = v_y = T_y = 0 \tag{17}$$

In the level set formulation, the vapor-liquid interface is described as $\phi = 0$. The zero level set of ϕ is advanced by the interfacial velocity while solving the following equation:

$$\phi_t = -\vec{u}_i \cdot \nabla\phi, \tag{18}$$

where

$$\vec{u}_i = \vec{u} + \rho^{-1}\dot{m}, \tag{19}$$

where ρ is the interpolated density. It was noted by Sussman et al. (1994) that the level set function should be maintained as a distance function at all times to prevent excessive numerical errors. Therefore, at each time step the level set function is reinitialized as a distance function, $|\nabla\phi| = 1$, from the interface by obtaining a steady-state solution of the equation

$$\phi_t = \frac{\phi_o}{\sqrt{\phi_o^2 + h^2}}(1 - |\nabla\phi|), \tag{20}$$

where ϕ_o is a solution of Eq. (18), and h is a grid spacing. While computing Eq. (20) numerically, the zero level set might be slightly changed due to discretization. Such a deviation, therefore, may be amplified by constant reinitialization of the level set function as indicated by Sussman et al. (1994). To prevent numerical instability arising from discontinuous material properties, the step function is smoothed as

$$\begin{aligned} H &= 1 \quad \text{if} \quad \phi \geq +1.5h \\ &= 0 \quad \text{if} \quad \phi \leq -1.5h \\ &= 0.5 + \phi/(3h) + \sin[2\pi\phi/(3h)]/(2\pi) \\ &\qquad \text{if} \quad |\phi| \leq 1.5h. \end{aligned} \tag{21}$$

This equation implies that the interface separating two phases is replaced by a transition region of finite thickness. The interface thickness can be maintained as constant for all the time while keeping the level set function as a distance function. When the interface thickness was varied from $2h$ to $4h$, the effect of the interface thickness on the evolution of the interface was observed to be negligible.

When discretizing the governing equations temporally, the diffusion terms are treated by a fully implicit scheme and the convection and source terms by a first-order explicit method. Then, the discretized governing equations are expressed as

$$(\phi^{n+1} - \phi^n)/\Delta t = -\vec{u}_i^n \cdot \nabla\phi^n \tag{22}$$

$$|\nabla\phi^{n+1}| = 1 \quad \text{for} \quad \phi \neq 0 \tag{23}$$

$$\rho_v c_{pv}(T^{n+1} - T^n)/\Delta t = -\rho_v c_{pv}\vec{u}^n \cdot \nabla T^n + \nabla \cdot k\nabla T^{n+1} \tag{24}$$

$$\rho(\vec{u}^{n+1} - \vec{u}^n)/\Delta t = -\rho\vec{u}^n \cdot \nabla\vec{u}^n - \nabla p^{n+1} - \sigma\kappa\nabla H + \rho\vec{g} + \nabla \cdot \mu\nabla\vec{u}^{n+1} + \vec{S}_u^n \tag{25}$$

$$\nabla \cdot \vec{u}^{n+1} = v_{fg}\dot{m}^{n+1} \cdot \nabla H, \tag{26}$$

where superscript n and $n + 1$ represent n and $n + 1$ time steps, respectively. Fluid properties and the step function are evaluated from ϕ^{n+1}.

In order to obtain the governing equation for pressure which achieves mass conservation, the fractional-step method or projection method, is used. This method has been developed by Chorin (1968), Kim and Moin (1985), and Bell et al. (1989). In this study, the projection method is formulated in a staggered grid system in which the locations for velocity components are displaced from those for pressure and temperature (refer to Fig. 3). This is done to avoid the difficulty caused by pressure boundary conditions. The momentum equation (25) is decomposed into two fractional steps:

$$\rho \frac{\vec{u}^* - \vec{u}^n}{\Delta t} = -\rho \vec{u}^n \cdot \nabla \vec{u}^n - \nabla p^n + \rho \vec{g} - \sigma \kappa \nabla H + \nabla \cdot \mu \nabla \vec{u}^* + \vec{S}_u^n \quad (27)$$

$$\vec{u}^{n+1} = \vec{u}^* - \Delta t (p^{n+1} - p^n)/\rho. \quad (28)$$

First, Eq. (27) is solved using the pressure evaluated at the previous time step. Then, the resulting velocity, $\vec{u}^*$, which does not satisfy the continuity equation, is corrected, as given by Eq. (28). When substituting Eq. (28) into Eq. (27), and then comparing with Eq. (25), the projection error can be estimated to be of the order of $\Delta t(p^{n+1} - p^n)$. Using Eq. (28) and continuity equation (26), the governing equation for pressure is obtained as

$$\nabla \cdot \frac{1}{\rho} \nabla p^{n+1} = \nabla \cdot \frac{1}{\rho} \nabla p^n + \frac{1}{\Delta t} \nabla \cdot \vec{u}^* - \frac{1}{\Delta t} v_{fg} \vec{m}^{n+1} \cdot \nabla H. \quad (29)$$

While discretizing the differential equations spatially, a second-order central difference method is used for the diffusion terms and the interfacial curvature, κ. However, to prevent numerical oscillations, a second-order ENO method described by Chang et al. (1996) is adopted for the convection terms and the distance function, $|\nabla \phi| = 1$.

The discretized equations are solved iteratively by a line-by-line TDMA (Tridiagonal-Matrix Algorithm) supplemented by the Gauss-Seidel method, which was suggested by Patankar (1980). To enhance the rate of iteration convergence, a relaxation factor is obtained from an orthogonal-residual method. Also, the iterative procedure to solve the pressure equation is combined with a sawtooth type of multigrid method (Sonneveld and Wesseling, 1985).

Results and Discussion

In carrying out numerical simulation, characteristic length, l_o, and characteristic velocity, u_o, are defined as

$$l_o = \sqrt{\sigma / g(\rho_l - \rho_v)}; \; u_o = \sqrt{g l_o}. \quad (30)$$

Also, the following parameters are defined:

$$\mathrm{Re} = \frac{\rho_v u_o l_o}{\mu_v}; \quad \mathrm{Pr} = \frac{c_{pv}\mu_v}{k_v}; \quad \beta = \frac{c_{pv}\Delta T}{h_{fg}}; \quad \mathrm{Nu} = \frac{l_o q_w}{k_v \Delta T},$$

where $\Delta T = T_w - T_{\mathrm{sat}}$, and q_w is a wall heat flux.

First, the computations are made to validate the volume source term, $v_{fg}\vec{m} \cdot \nabla H$, that has been included in Eq. (26) to account for liquid-vapor phase change. An unsteady one-dimensional problem with phase change is chosen as a test problem, which can be solved analytically (Alexiades and Solomon, 1993):

$$\rho_v c_{pv} T_t = k T_{yy} \quad \text{for} \quad 0 < y < \delta \quad (31)$$

$$T = T_{\mathrm{sat}} \quad \text{for} \quad y \geq \delta \quad (32)$$

$$T = T_w \quad \text{at} \quad y = 0 \quad (33)$$

$$\rho_v \delta_t h_{fg} = -k T_y \quad \text{at} \quad y = \delta. \quad (34)$$

Here, δ is the vapor film thickness and its time derivative can be obtained analytically:

$$\delta \delta_t = \frac{k_v \Delta T}{\rho_v h_{fg}} \frac{2z}{\sqrt{\pi} erf(z)}, \quad (35)$$

where z is the root of the equation

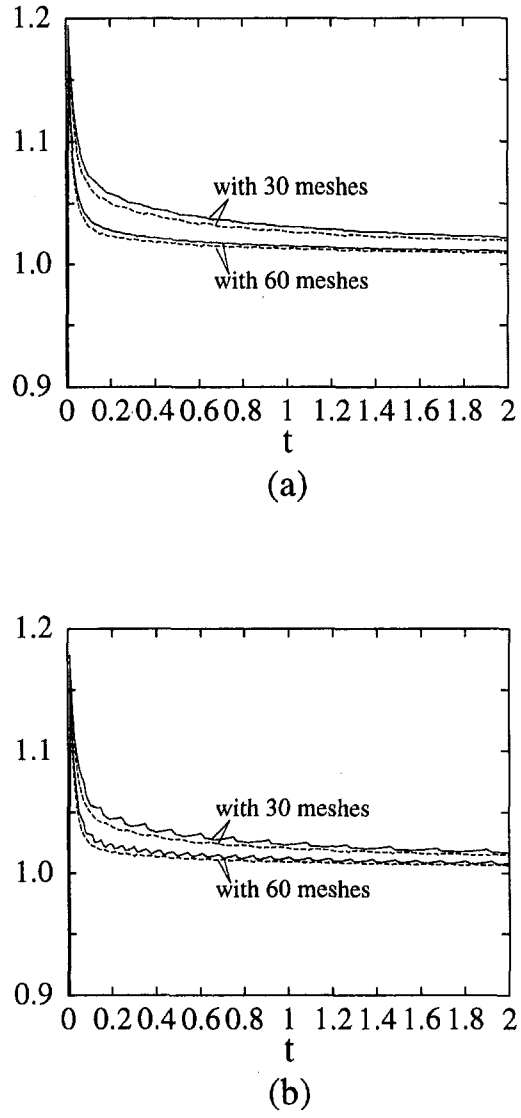

Fig. 4 Ratios of the numerical solutions to the exact solutions for an unsteady one-dimensional phase change problem: (*a*) for $\rho_l = 1000\rho_v$ and (*b*) for $\rho_l = 2\rho_v$. The solid lines and the dashed lines represent the interfacial velocities and the liquid velocities, respectively.

$$z e^{z^2} erf(z) = \beta / \sqrt{\pi}. \quad (36)$$

The normal liquid velocity caused by liquid-vapor phase change is expressed as

$$v_l = \delta_t (1 - \rho_v / \rho_l). \quad (37)$$

For $\beta = 1$, $\mathrm{Re} = 1$, $\mathrm{Pr}_v = 1$, $\mu_v = \mu_l$, and $\rho_l = 2\rho_v$ or $\rho_l = 1000\rho_v$, the test problem is computed numerically using the algorithm developed in this study. Initially, the dimensionless interface height, δ, is taken to be 0.5, and the temperature profile is assumed to be linear. The numerical results are compared with the exact solutions as shown in Fig. 4. The solid and dashed lines in Fig. 4 represent the ratios of the interfacial velocity and the normal liquid velocity obtained from the computations compared to those obtained analytically. The numerical errors are less than 2 percent at $t = 2$ when using the 30 mesh points, regardless of the density ratios. As the mesh points are increased by a factor of two, the errors are reduced to less than 1 percent.

During numerical simulations of film boiling near critical pressures, the properties of water listed in Table 1 are used.

Table 1 Properties of water near critical pressures

Pressure (atm.)	T_{sat} (^oC)	ρ_v/ρ_l	l_o (mm)	μ_v/μ_l	Gr	Pr	c_{pv}/h_{fg} ($1/^oC$)
216	373.3	0.66	0.20	0.90	2110	147.	4.034
217	373.8	0.77	0.11	0.96	216	420.	17.60

Initially, the vapor-liquid interface is disturbed asymmetrically as

$$\delta = 0.3 + 0.2J_o(3.832r/R) \quad \text{for} \quad x < 0$$
$$= 0.3 + 0.1J_o(3.832r/R) + 0.1J_o(3.832)$$
$$\text{for} \quad x > 0, \quad (38)$$

where J_o is Bessel's function of order 0, and a value of 3.832 is the first root satisfying $dJ_o/dr = 0$. The initial vapor temperature profile is taken to be linear and fluid velocity is set to be zero. Since, in reality, film boiling is a cyclic process, the computations should be carried out over several cycles until the effect of initially specified conditions disappears. For T_{sat} = 373.3°C and ΔT = 30°C, the computations are performed with grid points of 128 × 256 using the following three different initial conditions for the temperature profile: (a) it is linear; (b) it is uniform at the saturation temperature; and (c) it is extrapolated from a nearly steady-state solution obtained on coarse grids. Figure 5 shows the dependence on the initial conditions of the Nusselt numbers based on heat transfer coefficients averaged over a cell area. It is seen that the curves for the three cases attain the same values at dimensionless time of 150. At this time the effect of initial conditions appears to have completely vanished.

To select an appropriate mesh size, convergence for grid resolutions was tested with mesh points of 32 × 64, 64 × 128, 128 × 256, and 256 × 512. The results are plotted in Fig. 6. The interface shapes, the velocity fields, and the temperature fields for the two finest grids have shown insignificant differences. Table 2 lists the nearly steady-state Nusselt numbers based on the heat transfer coefficient averaged over a cell area for the different mesh sizes. As the mesh points increase, the relative difference of Nusselt numbers between successive mesh sizes becomes small. For 128 × 256 and 256 × 512 meshes, the difference is less than 1 percent. Therefore, most of computations in this study are done on 128 × 256 grid points to save the computing time, without losing the accuracy of numerical

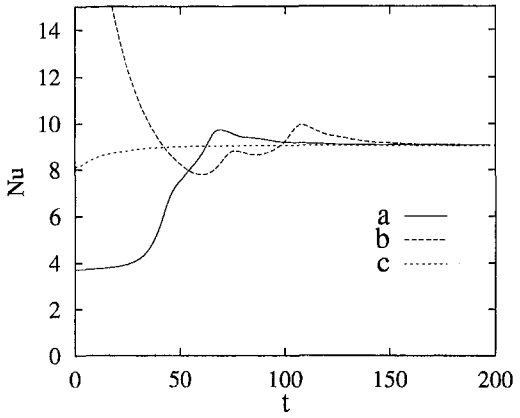

Fig. 5 Dependence of Nusselt number averaged over a cell area on initial conditions for T_{sat} = 373.3°C and ΔT = 30°C: the liquid temperature profile (*a*) is linear, (*b*) is uniform at the saturation temperature, and (*c*) is extrapolated from a nearly steady-state solution obtained on coarse grids.

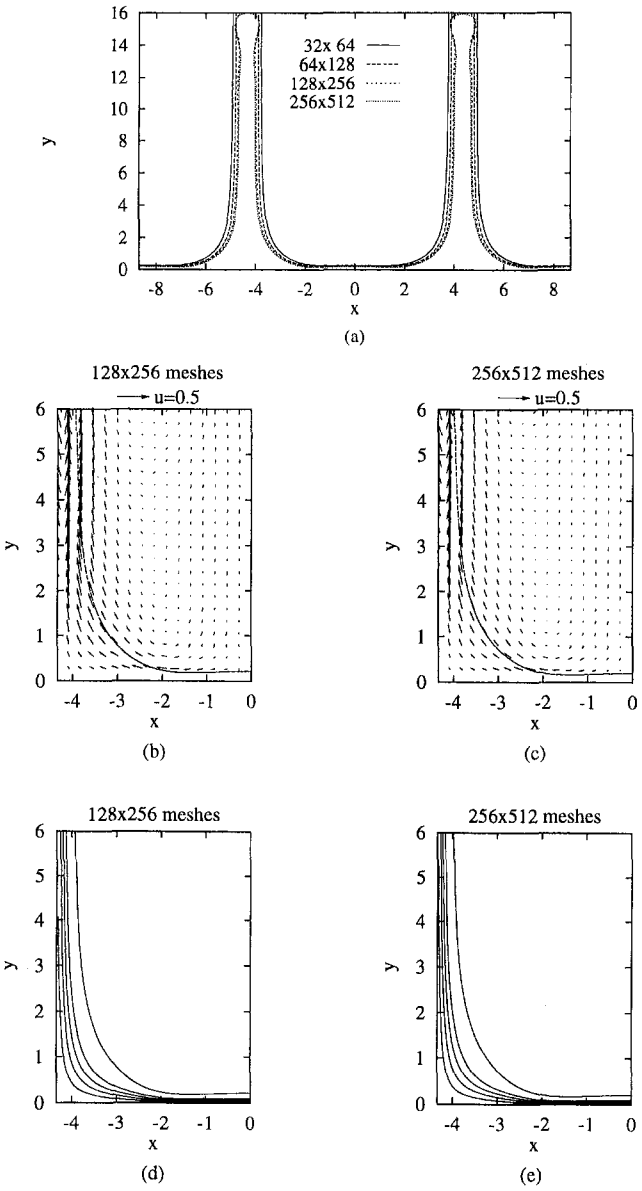

Fig. 6 Effect of mesh size on the numerical results at t = 200 for T_{sat} = 373.3°C and ΔT = 30°C: (*a*) the vapor-liquid interface, (*b*), (*c*) velocity fields, and (*d*), (*e*) temperature fields with temperature intervals of 6°C.

Table 2 Dependence of Nusselt number on grid resolutions for T_{sat} = 373.3°C and ΔT = 30°C

No. of Grids	Nu	difference of Nu between successive meshes
32 x 64	6.09	
64 x 128	8.14	-25.2 %
128 x 256	9.06	-10.2 %
256 x 512	9.10	-0.4 %

results. During the computations, time steps were chosen to satisfy the CFL condition, $\Delta t \leq (|u| + |v|)/h$, due to the explicit treatment of the convection terms and the condition that the numerical results should not change if the time steps are halved. An appropriate time step is approximately a dimensionless time of 0.01.

Figure 7 shows the evolution of the vapor-liquid interface for different wall superheats at T_{sat} = 373.3°C. The corresponding

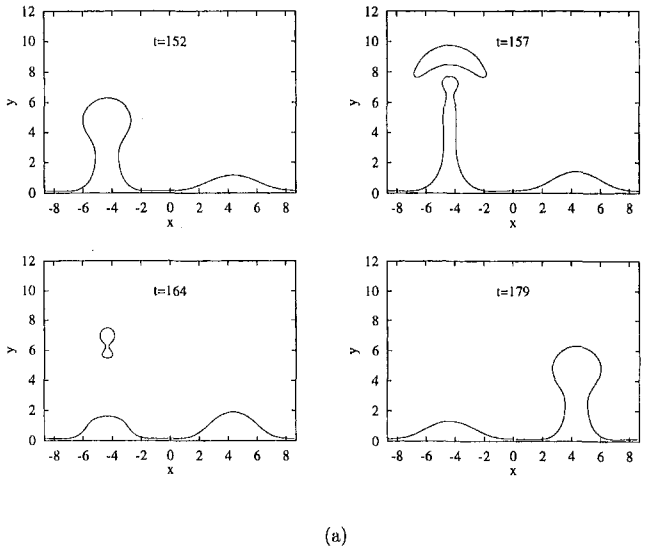

Fig. 7 Evolution of the interface for different wall superheats at T_{sat} = 373.3°C: (*a*) ΔT = 10°C, (*b*) ΔT = 22°C, and (*c*) ΔT = 30°C.

saturation pressure is 21.90 MPa, which is 0.99 times the critical pressure for water. It is found from Fig. 7(a) that at the low wall superheat, ΔT = 10°C, discrete vapor bubbles are released alternatively at the nodes and antinodes like film boiling at low pressures. After the vapor bubble pinches off, the vapor stem also breaks off as shown at t = 157 and t = 164. Such a breakoff leads to formation of small secondary bubbles. After bubble breakoff, the interface in the peak region rapidly drops down because of the restoring force of surface tension. When the wall superheat is increased to ΔT = 22°C, the bubble release pattern

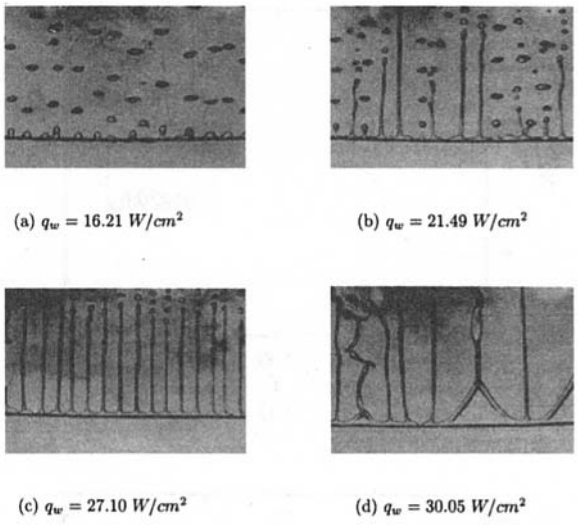

Fig. 8 Hydrodynamic transition in bubble release pattern observed by Reimann and Grigull (1975), which was presented in the paper of Dhir and Taghavi-Tafreshi (1981)

changes, as shown in Fig. 7(b). A stable vapor jet starts to be formed on the node ($x = -R$), while the pattern of discrete bubble release still exists on the antinode ($x = R$). At a higher superheat, ΔT = 30°C, stable jets are formed on both the node and antinode. Fig. 7(c) shows that the interface is nearly stationary except for the fact that bubbles are released from the upper end of the vapor columns. Also, at the nearly steady-state condition, the interface is found to be almost symmetric with respect to x = 0. These hydrodynamic transitions in bubble release pattern are consistent with those observed by Reimann and Grigull (1975). They observed that during film boiling of water on 0.1 mm diameter platinum wire at T_{sat} = 373.3°C, vapor left in several different modes, as shown in Fig. 8. With increase in heat flux, the modes of vapor removal shift from (a) to (d). The modes (a), (b), and (c) are similar to the bubble release pattern simulated numerically in the present study. It is interesting to note that the heat fluxes for Fig. 8(b) and (c) are comparable to the heat fluxes q_w = 21.6 (W/cm^2) and q_w = 29.9 (W/cm^2) in Table 3, obtained numerically for different bubble release modes, though the geometry of boiling surface is not the same.

Nusselt numbers averaged over the cell area for ΔT = 10 and 22°C are plotted in Fig. 9 for several cycles. It is seen that the temporal variation of Nusselt numbers is nearly cyclic after the effect of the initial condition disappears. Just after the bubble pinches off, the heat transfer rate decreases. This can be explained by noting that the surface tension acting as a restoring force pushes down the interface at the peak, and, in turn, the interface in the valley region moves upward to conserve vapor volume. Thereafter, the Nusselt number increases again as the

Table 3 Comparison of Nusselt number

T_{sat}(°C)	ΔT(°C)	β	Nu_B^*	Nu_K	Nu	q_w(W/cm^2)	No. of stable vapor jets
373.3	10	40.3	8.53	12.9	8.44	9.28	0
373.3	20	80.7	8.49	12.9	8.85	19.5	0
373.3	22	88.7	8.48	12.9	8.91	21.6	1
373.3	30	121.	8.47	12.9	9.06	29.9	2
373.8	4	70.4	6.25	8.54	6.57	5.52	0
373.8	5	88.0	6.24	8.54	6.90	7.25	1
373.8	6	106.	6.23	8.54	6.90	8.69	1
373.8	7	123.	6.23	8.54	6.97	10.2	2
373.8	8	141.	6.23	8.54	7.02	11.8	2

* For Nu_B, β in Eq. (1) is replaced by β'.

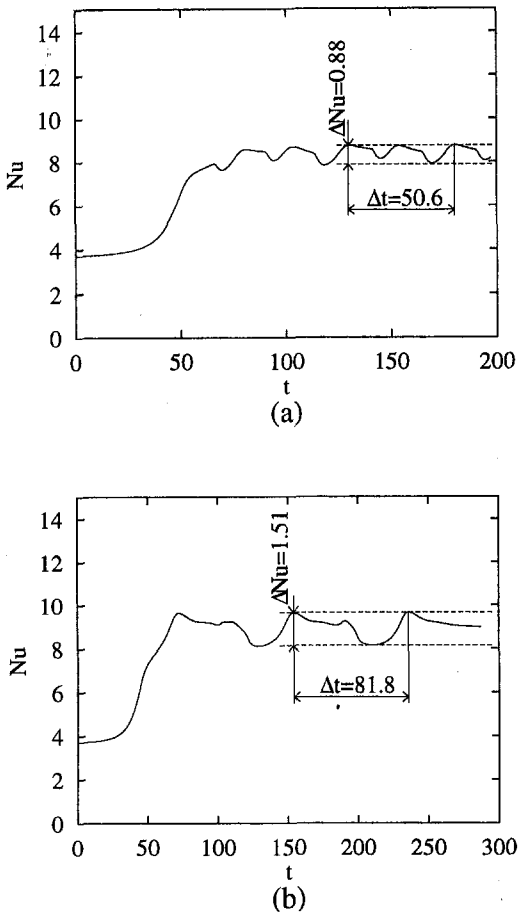

Fig. 9 Nusselt number averaged over a cell area for T_{sat} = 373.3°C: (*a*) ΔT = 10°C and (*b*) ΔT = 22°C.

interface in the peak region moves upward, and in the valley region it moves downward. The Nusselt numbers based on the heat transfer coefficient averaged over a cell and over one cycle are listed in Table 3. In this table, the values of Nu are compared with the predictions from Berenson's model (Eq. 1) and the correlation of Klimenko (Eq. 2). In Eq. 1, β' ($=\beta/(1+0.5\beta)$) rather than β is used to account for sensible heat transfer. If β instead of β' as originally proposed by Berenson was used, correlation equation (1) will predict Nusselt numbers much smaller than those predicted from the present work and from Klimenko's correlation. This difference is due to the fact that at low pressures sensible heat correction is small in comparison to latent heat of vaporization. But this is not true near the critical pressure. Near the critical pressures, while the Nusselt numbers predicted from the correlations remain almost constant at large β, those predicted numerically increase slightly with ΔT. This increase results from the fact that the formation of stable vapor jets at high wall superheat increases the pressure difference between the peak and the valley region of the interface, which provides more efficient flow passages for vapor removal. Such hydrodynamic transition in bubble release pattern was not considered in Berenson's and Klimenko's models, where the ratio of bubble height to the bubble spacing was assumed to be constant regardless of the wall superheat. It is interesting to note that the Nusselt numbers obtained from the present analysis are bounded by those predicted from Berenson's and Klimenko's correlations. Table 3 shows that the Nusselt numbers obtained in the present work are closer to the values obtained from the modified Berenson's model than those predicted by the Klimenko's correlations, which are about 31 percent ~ 19 percent higher.

The Nusselt numbers averaged over a cell area are plotted in Fig. 10 for a pressure of 22.03 MPa and T_{sat} = 373.8°C. It is observed that at a low wall superheat the Nusselt numbers vary cyclically. However, at the highest superheat an asymptotic value is obtained. Interestingly, the upper values obtained during cyclic variations are bounded by the Nusselt number for the highest wall superheat (8°C).

Table 3 lists the number of stable jets as well as the average Nusselt numbers for the different system pressures and wall superheats. It is found that a critical value of β ($=c_{pv}\Delta T/h_{fg}$) exists at which the bubble release pattern changes. For $\beta \geq 120$, approximately, stable vapor jets are formed on both the nodes and antinodes. For $85 \leq \beta \leq 120$, vapor release occurs in the forms of stable vapor jets and bubbles. However, for $\beta \leq 80$, no stable vapor jets exist and bubbles are released cyclically from nodes and antinodes. The latter condition has been found to prevail for film boiling at low pressures.

The numerical simulations of film boiling at high pressures in the present work, which performed as well as at low pressures carried out in the earlier work (Son and Dhir, 1997), provide a completely theoretical basis for correlation of the Nusselt number for film boiling on a horizontal surface. The range of parameters varied during the computations are as follows:

$$\mathrm{Gr} = 210 \sim 2.2 \times 10^6, \quad \mathrm{Pr} = 0.72 \sim 420,$$

$$\beta = 0.09 \sim 140.$$

The Nusselt numbers obtained numerically are fitted within, at most, a ±6 percent deviation by the following equation:

$$\mathrm{Nu} = 0.265(\mathrm{Gr}\,\mathrm{Pr})^{1/4}(\beta^{-1} + 0.5 + 1.3\beta^{0.25})^{1/4}. \quad (39)$$

In Eq. (39), a radiation effect was not included. Therefore, the correlation is valid as long as T_w is less than 400°C. The predictions from Eq. (39) are plotted in Fig. 11. It is seen that for low β, corresponding to low pressures, the Nusselt numbers vary as $\beta^{-1/4}$, which is consistent with Berenson's prediction (even though the Nusselt numbers obtained from the numerical simulations are about 34 percent lower than those obtained from Berenson's model). However, for high β the Nusselt numbers predicted numerically increase slightly with β, unlike Berenson's prediction. It is noted that this correlation of Nusselt number for film boiling was obtained from a purely numerical simulation (which has not been done so far) even though the computations were restricted to two-dimensional cases. Furthermore, near critical pressures the cell fractional area occupied by an evolving vapor bubble or a vapor column is much smaller than that for an evolving vapor bubble during film boiling at low pressures. This, in turn, causes the film boiling near critical pressures to be closer to a two-dimensional (axisymetric) situation than is film boiling at low pressures.

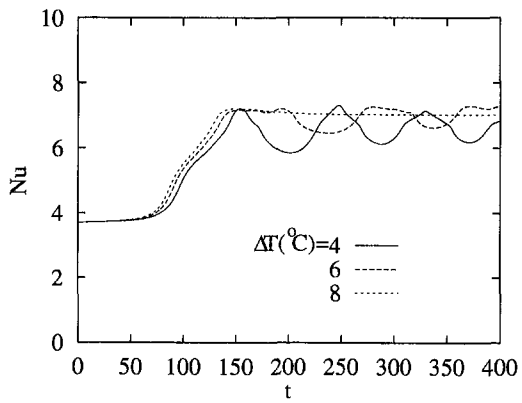

Fig. 10 Nusselt number averaged over a cell area for T_{sat} = 373.8°C

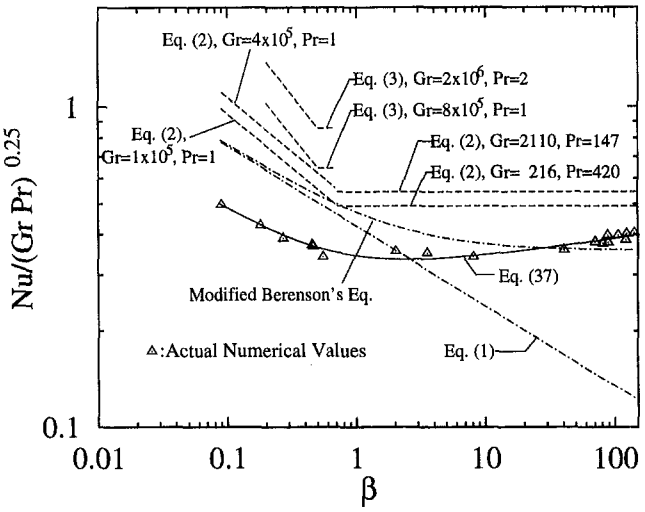

Fig. 11 Correlation of Nusselt numbers obtained from the numerical simulations. (Effect of radiation has not been included.)

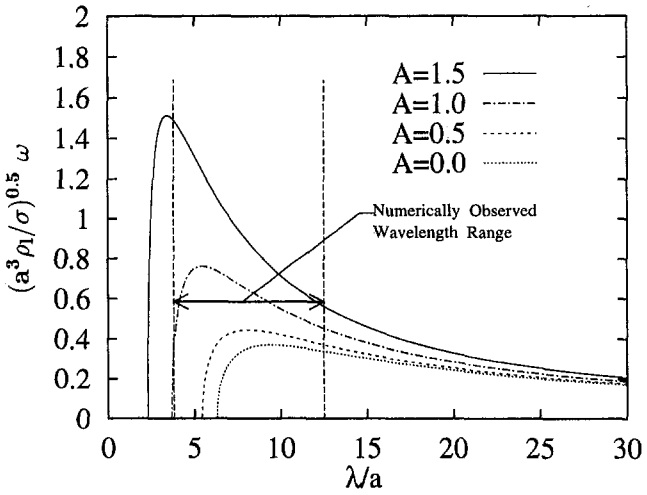

Fig. 12 Effect of the magnitude of the vapor velocity on the growth rates obtained from a linear inviscid Kelvin-Helmholtz stability analysis

During the numerical simulation of film boiling near critical pressures it is observed that the narrow and straight vapor columns formed at high superheat are subject to Kelvin-Helmholtz instability. To investigate the instability characteristics, a linear inviscid stability analysis as well as the numerical simulation is performed for $T_{sat} = 373.3°C$ and $\Delta T = 30°C$. For a cylindrical vapor jet in liquid, assuming that the base flow of the vapor jet is uniform, inviscid, and parallel to the gravity vector, the growth rate, ω, of an interfacial disturbance is derived as (refer to Drazin and Reid, 1981):

$$\frac{a^3}{\sigma}\omega^2 = \frac{(\rho_v + \rho_l)IKA^2\alpha^2 + (\rho_v I + \rho_l K)(\alpha - \alpha^3)}{(\rho_v I + \rho_l K)^2}, \quad (40)$$

where a is a radius of the vapor jet and

$$\alpha = 2\pi a/\lambda \quad (41)$$

$$I = I_o(\alpha)/I_1(\alpha) \quad (42)$$

$$K = K_o(\alpha)/K_1(\alpha) \quad (43)$$

$$A = (V_v - V_l)\sqrt{a\rho_v\rho_l/\sigma(\rho_v + \rho_l)}, \quad (44)$$

where λ is a wavelength, I_o, I_1, K_o, K_1 are modified Bessel's functions, and V_v and V_l are the base velocities of the vapor and the liquid, respectively. It is noted from Eq. (40) that for a stationary vapor jet, $A = 0$, the critical wavelength is equal to the circumference of the jet. Neglecting the curvature effect ($I = K = 1$, $\alpha - \alpha^3 \rightarrow -\alpha^3$), Eq. (40) becomes

$$\frac{a^3}{\sigma}\omega^2 = \frac{A^2\alpha^2 - \alpha^3}{\rho_v + \rho_l}. \quad (45)$$

For a wavelength of $2\pi a$, the critical velocity, V_c, corresponding to the zero growth rate is obtained as

$$V_c = \sqrt{\sigma(\rho_v + \rho_l)/a\rho_v\rho_l}. \quad (46)$$

Such a critical velocity was used by Zuber (1959) while evaluating the maximum heat flux for pool boiling. The effect of A on the growth rate of the interfacial disturbance is plotted in Fig. 12. As the jet velocity increases, the growth rate increases, whereas the most unstable wavelength decreases. In reality, the vapor jet velocity in liquid is not uniform and the flow is not inviscid; waves of various lengths, $\lambda = 3.8a \sim 11.5a$ (as shown in Fig. 12) are observed during the numerical simulation for $T_{sat} = 373.3°C$ and $\Delta T = 30°C$. Figure 13(a) shows the velocity profiles obtained numerically. It is seen that the vapor velocity is maximum at the center of the jet and the liquid velocity induced by the vapor jet decays and reaches nearly zero for $r > 4a \sim 5a$. The vapor jet injected into liquid breaks up as the disturbance amplitude approaches the jet radius.

The volume rate, $\dot{V}_v$, through the vapor jet can be obtained from the energy balance

$$\dot{V}_v = \pi R^2 q_w/\rho_v h_{fg}(1 + 0.5\beta). \quad (47)$$

The value of $\dot{V}_v$ is 1.86×10^{-10} m^3/s. This value is compared with that observed by Dhir and Taghavi-Tafreshi (1981) during dripping of a liquid from underside of a horizontal tube. According to their experiments, stable liquid jets were formed when the liquid volume rate per jet, $\dot{V}_l$, was 1.66×10^{-7} m^3/s. This transition flow rate is three orders of magnitude larger than $\dot{V}_v$ obtained numerically for film boiling. However, when the transition flow rates are normalized with $l_o^2 u_o$ ($l_o = 1.46 \times 10^{-3}$ m and $u_o = 0.12$ m/s for the fluids used in the experi-

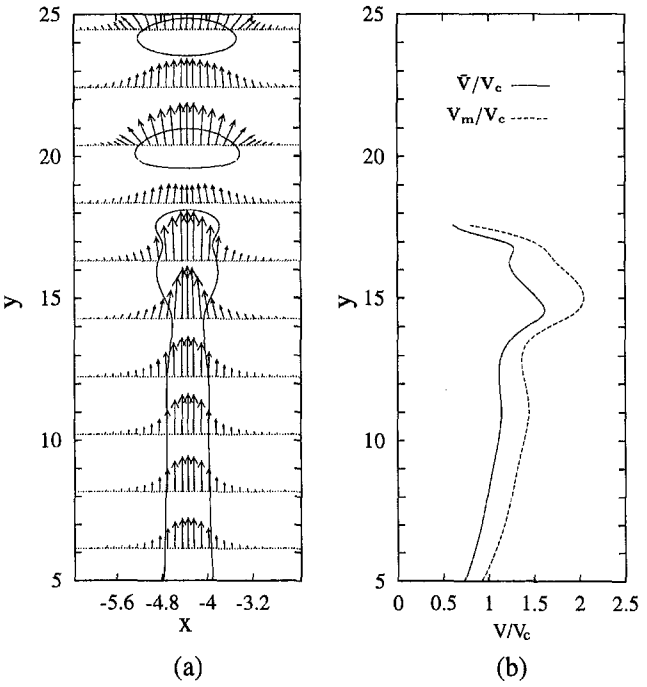

Fig. 13 Velocity profiles at $t = 300$ for $T_{sat} = 373.3°C$ and $\Delta T = 30°C$: (*a*) velocity vectors and (*b*) average and maximum vapor velocities. (The velocities are normalized with V_c.)

ments), the values for both cases are in the same order of magnitude: $\dot{V}_v/l_o^2 u_o = 0.11$ and $\dot{V}_l/l_o^2 u_o = 0.65$, respectively. The liquid jet radius obtained from the pictures of Dhir and Taghavi-Tafreshi is about 0.5 mm or 5 percent of the jet spacing. This ratio of the jet radius to jet spacing is comparable to that for film boiling, $a/2R = 0.046$, where the jet is nearly uniform in size ($5 \leq y \leq 12$), as shown in Fig. 13(a). Also, they found that when the flow rate was increased to $\dot{V}_l = 1.28 \times 10^{-6}$ m^3/s, the liquid jet got fatter by a factor of two. However, during the computations for film boiling near critical pressures, the jet radius is not found to significantly increase even though the wall superheat is increased substantially. For large β the jet flow rate does not increase with the wall superheat because additional energy is utilized in superheating the vapor. The vapor velocity averaged over the cross section of the vapor jet and the maximum vapor velocity in the jet are plotted in Fig. 13(b). The velocities are normalized with V_c. The maximum vapor velocity, V_m, is found to be about 1.25 times the average vapor velocity, $\bar{V}$. Also, it is seen that the average vapor velocity varies from $0.75V_c$ to $1.13V_c$ with elevation, as long as the vapor jet is not deformed substantially.

Conclusions

1 The numerical algorithm that can handle breaking and merging of the interface and account for the effect of liquid-vapor phase change has been developed successfully.
2 A numerical simulation of the evolution of the vapor-liquid interface during saturated film boiling near the critical pressures has been carried out.
3 From the numerical simulation it is shown that at low wall superheat discrete bubbles are released alternatively at the nodes and antinodes. However, with increase in wall superheat, vapor jets are formed on both the nodes and antinodes. This is consistent with visual observations reported in the literature, and a definite value of β is found to be associated with these transitions.
4 The Nusselt numbers obtained from the present analysis are bounded by those predicted from Berenson's and Klimenko's correlations. However, it is noted that the Nusselt number increases very weakly with wall superheat.

Acknowledgment

This work received support from the National Science Foundation under Grant No. CTS-9322418.

References

Alexiades, V., and Solomon, A. D., 1993, *Mathematical Modeling of Melting and Freezing Processes,* Hemisphere, Washington, D.C., pp. 34–37, pp. 215–216.

Bell, J. B., Colella, P., and Glaz, H. M., 1989, "A Second-Order Projection Method for the Incompressible Navier-Stokes Equations," *J. of Comput. Phys.,* Vol. 85, pp. 257–283.

Berenson, P. J., 1961, "Film Boiling Heat Transfer From a Horizontal Surface," ASME JOURNAL OF HEAT TRANSFER, Vol. 83, pp. 351–362.

Brackbill, J. U., Kothe, D. B., and Zemach, C., 1992, "A Continuum Method for Modeling Surface Tension," *J. of Comput. Phys.,* Vol. 100, pp. 335–354.

Chang, Y. C., Hou, T. Y., Merriman, B., and Osher, S., 1996, "A Level Set Formulation of Eulerian Interface Capturing Methods for Incompressible Fluid Flows," *J. of Comput. Phys.,* Vol. 124, pp. 449–464.

Chorin, A. J., 1968, "Numerical Solution of the Navier-Stokes Equations," *Math. Comput.,* Vol. 22, pp. 745–762.

Dhir, V. K., Castle, J. N., and Catton, I., 1977, "Role of Taylor Instability on Sublimation of a Horizontal Slab of Dry Ice," ASME JOURNAL OF HEAT TRANSFER, Vol. 99, pp. 411–418.

Dhir, V. K., and Taghavi-Tafreshi, K., 1981, "Hydrodynamic Transitions During Dripping of a Liquid from Underside of a Horizontal Tube," ASME paper, 81-WA/HT-12, ASME, New York.

Drazin, P. G., and Reid, W. H., 1981, *Hydrodynamic Stability,* Cambridge, New York, pp. 14–30.

Juric, D., and Tryggvason, G., 1996, "Computations of Film Boiling," presented at the ASME FED summer meeting, San Diego, July 7–11.

Kim, J., and Moin, P., 1985, "Application of a Fractional-Step Method to Incompressible Navier-Stokes Equations," *J. of Comput. Phys.,* Vol. 59, pp. 308–323.

Klimenko, V. V., 1981, "Film Boiling on a Horizontal Plate-New Correlation," *Int. J. Heat Mass Transfer,* Vol. 24, pp. 69–79.

Patankar, S. V., 1980, *Numerical Heat Transfer and Fluid Flow,* Hemisphere, Washington, D.C., pp. 44–47, pp. 61–66.

Reimann, M., and Grigull, U., 1975, "Warmeubergang bei freier Konvektion und Filmsieden im kritischen Gebiet von Wasser und Kohlendioxid," *Warme- und Stof-fubertragung,* Vol. 8, pp. 229–239.

Son, G., and Dhir, V. K., 1997, "Numerical Simulation of Saturated Film Boiling on a Horizontal Surface," ASME JOURNAL OF HEAT TRANSFER, Vol. 119, pp. 525–533.

Sonneveld, P., and Wesseling, P., 1985, "Multigrid and Conjugate Gradient Methods as Convergence Acceleration Techniques," *Multigrid Methods for Integral and Differential Equations,* D. J. Paddon, and H. Holstein, Clarendon Press, Oxford.

Sussman, M., Smereka, P., and Osher, S., 1994, "A Level Set Approach for Computing Solutions to Incompressible Two-Phase Flow," *J. of Comput. Phys.,* Vol. 114, pp. 146–159.

Zuber, N., 1959, *Hydrodynamic Aspects of Boiling Heat Transfer,* Ph.D. dissertation, University of California, Los Angeles, Los Angeles, CA.

Condensation in Smooth Horizontal Tubes

M. K. Dobson
Exxon Production Research Co.,
Houston, TX 77252
Mem. ASME.

J. C. Chato
Professor Emeritus,
Department of Mechanical and Industrial Engineering,
University of Illinois at Urbana-Champaign,
1206 W. Green Street,
Urbana, IL 61801
j-chato@uiuc.edu
Life Mem. ASME.

An experimental study of heat transfer and flow regimes during condensation of refrigerants in horizontal tubes was conducted. Measurements were made in smooth, round tubes with diameters ranging from 3.14 mm to 7.04 mm. The refrigerants tested were R-12, R-22, R-134a, and near-azeotropic blends of R-32/R-125 in 50 percent/50 percent and 60 percent/40 percent compositions. The study focused primarily on measurement and prediction of condensing heat transfer coefficients and the relationship between heat transfer coefficients and two-phase flow regimes. Flow regimes were observed visually at the inlet and outlet of the test condenser as the heat transfer data were collected. Stratified, wavy, wavy annular, annular, annular mist, and slug flows were observed. True mist flow without a stable wall film was not observed during condensation tests. The experimental results were compared with existing flow regime maps and some corrections are suggested. The heat transfer behavior was controlled by the prevailing flow regime. For the purpose of analyzing condensing heat transfer behavior, the various flow regimes were divided into two broad categories of gravity-dominated and shear-dominated flows. In the gravity dominated flow regime, the dominant heat transfer mode was laminar film condensation in the top of the tube. This regime was characterized by heat transfer coefficients that depended on the wall-to-refrigerant temperature difference but were nearly independent of mass flux. In the shear-dominated flow regime, forced-convective condensation was the dominant heat transfer mechanism. This regime was characterized by heat transfer coefficients that were independent of temperature difference but very dependent on mass flux and quality. Heat transfer correlations that were developed for each of these flow regimes successfully predicted data from the present study and from several other sources.

Introduction

Studies of condensation are numerous in the technical literature. These studies include analytical efforts to model the physics of condensation processes, experimental efforts to measure the heat transfer behavior of certain fluids, and various combinations of the two. Most investigators have collected data for a limited number of fluids under a range of operating conditions that was suitable for the applications of their interest. Efforts to match their data with existing correlations or to develop correlations to fit their own data have met with some success. Many correlations that are available come with no explicit range of parameters over which they can be expected to give accurate results. Although there are handbooks and design manuals supplying reasonable recommendations for a design engineer who is searching the technical literature, the overall literature provides seemingly diverse reports about what correlation is "best." The differences between the lowest and highest predicted heat transfer coefficients, in certain cases, can be as high as a factor of two or three (Hinde et al., 1992).

There is agreement in the literature that the mechanisms of heat transfer and pressure drop are intimately linked with the prevailing two-phase flow regime. This has led to many studies aimed at predicting what dimensionless parameters govern specific flow regime transitions, and at what values of these dimensionless parameters certain transitions are expected to occur. Although debates still exist in the literature concerning differences in the flow regime predictions of various researchers, a basic understanding has been established of what the various flow regimes are and, in most cases, what parameters are suitable for determining the transition from one flow regime to the next. The work described herein represents an extensive effort to combine the topics of heat transfer and flow regimes in order to develop correlations that can be used in the design of condensers.

Background Review

A detailed discussion of the background and the literature was given by Dobson (1994) and Dobson et al. (1994a, 1994b). Other summaries were published by Breber (1988), Palen et al. (1993), and Wang and Chato (1995). Here, only the most significant points will be described.

Flow Regimes in Horizontal Two-Phase Flow. Fundamentally, the two factors controlling the flow are gravity and vapor shear. At low vapor velocities gravity dominates and the condensate forms primarily on the top portion of the tube and flows downward into a liquid pool which is driven out axially partly by the vapor flow and partly by a gravitational head. In terms of void fraction, the flow regimes can be divided into the following two groups: (1) those that occur at high void fractions; and (2) those that occur only at low void fractions. The first category includes five flow regimes: stratified flow, wavy flow, wavy-annular flow, annular flow, and annular-mist flow. The second category includes slug, plug, and bubbly flow. The five flow regimes in the first category are arranged such that each successive flow regime corresponds to an increase in the vapor velocity. Thus, the first two are gravity dominated, the third is influenced about equally, and the last two are vapor shear dominated. The three flow regimes in the second category are arranged such that the transition from one flow regime to the next corresponds to an increase in the liquid inventory (i.e., decrease in α).

Contributed by the Heat Transfer Division for publication in the JOURNAL OF HEAT TRANSFER. Manuscript received by the Heat Transfer Division August 19, 1996; revision received August 4, 1997; Keywords: Condensation; Heat Exchangers; Multiphase Flows. Associate Technical Editor: T. J. Rabas.

At very low vapor velocities, the gravity controlled stratified flow regime is observed. Because the vapor velocity is low, the liquid-vapor interface remains smooth (Chato, 1962).

As the vapor velocity is increased, the liquid-vapor interface becomes Helmholtz unstable, giving rise to surface waves (Carey, 1992) and wavy flow. The condensation process on the top of the tube is similar to that in stratified flow. The condensation process on the portion of the tube wall near the interface between the liquid pool and the vapor is affected by the waves since it is alternately exposed to a thin condensate film flowing downward and the crest of a wave moving in the mean flow direction.

As the vapor velocity is increased further, the wavy flow becomes unstable and can result in two different transitions. At high liquid fractions, the slug flow case that is described subsequently occurs. At lower liquid fractions, the waves begin to wash up and around the tube wall leading to an annular flow. Before the annular flow pattern is reached, however, a transitional flow pattern called wavy-annular flow is observed in which some liquid from the waves begins to wash up and around the circumference of the tube, but not enough to create a symmetric annular film. This liquid moves primarily in the mean flow direction rather than downward, creating the primary difference from the wavy flow regime.

With still further increases in the vapor velocity, the liquid migration from the pool at the bottom of the tube to the top of the tube continues until the film thickness becomes nearly uniform. The visual appearance of this type of flow is one of an annular film of liquid on the wall and a high-speed vapor core in the center, hence the name annular flow. The liquid-vapor interface in annular flow is nearly always characterized by surface waves due to the high-speed vapor flowing over it.

At yet higher vapor velocities, the crests of the waves on the liquid film are sheared off by the vapor flow and entrained in the core in the form of liquid droplets. This is referred to as the annular-mist flow regime because of the appearance of an annular film with a mixture of vapor and mist in the core flow.

At low void fractions slug flow is formed when interfacial waves grow sufficiently in amplitude to block the entire cross section at some axial locations, leading to the visual appearance of slugs of liquid flowing down the tube. These slugs have been shown by Hubbard and Dukler (1966) and Lin and Hanratty (1989) to create large pressure spikes due to rapid deceleration of the vapor flow. In other cases, a flow that would visually be identified as slug flow does not create these large pressure spikes. This regime has been designated by Lin and Hanratty as pseudo-slug flow. They proposed that, unlike true slugs, pseudo slugs either did not entirely block the tube or did so only momentarily. A regime with a similar qualitative description to pseudo-slug flow was designated as proto-slug flow by Nicholson et al. (1978), and wavy-annular flow by Barnea et al. (1980). This illustrates the considerable subjectivity in flow regime classifications.

As condensation continues, the slugs coalesce into a predominantly liquid flow with large bubbles within. This is referred to as the plug flow regime. Turbulent fluctuations within the liquid eventually break these plugs into smaller vapor bubbles that become dispersed throughout the liquid. This is called the bubbly flow regime. The slug, plug, and bubbly flow regimes occur at the end of the condensation process when the liquid inventory is large (i.e., α is small). In combination, they occupy only 10 percent to 20 percent of the total quality range. The plug and bubbly flow regimes are confined to the bottom of the quality range, and will not be discussed in detail because they were not encountered in our experiments.

Flow Regime Mapping. Since the flow patterns strongly influence the heat and momentum transfer processes, it is important for designers to predict what flow pattern is expected based on the flow rate, quality, fluid properties, and tube diame-

Nomenclature

$\tilde{A}_g$ = dimensionless cross-sectional area occupied by vapor, A_g/D^2
Bd = Bond number, $g(\rho_l - \rho_g)D^2/\sigma$
Bo = boiling number, q''/Gi_{lg}
$c_{p,l}$ = specific heat at constant pressure for liquid
D = tube inner diameter
D^+ = dimensionless diameter, $D\sqrt{\tau_w \rho_l}/\mu_l$
F = two-phase multiplier defined in Eq. (19)
F_2 = denominator in Eq. (27)
F_{td} = defined by Eq. (2)
Fr_l = Froude number, $G^2/\rho_l^2 gD$
Fr_{so} = Soliman's modified Froude number, Eqs. (4a, b)
g = acceleration due to gravity
G = mass flux
Ga = Galileo number, $g\rho_l(\rho_l - \rho_g)D_g^3/\mu_l^2$
h = heat transfer coefficient
$\tilde{h}_l$ = dimensionless liquid level height, h_l/D
i_{lg} = enthalpy of vaporization
i'_{lg} = Rohsenow's (1956) modified enthalpy of vaporization, Eq. (10)
Ja_l = liquid Jakob number, $(c_{p,l}(T_{sat} - T_s)/i_{lg}$
k_l = liquid thermal conductivity
K_{td} = defined by Eq. (1)
L = test-section length
Nu = Nusselt number (subscript indicates characteristic length, other than D), hD/k_l
P = pressure
P_{red} = reduced pressure, $P/P_{critical}$
Pr_l = liquid Prandtl number, $\mu_l c_{p,l}/k_l$
q'' = heat flux
R = radius of curvature
Re_g = superficial vapor Reynolds number, GDx/μ_g
Re_l = superficial liquid Reynolds number, $GD(1 - x)/\mu_l$
Re_{lo} = liquid only Reynolds number, GD/μ_l
Re_{vo} = vapor only Reynolds number, GD/μ_g
Su_g = Suratman number, $\rho_g D\sigma/\mu_g^2$
T_{sat} = saturation temperature
T_s = surface temperature of tube wall
$\tilde{u}_g$ = vapor velocity/superficial vapor velocity
$\tilde{u}_l$ = liquid velocity/superficial liquid velocity
We_{so} = Soliman's modified Weber number, Eqs. (5a, b)
x = location from leading edge or vapor quality
X_{lt} = laminar-turbulent Lockhart Martinelli parameter
X_{tt} = turbulent-turbulent Lockhart Martinelli parameter, $(\rho_g/\rho_l)^{0.5}(\mu_l/\mu_g)^{0.1}((1 - x)/x)^{0.9}$
x = vapor quality
z = axial location in tube

Greek Letters

α = void fraction
α_T = angle of inclination in Taitel-Dukler criterion
β = fraction of the circumference where filmwise condensation prevails, Eqs. (17a, b)
θ_l = angle subtended from the top of tube to the liquid level
μ_g = dynamic viscosity of vapor refrigerant
μ_l = dynamic viscosity of liquid refrigerant
ν_l = kinematic viscosity of liquid, μ_l/ρ_l
ρ_a = density of air
ρ_g = density of vapor
ρ_l = density of liquid
σ = surface tension of refrigerant
τ_w = shear stress at the wall
ϕ_l^2 = two-phase pressure drop multiplier, $(dP/dz)/(dP/dz)_l$
$\phi_{l,lt}$ = defined by Eq. (16)
ϕ_g^2 = two-phase pressure drop multiplier, $(dP/dz)/(dP/dz)_g$
ω_o = mass fraction of oil in refrigerant

ter. One of the earliest attempts at a flow regime map was by Baker (1954). The Baker map was based on observations of adiabatic gas-liquid flows in tubes ranging from 25.4 to 101.6 mm in diameter. The data used included both air-water and oil-water flows, providing a fairly wide range of fluid properties. The horizontal and vertical coordinates on the Baker map are the superficial liquid and vapor mass fluxes, times scaling factors, that account for fluid property variations. Although subsequent flow regime maps have achieved improved accuracy, Baker's work is historically the first widely recognized flow regime map.

Mandhane et al. (1974) developed a flow regime map similar to Baker's using a larger database of 5935 observations. The abscissa and ordinate of the Mandhane map are the superficial gas velocity and superficial liquid velocity, which makes it rather simple to use. The Mandhane map correctly predicted the flow regime for 68 percent of the observations in their database, as opposed to 42 percent for the original Baker map. The boundaries of the Mandhane map were constructed primarily for air-water data in tubes larger than those used in the present study. Comparisons with recent data for refrigerants revealed systematic problems with the Mandhane map (Wattelet, 1994; Wattelet et al., 1994). These problems were caused primarily by the much higher vapor densities of the refrigerants in Wattelet's study than the air densities in the Mandhane data. This problem would be worse for the data from the present study, since the vapor density is considerably higher at condensation temperatures than at evaporation temperatures.

Perhaps the most theoretically based flow regime map is that of Taitel and Dukler (1976). They reasoned that each flow regime transition was based on a different set of competing forces and that a single parameter or set of coordinates should not be expected to predict all flow regime transitions. The Taitel-Dukler map includes five flow regimes: stratified smooth, stratified wavy, annular, intermittent (plug and slug), and dispersed bubble. The map was developed for adiabatic flows, but has been used with success by other investigators for diabatic flows (Barnhart, 1992; Wattelet, 1994; Wattelet et al., 1994). Taitel and Dukler developed various approaches for predicting the transitions between the various flow regimes based on the appropriate physical mechanisms. For the stratified to wavy flow transition, they hypothesized that waves would be formed when the pressure and shear forces acting on a wave were sufficient to overcome viscous dissipation in the wave. Their ideas were based on the work of Jeffreys (1925, 1926), and in dimensional form they deduced that waves would be expected to form when a critical vapor velocity was exceeded. In dimensionless form, the inequality can be expressed as

$$K_{td} = F_{td}\sqrt{\mathrm{Re}_l} \geq \frac{20}{\tilde{u}_g\sqrt{\tilde{u}_l}}. \qquad (1)$$

The right hand side of Eq. (1) follows the nomenclature set forth by Taitel and Dukler, where all quantities with tildes are dimensionless variables. In this scheme, actual phase velocities are scaled by superficial phase velocities and lengths are scaled by the tube diameter.

The first term on the right of the equal sign, referred to by Taitel and Dukler as a modified Froude number, is defined as follows:

$$F_{td} = \sqrt{\frac{\rho_g}{\rho_l - \rho_g}}\frac{Gx/\rho_g}{\sqrt{Dg\cos\alpha_T}}. \qquad (2)$$

The second term in Eq. (2) is a superficial vapor Froude number (ratio of inertial to gravity forces in the vapor), while the first is a modifier depending on the density ratio.

The transition from a stratified-wavy flow to an intermittent or annular flow was observed experimentally by Butterworth (1972) and Dukler and Hubbard (1975). They described wave growth on a stratified-wavy flow which led to one of two effects. At low liquid fractions the wave washed liquid around the circumference of the tube leading to an annular flow. At high liquid fractions the wave bridged the tube cross section and led to an intermittent (slug or plug) flow. Taitel and Dukler predicted this transition based on a modification of the Kelvin-Helmholtz stability analysis for an infinitesimal wave between two horizontal plates. Taitel and Dukler extended this theory to predict the stability of finite waves inside a tube. In dimensionless form, their result can be expressed as follows:

$$F_{td}^2\left[\frac{1}{(1-\tilde{h}_l)^2}\frac{\tilde{u}_g^2\sqrt{1-(2\tilde{h}_l-1)^2}}{\tilde{A}_g}\right] \geq 1. \qquad (3)$$

All terms in the bracketed portion of Eq. (3) are exclusive functions of the Martinelli parameter, so the boundary is a function of only F_{td} and X_{tt}. As discussed below, the two transition criteria expressed by Eqs. (1) and (3) are the only ones relevant to cases studied here.

Another approach to predicting flow regime transitions, specifically for condensation, has been developed by Soliman (1982, 1983). Soliman distinguished between three flow regimes that he deemed to be important for condensing flows: wavy flow, annular flow, and mist flow. He developed two flow regime transition criteria, one for the wavy-to-annular transition and one for the annular-to-mist transition. It is important to note that the wavy flow regime of Soliman includes the regimes commonly called stratified, slug, and wavy flow. While these regimes have important differences from the standpoint of flow regime classification, particularly concerning the stability of the wavy interface, Soliman apparently concluded that these differences were less important than the significant stratification that they all had in common.

Soliman (1982) postulated that the wavy-to-annular transition was based on a balance between inertial and gravitational forces on the liquid film. The Froude number, V^2/gL, represents a balance between these forces. Soliman proposed that the appropriate velocity was the actual liquid velocity and the appropriate length scale was the film thickness, δ. These parameters were not known based solely on G, x, and the fluid properties. Soliman obtained expressions for them based on relations for two-phase pressure drop in annular flow. Thus, his transition criterion is opposite to that of Taitel and Dukler in that it assumes that an annular flow exists and seeks to determine when gravitational forces will cause a transition to wavy flow. The resulting expression for the Froude number is given by

$$\mathrm{Fr}_{so} = 0.025\,\mathrm{Re}_l^{1.59}\left(\frac{1+1.09X_{tt}^{0.039}}{X_{tt}}\right)^{1.5}\frac{1}{\mathrm{Ga}^{0.5}} \quad \text{for} \quad \mathrm{Re}_l \leq 1250, \qquad (4a)$$

$$\mathrm{Fr}_{so} = 1.26\,\mathrm{Re}_l^{1.04}\left(\frac{1+1.09X_{tt}^{0.039}}{X_{tt}}\right)^{1.5}\frac{1}{\mathrm{Ga}^{0.5}} \quad \text{for} \quad \mathrm{Re}_l > 1250. \qquad (4b)$$

Based on comparisons with data in tubes of 4.8 mm to 25 mm in diameter, and with fluids including water, refrigerants, and acetone, Soliman (1982) concluded that wavy flow was observed for $\mathrm{Fr}_{so} < 7$, and annular flow was observed for $\mathrm{Fr}_{so} > 7$. Dobson (1994) and Dobson et al. (1994a, 1994b) reported that $\mathrm{Fr}_{so} = 7$ served as a good indicator of the transition from wavy to wavy-annular flow, although a symmetric annular flow was not observed until around $\mathrm{Fr}_{so} = 18$.

Soliman (1983, 1986) also developed a parameter for predicting the transition from annular to mist flow. He postulated that the primary forces tending to prevent entrainment were liquid viscous forces and surface tension forces, and that the

primary force which promoted mist formation was vapor inertia. He formulated a modified Weber number that represented a balance between these forces:

$$\mathrm{We}_{so} = 2.45 \frac{\mathrm{Re}_g^{0.64}}{\mathrm{Su}_g^{0.3}(1 + 1.09X_{tt}^{0.039})^{0.4}} \quad \text{for} \quad \mathrm{Re}_l \leq 1250, \quad (5a)$$

$$\mathrm{We}_{so} = 0.85\left[\left(\frac{\mu_g}{\mu_l}\right)^2\left(\frac{\rho_l}{\rho_g}\right)\right]^{0.084} \frac{\mathrm{Re}_g^{0.79}X_{tt}^{0.157}}{\mathrm{Su}_g^{0.3}(1 + 1.09X_{tt}^{0.039})^{0.4}}$$

$$\text{for} \quad \mathrm{Re}_l > 1250. \quad (5b)$$

Based on visual observations from various studies, Soliman (1986) concluded that annular flow was always observed for $\mathrm{We}_{so} < 20$, and pure mist flow with no stable liquid film on the wall was always observed for $\mathrm{We}_{so} > 30$. The region of We_{so} between 20 and 30 was reported to be a mix of annular and mist flow, called annular-mist flow.

Gravity-Driven Condensation. The gravity-driven flow regimes as discussed in this report include the stratified, wavy, and slug flow regions. These regimes are lumped together primarily because the dominant heat transfer mechanism in each regime is conduction across the film at the top of the tube. This type of condensation is commonly referred to as film condensation. Analytical studies of condensation began with Nusselt's pioneering analysis (1916) of gravity-driven condensation of a pure component on a vertical plate. He derived the local and mean Nusselt numbers. The mean Nusselt number at $x = L$ is given by

$$\overline{\mathrm{Nu}}_L = \frac{\bar{h}L}{k_l} = 0.943\left[\frac{g(\rho_l - \rho_g)i_{lg}L^3}{k_l\nu_l(T_{\mathrm{sat}} - T_s)}\right]^{1/4}. \quad (6)$$

The bracketed term in Eq. (6) can be expressed in dimensionless form as

$$\overline{\mathrm{Nu}}_L = 0.943\left[\frac{\mathrm{Ga}^*\mathrm{Pr}_l}{\mathrm{Ja}_l}\right]^{1/4}. \quad (7)$$

Dhir and Lienhard (1971) devised a simple way to extend the analysis for the vertical wall to arbitrary axisymmetric bodies. They showed that the local Nusselt number can be predicted by replacing "g" in Eq. (6) with an effective acceleration of gravity:

$$g_{eff} = \frac{x(gR)^{4/3}}{\int_0^x g^{1/3}R^{4/3}dx}. \quad (8)$$

In Eq. (8), $R(x)$ is the local radius of curvature and $g(x)$ is the local gravity component in the x-direction. For the horizontal cylinder, the effective gravity can be evaluated numerically and averaged over the circumference of the tube to show

$$\mathrm{Nu} = 0.729\left[\frac{\mathrm{Ga}_D^*\mathrm{Pr}_l}{\mathrm{Ja}_l}\right]^{1/4}. \quad (9)$$

The subscript in Ga_D indicates that the diameter is the length scale.

Based on integral analyses, Bromley (1952) and Rohsenow (1956) corrected for the assumption of a linear temperature profile. This is equivalent to including the convective terms which were originally neglected in the energy equation. Once Bromley included cross-flow terms which were neglected in his original analysis, he and Rohsenow agreed that this effect could be corrected for by replacing the latent heat in Eq. (6) by a modified latent heat given by

$$i'_{lg} = i_{lg}(1 + 0.68\ \mathrm{Ja}_l). \quad (10)$$

This correction shows that the assumption of a linear temperature profile in the original analysis is quite acceptable for Ja much less than unity.

During condensation inside horizontal, smooth tubes at low vapor velocities, gravitational forces, which tend to pull condensate down the tube wall, are much stronger than vapor shear forces, which tend to pull the condensate in the direction of the mean flow. Thus, a condensate film forms on the top of the tube and grows in thickness as it flows around the circumference. The bottom portion of the tube is filled with a liquid pool that transports the condensed liquid along the tube in the direction of the mean flow. This heat transfer mechanism is very similar to that in external falling-film condensation for which extensive theory has been developed.

Chato (1962) concentrated on stratified flows with low vapor velocities. He developed a similarity solution for the condensate film which was patterned after Chen's (1961) analysis of falling film condensation outside of a horizontal cylinder. He applied this solution to the upper portion of the tube where falling-film condensation existed (i.e., to the liquid pool on the bottom). To predict the depth of the liquid pool, he developed a separate model for it based on open channel hydraulics. Both his analytical model and experimental results for R-113 showed that the depth of the liquid level was relatively constant. This allowed his heat transfer data to be approximated quite well by the following Nusselt type correlation:

$$\mathrm{Nu} = \frac{\bar{h}D}{k_l} = 0.555\left[\frac{\rho_l(\rho_l - \rho_g)gi'_{lg}D^3}{k_l\mu_l(T_{\mathrm{sat}} - T_s)}\right]^{1/4}. \quad (11)$$

The constant 0.555 is 76 percent of the value of 0.728 for external condensation on a cylinder. This decrease in heat transfer is due to the thickness of the liquid pool on the bottom of the tube which reduces the heat transfer to negligible amounts.

Jaster and Kosky (1976) proposed a correlation similar to Chato's for stratified flow condensation. To account for the variation of the liquid pool depth in a manner consistent with pressure-driven flow, they replaced the constant in the Chato correlation with a function of the void fraction, α. This resulted in

$$\mathrm{Nu} = \frac{\bar{h}D}{k_l} = 0.728\alpha^{3/4}\left[\frac{\rho_l(\rho_l - \rho_g)gi'_{lg}D^3}{k_l\mu_l(T_{\mathrm{sat}} - T_s)}\right]^{1/4}. \quad (12)$$

They recommend using Zivi's (1964) correlation for the void fraction:

$$\alpha = \left[1 + \frac{1 - x}{x}\left(\frac{\rho_g}{\rho_l}\right)^{2/3}\right]^{-1} \quad (13)$$

Jaster and Kosky's correlation overpredicts the Chato correlation for all qualities greater than about 0.2. It had a mean deviation of 37 percent with their own data, which it appeared to consistently overpredict.

The correlations of Chato, and Jaster and Kosky, both neglect the heat transfer that occurs in the liquid pool at the bottom of the tube. Chato showed that this heat transfer was normally negligible compared to that through the upper part of the tube based on conduction only. This assumption is reasonable for his low speed stratified flows, but might not be for higher mass flux, low quality situations where wavy or stratified flow could prevail in the presence of substantial convective heat transfer in the bottom of the tube. Rosson and Myers (1965) collected experimental data in what they called the intermittent flow regime, which included stratified, wavy, and slug flows. They measured the variation of heat transfer coefficient with angle around the tube and found that the heat transfer coefficient

continuously decreased from the top to the bottom of the tube. Their data suggested that filmwise condensation occurred in the top of the tube with superimposed effects of vapor shear. They proposed replacing the constant in the Nusselt's solution with an empirically determined function of vapor Reynolds number:

$$\mathrm{Nu}_{\mathrm{top}} = 0.31\ \mathrm{Re}_g^{0.12}\left[\frac{\rho_l(\rho_l - \rho_g)g i'_{lg} D^3}{k_l \mu_l (T_{\mathrm{sat}} - T_s)}\right]^{1/4}. \quad (14)$$

In the bottom of the tube, they postulated forced-convective heat transfer. Using a heat and momentum transfer analogy, they recommended the following correlation:

$$\mathrm{Nu}_{\mathrm{bot}} = \frac{\phi_{l,lt}\sqrt{8\ \mathrm{Re}_l}}{5\left[1 + \dfrac{\ln(1 + 5\ \mathrm{Pr}_l)}{\mathrm{Pr}_l}\right]}, \quad (15)$$

where

$$\phi_{l,lt} = \sqrt{1 + \frac{1}{X_{lt}} + \frac{12}{X_{lt}^2}}. \quad (16)$$

Rosson and Myers defined a parameter, β, that represented the fraction of the tube perimeter over which filmwise condensation occurred. They recommended predicting the value of β as follows:

$$\beta = \mathrm{Re}_g^{0.1} \quad \text{if} \quad \frac{\mathrm{Re}_g^{0.6}\ \mathrm{Re}_l^{0.5}}{\mathrm{Ga}} < 6.4 \times 10^{-5} \quad (17a)$$

$$\beta = \frac{1.74 \times 10^{-5}\ \mathrm{Ga}}{\sqrt{\mathrm{Re}_g\ \mathrm{Re}_l}} \quad \text{if} \quad \frac{\mathrm{Re}_g^{0.6}\ \mathrm{Re}_l^{0.5}}{\mathrm{Ga}} > 6.4 \times 10^{-5}. \quad (17b)$$

Then, the circumferentially averaged Nusselt number was given by

$$\mathrm{Nu} = \beta\ \mathrm{Nu}_{\mathrm{top}} + (1 - \beta)\ \mathrm{Nu}_{\mathrm{bot}}. \quad (18)$$

Rosson and Myers compared their predicted values to their own experimental data for acetone and methanol, and the agreement was reasonable. A large amount of scatter was inherent due to inaccuracies in their experimental technique, so it is difficult to discern whether the deviations were due to theoretical deficiencies or experimental scatter.

Tien et al. (1988) presented an analysis for gravity-driven condensation that they proposed to be valid for stratified, wavy, and slug flow. Their analysis was similar to that of Rosson and Myers, although more deeply rooted in conservation equations than empirically determined expressions. This analysis approaches the correct values in the asymptotic limits. That is, for a quality of zero it predicts a single-phase liquid Nusselt number, and for situations where stratified flow exists rather than slug flow, it reduces to the form of Rosson and Myers. To use the Tien model, six simultaneous nonlinear equations must be solved. Although novel and well structured, the technique is probably too involved for a practical design correlation.

Annular Flow Condensation. The annular flow regime represents the situation where the interfacial shear stresses dominate the gravitational forces and result in a nearly symmetric annular film with a high speed vapor core. As might be expected, the heat transfer characteristics in the annular flow regime differ significantly from those in the gravity-driven regime.

A variety of approaches for predicting heat transfer during annular flow condensation have been developed. While these approaches can be divided into many different categories, they will be reduced to the following three for the purposes of this review: (1) two-phase multiplier approaches; (2) shear-based approaches; and (3) boundary-layer approaches. These three categories of correlations will be discussed separately.

Two-Phase Multiplier Correlations. The simplest method of heat transfer prediction in the annular flow regime is the two-phase multiplier approach. This approach was pioneered for predicting convective evaporation data by Denglor and Addoms (1956), and was adapted for condensation by Shah (1979). The theoretical hypothesis is that the heat transfer process in annular two-phase flow is similar to that in single-phase flow of the liquid (through which all of the heat is transferred), and thus their ratio may be characterized by a two-phase multiplier. This reasoning is in fact very similar to that of Lockhart and Martinelli (1947), who pioneered the two-phase multiplier approach for predicting two-phase pressure drop. The single-phase heat transfer coefficients are typically predicted by modifications of the Dittus and Boelter (1930) correlation, which results in the following form:

$$\mathrm{Nu} = 0.023\ \mathrm{Re}_l^{0.8}\ \mathrm{Pr}_l^m F\left(x, \frac{\rho_l}{\rho_g}, \frac{\mu_l}{\mu_g}, \mathrm{Fr}_l\right), \quad (19)$$

where m is a constant between 0.3 and 0.4, and F is the two-phase multiplier. While the two-phase multiplier can depend on more dimensionless groups than those indicated in Eq. (19), the groups shown are the most prevalent. The type of single-phase correlation shown is valid for turbulent flow, and is based primarily on an analogy between heat and momentum transfer. It then follows that the same assumptions which are made in its development are implicitly included in the form given by Eq. (19).

The most widely cited correlation of the two-phase multiplier type is that of Shah (1979). It was developed from his observation that the mechanisms of condensation and evaporation were very similar in the absence of nucleate boiling. With this idea, he set out to modify the convective component of his flow boiling correlation for use during condensation. The form of his correlation is

$$\mathrm{Nu} = 0.023\ \mathrm{Re}_l^{0.8}\ \mathrm{Pr}_l^{0.4}\left[1 + \frac{3.8}{P_{\mathrm{red}}^{0.38}}\left(\frac{x}{1 - x}\right)^{0.76}\right]. \quad (20)$$

The bracketed term is the two-phase multiplier. It properly approaches unity as x approaches 0, indicating that it predicts the single-phase liquid heat transfer coefficient when all liquid is present. As the reduced pressure is increased, the properties of the liquid and vapor become more alike and the two-phase multiplier decreases. Thus, the qualitative behavior is as expected. Shah compared his correlation with data from the open literature for refrigerants, water, methanol, benzene, toluene, trichloroethylene, and ethanol. The mean deviation between his correlation and the experimental data (474 points) was 17 percent. Although he classified his correlation as a "generalized" correlation which was independent of flow regime, it is categorized herein as an annular flow correlation since it will later be shown to be appropriate only for this flow regime.

Cavallini and Zecchin (1974) used the results of a theoretical annular flow analysis to deduce the dimensionless groups that should be present in an annular flow correlation. They then used regression analysis to justify neglecting many of the groups that did not appear in their empirically developed correlation, which can be shown to be of the two-phase multiplier form by writing it in the following way:

$$\mathrm{Nu} = 0.023\ \mathrm{Re}_l^{0.8}\ \mathrm{Pr}_l^{0.33}\left\{2.64\left[1 + \left(\frac{\rho_l}{\rho_g}\right)^{0.5}\left(\frac{x}{1 - x}\right)\right]\right\}^{0.8}. \quad (21)$$

Here, the bracketed term represents the two-phase multiplier. Cavallini and Zecchin compared their correlation with experimental data from six different studies with R-113, R-12, and

R-22. The standard deviation between their correlation and the experimental data sets varied from 8 percent to 47 percent. The mean deviation of all the data combined was 30 percent, if each point was given equal weight, and 22 percent, if each set was given equal weight.

Shear-Based Correlations. The use of shear-based correlations for annular flow condensation dates back to the early work of Carpenter and Colburn (1951). They argued that the resistance to heat transfer in the turbulent liquid flow was entirely inside the laminar sublayer and that the wall shear stress was composed of additive components due to friction, acceleration, and gravity. Although it was later pointed out by Soliman et al. (1968) that their equation for the accelerational shear component was incorrect, the framework that they established at a relatively early point in the history of forced-convective condensation remains useful.

Soliman et al. utilized the framework established by Carpenter and Colburn to develop their own semi-empirical heat transfer correlation for annular flow. They accepted the basic validity of the form presented by Carpenter and Colburn, but refined it in several ways. First, they corrected the equation for predicting the wall shear stress due to phase change. Their corrected form showed that this component was normally negligible in comparison to the frictional component except at low qualities. Second, they implemented an improved correlation for the frictional pressure drop. Third, they used data from other researchers to determine new values of the constants. Neglecting the gravitational term, which is appropriate for horizontal flow, the Soliman correlation can be written as

$$\mathrm{Nu} = 0.036\ \mathrm{Re}_{lo}\ \mathrm{Pr}_l^{0.65}\left(\frac{\rho_l}{\rho_g}\right)^{0.5} \times \sqrt{\frac{2(.046)x^2}{\mathrm{Re}_g^{0.2}}\phi_g^2 + \mathrm{Bo}\sum_{n=1}^{5} a_n\left(\frac{\rho_g}{\rho_l}\right)^{n/3}} \quad (22a)$$

where

$$a_1 = x(2-\gamma) - 1$$

$$a_2 = 2(1-x)$$

$$a_3 = 2(\gamma - 1)(x-1),$$

$$a_4 = \frac{1}{x} - 3 + 2x$$

$$a_5 = \gamma\left[2 - \frac{1}{x} - x\right] \quad (22b\text{–}f)$$

$$\gamma = \frac{\text{interface velocity}}{\text{mean film velocity}} = 1.25 \text{ for turbulent liquid.} \quad (22g)$$

Soliman et al. (1968) compared the predictions of their correlation to data for steam, R-113, R-22, ethanol, methanol, toluene, and trichloroethylene. The agreement was correct in trend, although even on log-log axes the deviations appeared quite large. No statistical information regarding deviations was given.

Chen et al. (1987) developed a generalized correlation for vertical flow condensation which included several effects combined with an asymptotic model. They stated, as did Carey (1992), that their correlation for the shear-dominated regime was also appropriate for horizontal flow. Their correlation used the general form of Soliman et al. (1968) with two modifications. First, the acceleration terms were neglected since they were normally negligible at the relatively high quality conditions at which annular flow was expected to exist. Second, the pressure drop model was replaced by one from Dukler (1960). The final result can be written as

$$\mathrm{Nu} = 0.018\left(\frac{\rho_l}{\rho_g}\right)^{0.39}\left(\frac{\mu_g}{\mu_l}\right)^{0.078} \times \mathrm{Re}_l^{0.2}[\mathrm{Re}_{lo} - \mathrm{Re}_l]^{0.7}\ \mathrm{Pr}_l^{0.65}. \quad (23)$$

Chen et al. (1987) made no comparison with horizontal flow data for the annular flow regime.

Experimental Facility

Refrigerant and Water Circuits. Detailed descriptions of the facility were given by Dobson (1994) and Dobson et al. (1994a, 1994b). The refrigerant flow in the loop is driven by a variable-speed gear pump. Because the gear pump requires no lubrication, the loop can be operated in an oil-free environment. Following the pump, the refrigerant flow rate is measured by one of two flow meters. A Coriolis-type mass flow meter is used for all flows that fall inside of its 0.90 kg/min range. A positive-displacement flow meter with a 0–3.8 l/min range is used at high flow rates. A serpentine preheater is used to heat the subcooled liquid refrigerant to the desired state at the inlet of the test condenser. Immediately after the preheater is a horizontal, adiabatic section. This adiabatic section provides fully developed flow to the test section. In this section, heat is transferred from the two-phase refrigerant to water in a counterflow heat exchanger. The flow regime is observed visually at the inlet and outlet of the test condenser in sight glasses of inner diameters that match the test condenser. The ball valves in the loop create no disturbance in the flow in the open position. After exiting the test condenser, the refrigerant is returned to a subcooled liquid state by extracting heat from it in a water-cooled after-condenser and in a second water-cooled heat exchanger. A receiver between the after condenser and the heat exchanger contains a two-phase mixture of the refrigerant. The temperature of the receiver and, consequently, the pressure of the entire system is maintained at the required level by a controlled-temperature water bath around the receiver. In earlier experiments, the pressure was maintained by an externally pressurized bladder. The refrigerant then passes through a filter and is recirculated through the pump.

The test section is cooled by water from the building supply flowing counter currently through a concentric annular tube. The temperature of the cooling water is set by a 1.5 kW, variac-controlled heating element. At various axial and circumferential locations (dependent on tube size) along the outer surface of the test section, thermocouples were soldered into machined grooves and mounted so that they did not protrude into the water flow. This arrangement provided an accurate measurement of the tube wall temperature with negligible fin effects. Static pressure taps at either end of the test section and at other, strategic points in the loop provide direct or differential pressure readings.

Three tube sizes were chosen. The parametric ranges used are summarized in Tables 1–3.

Instrumentation and Data Acquisition Systems. The measurement devices used in this study included thermocouples, absolute pressure transducers, differential pressure trans-

Table 1 Condensation test envelope for the 4.57 mm i.d. tube

Quantity	Range
Mass flux	75-650 kg/m^2-s
Average quality	10%-90%
Heat flux	5-15 kW/m^2
T_{sat} -T_s	1.8-4.0 °C
Saturation temperature	35 - 60 °C
Refrigerant	R-134a, R-12, R-22, R-32/R-125
Reduced pressure	0.21-0.40
Flow regimes	Wavy, annular, annular-mist

Table 2 Condensation test envelope for the 3.14 mm i.d. tube

Quantity	Range
Mass flux	75-800 kg/m^2-s
Average quality	10%-90%
Heat flux	5-15 kW/m^2
T_{sat} - T_s	1.8-4.0 °C
Saturation temperature	35 - 45 °C
Refrigerant	R-134a, R-22, R-32/R-125
Reduced pressure	0.21-0.57
Flow regimes	Wavy, annular, annular-mist

ducers, watt-hour transducers, and flow meters. The uncertainties of the refrigerant temperature measurements with calibrated type-T copper-constantan thermocouples were ±0.2°C, except at the heater inlet where they were ±0.3°C. The uncertainties of the water temperature measurements were ± 0.1°C.

Absolute and differential pressures were measured throughout the refrigerant loop with calibrated strain-gage-type pressure transducers. The uncertainties of the absolute pressure measurements were ±7 kPa at the test section inlet and ±35 kPa at the other locations. The pressure drop across each of the test-condensers was measured with differential pressure transducers. Different combinations of transducers were used for experiments in the different tubes. Three kinds of differential pressure transducers were used, the uncertainties of which were ±0.2 kPa for the 0–7 kPa unit, ±0.5 kPa for the 0–35 kPa unit, and ±1 kPa for the 0–105 kPa unit.

The power input into the refrigerant heater was measured using two watt-hour transducers. One transducer measured the power input into the nine heaters that were controlled by the variac, while the other transducer measured the power input into the remaining eleven heaters. Both transducers produced a pulse output for each 100 mJ of energy input. These pulses were counted over the monitored period and divided by the elapsed time to yield a power measurement. The uncertainty of these devices was factory estimated at 0.2 percent of the reading. They were indirectly verified by energy balance checks across the refrigerant heater.

Two flow meters were used to monitor the refrigerant flow rate. For flow rates below 0.015 kg/s, a Coriolis-type mass flow meter was used with an uncertainty of ±0.1 percent of the reading. For higher flow rates, a calibrated positive-displacement flow meter was used to measure the volumetric flow rate with an uncertainty of 0.75 percent of its full-scale reading. The range of this flow meter was 0–3.8 l/min, which corresponds to a mass flow range of approximately 0–0.07 kg/s with R-134a at 35°C. The lowest flow rate at which this flow meter was used, which was over 20 percent of its full scale range, corresponded with the upper limit of the Coriolis-type flow meter.

The flow rate of the water was determined by weighing a time sample using a graduated cylinder and stopwatch. The estimated uncertainty of these mass measurements is ±1 gm.

All data were logged into a computer using data acquisition hardware and software. The data acquisition program displayed all measured quantities on a graphical display in real time. In addition, secondary quantities such as refrigerant quality, heat transfer coefficient, and various dimensionless groups were presented on the screen. This allowed the user to closely monitor the system parameters.

Uncertainties in the experimental data were calculated using the familiar methods described by Moffat (1988). The data from the present study were classified as single sample. The uncertainty of each measured quantity consisted of the uncertainty of the measurement device, the uncertainty of the data-acquisition system, interactions between the sensor and the experimental system, and conceptual errors. Two uncertainties were of interest in the present study, (1) the measured heat transfer coefficient, and (2) the quality at the inlet and outlet of the test section. For the two-phase experiments, the heat transfer coefficient was corrected for entrance effects, as discussed by Dobson (1994) and Dobson et al. (1994a, b). The significant components that contributed to uncertainty in the two-phase experiments are the wall temperature, the saturation temperature, the inlet and outlet water temperatures, the heat loss to the environment, the surface area of the test section, and the water flow rate. The fractional uncertainties of the heat transfer coefficients were well under 0.15 for all but about a dozen tests, the highest value being 0.19. The maximum uncertainty in the value of the quality was 0.1, with the vast majority being at or under 0.03.

Flow Regime Observations

This section presents the experimental flow regime observations from this study and compares them to various flow regime predictors from the literature. As described before, these observations were gathered in tubes of 3.14, 4.57, and 7.04 mm inner diameters. The refrigerants used were R-134a, R-22, and 60/40 and 50/50 blends of R-32 and R-125. The properties of the 60/40 and 50/50 blends of R-32 and R-125 were so similar to each other and so different from the other fluids that they will both be referred to only as R-32/R-125 for the remainder of this paper.

Effect Of Mass Flux and Quality. The dominant factors affecting the flow regimes were the mass flux and the quality. At the lowest mass flux in the study, 25 kg/m^2-s, smooth-stratified flow was observed across the entire range of quality. As the mass flux was increased to 75 kg/m^2-s, interfacial waves developed and wavy flow was observed for the entire range of quality. For these two mass fluxes, the flow regime was not affected by changes in diameter or refrigerant.

At mass fluxes of 150 and 300 kg/m^2-s, several different flow regimes were observed as the quality was changed. Slug flow was observed at low qualities, followed sequentially by wavy, wavy-annular, and annular flow. At these mass fluxes, the tube diameter and fluid properties influenced the range of quality over which each of the flow regimes occurred. These effects are discussed later.

At the highest mass fluxes in this study, 500, 650, and 800 kg/m^2-s, the flow regimes included slug flow at low quality, followed by wavy-annular, annular, and annular-mist flow as the quality was increased. Although the quality range over which each of these regimes occurred depended somewhat on fluid properties and diameter, annular or annular-mist flow normally occurred for 70 percent to 80 percent of the condensation path. These were the only mass fluxes where significant entrainment occurred. Detecting any details of the mist was difficult because it normally flowed inside a wall film, but it was clearly visible at high qualities. The amount of mist showed significant temporal variations, with periods of no entrainment being followed by periods with a rather dense mist in the core flow. This is consistent with the findings reported by Barnhart (1992), who found that droplets formed at slug initiation propagated far downstream. Perhaps the most significant observation at these

Table 3 Condensation test envelope for the 7.04 mm i.d. tube

Quantity	Range
Mass flux	25-800 kg/m^2-s
Average quality	10%-90%
Heat flux	5-15 kW/m^2
T_{sat} - T_s	1.8-4.0 °C
Saturation temperature	35 - 45 °C
Refrigerant	R-134a, R-22, R-32/R-125
Reduced pressure	0.21-0.57
Flow regimes	Stratified, wavy, annular, annular-mist

Table 4 Property comparison of R-134a, R-22, and 50/50 R-32/R-125

Property	R-134a 35 °C/45 °C	R-22 35 °C/45 °C	R-32/R-125 35 °C/45 °C
ρ_l (kg/m^3)	1167/1126	1148/1073	1013/950
ρ_g (kg/m^3)	43/56	58/77	86/114
ρ_l / ρ_g	27.2/19.9	19.9/13.9	11.8/8.4
μ_l (μPa-s)	179/163	190/179	135/120
μ_g (μPa-s)	12/13	14/15	14/15
μ_l / μ_g	14.4/12.8	13.6/12.2	9.5/7.9
$(\mu_l / \mu_g)^{0.1}(\rho_g / \rho_l)^{0.5}$	0.250/0.289	0.291/0.344	0.365/0.425
σ (mN-m)	6.82/5.60	6.70/5.38	5.93/4.26
P_{red}	0.218/0.285	0.268/0.343	0.430/0.549

high mass fluxes was that pure mist flow (without a stable wall film) was observed only at qualities over 90 percent, and even then never at the outlet sight glass. Thus, what was mist flow in the adiabatic section appeared to develop a stable liquid film as soon as condensation began. Over the range of parameters tested in this study, then, Soliman's (1986) idea of pure mist flow as a distinct condensation regime was not verified.

Effects of Fluid Properties and Tube Diameter. Although mass flux and quality were the primary factors affecting the flow regimes, the thermophysical properties of the fluids and the tube diameter played a secondary role. Their influence was most evident at the intermediate mass fluxes of 150 and 300 kg/m^2-s, where the mass velocities were not so high or low as to allow one flow regime to clearly dominate over another. The primary fluid properties that affect the flow regimes are the vapor and liquid densities and viscosities, the ratios between these quantities, and the surface tension. Values of these properties for the three fluids used in this study are listed in Table 4 for saturation temperatures of both 35°C and 45°C. Much of the variation in the fluid properties can be explained by the reduced pressure. At high values of reduced pressure, the liquid and vapor phases are more similar. This dictates higher values of vapor density and viscosity and lower values of liquid density and viscosity. The surface tension, which has the interpretation of the work required to increase the interfacial area (Carey, 1992), also decreases as the reduced pressure increases and the phases become more similar. At a given temperature, the reduced pressure is lowest for R-134a, followed by R-22 and R-32/R-125. The values of the other properties follow accordingly.

The most noticeable effect of the property differences on the flow regimes was the extent to which annular flow prevailed over wavy or wavy-annular flow. At a given mass flux where wavy, wavy-annular, and annular flows all occurred, the size of the quality range occupied by annular flow was greater at lower reduced pressures. Thus, the most annular flow was observed for R-134a at 35°C, and the least annular flow was observed for R-32/R-125 at 45°C. The differences in the observed flow regimes for these two cases were significant. At a mass flux of 300 kg/m^2-s, the transition to annular flow that occurred at 25 percent quality for the low-temperature R-134a case was delayed until 50 percent for the high-temperature R-32/R-125 case. Even at the highest mass flux of 650 kg/m^2-s, significant stratification was observed across the entire quality range for the high-temperature R-32/R-125 case. For the low-temperature R-134a case at the same mass flux, a symmetric annular film was established at 15 percent quality. Smaller changes in reduced pressure, such as changing the temperature of the same fluid, produced similar but smaller changes.

Another item that is affected by the reduced pressure is the length of the slug flow region. Taitel and Dukler's (1976) criterion for slug flow is that $X_{tt} > 1.6$. Combining this with the fact that $(\rho_v/\rho_l)^{0.5}(\mu_l/\mu_v)^{0.1} \cong 0.551 P_{red}^{0.492}$ (Wattelet, 1994; Wattelet et al., 1994) yields an algebraic expression for the quality below which slug flow is expected to occur:

$$x_{slug} \leq \frac{1}{1 + 3.27 P_{red}^{-0.547}}. \quad (24)$$

This equation predicts that the most slug flow will occur for R-32/R-125, followed by R-22 and R-134a. For R-32/R-125 at 45°C; for instance, Eq. (24) predicts that slug flow will be observed for all qualities below 19 percent. For R-134a at 35°C, it predicts a slug flow region confined to qualities below 11 percent. This lengthening of the slug flow region with increases in reduced pressure was observed experimentally.

The tube diameter also affected the flow regime transitions. As the tube diameter was reduced at a fixed mass flux, the transition from wavy flow to wavy-annular flow, and the transition from wavy-annular flow to annular flow shifted to lower qualities. This trend is summarized in Table 5, which shows the estimated quality at which these transitions occurred in each of the tubes for R-134a at 35°C. The quality where the wavy to wavy-annular transition occurred shifted the most at a mass flux of 150 kg/m^2-s, where it decreased from 37 percent in the 7.04 mm i.d. tube to 23 percent in the 3.14 mm i.d. tube. The quality at which the wavy-annular to annular transition occurred decreased from 65 percent to 45 percent at this same mass flux. At higher mass fluxes most of the quality range was associated with annular flow even in the 7.04 mm i.d. tube. Thus, the diameter effects were less pronounced.

Pure stratified flow was observed only in the 7.04 mm i.d. tube, primarily because this was the only tube where a mass flux of 25 kg/m^2-s could be stabilized. The cause of the instabilities could not be pinpointed, but it was probably due to interactions among the components of the entire loop. Thus, no observations on the effect of diameter could be made with respect to this transition. Entrainment was only observed at mass fluxes of 500 kg/m^2-s and above in each of the tubes. Although visually estimating the amount of entrainment was difficult, it appeared that entrainment was less pronounced in the smaller tubes.

Comparison With Flow Regime Maps

A major goal of this study was to eliminate the need for testing with every refrigerant that might be considered as a candidate in the future. Since the flow regimes clearly affect the heat transfer processes, it was necessary to evaluate the potential of existing flow regime prediction techniques for condensation conditions. Evaluations will be made herein for the maps of Mandhane et al. (1974), Taitel and Dukler (1976), and Soliman (1982, 1983). The potential role of surface tension will also be briefly explored for the data in the 3.14 mm i.d. tube. The baseline case that will be used to evaluate each of these maps will be R-134a in the 7.04 mm i.d. tube at 35°C. The validity of the maps for other diameters, fluids, and temperatures will be addressed by examining how their predictions change with diameter and reduced pressure.

Mandhane Map. The predictions of the original Mandhane map are grossly different from the experimental observations, but this map was developed primarily from air-water data. At atmospheric pressure and temperature, the density of air is about 1.15 kg/m^3. This is between 40 and 100 times lower than the vapor densities from this study. Hanratty (1994) pointed out that the Mandhane map could be brought into better agreement

Table 5 Effect of tube diameter on R-134a flow regime transitions at 35°C

Tube i.d. (mm)	Wavy to wavy-annular		Wavy-annular to annular	
	x for G=150 kg/m^2-s	x for G=300 kg/m^2-s	x for G=150 kg/m^2-s	x for G=300 kg/m^2-s
3.14	0.23	0.15	0.45	0.29
4.57	0.35	0.25	0.50	0.38
7.04	0.37	0.25	0.65	0.41

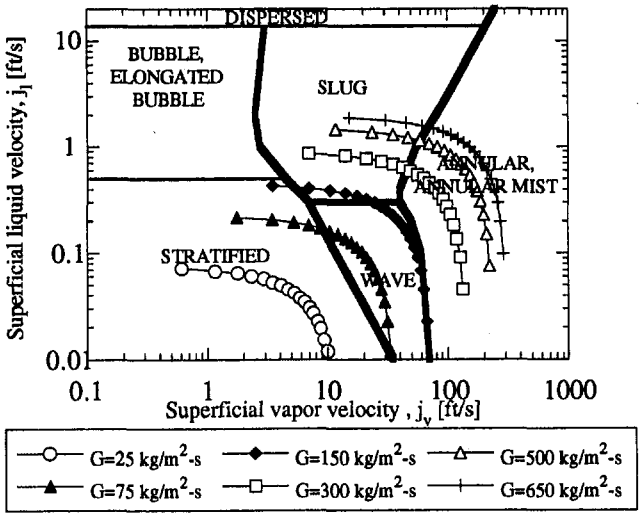

Fig. 1 Predicted flow patterns for R-134a on the Mandhane et al. (1974) map using corrected superficial velocities

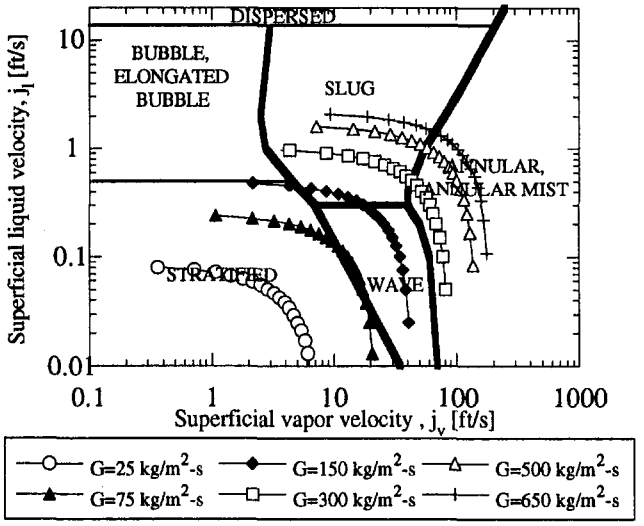

Fig. 2 Predicted flow patterns for R-32/R-125 at 45°C on the Mandhane et al. (1974) map using corrected superficial velocities

with refrigerant data by accounting for the large differences in vapor density. To effect this change, the superficial vapor velocity of the refrigerant was multiplied by the square root of the ratio of the vapor density to the density of atmospheric air. The resulting quantity is referred to herein as a modified superficial vapor velocity:

$$j_v^{\text{corr}} = \sqrt{\rho_g/\rho_a}\, j_v. \tag{25}$$

From a physical standpoint, this modified superficial velocity is proportional to the square root of the vapor kinetic energy. This simple change was made in both the vapor and liquid superficial velocities and the results are plotted on the Mandhane coordinates in Fig. 1. The condensation paths are for mass fluxes ranging from 25 kg/m^2-s to 650 kg/m^2-s of R-134a. The points on the map cover a range of quality from 5 percent to 95 percent in 5 percent increments. Decreasing the quality corresponds to moving right to left on the map.

Making this simple correction to the Mandhane map produced much better agreement with the experimental data. The 25 kg/m^2-s data were still correctly predicted to be in the stratified flow regime. The data at 75 and 150 kg/m^2-s were moved from the being exclusively in the stratified flow regime to being predominantly wavy flow, consistent with experimental observations. Furthermore, the highest quality data at 150 kg/m^2-s were correctly predicted to be on the line between wavy and annular flow. The data at the high mass fluxes of 300, 500, and 650 kg/m^2-s were all predominantly in the annular or annular-mist flow regime. The only obvious deficiency was an overprediction in the length of the slug flow region, particularly at 300 kg/m^2-s. Barnea et al. (1980), however, also noted that their wavy-annular flow data occupied the slug flow region on the Mandhane map. They suggested this was due to different interpretations of what constituted slug flow, and that data observed to be in the wavy-annular flow regime should be classified as slug flow for comparisons with the Mandhane map (or conversely that points lying near the right edge of Mandhane's slug flow region might be expected to correspond to wavy-annular flow). Incorporating this suggestion results in excellent agreement with the Mandhane map.

Having established the basic validity of the corrected Mandhane map for the case of R-134a in the 7.04 mm i.d. tube, questions remain about how it incorporates the effects of diameter and reduced pressure. Neither coordinate on the Mandhane map includes a diameter term, and investigators as early as Taitel and Dukler (1976) have noted systematic deviations in the Mandhane map because of this deficiency. Thus, the increased amount of annular flow from the 3.14 mm i.d. tube would not be predicted using the Mandhane map.

The effect of reduced pressure is addressed in Fig. 2, which plots the condensation paths for R-32/R-125 at 45°C on the corrected Mandhane map. This combination of refrigerant and temperature was selected for comparison because it corresponded to the highest reduced pressure tested in this study. The trends predicted by the Mandhane map regarding the change in fluid properties are consistent with the experimental observations. Compared to the predictions of the low reduced-pressure case (Fig. 1), the lines for a given mass flux were shifted left for the high reduced-pressure case (Fig. 2). The mass flux of 150 kg/m^2-s was correctly predicted to lie entirely in the wavy flow regime. The quality at which annular flow was expected to begin for the high mass flux cases was correctly increased over the R-134a case, although a portion of the slug flow region was again occupied by either wavy or wavy-annular flow.

Taitel-Dukler Map. Figure 3 traces condensation paths for the baseline R-134a case on the Taitel-Dukler map. The points again range from 5 percent to 95 percent quality at 5 percent increments, with increasing quality corresponding to moving left on the map. Since the Taitel-Dukler map uses different coordinates for different transitions, in general three different lines would be needed for each mass flux. However, for the range of parameters in this study, no dispersed bubble flow was

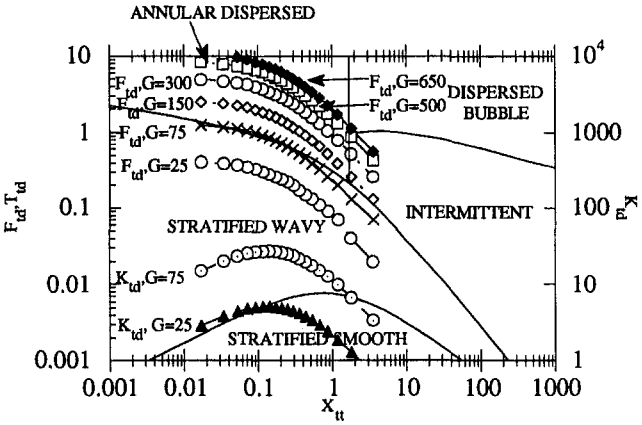

Fig. 3 Flow regime predictions of the Taitel-Dukler (1976) map for R-134a at 35°C in the 7.04 mm i.d. tube

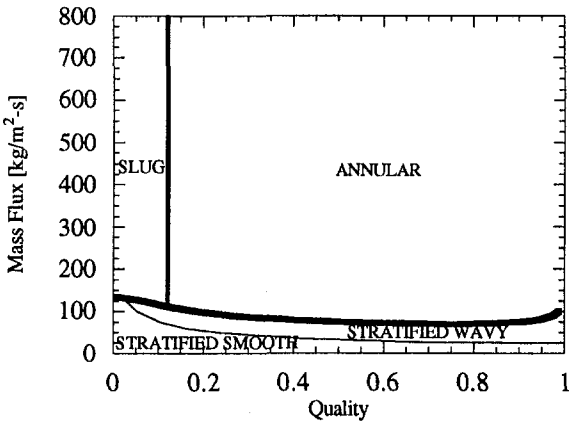

Fig. 4 Taitel-Dukler (1976) predictions on *G-x* coordinates for R-134a at 35°C in the 7.04 mm i.d. tube

observed or predicted. Thus, the only two parameters that were needed were K_{td} and F_{td}, used, respectively, for predicting the stratified to wavy and wavy to annular, or intermittent, transitions.

Plots of K_{td} versus X_{tt} are shown for the two lowest mass fluxes only, since these were the only mass fluxes at which any stratified flow was predicted. The map predicted stratified flow up to 80 percent for the 25 kg/m^2-s flux case, where stratified flow was observed across the entire range of quality. For a mass flux of 75 kg/m^2-s, the Taitel-Dukler map correctly predicted nearly all wavy flow.

Plots of F_{td} versus X_{tt}, used for predicting the transition from wavy to annular or intermittent flow, are shown for all the mass fluxes in the study. It is interesting to note that the transition boundary is nearly parallel to the condensation path lines. This implies that a particular mass flux, to a close approximation, will be either wavy or annular across the entire range of quality. This causes no problems for the 25 and 75 kg/m^2-s mass fluxes, where the map correctly predicts that no annular flow will be observed. For mass fluxes slightly above the transition boundary (in the annular regime), the slug flow regime at low qualities was always followed by regions of wavy, wavy-annular, then annular flow. The quality range over which the wavy and wavy-annular flow regimes occurred decreased as mass flux was increased. At a mass flux of 150 kg/m^2-s, the wavy regime persisted up to 25 percent quality, followed by wavy-annular flow up to 65 percent quality, and annular flow at higher qualities.

The predictions of the Taitel-Dukler map are translated onto mass flux-quality (G-x) coordinates in Fig. 4. At low mass fluxes, stratified flow is predicted across the entire range of quality. At slightly higher mass fluxes, wavy flow is predicted across most of the quality range with a small amount of stratified flow at low quality. At mass fluxes above 140 kg/m^2-s, slug flow is predicted for qualities below 11.8 percent and annular flow is predicted for all higher qualities. It is close to this boundary that the observed flow regimes deviated most significantly from the Taitel-Dukler predictions. The length of the slug flow region was underpredicted, and this was consistently followed by some wavy or wavy-annular flow that was not predicted by the Taitel-Dukler map.

The apparent discrepancy between the observed and predicted flow regimes at mass fluxes slightly above the annular boundary of the Taitel-Dukler map is largely due to differences in terminology. In an early experimental verification of the Taitel-Dukler map, Barnea et al. (1980) used the term wavy-annular flow to refer to a hybrid pattern observed at the lowest gas rates where the slug-to-annular transition occurred. A similar regime has been termed "proto-slug" flow by Nicholson et al. (1978), and "pseudo-slug" flow by Lin and Hanratty (1989). Since this pattern occurs after the wavy flow has become unstable, it is properly labeled as intermittent or annular flow in Taitel-Dukler terminology. From a heat transfer standpoint, however, the instability of the wavy flow near this boundary is less important than the significant stratification due to gravity. At higher mass fluxes, the range of quality occupied by this hybrid flow pattern becomes so small that proper classification is unimportant.

Of the boundaries from the Taitel-Dukler map that were used in this study, only that between wavy and intermittent or annular flow depends on the diameter. The parameter used for predicting this transition, F_{td}, is proportional to $D^{-0.5}$ at a fixed mass flux and quality. Thus, decreasing the diameter increases the Froude number and decreases the mass flux at which the annular transition is expected to occur. This is consistent with the observed trend of more annular flow in the smaller tubes. While the trend is physically correct, the predictions themselves were incorrect when applied to the data in the 3.14 mm i.d. tube. The Taitel-Dukler method predicts annular flow across nearly the entire range of quality at a mass flux of 75 kg/m^2-s, while wavy flow was observed exclusively at this mass flux. The predicted trend of the Taitel-Dukler map to an increase in the reduced pressure was consistent with the experimental observations. For example, the slug flow region was wider, as predicted by Eq. (24).

At higher reduced pressures one would also expect the stratified-to-wavy and wavy-to-annular transitions to be shifted to higher mass fluxes due to the lower vapor velocity at a given mass flux and quality. Although this expected trend did occur, the observed shift was very modest. At a quality of 50 percent, for instance, the wavy-to-annular transition shifted from a mass flux of 75 kg/m^2-s for the R-134a case to 83 kg/m^2-s for the R-32/R-125 case. This small shift was due to two opposing trends brought about by the changes in fluid properties. At constant mass flux and quality, the value of F_{td} for the high-temperature R-32/R-125 refrigerant was only 71 percent of that for the low-temperature R-134a case, moving the curve downward relative to the transition boundary on the Taitel-Dukler map. However, the value of X_{tt} for R-32/R-125 was 70 percent greater than that for the R-134a case at constant quality, moving the curve to the right on the Taitel-Dukler map and therefore closer to the boundary. At 50 percent quality, for an example, these two effects result in the low-temperature R-134a case being only 11 percent higher relative to the transition boundary than the high-temperature R-32/R-125 case. From a practical standpoint, this predicted shift in the transition boundary is insignificant. The apparent discrepancy between the predictions and the observations at mass fluxes slightly above the annular flow boundary was also present with all the refrigerants used in this study. For example, at a mass flux of 150 kg/m^2-s wavy flow persisted at qualities up to 50 percent, while the Taitel-Dukler map predicted annular flow above 20 percent quality.

Soliman Transitions. Soliman (1982, 1986) developed criteria for two flow-regime transitions for condensation: (1) wavy or slug flow to annular flow, and (2) annular flow to mist flow. His transition criteria are displayed on G-x coordinates in Fig. 5. Several interesting observations can be made from comparing the predictions of Soliman to those of Taitel and Dukler. First, at high qualities, Soliman's prediction of the wavy-to-annular transition agrees fairly well with that of Taitel and Dukler. Unlike the Taitel-Dukler map, however, Soliman predicts a wavy region at low qualities over the entire mass flux range of this study. This occurs partially because Soliman lumps the wavy and slug flow regions together. At high mass fluxes, the region predicted to be wavy flow by Soliman corresponds almost exactly with the slug flow region on the Taitel-Dukler map. At lower mass fluxes however, the region predicted to be occupied by wavy flow extends to higher qualities than the slug flow boundary on the Taitel-Dukler map. This is consistent with the experimental data in both magnitude and trend if

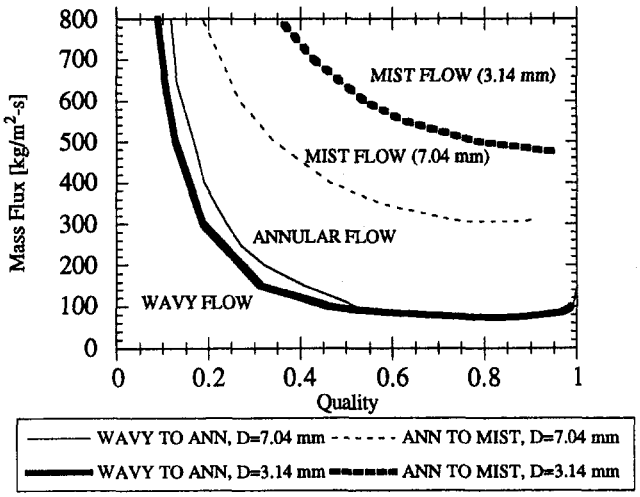

Fig. 5 Soliman (1982, 1983) predicted flow regimes on *G-x* coordinates for R-134a at 35°C

the predicted transition line is considered to be that of wavy flow to wavy-annular flow. It was shown by Dobson (1994) and Dobson et al. (1994a, 1994b) that the transition from wavy-annular flow to annular flow was well predicted by a value of $Fr_{so} = 18$, as opposed to $Fr_{so} = 7$ for the wavy to wavy-annular transition.

Soliman's map also includes a distinct mist flow region, unlike the maps of Mandhane and Taitel-Dukler. According to Soliman, mist or spray flow is a regime with all the liquid flowing as entrained droplets in the core flow and no stable film on the wall. Annular mist flow would refer to a regime with a stable liquid film on the wall and significant entrainment in the core flow. According to the observations made in the present study, most of the region labeled as mist flow by Soliman's map would more properly be called annular-mist flow. Although the amount of entrainment was very significant, a stable liquid film was always observed on the wall at qualities below 90 percent. Even when the flow entered the first sight glass (after the adiabatic section) as mist flow, the outlet sight glass always had annular-mist flow. This suggests that the net mass flux toward the wall during condensation always results in a stable liquid film, no matter what the observations might indicate in an adiabatic section. This finding is important for interpreting the annular-mist flow heat transfer data.

If Soliman's mist flow region is interpreted as annular-mist flow, the predictions seem quite reasonable. No mist flow is predicted at mass fluxes below 300 kg/m^2-s, which is consistent with the observations. At a mass flux of 650 kg/m^2-s, mist flow is predicted for qualities greater than about 20 percent. This again seems consistent with the experimental data, although a great amount of subjectivity was present in categorizing a regime as annular or annular mist.

The diameter effects predicted by Soliman's transition criteria are also shown in Fig. 5. The lower mass flux limit at which annular flow is predicted is relatively insensitive to the diameter change, much like the predictions of Taitel and Dukler. At mass fluxes slightly above this, however, the wavy to annular transition line was shifted to lower qualities with decreasing diameter. This was consistent with the experimental observations in both direction and magnitude. The predicted effect on the mist flow regime was much more dramatic, with a significant stabilizing effect on the liquid film being predicted as the tube diameter was decreased. This was consistent with the trend of the observations, although the transition was very difficult to detect visually.

The effect that increasing the reduced pressure has on the wavy to annular flow regime transition predicted by Soliman is explored in Fig. 6. This figure compares the predicted wavy to annular transition lines for R-134a at 35°C and R-32/R-125 at 45°C (low and high reduced pressures). The predicted trends are consistent with the experimental observations. The mass flux below which no annular flow is predicted was increased by approximately 30 kg/m^2-s. Because testing was not performed at mass fluxes between 75 and 150 kg/m^2-s, this prediction could not be verified. At the 150 kg/m^2-s mass flux, Fig. 6 predicts a transition from wavy to wavy-annular flow at 41 percent quality for R-134a and 57 percent quality for R-32/R-125. These predictions agree well with the experimentally observed values, which were estimated at 37 percent and 50 percent, respectively. At mass fluxes near 1000 kg/m^2-s, the predicted quality range for wavy flow for R-32/R-125 is very near the 19 percent range for the slug flow regime predicted by Taitel and Dukler.

Because reliable surface tension data are not yet available for this mixture, and drawing any conclusions concerning mist flow from the visualization was difficult, only the lines for the wavy to annular transition were included in Fig. 6. As another way of assessing the effect of increasing reduced pressure, the magnitude of the Weber number was examined as the temperature was increased for both R-134a and R-22. The Weber number increased as temperature increased due to the reduced liquid viscosity and surface tension, but only slightly (less than 10 percent as the temperature of both fluids was raised from 35 to 55°C). This small change indicates that the decreased surface tension and liquid viscosity are nearly balanced by corresponding decreases in the density ratio. Based on these trends, one would expect slightly more entrainment to occur for R-32/R-125 than the other refrigerants at identical mass flux and quality.

Potential Role of Surface Tension. In any situation where a free surface exists, the potential role of surface tension should not be overlooked. The analytical approach in the original Taitel-Dukler maps clearly does ignore surface tension forces. The consensus of subsequent investigators is that surface tension forces become increasingly important as the diameter is decreased, and may dominate for sufficiently small tube sizes. Of primary interest in this study was the effect on the wavy to annular transition, particularly in the 3.14 mm i.d. tube.

Galbiatti and Andreini (1992) started with Taitel and Dukler's analysis of a Kelvin-Helmholtz instability for the wavy to annular flow transition. In the original analysis, the stabilizing effect of gravity is opposed by the effect of an accelerating vapor flowing over a wave. Galbiatti and Andreini included surface tension forces that supplement the stabilizing gravity

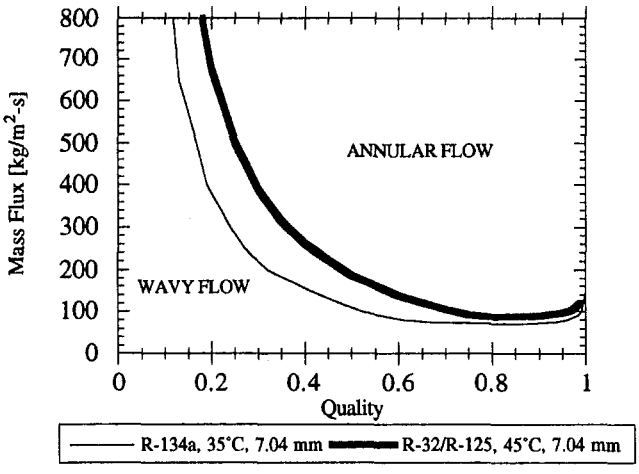

Fig. 6 Effect of reduced pressure on Soliman's (1982) wavy to annular flow regime transition

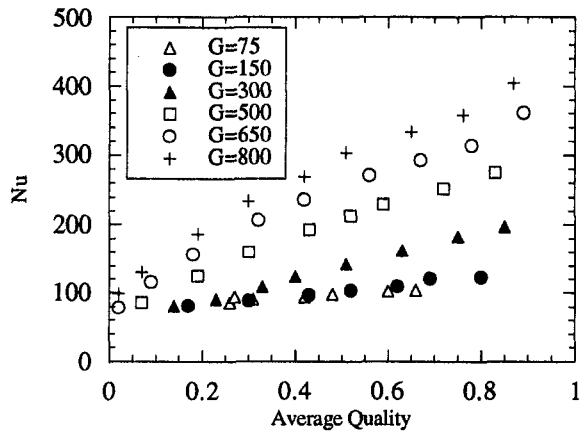

Fig. 7 Variation of Nusselt number with quality for 60 percent/40 percent R-32/R-125 mixture at 35°C in 3.14 mm i.d. test-section

forces. Their final result for the transition criterion can be obtained by plotting the following modified form of F_{td} on the Taitel-Dukler map:

$$\frac{F_{td}}{\sqrt{1+\dfrac{1.305\sigma}{gD^2(\rho_l-\rho_g)}}}=\frac{F_{td}}{\sqrt{1+\dfrac{1.305}{\mathrm{Bd}}}}. \qquad (26)$$

For values of the Bond number, Bd, that are much greater than unity, surface tension plays no significant stabilizing role. The lowest value of the Bond number for this study, that for R-134a at 35°C in the 3.14 mm i.d. tube, was about 16. This Bond number results in a value of the denominator of Eq. (26) of only 1.04, indicating gravity dominance. This is surprising because Galbiatti and Andreini stated that the surface tension and gravity forces were of equal magnitude for D = 3 mm, but the value of surface tension for their air-water system was significantly larger than that for the high-temperature refrigerants in this study. The value of diameter at which surface tension forces become important is quite sensitive to what wavelength is considered most unstable ($l = 5.5D$ was used by Galbiatti and Andreini), so this issue might warrant further attention if tubes in the 3 mm range are implemented commercially. While the experimental observations from this study did not reveal large differences that could be attributed to surface tension forces, the addition of oil that is present in real condensers could alter this finding.

Experimental Heat Transfer Data

Only the data from the 3.14 mm and 7.04 mm i.d. tubes were used to develop the heat transfer coefficient models because of increased accuracy in these tubes. Overall, 261 heat transfer points were collected in the 3.14 mm i.d. tube and 387 heat transfer points were collected in the 7.04 mm i.d. tube. These points included data in the smooth-stratified, wavy-stratified, wavy-annular, annular, and annular-mist flow regimes.

Overall Trends—Effect of Mass Flux and Quality. Figure 7 presents heat transfer data for R-32/R-125 (60/40 percent) in the 3.14 mm i.d. tube at a saturation temperature of 35°C. These data illustrate the general effects of mass flux and quality rather clearly. At the lowest mass flux of 75 kg/m^2-s, the Nusselt number increased very modestly as the quality was increased. A similar quality dependence was exhibited as the mass flux was doubled to 150 kg/m^2-s. Perhaps more interestingly, the Nusselt numbers remained nearly identical as the mass flux was doubled. As the mass flux was doubled once again to 300 kg/m^2-s, a different trend began to emerge. At low qualities, the heat transfer coefficients remained nearly identical to the lower mass flux cases. As the quality was increased to around 30 percent, the Nusselt number began to display a much more pronounced effect of quality. At mass fluxes above 300 kg/m^2-s, the dependence of the Nusselt number on quality remained similar. Even at low qualities, the Nusselt numbers were substantially higher than those for the low mass flux cases. If the same data were plotted as Nusselt number versus mass flux, the heat transfer coefficient remained relatively constant at low mass fluxes. At a sufficiently high mass flux, the slope of the heat transfer versus mass flux curve exhibited a distinct change in slope which remained relatively constant. The mass flux at which this change in slope occurred increased as the quality was decreased. For the 25 percent quality points, this shift was delayed to a mass flux of 300 kg/m^2-s.

The change in heat transfer behavior exhibited in Fig. 7 is closely linked to changes in the two-phase flow regime. For the two lowest mass fluxes, 75 and 150 kg/m^2-s, wavy or wavy-annular flow prevailed over much of the quality range. In the wavy flow regime, heat is transferred primarily by conduction across the thin condensate film at the top of the tube. This condensate flows down the tube under the action of gravity, and is then transported out of the tube in the liquid pool at the bottom of the tube. The modest increase in heat transfer coefficient with quality in this flow regime occurs because of the corresponding increase in interfacial area. The primary item affecting the heat transfer coefficient in this flow regime is the film thickness. Since the film thickness is insensitive to mass flux in the wavy flow regime, wavy flow heat transfer coefficients are also relatively insensitive to mass flux.

At the highest mass fluxes of 500, 650, and 800 kg/m^2-s, annular flow prevailed over most of the quality range. In the annular flow regime, correlations such as those of Soliman et al. (1968) and Traviss et al. (1973) clearly illustrate the interdependence between pressure drop and heat transfer ($h \propto \sqrt{\Delta P/\Delta z}$). Since the pressure drop increases sharply as the quality is increased, the heat transfer coefficients in the annular flow regime show significant quality dependence.

Perhaps the most interesting heat transfer trends were displayed at a mass flux of 300 kg/m^2-s. At this mass flux, the flat Nusselt number versus quality behavior that is characteristic of wavy flow was observed at low qualities while annular flow behavior was observed at higher qualities. The change in slope of the Nusselt number versus quality graph occurred between 30 percent and 40 percent quality, which corresponded closely with an observed change from the wavy-annular to the annular flow regime. At this mass flux, it would be inappropriate to use a single heat transfer model over the entire quality range.

Tube Diameter Effects. The relationships between h and D that were predicted by annular and wavy flow heat transfer correlations agreed well with the experimental data. Although this was expected for the 7.04 mm i.d. tube, a commonly used and tested size, some doubt existed about whether the heat transfer behavior in the 3.14 mm i.d. tube would correspond with that predicted by "large tube" correlations.

The most noticeable effect of the tube diameter had to do with the point at which the heat transfer mechanism changed from filmwise (wavy) to forced convective (annular). The primary difference in the heat transfer behavior in the two tubes was observed at a mass flux of 300 kg/m^2-s. In the 3.14 mm i.d. tube, the heat transfer behavior showed a change in slope between 30 percent and 40 percent quality as the flow regime changed from wavy annular to annular. In the larger 7.04 mm i.d. tube, this transition was only observed for the highest quality point (89 percent). Again, it corresponded closely with an observed transition to annular flow at around 80 percent quality. The heat transfer characteristics at the other mass fluxes were similar in both tubes.

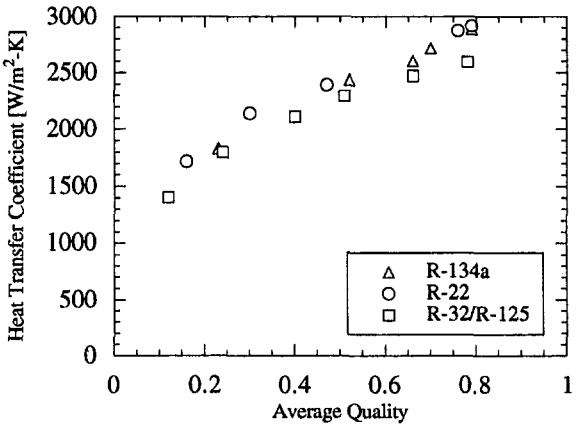

Fig. 8 Wavy flow heat transfer comparison for R-134a, R-22, and 50 percent/50 percent R-32/R-125 in the 7.04 mm i.d. tube at 35°C, G = 75 kg/m²-s, $\Delta T \approx 3$°C

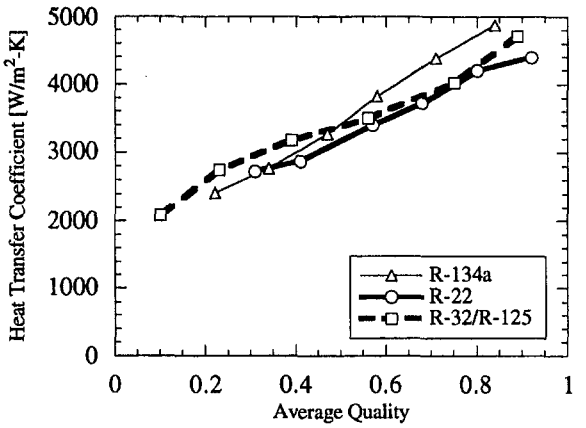

Fig. 10 Mixed flow regime heat transfer comparison for R-134a, R-22, and 50 percent/50 percent R-32/R-125 in the 7.04 mm i.d. tube at 35°C, G = 300 kg/m²-s

Effect of Refrigerants. A comparison of wavy flow heat transfer for R-134a, R-22, and 50 percent/50 percent R-32/R-125 is made in Fig. 8. This figure shows the heat transfer coefficients at a mass flux of 75 kg/m²-s and a saturation temperature of 35°C in the 7.04 mm i.d. tube. Since the wavy flow heat transfer coefficients are dependent on the refrigerant-to-wall temperature difference, it was maintained near 3°C (2.87°C to 3.11°C) for all the tests. Perhaps the primary conclusion from these data is that little difference exists in the wavy flow heat transfer coefficients of the three fluids, with a maximum difference of around 10 percent. It appeared that the highest heat transfer coefficients were obtained for R-22, followed by R-134a and R-32/R-125. Based on the wavy flow property index from the Chato (1962) correlation, $[\rho_l(\rho_l - \rho_g)k_l^3 i_{lg}/\mu_l]^{0.25}$, R-32/R-125 would be expected to have the highest wavy flow heat transfer coefficients (4.7 percent above R-134a), followed by R-22 (3.5 percent above R-134a) and R-134a. These predicted differences are very small in light of the considerable uncertainty in transport properties. The index itself also neglects the effect of void fraction variations between the fluids, which would tend to reverse the predicted differences.

Figure 9 compares the annular flow heat transfer coefficients of R-134a, R-22, and 50 percent/50 percent R-32/R-125. These data were collected at a mass flux of 650 kg/m²-s and a saturation temperature of 35°C in the 7.04 mm i.d. tube. The best fluid for annular flow heat transfer was R-134a, while the heat transfer coefficients of R-22 and R-32/R-125 were nearly identical. The single-phase, liquid heat transfer index, $k_l^{0.6} c_{pl}^{0.4}/\mu_l^{0.4}$, was highest for R-32/R-125, followed by nearly identical values for R-134a and R-22. This resulted in R-32/R-125 having slightly better annular flow heat transfer than the other fluids at low qualities, where the heat transfer coefficient was close to the single-phase liquid value. As the quality was increased, the two-phase multiplier increased in value and became increasingly important. The two-phase multiplier was highest for R-134a, the lowest reduced pressure fluid. This resulted in R-134a having higher heat transfer coefficients than the other fluids at high qualities.

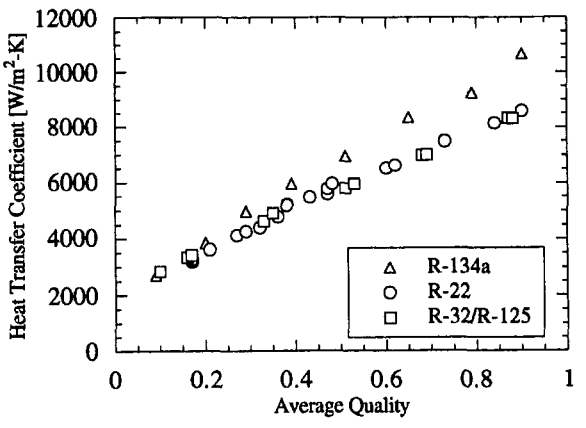

Fig. 9 Annular flow heat transfer comparison for R-134a, R-22, and 50 percent/50 percent R-32/R-125 in the 7.04 mm i.d. tube at 35°C, G = 650 kg/m²-s

Figures 8 and 9 compared the heat transfer coefficients of the fluids at mass fluxes where one flow regime prevailed over the entire quality range. At intermediate mass fluxes, a transition quality was reached where the flow regime and heat transfer characteristics changed from wavy flow to annular flow. This point was also affected by the fluid. Based on the flow regime results, one would expect annular flow to occur at lower qualities for R-134a than for R-32/R-125. This is demonstrated in Fig. 10, which compares the heat transfer coefficients of R-134a, R-22, and R-32/R-125 at a mass flux of 300 kg/m²-s. At this mass flux, the quality where the wavy-annular to annular transition occurred was 40 percent for R-134a, 50 percent for R-22, and 72 percent for R-32/R-125. The heat transfer points were connected with lines in this figure to make changes in slope clearer. The data showed that, as expected, the change in slope occurred slightly earlier for R-134a than for the other fluids. At the highest qualities, where annular flow was observed for all fluids, R-134a had the highest heat transfer coefficients of the three fluids. Across the full range of quality, the heat transfer coefficients of the three fluids were within 10 percent.

Effect of Temperature Difference. The refrigerant-to-wall temperature difference has an impact on the heat transfer coefficients in the wavy flow regime. This dependence occurs because, for a falling film, a larger driving temperature difference results in a thicker film at a given location (hence lower heat transfer coefficients). In the annular flow regime, a significant amount of experimental and analytical evidence suggests a negligible impact of temperature difference or heat flux. Studying the impact of temperature difference on the heat transfer coefficients then provides a nonvisual method of assessing the extent of filmwise and/or forced-convective condensation.

Precisely controlling the temperature difference during internal condensation experiments is very difficult. For this reason, few internal condensation data are available for which the temperature difference was deliberately controlled. To gain an added understanding of ΔT effects, the temperature difference was controlled at two different levels for all mass fluxes during testing with R-22 and R-32/R-125 in the 7.04 mm i.d. tube.

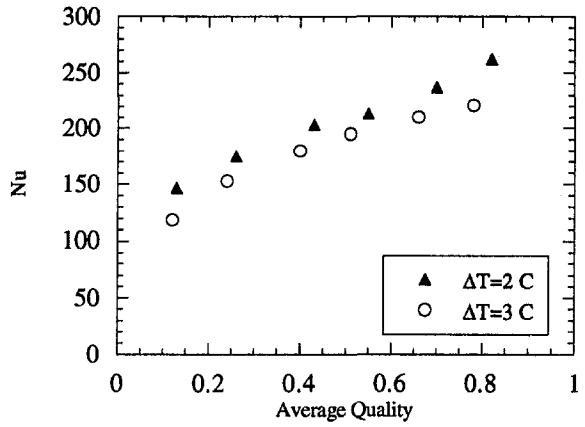

Fig. 11 Effect of ΔT on Nu for R-32/R-125 in the 7.04 mm test-section, G = 75 kg/m^2-s, T_{sat} = 35°C

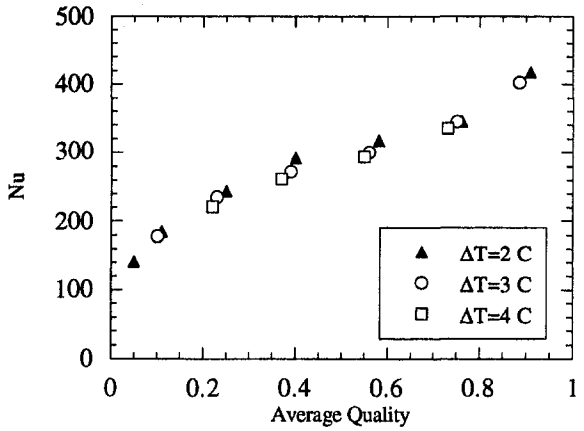

Fig. 13 Effect of ΔT on Nu for R-32/R-125 in 7.04 mm test-section, G = 300 kg/m^2-s, T_{sat} = 35°C

Figure 11 shows the variation of Nusselt number with quality for R-32/R-125 at a saturation temperature of 35°C and a mass flux of 75 kg/m^2-s. The two different sets of points correspond to temperature differences of approximately 2°C (1.88°C to 2.12°C) and 3°C (2.87°C to 3.11°C). As predicted by Nusselt theory, the Nusselt numbers were lower for the higher temperature difference data across the full range of quality. These same data were corrected for varying temperature differences by computing the quantity $Nu/[Ga*Pr/Ja_l]^{0.25}$ based on liquid properties. If all of the heat transfer occurred by filmwise condensation and none occurred in the bottom of the tube, this correction should collapse the two different sets of data onto a single line. Figure 12 shows that, to a large extent, making this correction does just that. As the quality approaches unity and the liquid pool vanishes, moreover, the value of $Nu/[Ga*Pr/Ja_l]^{0.25}$ appears to properly approach the accepted value of 0.728 for condensation outside of a horizontal cylinder.

Figures 13 through 15 present similar plots for R-32/R-125 in the 7.04 mm tube as the mass flux was increased to 300 kg/m^2-s and 650 kg/m^2-s. The trends are very interesting. At 300 kg/m^2-s, the unmodified Nusselt numbers increased with decreasing temperature difference up to a quality of 75 percent. At that point, they appeared to converge as would be expected for annular flow. In Fig. 14, the quantity $Nu/[Ga*Pr/Ja_l]^{0.25}$ is plotted for the same set of data. The trends on this plot are "flipped" in comparison to the data of Fig. 13, with the highest values of $Nu/[Ga*Pr/Ja_l]^{0.25}$ occurring for the highest values of ΔT. This indicates that at this mass flux, additional heat transfer by forced-convective condensation resulted in a dependence on ΔT less than the -0.25 power dependence from Nusselt theory. Stated another way, the heat transfer in the bottom of the liquid pool was no longer negligible. Figure 15 shows that at a mass flux of 650 kg/m^2-s, the unmodified Nusselt numbers exhibited no dependence on temperature difference, as expected for annular flow.

Comparisons with Existing Heat Transfer Correlations

Several correlations from the literature were selected for comparison with the experimental data. For the wavy flow data, the correlations of Chato (1962), Jaster and Kosky (1976), and Rosson and Myers (1965) were selected. The correlations of Shah (1979), Cavallini and Zecchin (1974), Traviss et al. (1973), and Chen et al. (1987) were selected for comparison with the annular flow data.

Gravity-Dominated Correlations. Chato's correlation was developed for stratified flow and recommended for use at vapor Reynolds numbers of less than 35,000. It was compared with 210 experimental data points that met this criteria, and had a mean deviation of 12.8 percent. The primary deficiency in the Chato correlation was that it predicted no variation of the Nusselt number with quality. Comparisons with the wavy flow data show that such variations did exist.

The range of applicability of the Jaster and Kosky correlation is specified by an upper limit of a dimensionless wall shear. The mean deviation between the 213 experimental points which

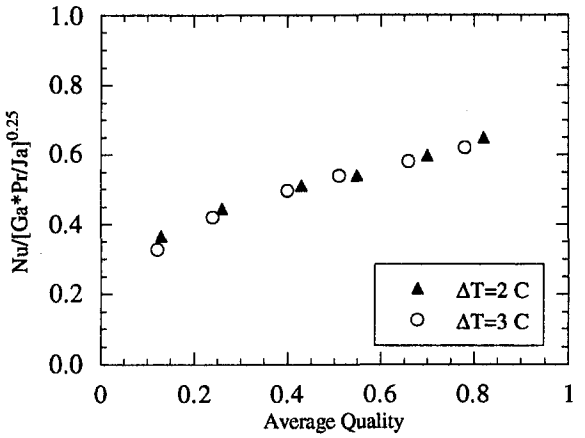

Fig. 12 Effect of ΔT on $Nu/[Ga*Pr/Ja]^{0.25}$ for R-32/R-125 in the 7.04 mm i.d. test-section, G = 75 kg/m^2-s, T_{sat} = 35°C

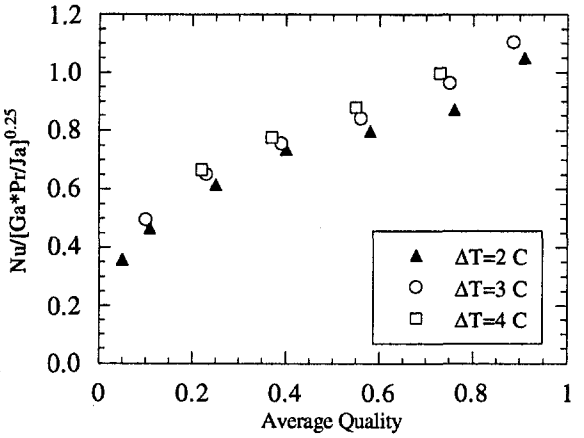

Fig. 14 Effect of ΔT on $Nu/[Ga*Pr/Ja]^{0.25}$ for R-32/R-125 in the 7.04 mm i.d. test-section, G = 300 kg/m^2-s, T_{sat} = 35°C

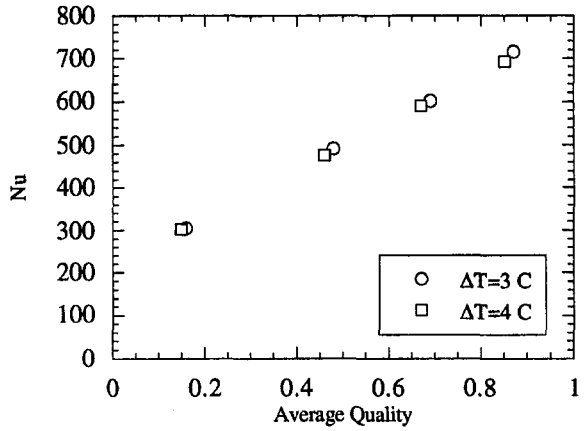

Fig. 15 Effect of ΔT on Nu for R-32/R-125 in the 7.04 mm tube, G = 650 kg/m^2-s, T_{sat} = 35°C

met this criterion and the predicted values was 14.5 percent, slightly higher than the simpler Chato correlation. Although the deviations between their correlation and the present data were sometimes large, the mean deviation of 14.5 percent was substantially better than the 37 percent standard deviation with their own data.

The correlations of Chato, and Jaster and Kosky, were both able to predict most of the experimental data for the wavy flow regime within a range of ±25 percent. Neither predicted the variation with quality successfully, and neither accounted for heat transfer in the bottom of the liquid pool. For very low mass fluxes, this assumption is reasonable.

Because no guidelines were given the use of the Rosson and Myers correlation, it was compared against the full database of points that were later used to develop the wavy flow correlation for this study. Although Rosson and Myers attempted to account for forced-convective condensation in the liquid pool at the bottom of the tube, their correlation was actually a poor predictor of the experimental data. The correlation had a mean deviation of 21.3 percent with the experimental data, almost 10 percent worse than the simpler Chato and Jaster and Kosky correlations. The most problematic part of the correlation seemed to be prediction of the parameter β, which represents the fraction of the tube circumference occupied by filmwise condensation. At low mass fluxes, this parameter should clearly be related to the void fraction and approach unity as the quality approaches unity. However, the empirical expressions developed by Rosson and Myers do not behave in this manner. The trends were very erratic, particularly for mass fluxes over 25 kg/m^2-s, where the relationship was not even monotonic.

Annular Flow Correlations. The annular flow correlations that were selected for comparison with the experimental data encompass at least one member of each of the three broad classes—two-phase multiplier correlations (Shah, Cavallini, and Zecchin), shear-based correlations (Chen et al.), and boundary layer analyses (Traviss et al.).

Of the four correlations, only Shah's came with specific guidelines for a lower limit of applicability. His correlation should not be used at mass fluxes where the vapor velocity with x = 1 was less than 3 m/s. For R-134a at 35°C, this corresponds to a lower mass flux limit of 130 kg/m^2-s. This value is higher for the other refrigerants, which have higher vapor densities. In all cases, this represents a vapor velocity well above the wavy to annular transition line on the Taitel-Dukler map. This criterion was selected for each of the correlations so that they would be compared on an equal basis.

The predictions of the Shah correlation agree fairly well with the data, with a mean deviation of 9.1 percent. Nearly all of the data were predicted within ±25 percent. The most significant deviations occurred for some low Nusselt number data that were in the wavy-annular flow regime and for some very high mass flux, high quality data. In general, the Shah correlation seemed to underpredict the experimental data.

The mean deviation of the Cavallini and Zecchin correlation with the experimental data was 11.6 percent, slightly higher than the Shah correlation. Despite the slightly higher mean deviation, though, the predictions of the Cavallini and Zecchin correlation were more correct in trend than those of the Shah correlation. When the Cavallini and Zecchin correlation was in error, it tended to overpredict the experimental data. The largest errors occurred at low qualities because this correlation approaches a value of 2.18 times the single-phase Nusselt number at a quality of zero.

The mean deviation of the Traviss correlation was 11.8 percent, slightly higher than the Cavallini and Zecchin correlation. The Traviss correlation tended to overpredict the experimental data, particularly at high qualities, where their empirical correction was used. If this correction was omitted, their correlation would have underpredicted the high quality data.

The Chen correlation was the worst predictor of the annular flow data with a mean deviation of 23.3 percent. This correlation significantly underpredicted nearly all of the data. The correlation of Soliman et al. (1968) generally predicts lower Nusselt numbers than the Chen correlation. Thus, it would have performed even worse against the present data.

One problem with the annular flow correlations that is not apparent in a plot of experimental versus predicted Nusselt numbers concerns their range of applicability. Figure 16 compares experimental and predicted Nusselt numbers versus quality for R-22 in the 7.04 mm i.d. tube at a mass flux of 225 kg/m^2-s and a saturation temperature of 35°C. According to the Taitel-Dukler maps, this mass flux should be annular at all qualities above 12 percent. The velocity, with vapor only, would be 3.9 m/s, 30 percent above the lower limit of applicability specified by Shah. Thus, the best information available in the literature would suggest that annular flow correlations should be applicable over nearly the entire quality range. Still, Fig. 16 shows that the Nusselt numbers were well above the annular flow predictions at low qualities. As the quality reached about 70 percent and the flow pattern became fully annular, the predictions of the Cavallini and Zecchin correlation agreed very well with the experimental data. These data suggest the need for further development of heat transfer models in the wavy or wavy-annular regions at higher mass fluxes.

Development of the Heat Transfer Correlations

In this section, the development of the annular flow correlation for forced-convective condensation is first described. This

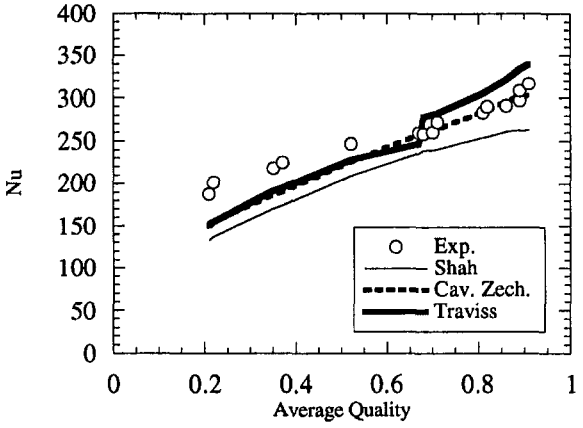

Fig. 16 Comparison of annular flow correlations with heat transfer data for R-22 in the 7.04 mm tube, T_{sat} = 35°C, G = 225 kg/m^2-s

discussion establishes the strong similarities between the most theoretical approach for annular flow condensation, the boundary-layer analyses, and the simpler two-phase multiplier approaches. Then, an annular flow correlation is developed using the two-phase multiplier approach. Next, the wavy flow data from this study are used to develop a wavy flow correlation. This correlation uses a similar approach to that tried unsuccessfully by Rosson and Myers (1965), but with more attention paid to carefully weighting the forced-convective and filmwise components. Finally, the data from the wavy-annular flow regime are compared with predictions of the wavy and annular flow correlations. These comparisons are used to develop limits of applicability for the two correlations.

Annular Flow Correlation. The most theoretical correlation that has been widely used is the Traviss correlation. Under its rather stringent assumptions, this method provides an analytical prediction of the Nusselt number. Before a pressure drop model is assumed, the correlation can be written as follows:

$$\mathrm{Nu} = \frac{D^+ \mathrm{Pr}_l}{F_2(\mathrm{Re}_l, \mathrm{Pr}_l)}. \tag{27}$$

The term D^+ is the tube diameter scaled by the turbulent length scale, $\mu_l/\sqrt{\tau_w \rho_l}$. A simple force balance indicates the proportionality between the wall shear and the pressure drop, establishing the fact that the annular flow Nusselt number is proportional to the square root of the pressure drop per unit length.

The denominator of Eq. (27), F_2, can be thought of as a dimensionless heat transfer resistance. Physically, this resistance increases as the dimensionless film thickness increases, as would be expected from conduction arguments. It also increases with increasing Prandtl numbers, since high Prandtl numbers reflect more effective transfer of momentum than heat. This function is dependent upon the liquid Reynolds number because, under the assumptions of a symmetric annular film and no entrainment, specifying the liquid Reynolds number uniquely specifies the dimensionless film thickness. A plot of F_2 versus Re_l for various values of Pr_l shows that as Re_l increases from 0 to 1125 (the value where the fully turbulent region begins), F_2 increases very rapidly. As Re_l is increased further, F_2 increases much more slowly. Physically, this occurs because the primary resistance to heat transfer is contained in the laminar sublayer and buffer regions.

Although the Traviss analysis was performed after the advent of the simple shear-based correlations, it provides a useful method for understanding them. For relatively small changes in Re_l when $\mathrm{Re}_l > 1125$, one could reasonably assume a constant value of F_2 at a fixed Prandtl number. If the Prandtl number dependence could be expressed as a power law function, the Nusselt number could then be expressed as

$$\mathrm{Nu} = aD^+ \mathrm{Pr}_l^m. \tag{28}$$

This is exactly the form of the original shear-based correlation of Carpenter and Colburn (1951). Thus, these correlations are justified for a narrow range of conditions by the more theoretically sound analysis of Traviss.

Only a few more manipulations are required to show the equivalence between the Traviss analysis and the two-phase-multiplier approaches. The first important observation is that annular flow is seldom encountered for liquid Reynolds numbers less than 1125. Using the criterion for annular flow that $\mathrm{Fr}_{so} = 18$ (Eqs. (4*a*) and (4*b*)), the corresponding equation was solved for the quality above which annular flow could exist with $\mathrm{Re}_l = 1125$. For R-134a at 35°C, a value of over 99.5 percent was obtained in the 7.04 mm i.d. tube and a value of over 97.5 percent was obtained in the 3.14 mm i.d. tube. This indicates that the liquid film is seldom so thin that the fully turbulent region is not reached, thus the piecewise definition of F_2 is seldom necessary. With F_2 confined to values of $\mathrm{Re}_l > 1125$, a power law function of Re_l and Pr_l was used to curve fit the function F_2. For a range of Re_l from 1125 to 10^5 and Pr_l from 1 to 10. F_2 was well approximated by the following function:

$$F_2 \cong 10.25\ \mathrm{Re}_l^{0.06}\ \mathrm{Pr}_l^{0.59}. \tag{29}$$

If this approximation is used in Eq. (28), and D^+ is evaluated with a pressure drop correlation using Lockhart and Martinelli's two-phase liquid multiplier approach, the following equation is obtained for the Nusselt number:

$$\mathrm{Nu} = \frac{\sqrt{0.079/2}\ \mathrm{Re}_l^{0.87} \phi_l(X_{tt})\ \mathrm{Pr}_l}{10.25\ \mathrm{Re}_l^{0.06}\ \mathrm{Pr}_l^{0.59}} = 0.0194\ \mathrm{Re}_l^{0.81}\ \mathrm{Pr}_l^{0.41} \phi_l(X_{tt}). \tag{30}$$

This is identical in form, and close in value, to the commonly used two-phase multiplier correlations. A two-phase multiplier correlation using the Dittus-Boelter correlation for the single-phase heat transfer coefficient, such as the one of Shah (1979), takes the following form:

$$\mathrm{Nu} = 0.023\ \mathrm{Re}_l^{0.8}\ \mathrm{Pr}_l^{0.4} \underbrace{F\left[P_{\mathrm{red}}^{0.4}\left(\frac{1-x}{x}\right)^{0.8}\right]}_{\text{two-phase multiplier}}. \tag{31}$$

There is little difference in the form of Eq. (30) and (31), except that Shah used a slight modification of the Lockhart-Martinelli parameter for correlating his two-phase multiplier.

If the correlation of Traviss et al. (1973) proved to be the most accurate predictor of experimental data, modifying it would make little sense. In fact, even Traviss found that their correlation underpredicted their own data at high qualities. For this reason, they arbitrarily replaced their two-phase multiplier (which they call F rather than ϕ_l) with $F^{1.15}$ at high qualities ($X_{tt} < 0.155$). Rather than modifying this function, which was an empirical fit to two-phase pressure drop data to begin with, it appears equally reasonable to determine the function directly from condensing heat transfer data. This is exactly the approach of the two-phase multiplier correlations.

One additional benefit of dissecting the Traviss correlation is that it demonstrates the robustness of the heat transfer correlation for annular flow with respect to the rather serious assumptions used in their derivation. These assumptions are (1) extrapolating the universal velocity profile from single-phase pipe flow, (2) symmetric annular film, and (3) no entrainment of liquid in the vapor core.

With regard to the first assumption, the presence of waves at the free surface would be expected to cause deviations from the universal velocity profile. However, the impact of these waves is likely to be small in the region closest to the wall where most of the resistance to heat transfer occurs.

With respect to the second assumption (the symmetric annular film), gravity definitely creates a thinner film at the top of the tube than at the bottom. Since the heat transfer is relatively insensitive to variations in film thickness provided that the film remains thicker than the buffer layer, these effects would not be expected to significantly alter the heat transfer results.

The impact of violating the third serious assumption (that of no entrainment), can also be assessed from Traviss' analysis. This assumption is necessary when invoking the conservation of liquid statement, which in turn determines the dimensionless film thickness. Since F_2 only depends on Re_l to the 0.06 power, though, it appears that the role of entrainment on heat transfer should be small, provided that the entrainment rate does not become high enough to remove liquid from the laminar sublayer or buffer layer.

Based on the work above, the two-phase multiplier approach was selected for correlating the annular flow heat transfer data from this study. To make sure that the correlation was not biased by data outside of the annular flow regime, only data with $Fr_{so} > 20$ were used to develop the correlation. This value was reported by Dobson (1994) to provide a good indicator of the transition from wavy-annular to annular flow, and agreed well with the data from this study. The correlation developed was

$$\mathrm{Nu} = 0.023\ \mathrm{Re}_l^{0.8}\ \mathrm{Pr}_l^{0.4}\left[1 + \frac{2.22}{X_{tt}^{0.89}}\right]. \tag{32}$$

This form utilizes the single-phase heat transfer correlation of Dittus and Boelter (1930) with a Prandtl exponent of 0.4. This value would normally be used for heating rather than cooling, but was selected for the following three reasons: (1) it was nearly identical to the value obtained by curve-fitting the Traviss correlation; (2) it provided a better fit to the more accurate single-phase correlations in the range of Re and Pr from this study; and (3) it has been used with some success by Shah for fluids other than refrigerants. At a quality of zero, the Lockhart-Martinelli parameter approaches infinity and Eq. (32) predicts the single-phase liquid Nusselt number. Values of the constants in Eq. (32) were determined by regression analysis of the entire set of data. The results show that Eq. (32) is a better predictor of the experimental data than any of the correlations from the literature.

Wavy Flow Correlation. During wavy flow condensation at sufficiently low mass fluxes, heat is transferred in the upper portion of the tube by filmwise condensation and in the pool at the bottom of the tube by forced-convective condensation. At very low vapor velocities, the heat transfer in the bottom of the tube is much smaller than that in the top and can be readily neglected. Under these same conditions, the vapor flow has little effect on the liquid film at the top of the tube and Nusselt's solution for external condensation on a cylinder can be used. This approach was adopted by Chato (1962) and Jaster and Kosky (1976).

As the vapor velocity is increased, several deviations from ideal stratified flow conditions begin to emerge. First, the heat transfer in the bottom of the tube may become significant enough to warrant inclusion. This effect was observed experimentally at mass fluxes above 75 kg/m^2-s, where the $\mathrm{Nu}/[\mathrm{Ga}\ \mathrm{Pr}/\mathrm{Ja}]^{0.25}$ curves for different ΔT's no longer converged onto a single line. The second deviation from ideal stratified flow has to do with the interfacial shear exerted by the vapor on the condensate film. For conditions approaching stagnant vapor, little shear is exerted on the condensate. Under these conditions, the condensate falls almost vertically down the tube and each axial location is independent of those around it. In this situation, applying solutions from external condensation is certainly justified. In the opposite extreme, that of very high vapor velocity and interfacial shear, gravitational forces become negligible and annular flow is observed. Now the film thickness is nearly independent of angle and filmwise condensation solutions are inappropriate. In the intermediate region, the vapor velocity is high enough to exert a significant shear on the condensate film but not great enough to overwhelm gravity forces. Here, the condensate flows in a path with both axial and circumferential components.

Based on the data from this study, it appeared that some film condensation was occurring in this intermediate regime. The first question was whether the solutions from external filmwise condensation would remain valid in this region. This question was addressed by solving the conservation equations for the film thickness in the entry and in the fully developed region. The solutions indicated that downstream of the entry region, the film thickness and the heat transfer coefficient is identical to the zero shear case. The primary role of the vapor shear is to determine the relative sizes of the entry and fully developed regions. Low shear cases correspond to short entry regions, and the converse is true for high shear cases. However, only relatively low shear cases are amenable to film condensation analysis because high interfacial shear cases correspond to turbulent annular flows. The primary result of the analysis was to demonstrate the validity of filmwise condensation solutions that assume no axial velocity component for cases where a relatively small axial velocity does exist.

The development of the correlation was guided by a combination of careful data analysis and physical guidance from analytical solutions. The details are described by Dobson (1994) and Dobson et al. (1994a). The final correlation separates the heat transfer by film condensation in the upper part of the horizontal tube from the forced-convective heat transfer in the bottom pool:

$$\mathrm{Nu} = \frac{0.23\ \mathrm{Re}_{vo}^{0.12}}{1 + 1.11 X_{tt}^{0.58}}\left[\frac{\mathrm{Ga}\ \mathrm{Pr}_l}{\mathrm{Ja}_l}\right]^{0.25} + (1 - \theta_l/\pi)\ \mathrm{Nu}_{\mathrm{forced}}, \tag{33}$$

where θ_l = angle subtended from the top of tube to the liquid level and

$$\mathrm{Nu}_{\mathrm{forced}} = 0.0195\ \mathrm{Re}_l^{0.8}\ \mathrm{Pr}_l^{0.4}\phi_l(X_{tt}) \tag{34}$$

$$\phi_l(X_{tt}) = \sqrt{1.376 + \frac{c_1}{X_{tt}^{c_2}}}. \tag{35}$$

For $0 < \mathrm{Fr}_l \leq 0.7$,

$$c_1 = 4.172 + 5.48\ \mathrm{Fr}_l - 1.564\ \mathrm{Fr}_l^2 \tag{36a}$$

$$c_2 = 1.773 - 0.169\ \mathrm{Fr}_l \tag{36b}$$

For $\mathrm{Fr}_l > 0.7$,

$$c_1 = 7.242 \tag{37a}$$

$$c_2 = 1.655 \tag{37b}$$

Fr_l is the liquid Froude number. Due to the 1.376 inside the radical of Eq. (35), the correlation above matches the Dittus-Boelter single-phase correlation when $x = 0$.

θ_l is geometrically related to the void fraction by the following formula if the area occupied by the thin condensate film is neglected:

$$\alpha = \frac{\theta_l}{\pi} - \frac{\sin(2\theta_l)}{2\pi}. \tag{38}$$

If a void fraction model is assumed, this transcendental equation must be solved to obtain the desired quantity, θ_l. Jaster and Kosky (1976) deduced an approximate relationship which is much easier to use, albeit for a slightly different purpose. In the context of the present problem, their simplification can be stated as

$$1 - \frac{\theta_l}{\pi} \cong \frac{\arccos(2\alpha - 1)}{\pi}. \tag{39}$$

The simplicity achieved by this assumption is well worth the modest errors associated with it. These errors are themselves mitigated by the fact that the forced-convective Nusselt number, by which the quantity in Eq. (39) is multiplied, is normally considerably smaller than the filmwise Nusselt number. A void fraction correlation must be assumed to solve this equation. The calculations presented hereafter were made using the approximation of Eq. (39) and the void fraction correlation of Zivi (1964), Eq. (13).

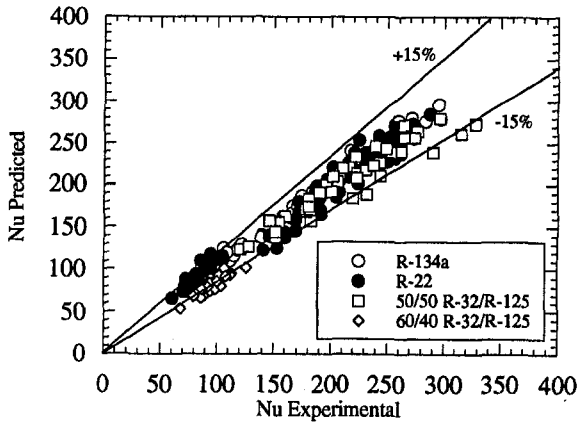

Fig. 17 Comparison of the wavy flow correlation, Eq. (33), with the experimental data of the present study

The predictions of Eq. (33) are compared to the wavy flow data in Fig. 17. Overall, the agreement is very good. The mean deviation between the predicted and experimental values was 6.6 percent, considerably better than the correlations from the literature. The worst deviations were found for the data at a saturation temperature of 45°C and some of the data in the 3.14 mm i.d. tube. For both of these situations, the uncertainties in both the heat transfer coefficients and the qualities were rather large because the heat losses to the environment became a significant fraction of the overall heat transfer. For the lowest mass flux tests in the 3.14 mm i.d. tube, for instance, the heat transfer rates in the test section were on the order of only 50 W.

Limits of Application—Wavy-Annular Flow Regime. The correlations developed above were for the annular and wavy flow regimes, respectively. The annular flow correlation was developed using a set of data restricted to values of $Fr_{so} > 20$, which excluded wavy-annular flow. The wavy flow correlation was developed primarily with data for which $Fr_{so} < 10$, including primarily wavy flow. A region exists in between these limits where the physics of the condensation process is not so clear cut. The applicability of the wavy and annular flow correlations were assessed for data in this transition region. As a first step, the wavy and annular flow correlations were used to predict the Nusselt numbers for the entire set of data, regardless of the flow regime. At values of $Fr_{so} < 10$, the Nusselt numbers were much higher than predicted by the annular flow correlation. In the worst case, this deviation was over a factor of 4. At values of $Fr_{so} > 20$, the data were entirely in the annular flow regime, and the predictions were very good. At values of Fr_{so} between 10 and 20, some points were well predicted by the annular flow correlations, and others were predicted poorly. With the wavy flow correlation, at values of $Fr_{so} < 10$, all of the data were predicted within a 20 percent range. At values of $Fr_{so} > 20$, the measured Nusselt numbers were substantially larger than the predicted values. For the range of Fr_{so} between 10 and 20, the error in the prediction of the wavy flow correlation was much less than the error produced by the annular flow correlation. At mass fluxes at or above 500 kg/m^2-s, all experimental Nusselt numbers were substantially higher than those predicted by the wavy flow correlation, but were quite well predicted by the annular flow correlation.

Mist Flow Effects. Pure mist flow with no stable wall film was never observed at qualities below 95 percent. Moreover, when it was observed at the highest qualities, it was always after the adiabatic section and before the test-section inlet. At the outlet sight glass, after condensation had begun in the test section, a stable wall film was always observed. This was true for test-section outlet qualities as high as 90 percent. This evidence implies that a stable wall film is formed as soon as condensation begins. Stated another way, the nature of the condensation process itself tends to preclude a dry wall. Although a substantial amount of mist was entrained in the core flow at high mass fluxes, the excellent agreement of the annular flow correlation with experimental data containing significant entrainment indicates that the entrainment did not have a significant effect on the heat transfer. These findings do not agree with those of Soliman (1986), and are discussed in detail by Dobson (1994) and Dobson et al. (1994a).

Design Recommendations.

For $G \geq 500$ kg/m^2-s, use Eq. (32) for all qualities. For $G < 500$ kg/m^2-s, use Eq. (33) if $Fr_{so} < 20$, and use Eq. (32) if $Fr_{so} > 20$.

Comparison With Experimental Data. The recommended correlations were applied to data from this study and from the literature. The comparisons are summarized in Table 6 and discussed in detail by Dobson (1994).

Effect of Oil. Oil in the refrigerant decreases the heat transfer and increases the pressure drop. Gaibel et al. (1994) discussed these effects. He found that for oil mass fractions $\omega_o < 0.05$, the correction factor developed by Schlager et al. (1990) gave acceptable values for the heat transfer when applied to the Dobson correlations (Eqs. (32) and (33)).

$$Nu_{oil} = Nu_{Dobson} * \exp(-3.2\omega_o). \quad (40)$$

For the pressure drop, the Souza et al. (1992) correction factor was found acceptable in the same oil concentration range.

$$\Delta P_{oil} = \Delta P_{pure}(1 + 12.4\omega_o - 110.8\omega_o^2). \quad (41)$$

Insufficient data were developed to investigate the effects of oil on the flow-regime transitions.

Condensation of Zeotropes. Sweeney (1996) and Sweeney and Chato (1996) correlated the data of Kenney et al. (1994) obtained with Refrigerant 407c, a zeotropic mixture of R-32, R-125, and R-134a (23, 25, and 52 percent by mass), in a smooth tube. They found that the heat transfer rates could be predicted by the following simple modification of the Dobson correlations (Eqs. (32) and (33)):

$$Nu_{wavy,zeotrope} = \left(\frac{G}{300}\right)^{0.3} Nu_{Eq.(33)} \quad (42)$$

$$Nu_{annular,zeotrope} = 0.7\left(\frac{G}{300}\right)^{0.3} Nu_{Eq.(32)}, \quad (43)$$

where the mass flux, G, is in kg/m^2-s. Figure 18 shows the agreement between these correlations and a typical set of experimental data covering both wavy and annular flow regimes.

These correlations cannot be assumed to be generally applicable to zeotropes without additional data on other zeotropes, but they do indicate that the equations represent the underlying physical phenomena well.

Table 6 Comparison between the heat transfer correlations and experimental data

Source	Fluid	Tube Diameter mm	Mass Flux kg/m^2-s	Mean Deviation %
Dobson (1994)	R-134a	3.14 & 7.04	25 - 800	4.4
Dobson (1994)	R-22	3.14 & 7.04	25 - 800	4.9
Dobson (1994)	50/50 R-32/R-125	3.14 & 7.04	25 - 800	5.9
Dobson (1994)	60/40 R-32/R-125	3.14 & 7.04	25 - 800	6.1
Altman (1960)	R-22	8.7	300 - 860	7.0
Bae (1970)	R-22	12.5	320 - 660	13.5
Traviss (1973)	R-12	8.0	162 - 1540	13.7

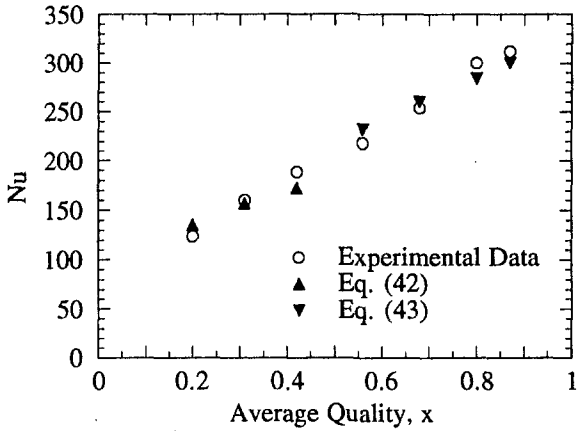

Fig. 18 Comparison between smooth tube data and predictions of Eqs. (42) and (43), G = 300 kg/m^2-s (220 klb$_m$/ft^2-hr)

Instabilities. Probably because we were studying only local condensation, as opposed to complete condensation, we have not encountered any instabilities, such as those reported by Rabas and Minard (1987). Instabilities, however, could occur in complete systems but would depend very strongly on the interactions among the various components.

Summary and Recommendations

Local (i.e., for small changes in quality) heat transfer and fluid flow data were collected and analyzed for four refrigerants in two smooth tubes. Flow regimes were observed visually in three smooth tubes with diameters ranging from 3.14 to 7.04 mm inner diameter. These observations were made over the entire range of quality and a range of mass flux that comprises the fluxes used from refrigerators to automotive air conditioners. Based on these observations and their comparisons with three commonly used flow regime predictors, several conclusions can be made.

The primary flow patterns that can be expected in refrigeration condensers are wavy, wavy annular, annular, and annular mist. At low qualities, slug or pseudo-slug flow will occur. From this study, it appears that mist flow without a stable liquid film does not exist during condensation. At low vapor velocities, the flow is gravity dominated, and the liquid tends to collect at the bottom of the tube. At high velocities, vapor shear controls and the liquid is distributed around the circumference in annular fashion. Stratified flow without any interfacial waves was obtained at the lowest mass flux in this study, but it is unlikely that such a low mass flux will be encountered in typical applications.

Three techniques for flow regime prediction were compared to the experimental observations. Comparing these flow regime predictors to each other presents several problems which would reduce the usefulness of such an exercise. First, the subjectivity involved in visually determining the flow regimes is considerable. Differentiating between similar flow patterns is quite difficult. Second, the number of categories included in the different maps also presents a problem. While Soliman includes stratified, wavy, and slug flows in one regime, the Mandhane and Taitel-Dukler maps treat these as three separate regimes. Similarly, the Mandhane and Taitel-Dukler maps do not have a separate mist flow regime, while Soliman's map does. The possibility for an incorrect placement clearly increases with the number of distinct flow regimes. Given these difficulties, a discussion of the merits and drawbacks of each technique seems more suitable.

The original map of Mandhane was an extremely poor predictor of the experimental data from this study. This was because the vapor densities from this study were much higher than those from which the map was developed. A simple correction with the ratio of vapor and air densities of the superficial velocities of the vapor and liquid phases overcomes this problem, and gives each axis the physical interpretation of square root of kinetic energy. With this correction applied, the Mandhane map was an excellent predictor of the experimental data and the easiest of the three methods to use. Based on the data from this study and earlier suggestions from the literature, the flow regime described as wavy annular in this study lies in the right portion of the slug flow region on the Mandhane map. The region labeled as annular flow corresponds closely with the establishment of a nearly axisymmetric annular film. The absence of a diameter dependence could prove problematic for very small tubes, but was not a significant problem for the range of this study.

The Taitel-Dukler map successfully distinguished the stratified and wavy flow regimes at 25 and 75 kg/m^2-s for each refrigerant. Also, the increase in the length of the slug flow region as reduced pressure was increased was correctly predicted. The main difference between the predictions of the Taitel-Dukler map and the observed flow regimes was found at mass fluxes slightly above the wavy flow transition line. For these, the Taitel-Dukler map predicts that slug flow at low qualities is followed immediately by annular flow for the remainder of the quality range. The experimental observations in this region indicated that the slug flow regime was consistently followed by wavy, wavy annular, and annular flows, as the quality was increased. Observations of wavy-annular flow in the region predicted to be annular flow are not due to a deficiency in the Taitel-Dukler technique, since wavy-annular flow represents an early stage of annular flow in their terminology. Observations of wavy flow where annular flow was predicted do represent an error, but are possibly due to subjectivity in classification. Perhaps the most important conclusion concerning this map is that significant stratification of the liquid can be expected in the lower part of the range labeled as annular flow. This stratification is most significant at low qualities, or high values of the Lockhart-Martinelli parameter. For pipe diameters smaller than those used in this study, each of the flow regime transitions predicted by the Taitel-Dukler map should be examined for surface tension influences.

The Soliman flow regime predictors, although less theoretically justified than those of Taitel and Dukler, matched the experimental observations very well. However, the definitions of the different regimes must be clearly understood. The wavy flow region of Soliman includes stratified flow, wavy flow, and slug flow. With this in mind, the annular flow transition predicted by Soliman corresponded very well with the wavy to wavy-annular transition from this study. It has been shown by Dobson (1994) and Dobson et al. (1994a, b) that the transition from wavy-annular to annular flow is well predicted by a value of Fr_{so} = 18 (as opposed to 7 for the wavy to wavy-annular transition). The region labeled as mist flow by Soliman was found to correspond well with the annular-mist flow regime in this study. However, pure mist flow without a stable wall film was confined to qualities greater than 90 percent, and even then appeared to become annular mist once condensation began.

The heat transfer behavior depended significantly on the flow regime. At low mass fluxes, gravity-dominated wavy flow prevailed, and film condensation was the dominant heat transfer mode. In this flow regime, the heat transfer coefficients increased slightly with increasing quality and mass flux. At the highest mass fluxes, vapor shear dominated and annular or annular-mist flow prevailed over nearly the entire quality range with forced-convective condensation as the prevailing heat transfer mode. This regime was characterized by heat transfer coefficients that increased substantially with increases in quality and mass flux. At intermediate mass fluxes, wavy flow heat transfer behavior was observed at low qualities but became dominated by annular flow at higher mass fluxes. The quality at which this

transition to forced-convective condensation occurred increased with increases in tube diameter and reduced pressure of the refrigerant. The effect of temperature difference on heat transfer followed the expected -0.25 power dependence at low mass fluxes in the wavy flow regime. As the mass flux was increased, heat transfer contributions from the forced-convective condensate flow in the liquid pool reduced the dependence on temperature difference.

The experimental data were compared to several correlations from the literature and significant discrepancies were found. The main problem with these correlations had to do with their range of applicability, i.e., they tended to yield good results only in specific flow regimes. New correlations were developed for the annular and wavy flow regimes. The annular flow correlation was developed using a two-phase multiplier approach. It agreed with the data from this and other studies very well. Analysis of the more theoretical approaches to annular flow condensation revealed the similarity between these approaches and that of the two-phase multiplier. A wavy flow correlation was developed that accounted for both film condensation at the top of the tube and forced-convective condensation in the liquid pool at the bottom of the tube. This correlation approaches the correct limits in extreme cases—a single-phase liquid correlation at a quality of zero, and an external condensation for a quality of 1 at low mass fluxes. Based on a systematic analysis, a limit for switching from the wavy to the annular correlation was determined using Soliman's Froude number. Above a given mass flux limit, the annular flow correlation could be applied regardless of the Froude number.

Although one of the new correlations could be used with a zeotropic refrigerant with he application of a simple multiplier, considerably more analyses and experimental data are needed for the development of satisfactory understanding and reliable correlations for zeotropes. In addition, more reliable data are needed to ascertain the void fraction under various flow conditions.

Acknowledgments

This work was supported in part by the Air Conditioning and Refrigeration Center of the University of Illinois, a consortium of the University, eighteen industrial sponsors, and the National Science Foundation.

References

Altman, M., Staub, F. W., and Norris, R. H., 1960, "Local Heat Transfer and Pressure Drop for Refrigerant 22 Condensing in Horizontal Tubes," *Chemical Engineering Progress Symposium Series,* Vol. 56, No. 30, pp. 151–159.

Bae, S., Maulbetsch, J. S., and Rohsenow, W. M., 1970, "Refrigerant Forced-Convection Condensation Inside Horizontal Tubes," Report No. DSR 72591-71, Massachusetts Institute of Technology, Cambridge, MA.

Baker, O., 1954, "Simultaneous Flow of Oil and Gas," *Oil and Gas Journal,* Vol. 53, pp. 185–195.

Barnea, D., Shoham, O., Taitel, Y., and Dukler, A. E., 1980, "Flow Pattern Transition for Gas-Liquid Flow in Horizontal and Inclined Pipes: Comparisons of Experimental Data with Theory," *International Journal of Multiphase Flow,* Vol. 6, pp. 217–225.

Barnhart, J., 1992, "An Experimental Investigation of Flow Patterns and Liquid Entrainment in a Horizontal-Tube Evaporator," Ph.D. thesis, Dept. of Mechanical and Industrial Engineering, University of Illinois at Urbana-Champaign.

Breber, G., 1988, "Intube Condensation," *Heat Transfer Equipment Design,* R. K. Shah, E. C. Subbarao, and R. A. Mashelkar, eds., Hemisphere Publishing Corp., New York, pp. 1–23.

Bromley, L. A., 1952, "Effect of Heat Capacity on Condensation," *Industrial and Engineering Chemistry,* Vol. 44, pp. 2966–2969.

Butterworth, D., 1972, "A Visual Study of Mechanisms in Horizontal, Air-Water Flow," *AERE Report M2556,* Harwell, England.

Carey, V. P., 1992, *Liquid-Vapor Phase Change Phenomena: An Introduction to the Thermophysics of Vaporization and Condensation Processes in Heat Transfer Equipment,* Hemisphere, New York.

Carpenter, E. F. and Colburn, A. P., 1951, "The Effect of Vapor Velocity on Condensation Inside Tubes," *Proceedings of General Discussion on Heat Transfer,* Inst. Mech. Eng. and ASME, pp. 20–26.

Cavallini, A., and Zecchin, R., 1974, "A Dimensionless Correlation for Heat Transfer in Forced-Convective Condensation," *Proceedings of the Fifth International Heat Transfer Conference,* Japan Society of Mechanical Engineers, Vol. 3, pp. 309–313.

Chato, J. C., 1962, "Laminar Condensation Inside Horizontal and Inclined Tubes," *ASHRAE Journal,* Vol. 4, pp. 52–60.

Chen, M. M., 1961, "An Analytical Study of Laminar Film Condensation. Part II: Single and Multiple Horizontal Tubes," ASME JOURNAL OF HEAT TRANSFER, Vol. 83, pp. 55–60.

Chen, S. L., Gerner, F. M., and Tien, C. L., 1987, "General Film Condensation Correlations," *Experimental Heat Transfer,* Vol. 1, pp. 93–107.

Denglor, C. E. and Addoms, J. N., 1956, "Heat Transfer Mechanism for Vaporization of Water in a Vertical Tube," *Chemical Engineering Progress Symposium Series,* Vol. 52, No. 18, pp. 95–103.

Dhir, V., and Lienhard, J., 1971, "Laminar Film Condensation on Plane and Axisymmetric Bodies in Nonuniform Gravity," ASME JOURNAL OF HEAT TRANSFER, Vol. 93, pp. 97–100.

Dittus, F. W., and Boelter, L. M. K., 1930, "Heat Transfer in Automobile Radiators of the Tubular Type," University of California Publications on Engineering, Vol. 2, No. 13, Berkeley, CA, p. 443.

Dobson, M. K., 1994, "Heat Transfer and Flow Regimes During Condensation in Horizontal Tubes," Ph.D. thesis, Dept. of Mechanical and Industrial Engineering, University of Illinois at Urbana-Champaign.

Dobson, M. K., Chato, J. C., Wattelet, J. P., Gaibel, J. A., Ponchner, M., Kenney, P. J., Shimon, R. L., Villaneuva, T. C., Rhines, N. L., Sweeney, K. A., Allen, D. G., and Hershberger, T. T., 1994a, "Heat Transfer and Flow Regimes During Condensation in Horizontal Tubes," *ACRC Technical Report 57,* University of Illinois at Urbana-Champaign.

Dobson, M. K., Chato, J. C., Hinde, D. K., and Wang, S. P., 1994b, "Experimental Evaluation of Internal Condensation of Refrigerants R-12 and R-134a," *ASHRAE Transactions,* Vol. 100, No. 1, pp. 744–754.

Dukler, A. E., 1960, "Fluid Mechanics and Heat Transfer in Vertical Falling-Film Systems," *Chemical Engineering Progress Symposium Series,* Vol. 56, No. 30, pp. 1–10.

Dukler, A. E., and Hubbard, M. G., 1975, "A Model for Gas-Liquid Slug Flow in Horizontal and Near Horizontal Tubes," *Ind. Eng. Chem. Fundamentals,* Vol. 14, No. 4, pp. 337–347.

Gaibel, J. A., Chato, J. C., Dobson, M. K., et al., 1994, "Condensation of a 50/50 Blend of R-32/R-125 in Horizontal Tubes with and without Oil," *ACRC Technical Report 56,* University of Illinois at Urbana-Champaign.

Hanratty, T. J., 1994, personal communication, University of Illinois at Urbana-Champaign, IL.

Hinde, D. K., Dobson, M. K., Chato, J. C., Mainland, M. E., and Rhines, N., 1992, "Condensation of R-134a With and Without Oils," *ACRC Technical Report 26,* University of Illinois at Urbana-Champaign.

Hubbard, M. G., and Dukler, A. E., 1966, "The Characterization of Flow Regimes for Horizontal Two-Phase Flow: Statistical Analysis of Wall Pressure Fluctuations," Proceedings of the 1966 Heat Transfer and Fluid Mechanics Institute, Stanford University Press, Stanford, CA, pp. 100–121.

Jaster, H. and Kosky, P. G., 1976, "Condensation in a Mixed Flow Regime," *International Journal of Heat and Mass Transfer,* Vol. 19, pp. 95–99.

Jeffreys, H., 1925, "On the Formation of Water Waves by Wind," *Proceedings of the Royal Society,* Vol. A107, p. 189.

Jeffreys, H., 1926, "On the Formation of Water Waves by Wind," *Proceedings of the Royal Society,* Vol. A110, p. 241.

Kenney, P. J., Chato, J. C., Dobson, M. K., Wattelet, J. P., et al., 1994, "Condensation of a Zeotropic Refrigerant R-32/R-125/R-134a (23 percent/25 percent/52 percent) in a Horizontal Tube," *ACRC Technical Report 62,* University of Illinois at Urbana-Champaign.

Lin, P. Y. and Hanratty, T. J., 1989, "Detection of Slug Flow from Pressure Measurements," *International Journal of Multiphase Flow,* Vol. 15, No. 2, pp. 209–226.

Lockhart, R. W., and Martinelli, R. C., 1947, "Proposed Correlation of Data for Isothermal, Two-Phase, Two-Component Flow in Pipes," *Chemical Engineering Progress,* Vol. 45, No. 1, pp. 39–48.

Mandhane, J. M., Gregory, G. A., and Aziz, K., 1974, "A Flow Pattern Map for Gas-Liquid Flow in Horizontal Pipes," *International Journal of Multiphase Flow,* Vol. 1, pp. 537–553.

Moffat, R. J., 1988, "Describing the Uncertainties in Experimental Results," *Experimental Thermal and Fluid Science,* Vol. 1, pp. 3–17.

Nicholson, M. K., Aziz, K., and Gregory, G. A., 1978, "Intermittent Two Phase Flow: Predictive Models," *27th Canadian Chemical Engineering Conference,* Calgary, Alberta.

Nusselt, W., 1916, "Die Oberflachenkondensation des Wasserdampfes," *Z. Verein Deutscher Ingeniuere,* Vol. 60, pp. 541–575.

Palen, J. W., Kistler, R. S., and Yang, Z. F., 1993, "What We Still Don't Know about Condensation in Tubes," *ASME Symposium, Condensation and Condenser Design,* ASME, NY, pp. 19–53.

Rabas, T. J. and Minard, P. G., 1987, "Two Types of Flow Instabilities Occurring Inside Horizontal Tubes with Complete Condensation," *Heat Transfer Engineering,* Vol. 8, No. 1, pp. 40–49.

Rohsenow, W. M., 1956, "Heat Transfer and Temperature Distribution in Laminar Film Condensation," *Transactions ASME,* Vol. 78, pp. 1645–1648.

Rosson, H. F., and Meyers, J. A., 1965, "Point Values of Condensing Film Coefficients Inside a Horizontal Tube," *Chemical Engineering Progress Symposium Series,* Vol. 61, No. 59, pp. 190–199.

Schlager, L. M., Pate, M. B., and Bergles, A. E., 1990, "Performance Predictions of Refrigerant-Oil Mixtures in Smooth and Internally Finned Tubes," *ASHRAE Transactions,* Vol. 96, Part 1, pp. 161–182.

Shah, M. M., 1979, "A General Correlation for Heat Transfer During Film Condensation Inside Pipes," *International Journal of Heat and Mass Transfer,* Vol. 22, pp. 547–556.

Soliman, H. M., 1982, "On the Annular-to-Wavy Flow Pattern Transition During Condensation Inside Horizontal Tubes," *The Canadian Journal of Chemical Engineering,* Vol. 60, pp. 475–481.

Soliman, H. M., 1983, "Correlation of Mist-to-Annular Transition During Condensation," *The Canadian Journal of Chemical Engineering,* Vol. 61, pp. 178–182.

Soliman, H. M., 1986, "The Mist-Annular Transition During Condensation and its Influence on the Heat Transfer Mechanism," *International Journal of Multiphase Flow,* Vol. 12, No. 2, pp. 277–288.

Soliman, H. M., Schuster, J. R., and Berenson, P. J., 1968, "A General Heat Transfer Correlation for Annular Flow Condensation," ASME JOURNAL OF HEAT TRANSFER, Vol. 90, pp. 267–276.

Souza, A. M., Chato, J. C., and Wattelet, J. P., 1992, "Pressure Drop During Two-Phase Flow of Refrigerants in Horizontal Smooth Tubes," *ACRC Technical Report 25,* University of Illinois at Urbana-Champaign.

Sweeney, K. A., 1996, "The Heat Transfer and Pressure Drop Behavior of a Zeotropic Refrigerant Mixture in a Microfinned Tube," M.S. thesis, Dept. of Mechanical and Industrial Engineering, University of Illinois at Urbana-Champaign.

Sweeney, K. A. and Chato, J. C., 1996, "The Heat Transfer and Pressure Drop Behavior of a Zeotropic Refrigerant Mixture in a Microfinned Tube," *ACRC Technical Report 95,* University of Illinois at Urbana-Champaign.

Sweeney, K. A., Chato, J. C., Ponchner, M., and Rhines, N. L., 1995, "The Effect of Oil on Condensation in a Microfinned Tube," *ACRC Technical Report 87,* University of Illinois at Urbana-Champaign.

Taitel, Y., and Dukler, A. E., 1976, "A Model for Predicting Flow Regime Transitions in Horizontal and Near Horizontal Gas-Liquid Flow," *American Institute of Chemical Engineering Journal,* Vol. 22, No. 1, pp. 47–55.

Tien, C. L., Chen, S. L., and Peterson, P. F., 1988, "Condensation Inside Tubes," *EPRI Project 1160-3 Final Report,* EPRI, Palo Alto, CA.

Traviss, D. P., Rohsenow, W. M., and Baron, A. B., 1973, "Forced-Convective Condensation in Tubes: A Heat Transfer Correlation for Condenser Design," *ASHRAE Transactions,* Vol. 79, No. 1, pp. 157–165.

Wang, S.-P., and Chato, J. C., 1995, "Review of Recent Research on Heat Transfer with Mixtures—Part 1: Condensation," *ASHRAE Trans.,* Vol. 101, No. 1, pp. 1376–1386.

Wattelet, J. P., 1994, "Heat Transfer Flow Regimes of Refrigerants in a Horizontal-Tube Evaporator," Ph.D. thesis, Dept. of Mechanical and Industrial Engineering, University of Illinois at Urbana-Champaign.

Wattelet, J. P., Chato, J. C., Christoffersen, B. R., Gaibel, J. A., Ponchner, M., Kenney, P. J., Shimon, R. L., Villaneuva, T. C., Rhines, N. L., Sweeney, K. A., Allen, D. G., and Hershberger, T. T., 1994, "Heat Transfer Flow Regimes of Refrigerants in a Horizontal-Tube Evaporator," *ACRC Technical Report 55,* University of Illinois at Urbana-Champaign.

Zivi, S. M., 1964, "Estimation of Steady-State Steam Void-Fraction by Means of the Principle of Minimum Entropy Production," ASME JOURNAL OF HEAT TRANSFER, Vol. 86, pp. 247–252.

Thermocapillary Driven Turbulent Heat Transfer

V. S. Arpaci
Professor.
arpaci@engin.umich.edu
Fellow ASME.

S.-H. Kao
Department of Mechanical Engineering and Applied Mechanics,
The University of Michigan,
2142 G. G. Brown,
2350 Hayward,
Ann Arbor, MI 48109-2125

A dimensionless number depending on the usual Prandtl and Marangoni numbers, $\Pi_S \sim Ma/(1 + Pr^{-1}) = Ma\ Pr/(1 + Pr)$, is introduced for thermocapillary driven flows. Three heat transfer models are proposed in terms of Π_S. The first model on laminar flow, using some dimensional arguments with a flow scale and the boundary layer concept, leads to $Nu \sim \Pi_S^{1/4}$, Nu being the usual Nusselt number. The second model on transition flow, extending Landau's original idea on the amplitude of disturbances past marginal stability of isothermal flow, leads to $Nu - 1 \sim (\Pi_S - \Pi_{S_c})^{1/2}$, Π_{S_c} corresponding to the critical value of Π_S for the marginal state. The third model on turbulent flow, introduces a thermal microscale $\eta_\theta \sim (1 + Pr^{-1})^{1/4}(\nu\alpha^2/\mathcal{P}_S)^{1/4} = (1 + Pr)^{1/4}(\alpha^3/\mathcal{P}_S)^{1/4}$, with ν and α, respectively, being kinematic and thermal diffusivities, and $\mathcal{P}_S$ the production rate of thermocapillary energy. The first expression relating η_θ to Prandtl number explicitly includes its limit for $Pr \to \infty$, $\eta_\theta^B \sim (\nu\alpha^2/\epsilon)^{1/4}$, which is a Batchelor scale, and the second one explicitly includes its limit for $Pr \to 0$, $\eta_\theta^C \sim (\alpha^3/\epsilon)^{1/4}$, which is an Oboukhov-Corrsin scale. In terms of η_θ and an integral scale l, the model leads to $Nu \sim l/\eta_\theta \sim \Pi_S^{1/3}$. Recent experimental literature are interpreted by special cases of the foregoing models corresponding to $Pr > 1$.

1 Introduction

Block's (1956) experimental observations, supported by Pearson's (1958) analytical study about four decades later than Rayleigh, demonstrated that thermocapillarity rather than buoyancy is responsible for instability in some of the Bénard experiments. For example, drying paints are now known to display steady cellular circulatory flow of the "Bénard type" whether the free surface was at the top or the bottom of the paint layer. In some of these cases, the critical Rayleigh number fails to predict the flow initiation. Pearson has shown in terms of the classical stability theory that the thermocapillary forces are sufficient to cause this instability characterized by the Marangoni number,

$$\mathrm{Ma} = \frac{\Delta\sigma l}{\mu\alpha}, \tag{1}$$

$\Delta\sigma$ being net surface tension, l the thickness of the horizontal liquid layer, μ the dynamic viscosity, and α the thermal diffusivity.

The same class of problems now attract increased experimental, analytical, and computational attention because of their importance to space explorations. A variety of geometric configurations and heating conditions have been investigated (e.g., Chang and Wilcox, 1976; Fu and Ostrach, 1983; Cowley and Davis, 1983; Zebib et al., 1985; Bergman and Ramadhyani, 1986; Chen, 1987; Carpenter and Homsy, 1989, 1990; Keller and Bergman, 1990; Mundrane and Zebib, 1993; Kamotani et al., 1993, 1994). The present work is motivated by the latest Kamotani experiments and scaling analysis. The main objective is to demonstrate the microscale (Kolmogorov, 1941; Oboukhov, 1949; Corrsin, 1951; Batchelor, 1959) foundations of their scale considerations.

Note that, by definition,

$$\mathrm{Ma} = \left(\frac{F_S}{F_V}\right)\left(\frac{Q_H}{Q_K}\right), \tag{2}$$

F_S and F_V, respectively, being the thermocapillary tension and viscous forces, and Q_H and Q_K being the enthalpy flow and conduction. Also, by definition, the Prandtl number is

$$\mathrm{Pr} = \left(\frac{Q_H}{Q_K}\right)\left(\frac{F_V}{F_I}\right), \tag{3}$$

F_I being the inertial force. An infinitesimal theory, resting on linearized governing equations, ignores the nonlinear inertial effects and is independent of the Prandtl number. It is then governed by the Marangoni number alone. A nonlinear theory for thermocapillary driven flows past the Marangoni instability depends on the Prandtl number as well as the Marangoni number. A fundamental dimensionless number including the effect of both Ma and Pr so far appears to be overlooked in the archival literature. The first objective is to introduce this dimensionless number, say Π_S. The second and final objective is to develop the scales of and heat transfer in three (laminar, transition, and turbulent) flow regimes in terms of Π_S.

2 Dimensional Considerations

On dimensional grounds, consider first a flow driven by thermocapillary forces F_S,

$$F_S \sim F_I + F_V, \tag{4}$$

F_I and F_V being the inertial and viscous forces. The thermal energy balance for this flow is

$$Q_H \sim Q_K, \tag{5}$$

Q_H and Q_K being the enthalpy flow and heat conduction. Now, rearrange Eq. (4) as

$$\frac{F_S}{F_I + F_V} \sim \frac{F_S/F_V}{1 + F_I/F_V} \tag{6}$$

and Eq. (5) as

Contributed by the Heat Transfer Division for publication in the JOURNAL OF HEAT TRANSFER and presented at 1996 Winter Annual Meeting. Manuscript received by the Heat Transfer Division August 21, 1996; revision received August 22, 1997; Keywords: Heat Transfer; Microgravity; Microscale; Turbulence. Associate Technical Editor: K. Vafai.

$$Q_H/Q_K. \tag{7}$$

Note that the numeral 1 in the denominator of Eq. (6) implies order of magnitude. Explicitly,

$$F_S \sim \Delta\sigma l, \quad F_I \sim \rho V^2 l^2, \quad F_V \sim \mu V l,$$

$$Q_H \sim \rho c_p V T l^2, \quad Q_K \sim k T l,$$

and

$$\frac{F_S}{F_V} \sim \frac{\Delta\sigma}{\mu V}, \quad \frac{F_I}{F_V} \sim \frac{\rho V l}{\mu}, \tag{8}$$

$$\frac{Q_H}{Q_K} \sim \frac{\rho c_p V l}{k}, \tag{9}$$

where ρ is the density, c_p the specific heat at constant pressure, V the velocity, T the temperature, l a characteristic length, and Δ is the difference in surface tension.

Eq. (6) yields, in terms of Eq. (8),

$$\frac{\Delta\sigma/\mu V}{1 + \rho V l/\mu}, \tag{10}$$

and Eq. (7) gives, in terms of Eq. (9),

$$\rho c_p V l/k. \tag{11}$$

For thermocapillary driven flows, V is a dependent variable. Consequently, neither Eq. (10) nor Eq. (11) is an ultimate dimensionless number characterizing these flows. The elimination of V between Eq. (10) and Eq. (11) leads to this number,

$$\frac{(F_S/F_V)Q_H/Q_K}{(1 + F_I/F_V)Q_K/Q_H},$$

or, explicitly,

$$\Pi_S \sim \frac{\Delta\sigma l/\mu\alpha}{1 + \alpha/\nu}, \tag{12}$$

or

$$\Pi_S \sim \frac{\mathrm{Ma}}{1 + \mathrm{Pr}^{-1}} = \frac{\mathrm{Ma\ Pr}}{1 + \mathrm{Pr}}. \tag{13}$$

Note that the numeral 1 in the denominator of Eqs. (10), (12), and (13), in a manner similar to that in Eq. (6), implies an order of magnitude. The two limits of Eq. (13), respectively corresponding to large and small Prandtl numbers, are

$$\lim_{\mathrm{Pr}\to\infty} \Pi_S \to \mathrm{Ma}, \tag{14}$$

$$\lim_{\mathrm{Pr}\to\infty} \Pi_S \to \mathrm{Ma\ Pr}. \tag{15}$$

Foregoing dimensional considerations are utilized in the next three sections on laminar, transition, and turbulent flow regimes.

3 Laminar Flow

On dimensional grounds, let the momentum balance given by Eq. (4) be

$$\frac{\Delta\sigma}{\rho l^2} \sim V\frac{V}{l} + \nu\frac{V}{\delta^2}, \tag{16}$$

where δ the thickness of the momentum boundary layer, and l an integral scale characterizing geometry. Also, let the thermal energy balance be

$$V\frac{\theta}{l} \sim \alpha\frac{\theta}{\delta_\theta^2}, \tag{17}$$

where δ_θ the thickness of the thermal boundary layer. Solve Eq. (17) for velocity,

$$V \sim \alpha\frac{l}{\delta_\theta^2}. \tag{18}$$

To proceed further, following Squire (1938), let

$$\delta \sim \delta_\theta \tag{19}$$

in Eq. (16). This is an often misinterpreted pivotal assumption. It postulates the secondary importance of the difference between δ and δ_θ for heat transfer rather than suggesting equality of these boundary layer thicknesses. Now, elimination of velocity between Eqs. (16) and (18) gives, for the thickness of thermal boundary layer,

$$\frac{\Delta\sigma}{\rho l^2} \sim \frac{\nu\alpha l}{\delta_\theta^4}\left(1 + \frac{\alpha}{\nu}\right), \tag{20}$$

or, relative to the integral scale,

$$\frac{\delta_\theta}{l} \sim \Pi_S^{-1/4}. \tag{21}$$

The next section is devoted to transition flow in terms of Π_S.

Nomenclature

c_p = specific heat at constant pressure
F = force
h = heat transfer coefficient
k = thermal conductivity
l = a characteristic length of geometry
Ma = Marangoni number
Nu = Nusselt number
Pr = Prandtl number
Q = heat flux
q_w = heat flux at wall
s_{ij} = fluctuating rate of strain
S_{ij} = mean rate of strain
T = temperature
u = root mean square of velocity fluctuation
V = a characteristic velocity

Greek Symbols

α = thermal diffusivity
δ = boundary layer thickness
Δ = difference
ϵ = viscous dissipation
η = Kolmogorov length scale
θ = temperature fluctuation
Θ = mean temperature
λ = Taylor scale
μ = dynamic viscosity
ν = kinematic viscosity
$\mathcal{P}$ = production
Π_S = dimensionless number for surface tension driven flows
ρ = density
σ = surface tension
σ_T = surface tension expansion coefficient

Subscripts

c = critical
H = enthalpy
I = inertial
K = conduction
S = surface tension
V = viscous
θ = thermal

Superscripts

$\tilde{}$ = instantaneous value
$\bar{}$ = mean values
B = Batchelor scales
C = Oboukhov-Corrsin scales

4 Transition Flow

Dimensional arguments of the preceding sections assume that in the case of steady convection, a balance is maintained between production and dissipation of energy. It was Landau (1944) who originally suggested from general considerations that the amplitude of disturbances past marginal stability must increase like

$$A \sim (\mathrm{Re} - \mathrm{Re}_c)^{1/2}, \tag{22}$$

where Re is the Reynolds number characterizing flow beyond the onset of instability at Re_c. Chandrasekhar (1961), following Stuart (1958) on the Couette flow, extended the idea to buoyancy driven flow and showed from variational considerations that

$$A \sim (\mathrm{Ra} - \mathrm{Ra}_c)^{1/2}, \tag{23}$$

Ra being the Rayleigh number (also, for some earlier work, refer to Malkus, 1954; Malkus and Veronis, 1958; Gorkov, 1958; Stuart, 1958; Landau and Lifshitz, 1959; Veronis, 1959; Nakagawa, 1960). It is clear from Landau's general considerations, as well as from Chandrasekhar's variational demonstration, that the amplitude of thermocapillary flow past marginal stability is

$$\frac{A}{k\Delta T/l} \sim (\Pi_S - \Pi_{S_c})^{1/2}, \tag{24}$$

where k is the thermal conductivity, l a characteristic length for geometry, and ΔT the imposed temperature difference. The next section is devoted to development of turbulent microscales in terms of Π_S.

5 Turbulent Flow

Following the usual practice, decompose the instantaneous velocity and temperature of a surface tension driven turbulent flow into a temporal mean (denoted by capital letters) and fluctuations

$$\tilde{u}_i = U_i + u_i \quad \text{and} \quad \tilde{\theta} = \Theta + \theta$$

and let U_i and Θ be statistically steady. Then, the balance of the mean kinetic energy of velocity fluctuations

$$\mathcal{K} = \tfrac{1}{2}\,\overline{u_i u_i}$$

yields (e.g., Tennekes and Lumley, 1972)

$$U_j \frac{\partial \mathcal{K}}{\partial x_j} = -\frac{\partial \mathcal{D}_j}{\partial x_j} - \mathcal{P}_S + \mathcal{P} + \epsilon \tag{25}$$

where

$$\mathcal{D}_j = -\overline{\frac{p}{\rho}\,u_j} + \tfrac{1}{2}\,\overline{u_i u_j u_j} - 2\nu\overline{u_i s_{ij}}$$

is the transport,

$$\mathcal{P}_S = \sigma_T \overline{u_i \theta}/\rho l^2, \tag{26}$$

is the rate of thermocapillary energy production, σ_T being the surface tension expansion coefficient,

$$\mathcal{P} = -\overline{u_i u_j} S_{ij} \tag{27}$$

is the inertial production rate of turbulent energy by Reynolds stresses, and

$$\epsilon = -2\nu\overline{s_{ij} s_{ij}} \tag{28}$$

is the rate of viscous dissipation of turbulent fluctuations.

Also, the balance of the root mean square of temperature fluctuations

$$\mathcal{K}_\theta = \tfrac{1}{2}\,\overline{\theta^2}$$

gives

$$U_j \frac{\partial}{\partial x_j}(\mathcal{K}_\theta) = -\frac{\partial}{\partial x_j}(\mathcal{D}_\theta)_j + \mathcal{P}_\theta - \epsilon_\theta \tag{29}$$

where

$$(\mathcal{D}_\theta)_j = \frac{1}{2}\,\overline{\theta^2 u_j} - \alpha \frac{\partial}{\partial x_j}\left(\frac{1}{2}\,\overline{\theta^2}\right)$$

is the thermal transport,

$$\mathcal{P}_\theta = -\overline{u_j \theta}\,\frac{\partial \Theta}{\partial x_j} \tag{30}$$

is the thermal production, and

$$\epsilon_\theta = \alpha\,\overline{\frac{\partial \theta}{\partial x_j}\,\frac{\partial \theta}{\partial x_j}} \tag{31}$$

is the thermal dissipation.

For a homogeneous flow (in which all averaged quantities except U_i and Θ are independent of position and S_{ij} and $\partial\Theta/\partial x_i$ are constants) the mean kinetic energy of turbulent fluctuations is reduced to (Arpaci, 1986, 1990, 1994a, b, 1995a, b)

$$\mathcal{P}_S = \mathcal{P} + \epsilon, \tag{32}$$

and the rate of thermal energy to

$$\mathcal{P}_\theta = \epsilon_\theta. \tag{33}$$

Equation (32) states that the thermocapillary energy production is partly converted into inertial production and partly into viscous dissipation.

On dimensional grounds, Eqs. (32) and (33) lead to

$$\mathcal{P}_S \sim \frac{u^3}{l} + \nu\,\frac{u^2}{\lambda^2} \tag{34}$$

and

$$u\,\frac{\theta^2}{l} \sim \alpha\,\frac{\theta^2}{\lambda_\theta^2}. \tag{35}$$

5.1 Thermal Scales. It seems reasonable to assume Eq. (19) postulated by Squire (1938) to be a general property of body-force driven flows and valid also for turbulent thermal scales (this assumption is justified later by experimental support to be discussed in Section 7). Accordingly, let

$$\lambda \sim \lambda_\theta. \tag{36}$$

Then, elimination of velocity between Eqs. (34) and (35) leads to a thermal microscale for homogeneous flow,

$$\lambda_\theta \sim l^{1/3}\left(1 + \frac{1}{\mathrm{Pr}}\right)^{1/6}\left(\frac{\nu\alpha^2}{\mathcal{P}_S}\right)^{1/6} = l^{1/3}(1 + \mathrm{Pr})^{1/6}\left(\frac{\alpha^3}{\mathcal{P}_S}\right)^{1/6}. \tag{37}$$

The first expression of Eq. (37) explicitly includes the limit for $\mathrm{Pr} \to \infty$ and is useful for fluids with $\mathrm{Pr} \geq 1$, the second expression explicitly includes the limit for $\mathrm{Pr} \to 0$ and is useful for fluids with $\mathrm{Pr} \leq 1$, and both relations are identical for $\mathrm{Pr} = 1$.

For the isotropic limit of the homogeneous flow, letting

$$\left(\frac{\lambda_\theta}{l}\right) \to \eta_\theta, \tag{38}$$

Eq. (37) is reduced to a thermal Kolmogorov scale

$$\eta_\theta \sim \left(1 + \frac{1}{\mathrm{Pr}}\right)^{1/4}\left(\frac{\nu\alpha^2}{\mathcal{P}_S}\right)^{1/4} = (1 + \mathrm{Pr})^{1/4}\left(\frac{\alpha^3}{\mathcal{P}_S}\right)^{1/4}. \quad (39)$$

Now, it is a simple matter to show from Eq. (39) that

$$\lim_{\mathrm{Pr}\to\infty} \eta_\theta \to \left(\frac{\nu\alpha^2}{\mathcal{P}_S}\right)^{1/4}, \quad (40)$$

which, in view of

$$\lim_{\mathrm{Pr}\to\infty} \mathcal{P} \to 0 \quad (41)$$

and

$$\mathcal{P}_S \to \epsilon, \quad (42)$$

leads to the Batchelor scale,

$$\lim_{\mathrm{Pr}\to\infty} \eta_\theta \to \eta_\theta^B \sim \left(\frac{\nu\alpha^2}{\epsilon}\right)^{1/4}. \quad (43)$$

Also, from Eq. (39),

$$\lim_{\mathrm{Pr}\to 0} \eta_\theta \to \left(\frac{\alpha^3}{\mathcal{P}_S}\right)^{1/4}, \quad (44)$$

which, in view of

$$\lim_{\mathrm{Pr}\to 0} \epsilon \to 0, \quad (45)$$

$$\mathcal{P}_S \to \mathcal{P}, \quad (46)$$

and in a viscous layer order of magnitude thinner than η_θ,

$$\mathcal{P} \to \epsilon, \quad (47)$$

leads to the Oboukhov-Corrsin scale,

$$\lim_{\mathrm{Pr}\to\infty} \eta_\theta \to \eta_\theta^C \sim \left(\frac{\alpha^3}{\epsilon}\right)^{1/4}. \quad (48)$$

Finally, for $\mathrm{Pr} \sim 1$, because of the equipartition (on dimensional grounds) of thermocapillary production into inertial production and viscous dissipation, Eq. (32) becomes

$$\mathcal{P}_S \sim 2\epsilon, \quad (49)$$

and, Eq. (39) leads to the Kolmogorov scale,

$$\lim_{\mathrm{Pr}\to 1} \eta_\theta \to \eta \sim \left(\frac{\nu^3}{\epsilon}\right)^{1/4}. \quad (50)$$

The relation between the thermal scales and the integral scale may now be obtained by eliminating the factor $(1 + \mathrm{Pr}^{-1})(\nu\alpha^2/\mathcal{P}_S)$ between Eqs. (37) and (39). Thus,

$$\left(\frac{\eta_\theta}{\lambda_\theta}\right)^2 = \frac{\lambda_\theta}{l} \quad (51)$$

which is analogous to a model proposed by Tennekes (1968) for dynamic intermittency.

5.2 Kinetic Scales. In the preceding section, the difference between kinetic and thermal scales was assumed to be of second order. Valid only for construction of thermal scales, this assumption provides no information for kinetic scales. These scales are developed in this section after some remarks on kinetic scales of buoyant flows.

As is well known, for buoyant flow of a fluid with $\mathrm{Pr} \neq 1$, the kinetic scales are different from the thermal scales. For example, the kinetic scales for $\mathrm{Pr} \gg 1$ (viscous oils) are order of magnitude larger than the thermal scales. That is, flow in this case extends far beyond the influence of buoyancy, it is basically isothermal and governed by the usual Kolmogorov scale. This scale in the present case, obtained by replacing buoyant production with thermocapillary production, is

$$\eta \sim \left(\frac{\nu^3}{\mathcal{P}_S}\right)^{1/4}. \quad (52)$$

On the other hand, the kinetic scales for $\mathrm{Pr} \ll 1$ (liquid metals) are order of magnitude smaller than the thermal scales of this case. That is, buoyant (or thermocapillary) production within η is of second order and η continues to be governed by Eq. (52). Then, Eq. (52) relative to Eq. (39) gives

$$\frac{\eta}{\eta_\theta} \sim \frac{\mathrm{Pr}^{3/4}}{(1 + \mathrm{Pr})^{1/4}}. \quad (53)$$

For $\mathrm{Pr} \to 0$, Eq. (53) is reduced to

$$\frac{\eta}{\eta_\theta} \sim \mathrm{Pr}^{3/4}, \quad (54)$$

which is the ratio between Kolmogorov and Oboukhov-Corrsin scales and, for $\mathrm{Pr} \to \infty$, is reduced to

$$\frac{\eta}{\eta_\theta} \sim \mathrm{Pr}^{1/2} \quad (55)$$

which is the well-known ratio between Kolmogorov and Batchelor scales. For these well-known scale ratios see, for example, Hinze (1959) or Tennekes and Lumley (1972).

6 Heat Transfer

Note that η_θ introduced by Eq. (39), $\mathcal{P}_S$ depends on velocity, and this scale cannot be in ultimate form of the thermal microscale for thermocapillary flows. To eliminate velocity dependence, reconsider, for example, the first relation given for η_θ in Eq. (39),

$$\eta_\theta \sim \left(1 + \frac{1}{\mathrm{Pr}}\right)^{1/4}\left(\frac{\nu\alpha^2}{\mathcal{P}_S}\right)^{1/4},$$

and assume, on dimensional grounds,

$$\mathcal{P}_S \sim \sigma_T u\theta/\rho l^2. \quad (56)$$

or, with the local velocity obtained from the limit of Eq. (35),

$$u \sim \alpha/\eta_\theta, \quad (57)$$

as

$$\mathcal{P}_S \sim \sigma_T \alpha\theta/\rho l\eta_\theta. \quad (58)$$

Insertion of Eq. (58) into Eq. (39) yields, after some rearrangement,

$$\eta_\theta \sim \left(1 + \frac{1}{\mathrm{Pr}}\right)^{1/3}\left(\frac{\mu\alpha l^2}{\sigma_T\theta}\right)^{1/3}. \quad (59)$$

Finally, assuming the rms of temperature fluctuations to be proportional to the imposed temperature difference,

$$\theta \sim \Delta T, \quad \sigma_T\theta \sim \sigma_T\Delta T \sim \Delta\sigma, \quad (60)$$

Eq. (59) becomes

$$\eta_\theta \sim \left(1 + \frac{1}{\mathrm{Pr}}\right)^{1/3}\left(\frac{\mu\alpha l^2}{\Delta\sigma}\right)^{1/3}, \quad (61)$$

or, in terms of an integral scale l,

$$\frac{\eta_\theta}{l} \sim \left(1 + \frac{1}{\mathrm{Pr}}\right)^{1/3} \mathrm{Ma}^{-1/3} \sim \Pi_S^{-1/3}, \tag{62}$$

where

$$\mathrm{Ma} = \frac{\Delta\sigma l}{\mu\alpha}$$

is the Marangoni number. The foregoing scale considerations are utilized below in the construction of three heat transfer models.

6.1 Laminar Flow. The usual definition of the coefficient of heat transfer gives, in terms of thermal boundary layer thickness δ_θ,

$$q_w \sim h\theta \sim k\left(\frac{l}{\delta_\theta}\right), \tag{63}$$

which can be rearranged as

$$\mathrm{Nu} = \frac{hl}{k} \sim \frac{l}{\delta_\theta}. \tag{64}$$

Then, in terms of Eq. (21),

$$\mathrm{Nu} \sim \frac{l}{\delta_\theta} \sim \Pi_S^{1/4} \tag{65}$$

whose limits for large and small Prandtl numbers are

$$\lim_{\mathrm{Pr}\to\infty} \mathrm{Nu} \sim \mathrm{Ma}^{1/4}, \tag{66}$$

and

$$\lim_{\mathrm{Pr}\to 0} \mathrm{Nu} \sim (\mathrm{Ma}\ \mathrm{Pr})^{1/4}. \tag{67}$$

6.2 Transition Flow. Relative to conduction prevailing up to the marginal stability,

$$\left(h - \frac{k}{l}\right)\Delta T \sim A \tag{68}$$

which yields, in view of Eq. (24)

$$\mathrm{Nu} - 1 \sim (\Pi_S - \mathrm{Ma}_{S_c})^{1/2} \tag{69}$$

whose limit for the first transition is

$$\mathrm{Nu} - 1 \sim (\mathrm{Ma} - \mathrm{Ma}_c)^{1/2}. \tag{70}$$

6.3 Turbulent Flow. The usual definition of the coefficient of heat transfer gives, in terms of the thermal microscale η_θ,

$$q_w \sim h\theta \sim k\left(\frac{l}{\eta_\theta}\right), \tag{71}$$

which can be rearranged as

$$\mathrm{Nu} = \frac{hl}{k} \sim \frac{l}{\eta_\theta}. \tag{72}$$

Then, in terms of Eq. (62),

$$\mathrm{Nu} \sim \frac{l}{\delta_\theta} \sim \Pi_S^{1/3} \tag{73}$$

whose limits for large and small Prandtl numbers are

$$\lim_{\mathrm{Pr}\to\infty} \mathrm{Nu} \sim \mathrm{Ma}^{1/3}, \tag{74}$$

and

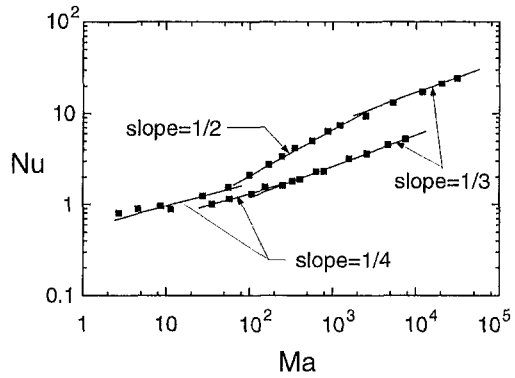

Fig. 1 Dimensionless heat transfer rate as a function of Marangoni number based on heating zone radius (Kamotani et al., 1996)

$$\lim_{\mathrm{Pr}\to 0} \mathrm{Nu} \sim (\mathrm{Ma}\ \mathrm{Pr})^{1/3}. \tag{75}$$

7 Conclusions

A fundamental dimensionless number, Π_S, for thermocapillary driven flows is introduced. Heat transfer in laminar and transition flows is expressed in terms of $\Pi_S^{1/4}$ and $\Pi_S^{1/2}$, respectively. A microscale for thermocapillary driven turbulent flow is proposed in terms of Π_S. Three limits of this scale are shown to be classical Kolmogorov, Oboukhov-Corrsin, and Batchelor scales. Heat transfer in turbulent flow is given in terms of $\Pi_S^{1/3}$.

Two limits of the three flow regimes corresponding to $\mathrm{Pr} \to \infty$ and $\mathrm{Pr} \to 0$ are ($\mathrm{Ma}^{1/4}$, $\mathrm{Ma}^{1/2}$, $\mathrm{Ma}^{1/3}$) and [$(\mathrm{Ma}\ \mathrm{Pr})^{1/4}$, $(\mathrm{Ma}\ \mathrm{Pr})^{1/2}$, $(\mathrm{Ma}\ \mathrm{Pr})^{1/3}$], respectively. The first set of limits corresponding to $\mathrm{Pr} \to \infty$ explain the flow regimes discussed in the recent dimensional, computational, and experimental study of Kamotani et al. (1996) who follow arguments different than those presented here. Figure 1, borrowed from Kamotani et al. (1996), illustrates these regimes. For experimental support of the second set of limits corresponding to $\mathrm{Pr} \to 0$, new data are needed covering a significant range of liquid metals. With future data to be coupled with the Kamotani data, the three flow regimes are expected to be correlated with the third set ($\Pi_S^{1/4}$, $\Pi_S^{1/2}$, $\Pi_S^{1/3}$) whose limits for $\mathrm{Pr} \to \infty$ and $\mathrm{Pr} \to 0$ are the first two sets.

There are analytical studies for heat transfer leading to $\mathrm{Nu} \sim \mathrm{Ma}^{2/7}$ for large Pr and to $\mathrm{Ma}^{2/7}\ \mathrm{Pr}^{1/10}$ for small Pr (Cowley and Davis, 1983). These results do not appear to have a microscale foundation.

References

Arpacı, V. S., 1986, "Microscales of Turbulence and Heat Transfer Correlations," *Int. J. Heat Mass Transfer,* Vol. 29, No. 8, pp. 1071–1078.

Arpacı, V. S., 1990, "Microscales of Turbulence and Heat Transfer Correlations," *Annual Review of Heat Transfer,* Vol. 3, pp. 195–231.

Arpacı, V. S., 1994a, Microscales of Turbulence-Mass Transfer Correlations, keynote lecture in the International Symposium on Turbulence and Heat Mass Transfer, Lisbon.

Arpacı, V. S., 1994b, Microscales of Turbulence-Heat Transfer Correlations, keynote lecture in the Tenth International Heat Transfer Conference, Brighton, UK.

Arpacı, V. S., 1995a, "Buoyant Turbulent Flow Driven by Internal Energy Generation," *Int. J. Heat Mass Transfer,* Vol. 38, No. 15, pp. 2761–2770.

Arpacı, V. S., 1995b, "Microscales of Turbulent Combustion," *Prog. Energy Combust. Sci.,* Vol. 21, pp. 153–171.

Batchelor, G. K., 1959, "Small-Scale Variation of Convected Quantities Like Temperature in a Turbulent Fluid," *J. Fluid Mech.,* Vol. 5, pp. 113–139.

Bergman, T. L., and Ramadhyani, S., 1986, "Combined Buoyancy and Thermocapillary-Driven Convection in Open Square Cavities," *Numerical Heat Transfer,* Vol. 9, pp. 441–451.

Block, M. J., 1956, "Surface Tension as the Cause of Bénard Cells and Surface Deformation in a Liquid Film," *Nature,* Vol. 178, p. 650.

Carpenter, B. M., and Homsy, G. M., 1989, "Combined Buoyant and Thermocapillary Flow in a Cavity," *J. Fluid Mech.,* Vol. 207, pp. 121–132.

Carpenter, B. M., and Homsy, G. M., 1990, "High Marangoni Number Convection in a Square Cavity: Part II," *Phys. Fluids A,* Vol. 2, pp. 137–149.

Chandrasekhar, S., 1961, *Hydrodynamic and Hydromagnetic Stability,* Oxford University Press, England.

Chang, C. E., and Wilcox, W. R., 1976, "Analysis of Surface Tension Driven Flow in Floating Zone Melting," *Int. J. Heat Mass Transfer,* Vol. 19, pp. 355–366.

Chen, M. M., 1987, "Thermocapillary Convection in Materials Processing," *Interdisciplinary Issues in Materials Processing and Manufacturing,* Vol. 2, ASME, NY, pp. 541–558.

Corrsin, S., 1951, "On Spectrum of Isotropic Temperature Fluctuations in Isotropic Turbulence," *J. Appl. Phys.,* Vol. 22, No. 4, pp. 469–473.

Cowley, S. J., and Davis, S. H., 1983, "Viscous Thermocapillary Convection at High Marangoni Number," *J. Fluid Mech.,* Vol. 135, pp. 175–188.

Fu, B. I., and Ostrach, S., 1983, "Numerical Solutions of Floating-Zone Thermocapillary Flow," *Proceedings of the 4th European Symposium on Materials Sciences Under Microgravity,* pp. 239–245.

Gorkov, L. P., 1958, "Stationary Convection in a Plane Liquid Layer Near the Critical Heat Transfer Point," *Soviet Physics, JETP,* Vol. 6, pp. 311–315.

Hinze, J. O., 1959, *Turbulence,* McGraw-Hill, New York.

Kamotani, Y., Ostrach, S., and Pline, A., 1993, "A Thermocapillary Convection Experiment in Microgravity," *Heat Transfer in Microgravity,* C. T. Avedesian and V. S. Arpaci, eds., ASME HTD-Vol. 269, pp. 23–30.

Kamotani, Y., Chang, A., and Ostrach, S., 1994, "Effects of Heating Mode on Steady Axisymmetric Thermocapillary Flows in Microgravity," *Heat Transfer in Microgravity Systems,* S. S. Sadhal and A. Gopinath, eds., ASME HTD-Vol. 290, pp. 53–62.

Kamotani, Y., Chang, A., and Ostrach, S., 1996, "Effects of Heating Mode on Steady Axisymmetric Thermocapillary Flows in Microgravity," ASME JOURNAL OF HEAT TRANSFER, Vol. 118, pp. 191–197.

Keller, J. R., and Bergman, T. L., 1990, "Thermocapillary Cavity Convection in Wetting and Nonwetting Liquids," *Numerical Heat Transfer,* Vol. 18, pp. 33–49.

Kolmogorov, A. N., 1941, "Local Structure of Turbulence in Incompressible Viscous Fluid for Very Large Reynolds Numbers," *C. R. Acad. Sci. URSS,* Vol. 30, pp. 299–301.

Landau, L. D., 1944, "On the Problem of Turbulence," *C. R. Doklady Acad. Sci. URSS,* Vol. 44, pp. 311–314.

Landau, L. D., and Lifshitz, E. M., 1959, *Fluid Mechanics,* Pergamon, Oxford, England.

Malkus, W., 1954, "The Heat Transport and Spectrum of Thermal Turbulence," *Proc. Roy. Soc. (London) A,* Vol. 225, pp. 196–212.

Malkus, W., and Veronis, G., 1958, "Finite Amplitude Cellular Convection," *J. Fluid Mech.,* Vol. 4, pp. 225–260.

Mundrane, M., and Zebib, A., 1993, "Two and Three-Dimensional Buoyant Thermocapillary Convection," *Phys. Fluids A,* Vol. 5, pp. 810–818.

Nakagawa, Y., 1960, "Heat Transport by Convection," *Physics of Fluids,* Vol. 3, pp. 82–86.

Oboukhov, A. M., 1949, "Structure of the Temperature Field in Turbulent Flows," *Izv. Nauk. SSSR, Geogr. i. Geofiz.,* Vol. 13, p. 58.

Pearson, J. R. A., 1958, "On Convection Cells Induced by Surface Tension," *J. Fluid Mech.,* Vol. 4, pp. 489–500.

Squire, H. B., 1938, "Free Convection from a Heated Vertical Plate," *Modern Developments in Fluid Mechanics,* S. Goldstein, ed. Oxford, Vol. 2, p. 638.

Stuart, J. T., 1958, "On the Nonlinear Mechanics of Hydrodynamic Stability," *J. Fluid Mech.,* Vol. 4, pp. 1–21.

Tennekes, H., 1968, "Simple Model for the Small Scale Structure of Turbulence," *Phys. Fluids,* Vol. 11, pp. 669–671.

Tennekes, H., and Lumley, O. L., 1972, *A First Course in Turbulence,* MIT Press, Cambridge, MA.

Veronis, G., 1959, "Cellular Convection with Finite Amplitude in a Rotating Fluid," *J. Fluid Mech.,* Vol. 5, pp. 401–435.

Zebib, A., Homsy, G. M., and Meiburg, E., 1985, "High Marangoni Number Convection in a Square Cavity," *Phys. Fluids,* Vol. 28, pp. 3467–3476.

D. M. Pratt
Air Force Research Laboratory,
AFRL/VAVE,
2130 Eighth Street, Suite 1,
Wright-Patterson AFB, OH 45433-7542
prattdm@wl.wpafb.af.mil

J. R. Brown
Air Force Research Laboratory,
AFRL/PR,
1950 Fifth Street,
Wright-Patterson AFB, OH 45433-7251

K. P. Hallinan
Department of Mechanical and
Aerospace Engineering,
University of Dayton,
Dayton, OH 45409

Thermocapillary Effects on the Stability of a Heated, Curved Meniscus

An investigation of thermocapillary effects on heated menisci formed by volatile liquids in capillary pumped heat transfer devices has been conducted. This research was motivated by the importance of the evaporation process from porous or grooved media integral to the operation of capillary pumped heat transport devices such as heat pipes and capillary pumped loops. From analysis, a criteria was established which predicts the thermal conditions at which the destablizing influences of thermocapillary stresses near the contact line of a heated and evaporating meniscus cause the meniscus to become unstable. Experimentally, two different idealized models of capillary pumped phase change loops were investigated to assess the suitability of the predictions. Correspondence between theory and experiment was observed. Given the observed dry-out of the evaporator at higher heat inputs after the meniscus becomes unstable, the importance of predicting the conditions at the instability onset is made clear.

Introduction

Much of the current work in the development of novel heat transfer equipment for handling high heat fluxes concentrates on liquid-vapor phase change due to the enormous latent heat benefits. One such device is the conventional heat pipe (reviewed by Chi, 1976; Dunn and Reay, 1994; and Faghri, 1995), which relies on the vaporization of a working fluid in a porous media within the evaporator section, movement of the vapor to the cooler section of the pipe where heat removal causes the vapor to condense, and finally upon return of the liquid to the evaporator by the capillary action of a porous "wick." These closed system devices operate reliably in a passive mode, but have not been able to operate against gravity in significant adverse elevations. To overcome these constraints, capillary pumped loop (CPL) and loop heat pipe (LHP) concepts have recently been developed.

Reviews of CPL operation and usage have been provided by Ku (1993), Cullimore (1993), and Faghri (1995). The unique feature of the CPL, in contrast to conventional heat pipes, is that the wick structure is isolated in the evaporator section permitting greater distances between the condenser and the evaporator. The LHP, developed by Maidanik et al. (1985), is considered to be an improvement over the CPL due to its perceived ability to work against significant adverse elevations and because it offers a more reliable start-up.

Despite the theoretical ability of CPLs and LHPs to outperform heat pipes, they have both suffered from performance anomalies. For the CPL, both evaporator deprime during rapid power reduction and pressure oscillations during steady operation have been observed. They have not been successfully operated in low gravity without a starter pump. For low temperature operation, design predictions have been observed to significantly over-predict the experimentally realized heat transport capability (Richter and Gottschlich, 1994). Further, in experimental work by Ku et al. (1988), the pressure differential across the evaporators sometimes showed oscillations with a magnitude as large as 700 Pa (0.1 psi). Ku (1995) has shown that, when these oscillations are present, the maximum heat transport capability can be as little as 10 percent of the design value. Tests at NASA/GSFC have indicated a correlation between pressure oscillations and an observed radial liquid motion into and out of the wick due to evaporation. With respect to the LHP, Baumann (1994) showed that some successful start-ups were observed to initially have a reversed flow condition that corrected itself after a few minutes. Other random start-up failures occurred in 12 percent of the tests with no explanation. Maidanik et al. (1995) and Dickey and Peterson (1994) also observed peculiarities of LHP operation, particularly associated with startup with the evaporator region initially flooded. These peculiarities, namely pressure oscillations and radial liquid motions, are characteristics associated with unstable system operation.

The investigations by Hoang and Ku (1995) and also Ku and Hoang (1995) have established a direct association between the pressure oscillations and device instabilities. However, their theoretical analysis of the device stability did not offer any insight on the physics leading to the instability (pressure oscillation). Rather, it determined the magnitude of a pressure oscillation required to cause unstable operation.

The current knowledge of the operation of capillary driven heat transfer devices, especially when operating in an unstable mode, is limited. Device instabilities for both CPLs and LHPs have been shown to have in some cases a deleterious effect on their heat transport capacity. However, the mechanisms leading to device instability are unknown.

One basis for the instability may be due to the evaporating meniscus. Preiss and Wayner (1976), Welter (1991), and Valociek (1994) have all observed that a heated and evaporating meniscus within a capillary pore may become unstable presumably due to thermal conditions present at the evaporating meniscus. Based upon these considerations, the objectives of the present research are as follows:

- demonstrate that the device instabilities are in part a consequence of instabilities present at the evaporator menisci within the heated pores
- identify the conditions leading to the onset of these instabilities
- show the impact of these instabilities on heat transfer and device operation

Contributed by the Heat Transfer Division for publication in the JOURNAL OF HEAT TRANSFER. Manuscript received by the Heat Transfer Division, February 7, 1997; revision received August 11, 1997; Keywords: Heat Pipes and Thermosyphons; Porous Media; Thermocapillary Flows. Associate Technical Editor: M. Kaviany.

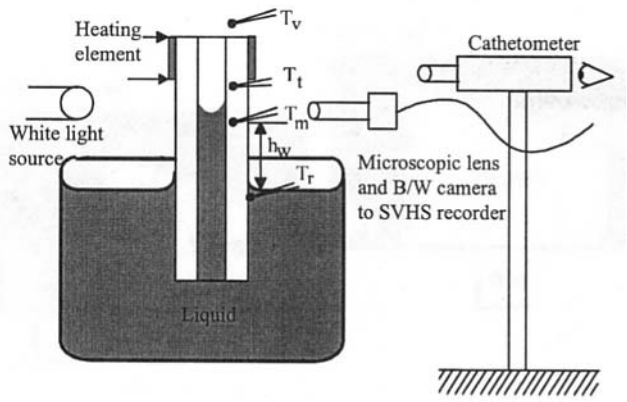

Fig. 1 Schematic of single pore capillary pumped heat transfer device

Both experiments and analysis were conducted to achieve these goals.

Experiments

Two different experimental configurations were designed to both examine the stability of a heated, evaporating meniscus within a porous media and to investigate the effect of the instabilities arising from this region on device operation. The first of these configurations was designed strictly to examine the stability of such a meniscus to enable a better understanding of the mechanism for the instability. To this end, a simple experimental model permitting visual observation of the meniscus, while allowing for accurate measurement of the wall temperature near the meniscus was designed and fabricated. A schematic of this design is shown in Fig. 1. In this set up, the single capillary pore could be heated from either above or below the meniscus using a nichrome electrical resistance heating element spirally wrapped on the outer diameter of the tube. A portion of the tube was immersed in a reservoir of liquid n-pentane causing the liquid to wick partially into the tube. N-pentane was chosen due to its relatively low surface energy, high volatility, and excellent wetting characteristics on glass. The temperature of the liquid n-pentane within the reservoir was controllable by circulating liquid from a refrigerated bath through a heat exchanger placed within the reservoir. The system was placed within a chamber for isolation from the ambient environment and for control of the test conditions. A vertical translation system, manipulated exterior to the chamber via a rotational feed through, was used to locate the base of the meniscus at the same level for each test.

Table 1 Capillary tube dimensions

ID (mm)		OD	L	L_f	L_1	L_{tc}
Reference	Actual	(mm)	(cm)	(cm)	(cm)	(cm)
0.5	0.4826	6.3	9	1	0.21	0.51
1	0.9906	6.3	9	1.2	0.07	0.65
2	1.77	7.5	9.1	1.2	0.08	0.49

The dimensions for the capillary tubes used in this model during testing are detailed in Table 1. In this table, L is the length of the capillary tube, L_f is the length of the heating element, L_1 is the distance between the bottom of the heater and the first thermocouple, and L_{tc} is the distance between the thermocouples. All lengths were measured using a cathetometer that has an associated bias limit of ±0.0025 mm leading to an error for the length measurements of 0.0005 cm at a 95 percent confidence interval. The inner and outer diameter measurements have errors of ±0.00005 mm and 0.05 mm, respectively.

Calibrated thermocouples were used to measure wall temperatures along the capillary tube and to measure the temperature of the vapor space and liquid reservoir as shown in Fig. 1. The thermocouples were mounted within drilled holes that were machined to within 0.5 mm of the inside wall. The thermocouple voltages were recorded using an Iotech 16 bit A/D board interfaced to a 486-66 PC. This lead to an error in the temperature readings of ±0.3°C with a 95 percent confidence interval. A video microscope system was used to image the meniscus so that the contact angle could be determined. It consisted of a long distance Infinovar microscope connected to a Hi-8 resolution black and white video camera. This image was recorded using an SVHS video recorder. The meniscus was back lit with a high intensity white light source filtered to allow transmission

Nomenclature

A = Hamaker constant (J)
$\bar{A}$ = modified Hamaker constant, $A/6\pi$ (J)
c_p = specific heat (J/kg·K)
E = evaporation number, $k\Delta T/\mu h_{fg}$
g = acceleration due to gravity (m/s^2)
h = film thickness (m)
h_{fg} = latent heat of vaporization (J/kg)
h_w = wicking height (m)
H = aspect ratio
ID = inner diameter (m)
J = evaporative flux (kg/m^2)
k = thermal conductivity (W/m·K)
K = curvature (m^{-1})
$\hat{K}$ = evaporation resistance
L = length (m)
Ma = marangoni number, $\rho c_p \gamma \Delta \mathrm{Th}_{tr}^2/x_c \mu k$
$\hat{n}$ = unit normal vector
OD = outer diameter (m)
P = pressure (Pa)
Pr = Prandtl number, $\mu c_p/k$
Q = heat transfer rate (W)
r = radius (m)
s = parametric
S = dimensionless curvature, $\sigma \rho h X^2/\mu^2$
T = temperature (°C)
t = time (s)
$\hat{t}$ = unit tangent vector
U = velocity in the x-direction (m/s)
V = velocity in the y-direction (m/s)
x = Cartesian coordinate (m)
y = Cartesian coordinate (m)
α = evaporation coefficient
δ = perturbation amplitude
γ = $d\sigma/dT$ (N/m·K)
η = nondimensional y-direction coordinate
λ = wave number
μ = absolute viscosity (Pa s)
Π = disjoining pressure (Pa)
ρ = density (kg/m^3)
σ = surface tension (N/m)
τ = nondimensional time
$\underline{T}$ = stress tensor
ξ = nondimensional x-direction coordinate

Subscripts

a = actual; amplitude
A = air
bot = bottom (at the meniscus)
c = characteristic; critical
f = heating element
g = glass
m = meniscus
o = initial; adsorbed
r = reservoir
tc = thermocouple
t = top (above the meniscus)
tr = transition
v = vapor
w = wall

Superscripts

$\tilde{X}$, $\bar{X}$ = nondimensional forms of any term X

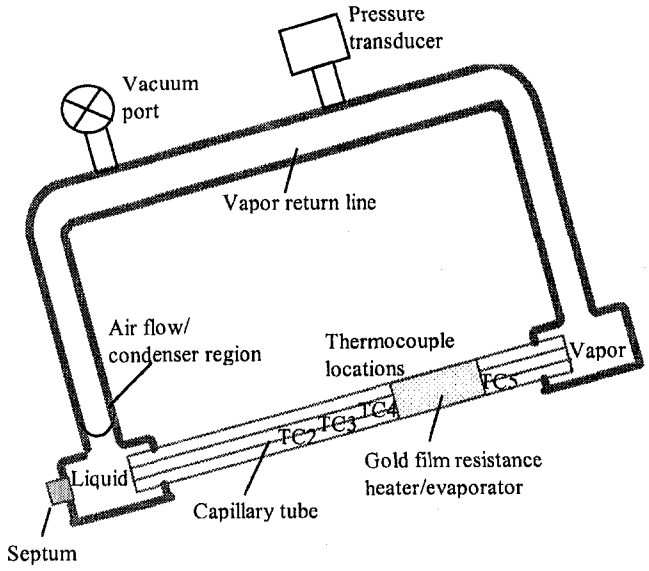

Fig. 2 Heat transport loop (HTL) schematic in an inclined orientation

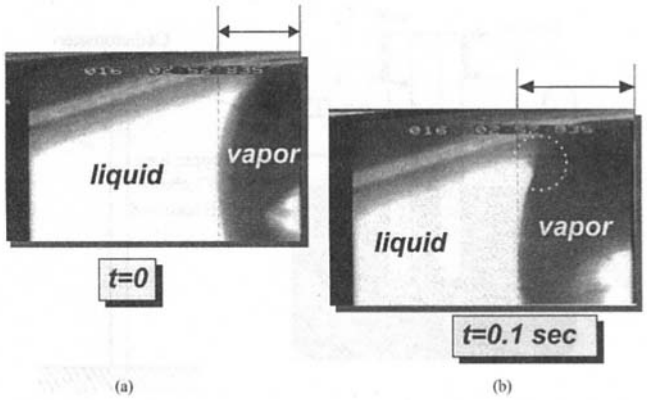

Fig. 3 Near contact line region of a heated and evaporating pentane meniscus within a 1 mm capillary pore (*a*) just prior to the origination of an instability and (*b*) $\frac{1}{10}$ second later

of light in the green spectrum only for video image enhancement and to prevent transmission of much of the thermal radiation in the infrared spectrum. A shunt resistor connected in series with the heating element allowed the current flowing through the circuit to be determined by measuring the voltage drop across it.

The second experimental configuration was designed to investigate the effect of evaporator meniscus instabilities on device operation and to gain information of the instability mechanism. This device was also made entirely of glass to allow for viewing of fluid movement during operation. The apparatus consists of a precision bore capillary tube fused to square glass tubing to produce an enclosed heat transport loop system, as shown in Fig. 2. The primary components are a capillary tubing region for generation of highly curved menisci, liquid reservoirs, and a connecting vapor space. The capillary tubing, which is 95 mm long, extends into the reservoirs on both ends approximately 6 mm. The two liquid reservoirs are identical, except for the addition of a port on one reservoir to allow injection of the n-pentane working fluid. The dimensions of these reservoirs are 10 mm square by 19 mm long. The vapor lines were made of 6.35 mm glass tubing. To allow for evacuation and filling of the loop and the measurement of the bulk vapor pressure, two ports were fused onto the vapor lines. The angle of inclination of the loop was variable. The primary orientation of the HTL for the purpose of the present research was inclined at an angle of $15 \pm 1°$, with the heated section above the liquid reservoir; the fluid return to this heated section is by capillarity. The liquid fill was 2.4 ml for the majority of tests.

A 0.020 m long gold film (~400 A thick) was vapor deposited on one end of the capillary tube (0.015 m from the tube end) to serve as a resistance heating element. This allowed viewing of the meniscus present beneath the heater. The gold film resistance heater was placed in series with a calibrated 10 Ω shunt resistor and a DC power supply. Power input to the gold film was determined by simultaneously measuring the voltage drop across the shunt resistor and across the gold film. Calibrated, type T thermocouples were used to determine the temperatures in the locations shown in Fig. 2. Thermocouples 2 through 4 were placed 5 mm apart with thermocouple 4 (TC4) and thermocouple 5 (TC5) being 3 mm below and above the heater, respectively. The data presented for these thermocouples is considered to be accurate to ±0.1°C at a certainty of 95 percent. An electronic pressure transducer with a calibrated accuracy of 0.05 percent of full scale (±172 Pa) was mounted at one of the HTL ports to monitor changes in the vapor space pressure during HTL operation. Recording of thermocouple and pressure transducer readings were made every 0.7 s with an uncertainty of 0.001 s at a 95 percent confidence interval.

Initial Experimental Observations

In order to obtain some a priori knowledge of the mechanism for the oscillations which have been observed by Welter (1991) and Valociek (1994) at heated and evaporating menisci within capillary geometries, high speed video records showing oscillations of the near contact line region were obtained. Figure 3(*a*) shows the near contact line region of the evaporating pentane meniscus prior to an instability. Figure 3(*b*) shows the same region just $\frac{1}{10}$ s later, just as the meniscus has begun to rapidly recede. It is clear from a comparison of these two figures that the instability or trigger for the oscillation emanates from the near contact line region. In fact, the thin wetting film initially present has disintegrated, producing an apparent contact angle at the wall greater than 90°, at least for short duration. This disintegration of the near contact line region has produced an accelerating vapor phase which applies vapor recoil forces to the meniscus causing it to noticeably recede.

Evidence that the driver for the oscillation is due to the vapor recoil stresses associated with the rapid increase in evaporation is apparent from Fig. 4, which presents the change in the pressure of the vapor with time and capillary wall temperature (near-

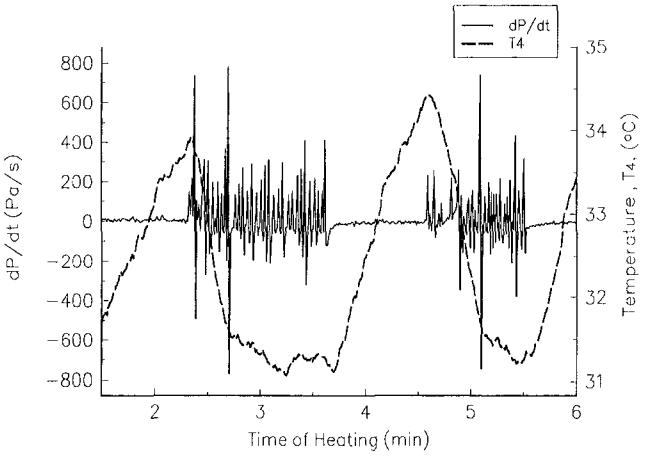

Fig. 4 Vapor pressure gradient and capillary wall capillary wall temperature in the vicinity of the meniscus as a function of time (applied heat is 1.3 W)

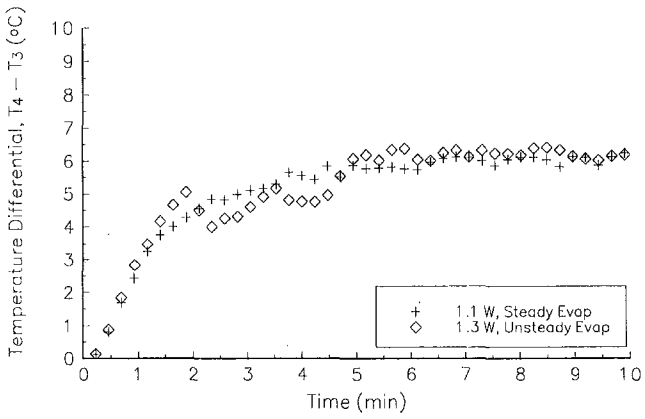

Fig. 5 Temperature differential comparison for 1.0 mm inclined HTL, steady evaporation, 1.1 W, versus unsteady evaporation, 1.3 W

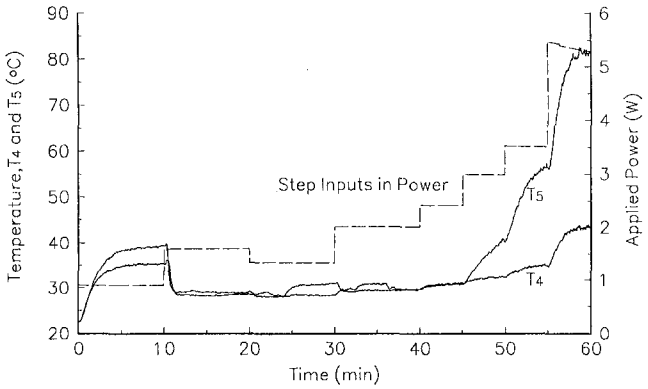

Fig. 6 Dry-out evidenced by rapid rise in wall temperature for the HTL configuration

est the meniscus) during heating as a function of time. For the case shown, there was an applied heat of 1.3 W. It is of primary importance that, as shown in this figure, there are rapid variations in the pressure of the vapor which are closely in phase with reductions in wall temperature. The instability phenomenon can be explained by rapid increases in evaporation that cools the fluid and capillary structure in the vicinity of the meniscus and which subsequently increases the vapor pressure. The uncertainty in the pressure data, dP/dt, are ± 34 at a 95 percent confidence level. This rapid change in pressure is used only as an indicator of the onset of device instability and thus exact numerical values are not required. Further investigations of the impact of these instabilities on heat transfer have been presented by Brown (1995).

The impact of these instabilities on the heat transfer is now discussed using the temperature difference between thermocouples embedded in the wall beneath the heater of the inclined HTL as the basis for assessing the role of instabilities on heat transfer. This temperature difference is the driver for heat conduction down the tube away from the heater.

Improvement in evaporation heat transport is possible when an oscillating evaporating meniscus is present. This is apparent from a comparison of a 1.3 W heating case, which produces an unsteady, oscillating meniscus to a 1.1 W heating case where evaporation occurs from a stationary meniscus. Temperature profiles versus time for these two cases are shown in Fig. 5. Notice that the same temperature differential is realized for the 1.3 W case as for the 1.1 W case, indicating that more of the heat is being dissipated by evaporation from the meniscus than by conduction down the tube for the 1.3 W case. In this case, during the recession of the oscillating meniscus, a liquid film is left behind which increased the liquid-vapor surface area. This promotes increased evaporation.

As the heat input is increased, however, the induced oscillations have a negative effect on the heat transfer. Here, increases in heat input ultimately produce a dry-out condition in the evaporator as evidenced by rapid increases in wall temperatures near the heater as is shown in Fig. 6. Therefore, the oscillation itself appears to have an overall negative effect on heat transfer.

Analysis

The initial experimental results clearly indicated that instabilities in the near contact line region were responsible for the oscillations observed. It was also shown that these oscillations could have a deleterious effect on device operation under certain conditions. The following analysis is designed to predict the conditions which can cause the meniscus to become unstable. This analysis, along with the experimental observations, links the stability of the meniscus with that of the thin liquid film near the contact line.

The stability of planar thin films has been examined by Ruckenstein and Jain (1974), Palmer (1976), William and Davis (1982), Burelbach et al. (1988), Sharma and Ruckenstein (1988), Joo et al. (1991), and Bankoff (1994). These serve as the basis for estimating the marginal stability conditions present at a heated and evaporating meniscus within a capillary pore. Previous researchers, namely Neogi and Berryman (1982) and Mirzamoghadam and Catton (1988), investigated the stability of a heated and evaporating meniscus along an inclined heated plate, and speculated that the location of an instability was the thin film region near the contact line. They performed a stability analysis of a planar liquid film (thereby neglecting the role of the curved meniscus which terminates into the film). Their analysis focused on Marangoni and mass transfer modes of instabilities.

In the present analysis, it is assumed that the thinnest portion of the film near the adsorbed film is implicitly stable due to the stabilizing effects of solid-liquid adhesive forces. It is also postulated that the most likely location for the onset of an instability is at the end of the transition region ($h = h_{tr}$), where the effects of the adhesive forces are no longer dominant relative to surface tension. This region is also where thermocapillary stresses are most severe, i.e., the interfacial temperature gradients are maximum. (At greater film thicknesses, He and Hallinan (1996), using microscopic flow visualization techniques, have determined that a reversed flow away from the contact line is present. This occurs at film thicknesses on the order of tens of microns. Thus, these reversed interfacial flows, arising from a cooler meniscus temperature away from the contact line, will have the effect of making the interfacial temperature in the thicker regions more isothermal.)

The origination and evolution of thermocapillary instabilities in the near contact line region of the curved meniscus is envisioned to occur via the following scenario. If the surface is perturbed near $h = h_{tr}$, the meniscus becomes locally depressed, thereby increasing in temperature. As a result, there is a greater pull on the liquid-vapor (l-v) interface from the intrinsic meniscus. At the same time, there is still a disjoining pressure potential from $h = h_{tr}$ to $h = h_o$ (where h_o is the adsorbed film thickness) to drive liquid toward the adsorbed film region. On the upstream side of the depression, the concave curvature increases producing a curvature gradient which tends to reduce the flow of liquid into the thin film at the wall while the curvature gradient on the downstream side of the depression tends to draw liquid from beneath the depression. These effects combine to amplify the disturbance. The superheated liquid then needs only this trigger to flash to vapor; ultimately, producing significant vapor recoil stresses.

To perform a stability analysis on these curved, evaporating thin films, the approach used by Burelbach et al. (1988) for

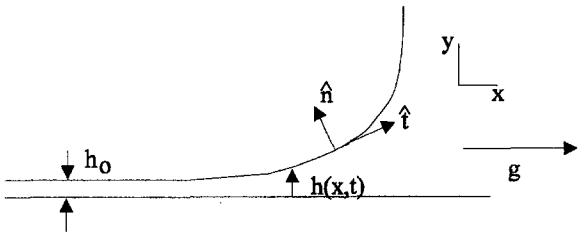

Fig. 7 Thin film region of the extended meniscus

planar films is used, differing only in the parameters unique to the capillary confined geometry.

The governing equations for the conservation of mass, momentum, and energy for the physical system, depicted in Fig. 7, are described below.

$$U_x + V_y = 0 \tag{1}$$

$$\rho(U_t + UU_x + VU_y) = -P_x + \mu(U_{xx} + U_{yy}) + \rho g \tag{2}$$

$$\rho(V_t + UV_x + VV_y) = -P_y + \mu(V_{xx} + V_{yy}) \tag{3}$$

$$\rho c_p(T_t + UT_x + VT_y) = k(T_{xx} + T_{yy}) \tag{4}$$

This system of equations is constrained by the following boundary conditions in the thin film region.

At $y = 0$.

$$U = V = 0 \tag{5}$$

At the Interface (Liquid-Vapor).

Kinematic Condition.

$$J = \rho\vec{V}\cdot\hat{n} \tag{6}$$

where $\vec{V} = (U, V - h_t)$ and $\hat{n} = \nabla s/|\nabla s|$, $s = y - h(x, t) = 0$ (parametric equation describing the liquid vapor interface)

$$\nabla s = -h_x\hat{i} + \hat{j},$$

$$|\nabla s| = (1 + h_x^2)^{1/2},$$

or

$$\hat{n} = (-h_x\hat{i} + \hat{j})(1 + h_x^2)^{-1/2} \tag{7}$$

lead to

$$J = \rho(-h_t - h_xU + V)(1 + h_x^2)^{-1/2}. \tag{8}$$

Energy Balance.

$$J(h_{fg}) = -k\nabla T_1\cdot\hat{n} \tag{9}$$

or

$$J(h_{fg}) = k(T_xh_x - T_y)(1 + h_x^2)^{-1/2} \tag{10}$$

Conservation of Momentum.

$$J(\vec{U}_1 - \vec{U}_2) + (P_v - P_1)\hat{n} + (\underline{\underline{T}}_2 - \underline{\underline{T}}\,I) = \sigma K\hat{n} + \Pi\hat{n} \tag{11}$$

Normal Stress Balance (Eq. (10)$\cdot\,\hat{n}$).

$$P_v - P_l = \sigma K + \Pi - \frac{J^2}{\rho_v} \tag{12}$$

Tangential Stress Balance (Eq. (11)$\cdot\,\hat{t}$).

$$\mu(U_y + V_x)(1 - h_x^2) - 4\mu U_xh_x = -\gamma(T_xh_x - T_y)(1 + h_x^2)^{-1/2} \tag{13}$$

A linearized evaporative mass flux constitutive equation was used similar to Burelbach et al. (1988).

This system of equations was nondimensionalized using viscous scales for pressure, velocity, and time, just as in Burelbach et al. (1988), only differing by the choice of the length scales in the x and y-directions to be consistent with the experimental observations. As it is expected that the instability arises from the near contact line region where the thermocapillary stresses and heat transfer are greatest, an appropriate scale factor in the y-direction for the thin film portion of the meniscus within a capillary tube is the transition film thickness, h_{tr}. At this film thickness, the stabilizing effects of the adhesive forces are small but the l-v temperature gradient is large. The transition film thickness can be defined as the film thickness where the capillary pressure is equal to the disjoining pressure, i.e.,

$$h_{tr} = \left(\frac{\bar{A}r}{2\sigma}\right)^{1/3}. \tag{14}$$

In the x-direction, h_{tr} is not an appropriate reference length since the film length is much greater than the film thickness for a well-wetting liquid. Therefore, another scaling factor, x_c, is obtained using the following reasoning. Approximating the curvature, K, as h_{xx} (scaled as h_{tr}/x_c^2) in the extended meniscus where the slope is small, and equating the curvature near the contact line to the curvature of the intrinsic meniscus, $1/r$, provides a relationship between x_c and h_{tr} of the form $x_c = (rh_{tr})^{1/2}$. It follows that $r \gg h_{tr}$, $x_c \gg h_{tr}$.

The dimensionless independent variables in the system of equations obtained from this analysis (Pratt, 1996) are then expanded in terms of the characteristic slope, X, which is assumed to be small, ultimately resulting in the following evolution equation:

$$\tilde{h}_{\hat{\tau}} = -\bar{E}J_o + \frac{2\bar{\Pi}\tilde{h}_{\xi\xi}}{\tilde{h}} - \frac{2}{3}\bar{S}\tilde{h}^3\tilde{h}_{\xi\xi\xi\xi} - \frac{\mathrm{Ma}}{2\,\mathrm{Pr}}(J_o\tilde{h})_{\xi\xi}\tilde{h}^2. \tag{15}$$

Above, J_0 is the dimensionless linearized evaporative mass flux which is equal to

$$J_o = \frac{1}{(\tilde{h} + \hat{K})}. \tag{16}$$

Equation (15) describes the film thickness as both a function of time and position, and it can therefore be used to investigate the marginal stability of the extended meniscus by applying a linearization scheme and perturbing the linearized differential equation. Additionally, it should be noted that $\tilde{h}$ is approximately unity in the portion of the meniscus that is likely the most unstable (i.e., $h/h_{tr} \to 1$).

For determination of a critical wave number, above which the system is unstable, a perturbation of the following form is imposed:

$$\tilde{h} = \delta H(\hat{\tau})e^{i\lambda\xi}. \tag{17}$$

Substituting Eq. (16) and (17) into Eq. (15) and noting that $\bar{E}$ is small leads to the following evolution equation:

$$\frac{\dot{H}}{H} = -\lambda^2\left(\frac{2\bar{\Pi}}{h_o} + \frac{2}{3}\bar{S}h_o^3\lambda^2 - \frac{\mathrm{Ma}}{2\,\mathrm{Pr}}\frac{h_o^2}{\hat{K} + h_o}\right). \tag{18}$$

This equation is stable when

$$\frac{2\bar{\Pi}}{h_o} + \frac{2}{3}\bar{S}h_o^3\lambda^2 - \frac{\mathrm{Ma}}{2\,\mathrm{Pr}}\frac{h_o^2}{\hat{K} + h_o} > 0 \tag{19}$$

or

$$\lambda^2 > \frac{3\,\mathrm{Ma}}{4\,\mathrm{Pr}\bar{S}h_o(\hat{K} + h_o)} - \frac{3\bar{\Pi}}{\bar{S}h_o^4}. \tag{20}$$

Applying $\hat{K} + h_o \approx h_o \approx 1$ yields[1]

[1] Burelbach et al. (1988) showed that $\hat{K} \to 0$.

Table 2 ΔT_c for *n*-pentane

ID (mm)	T_m (°C)	$\Delta T_c/x_c$ (K/cm)
0.5	10	207.9
0.5	20	196.7
0.5	30	185.3
0.5	40	173.9
1	10	79.1
1	20	74.8
1	30	70.5
1	40	66.2
1.8	10	36.5
1.8	20	34.5
1.8	30	32.5
1.8	40	30.5

$$\lambda_c^2 > \frac{3\ \mathrm{Ma}}{4\ \mathrm{Pr}\bar{S}} - \frac{3\bar{\Pi}}{\bar{S}}, \tag{21}$$

where λ_c represents the critical wave number.

From observation of Eq. (21), the system is inherently unstable regardless of wave number if

$$\frac{\mathrm{Ma}}{4\ \mathrm{Pr}} \geq \bar{\Pi}. \tag{22}$$

Physically, this critical condition corresponds to the situation when the Marangoni or thermocapillary effects are of the same order as the disjoining pressure effects. In the thin film region, gravity effects have a negligible bearing on the film stability.

Rewriting Eq. (22) in dimensional terms offers insight into the physical parameters which can lead to an unstable meniscus.

$$\frac{\rho\gamma\Delta T h_{lv}^2}{2\mu^2 x_c} = \frac{\rho\bar{A}}{x_c\mu^2} \tag{23}$$

or

$$\Delta T_c = \frac{2\bar{A}}{\gamma h_{lv}^2} \tag{24}$$

Using the expression for h_{lv} in Eq. (14) leads to the following critical interfacial temperature difference over the length scale x_c:

$$\Delta T_c = \frac{2}{\gamma}\left(\frac{2\bar{A}^{1/2}\sigma}{r}\right)^{2/3}. \tag{25}$$

Stability Results

Analytical predictions for the critical wall temperature gradients are presented in Table 2 for various meniscus temperatures, T_m, and pore diameters. These predictions indicate that heated menisci in smaller pores are significantly more stable than in larger pores. Also, the results indicate that as the system temperature increases, the meniscus tends to be more unstable due to the reduction in surface tension.

Table 3 shows the measured wall temperature gradients in the vicinity of the evaporating meniscus just at the onset of an instability in the vertical capillary geometry. Also presented in the table are the analytical predictions for the experimental conditions. (In these predictions the experimentally measured temperatures were used to evaluate the fluid properties.) The ranges shown in the experimental data correspond to the range of conditions which produced initial instabilities. The corresponding range of analytical values is due to the variable thermal conditions present in the experimental data, and, therefore, variations in fluid properties. There is good correspondence between the experimental data and the theoretical predictions. Moreover, the trend of diminished meniscus stability with increasing pore size, which was predicted, is realized in the experiments. Such experimental corroboration supports the validity of the lengthscales used in the analysis and the hypothesis that a thermocapillary destablizing mechanism can control the stability of a meniscus in a heated capillary pore.

Table 3 Measured and predicted critical temperature gradient at the onset of meniscus instability

Pore ID (mm)	$\Delta T_c / L_{tc}$ (K/cm) Experimental (±1.7% at {95})	$\Delta T_c / x_c$ (K/cm) Analytical
0.5	100-160	170-210
1	45-70	60-80
2	20-50	30-40

Additional evidence of the role of thermocapillary stresses in causing the initial instability is observed for similar tests conducted for heat input beneath the meniscus (i.e., on the liquid side of the meniscus). In these tests, heating rates three times greater than for heat input above the meniscus could be sustained prior to the onset of an instability. The higher heat inputs also translated into a 20 percent increase in the tolerated superheat prior to the origination of the instability. The improved stability when heating from below is expected since, as is apparent from Eq. (18) with a negative Marangoni number ($dT_w/dx < 0$), the thermocapillary stress term provides a stabilizing influence.

Conclusions

This work demonstrated experimentally that capillary pumped device instabilities are in part due to thermocapillary instabilities of the contact line region of evaporating menisci within capillary pores. It was shown that these instabilities can emanate from the near contact line region of the extended meniscus formed within the capillary pores and that for low heat inputs these instabilities can enhance the heat transport capacity of the HTL as much as 18 percent, due to the increase in the extent of the evaporating thin film. However, for higher heat transfer levels, the instabilities will degrade the transport capability of this system. Additionally, it was shown that the location of the input heating relative to the meniscus drastically affects the energy transport capability and stability of an evaporating meniscus formed within a capillary pore. In fact, for the heating from below case, a 20 percent increase in superheat was obtainable prior to instability onset. Finally, a theoretical marginal stability criteria was developed that agrees with the experimentally realized data. This work was completed using n-pentane as the working fluid for model verification. Additional work should be completed that incorporates other fluids and binary fluid mixtures.

References

Bankoff, S. G., 1995, "Stability and Dynamics of Thin Heated Liquid Films," *Transport Phenomena in Thermal Engineering,* Vol. 1, Begell House, NY, pp. 9–17.

Baumann, J., 1994, "Loop Heat Pipe Technology Performance Evaluation," Martin Marietta Astronautics Group Internal Report No. D-19D-93-01, Martin Marietta Astronautics Group, Denver, CO.

Brown, J. R., 1995, "Effect of Interfacial Dynamics on the Heat Transfer of an Evaporating Menisucus," Ph.D. dissertation, University of Dayton, Dayton, OH.

Burelbach, J. P., Bankoff, S. G., and Davis, S. H., 1988, "Nonlinear Stability of Evaporating/Condensing Liquid Films," *Journal of Fluid Mechanics,* Vol. 195, pp. 463–494.

Chi, S. W., 1976, *Heat Pipe Theory and Practices, A Source Book,* McGraw-Hill, New York.

Cullimore, B., 1993, "Capillary Pumped Loop Application Guide," SAE Technical Paper Series, Paper No. 932156.

Dickey, J. T., and Peterson, G. P., 1994, "Experimental and Analytical Investigation of a Capillary Pumped Loop," *Journal of Thermophysics and Heat Transfer,* Vol. 8, No. 3, pp. 602–607.

Dunn, P. D. and Reay, D. A., 1994, *Heat Pipes,* 4th ed., BPCC Wheatons LTD, Exeter, Great Britain.

Faghri, A., 1995, *Heat Pipe Science and Technology,* Taylor and Francis, Washington, D.C..

He, Q., and Hallinan, K. P., 1996, "The Development of a Full-Field Three-Dimensional Flow Measurement Technique for Applications to Near Contact Line Flows," presented at the Microgravity Fluids Conference, Cleveland, OH.

He, Q., 1994, Personal Communication, University of Dayton, Datyon, OH.

Hoang, T., and Ku, J., 1995, "Theory of Hydrodynamic Stability of a Capillary Pumped Loop," *Proceeding of the 30th 1995 National Heat Transfer Conference,* HTD-Vol. 307, ASME, NY, pp. 33–40.

Joo, S. W., Davis, S. H., and Bankoff, S. G., 1991, "Long-Wave Instabilities of Heated Falling Films: Two-Dimensional Theory of Uniform Layer," *Journal of Fluid Mechanics,* Vol. 230, pp. 117–146.

Ku, J., 1993, "Overview of Capillary Pumped Loops," *Heat Pipes and Capillary Pumped Loops,* HTD-Vol. 236, ASME, NY, pp. 1–17.

Ku, J., Kroliczek, E. J., McCabe, M., and Benner, S. M., 1988, "A High Power Spacecraft Thermal Management System," AIAA Paper No. 88-2702.

Ku, J., 1995, "Start-Up Issues in Capillary Pumped Loops," presented at the 9th International Heat Pipe Conference, Albuquerque, New Mexico.

Ku, J. and Hoang, T., 1995, "An Experimental Study of Pressure Oscillation and Hydrodynamic Stability in a Capillary Pumped Loop," *Proceeding of the 30th 1995 National Heat Transfer Conference,* HTD-Vol. 307, ASME, NY, pp. 25–32.

Maidanik, Y. F., Vershinin, S. V., Kholodov, V. F., and Dolgirev, Y. D., 1985, Heat Transfer Apparatus. U.S. Patent No. 4,515,209.

Maidanik, Y., Solodovnik, N., and Fershtater, Y., 1995, "Investigation of Dynamic and Stationary Characteristics of a Loop Heat Pipe," presented at the 9th International Heat Pipe Conference, Albuquerque, NM.

Mirzamoghadam, A., and Catton, I., 1988, "A Physical Model of the Evaporating Meniscus," ASME JOURNAL OF HEAT TRANSFER, Vol. 110, pp. 201–204.

Neogi, P., and Berryman, J. B., 1982, "Stability of Thin Liquid Films Evaporating into Saturated Vapor," *Journal of Colloid and Interface Science,* Vol. 88, pp. 100–109.

Palmer, H. J., 1976, "The Hydrodynamic Stability of Rapidly Evaporating Liquids at Reduced Pressure," *Journal of Fluid Mechanics,* Vol. 75, pp. 487–511.

Pratt, D. M., 1996, "The Effects of Thermocapillary Stresses on the Wetting Characteristics, Heat Transfer Effectiveness, and Stability of an Evaporating, Capillary Re-Supplied, Curved Meniscus within a Capillary Tube," Ph.D. dissertation, University of Dayton, Dayton, OH.

Preiss, G., and Wayner, P. C., Jr., 1976, "Evaporation From a Capillary Tube," ASME JOURNAL OF HEAT TRANSFER, Vol. 98, pp. 178–181.

Richter, R., and Gottschlich, J. M., 1994, "Thermodynamic Aspects of Heat Pipe Operation," *Journal of Thermophysics and Heat Transfer,* Vol. 8, No. 2, pp. 334–340.

Ruckenstein, E., and Jain, R. K., 1974, "Spontaneous Rupture of Thin Liquid Films," *Journal of Chemical Society, Faraday Transactions* 2, Vol. 70, pp. 132–147.

Sharma, A., and Ruckenstein, E., 1988, "Dynamics and Lifetimes of Thin Evaporating Liquid Films: Some Non-Linear Effects," *PhysicoChemical Hydrodynamics,* Vol. 10, No. 5/6, pp. 675–691.

Valociek, D. A., 1994, "The Effect of Low Frequency Vibrations on an Evaporating Meniscus For a Near Perfect Wetting Fluid," Masters thesis, University of Dayton, Dayton, OH.

Welter, D., 1991, "The Effects of Evaporation on the Dynamic Capillary Pressure in Heat Pipes," M.S.M.E. thesis, University of Dayton, Dayton, OH.

Williams, M. B. and Davis, S. H., 1982, "Nonlinear Theory of Film Rupture," *Journal of Colloid and Interface Science,* Vol. 90, No. 1, pp. 220–228.

The Minimum Meniscus Radius and Capillary Heat Transport Limit in Micro Heat Pipes

H. B. Ma
Research Associate.
Mem. ASME

G. P. Peterson
Associate Vice Chancellor.
GPP5386@teesmail.tamu.edu
Fellow ASME

Department of Mechanical Engineering,
Texas A&M University,
College Station, TX 77843-3123

Based on the momentum conservation and Laplace-Young equations, an analytical expression for the minimum meniscus radius was derived and an expression for the maximum capillary heat transport limit in micro/small heat pipes was obtained. These expressions incorporated the shear stresses at the liquid/solid and liquid/vapor interfaces, contact angle effects, vapor pressure drop, tilt angle, groove dimensions, and channel angle effects. In order to verify the expressions derived herein, comparisons with experimental data from triangular grooves and micro heat pipes were made; they demonstrated that these equations can be used to predict the maximum capillary heat transport in the micro/small triangular grooves or micro heat pipes with a higher degree of accuracy, and they can explain the behavior better than previously developed models.

Introduction

Micro heat pipes have been successfully used in the thermal control of electronic systems in a number of applications, and they have been shown to be particularly useful in obtaining a high degree of temperature uniformity on the surface of silicon wafers (Peterson, 1992; Peterson et al., 1993). In a majority of the previously developed models, the typical approach utilized has been to balance the capillary pressure and the viscous pressure drops of the liquid and vapor flow streams (Peterson, 1994). Aside from issues surrounding the rewetting of hot surfaces (Peterson et al., 1992b) and the capillary flow in small grooves or porous materials (Peterson et al., 1992a), the principle shortcoming of this approach is that the capillary pumping pressure is based upon a minimum capillary radius, the value of which is relatively unknown (Babin et al., 1990; Wu and Peterson, 1991; Longtin et al., 1994). Obtaining expressions for this minimum meniscus radius and maximum heat transport can be a significant help in the design and optimization of the size and shape of micro heat pipes, particularly those fabricated as an array of vapor deposited micro heat pipes where the size, shape, and channel coating material can be carefully controlled (Peterson and Mallik, 1995).

Typically, the maximum capillary pressure can be found from the Laplace-Young equation as

$$\Delta p_{\max} = \frac{2\sigma}{r_{\text{cap}}}. \tag{1}$$

For conventional heat pipe wicking structures, the minimum meniscus radius can be found by measuring the maximum capillary pumping head (Tien and Sun, 1971),

$$\frac{H}{\sigma/(\rho_l - \rho_v)g} = \frac{2}{r_{\text{cap}}}. \tag{2}$$

Because a typical micro heat pipe consists of small noncircular channels and utilizes the sharp angled corner regions as liquid arteries, it is difficult to use Eq. (2) to find the minimum meniscus radius for micro heat pipes. In addition, due to differences in the fundamental flow characteristics in the micro channels used in micro heat pipes and the measurement of stationary liquid/vapor interfaces in porous wicking structures, the relationships developed for calculating the minimum meniscus radius in conventional heat pipes are not appropriate. As a result, Cotter (1984) developed a method for estimating the minimum meniscus radius as

$$r_{\text{cap}} = \frac{A^{1/2}}{\beta}, \tag{3}$$

where β is a constant for a given wick structure, and A is the cross-sectional area of the liquid and vapor flow region. Later, Babin et al. (1990) employed the expression

$$r_{\text{cap}} = \frac{\omega}{\cos\phi\cos\alpha} \tag{4}$$

to determine the minimum meniscus radius, where ω is the width of the groove. In the model of Gerner et al. (1992), the meniscus radius was defined as

$$r_{\text{cap}} = \frac{D}{2}, \tag{5}$$

where D was used to represent the hydraulic diameter of the liquid and vapor flow region in the micro heat pipe. In more recent work (Ma et al., 1994; Khrustalev and Faghri, 1994; Peterson and Ma, 1996c), the vapor flow in micro heat pipes has been shown to exhibit significant influence on the capillary heat transport capacity.

Although the models developed by Cotter (1984), Babin et al. (1990), and Gerner et al. (1992) neglected or underestimated the vapor influence on the heat transport capacity of micro heat pipes, the predicted results obtained from these models are in good agreement with the experimental data. One possible explanation for this contradiction is that the relationships given by Eqs. (3), (4), and (5) used to calculate the minimum meniscus radius would underestimate the capillary pumping pressures. These two opposing mechanisms combined to make the predictions given by Babin et al. (1990) and Gerner et al. (1992) appear to be in good agreement with the experimental data, while masking the contrasting effects of these two simplifying assumptions. For this reason, it is necessary to identify a better method for predicting the minimum meniscus radius in micro heat pipes in order to accurately predict the maximum capillary heat transport limit. In the recent model of Longtin et

Contributed by the Heat Transfer Division for publication in the JOURNAL OF HEAT TRANSFER. Manuscript received by the Heat Transfer Division July 21, 1997; revision received November 20, 1997; Keywords: Heat Pipes and Thermosyphons; Phase-Change Phenomena; Thermocapillary Flows. Associate Technical Editor: M. Kaviany.

al. (1994), a critical radius of curvature was proposed and used to predict the maximum capillary heat transport based on the numerical analysis. In the most recent model, which was based on the control volume technique and utilized a numerical method, Peterson and Ma (1996a) found an approximate expression for the minimum meniscus radius in a micro heat pipe with triangular grooves. However, because this expression was based on the numerical results of a micro heat pipe with triangular grooves, its application was limited. It is therefore necessary to reformulate this model for the more general case and develop a simple general expression for determining the minimum meniscus radius in micro heat pipes in order to determine the true maximum capillary heat transport limit.

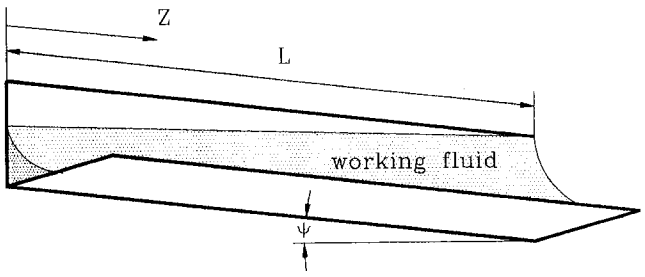

Fig. 1 A triangular groove in micro heat pipes

Theoretical Analysis

For a micro heat pipe with longitudinal grooves, the capillary pumping head arises due to a decrease in the meniscus radius caused by the working fluid receding into the apex of the groove in the evaporator and flattening out in the condenser. When the heat added to the evaporator is larger than the maximum heat transport capacity, the sharp angled corner region in the micro heat pipe cannot pump sufficient working fluid back to the evaporator and dryout will occur.

To simplify the problem, consider the case of a single longitudinal groove, which transports the working fluid from the condenser to the evaporator, as shown in Fig. 1. Because the Bond number is very small, the liquid-vapor interface can be assumed to have a nearly constant radius of curvature in the direction perpendicular to the groove. In the axial direction, the curvature is assumed to be infinite. Therefore, the liquid meniscus assumes the shape shown in Fig. 1, and there exists a pressure difference across the vapor-liquid interface that can be described by the Laplace-Young equation, i.e.,

$$p_v - p_l = \sigma\left(\frac{1}{r_l} + \frac{1}{r_{II}}\right). \tag{6}$$

For the groove shown in Fig. 1, where one of the radii of curvature is constant and the other is infinite, the liquid pressure in the liquid can be written as

$$p_l = p_v - \frac{\sigma}{r_l}. \tag{7}$$

From Eq. (7), it can be found that the liquid pressure is related to the meniscus radius of curvature of liquid flow and the vapor pressure. The total capillary pressure pumping head in a micro heat pipe can be found as

$$\Delta p_c = \Delta p_v - \sigma\left(\frac{1}{r_{\text{cap},e}} - \frac{1}{r_{\text{cap},c}}\right), \tag{8}$$

where Δp_v is the vapor pressure drop occurring in the micro heat pipe, and $r_{\text{cap},e}$ and $r_{\text{cap},c}$ are the average capillary meniscus radii of curvature occurring in the evaporator and condenser, respectively.

The frictional pressure drop of the liquid flow can be found by evaluating the shear forces at the liquid-solid and liquid-vapor interfaces. For steady-state heat addition and heat rejection, the liquid pressure drop in the differential form can be found as

$$\frac{dp}{dz} = -\frac{f_l \cdot \text{Re}_{h,l}\mu_l \dot{m}}{2r_{h,l}^2 A_l \rho_l}, \tag{9}$$

where the Reynolds number is defined by $\text{Re}_{h,l} = 2r_{h,l}\rho_l V_l/\mu_l$, $r_{h,l}$ is the average hydraulic radius of liquid flow, and A_l is the cross-sectional area of liquid flow. For a given longitudinal groove, there exists a fixed relationship between the cross-sectional area of liquid flow, A_l, and the hydraulic radius of liquid flow, $r_{h,l}$, i.e.,

$$A_l = C_1 r_{h,l}^2, \tag{10}$$

where C_1 depends on the geometric shape of the groove and the contact angle of the working fluid. Substituting Eq. (10) into Eq. (9) and integrating Eq. (9), the liquid pressure drop can be found as

$$\Delta p_l = -\frac{f_l \cdot \text{Re}_{h,l}\mu_l}{2C_1\rho_l r_{h,l}^4}\int_0^L \dot{m}dz, \tag{11}$$

where L is the heat pipe length. If

$$L_{eff} = \frac{\int_0^L \dot{m}dz}{\dot{m}_a}, \tag{12}$$

Nomenclature

A = cross-sectional area, m^2
C_1 = coefficient defined by Eq. (10)
C_2 = coefficient defined by Eq. (16)
C^* = coefficient defined by Eq. (13)
D = diameter, m
f = friction factor
g = gravitational acceleration, m/s^2
h_{fg} = latent heat of vaporization, kJ/kg
H = highness, m
L = length, m
L_{eff} = effective length defined by Eq. (12)
$\dot{m}$ = mass flow rate, kg/s
p = pressure, N/m^2
P = perimeter, m
q = heat transport, W
r = radius, m
R = length, m
Re = Reynolds number
w = groove width, m
z = coordinate, m

Greek Symbols

α = contact angle, degree
θ = coordinate, degree
μ = viscosity, Ns/m^2
$\xi = \sigma/r_{\text{cap},c} + \Delta p_v + \rho_1 gL \sin\psi$
ρ = density, kg/m^3
σ = surface tension, N/m
τ = shear stress, N/m^2
ϕ = half channel angle, degree
ψ = tilt angle, degree

Subscripts

a = adiabatic
c = condenser
cap = capillary
e = evaporating
h = hydraulic
l = liquid
max = maximum
s = surface
v = vapor
w = wall

where $\dot{m}_a$ is the mass flow rate of liquid through the adiabatic section, and

$$C^* = \frac{r_{h,l}}{r_{h,e}}. \tag{13}$$

Recognizing

$$\dot{m}_a = \frac{q}{h_{fg}}, \tag{14}$$

Eq. (11) can be transformed into

$$\Delta p = -\frac{f_l \cdot \mathrm{Re}_{h,l}\mu_l L_{eff}}{2C_1(C^* r_{h,e})^4 \rho_l h_{fg}} q. \tag{15}$$

The average hydraulic radius of liquid flow in the evaporator, $r_{h,e}$, can be further expressed as

$$r_{h,e} = C_2 r_{\mathrm{cap},e}. \tag{16}$$

Substituting Eq. (16) into Eq. (15), the total liquid pressure drop due to the shear stresses at the liquid-solid and liquid-vapor interfaces can be found as

$$\Delta p_l = -\left(\frac{f_l \cdot \mathrm{Re}_{h,l}\mu_l L_{eff}}{2C_1(C^* C_2 r_{\mathrm{cap},e})^4 \rho_l h_{fg}}\right) q. \tag{17}$$

The total pressure drop due to the gravitational body force can be found as

$$\Delta p_g = \rho_l g L \sin \psi. \tag{18}$$

The operation of micro heat pipes requires that the capillary pumping pressure be greater than the sum of all the pressure drops occurring in the liquid flow. This relationship can be expressed as

$$\frac{\sigma}{r_{\mathrm{cap},e}} - \frac{\sigma}{r_{\mathrm{cap},c}} = \left(\frac{f_l \cdot \mathrm{Re}_{h,l}\mu_l L_{eff}}{2C_1(C^* C_2 r_{\mathrm{cap},e})^4 \rho_l h_{fg}}\right) q + \Delta p_v + \rho_l g L \sin \psi, \tag{19}$$

where the momentum variation effect was neglected. Rewriting Eq. (19), the heat transport, q, can be determined as

$$q = \left(\frac{\sigma}{r_{\mathrm{cap},e}} - \frac{\sigma}{r_{\mathrm{cap},c}} - \Delta p_v - \rho_l g L \sin \psi\right) \times \left(\frac{2C_1(C^* C_2 r_{\mathrm{cap},e})^4 \rho_l h_{fg}}{f_l \cdot \mathrm{Re}_{h,l}\mu_l L_{eff}}\right). \tag{20}$$

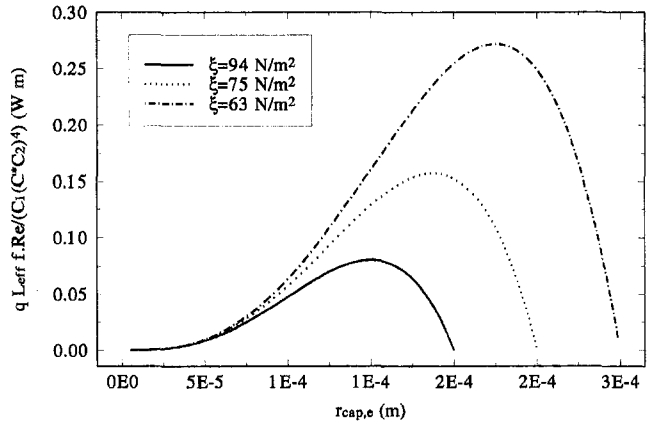

Fig. 2 Meniscus radius effect on the heat transport capability ($\xi = \sigma/r_{\mathrm{cap},c} + \Delta p_v + \rho_l g L \sin \psi$)

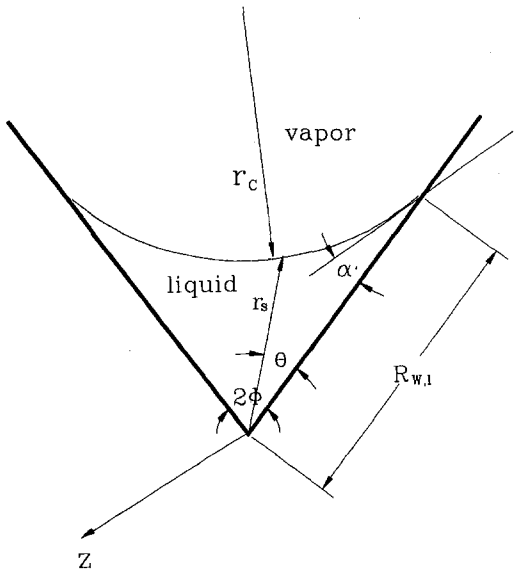

Fig. 3 Triangular groove and coordinate system

From Eq. (20), it can be found that the heat transport is largely dependent on the meniscus radius of curvature in the evaporator, and there exists a maximum value of the heat transport which can be determined by

$$\frac{\partial q}{\partial r_{\mathrm{cap},e}} = 0. \tag{21}$$

Substituting Eq. (20) into Eq. (21) and rearranging, this value can be expressed as

$$r_{\mathrm{cap},e} = \frac{3\sigma}{4\left(\frac{\sigma}{r_{\mathrm{cap},c}} + \Delta p_v + \rho_l g L \sin \psi\right)}. \tag{22}$$

When the average meniscus radius in the evaporator is equal to that defined by Eq. (22), the micro heat pipe has the largest capillary heat transport capability which is obtained by substituting Eq. (22) into Eq. (20). Traditionally, this meniscus radius is called the minimum meniscus radius (Tien and Sun, 1971). Examining Eq. (22), it can be found that this minimum meniscus radius depends on $r_{\mathrm{cap},c}$, Δp_v, L, ρ_l, σ, and ψ, which all directly affect the capillary heat transport capability as shown in Fig. 2, where $\xi = \sigma/r_{\mathrm{cap},c} + \Delta p_v + \rho_l g L \sin \psi$.

Discussion

The above derivation did not set any limitation on the cross-sectional shape of the longitudinal grooves in the micro heat pipe. This implies that Eqs. (20) and (22) can be used to calculate the capillary heat transport capability and minimum meniscus radius occurring in a micro heat pipe with any cross-sectional shape, provided that the Bond number is small. For a specific micro heat pipe, the geometric shape and the working fluid are typically given, and the values of C_1 and C_2 can be readily found. As shown in Eqs. (12) and (13), L_{eff} and C^* depend on the heat flux distribution and the cross-sectional area distribution of the liquid flow along the axial direction. For a given operating condition where the heat flux distribution is given, the cross-sectional area distribution of liquid flow can be found, and the values of L_{eff} and C^* can be determined using Eqs. (12) and (13).

As discussed previously, for a given micro heat pipe, the coefficients, C_1 and C_2, are singularly fixed. In order to show how to obtain C_1 and C_2, the triangular longitudinal groove shown in Fig. 3 is taken as an example. The cross-sectional area of the liquid flow can be determined by

$$A_l = \frac{1}{2}\int_0^{2\phi} r_s^2\, d\theta = \frac{1}{2}\int_0^{2\phi} R_{w,l}^2\left[\frac{\cos\alpha\cos(\phi-\theta) - [\sin^2\phi - \cos^2\alpha\sin^2(\phi-\theta)]^{0.5}}{\cos(\alpha+\phi)}\right]^2 d\theta. \quad (23)$$

Recalling the expression of the hydraulic radius, i.e., $r_{h,l} = 4A_l/P_l$, where P_l is equal to $2R_{w,l}$, the hydraulic radius of the liquid flow can be found as

$$r_{h,l} = \int_0^{2\phi} R_{w,l}\left[\frac{\cos\alpha\cos(\phi-\theta) - [\sin^2\phi - \cos^2\alpha\sin^2(\phi-\theta)]^{0.5}}{\cos(\alpha+\phi)}\right]^2 d\theta. \quad (24)$$

Substituting Eq. (24) into Eq. (10) and comparing with Eq. (23), it can found that

$$\frac{1}{C_1} = 2\int_0^{2\phi}\left[\frac{\cos\alpha\cos(\phi-\theta) - [\sin^2\phi - \cos^2\alpha\sin^2(\phi-\theta)]^{0.5}}{\cos(\alpha+\phi)}\right]^2 d\theta. \quad (25)$$

Following the same procedure, C_2, in Eq. (16) can be readily found as

$$C_2 = \frac{1}{\cos(\alpha+\phi)\sin\phi}\int_0^{2\phi}[\cos\alpha\cos(\phi-\theta) - [\sin^2\phi - \cos^2\alpha\sin^2(\phi-\theta)]^{0.5}]^2 d\theta. \quad (26)$$

From Eqs. (25) and (26), it is apparent that C_1 and C_2 depend only on the channel angle of the groove and the contact angle of the liquid flow as shown in Figs. 4 and 5, respectively.

If the heat pipe consists of three sections, i.e., evaporator, adiabatic section, and condenser with lengths, L_e, L_a, and L_c, respectively, the effective length, L_{eff}, can be rewritten as

$$L_{eff} = \frac{\int_0^{L_e}\dot{m}dz}{\dot{m}_a} + L_a + \frac{\int_{L_e+L_a}^{L}\dot{m}dz}{\dot{m}_a}. \quad (27)$$

From Eq. (27), it can be found that if the heat distribution is given, the effective length, L_{eff}, can be readily found and the coefficients, C_1 and C_2, can be determined. The remaining term, C^* is defined by Eq. (14). If the average hydraulic radius of the liquid flow in the condenser is $r_{h,c}$, the total average hydraulic radius of the liquid flow can be approximated as

$$r_{h,l} = \frac{r_{h,e} + r_{h,c}}{2}. \quad (28)$$

Substituting Eq. (28) into Eq. (13) and considering Eq. (16), the coefficient, C^*, can be further expressed as

$$C^* = \frac{1}{2}\left(1 + \frac{r_{h,c}}{r_{h,e}}\right) = \frac{1}{2}\left(1 + \frac{r_{\text{cap},c}}{r_{\text{cap},e}}\right), \quad (29)$$

where $r_{\text{cap},e}$ can be determined by Eq. (22), and $r_{h,c}$ and $r_{\text{cap},c}$ can be found from the average cross-sectional area of grooves in the micro heat pipe and an assumption of constant meniscus radius of curvature.

Experimental Verification.

Triangular Grooves. In order to verify the derivation presented here, results obtained using Eqs. (20) and (22) were first compared with the experimental data reported by Ma and Peterson (1996) who conducted an experimental investigation on the capillary heat transport limit in small triangular grooves as shown in Fig. 6. Using methanol as the working fluid, the maximum capillary heat transport capability was experimentally determined for ten grooved plates with 60 degree apex angles and varying groove widths from D_h = 0.17 mm to D_h = 1.43 mm. As shown in Fig. 6, one end of the grooved plate was immersed in a liquid pool and held stationary at a specified tilt angle. The liquid wicked up the grooves by the capillary pressure, against the gravitational force and the frictional pressure drop. To simulate typical micro heat pipe operation, an axial adiabatic section was included between the point of origin (where the groove plate emerges from the liquid pool) and the junction point (the start of the region where a heat flux was applied). As shown in Fig. 6, the evaporating section extended from the junction point to the dryout point. No condensing section was included, thereby eliminating the influence of the condenser region on the measured maximum capillary heat transport. In that way, it was possible to determine the true capillary limit of the liquid flow in the longitudinal V-shaped grooves and to approximate the conditions occurring in an actual micro heat pipe.

From Fig. 6, it can be found that the meniscus radius of curvature at the point of origin approaches infinity, i.e., $r_{\text{cap},c} \rightarrow$

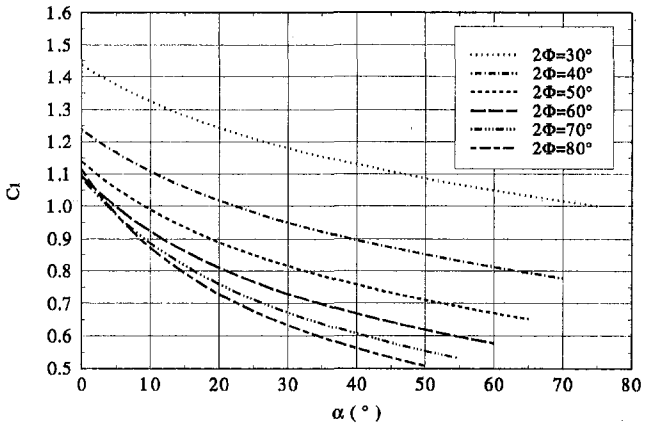

Fig. 4 Channel angle and contact angle effects on the value of C_1 in a triangular groove

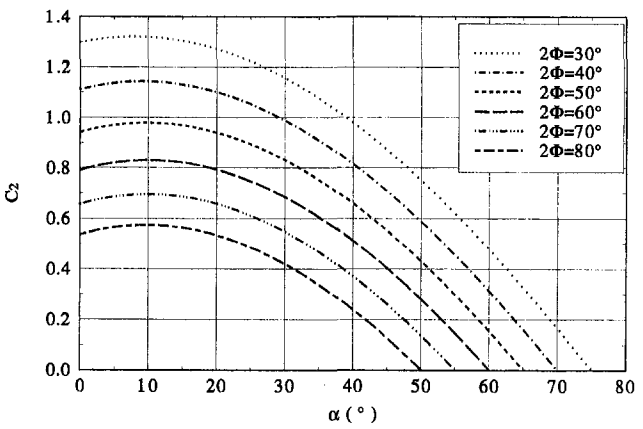

Fig. 5 Channel angle and contact angle effects on the value of C_2 in a triangular groove

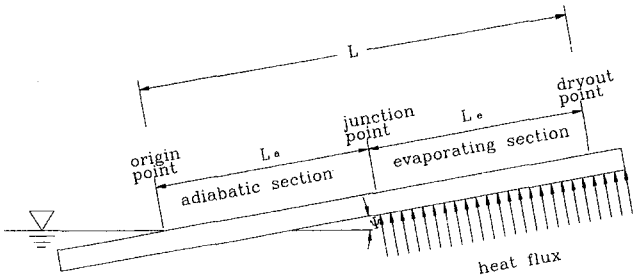

Fig. 6 Schematic of a grooved plate

∞. Since the vapor pressure is constant, there is no vapor pressure drop, i.e., $\Delta p_v = 0$ and Eq. (20) becomes

$$q = \left(\frac{\sigma}{r_{\text{cap},e}} - \rho_l g L \sin\psi\right)\left(\frac{2C_1(C^*C_2 r_{\text{cap},e})^4 \rho_l h_{fg}}{f_l \cdot \text{Re}_{h,l}\mu_l L_{eff}}\right), \quad (30)$$

where $r_{\text{cap},e}$ can be found by Eq. (22), and C_1 and C_2 are equal to 1.10 and 0.79, respectively, for the channel angle, $2\phi = 60$ deg and contact angle, $\alpha = 0$ deg. Although the heat flux added to the bottom of the evaporating section is uniform, the evaporating heat flux through the evaporating film is not, resulting in a nonuniform evaporating heat flux distribution along the evaporating section. Xu and Carey (1990) found that an approximate heat flux was found to have a nearly linear relationship with the plate length coordinate. Also, Peterson and Ma (1996c) used a linear heat flux distribution along the axial direction in the evaporating section and found a good agreement with the experimental data. For these reasons, a linear heat flux distribution along the axial direction of the evaporating section was assumed and the effective length, L_{eff}, can be found as

$$L_{eff} = L_a + \tfrac{2}{3}L_e. \quad (31)$$

The coefficient, C^*, can be determined by Eq. (29), which is approximately equal to 1.61 for the hydraulic radius of 0.23 mm. Substituting this value into Eq. (20), good agreement with the experimental data was obtained. With increases in the hydraulic radius, the value of C^* increases, but during the derivation of Eqs. (20) and (22), the assumption of constant meniscus radius was used. This resulted in an increase of C^* with an increase in the hydraulic radius, which is not correct when the Bond number becomes large. Based on the investigation conducted by Ma and Peterson (1996), when the hydraulic radius of the grooves, r_h, is larger than 0.35 mm, the assumption of constant meniscus radius of curvature may not be appropriate. This implies that when the hydraulic radius is larger than 0.35 mm, it is inappropriate to use Eq. (29) to determine the coefficient, C^*. For this reason, the value of C^* should be based on experimental data. This procedure was followed here and indicated that when a value of C^* obtained at the hydraulic radius of 0.23 mm was used, good agreement resulted.

When the hydraulic radius of the groove is less than those corresponding to the minimum meniscus radius, the dimension of the grooves directly limits the heat transport capability, resulting in a decrease in the heat transport capability in the triangular grooves as shown in Fig. 7. When this occurs, an optimum meniscus radius does not exist in the evaporator and the heat transport capability depends on the hydraulic radius of the grooves. That is why the capillary heat transport capability decreases so fast when the hydraulic radius of the grooves becomes smaller. When the hydraulic radii of those grooves are smaller than that corresponding to the minimum meniscus radius found by Eq. (22), an error occurs. Therefore, the meniscus radius in Eq. (30) should be approximated by those corresponding to the hydraulic radius. The results predicted by Eq. (30)

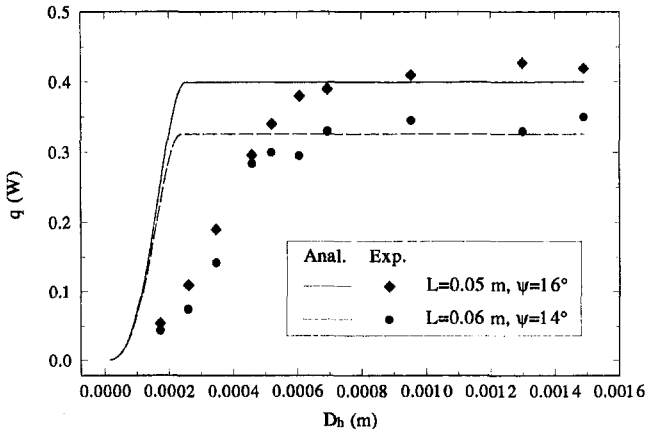

Fig. 7 Comparison with experimental data for triangular grooves

are shown in Fig. 7 and are in good agreement with the experimental data.

Micro heat pipes. Wu and Peterson (1991) conducted an experimental investigation on the heat transport limits in trapezoidal micro heat pipes, made of copper or silver, with outer dimensions of 1 × 1 mm and a length of 57 mm, as shown in Fig. 8. The working fluid, ultrapure water, was pumped back through four corners with a channel angle of 60 deg. Since the micro heat pipe was placed horizontally, the gravitational force effect could be neglected and Eq. (20) becomes

$$q = \left(\frac{\sigma}{r_{\text{cap},e}} - \frac{\sigma}{r_{\text{cap},c}} - \Delta p_v\right)\left(\frac{2C_1(C^*C_2 r_{\text{cap},e})^4 \rho_l h_{fg}}{f_l \cdot \text{Re}_{h,l}\mu_l L_{eff}}\right), \quad (32)$$

where $r_{\text{cap},e}$ can be determined by Eq. (22). Since the term, Δp_v, is included in Eq. (32), the value of Δp_v should first be

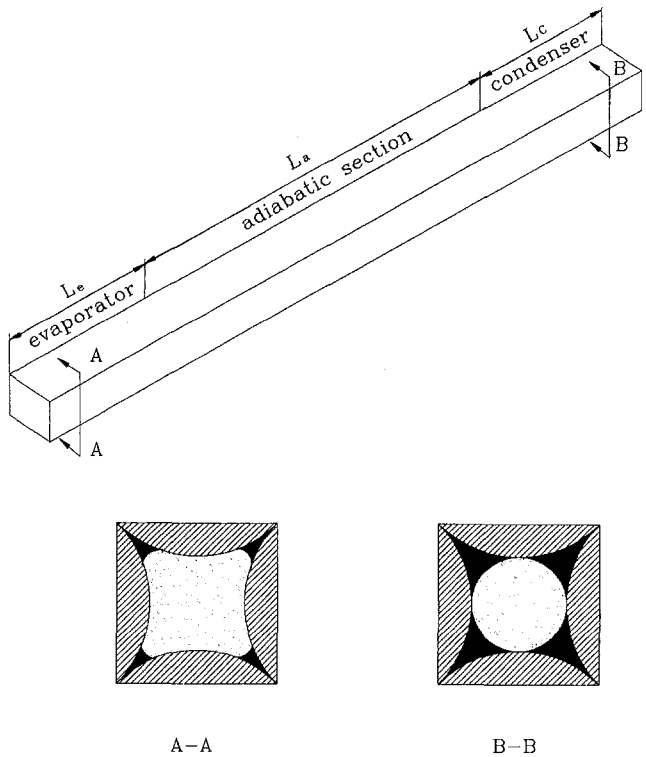

Fig. 8 Schematic of a micro heat pipe

obtained. Based on momentum conservation, the expression for vapor pressure drop can be found as (Babin et al., 1990)

$$\Delta p_v = \left(\frac{f_v \cdot \mathrm{Re}_{h,v} \mu_v}{2 r_{h,v}^2 A_v \rho_v h_{fg}} \right) L_{eff} q, \tag{33}$$

where $r_{h,v}$ is the average hydraulic radius of the vapor space and is equal to $4A_v/P_v$, where A_v and P_v are the average cross-sectional area and perimeter of the vapor space, respectively. Since the cross-sectional shape varies from an approximate square to an approximate circle, the friction factor will change from 14.23 to 16, therefore, an average value of $f_v \cdot \mathrm{Re}_{h,v}$ was taken.

Since the length of the evaporator and the condenser was equal to 12.7 mm, which is much shorter than the length of the adiabatic section, a uniform heat flux distribution, similar to that used previously by Babin et al. (1990) and Wu and Peterson (1991), was assumed. The effective length, L_{eff}, can be found by using

$$L_{eff} = \frac{L_e}{2} + L_a + \frac{L_c}{2}. \tag{34}$$

From Figs. (4) and (5), it can be found that C_1 and C_2 depend not only on the channel angle, but also on the contact angle. The measured contact angles of water with copper and silver are 55 deg and 45 deg, respectively (Wu and Peterson, 1991), and the contact angle at the condenser was assumed to be zero due to condensation. The contact angle will vary from the evaporator to condenser; hence, an average value of the contact angle of 27.5 deg for copper and 22.5 deg for silver is assumed, and the values of C_1 and C_2 can be obtained using Eqs. (25) and (26).

Since the vapor flow has an important effect on the capillary heat transport in a micro heat pipe (Ma et al., 1994), the term $f_l \cdot \mathrm{Re}_{h,l}$, should consider the vapor flow effect. Although Peterson and Ma (1996b) obtained a complete solution for the value of $f_l \cdot \mathrm{Re}_{h,l}$ with the vapor flow effect in a micro heat pipe, the model did not consider the surface roughness and shape effects, which will have an important influence on the liquid flow due to the dimensions being so small. Also, the solution by Peterson and Ma (1996b) are correct only where the ratio of the average vapor velocity to the average liquid velocity is less than 50. For these reasons, a modification coefficient based on experimental data should be used for the vapor flow effect. Using the experimental data at the operating temperature of 62.8°C for the silver-water micro heat pipe obtained by Wu and Peterson (1991), this coefficient was found as 15.0, where the value of $f_l \cdot \mathrm{Re}_{h,l}$ was taken at $Lv = 1$ (Peterson and Ma, 1996b). Figures 9 and 10 illustrate the results predicted by Eqs. (20) and (22) and compare the experimental data presented by Wu and Peterson (1991) for the silver-water and copper-water heat pipes, respectively. As shown, the equations developed in this paper predict the maximum capillary heat transport with a reasonable degree of accuracy.

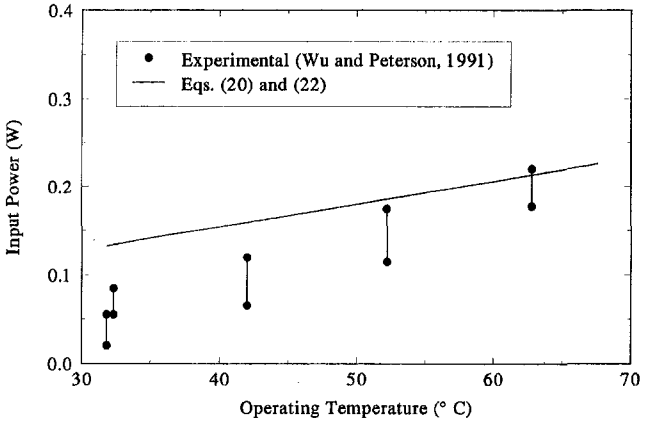

Fig. 9 Comparison with experimental data for a silver-water heat pipe

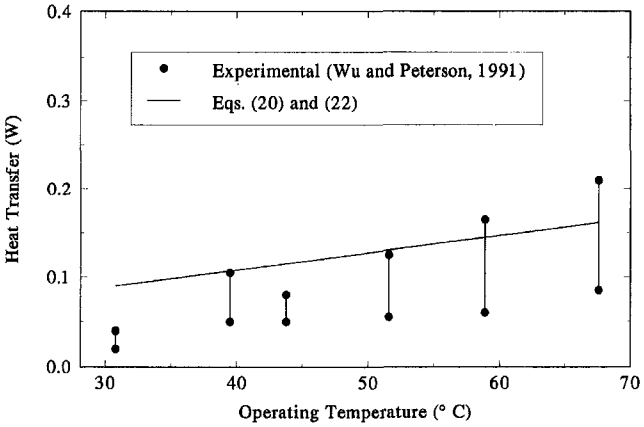

Fig. 10 Comparison with experimental data for a copper-water heat pipe

Conclusions

Based on the momentum conservation and Laplace-Young equations, expressions to predict the minimum meniscus radius and the maximum capillary heat transport were obtained. In order to verify these expressions, a comparison with experimental results for triangular grooves was made and was shown to be in good agreement. These expressions verify that there exists an optimum hydraulic radius for the grooves that have a maximum capillary heat transport capability, and when the hydraulic radius is less than the optimum hydraulic radius, the groove dimension will directly limit the capillary heat transport capability occurring in the triangular grooves. Also, when the hydraulic radius of the cross section of the grooves is much larger than the optimum hydraulic radius, no increase in the capillary pumping occurs. The results predicted by Eqs. (20) and (22) were compared with experimental data for silver-water and copper-water micro heat pipes, and they were shown to be in good agreement. The equations developed here not only predict the operating temperature effect, but also predict the case material effect on the maximum capillary heat transport capability. These expressions are of particular importance in the design of micro/small heat pipes for practicing engineers, and they better explain the physical phenomena that exists.

References

Babin, B. R., Peterson, G. P., and Wu, D., 1990, "Steady-State Modeling and Testing of a Micro Heat Pipe," ASME JOURNAL OF HEAT TRANSFER, Vol. 112, pp. 595–601.

Cotter, T. P., 1984, "Principle and Prospects of Micro Heat Pipes," *Proc. 5th Int. Heat Pipe Conf.*, Tsukuba, Japan, pp. 328–335.

Gerner, F. M., Longtin, J. P., Henderson, H. T., Hsieh, W. M., Ramadas, P., and Chang, W. S., 1992, "Flow and Heat Transfer Limitation in Micro Heat Pipes," *Proc. ASME Annual Meeting*, HTD-Vol. 206-3, ASME, NY, pp. 99–104.

Khrustalev, D., and Faghri, A., 1994, "Thermal Analysis of A Micro Heat Pipe," ASME JOURNAL OF HEAT TRANSFER, Vol. 116, No. 1, pp. 189–198.

Longtin, J. P., Badran, B., and Gerner, F. M., 1994, "A One-Dimensional Model of Micro Heat Pipe During Steady-State Operation," ASME JOURNAL OF HEAT TRANSFER, Vol. 116, pp. 709–715.

Ma, H. B., Peterson, G. P., and Lu, X. J., 1994, "The Influence of Vapor-Liquid Interaction on the Liquid Pressure Drop in Triangular Microgrooves," *International Journal of Heat and Mass Transfer*, Vol. 37, No. 15, pp. 2211–2219.

Ma, H. B., and Peterson, G. P., 1996, "Experimental Investigation of the Maximum Heat Transport in Triangular grooves," ASME JOURNAL OF HEAT TRANSFER, Vol. 118, No. 3, pp. 740–746.

Peterson, G. P., 1992, "An Overview of Micro Heat Pipe Research," *Applied Mechanics Review*, invited review article, Vol. 45, No. 5, pp. 175–189.

Peterson, G. P., 1994, *An Introduction to Heat Pipes,* John Wiley & Sons, Inc., New York.

Peterson, G. P., Duncan, A. B., and Weichold, M. H., 1993, "Experimental Investigation of Micro Heat Pipes Fabricated in Silicon Wafers," ASME JOURNAL OF HEAT TRANSFER, Vol. 115, No. 3, pp. 751–756.

Peterson, G. P., and Ma, H. B., 1996a, "The Characteristics of the Minimum Meniscus Radius in Micro Heat Pipes," *34th AIAA Aerospace Sciences Conference,* AIAA 96-0476, Reston, VA, pp. 15–18.

Peterson, G. P., and Ma, H. B., 1996b, "Analysis of Countercurrent Liquid-Vapor Interactions and the Effect on the Liquid Friction Factor," *International Journal of Experimental Thermal and Fluid Science,* Vol. 12, No. 1, pp. 13–24.

Peterson, G. P., and Ma, H. B., 1996c, "The Theoretical Analysis of the Maximum Heat Transport in Triangular Grooves—A Study of Idealized Micro Heat Pipes," ASME JOURNAL OF HEAT TRANSFER, Vol. 118, No. 3, pp. 731–739.

Peterson, G. P., and Mallik, A. K., 1995, "Transient Response Characteristics of Vapor Deposited Micro Heat Pipe Arrays," *ASME Journal of Electronic Packaging,* Vol. 117, No. 1, pp. 82–87.

Peterson, G. P., and Lu, X. J., Peng, X. F., and Wang, B. X., 1992a, "Analytical and Experimental Investigation of the Rewetting of Circular Channels with Internal V-Grooves," *Int. J. Heat and Mass Transfer,* Vol. 35, No. 11, pp. 3085–3094.

Peterson, G. P., Peng, X. F., and Wang, B. X., 1992b, "The Effect of Plate Temperature on the Onset of Rewetting," *Int. J. Heat & Mass Transfer,* Vol. 35, No. 6, June, pp. 1605–1614.

Tien, C. L., and Sun, K. H., 1971, "Minimum Meniscus Radius of Heat Pipe Wicking Materials," *International Journal of Heat and Mass Transfer,* Vol. 14, pp. 1853–1855.

Wu, D., and Peterson, G. P., 1991, "Investigation of the Transient Characteristics of Micro Heat Pipes," *AIAA Journal of Thermophysics and Heat Transfer,* Vol. 5, No. 2, pp. 129–134.

Xu, X., and Carey, Y. P., 1990, "Film Evaporation from a Micro-Grooved Surface—An Approximate Heat Transfer Model and Its Comparison with Experimental Data," *AIAA Journal of Thermophysics and Heat Transfer,* Vol. 4, No. 4, pp. 512–520.

Double Diffusive Natural Convection in a Composite Fluid-Porous Layer

D. Gobin
gobin@fast.u-psud.fr

B. Goyeau

J.-P. Songbe

Fluides, Automatique et Systèmes Thermiques-FAST-URA 871, Campus Universitaire, Bât. 502, 91405 Orsay Cedex, France

This study deals with natural convection driven by combined thermal and solutal buoyancy forces in a binary fluid. The consequence of thermosolutal convection on heat and mass transfer is examined in a confined enclosure partially filled with a porous medium. The mathematical description of the problem makes use of a one-domain formulation of the conservation equations. The presented numerical results quantitatively show the significant influence of the presence of a relatively thin porous layer on the flow structure and on heat and species transfer in the enclosure. The paper is dedicated to the analysis of the influence of the thickness and permeability of the porous layer in a range of governing parameters. For a low permeability porous layer, the numerical results are compared to an analysis based on simple scaling laws, which provide a good interpretation in terms of the wall transfer decrease with the porous layer thickness. The effect of permeability is investigated and it is shown that flow penetration in the porous layer induces a specific behavior of the flow structure and average heat transfer in the enclosure.

1 Introduction

This study deals with heat and solute transport at a fluid-porous interface. This problem is related to a wide range of industrial or environmental applications. Heat transfer and fluid flow through a fibrous insulation (Le Breton et al., 1991), natural convection heat and mass transfer in a mushy zone (Prescott and Incropera, 1996), or solute exchange in sediments in coastal environments (Webster et al., 1996) are some examples of such fields where transport phenomena take place at an interface between a fluid phase and a porous medium.

Our study focuses on combined thermal and solutal natural convection of a binary fluid confined in an enclosure partially filled by a porous medium. Among others, the motivation for this work arises from macroscopic modeling of solidification processes in multicomponent systems—where the importance of the interaction between natural convection in the melt and heat and species transfer in the interfacial phase-change domain is recognized (Prescott and Incropera, 1996).

A good description of these transfers may be of primary importance in materials processing because the solidification kinetics, and thus the internal structure and mechanical properties of the solid, result from this coupling. In the present approach, our purpose is not to propose a full solidification model, but to retain some important features of macroscopic transport phenomena in such systems in order to analyze their consequence. Namely, the first important feature of solidification processes in multicomponent mixtures is the segregation of components during phase change, due to solute redistribution at the interface. This results in composition gradients in the liquid phase which, combined with the temperature gradients imposed to the system, locally modify the fluid density and give rise to buoyancy induced double diffusive convection. This is the reason why thermosolutal convection is considered in this work. The second significant feature retained in our analysis is the fact that the growth conditions very often lead to the formation of a two-phase region, known as "mushy layer", where phase change takes place between the solid dendrites and the interstitial liquid phase. Heat and mass transfer modeling in this domain generally uses a macroscopic representation of the mushy layer as a saturated porous medium, where the expression of momentum conservation is based on a volume averaged formulation, leading to the Darcy equation or one of its extensions.

The real flow problem in mushy layers is actually much more complex, since the time-dependent porosity of the porous medium (the liquid fraction) is one of the main unknowns of the problem and the assessment of porosity-permeability relationships is still one of the open difficulties of such models. In this frame, it is therefore relevant to analyze the interaction between the flow in the melt and in a porous layer for thermosolutal natural convection in such a composite domain in the absence of phase change.

This approach is not intended to model the coupled heat, species, and fluid flow problem in the columnar growth zone, but it allows for focus on the influence of flow penetration on heat and species transfer in such a close situation. The purpose of the present paper is to present and to analyze a set of numerical results concerning thermosolutal natural convective flows in a binary fluid, confined in a rectangular enclosure, divided into a porous and a fluid vertical layer. Actually, such a configuration has been previously studied in the case of thermal convection, either in the context of wall insulation (Arquis and Caltagirone, 1984; Sathe et al., 1988; Le Breton et al., 1991) or solidification (Beckermann et al., 1987, 1988; Song and Viskanta, 1994). Extensively studied in the literature, the analysis of thermosolutal convective flows, either in a fully fluid or in a fully porous cavity, has shown that many different flow structures could be expected, depending on the governing parameters.

The originality of the present study is to combine the presence of the porous layer and the complex structure of double diffusive convection flows, and to study the consequence on heat and species transfer.

II Problem Formulation

II.1 Problem Description. The geometry under consideration is the two-dimensional rectangular cavity (height H, total width L) sketched in Fig. 1, the left part of which is filled with a porous layer (thickness x_P^*) and is assumed to be homoge-

Contributed by the Heat Transfer Division for publication in the JOURNAL OF HEAT TRANSFER. Manuscript received by the Heat Transfer Division July 25, 1996; revision received June 27, 1997; Keywords: Double Diffusion Systems; Enclosure Flows; Porous Media. Associate Technical Editor: K. Vafai.

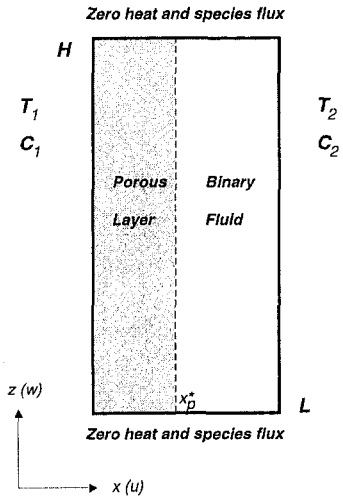

Fig. 1 Problem description

neous and isotropic. With respect to the preceding introductory remarks, this description represents a major assumption of our approach, since real structures are expected to present porosity gradients and anisotropic permeability. In the present state of our work, this limitation is accepted since it is relevant to analyze the characteristics of thermosolutal natural convection in a standard porous partition. However, it is clear that further extensions should question the homogeneous isotropic model. This is presently a field of current research (Goyeau et al., 1997) and the numerical implementation of this more complex formulation is under study. Also, it could be necessary to consider a three-dimensional model to study some limiting situations, but it is known that such flows are two-dimensional over a sufficiently wide range of parameters to allow for this assumption and reasonable computational costs.

The porous medium is saturated by the same binary fluid which fills the remainder of the enclosure. Different and uniform temperatures and concentrations are specified at the external vertical walls of the cavity, and zero heat and species fluxes are imposed at the horizontal boundaries. The flow is assumed to be laminar and incompressible, and the binary fluid is assumed to be newtonian and to satisfy the Boussinesq approximation:

$$\rho = \rho_0[1 - \beta_T(T - T_0) - \beta_C(C - C_0)]. \qquad (1)$$

Finally, the porous matrix is supposed to be in thermodynamical equilibrium with the fluid, and the Soret and Dufour effects are neglected (Bergman and Srinivasan, 1989).

The underlying problem in modeling this situation is the coupling of the momentum equation in the fluid and the porous regions and the appropriate boundary conditions at the fluid/porous interface. This has been, and still is, a controversial subject of intense research activity, which has been reviewed by Nield and Bejan (1992) and Kaviany (1995). Two different approaches are generally proposed.

Two-Domain Approach. In this approach, the fluid layer and the porous medium are considered separately. The Navier-Stokes equation is written in the fluid, while the flow in the porous medium is governed by the Darcy law or one of its extensions. Beavers and Joseph (1967) used the Darcy equation and proposed an empirical slip-flow boundary condition at the interface describing the proportionality between the shear rate at the interface and the slip velocity through a dimensionless slip coefficient, which depends on the surface structure and on the flow (Sahraoui and Kaviany, 1992). This condition has been justified theoretically (Saffman, 1971) and verified experimentally (Beavers and Joseph, 1967; Beavers et al., 1970, 1974). Neale and Nader (1974) have used the Brinkman extension of the Darcy equation (Brinkman, 1947) in order to account for the boundary layer in the porous medium. In this case, one must write the continuity of the velocity and of the shear stress at the interface, which has been extensively discussed in the

Nomenclature

A = aspect ratio of the enclosure, H/L
C = solute mass fraction
D = mass diffusivity of the solute in the liquid phase
Da = Darcy number, K/H^2
g = acceleration of gravity
Gr_S = solutal Grashof number, $g\beta_C\Delta CH^3/\nu^2 = N\,\mathrm{Gr}_T$
Gr_T = thermal Grashof number, $g\beta_T\Delta TH^3/\nu^2$
H = initial height of liquid in the enclosure
$\vec{j}$ = dimensional mass flux
$\vec{k}$ = unit vector in the vertical direction
k = thermal conductivity of the liquid
K = permeability of the porous medium (m^2)
L = width of the enclosure
Le = Lewis number: α/D
N = buoyancy ratio: $\beta_C\Delta C/\beta_T\Delta T$
Nu = average Nusselt number (Eq. 6)
P = dimensionless pressure
Pr = Prandtl number, ν/α
Ra_S = solutal fluid Rayleigh number, $N\,\mathrm{Le}\,\mathrm{Ra}_T$
Ra_T = thermal fluid Rayleigh number, $\mathrm{Pr}\,\mathrm{Gr}_T$
Ra_T^* = porous thermal Rayleigh number, $\mathrm{Da}\,\mathrm{Pr}\,\mathrm{Gr}_T$
Sc = Schmidt number, ν/D
Sh = average Sherwood number (dimensionless mass flux)
Sh_R = normalized Sherwood number (Section V.2)
T = dimensional temperature
$\vec{V}$ = dimensionless fluid velocity ($\vec{v}^*H/\nu$)
$w(u)$ = vertical (horizontal) component of $\vec{V}$
x_P^* = dimensional width of the porous layer
x_P = dimensionless width of the porous layer, (x_P^*/L)
$x(z)$ = dimensionless coordinates, $x^*/H(z^*/H)$
Z = variable defined in Eq. (11)

Greek Symbols

α = thermal diffusivity
β_T = coefficient of volumetric thermal expansion
β_C = coefficient of solutal expansion
ΔC = concentration difference between the external walls
ΔC_P = concentration difference in the porous layer
ΔT = temperature difference between walls
δ = ratio $\Delta C_P/\Delta C$
γ = slip coefficient at the fluid-porous interface
ϵ = porosity of the porous layer
μ = dynamic viscosity of the fluid
ν = kinematic viscosity
ϕ = dimensionless concentration, $\phi = (C - C_o)/\Delta C$
ψ = stream function
ρ = fluid density
θ = dimensionless temperature, $\theta = (T - T_o)/\Delta T$

Subscripts

eff = effective property of the porous layer
F = refers to the fluid domain
P = refers to the porous medium
S or C = solutal parameter
T = thermal parameter

literature (Vafai and Kim, 1990, 1995; Nield, 1991; Chen and Chen, 1992; Ochoa-Tapia and Whitaker, 1995). Neale and Nader show that both formulations (slip or no-slip conditions) lead to the same result if in the slip coefficient γ is taken equal to $(\mu_{eff}/\mu)^{1/2}$. μ is the fluid dynamic viscosity, and μ_{eff} is the effective viscosity in the Brinkman term whose determination remains an open problem (Lundgren, 1972; Koplik et al., 1983; Sahraoui and Kaviany, 1992; Givler and Altobelli, 1994).

One-Domain Approach. By contrast, the one-domain approach considers the porous layer as a pseudo-fluid and the composite region is treated as a continuum. This leads to solve only one modified Navier Stokes equation, which includes the Darcy term and eventually the Forchheimer term. In this equation, the transition from the fluid to the porous medium is achieved through a spatial variation of the permeability (Arquis and Caltagirone, 1984; Turki and Lauriat, 1990; Le Breton et al., 1991; Ettefagh et al., 1991). This formulation has been widely used in previous numerical computations since it avoids explicitly considering the conditions at the fluid/porous interface. In the field of thermal natural convection, results obtained with $\mu_{eff} = \mu$ are shown to be in good agreement with the experimental studies (Beckermann et al., 1987, 1988; Sathe et al., 1988; Song and Viskanta, 1994).

In our work, this later formulation has been retained because of the future extensions of the present study: a single domain formulation of the conservation equations is preferred in a solidifying system since the transition from the fluid to the mushy layer is not clear-cut due to the progressive porosity (and permeability) change.

II.2 Governing Equations. Under the foregoing hypotheses, the problem is to write macroscopic conservation equations which might continuously shift from the Darcy-Brinkman formulation to the Navier-Stokes description. A unique expression is retained with permeability as a function of space. The following dimensionless variables are introduced: $x = x^*/H$, $z = z^*/H$, $\theta = (T - T_0)/\Delta T$ and $\phi = (C - C_0)/\Delta C$, $\vec{V} = \vec{v}^* H/\nu$, where $\vec{v}^*$ is the filtration velocity. The steady-state macroscopic conservation equations resulting from the aforementioned hypotheses are written as

$$\vec{\nabla} \cdot \vec{V} = 0 \tag{2}$$

$$\frac{1}{\epsilon^2}(\vec{V} \cdot \vec{\nabla})\vec{V} = -\vec{\nabla} P + (\mathrm{Gr}_T\,\theta + \mathrm{Gr}_S\,\phi)\vec{k} - \frac{1}{\mathrm{Da}}\vec{V} + \frac{\mu_{eff}}{\mu}\nabla^2\vec{\nabla} \tag{3}$$

$$\vec{V} \cdot \vec{\nabla}\theta = \frac{1}{\mathrm{Pr}}\frac{k_{eff}}{k}\nabla^2\theta \tag{4}$$

$$\vec{V} \cdot \vec{\nabla}\phi = \frac{1}{\mathrm{Sc}}\frac{D_{eff}}{D}\nabla^2\phi, \tag{5}$$

with zero flux conditions at the horizontal walls and Dirichlet boundary conditions at the vertical walls: $\theta = \phi = -0.5$ at $x = 0$ (on the porous medium side), $\theta = \phi = 0.5$ at $x = 1/A$ (on the fluid side).

The dimensionless parameters of the problem are the thermal and solutal Grashof numbers defined with the fluid properties $\mathrm{Gr}_T = (g\beta_T \Delta T H^3)/\nu^2$ and $\mathrm{Gr}_s = (g\beta_C \Delta C H^3)/\nu^2$, the Darcy number $\mathrm{Da} = K/H^2$, and the Prandtl and Schmidt numbers. In the following we will also use combinations of those parameters, such as the Lewis number ($\mathrm{Le} = \mathrm{Sc}/\mathrm{Pr}$) and the ratio of the buoyancy forces ($N = \mathrm{Gr}_S/\mathrm{Gr}_T$). μ, k and D refer to the fluid viscosity, thermal conductivity, and molecular diffusivity, respectively, while subscript "eff" refers to the corresponding effective property of the porous medium. The Nusselt and Sherwood numbers are the dimensionless averages of the heat and mass fluxes along a vertical surface:

$$\mathrm{Nu} = \int_0^1 \left[\frac{\partial\theta}{\partial x} - \mathrm{Pr}(u\theta)\right] dz,$$

$$\mathrm{Sh} = \int_0^1 \left[\frac{\partial\phi}{\partial x} - \mathrm{Sc}(u\phi)\right] dz. \tag{6}$$

II.3 Numerical Procedure. The numerical resolution of the set of Eqs. (2)–(5) is based on a standard finite volume procedure. The details concerning this procedure may be found elsewhere and will not be repeated here, except for a few specific aspects.

The discretization scheme used for the conservation equations is the hybrid scheme of Patankar and Spalding which retains the second-order accuracy of the centered scheme when the local Peclet number is less than 2. This technique ensures numerical stability of the solution, but in our case, especially at the high Lewis numbers considered hereafter, the convective terms often dominate over the diffusive ones in the major part of the domain. Consequently the use of upwinding (i.e., first-order space discretization) may result in numerical diffusion, which may affect the results, especially in multicellular regimes. In a few cases, the results were compared with those obtained using central differencing (CDS): similar flow structures and average wall transfers (on the order of 1 percent) were obtained at a much higher computational cost due to slower convergence of the CDS. The solution procedure for the pressure-velocity coupling makes use of the SIMPLEC algorithm (or SIMPLE when divergence problems are met).

In the present configuration, it has been first verified that thermal and thermosolutal natural convection results for $x_P \to 1$ at any value of the Da number were in agreement with the standard Darcy-Brinkman version of the code (Goyeau et al., 1996). It has also been assessed that, at high values of the Darcy number (1 and more), the results at any value of x_P were identical to the results obtained for the pure fluid problem (Gobin and Bennacer, 1996).

In the absence of published results for double diffusive convection in the two-layer cavity, comparisons have been performed for the problem of thermal convection in a partially porous cavity (Le Breton et al., 1991). For a set of simulations presented by these authors (in our terms $\mathrm{Ra}_T = 10^7$, $\mathrm{Pr} = 0.71$, $N = 0$, $A = 1$, and $x_P = 0.1$), we obtain the same results over a Darcy number range extending from $\mathrm{Da} = 10^{-8}$ to $\mathrm{Da} = 10^{-1}$, when using similar grids (48 nodes; exponential distribution in the horizontal direction; regular distribution in the vertical direction).

However, at low Darcy numbers it appears that the development of thin boundary layers in the fluid at the fluid/porous interface does not allow a sufficient accuracy, and grid independence is difficult to satisfy if a simply irregular horizontal node distribution is used. This led us to use an irregular node distribution (exponential, sinusoidal or geometrical) in each domain in the horizontal direction. In the previous example, the results at $\mathrm{Da} = 10^{-1}$ are grid independent for the horizontal 48-node exponential grid—using complementary meshes for the fluid and porous domains does not improve the accuracy. On the contrary, at $\mathrm{Da} = 10^{-8}$, the simply irregular 48-node grid overestimates by more than 7 percent the wall Nusselt number, by comparison with the grid-independent result achieved for a 145-node grid. A 48-node hybrid mesh (7 regular nodes in each porous wall and 34 exponentially distributed nodes in the central fluid domain) leads to the same accuracy.

In many situations analyzed hereafter, which are characterized by high solutal Rayleigh numbers and low permeability porous walls, it is then particularly relevant to use such compound grids in order to limit the computational cost. In the

horizontal direction, 91 nodes are generally used for moderate Rayleigh numbers and up to 145 nodes have been necessary to solve for the thin boundary layers met in some extreme situations. The number of nodes in the porous layer also depends on its thickness and permeability, generally ranging between 21 and 41 for $x_P = 0.1$. In the vertical direction, the spatial nodes are regularly spaced (typically, 125 nodes, and up to 201 nodes for multicellular regimes).

III Numerical Results

The problem under consideration is characterized by a large number of parameters and their influence cannot be individually analyzed in the frame of the present study. Thus, we have limited the scope of this paper to the influence of the relative thickness of the porous layer ($x_P = x_P^*/L$) and its permeability on the heat and species transfer in a cavity of a given global aspect ratio ($A = H/L = 2$). The Prandtl number of the fluid is taken as equal to 10, corresponding to aqueous solutions which are often used in the experiments on double diffusive convection (Bénard et al., 1996). For the same reason, we are concerned with the range of relatively high Lewis numbers characterizing liquids. We only consider the case of cooperating thermosolutal convection (the thermal and solutal body forces are acting in the same direction), and the solutal component of the buoyancy force is assumed to be dominating ($N > 1$), all the results being presented for $N = 10$.

Concerning the value of the effective transport properties, a complete calculation should consider the detailed description of the structure of the porous medium in order to account for the effect of the tortuosity and dispersion phenomena. For the sake of simplicity and consistancy, and in the absence of information concerning the porous medium to be considered, the effective transport coefficients are given the value of the corresponding fluid properties; that is, the ratios shown in the diffusive terms of Eqs. (3)–(5) are equal to 1. This is consistent with the usual hypothesis that $\mu_{\text{eff}} = \mu$ in the Brinkman term.

The set of simulation results displayed in Fig. 2 shows the variation of the average Sherwood number in a vertical plane as a function of x_P for $\text{Ra}_T = 10^7$, $\text{Da} = 10^{-7}$, Le = 100, and $N = 10$.

One striking feature of those results is the very strong decrease of the Sherwood number with the increasing x_P for the thin porous layers ($0 \leq x_P \leq 0.20$). Qualitatively, this result is expected from the observations made for heat transfer in purely thermal convection (Sathe et al., 1988; Le Breton et al., 1991). This marked influence of the presence of a thin porous layer confirms the relevance of this study in the context of solidification because it reveals that convective mass transfer at the interface may be drastically affected as soon as a zone of columnar growth is present. Thus, it is important to study this influence, even for relatively thin mushy layers.

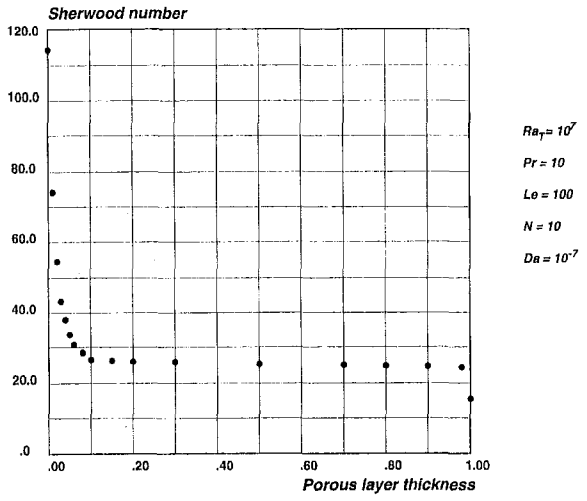

Fig. 2 Influence of the porous layer thickness on the average mass transfer. ($\text{Ra}_T = 10^7$; Pr = 10; Le = 100; $N = 10$; $\text{Da} = 10^{-7}$; $A = 2$.)

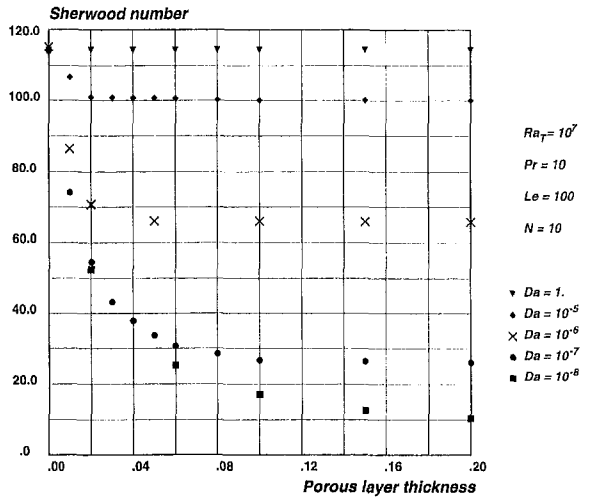

Fig. 3 Variation of the average mass transfer with the porous layer thickness—influence of the Darcy number. ($\text{Ra}_T = 10^7$; Pr = 10; Le = 100; $N = 10$; $A = 2$.)

For thicker porous layers (between 0.20 and 1.0), the Sherwood number is not very sensitive to x_P. Only for $x_P \to 1$, a slight decrease of Sh may be noted on the curve, which also may be observed on the Nu results proposed by Sathe et al. (1988).

Since the permeability of the solid matrix governs flow penetration inside the porous layer, it is important to study the influence of Da and to complete the previous results with simulations performed for other Darcy numbers. The influence of the porous layer permeability, in the zone of strong decrease in mass transfer, is shown in Fig. 3 for $\text{Da} = 10^{-8}$, 10^{-7}, 10^{-6}, 10^{-5}, and 1.0. It is clear that the Sh decrease with increasing x_P depends largely on the permeability. As expected, the influence of the porous layer is much weaker at high permeabilities, and in the present case it is not significant for $\text{Da} > 10^{-5}$. It is also possible to verify that decreasing from $\text{Da} = 10^{-7}$ to 10^{-8} has a strong influence at intermediate x_P values, and that below 10^{-8} no significant change is noticed.

In the following sections the analysis of the results is presented in two parts. In Section IV the influence of the porous layer thickness is studied in the limit of low permeability porous media. Section V is dedicated to the influence of the Darcy number.

IV The Limit of Low Permeability Porous Layers

Since it has been made clear in the previous section that both the geometry and the structure of the porous layer were two important parameters of this problem, let us first analyze the influence of the porous wall thickness in the Darcy regime; that is, in the range of low permeabilities where the results are not sensitive to the Darcy number. It is well known from previous studies on thermal convection in porous enclosures (e.g., see Lauriat and Prasad, 1987) that the corresponding limit in Darcy number depends on the Rayleigh number, but in the present situation no criterion is available and the "low permeability limit" has to be determined for each case. In this section we analyze the effect of increasing x_P on the heat and species transfer decrease for different conditions.

IV.1 Analysis of Mass Transfer. Figure 4 shows the streamlines and temperature and concentration fields for $\text{Ra}_T = 10^7$, $\text{Da} = 10^{-8}$, Le = 100, Pr = 10, and $x_P = 0.2$. It may be

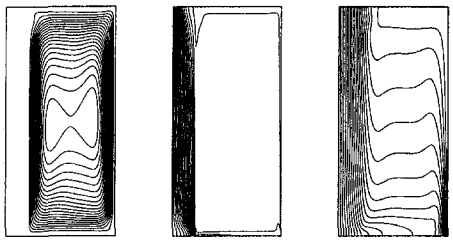

Fig. 4 Structure of the fields: (*a*) streamlines ($\Delta\psi = 0.10$); (*b*) composition ($\Delta\phi = 0.05$); (*c*) isotherms ($\Delta\theta = 0.05$). ($Ra_T = 10^7$; Pr = 10; Le = 100; N = 10; Da = 10^{-6}; A = 2; x_P = 0.20.)

seen that the low permeability porous wall behaves like a solid wall (Fig. 4(*a*)). The very weak flow penetration is then characterized by a quasi-diffusive mass transfer in the porous layer, where the isoconcentration lines are parallel to the vertical walls (Fig. 4(*b*)).

From this observation one may estimate the global mass transfer at low x_P from the diffusion flux in the porous layer. If we assume that the porous medium is impermeable to the flow, mass transfer may be considered to be purely diffusive and one-dimensional. The fluid-porous interface is then assumed to be at a uniform concentration. Let ΔC be the imposed concentration difference between the external walls of the enclosure and ΔC_P the concentration gap (supposed to be uniform) between the boundaries of the porous medium. In the steady state, the diffusive mass flux in the porous layer

$$\left(j_P = D \frac{\Delta C_P}{x_P^*} \right)$$

is equal to the convective mass flux in the fluid

$$\left(j_F = D \frac{\Delta C_F}{H} \mathrm{Sh}_F \right),$$

where $\Delta C_F = \Delta C - \Delta C_P$ and Sh_F is the Sherwood number induced by ΔC_F. If the boundary layer regime with dominating solutal buoyancy is assumed, Sh_F may be written as a function of Ra_{SF}, the solutal Rayleigh number built on ΔC_F, by a classical power-law correlation:

$$\mathrm{Sh}_F \sim \mathrm{Ra}_{SF}^{1/4} = \left[\frac{g\beta_C H^3}{\nu D} \Delta C_F \right]^{1/4}$$

$$= \mathrm{Ra}_S^{1/4} \left[1 - \frac{\Delta C_P}{\Delta C} \right]^{1/4}, \qquad (7)$$

with $\mathrm{Ra}_S = N\mathrm{LePrGr}_T$.

The constant of proportionality corresponding to high values of the Schmidt number (typically of order 1000) is about 0.35 (Bejan, 1995). Using (7), the equality $j_P = j_F$ leads to a relation between x_P and the relative composition difference in the porous layer, $\delta = \Delta C_P/\Delta C$:

$$\frac{\delta}{(1-\delta)^{5/4}} = 0.35 \frac{x_P}{A} \mathrm{Ra}_S^{1/4}. \qquad (8)$$

If A and Ra_S are specified, Eq. (8) gives δ and thus the Sherwood number as a function of the porous layer thickness, x_P. Figure 5 presents the values of the Sherwood number resulting from this analysis for Le = 10 or 100, and $\mathrm{Ra}_T = 10^6$ or 10^7, corresponding to three different values of the solutal Rayleigh number ($\mathrm{Ra}_S = 10^8$, 10^9, or 10^{10}). For each set of parameters, the figure also displays the values of the Sherwood number obtained numerically. The first observation is that the solutal Rayleigh number is the relevant parameter for defining

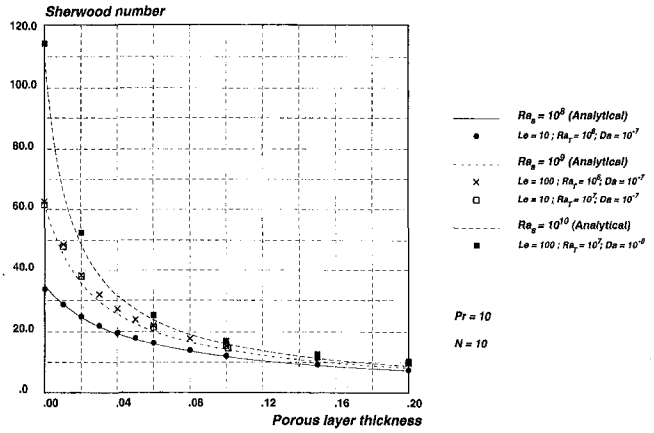

Fig. 5 Variation of the average mass transfer with the porous layer thickness at low permeability: comparison of the numerical simulations with the analytical model. (Pr = 10; N = 10; A = 2.)

the mass transfer in this range of parameters (dominating solutal buoyancy and high Lewis numbers) since the results at Le = 10 and $\mathrm{Ra}_T = 10^7$, and those at Le = 100 and $\mathrm{Ra}_T = 10^6$ ($\mathrm{Ra}_S = 10^9$ for both), are identical.

Besides, at the low values of x_P ($x_P < 0.2$), the above analysis is shown to give a fairly good interpretation of the numerical computations for solutal Rayleigh numbers ranging from 10^8 to 10^{10}.

IV.2 Heat Transfer. Figure 6 displays the values of the Nusselt numbers corresponding to the same set of results. It may first be seen that, for the range of parameters under consideration, the heat transfer is mainly conductive (Nu = A) when the thickness of the porous layer is larger than 70 percent of the total width of the enclosure ($x_P > 0.7$). This is due to the small value of the filtration thermal Rayleigh number ($\mathrm{Ra}_T^* = \mathrm{Pr}\,\mathrm{Gr}_T\,\mathrm{Da}$ is at most equal to 1), as may be verified on the corresponding isotherm plots (not shown). Secondly, the results show a low sensitivity of the heat transfer to the Lewis number, which indicates that the thermal Rayleigh number is the governing parameter for the Nusselt number. However, the validity of this result is limited because it is known that: (1) in fluids, thermosolutal natural convection may lead to multicellular regimes according to the values of Le, N, and Ra_T, with a strong influence on heat transfer (Gobin and Bennacer, 1996); and (2) in porous media, increasing the value of the buoyancy ratio N at high Lewis numbers may lead to decreasing heat transfer

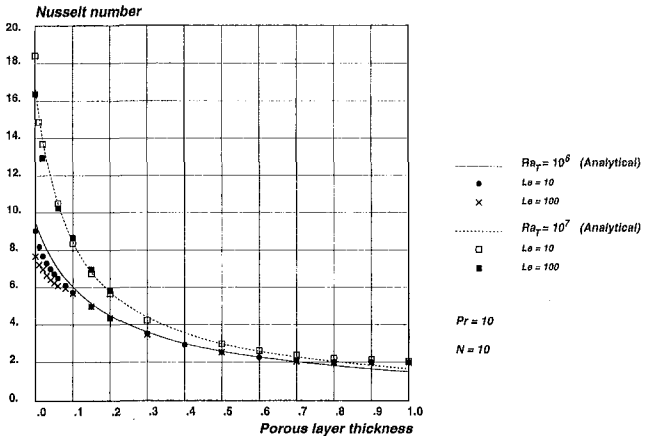

Fig. 6 Variation of the average heat transfer with the porous layer thickness: comparison of the numerical simulations with the analytical model. (Pr = 10; N = 10; A = 2.)

(Goyeau et al., 1996). It may be seen in Fig. 6 that the sensitivity to Le at a given value of Ra_T is stronger at small values of x_P.

Keeping this restriction in mind one may apply the previous analysis to the average heat transfer in the cavity using the thermal Rayleigh number as the governing parameter. In this case, the correlation coefficient corresponding to moderate values of the Prandtl number (Pr = 10) is chosen to be 0.30 (Bejan, 1995).

The analytical model for the thermal Rayleigh numbers considered here ($Ra_T = 10^6$ and 10^7) leads to the continuous curves displayed on the figure. It is clear that this simplified analysis constitutes a good approximation of the behavior of the numerical solution (except for high values of x_P) where the assumption of boundary layer convection in the very thin liquid region is not appropriate.

V Influence of Permeability

The results of the previous section have been obtained considering a low permeability porous layer. We now focus our attention on the role of permeability of the porous medium, which appears through the Darcy number in the dimensionless equations presented above. In this section we will examine variations of Da ranging from the small values corresponding to the low permeability layer considered previously, up to the high values for which the Darcy term in Eq. (3) is so small that the porous layer has the same behavior as a fluid.

V.1 Influence of Da. Considering the largely investigated field of thermal natural convection in porous media, it is well known that for very low values of the Darcy number (such as $Ra_T Da < 10^2$, see Lauriat and Prasad, 1987), the viscous (Brinkman) term in the macroscopic momentum equation may be discarded and the Darcy model prevails. On the other hand, it has been shown that at high Da values ($Ra_T Da > 10^6$), the Darcy term is very small and the flow in the porous medium is similar to a usual fluid flow, if the inertia term is retained in the formulation (Kaviany, 1995).

In the present configuration it is relevant to analyze how the permeability of the porous layer affects the heat and species transfer in the enclosure. In this section the set of numerical simulations is intended to span a large range of Darcy numbers—all other parameters but the Darcy number being maintained constant ($Ra_T = 10^6$; $N = 10$; Le = 100; Pr = 10; $A = 2$) for a given thickness of the porous layer ($x_P = 0.1$).

Figure 7(a) displays the average wall Nusselt and Sherwood numbers as a function of the Darcy number. The average mass transfer is constant at the low Darcy numbers corresponding to very impermeable porous layers. It increases significantly at high Da values (roughly by a factor of 4) in agreement with the observations of the previous section. The transition between these extreme values of Sh takes place over about four decades of Da numbers ranging between 10^{-7} and 10^{-3}.

This general variation of mass transfer with Da is expected. It is similar to what has already been observed for heat transfer when only the thermal component of the buoyancy force is present (Le Breton et al., 1991).

The variation of the Nusselt number is very different. It is possible to observe a global enhancement of the heat transfer from the low to the high Darcy number domain, but the increase is limited (only about 30 percent). The Nusselt number varies approximately in the same range of Da as the Sherwood number, but the main feature is that it does not vary monotonically and exhibits a significant minimum. This result is not intuitively expected since the permeability increase should result in a better penetration of the flow in the porous layer and finally in the enhancement of the overall heat transfer.

In order to illustrate the relation between the flow structure and the heat transfer characteristics, streamlines are represented

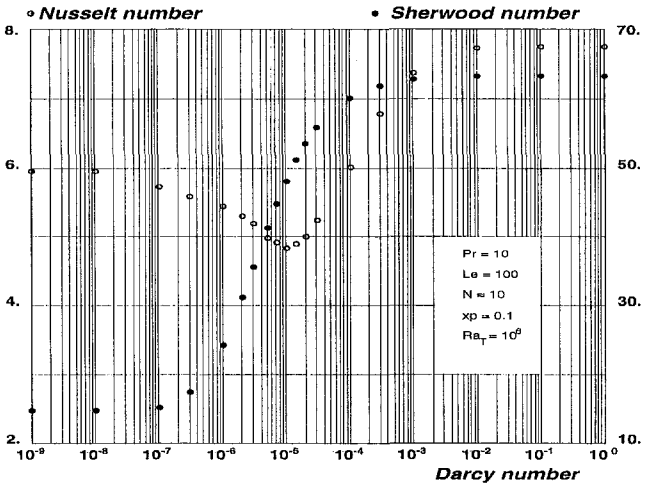

Fig. 7(a) Influence of the Darcy number on the average heat and mass transfer. ($Ra_T = 10^6$; Pr = 10; Le = 100; $N = 10$; $A = 2$; $x_P = 0.10$.)

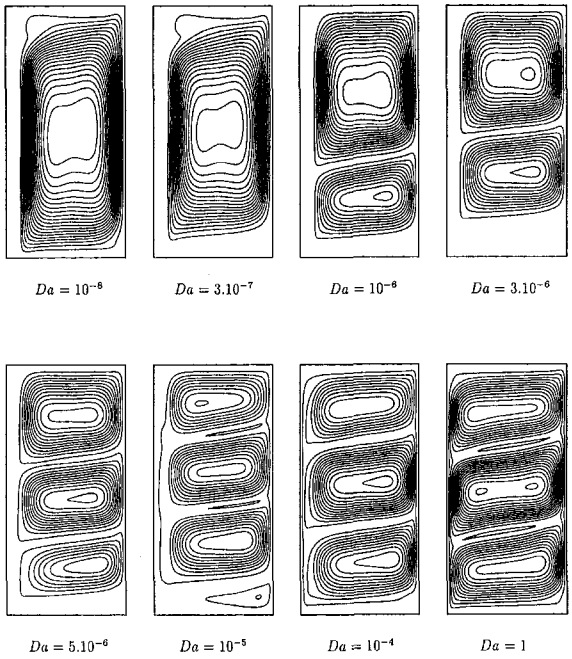

Fig. 7(b) Flow structure at different Darcy numbers ($\psi_{max} = 1.30$; $\Delta\psi = 0.065$). ($Ra_T = 10^6$; Pr = 10; Le = 100; $N = 10$; $A = 2$; $x_P = 0.10$.)

in Fig. 7(b) for different values of the Darcy number. To get a comparative idea of the flow intensity, a common value of the maximum stream function ψ_M is chosen, corresponding to the maximum of ψ for all the presented simulations so that the $\Delta\psi$ is the same for all the graphs. The results clearly show that the major difference between the low and high Da solutions is not only the intensity but the structure of the flow, ranging from a monocellular regime at $Da = 10^{-8}$ to a multicellular flow at Da = 1. Between these extreme situations the variation of the flow structure, when Da increases, shows two successive stages. First, a reorganization of the flow structure from one to three cells, to be compared to the decrease in Nusselt number. Then, the flow penetration in the porous layer increases without change of the flow structure, corresponding to the increase of the heat transfer.

The interpretation and the conditions of existence of the minimum are not well understood so far and a more complete analysis has to be performed on the basis of a more detailed parametric study. The formation of multicellular regimes has already been observed in many previous studies on thermosolutal natu-

ral convection in fluid enclosures at high Lewis numbers. It has been shown to appear for sufficiently high thermal Rayleigh numbers and moderate buoyancy ratios, but the range of transition has still to be determined (e.g., Gobin and Bennacer, 1996). In order to assess the observed behavior in other situations, the next section presents the sensitivity of the results to the variation of the thermal Rayleigh (Grashof) number.

V.2 Influence of the Thermal Rayleigh Number. Among the many parameters of the problem, we have chosen to analyze the influence of the thermal fluid Rayleigh number for different values of the Darcy number. Three values of the Rayleigh numbers are considered (for Pr = 10): $Ra_T = 10^5$, 10^6, and 10^7, corresponding to the same solutal Rayleigh numbers as in Section IV ranging between 10^8 and 10^{10}.

For all simulations the variations of the Sherwood and Nusselt numbers with Da have the same characteristics as those discussed in the previous section:

1 The continuous and significant increase of mass transfer in the domain of intermediate permeabilities (Fig. 8(*a*))

2 The existence of a heat transfer minimum in the same domain (Fig. 8(*b*))

The relative importance of the overall increase of Nu or Sh with Da is more significant at the higher values of the thermal Rayleigh number (for the Sherwood number it is about a factor of 7 at $Ra_T = 10^7$ and 3 at $Ra_T = 10^5$). Moreover, it may be noticed that the Da range for the variation of Sh or the position

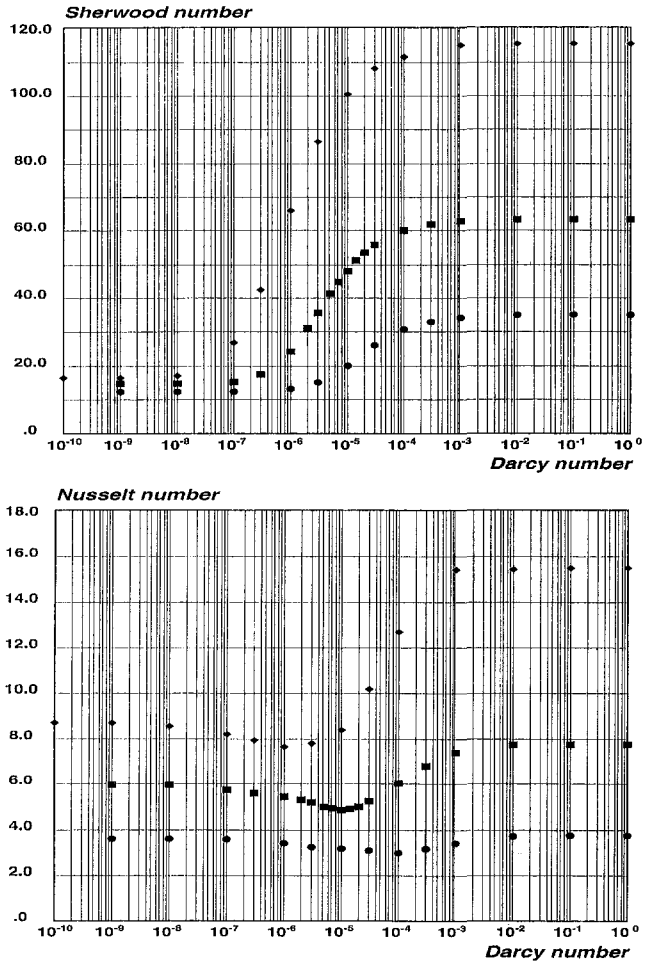

Fig. 8 Variation of the average (*a*) mass transfer and (*b*) heat transfer with the Darcy number. (●: $Ra_T = 10^5$; ■: $Ra_T = 10^6$; ♦: $Ra_T = 10^7$; Pr = 10; Le = 100; N = 10; A = 2; x_P = 0.10.)

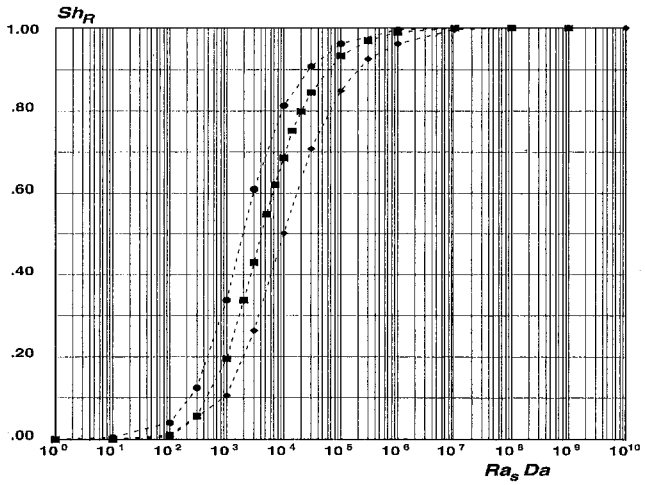

Fig. 9 Variation of the reduced mass transfer with the group $Ra_s Da$. (●: $Ra_T = 10^5$; ■: $Ra_T = 10^6$; ♦: $Ra_T = 10^7$; Pr = 10; Le = 100; N = 10; A = 2; x_P = 0.10.)

of the Nu minimum is shifted towards the higher Darcy numbers as Ra_T increases.

Concerning the Sherwood number dependence on Ra_T, it should be first emphasized that in the low Da range Sh increases from roughly 12 to 16 (a 30 percent increase) for a factor of 10^2 on Ra_T. However, in the range of high permeabilities Sh varies from about 35 to 115 (more than a factor of 3). A second feature of the results displayed in Fig. 8 is that the Da domain where the variation of Sh (or Nu) takes place has a roughly constant width (approximately four decades) but is shifted towards lower values of Da at large Ra_T (centered around 10^{-5} at $Ra_T = 10^7$ and 3×10^{-4} at $Ra_T = 10^5$).

This observation appears more clearly in the representation given in Fig. 9 where the mass transfer results, in terms of the relative variation of the Sherwood number over the Da range, are displayed as a function of the dimensionless group Ra_S Da:

$$Sh_R = \frac{Sh - Sh_{min}}{Sh_{max} - Sh_{min}}$$

The use of this dimensionless group is intended to recognize the primary influence of the solutal Rayleigh number on mass transfer in solutally dominated double diffusive convection (recall that $N = 10$ in this analysis). It is also intended to introduce a parameter which would be relevant if the whole cavity were filled with the porous medium, that is, the modified solutal Rayleigh number. Figure 9 clearly shows the similarity of the Sh variations at different Ra_T, the slope of the curves being identical in the range of significant increase. The location of the center of the corresponding Da domain still shows a clear dependence on Ra_S, but the graphs are fairly centro-symmetrical with respect to the position corresponding to $Sh_R = 0.5$. In terms of $Ra_S Da$, a good correlation for this location is obtained from our numerical results:

$$(Ra_S\ Da)_0 \approx 4.5\ Ra_S^{1/3}. \quad (9)$$

This gives a possibility of correlating the overall evolution of the Sherwood number with Da depending on the solutal fluid Rayleigh number. Indeed, it has been seen in Section IV that mass transfer in the high permeability range (the limit of fluid behavior) could be described by an expression derived from the classical scaling laws, providing a relevant estimation of Sh_{max}:

$$Sh_{max} = 0.35\ Ra_S^{1/4}. \quad (10)$$

If we now use the analysis presented in the previous section

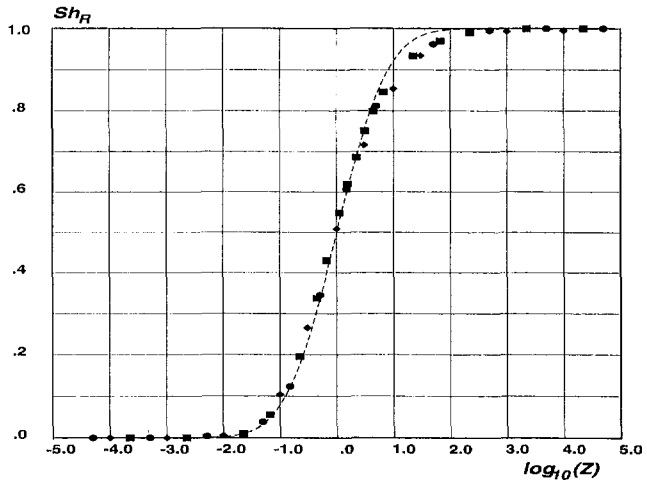

Fig. 10 Variation of the reduced mass transfer with the reduced variable $Z = 0.22\ \mathrm{Da}\ \mathrm{Ra}_S^{2/3}$. (●: $\mathrm{Ra}_T = 10^6$; ■: $\mathrm{Ra}_T = 10^6$; ♦: $\mathrm{Ra}_T = 10^7$; solid line: erf [$\log_{10}(Z)$]; Pr = 10; Le = 100; N = 10; A = 2; x_P = 0.10.)

for determining the Sherwood number in the low permeability limit (given A, x_P, and Ra_S, Eqs. (7) and (8)), it is possible to analytically determine the value of $\mathrm{Sh}_{\min}$.

Finally, considering the symmetry of the Sh_R curves and the similarity with the error function erf(Z), we may propose a simplified model of the Sherwood number dependance for a large range of Da, Ra_S, A, and x_P, provided that the double diffusive process is laminar and is dominated by the solutal component of the buoyancy force:

$$\mathrm{Sh}_R = \mathrm{erf}\,[\log_{10}(Z)], \qquad (11)$$

where

$$Z = \frac{\mathrm{Ra}_S\,\mathrm{Da}}{(\mathrm{Ra}_S\,\mathrm{Da})_0} = 0.22\ \mathrm{Da}\ \mathrm{Ra}_S^{2/3}.$$

The representation of the expression (11) given on Fig. 10 shows that such a correlation allows to cluster the numerical results obtained over the Ra_S range considered in this study. Let us insist that this analysis is limited to the domain of dominating solutal buoyancy force and high Lewis numbers. The range of validity of such an approach has still to be determined by a closer analysis of the influence of N, which has not been covered by the present study.

VI Conclusion

This paper represents a first approach to the problem of thermosolutal natural convection in a partially porous enclosure. The numerical results confirm the definite influence of the presence of an even relatively thin porous layer on heat and mass transfer in such a geometry. The permeability of the porous matrix is seen to be a parameter of first importance. Although the boundary conditions are somewhat different from the actual conditions met in solidification processes, it is possible to conclude that the formation of a columnar growth layer significantly affects the transfers and thus the overall dynamics of the process.

As an extension of this study it is necessary to perform a more systematical analysis of the influence of other important parameters, such as the buoyancy ratio or the aspect ratio, which are presently the subjects of a current investigation by the authors. Moreover, it is particularly relevant to take into account some specific aspects of the porous structure used to model the dendritic layer. The analysis of the permeability anisotropy and of the nonhomogeneous porosity field are presently studied by the authors.

Acknowledgments

The calculations have been performed on the Cray C98 of the National Computer Center of CNRS (IDRIS) with the support of the SPI Departement of CNRS under project 96-0336. The authors wish to gratefully thank Eric ARQUIS (University of Bordeaux) for providing detailed numerical results in the validation phase of this work. One of us (J.-P. Songbe) acknowledges the research fellowship from DSPT8 of the French Ministry of Research.

References

Arquis, E., and Caltagirone, J.-P., 1984, "Sur les Conditions Hydrodynamiques au Voisinage d'une Interface Milieu Fluide-Milieu Poreux: Application à la Convection Naturelle," *C. R. Acad. Sc.*, Vol. 299-II, pp. 1–4.

Beavers, G. S., and Joseph, D. D., 1967, "Boundary Conditions at a Naturally Permeable Wall," *J. Fluid Mech.*, Vol. 30, pp. 197–207.

Beavers, G. S., Sparrow, E. M., and Magnuson, R. A., 1970, "Experiments on Coupled Parallel Flows in a Channel and a Bounding Porous Medium," *Trans. of ASME Journal of Basic Engineering*, Vol. 92, pp. 843–848.

Beavers, G. S., Sparrow, E. M., and Masha, B. A., 1974, "Boundary Condition at a Porous Surface Which Bounds a Fluid Flow," *AIChE Journal*, Vol. 20-3, pp. 596–597.

Beckermann, C., Ramadhyani, S., and Viskanta, R., 1987, "Natural Convection Flow and Heat Transfer Between a Fluid Layer and a Porous Layer Inside a Rectangular Enclosure," ASME JOURNAL OF HEAT TRANSFER, Vol. 109, pp. 363–370.

Beckermann, C., Viskanta, R., and Ramadhyani, S., 1988, "Natural Convection in Vertical Enclosures Containing Simultaneously Fluid and Porous Layers," *J. Fluid Mech.*, Vol. 186, pp. 257–284.

Bejan, A., 1995, *Convection heat transfer*, 2nd ed., John Wiley & Sons Inc., NY.

Bénard, C., Bénard, R., Bennacer, R., and Gobin, D., 1996, "Melting Driven Thermo-Haline Convection," *Phys. Fluid A*, Vol. 8, pp. 112–130.

Bergman, T. L., and Srinivasan, R., 1989, "Numerical Simulation of Soret-Induced Double Diffusion in an Initially Uniform Concentration Binary Liquid," *Int. J. Heat Mass Transfer*, Vol. 32, pp. 679–687.

Brinkman, H. C., 1947, "A Calculation of the Viscous Force Exerted by a Flowing Fluid on a Dense Swarm of Particles," *Appl. Sci. Res.*, Vol. A1, pp. 27–34.

Chen, F., and Chen, C. F., 1992, "Double-Diffusive Fingering Convection in a Porous Medium," *Int. J. Heat Mass Transfer*, Vol. 36-3, pp. 793–807.

Ettefagh, J., Vafai, K., and Kim, S. J., 1991, "Non-Darcian Effects in Open-Ended Cavities Filled With a Porous Medium," ASME JOURNAL OF HEAT TRANSFER, Vol. 113, pp. 747–756.

Givler, R. C., and Altobelli, S. A., 1994, "A Determination of the Effective Viscosity for the Brinkman-Forchheimer Flow Model," *J. Fluid Mech.*, Vol. 258, pp. 355–370.

Gobin, D., and Bennacer, R., 1996, "Cooperating Thermosolutal Convection in Enclosures: 1. Scale Analysis and Mass Transfer; 2. Heat Transfer and Flow Structure," *Int. J. Heat Mass Transfer*, Vol. 39-13, pp. 2671–2681; pp. 2683–2697.

Goyeau, B., Songbe, J.-P., and Gobin, D., 1996, "Numerical Study of Double-Diffusive Natural Convection in a Porous Cavity Using the Darcy-Brinkman Formulation," *Int. J. Heat Mass Transfer*, Vol. 39-7, pp. 1363–1378.

Goyeau, B., Benihaddadene, T., Gobin, D., and Quintard, M., 1997, "Averaged Momentum Equation for Interdendritic Flow During Solidification," *Transport in Porous Media*, Vol. 28, pp. 19–50.

Kaviany, M., 1995, *Principles of Heat Transfer in Porous Media*, Springer-Verlag Inc., NY.

Koplik, J., Levine, H., and Zee, A., 1983, "Viscosity Renormalization in the Brinkman Equation," *Phys. Fluids*, Vol. 26-10, pp. 2864–2870.

Lauriat, G., and Prasad, V., 1987, "Natural Convection in a Vertical Porous Cavity: a Numerical Study for Brinkman-Extended Darcy Formulation," ASME JOURNAL OF HEAT TRANSFER, Vol. 109, pp. 688–696.

Le Breton, P., Caltagirone, J. P., and Arquis, E., 1991, "Natural Convection in a Square Cavity With Thin Porous Layers on its Vertical Walls," ASME JOURNAL OF HEAT TRANSFER, Vol. 113, pp. 892–898.

Lundgren, T. S., 1972, "Slow Flow Through Stationary Random Beds and Suspensions of Spheres," *J. Fluid Mech.*, Vol. 51, pp. 273–299.

Neale, G., and Nader, W., 1974, "Practical Significance of Brinkman's Extension of Darcy's Law: Coupled Parallel Flows Within a Channel and a Bounding Porous Medium," *The Canadian Journal of Chemical Engineering*, Vol. 52, pp. 475–478.

Nield, D. A., 1991, "The Limitation of the Brinkman-Forchheimer Equation in Modeling Flow in a Saturated Porous Medium and at an Interface," *Int. J. Heat Fluid Flow*, Vol. 12, pp. 269–272.

Nield, D. A., and Bejan, A., 1992, *Convection in porous media*, Springer-Verlag New York Inc., NY.

Ochoa-Tapia, J. A., and Whitaker, S., 1995, "Momentum Transfer at the the Boundary Between a Porous Medium and a Homogeneous Fluid—I. Theoretical Development," *Int. J. Heat Mass Transfer*, Vol. 38, pp. 2635–2646.

Prescott, P., and Incropera, F. P., 1996, "Convection Heat and Mass Transfer in Alloy Solidification," *Adv. in Heat Transfer*, Vol. 28, pp. 231–338.

Saffman, P. G., 1971, "On the Boundary Condition at the Surface of a Porous Medium," *Studies in Applied Mathematics L*, Vol. 2, pp. 93–101.

Sahraoui, M., and Kaviany, M., 1992, "Slip and No-Slip Velocity Boundary Conditions at the Interface of Porous, Plain Media," *Int. J. Heat Mass Transfer,* Vol. 35-4, pp. 927–943.

Sathe, S. B., Lin, W. Q., and Tong, T. W., 1988, "Natural Convection in Enclosures Containing an Insulation With Permeable Fluid-Porous Interface," *Int. J. Heat Fluid Flow,* Vol. 9-4, pp. 389–395.

Song, M., and Viskanta, R., 1994, "Natural Convection Flow and Heat Transfer Within a Rectangular Enclosure Containing a Vertical Porous Layer," *Int. J. Heat Mass Transfer,* Vol. 37-16, pp. 2425–2438.

Turki, S., and Lauriat, G., 1990, "An Examination of Two Numerical Procedures for Natural Convection in Composite Enclosures," *Numerical Heat Transfer* proceedings of AIAA-ASME Thermophysics and Heat Transfer Conference, HTD No. 130, pp. 107–113.

Vafai, K., and Kim, S. J., 1990, "Fluid Mechanics of the Interface Region Between a Porous Medium and a Fluid Layer–An Exact Solution," *Int. J. Heat Fluid Flow,* Vol. 11-3, pp. 254–256.

Vafai, K., and Kim, S. J., 1995, "On the Limitations of the Brinkman-Forchheimer-Extended Darcy Equation," *Int. J. Heat Fluid Flow,* Vol. 16-1, pp. 11–15.

Webster, I. T., Norquay, S. J., Ross, F. C., and Wooding, R. A., 1996, "Solute Exchange by Convection Within Estuarine Sediments," *Estuarine, Coastal and Shelf Science,* Vol. 42, pp. 171–183.

Two-Phase Heat Dissipation Utilizing Porous-Channels of High-Conductivity Material

G. P. Peterson
Associate Vice Chancellor and Executive Associate Dean of Engineering
GPP5386@teesmail.tamu.edu
Fellow ASME.

C. S. Chang[1]

Department of Mechanical Engineering,
Texas A&M University,
College Station, TX 77843-3123

The results of an experimental study of two-phase heat dissipation in high-conductivity porous channel heat sinks are presented. Porous channels of various sizes were fabricated using sintered copper particles inside rectangular copper channels with base dimensions of 25 mm by 25 mm, either 3 or 10 mm in height. The experiments were conducted using subcooled water as the working fluid and test conditions ranged from an inlet temperature of 85 to 95°C, inlet pressures of 1.062 to 1.219 bars, flow rates of 22.5 to 150 ml/min, and heat fluxes of 10 to 25 W/cm². The experimental results were compared to the results predicted using a previously developed numerical model. For water with inlet subcooling in the range of 6.6 to 10.8°C, heat transfer coefficients for open channel flow were increased from 1.25 to 1.94 W/cm²°C to 1.79 to 3.33 W/cm²°C, or a 43 to 142 percent improvement through the use of porous channels with mean particle diameters of 0.97, 0.54, 0.39, or 0.33 mm. The results indicate that the high thermal conductivity of the porous material and the large solid-fluid contact area combine to create a highly effective, two-phase heat sink, which may provide an effective mechanism for cooling high heat flux microelectronics.

Introduction

Advances in modern electronics have resulted in dramatic increases in the level of heat fluxes that must be removed for reliable operation of electronic packages. The packages typically require that operating temperatures be maintained below 130°C and temperature nonuniformity be minimized. With chip heat flux levels of 100 W/cm² or more for mainframe computers by the year 2000 (Jacobs and Hartnett, 1991), conventional single-phase heat transfer techniques utilizing natural or forced convection will clearly not be capable of meeting the future requirements. For this reason, considerable research on new cooling technologies is currently underway (Peterson and Ortega, 1990).

Typically, forced single-phase convective cooling exhibits a nearly linear increase in stream temperature with increasing heat loads. This, in turn, leads to greater surface temperature gradients. Because of the large increases in heat transfer area, the use of channels packed with high-conductivity porous or fibrous material has been proposed as an effective alternative for enhancing these forced single-phase convective cooling systems (Koh and Colony, 1974; Kuo and Tien, 1981; Hwang and Chao, 1994). Alternatively, the use of phase-change cooling presents a technique for heat rejection that offers several inherent advantages over single-phase cooling. Most important among these is the more uniform surface temperatures that can be achieved through boiling and evaporation with surface temperatures only a few degrees higher than the fluid saturation temperature. In addition, the latent heat exchange provides the capability of high heat flux dissipation with very low flow rates.

Using this concept, an investigation to determine the feasibility of using high-conductivity porous channels with two-phase cooling as high efficiency heat sinks for microelectronics was conducted. Previously, a two-phase mixture model for two-phase flow in porous media was developed by Wang and Beckermann (1993, 1994); Darcy's law was applied for both liquid and vapor phases, and local-thermodynamic equilibrium between phases was assumed. In addition, governing equations and boundary conditions which were valid throughout the entire domain were derived based on phase-averaged properties of the fluid, which would tremendously simplify computational tasks. Based on the model developed by Wang and Beckermann (1993, 1994), Peterson and Chang (1997) accounted for the heat transfer from the solid phase to the fluid (i.e., nonlocal thermodynamic equilibrium between phases) in their two-dimensional numerical model to provide an analytical tool through which the two-phase flow and heat transfer characteristics in these high-conductivity porous-channel heat sinks could be determined. The present experimental study focuses on verifying the predictions obtained in this numerical model and on the determination of the feasibility of the concept.

Experimental Apparatus and Procedure

The experimental test facility for measuring the thermal characteristics of porous channels fabricated from sintered copper beads is shown in Fig. 1. As illustrated, deionized water was pumped from a reservoir and circulated through the test loop by a $\frac{1}{5}$ HP magnetically coupled centrifugal pump. Exiting the pump, the main stream of water was split: a portion passed through a 7 μm in-line filter before entering the test section, and the remaining amount returned to the reservoir through a by-pass loop. The amount of water entering the test section was determined using a flowmeter, and then it was heated to the desired temperature at the inlet of the test section by an electrical resistance heater. Exiting the test section, the fluid passed through a cooling coil to condense the vapor, and then into the reservoir where the flow was remixed with the by-passed liquid. To control the liquid pressure at the inlet of the test section, a liquid-vapor mixture was maintained in the pressure control tank by adjusting the tank temperature.

The test section, which is shown in Fig. 2, consisted of a porous channel, an inlet flow channel upstream of the test channel, and an outlet flow channel immediately downstream. The porous channel was fabricated by sintering copper beads inside the center section of a rectangular copper channel with base dimensions of 25 mm by 25 mm. Channels of two cross-sec-

[1] Researcher, Energy and Resources Laboratories, ITRI, Taiwan.

Contributed by the Heat Transfer Division for publication in the JOURNAL OF HEAT TRANSFER. Manuscript received by the Heat Transfer Division August 29, 1996; revision received September 23, 1997; Keywords: Multiphase Flows; Thermocapillary Flows; Thin Film Flow. Associate Technical Editor: K. Vafai.

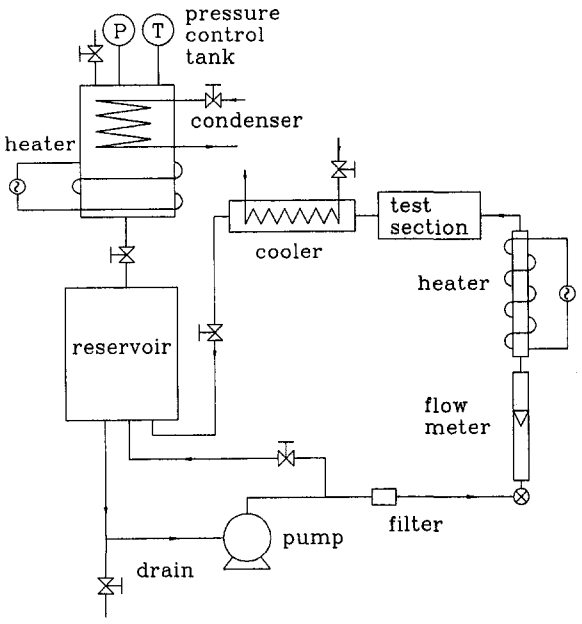

Fig. 1 Experimental system

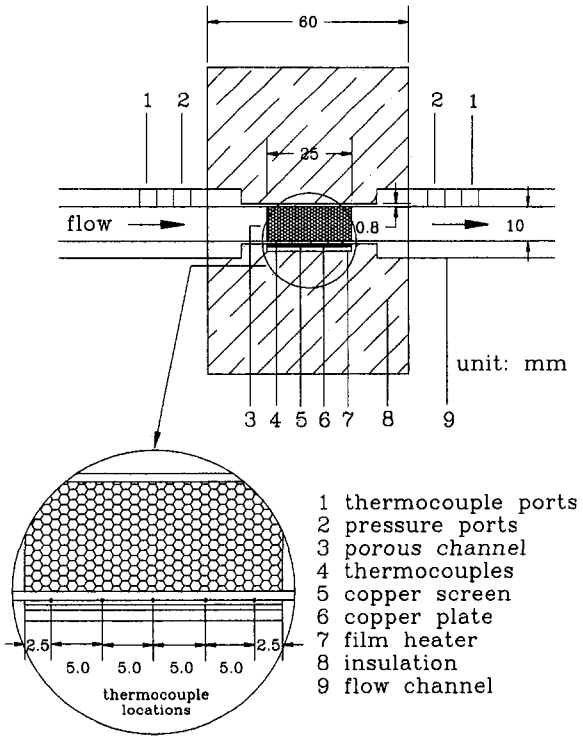

Fig. 2 Test section

tional flow areas were evaluated, 25 mm × 10 mm and 25 mm × 3 mm, and the porous material in both test configurations was 60 mm long. The inlet and outlet flow channels were each 200 mm long and were made of Polycarbonate, with the same internal flow dimensions as the test section. Once fabricated, the porous channel was fitted between the two flow channels and attached mechanically. Each flow channel was instrumented with a pressure transducer and a T-type shield thermocouple, located 35 mm and 65 mm apart from the end section of the copper particles in the channel, respectively. A 0.14 mm thick film heater (25 mm × 25 mm base, A_b) of 18 omhs was used along with a 0–110 V a.c. variac to simulate a constant heat flux condition at the bottom wall of the porous channel. Five T-type thermocouples, 0.127 mm diameter, were evenly spaced along the flow direction at the bottom wall centerline, to measure the wall temperature variation in the flow direction. The arrangement of the thermocouples is shown in Fig. 2.

To enhance the thermal contact between the heated wall and the heater, a layer of 100-mesh size copper screen, a 0.4 mm thick copper plate, and the film heater were bonded successively against the thermocouples using a high thermal conductivity epoxy adhesive (OMEGABOND 200). A series of dry tests for each test article without filling water in the test section were conducted in advance to find the steady-state relationship between the net heat loss and the measured temperature difference in the heater wall and the ambient. In these tests the energy gain of the air in the channel was neglected and the net heat loss was approximately equivalent to the heat input. Hence, during the normal tests, the amount of heat loss from the test

Nomenclature

A_b = base area
c = specific capacity
d_p = particle diameter
g = gravitational constant
H = volumetric enthalpy, $H = \rho_l s h_l + \rho_v(1 - s)h_v - \rho_l h_{vsat}$
h = enthalpy
h_{fg} = latent heat
h_{sf} = heat transfer coefficient
K = permeability
k = thermal conductivity
k^* = effective thermal conductivity
$k_{rl}(s)$ = relative permeability for liquid phase, $k(s)_{rl} = s$
$k_{rv}(s)$ = relative permeability for vapor phase, $k(s)_{rl} = 1 - s$
L = length
$\dot{m}$ = mass flow rate
P = pressure
Q'_{sf} = volumetric heat transfer rate from the solid phase to the fluid
q = heat flux
Re_K = Reynolds number based on permeability, $u\sqrt{K}/\nu$
Re_p = Reynolds number based on particle diameter, ud_p/ν
s = liquid saturation, the volume fraction of the void space occupied by liquid
T = temperature
u = mixture superficial velocity component in x-direction
$\mathbf{u}$ = mixture superficial velocity vector, $\rho\mathbf{u} = \rho_l\mathbf{u}_l + \rho_v\mathbf{u}_v$
x, y = space coordinates

Greek Symbols

Γ = effective diffusion coefficient, $\Gamma = [\varphi s k_l^* + \varphi(1 - s)k_v^*]dT_f/dH$
γ = two-phase advection correlation, $\gamma = \lambda_l(s)[1 + \rho_v(1 - s)/(\rho_l s)]$
λ_l = liquid phase relative mobility, $\lambda_l(s) = [k_{rl}(s)/\nu_l]/[k_{rl}(s)/\nu_l + k_{rv}(s)/\nu_v]$
λ_v = vapor phase relative mobility, $\lambda_v(s) = [k_{rv}(s)/\nu_v]/[k_{rl}(s)/\nu_l + k_{rv}(s)/\nu_v]$
φ = porosity
μ = mixture viscosity, $\mu = [\rho_l s + \rho_v(1 - s)]/[k_{rl}(s)/\nu_l + k_{rv}(s)/\nu_v]$
ν = kinetic viscosity
ρ = mixture density, $\rho = \rho_l s + \rho_v(1 - s)$
ρ_k = mixture kinetic density, $\rho_k = \rho_l\lambda_l + \rho_v\lambda_v$

Subscripts

f = fluid
in = inlet
l = liquid
s = solid
sat = saturated state
v = vapor

Table 1 Physical parameters and dimensions of the porous channels

Test article #	Mean diameter d_p (mm)	Porosity φ	Permeability K×10^{10} (m^2)	Internal dimension of the porous channel W(mm)×H(mm)×L(mm)
1	0.97	0.40	5.10 (9.29)*	25×10×25
2	0.54	0.41	1.19 (2.88)*	25×10×25
3	0.39	0.35	0.714 (0.762)*	25×3×25
4	0.33	0.34	0.501 (0.545)*	25×3×25
5	empty channel	-	-	25×10×25

*calculated from Carman-Kozeny equation (Nield and Bejan, 1992):

$$K = \frac{d_p^2 \varphi^3}{180(1-\varphi)^2}$$

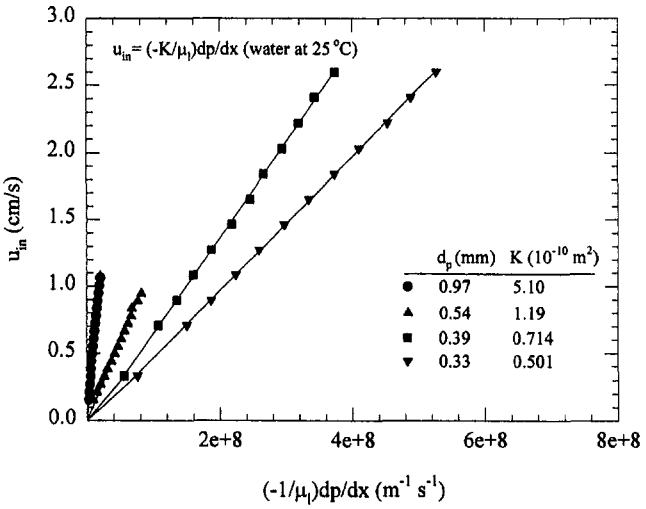

Fig. 3 The quantity $(-1/\mu_l)(dp/dx)$ versus u_{in} for the porous channels

section to the ambient was evaluated by referring to the temperature difference between the heater wall and the ambient.

Porous Media and Test Articles. Table 1 illustrates the physical parameters and dimensions of the test articles. Copper beads (99.95 percent purity, 10–50 mesh sizes) were first separated into four different size ranges (20–22, 30–32, 42–44, and 48–50 mesh sizes) using a set of stainless-steel screens of standard sizes. The particles in each group were measured randomly 200 times to calculate the mean diameter, d_p, before they were sintered into place in the copper channel. Four test articles of porous channels and one empty channel were fabricated for the present experimental investigation and comparison. The porosity, φ, of each test article was evaluated using the expression, $\varphi = (V - V_s)/V$, where V is the volume of the channel section occupied by the porous media, and V_s is the volume of the porous media (determined by dividing the weight of the porous media by its density). Table 1 shows the porosities of the four test articles which fell into two narrow ranges, 0.40–0.41 and 0.34–0.35, for the two different channel dimensions, respectively.

The permeability of the porous channel was determined from the adiabatic data by measuring the pressure drop of a water column across the porous channel for a range of flow rates. The pressure drop was monitored by a differential pressure transmitter (0.013 bar full range) or calculated from the two absolute pressure transducers (2.068 bar full range), depending on the scale of the pressure drop. The pressure drop contribution of the empty channel section, from each end of the porous section to the location of the pressure tap on its corresponding side, was found to be too small to be considered. Darcy's equation was used to correlate the data and calculate the permeability because of its validity for the present study ($u_l\sqrt{K}/\nu_l < 1$). As shown in Fig. 3, the inlet velocity, u_{in}, is nearly linearly proportional to the quantity $(-1/\mu_l)(dP/dx)$, and the slope of the regression line approximates the permeability of the porous media. The permeabilities determined in this way were found to be somewhat smaller than those predicted using the Carman-Kozeny equation (Nield and Bejan, 1992), as shown in Table 1. Because the copper particles, sintered in each of the test articles, were not exactly of the same size, they were supposed to pack more closely than those of a uniform size, and this resulted in a lower permeability than the one predicted.

Data Acquisition. Two pressure transducers (2.068 bar full range) connected to the pressure taps of the flow channels were used to record the absolute inlet and outlet fluid pressures. The output signals of the pressure transducers as well as the temperature readings of the thermocouples were transmitted from the test section to a 3497A data acquisition system. The AC voltage across the film heater and the current through it were used to calculate the electric heat input. Both were measured by an HP 3478A digital multimeter.

For normal tests, the electrical power to the film heater was adjusted to the desired level using a variac, while the flow rate, inlet temperature, and inlet pressure of water were simultaneously maintained at the desired conditions. Once the flow conditions were stabilized, typically 30–40 minutes, the porous channel heat sink would reach steady state within 10 minutes. The raw data were collected every 20 seconds, and steady-state was assumed to have been reached when the variation in the wall temperature measurements were within ±0.2°C over a period of 2 minutes.

Measurement Uncertainties. Errors in temperature measurements with thermocouples were estimated to be less than 0.2°C. The uncertainty associated with the absolute pressure measurements was estimated to be less than 0.4 percent (0.004 bar), and the uncertainty with the differential pressure measurements by the differential pressure transmitter was less than 1 percent (0.00013 bar). The maximum error in flow rate measurements calibrated by the weighing method was estimated to be less than 6 percent at a volumetric flow rate of 10 ml/min.

For normal tests, the net heat input to the test section was calculated as the difference between the electric heat input and the heat loss. The method to evaluate the heat loss has been described in the previous section. The maximum heat loss was estimated to be less than 7 percent (11 W) at an electric heat input of 170 W and a temperature difference of 125°C between the heater wall and the ambient. In addition, by performing a series of single-phase experiments, the difference in the net heat input to the test section and the enthalpy increase in the cooling water across it was found to be within ±5 percent. Throughout this experimental study, the heat flux imposed to the porous channel was calculated based on the net heat input and the heater area, A_b.

Numerical Analysis

The major assumptions and simplifications in the numerical analysis are: (1) the porous medium is rigid, uniform, isotropic and fully saturated with fluid; (2) Darcy's law is applicable to both the liquid and vapor phases, and the capillary pressure is neglected because of lack of sufficient information; (3) the thermal diffusion and thermal dispersion due to the microstructure of the solid matrix are neglected, hence, the effective thermal conductivity of each phase is assumed to be its intrinsic value; (4) the heat transfer between the solid phase and the fluid is considered and can be modeled by the relation (Wakao

and Kaguei, 1982), $h_{sf} = k_l(2 + 1.1\ \mathrm{Pr}_l^{1/3}\ \mathrm{Re}_{p,l}^{0.6})/d_p$, in the single-phase region and by Rohsenow's pool boiling correlation (Carey, 1992) in the two-phase region; (5) the effect of pressure drop on the fluid saturation temperature is neglected, and the two-phase region is assumed to be isothermal at the saturation temperature corresponding to the inlet pressure; and (6) the thermophysical properties of the fluid are assumed to be constant at the same saturation state. Compared to the assumptions used in Wang and Beckermann's model (1993, 1994), capillary pressure was neglected, but a nonlocal thermodynamic equilibrium was employed in this study. The steady-state volume-averaged governing equations, which were valid throughout the entire domain, could be derived based on the two-phase mixture model (Wang and Beckermann, 1993, 1994). The major difference was that the energy conservations for the solid phase and the fluid were considered separately. Details of the numerical analysis can be found in a previous study (Peterson and Chang, 1997). The resulting governing equations for the mixture are as follows:

Continuity.

$$\nabla\cdot(\rho\mathbf{u}) = 0 \tag{1}$$

Momentum.

$$\mathbf{u} = -\frac{K}{\mu}(\nabla P - \rho_k\mathbf{g}) \tag{2}$$

Fluid Energy.

$$\nabla\cdot(\gamma\mathbf{u}H) = \nabla\cdot(\Gamma\nabla H) + \nabla\cdot\left[k_{rv}(s)\lambda_l(s)\frac{K(\rho_l - \rho_v)h_{fg}}{\nu_v}\mathbf{g}\right] + Q'_{sf} \tag{3}$$

Solid Phase Energy.

$$\nabla\cdot[(1-\varphi)k_s^*\nabla T_s] - Q'_{sf} = 0 \tag{4}$$

In the above equations and what follows, a quantity without a subscript is reserved for the mixture, and the subscripts l and v stand for liquid and vapor properties, respectively. In Eq. (1) ρ is mixture density which is a weighting function of the liquid saturation, s, and $\boldsymbol{u}$ is the superficial mixture velocity vector based on the total cross-sectional area of the fluid and the porous media. In Eq. (2), μ is the mixture viscosity, and P is the liquid pressure, which in this study is also equal to the vapor pressure in the two-phase region. Once the pressure field and the liquid saturation are solved, the individual phase velocity can be obtained by solving the Darcy's equation for each phase (Nield and Bejan, 1992). It should be noted that in Eq. (3), Q'_{sf} stands for the volumetric heat transfer rate from the solid phase to the fluid, and H is the volumetric enthalpy for the mixture (Wang and Beckermann, 1993). The derivations of the other variables or coefficients, ρ_k, μ, γ, Γ, and λ are similar to those proceeded by Wang and Beckermann (1993, 1994).

The fluid temperature and liquid saturation can be recovered from the volumetric enthalpy by the following relations (Wang and Beckermann, 1994):

$$T_f = \frac{H + \rho_l h_{\mathrm{vsat}}}{\rho_l c_l} \quad H \le -\rho_l h_{fg} \tag{5a}$$

$$T_f = T_{\mathrm{sat}} \quad -\rho_l h_{fg} < H < 0 \tag{5b}$$

$$T_f = T_{\mathrm{sat}} + \frac{H}{\rho_v c_v} \quad 0 \le H \tag{5c}$$

$$s = 1 \quad H \le -\rho_l h_{fg} \tag{6a}$$

$$s = \frac{H}{-\rho_l h_{fg}} \quad -\rho_l h_{fg} < H < 0 \tag{6b}$$

$$s = 0 \quad 0 \le H \tag{6c}$$

The appropriate boundary conditions for the two-dimensional system are summarized as follows:

At $x = 0$.

$$u = u_{\mathrm{in}} \tag{7a}$$

$$(1-\varphi)k_s^*\frac{\partial T_s}{\partial x} = 0 \tag{7b}$$

$$H = \rho_l(c_l T_{\mathrm{in}} - h_{\mathrm{vsat}}) \tag{7c}$$

At $y = 0$.

$$\frac{\partial P}{\partial y} = -\rho_k g \tag{8a}$$

$$-(1-\varphi)k_s^*\frac{\partial T_s}{\partial y} = q_s \tag{8b}$$

$$-\Gamma\frac{\partial H}{\partial y} + k_{rv}(s)\lambda_l(s)\frac{K(\rho_l - \rho_v)h_{fg}}{\nu_v}g = q_f \tag{8c}$$

where

$$q_s + q_f = q \tag{8d}$$

At $y = L_y$.

$$\frac{\partial P}{\partial y} = -\rho_k g \tag{9a}$$

$$(1-\varphi)k_s^*\frac{\partial T_s}{\partial y} = 0 \tag{9b}$$

$$\Gamma\frac{\partial H}{\partial y} - k_{rv}(s)\lambda_l(s)\frac{K(\rho_l - \rho_v)h_{fg}}{\nu_v}g = 0 \tag{9c}$$

At $x = L_x$.

$$(1-\varphi)k_s^*\frac{\partial T_s}{\partial x} = 0 \tag{10}$$

The set of the governing equations described above was solved simultaneously using a line-by-line procedure, which is a combination of Gauss-Seidel and the Tri-Diagonal Matrix algorithm. The criterion of convergence for P, T_s, and H was based on the normalized residual, as

$$\bar{R} = \frac{\sum_{\mathrm{nodes}P} |a_E\phi_E + a_W\phi_W + a_N\phi_N + a_S\phi_S + b - a_P\phi_P|}{\sum_{\mathrm{nodes}P} |a_P\phi_P|} \le 10^{-7}. \tag{11}$$

In addition, relative changes between successive iterations in mixture velocity fields, fluid and solid phase temperatures, and liquid saturations were all less than 10^{-5} when convergence was achieved.

The rectangular domain is divided into uniform control volumes. Staggered grids (Patankar, 1980) are used for velocity control volumes. The influence of grid sizes on the wall temperature distributions was examined while the size of the control volume (the volume in which variables were taken averaged) was kept larger than the particle size of the porous medium. Grid independence was declared when the maximum change in the wall temperature was less than 2 percent. Finally, grid sizes of 22 × 12 and 22 × 6 were chosen for channel heights of 10 and 3 mm, respectively.

Results and Discussion

In order to compare experimental data with numerical predictions for the heated wall temperature distribution of each test article, numerical calculations using the same measured permeability and test conditions (inlet velocity, temperature, and pres-

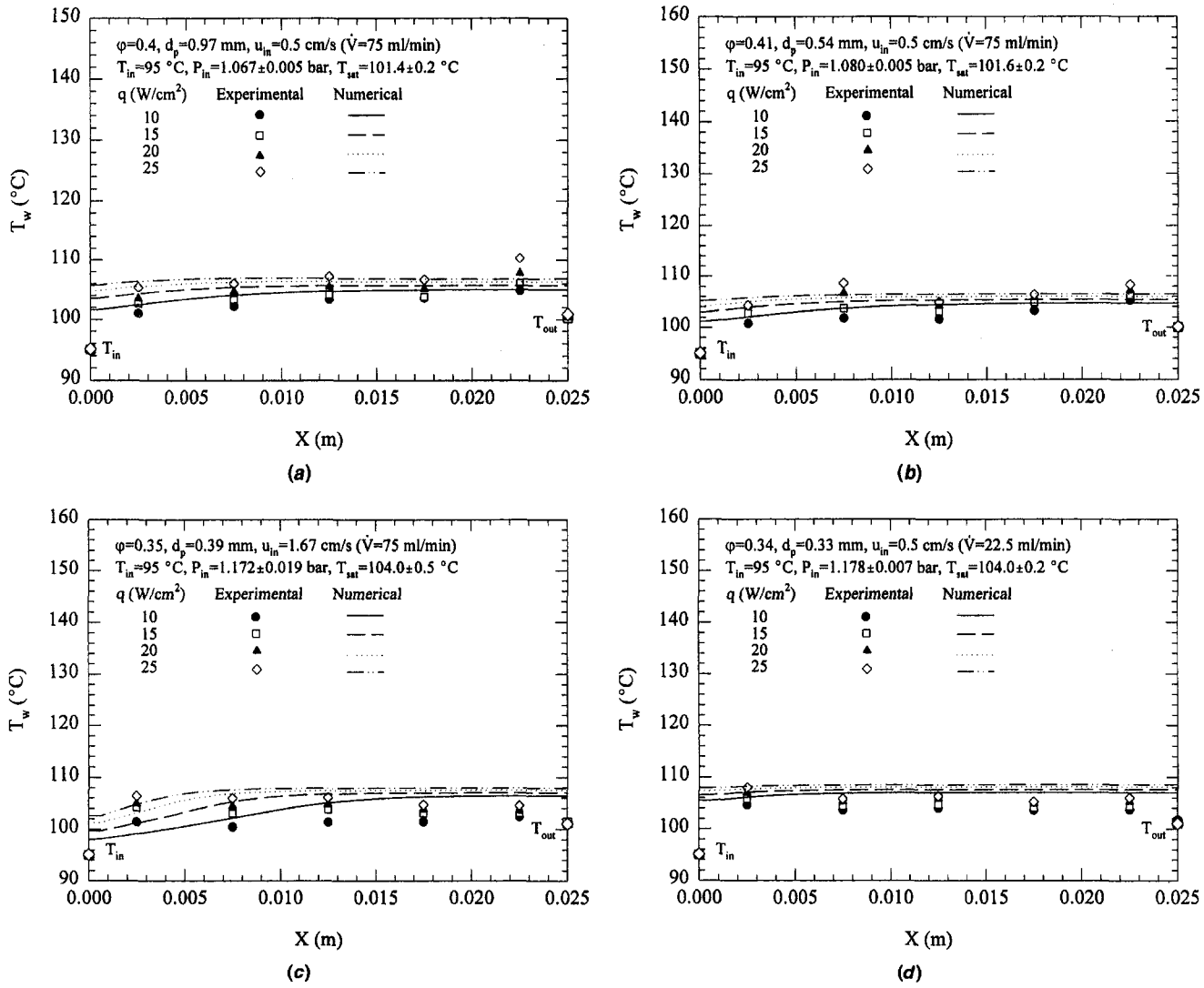

Fig. 4 Variation of heat flux on wall temperature distribution: (*a*) d_p = 0.97 mm; (*b*) d_p = 0.54 mm; (*c*) d_p = 0.39 mm; and (*d*) d_p = 0.33 mm.

sure) were performed. For Darcy's law to be applicable for the comparison, numerically calculated nodal values of the Reynolds numbers (Re_K, for both liquid and vapor phases) were examined to be less than 1 for all the ranges of test conditions. In this study, the test ranges were 10 to 25 W/cm^2 for heat flux, 22.5 to 150 ml/min for volumetric flow rate, 1.062 to 1.219 bars for inlet pressure, and 85 to 95°C for inlet temperature.

Variation of Heat Flux. For each test article, tests were performed for heat fluxes from 10 to 25 W/cm^2 by an increasing step of 5 W/cm^2, while the flow rate and inlet temperature were maintained constant. The inlet pressures were maintained within a very narrow range (±0.019 bar maximum throughout the experiments) for these cases, therefore, the mean value of the inlet pressures and the corresponding saturation temperature was used for numerical calculations.

The influence of the heat fluxes on the heated wall temperature distributions for the four porous channel test articles is shown in Figs. 4(*a*)–(*d*). As shown in each figure, both experimental data (including five wall temperatures and the inlet and the outlet fluid temperature measurements) and the corresponding numerical calculations are plotted for comparison. As shown, wall temperature increased with increases in the heat flux, and the temperature measurements are close to the numerical calculations for most of the cases. It should also be noted that the fluid outlet temperature corresponded closely to the saturation temperature (with errors within ±0.6°C) at the outlet pressure of the porous channel for each test.

Several other observations can be made from this comparison. First, as shown in Figs. 4(*a*) and 4(*b*), one or two hot spots on the heated wall of these porous channels were observed to form as the heat flux was increased. This phenomenon was most probably due to the sintering of nonuniform sized copper particles near the wall region, which resulted in a local blockage to the liquid flow at the wall. Second, for some cases where the bulk fluid pressure drop across the porous channel was large enough, decrease in the fluid saturation temperature due to the pressure drop in the flow direction was reflected in the wall temperature readings. For example, as shown in Fig. 4(*c*) for the porous channel comprised of 0.39 mm mean particle diameter spheres tested at an inlet velocity of 1.67 cm/s, the measured heated wall temperatures started to decrease from the beginning of the two-phase region along the flow direction when the heat flux exceeded 10 W/cm^2. The numerical model, however, did not account for this effect because of the aroused complexity and difficulty, hence, as shown, the numerical model predicted that the wall temperatures would remain quite uniform in the two-phase region. Figure 4(*d*) shows a similar trend for the porous channels of 0.33 mm diameter spheres. The bulk fluid pressure drops across the porous channel for the above cases ranged from 0.068 to 0.11 bar and the corresponding decreases

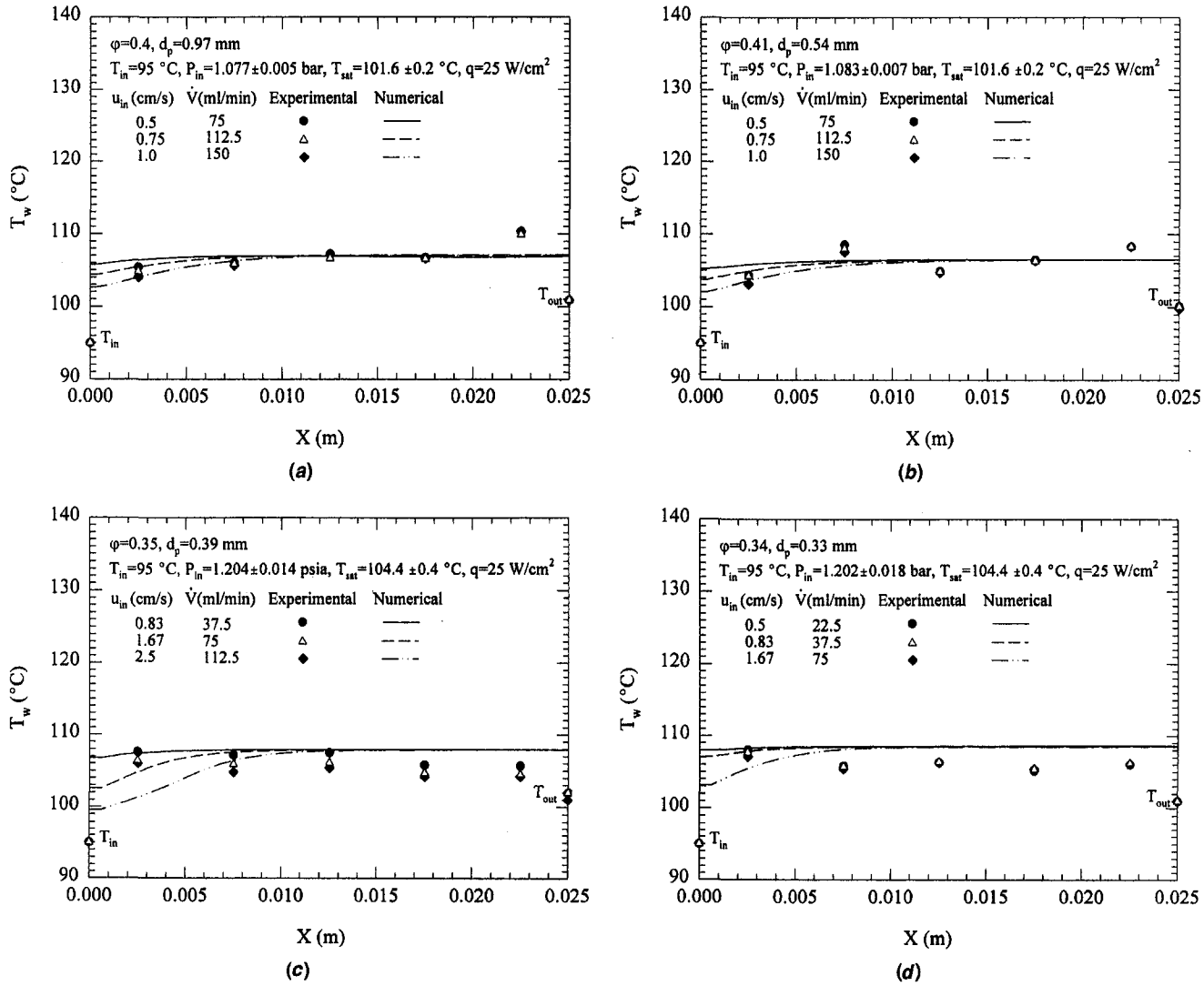

Fig. 5 Variation of inlet velocity on wall temperature distribution: (*a*) d_p = 0.97 mm; (*b*) d_p = 0.54 mm; (*c*) d_p = 0.39 mm; and (*d*) d_p = 0.33 mm.

in the saturation temperature are about 1.6 to 2.8°C. Alternatively, for porous channels of 0.97 and 0.54 mm tested at inlet velocities of 0.5 to 1.0 cm/s and heat fluxes up to 25 W/cm^2 (Figs. 4(*a*) and 4(*b*)), the bulk fluid pressure drops were less than 0.047 bar, therefore, no clear observation of this effect could be made.

Variation of Fluid Inlet Velocity. The fluid inlet velocity for each test article was varied to determine the effect on the heated wall temperature distribution. The maximum inlet velocity was limited to a reasonably acceptable pressure drop to maintain the validity of the Darcy's law ($Re_K < 1$) assumption used in the numerical model for comparison. Figures 5(*a*) and 5(*b*) show that for the porous channels of 0.97 and 0.54 mm, the experimental results agree well with the numerical predictions, except for the hot spots mentioned previously. As shown in the figures, increasing the inlet velocity from 0.5 to 1.0 cm/s only served to improve the single-phase forced convection heat transfer in the entrance region and had no significant influence on the wall temperature distribution in the two-phase region.

Figure 5(*c*) shows the experimental results for the porous channel comprised of 0.39 mm diameter spheres tested at higher inlet velocities (0.83 to 2.5 cm/s). Here, two observations can be made from the experimental data. First, the measured wall temperatures decrease along the flow direction in the two-phase region, which reflects the decrease in the fluid saturation temperature due to the pressure drop; again, the numerical prediction did not account for this effect. Second, while the inlet pressures for these cases were close (1.190–1.217 bar), the pressure drops were distinct and relatively large (0.103–0.140 bar) compared with the other cases due to the high inlet velocities. This resulted in obvious offsets of the fluid saturation temperatures throughout the porous channel (taking the constant saturation temperature used in the numerical calculation as a basis). Hence, increasing the inlet velocity leads to a lower wall temperature distribution in both the single-phase region and the two-phase region. For the porous channels comprised of 0.33 mm diameter spheres shown in Fig. 5(*d*), the inlet velocity within the test range of 0.5 to 1.67 cm/s had a smaller influence on the wall temperature distribution, although some discrepancies between the experimental data and the numerical predictions are apparent.

Variation of Fluid Inlet Temperature and Subcooling. The present study focused on the two-phase heat dissipation. However, to emphasize the originality, single-phase forced convection heat transfer tests were also performed for the porous channels comprised of 0.97, 0.54, and 0.39 mm diameter spheres. Here, there is no attempt to make strict comparisons between experimental data and numerical calculations for the cases of single-phase heat transfer tests because some assump-

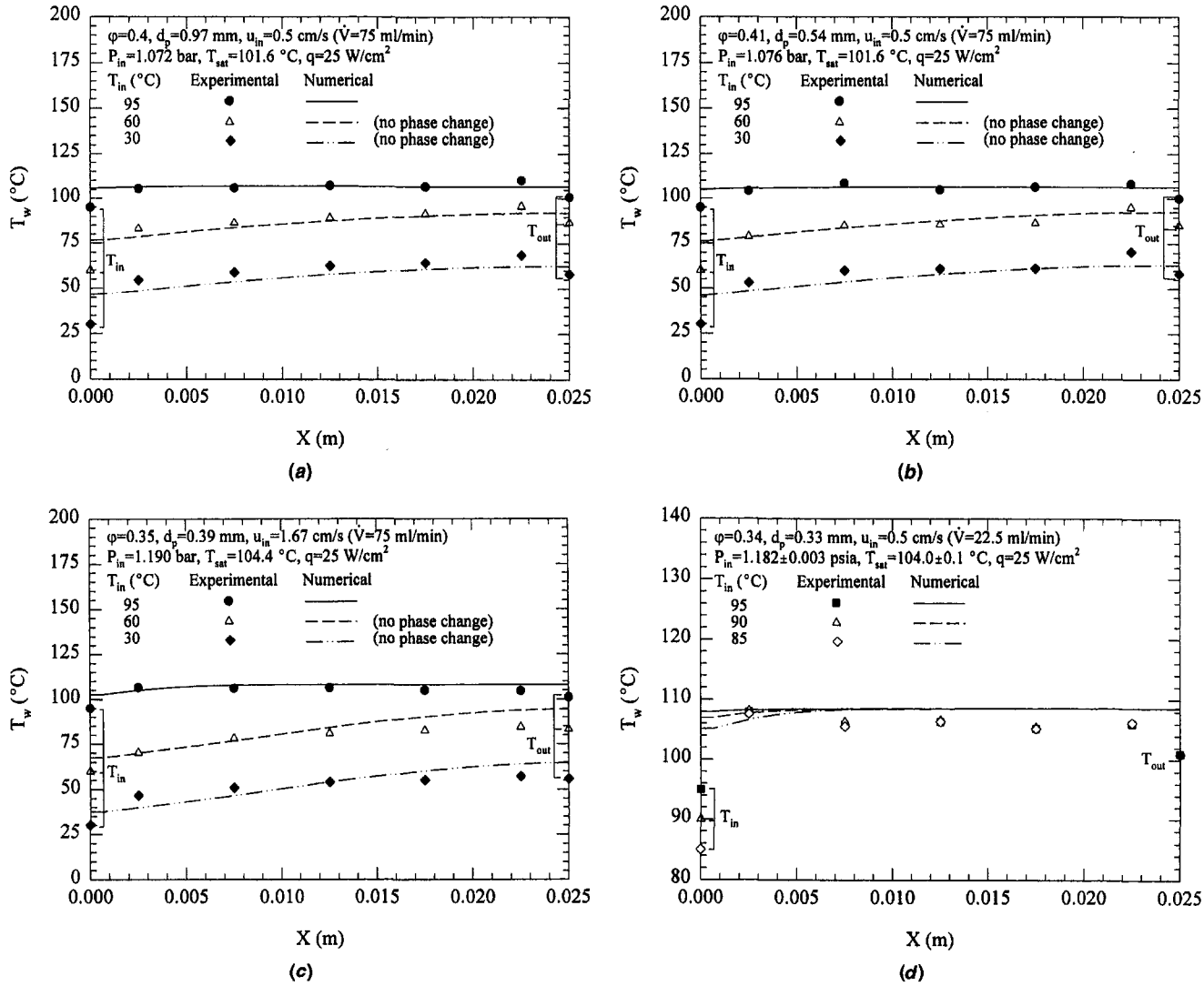

Fig. 6 Variation of inlet temperature on wall temperature distribution: (*a*) d_p = 0.97 mm; (*b*) d_p = 0.54 mm; (*c*) d_p = 0.39 mm; and (*d*) d_p = 0.33 mm.

tions in the numerical model may not be suitable and could lead to large errors for these cases.

Figures 6(*a*) through 6(*c*) show both the experimental and numerical results for the porous channels comprised of 0.97, 0.54, and 0.39 mm diameter spheres tested at three inlet temperatures, 95, 60, and 30°C. As shown in each figure, the heated wall temperature gradients of the porous channel tested at inlet temperatures 60 and 30°C (without phase change of water) are large compared to that measured at an inlet temperature 95°C (with phase change of water). It is anticipated that larger differences will be observed if heat flux continues to increase beyond the capability of the experimental limit, 25 W/cm^2, and phase change of the fluid will eventually occur in the porous channel unless the inlet velocity of the fluid is increased to a level high enough to compensate for the energy increase through sensible heating.

Figure 6(*d*) illustrates the subcooling effect on the wall temperature distribution for the porous channel comprised of 0.39 mm diameter spheres. Within the range of subcooling tested (approximately 9, 14, and 19°C subcoolings), no significant differences in the wall temperature measurements were observed outside the entrance region. Again, the experimental data show a lower level of wall temperature distribution than the numerical prediction due to the pressure drop effect.

Variation of Particle Sizes of the Porous Media. In the present experimental study, it was difficult to obtain exactly the same operating conditions for any two channels of different mean particle diameters. For channels of the same dimension, experimental data obtained at similar inlet test conditions were plotted to show the influence of the particle size. Heat transfer tests for an empty channel of dimension 25 mm by 10 mm by 25 mm were also performed to serve as a basis of comparison.

Figure 7(*a*) shows that, for channels of dimension 25 mm by 10 mm by 25 mm, tested at the same conditions (the difference in porosities and inlet pressures are small and neglected), a channel of a smaller mean particle diameter (0.54 mm compared to 0.97 mm) results in a lower wall temperature distribution (despite the hot spots) compared to that for an empty channel. This is consistent with the theoretical predictions, which indicate that the specific surface area of a packed bed of spheres is inversely proportional to the particle diameter (Dullien, 1979). This indicates that the heat transfer performance of a porous channel can be improved by using a smaller size of copper particles because of a larger solid-fluid contact surface area.

Figure 7(*b*) illustrates a comparison between the porous channels of dimension 25 mm by 3 mm by 25 mm and the empty channel (10 mm depth), which were tested at the same

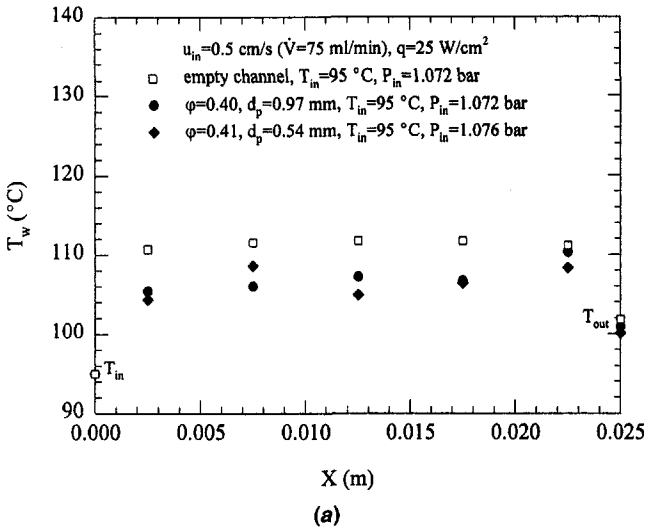

(a)

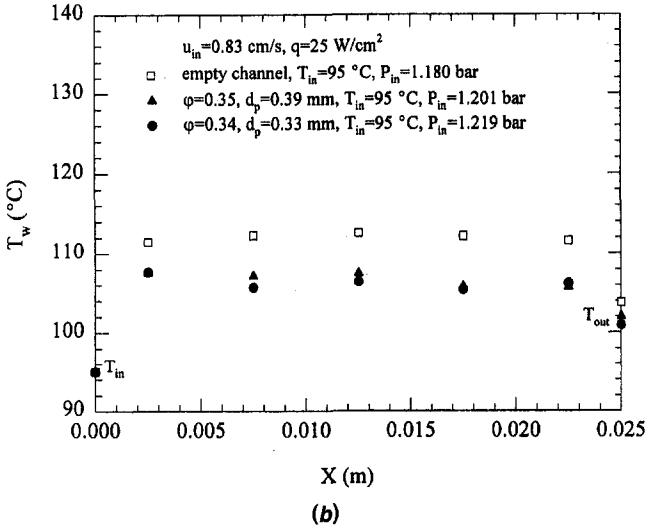

(b)

Fig. 7 Variation of particle diameters on wall temperature distribution: (a) d_p = 0.97 and 0.54 mm and (b) d_p = 0.39 and 0.33 mm

inlet velocity 0.83 cm/s (37.5 and 125 ml/min, respectively). The results indicate that for a smaller supply of water, a smaller channel (lower depth) sintered with copper particles can achieve a lower wall superheat than a larger empty channel at the same test conditions. It is noticed that the experimental data shown in Fig. 7(*b*) do not clearly reflect the influence of the particle size because of the small differences in the mean particle diameters (0.39–0.33 mm) and the large differences in the fluid inlet pressures (1.201–1.219 bar). Basically, a higher fluid inlet pressure results in higher fluid saturation temperatures in the porous channel, which has an adverse effect on the heated wall temperature. Therefore, the influence of the particle size on the wall temperature is expected to be much clearer if comparisons are made at identical inlet pressures.

Pressure Drops. Figure 8 illustrates the relationship between bulk fluid pressure drop and liquid inlet velocity. The pressure drop data are also listed in Table 2 in which the vapor quality at the outlet of the porous channel, x_e, was calculated by the following equations: $x_e = (h_{out} - h_{f,T_{out}})/h_{fg,T_{out}}$ and $h_{out} = h_{in} + qA_b/\dot{m}$, where $h_{f,T_{out}}$ and $h_{fg,T_{out}}$ are saturated liquid enthalpy and latent heat at the outlet temperature.

For each channel tested at a constant flow rate (inlet velocity), the pressure drop increased with increasing heat flux. For simplicity, as shown in Fig. 8, a symbol with error bars repre-

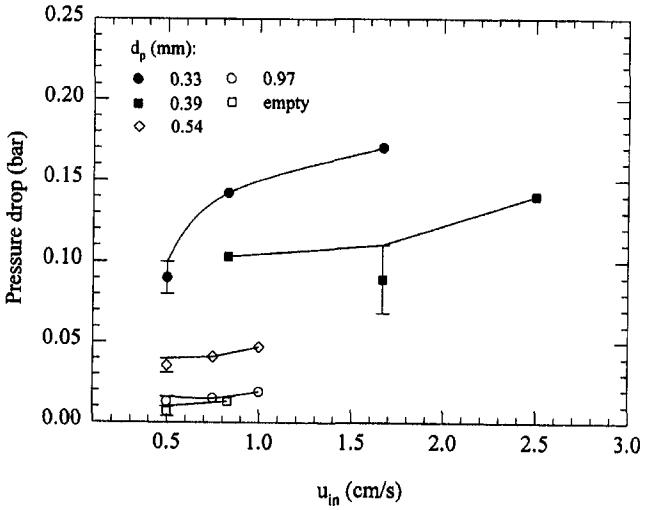

Fig. 8 Influence of inlet velocity on pressure drop

sents the lower and upper bounds of the pressure drops for heat fluxes from 10 to 25 W/cm^2, and the other symbols without error bars represent data for heat fluxes at 25 W/cm^2. Two trends are visible from this plot. First, for each channel tested at the same inlet velocity, the pressure drop increases with increasing heat flux (and increasing vapor quality) within the test range. This is more pronounced for porous channels with smaller particle diameters or those tested at higher flow rates. Second, for each channel tested at a given heat flux, the pressure drop increases with increasing inlet velocity (and decreasing vapor quality). That is, pressure drop is high at larger flow rates even though the quality is low. For all of the cases considered here, the fluid pressure drops range from 0.01 to 0.17 bar for the porous channels and from 0.004 to 0.013 bar for the empty channel.

Mean Heat Transfer Coefficients. In the present experimental study, the mean heat transfer coefficient for subcooled flow boiling as well as forced single-phase convection in the porous channel is defined as $\bar{h} = q/(\bar{T}_w - \bar{T}_f)$, where $\bar{T}_w$ is the mean wall temperature calculated from the measured data of the five thermocouples using the formula, $(\sum_{i=1}^{5} T_i \Delta x_i)/L_x$, and $\bar{T}_f$ is mean fluid temperature, which is evaluated as the arithmetic average of the fluid inlet and outlet temperatures. Table 2 lists the calculated mean heat transfer coefficients for all the experiments. As shown, for subcooled flow boiling, the mean heat transfer coefficient increases with increasing heat flux for each channel tested at the same inlet temperature and velocity. Within the test range, the influence of inlet velocity on the heat transfer coefficient is not obvious.

As shown in Table 2, for water at 95°C inlet temperature (about 6.6–10.8°C subcooling) and 0.5 cm/s inlet velocity (75 ml/min), the mean heat transfer coefficients for the empty channel ranged from 1.25 to 1.94 W/cm^2°C, which could be increased to the ranges of 1.92 to 2.74 W/cm^2°C and 2.00 to 2.81 W/cm^2°C by inserting (sintering) copper particles of mean diameters of 0.97 and 0.54 mm, respectively, into a channel of similar dimensions. Improvements of the mean heat transfer coefficients ranged from 40 to 60 percent.

Comparing porous channels of 3 mm depth to the empty channel, improvements of 71 to 142 percent ($\bar{h}$: 3.03–3.33 W/cm^2°C) are observed for channels comprised of 0.39 mm in diameter when tested at the same volumetric flow rate ($\dot{V}$ = 75 ml/min, u_{in} = 0.83, and 0.5 cm/s, respectively), and improvements of 43 to 55 percent ($\bar{h}$: 1.79–3.01 W/cm^2°C) for the sintered 0.33 mm diameter particles when tested at the same

Table 2 Mean heat transfer coefficients and pressure drops

u_{in} (cm/s)	q (W/cm²)	$\bar{T}_w$ (°C)	T_{in} (°C)	T_{out} (°C)	$\bar{T}_f$ (°C)	$\bar{h}$ (W/cm²°C)	P_{in} (bar)	ΔP (bar)	x_e quality
Channel dimension: 25 mm× 10 mm× 25 mm, empty channel									
0.5	10	106.3	95.0	101.5	98.3	1.25	1.076	0.004	0.010
0.5	15	108.5	95.0	101.9	98.5	1.49	1.092	0.006	0.020
0.5	20	109.7	95.0	102.0	98.5	1.79	1.098	0.010	0.031
0.5	25	111.3	95.0	101.8	98.4	1.94	1.072	0.010	0.043
0.83	25	112.0	95.0	103.8	99.4	1.98	1.180	0.013	0.017
Channel dimension: 25 mm× 10 mm× 25 mm, d_p: 0.97 mm									
0.5	10	103.0	95.0	100.5	97.8	1.92	1.062	0.010	0.012
0.5	15	104.0	95.0	100.3	97.7	2.38	1.066	0.012	0.023
0.5	20	105.3	95.0	100.5	97.8	2.67	1.071	0.013	0.034
0.5	25	107.1	95.0	100.9	98.0	2.75	1.072	0.016	0.044
0.75	25	106.7	95.0	100.8	98.0	2.87	1.077	0.015	0.026
1.0	25	106.7	95.0	101.4	98.2	2.94	1.082	0.019	0.016
0.5	25	89.3	60.0	86.9	73.5	1.58	1.068	0.006	-
0.5	25	61.7	30.0	58.0	44.0	1.41	1.076	0.007	-
Channel dimension: 25 mm× 10 mm× 25 mm, d_p: 0.54 mm									
0.5	10	102.5	95.0	100.0	97.5	2.00	1.085	0.028	0.013
0.5	15	104.1	95.0	100.0	97.5	2.27	1.079	0.031	0.024
0.5	20	105.6	95.0	100.1	97.6	2.50	1.074	0.036	0.035
0.5	25	106.5	95.0	100.1	97.6	2.81	1.076	0.040	0.046
0.75	25	106.3	95.0	99.8	97.4	2.81	1.078	0.041	0.028
1.0	25	106.0	95.0	100.7	97.9	3.09	1.089	0.047	0.017
0.5	25	86.2	60.0	85.2	72.6	1.84	1.074	0.012	-
0.5	25	61.4	30.0	58.2	44.1	1.45	1.071	0.013	-
Channel dimension: 25 mm× 3 mm× 25 mm, d_p: 0.39 mm									
1.67	10	101.4	95.0	101.1	98.1	3.03	1.153	0.068	0.011
1.67	15	103.5	95.0	101.3	98.2	2.83	1.178	0.085	0.021
1.67	20	104.3	95.0	101.0	98.0	3.17	1.178	0.096	0.033
1.67	25	105.5	95.0	101.0	98.0	3.33	1.190	0.110	0.044
2.5	25	104.9	95.0	101.1	98.1	3.68	1.217	0.140	0.026
0.83	25	106.8	95.0	102.0	98.5	3.01	1.201	0.103	0.098
1.67	25	79.2	60.0	83.3	71.7	3.33	1.092	0.038	-
1.67	25	52.7	30.0	55.8	42.9	2.55	1.130	0.057	-
Channel dimension: 25 mm× 3 mm× 25 mm, d_p: 0.33 mm									
0.5	10	103.9	95.0	101.5	98.3	1.79	1.176	0.080	0.062
0.5	15	104.7	95.0	101.1	98.1	2.27	1.171	0.086	0.100
0.5	20	105.7	95.0	101.1	98.1	2.63	1.178	0.090	0.137
0.5	25	106.3	95.0	101.0	98.0	3.01	1.184	0.100	0.174
0.5	25	106.5	90.0	100.9	95.5	2.27	1.179	0.105	0.164
0.5	25	106.0	85.0	100.9	93.0	1.92	1.181	0.105	0.155
0.83	25	106.5	95.0	100.9	98.0	2.94	1.219	0.142	0.100
1.67	25	106.1	95.0	100.5	97.8	3.01	1.204	0.170	0.045

inlet velocity (u_{in} = 0.5 cm/s). It should be noted that in the above comparisons, the porous channels were tested at higher inlet pressures, which actually had an adverse effect on the heat transfer coefficients.

As indicated by the above results, two-phase heat dissipation utilizing high-conductivity porous channels can achieve very high heat transfer coefficients. The present results also show that forced water (single phase) in porous channels results in a competitive level of heat transfer coefficients (1.41 to 3.33 W/cm²°C), but carries with it plenty of larger wall temperature gradients.

A previous investigation conducted by Vafai and Kim (1989, 1995) examined the boundary and inertia effects on fully developed forced convection in a porous channel bounded by parallel plates. In this study, it was concluded that for a low-permeability porous media the thickness of the momentum boundary layer was dependent only on the Darcy number, while for a high-permeability porous media it was dependent upon both the Darcy number and the inertia parameter. In addition, it was observed that there was a significant increase in the heat transfer rate as the inertia parameter increased especially for high to medium permeability porous media. In the present study, the numerical model was based on the Darcy flow assumption, that is, both the boundary and inertia effects were neglected. As a result, the fluid in the porous channel experienced phase change through absorbing heat from the porous medium, and fully developed flow, if occurring at all, would only occur in the very upstream single-phase region. While the current study has a different dominant heat transfer mechanism than the investigation conducted by Vafai and Kim (1989, 1995), i.e., pure single-phase forced convection throughout a porous channel, the latter results can be used to benchmark the current model.

Table 3 The range of the Darcy number (Da) in the present study

Test article #	Mean diameter d (mm)	porosity δ	Half the channel width H(m)	Permeability $K(10^{-10}\ m^2)$	Darcy number $Da=K/(H^2\delta)$	$Da^{-1/2}$
1	0.97	0.4	0.05	5.1	5.1×10^{-7}	1400
2	0.54	0.41	0.05	1.19	1.16×10^{-7}	2936
3	0.39	0.35	0.015	0.714	9.06×10^{-7}	1050
4	0.33	0.34	0.015	0.501	6.55×10^{-7}	1236

To illustrate the effect of neglecting the boundary and inertia effects in the present study, Darcy numbers and the inertial parameters for the present numerical study, defined in the same way as by Vafai and Kim, are listed in Tables 3 and 4, respectively. Table 3 illustrates that $Da^{-1/2}$ ranges from 1050 to 2936, which indicates that the permeability is much lower than those considered in the reference by Vafai and Kim (1989, 1995), and, as a result, the boundary and inertia effects should have less influence on the velocity and temperature profiles. As mentioned by Vafai and Kim (1989, 1995) the thickness of the momentum boundary layer will be of the order of $(Da^{1/4}/\Lambda_I^{\frac{1}{2}})$ for $\Lambda_I \gg 1$. Hence, in the present study it will be on the order of 10^{-3}.

Although there are some differences in the present study and the one presented by Vafai and Kim (1989, 1995), the previously obtained results verify that utilizing the Darcy flow assumption for the present study is acceptable.

Conclusions

The results of the current investigation can be summarized as follows. First, generally speaking, the experimental results agree well with the numerical predictions, however, some deviation is apparent when fluid pressure drop is large because the numerical model did not account for its effect on saturation temperature. Second, porous channels comprised of smaller diameter spheres result in a higher heat transfer coefficient because of a larger heat transfer area. Third, for water at 6.6 to

Table 4 The range of the inertia parameter (Λ_I) in the present study

Test article #	Mean diameter d (mm)	porosity δ	Half the channel width H(m)	Dimensionless form drag constant $F=0.55(1-5.5d/D_e)^{1/2}$ F	Inertia parameter $(\Lambda_I=\delta^{3/2}F\,U_\infty H/\nu_f)$ Λ_I
1	0.97	0.4	0.05	0.35	71.4
2	0.54	0.41	0.05	0.44	93.2
3	0.39	0.35	0.015	0.33	16.5
4	0.33	0.34	0.015	0.37	17.7

10.8°C inlet subcooling, the heat transfer coefficients of the empty channel ranged from 1.25 to 1.94 W/cm^2°C, which could be increased to 1.79 to 3.33 W/cm^2°C (an improvement of 43 to 142 percent using the porous channels comprised of 0.97 to 0.29 mm diameter spheres). Fourth, for subcooled flow boiling tests, the influence of inlet velocity on the mean heat transfer coefficient is not obvious within the test range. Fifth, the experimental results indicate that the fluid pressure drop increases with increasing heat flux, and this increase is more pronounced for either a porous channel of smaller particles or a porous channel tested at a higher flow rate. The influence of inlet velocity on pressure drop increases with decreasing particle diameter, and the pressure drop is large at higher velocities even when the vapor outlet quality is low. The pressure drops across the porous channels are 0.01 to 0.17 bar within the ranges tested.

Finally, in real applications, refrigerants of lower boiling points are suggested instead of water as used in the current study, but improvements in heat transfer coefficients should still be anticipated.

Acknowledgments

This work was supported in part by the Texas Higher Education Coordinating Board through the Advanced Technology Program, project 71710. Support of the test articles for this study by Energy & Resources Laboratories of Industrial Technology Research Institute in Taiwan is appreciated.

References

Carey, V. P., 1992, *Liquid-Vapor Phase-Change Phenomena,* Taylor & Francis, PA.

Dullien, F. A. L., 1979, *Porous Media Fluid Transport and Pore Structure,* Acade Press, NY.

Hwang, G. J., and Chao, C. H., 1994, "Heat Transfer Measurement and Analysis for Sintered Porous Channels," ASME JOURNAL OF HEAT TRANSFER, Vol. 116, pp. 456–464.

Jacobs, H. R., and Hartnett, J. P., 1991, *Thermal Engineering: Engineering Technologies and Critical Phenomena,* Workshop Report, NSF Grand No. CTS-90-04006, pp. 139–176.

Koh, J. C. Y., and Colony, R., 1974, "Analysis of Cooling Effectiveness for Porous Material in a Coolant Passage," ASME JOURNAL OF HEAT TRANSFER, Vol. 96, pp. 324–330.

Kuo, S. M., and Tein, C. L., 1981, "Heat Transfer Augmentation in a Form-Material Filled Duct With Discrete Heat Sources," *Proceedings of IEEE Thermal Phenomena in Electronic Components Conference,* IEEE, NY, pp. 87–91.

Nield, D. A., and Bejan, A., 1992, *Convection in Porous Media,* Springer-Verlag, NY.

Patankar, S., 1980, *Numerical Heat Transfer and Fluid Flow,* McGraw-Hill, NY.

Peterson, G. P., and Chang, C. S., 1997, "Heat Transfer Analysis and Evaluation for Two-Phase Flow in Porous-Channel Heat Sinks," *Numerical Heat Transfer,* Part A, Vol. 31, pp. 113–130.

Peterson, G. P., and Ortega, A., 1990, "Thermal Control of Electronic Equipment and Devices," *Advances in Heat Transfer,* Vol. 20, J. P. Hartnett and T. F. Irvine, eds, Pergamon Press, New York, NY, pp. 181–314.

Vafai, K., and Kim, S. J., 1989, "Forced Convection in a Channel Filled With a Porous Medium: and Exact Solution," ASME JOURNAL OF HEAT TRANSFER, Vol. 111, pp. 1103–1106.

Vafai, K., and Kim, S. J., 1995, "Discussion of Forced Convection in a Channel Filled With a Porous Medium: and Exact Solution," ASME JOURNAL OF HEAT TRANSFER, Vol. 117, pp. 1097–1098.

Wakao, N., and Kaguei, S., 1982, *Heat and Mass Transfer in Packed Beds,* Gordon and Breach, NY.

Wang, C. Y., and Beckermann, C., 1993, "A Two-Phase Mixture Model of Liquid-Gas Flow and Heat Transfer in Capillary Porous Media-I, Formulation," *Int. J. Heat Mass Transfer,* Vol. 36, pp. 2747–2758.

Wang, C. Y., Beckermann, C., and Fan, C., 1994, "Numerical Study of Boiling and Natural Convection in Capillary Porous Media Using the Two-Phase Mixture Model," *Numerical Heat Transfer,* Part A, Vol. 26, pp. 375–398.

J. H. Lienhard V
lienhard@mit.edu

D. S. Napolitano

W. M. Rohsenow Heat and
Mass Transfer Laboratory,
Department of Mechanical Engineering,
Room 3-162,
Massachusetts Institute of Technology,
Cambridge, MA 02139-4307

Yield Limits of Plates at Extremely High Heat Flux

For heat fluxes ranging above 10 MW/m^2 or so, solid surfaces usually experience large thermal stresses and degradation of mechanical properties. The resulting mechanical failure of such surfaces is a primary limitation to the design of thermal systems at extremely high heat flux. This investigation considers the elastic stresses in circular plates subjected to extremely high heat fluxes. A gaussian distributed heat load is applied to one surface of the plate and the heat flux at which yielding occurs is identified. Several candidate materials are examined, accounting for the temperature dependence of yield strength and other properties. The mechanical boundary conditions on the plate are varied. Figures of merit are given for the high flux performance of a number of materials.

1 Introduction

The creation of steady heat fluxes on the order of 100 MW/m^2 through solids is usually hampered by mechanical failure of the heat transfer surface, resulting from thermal stress and loss of material strength. Unique features of thermal stress management at extremely high heat fluxes include temperatures that may approach the melting point of the solid surface and temperature differences of more than 1000°C imposed over distances of only a few millimeters. Yield strength may become very low on the hot side of the solid, leading to plastic deformation or rupture.

For a solid of a given thickness, the highest one-dimensional heat flux that may be sustained places one surface at the melting point while the opposite surface is held at low temperature (typically the temperature of a coolant, such as water near 25°C). Conditions of this sort have produced the highest steady-state heat fluxes to be obtained. In particular, Liu and Lienhard (1993) achieved fluxes of up to 400 MW/m^2 through a molybdenum plate cooled by a high speed water jet on one side and heated to its melting point by a plasma arc struck to its opposite side; in this state, the unmelted thickness of the molybdenum sheet was less than 1 millimeter. Tests run on other materials of similar thermal conductivity showed failures at lower heat fluxes, typically by plastic rupture or brittle fracture. All evidence suggested that failure was a function of the solid material used and did not derive from limitations of the cooling process (such as a critical heat flux phenomenon). Thermal stresses were the apparent cause of these failures.

Simple one-dimensional thermal stress calculations show that stresses in a plate subjected to the melting point flux can easily exceed the elastic strength, and finite-element simulations allowing for plasticity show that the stresses may exceed ultimate strength (Lienhard and Napolitano, 1996). The stress levels actually achieved depend on the specific material used, the mechanical boundary conditions of the plate, and the temperature difference developed across the plate for a given heat flux.

This paper identifies the flux at which thermal stress reaches yield strength for several promising materials in a configuration generically similar to that found in some of the highest heat flux systems. Our focus is on planar surfaces that are heated from one face and cooled from the opposite face; this geometry is typical of various extremely high flux systems, notably those involving jet impingement cooling. Heat loads are taken to be gaussian distributed on the hot surface, as is typical of the optical beam heating or plasma-arc heating that is frequently used to reach the highest fluxes. Our objective is to sort out the influence of several factors affecting the mechanical performance of extremely high flux systems. These factors include material properties, heat load distributions, and mechanical constraints. The onset of yielding is taken as a measure of material performance; other important issues, such as creep and thermal fatigue, are not considered.

We assume steady state in analyzing the stresses. Transient stresses can be larger in systems that experience an abrupt change in boundary temperature, owing to the highly nonlinear temperature distributions that may occur during transients. However, current extremely high heat flux systems most often involve applied heat fluxes (e.g., laser beams), and for those cases the maximum stress may occur in either the steady or transient state depending on the heating profile and the mechanical boundary condition. We assume our steady states to be reached through a quasi-steady heating process in which the temperature distribution through the plate thickness is always linear.

2 Materials for High Heat Fluxes

Materials for use at extremely high heat fluxes must have a combination of high thermal conductivity, high strength at elevated temperature, low thermal expansion, and/or low elastic modulus. In this paper, we consider some typical metals, either high conductivity metals (copper and aluminum) or refractory metals (tungsten and molybdenum). A cold-worked stainless steel is examined for comparison. Yield strengths of these materials are shown in Fig. 1 and properties of these and other materials are listed in Table 1 (Touloukian, 1979; Holt et al., 1995; Peckner and Bernstein, 1977; ASM, 1985).

Precipitation-hardening coppers, such as chromium copper (C18200) and zirconium copper (C15000), are useful owing to their high strength after cold-working and aging. This strength is retained for temperatures up to a few hundred degrees Celsius. Dispersion-strengthed coppers, such as C15715, obtain strength from aluminum oxide powder dispersed in the copper matrix. These coppers have thermal and elastic properties nearly identical to aged-hardened coppers, but they soften less at high temperatures and exhibit much better creep/rupture characteristics. Aluminum alloys do not retain their strength beyond about 150°C. The coppers and aluminums in the table are hardened to the tempers indicated.

Refractory metals have reasonably high thermal conductivities and can retain cold working at high temperatures (recrystallization above 900°C for molybdenum and 1300°C for tung-

Contributed by the Heat Transfer Division for publication in the JOURNAL OF HEAT TRANSFER and presented at the 1996 ASME IMECE. Manuscript received by the Heat Transfer Division April 11, 1997; revision received September 30, 1997; Keywords: Analytical; Heat Transfer; Materials; Stress. Associate Technical Editor: T. Bergman.

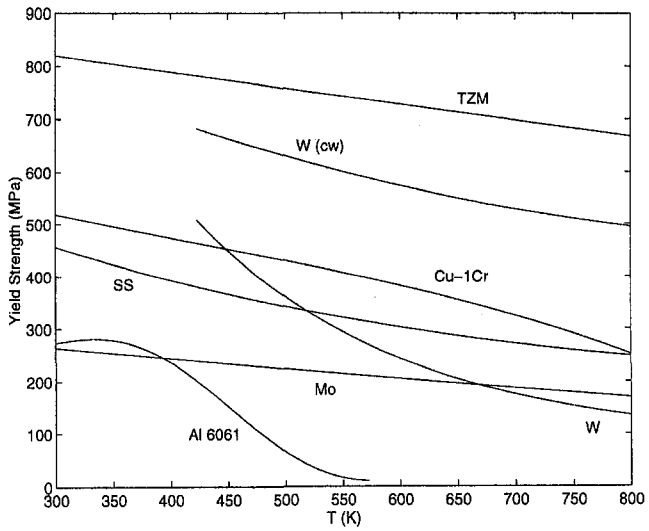

Fig. 1 Temperature dependence of 0.2 percent yield stress σ_Y for various metals: aluminum (6061-T651), molybenum (recrystalized), tungsten (recrystalized), 304L stainless steel (10 percent cold work), chromium copper (18200-TH04), tungsten (wrought), TZM (stress-relieved)

sten). Some refractory metals will have ductile-to-brittle transition temperatures in the operating temperature range (DTBT around 200°C for tungsten, near room temperature for molybdenum, but near absolute zero for tantalum). Most refractories require protection from oxidation at high temperatures. The molybdenum alloy TZM (Mo-0.5Ti-0.1Zr) has higher strength than pure molybdenum, a higher recrystallization temperature, and better creep characteristics.

Stainless steels and superalloys have low thermal conductivity and are usually unsuitable for extremely high heat flux applications. To illustrate this, 304L stainless steel with 10 percent cold reduction is examined in some the following sections. Other materials of interest for high heat fluxes include synthetic diamond (see Table 1) and ceramics such as silicon carbide.

Previous studies (Abdou et al., 1984; Lienhard and Khounsary, 1993) have proposed the following figure of merit for the elastic performance of high heat flux materials:

$$Q_{\text{efm}} \equiv \frac{(1-\nu)k\sigma_Y}{E\alpha}. \tag{1}$$

This figure is effectively based on the thermal stress in a uniformly heated, fixed-edge plate; it represents the flux that causes yield stress in a plate of unit thickness. Values are listed in Table 1 for various materials. This figure of merit gives a reasonable first-order approximation to the performance of a particular material, but for some materials it decreases sharply as temperature rises owing to the temperature dependence of yield strength. Moreover, stresses can be lower for plates that have only localized heating or for plates that are allowed to expand laterally. Consequently, a more complete analytical ranking of materials is desirable.

Table 1 Thermal and elastic properties of various materials at room temperature (unless otherwise indicated). Properties that have been estimated are italicized. Units are as follow: α, 10^{-6} K^{-1}; E, GPa; k, W/m·K; σ_Y, MPa; Q_{efm}, MW·mm/m^2; $\Delta T = Q_{\text{efm}}/k$, K; T_{melt}, K. σ_Y for ductile materials is for 0.2 percent offset. For brittle materials, σ_Y is the compressive strength. T_{melt} is the solidus temperature for metallic alloys; for diamond, it is the temperature above which pyrolysis occurs. α is based on total expansion from 20°C to the indicated temperature.

Material	α	E	k	σ_Y	ν	Q_{efm}	ΔT	T_{melt}
Diamond (single crystal)	0.8	1050	2100	3000	0.15	6400	3	973
DS Copper (C15715-H04)								1356
20°C	*16*	130	365	430	*0.3*	52.8	145	
200°C	17.2	*120*	345	375	*0.3*	43.9	127	
400°C	18.8	*110*	320	307	*0.3*	33.3	104	
Copper-Cr (C18200-TH04)								1343
20°C	16.3	130	324	520	*0.3*	55.6	172	
200°C	17.2	*120*	351	441	*0.3*	55.5	150	
400°C	18.9	109	364	343	*0.3*	42.4	117	
Copper-Zr (C15000-TH04)	16.9	129	367	411	0.34	45.7	124	1253
Molybdenum (TZM)								2883
Stress relieved, 21°C	4.9	315	120	860	*0.3*	46.8	390	
Stress relieved, 1090°C	5.6	205	100	435	*0.3*	26.5	265	
Tantalum (T-222)								3293
Stress relieved, 20°C	5.9	200	54	950	*0.3*	30.4	563	
Stress relieved, 1000°C	6.8	*140*	59	700	*0.3*	30.3	514	
Tungsten								3683
Wrought, 200°C	4.3	400	150	640	0.28	40.0	267	
Wrought, 500°C	4.4	388	130	517	0.29	28.0	215	
Wrought, 1000°C	4.7	367	110	413	0.29	18.4	168	
Recrystallized, 200°C	4.3	400	150	405	0.28	25.3	169	
Recrystallized, 500°C	4.4	388	130	131	0.29	7.1	54	
Niobium (FS-85)								2741
Stress relieved, 20°C	7.1	140	45	735	*0.3*	23.3	518	
Stress relieved, 500°C	7.4	130	49	560	*0.3*	20.0	407	
Recrystalized, 1090°C	9.0	125	57	200	*0.3*	7.1	124	
Aluminum (6061-T651)								855
20°C	23.6	70	167	276	0.33	18.8	112	
149°C	24.2	64	175	215	*0.33*	16.8	96	
371°C	25.3	39	181	12	*0.33*	1.5	9	
Vanadium (V-15Cr-5Ti)	9	124	24	500	*0.3*	10.8	448	2173
Inconel 713C	10.6	205	11	740	*0.3*	2.6	238	1533
Stainless 304L (10% cw)	17.3	193	15	450	*0.27*	1.5	98	1673

3 Localized Heating of an Axisymmetric Disk

We consider a steady localized heat source applied to one side of a circular disk and compute the heat flux at which yielding first occurs within the disk. Our objective is to identify major factors affecting stresses during localized heating and to estimate the heat fluxes achievable without plastic deformation.

Nomenclature

Roman Letters

a = gaussian decay rate (see Eq. (2); m)
b = plate radius (m)
E = Young's modulus (N/m^2)
$F(r)$ = see Eq. (7)
H = thickness of plate (m)
k = thermal conductivity (W/m·K)
M_r, M_θ = bending moment in the r, θ direction per unit length (N)
N_r, N_θ = membrane force in the r, θ direction per unit length (N/m)
q = heat flux (W/m^2)
Q_{efm} = material figure of merit for elastic deformation (MW·mm/m^2)
(r, z, θ) = cylindrical coordinates
T = temperature distribution (K)
$\bar{T}(r)$ = mean temperature over plate thickness (see Eq. (3); K)
T_c = low temperature at top of plate (K)
T_h = high temperature at bottom of plate (see Eq. (2); K)
T_{melt} = melting or solidus temperature of material (K)
T_0 = temperature of plate in unstressed initial state (K)

Greek Letters

α = thermal expansion coefficient (K^{-1})
$\Delta T(r)$ = temperature difference across plate thickness (see Eq. (3); K)
ν = Poisson's ratio
σ_{jj} = normal stress in the j-direction (N/m^2)
σ_v = von Mises stress (N/m^2)
σ_Y = 0.2 percent yield stress (N/m^2)

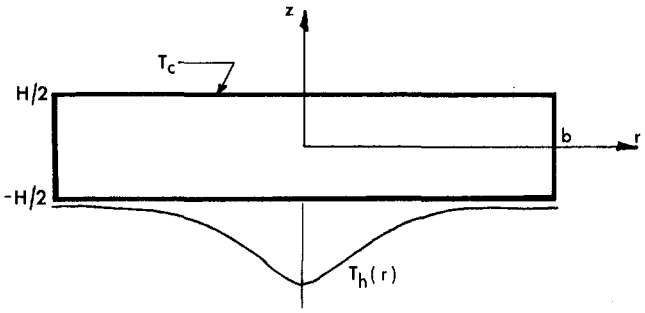

Fig. 2 A circular disc subjected to a gaussian temperature distribution on one surface

A circular plate of radius b and thickness H is considered (Fig. 2). Cylindrical coordinates (r, z, θ) are located at the plate center with the z-axis directed upward. Calculations are based on classical plate theory. The plate's material properties, other than yield stress, are treated as homogeneous and temperature independent; yield stress is evaluated at the local temperature to determine the elastic limit. Comparison to finite element simulations with fully variable properties shows that the present property approximation is accurate to within 10 to 15 percent if properties other than yield strength are evaluated at the average temperature of the plate (Dahbura, 1996).

A gaussian distributed temperature profile is assumed; as previously noted, such temperature profiles are typical of localized heating by optical beams or plasma arcs. The plate is unstressed at a temperature of $T_0 = 25°C$. The imposed temperature distribution on the bottom surface of the plate ($z = -H/2$) is an axisymmetric gaussian profile

$$T_h(r) = T_c + (T_{\max} - T_c)\exp\left(-\frac{2r^2}{a^2}\right) \tag{2}$$

and the upper surface is held (as by intense convective cooling) to $T_c = T_0$. The gaussian temperature distribution is assumed to decay slowly enough with radius that the temperature variation in z for fixed r is essentially a linear variation between the upper and lower surface temperatures.[1] The temperature field in the plate is thus

$$T(r, z) = \left(\frac{T_h(r) + T_c}{2}\right) + \left(\frac{z}{H}\right)(T_h(r) - T_c)$$

$$\equiv T_0 + \bar{T}(r) - \left(\frac{z}{H}\right)\Delta T(r). \tag{3}$$

The stresses in the plate can be calculated by integration of standard equations from classical plate theory (Johns, 1965; Tauchert, 1986; Boley and Weiner, 1960). Plate theory leads to general expressions for the membrane forces per unit length, N_r and N_θ, and for the bending moments per unit length, M_r and M_θ; for brevity, we omit the general equations, which are well known. The moments and forces must be calculated for our particular temperature field; then, the stresses resulting from a temperature field of the form (3) may be calculated as follows:

$$\sigma_{rr} = \frac{N_r}{H} + \left(\frac{12z}{H^3}\right)M_r, \tag{4}$$

$$\sigma_{\theta\theta} = \frac{N_\theta}{H} + \left(\frac{12z}{H^3}\right)M_\theta. \tag{5}$$

[1] This condition is satisfied when radial heat conduction is negligible, i.e., for $(H/a)^2 \ll 1$.

3.1 Simply Supported Plate. In this case, the edge of the plate has zero vertical deflection and zero radial stress or bending moment. The solutions for the bending moments on the interior are (Johns, 1965)

$$M_r = \frac{EH^2}{12}\left(\frac{1}{r^2}F(r) - \frac{1}{b^2}F(b)\right)$$

$$M_\theta = \frac{EH^2}{12}\left(\alpha\Delta T(r) - \frac{1}{r^2}F(r) - \frac{1}{b^2}F(b)\right) \tag{6}$$

where

$$F(r) = \int_0^r r\alpha\Delta T(r)dr \tag{7}$$

and the membrane forces are

$$N_r = \frac{E\alpha H}{r^2}\left(\frac{r^2}{b^2}\int_0^b r\bar{T}(r)dr - \int_0^r r\bar{T}(r)dr\right)$$

$$N_\theta = \frac{E\alpha H}{r^2}\left(\frac{r^2}{b^2}\int_0^b r\bar{T}(r)dr + \int_0^r r\bar{T}(r)dr - r^2\bar{T}(r)\right). \tag{8}$$

Integration of these equations using Eq. (3) leads to the following stresses:

$$\sigma_{rr} = \left[\frac{E\alpha(T_{\max} - T_0)}{8}\right]\left[\left(\frac{a}{b}\right)^2(1 - e^{-2b^2/a^2}) - \left(\frac{a}{r}\right)^2(1 - e^{-2r^2/a^2})\right]\left(1 - \frac{2z}{H}\right); \tag{9}$$

$$\sigma_{\theta\theta} = \left[\frac{E\alpha(T_{\max} - T_0)}{8}\right]\left[\left(\frac{a}{b}\right)^2(1 - e^{-2b^2/a^2}) + \left(\frac{a}{r}\right)^2(1 - e^{-2r^2/a^2}) - 4e^{-2r^2/a^2}\right]\left(1 - \frac{2z}{H}\right). \tag{10}$$

The radial stress (Fig. 3) has a single compressive extremum at $(r, z) = (0, -H/2)$. The hoop stress has a compressive extremum at $(r, z) = (0, -H/2)$ and a tensile extremum at $(r, z) = (1.2676a, -H/2)$; the tensile extremum is located at the edge of the plate ($r = b$) for $a/b > 0.789$. The compressive extremum of hoop stress has a larger magnitude than the tensile extremum if $a/b < 0.96468$; both stresses tend to zero as $a/b \to \infty$ (the limit of uniform surface temperature).

Onset of yielding was determined using distortion energy theory (Ugural and Fenster, 1975). To find the flux at onset of yielding, $T_{\max}$ was increased until the von Mises stress, $\sigma_v = (\sigma_{rr}^2 - \sigma_{rr}\sigma_{\theta\theta} + \sigma_{\theta\theta}^2)^{1/2}$, exceeded σ_Y at some point in the plate. The yield stress, σ_Y, was evaluated at the local temperature of the plate at the points of maximum stress, while other mechanical properties were evaluated at the thickness-average temperature for $r = 0$.

Values of $T_{\max}$ and the heat flux at onset of yielding are given in Table 2. (Data have been omitted from the table where temperatures exceeded the range in which reliable property data were available.) Note that the stresses depend on the temperature difference, rather than the heat flux, so that plates of different thickness will reach yielding for the same value of $T_{\max}$ but with different values of the flux. The numerical values of $q \cdot H$ in the table correspond to the flux at $r = 0$ through a 1 mm plate; for other thicknesses, the flux can be found by dividing the tabulated value by H in millimeters. For example, with $a/b = 0.1$, a DS copper plate of 1 mm thickness yields at a heat flux of 112 MW/m^2 at the plate center, while a 3 mm thick

plate will yield at a flux of 37 MW/m^2. The total power of the gaussian source (from $r = 0$ to ∞) is $q(\pi a^2/2)$ at yielding.

In the uniform temperature limit ($a/b \to \infty$), where theoretical stresses are zero, the melting point temperature and flux are given. For real plates this flux is optimistic, in so far as variations of thermal conductivity over these large temperature ranges can be expected to produce nonlinearities in the temperature distributions which will cause significant thermal stresses.

Hardened copper alloys show the highest flux among these materials prior to yielding. Tungsten behaves as both a brittle and ductile material in this configuration (in the cold and hot regions, respectively); thus, its failure point is determined by comparing its stress field to both the ultimate and yield strengths. Aluminum loses strength quickly with increasing temperature, and does not perform well in spite of its high conductivity. Tungsten and molybdenum require protection from oxidation for service temperatures above 770 K.

3.2 Fixed-Edge Plate. Here, the edge has zero vertical or radial deflection and zero slope. The solutions for the bending moments are (Goodier, 1957)

$$M_r = \frac{EH^2}{12}\left[\frac{1}{r^2}F(r) + \left(\frac{1+\nu}{1-\nu}\right)\frac{1}{b^2}F(b)\right]$$

$$M_\theta = \frac{EH^2}{12}\left[\alpha\Delta T(r) - \frac{1}{r^2}F(r) + \left(\frac{1+\nu}{1-\nu}\right)\frac{1}{b^2}F(b)\right]. \quad (11)$$

The membrane forces are (Napolitano, 1995)

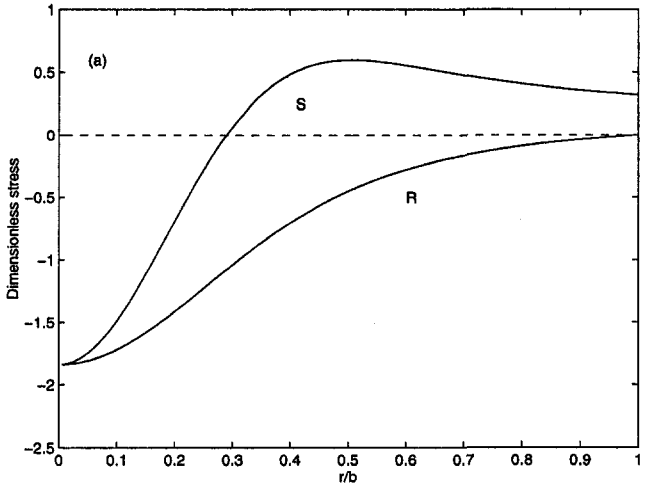

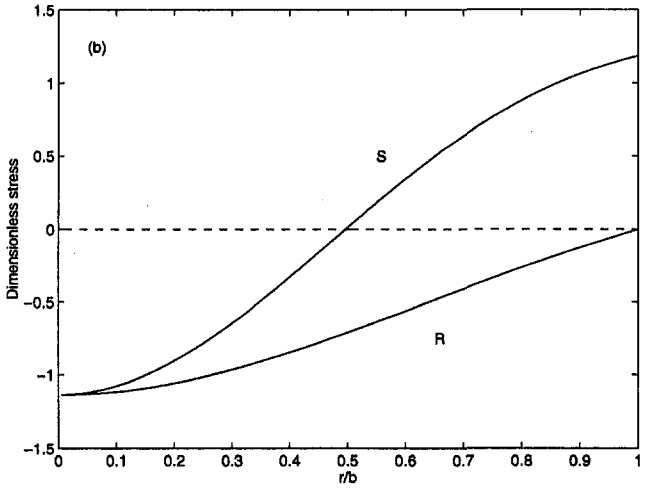

Fig. 3 Normalized distributions of σ_{rr} and $\sigma_{\theta\theta}$ at $z = -H/2$ in a simply supported circular disk: (a) $a/b = 0.4$; and (b) $a/b = 1.0$. $R = 4\sigma_{rr}/[E\alpha(T_{max} - T_0)]$, $S = 4\sigma_{\theta\theta}/[E\alpha(T_{max} - T_0)]$.

Table 2 Temperature and heat flux at which a simply supported plate reaches yield stress during localized heating: T_{max} in kelvin and $q \cdot H$ in MW · mm/m^2

Material		a/b				
		0.1	0.4	0.75	1.0	∞
DS Copper (C15715-H04)	T_{max}	616	633	696	766	1343
	$q \cdot H$	*112*	*118*	*138*	*160*	*323*
Chromium Copper (C18200-TH04)	T_{max}	641	659	711	765	1343
	$q \cdot H$	*120*	*127*	*146*	*167*	*376*
Tungsten (wrought)	T_{max}	873	907			3683
	$q \cdot H$	*78*	*82*			*376*
Tungsten (recrystallized)	T_{max}	599	610	645	688	3683
	$q \cdot H$	*43*	*45*	*50*	*55*	*340*
Molybdenum (recrystallized)	T_{max}	556	575	630	705	2883
	$q \cdot H$	*35*	*37*	*44*	*53*	*200*
Aluminum (6061-T651)	T_{max}	461	466	477	491	885
	$q \cdot H$	*28*	*29*	*31*	*33*	*106*
Stainless Steel (304L, 10% cw)	T_{max}	502	515	561	615	1670
	$q \cdot H$	*3*	*3*	*4*	*5*	*35*

$$N_r = -\frac{E\alpha H}{r^2}\left[\frac{r^2}{b^2}\left(\frac{1+\nu}{1-\nu}\right)\int_0^b r\bar{T}(r)dr + \int_0^r r\bar{T}(r)dr\right]$$

$$N_\theta = -\frac{E\alpha H}{r^2}\left[\frac{r^2}{b^2}\left(\frac{1+\nu}{1-\nu}\right)\int_0^b r\bar{T}(r)dr - \int_0^r r\bar{T}(r)dr + r^2\bar{T}(r)\right]. \quad (12)$$

Integration of these equations using Eq. (3) provides the stresses:

$$\sigma_{rr} = -\left[\frac{E\alpha(T_{max} - T_0)}{8}\right]\left[\left(\frac{a}{r}\right)^2(1 - e^{-2r^2/a^2}) + \left(\frac{1+\nu}{1-\nu}\right)\left(\frac{a}{b}\right)^2(1 - e^{-2b^2/a^2})\right]\left(1 - \frac{2z}{H}\right); \quad (13)$$

$$\sigma_{\theta\theta} = -\left[\frac{E\alpha(T_{max} - T_0)}{8}\right]\left[\left(\frac{1+\nu}{1-\nu}\right)\left(\frac{a}{b}\right)^2(1 - e^{-2b^2/a^2}) - \left(\frac{a}{r}\right)^2(1 - e^{-2r^2/a^2}) + 4e^{-2r^2/a^2}\right]\left(1 - \frac{2z}{H}\right). \quad (14)$$

The radial stress has a single compressive extremum at (r, z) = (0, $-H/2$) (Fig. 4). The hoop stress has a compressive extremum at (r, z) = (0, $-H/2$) and a tensile extremum at (r, z) = ($1.2676a$, $-H/2$). The compressive extremum of hoop stress has a larger magnitude than the tensile extremum; the tensile extremum becomes a compressive extremum for $a/b > 0.485$ (with $\nu = 0.3$) and is located at the edge of the plate ($r = b$) for $a/b > 0.789$.

Values of T_{max} and the heat flux at the onset of yielding are given in Table 3. When $a/b \ll 1$ (a localized hot-spot), the results are identical to those for a simply supported plate: edge constraints are unimportant in this limit. For larger a/b, the heat fluxes at onset of yielding are considerably lower for a fixed plate than for a simply supported plate, owing to higher compressive membrane stresses. One consequence is that allowable temperatures prior to yielding are much lower. As a result, materials with poor high temperature strength, like aluminum, perform somewhat less poorly relative to other materials.

The solution for uniform heating can be obtained from Eqs. (13–14) by letting $a/b \to \infty$. The results are generally well-known (Johns, 1965) and contain both membrane stress and bending stress:

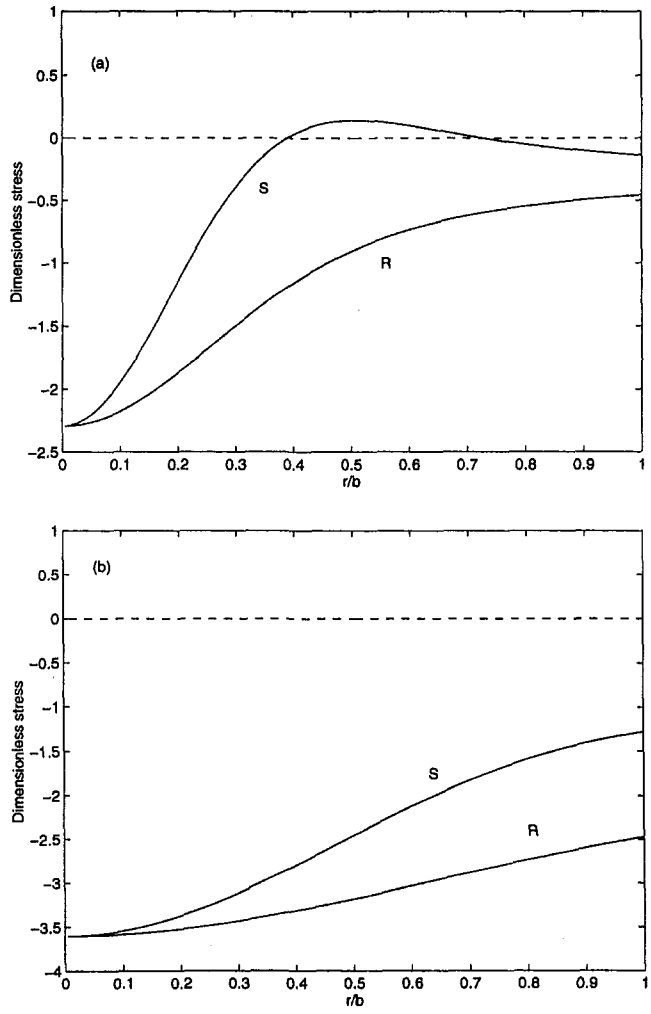

Fig. 4 Normalized distributions of σ_{rr} and $\sigma_{\theta\theta}$ at $z = -H/2$ in a circular disk fixed along its outer radius: (a) $a/b = 0.4$; and (b) $a/b = 1.0$. $R = 4\sigma_{rr}/[E\alpha(T_{max} - T_0)]$, $S = 4\sigma_{\theta\theta}/[E\alpha(T_{max} - T_0)]$.

$$\sigma_{rr} = \sigma_{\theta\theta} = -\left[\frac{E\alpha(T_{max} - T_0)}{2(1-\nu)}\right]\left(1 - \frac{2z}{H}\right). \quad (15)$$

The maximum stresses are compressive and occur on the hot surface ($z = -H/2$); the stress at the opposite surface is zero.

Table 3 Temperature and heat flux at which a fixed-edge plate reaches yield stress during localized heating: T_{max} in kelvin and $q \cdot H$ in MW · mm/m²

Material		a/b				
		0.1	0.4	0.75	1.0	∞
DS Copper (C15715-H04)	T_{max}	610	581	525	494	429
	$q \cdot H$	*110*	*100*	*82*	*71*	*49*
Chromium Copper (C18200-TH04)	T_{max}	639	610	555	523	450
	$q \cdot H$	*119*	*109*	*89*	*77*	*52*
TZM Alloy (wrought)	T_{max}	1052	980	841	764	606
	$q \cdot H$	*94*	*86*	*70*	*60*	*41*
Tungsten (wrought)	T_{max}	864	811	714	643	557
	$q \cdot H$	*77*	*71*	*59*	*49*	*38*
Tungsten (recrystallized)	T_{max}	598	579	543	522	473
	$q \cdot H$	*43*	*41*	*36*	*33*	*26*
Molybdenum (recrystallized)	T_{max}	556	525	478	450	395
	$q \cdot H$	*35*	*31*	*24*	*21*	*13*
Aluminum (6061-T651)	T_{max}	461	455	442	430	400
	$q \cdot H$	*28*	*27*	*25*	*23*	*17*
Stainless Steel (304L, 10% cw)	T_{max}	502	478	438	420	381
	$q \cdot H$	*3*	*3*	*2*	*2*	*1*

Table 4 Values of $\zeta = (1 + \nu)\alpha\Delta T(b/H)^2$ below which classical plate results are applicable

Boundary Condition	a/b				
	0.1	0.4	0.75	1.0	∞
Fixed edge	16.4	2.4	0.85	0.50	2.4
Simply supported	12.5	1.4	0.60	0.45	0.26

In this situation, both temperature and stress are independent of radius. The uniformly heated fixed-edge limit is the most unfavorable situation for thermal stress. To reach higher fluxes without yielding in a uniform heating configuration, the heat transfer surface should be designed to allow lateral expansion that relieves the membrane stresses.

Restrictions

Cooling system pressure will add additional stress within the plate which may either exacerbate or ameliorate the thermal stress. Such stresses should be compared to thermal stresses in any effort to design with the present results (see, e.g., Lienhard et al., 1996). Generally, pressure stresses will be proportional to $p(b/H)^2$, for p the gage pressure, so that these stresses are most significant for high aspect ratio plates.

The solutions given above are based on classical plate theory, which is valid only when the membrane stresses do not contribute to the bending deflection and when nonlinear strains can be neglected. These conditions are generally met when the plate deflection w is small compared to the plate thickness H. Since the size of the deflection increases with plate diameter, this implies that our solutions are valid only for sufficiently small values of b/H.

The limiting value of b/H can be estimated by finding the value of $\zeta = (1 + \nu)\alpha\Delta T(b/H)^2$ below which the nonlinear strains can be ignored (roughly $w/H < 0.1$) and the error in the classical solution for w is less than 10 percent (the contribution of bending deflection to the stress is order of unity for all cases other than the fixed-edge case with $a/b \to \infty$). The error in the fixed-edge solution has been estimated using Pal's finite amplitude equations (Pal, 1969) for $a/b \geq 0.7$.

The limiting value of ζ is given for each case in Table 4. For all simply supported cases and the fixed-edge case with $a/b = 0.1$ and 0.4, the limiting values are those at which the classical plate solution for w/H (Goodier, 1957) reaches 10 percent. For the other fixed-edge cases, the values are those at which the classical deflection differs from Pal's solution by 10 percent; when $a/b \to \infty$, the fixed-edge limit is that for buckling of the plate.

As an example, a fixed-edge TZM plate with $a/b = 0.75$ will be described by our solutions while $\zeta \leq 0.85$ or, with $\alpha\Delta T$ calculated from data in Tables 1 and 3, for $b/H \leq 15$—plates whose diameters are no more than 30 times their thickness. For a DS copper plate under the same conditions, the diameter should not exceed 26 times the thickness.

Acknowledgments

JHL was funded by the INEEL University Research Consortium. The INEEL is managed by Lockheed Martin Idaho Technologies Company for the U.S. Department of Energy, Idaho Operations Office under Contract No. DE-AC07-94ID13223. DSN was supported by a fellowship from the Defense Nuclear Facilities Safety Board.

References

Abdou, M. A., et al., 1984, *Technical Assessment of the Critical Issues and Problem Areas in High Heat Flux Materials and Component Development*, vol. 2 of *Magnetic Fusion Energy Plasma Interactive and High Heat Flux Components*, DOE Office of Fusion Energy Task Group on High Heat Flux Material

and Component Development, Center for Plasma Physics and Fusion Engr., UCLA, Los Angeles, CA.

ASM, 1985, *Metals Handbook,* 9th ed., American Society for Metals, Metals Park, OH.

Boley, B. A., and Weiner, J. E., 1960, *Theory of Thermal Stresses,* John Wiley, New York.

Dahbura, R. S., 1996, personal communication, MIT, Cambridge, MA.

Goodier, J. N., 1957, "Thermal Stress and Deformation," *ASME Journal of Applied Mech.,* September, pp. 467–474.

Holt, J. M., Mindlin, H., and Ho, C. Y., eds., 1995, *Structural Alloys Handbook,* CINDAS, Purdue University, West Lafayette, IN.

Johns, D. J., 1965, *Thermal Stress Analyses,* Pergamon Press, Oxford.

Lienhard V, J. H., Dahbura, R. S., Younis, H. F., and Oh, C. H., 1996, "Large Area Jet-Array Cooling Modules for High Heat Fluxes," *High Heat Flux Engineering III,* Society of PhotoOptical Instrumentation Engineers (SPIE); Bellingham, WA, Vol. 2855, pp. 66–81.

Lienhard V, J. H., and Khounsary, A. M., 1993, "Liquid Jet Impingement Cooling in Conjunction with Diamond Substrates for Extremely High Heat Flux Applications," *High Heat Flux Engineering II,* Society of PhotoOptical Instrumentation Engineers (SPIE), Bellingham, WA, Vol. 1997, pp. 29–43.

Lienhard V, J. H., and Napolitano, D. S., 1996, "Thermal Stress Limits of Plates Subjected to Extremely High Heat Flux," *Proc. Heat Transfer Division Vol. 2,* ASME HTD-Vol. 333, pp. 23–35.

Liu, X., and Lienhard V, J. H., 1993, "Extremely High Heat Fluxes Beneath Impinging Liquid Jets," ASME JOURNAL OF HEAT TRANSFER, Vol. 115, pp. 472–476.

Napolitano, D. S., 1995, "Stress Induced Failure in Materials Subjected to Extremal Heat Fluxes," S. M. thesis in Mechanical Engineering, MIT, Cambridge, MA.

Pal, M. C., 1969, "Large Deflections of Heated Circular Plates," *Acta Mechanica,* Vol. 8, pp. 82–103.

Peckner, D., and Bernstein, I. M., eds., 1977, *Handbook of Stainless Steels,* McGraw-Hill, New York.

Tauchert, T. R., 1986, "Thermal Stresses in Plates—Statical Problems," in *Thermal Stresses,* R. B. Hetnarski, ed., Vol. 1, Elsevier Science Publishers, New York.

Tietz, T. E., and Wilson, J. W., 1965, *Behavior and Properties of Refractory Metals,* Stanford University Press, Stanford, CA.

Touloukian, Y. S., 1979, *Thermophysical Properties of Matter,* Vol. 1, Purdue University, West Lafayette, IN.

Ugural, A. C., and Fenster, S. K., 1975, *Advanced Strength and Applied Elasticity,* Elsevier, New York.

B. Xiong

C. M. Megaridis
Assoc. Mem. ASME
cmm@uic.edu

Department of Mechanical Engineering,
M/C 251,
University of Illinois at Chicago,
842 W. Taylor Street,
Chicago, IL 60607-7022

D. Poulikakos
Institute of Energy Technology,
Swiss Federal Institute of Technology,
ETH Center,
Zurich, Switzerland

H. Hoang
Corporate Manufacturing Research Center,
Motorola,
Schaumburg, IL 60196

An Investigation of Key Factors Affecting Solder Microdroplet Deposition

This paper combines a theoretical model with experimental measurements to elucidate the role of key operating parameters affecting solder microdroplet deposition in the electronics manufacturing industry. The experimental investigation is used to evaluate the final deposit (bump) shapes and trends predicted by the model. The effects of substrate temperature, material composition, layer thickness, and thermal contact resistance (including surface oxidation) are delineated. Solder-deposit shape comparisons between experiments and modeling suggest that the value of thermal contact resistance may change with process parameters, and is probably dependent on the solder phase. It is established that inferences regarding the overall shape or solidification times of solder bumps using limited modeling trends should be made only after careful consideration of the substrate composition, accurate representation of the thermal contact resistance, and adequate resolution of the fluid dynamical oscillatory motion and its effects on solidification rates. It is shown that modeling tools can be used in conjunction with experiments to promote our fundamental understanding of the transport processes in the complex solder jetting technology.

Introduction

The dynamic spreading and solidification of solder droplets during impact onto cooler substrates are phenomena of critical importance to the mounting of microelectronic components (Hayes et al., 1993). Solder bead deposits (bumps) in the size range of 25 μm–100 μm provide efficient contact between electronic circuit components. These deposits are dispensed on substrates in their liquid state with injection velocities typically around 1 m/s. The distance from the injection orifice to the substrate is of the order of 1 mm. During flight, solder droplets cool convectively before they collide with the substrate. During impact, each solder droplet spreads and may possibly recoil before solidification occurs. The final shape of the solder deposit (or bump) is critical in solder jetting applications and is influenced not only by the impact dynamics, but also by the heat removal process from the molten metal to the substrate. The technological need for reliable prediction of solder bump shapes has sparked renewed interest in understanding the complex transport phenomena pertinent to solder jetting.

The basic problem configuration in solder microdispensing is illustrated in Fig. 1. A comprehensive review of the operating parameter ranges and the relative importance of the pertinent physical mechanisms has been published by Poulikakos and Waldvogel (1996). As seen in Fig. 1, there exist two distinct stages of solder jetting, namely flight and impact. A detailed study by Megaridis (1993) focused on the presolidification fluid dynamics and energy transport phenomena of a superheated liquid-metal droplet injected in a uniform inert-gas stream. It was reported that the high thermal conductivity of most metals cause the droplet to be nearly isothermal throughout its flight path.

The spreading and simultaneous solidification of liquid droplets on flat surfaces has been examined using an array of simplifying assumptions needed to make the analysis or the interpretation of experiments more tractable (Madejski, 1976; Collings et al., 1990; Kang et al., 1995; Liu et al., 1995; Wang and Matthys, 1996). Most recent investigations in this area have adopted detailed approaches which involved experiments (Zhao et al., 1996b), numerical simulations (Delplanque et al., 1996; Zhao et al., 1996a), or a combination of the two (Watanabe et al., 1992; Trapaga et al., 1992).

Watanabe et al. (1992) combined modeling and experiments to study the spreading and solidification of large molten hydrocarbon droplets impinging on cold substrates with velocities of the order of 1 m/s. The solution of the Navier-Stokes equations was performed using the simplified marker and cell approach to track shape deformation. Trapaga et al. (1992) also employed a combination of modeling and experiments to study droplet spreading and solidification on a flat surface. They implemented a commercially available code (FLOW-3D) to solve the Navier-Stokes equations, and used high-speed videography to record the spreading of large molten-metal droplets during impact.

Gao and Sonin (1994) studied the deposition of molten wax microdrops (using single droplets), low and high frequency deposition of multiple droplets to produce columns, sweep deposition of continuous beads, and repeated sweep deposition to build layered objects. Their theoretical analysis made order-of-magnitude estimations of the time needed to remove the initial superheat, the time to remove the latent heat during freezing, and the time required to cool the deposit to ambient temperature. Convection effects within the droplet and thermal contact resistance at the splat-substrate interface were neglected.

Liu et al. (1995) estimated the thermal contact coefficient between molten nickel droplets and different substrates by matching their experimental data to predictions of a one-dimensional heat conduction and phase change model. A follow-up study by Wang and Matthys (1996) used similar techniques but with improved time resolution to quantify the same coefficient for large molten copper drops impacting on cold metallic substrates. Both studies showed that interfacial thermal contact resistance can increase by an order of magnitude during solidification on metal substrates.

Amon et al. (1996) investigated the remelting phenomena occurring in microcasting, a process utilizing the continuous dispension of molten-metal drops for the rapid manufacture of

Contributed by the Heat Transfer Division for publication in the JOURNAL OF HEAT TRANSFER and presented at 1997 NHTC, Baltimore. Manuscript received by the Heat Transfer Division December 20, 1996; revision received November 6, 1997; Keywords: Electronic Equipment; Liquid Metals; Sprays/Droplets. Associate Technical Editor: A. S. Lavine.

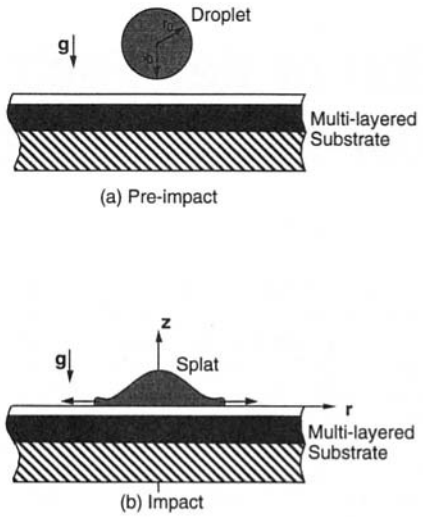

Fig. 1 Basic stages in solder microdroplet dispensing: (*a*) flight; (*b*) impact

near net shape objects. They combined analytical, numerical, and experimental methods to examine the metallurgical bonding between the impinging droplets and the already deposited material. The modeling in that work neglected convection and multidimensional effects. Orme et al. (1996) described a precision droplet-based manufacturing technique for the production of structural materials of superior mechanical characteristics. They presented experimental and computational results defining trajectories and thermal conditions at impact of electrostatically charged molten droplets used as deposition elements.

Delplanque et al. (1996) presented a numerical investigation of micropore formation in solidifying molten metal droplets impinging with high velocities (several hundred meters per second) on a colder substrate. Zhao et al. (1996a) reported a finite-element model studying the fluid dynamics and heat transfer phenomena during droplet impingement upon a substrate. They presented detailed data on the transient behavior of temperature fields during the impact of molten-metal drops on cooler substrates and of water droplets on hot surfaces. In an experimental study conducted simultaneously with their modeling work, Zhao et al. (1996b) utilized two-reference-beam pulse holography to visualize droplet deformation, and devised a novel photoelectric method to record the radius of an impacting opaque droplet as a function of time.

Because experimental measurements are intrinsically handicapped in resolving the time and space resolution necessary for solder jetting applications, numerical modeling offers itself as an attractive alternative for advancing knowledge in solder dispensing technologies. As solder microdroplet dispensing utilizes relatively low droplet injection speeds, it is particularly important to consider multidimensional transport effects (Rein, 1995). The first detailed study to address the unsteady multidimensional fluid dynamics coupled with heat transfer in soldering applications was conducted by Waldvogel et al. (1996) who used a finite-element method with a shape-adaptive mesh to track the large domain nonuniformities characteristic of such spreading processes. Subsequently, Waldvogel and Poulikakos (1997) extended this model to account for solidification, and modeled the impact of eutectic 63% Sn-37% Pb solder droplets on composite, two-layer substrates. They analyzed the influence of four process parameters, namely, initial droplet temperature, impact velocity, thermal contact resistance at the droplet-substrate interface, and substrate temperature. The relative time scales of the deformation, cooling and solidification processes were found to be crucial in the determination of the solidified droplet shape.

The current work extends the recent model of Waldvogel and Poulikakos (1997) to accommodate complex substrate configurations—such as circuit board pads and multilayer substrate compositions—which are more representative of practical applications than the two-layered flat substrates considered previously. Furthermore, the model is employed to investigate the effects of substrate material composition, layer thickness, and thermal contact resistance (including surface oxidation), all of which are process parameters of critical importance in solder jetting applications and have not been examined previously. Finally, an experimental investigation of solidified solder droplets deposited by a prototype apparatus is used to evaluate the bump shapes and trends predicted by the model.

Model Description

The model simulates the axisymmetric impact and subsequent solidification of an initially spherical, molten solder droplet on a flat horizontal multilayer composite substrate. The model of Waldvogel and Poulikakos (1997) was extended in this study to accommodate substrates in the shape of cylindrical pads which are of interest in electronic component assembly. In all cases considered herein, the droplet is injected along the gravitational direction that is orthogonal to the target surface. The Navier-Stokes equations, combined with heat transfer and solidification equations, are solved in the liquid phase using a Lagrangian approach. The heat conduction equation is solved in the solid phase, i.e., substrate and solidified sector of the splat. It is noted that the employed axisymmetric approach is valid for situations where the solder droplet impinges on the substrate at an angle equal or approaching 90 deg. The mathematical model formulation has been described elsewhere in detail (see Waldvogel and Poulikakos, 1997), and will not be repeated here for brevity. However, a brief description is given in the following for completeness.

Fluid Dynamics. Laminar flow of a constant property fluid (molten solder) is assumed. The radial and axial components of the momentum equation are considered along with the continuity equation. The artificial compressibility method is employed, thus introducing a pressure term to the mass conservation equation. The free surface deformation is tracked by the two corresponding stress balance equations (along r and z). The wetting force at the dynamic contact line between the liquid droplet and the substrate is neglected throughout the analysis. This assumption is valid during the initial stages of droplet impact where inertia forces are high with respect to the retarding forces of viscosity and surface tension. In the case of solder jetting, solidification is likely to occur very quickly at the contact area, thus eliminating the need for a wetting condition altogether. The moving contact line is treated by allowing for slipping along the radial direction (Dussan, 1979). In this formulation, the slip distance l_s relates velocity and velocity gradient at the contact line according to

$$\left.\frac{\partial u}{\partial z}\right|_c = \frac{u|_c}{l_s}. \tag{1}$$

A sensitivity analysis using the model showed that variations of the value of l_s over a range from $10^{-3}\ d_o$ to $10^3\ d_o$ had little influence on the final bump shape. This is probably the combined outcome of the spatially limited region of the flow field on which the slip condition is applied, the dominance of fluid inertia, and the rapid solidification which abruptly halts liquid spreading. A value of $l_s = 10^3\ d_o$ was used for the slip distance in all simulations presented in this study.

Heat Transfer. The Lagrangian formulation is used for the conjugate heat transfer process in the droplet and the substrate. The energy conservation equation is solved in the droplet interior as well as in the substrate. Heat transfer from all exposed

surfaces is neglected. The thermal contact resistance between the droplet and the substrate is modeled by a thin layer of arbitrary thickness. This layer is assigned zero heat capacity and experiences only axial conduction.

Solidification. The following assumptions are made regarding the solidification of the molten-solder droplet. First, since a eutectic alloy is studied, a sharp boundary separating distinct liquid and solid regions is included in the model. Furthermore, it is assumed that phase change occurs at the equilibrium freezing temperature. It is noted that the droplet solid and liquid phase densities are nearly identical since the 63% Sn-37% Pb solder material experiences only a 0.2 percent contraction upon freezing. The exact specific heat method proposed by Bushko and Grosse (1991) was adopted to model solidification. This approach facilitates the finite element formulation and has the added advantage that it is very accurate in conserving energy as the droplet solidifies.

Numerical Solution Procedure

The computational domain was discretized with a mesh of triangular elements, and the numerical model was solved using a Galerkin finite element method. Quadratic and linear shape functions were used for velocity and pressure, respectively. An implicit method was utilized for the numerical integration of the fluid dynamics equations in time, while a Crank-Nicholson scheme was used for the energy equation. The details of the iterative solution technique and mesh generation algorithm are given in Waldvogel and Poulikakos (1997). As reported therein, the spatial resolution found to provide grid and time-step independence featured 604 nodes in the droplet and 1154 nodes in the substrate. A slightly finer grid (633 × 1374) was used in the flat substrate simulations reported herein, while an even finer grid (713 × 1384) was used in the pad simulations to assure grid-size independence. A dimensionless time step of $\delta t U_o/d_o = 5 \times 10^{-4}$ was found adequate for time-step insensitive results.

Experimental Work

The prototype jetting apparatus employed in the experiments is depicted schematically in Fig. 2. The device features a heated reservoir in which high-purity 63% Sn-37% Pb solder is melted and maintained at 210°C during the tests. Nitrogen gas is used to pressurize the system forming the droplets and hinder the formation of oxides within the reservoir. Individual droplets are generated as a voltage pulse excites a piezoelectric transducer mounted within the device. The solder jetting assembly is mounted to a Universal Instruments high-accuracy XY positioning system which facilitates printing of solder droplets on precisely spaced locations on the heated substrate (Fig. 2). The droplet flight occurs in a nitrogen atmosphere to avoid formation of oxides. A vision system is utilized to follow the solder jet print head assembly as it is moved into position above the stationary substrate with a placement accuracy of the order of 10 μm. The motion of the solder print head and the operation of the droplet generator are controlled by a personal computer. The droplet impact velocity U_o is determined using a stroboscope and a steady stream of droplets generated at a known injection frequency.

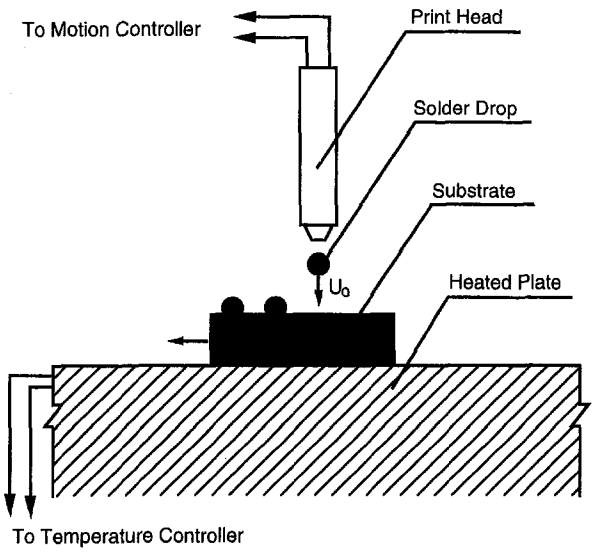

Fig. 2 Schematic of the prototype solder jetting apparatus used in the experiments

The solidified solder droplet shape was evaluated under a variety of conditions using scanning electron microscopy (SEM). Because the experimental shapes were recorded at an angle with respect to the plane of the substrate surface, a parallax error correction had to be applied to the experimentally observed bump outlines. This corrective procedure was performed for all experimental shapes, and allowed the zero-angle view of each bump to be reconstructed for direct comparisons with the model predictions. The reverse procedure was used to produce the model-predicted shape of the bump when viewed at an angle similar to that used in the experiment. The experimental results reported herein were obtained using a two-layer composite substrate consisting of 2 μm Ni on 212 μm Si.

Results and Discussion

The numerical simulations conducted are divided in sections, each corresponding to the influence of a specific solder jetting parameter. Some material properties are given first for completeness.

Thermophysical Properties. The following values are used for 63% Sn-37% Pb solder in the molten phase: surface tension coefficient 0.345 N/m; viscosity 0.00262 kg/m s. The melting temperature for this eutectic solder is 183°C, and its latent heat of fusion is 42 kJ/kg. Table 1 lists additional thermophysical properties of solder, as well as those of several substrate materials. These properties were obtained from Hewitt et al. (1994) and Lide (1995).

Baseline Conditions. The base case conditions correspond to a 63% Sn-37% Pb solder droplet with preimpact diameter d_o = 53 μm, velocity U_o = 1.6 m/s, and temperature T_{inj} = 210°C. This droplet is considered to collide with a substrate of initial temperature T_{sub} = 35°C. The nondimensional numbers relevant to the baseline conditions are as follows:

$$\text{Re} = 266, \quad \text{We} = 3.23, \quad \text{Fr} = 4930,$$

$$\text{Pr} = 0.025, \quad \text{and} \quad \text{Ste} = 0.77.$$

Thermal Contact Resistance. The thermal contact resistance between an impinging droplet and the target substrate is quantified by a dimensionless coefficient (Biot number), defined by

$$\text{Bi} = h_c d_o / k_o. \tag{2}$$

In this definition, h_c denotes the heat transfer coefficient for the thin contact area between the droplet and the substrate, while k_o denotes the thermal conductivity of the solder, and d_o denotes the droplet diameter before impact. Unfortunately, no correlations published to date have been identified to determine the value of h_c in the parametric domain of solder jetting. To this end, specific attention is given in the current study to identify the thermal contact resistance in solder microdroplet dispensing and, in turn, facilitate future studies in this area. It is noted that Liu et al. (1995) and Wang and Matthys (1996) reported that

Table 1 Thermophysical properties of solder and substrate materials

Substance	Density (kg/m^3)	Specific Heat (J/kg K)	Thermal Conductivity (W/m K)
63%Sn–37%Pb Solder (Liquid)	8,218	238	25
63%Sn–37%Pb Solder (Solid)	8,240	176	48
Copper (Cu)	8,933	385	401
Nickel (Ni)	8,900	444 (at 25°C)	90.7 (at 25°C)
		485 (125°C or 180°C)	80 (125°C or 180°C)
Gold (Au)	19,300	129	317
Silicon (Si)	2,330	712	148 (at 25°C)
			98.9 (at 125°C)
			94 (180°C)
FR4*	1,924	1,570	0.26

* Common organic circuit board material consisting of epoxy with fiberglass reinforcement

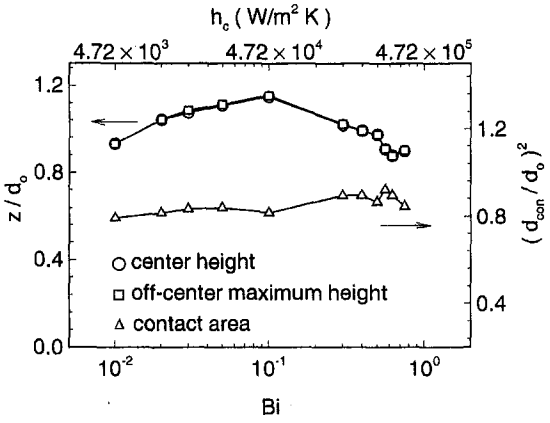

Fig. 3 Geometric parameters describing the solder bump shape and its dependence on thermal contact resistance: z/d_o denotes the dimensionless height either on the symmetry axis (circles) or at the off-axis location of maximum elevation (squares); $(d_{con}/d_o)^2$ denotes the dimensionless contact area between the solidified solder droplet and the substrate

the thermal contact coefficient between large molten nickel or copper droplets and copper, aluminum, or stainless steel substrates can decrease by an order of magnitude during solidification.

Thermal Contact Resistance of Solder on a Ni/Si Substrate. The effect of thermal contact resistance between substrate and the impacting solder droplet is examined first to evaluate the influence of this parameter on deposited solder bump shape. A two-layer composite substrate is considered with the top layer composed of nickel with a thickness of 2 μm, and the bottom layer consisting of silicon (212 μm thick). This composition is characteristic of practical situations and has been chosen primarily because of the availability of experimental data in these conditions; see Waldvogel and Poulikakos (1997). A series of model simulations was performed with all process parameters fixed to the baseline values stated above, while the values of Bi were varied over a range from 0.01 to 0.75. Even though the value of Bi changed from run to run, it was kept constant throughout each simulation. The above values of Bi correspond to contact heat transfer coefficients h_c in the range 4–350 kW/m^2 K. This range covers the values utilized in previous studies; for example, the values of h_c examined by Waldvogel and Poulikakos (1997) varied from 5 to 25 kW/m^2 K.

The simulations performed regarding the influence of thermal contact resistance can also be viewed as indicative of practical situations where the substrate surface is partially oxidized. The presence of an oxide on the substrate surface increases the thermal contact resistance (reduces the value of Bi). For example, the thermal conductivity of pure copper is 401 W/m K, while the same property for CuO is around 15 W/m K, and 5 W/m K for Cu_2O. Thus, partial coverage of the surface of a pure-copper substrate by copper oxide(s) would result in thermal contact resistance in between the values corresponding to Cu and Cu_2O. It is recognized, however, that the presence of a surface oxide affects not only thermal contact resistance, but may also cause changes in the wetting angle or the smoothness of the substrate surface. Such changes are expected to influence the droplet spreading rate, but are neglected in this work.

Figure 3 presents two geometric parameters describing the solidified-bump shape and its dependence on thermal contact resistance. Both parameters are plotted in their dimensionless form versus Biot number (or heat transfer coefficient h_c). Two values of height (z/d_o) for each solidified bump appear in Fig. 3: one on the symmetry axis and another at the off-axis location of maximum elevation (the maximum elevation may not lie on the axis). It is clear that for all values of Bi examined, these two heights are essentially identical. Figure 3 also shows that the bump height varies by up to 20 percent depending on thermal contact resistance; the maximum height is realized at Bi = 0.1 (or h_c = 47.2 kW/m^2 K). These variations of bump dimensions with thermal contact resistance can be critical in solder jetting, as solder bump height deviations of only a few percent can be detrimental to the successful implementation of the technique in high-precision electronic component manufacturing. The dimensionless contact area $(d_{con}/d_o)^2$ between the solidified solder droplet and the substrate demonstrates a weaker dependence on thermal contact resistance, with an overall increasing trend towards higher values of Bi or h_c. According to this trend, more efficient heat transport results in larger contact area, and, in turn, better attachment of the bump on the substrate.

Figure 4 displays the solder bump outline for each value of Bi and reveals that this shape is very sensitive to the contact

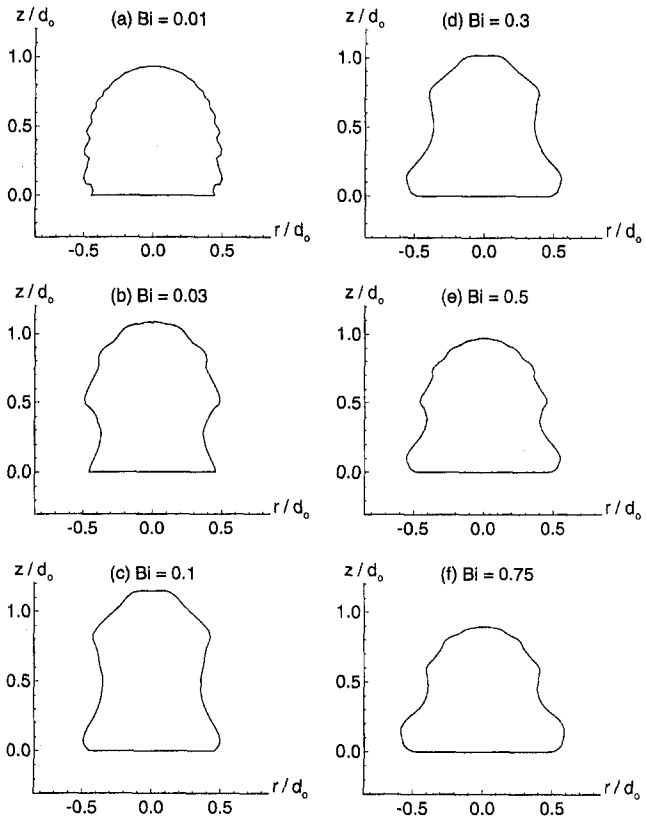

Fig. 4 Series of solidified solder bump shapes as predicted by the model for the different values of thermal contact resistance at the base case operating conditions: 63 percent Sn-37 percent Pb solder, d_o = 53 μm, U_o = 1.6 m/s, T_{inj} = 210°C, T_{sub} = 35°C

resistance between droplet and substrate. The number of surface ripples on each bump as well as the significant changes in their respective distances from the substrate indicate the dynamic competition between surface tension and fluid inertial forces (which cause droplet oscillations) with the upward propagation of the solidification front. A detailed comparison of the shapes given in Fig. 4 (obtained via modeling) with the shape determined experimentally for the baseline conditions led to the conclusion that the value Bi = 0.5 (or h_c = 235 kW/m^2 K) provides the best agreement between observed and predicted bump shapes. Shape comparisons were conducted by means of the morphology of the ripples on the outline of the bump and by measuring the contact area at the bump base. Figure 5 demonstrates the agreement leading to the designation of Bi = 0.5 (likewise h_c = 235 kW/m^2 K) as the base case value of this quantity. Figure 5(a) shows the bump geometry obtained in the experiments when the solder deposit was viewed at an angle. Figure 5(b) shows the model-predicted shapes for (I) constant Bi = 0.5, and (II) variable Bi (see discussion below).

The average value of Bi = 0.5, as providing the best agreement between experiment and modeling at T_{sub} = 35°C, was also utilized in an additional simulation for T_{sub} = 85°C where experimental bump shapes are available. For the elevated substrate temperature, the Stefan number is 0.5, being slightly lower than the base case value of 0.77. Figure 6 presents a comparison between (a) the shape of the bump observed experimentally at T_{sub} = 85°C, and (b) the outline predicted by the model using the constant value Bi = 0.5 (shape I). The apparent differences between these two bump geometries suggest that the value of thermal contact resistance (and thus the value of Bi or h_c)

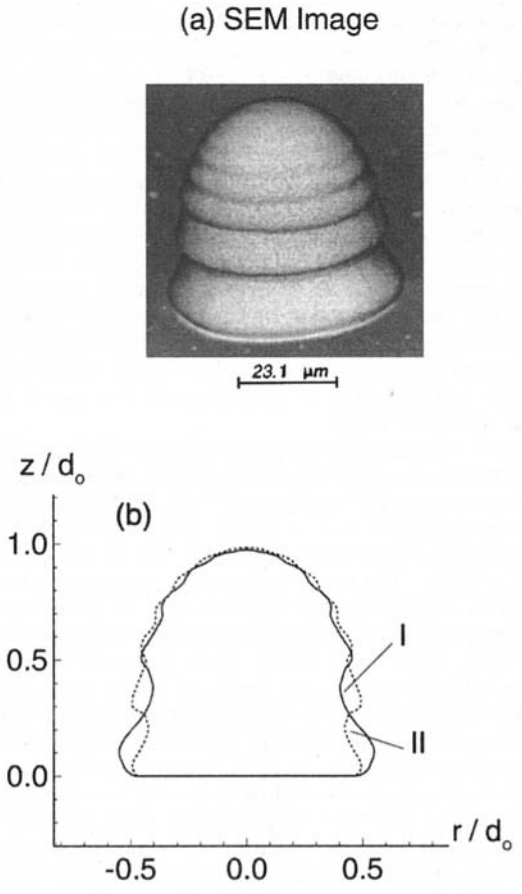

Fig. 5 (a) Solder bump geometry obtained in the experiments for the baseline conditions and a substrate temperature T_{sub} = 35°C; (b) model-predicted shapes for: (I) constant Bi = 0.5, and (II) Bi changing with phase, i.e., Bi$_l$ = 0.5 and Bi$_s$ = 0.0275

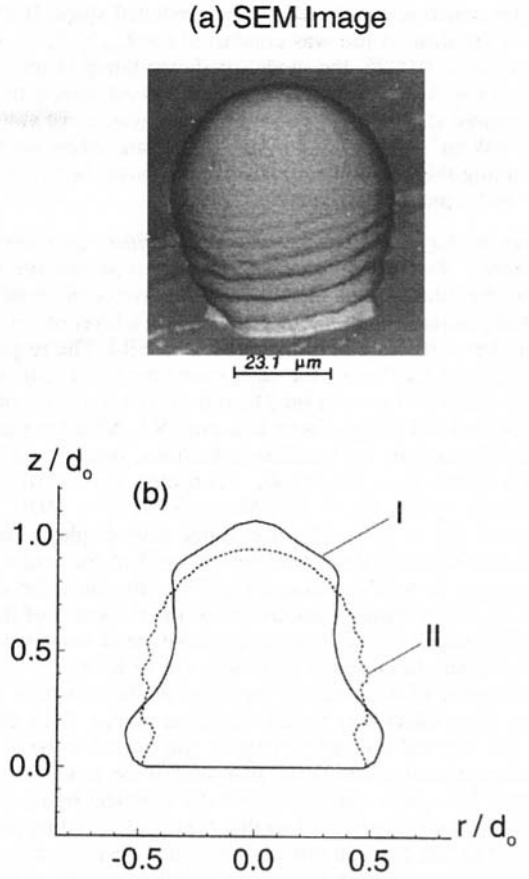

Fig. 6 (a) Solder bump geometry obtained experimentally for the baseline conditions and a substrate temperature T_{sub} = 85°C; (b) model-predicted shapes for: (I) constant Bi = 0.5, and (II) Bi changing with phase, i.e., Bi$_l$ = 0.5 and Bi$_s$ = 0.0275

changes with process parameters. The bump shape discrepancy seen in Fig. 6 further suggests the possibility of time-varying thermal contact resistance during the droplet impact period and subsequent solidification. This is consistent with the studies of Liu et al. (1995) as well as Wang and Matthys (1996) who reported that h_c can drop by an order of magnitude during solidification of a splat on a metal substrate. This possibility was investigated by conducting a series of additional simulations with values of Bi (or h_c) changing with the solder phase. A constant value Bi$_l$ was used for liquid solder/substrate contact, while a reduced value Bi$_s$ was used for solid solder/substrate contact. The respective values of Bi$_l$ and Bi$_s$ were determined as follows, taking into account that solidification halts the radial spreading of the droplet on the substrate. First, Bi$_l$ was designated to provide the same solder/substrate contact area as that measured in the experimental bumps. Subsequently, the value of Bi$_s$ was determined as the one providing the best agreement between the predicted and measured bump outlines at complete solidification. According to the results presented for a substrate temperature T_{sub} = 35°C, the value Bi$_l$ = 0.5 (h_c = 235 kW/m^2 K) is suggested for liquid solder/substrate contact. At T_{sub} = 85°C only fair agreement between experimental and predicted contact areas was obtained for Bi = 0.5. The value Bi$_s$ = 0.0275 (h_c = 13 kW/m^2 K) provided the best possible agreement between experiments and modeling at T_{sub} = 85°C. Figure 6(b) includes the model-predicted bump shape (curve II) for T_{sub} = 85°C, Bi$_l$ = 0.5, Bi$_s$ = 0.0275, and demonstrates the better agreement between experiment and modeling when the thermal contact is reduced nearly by twenty-fold with the appearance of the solid phase. It is noted, however, that the experimental bump of Fig. 6(a) demonstrates a "top-heavy"

character which is not shown by the predicted shape II of Fig. 6(*b*). A verification run was conducted for T_{sub} = 35°C, Bi_l = 0.5, and Bi_s = 0.0275; the model-predicted bump shape is displayed in Fig. 5(*b*) (curve II), and shows good agreement with the measured shape (Fig. 5(*a*)). Thus, the respective values h_c = 235 kW/m^2 K and 13 kW/m^2 K are suggested herein as representing thermal contact resistance between liquid or solid solder and a nickel substrate.

Effect of Layer Thickness and Composition in Composite Substrates. Two-layer substrates. Figure 7 shows the influence of the thickness of the top layer for two composite substrates of practical interest: one consisting of a layer of Au on Si, and another consisting of a layer of Cu on FR4. The respective thicknesses of the layers for each case are: (a) 1 μm Au on 212 μm Si; (b) 10 μm Au on 212 μm Si; (c) 2 μm Cu on 212 μm FR4; and (d) 10 μm Cu on 212 μm FR4. All other parameters are identical to the baseline conditions, namely, 63% Sn-37% Pb solder, d_o = 53 μm, U_o = 1.6 m/s, T_{inj} = 210°C, T_{sub} = 35°C, Bi = 0.5, Re = 266, We = 3.23, Fr = 4930, Pr = 0.025, and Ste = 0.77. The first frame also displays the fine spatial resolution of the finite-element grid at the end of this computation. In both Au/Si and Cu/FR4 substrates, the solidified bump shape remains insensitive to the thickness of the top layer. The origin of this counter-intuitive trend was examined by determining the thermal resistance (in m^{2}K/W) of the thin contact region ($1/h_c$) and the top layer of the substrate (L/k; L is the layer thickness) for all situations of Fig. 7. In all four cases, the thermal contact resistance was found to be at least two orders of magnitude larger than that of the top layer of the substrate. Thus, it is concluded that the identical bump shapes seen in Fig. 7 are due to the fact that the droplet cooling process is limited by the thermal contact resistance between the solder and the substrate, which is identical in all cases (Bi = 0.5).

Three-layer substrates. Figure 8 presents the influence of the substrate middle-layer thickness when a 70 μm diameter 63% Sn-37% Pb solder droplet impinges with a velocity 1.6 m/s on a three-layer substrate (Au on Ni on Si) which is at a temperature of 125°C. The preimpact temperature of the droplet is 210°C. The respective thicknesses of the layers for each case are: (a) 1 μm Au on 2 μm Ni on 175 μm Si, (b) 1 μm Au on 7 μm Ni on 175 μm Si, and (c) 1 μm Au on 10 μm Ni on 175 μm Si. In all cases, Bi = 0.5 (h_c = 178 kW/m^2 K), Re = 351, We = 4.2, Fr = 3730, Pr = 0.025, and Ste = 0.3. The solidified bump shapes shown in Fig. 8 indicate that for a 1 μm thick top layer of Au, the effect of the nickel sublayer thickness is practically negligible. The thermal conductivity of nickel at 125°C is about 80 W/m K, which is similar to the corresponding value for silicon at that temperature (98.9 W/m K). The close values of thermal conductivity of the substrate layers are responsible for the similar solidified bump shapes seen in Fig. 8. It is noted, however, that this trend may not hold at different substrate temperatures. For example, at a temperature of 35°C, the thermal conductivity of nickel is 40 percent lower than that of silicon.

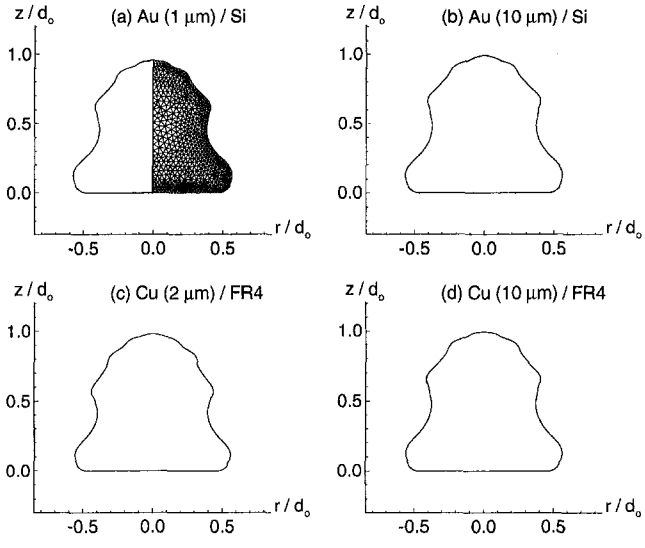

Fig. 7 Influence of thickness of the top layer for two composite substrates: one consisting of a layer of Au on Si, and another consisting of a layer of Cu on FR4. The thickness of the top layer is marked on each frame, while the thickness of the Si or the FR4 layer is 212 μm. All other parameters are identical to the baseline conditions. The first half frame also displays the fine spatial resolution of the finite-element grid at the end of this computation.

Figure 9 shows the influence of the thermal properties of the bottom layer, as well as the thickness of the top layer. Frames *a* and *b* of this figure correspond to three-layer substrates (1 μm Au on 2 μm Ni on 175 μm Si or FR4). All other conditions and dimensionless parameters are identical to those of Fig. 8. Comparison of Figs. 9(*a*) and 9(*b*) shows that the effect of the bottom layer is very important when the top layers are thin (of the order of a few microns). The insulating properties of FR4 result in prolonged solidification times, which, in turn, cause a different bump shape than that seen for Si. Figure 9(*c*) shows the final bump shape for a two-layer substrate (2 μm Ni on 175 μm Si). This case can be viewed as a limit of the three-layer (Au on Ni on Si) substrate case where the top layer of Au is infinitely thin. Our results indicate that the bump shape should be affected when the top layer of Au is extremely thin. This is expected physically, as the thermal conductivity of gold is 317 W/m K, which is significantly higher than that of nickel (80 W/m K) at the substrate temperature considered in Fig. 9.

Two-Layer Substrate: Effect of Surface Oxidation, Temperature, and Composition. In this set of simulations, 70 μm diameter 63% Sn-37% Pb solder droplets were considered to impinge with U_o = 1.6 m/s and T_{inj} = 210°C on two kinds of flat substrates: Ni (2 μm) either on Si or FR4 (both 175 μm). Three substrate temperatures were examined; T_{sub} = 25°C, 125°C, and 180°C. Oxidized substrate surface conditions were simulated by decreasing the value of the contact Biot number by a factor of 10, compared to the base case value of 0.5. The respective values of the contact heat transfer coefficient are h_c = 178 kW/m^2 K for Bi = 0.5, and 17.8 kW/m^2 K for Bi = 0.05. Since thermal contact resistance is inversely proportional to h_c, we deduce that the lower value of Bi for the oxidized substrate cases corresponds to higher values of thermal contact resistance. For all cases, Re = 351, We = 4.2, Fr = 3730, and Pr = 0.025. Also, Ste = 0.82 at T_{sub} = 25°C, Ste = 0.3 at T_{sub} = 125°C, and Ste = 0.02 at 180°C.

Figure 10 displays the temporal variations of dimensionless contact radius (r_{con}/d_o) and solder-droplet height (z_{top}/d_o on-axis) for substrates of 2 μm Ni on 175 μm Si. The time abscissa has been normalized as $\tau = tU_o/d_o$. Each column in Fig. 10 corresponds to a fixed value of Bi ((*a*)–(*c*) Bi = 0.5; (*d*) and (*e*) Bi = 0.05). The lower value of Bi represents a ten-fold increase in thermal contact resistance due to oxidation. Each row corresponds to one of the following three substrate temperatures: 25°C, 125°C, and 180°C. Each frame of Fig. 10 also contains an inset showing the predicted solder bump shape at complete solidification. The times required for complete solidification t_{solid} are also listed in Fig. 10 for comparison. Note that no frame is shown for T_{sub} = 180°C and Bi = 0.05, as no signs of solidification were detected up to t = 543 μs where the run was terminated. For Bi = 0.5, moderate heating of the Ni/Si substrate causes some deviation in the bump shape (compare Figs. 10(*a*) and 10(*b*)). The bump shape differences with temperature are more pronounced when Bi = 0.05, thus attesting to the high sensitivity of bump morphology at increased thermal contact resistance. In general, the time required for complete solidification increases with substrate temperature. It is noted,

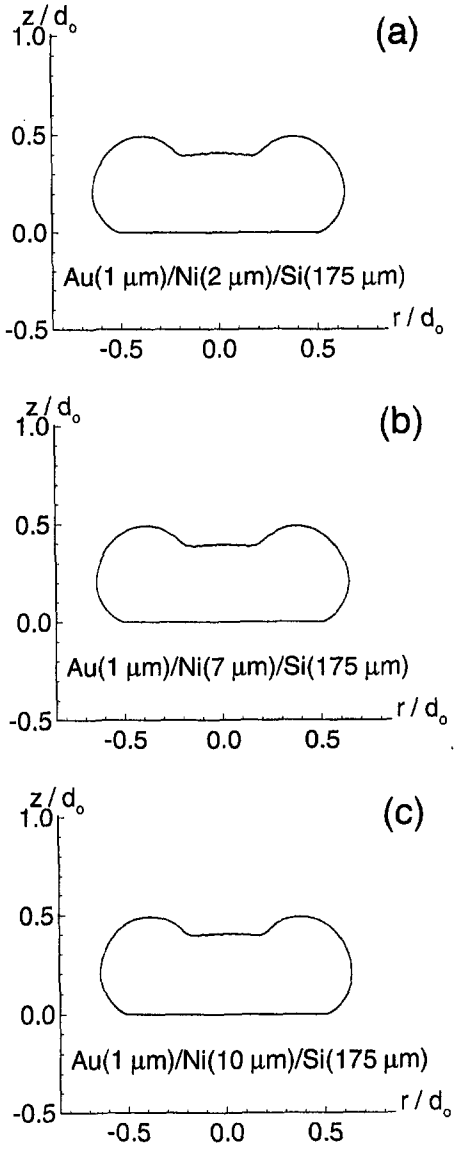

Fig. 8 Effect of the substrate middle-layer thickness when a 70 μm diameter 63 percent Sn-37 percent Pb solder droplet impinges with a velocity 1.6 m/s and a temperature 210°C on a three-layer substrate (Au on Ni on Si) which is at a temperature 125°C. The respective thickness of each layer is marked on the frames.

however, that the solidification times are almost identical when T_{sub} = 25°C and 125°C for Bi = 0.5, but are distinctly different when Bi = 0.05. Substrate temperatures near the melting point of the solder prolong the period for complete solidification and, in turn, affect the final bump shape (notice, for example, the multiple frozen-wave patterns on the periphery of the bump in Fig. 10(*c*)). A comparison of the two columns of Fig. 10 reveals that oxidation of the top substrate layer prolongs solidification, thus causing a more complex outer surface of the solidified bump. It is also well known that oxidation can prevent adherence of the deposit onto the substrate, thus hindering solder jetting accuracy and efficiency.

Figure 11 displays the temporal variations of contact radius and solder-droplet height for substrates of Ni (2 μm) on FR4 (175 μm). The left and right column correspond to Bi = 0.5 and 0.05, respectively. No frame is displayed for T_{sub} = 180°C and Bi = 0.05, as no solidification had commenced up to t = 513 μs when the run was terminated. As seen for the Ni/Si substrates, the bump shape differences with temperature are more pronounced when Bi = 0.05. Also, the time required for complete solidification increases monotonically with substrate temperature. The solidification times are almost identical when T_{sub} = 25°C and 125°C for Bi = 0.5, but are distinctly different when Bi = 0.05.

Careful examination of Figs. 10 and 11 reveals that the number of fluid oscillatory cycles seen in all z_{top}/d_o curves matches the number of ripples formed on the solidified bump. This is expected physically, as each ripple is created when the downward moving fluid mass meets the upward-propagating solidification front. In that respect, each ripple forms a marker of one fluid recoiling cycle. Comparison of Fig. 10 (Si base) and Fig. 11 (FR4 base) further shows that for Bi = 0.5 the number of ripples on the bump periphery increases when an insulating layer (such as FR4) is present in the substrate. However, this trend is not maintained when Bi = 0.05. The origin of this behavior was sought by tabulating the components of thermal resistance to the outflowing heat from the solidifying droplet to the substrate.

The first element of thermal resistance between the solder and the substrate bulk is the thin contact layer between the droplet and the top substrate surface. The contact layer resis-

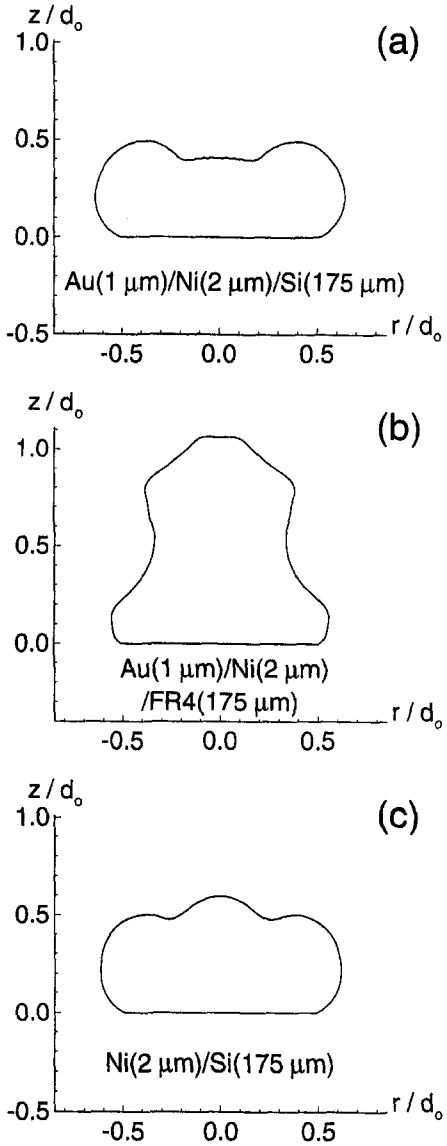

Fig. 9 Effect of thermal properties of the bottom substrate layer, as well as the thickness of the top layer. The respective thickness of each layer is marked on the figure. All other conditions are identical to those of Fig. 7.

tance has been quantified by the Biot number Bi = $h_c d_o/k_o$ in each simulation. As stated previously, the lower value of Bi for the oxidized substrate cases corresponds to higher values of thermal contact resistance. The substrate layers also contribute to the thermal resistance between the solder droplet and the bulk of the substrate. For conductive heat transfer, thermal resistance is proportional to the thickness of the substrate layer and inversely proportional to its thermal conductivity. The calculated components of thermal resistance for the runs of Figs. 10 and 11 are listed in Table 2. The ranges seen for the thermal resistance of Ni or Si layers reflect the variation of thermal conductivities of these semiconductor materials with temperature.

As seen for all cases listed in Table 2, the thermal resistance of the Ni layer remains negligible compared to the contributions of the interface contact or the bottom layer. The replacement of Si by FR4 when Bi = 0.5 causes the resistance of the bottom layer to become the heat-transport limiting factor, thus affecting the bump shape considerably (compare differences between Figs. $10(a)-(c)$ and Figs. $11(a)-(c)$). On the other hand, when Bi = 0.05 the contact layer maintains its important role in heat transport, even after the replacement of Si by FR4; note the overall similar solder bump shapes of Figs. $10(d)$, (e) and Figs. $11(d)$, (e).

Figure 12 presents a comparison of solidification times t_{solid} for all simulations relevant to Figs. 10 and 11. The dependence of t_{solid} on substrate temperature T_{sub} and contact resistance (or Bi likewise) is quite complex and needs to be ratified in conjunction with the thermal resistance data given in Table 2. As reported by Waldvogel and Poulikakos (1997), an increasing substrate temperature causes a delay of the onset of solidification. However, the additional time required for complete solidification of the solder droplet does not correlate monotonically with T_{sub}. In fact, as reported by Waldvogel and Poulikakos (1997), there exist situations where increasing substrate temperature leads to decreasing solder solidification time—a trend that appears counterintuitive. It was speculated that this is caused by the intense droplet dynamical motion which can have a drastic effect on freezing rates and, in turn, provide trends that contradict those obtained by using simplified physical considerations. Such trends were further displayed and verified in the current work; see, for example, the insensitivity of solder solidification time on substrate temperature for the baseline value of Bi and T_{sub} = 25°C or 125°C (Fig. 12).

The combined use of Table 2 and Fig. 12 can provide additional insight for the solder jetting process. For a substrate consisting of Ni (2 μm) on Si (175 μm) with the base value of Bi (0.5), the thermal resistance of the contact layer is of the same order with the resistance of the bottom layer of the substrate (see column marked Fig. $10(a)-(c)$ in Table 2). When the contact resistance is increased by a factor of ten, the contact layer becomes the limiting component for heat transport (see column labeled Fig. $10(d)$, (e) in Table 2). As a result, the solidification time and number of ripples at a fixed T_{sub} in Fig. 12 increase with degree of oxidation (or decreasing Bi). As

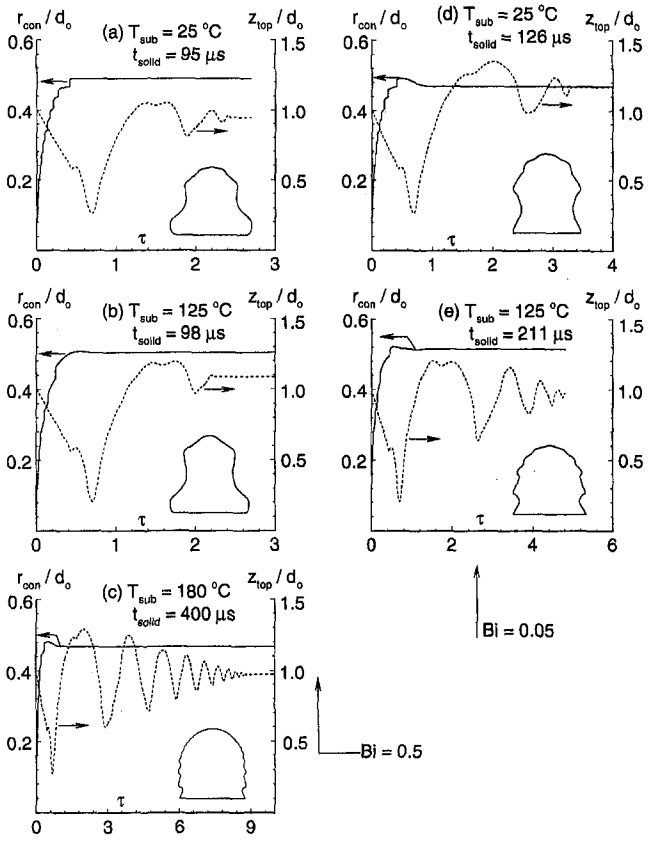

Fig. 10 Temporal variations of contact radius and solder-droplet height for 70 μm diameter 63 percent Sn-37 percent Pb droplets impinging with U_o = 1.6 m/s and T_{inj} = 210°C on flat substrates consisting of Ni (2 μm) on Si (175 μm). The time abscissa has been normalized as $\tau = tU_o/d_o$. Each column corresponds to a fixed value of Bi ((a)–(c) Bi = 0.5; (d) and (e) Bi = 0.05). Each row corresponds to one of three substrate temperatures considered: T_{sub} = 25°C, 125°C, or 180°C. The insets have been drawn to the same scale and depict the predicted solder bump shape at complete solidification. The times required for complete solidification t_{solid} are also indicated.

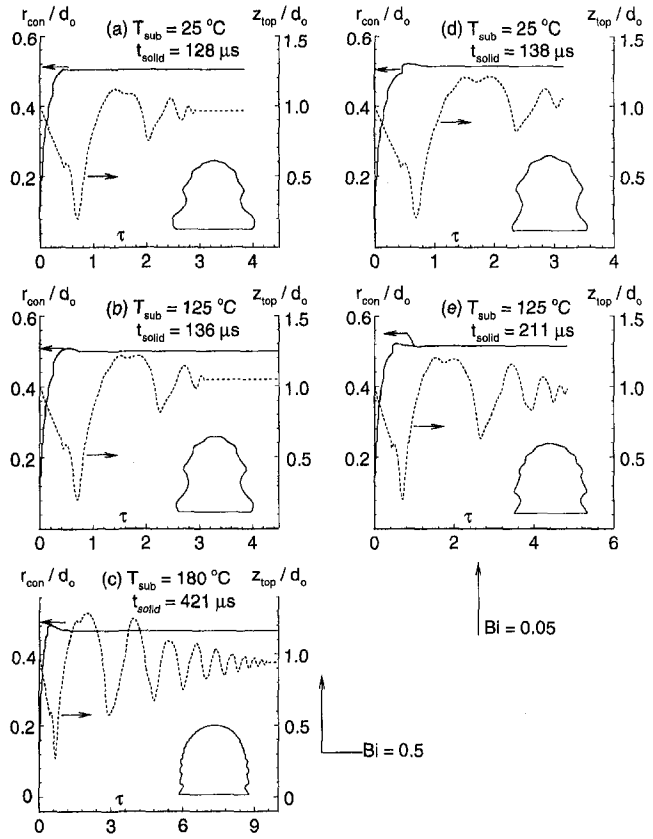

Fig. 11 Temporal variations of contact radius and solder-droplet height for 70 μm diameter 63 percent Sn-37 percent Pb droplets impinging with U_o = 1.6 m/s and T_{inj} = 210°C on flat substrates consisting of Ni (2 μm) on FR4 (175 μm). The time abscissa has been normalized as $\tau = tU_o/d_o$. Each column corresponds to a fixed value of Bi ((a)–(c) Bi = 0.5; (d) and (e) Bi = 0.05). Each row corresponds to one of three substrate temperatures considered: T_{sub} = 25°C, 125°C, or 180°C. The insets have been drawn to the same scale and depict the predicted solder bump shape at complete solidification. The times required for complete solidification t_{solid} are also indicated.

Table 2 Thermal resistance for heat transport from droplet to substrate (in m^2K/W)

Component	Figure 10 (a-c)	Figure 10 (d,e)	Figure 11 (a-c)	Figure 11 (d,e)
Interface	5.6×10^{-6}	5.6×10^{-5}	5.6×10^{-6}	5.6×10^{-5}
Top Layer	2.2×10^{-8}	2.2×10^{-8}	2.2×10^{-8}	2.2×10^{-8}
(*Ni*)	to 2.5×10^{-8}	to 2.5×10^{-8}	to 2.5×10^{-8}	to 2.5×10^{-8}
Bottom Layer	1.2×10^{-6}	1.2×10^{-6}	6.7×10^{-4}	6.7×10^{-4}
	to 1.9×10^{-6}	to 1.9×10^{-6}		

also seen in Fig. 12, the effect of oxidation on extending solidification times gets stronger at higher substrate temperatures. For a substrate of Ni (2 μm) on FR4 (175 μm) and for both values of thermal contact resistance, the bottom insulating layer appears to be dominant in heat transport (see columns labeled Fig. 11(*a*)–(*c*) and 11(*d*), (*e*) in Table 2). As a result, the degree of oxidation of the substrate surface has a weak influence on extending solidification times at low values of T_{sub} (see Fig. 12). However, this influence becomes stronger at higher substrate temperatures.

The above discussion leads to the conclusion that inferences regarding the overall shape or solidification times of solder bumps using limited modeling trends should be made only after careful consideration of the substrate composition, accurate representation of the thermal contact resistance, and adequate evaluation of the effects of fluid dynamical motion on solidification rates.

Cylindrical Pad: Effect of Surface Oxidation, Temperature, and Composition. In this set of simulations, 70 μm diameter solder droplets were considered to impinge with U_o = 1.6 m/s and T_{inj} = 210°C on a cylindrical pad that had a radius of 50 μm and consisted of Au (1 μm) on Ni (5 μm) on Cu (25 μm). The pad was mounted on FR4 (100 μm). Three substrate temperatures were considered: T_{sub} = 25°C, 125°C, and 180°C. Oxidized substrate conditions were simulated by decreasing the value of the contact Biot number by a factor of 10 compared to the base case value of 0.5. The respective values of the contact heat transfer coefficient are h_c = 178 kW/m^2 K for Bi = 0.5, and 17.8 kW/m^2 K for Bi = 0.05. For all cases Re = 351, We = 4.2, Fr = 3,730 and Pr = 0.025. Also, Ste = 0.82 at T_{sub} = 25°C, Ste = 0.3 at T_{sub} = 125°C, and Ste = 0.02 at 180°C.

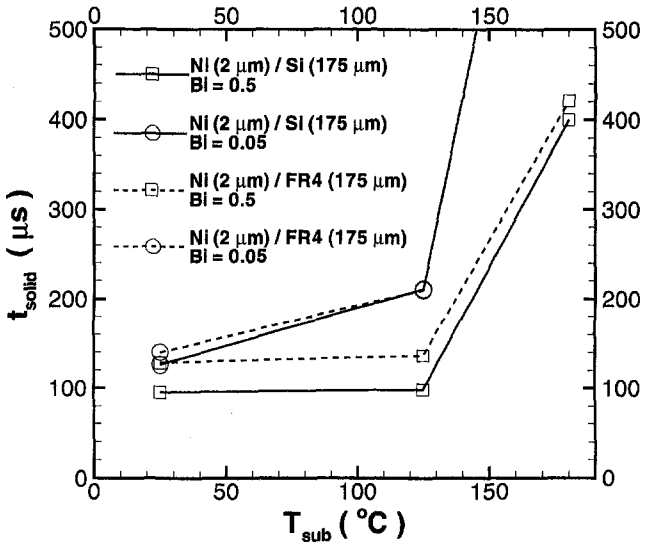

Fig. 12 Times for complete solidification t_{solid} versus substrate temperature T_{sub} for all simulations relevant to Figs. 10 and 11. The dependence of t_{solid} on contact resistance (or Bi likewise) is also shown.

Figure 13 illustrates the results; each column corresponds to a fixed value of Bi ((*a*)–(*c*) Bi = 0.5; (*d*) and (*e*) Bi = 0.05). Each row corresponds to a fixed substrate temperature: 25°C, 125°C, or 180°C. Each frame of Fig. 13 also contains an inset showing the predicted solder bump shape at complete solidification. Only the first two substrate-temperature cases were considered at Bi = 0.05, as solidification occurs very slowly at T_{sub} = 180°C. For both values of Bi, heating of the pad causes substantial changes in the bump shape (compare Figs. 13(*a*), (*b*) and (*c*)). Also, the time required for complete solidification t_{solid} increases monotonically with substrate temperature. A comparison of the two columns of Fig. 13 reveals that increased oxidation of the top substrate layer causes longer solidification times and a more complex outer surface of the solidified bump. It is also important to note that the contact areas of the solidified bumps remain similar (within 10 percent) for all three values of T_{sub}.

The constitutive components of thermal resistance are listed in Table 3. The range seen for the Ni layer reflects the variation of thermal conductivity of this semiconductor material with temperature. As seen in Table 3, the thermal resistance of the Au layer remains negligible compared to all other contributions. For both values of Bi, the thermal resistance of the bottom layer is highest. Since this insulating layer lies below a 31 μm thick layer of Au/Ni/Cu, significant cooling is achieved before the effect of the bottom layer is felt by the droplet. As a result, the increase of the contact resistance causes a substantial prolongation of the solidification times.

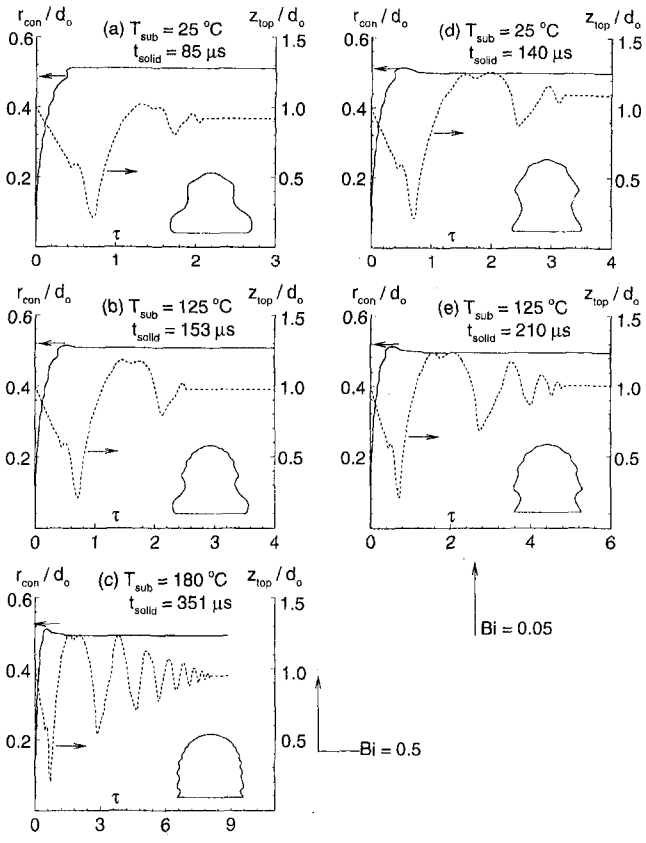

Fig. 13 Temporal variations of contact radius and solder-droplet height for 70 μm diameter 63 percent Sn-37 percent Pb droplets impinging with U_o = 1.6 m/s and T_{inj} = 210°C on a cylindrical pad of radius of 50 μm and consisting of Au (1 μm) on Ni (5 μm) on Cu (25 μm) on FR4 (100 μm). The time abscissa has been normalized as $\tau = tU_o/d_o$. Each column corresponds to a fixed value of Bi ((*a*)–(*c*) Bi = 0.5; (*d*) and (*e*) Bi = 0.05). Each row corresponds to one of three substrate temperatures: T_{sub} = 25°C, 125°C, or 180°C. The insets depict the predicted solder bump shape at complete solidification. The times required for complete solidification t_{solid} are also indicated.

Table 3 Thermal resistance for heat transport from droplet to pad (in m^2K/W)

Component	Figure 13 (a–c)	Figure 13 (d,e)
Contact Interface	5.6×10^{-6}	5.6×10^{-5}
First Pad Layer (Au)	3.2×10^{-9}	3.2×10^{-9}
Second Pad Layer (Ni)	5.6×10^{-8} to 6.3×10^{-8}	5.6×10^{-8} to 6.3×10^{-8}
Third Pad Layer (Cu)	6.2×10^{-8}	6.2×10^{-8}
Substrate Layer (FR4)	10^{-4}	10^{-4}

Fluid Dynamical Considerations. Figure 14 applies to the baseline pad simulation and identifies some fine flow features that are present in all z_{top}/d_o curves seen in Figs. 10, 11, and 13. A thorough explanation for the existence of these features was sought. The letter markings along the z_{top}/d_o (dashed) curve in Fig. 14 correspond to specific instances in the simulation, and are used to correlate Fig. 14 to the velocity fields shown in Fig. 15. Each row in Fig. 15 shows the velocity field in the droplet interior (left) and an enlarged detail of this field around the center top of the droplet (right). In addition, the propagation of the solidification front is shown within the left column images of Fig. 15. After the initial impact, the downward fluid motion at the droplet top stalls at instant B, when the flow locally reverses its direction. The locally upward motion continues until instant D when, once again, the flow reverses direction on the axis. From D to F, the flow descends and then starts recoiling upward (F-G-H). The fluid motion is downward in H-I-J and upward in J-K. Finally, the fields at L correspond to a late instant when a small amount of fluid remains in the molten state before complete solidification. The radially outward velocities above the solidification front seen in L are responsible for the formation of the bulging ripples around the periphery of the solder bump. The wavy feature A-B-C-D appearing in Fig. 14 corresponds to time intervals where the fluid near the axis moves in the opposite direction from the surrounding fluid. This feature at the droplet top is more intense early on, but maintains its presence at later cycles of the fluid oscillating motion (see feature H-I-J-K). If one considers the possibility of the freezing front "capturing" the droplet surface at the axis before freezing of the outer regions occurs (see Fig. 15, F, for example), then

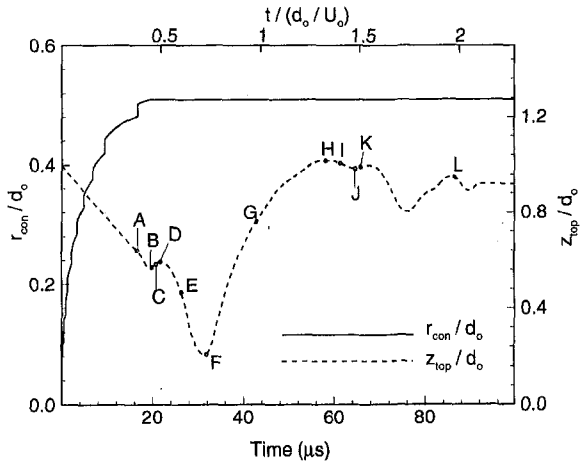

Fig. 14 Early temporal variations of dimensionless contact radius (r_{con}/d_o) and solder-droplet height (z_{top}/d_o on axis) for the baseline pad simulation. The letter markings along the dashed curve correspond to specific instances in the simulation and are used to correlate this figure to the velocity fields shown in Fig. 15.

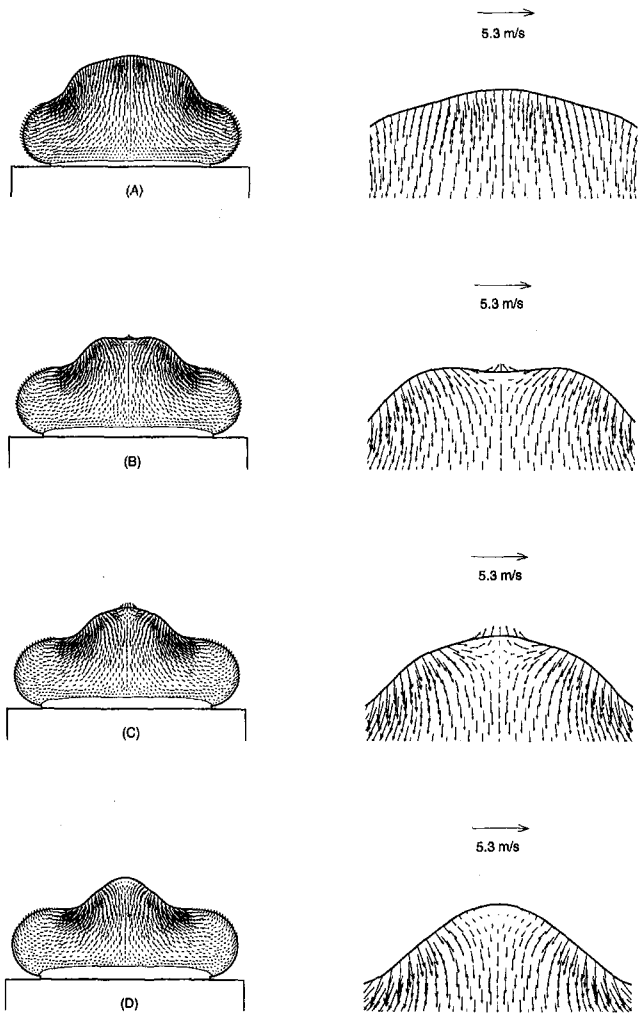

Fig. 15 Temporal variation of velocity fields for the droplet impacting on the baseline pad. The letters below the left frames correspond to an instant identified in Fig. 14. Each row shows the velocity field in the droplet interior (left) and an enlarged detail of this field around the center top of the droplet (right). The propagation of the solidification front is shown within the left images.

it becomes apparent how the formation of a dimple at the top of the droplet can take place. Figure 16 shows a bump obtained when a 63% Sn-37% Pb solder droplet collided with d_o = 53 μm, U_o = 1.6 m/s, and T_{inj} = 210°C, with a substrate of T_{sub} = 115°C. The dimple identified by the arrow at the top of this bump was a consistent feature obtained repeatedly in the experiments conducted under these conditions. The above explanation for the formation of the dimple was suggested by Waldvogel and Poulikakos (1997), and is further corroborated by the current work. Finally, the nonplanar character of the solidification front (as seen in frames F, G, and L of Fig. 15) emphasizes the importance of a multidimensional formulation in problems of this kind.

Conclusions

This study extended the recent work of Waldvogel and Poulikakos (1997) to accommodate complex substrate configurations—such as circuit board pads and multilayer compositions—which are characteristic of realistic applications in the electronics manufacturing industry. An experimental investigation of solidified solder droplets deposited by a prototype apparatus was also used to evaluate the final bump shapes and trends predicted by the model. 63% Sn-37% Pb solder droplets with

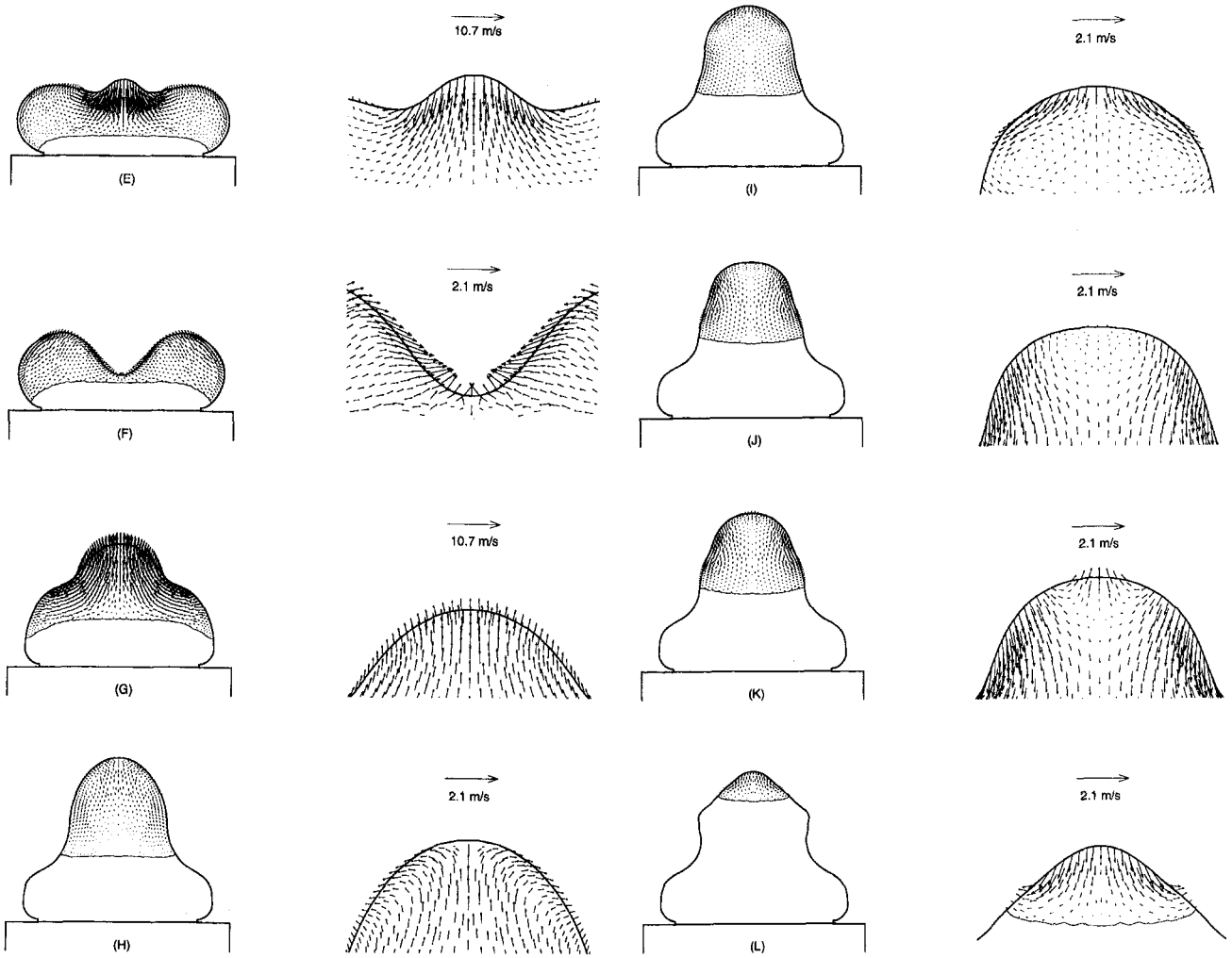

Fig. 15 (Continued)

preimpact diameters around 50 μm, velocities around 2 m/s and temperatures around 210°C were considered to impact on substrates at temperatures ranging from 35°C to 180°C. Specific attention was paid to the thermal contact resistance between solder droplets and nickel substrates. To this end, the model predicted variations in solder bump height up to 20 percent with thermal contact resistance, while the contact area between solder deposits and the substrate demonstrated a weaker dependence on that quantity. Changes of thermal contact coefficient also affected the number of surface ripples on each solidified solder bump and their respective distances from the substrate.

Solder-deposit shape comparisons between experiments and modeling were conducted by means of the spatial morphology of the ripples on the outline of each bump, and by measuring the deposit height and contact area at the bump base. These comparisons suggested that the value of thermal contact resistance may change with process parameters, and is probably dependent on the solder phase. The respective values of heat transfer coefficient h_c = 235 kW/m^2 K and 13 kW/m^2 K were determined as representing thermal contact resistance between liquid or solid solder and an unoxidized smooth nickel substrate.

In general, the time required for compete solidification of an impacting solder droplet increased with substrate temperature. However, there existed situations where this time did not correlate monotonically with the temperature of the substrate. In several occasions involving low to moderate substrate temperatures, increasing this temperature did not affect the solder solidification time—a trend that appears counterintuitive. This is caused by the intense droplet dynamical motion which can have a drastic effect on freezing rates and, in turn, provide trends that contradict those obtained by using simplified physical considerations. Substrate temperatures near the melting point of the solder (183°C) prolong the period for complete solidification and, in turn, affect the final bump shape. Furthermore, surface oxidation of the top substrate layer delays solidification, thus causing a more complex outer surface of the solidified bump.

The modeling results revealed that the number of liquid-solder oscillatory cycles completed before final solidification matches exactly the number of ripples formed around the periphery of each solidified bump. This is an outcome of the dynamics of formation of each ripple which is created when the downward moving fluid mass meets the upward-propagating solidification front. In that respect, each ripple forms a marker of one fluid recoiling cycle. A plausible explanation was also provided for the formation of dimples at the top of solder bumps as observed consistently under certain experimental conditions. The nonplanar character of the solidification front within the droplet added emphasis to the importance of a multidimensional formulation in problems of this kind.

Simulations regarding pad substrates showed a complex influence on solder-droplet solidification dynamics. In general, inferences regarding the overall shape or solidification times of solder bumps using limited modeling trends should be made only after careful consideration of the substrate composition, accurate representation of the thermal contact resistance, and adequate resolution of the fluid dynamical oscillatory motion

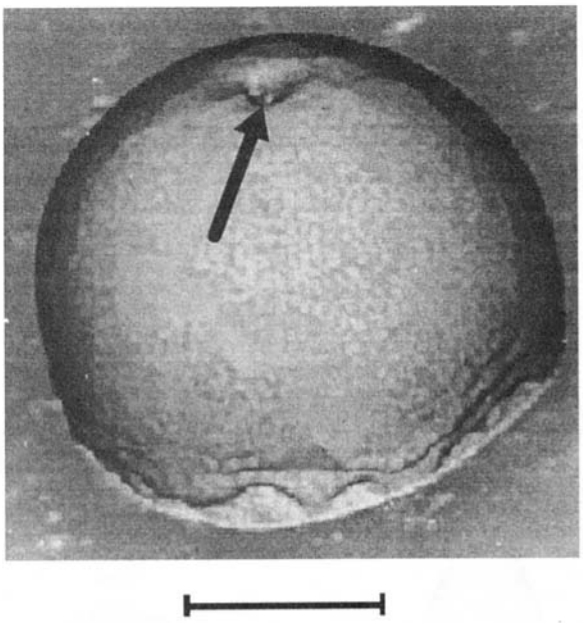

Fig. 16 SEM micrograph of a bump obtained when a 63 percent Sn-37 percent Pb solder droplet collided with d_o = 53 μm, U_o = 1.6 m/s, and T_{inj} = 210°C on a two-layer composite substrate (2 μm Ni on 212 μm Si) heated to T_{sub} = 115°C. The dimple pointed by the arrow at the top of this bump was a consistent feature obtained in the experiments conducted under these conditions. The length scale below the image corresponds to 23.1 μm.

and its effects on solidification rates. It has been shown that modeling tools can be used in conjunction with experiments to further understand the physics of the complex solder jetting technology.

Acknowledgment

This work has been partially supported by Motorola Inc. under an MRC-MCM Grant. The authors wish to thank Dr. Jie Zhang of Motorola for useful discussions and Mr. Ather Qureshi for performing the experiments.

References

Amon, C. H., Schmaltz, K. S., Merz, R., and Prinz, F. B., 1996, "Numerical and Experimental Investigation of Interface Bonding via Substrate Remelting of an Impinging Molten Metal Droplet," ASME JOURNAL OF HEAT TRANSFER, Vol. 118, pp. 164–172.

Bushko, W., and Grosse, I. R., 1991, "New Finite Element Method for Multidimensional Phase Change Heat Transfer Problems," *Num. Heat Transfer,* Part B, Vol. 19, pp. 31–48.

Collings, E. W., Markworth, A. J., McCoy, J. K., and Saunders, J. H., 1990, "Splat-Quench Solidification of Freely Falling Liquid-Metal Drops by Impact on a Planar Substrate," *J. Mater. Sci.,* Vol. 25, pp. 3677–3682.

Delplanque, J.-P., Lavernia, E. J., and Rangel, R. H., 1996, "Multidirectional Solidification Model for the Description of Micropore Formation in Spray Deposition Processes," *Numer. Heat Transfer A,* Vol. 30, pp. 1–18.

Dussan, V. E. B., 1979, "On the Spreading of Liquids on Solid Surfaces: Static and Dynamic Contact Lines," *Ann. Rev. Fluid Mech.,* Vol. 11, pp. 371–400.

Gao, F., and Sonin, A. A., 1994, "Precise Deposition of Molten Microdrops: the Physics of Digital Microfabrication," *Proc. R. Soc. Lond. A,* Vol. 444, pp. 533–554.

Hayes, D. J., Wallace, D. B., Boldman, M. T., and Marusak, R. E., 1993, "Picoliter Solder Droplet Dispensing," *Int. J. Microcircuits and Electronic Packaging,* Vol. 16, pp. 173–180.

Hewitt, G. F., Shires, G. L., and Bott, T. R., 1994, *Process Heat Transfer,* CRC Press, Boca Raton, FL.

Kang, B., Waldvogel, J. M., and Poulikakos, D., 1995, "Remelting Phenomena in the Process of Splat Solidification," *J. Mater. Sci.,* Vol. 30, pp. 4912–4925.

Lide, D. R., ed., 1995, *CRC Handbook of Chemistry and Physics,* 75th ed., CRC Press, Cleveland, OH.

Liu, W., Wang, G. X., and Matthys, E. F., 1995, "Thermal Analysis and Measurements for a Molten Metal Drop Impacting on a Substrate: Cooling, Solidification and Heat Transfer Coefficient," *Int. J. Heat/Mass Transfer,* Vol. 38, pp. 1387–1395.

Madejski, J., 1976, "Solidification of Droplets on a Cold Substrate," *Int. J. Heat Mass Transfer,* Vol. 19, pp. 1009–1013.

Megaridis, C. M., 1993, "Presolidification Liquid Metal Cooling Under Convective Conditions," *Atomization and Sprays,* Vol. 3, pp. 171–191.

Orme, M. E., Huang, C., and Courter, J., 1996, "Precision Droplet-Based Manufacturing and Material Synthesis: Fluid Dynamics and Thermal Control Issues," *Atomization and Sprays,* Vol. 6, pp. 305–329.

Poulikakos, D., and Waldvogel, J. M., 1996, "Heat Transfer and Fluid Dynamics in the Process of Spray Deposition," *Advances in Heat Transfer,* Vol. 28, pp. 1–73.

Rein, M., 1995, "Nonlinear Analysis of Two-Dimensional Compressible Liquid-Liquid Impact," *Eur. J. Mech., B/Fluids,* Vol. 14, pp. 301–322.

Trapaga, G., Matthys, E. F., Valencia, J. J., and Szekely, J., 1992, "Fluid Flow, Heat Transfer, and Solidification of Molten Metal Droplets Impinging on Substrates: Comparison of Numerical and Experimental Results," *Metall. Trans. B,* Vol. 23B, pp. 701–718.

Waldvogel, J. M., Poulikakos, D., Wallace, D. B., and Marusak, R., 1996, "Transport Phenomena in Picoliter Size Solder Droplet Dispension," ASME JOURNAL OF HEAT TRANSFER, Vol. 118, pp. 148–156.

Waldvogel, J. M., and Poulikakos, D., 1997, "Solidification Phenomena in Picoliter Size Solder Droplet Deposition on a Composite Substrate," *Int. J. Heat Mass Transfer,* Vol. 40, pp. 295–309.

Wang, G. X., and Matthys, E. F., 1996, "Experimental Investigation of Interfacial Thermal Conductance for Molten Metal Solidification on a Substrate," ASME JOURNAL OF HEAT TRANSFER, Vol. 118, pp. 157–163.

Watanabe, T., Kuribayashi, I., Honda, T., and Kanzawa, A., 1992, "Deformation and Solidification of a Droplet on a Cold Substrate," *Chem. Eng. Sci.,* Vol. 47, pp. 3059–3065.

Zhao, Z., Poulikakos, D., and Fukai, J., 1996a, "Heat Transfer and Fluid Dynamics During the Collision of a Liquid Droplet on a Substrate—I. Modeling," *Int. J. Heat Mass Transfer,* Vol. 39, pp. 2771–2789.

Zhao, Z., Poulikakos, D., and Fukai, J., 1996b, "Heat Transfer and Fluid Dynamics During the Collision of a Liquid Droplet on a Substrate—II. Experiments," *Int. J. Heat Mass Transfer,* Vol. 39, pp. 2791–2802.

Journal of Heat Transfer

Technical Notes

This section contains shorter technical papers. These shorter papers will be subjected to the same review process as that for full papers.

A Numerical Analysis of the Stratification Properties of Chilled Water Storage Tanks Charged at the Freezing Point Temperature

R. E. Spall[1]

Introduction

The stratification properties of water at and near the density maximum are of interest in applications such as thermal storage systems in which water is cooled by a chiller and stored in a tank for later use. Natural chilled water storage systems depend upon the establishment of a well defined thermocline separating the chilled water stored in the tank from the warm return water. To promote stratification, chilled water storage systems are typically charged with water at temperatures above the density maximum of 4°C. Charge temperatures below 4°C are generally avoided due to a potential for buoyancy induced mixing.

A considerable amount of experimental and numerical research into the stratification properties of chilled water storage tanks appears in the literature. Representative numerical works include those of Chan et al. (1983), Guo and Wu (1985), Cai and Stewart (1993), Mo and Miyatake (1996), and Bouhdjar et al. (1997). These numerical works have investigated primarily two-dimensional configurations and have considered both laminar and turbulent flows, with turbulence closure through two-equation $K - \epsilon$ models. In each case, the variation of density with temperature was accounted for via the Boussinesq approximation. (The Boussinesq approximation involves treating density as a constant in the equations of motion, except for the gravitational term. In addition, a relation of the form $\rho = \rho_0(1 - \beta\Delta T)$ is usually employed to eliminate the density.) In general, there is reasonable agreement between experiment and numerical simulations, albeit the numerical results may tend to over-predict the thermocline thickness. This issue is discussed in Bouhdjar et al. (1997); their resolution being that higher-order differencing of only the energy equation will produce a significant reduction in the thickness of the thermocline. Experimental results (c.f. Miyatake et al., 1986) indicate that the Archimedes number (defined as the ratio of the Grashof to Reynolds number squared) is the only parameter that governs the transient turbulent flow field in a storage tank—the inlet Reynolds number having little influence on the stratification properties as long as the Archimedes number is held constant.

The present work involves a numerical investigation of the stratification properties of cylindrical and rectangular chilled water storage tanks. This involves a transient analysis in which water at the freezing point temperature is injected into a storage tank filled with initially quiescent water at a temperature above 4°C. Accordingly, the Boussinesq approximation is not implemented (as the thermal expansion coefficient β changes sign at the temperature corresponding to the density maximum). Since the temperature at which the density is a maximum lies between the initial temperature of the water in the tank (which is greater than 4°C) and the inlet water, buoyancy forces may act to destabilize the thermocline. The purpose of the present work then is to investigate the potential for buoyancy induced stratification and/or turbulent mixing as a function of the Archimedes number. Both axisymmetric cylindrical and rectangular storage tanks are considered.

Numerical Method

The governing equations consist of the incompressible Reynolds-averaged momentum, continuity, and energy equations. Turbulence closure was achieved through a differential Reynolds stress model (RSM). The governing equations were solved using the pressure-based finite-volume code FLUENT (Fluent Inc., 1996). Interpolation to cell faces (for all equations) was performed using a QUICK (Leonard, 1979) third-order interpolation scheme. First-order implicit differencing was employed for the temporal discretization and pressure-velocity coupling was based on the SIMPLE procedure (c.f. Patankar, 1980). A (piecewise linear) functional dependence of density on temperature is specified, and is shown in Fig. 1.

Since the governing differential equations are well known, they are, for purposes of brevity, not listed (c.f. Hinze, 1987). However, a brief description of the modeling assumptions employed in the RSM is provided. The diffusive transport term was represented by a simplified form of the generalized gradient diffusion hypothesis as

$$-\frac{\partial}{\partial x_k}\left[\overline{(u_i' u_j' u_k')} + \frac{p}{\rho}(\delta_{kj}u_i' + \delta_{ik}u_j') - \nu\frac{\partial}{\partial x_k}\overline{(u_i' u_j')}\right] = \frac{\partial}{\partial x_k}\left(\frac{\nu_t}{\sigma_k}\frac{\partial}{\partial x_k}\overline{(u_i' u_j')}\right). \quad (1)$$

[1] Department of Mechanical and Aerospace Engineering, Utah State University, Logan, UT 84322-4130; e-mail: spall@fluids.me.usu.edu; Mem. ASME.

Contributed by the Heat Transfer Division of THE AMERICAN SOCIETY OF MECHANICAL ENGINEERS. Manuscript received by the Heat Transfer Division May 12, 1997; revision received September 26, 1997; Keywords: Mixed Convection; Stratified Flows; Transient and Unsteady Heat Transfer. Associate Technical Editor: T. L. Bergman.

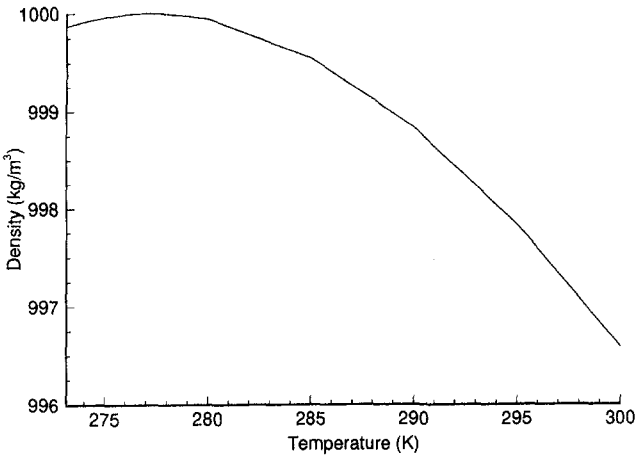

Fig. 1 Specification of density as a function of temperature

The pressure-strain term was approximated as (c.f. Launder et al., 1975; Launder 1989)

$$\overline{\frac{p}{\rho}\left[\frac{\partial}{\partial x_j}u_i' + \frac{\partial}{\partial x_i}u_j'\right]} = -C_1\frac{\epsilon}{k}\left[\overline{u_i'u_j'} - \frac{2}{3}\delta_{ij}k\right] - C_2\left[P_{ij} - \frac{2}{3}\delta_{ij}P - S_{ij}\right], \quad (2)$$

where the constants C_1 and C_2 were taken as 1.8 and 0.60, respectively, and $P = P_{ii}/2$. S_{ij} is a curvature related source term arising from the implementation of a cylindrical velocity formulation (as was the case for the cylindrical storage tank). In addition,

$$P_{ij} = -\overline{u_i'u_k'}\frac{\partial u_j}{\partial x_k} - \overline{u_j'u_k'}\frac{\partial u_i}{\partial x_k}. \quad (3)$$

Finally, the dissipation term was assumed isotropic and was approximated by the scalar dissipation rate

$$2\nu\overline{\frac{\partial u_i'}{\partial x_k}\frac{\partial u_j'}{\partial x_k}} = \frac{2}{3}\delta_{ij}\epsilon, \quad (4)$$

where the dissipation rate ϵ was computed via the modeled transport equation.

Geometry and Problem Formulation

The baseline geometries consisted of axisymmetric cylindrical and rectangular storage tanks. The cylindrical geometry is shown in Fig. 2. (The rectangular geometry is similarly defined.) The cylindrical tank was of radius R and depth H, and contained an inlet annulus of height h around the circumference of the tank base. The rectangular tank was of width W and depth H, with an inlet slit of height h along one side of the tank base. For each geometry the gravity vector was oriented in the negative x-direction.

The importance of buoyancy forces in mixed convection flows is indicated by the ratio of the Grashof to Reynolds number squared as $(\Delta\rho g h)/(\rho_0 U_0^2)$, which is also referred to as the Archimedes number. The relevant inlet Reynolds number for the problem is given as $\mathrm{Re} = (\rho_0 U_0 h)/\mu_0$. In the above parameters, ρ_0 represents the density of the inlet water, μ_0 a reference viscosity (at the inlet temperature), and U_0 is a (uniform) inlet velocity. In addition, $\Delta\rho = \rho_0 - \rho_i$, where ρ_i is the temperature dependent density of the initially quiescent fluid in the tank at time $t = 0$.

The magnitude of the turbulence kinetic energy (k) at the jet inlet was derived from a fixed turbulence intensity (I) of 1 percent via the relationship $k = 1.5(U_0 I)^2$. Based upon scaling arguments, the dissipation rate was then given as $C_\mu^{0.75}k^{1.5}/L$, where $C_\mu = 0.09$ and the turbulence length scale L was taken as $0.07h$. The inlet Reynolds shear stresses were then set to zero, and the normal stresses to $2k/3$ (isotropic turbulence assumption). For the cylindrical geometry calculations symmetry conditions were imposed along the cylinder centerline, $r = 0$. In each case zero gradient conditions were imposed at the outlet boundary defined at $x = H$ (where $H = 3R$ for the cylindrical geometry, and $H = 3W$ for the rectangular geometry). The intent was to develop an outlet boundary that would have minimum impact on the stratification properties of the flow (implying that a region of one-dimensional flow exists between the stratification zone and the outlet). Wall boundary conditions for the mean velocity, temperature (adiabatic wall), and ϵ were implemented using standard equilibrium wall functions.

At time $t = 0$ the fluid in the tanks was assumed stationary and assigned a constant temperature $T_i > T_0$. The turbulence kinetic energy was initialized to a negligibly small value, $k = 10^{-6}U_0^2$. Correspondingly, the initial condition for the dissipation rate was set to $\epsilon = (C_\mu^{0.75}k^{1.5}/L)$.

It is useful to define a characteristic time, which for the cylindrical geometry is given as

$$t^* = RH/(2U_0 h) \quad (5)$$

and for the rectangular geometry as

$$t^* = DH/hU_0. \quad (6)$$

These scales represent the time necessary to fully replace the water in the tank when a plug flow occurs. The transient calculations were carried out over a time span $0.32t^*$, which was sufficient to determine the stratification properties of the flow. The time steps were chosen such that 800 time steps were required to reach the time level $0.32t^*$ (resulting in a dimensionless time step, based upon the characteristic time described above, of 0.0004). Approximately 30 iterations per time step were required to drive the residuals to sufficiently low levels.

For a more detailed discussion regarding scaling analysis for large stratified volumes, the reader is referred to the theoretical work in Peterson (1994) and experimental work in Jirka (1982).

Results

Results are presented for both cylindrical and rectangular geometries at a fixed inlet Reynolds number of 1000. Calculations were performed for a fixed inlet temperature of 273°K, with initial conditions within the tank of 280, 285, and 290°K. For the calculations performed at 285 and 290°K, the density of the inlet water is greater than the tank water, and hence the possibility of stratification exists. These cases correspond to Archimedes number of 1.25 and 4.0, respectively. However, for initial conditions at 280°K, the density of the tank water is greater than that of the inlet water, and hence buoyancy forces are expected to increase mixing, and stratification is unlikely

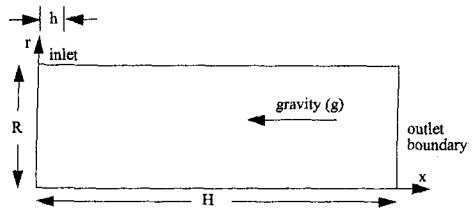

Fig. 2 Computational domain and coordinate system for axisymmetric configuration

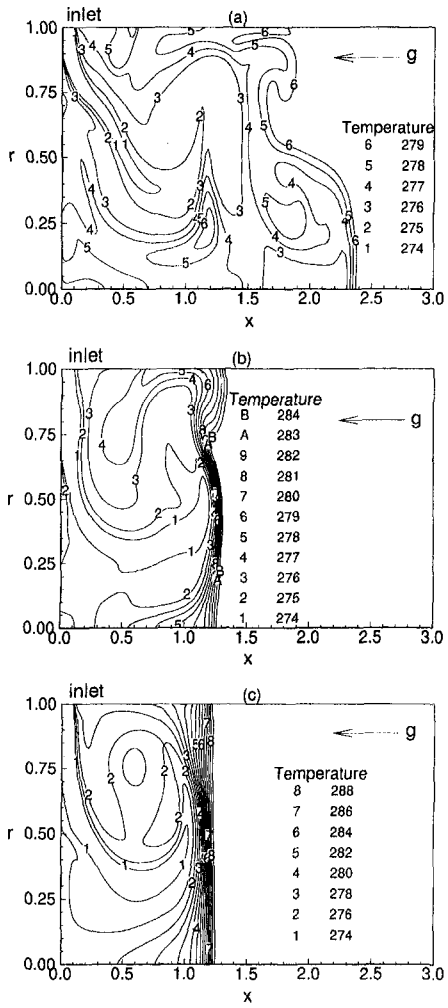

Fig. 3 Contours of constant temperature for axisymmetric configuration at time $t = 0.32t^*$: (*a*) $T_i = 280$°K; (*b*) $T_i = 285$°K, $Ar = 1.25$; and (*c*) $T_i = 290$°K, $Ar = 4.0$.

to occur. (Correspondingly, we do not refer to an Archimedes number for that case.)

The domain was discretized using 160 cells in the x-direction and 100 cells in the radial (r) (or transverse, y) direction. The grid was clustered toward the boundary at $x = 0$ so that approximately 75 cells were contained over $0 \le x \le H/3$ (which bounds the inlet-to-stratification region over the time spans investigated). Cells were also clustered toward the wall (and symmetry line) regions. To assess the level of grid and time step convergence of the solution, additional calculations (discussed at the end of this section) were performed on a refined (320×200) grid, and on the original 160×100 grid with the time step halved to $\Delta t = 0.0002$.

Shown in Figures $3(a)-(c)$ are contours of constant temperature for the cylindrical tank configuration at $t = 0.32t^*$. The results for $T_i = 280$°K, which are shown in Figure $3(a)$, reveal considerable mixing between the inlet water and the fluid within the tank. This result is not unexpected since the density minimum within the system occurs at the inlet temperature. Consequently, buoyancy forces act to increase mixing within the tank. The more interesting results are those for which the density of the inlet water is greater than that within the tank at $t = 0$. In that case, due to diffusion and mixing, we can expect regions of fluid with densities greater than that of the inlet stream to develop. Hence, the possibility for some degree of buoyancy induced mixing still exists. Shown in Figures $3(b)$, (c) are temperature contours for which T_i was initialized to 285 and 290°K, respectively (which correspond to $Ar = 1.25$ and 4.0). For these cases the 277°K contour line appears to provide reasonable demarcation between regions of appreciable fluid mixing (at temperatures below 277°K) and a stratification zone (at temperatures above 277°K). Although fluid mixing does occur, this is limited primarily to regions for which the temperature is below that of the density maximum, and thus impacts minimally the thermal storage capacity of the tank.

Shown in Figures $4(a)-(c)$ are temperature contours for the rectangular geometry. The results are qualitatively similar to the cylindrical geometry, albeit the mixing involved in the 280°K case is less complete and we do see evidence of stratification at temperatures above 278°K. However, we also see the emergence of fluid layers at the density maximum along the bottom of the tank. This temperature inversion was not observed for the 285 and 290°K cases. The stratification zone is quite well defined for the 290°K case ($Ar = 4.0$), demarcated from the mixing region by the 279°K contour.

Results in terms of levels of turbulence kinetic energy (TKE) have also been investigated, although limitations on space dictate that contour plots not be presented. Qualitatively however, it was found that when stratification took place, the highest levels of TKE occurred within the (thin) stratification zone. Maximum levels of dissipation rate were then associated with the maximums in TKE. For the case in which no stratification occurred ($T = 280$ K), maximum levels of TKE were roughly

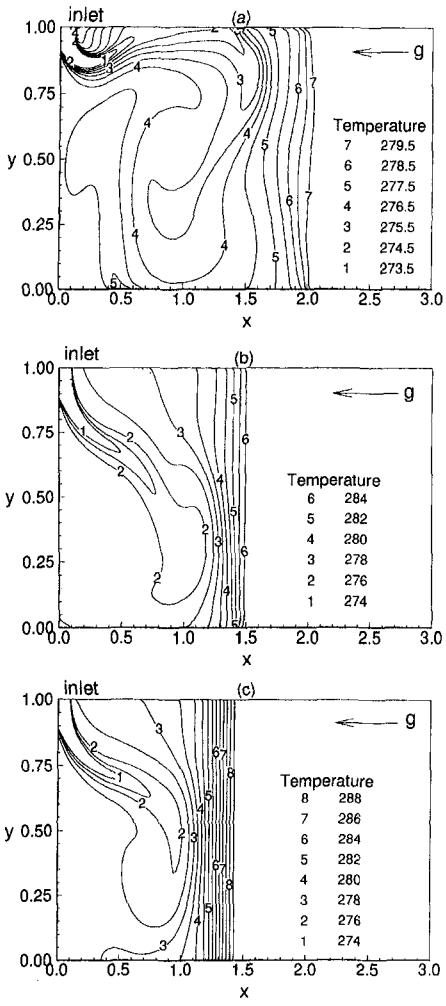

Fig. 4 Contours of constant temperature for rectangular configuration at $t = 0.32t^*$. (*a*) $T_i = 280$°K; (*b*) $T_i = 285$°K, $Ar = 1.25$ and (*c*) $T_i = 290$°K, $Ar = 4.0$.

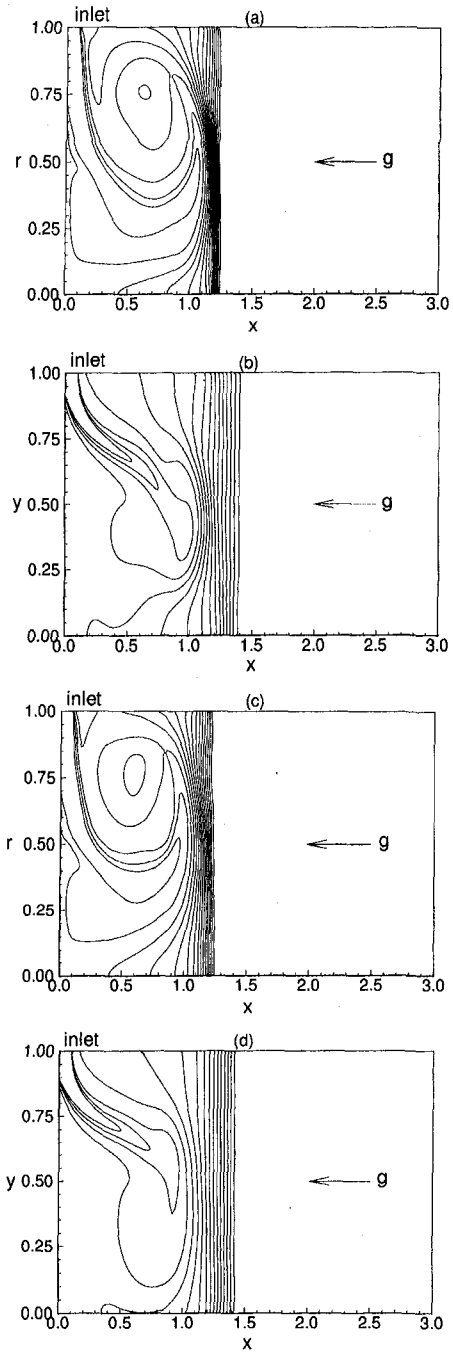

Fig. 5 Effect of grid resolution and time step on stratification properties at time level $t = 0.32t^*$: (*a*) axisymmetric geometry—temperature contours for $Ar = 4.0$, $\Delta t = 0.0004$, 320 × 200 grid; (*b*) rectangular geometry—temperature contours for $Ar = 4.0$, $\Delta t = 0.0004$, 320 × 200 grid; (*c*) axisymmetric geometry—temperature contours for $Ar = 4.0$, $\Delta t = 0.0002$, 160 × 100 grid; and (*d*) rectangular geometry—temperature contours for $Ar = 4.0$, $\Delta t = 0.0002$, 160 × 100 grid.

half those of the $Ar = 4$ case, with several regions of local maximums dispersed throughout the domain.

To assess the suitability of the spatial discretizations, calculations were performed on a 320 × 200 grid (with $\Delta t = 0.0004$) for the case $Ar = 4.0$. These results are shown in Figs. 5(*a*), (*b*) for the axisymmetric and rectangular geometries, respectively. (Contour spacings are identical to those in Fig. 3(*c*) and Fig. 4(*c*).) A comparison between these figures, and Figs. 3(*c*) and 4(*c*) reveals only minor differences between the solutions. For instance, results for the axisymmetric case indicate that the width of the stratification zone is decreased slightly as the grid is refined. For the purposes of this work the original 160 × 100 grid was deemed to be sufficient. Similarly, calculations with the time step halved to $\Delta t = 0.0002$ (on the original 160 × 100 grid) are shown in Figs. 5(*c*), (*d*) for the axisymmetric and rectangular geometries. Again, comparison with Figs. 3(*c*) and 4(*c*) reveal that the original time step was adequate.

Summary

Calculations have been performed for the transient analysis of the stratification properties of axisymmetric and rectangular chilled-water storage tanks charged at the freezing point of water. The Boussinesq approximation and associated linear variation of density with temperature was not employed (as it has been in previous numerical studies). Rather, density was specified as a piecewise linear function of temperature. In addition, in lieu of the commonly employed two-equation $k - \epsilon$ model, turbulence closure was achieved through a differential Reynolds stress model. The results indicate that for Archimedes numbers near unity, partial stratification can be expected.

Previous numerical work available in the literature for which the Boussinesq approximation was employed (and hence the density maximum occurs at the inlet temperature) also reveal stratification at Archimedes numbers of approximately unity for the rectangular configuration (c.f. Mo and Miyatake, 1996). Under charge conditions for which the inlet density is less than the density of the initial quiescent fluid within the tank, buoyancy acts to increase mixing, and no stratification zone forms. The results indicate that it may be feasible to increase the cooling capacity of chilled water storage tanks by charging the tanks at temperatures below that of the density maximum of water. For stratification to occur the density of the initial quiescent water within the tank should be less than that of the charge water—the Archimedes number serving as the relevant parameter.

References

Bouhdjar, A., Benkhelifa, A., and Harhad, A., 1997, "Numerical Study of Transient Mixed Convection in a Cylindrical Cavity," *Numerical Heat Transfer,* A, Vol. 31, pp. 305–324.

Cai, L., and Stewart, Jr., W. E., 1993, "Turbulent Buoyant Flows into a Two-Dimensional Storage Tank," *Int. J. Heat Mass Transfer,* Vol. 36, pp. 4247–4256.

Chan, A. M. C., Smereka, P. S., and Giusti, D., 1983, "A Numerical Study of Transient Mixed Convection Flows in a Thermal Storage Tank," *J. Solar Energy Engineering,* Vol. 105, pp. 246–253.

Fluent Inc., 1996, *Fluent Users Guide,* Lebanon, NH.

Guo, K. L., and Wu, S. T., 1985, "Numerical Study of Flow and Temperature Stratifications in a Liquid Thermal Storage Tank," *J. Solar Energy Engineering,* Vol. 107, pp. 15–20.

Jirka, G. H., 1982, "Turbulent Buoyant Jets in Shallow Fluid Layers," in *Turbulent Buoyant Jets and Plumes,* W. Rodi, ed., Pergamon Press, NY.

Hinze, J. O., 1987, *Turbulence,* McGraw-Hill, New York, NY.

Launder, B. E., Reece, G. J., and Rodi, W., 1975, "Progress in the Development of a Reynolds-Stress Turbulence Closure," *J. Fluid Mech.,* Vol. 68, pp. 537–566.

Launder, B. E., 1989, "Second-Moment Closure: Present . . . and Future?," *Inter. J. Heat Fluid Flow,* Vol. 10, pp. 282–300.

Leonard, B. P., 1979, "A Stable and Accurate Convective Modeling Procedure Based on Quadratic Upstream Interpolation," *Comput. Methods Appl. Mech. Eng.,* Vol. 19, pp. 59–98.

Miyatake, O., Nagafuchi, N., Nobuaki, S., and Tanka, I., 1986, "Studies on the Internal Characteristics of a Temperature Stratified-Type Thermal Storage Water Tank: Part 1—Temperature Stratification Process for the Case of Hot Water Input," *Trans. Soc. Heating Air-Conditioning Sanitary Eng. Jpn.,* Vol. 32, pp. 35–43.

Mo, Y., and Miyatake, O., 1996, "Numerical Analysis of the Transient Turbulent Flow Field in a Thermally Stratified Thermal Storage Water Tank," *Numerical Heat Transfer, A,* Vol. 30, pp. 649–667.

Patankar, S. V., 1980, *Numerical Heat Transfer and Fluid Flow,* Hemisphere Publishing Corp., Washington, DC.

Peterson, P. F., 1984, "Scaling and Analysis of Mixing in Large Stratified Volumes," *Int. J. Heat Mass Transfer,* Vol. 37, pp. 97–106.

Radiative Net Exchange Formulation Within One-Dimensional Gas Enclosures With Reflective Surfaces

M. Cherkaoui[1], J.-L. Dufresne[1,3], R. Fournier[2], J.-Y. Grandpeix[1], and A. Lahellec[1]

1 Introduction

The Net Exchange Formulation (NEF) and the Exchange Monte Carlo Method (EMCM) were proposed in (Cherkaoui et al., 1996) for accurate computation of infrared radiative exchanges within gas enclosures. This formulation has some common principles with the exchange factor methods (zone method) although the volume is not supposed to be isothermal and the fundamental variable is not the exchange, but the net-exchange flux.

For gray absorbing-emitting/isotropically-scattering medium confined in a Lambert enclosure, the total exchange areas are completely defined by (Noble, 1975). To deal with nongray medium surrounded by reflective surfaces, the radiative exchanges should be followed along a lot of reflections or scatterings. Up to now, only low order closure algorithms were used (Naraghi and Huan, 1991; Menart et al., 1993). The aim of this technical note is to address, in a simple problem (no scattering, one-dimensional) the exact solution of the radiative exchanges, but for a wide range of optical properties.

The extension of the NEF to the case of reflective surfaces (Section 2) and the derivation of an estimator of the truncation error (Section 3) are presented first. Optically thin gas problems with highly reflective surfaces are then studied (Section 4).

2 Generalization of the Net-Exchange Formulation With Multiple Reflections

In the NEF, radiative transfer is described in terms of Net Exchange Rates (NER) $\Psi(i, j)$ between zone pairs i, j. The radiation budget $\Psi(i)$ of one zone i is the sum of all NER between i and the other zones of the discretized system.

$$\Psi(i) = \sum_j \Psi(i, j) \tag{1}$$

The configuration considered in this note is a one-dimensional slab with reflective surfaces. Under the assumption that the gas refraction index is uniform, any optical path γ is a set of broken lines and is entirely defined with the abscissas x_γ and y_γ of origin and end, the number r_γ of surface reflections, the vector $\vec{\mu}_\gamma$ of the segment cone angle cosines (the dimension of $\vec{\mu}_\gamma$ is $r_\gamma + 1$) and, in the case of the exchange between two gas volumes, the first encountered surface number n_γ (see Fig. 1):

$$\gamma = \Gamma(x_\gamma, y_\gamma, r_\gamma, \vec{\mu}_\gamma, n_\gamma) \tag{2}$$

The monochromatic optical depth of the path γ is given as

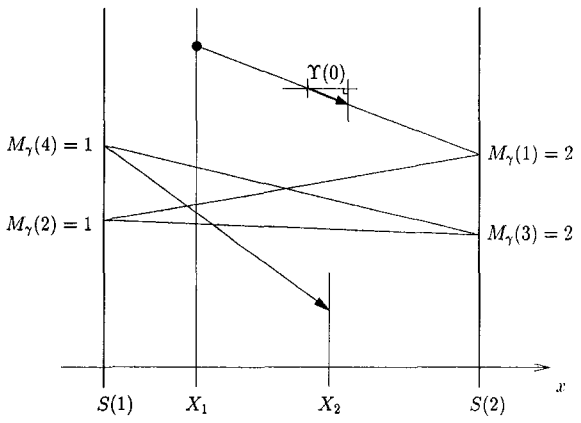

Fig. 1 This figure displays an optical path $\gamma = \Gamma(X_1, X_2, 4, \vec{\Upsilon}, 2)$, i.e., going from $x_\gamma = X_1$ to $y_\gamma = X_2$, leaving X_1 towards surface $n_\gamma = 2$, with $r_\gamma = 4$ reflections. The optical path is made of five straight segments, which yields a vector of cone angle cosines $\vec{\mu}_\gamma = \vec{\Upsilon}$ which has a dimension of 5 (only the first component $\Upsilon(0)$ is shown).

$$\tau_{\nu,\gamma} = \begin{cases} \tau_\nu(x_\gamma, y_\gamma, \mu_\gamma(0)) & \text{if} \quad r_\gamma = 0, \\ \tau_\nu(x_\gamma, S(n_\gamma), \mu_\gamma(0)) + \sum_{s=1}^{r_\gamma - 1} \tau_\nu(S(1), S(2), \mu_\gamma(s)) & \\ \qquad + \tau_\nu(S(M_\gamma(r_\gamma)), y_\gamma, \mu_\gamma(r_\gamma)) & \text{if} \quad r_\gamma \geq 1, \end{cases} \tag{3}$$

where $\tau_\nu(x, y, \mu)$ is the optical depth of the x to y segment with a cone angle cosine μ, $S(1)$ and $S(2)$ are the abscissas of the two surfaces, and $M_\gamma(s)$ is the index of the surface encountered at the sth reflection.

The monochromatic directional-directional reflectivity of the mth surface is denoted:

$$\rho_\nu^{dd}(\mu_r, \mu_i, m) = \rho_\nu^{dh}(\mu_i, m) q_\nu(\mu_r; \mu_i, m), \tag{4}$$

where ρ^{dh} is the directional-hemispheric reflectivity and q is the probability density function of the reflection cosine μ_r for an incident cosine μ_i. The compound reflection factor $R_{\nu,\gamma}$ is then defined as the directional-directional reflectivity product for all reflections along the path γ:

$$R_{\nu,\gamma} = 1 \quad \text{if} \quad r_\gamma = 0$$

$$R_{\nu,\gamma} = \prod_{s=1}^{r_\gamma} \rho_\nu^{dh}(\mu_\gamma(s-1), M_\gamma(s)) \times q_\nu(\mu_\gamma(s); \mu_\gamma(s-1), M_\gamma(s)) \quad \text{if} \quad r_\gamma \geq 1.$$

We now consider a gas layer i between abscissas X_i and X_{i+1} and a gas layer j between abscissas X_j and X_{j+1}. The monochromatic NER between i and j (see Cherkaoui et al., 1996) can be expressed by summing the contributions of optical paths involving r reflections with r varying from zero to infinity:

$$\psi_\nu^{gg}(i, j) = \sum_{r=0}^{\infty} \int_{X_i}^{X_{i+1}} dx \int_{X_j}^{X_{j+1}} dy \int_0^1 d\mu(0) \ldots \times \int_0^1 d\mu(r) \{ \sum_{n=1}^{2} h_\nu^{gg}(\Gamma(x, y, r, \vec{\mu}, n)) \}, \tag{5}$$

where

$$h_\nu^{gg}(\gamma) = \pi[B_\nu(y_\gamma) - B_\nu(x_\gamma)] \times 2\mu_\gamma(0) R_{\nu,\gamma} \left| \frac{\partial^2 \exp(-\tau_{\nu,\gamma})}{\partial x_\gamma \partial y_\gamma} \right|. \tag{6}$$

An assumption made when averaging monochromatic NER over

[1] Laboratoire de Météorologie Dynamique, C.N.R.S-Université Paris 6, E.N.S. 24 Rue Lhomond, F-75231, Paris, Cedex 05, France.
[2] LESETH, Université Paul Sabatier, 118, route de Narbonne, F-31062 Toulouse Cedex, France
[3] jldufres@lmd.ens.fr

Contributed by the Heat Transfer Division of THE AMERICAN SOCIETY OF MECHANICAL ENGINEERS. Manuscript received by the Heat Transfer Division December 20, 1996; revision received July 7, 1997; Keywords: Numerical Methods; Radiation. Associate Technical Editor: M. P. Menguc.

a spectral narrow band is that monochromatic black body intensities and reflection properties are assumed uniform ($B_\nu \approx \bar{B}$, $\rho_\nu^{dh} \approx \bar{\rho}^{dh}$ and $q_\nu \approx \bar{q}$). With only these two assumptions, and by inverting angular and spectral integrals, the average over a narrow band l of the NER between two gas layers is

Gas-gas exchanges.

$$\bar{\psi}_l^{gg}(i,j) = \sum_{r=0}^{\infty} \int_{X_i}^{X_{i+1}} dx \int_{X_j}^{X_{j+1}} dy \int_0^1 d\mu(0) \ldots \times \int_0^1 d\mu(r) \{ \sum_{n=1}^{2} \bar{h}^{gg}(l, \Gamma(x, y, r, \tilde{\mu}, n)) \}, \quad (7)$$

where

$$\bar{h}^{gg}(l, \gamma) = \pi[\bar{B}_l(y_\gamma) - \bar{B}_l(x_\gamma)] 2\mu_\gamma(0) \bar{R}_{l,\gamma} \left| \frac{\partial^2 \bar{F}_l(\gamma)}{\partial x_\gamma \partial y_\gamma} \right| \quad (8)$$

$$\bar{F}_l(\gamma) = \frac{1}{\Delta\nu} \int_{\Delta\nu} \exp(-\tau_{\nu,\gamma}) d\nu. \quad (9)$$

$\bar{F}_l$ is defined as the spectral average transmission function, which can be approximated using narrow band models. The NER between surface m and gas layer i and between surface m and surface m' can be formulated similarly:

Surface-gas exchanges.

$$\bar{\psi}_l^{sg}(m, i) = \sum_{r=0}^{\infty} \int_{X_i}^{X_{i+1}} dy \int_0^1 d\mu(0) \ldots \times \int_0^1 d\mu(r) \bar{h}^{sg}(l, \Gamma(S(m), y, r, \tilde{\mu}, m')), \quad (10)$$

where m' is the index of the surface facing m and

$$\bar{h}^{sg}(l, \gamma) = \pi[1 - \bar{\rho}_l^{dh}(\mu_\gamma(0), m)] \times [\bar{B}_l(y_\gamma) - \bar{B}_l(S(m))] 2\mu_\gamma(0) \bar{R}_{l,\gamma} \left| \frac{\partial \bar{F}_l(\gamma)}{\partial y_\gamma} \right|. \quad (11)$$

Surface-surface exchanges.

$$\bar{\psi}_l^{ss}(m, m') = \sum_{r=0}^{\infty} \int_0^1 d\mu(0) \ldots \times \int_0^1 d\mu(r) \bar{h}^{ss}(l, \Gamma(S(m), S(m'), r, \tilde{\mu}, m')), \quad (12)$$

where

$$\bar{h}^{ss}(l, \gamma) = \pi[1 - \bar{\rho}_l^{dh}(\mu_\gamma(0), m)][1 - \bar{\rho}_l^{dh}(\mu_\gamma(r_\gamma), m')] \times [\bar{B}_l(S(m')) - \bar{B}_l(S(m))] 2\mu_\gamma(0) \bar{R}_{l,\gamma} \bar{F}_l(\gamma). \quad (13)$$

3 Truncation Error Over-Estimates

The preceeding NER expressions involve infinite sums over surface reflections. The present section aims at finding an estimate of the errors made when omitting higher-order terms. Since all terms in, say, Eq. 10 do not have the same sign (because points in layer i may be warmer as well as colder than surface m), we shall seek an estimate of the truncation error on the spatial density. For Eq. 10, the absolute value of this density reads:

$$\left| \frac{\partial \bar{\psi}^{sg}(m, y)}{\partial y} \right| = \sum_{r=0}^{\infty} \int_0^1 d\mu(0) \ldots \times \int_0^1 d\mu(r) |\bar{h}^{sg}(l, \Gamma(S(m), y, r, \tilde{\mu}, m'))|. \quad (14)$$

Clearly, the partial sum of the r_0 first terms yields an under estimate of the full sum. What is sought for now is an overestimate function ξ^{sg} such that

$$\int_0^1 d\mu(0) \ldots \int_0^1 d\mu(r_0) \left| \sum_{r=r_0+1}^{\infty} \int_0^1 d\mu(r_0+1) \ldots \times \int_0^1 d\mu(r) \bar{h}^{sg}(l, \Gamma(S(m), y, r, \tilde{\mu}, m')) \right| \leq \int_0^1 d\mu(0) \ldots \int_0^1 d\mu(r_0) \xi^{sg}(l, \Gamma(S(m), y, r_0, \tilde{\mu}, m')). \quad (15)$$

The domain of integration of the truncated sum and the one of the overestimate function ξ^{sg} are the same: the angles of the first r_0 terms. So, these two numerical integrations can be computed together.

Simple over-estimate functions ξ^{sg} could be derived by only considering surface extinction after the $(r_0 + 1)$th reflection. As an alternative, other overestimates are proposed here for which only gas extinction is considered. The derivations are made with the assumption that the spectral average transmission function is a direct function of the effective pressure path length u_γ (common to most narrow band models):

$$\bar{F}_l(\gamma) = \bar{T}_l(u_\gamma). \quad (16)$$

u_γ is defined similarly to the $\tau_{\nu,\gamma}$ expression (Eq. 3):

$$u_\gamma = \begin{cases} u(x_\gamma, y_\gamma, \mu_\gamma(0)) & \text{if} \quad r_\gamma = 0 \\ u(x_\gamma, S(n_\gamma), \mu_\gamma(0)) + \sum_{s=1}^{r_\gamma - 1} u(S(1), S(2), \mu_\gamma(s)) & \\ \quad + u(S(M_\gamma(r_\gamma)), y_\gamma, \mu_\gamma(r_\gamma)) & \text{if} \quad r_\gamma \geq 1, \end{cases} \quad (17)$$

where $u(x, y, \mu)$ is the effective pressure path length of the segment from abscissa x to abscissa y with a cone angle cosine μ (see Cherkaoui et al., 1996). For any path γ we shall need extended path $\gamma|r$, for reflection numbers $r > r_\gamma$, defined as

$$\gamma|r = \Gamma(x_\gamma, y_\gamma, r, \tilde{\mu}_{\gamma|r}, n_\gamma), \quad (18)$$

where

$$\mu_{\gamma|r}(s) = \mu_\gamma(s) \quad \text{if} \quad 0 \leq s \leq r_\gamma - 1 \quad (19)$$

$$\mu_{\gamma|r}(s) = \mu^* \quad \text{if} \quad r_\gamma \leq s \leq r - 1 \quad (20)$$

$$\mu_{\gamma|r}(r) = \mu_\gamma(r_\gamma). \quad (21)$$

$\mu^* = 1$ in the general case and could be taken as $\mu^* = \mu_\gamma(0)$ in the simple case of two specular reflecting surfaces. $\gamma|r$ is therefore an optical path that is identical to γ up to the $(r_\gamma - 1)$th reflection, other cone angle cosines being attributed the value μ^* except for the last direction that corresponds to the last direction of the path γ. A first over estimate can be obtained by use of the properties that: (i) directional-hemispheric reflectivities are lower than unity; and (ii) the first derivative of $\bar{T}$ (which is negative) is an increasing function of the effective pressure path length.

$$\left| \sum_{r=r_0+1}^{\infty} \int_0^1 d\mu(0) \ldots \int_0^1 d\mu(r) \bar{h}^{sg}(l, \Gamma(S(m), y, r, \tilde{\mu}, m')) \right| \leq \int_0^1 d\mu(0) \ldots \int_0^1 d\mu(r_0) \left\{ \pi[1 - \bar{\rho}_l^{dh}(\mu_\gamma(0), m)] \times |\bar{B}_l(y_\gamma) - \bar{B}_l(S(m))| \times 2\mu_\gamma(0) \bar{R}_{l,\gamma} \bar{\Xi}_{l,\gamma} \right.$$

$$\times \sum_{r=r_\gamma+1}^{\infty} \left[-\frac{\partial \bar{T}_l}{\partial u}(u_{\gamma|r}) \right] \Bigg\} \gamma$$

$$= \Gamma(S(m), y, r_0, \vec{\mu}, m'), \tag{22}$$

where

$$\bar{\Xi}_{l,\gamma} = \max_{\substack{\alpha \in [0,1] \\ i \in \{1,2\}}} \left(\frac{\bar{q}_l(\mu_\gamma(r_\gamma); \alpha, i)}{\bar{q}_l(\mu_\gamma(r_\gamma); \mu_\gamma(r_\gamma - 1), M_\gamma(r_\gamma))} \right). \tag{23}$$

Note that $\bar{\Xi}_{l,\gamma} = 1$ for specular or diffuse reflecting surfaces. Further simplification of this overestimate can be obtained by use of the following relation:

$$u_{\gamma|r+2t} = u_{\gamma|r} + 2tu(S(1), S(2), \mu^*), \tag{24}$$

together with the following property of positive monotonous decreasing functions:

$$\sum_{t=1}^{\infty} g(a + th) \le \frac{1}{h} \int_a^{\infty} g(y)dy. \tag{25}$$

In the present case, $g = -(\partial \bar{T}_l/\partial u)$ and $h = 2u(S(1), S(2), \mu^*)$ leads to

$$\sum_{r=r_\gamma+1}^{\infty} \left[-\frac{\partial \bar{T}_l}{\partial u}(u_{\gamma|r}) \right]$$

$$= -\frac{\partial \bar{T}_l}{\partial u}(u_{\gamma|r_\gamma+1}) - \sum_{t=1}^{\infty} \frac{\partial \bar{T}_l}{\partial u}(u_{\gamma|r_\gamma+2t}) - \sum_{t=1}^{\infty} \frac{\partial \bar{T}_l}{\partial u}(u_{\gamma|r_\gamma+1+2t})$$

$$\le -\frac{\partial \bar{T}_l}{\partial u}(u_{\gamma|r_\gamma+1}) + \frac{\bar{T}_l(u_\gamma)}{2u(S(1), S(2), \mu^*)}$$

$$+ \frac{\bar{T}_l(u_{\gamma|r_\gamma+1})}{2u(S(1), S(2), \mu^*)}$$

$$\le -\frac{\partial \bar{T}_l}{\partial u}(u_{\gamma|r_\gamma+1}) + \frac{\bar{T}_l(u_\gamma)}{u(S(1), S(2), \mu^*)}. \tag{26}$$

The final retained overestimate (see Eq. (15), (22), and (26)) is:

$$\xi^{sg}(l, \gamma) = \pi[1 - \bar{\rho}_l^{dh}(\mu_\gamma(0), m)] |\bar{B}_l(y_\gamma) - \bar{B}_l(S(m))|$$
$$\times 2\mu_\gamma(0)\bar{R}_{l,\gamma}\bar{\Xi}_{l,\gamma} \left\{ -\frac{\partial \bar{T}_l}{\partial u}(u_\gamma) + \frac{\bar{T}_l(u_\gamma)}{u(S(1), S(2), \mu^*)} \right\}. \tag{27}$$

Gas-gas and surface-surface overestimates are derived similarly:

$$\xi^{gg}(l, \gamma) = \pi |\bar{B}_l(y_\gamma) - \bar{B}_l(S(m))| 2\mu_\gamma(0)\bar{R}_{l,\gamma}\bar{\Xi}_{l,\gamma}$$
$$\times \left\{ \frac{\partial^2 \bar{T}_l}{\partial u^2}(u_\gamma) - \frac{\frac{\partial \bar{T}_l}{\partial u}(u_\gamma)}{u(S(1), S(2), \mu^*)} \right\} \tag{28}$$

$$\xi^{ss}(l, \gamma) = \pi[1 - \bar{\rho}_l^{dh}(\mu_\gamma(0), m)]$$
$$\times [1 - \bar{\rho}_l^{dh}(\mu_\gamma(r_\gamma), M_\gamma(r_\gamma))] |\bar{B}_l(S(1)) - \bar{B}_l(S(2))|$$
$$\times 2\mu_\gamma(0)\bar{R}_{l,\gamma}\bar{\Xi}_{l,\gamma} \left\{ \bar{T}_l(u_\gamma) + \frac{\int_0^{u_\gamma} \bar{T}_l(u')du'}{u(S(1), S(2), \mu^*)} \right\}. \tag{29}$$

For surface-surface exchanges, the primitive of $\bar{T}$ is difficult to handle. In Cherkaoui et al., 1996, a simpler overestimate was used that is valid in the specular and diffuse cases: gas extinction is neglected after the $(r_0 + 1)$th reflection and reflectivities are assumed either Dirac-like or independent of the incident angle:

$$\xi^{ss}(l, \gamma) = \pi[1 - \bar{\rho}_l^{dh}(\mu_\gamma(0), m)]$$
$$\times [1 - \bar{\rho}_l^{dh}(\mu_\gamma(r_\gamma), M_\gamma(r_\gamma))] |\bar{B}_l(S(1)) - \bar{B}_l(S(2))|$$
$$\times 2\mu_\gamma(0)\bar{R}_{l,\gamma}\bar{\Xi}_{l,\gamma}\bar{T}_l(u_\gamma) \cdot \frac{\bar{\rho}_l^{dh}(\mu^*, 1) \cdot \bar{\rho}_l^{dh}(\mu^*, 2)}{1 - \bar{\rho}_l^{dh}(\mu^*, 1) \cdot \bar{\rho}_l^{dh}(\mu^*, 2)}. \tag{30}$$

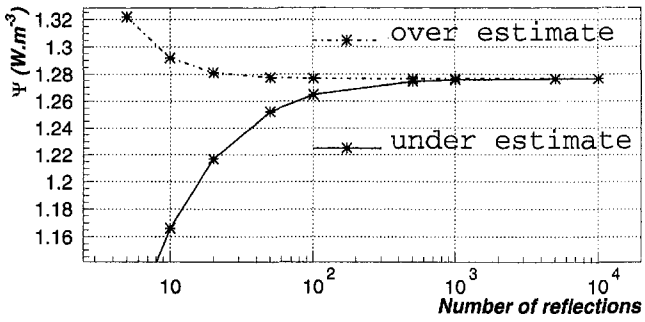

Fig. 2 Under and over estimate of the radiation budget for a particular layer (located at ≈ 0.04 m from S(1)) as a function of the number of reflection. $P_{CO_2} = 10^{-3}$, the two surfaces are perfect specular reflectors ($\epsilon_1 = \epsilon_2 = 0$), the temperature profile is linear (295 K at S(1) = 0 to 305 K at S(2) = 1 m).

4 Test Results

The preceding derivations allow the use of the EMCM algorithm (Cherkaoui et al., 1996) for configurations with large numbers of multiple reflections. Simulation results are presented for one-dimensional slab configurations with air-CO_2 mixtures and purely specular or purely diffuse surfaces. Spectral data are those of Soufiani et al. (1985) and Soufiani (1994).

A first series of simulations was made to validate the overestimation properties of the truncation error estimates derived in Section 3. The truncated volumetric radiation budget is an underestimate of the total budget, and adding to it the truncation error overestimate, yields an overestimate. Both under and overestimates have to converge when the number of considered reflections increases to infinity. Such a test is presented in Fig. 2 for a configuration with two perfect reflector surfaces: convergence of the radiation budget is achieved without noticeable bias, even for several hundred reflections. Also to be mentioned is the fact that the overestimate converges rapidly to the final solution; after a few reflections, the truncation error overestimate proposed in Section 3 provides a precise estimate of the sum of all radiative exchange via the infinite number of further reflections.

These tests were required to gain confidence in the EMCM as a method for production of reference solutions that may be useful for the design of approximate methods such as those presented in (Menart et al., 1993). Important information for this goal is the number of multiple reflections to be taken into account for a given accuracy and a given configuration type. Let $\zeta(i, j; r)$ be the ratio of the NER between the ith and the jth gas layers via r reflections over the full NER $\psi(i, j)$. Since the ratio $\zeta(i, j; r)$ is, for highly reflective configurations and relatively thin media, approximately identical for all layer pairs, only its average value $\zeta(r)$ will be considered. Figure 3 gives the evolution of $\zeta(r)$ versus the number of reflections for three dioxyde partial pressure P_{CO_2} values. For $P_{CO_2} = 10^{-4}$, 50 percent of the exchanges are due to the first 10 reflections; however, it is interesting to note that 10 percent of the exchanges are occurring via more than 100 reflections, and 1 percent via more than 800 reflections. Of course, the number of reflections decreases strongly as soon as the surface emissivities are not strictly zero: for emissivity values of 0.1 and $P_{CO_2} = 10^{-4}$, the

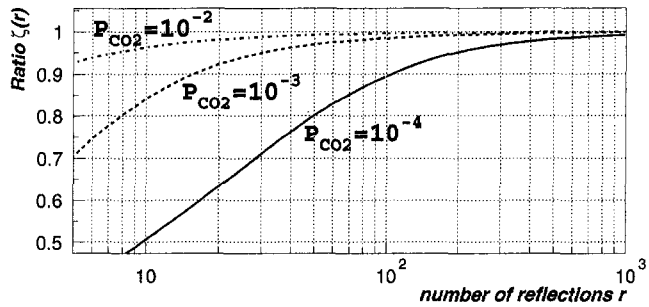

Fig. 3 Ratio $\zeta(r)$ between the energy net-exchange rate through the r first reflections and the net-exchange rate through an infinite number of reflections as a function of r. The two surfaces are perfect diffuse reflectors ($\epsilon_1 = \epsilon_2 = 0$), the temperature profile is linear (295 K at $S(1) = 0$ to 305 K at $S(2) = 1$ m).

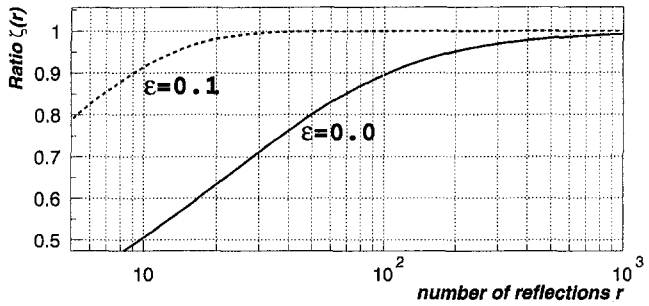

Fig. 4 Same ratio $\zeta(r)$ as Fig. 3 but for two values of the surface reflectivity ($\epsilon_1 = \epsilon_2 = \epsilon$). The dioxyde partial pressure is $P_{CO_2} = 10^{-4}$.

25 first reflections contribute to 99 percent of the average energy NER (Fig. 4).

Finally, some results are presented that illustrate the difference between the purely specular and purely diffuse assumptions. The ratio between the radiation budget for diffuse surfaces and the one for specular surfaces is plotted in Fig. 5 (for three specific layers), versus the partial pressure of CO_2. Along the reflective surface, the ratio of diffuse/specular starts at a value of one for extremely small concentrations of absorbing material and increases regularly with P_{CO_2}, up to 13 percent for pure carbon dioxide. For gas volumes farther from the surface, the sensitivity to the reflective properties is much smaller (a few percent). The surface radiation budget appears to be much less sensitive to the reflective properties, as it was previously observed by Nelson (1979) for an isothermal gas volume. The same kind of results were obtained in the case of two highly reflective surfaces ($\epsilon_1 = \epsilon_2 = 0.1$).

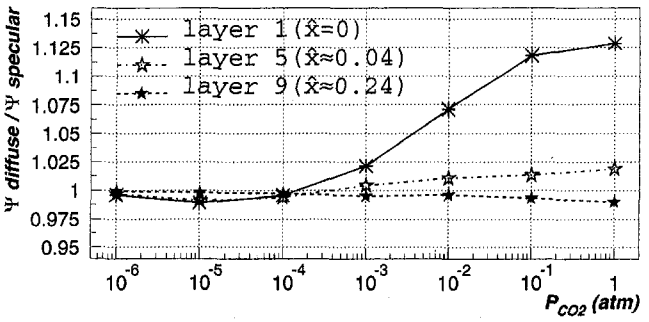

Fig. 5 Ratio between the radiation budgets for diffuse reflections and the one for specular reflections versus partial pressures of absorbing gas (CO_2), in the case of one perfect reflector and one black surface ($\epsilon_1 = 0$, $\epsilon_2 = 1$). The temperature profile is linear (295 K at $S(1) = 0$ to 305 K at $S(2) = 1$ m). Layer 1 is zero thickness and located along the reflective surface, Layer 5 and Layer 9 are, respectively, located at 0.04 m and at 0.24 m.

5 Conclusion

NEF and EMCM have been extended to configurations involving multiple reflection processes. Reference solutions are therefore available that should be very useful to test approximate methods, especially concerning spectral correlation problems. It is of interest to note that:

1 Specular and diffuse reflection assumptions yield very similar results for most configuration types: the multiple angular integration complexity can be avoided for first approximation computations.
2 Truncation errors can be precisely estimated: in the specular case, such estimates take simple mathematical forms. Thus, multiple reflection exchanges should be easy to model with better accuracy than the commonly encountered assumption of spectrally uncorrelated reflections.

Acknowledgments

We would like to thank L. Fairhead for English editing. This work was sponsored by PIRSEM/CNRS, ADEME, "Service Habitat et Tertiaire" and "Ministère de la Recherche et de la Technologie."

References

Cherkaoui, M., Dufresne, J. L., Fournier, R., Grandpeix, J. Y., Lahellec, A., 1996, "Monte Carlo Simulation of Radiation in Gases With a Narrow-Band Model and a Net-Exchange Formulation," ASME JOURNAL OF HEAT TRANSFER, Vol. 118, pp. 401–407.

Green, J. S. A., 1967, "Division of Radiative Streams into Internal Transfer and Cooling to Space," *Quarterly Journal of the Royal Meteorological Society*, Vol. 93, pp. 371–372.

Joseph, J. M., Bursztyn, R., 1976, "A Radiative Cooling Model in the Thermal Infrared for Application to Models of the General Circulation," *Journal of Applied Meteorology*, Vol. 15, pp. 319–325.

Menart, J. A., Lee, H. S., Kim, T. K., 1993, "Discrete Ordinate Solutions of Nongray Radiative Transfer with Diffusely Reflecting Walls," ASME JOURNAL OF HEAT TRANSFER, Vol. 115, pp. 184–193.

Naraghi, M. H. N., Huan, J., 1991, "An n-Bounce Method for Analysis of Radiative Transfer in Enclosure With Anisotropically Scattering Media," ASME JOURNAL OF HEAT TRANSFER, Vol. 113, pp. 774–777.

Nelson, D. A., 1979, "Band Radiation Within Diffuse-Walled Enclosures: Part 1—Exact Solutions for Simple Enclosures," ASME JOURNAL OF HEAT TRANSFER, Vol. 101, pp. 81–84.

Noble, J. J., 1975, "The Zone Method: Explicit Matrix Relations for Total Exchange Areas," *Int. J. Heat Mass Transfer*, Vol. 18, pp. 261–269.

Soufiani, A., 1994, personnal communication, EM2C Laboratory (ECP-CNRS), Chatenay-Malabry, France.

Soufiani, A., Hartmann, J. M., and Taine, J., 1985, "Validity of Band-Model Calculations for CO_2 and H_2O Applied to Radiative Properties and Conductive-Radiative Transfer," *Journal of Quantitative Spectroscopy and Radiative Transfer*, Vol. 33, No. 3, pp. 243–257.

A New Semianalytical Algorithm for Calculating Diffuse Plane View Factors

A. Mavroulakis[1] **and A. Trombe**[1,2]

A new semianalytical algorithm for calculating diffuse plane view factors which is based on an extension of Nusselt's sphere method is presented. For simple cases of view factor calculations where exact solutions exist, the accuracy of the algorithm is tested and compared with the accuracy of others.

Nomenclature

A = area
dA = elementary area
dA_h = projection of dA_2 onto the unit sphere
F = configuration factor
l = element of contour
n_L = discretisation parameter
R = unit radius
S = distance between two differential elements
$X, Y, Z - x, y, z$ = cartesian coordinate systems

Greek Symbols

α = tilted angle between plane ES_1S_2 and the coordinate system Exy
φ = eccentric angle between radius and abcissa EX
φ_1, φ_2 = angles between EH_1, EH_2, and axis EA
θ_1, θ_2 = angles between EP_1 and EP_2 and EX
γ = angle between coordinate systems Exy and EXY

Subscripts

1, 2 = at area 1 or 2
d_1, d_2 = evaluated as differential element d_1 or d_2

1 Description of the New Semianalytical Algorithm

The geometrical view factor between two isothermal blackbody diffusely emitting and reflecting surfaces, A_1 and A_2, is given by Eq. (1).

$$F_{12} = \frac{1}{A_1}\int_{A_1}\int_{A_2}\frac{\cos\theta_1\cos\theta_2}{\pi S^2}dA_2dA_1 \qquad (1)$$

It represents the proportion of the energy leaving area A_1 that is intercepted by area A_2.

Several methods can be used to determine view factors. For relatively simple geometries, analytical, graphical, or tabular values of F_{12} are available; a great number of references are given by Siegel and Howell (1992). But as we intend to develop view factor calculations for real structures in which surface geometries can become complex, analytical relations are not available. For such cases approximate methods using numerical algorithms and computers must be used.

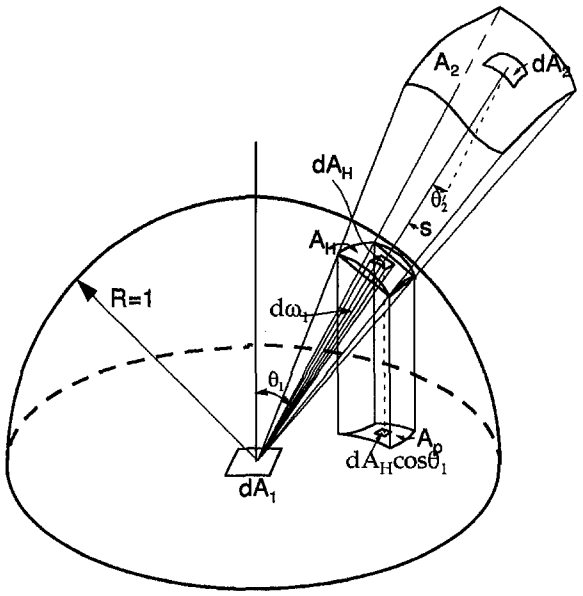

Fig. 1 Geometrical representation of Nusselt's analogy

The first algorithm is known as the "double area integral method." Its accuracy is poor, particularly when areas are close together (Walton, 1986) or present a common edge. It is often used, if lower accuracy is acceptable, for configurations filled with obstacles because of its algorithmic simplicity and of its speed (Walton, 1986; Shapiro, 1985; Emery et al., 1991). Note that an improvement of this method has been proposed for irregular geometries using isoparametric element functions (Chung and Kim, 1982).

The second is the "line integral method". From Eq. (1), the value of F_{12} is given by a double integral. In this representation the mathematical task required is a two-dimensional integration, but it is possible to reduce the remaining mathematical integration using Stokes's theorem (Sparrow, 1963). Sparrow's method (or contour integration), although it allows the analytical calculation of view factors for some cases, is of no use if the two surfaces share a part of their contour. In order to avoid this problem, Mitalas and Stephenson (1966) proposed an analytical formulation for one of the equation integrals in the case of polygonal surfaces. For two quadrilaterals it has the following form (Eq. (2)).

$$F_{12} = \frac{1}{2\pi A_1}\sum_{p=1}^{4}\sum_{q=1}^{4}\Phi(p,q)\oint_{C_{1p}}[(T\cos\phi\ln T + S\cos\theta\ln S + U\omega - R)dl_1]_{p,q} \qquad (2)$$

The third algorithm is based on Nusselt's method (Nusselt, 1928), initially used for the experimental determination of the configuration factors, Fig. (1). The elementary configuration factor F_{d1-2} of dA_1, with regard to the finite area A_2, can be expressed in terms of the projection dA_H of dA_2 onto the surface of the unit hemisphere.

$$F_{d1-2} = \frac{1}{\pi}\int_{A_2}\cos\theta_1 dA_H = \frac{A_p}{\pi} \qquad (3)$$

Where A_p is the orthographic projection of A_H onto the base of the hemisphere.

The proposed algorithm is based on an extension of the Nusselt's initial sphere method. Equation (3), with an appropriate evaluation of the projected surface A_p, would allow the determi-

[1] Laboratoire D'Etudes Thermiques et Mécaniques, Département de Génie-Civil, Complexe Scientifique de Rangueil, 31077, Toulouse cedex, France
[2] trombe@insatlse.insa-tlse.fr

Contributed by the Heat Transfer Division of THE AMERICAN SOCIETY OF MECHANICAL ENGINEERS. Manuscript received by the Heat Transfer Division July 26, 1996; revision received October 13, 1997; Keywords: Building Heat Transfer; Computer Codes; Radiation. Associate Technical Editor: T. Tong.

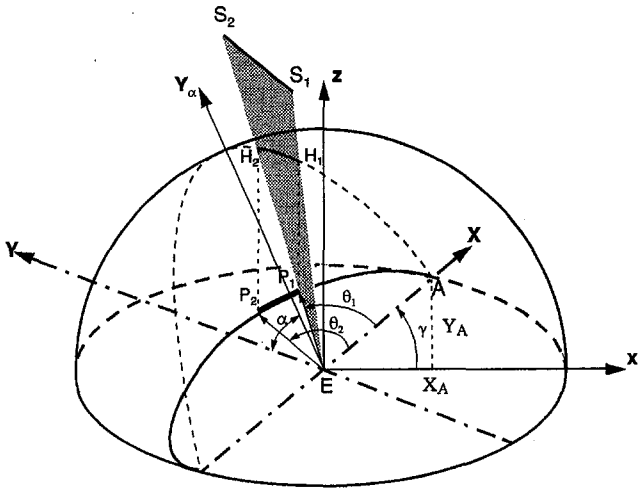

Fig. 2 Definition of the arc of an ellipse P_1P_2

nation of F_{d1-2} without a previous subdivision of the receiving area A_2. We can consider that the contour of the receiver can be given by a series of straight segments or by planar segments of curves, each of them situated as a whole inside the plane defined by the centroid of dA_1 and the two arc's ends. Then, the contour of the projection will be a series of unit circle arcs onto the unit sphere. Finally, every unit circle arc which is projected onto the base of the hemisphere becomes an arc of an ellipse (or a unit circle arc of the base, or a diameter segment of it) and we thus obtain the contour of A_p, Fig. (2). Consequently, we intend to provide the analytical formulation of the projected area A_p. To do so we are going to consider a straight segment S_1S_2, situated inside the positive half space ($z > 0$) of the base hemisphere, which represents one of the edges of the receiving surfaces A_2.

The vertices S_1 and S_2 are known by their cartesian coordinates x_{S_1}, y_{S_1}, z_{S_1}, and x_{S_2}, y_{S_2}, z_{S_2}, respectively seen under the coordinate system $Exyz$, with E the centroid of dA_1 and the axis Ez the normal to the base of the hemisphere. The projection of S_1 and S_2 upon the unit hemisphere provides the points H_1 and H_2 of which we know the following:

$$\underline{EH_1} = [x_{H_1} y_{H_1} z_{H_1}]^T = \left[\frac{x_{S_1}}{\|\underline{ES_1}\|} \quad \frac{y_{S_1}}{\|\underline{ES_1}\|} \quad \frac{z_{S_1}}{\|\underline{ES_1}\|} \right]^T, \quad \|\underline{EH_1}\| = 1$$

and

$$\underline{EH_2} = [x_{H_2} y_{H_2} z_{H_2}]^T = \left[\frac{x_{S_2}}{\|\underline{ES_2}\|} \quad \frac{y_{S_2}}{\|\underline{ES_2}\|} \quad \frac{z_{S_2}}{\|\underline{ES_2}\|} \right]^T, \quad \|\underline{EH_2}\| = 1.$$

The straight segment S_1S_2 projects itself upon the arc H_1H_2 of the unit circle situated inside the plane defined by E, S_1, and S_2—gray area, Fig. (2)—whose tilted angle α can vary between ($0 \le \alpha \le \pi/2$) with respect to the base of the hemisphere (plane xEy).

The orthographic projection of the unit circle tilted upon the base will then be an ellipse of unitary semimajor axis and of semiminor axis cos α. Its semimajor axis EA presents an azimuth angle γ with respect to the axis Ex which we can determine if we note that the points E of coordinates $([x_E, y_E, z_E]^T = [0, 0, 0]^T)$, H_1, H_2, and A ($\underline{EA} = [x_A\ y_A\ 0]^T$) will have to belong to plane (ES_1S_2). For that we have to set the triple scalar product to zero, as follows:

$$\begin{vmatrix} x_A - x_E & y_A - y_E & z_A - z_E \\ x_{H_1} - x_E & y_{H_1} - y_E & z_{H_1} - z_E \\ x_{H_2} - x_E & y_{H_2} - y_E & z_{H_2} - z_E \end{vmatrix} = \begin{vmatrix} x_A & y_A & 0 \\ x_{H_1} & y_{H_1} & z_{H_1} \\ x_{H_2} & y_{H_2} & z_{H_2} \end{vmatrix}$$

$$= \begin{vmatrix} y_{H_1} & z_{H_1} \\ y_{H_2} & z_{H_2} \end{vmatrix} x_A - \begin{vmatrix} x_{H_1} & z_{H_1} \\ x_{H_2} & z_{H_2} \end{vmatrix} y_A = 0.$$

then

$$\tan \gamma = \frac{y_A}{x_A} = \frac{\begin{vmatrix} y_{H_1} & z_{H_1} \\ y_{H_2} & z_{H_2} \end{vmatrix}}{\begin{vmatrix} x_{H_1} & z_{H_1} \\ x_{H_2} & z_{H_2} \end{vmatrix}} = \frac{y_{H_1} z_{H_2} - y_{H_2} z_{H_1}}{x_{H_1} z_{H_2} - x_{H_2} z_{H_1}}.$$

The classical equation of the ellipse can be written in the coordinate system EXY,

$$X^2 + \frac{Y^2}{\cos^2 \alpha} = 1, \tag{4}$$

with

$$X = x \cos \gamma + y \sin \gamma \quad Y = y \cos \gamma - x \sin \gamma \tag{5}$$

$$x = X \cos \gamma - Y \sin \gamma \quad y = X \sin \gamma + Y \cos \gamma, \tag{6}$$

the transformations between the coordinate systems EXY and Exy.

The projection coordinates P_1 and P_2 of points H_1 and H_2 of the hemisphere are written as follows:

$$\text{In } Exy: \quad xp_{1,2} = xH_{1,2} \quad yp_{1,2} = yH_{1,2} \quad zp_{1,2} = 0 \tag{7}$$

$$\text{In } EXY: \quad Xp_{1,2} = \cos \varphi_{1,2} \quad Yp_{1,2} = \cos \alpha \sin \varphi_{1,2}$$

$$-\pi \le \varphi_{1,2} \le \pi \tag{8}$$

The parametric equations (8) of the ellipse make it necessary to use the eccentric angle; between this angle and the angle θ, the relation is

$$\tan \theta = \cos \alpha \tan \varphi. \tag{9}$$

Relations (5) and (6) allow $X_{P_{1,2}}$ and $Y_{P_{1,2}}$ to be calculated in order to obtain cos α with help of Eq. (4):

$$\cos \alpha = \frac{|Y_{P_{1,2}}|}{\sqrt{1 - X^2_{P_{1,2}}}}. \tag{10}$$

The absolute value of the numerator is justified by the fact that cos α can only take positive values, the end values 0 and $\pi/2$ of α do not correspond to an elliptic projection of the unit circle.

The angles φ_1 and φ_2 of points P_1 and P_2 of the ellipse can be calculated easily with relations (8, 9), which are injected into relations (5, 6) to lead to the parametric equations of the ellipse arc P_1P_2 in the coordinate system Exy:

$$x(\varphi) = \cos \gamma \cos \varphi - \cos \alpha \sin \gamma \sin \varphi$$

$$y(\varphi) = \sin \gamma \cos \varphi + \cos \alpha \cos \gamma \sin \varphi$$

$$\varphi = \varphi_1 + \lambda(\varphi_2 - \varphi_1), \quad 0 \le \lambda \le 1 \tag{11}$$

The angles φ_1 and φ_2 of points P_1 and P_2 of the ellipse can be calculated easily with relations (11), which are injected into relation (8) to lead to the parametric equations of the ellipse arc P_1P_2 in the coordinate system Exy:

$$x(\varphi) = \cos\gamma\cos\varphi - \cos\alpha\sin\gamma\sin\varphi$$

$$y(\varphi) = \sin\gamma\cos\varphi + \cos\alpha\cos\gamma\sin\varphi$$

$$\varphi = \varphi_1 + \lambda(\varphi_2 - \varphi_1), \quad 0 \le \lambda \le 1 \qquad (12)$$

The thought process that we just have described can be repeated again for all the edges of the receiving area in order to establish the expressions of $x(\varphi)$ and $y(\varphi)$ governing the arcs of ellipses which constitute the contour of the projection A_p.

The area A_p will be determined using the Green's formulation (Eq. (13)).

$$\iint_D \left(\frac{\partial V}{\partial x} - \frac{\partial U}{\partial y}\right) dxdy = \oint_C Udx + Vdy \qquad (13)$$

For our case, for a receiving polygon with n vertices $S_i (i = 1, \ldots, n)$, we can express the area A_p with the help of expressions (14) applied to the successive arcs of ellipses:

$$P_1P_2(\alpha_1, \gamma_1, \varphi_1, \varphi_2), \ldots, P_{n-1}P_n(\alpha_{n-1}, \gamma_{n-1}, \varphi_{n-1}, \varphi_n),$$
$$P_nP_1(\alpha_n, \gamma_n, \varphi_n, \varphi_1)$$

$$A_p = \left| \sum_{i=1}^{n-1} \oint_{P_iP_{i+1}} xdy + \oint_{P_nP_1} xdy \right|. \qquad (14)$$

The sum of the contour integrations is calculated in terms of the absolute value to take into account a possible orientation of the contour integral following the clockwise direction.

The curvilinear intégral $\mathbf{I_q}$, which corresponds to the edge S_qS_r and to the arc of an ellipse P_qP_r, becomes

$$\mathbf{I_q} = \tfrac{1}{4}[\cos\alpha_q\{2(\varphi_r - \varphi_q) + \cos 2\gamma_q(\sin 2\varphi_r - \sin 2\varphi_q)\}$$
$$- \sin 2\gamma_q(1 + \cos^2\alpha_q)(\sin^2\varphi_r - \sin^2\varphi_q)]. \qquad (15)$$

Particular Cases.

1 *1.* $\alpha_q = 0$. The edge S_qS_r, being situated inside the base plane, is: $H_qH_r \equiv P_qP_r$ = unit circle arc with

$$x_{P_{q,r}} = x_{H_{q,r}} = \cos\theta_{q,r} \quad y_{P_{q,r}} = y_{H_{q,r}} = \sin\theta_{q,r}$$

and

$$\mathbf{I_q} = \oint_{P_qP_r} xdy = \int_{\theta_q}^{\theta_r} \cos^2\theta d\theta$$
$$= \tfrac{1}{4}[2(\theta_r - \theta_q) + \sin 2\theta_r - \sin 2\theta_q]. \qquad (16)$$

2 $\alpha_q = \pi/2$. The edge S_qS_r projects itself onto the line segment P_qP_r of slope $\tan\beta_q$ which goes through the center of the hemisphere.

$2\alpha)$ $\beta_q = 0$ or $\beta_q = \pi$: $y_{P_{q,r}} = y_{H_{q,r}} = 0 \quad \mathbf{I_q} = 0$

$2\beta)$ $\beta_q = \pm\pi/2$: $x_{P_{q,r}} = x_{H_{q,r}} = 0 \quad \mathbf{I_q} = 0$

2c) $\tan\beta_q \neq 0$ and $\tan\beta_q \neq \pm\infty$ $x = y/\tan\beta_q$

$$y = y_{P_q} + \lambda(y_{P_r} - y_{P_q}), \quad 0 \le \lambda \le 1$$

$$\text{and} \quad \mathbf{I_q} = \frac{1}{\tan\beta_q}\int_{y_{P_q}}^{y_{P_r}} ydy = \frac{y_{P_r}^2 - y_{P_q}^2}{2\tan\beta_q} \qquad (17)$$

The equations (15), (16), and (17) provide a quick and real mean of determining the true value of $F_{d1-2}(=A_p/\pi)$.

2 Performance of the Method for Simple and Known Analytical Configurations

The double area integral algorithm and the line integral algorithm provided by Mitalas and Stephenson (1966) have often been used for complex view factor calculations with computers:

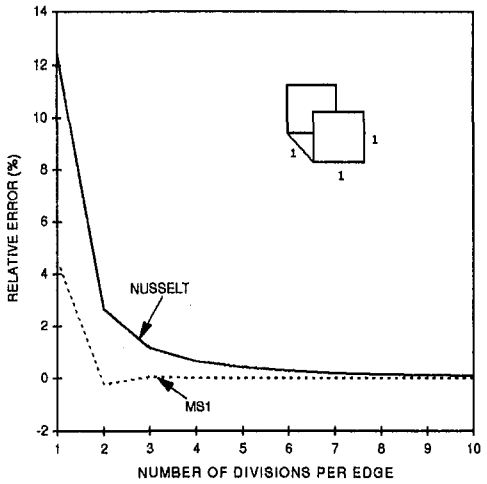

Fig. 3 Comparison of Nusselt and of Mitalas-Stephenson for configuration A

VLITE (Walton, 1993), VIEW (Emery, 1988), and FACET (Shapiro, 1983). It is worth noting that the last two employ a hybrid technique which uses a combination of contour and double area integrals depending on the configuration. So, we thought it would be interesting to compare the results obtained from our method with those given by sophisticated methods such as the Mitalas-Stephenson's method and reported by Walton, (1986).

2.1 Parallel Unit Squares, Facing Each Together, One Meter Apart (configuration A). Figure (3) may be used to compare the accuracy of our method (Nusselt's curve) to that of Mitalas-Stephenson's (curve MS1) for n_L varying between 1 and 10. It should be noted that the single contour integral used is very economical in computer time since for the emitting element it involves n_L length elements instead of n_L^2 area elements.

The relative error (results − exact value/exact value) is equally in favour of this method; with $n_L = 2$ it gives −0.22 percent as 2.64 percent for our Nusselt's method, the latter giving the same relative error for $n_L = 7$ (0.21 percent). This good performance of Mitalas-Stephenson's method is generally assigned to the efficiency of the numerical integration diagrams (Gaussian) used, allowing each edge of the emitting surface to be divided into n_L elements of different lengths. One can add the fact that, as we shall see further on, this method like Sparrow's initial method can be easy to use when there is no common edge between the two areas.

2.2 Perpendicular Unit Squares, With a Common Edge (configuration B). This result is shown, Fig. (4), where the situation is reversed relative to configuration A. We note that our Nusselt's method is more accurate than MS1; for $n_L = 1$ ($n_L = 2$) the errors are 3.12 percent (−0.66 percent) and 11.8 percent (1.25 percent), respectively. This increasing error of MS1 indicates the weakness of numerical integration on the common edges of the areas.

The solution consists of analytically evaluating the integral of expression (2) upon the common edge or, more generally, on the two collinear edges (Walton, 1986). The curve MS2 of Fig. (4) shows the positive effect on the accuracy: the error for $n_L = 2$ decreases to 0.12 percent.

This improvement given by Mitalas-Stephenson's method depends on the detection of the collinearity amongst the edges of two polygons. Even if the calculation time is not increased as Walton (1986) claims, this operation remains of extreme algorithmic sensitivity and needs very long and rigorous numer-

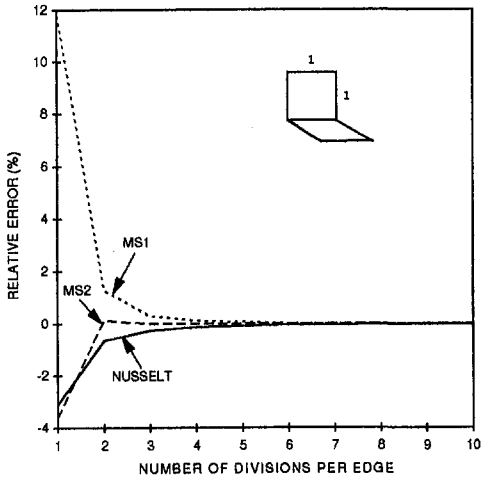

Fig. 4 Comparison of Nusselt and of Mitalas-Stephenson for configuration B

ical validations before putting it into service. This is not the case for our Nusselt's method, for which, guided by far more simple geometrical tests, can adapt itself to any application situation, except for analytical support of section (1).

3 Conclusion

The authors have presented here an improvement of Nusselt's analogy. Even if its accuracy is not as good as the latest improved methods recently proposed, particularly for small values of discretisation parameters, it is very easy to use for diffuse view factor calculations. This is specially true for complex enclosures where colinear surfaces are frequent. So, the authors intend to use it for their future works in obstacle-filled cavities.

Acknowledgements

The authors wish to acknowledge the support of G. N. Walton who provided a very interesting bibliographic support.

4 References

Chung, T. J., and Kim, J. Y., 1982, "Radiation View Factors by Finite Elements," ASME JOURNAL OF HEAT TRANSFER, Vol. 104, pp. 792–795.

Emery, A. F., 1983, VIEW—A Radiation View Factor Computer Program With Interactive Graphics for Geometry Definition (version 5.5.3), Nasa Computer Software Management and Information Center, Atlanta GA.

Emery, A. F., Johansson, O., Lobo, M., Abrous, A., 1991, "A Comparative Study of Methods for Computing the Diffuse Radiation View Factors for Complex Structures," ASME JOURNAL OF HEAT TRANSFER, Vol. 113, pp. 413, 422.

Mitalas, G. P., and Stephenson, D. G., 1966, *Fortran Programs to Calculate Radiant Interchange Factors,* Report DBR-25, National Research Council of Canada, Division of Building Research, Ottawa, Canada.

Nusselt, W., 1928, "Graphische bestimmung des winkelverhaltnisses bei der warmestrahlung VDI Z," Vol. 72, p. 673.

Siegel, R., and Howell, J. R., 1992, "Thermal Radiation Heat Transfer," Hemisphere Publishing Corporation, Washington, D.C.

Shapiro, A. B., 1985, "Computer Implementation, Accuracy and Timing of Radiation View Factor Algorithms," ASME JOURNAL OF HEAT TRANSFER, Vol. 107, pp. 730–732.

Shapiro, A. B., 1983, FACET—A Radiation View Factor Computer Code for Axisymmetric, 2D Planar, and 3D Geometries With Shadowing, University of California, Lawrence Livermore National Laboratory, UCID-19887.

Sparrow, E. M., 1963, "A New and Simpler Formulation for Radiative Angle Factors," ASME JOURNAL OF HEAT TRANSFER, Vol. 85, pp. 81–88.

Walton, G. N., 1986, Algorithms for Calculating Radiation View Factors Between Plane Convex Polygons With Obstructions, Report 86-3463, National Bureau of Standards, Gaithersburg, MD.

Walton, G. N., 1993, VLITE—Computer Programs for Simulation of Lighting/HVAC Interactions, National Institute of Standards and Technology, Gaithersburg, Maryland.

Effect of Ultrasonic Vibration on Transient Boiling Heat Transfer During Rapid Quenching of a Thin Wire in Water

H. Yamashiro,[1] H. Takamatsu,[1] and H. Honda[1,2]

Introduction

The enhancement of cooling rate is very important for the production of amorphous metallic wires by the in-rotating-water spinning method, in which a jet of molten alloy is ejected through a nozzle into a water layer formed on the inner surface of a rotating drum. As a basic study of the cooling characteristics during this process, Honda et al. (1992, 1994) performed rapid quenching experiments of thin horizontal platinum wires in subcooled water, $CaCl_2$/water solution and ethanol. The transient boiling curve obtained from the measured cooling curve showed two minimum-heat-flux (MHF) points. Measurement of liquid-solid contact using a conductance probe showed that the first MHF point with a higher wall superheat ($M1$ point) corresponded to the onset of significant liquid-solid contact. Addition of $CaCl_2$ into water was very effective in enhancing heat transfer in the region of wall superheat below the $M1$ point. However, it was not effective in increasing the wall superheat at the $M1$ point. Thus, a new method for promoting the liquid-solid contact is required to enhance heat transfer in the higher wall superheat region.

The effect of ultrasonic vibration on the quenching process has been studied by a number of investigators. Iida et al. (1990) performed quenching experiments of silver cylinders with water as a quenching liquid. Loosle and Holdredge (1970) used liquid nitrogen and liquid helium as quenching liquids. This work showed that the ultrasonic vibration was effective in raising the quench temperature and enhancing the cooling rate. However, the range of wall temperature tested by these investigators was limited to below 700°C, which was not high enough to cover the temperature range encountered in the rapid solidification processing. The effect of ultrasonic vibration on the steady heat transfer has been examined by Wong and Chon (1969), Park and Bergles (1988), Iida and Tsutsui (1989), Nakayama and Kano (1990), and Nomura and Nakagawa (1993). Summarizing these results, the ultrasonic vibration improves the heat transfer coefficient about eight times for free convection and two to three times for nucleate and film boiling. While the heat transfer enhancement described above is ascribed to the generation of the sound pressure, cavitation and acoustic streaming, more work is required to identify the contribution of each factor. In the present work the effect of ultrasonic vibration on the heat transfer during the rapid quenching of a thin horizontal wires in subcooled water is studied experimentally. Parametric effects of the sound pressure and the frequency of ultrasonic vibration on the transient boiling curve and the $M1$ point are examined. The distributions of the sound pressure and cavitation

[1] Institute of Advanced Material Study, Kyushu University, Kasuga, Fukuoka, 816, Japan.

[2] E-mail: hhonda@cm.kyushu-u.ac.jp

Contributed by the Heat Transfer Division of THE AMERICAN SOCIETY OF MECHANICAL ENGINEERS. Manuscript received by the Heat Transfer Division November 12, 1996; revision received October 7, 1997; Keywords: Augmentation and Enhancement; Building Heat Transfer; Transient and Unsteady Heat Transfer. Associate Technical Editor: M. Kaviany.

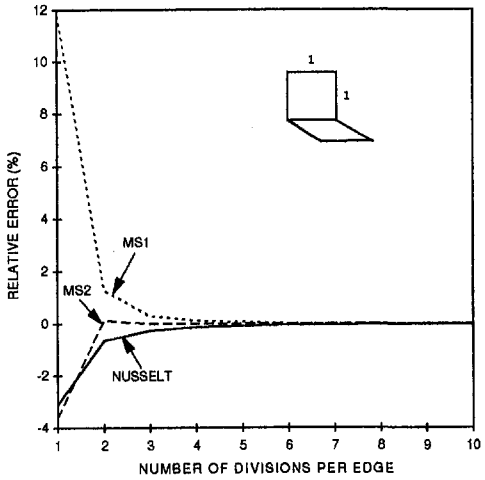

Fig. 4 Comparison of Nusselt and of Mitalas-Stephenson for configuration B

ical validations before putting it into service. This is not the case for our Nusselt's method, for which, guided by far more simple geometrical tests, can adapt itself to any application situation, except for analytical support of section (1).

3 Conclusion

The authors have presented here an improvement of Nusselt's analogy. Even if its accuracy is not as good as the latest improved methods recently proposed, particularly for small values of discretisation parameters, it is very easy to use for diffuse view factor calculations. This is specially true for complex enclosures where colinear surfaces are frequent. So, the authors intend to use it for their future works in obstacle-filled cavities.

Acknowledgements

The authors wish to acknowledge the support of G. N. Walton who provided a very interesting bibliographic support.

4 References

Chung, T. J., and Kim, J. Y., 1982, "Radiation View Factors by Finite Elements," ASME JOURNAL OF HEAT TRANSFER, Vol. 104, pp. 792–795.

Emery, A. F., 1983, VIEW—A Radiation View Factor Computer Program With Interactive Graphics for Geometry Definition (version 5.5.3), Nasa Computer Software Management and Information Center, Atlanta GA.

Emery, A. F., Johansson, O., Lobo, M., Abrous, A., 1991, "A Comparative Study of Methods for Computing the Diffuse Radiation View Factors for Complex Structures," ASME JOURNAL OF HEAT TRANSFER, Vol. 113, pp. 413, 422.

Mitalas, G. P., and Stephenson, D. G., 1966, *Fortran Programs to Calculate Radiant Interchange Factors,* Report DBR-25, National Research Council of Canada, Division of Building Research, Ottawa, Canada.

Nusselt, W., 1928, "Graphische bestimmung des winkelverhaltnisses bei der warmestrahlung VDI Z," Vol. 72, p. 673.

Siegel, R., and Howell, J. R., 1992, "Thermal Radiation Heat Transfer," Hemisphere Publishing Corporation, Washington, D.C.

Shapiro, A. B., 1985, "Computer Implementation, Accuracy and Timing of Radiation View Factor Algorithms," ASME JOURNAL OF HEAT TRANSFER, Vol. 107, pp. 730–732.

Shapiro, A. B., 1983, FACET—A Radiation View Factor Computer Code for Axisymmetric, 2D Planar, and 3D Geometries With Shadowing, University of California, Lawrence Livermore National Laboratory, UCID-19887.

Sparrow, E. M., 1963, "A New and Simpler Formulation for Radiative Angle Factors," ASME JOURNAL OF HEAT TRANSFER, Vol. 85, pp. 81–88.

Walton, G. N., 1986, Algorithms for Calculating Radiation View Factors Between Plane Convex Polygons With Obstructions, Report 86-3463, National Bureau of Standards, Gaithersburg, MD.

Walton, G. N., 1993, VLITE—Computer Programs for Simulation of Lighting/HVAC Interactions, National Institute of Standards and Technology, Gaithersburg, Maryland.

Effect of Ultrasonic Vibration on Transient Boiling Heat Transfer During Rapid Quenching of a Thin Wire in Water

H. Yamashiro,[1] H. Takamatsu,[1] and H. Honda[1,2]

Introduction

The enhancement of cooling rate is very important for the production of amorphous metallic wires by the in-rotating-water spinning method, in which a jet of molten alloy is ejected through a nozzle into a water layer formed on the inner surface of a rotating drum. As a basic study of the cooling characteristics during this process, Honda et al. (1992, 1994) performed rapid quenching experiments of thin horizontal platinum wires in subcooled water, $CaCl_2$/water solution and ethanol. The transient boiling curve obtained from the measured cooling curve showed two minimum-heat-flux (MHF) points. Measurement of liquid-solid contact using a conductance probe showed that the first MHF point with a higher wall superheat ($M1$ point) corresponded to the onset of significant liquid-solid contact. Addition of $CaCl_2$ into water was very effective in enhancing heat transfer in the region of wall superheat below the $M1$ point. However, it was not effective in increasing the wall superheat at the $M1$ point. Thus, a new method for promoting the liquid-solid contact is required to enhance heat transfer in the higher wall superheat region.

The effect of ultrasonic vibration on the quenching process has been studied by a number of investigators. Iida et al. (1990) performed quenching experiments of silver cylinders with water as a quenching liquid. Loosle and Holdredge (1970) used liquid nitrogen and liquid helium as quenching liquids. This work showed that the ultrasonic vibration was effective in raising the quench temperature and enhancing the cooling rate. However, the range of wall temperature tested by these investigators was limited to below 700°C, which was not high enough to cover the temperature range encountered in the rapid solidification processing. The effect of ultrasonic vibration on the steady heat transfer has been examined by Wong and Chon (1969), Park and Bergles (1988), Iida and Tsutsui (1989), Nakayama and Kano (1990), and Nomura and Nakagawa (1993). Summarizing these results, the ultrasonic vibration improves the heat transfer coefficient about eight times for free convection and two to three times for nucleate and film boiling. While the heat transfer enhancement described above is ascribed to the generation of the sound pressure, cavitation and acoustic streaming, more work is required to identify the contribution of each factor. In the present work the effect of ultrasonic vibration on the heat transfer during the rapid quenching of a thin horizontal wires in subcooled water is studied experimentally. Parametric effects of the sound pressure and the frequency of ultrasonic vibration on the transient boiling curve and the $M1$ point are examined. The distributions of the sound pressure and cavitation

[1] Institute of Advanced Material Study, Kyushu University, Kasuga, Fukuoka, 816, Japan.

[2] E-mail: hhonda@cm.kyushu-u.ac.jp

Contributed by the Heat Transfer Division of THE AMERICAN SOCIETY OF MECHANICAL ENGINEERS. Manuscript received by the Heat Transfer Division November 12, 1996; revision received October 7, 1997; Keywords: Augmentation and Enhancement; Building Heat Transfer; Transient and Unsteady Heat Transfer. Associate Technical Editor: M. Kaviany.

intensity in the liquid are also measured and their effects on the heat transfer characteristics are discussed.

Experimental Apparatus and Procedures

The experimental apparatus was the same as that used in the previous studies (Honda et al., 1992, 1994, 1995) except that an ultrasonic vibrator was newly added. The test section was a platinum wire of 0.5 mm in diameter having the shape of letter "U". Both the horizontal and vertical parts of the wire were 80 mm long. Two 0.02 mm diameter platinum filaments were spot welded 25 mm apart to the center of the horizontal part to form voltage taps. The test section was mounted on a falling stand driven by a pulse motor. The test section was electrically heated by a dc power supply up to a prescribed initial wire temperature T_{W0} (=700–1150°C). Then, the test section was forced to fall at a constant speed u (=0.6–1.0 m/s) into a liquid bath in which the ultrasonic vibration was applied. Just before the horizontal part of the wire reached the liquid surface, the dc power supply was switched off and a 1-A dc supply was switched on. This was done by use of a controller equipped with photosensors and a relay unit. The voltage drop E at the 25 mm long section of the horizontal part during the quenching process was measured by an analyzing recorder. The voltage drop at a 100 mΩ standard resistor connected in series was also measured to calculate the electric current I. These data were read every 0.02 to 0.1 ms depending on the cooling rate. Since the measured data included a high-frequency noise of 1.1 kHz generated by the controller, the running average of the data for 0.9 ms were recorded.

The measured values of E and I are related with the electric resistivity of the wire γ as

$$2\pi \int_0^{d/2} \frac{r}{\gamma}\, dr = \frac{lI}{E}, \tag{1}$$

where d is the wire diameter, r is the radial coordinate, and l is the distance between the voltage taps. Since γ is a function of the temperature, the left side of Eq. (1) depends on the radial temperature distribution. Assuming the one-dimensional radial conduction, the transient heat conduction equation for the wire is written as

$$\frac{\partial T}{\partial t} = a_W \frac{1}{r}\frac{\partial}{\partial r}\left(r\frac{\partial T}{\partial r}\right), \tag{2}$$

where t is time and a_W is the thermal diffusivity of the wire. Equation (2) was solved numerically with a finite difference method assuming a uniform initial wire temperature T_{W0}. At each time step, calculation was repeated assuming a new value of the heat flux q_W until a temperature distribution that satisfied Eq. (1) to within 0.001 percent was obtained. The uncertainty in the measured q_W was estimated to be within $\pm 10^5$ W/m^2. The maximum temperature difference between the center and surface of the wire was about 27°C.

The ultrasonic vibrator had seven transducers (45 mm in diameter) attached to a 170 × 150 mm^2 wide upper surface of the vibrator. The power input to the transducers P ranged from 0 to 280 W. The frequency of the ultrasonic vibration ν was 24 and 44 kHz. The vibrator was immersed in the water bath at the bottom. The ultrasonic vibration radiated from the vibrator propagates with the sound velocity c and is reflected at the wall and at the water surface. As a result, an acoustic field is formed in the water bath. When the water level above the vibrator surface is set at a multiple of the half wavelength, resonance of the radiated wave and the reflected wave at the water surface occurs and a standing wave will be formed. In the present experiment the water level was set at 129 mm and 141 mm for ν = 24 kHz and 44 kHz, respectively, which corresponded to the two times and four times the wavelength, respectively. The

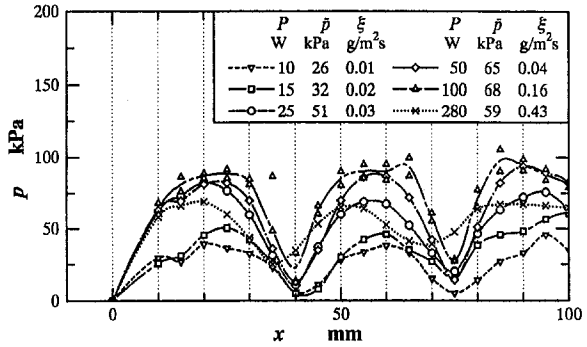

Fig. 1 Vertical distribution of sound pressure in water bath; ΔT_{sub} = 40 K and ν = 24 kHz.

sound pressure p was measured by using a sound pressure meter with a piezoelectric probe 4 mm in diameter. The distribution of the sound pressure in the liquid bath was measured by traversing the sound probe horizontally and vertically. The average sound pressure $\bar{p}$ was defined as the average value of p along the path of the center of the test wire. The cavitation intensity in the liquid bath was measured quantitatively using a method similar to that developed by Nomura and Nakagawa (1993). A 15 μm thick, 150 × 100 mm^2 wide aluminum foil was fixed vertically in the liquid bath along the path of the test wire and was exposed to the ultrasonic vibration for 10 to 20 s. Then a lot of holes appeared on the foil at the hills of the sound pressure due to the occurrence of cavitation. The cavitation intensity ξ was defined by the loss in weight per unit time and area of the aluminum foil.

Experimental Results and Discussions

Measurement of Sound Pressure and Cavitation Intensity. Figure 1 shows the vertical distribution of the local sound pressure p in the water bath at the center of the ultrasonic vibrator for ΔT_{sub} = 40 K, ν = 24 kHz, and P = 10–280 W, where p is plotted as a function of the distance measured from the water surface x. In Fig. 1 the values of ξ and $\bar{p}$ are also shown. For $P \leq 100$ W, p showed a periodic distribution with the wavelengths of about 36 mm and 19 mm for ν = 24 kHz and 44 kHz, respectively, indicating the existence of the standing wave. For $P \geq 100$ W, however, the distribution became somewhat irregular. The amplitude of p first increased with increasing P, then took a maximum value, and then decreased with further increasing P. The horizontal distribution of the sound pressure was not periodic but showed an undulation which was roughly symmetrical with respect to the center of the vibrator. The value of p was almost uniform along the 25 mm long horizontal test section.

Figure 2 shows the variations of $\bar{p}$ and ξ with P. The $\bar{p}$ first increases with P. For $P \leq 30$ W, the values of $\bar{p}$ are almost the same for ν = 24 kHz and 44 kHz. It takes a maximum value at P = 100 W and 35 W for ν = 24 kHz and 44 kHz, respectively, and then decreases gradually with further increasing P. In the case of ν = 44 kHz, it increases again in the region of $P > 140$ W. A strange behavior of $\bar{p}$ at a high P is probably due to the effect of cavitation bubbles generated in the water bath, which reduced the transmission of acoustic energy from the vibrator to the probe. The ξ increases monotonically with increasing P and its value is larger for ν = 24 kHz than for ν = 44 kHz. For ν = 24 kHz, it increases rather rapidly at P = 80–100 W where large cavitation bubbles appeared. Visual observation of the cavitation bubbles revealed that the acoustic streaming was much stronger for ν = 24 kHz than for ν = 44 kHz. In the region of $\xi \leq 0.08$ g/m^{2}s it was not significant even in the case of ν = 24 kHz. However, it became significant with further increasing ξ, and violent agitation of

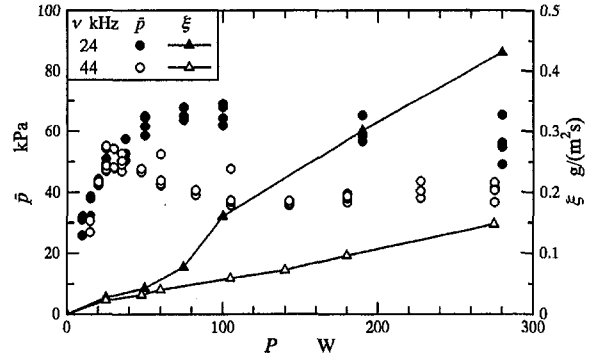

Fig. 2 Variations of average sound pressure and cavitation intensity with power input to transducer; ΔT_{sub} = 40 K.

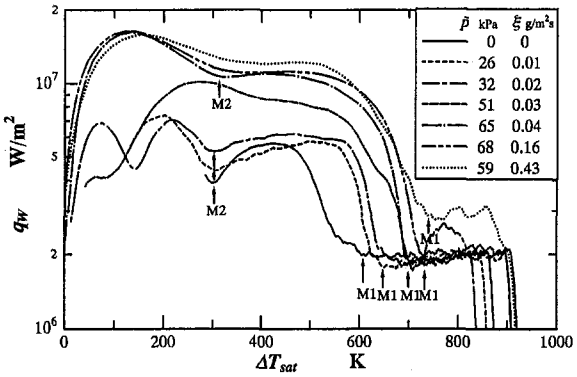

Fig. 4 Effect of ultrasonic vibration on boiling curve; u = 1.0 m/s, T_{wo} ≒ 1000°C, ΔT_{sub} = 40 K, and ν = 24 kHz.

water caused by the acoustic streaming was observed at ξ = 0.43 g/m²s. In the case of ν = 44 kHz the cavitation bubbles were trapped within the standing wave even at the highest ξ.

Heat Transfer Characteristics. Figure 3 shows the cooling curves for u = 1.0 m/s, T_{W0} ≒ 1000°C, ΔT_{sub} = 40 K, ν = 24 kHz, and ξ = 0–0.43 g/m²s ($\bar{p}$ = 0–68 kPa), where the wire surface temperature T_W is plotted as a function of the elapsed time after the wire was immersed in the water bath t (or the distance from the water surface x). The curves are shown only for the period of $t \leq$ 80 ms where a constant falling velocity of the wire was obtained. Generally, the wire temperature T_W decreases gradually after it is immersed in the water. For ξ = 0, the cooling curve shows a bend (the quench point) at t ≒ 60 ms and T_W ≒ 650°C, indicating a rather abrupt increase in the cooling rate. For ξ = 0–0.04 g/m²s, the slope of the cooling curve above the quench point is almost the same. For $\xi \geq$ 0.16 g/m²s, it is steeper than that for $\xi \leq$ 0.16 g/m²s. The quench point moves toward a higher T_W as ξ increases and the time required to cool down the wire decreases. Comparison of Fig. 3 with the sound pressure distribution shown in Fig. 1 reveals that the wire moves a distance corresponding to 1.7 to 2.5 times the wavelength of the sound pressure while it is cooled down to the bulk temperature. This makes the interpretation of experimental results somewhat difficult because the transient heat transfer characteristics is supposed to be affected by the distributions of p and the local cavitation intensity.

Figure 4 shows the transient boiling curves obtained from the cooling curves shown in Fig. 3. The heat flux q_W increases abruptly when the wire is immersed in the water bath. For $\xi \leq$ 0.04 g/m²s, q_W decreases very slowly until the first MHF point ($M1$ point) is reached and the effect of ultrasonic vibration is negligible in the film boiling region ($\Delta T_{sat} \geq \Delta T_{sat,M1}$). For $\xi \geq$ 0.16 g/m²s, q_W takes a much higher value than that for $\xi \leq$ 0.04 g/m²s in the film boiling region. This suggests the occurrence of partial liquid-solid contact. Considering the fact that the value of p for ξ = 0.43 g/m²s is even smaller than that for ξ = 0.03 g/m²s in the region of $x \leq$ 30 mm where film boiling occurs (see Fig. 1), the sound pressure will not be responsible for the occurrence of liquid-solid contact. Thus, the disturbance in the water that was caused by the acoustic streaming and violent cavitation will be responsible for this phenomena. The $\Delta T_{sat,M1}$ increases as ξ increases. However, the increase is not so significant (≤160 K). After the $M1$ point q_W increases significantly with decreasing ΔT_{sat}. For $\xi \leq$ 0.02 g/m²s and ξ = 0.04 g/m²s, q_W decreases with further decreasing ΔT_{sat} and reaches the second MHF point ($M2$ point). The $M2$ point is not obvious for the other cases. Comparison of the results for different ξ reveals that q_W increases first rapidly, and then gradually, with increasing ξ. At ΔT_{sat} = 600 K, the maximum value of q_W, which is obtained for ξ = 0.16 g/m²s, is 4.7 times as large as that for ξ = 0. It is also seen that for ξ = 0.04–0.43 g/m²s, the boiling curve after the $M1$ point is almost unchanged except for a small region near the $M1$ point. For these data the change in $\bar{p}$ is also small. These results suggest either that the effect of ultrasonic vibration is saturated at high ξ or that the sound pressure is the key factor that affects the heat transfer characteristics.

The experimental results for ν = 44 kHz showed a smaller heat transfer enhancement than the case of ν = 24 kHz. For the same experimental conditions of d, u, T_{W0}, and ΔT_{sub} as Fig. 4, the maximum value of q_W obtained for ν = 44 kHz at ΔT_{sat} = 600 K was 2.1 times as large as that for ξ = 0. The $\Delta T_{sat,M1}$ first increased with ξ and then decreased with further increasing ξ. At ξ = 0.15 g/m²s, the value of $\Delta T_{sat,M1}$ (=580 K) was even smaller than that for ξ = 0 (=610 K).

Figures 5 shows the effect of initial wire temperature T_{W0} on the transient boiling curve for u = 0.6 m/s, ΔT_{sub} = 40 K, ν = 24 kHz, and ξ = 0.03 g/m²s. The boiling curve in the film boiling region and the value of $\Delta T_{sat,M1}$ are not affected by T_{W0}. However, the boiling curve after the $M1$ point changes considerably depending on T_{W0}. This suggests the interaction of the transient boiling process with the distributions of p and the cavitation intensity in the water bath. In Fig. 5, an example of the boiling curve for P = 0 is also shown for comparison. In this case the boiling curve was not affected by T_{W0} except for a small region just after the $M1$ point. It is relevant to note here that the transient boiling curve for ξ = 0.43 g/m²s was also not affected by T_{W0}, except for a small region after the $M1$ point. Thus, the effect of ultrasonic vibration is considered to be saturated at high ξ.

Figure 6 shows the transient heat transfer data corresponding to Fig. 5 plotted on the coordinates of q_W versus x. As expected, the coordinate x at the $M1$ point is larger for higher T_{W0}. Comparison of Fig. 6 with the vertical distribution of p shown in

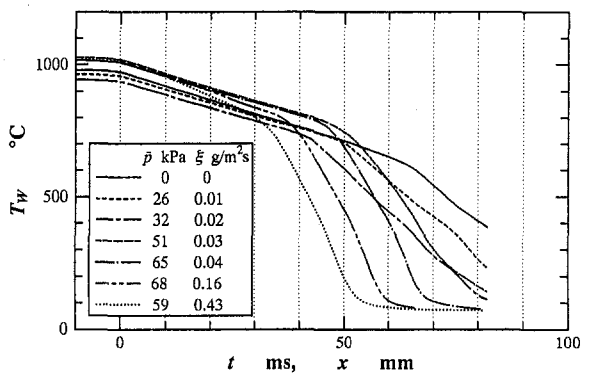

Fig. 3 Effect of ultrasonic vibration on cooling curve; u = 1.0 m/s, T_{W0} ≒ 1000°C, ΔT_{sub} = 40 K, and ν = 24 kHz.

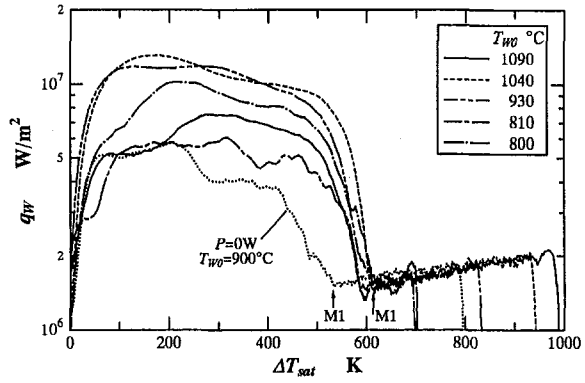

Fig. 5 Effect of initial wire temperature on boiling curve; u = 0.6 m/s, ΔT_{sub} = 40 K, ν = 24 kHz, and ξ = 0.03 g/m^{2}s.

Fig. 1 reveals that the q_W value before the $M1$ point is not affected by the local sound pressure (or the local cavitation intensity). For the five runs shown in Fig. 6, the average vapor film thickness at the $M1$ point δ_{M1}, defined by the $\delta_{M1} = \lambda_v \Delta T_{sat,M1}/q_{W,M1}$, is about 22 μm, irrespective of T_{W0}, where λ_v is the thermal conductivity of vapor. On the other hand, δ_{M1} for $\xi = 0$ is calculated to be 17 μm. Thus, the vapor film is destabilized by applying the ultrasonic vibration. However, it is seen from Figs. 1 and 6 that the local sound pressure is not responsible for the destabilization of the vapor film because the value of p at the $M1$ point changes considerably depending on T_{wo}. Therefore, the disturbance in the water bath caused by the acoustic streaming and cavitation will be responsible for the destabilization of the vapor film. As expected, the q_W value after the $M1$ point is affected significantly by the local sound pressure (or the local cavitation intensity). It takes a high maximum value at the increasing phase and the hill of the sound pressure distribution and a low maximum value near the valley (about 50 percent of the former). These results are in accord with the previous results by Loosle and Holdrege (1970), where the cool down time was longest at the node (valley) of the sound pressure. Thus, in the practical application care must be taken to minimize the nonuniformity of the sound pressure distribution on the surface of the material to be quenched. This will be relatively easy for a slender body like the present experiment because the sound pressure distribution in the water bath parallel to the vibrator surface is almost uniform at the central part.

For the production of amorphous alloys by the rapid solidification processing, a high cooling rate ($>10^5$ K/s) is required in the temperature range between the melting point (700–1300°C) and the glass-transition point (300–600°C). Figures 7(a) and 7(b) show the average heat flux $\bar{q}_W$ in the range of T_W = 900–550°C plotted as a function of $\bar{p}$ and ξ, respectively.

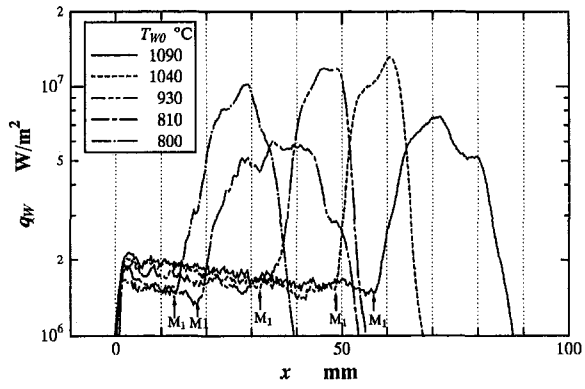

Fig. 6 Variation of heat flux with distance from water surface; u = 0.6 m/s, ΔT_{sub} = 40 K, ν = 24 kHz, and ξ = 0.03 g/m^{2}s.

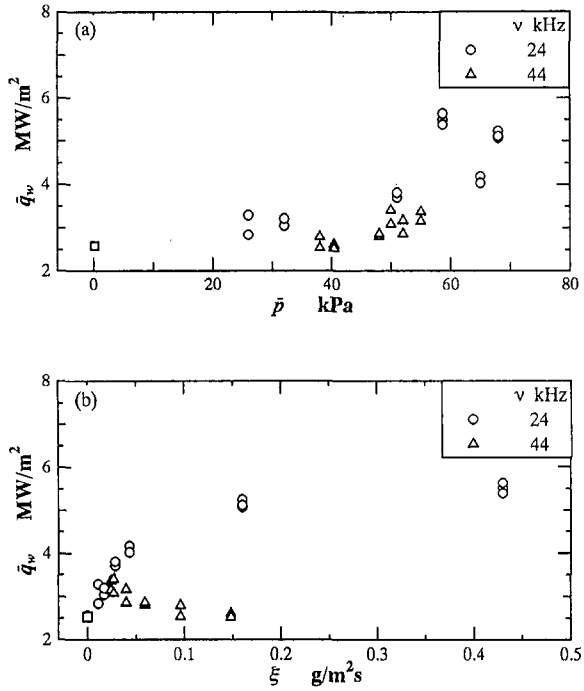

Fig. 7 Variation of average heat flux for T_W = 900 – 550°C with (a) average sound pressure and (b) cavitation intensity; u = 1.0 m/s, $T_{W0} \fallingdotseq$ 1000°C, ΔT_{sub} = 40 K.

The experimental data are those for d = 0.5 mm, u = 1.0 m/s, $T_{W0} \fallingdotseq$ 1000°C, and ΔT_{sub} = 40 K. In the case of ν = 24 kHz, the data for ξ = 0.01–0.04 g/m^{2}s were obtained under the condition in which the wire experienced the increasing phase and the hill of p in the temperature range between the quench point and 550°C. Thus, the measured value of $\bar{q}_W$ is considered to be close to the maximum value. On the other hand, the data for ξ = 0.16 and 0.43 g/m^{2}s correspond to the valley of p. However, these data are considered to be not affected by the sound pressure distribution (or the cavitation intensity distribution) because ξ is sufficiently high. In the case of ν = 44 kHz, the wire experienced about one wavelength in the foregoing temperature range. In Fig. 7(a) the experimental data for ν = 24 kHz show a positive correlation between $\bar{p}$ and $\bar{q}_W$ in the range of $\bar{p}$ = 0–56 kPa. However, such a correlation is lost for $\bar{p} \geq$ 59 kPa. The data for ν = 44 kHz also show a positive correlation between $\bar{q}_W$ and $\bar{p}$, but the value of $\bar{q}_W$ is smaller than that for ν = 24 kHz. In Fig. 7(b) the data for ν = 24 kHz show a positive correlation between ξ and $\bar{q}_W$. The $\bar{q}_W$ increases rapidly at first, and then gradually with increasing ξ. At ξ = 0.43 g/m^{2}s, the value of $\bar{q}_W$ is about 2.2 times as large as that for ξ = 0. The data for ν = 44 kHz show almost the same $\bar{q}_W$ as that for ν = 24 kHz at the smallest ξ (=0.025 g/m^{2}s). However, $\bar{q}_W$ decreases as ξ increases. These results indicate that the effect of ultrasonic vibration with different ν can not be represented adequately by $\bar{p}$ or ξ. More data covering a wide range of ν are required to clarify the mechanism of heat transfer enhancement during the rapid quenching process by the ultrasonic vibration.

References

Honda, H., Takamatsu, H., and Yamashiro, H., 1992, "Heat Transfer Characteristics During Rapid Quenching of a Thin Wire in Water," *Heat Transfer Japanese Research*, Vol. 21, No. 8, pp. 773–791.

Honda, H., Takamatsu, H., and Yamashiro, H., 1994, "Heat Transfer and Liquid-Solid Contact During the Rapid Quenching of Thin Wires in Water and $CaCl_2$/Water Solution," *Proc. 10th Int. Heat Transfer Conf.*, Vol. 5, ASME, New York, pp. 55–62.

Honda, H., Takamatsu, H., and Yamashiro, H., 1995, "Minimum Heat Flux Point and Liquid-Solid Contact During Rapid Quenching of Thin Wires," *Trans. JSME*, Ser. B, Vol. 61, No. 592, pp. 4440–4447.

Iida, Y., and Tsutsui, K., 1989, "Augmentation of Film Boiling Heat Transfer by an Ultrasonic Wave," *Trans. JSME,* Ser. B, Vol. 55, No. 509, pp. 194–198.

Iida, Y., Tsutsui, K., and Sasaki, J., 1990, "The Effect of Ultrasonic Wave Application for the Rapid Cool-Down Process of High-Temperature Solids Submerged in Liquid," *Trans. JSME,* Ser. B, Vol. 56, No. 562, pp. 210–213.

Loosle, D. G., and Holdredge, R. M., 1970, "The Effect of Acoustic Vibrations on the Cooldown Time of Bodies in Cryogenic Liquids," *Proc. 4th Int. Heat Transfer Conf.,* Vol. 4, NC 4.6., Elsevier, Amsterdam.

Nakayama, A., Kano, M., 1990, "Enhancement of Saturated Pool Nucleate-Boiling Heat Transfer by Ultrasonic Vibrations," *Trans. JSME,* Ser. B, Vol. 56, No. 524, pp. 185–190.

Nomura, S., and Nakagawa, M., 1993, "Ultrasonic Enhancement of Heat Transfer on Narrow Surface," *Trans. JSME,* Ser. B, Vol. 59, No. 565, pp. 132–137.

Park, K. A., and Bergles, A. E., 1988, "Ultrasonic Enhancement of Saturated and Subcooled Pool Boiling," *Int. J. Heat Mass Transfer,* Vol. 31, No. 3, pp. 664–667.

Wong, S. W., and Chon, W. Y., 1969, "Effect of Ultrasonic Vibration on Heat Transfer to Liquids by Natural Convection by Boiling," *AIChE J.,* Vol. 15, No. 2, pp. 281–288.

Multidimensional Modeling of Steam Injection into Porous Media

C. Y. Wang[1] and P. Cheng[2]

1 Introduction

Steam injection is an established method to enhance oil recovery from petroleum reservoirs (Boberg, 1988). Recently, steam injection has also been applied to remediate industrial sites contaminated by nonaqueous phase liquids (NAPLs), such as hydrocarbon fuels and halogenated compounds (Hunt et al., 1988; Stewart and Udell, 1988; Udell and Stewart, 1990).

There is a wealth of information on steam injection in the petroleum industry. Examples are the experimental study of Baker (1973) and the numerical work of Coats (1976, 1980). Unfortunately, because of the commercial value of this technology, limited information has been available in the open literature and a fundamental understanding of the steam injection process remains lacking. This is why the recent environmental application, i.e., groundwater contamination by NAPLs and subsequent remediation by steam injection, has renewed interest in this rather old problem (Hunt et al., 1988; Basel and Udell, 1989; Falta et al., 1992).

The experiments by Hunt et al. (1988) demonstrated that in a one-dimensional column, steam displaces a NAPL in a piston-like manner thereby resulting in virtually complete removal of the contaminant from porous media. Subsequent two-dimensional steam injection experiments and field tests by Udell and co-workers (Udell and Stewart, 1990; Basel, 1991) have shown promise but have not resulted in fast and complete contaminant removal. Basel and Udell (1989) experimentally measured the two-dimensional condensation front location using liquid crystals painted on the front pane of the test cell. Previous modeling efforts on steam injection (excluding those proprietary in the petroleum industry) are limited to one-dimensional cases (Hunt et al., 1988; Falta et al., 1992; Yuan and Udell, 1993; Hanamura and Kaviany, 1995; Brouwers, 1996). Exceptions are the works of Falta (1990) and Chung and Catton (1993). Two-dimensional simulations of steam injection into initially water-saturated porous media were attempted by Falta (1990) using a coarse grid (i.e., 6×15), and time step and grid-independence of numerical results could not be established.

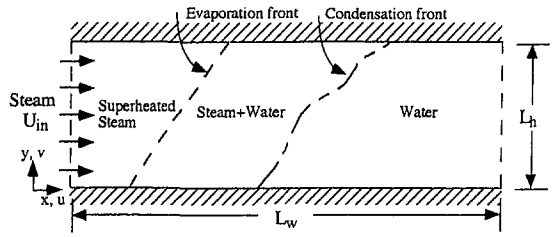

Fig. 1 Geometry and nomenclature of the physical problem under consideration

For a somewhat different application (i.e., thermal energy storage), Sözen and Vafai (1990) numerically studied steam injection (Freon-12) into an initially dry porous medium. Detailed two-dimensional numerical results were presented. Within their parametric range of interest, the maximum liquid saturation remained below the irreducible threshold value, and therefore the liquid was immobile in their work (Sözen and Vafai, 1990).

The present work attempts to address a fundamental problem of steam injection into an initially water-saturated two-dimensional reservoir using the recently developed two-phase mixture model (Wang and Beckermann, 1993). The objective is to identify the inherently multidimensional transport phenomena occurring during steam injection in porous media, such as multidimensional two-phase flow, phase change heat transfer at boiling and condensation fronts, and thermal convection in individual phases. A series of numerical simulations for both one and two-dimensional geometries will be reported, and the results are compared to the corresponding experimental data to unravel critical modeling issues. Finally, superheated steam injection is numerically assessed for its potential applications.

2 Numerical Model

The geometry considered is a two-dimensional horizontal reservoir as shown in Fig. 1 where the top and bottom surfaces are thermally insulated. The porous medium is isotropic, homogeneous, and initially saturated fully with liquid water at a constant temperature, T_o. Saturated or superheated steam is uniformly injected, at a rate of $\dot{m}_{in}$, from the left permeable boundary to displace liquid water. A condensation front forms in the porous formation where the hot steam comes in contact with subcooled water. Behind the condensation front a two-phase zone appears in which vapor co-exists with liquid. In the case of superheated steam injection, the two-phase zone is bounded by an all-vapor region (superheated) next to the inlet, as schematically shown in Fig. 1. The present problem is chosen for a detailed study partly because of its fundamental nature as a baseline case of steam injection and partly due to the availability of corresponding experimental data (Hunt et al., 1988; Basel and Udell, 1989) for model validation.

The following assumptions are made in the development of governing equations:

1 The generalized Darcy's law, with the relative permeabilities introduced to account for a reduction in the effective flow cross section due to the presence of the other fluid, is adopted for the two-phase flow. This is justified by the fact that the maximum values of the Reynolds number for vapor and liquid are around 5.4 and 0.05, respectively.

2 The two-phase zone is isothermal at the saturation temperature, T_{sat} (Udell, 1985).

3 Natural convection in all vapor and liquid regions is considered, and the Boussinesq approximation is used.

[1] Department of Mechanical Engineering, The Pennsylvania State University, University Park, PA 16802; e-mail: cxw31@psu.edu

[2] Department of Mechanical Engineering, The Hong Kong University of Science and Technology, Clear Water Bay, Kowloon, Hong Kong.

Contributed by the Heat Transfer Division of THE AMERICAN SOCIETY OF MECHANICAL ENGINEERS. Manuscript received by the Heat Transfer Division September 3, 1996; revision received September 5, 1997; Keywords: Multiphase Flows; Phase-Change Phenomena; Porous Media. Associate Technical Editor: K. Vafai.

Iida, Y., and Tsutsui, K., 1989, "Augmentation of Film Boiling Heat Transfer by an Ultrasonic Wave," *Trans. JSME,* Ser. B, Vol. 55, No. 509, pp. 194–198.

Iida, Y., Tsutsui, K., and Sasaki, J., 1990, "The Effect of Ultrasonic Wave Application for the Rapid Cool-Down Process of High-Temperature Solids Submerged in Liquid," *Trans. JSME,* Ser. B, Vol. 56, No. 562, pp. 210–213.

Loosle, D. G., and Holdredge, R. M., 1970, "The Effect of Acoustic Vibrations on the Cooldown Time of Bodies in Cryogenic Liquids," *Proc. 4th Int. Heat Transfer Conf.,* Vol. 4, NC 4.6., Elsevier, Amsterdam.

Nakayama, A., Kano, M., 1990, "Enhancement of Saturated Pool Nucleate-Boiling Heat Transfer by Ultrasonic Vibrations," *Trans. JSME,* Ser. B, Vol. 56, No. 524, pp. 185–190.

Nomura, S., and Nakagawa, M., 1993, "Ultrasonic Enhancement of Heat Transfer on Narrow Surface," *Trans. JSME,* Ser. B, Vol. 59, No. 565, pp. 132–137.

Park, K. A., and Bergles, A. E., 1988, "Ultrasonic Enhancement of Saturated and Subcooled Pool Boiling," *Int. J. Heat Mass Transfer,* Vol. 31, No. 3, pp. 664–667.

Wong, S. W., and Chon, W. Y., 1969, "Effect of Ultrasonic Vibration on Heat Transfer to Liquids by Natural Convection by Boiling," *AIChE J.,* Vol. 15, No. 2, pp. 281–288.

Multidimensional Modeling of Steam Injection into Porous Media

C. Y. Wang[1] and P. Cheng[2]

1 Introduction

Steam injection is an established method to enhance oil recovery from petroleum reservoirs (Boberg, 1988). Recently, steam injection has also been applied to remediate industrial sites contaminated by nonaqueous phase liquids (NAPLs), such as hydrocarbon fuels and halogenated compounds (Hunt et al., 1988; Stewart and Udell, 1988; Udell and Stewart, 1990).

There is a wealth of information on steam injection in the petroleum industry. Examples are the experimental study of Baker (1973) and the numerical work of Coats (1976, 1980). Unfortunately, because of the commercial value of this technology, limited information has been available in the open literature and a fundamental understanding of the steam injection process remains lacking. This is why the recent environmental application, i.e., groundwater contamination by NAPLs and subsequent remediation by steam injection, has renewed interest in this rather old problem (Hunt et al., 1988; Basel and Udell, 1989; Falta et al., 1992).

The experiments by Hunt et al. (1988) demonstrated that in a one-dimensional column, steam displaces a NAPL in a piston-like manner thereby resulting in virtually complete removal of the contaminant from porous media. Subsequent two-dimensional steam injection experiments and field tests by Udell and co-workers (Udell and Stewart, 1990; Basel, 1991) have shown promise but have not resulted in fast and complete contaminant removal. Basel and Udell (1989) experimentally measured the two-dimensional condensation front location using liquid crystals painted on the front pane of the test cell. Previous modeling efforts on steam injection (excluding those proprietary in the petroleum industry) are limited to one-dimensional cases (Hunt et al., 1988; Falta et al., 1992; Yuan and Udell, 1993; Hanamura and Kaviany, 1995; Brouwers, 1996). Exceptions are the works of Falta (1990) and Chung and Catton (1993). Two-dimensional simulations of steam injection into initially water-saturated porous media were attempted by Falta (1990) using a coarse grid (i.e., 6×15), and time step and grid-independence of numerical results could not be established.

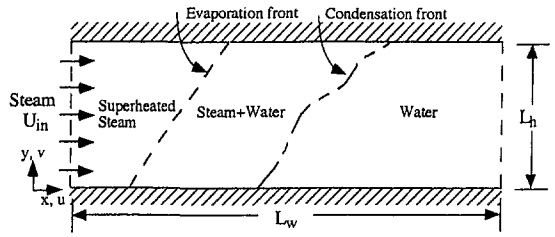

Fig. 1 Geometry and nomenclature of the physical problem under consideration

For a somewhat different application (i.e., thermal energy storage), Sözen and Vafai (1990) numerically studied steam injection (Freon-12) into an initially dry porous medium. Detailed two-dimensional numerical results were presented. Within their parametric range of interest, the maximum liquid saturation remained below the irreducible threshold value, and therefore the liquid was immobile in their work (Sözen and Vafai, 1990).

The present work attempts to address a fundamental problem of steam injection into an initially water-saturated two-dimensional reservoir using the recently developed two-phase mixture model (Wang and Beckermann, 1993). The objective is to identify the inherently multidimensional transport phenomena occurring during steam injection in porous media, such as multidimensional two-phase flow, phase change heat transfer at boiling and condensation fronts, and thermal convection in individual phases. A series of numerical simulations for both one and two-dimensional geometries will be reported, and the results are compared to the corresponding experimental data to unravel critical modeling issues. Finally, superheated steam injection is numerically assessed for its potential applications.

2 Numerical Model

The geometry considered is a two-dimensional horizontal reservoir as shown in Fig. 1 where the top and bottom surfaces are thermally insulated. The porous medium is isotropic, homogeneous, and initially saturated fully with liquid water at a constant temperature, T_o. Saturated or superheated steam is uniformly injected, at a rate of $\dot{m}_{in}$, from the left permeable boundary to displace liquid water. A condensation front forms in the porous formation where the hot steam comes in contact with subcooled water. Behind the condensation front a two-phase zone appears in which vapor co-exists with liquid. In the case of superheated steam injection, the two-phase zone is bounded by an all-vapor region (superheated) next to the inlet, as schematically shown in Fig. 1. The present problem is chosen for a detailed study partly because of its fundamental nature as a baseline case of steam injection and partly due to the availability of corresponding experimental data (Hunt et al., 1988; Basel and Udell, 1989) for model validation.

The following assumptions are made in the development of governing equations:

1 The generalized Darcy's law, with the relative permeabilities introduced to account for a reduction in the effective flow cross section due to the presence of the other fluid, is adopted for the two-phase flow. This is justified by the fact that the maximum values of the Reynolds number for vapor and liquid are around 5.4 and 0.05, respectively.

2 The two-phase zone is isothermal at the saturation temperature, T_{sat} (Udell, 1985).

3 Natural convection in all vapor and liquid regions is considered, and the Boussinesq approximation is used.

[1] Department of Mechanical Engineering, The Pennsylvania State University, University Park, PA 16802; e-mail: cxw31@psu.edu

[2] Department of Mechanical Engineering, The Hong Kong University of Science and Technology, Clear Water Bay, Kowloon, Hong Kong.

Contributed by the Heat Transfer Division of THE AMERICAN SOCIETY OF MECHANICAL ENGINEERS. Manuscript received by the Heat Transfer Division September 3, 1996; revision received September 5, 1997; Keywords: Multiphase Flows; Phase-Change Phenomena; Porous Media. Associate Technical Editor: K. Vafai.

4 Dispersion effects in the single-phase regions are negligible due to low Peclet numbers (i.e., 0.04 and 0.3 for vapor and liquid flows, respectively). The thermal dispersion effect in the two-phase zone becomes irrelevant because of assumption No. 2.

5 The vapor, liquid, and solid phases are in local thermal equilibrium. According to Vafai and Sözen (1990), this assumption is justified in situations where the particle Reynolds number is of the order of unity and the Darcy number (i.e., K/L^2) is of the order of 10^{-7} for sandpacks. In the present work the Darcy number is two orders of magnitude below 10^{-7}.

Numerical analysis for the present problem is based on the two-phase mixture model of Wang and Beckermann (1993) and its numerical version of Wang (1997); see the original references for details. The initial/boundary conditions are given in terms of the mixture pressure, p, and enthalpy, H, as they represent the primary variables in the present numerical model. The porous formation is initially saturated with quiescent liquid water at a constant temperature; hence,

$$\text{at } t = 0 \quad \frac{\partial p}{\partial y} = -\rho_l g; \quad \frac{\partial p}{\partial x} = 0; \quad H = \rho_l(c_l T_o - 2h_{\text{vsat}}). \quad (1)$$

The boundary conditions are as follows:

$$\text{at } y = 0 \text{ and } L_h \text{ (bottom and top surfaces)},$$

$$\frac{\partial p}{\partial y} = -\rho_\kappa g \text{ (impermeable)};$$

$$-\Gamma_h \frac{\partial H}{\partial y} + f(s)\frac{K\Delta\rho h_{fg}}{\nu_v} g = 0 \text{ (adiabatic)}. \quad (2)$$

The inlet boundary condition is represented by the given mass fluxes for each phase as follows:

$$\rho_l u_l = (1 - X)\dot{m}_{\text{in}}; \quad \rho_v u_v = X\dot{m}_{\text{in}}, \quad (3)$$

where X denotes the steam quality of the injected fluid. From Eq. (3) one has

$$\rho u = \dot{m}_{\text{in}}; \quad j_x = -\rho_l D(s)\frac{\partial s}{\partial x} = (1 - \lambda_l - X)\dot{m}_{\text{in}}. \quad (4)$$

In terms of the mixture variables, p and H, these can be further expressed as follows:

at $x = 0$ (inlet)

$$-\frac{\partial p}{\partial x} = \frac{\nu\dot{m}_{\text{in}}}{K} \text{ (constant mixture mass flux)};$$

$$D(s)\frac{\partial H}{\partial x} = (1 - \lambda_l - X)\dot{m}_{\text{in}}h_{fg} \quad (5)$$

for saturated steam injection with a steam quality, X. In the case of superheated steam injection with the superheat of ΔT_{sup}, the latter part of Eq. (5) will be replaced by

$$H = \rho_v(c_v\Delta T_{\text{sup}} - h_{\text{vsat}}). \quad (6)$$

At the exit of the reservoir, i.e., at $x = L_w$ (outlet),

$$\frac{\partial p}{\partial y} = -\rho_k g \text{ (fully developed flow)};$$

$$\frac{\partial H}{\partial x} = 0 \text{ (thermally fully developed)}. \quad (7)$$

The pressure boundary condition, Eq. (2), simply reflects the fact that the bottom and top surfaces of the porous formation are impermeable, so that the vertical component of the velocity vanishes. The adiabatic boundary conditions for the top and bottom surfaces of the porous formation are used in order to match the laboratory experiments of Hunt et al. (1988) and Basel and Udell (1989). These conditions can be easily relaxed to accommodate conductive top and bottom surfaces as encountered in reality. Equation (7) represents the thermally and hydrodynamically developed conditions for the two-phase mixture leaving the channel. This assumption of the exit conditions was justified by a parametric test in which the computational domain was extended beyond the physical length, and no appreciable variations in the simulation results were observed.

Details of the numerical procedures were presented in Wang (1997) and thus are not repeated here. The equations were solved as a simultaneous set, and convergence was enforced with the criterion that the relative errors between iterations in both the enthalpy and velocity fields be less than 10^{-5} and that mass and energy conservation in the system is ensured to within 0.1 percent. For simplicity, uniform and fixed grids were chosen. Stringent numerical tests were performed to ensure that the solutions are independent of both grid size and time step. A typical transient two-dimensional simulation presented below required a CPU time of approximately 1 h on a HP 715/100 workstation.

Table 1 Thermophysical property data for a water-steam-sand system

Property	Symbol	Solid Matrix	Liquid	Vapor	Unit
Density	ρ	2650	995.7	0.598	kg/m^3
Specific heat	c	1350	4.178×10^3	1.548×10^3	J/kg·K
Kinetic viscosity	ν	-	4.67×10^{-7}	2.012×10^{-5}	m^2/s
Expansion coefficient	β	-	5.23×10^{-4}	2.4×10^{-3}	K^{-1}
Thermal conductivity	k_{eff}	-	3.10	2.86	W/m·K
Interfacial tension	σ	-	0.0588		N/m
Latent heat of evaporation	h_{fg}	-	2.257×10^6		J/kg

3 Results and Discussion

A series of laboratory-scale steam injection experiments were conducted by Hunt et al. (1988) in a one-dimensional column, and by Basel and Udell (1989) in a two-dimensional sand pack. In what follows, these experiments are used to validate the present model. A simulation of superheated steam injection is subsequently performed to assess its potential applications. The thermophysical properties needed in all simulations are listed in Table 1, where the effective thermal conductivity of 3.1 W/m·K for liquid-saturated porous media was suggested by Hunt et al. (1988) to be representative of water saturated silica sand and the dry media thermal conductivity is approximately equal to 2.86 W/m·K. The effective specific heat of 1350 J/kg·K for soil, which is higher than its physical value of 1000 J/kg·K, was suggested by Falta (1990) to account for heat loss through the walls of the test section. The relative permeabilities and capillary pressure were given in Table 2 of Wang (1997). These are widely used correlations and were developed based on measurements for sandy porous media (Udell, 1985; Basel and Udell, 1989). In model validation against experimental data, the irreducible liquid saturation is set to be 0.2, following Basel and Udell (1989). It should, however, be mentioned that both Hunt et al. (1988) and Basel and Udell (1989) did not actually measure the relative permeabilities and capillary pressure of their sandpacks.

3.1 One-Dimensional Steam Injection. The experiments of Hunt et al. (1988) correspond to the following input parameters: $\epsilon = 0.385$; $K = 1.6 \times 10^{-11}$ m^2; $L_w = 0.91$ m; $T_o = 22$°C and $\dot{m}_{\text{in}} = 0.0173$ kg/m^2·s. Hunt et al. (1988) observed in their experiments that an initial period of 485 s was required for the steam to heat up the inlet section before steam began to enter the sandpack. Hence, in the simulations the boundary condition for the inlet enthalpy corresponds to the injection of liquid water at $T_{\text{sat}} = 100$°C during the first 468 s and a water-steam mixture at a quality of 0.5 thereafter. All simulations were terminated after steam breaks through at the outlet.

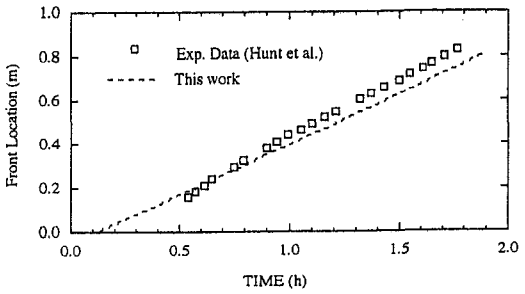

Fig. 2 Comparison of the predicted and measured (Hunt et al., 1988) steam condensation front locations in a one-dimensional silica sand column

A mesh of 62 grids and a time step of 5 s, carefully selected by a grid and time-step-independence study, were used in one-dimensional simulations. Figure 2 compares the measured with calculated steam condensation front locations. The good agreement suggests that the local thermal equilibrium assumption is adequate under the experimental conditions considered. This conclusion is also consistent with the finding of Brouwers (1996) in which the measured condensation front propagation during steam injection into an initially air-saturated porous medium was favorably compared with an analytical model assuming local thermal equilibrium.

3.2 Two-Dimensional Steam Injection. The three experiments of Basel and Udell (1989) correspond to the injection mass fluxes of 0.0274, 0.0494, and 0.118 kg/m$^2\cdot$s, respectively, and the other parameters are: $\epsilon = 0.4$, $K = 10^{-10}$ m^2, $L_w = 0.915$ m and $L_h = 0.305$ m, $X = 1.0$, and $T_o = 22$°C. Preliminary numerical tests indicated that the time steps for the various injection rates were 5, 2.5, and 1.5 s, respectively, while a uniform 22 × 62 grid produced sufficiently accurate results.

Comparisons of the numerical predictions with the experiments of Basel and Udell (1989) are shown in Figs. 3(a) through 3(c), in which the steam condensation front profiles are plotted at various times. In Basel and Udell (1989) a quantity called the pore volume was used to measure the lapsed time. This parameter is defined as the number of pore volumes filled with injected steam; namely,

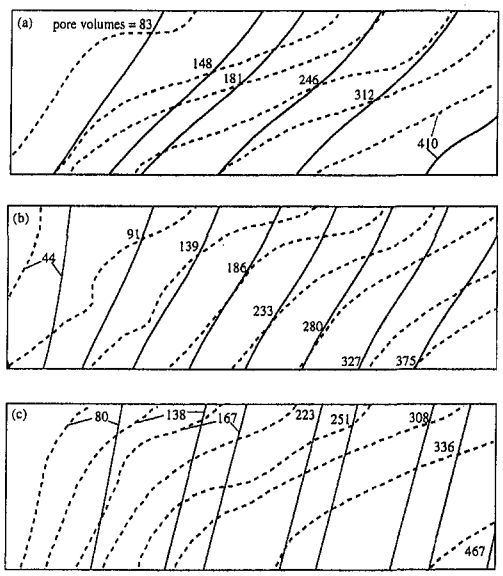

Fig. 3 Comparison of predicted (solid lines) and experimental (dashed lines; Basel and Udell, 1989) steam condensation front profiles at the injection mass flux of (a) 0.0274 kg/m$^2\cdot$s, (b) 0.0494 kg/m$^2\cdot$s, and (c) 0.118 kg/m$^2\cdot$s. The numbers in the figure refer to pore volumes of injected steam which are also dimensionless time (see text).

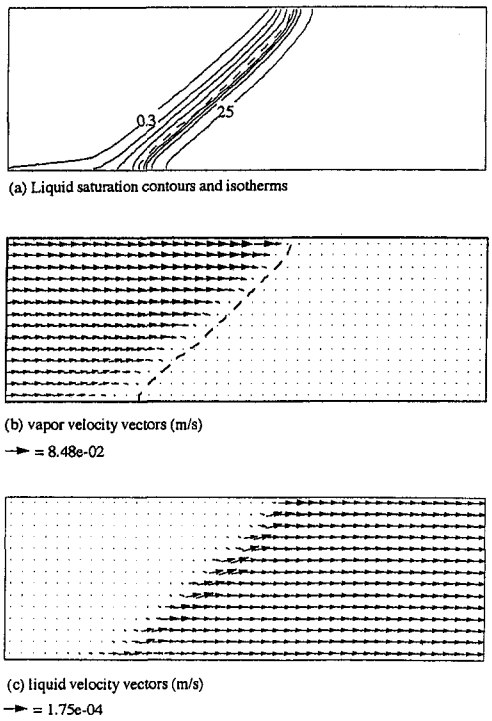

Fig. 4 Numerical results for two-dimensional steam injection at a flux of 0.0274 kg/m$^2\cdot$s (t = 0.4 h): (a) liquid saturation contours (Δs = 0.2) in the two-phase zone (left to the dashed line) and isotherms (ΔT = 15°C) in the pure liquid region (right to the dashed line); (b) vapor velocity field; and (c) liquid velocity field. The condensation front is denoted by the dashed line.

$$\text{Pore Volumes} = \frac{\text{volume of injected steam}}{\text{pore volume of formation}} = \left(\frac{\dot{m}_{\text{in}}}{\rho_v \epsilon L_w}\right) t, \quad (8)$$

where the incoming steam flow rate is equal to the total injection flux, provided that the inleting mixture has a steam quality of unity. Apparently, the term within the bracket of Eq. (8) has a unit of the inverse of time, and therefore the pore volume can also be interpreted as a dimensionless time. It can be seen from Figs. 3(a)–3(c) that the predicted curves are in fair agreement with the ones measured experimentally. In particular, there seems to be good agreement in terms of the mean front location as a function of time. Both experimental and predicted results indicate that the multi-dimensional effect diminishes as the injection rate increases, as would be expected. The experimental fronts are, however, more inclined from the vertical than the predicted counterparts. This is likely because during experimental preparation a high permeability zone was created at the top of the sandpack which allows the injected steam to preferentially invade along the top (Basel and Udell, 1989; Falta, 1990). The influence of this more permeable layer at the top of the sandpack on the measured steam front profiles is clearly visible in panels (a) of Figs. 3(a)–3(c). The present model could reconcile the discrepancies displayed in Figs. 3(a)–3(c) through adjusting the permeability of the upper region of the sandpack. But, steam injection in heterogeneous media is thought to be worthy of a separate and fundamental treatment.

To elucidate the fundamental transport phenomena occurring during steam injection, representative results of the temperature distribution ahead of the condensation front, liquid saturation contours within the two-phase zone, and vapor and liquid velocity fields are shown in Figs. 4(a) through 4(c) for the injection mass flux of 0.0274 kg/m$^2\cdot$s. In these figures, the isotherms are plotted for temperatures between 25 and 70°C with an equal increment of 15°C, and the liquid saturation contours from 0.3 to 0.9 with the increment of 0.2. An inclined steam front denoted

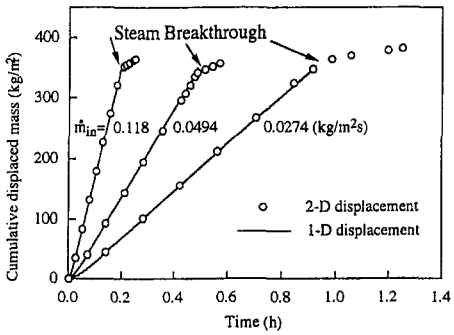

Fig. 5 Cumulative displaced mass per unit of cross sectional area for various injection fluxes and comparisons with one-dimensional predictions

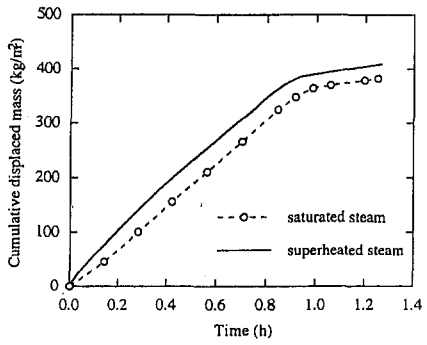

Fig. 6 Effect of superheat on steam displacement

by the dashed line in Fig. 4(a) indicates that the gravitational forces dominate the viscous forces. Far behind the steam front, the liquid saturation is nearly constant at the residual value, i.e., 0.2. Major changes in the temperature and liquid saturation occur over very small distances in the proximity of the steam condensation front. The vapor motion in the two-phase zone is primarily horizontal and uniform except in the neighborhood of the condensation front where the vapor velocity drastically decreases due to steam condensation (Fig. 4(b)). As a result, the liquid saturation increases rapidly, as can be seen from Fig. 4(a). The liquid motion features somewhat intricate characteristics in the vicinity of the condensation front. Immediately behind the front and within the two-phase zone, liquid tends to migrate downwards due to its density being much larger than the vapor. The migration, however, occurs at a small speed because of the large resistance for liquid flow in the two-phase zone. Ahead of the front and in the pure liquid region the liquid ascends owing to thermal buoyancy forces. Significantly away from the steam front, the liquid velocity field is characterized by the horizontal displacement.

An integral way to characterize steam displacement for oil recovery or contaminant removal is to examine the cumulative mass displaced out of the reservoir; namely,

$$m_{\text{out}} = \frac{1}{A}\int_o^t \int_A (\rho u)_{\text{out}} dA dt. \qquad (9)$$

From an experimental point of view, the displaced mass is also a convenient quantity to measure. Numerical results of cumulative displaced mass shown in Fig. 5 for the three steam injection experiments (i.e., circles) indicate that displaced mass increases almost linearly with time, implying that steam displacement occurs at a constant mean speed. Steam breakthrough is seen to be characterized by a sharp change in the slope of a displacement curve. At times sufficiently later than the steam breakthrough, the slope of the displacement curve should asymptotically approach the injection mass flux since the system has acquired steady state. The slopes of the displacement curves shown in Fig. 5 before steam breakthrough range between 3.0 and 3.3 times larger than their respective injection mass fluxes, indicating the steam injection is a viable method of removing oil or contaminants from the subsurface.

Also plotted in Fig. 5 are the solid lines obtained from one-dimensional simulations in which the gravitational acceleration is set to zero and other conditions remain the same. Apparently, two-dimensional displacement can be well approximated by the one-dimensional behavior, regardless of severe steam override and natural convection present in some cases. This might provide a reason why most one-dimensional models give good predictions of the performance curves, even though steam override is a complex multidimensional phenomenon.

3.3 Superheated Steam Injection. Superheated steam injection is studied for a moderate superheat of 100°C. Figure 6 compares the displacement curves for the saturated (i.e., the baseline case) and superheated steam injection, respectively. Apparently, the superheat helps to displace more liquid out of the porous formation. This enhanced performance is, however, not through an increase in the front propagation velocity; in fact, the steam front velocity, which is approximately equal to the slope of the displacement curve, remains almost the same between the two cases after the initial transients, as shown in Fig. 6. Inspection of the predicted liquid saturation contours reveals that the increase in the displaced mass is due to the evaporation of residual water as stimulated by the superheated steam. Considering that the residual liquid can be removed only by evaporation, superheated steam injection should be quite effective in removing the trapped liquid phases in realistic reservoirs.

4 Conclusion

A fundamental problem of steam injection into a water-saturated and homogeneous reservoir has been studied. Important transport phenomena such as steam override, phase change heat transfer at the moving condensation and evaporation fronts, simultaneous flows of liquid and vapor, natural convection in pure fluid regions, and multidimensional effects were accounted for. The two-phase mixture model previously developed was utilized to facilitate solutions to complicated steam injection problems. A series of one and two-dimensional simulations were carried out to compare to available experimental data with favorable agreement. It was also found that the superheated steam can aid in mobilizing residual liquid thus achieving complete recovery.

Future research should be focused on the effects of heterogeneity on steam injection, three-dimensional modeling of steam injection, extensions to multiphase, multicomponent systems so as to study multicomponent mass transfer and hence the steam distillation mechanism, and ultimately field-scale modeling of steam injection into stochastically heterogeneous subsurface.

Acknowledgments

The second author acknowledges the support of this work through a Hong Kong Research Council grant (No. HKUST814/96E). This work would not have been possible without earlier efforts by Dr. C. Beckermann and Mr. C. Fan of the University of Iowa.

References

Baker, P. E., 1973, "Effect of Pressure and Rate on Steam Zone Development in Steamflooding," *SPEJ*, Vol. 13, pp. 274–284.

Basel, M. D., 1991, "Two-Dimensional Propagation of Steam Through Partially Saturated Porous Media," Ph.D. dissertation, University of California at Berkeley, Berkeley, CA.

Basel, M. D., and Udell, K. S., 1989, "Two-Dimensional Study of Steam Injection into Porous Media," *Multiphase Transport in Porous Media—1989*, ASME, Vol. 127, pp. 39–46.

Boberg, T. C., 1988, *Thermal Methods of Oil Recovery*, John Wiley & Sons Inc., NY.

Brouwers, H. J. H., 1996, "An Experimental Study of Constant-Pressure Steam Injection and Transient Condensing Flow in an Air-Saturated Porous Medium," ASME JOURNAL OF HEAT TRANSFER, Vol. 118, pp. 449–454.

Chung, M., and Catton, I., 1993, "Steam Injection into a Slow Water Flow Through Porous Media," ASME JOURNAL OF HEAT TRANSFER, Vol. 115, pp. 734–743.

Coats, K. H., 1976, "Simulation of Steamflooding With Distillation and Solution Gas," *SPEJ*, Vol. 16, pp. 235–247.

Coats, K. H., 1980, "In-Situ Combustion Model," *SPEJ*, Vol. 20, pp. 533–554.

Falta, R. W., 1990, "Multiphase Transport of Organic Chemical Contaminants in the Subsurface," Ph.D. thesis, University of California at Berkeley, Berkeley, CA.

Falta, R. W., Pruess, K., Javandel, I., and Witherspoon, P. A., 1992, "Numerical Modeling of Steam Injection for the Removal of Nonaqueous Phase Liquids from the Subsurface: 1. Numerical Formulation and 2. Code Validation and Application," *Water Resour. Res.*, Vol. 28, pp. 433–465.

Hanamura, K., and Kaviany, M., 1995, "Propagation of Condensation Front in Steam Injection into Dry Porous Media," *Int. J. Heat Mass Transfer*, Vol. 38, pp. 1377–1386.

Hunt, J. R., Sitar, N., and Udell, K. S., 1988, "Non-Aqueous Phase Liquid Transport and Cleanup," *Water Resour. Res.*, Vol. 24, pp. 1247–1269.

Sözen, M., and Vafai, K., 1990, "Analysis of the Non-Thermal Equilibrium Condensing Flow of a Gas Through a Packed Bed," *Int. J. Heat Mass Transfer*, Vol. 33, pp. 1247–1261.

Stewart, L. D., and Udell, K. S., 1988, "Mechanisms of Residual Oil Displacement by Steam Injection," *SPE Reservoir Engineering*, pp. 1233–1242.

Udell, K. S., 1985, "Heat Transfer in Porous Media Considering Phase Change and Capillary—Heat Pipe Effect," *Int. J. Heat Mass Transfer*, Vol. 28, pp. 485–495.

Udell, K. S., and Stewart, L. D., 1990, "Combined Steam Injection and Vacuum Extraction for Aquifer Cleanup," Subsurface Contamination by Immiscible Fluids, K. U. Weyer et al., eds., Balkema Publishers, Calgary, Alberta, Canada.

Vafai, K., and Sözen, M., 1990, "Analysis of Energy and Momentum Transport for a Flow of a Gas Through a Porous Bed," ASME JOURNAL OF HEAT TRANSFER, Vol. 112, pp. 690–699.

Wang, C. Y., 1997, "A Fixed-Grid Numerical Algorithm for Two-Phase Flow and Heat Transfer in Porous Media," *Numerical Heat Transfer*, Vol. B31, pp. 85–105.

Wang, C. Y., and Beckermann, C., 1993, "A Two-Phase Mixture Model of Liquid-Gas Flow and Heat Transfer in Capillary Porous Media," *Int. J. Heat Mass Transfer*, Vol. 36, pp. 2747–2769.

Yuan, Z. G., and Udell, K. S., 1993, "Steam Distillation of a Single Component Hydrocarbon Liquid in Porous Media," *Int. J. Heat Mass Transfer*, Vol. 36, pp. 887–897.

Heat Transfer Enhancement in the Entrance Zone of a Vertical Channel

D. A. Roberts[1] and J. M. Floryan[2]

Introduction

Passive enhancements to heating or cooling effectiveness for heat transfer problems are generally those which involve subtle modifications to boundary geometry. Because such enhancements involve no additional apparatus or power input, they are desirable both in terms of cost effectiveness and simplicity. The present study investigates one such enhancement: the convective cooling of closely spaced, vertical, isothermal surfaces which may be of use in the cooling of assemblies of electronic circuit boards.

In a previous study of developing flow between isothermal vertical plates by Naylor et al. (1991), it was discovered that a separation bubble formed on the wall near the sharp-edged inlet corner. The separation bubble, as well as its effects on local Nusselt number, were found to become more pronounced at higher Grashof numbers. In the present study the previous work was extended such that the inlet corners were rounded slightly in order to inhibit separation and to explore the resulting improvements in both local and global cooling effectiveness.

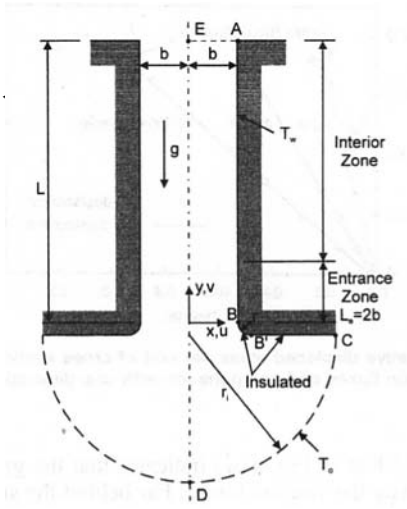

Fig. 1 Model geometry

Problem Formulation

Figure 1 shows the geometry of the flow system. Fluid flows by natural convection between two isothermal walls of length L and spacing $2b$, having constant temperature T_w. The channel inlet corners are rounded to a corner radius r_c and are insulated; the bottom walls of the channel are also insulated. An entrance zone is defined as the first $2b$ of the channel inlet. Below the channel, at a sufficient distance r_i from the inlet, the fluid is at ambient temperature T_o and its motion toward the channel inlet is described by the Jeffrey-Hamel solution. At the channel exit the flow is considered to be fully developed.

The Boussinesq model is adopted for fluid properties. The following dimensionless variables are used: $U = u/U_{\text{ref}}$, $V = v/U_{\text{ref}}$, $X = x/b$, $Y = y/b$, $r^* = r/b$, $r_c^* = r_c/b$, $\theta = (T - T_o)/(T_w - T_o)$, $P = pb/\mu U_{\text{ref}}$, where $U_{\text{ref}} = \alpha\,\text{Pr}\,(\text{Gr})^{1/2}/b$ and $\text{Gr} = g\beta(T_w - T_o)b^3/\nu^2$. Here, (u, v) denote the velocity components in the (x, y) directions; p stands for pressure; g represents the gravitational acceleration vector; μ denotes the dynamic viscosity; ν stands for the kinematic viscosity; β denotes the volumetric expansion coefficient; $\text{Pr} = \nu/\alpha$ is the Prandtl number; α represents the thermal diffusivity, and Gr stands for the Grashof number. Boundary conditions and the method of solution are similar to those described by Naylor et al. (1991). In all cases reported, Prandtl number Pr = 0.7, a channel aspect ratio of $L/b = 24$ and inlet domain radius of $r_i^* = 5$ were used.

Local (Nu_l) and mean (Nu_m) Nusselt numbers are defined by the relations given below. In addition, entrance (Nu_{ent}) and interior (Nu_{int}) zone (see Fig. 1) Nusselt numbers are introduced in order to assess differences in local cooling effectiveness.

$$\text{Nu}_l = \frac{h_l b}{k} = \left.\frac{\partial\theta}{\partial X}\right|_{X=1}, \quad \text{Nu}_m = \frac{h_m b}{k} = \frac{b}{L}\int_0^{L/b}\left.\frac{\partial\theta}{\partial X}\right|_{X=1} dY$$

$$\text{Nu}_{\text{ent}} = \frac{h_{\text{ent}} b}{k} = \frac{1}{2}\int_0^2 \left.\frac{\partial\theta}{\partial X}\right|_{X=1} dY,$$

$$\text{Nu}_{\text{int}} = \frac{h_{\text{int}} b}{k} = \frac{1}{L/b - 2}\int_2^{L/b}\left.\frac{\partial\theta}{\partial X}\right|_{X=1} dY.$$

[1] Department of Mechanical and Materials Engineering, The University of Western Ontario, London, Ontario, N6A 5B9, Canada.

[2] Professor, Department of Mechanical and Materials Engineering, The University of Western Ontario, London, Ontario, N6A 5B9, Canada; e-mail: MFloryan@eng-ntadmin.engga.u

Contributed by the Heat Transfer Division of THE AMERICAN SOCIETY OF MECHANICAL ENGINEERS. Manuscript received by the Heat Transfer Division January 9, 1997; revision received August 29, 1997; Keyword: Heat Transfer. Associate Technical Editor: P. G. Simpkins.

Brouwers, H. J. H., 1996, "An Experimental Study of Constant-Pressure Steam Injection and Transient Condensing Flow in an Air-Saturated Porous Medium," ASME JOURNAL OF HEAT TRANSFER, Vol. 118, pp. 449–454.

Chung, M., and Catton, I., 1993, "Steam Injection into a Slow Water Flow Through Porous Media," ASME JOURNAL OF HEAT TRANSFER, Vol. 115, pp. 734–743.

Coats, K. H., 1976, "Simulation of Steamflooding With Distillation and Solution Gas," *SPEJ*, Vol. 16, pp. 235–247.

Coats, K. H., 1980, "In-Situ Combustion Model," *SPEJ*, Vol. 20, pp. 533–554.

Falta, R. W., 1990, "Multiphase Transport of Organic Chemical Contaminants in the Subsurface," Ph.D. thesis, University of California at Berkeley, Berkeley, CA.

Falta, R. W., Pruess, K., Javandel, I., and Witherspoon, P. A., 1992, "Numerical Modeling of Steam Injection for the Removal of Nonaqueous Phase Liquids from the Subsurface: 1. Numerical Formulation and 2. Code Validation and Application," *Water Resour. Res.*, Vol. 28, pp. 433–465.

Hanamura, K., and Kaviany, M., 1995, "Propagation of Condensation Front in Steam Injection into Dry Porous Media," *Int. J. Heat Mass Transfer*, Vol. 38, pp. 1377–1386.

Hunt, J. R., Sitar, N., and Udell, K. S., 1988, "Non-Aqueous Phase Liquid Transport and Cleanup," *Water Resour. Res.*, Vol. 24, pp. 1247–1269.

Sözen, M., and Vafai, K., 1990, "Analysis of the Non-Thermal Equilibrium Condensing Flow of a Gas Through a Packed Bed," *Int. J. Heat Mass Transfer*, Vol. 33, pp. 1247–1261.

Stewart, L. D., and Udell, K. S., 1988, "Mechanisms of Residual Oil Displacement by Steam Injection," *SPE Reservoir Engineering*, pp. 1233–1242.

Udell, K. S., 1985, "Heat Transfer in Porous Media Considering Phase Change and Capillary—Heat Pipe Effect," *Int. J. Heat Mass Transfer*, Vol. 28, pp. 485–495.

Udell, K. S., and Stewart, L. D., 1990, "Combined Steam Injection and Vacuum Extraction for Aquifer Cleanup," Subsurface Contamination by Immiscible Fluids, K. U. Weyer et al., eds., Balkema Publishers, Calgary, Alberta, Canada.

Vafai, K., and Sözen, M., 1990, "Analysis of Energy and Momentum Transport for a Flow of a Gas Through a Porous Bed," ASME JOURNAL OF HEAT TRANSFER, Vol. 112, pp. 690–699.

Wang, C. Y., 1997, "A Fixed-Grid Numerical Algorithm for Two-Phase Flow and Heat Transfer in Porous Media," *Numerical Heat Transfer*, Vol. B31, pp. 85–105.

Wang, C. Y., and Beckermann, C., 1993, "A Two-Phase Mixture Model of Liquid-Gas Flow and Heat Transfer in Capillary Porous Media," *Int. J. Heat Mass Transfer*, Vol. 36, pp. 2747–2769.

Yuan, Z. G., and Udell, K. S., 1993, "Steam Distillation of a Single Component Hydrocarbon Liquid in Porous Media," *Int. J. Heat Mass Transfer*, Vol. 36, pp. 887–897.

Heat Transfer Enhancement in the Entrance Zone of a Vertical Channel

D. A. Roberts[1] and J. M. Floryan[2]

Introduction

Passive enhancements to heating or cooling effectiveness for heat transfer problems are generally those which involve subtle modifications to boundary geometry. Because such enhancements involve no additional apparatus or power input, they are desirable both in terms of cost effectiveness and simplicity. The present study investigates one such enhancement: the convective cooling of closely spaced, vertical, isothermal surfaces which may be of use in the cooling of assemblies of electronic circuit boards.

In a previous study of developing flow between isothermal vertical plates by Naylor et al. (1991), it was discovered that a separation bubble formed on the wall near the sharp-edged inlet corner. The separation bubble, as well as its effects on local Nusselt number, were found to become more pronounced at higher Grashof numbers. In the present study the previous work was extended such that the inlet corners were rounded slightly in order to inhibit separation and to explore the resulting improvements in both local and global cooling effectiveness.

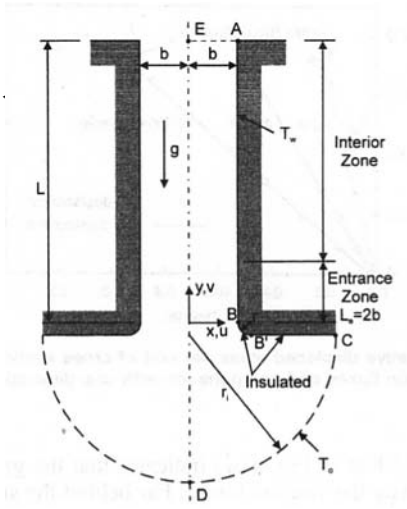

Fig. 1 Model geometry

Problem Formulation

Figure 1 shows the geometry of the flow system. Fluid flows by natural convection between two isothermal walls of length L and spacing $2b$, having constant temperature T_w. The channel inlet corners are rounded to a corner radius r_c and are insulated; the bottom walls of the channel are also insulated. An entrance zone is defined as the first $2b$ of the channel inlet. Below the channel, at a sufficient distance r_i from the inlet, the fluid is at ambient temperature T_o and its motion toward the channel inlet is described by the Jeffrey-Hamel solution. At the channel exit the flow is considered to be fully developed.

The Boussinesq model is adopted for fluid properties. The following dimensionless variables are used: $U = u/U_{\text{ref}}$, $V = v/U_{\text{ref}}$, $X = x/b$, $Y = y/b$, $r^* = r/b$, $r_c^* = r_c/b$, $\theta = (T - T_o)/(T_w - T_o)$, $P = pb/\mu U_{\text{ref}}$, where $U_{\text{ref}} = \alpha\,\text{Pr}\,(\text{Gr})^{1/2}/b$ and $\text{Gr} = g\beta(T_w - T_o)b^3/\nu^2$. Here, (u, v) denote the velocity components in the (x, y) directions; p stands for pressure; g represents the gravitational acceleration vector; μ denotes the dynamic viscosity; ν stands for the kinematic viscosity; β denotes the volumetric expansion coefficient; $\text{Pr} = \nu/\alpha$ is the Prandtl number; α represents the thermal diffusivity, and Gr stands for the Grashof number. Boundary conditions and the method of solution are similar to those described by Naylor et al. (1991). In all cases reported, Prandtl number Pr = 0.7, a channel aspect ratio of $L/b = 24$ and inlet domain radius of $r_i^* = 5$ were used.

Local (Nu_l) and mean (Nu_m) Nusselt numbers are defined by the relations given below. In addition, entrance (Nu_{ent}) and interior (Nu_{int}) zone (see Fig. 1) Nusselt numbers are introduced in order to assess differences in local cooling effectiveness.

$$\text{Nu}_l = \frac{h_l b}{k} = \left.\frac{\partial\theta}{\partial X}\right|_{X=1}, \quad \text{Nu}_m = \frac{h_m b}{k} = \frac{b}{L}\int_0^{L/b}\left.\frac{\partial\theta}{\partial X}\right|_{X=1} dY$$

$$\text{Nu}_{\text{ent}} = \frac{h_{\text{ent}} b}{k} = \frac{1}{2}\int_0^2 \left.\frac{\partial\theta}{\partial X}\right|_{X=1} dY,$$

$$\text{Nu}_{\text{int}} = \frac{h_{\text{int}} b}{k} = \frac{1}{L/b - 2}\int_2^{L/b}\left.\frac{\partial\theta}{\partial X}\right|_{X=1} dY.$$

[1] Department of Mechanical and Materials Engineering, The University of Western Ontario, London, Ontario, N6A 5B9, Canada.

[2] Professor, Department of Mechanical and Materials Engineering, The University of Western Ontario, London, Ontario, N6A 5B9, Canada; e-mail: MFloryan@eng-ntadmin.engga.u

Contributed by the Heat Transfer Division of THE AMERICAN SOCIETY OF MECHANICAL ENGINEERS. Manuscript received by the Heat Transfer Division January 9, 1997; revision received August 29, 1997; Keyword: Heat Transfer. Associate Technical Editor: P. G. Simpkins.

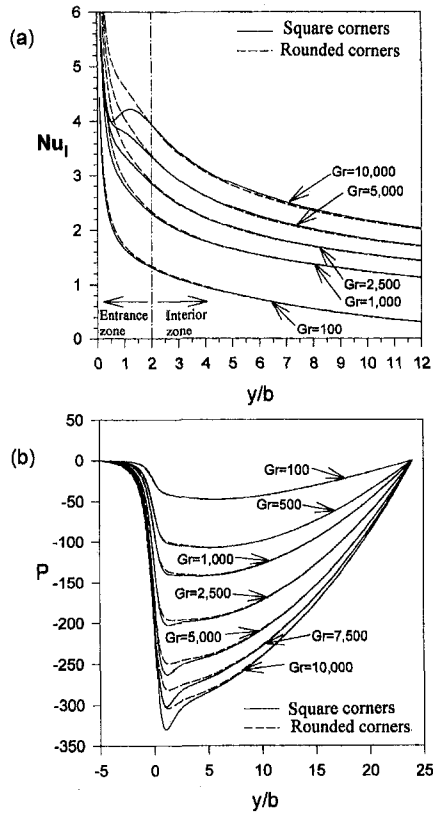

Fig. 2 Local (*a*) Nusselt number and (*b*) centerline pressure distributions along channel length for square and rounded corners for various values of Grashof number

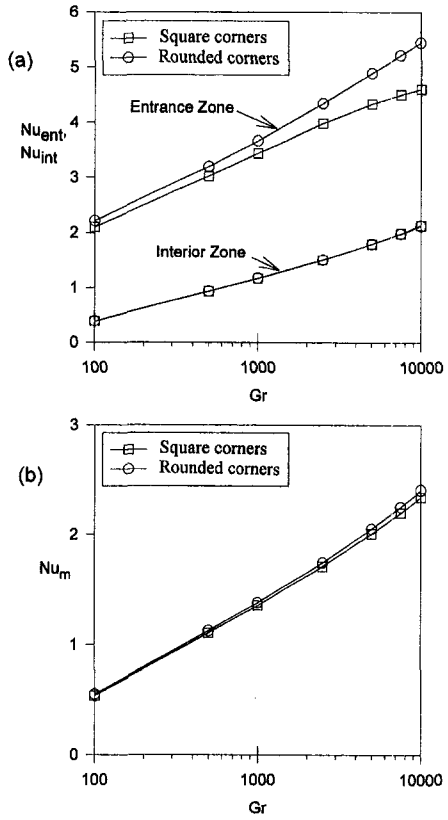

Fig. 3 Variations of the average Nusselt number as a function of Grashof number for channels with square and rounded corners: (*a*) entrance zone and interior zone Nusselt numbers and (*b*) mean Nusselt numbers

In the above expressions, k is the thermal conductivity, and h_l, h_m, h_{ent}, and h_{int} refer to the local, mean, entrance zone, and interior zone heat transfer coefficients, respectively.

Results and Discussion

By rounding the inlet corners to one-tenth the channel half-width, inlet separation is eliminated for all Grashof numbers examined. Figure 2(a) shows distribution of the local Nusselt number for channels with both square and rounded corners at various Grashof numbers. A decrease in the local Nusselt number can be seen in the entrance zone of a channel with square corners. This decrease is due to the appearance of a separation bubble. When the inlet corners are rounded, no such decrease of the local Nusselt number occurs. Figure 2(b) displays distribution of the centreline pressure. A localized decrease of the pressure can be seen just inside the channel entrance for square corners at higher Grashof numbers. This pressure decrease is another manifestation of the presence of a separation bubble which acts locally as a contraction in the flow.

Figure 3(a) shows that while the interior zone Nusselt numbers are similar for both square and round corners over all Grashof numbers, the entrance zone Nusselt numbers differ. As the Grashof number increases, the improvement in the entrance zone heat transfer becomes more pronounced. At the largest Grashof number, Gr = 10^4, the entrance zone Nusselt number increases by 18.4 percent while the interior zone Nusselt number increase by only 0.3 percent. Figure 3(b) shows a slight improvement in the overall cooling; at Gr = 10^4 the increase in overall Nusselt number is approximately 2.7 percent.

The rounded corners increase the effective length of the channel and thus induce a "chimney effect" (Haaland and Sparrow, 1983). Various tests showed that, because of a very small increase of the effective channel length, this effect is negligible. The gain in heat transfer occurs solely because of the elimination of flow separation in the entrance zone.

Although the addition of rounded inlet corners to the channel yields only a slight increase in the overall heat transfer, a significant enhancement of heat transfer occurs in the entrance zone. Such a simple, low cost enhancement to cooling is of particular interest to electronic applications in the prevention of localized "hot spots" in the entrance zone resulting from flow separation, and should be considered by the designer.

Acknowledgments

This work was supported by the Natural Sciences and Engineering Research Council of Canada.

References

Haaland, S. E., and Sparrow, E. M., 1983, "Solutions for the Channel Plume and the Parallel-Walled Chimney," *Numerical Heat Transfer,* Vol. 6, pp. 155–172.

Naylor, D., Floryan, J. M., and Tarasuk, J. D., 1991, "A Numerical Study of Developing Free Convection Between Isothermal Vertical Plates," ASME JOURNAL OF HEAT TRANSFER, Vol. 113, pp. 620–626.

Journal of Heat Transfer

Discussion

Elastoplastic Contact Conductance Model for Isotropic Conforming Rough Surfaces and Comparison With Experiments[1]

A Further Discussion by C. V. Madhusudana[2] and Y. Z. Li[2]. We have read carefully the response made by the authors to our discussion and note that several points still need satisfactory clarification.

1 Ratio of Elastoplastic to Plastic Contact Areas in a Single Contact Spot

For a single contact spot, ϵ_c^* is a function of the load and, since f_{ep} is a function of ϵ_c^* only, it follows that the ratio A_{ep}/A_p, the ratio of elastoplastic to plastic contact areas, must be a function of the load. It is only for the contact between rough surfaces that the authors' argument, that this ratio is independent of load, sounds plausible. The confusion has arisen, perhaps, because the authors have made no attempt to distinguish between the ϵ_c^* as defined by Eq. (26) for rough surfaces and the ϵ_c^* as defined by Eqs. (2) and (3) for a single contact spot.

2 The Mean Contact Size

In Eq. (24), the authors used the elastic hardness derived by Mikic (1974) for conforming rough surfaces. This then leads to Eq. (25) which indicates that the mean contact size a is a function of the radius of curvature β and the mean slope m, and is independent of the load. Equation (36), which is identical to Eq. (26), was then derived from Eq. (25).

In the iterative procedure to determine P/H_{ep}, Eqs. (31) to (37), two mean contact spot sizes were used: one in Eq. (33), which says that the contact radius is a function of the mean separation λ and is, therefore, a function of load (see Eq. (34)), and the other in Eq. (36), which assumes that the contact radius is independent of load. Which one of these is true?

3 A Typographic Error?

There seems to be an error in the very first sentence of the response. It implies $\beta = 1/(2\beta)$, which is absurd. Note that β has dimensions of length.

Reference

Mikic, B. B., 1974, "Thermal Contact Conductance: Theoretical Considerations," *Int. J. Heat Mass Transfer*, Vol. 17, pp. 205–214.

[1] By M. R. Sridhar and M. M. Yovanovich, published in the ASME JOURNAL OF HEAT TRANSFER, Vol. 119, No. 1, pp. 3–9; discussion and author's response published in the ASME JOURNAL OF HEAT TRANSFER, Vol. 119, No. 2, pp. 392–393.

[2] School of Mechanical and Manufacturing Engineering, The University of New South Wales, Sydney 2052, Australia. E-mail: c.madhusudana@unsw.edu.au

